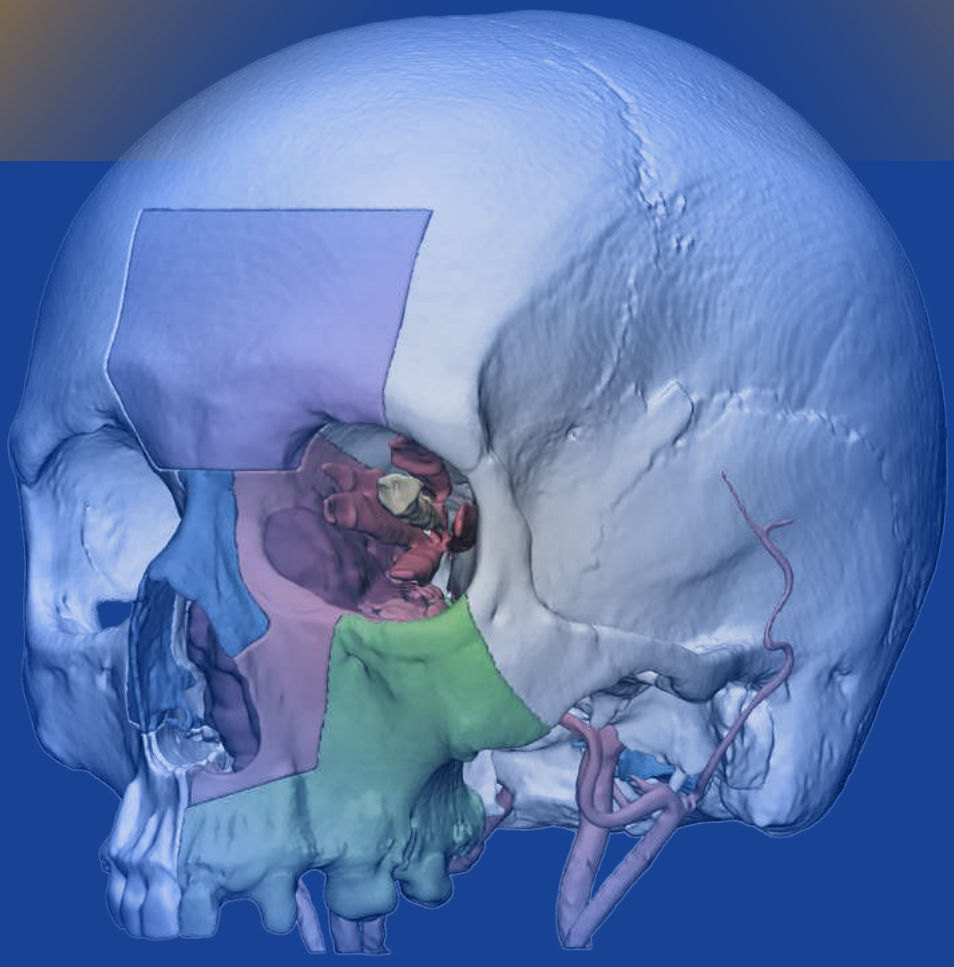
Alessandro Tel · Massimo Robiony
Editors

Atlas of Virtual Surgical Planning and 3D Printing for Cranio-Maxillo-Facial Surgery



Springer

Atlas of Virtual Surgical Planning and 3D Printing for Cranio-Maxillo-Facial Surgery

Alessandro Tel • Massimo Robiony
Editors

Atlas of Virtual Surgical Planning and 3D Printing for Cranio-Maxillo-Facial Surgery

Springer

Editors
Alessandro Tel
Lead Specialist for VSP and 3DP,
Maxillofacial Surgery Clinic,
Head & Neck and Neuroscience Department
Academic Hospital of Udine
Udine, Italy

Massimo Robiony
Chief of Maxillofacial Surgery Clinic
Director of the Postgraduate School
in Maxillofacial Surgery
Chief of Head & Neck and Neuroscience
Department
Academic Hospital - University of Udine
Udine, Italy

ISBN 978-3-031-94494-9 ISBN 978-3-031-94495-6 (eBook)
https://doi.org/10.1007/978-3-031-94495-6

© The Editor(s) (if applicable) and The Author(s), under exclusive license to Springer Nature Switzerland AG 2025

This work is subject to copyright. All rights are solely and exclusively licensed by the Publisher, whether the whole or part of the material is concerned, specifically the rights of translation, reprinting, reuse of illustrations, recitation, broadcasting, reproduction on microfilms or in any other physical way, and transmission or information storage and retrieval, electronic adaptation, computer software, or by similar or dissimilar methodology now known or hereafter developed.
The use of general descriptive names, registered names, trademarks, service marks, etc. in this publication does not imply, even in the absence of a specific statement, that such names are exempt from the relevant protective laws and regulations and therefore free for general use.
The publisher, the authors and the editors are safe to assume that the advice and information in this book are believed to be true and accurate at the date of publication. Neither the publisher nor the authors or the editors give a warranty, expressed or implied, with respect to the material contained herein or for any errors or omissions that may have been made. The publisher remains neutral with regard to jurisdictional claims in published maps and institutional affiliations.

This Springer imprint is published by the registered company Springer Nature Switzerland AG
The registered company address is: Gewerbestrasse 11, 6330 Cham, Switzerland

If disposing of this product, please recycle the paper.

Preface

This Atlas represents the evolution of a scientific and systemic thought, rooted in a profound reflection on the need for a new "humanization" of medicine that strongly considers technological innovation and progress at the same time not forgetting the responsibility of clinicians' role. The advent of technology and the introduction of artificial intelligence opened new scenarios regarding the care of the patient. It becomes essential to be engaged in a deep consideration of the ethical value of technology that enhances the human dimension of health professionals. Concretely, this means applying all the opportunities offered by technological innovation, including artificial intelligence, to good clinical practices while respecting Ethics and Morality. For this reason, the paradigm shift must allow technology and the humanization of care to pass through an emotional, relational, and practical educational path to meet population health needs, which today must consequently include innovation and technology, defining what we in Udine have named Techno-Humanization.

Each topic of this book is the result of a human relationship among colleagues worldwide who share a common passion: medicine as a Science that renews and enriches, and the human being as a Priority. Together, we have collaborated by highlighting in each chapter the innovative work in the field, expressing the best doctor-patient relationship, extraordinarily supported by virtual reality, which in the last decade has become an essential tool for providing the best care to our patients in the head and neck district. All this is an expression of the rapid progress of Medicine and Surgery, which recognizes its foundations in education, research, innovation, and the conscious use of technologies, and must inevitably consider the Humanization of Care a founding principle.

Humanizing Care, in the modern sense, also means putting technology at the service of the person. This Atlas clearly shows that attention to detail and meticulous description of the design phases are developed with the ultimate goal of spreading knowledge so that anyone who wishes can replicate the Real and Virtual care experiences for their patients. Dr. Alessandro Tel, the creator of this extraordinary project, a profound connoisseur and user of virtual planning software and 3D printing, along with the other Authors, guides the reader in a didactic presentation that makes the text a true guide to the most modern and sophisticated techniques of Virtual Planning and Surgery.

The growing role of new technologies in healthcare and their use cannot be separated from human intelligence, which will see in this volume the highest expression of surgical virtuosity expressed by the human hand. In the health chain, which must ensure the comprehensive care of the patient, it is now essential to train and benefit from multiple professional figures, beyond doctors and nurses, for true teamwork: IT specialists, robotics experts, AI, Virtual Reality, Augmented Reality, immersive navigation, intraoperative navigation, (data analysis experts, health statisticians, quality control experts, management engineers, clinical engineers, physicists, sociologists, psychologists, biotechnologists, legal experts, project managers), in order to develop aspects of 5P medicine (Personalized, Predictive, Preventive, Participatory, Populational) related to technology, such as Personalized and Precision Surgery.

The new healthcare professional must have the ability to use technologies creatively, not only to improve therapeutic and organizational effectiveness but also to increase the time available for patient relationships, facilitating communication and interactions. Technologies such

as virtual surgical planning support verbal descriptions with realistic images, enhancing patient understanding and making consent truly informed. This approach transforms the traditional parental doctor-to-patient model with a purely informative one, creating a more participatory and aware relationship with our patients.

Therefore, building a defined vision of techno-humanization means allowing health professionals to facilitate the integration of skills, generating interconnections between different disciplines that aspire to create a new model of prevention, diagnosis, and care.



Udine, Italy

Alessandro Tel
Massimo Robiony

Contents

Technological Updates in Cranio-Maxillo-Facial Surgery

Software Used for Virtual Surgical Planning 3
Lorenzo Arboit and Alessandro Tel

Dedicated Acquisition Protocols in Radiology for Virtual Surgical Planning and 3D Printing 27
Arnau Valls-Esteve, Núria Adell-Gómez, Josep Munuera, Daniele Bagatto, and Alessandro Tel

Overview of 3D Printing Technologies 51
Erik Kornfellner and Francesco Moscato

Virtual Surgical Planning and 3D Printing at the Point-of-Care Lab for Cranio-Maxillo-Facial Surgery 59
Shadi Daoud, Amjad Shhadeh, Idan Redenski, Adeeb Zoabi, and Samer Srouji

Regulation Perspectives for Point-of-Care Lab in Cranio-Maxillo-Facial Surgery . . . 71
María Gloria Álvarez Caballero

Personalized Implant Design in Cranio-Maxillo-Facial Surgery 83
Maarten Zandbergen

Augmented Reality in Cranio-Maxillo-Facial Surgery 95
Thomas J. J. Maal, Jene M. Meulstee, Dylan Duits, and Ruud Schreurs

Artificial Intelligence in Cranio-Maxillo-Facial Surgery 107
Stefanie van den Bosch, Niels van Nistelrooij, Michel Beyer, Wesley Do, Stefaan Bergé, and Shankeeth Vinayahalingam

Atlas of Procedures in Oro-Cranio-Maxillo-Facial Surgery

Applications of VSP for Customized Subperiosteal Implants for the Rehabilitation of the Atrophic Jaws 123
Luigi Angelo Vaira and Giacomo De Riu

Principles of Cranial Reconstruction 135
Alessandro Tel, Francesco Tuniz, and Massimo Robiony

Personalized Cranial Implants: Pioneering Techniques with Additive Manufacturing 161
Neha Sharma, Jokin Zubizarreta Oteiza, Daniel Seiler, and Florian M. Thieringer

Virtual Planning in Frontal Sinus and Anterior Skullbase 171
Alessandro Tel, Fabio Costa, Marc Generowitz, Robert Pellecchia, and Massimo Robiony

Virtual Surgical Planning in Craniofacial Surgery 191
Federica Ruggiero, Alberto Bianchi, Emanuela Marcelli, Owase Jeelani, Mino Zucchelli, Laura Cercenelli, and Alessandro Borghi

Introduction to Virtual Planning in Orbital Region and Applications in Orbital Trauma 211
Alessandro Tel and Massimo Robiony

Virtual Surgical Planning in Orbital Oncology 239
Alessandro Tel and Massimo Robiony

Computer-Guided Orthognathic Surgery: State of the Art and Innovation 263
Alessandro Tel, Tong Xi, and Massimo Robiony

Applications of VSP in Orthognathic Surgery 291
Alessandro Tel and Massimo Robiony

Application of VSP in Temporomandibular Joint Surgery 323
Salvatore Sembronio, Luca Raccampo, Massimo Robiony, and Alessandro Tel

Virtual Planning and 3D Printing in Midfacial Trauma 363
Alessandro Tel and Massimo Robiony

Virtual Surgical Planning in Midfacial Oncology 385
Alessandro Tel and Massimo Robiony

Virtual Surgical Planning in Midfacial Reconstruction 415
Alessandro Tel, Matthias Ureel, Maarten De Jong, Renaat Coopman, and Massimo Robiony

Virtual Planning and 3D Printing in Mandibular Fractures 447
Alessandro Tel and Massimo Robiony

Virtual Surgical Planning in Mandibular Oncology 469
Alessandro Tel and Massimo Robiony

Virtual Surgical Planning in Mandibular Reconstruction 489
Alessandro Tel, Matthias Ureel, Renaat Coopman, and Massimo Robiony

Full-Face Cranio-maxillo-facial Surgery Procedures 521
Alessandro Tel, Federico Bolognesi, Federico Biglioli, Silvano Ferrari, and Massimo Robiony

Comprehensive Guide and Atlas to Virtual Surgical Planning in Face Transplantation 547
Alay R. Shah, Sachin R. Chinta, and Eduardo D. Rodriguez

Conclusive Remarks

Medical 3D Printing: A Fruitful and Impactful Field for Collaboration and Interdisciplinarity 561
Giovanni Biglino, Karen Eich Hammer, Carina Hopfner, Francesco Moscato, Marina Nagel, Gunpreet Coudert Oberoi, Arnau Valls-Esteve, and Alessandro Tel

Technological Updates in Cranio-Maxillo-Facial Surgery

Software Used for Virtual Surgical Planning

Lorenzo Arboit and Alessandro Tel

1 Introduction to Virtual Surgical Planning Software

1.1 Definition and Purpose of VSP Software

Virtual Surgical Planning (VSP) is a technique that utilizes computer-based systems to digitize clinical data for diagnosis, design of surgical procedures, treatment planning, and outcome prediction. The process begins with data acquisition, primarily obtained from radiological imaging. This data is then transformed into a three-dimensional (3D) model within a virtual environment, serving as the focal point for analysis. VSP's development was driven by advancements in Computer-Aided Design (CAD) and Computer-Aided Manufacturing (CAM), which originated in mechanical engineering but were later adapted for medical use. Today, VSP is widely employed in craniomaxillofacial (CMF), orthopedic, and reconstructive surgeries. It has been shown to enhance surgical precision, assist in outcome prediction, and improve patient communication, resulting in safer surgeries and better-informed patients.

VSP encompasses essential features such as 3D model visualization, manipulation tools, and simulation capabilities, all contributing to its widespread adoption [1]. Its flexibility allows it to assist surgeons at multiple stages and integrate seamlessly with surgical practices and other technologies like 3D printing, advanced manufacturing techniques, and surgical navigation systems. The success of VSP is evident across many surgical departments, facilitated by the automation of processes from imaging acquisition to 3D rendering. This advancement has gained approval from regulatory bodies, notably the Food and Drug Administration (FDA) in the United States and the European Medicines Agency (EMA) in Europe, following the Medical Device Regulation (MDR).

1.2 Historical Background

The introduction of computed tomography (CT) in the 1970s marked a revolutionary shift in medical imaging by providing detailed cross-sectional images of the human body. Building on this advancement, Vannier et al. [2] developed the first computed three-dimensional (3D) reconstructions from CT data, significantly enhancing diagnostic capabilities and surgical planning compared to conventional two-dimensional (2D) images.

These innovations were quickly leveraged to create physical 3D models using computer numerically controlled (CNC) milling machines programmed with reconstructed CT scan slices. However, reproducing complex geometries was challenging due to the low resolution along the z-axis in early CT scans. This limitation was overcome through advancements in both imaging and manufacturing technologies. The introduction of spiral CT improved image resolution, while the advent of rapid prototyping technologies—such as selective laser sintering (SLS), stereolithography (SLA), and 3D printing—enabled the production of models with intricate internal contours [3]. Unlike CNC milling, these additive manufacturing systems were more compatible with digital data and allowed for accurate replication of complex anatomical structures.

In the early 1990s, these technological advancements were introduced into surgical departments, providing enhanced anatomical references for complex structures [3]. Shortly thereafter, fully computer-based virtual surgical planning systems emerged, which could be directly translated into navigation systems for orthopedic surgery and

L. Arboit (✉)
University of Strasbourg, CNRS, INSERM, ICube, Strasbourg, France
e-mail: lorenzo.arboit@ext.ihu-strasbourg.eu

A. Tel
Lead Specialist for VSP and 3DP, Maxillofacial Surgery Clinic, Head & Neck and Neuroscience Department, Academic Hospital of Udine, Udine, Italy
e-mail: alessandro.tel@uniud.it

© The Author(s), under exclusive license to Springer Nature Switzerland AG 2025

A. Tel, M. Robiony (eds.), *Atlas of Virtual Surgical Planning and 3D Printing for Cranio-Maxillo-Facial Surgery*,
https://doi.org/10.1007/978-3-031-94495-6_1

traumatology [4]. This comprehensive integration significantly improved surgical precision and reduced errors. Companies like Medtronic and Brainlab began releasing commercial neurosurgical planning systems that combined preoperative imaging with intraoperative guidance, marking a significant milestone in neurosurgical practice.

The early 2000s witnessed another technological leap with the incorporation of virtual reality (VR) and augmented reality (AR) technologies into the applied research field. Additionally, the development of 3D surface and texture scanning complemented volumetric CT data by fully rendering soft tissues, allowing for better prediction of postoperative aesthetic outcomes. As these implementations underwent extensive research and in silico trials, the simulation capabilities of virtual surgical planning techniques became more standardized [5]. Tools for performing virtual surgeries with custom implant designs and improved integration with widely available platforms and data formats—most notably DICOM—became extensively used and tested across multiple surgical fields.

1.3 Evolution of VSP Software

The first generation of virtual surgical planning (VSP) software emerged to assist surgeons in designing patient-specific prosthetics, primarily in orthopedics. Due to the complexity of these systems and their interfaces—often adapted from general-purpose CAD software—they were typically operated by engineers or specialized personnel.

- *Advancements in the 1990s*
  In the mid-1990s, significant advancements in computational power and the introduction of 3D acceleration in consumer graphics processing units (GPUs) enabled more extensive implementations of VSP software. This period witnessed the emergence of specialized software companies in the medical and surgical fields:
  - Materialise: Founded in 1990 to provide 3D-printed parts, Materialise released Mimics in 1992. Mimics was a platform that converted medical images into 3D models, integrating seamlessly into the company's main services.
  - Brainlab: Established in 1989 as a surgical planning and navigation software company, Brainlab released its first product 3 years later. The company's software facilitated the integration of CT and MRI data into digital workflows.

Research-oriented departments rapidly adopted these technologies, exploring applications such as elastography, volumetric modeling algorithms, surgical and radiation treatment planning, and image-guided diagnostics [6].

- *Innovations in the Early 2000s*
  The early 2000s were marked by:
  - Research Advancements: Engineering departments implemented VSP solutions incorporating virtual reality (VR) and augmented reality (AR) for surgical training simulators and interactive planning optimization [7].
  - Industry Commitments: A focus on providing safe and standardized software led to significant milestones. Materialise achieved FDA 510(k) premarket clearance for the SimPlant System in 2004, making it the first software for preoperative simulation and evaluation of surgical treatment—specifically dental implant placement—to receive such approval.
  - The following decade saw many other VSP tools receive clearance, leading to increased adoption by surgeons, particularly in CMF and orthopedic reconstructive surgeries. Key technical features at this stage included:
    Quantitative Measurements: Highly accurate measurements validated by numerous reports.
    3D Object Manipulation: Ability to separate and manipulate 3D objects for virtual osteotomies. Six Degrees of Freedom Movement: Comprehensive movement control of bone elements.
- *Transition to Patient-Specific Modeling*
  Advancements in imaging technologies such as cone beam CT (CBCT), 3D laser scanners, and 3D optical systems allowed for detailed capture of soft tissue textures and colors [8]. VSP software integrated these multimodal data sources to:
  - Build Realistic Digital Models: Enhanced models that accurately represent patient anatomy.
  - Simulate Soft Tissue Deformation: Improved predictions of how soft tissues respond to bone movements and implant insertions.

This period marked a transition to patient-specific modeling, making high-fidelity models widely available. The expansion of 3D printing—both in-house and through external companies—confirmed VSP software as a crucial tool for designing surgical guides and custom implants, reducing the need for extensive engineering support due to built-in software features.

- *Technological Innovations in the Last Decade*
  Recent years have seen the following improvements:
  - Artificial Intelligence (AI) and Computer Vision: Development of AI models to automate segmentation

tasks and detect anomalies, facilitating the identification of pathological lesions [9].
- Refined Biomechanical Modeling: Utilization of finite element analysis (FEA) to create optimized simulations that incorporate geometric, anatomical, and tissue property data, along with surgical manipulations [1]. This advancement allows for better risk assessment of potential complications.
- Cloud Computing: Migration of software to cloud platforms has enabled surgeons to access planning tools without specialized equipment. This shift has also improved research collaboration through secure, multidisciplinary data sharing.

These features are now standard in VSP software packages. Modern VSP tools, however, greatly benefit, compared to previous solutions, from improved user interfaces (UIs) and user experience (UX). Many groups have contributed to the development of surgeon-friendly solutions, which has ensured the success of VSP platforms.

1.4 Importance of VSP in CMF Surgery

CMF surgery, alongside orthopedics, has significantly benefited from Virtual Surgical Planning (VSP), with its applications widely explored [10]. Before VSP's advent, cephalometry and two-dimensional imaging techniques—such as panoramic radiographs and cephalograms—were the preferred solutions, complemented by dental cast models mounted on adjustable articulators for predicting and planning occlusion. The introduction of reliable three-dimensional virtual reconstruction and VSP tools has been recognized for their superiority, establishing VSP as the new standard of care. This innovation has been effectively complemented by manufacturing advancements, evolving from additive manufacturing to 3D printing and now expanding into bioprinting [11, 12].

Several domains have confirmed VSP's superiority over traditional surgical methods, notably: (I) decreased risks and complications; (II) reduced reliance on surgeons' expertise, serving as a tool that accelerates the learning curve for trainees; (III) increased surgical precision, resulting in improved anatomical alignment and occlusal relationships; (IV) reduced intraoperative time by shifting decision-making to the preoperative phase; and (V) enhanced aesthetic and functional outcomes. The shift toward patient-centric care and personalized surgical methods has thus been successful in all these areas. Finally, (VI) the ability to involve patients in surgical planning through accessible 3D models, as opposed to complex 2D imaging, has improved patient satisfaction rates by enabling doctors to better manage expectations [11].

2 Key Components of VSP Software

2.1 Imaging Integration

Data acquisition is the critical first step in Virtual Surgical Planning (VSP). It requires careful standardization and optimization to minimize patient exposure to radiation while maintaining accuracy and precision. Various imaging techniques provide both 2D and 3D data, and their combination enables a clearer understanding of the relative position and orientation of the surgical site, including bone and soft tissue relationships.

- *CT/CBCT/MRI Scanning*
  - CT (Computed Tomography) and CBCT (Cone Beam Computed Tomography) are widely used in clinical imaging for VSP. They generate tomographic images that can be reconstructed into a 3D model from digital data. While both techniques expose patients to ionizing radiation, CBCT is favored for CMF applications because of its lower radiation levels and localized scanning, making it more suitable for focused areas like the jaw or sinuses. However, CBCT offers reduced precision compared to traditional CT, particularly in imaging soft tissues, as it primarily excels at capturing hard tissues like bones and teeth.
  - MRI (Magnetic Resonance Imaging), unlike CT and CBCT, does not use ionizing radiation and is preferable for visualizing soft tissues. MRI sequences such as T1, T2, and FLAIR offer varying levels of contrast depending on the tissues of interest. However, its sensitivity to patient motion, which can cause image blurring, limits its utility in some cases.
- *3D Scanning*
- 3D scanners capture the external surface anatomy with high accuracy, making them ideal for applications like facial reconstruction, orthognathic surgery, and prosthetic design. These devices are non-invasive, radiation-free, and capable of producing detailed models quickly, even in clinical settings. Various types of 3D scanning technologies are available:
  - Laser Scanning: Utilizes a laser beam to map surface contours with high precision.
  - Structured Light Scanning: Projects a grid or light pattern onto the surface, capturing deformations via cameras to create a 3D model. It is ideal for larger or less complex surfaces.
  - Photogrammetry: Uses multiple 2D images from different angles to create a 3D model. This is the simplest

and most cost-effective method, commonly used in CMF surgery. Standard photo angles include lateral profiles, 45-degree views, and frontal views, all taken with the patient in a natural head position.

2.2 Imaging Formats and Data Standards

- DICOM (Digital Imaging and Communication in Medicine) is the standard format for radiological imaging in VSP. It encodes not only the imaging data but also acquisition parameters and settings, ensuring compatibility across different VSP software.
- 3D Scanners typically store data in STL (Standard Tessellation Language) or OBJ (Object File) formats, which represent surface geometries either as polygonal meshes or point clouds. Some software uses proprietary formats, limiting compatibility with other platforms, which can be a drawback when integrating different systems [13].

2.3 3D Modeling and Visualization Tools

The 3D modeling process in VSP begins with the importation of 2D medical images, followed by anatomical segmentation using algorithms such as thresholding and region growing. Subsequently, surface and volume rendering techniques are applied to generate a 3D model. Various methods are then employed to create a mesh—a representation that accurately describes the surface topology of bones and soft tissues. A mesh is composed of (Fig. 1):

- Vertices: Points in 3D space that serve as the corners or intersections of the mesh
- Edges: Straight lines connecting two vertices
- Faces: Flat surfaces formed when multiple edges connect in a closed loop, typically triangular or quadrilateral in shape

Once the 3D model is fully rendered, advanced visualization tools allow clinicians and engineers to explore different organs and correlate them with the corresponding 2D images, regardless of the imaging modality used.

2.4 Image Import and Segmentation Tools

Medical images, commonly stored in the DICOM format, are imported into VSP software. The first critical step after importation is denoising the images to enhance quality, as noise—unwanted random variations in pixel intensity—can degrade image quality and adversely affect subsequent 3D reconstruction and planning.

- *Denoising Techniques* [14]:
  1. Local Filtering (Fig. 2):
     - Linear Filters: Mean filtering, Gaussian filtering, Wiener filtering.
     - Nonlinear Filters: Median filtering, adaptive median filtering, bilateral filtering.
  2. Non-local Means (NLM) Filtering (Fig. 3):
     - Considers the similarity between patches of pixels across the entire image, providing effective noise reduction while preserving details.
  3. Deep Learning-Based Filtering:
     - Utilizes neural networks trained to distinguish between noise and meaningful signal, offering superior performance in noise reduction and feature preservation.

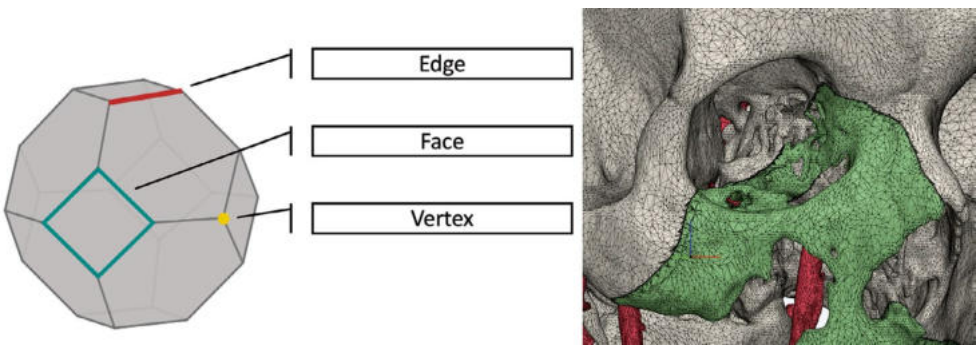


Fig. 1 Schematic representation of a 3D polyhedral model and of an anatomical STL file illustrating the fundamental components of a mesh structure. Right panel illustrates a complex maxillectomy mesh with the poly-wireframe displayed. Notably, curves need a substantial amount of triangulation to be defined

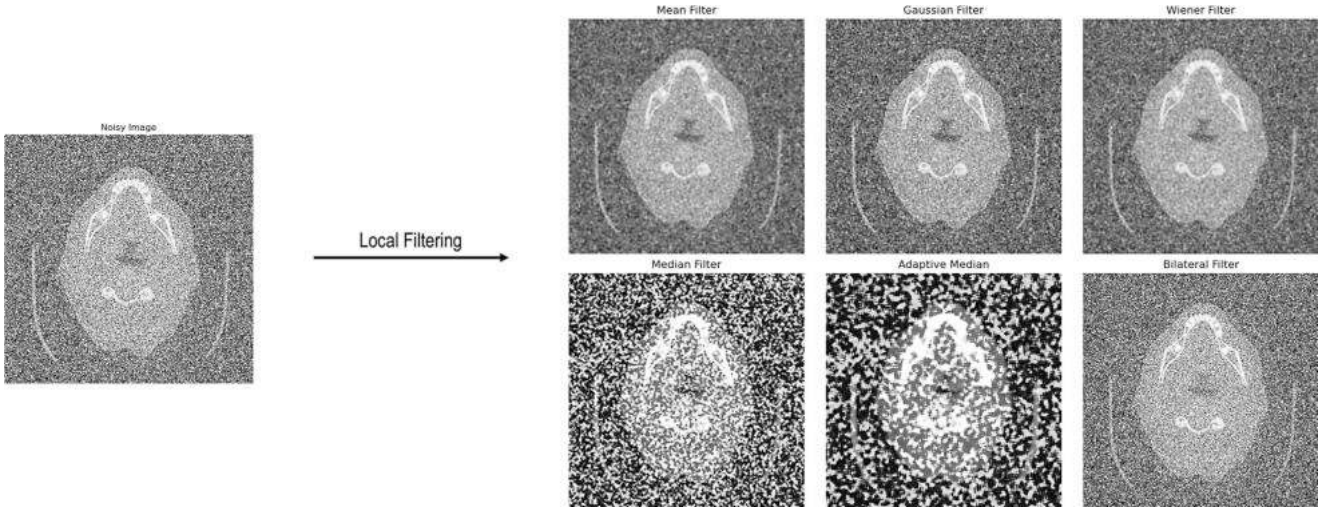


Fig. 2 Comparison of local filtering techniques applied to a noisy medical image (CT scan slice, on the left), including Mean, Gaussian, Wiener, Median, Adaptive Median, and Bilateral filters. Each method demonstrates varying noise reduction and detail preservation

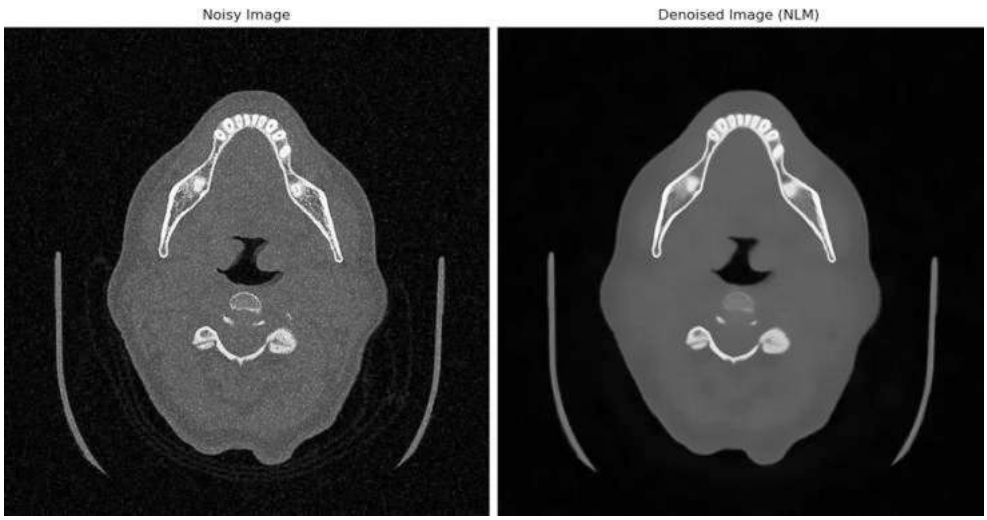


Fig. 3 Comparison of a noisy CT image (left) and its denoised counterpart using the Non-Local Means (NLM) algorithm (right), demonstrating significant noise reduction while preserving anatomical details

Non-local means filtering and deep learning-based denoising are increasingly popular due to their balance between noise reduction and preservation of anatomical details, particularly in high-resolution datasets used for complex procedures. After denoising, image enhancement techniques are applied to further improve the visibility and quality of anatomical structures.

While these are often automated, most software provides manual tools for fine-tuning. The main image enhancement techniques (Fig. 4) include [15]:

1. Contrast Enhancement:
   - Histogram Equalization: Adjusts the contrast by redistributing pixel intensity values.
   - Gamma Correction: Alters the luminance of the image to improve the visibility of specific structures.
2. Edge Enhancement:
   - Highlights critical anatomical boundaries to optimize accuracy in 3D reconstruction.
3. Intensity Windowing:
   - Adjusts the range of displayed intensity values to enhance specific features, commonly used to differentiate between bone and soft tissue.
4. Sharpening Filters:
   - High-Pass Filtering and Laplacian Sharpening: Enhance fine details and anatomical edges by increasing the contrast between neighboring pixels.

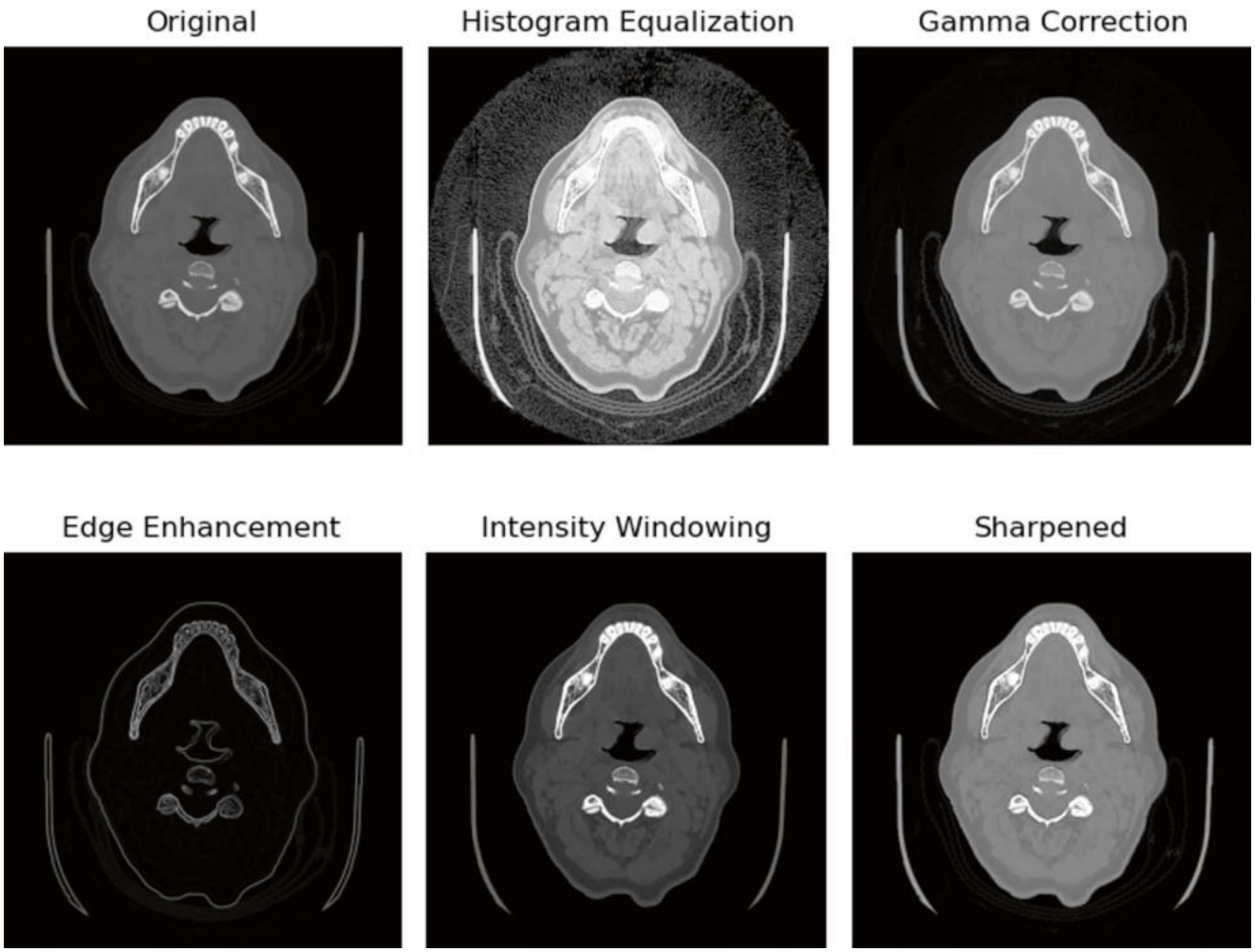


Fig. 4 Visualization of image enhancement techniques applied to a CT image, including Histogram Equalization, Gamma Correction, Edge Enhancement, Intensity Windowing, and Sharpening. Each method emphasizes specific features to improve contrast, detail visibility, or edge clarity compared to the original image

Following enhancement, image segmentation partitions the images into distinct regions with similar properties such as intensity, texture, or contrast. Precise segmentation is essential for accurate registration and anatomical labeling. Segmentation Methods [16, 17]:

1. Manual Segmentation:
   – Performed entirely by clinicians or engineers, providing high accuracy but is time-consuming.
2. Semi-automatic Segmentation:
   – Combines automated algorithms with manual input for initialization and correction, balancing efficiency and accuracy.
3. Automatic Segmentation:
   – Fully automated using algorithms, including deep learning methods that may be supervised (using annotated datasets), semi-supervised, or unsupervised [18].

Automatic segmentation is more effective for tissues with high contrast, such as bone and air-filled lungs. While it offers speed and efficiency, semi-automatic methods are often preferred clinically due to the need for expert oversight. Common segmentation algorithms (Fig. 5) are:

1. Thresholding:
   – Segments images based on intensity values, using thresholds derived from the image histogram. It does not consider spatial information, making it susceptible to noise.
2. Region Growing:
   – Expands regions by appending neighboring pixels that meet certain criteria, such as similar intensity. It utilizes spatial information but requires accurate denoising to function effectively.

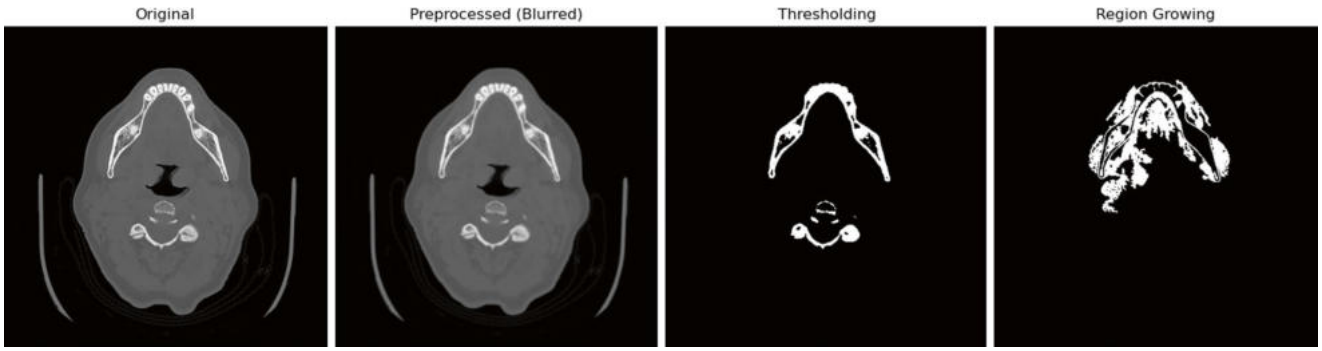


Fig. 5 Segmentation workflow applied to a CT image. The original image is preprocessed with blurring to reduce noise and smooth intensity variations, improving segmentation accuracy. Thresholding is used to separate regions based on intensity values, producing a binary mask. Region-growing segmentation groups connected pixels with similar intensities. Outputs highlight the distinct segmentation capabilities of each method

Combining thresholding with region-based methods enhances segmentation accuracy by leveraging both intensity and spatial information [17].

2.5 3D Model Generation and Mesh Optimization

From the denoised and segmented 2D images, a 3D model is constructed to enhance visualization of anatomical features and facilitate surgical planning. The transition to 3D visualization has significantly improved diagnostic accuracy and procedural planning. Many algorithms have been developed to extract a 3D representation from 2D imaging, and many of these are now incorporated in modern VSP software [19]. Volumetric rendering techniques are essential for visualizing the entire volume of medical imaging data without explicitly converting it into surface representations or polygonal meshes. Direct volume rendering (DVR) is a key method employed for this purpose. DVR allows for the direct visualization of volumetric data by mapping data values to optical properties like color and opacity, providing detailed views of internal structures. Techniques such as ray casting, which projects rays through the data volume to accumulate color and opacity values, are frequently utilized in VSP software.

While DVR is excellent for visualization, it falls short when manipulation of the 3D model is required—such as editing, measurement, or exporting to computer-aided design (CAD) applications—because it does not produce a surface or mesh representation that these applications can process. To address this limitation, algorithms like the Marching Cubes algorithm are employed to extract a polygonal mesh of an isosurface from the volumetric data. An isosurface represents a surface within the volume where the data value equals a constant (e.g., a specific tissue density threshold). The Marching Cubes algorithm examines the values at the corners of each voxel—the three-dimensional equivalents of pixels—and generates triangles to define the surface of the isosurface. This process efficiently produces a mesh suitable for real-time interaction, which is crucial in VSP applications (Fig. 6).

Once the 3D surface is generated, smoothing techniques are applied to reduce artifacts and enhance anatomical realism [20]. Laplacian smoothing is a commonly used method that adjusts the position of each vertex based on the average position of its neighboring vertices, effectively reducing noise and irregularities in the mesh (Fig. 7).

Other frequently applied smoothing techniques include recursive Gaussian smoothing, Taubin smoothing, and bilateral smoothing. Each method treats the mesh differently, and many software programs offer user-selectable options to choose the most appropriate technique for preserving small features and boundaries (Fig. 8). Smoothing is often essential when preparing models for 3D printing or simulation, where surface imperfections could adversely affect outcomes.

Following smoothing, mesh optimization techniques are employed to simplify the 3D-generated mesh, a critical step that enhances computational efficiency and allows for faster real-time interaction without compromising essential anatomical details. Decimation, or mesh simplification, reduces the number of polygons in a mesh using techniques such as edge collapse, where edges between neighboring vertices are collapsed, and methods based on quadric error metrics, which aim to preserve the overall anatomical structure and sharp edges while reducing complexity [21].

In contrast, when greater detail preservation is required—for instance, in areas like blood vessels or complex articular surfaces—the opposite process of decimation, known as subdivision, is applied. Subdivision enhances detail by subdi-

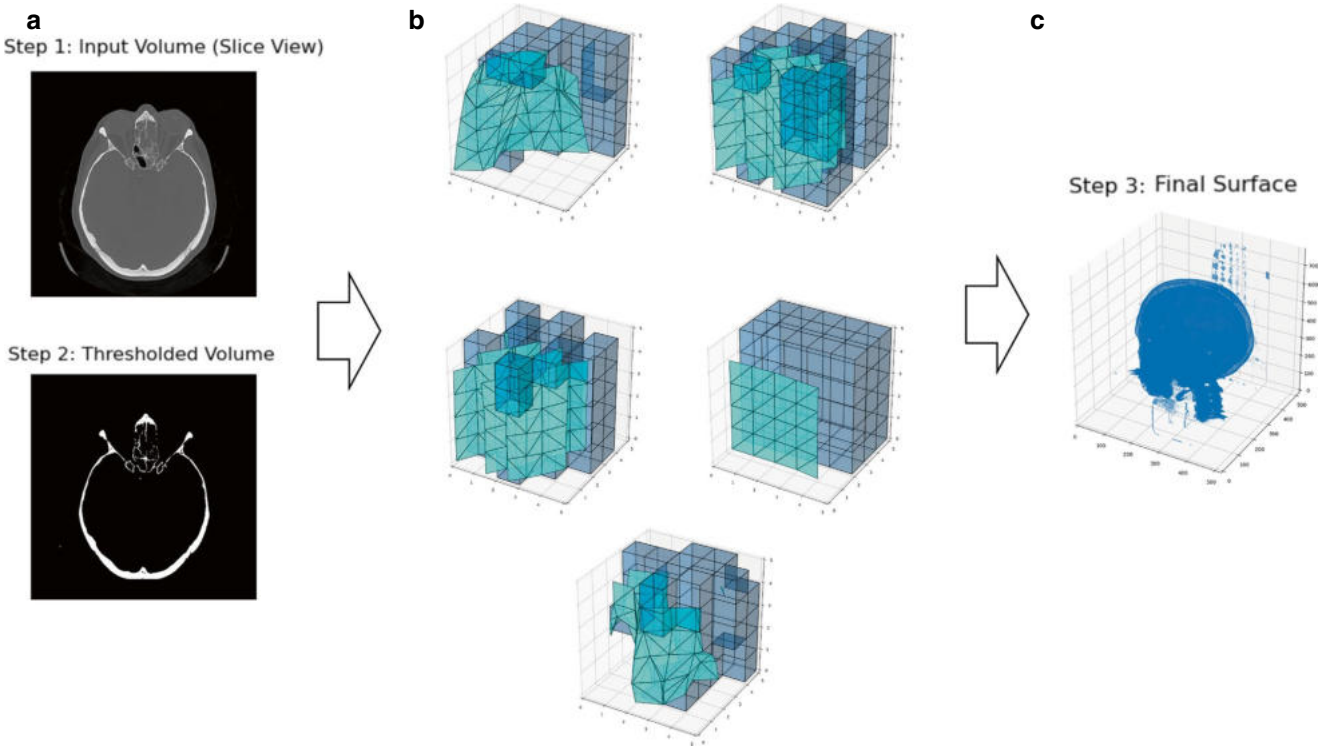


Fig. 6 Pipeline for 3D surface reconstruction from volumetric medical imaging. (**a**) Step 1 shows the input volume in slice view. Step 2 illustrates the thresholded volume, isolating regions of interest. (**b**) Intermediate steps in surface generation with the Marching Cubes algorithm, visualized with voxel grids and mesh triangulation. (**c**) Step 3 depicts the final 3D surface model of the anatomical structure

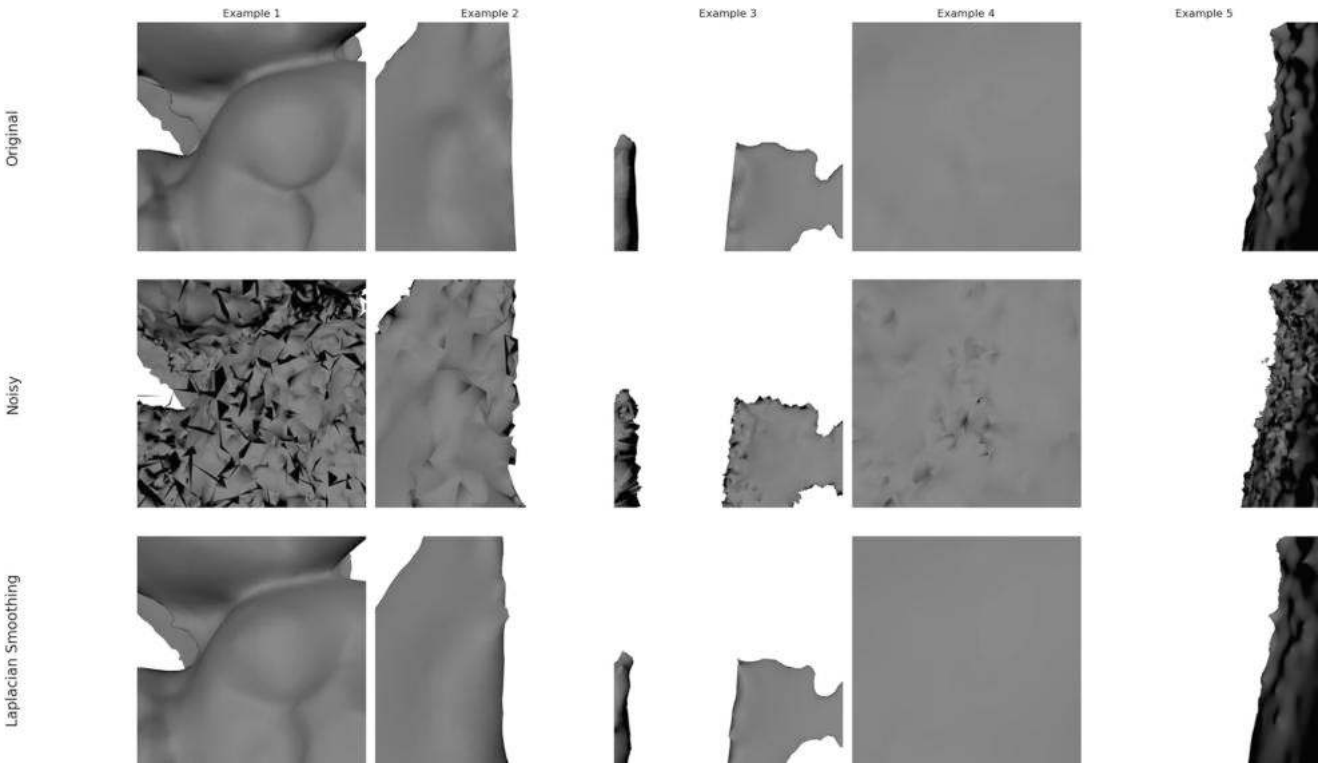


Fig. 7 3D skull model detailed views showcasing the application of Laplacian smoothing to enhance anatomical realism. Noise was introduced to the original surface, creating artifacts and irregularities. Laplacian smoothing was applied, repositioning each vertex based on the average position of its neighbors, effectively reducing noise and restoring surface smoothness. Examples 1 to 5 illustrate the process across various regions of the skull

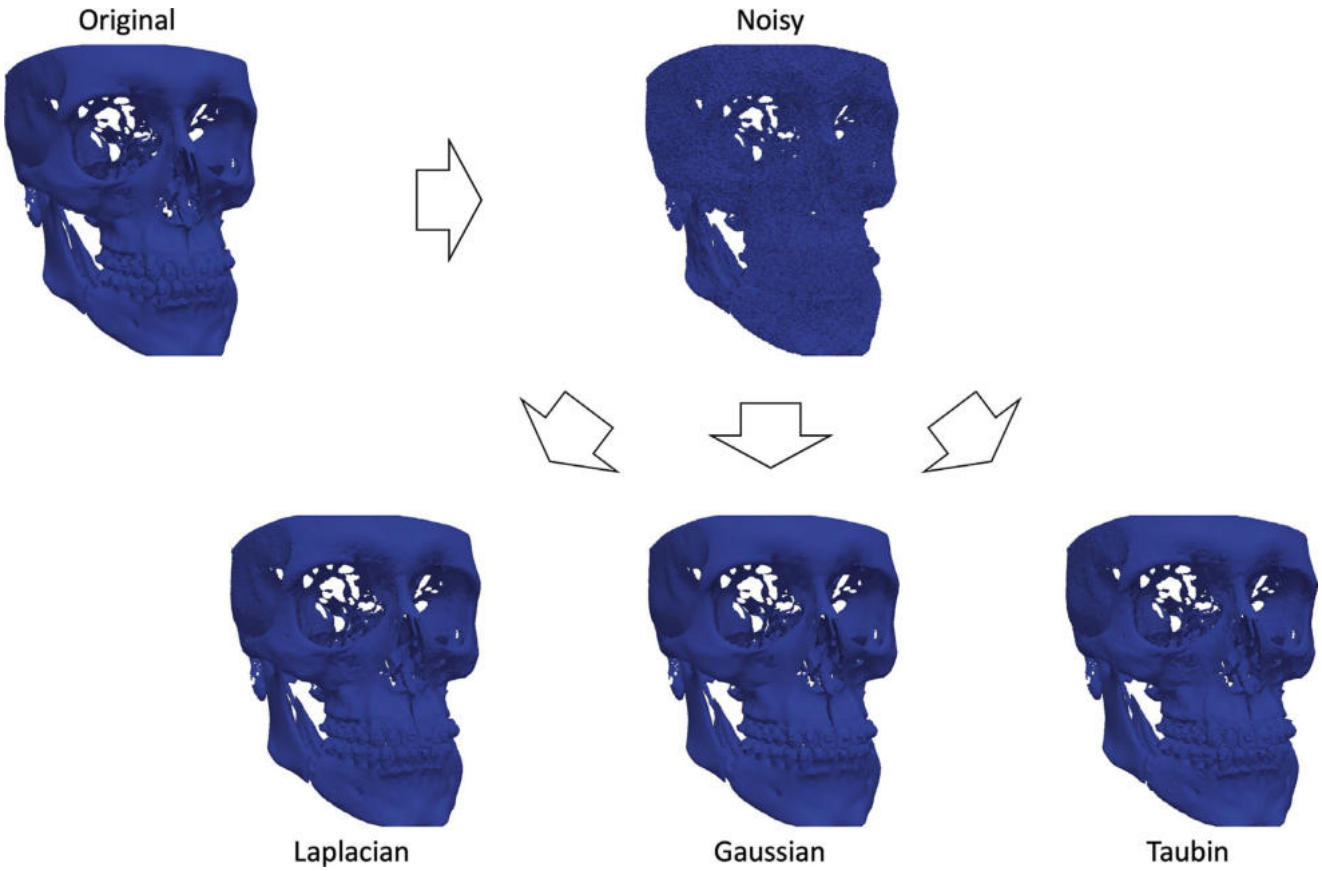


Fig. 8 Comparison of smoothing techniques applied to a noisy 3D skull model. The original model was artificially degraded with noise, followed by three smoothing approaches: Laplacian smoothing, Gaussian smoothing, and Taubin smoothing

viding and adding polygons to the mesh. Techniques such as the Catmull-Clark subdivision method are used to refine the mesh, providing increased detail and smoothness [22]. This process is particularly important for accurately representing intricate anatomical structures in surgical planning.

2.6 Multimodal 3D Registration

In VSP, software often requires the registration and alignment of three-dimensional models derived from various medical imaging modalities—such as CT, CBCT, MRI, and 3D surface scanners—to accurately represent a patient's anatomy by leveraging the strengths of each modality. Image registration involves determining the correct mapping that relates positions in one image to the corresponding positions in another. Several methods are employed to combine these multimodal datasets, classified into rigid, non-rigid, and hybrid approaches based on the type of alignment needed [23].

Rigid registration assumes that the surfaces are related by a rigid transformation (i.e., rotation and translation) without any structural deformation, which is often applicable to bone segments. An extension of rigid registration is the affine method, which allows for scaling and shearing transformations in addition to rotation and translation. Non-rigid registration, in contrast, permits free-form deformations to accommodate structural differences between images but requires longer processing times to identify corresponding features across different imaging modalities.

To achieve complete registration, algorithms must first identify similarities between images, create a transformation model with a set of numerical parameters that define a particular instance of the transformation, and then proceed with the optimization of the overlapping images. In the typical workflow of VSP software, the registration process begins with a preprocessing step. Here, images are resampled, and intensity values are normalized to facilitate comparisons between different imaging modalities. An initial transformation is then estimated to roughly align the datasets, either by manual selection of anatomical landmarks or, more commonly, by automatically detecting prominent features such as bone edges and vascular structures. Subsequently, similarity metrics are defined to measure the correspondence between the morphed (moving) image and the fixed (reference) image. A wide range of metrics has been developed,

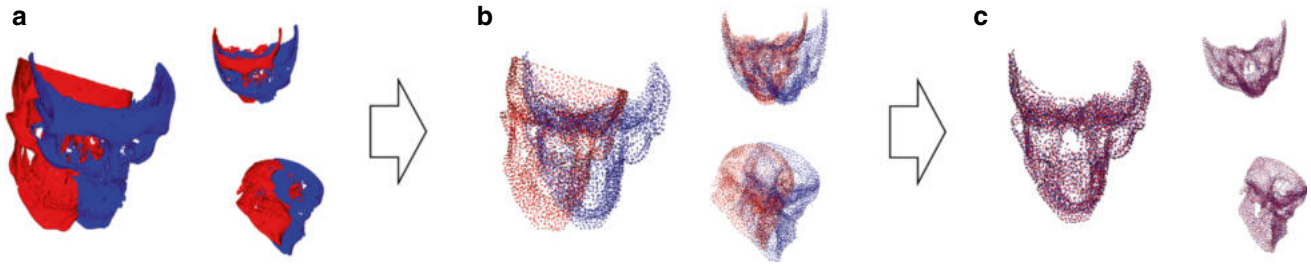


Fig. 9 Iterative Closest Point (ICP) algorithm applied to 3D anatomical models. (**a**) Initial surfaces (red and blue) before alignment. (**b**) Point cloud representation of the initial objects. (**c**) Final superimposed model after ICP convergence, showing minimized distances between corresponding points

with mutual information being preferred for registering images from different modalities. The transformation model is then applied and iteratively updated to improve alignment.

The most common registration techniques are [24]:

1. Rigid methods:
   - Iterative Closest Point (ICP): This method works by finding corresponding points between surfaces and iteratively minimizing the distance between these points through rotations and translations (Fig. 9). Various improved versions of ICP have been developed, and they perform optimally on bone 3D models.
   - Mutual Information (MI) Based Registration: This technique aligns images based on statistical dependencies rather than direct intensity similarities, making it suitable for combining CT's bone detail with MRI's superior soft tissue contrast.
2. Non-rigid methods [25]:
   - B-Spline Deformation: The anatomy is divided into a grid of control points in both the source and target images. A spline function defines correspondences between these points and extends them to the areas away from the control points. Commonly used in brain and abdominal organ alignment, it preserves local detail while adapting to changes in shape and is more computationally efficient compared to other spline techniques.
   - Demons Algorithm: Named for its ability to "push" and "pull" pixels across images until they align, this method is used in applications like brain imaging and tumor monitoring, where tissues may have shifted due to growth or other factors.

After registration is complete, an optimizer adjusts the transformation parameters to further improve image similarity until convergence is achieved. Finally, validation techniques are employed to ensure that the registration algorithm has correctly matched the input data, with an average error acceptable for the specific application in VSP.

2.7 Visualization Tools

After 3D model generation and registration have been performed, VSP software provides visualization tools to transform the 3D model into interactive views that allow surgeons to explore the anatomy from different perspectives. Some of these tools also provide a multi-view of the reconstructed model alongside the original DICOM images, with the plane identification to match the slice reference in the 3D model. Visualization is mostly used for diagnostic purposes, as little to no manipulation of the anatomies happens at this stage. For each of the available tools, a list of features and applications will be reported.

1. Multiplanar Reconstruction (MPR)

   MPR is a fundamental visualization technique that allows the viewing of medical imaging data in multiple planes (Fig. 10). Starting from a set of axial (horizontal) slices typically obtained from CT or MRI scans, MPR enables the reconstruction of images in other orthogonal planes: sagittal (vertical slices from left to right) and coronal (vertical slices from front to back). It also supports oblique and curved planar reconstructions [26]. Concurrent visualization of all these planes enhances spatial understanding of anatomical structures. Users can then scroll through slices in one plane, and the other planes will automatically update the view. It is widely used in most CMF applications, especially for the evaluation of fractures in facial trauma, localization of neoplasms, to assess skeletal discrepancies in orthognathic surgery, and to determine optimal implant sites with regards to bone density and proximity to vital structures.

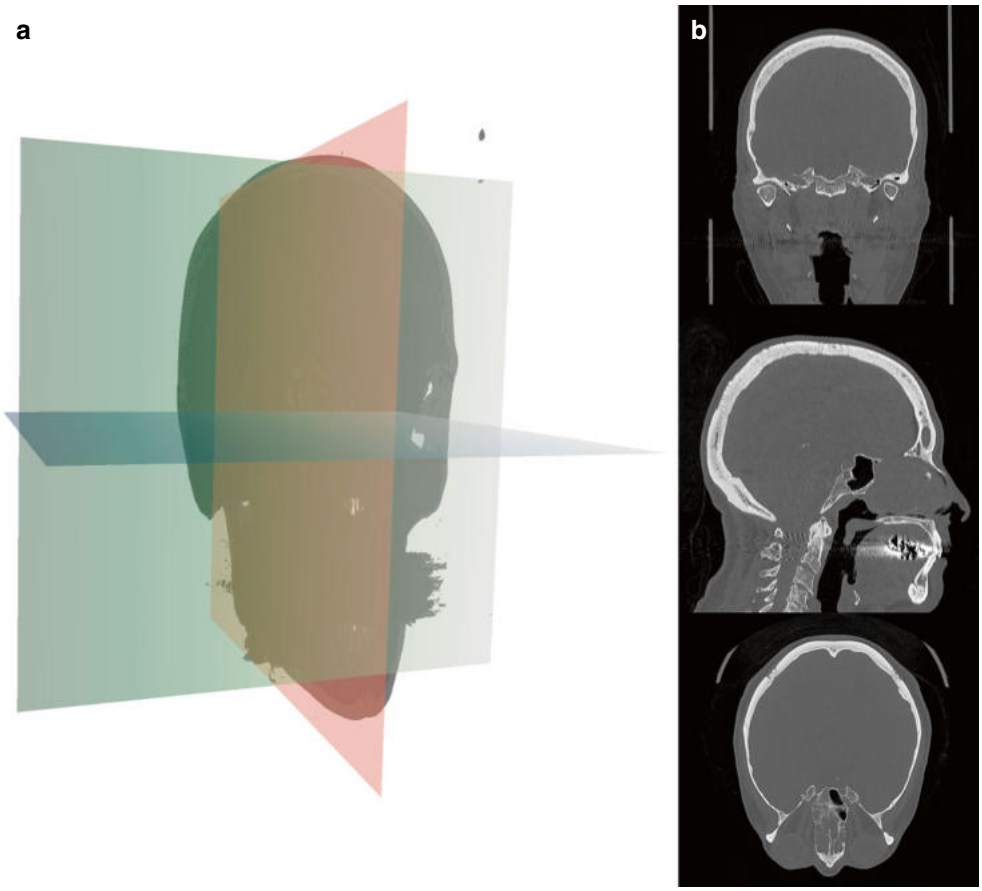


Fig. 10 Multiplanar reconstruction (MPR) of a CT scan for 3D anatomical visualization. (**a**) Representation of orthogonal planes (axial, sagittal, and coronal) intersecting the skull model in 3D space. (**b**) Corresponding 2D views along axial, sagittal, and coronal planes derived from the volumetric data

2. Transparency and Clipping

   Transparency and clipping tools enhance the visualization of internal structures by adjusting the opacity of overlying tissues or by virtually removing sections of the 3D model. They allow slicing at any angle, offering customized views tailored to the anatomical area of interest. It is relevant to correctly visualize impacted third molars or canines within the jawbone and to assist in visualizing the fit and positioning of bone grafts or alloplastic materials in reconstructive procedures.
3. Color Coding

   Color coding assigns specific colors to different anatomical structures or tissues within the 3D model, enhancing differentiation and recognition of smaller structures, such as nerves, and pathologic regions. It integrates with on-screen legend and labels for quick identification of anatomies, hence optimizing the understanding of complex anatomical relationships and better communication with research collaborators and patients.
4. Virtual Endoscopy and Fly-Through Navigation

   Virtual endoscopy simulates the experience of navigating within hollow anatomical structures using 3D imaging data, while fly-through navigation allows movement through any part of the anatomy. It has been used for preoperative exploration of the maxillary sinuses, a transantral approach to the inferior orbit [27], and airway assessment in patients with obstructive sleep apnea.
5. Annotations and Measurements

   Annotations and measurement tools allow users to mark points of interest, add textual notes, and perform quantitative assessments directly on the 3D model. Both linear and curved measurements can be performed to cover also nonlinear paths and surfaces. It is possible to determine angles between bones, implants, and other anatomical features, as well as computation of the volume of lesions and structures. Cephalometric analysis commonly performed in orthodontic and orthognathic surgery planning can be applied to the 3D model, and surgical guides can be created with precise measurements that inform their design and production.
6. Shading and Lighting Techniques

   Shading and lighting techniques simulate how light interacts with surfaces, enhancing the visual realism of 3D models and improving depth perception. Realistic shading helps visualize postoperative soft tissue contours, important in aesthetic surgeries and patient consultations,

and it highlights bone surface irregularities. This has been further improved with the advent of vertex shading, which assigns each mesh vertex its corresponding isovalue from the density map of a CT or MR. The aim is to represent polygonal anatomical structures with realistic color features.

7. Texture Mapping and Cinematic Rendering

   Texture mapping overlays 2D image data onto the surfaces of 3D models, adding detailed surface characteristics and enhancing visual realism. Cinematic rendering produces photorealistic images by simulating complex light-tissue interactions. It is possible to apply textures representing skin, muscles, bones, or organ surfaces that can help to predict potential scarring and facial reconstruction results, easing the discussions with patients regarding cosmetic outcomes.

8. Virtual Surgical Simulation

   3D model generation and tools that enhance anatomical visualization are essential components of VSP. However, they represent only the initial steps toward full manipulation and comprehensive simulation of surgical procedures. VSP software integrates a variety of tools and methods that enable surgeons to plan, practice, and optimize surgeries within a risk-free virtual environment. These tools enhance the surgeon's ability to visualize patient-specific anatomy, simulate surgical interventions, and predict postoperative outcomes. Their development is based on specific engineering methods, which serve as a common foundation for many of these tools.

2.8 Computational Modeling and Simulation

Computational modeling and simulation methods have led to the development of three main tools [28]:

1. Virtual osteotomy planning
2. Soft tissue simulation
3. Deformable modeling for soft tissue reconstruction

These tools use computational techniques to simulate the physical behavior of biological tissues under a variety of conditions. FEA and deformable modeling enable the prediction of soft tissue responses to skeletal changes, simulate tissue deformation during reconstructive procedures, and model the forces applied to bone segments after implant placement.

- Dynamic Osteotomy Simulation: This set of tools allows surgeons to simulate osteotomies in a 3D environment with real-time feedback on the impact of changes in bone structure. It is crucial for planning complex cuts and predicting postoperative alignment. For example, simulating a Le Fort I osteotomy to correct maxillary hypoplasia, allowing for precise planning of bone segment movements.
- Soft Tissue Prediction: These tools simulate the effects of skeletal adjustments on soft tissue outcomes, enhancing preoperative planning in aesthetic and reconstructive surgeries. For example, predicting facial contour changes after mandibular advancement in orthognathic surgery.
- Deformable Anatomical Modeling: This method simulates deformations in soft tissue and bone to reflect the dynamic nature of anatomical structures. It is often used in temporomandibular joint (TMJ) surgeries and complex trauma cases. For example, modeling soft tissue response in TMJ replacement surgery to optimize joint function and facial symmetry.

2.9 CAD/CAM Methods

CAD/CAM technologies are employed to design and fabricate patient-specific implants and surgical guides. Using CAD software, custom devices are created based on the patient's anatomical data and then manufactured using additive manufacturing techniques. The tools include:

1. Collision Detection and Constraint Modeling [29]: These tools identify potential interferences between anatomical structures or surgical instruments during virtual procedures, assisting in the evaluation of surgical pathways. For example, detecting potential collisions between surgical instruments and vital structures during mandibular reconstruction.
2. Patient-Specific Implant Simulation [30]: This tool facilitates the design and virtual fitting of implants tailored to individual patient anatomy. It integrates with additive manufacturing protocols to enable seamless transition from virtual design to 3D printing of implants. For example, designing a custom titanium mandibular implant for reconstruction after tumor resection.
3. Virtual Fixation and Splint Simulation [12]: These tools assist in planning the placement of fixation devices and surgical splints. They help determine the optimal placement of screws and plates for bone stabilization and predict dental alignment outcomes to ensure functional and aesthetic results. For example, planning the placement of miniplates and screws in a bilateral sagittal split osteotomy for mandibular setback.
4. Surgical Guide Creation [13]: This feature enables the design of precise surgical guides based on preoperative plans, helping surgeons accurately translate virtual simulations into physical templates. Guides can be fully cus-

tomized to align with planned osteotomies and implant placements. This tool also incorporates drill path planning, with STL files ready for production. For example, creating a surgical guide for accurate placement of zygomatic implants in maxillary atrophy cases.

2.10 Image-Guided Navigation and Augmented Reality

Image registration and real-time tracking—the most common methods adopted for image-guided navigation—allow surgeons to correlate the virtual surgical plan with the patient's actual anatomy during surgery. Augmented Reality (AR) overlays virtual models or surgical guides onto the surgeon's field of view, providing additional spatial information without diverting attention from the operative site [31]. This is achieved through:

1. Real-Time Overlay: Virtual images are superimposed onto the real-world view in real-time, enhancing spatial awareness.
2. Spatial Anchoring: Anatomical landmarks are used to anchor the virtual model, ensuring accuracy even when the surgeon or patient moves.

2.11 Artificial Intelligence and Machine Learning (ML)

AI and ML techniques are applied to analyze large datasets from previous surgical cases to assist in planning and predicting surgical outcomes. These algorithms can identify patterns, optimize surgical approaches, and provide decision support by suggesting procedural adjustments based on predicted results [9]. Applications include:

1. Predictive Modeling for Surgical Outcomes: AI models predict patient-specific outcomes based on planned surgical interventions. For example, forecasting the likelihood of postoperative occlusal stability after orthognathic surgery.
2. Personalized Biomechanical Simulation: Machine learning enhances biomechanical models to reflect individual patient variability. For example, simulating bone healing rates in mandibular fractures to optimize fixation methods.
3. Automated Surgical Planning Recommendations: AI suggests optimal surgical plans based on similar cases and outcomes. For example, recommending the best osteotomy approach for correcting asymmetrical mandibular prognathism.
4. Enhancing Virtual Surgical Simulation: Modeling tissue deformation and cutting patterns more accurately to improve simulation realism. For example, using AI to simulate soft tissue response during cleft lip repair for better aesthetic outcomes.
5. Implant Design Optimization: Algorithms optimize implant designs for improved fit and function. For example, refining the geometry of a custom orbital floor implant to enhance structural support and minimize weight.
6. Automated Quality Assurance for Surgical Plans: AI checks surgical plans for potential errors or oversights. For example, identifying inconsistencies in virtual osteotomy plans that could lead to misalignment.

Most of these tools are still in the research stage but are expected to revolutionize the approach to VSP by automating many of the required steps from imaging to a complete virtual plan.

By leveraging these advanced tools and engineering methods, virtual surgical simulation significantly enhances the precision, efficiency, and predictability of maxillofacial surgical procedures. Surgeons can perform detailed preoperative planning, anticipate potential challenges, and optimize both functional and aesthetic outcomes. As technology continues to evolve, the integration of computational modeling, CAD/CAM, image-guided navigation, augmented reality, and AI will further advance the capabilities of VSP in maxillofacial surgery.

3 Comparative Analysis of VSP Software

The market offers a diverse array of VSP software solutions, spanning from freely available tools to fully integrated platforms that emphasize workflow optimization and user accessibility. Over the past 14 years, more than 80 different software packages have been utilized, with several undergoing name changes or acquisitions. A general representation of the software reported in the literature from 2010 to November 2020 is reported in Fig. 11: it includes both still available tools and platforms that have now changed their name, as described further. The selection of software often depends on specific needs and applications, with some tools prioritizing surgeon-friendly designs, while others offer broader functionality for clinical research at the expense of more complex interfaces, which are typically managed by trained professionals, such as dedicated engineers. A comprehensive overview of the main software packages available will be provided, including an in-depth examination of the five most commonly used VSP software suites as identified by Tel et al. [32]. All the main software platforms are reported in Table 1.

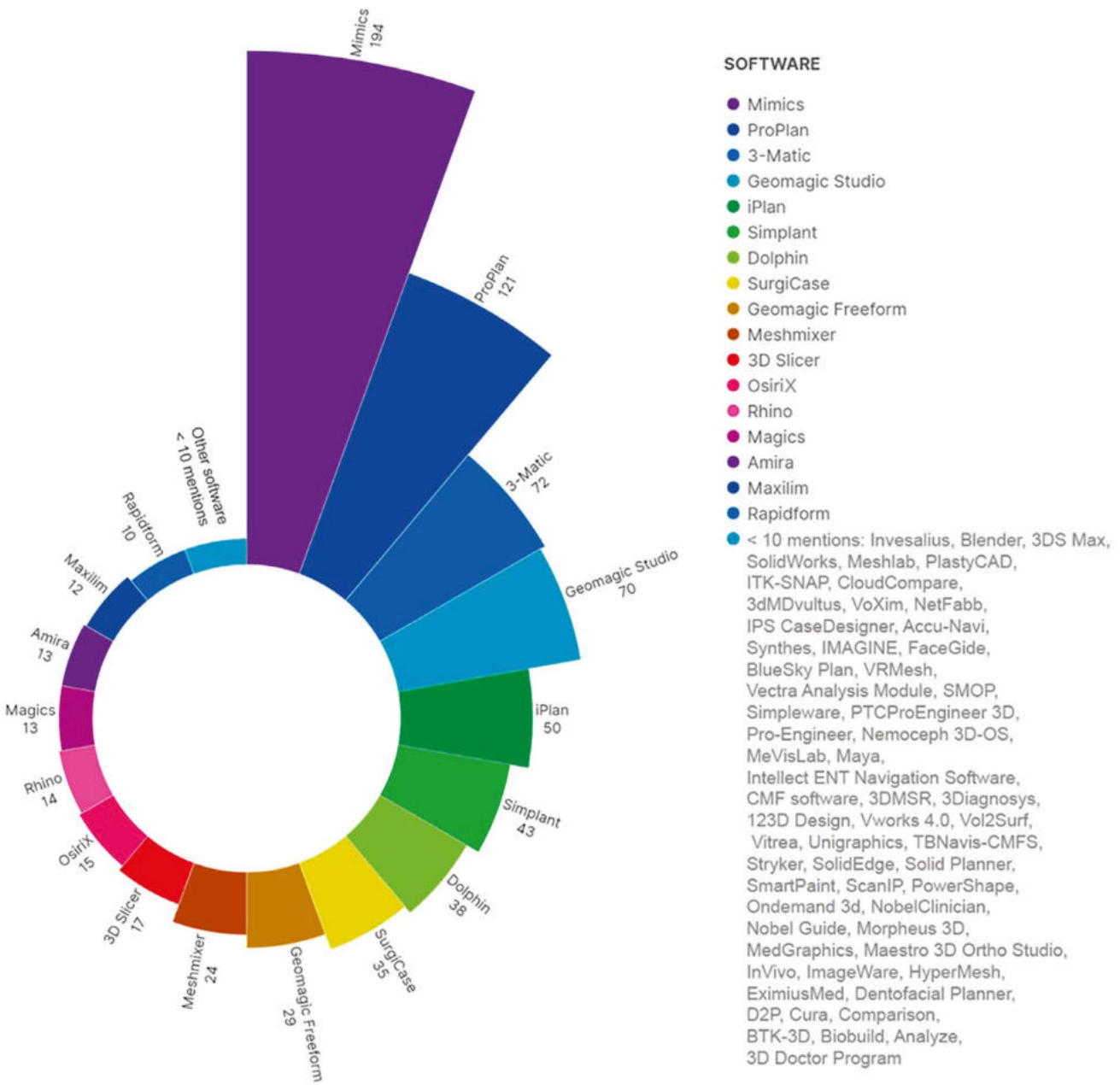


Fig. 11 Graphic diagram showing the prevalence of different software packages within articles published between 2010 and November 2020, as screened by Tel et al. [32]. In this spiral plot, the height of each colored block refers to the absolute prevalence of the software package. The last block includes packages mentioned in fewer than ten papers

Table 1 Overview of the main features and clearance for medical application of each software package currently available on the market

Software package	Cleared as a medical device	Manufacturer	Details	Free
Mimics	Yes	Materialise	Medical image segmentation and 3D model reconstruction	No
ProPlam	No	Materialise	CMF surgical planning	No
3-Matic	Yes	Materialise	Anatomical-CAD, alignment and analysis, design of PSIs	No
Enlight CMF	Yes	Materialise	Automated planning with surgeon-friendly interface	No
Magics	No	Materialise	3D printing pre-processing	No
Freeform	No	Oqton	Sculpting of organic surfaces (clays), design of PSIs	No
Geomagic Design X	No	Oqton	Scanning and reverse engineering	No
VSP Connect	No	3D Systems	Cloud-based surgical planning portal	No
Elements	Yes	Brainlab	Implemented by navigation systems with virtual planning capabilities	No
Dolphin	Yes	Dolphin Imaging and Management Solutions	Orthognathic surgical planning	No
IPS CaseDesigner	Yes	KLS Martin	Orthognathic surgical planning	No
Meshmixer	No	Autodesk	3D meshes modelling, design of guides	Yes/ No[a]
3D Slicer	No	Harvard University, NIH	Research software for segmentation, radiomics studies	Yes
OsiriX	Yes (only MD version)	Pixmeo	Medical image visualization software with simple segmentation	Yes/ No[b]
Horos	No	Horos Project	Medical image visualization software with simple segmentation, open-source	Yes
Amira	No	Thermo Fisher Scientific	Research for industrial and scientific data visualization	No
Rhino	No	Robert McNeel & Associates	Software for NURBS modelling in industrial design	No
ImmersiveView	Yes	ImmersiveTouch	CMF surgical planning in VR	No
Romexis CMF Surgery	Yes	Planmeca	AI-powered orthognathic surgery planning	No

3D three-dimensional, *CAD* computer-assisted design, *CMF* craniomaxillofacial, *NIH* National Institutes of Health, *NURBS* non-uniform rational basis spline, *PSI* patient-specific implant, *VR* virtual reality

[a]Meshmixer is a free software, but its successor, Fusion, is not

[b]OsiriX MD version with FDA clearance is not free

3.1 VSP Software Packages

3.1.1 Mimics Innovation Suite (Materialise NV, Leuven, Belgium)

Mimics Innovation Suite (MIS) has a modular structure to provide the surgeon/clinical engineer with high-quality tools to study anatomy in the digital space. Mimics and 3-matic, the two components of the Innovation Suite, are made of several modules, from basic segmentation and design, to advanced engineering, such as CAD format import and export, FEA, texturing, lattice structures, as well as dedicated workflows for cardiac, orthopedic, and pulmonary surgery. Overall, Mimics Innovation Suite was demonstrated to be the most frequently utilized software, with over one-third of published studies reporting their use. Another package, yet separate from the MIS, is to be mentioned: ProPlan CMF, which was dedicated to specific workflows in CMF surgery and accounted for two main workflows, orthognathics and reconstruction with fibula free flap. These platforms have been tested on a wide range of patient groups in clinical studies, encompassing both smaller studies (such as case reports, technical notes, case-control studies, and small cohort studies) and larger-scale clinical trials. Materialise also developed the Magics software, an industrial-focused 3D printing software with both CAD and mesh tools, which, regardless of the lack of medical approval, was found to be used in some papers to complement the Mimics Innovation Suite for in-house 3D printing of surgical guides and implants; yet, its main role is in industrial 3D printing.

Mimics

Mimics is considered the leading software suite for VSP in CMF surgery. It converts medical images (CT, MRI) into high-resolution, 3D anatomical models. The software's

robust algorithms are designed for accuracy in both bone and soft tissue segmentation, making it suitable for diverse surgical applications. This was proven as out of a wide range of surgical applications (TMJ, implant, malformation, reconstruction, oncology, oral surgery, orthognathic surgery, cranial surgery, trauma, and miscellaneous), Mimics in literature was consistently reported as the most used software in all of these scenarios, with the exception of reconstruction, where it was second to ProPlan.

3-matic

3-matic, part of the same suite, complements Mimics by offering CAD tools specifically tailored to anatomical models. This includes functions like Boolean operations, sketching, and alignment features, which are invaluable for tasks like surgical guide and implant design. 3-matic integration of engineering CAD functionalities makes the system more complex to a first-look, often requiring specialist knowledge in virtual planning and 3D modeling to manage it. The combination with Mimics has made Materialise a leader for VSP software, particularly because both Mimics and 3-matic are FDA-cleared.

ProPlan CMF

Initially derived from Materialise Simplant, ProPlan CMF is tailored for CMF surgery with modules optimized for orthognathic and reconstructive procedures. In particular, Simplant was split into a platform tailored for dentistry procedures, which kept the Simplant brand, and a dedicated version for CMF surgical procedures, which is the modern ProPlan. ProPlan CMF provides a structured workflow that integrates imaging data with 3D modeling and offers guided tools specifically designed to plan cases of orthognathic surgery or facial reconstruction with the fibula free flap.

ProPlan's user-friendly interface makes it accessible to clinicians who may not have an engineering background. As it integrates smoothly into CMF workflows and aligns well with Materialise Mimics, it has become a preferred choice in many institutions. Specifically, its application has been the most valued in literature in cases of reconstructive surgeries and orthognathic surgery, while falling short in trauma and craniofacial surgical procedures. ProPlan CMF still lacks a modern interface and an efficient rendering engine; thus, it was recently replaced by Enlight CMF for both its modules.

Enlight CMF

Mimics Enlight CMF by Materialise represents a new generation of VSP software specifically designed for CMF procedures. Developed in collaboration with surgeons, Enlight CMF aims to streamline and simplify the planning process for common CMF surgeries, specifically by providing dedicated workflows for orthognathic and reconstructive cases. This software stands out for its intuitive design and powerful rendering engine, which allows surgeons to perform comprehensive surgical planning in a few clicks, often completing complex orthognathic planning workflows in less than 25 minutes. Its streamlined step-by-step experience guides clinicians through each task—from segmentation to splint design—making it accessible to new users who can become proficient within few hours of use.

3.1.2 Geomagic Suite (3D Systems, Rock Hill, SC, USA & Oqton, San Francisco, CA, USA)

Following the Materialise family, which holds a leading position in research adoption, the Geomagic suite historically included Geomagic Studio, a comprehensive package developed and branded by 3D Systems with versatile applications in CMF surgery. Currently, the primary platform available within this suite is Geomagic Freeform Plus. Alongside other 3D Systems software products, Geomagic Freeform was transferred to Oqton in 2022 after 3D Systems acquired Oqton and established it as an independent software subsidiary. Freeform, as it is now rebranded, is distinct for its "digital clay" sculpting capabilities, allowing surgeons to model organic, intricate anatomical shapes. This feature has positioned Freeform as an essential tool for designing custom implants and for reconstructive surgery, as it overcomes traditional CAD modelling of 3-matic for its improved intuitiveness and versatility. The software excels at handling complex surface geometry and is especially valued for patient-specific implants and anatomical guide creation. Although Freeform is recognized for its design flexibility, it lacks regulatory clearance for medical use, limiting its application in regulated clinical environments. This has not prevented its widespread adoption in academia and prototyping, especially when detailed, high-fidelity models are required for non-clinical applications.

Within the Geomagic Suite now under Oqton, it is notable that Rapidform software, originally focused on 3D scan data processing and reverse engineering, was integrated into the suite and rebranded as Geomagic Design X.

Additionally, in 2017 at the Radiological Society of North America (RNSA), 3D Systems introduced its own FDA-cleared segmentation software, DICOM-to-PRINT (D2P), designed to handle medical images and create anatomical models for 3D printing [33].

Although Freeform, the Geomagic suite, and D2P have been transferred to the subsidiary Oqton, 3D Systems introduced a cloud-based, AI-powered VSP solution, VSP Connect, in 2023. Developed in partnership with Enhatch (Hasbrouck Heights, NJ, USA), VSP Connect combines FDA-cleared automated workflows with AI to streamline VSP by reducing planning times, enhancing a surgeon-friendly user interface, and integrating personalized implant and instrument design for 3D printing and manufacturing.

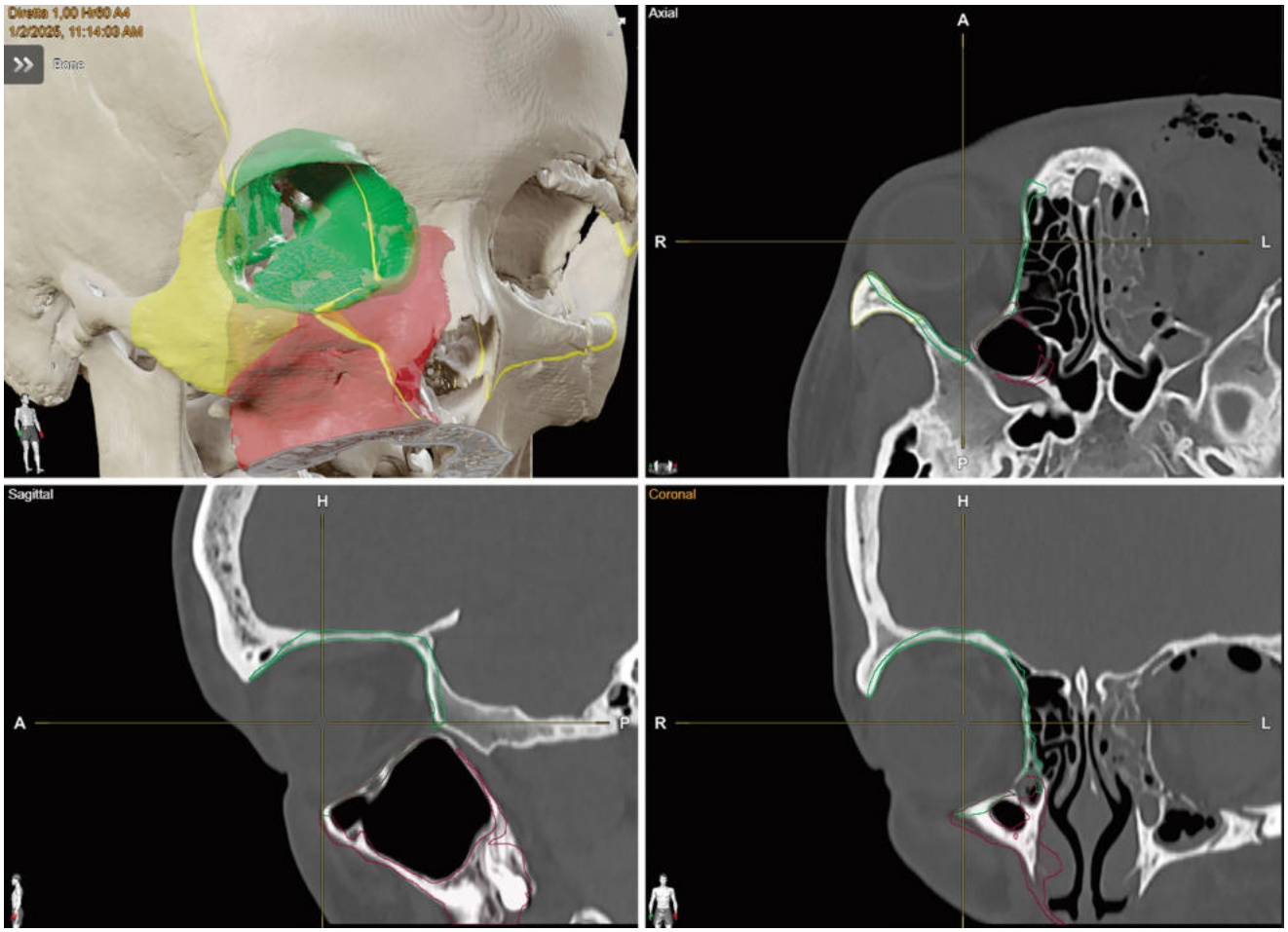


Fig. 12 Atlas-based autosegmentation performed using Brainlab Elements for the orbit (green), right ZMC (yellow), right maxilla (red). Autosegmentation is performed efficiently in a CT with normal anatomy (right side) but is not suitable to identify fractured fragments on the left side

3.1.3 Brainlab Suite (Brainlab, Munich, Germany)

Developed by Brainlab, iPlan (now rebranded as Elements) is a popular choice in trauma procedures due to its integration with navigation systems, coming second only to Mimics for frequency of utilization. It provides both manual and automated segmentation options, using anatomical atlases for precise structure recognition [34] (Fig. 12). This makes it especially useful for complex cases that require real-time navigation support. Its ability to combine segmentation with navigation systems makes iPlan unique among VSP software, setting it apart for procedures that demand high accuracy in spatial alignment and real-time adaptability. Its adoption is very limitedly extended to orthognathic, oral surgery, and implant design.

3.1.4 Dolphin (Dolphin Imaging and Management Solutions, Chatsworth, CA, USA)

Dolphin, developed specifically for orthodontic and orthognathic surgical planning, is widely used in orthognathic surgery for its advanced cephalometry modules and orthodontic alignment features, making it the third most common choice for this application after Mimics and ProPlan. It includes robust tools for measuring facial structures, angles, and occlusal relationships, making it highly applicable for surgeries aimed at correcting jaw alignment and occlusion. Dolphin's strength lies in its orthodontics-focused functionality, which is not as extensive in other VSP packages, but at the same time, it is not adopted for other types of procedures.

3.1.5 IPS CaseDesigner (KLS Martin, Tuttlingen, Germany)

Maxilim software was previously well-regarded in orthognathic surgery but was later succeeded by IPS CaseDesigner, acquired and rebranded by KLS Martin. IPS CaseDesigner is now still primarily used for orthognathic surgical planning, providing capabilities for diagnostic measurements, planning of individualized osteotomies and bite positions, and the generation of surgical splints. Simulation of soft tissue and facial modifications are also provided within the software.

3.1.6 Other Software

Amira (Thermo Fisher Scientific, Waltham, MA, USA) is a research package whose use has been reported in several papers. Mostly used in the biomedical field, it provides tools to process, visualize, and analyze imaging data, spacing from tissue imaging, neuroscience applications, anatomical imaging, and bioengineering. It also integrates components to perform segmentation and geometry reconstruction, compatible with 3D printing and rapid prototyping protocols.

NemoFab (Software Nemotec S.L., Madrid, Spain) is an FDA-cleared software that facilitates key processes in orthognathic surgical planning, such as volume orientation through automated clinical measurements, model fusion, and 3D cephalometric tracing, ensuring precise diagnostics and planning. It allows surgeons to customize osteotomies based on their techniques, improving accuracy and surgical outcomes.

Rhino (Robert McNeel & Associates, Seattle, WA, USA) is an industrial software used mostly as a freeform surface modeler. Its architecture is based on the non-uniform rational basis spline (NURBS) mathematical model to create, edit, render, and animate surfaces and solids. It supports complex surface modeling with features for Boolean operations, filleting, and trimming, which are essential for detailed CAD workflows. Rhino also integrates with Grasshopper—a visual programming language natively built into Rhino—for algorithmic modeling, allowing users to generate parametric designs and automate complex processes.

nTopology (nTopology Inc., New York, NY, USA) is advanced engineering software with biomedical applications, enabling optimized implant design with porous lattice structures to enhance osseointegration and bone fusion. It automates design iterations based on simulation results and parametric modeling and streamlines implant creation through reusable workflows [35].

Simpleware (Synopsys, Mountain View, CA, USA) is a tool that offers a range of features, including region-of-interest segmentation, image enhancement, and precise anatomical feature measurement. Moreover, Simpleware includes a comprehensive 3D printing toolkit that allows users to prepare, modify, and inspect models generated from imaging or CAD data.

3.1.7 Free Software

3D Slicer (Harvard University, Boston, MA, USA) is an open-source, research-focused software developed at Harvard University, frequently used for image segmentation, registration, and radiomics studies. Its modular design allows it to be highly customizable and extensible, suitable for users who are comfortable with adapting software to specific research needs.

Meshmixer (Autodesk Inc., San Rafael, CA, USA), OsiriX Lite (Pixmeo, Bernex, Switzerland), and Horos (Horos Project, Brooklyn, NY, USA), OsiriX open-source version, are also popular free options. Meshmixer is often used in early-stage prototyping for surgical guides and implant design, and starting in 2021, its tools have been implemented in Fusion (Autodesk Inc., San Rafael, CA, USA), which will be the leading software for industrial CAD/CAM applications in the Autodesk family. OsiriX Lite, primarily a DICOM viewer, is FDA-cleared in its MD version—which is not free—and offers basic segmentation and 3D modeling capabilities. OsiriX and Horos are available only for MacOS.

While free software solutions do not provide the full range of tools found in proprietary software, they serve as accessible options for research and prototyping. They are frequently used in academic settings where full-featured software is not essential, or budgets are limited.

3.1.8 Recent Advancements in Software Packages

Recent software development trends focus on four primary areas: enhanced user interfaces with surgeon-friendly tools, AI-powered functionalities, cloud-based computing, VR/AR integration, and FEA-enhanced modeling. As previously discussed, Mimics Enlight CMF incorporates an intuitive workflow and intelligent tools, such as automated segmentation, to reduce planning time. Similarly, VSP Connect leverages AI-powered features and cloud-based computing. Additional platforms have also been developed.

ImmersiveView (ImmersiveTouch Inc., Chicago, IL, USA) is an FDA-cleared VR-integrated software offering interactive VSP tools in a virtual environment for various applications, including TMJ surgery, trauma, oncology, and reconstructive procedures.

FEA-oriented software packages have increasingly been integrated into pure VSP software since maxillofacial surgical procedures are closely linked to understanding the pathomechanism of fractures, the biological responses of bone to biomechanical changes, and the behavior of osteosynthesis materials and intraosseous implants, both in healthy and pathological conditions. In this field, notable

packages include Ansys (Ansys Inc., Canonsburg, PA, USA), Abaqus FEA (Dassault Systèmes Simulia Corp., Johnston, RI, USA), and MSC Nastran (MSC Software Corporation, Newport Beach, CA, USA), which are widely used in various fields, ranging from trauma to orthognathic surgery [36].

3.2 Strengths, Weaknesses, and Specificities

The selection of software plays a key role in determining surgical precision, efficiency, and outcomes, making it essential to evaluate their strengths, limitations, and clinical suitability.

User Interface and Accessibility

Materialise Mimics provides advanced image processing and anatomical modeling for CMF applications, but its complexity requires substantial training. To address this, Materialise developed Enlight CMF, offering an intuitive interface that streamlines workflows for surgeons without sacrificing core functionality. Dolphin Imaging specializes in orthodontic and orthognathic procedures, offering user-friendly tools for cephalometric analysis and alignment but with limited application outside of dental and facial corrective surgeries. Geomagic Freeform provides advanced sculpting features for creating patient-specific implants and modeling complex anatomical structures, although it lacks medical regulatory clearance and requires expertise in 3D design.

Range of Surgical Application

Materialise software stands out for its broad applicability across CMF surgeries, including TMJ, reconstruction, oncology, and trauma, with Mimics excelling in segmentation and ProPlan CMF favored for orthognathic and reconstructive workflows. Brainlab's Elements integrates virtual surgical planning with real-time navigation, particularly benefiting trauma cases where spatial precision is crucial, though its reliance on navigation systems may limit broader adoption. Dolphin Imaging, IPS CaseDesigner, and Romexis CMF Surgery focus on orthodontic and orthognathic planning, excelling in their niche but offering limited functionality for trauma or reconstructive applications. A detailed overview of these platforms' clinical use is illustrated in Fig. 13.

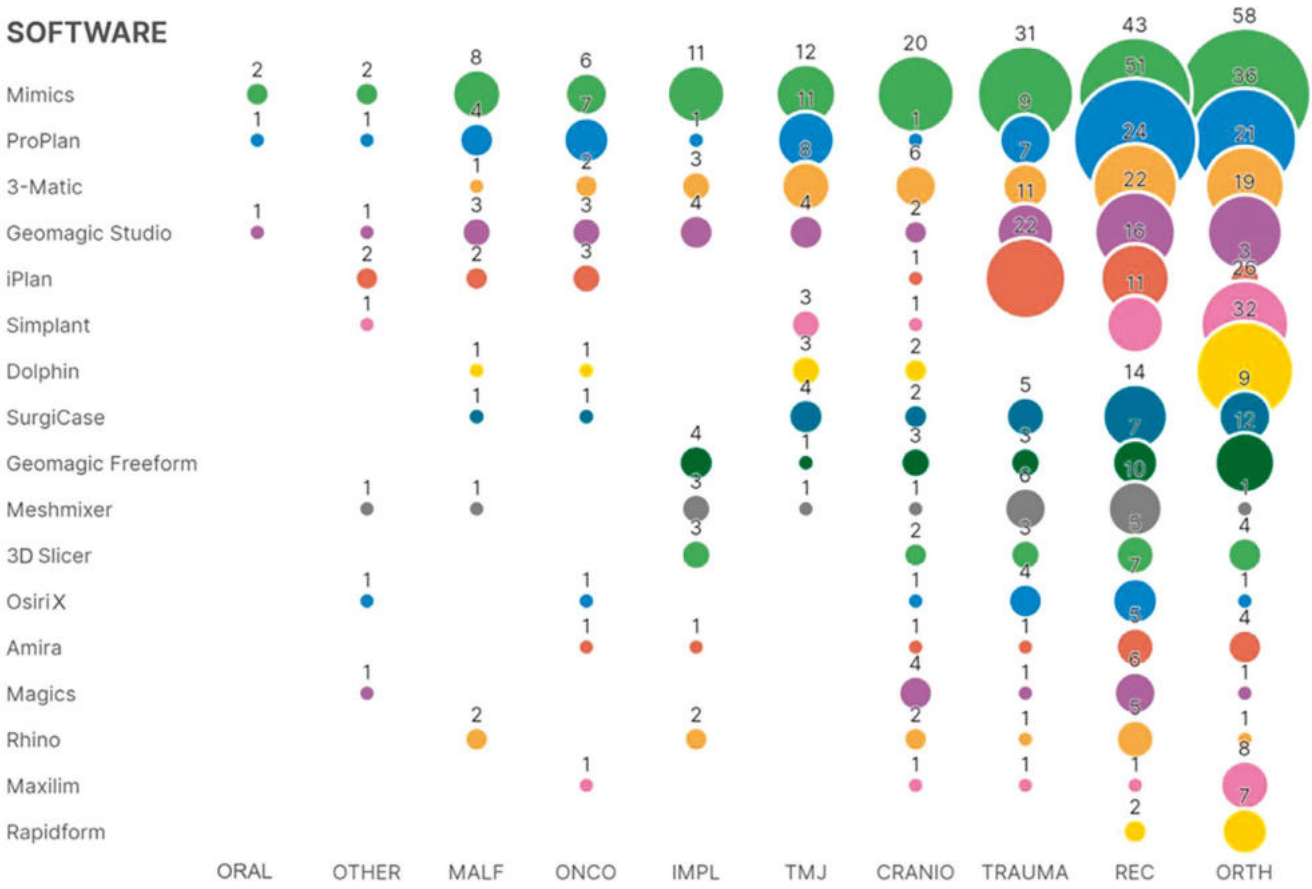


Fig. 13 Bubble plot showing the prevalence of each software for each type of surgical procedure. The size of each bubble accounts for the number of mentions of individual software within each class of procedure. (Reported from Tel et al. [32])

Advanced Features

Emerging technologies like artificial intelligence (AI) and cloud computing are shaping the future of VSP software. 3D Systems' VSP Connect, for example, leverages AI to automate and expedite the planning process, offering cloud-based collaboration and integration with manufacturing workflows for implants and guides. This innovation addresses the demand for efficiency and scalability in surgical planning. Moreover, the incorporation of virtual and augmented reality (VR/AR) technologies presents new dimensions in preoperative planning. Platforms like ImmersiveTouch's ImmersiveView enable surgeons to interact with 3D anatomical models in a virtual space, enhancing spatial understanding and potentially improving surgical outcomes in complex cases. The immersive experience facilitates better communication within surgical teams and with patients, offering a unique selling point that traditional platforms do not provide.

Regulatory Clearance and Clinical Use

Regulatory compliance is a pivotal consideration. Software with FDA clearance or equivalent regulatory approvals, such as Materialise Mimics and Enlight CMF, assures adherence to medical standards, making them suitable for clinical use. In contrast, platforms lacking such approvals, like Geomagic Freeform and industrial modeling tools like Rhino, are more appropriate for research, education, or preliminary design work rather than direct clinical application. Regulatory compliance will be further discussed in paragraph 1.4.

Open-source and free software options, such as 3D Slicer and Horos, present accessible alternatives for research and education. While they may not have the full feature set or regulatory approvals of commercial software, their modular design and community-driven development allow for customization and innovation. These platforms are valuable in academic settings and for institutions with budget constraints but may not meet the stringent requirements for clinical practice.

Literature reviews indicate that the choice of VSP software often correlates with the specific needs of the surgical procedure, the clinician's expertise, and institutional preferences. Studies have shown that platforms with regulatory approval and comprehensive features are more commonly used in clinical trials and larger cohort studies, underscoring the importance of reliability and compliance in clinical settings.

4 Ethical and Legal Considerations

Regulatory compliance is a critical consideration in the selection and application of VSP software in CMF surgery. Software used in clinical practice functions as a fundamental component of patient diagnosis and treatment, akin to any medical or surgical device. In the United States, such software must receive clearance from the US FDA to ensure it meets stringent safety and efficacy standards essential for patient care. Similarly, in Europe, the introduction of the MDR (Regulation (EU) 2017/745) in 2017, which became fully applicable in 2020, has reclassified software used in medical contexts, recognizing it as a medical device in its own right and subjecting it to rigorous regulatory scrutiny.

The MDR has brought significant changes to the classification and regulation of medical devices, including software, emphasizing their impact on health outcomes and patient safety. VSP software is now categorized into Class IIa or IIb, depending on its intended use and potential risks to patient health. Class IIa includes software used for diagnostic and therapeutic planning, while Class IIb applies to tools that directly influence surgical interventions. This reclassification highlights the critical role of software in ensuring surgical precision and reducing risks.

Regulatory approvals, such as FDA clearance, demonstrate adherence to medical standards and validate the software's safety and performance for clinical use. These approvals provide clinicians with confidence in the reliability of the tools for patient care. In contrast, platforms lacking regulatory approval are better suited for research, education, or early-stage design rather than direct clinical applications. While these tools may offer advanced modeling capabilities, their unregulated use in clinical settings poses risks, including potential inaccuracies and legal liabilities.

Non-compliance with MDR requirements can result in adverse events and significant legal repercussions. The MDR underscores the accountability of both manufacturers and clinicians to ensure that software used in medical settings is compliant and appropriate for its intended purpose. Given the integral role of software in surgical workflows, inaccuracies or errors can directly impact patient outcomes, underscoring the importance of selecting tools that meet regulatory standards for safety and reliability.

In addition to regulatory approvals, the concept of Software as a Medical Device (SaMD) has gained prominence. The

International Medical Device Regulators Forum (IMDRF) defines SaMD as software intended to be used for one or more medical purposes without being part of a hardware medical device. This definition reinforces the need for standalone software, such as VSP platforms, to meet regulatory requirements independently of any associated hardware.

4.1 FDA Clearance Process

For VSP software used in CMF surgery, the applicable regulatory pathway under the US FDA is typically the 510(k) premarket notification process, leading to the software being FDA-cleared rather than FDA-approved, which requires a Premarket Approval (PMA) and applies to Class III device—high risk and often life-sustaining or life-supporting (e.g., implantable devices, such as artificial heart valves and implantable pacemakers, or novel technologies without predicates). As part of the 510(k) premarket notification process, Manufacturers of VSP software must demonstrate that their product is substantially equivalent to a legally marketed predicate device. Upon successful review, the FDA issues a clearance letter, and the software is considered FDA-cleared. The main data requirements are performance testing and clinical data: Manufacturers submitting data must demonstrate that the software performs as intended, including accuracy assessments and validation studies, and while extensive clinical trial data may not always be required, evidence supporting the software's safety and effectiveness in its intended use is necessary. The FDA also requires detailed documentation of software development processes, including hazard analyses and mitigation strategies. Instructions for use must be clear, and any limitations or contraindications must be specified. FDA clearance applies to VSP software as it significantly influences surgical planning and outcomes but does not typically sustain or support life in a way that Class III devices do. Misuse or malfunction of the software could lead to incorrect surgical plans, but these risks are generally controllable and can be mitigated through design controls and proper use. Moreover, most VSP software introduces improvements or new features without fundamentally changing the intended use or technological characteristics. FDA clearance ensures, therefore, that VSP software has been evaluated for accuracy and reliability, reducing the risk of surgical errors. This helps clinicians meet legal requirements and adhere to professional standards.

4.2 FDA-Cleared Software

The first VSP software to receive FDA 510(k) premarket clearance was SimPlant System (Materialise) in 2004 as a tool for preoperative simulation and evaluation of surgical treatment in dental implant placement. iPlan was first released as software for medical imaging, with intraoperative functional planning where the output could be used for stereotactic image-guided surgery, hence its different classification category. The full list of FDA clearance details for software packages that are included in the review by Tel et al. [32] or currently present on the market is reported in Table 2.

Table 2 FDA clearance details for most commonly used software packages, both on the market or retired

Device name	Applicant	Decision date	510(k) Number	Device classification name
Simplant	Materialise	05/25/2004	K033849	System, Image Processing, Radiological
3-Matic	Materialise	05/18/2006	K060950	System, Image Processing, Radiological
Mimics	Materialise	04/02/2008	K073468	System, Image Processing, Radiological
SurgiCase Orthognathic Software Wizard[a]	Materialise	09/26/2011	K111641	System, Image Processing, Radiological
SurgiCase Viewer	Materialise	05/11/2017	K170419	System, Image Processing, Radiological
Mimics Enlight CMF	Materialise	05/31/2024	K223427	System, Image Processing, Radiological
iPlan[b]	Brainlab AG	06/03/2011	K101627	Neurological Stereotaxic Instrument
Brainlab Elements	Brainlab AG	12/16/2021	K212420	System, Image Processing, Radiological
Dolphin Imaging	Patterson Dental Supply, Inc.	05/11/2011	K110430	System, Image Processing, Radiological
OsiriX MD	Pixmeo SARL	08/20/2010	K101342	System, Image Processing, Radiological
Maxilim	Medicim NV	03/31/2006	K052424	System, Image Processing, Radiological
IPS CaseDesigner	Noberl Biocare USA LLC	11/10/2016	K161634	System, Image Processing, Radiological
ImmersiveTouch	ImmersiveTouch, Inc.	09/29/2021	K210726	System, Image Processing, Radiological
Planmeca Romexis	Planmeca Oy	06/16/2014	K140713	System, Image Processing, Radiological

In the table, only the main devices are reported. Most of them, however, include several modules that have received separate FDA clearance. The full list can be search at https://www.accessdata.fda.gov/scripts/cdrh/cfdocs/cfPMN/pmn.cfm

[a]SurgiCase Orthognathic Software Wizard is the device that first received the registration for ProPlan, its modern version

[b]iPlan CMF module and the added 3D functionalities were cleared on the 05/07/2012, 510(k) number K113732

5 Selection of the Appropriate Software

In conclusion, this introductory chapter establishes a foundational understanding of the diverse tools and methodologies integrated within VSP software platforms specific to maxillofacial surgery. While comprehensive, this overview acknowledges that the field is continually evolving, with new innovations and technologies emerging regularly. VSP platforms equip surgeons with advanced capabilities for detailed anatomical analysis, precise surgical planning, and simulation, thereby enhancing surgical accuracy and enabling personalized patient care.

The expansion of specialized instruments and software modules designed for a variety of surgical procedures underscores the rapid growth and adaptation within the field. This progression is propelled by an increasing body of clinical evidence demonstrating that VSP significantly reduces intraoperative complications, optimizes surgical outcomes, and accelerates the learning curve for complex procedures. The integration of three-dimensional imaging, CAD, and CAM within VSP has revolutionized preoperative planning, allowing surgeons to anticipate challenges and develop optimal surgical strategies.

As the technology continues to advance, surgeons are presented with an array of software options, each offering distinct features and capabilities. Making an informed choice becomes imperative to ensure that the selected VSP software aligns with specific clinical objectives and practice requirements. Factors influencing this decision include the surgeon's expertise with digital tools, the complexity and variety of cases managed, and the specific procedural needs.

Regulatory considerations are also critical. Medical software must comply with regional and international standards to guarantee patient safety, data security, and ethical practice. Technical resources such as hardware compatibility, integration with existing systems, and support infrastructure are essential for the seamless incorporation of VSP software into clinical workflows. Financial aspects, including initial acquisition costs and ongoing expenses related to training, updates, and maintenance, must be carefully evaluated to ensure sustainability.

Looking forward, the field of maxillofacial surgery is poised for further transformation driven by advancements in VSP technology. The incorporation of AI and ML holds the potential to automate aspects of surgical planning, provide predictive analytics, and enhance clinical decision-making processes. As these technologies mature, they are expected to become integral components of VSP platforms, offering even greater precision, efficiency, and patient-specific solutions.

In summary, VSP represents a significant advancement in surgical practice, offering benefits in terms of patient outcomes and operational efficiency. Surgeons who thoughtfully select and effectively implement VSP software that aligns with their clinical goals and resources are well-positioned to leverage the full potential of these advanced tools. Embracing VSP not only elevates the standard of care in maxillofacial surgery but also contributes to the ongoing evolution of surgical excellence and innovation.

References

1. Singh GD, Singh M. Virtual surgical planning: modeling from the present to the future. J Clin Med. 2021;10(23):5655.
2. Vannier MW, Marsh JL, Warren JO. Three dimensional CT reconstruction images for craniofacial surgical planning and evaluation. Radiology. 1984;150(1):179–84.
3. Stoker NG, Mankovich NJ, Valentino D. Stereolithographic models for surgical planning: preliminary report. J Oral Maxillofac Surg. 1992;50(5):466–71.
4. Marmulla R, Niederdellmann H. Surgical planning of computer-assisted repositioning osteotomies. Plast Reconstr Surg. 1999;104(4):938–44.
5. Kumari T, Ramanathan A. Digital technology in craniofacial surgery—historical perspectives to current applications. Dentistry Rev. 2022;2(1):100039.
6. Robb RA. Biomedical imaging, visualization, and analysis. Wiley; 1999.
7. Marmulla R, Hoppe H, Mühling J, Hassfeld S. New augmented reality concepts for craniofacial surgical procedures. Plast Reconstr Surg. 2005;115(4):1124–8.
8. Zhao L, Patel PK, Cohen M. Application of virtual surgical planning with computer assisted design and manufacturing technology to cranio-maxillofacial surgery. Arch Plast Surg. 2012;39(04):309–16.
9. Park JJ, Tiefenbach J, Demetriades AK. The role of artificial intelligence in surgical simulation. Front Med Technol. 2022;4:1076755.
10. Hua J, Aziz S, Shum JW. Virtual surgical planning in oral and maxillofacial surgery. Oral Maxillofac Surg Clin North Am. 2019;31(4):519–30.
11. Kim J-Y, Lee Y-C, Kim S-G, Garagiola U. Advancements in oral maxillofacial surgery: a comprehensive review on 3D printing and virtual surgical planning. Appl Sci. 2023;13(17):9907.
12. Zoabi A, Redenski I, Oren D, Kasem A, Zigron A, Daoud S, et al. 3D printing and virtual surgical planning in oral and maxillofacial surgery. J Clin Med. 2022;11(9):2385.
13. Kernen F, Kramer J, Wanner L, Wismeijer D, Nelson K, Flügge T. A review of virtual planning software for guided implant surgery - data import and visualization, drill guide design and manufacturing. BMC Oral Health. 2020;20(1):251.
14. H MGR, Nagaraja GS, editors. Noise removal techniques and quality analysis of X-ray images. 2019 1st International Conference on Advanced Technologies in Intelligent Control, Environment, Computing & Communication Engineering (ICATIECE); 2019.
15. Naidu S, Quadros A, Natekar A, Parvatkar P, Kumar KMC, Aswale S, editors. Enhancement of X-ray images using various image processing approaches. 2021 International Conference on Technological Advancements and Innovations (ICTAI); 2021.
16. Fasihi MS, Mikhael WB, editors. Overview of current biomedical image segmentation methods. 2016 International Conference on Computational Science and Computational Intelligence (CSCI); 2016.
17. An G, Hong L, Zhou X-B, Yang Q, Li M-Q, Tang X-Y. Accuracy and efficiency of computer-aided anatomical analysis using 3D visualization software based on semi-automated and automated segmentations. Ann Anat. 2017;210:76–83.

18. Sharma N, Aggarwal LM. Automated medical image segmentation techniques. J Med Phys. 2010;35(1):3–14.
19. Khan U, Yasin A, Abid M, Shafi I, Khan SA. A methodological review of 3D reconstruction techniques in tomographic imaging. J Med Syst. 2018;42(10):190.
20. Preim B, Botha C. Chapter 6 - Surface rendering. In: Preim B, Botha C, editors. Visual computing for medicine. 2nd ed. Boston: Morgan Kaufmann; 2014. p. 229–67.
21. Jermyn M, Ghadyani H, Mastanduno M, Turner W, Davis S, Dehghani H, et al. Fast segmentation and high-quality three-dimensional volume mesh creation from medical images for diffuse optical tomography. J Biomed Opt. 2013;18(8):086007.
22. Stam J. Exact evaluation of Catmull-Clark subdivision surfaces at arbitrary parameter values. In: Proceedings of the 25th annual conference on computer graphics and interactive techniques. Association for Computing Machinery; 1998. p. 395–404.
23. Garzia S, Capellini K, Gasparotti E, Pizzuto D, Spinelli G, Berti S, et al. Three-dimensional multi-modality registration for orthopaedics and cardiovascular settings: state-of-the-art and clinical applications. Sensors (Basel). 2024;24(4):1072.
24. Tam GKL, Cheng ZQ, Lai YK, Langbein FC, Liu Y, Marshall D, et al. Registration of 3D point clouds and meshes: a survey from rigid to nonrigid. IEEE Trans Vis Comput Graph. 2013;19(7):1199–217.
25. Crum W, Hartkens T, Hill D. Non-rigid image registration: theory and practice. Br J Radiol. 2004;77 Spec No 2:S140–53.
26. Zhang Q, Eagleson R, Peters TM. Volume visualization: a technical overview with a focus on medical applications. J Digit Imaging. 2011;24(4):640–64.
27. Tel A, Arboit L, Sembronio S, Costa F, Nocini R, Robiony M. The transantral endoscopic approach: a portal for masses of the inferior orbit—improving surgeons' experience through virtual endoscopy and augmented reality. Front Surg. 2021;8:715262.
28. Rubio-Palau J, Prieto-Gundin A, Cazalla AA, Serrano MB, Fructuoso GG, Ferrandis FP, et al. Three-dimensional planning in craniomaxillofacial surgery. Ann Maxillofac Surg. 2016;6(2):281–6.
29. Namías R, D'Amato JP, del Fresno M, Vénere M, Pirró N, Bellemare M-E. Multi-object segmentation framework using deformable models for medical imaging analysis. Med Biol Eng Comput. 2016;54(8):1181–92.
30. Huang MF, Alfi D, Alfi J, Huang AT. The use of patient-specific implants in oral and maxillofacial surgery. Oral Maxillofac Surg Clin North Am. 2019;31(4):593–600.
31. Ayoub A, Pulijala Y. The application of virtual reality and augmented reality in oral & maxillofacial surgery. BMC Oral Health. 2019;19(1):238.
32. Tel A, Arboit L, De Martino M, Isola M, Sembronio S, Robiony M. Systematic review of the software used for virtual surgical planning in craniomaxillofacial surgery over the last decade. Int J Oral Maxillofac Surg. 2023;52(7):775–86.
33. Oqton. Dicom to print. Available from: https://oqton.com/d2p/.
34. Brainlab. CMF planning: craniomaxillofacial surgical planning. Available from: https://www.brainlab.com/surgery-products/digital-cmf-surgery/cmf-planning/.
35. Tel A, Kornfellner E, Moscato F, Vinayahalingam S, Xi T, Arboit L, et al. Optimizing efficiency in the creation of patient-specific plates through field-driven generative design in maxillofacial surgery. Sci Rep. 2023;13(1):12082.
36. Lisiak-Myszke M, Marciniak D, Bieliński M, Sobczak H, Garbacewicz Ł, Drogoszewska B. Application of finite element analysis in oral and maxillofacial surgery-a literature review. Materials (Basel). 2020;13(14):3063.

Dedicated Acquisition Protocols in Radiology for Virtual Surgical Planning and 3D Printing

Arnau Valls-Esteve, Núria Adell-Gómez, Josep Munuera, Daniele Bagatto, and Alessandro Tel

1 Introduction to Imaging Acquisition Techniques for VSP and 3DP in CMF

Medical imaging has revolutionized the field of diagnostics, helping in the deep understanding of anatomy and pathophysiology. Since the discovery of the X-ray by Dr. Wilhelm Röntgen in 1895, imaging has become the main tool for diagnosis and treatment assessment. The revolution of CT scans and MRI in the 1970s marked significant milestones, offering detailed internal images of the body. Today, the integration of AI and 3D planning technologies is bringing a new era of personalized, efficient, and minimally invasive diagnostic imaging, particularly in surgery.

A. Valls-Esteve · N. Adell-Gómez
3D Unit (3D4H), Hospital Sant Joan de Déu, Esplugues de Llobregat, Spain

Innovation Department, Hospital Sant Joan de Déu, Esplugues de Llobregat, Spain

Medicina i Recerca Translacional. Facultat de Medicina i Ciències de la Salut. Universitat de Barcelona, Barcelona, Spain
e-mail: arnau.valls@sjd.es; nuria.adell@sjd.es

J. Munuera (✉)
Diagnostic Imaging Department, Hospital de la Santa Creu i Sant Pau, Barcelona, Spain

Advanced Medical Imaging, Artificial Intelligence, and Imaging-Guided Therapy, Institut de Recerca Sant Pau (IR SANTPAU), Barcelona, Spain
e-mail: jmunuera@santpau.cat

D. Bagatto
Neuroradiology Department, Academic Hospital of Udine, Udine, Italy
e-mail: daniele.bagatto@asufc.sanita.fvg.it

A. Tel
Lead Specialist for VSP and 3DP, Maxillofacial Surgery Clinic, Head & Neck and Neuroscience Department, Academic Hospital of Udine, Udine, Italy
e-mail: alessandro.tel@uniud.it

3D technologies enable the realistic visualization of 2D images acquired through various imaging techniques. They also allow for the combination of multiple reconstructions from different technologies within a single plan, surpassing the capabilities of each technique individually. Additionally, 3D printing transforms digital models into physical objects with defined colors and textures, enhancing surgical assessment and preparation.

AI algorithms have further improved acquisition times and image quality. In fact, radiology has been a pioneer in adopting AI technologies [1], significantly impacting patient care and workflow by reducing acquisition times and radiation exposure, enhancing pathology identification, and enabling automatic anatomy segmentation. This is evidenced by the number of AI algorithms approved by the FDA, with radiology leading by far in the number of cleared AI applications at the time of the writing of this book [2].

Nowadays, imaging diagnostics is the gold standard for surgical planning, integrating AI and 3D, and this is especially true in cranio-maxillofacial (CMF) surgery. CMF surgery is one of the most advanced specialties in adopting 3D technologies due to its focus on complex anatomical areas like the splanchnocranium, which involves intricate interactions between bone and other tissues.

In this section, various imaging acquisition techniques will be introduced, defining their characteristics for CMF surgery and their applications for different tissues, pathologies, and indications. The most important protocols and strategies for creating 3D reconstructions and biomodels will be discussed in both pre-surgical planning and the operating room from the imaging point of view.

The importance of combining different acquisition modalities to enhance the visualization of both soft and hard tissues will be elucidated, depending on their density and characteristics, and the protocols to ensure patient well-being. The relevance of selecting specific parameters to achieve the final diagnostic goal, particularly when using vir-

© The Author(s), under exclusive license to Springer Nature Switzerland AG 2025

A. Tel, M. Robiony (eds.), *Atlas of Virtual Surgical Planning and 3D Printing for Cranio-Maxillo-Facial Surgery*,
https://doi.org/10.1007/978-3-031-94495-6_2

tual surgical planning (VSP) or 3D printing (3DP) for surgical planning, will be highlighted.

Finally, particularities of specific maxillofacial cases will be examined, such as free flap harvesting, and considerations for specific populations, such as pediatric patients. The ecological impact of imaging acquisition techniques will be discussed as well.

2 Overview of Imaging Acquisition Technologies for VSP and 3DP

To achieve the most accurate 3D reconstruction, it is of utmost importance to select the appropriate imaging modality. Selecting the appropriate imaging modality is a fundamental initial step and depends on the advantages in spatial and contrast resolution. Spatial resolution is the ability for an image modality to differentiate between two separate objects in a radiographic image (e.g., a nerve canal within the mandible), whereas contrast resolution is the ability to differentiate image intensities between two areas (e.g., fat stranding vs normal adipose tissue). For this reason, depending on the clinical need, patients should be ideally investigated with both preoperative CT (for spatial resolution) and MR (for contrast resolution) imaging with dedicated protocols.

2.1 Computed Tomography (CT)

General Definition A computed tomography scan (CT scan), first described in the 1970s, is a medical imaging technique used to obtain detailed internal images of the body. CT scanners use a rotating X-ray tube and a row of detectors placed in a gantry to measure X-ray attenuations by different tissues inside the body. The multiple X-ray measurements taken from different angles are then processed on a computer using tomographic reconstruction algorithms to produce tomographic (cross-sectional) images (virtual "slices") of the body. In a CT scan image, pixels are shown based on their relative radiodensity. Each pixel represents the average density of the tissues it corresponds to, measured on the Hounsfield scale, which ranges from +3071 (most dense) to −1024 (least dense). A pixel is a two-dimensional unit determined by the matrix size and the field of view. When the thickness of the CT slice is included, the unit becomes a voxel, which is three-dimensional.

Fact *Water has an attenuation of 0 Hounsfield units (HU), while air is −1000 HU, cancellous bone is typically +400 HU, and cortical bone can reach 2000 HU.*

CT has become an important tool in medical imaging to supplement conventional X-ray imaging and medical ultrasonography. Although its widespread use in imaging diagnosis and preventive medicine is significant, its ionizing radiation limits its use and recommendations due to its impact on the body of the patient.

Fact *CT was invented by Sir Godfrey Hounsfield (British electrical engineer) and Dr. Allan Cormack (South African-American physicist), who shared the Nobel Prize in Physiology or Medicine in 1979 for their invention* [3].

Specificity for Cranio-Maxillofacial Surgery CT scans are essential for capturing high-resolution images of facial bones and soft tissues. Thin-slice CT scans, ranging from 0.5 to 0.75 mm, are commonly used to obtain detailed anatomical structures. These precise images are crucial for accurate virtual surgical planning and the 3D printing of patient-specific models and surgical guides (Fig. 1).

Advantages and Drawbacks CT provides detailed images and is widely used, but the ionizing radiation exposure is a significant drawback [4].

Positive

- Non-overlapping tissues, unlike it happens in 2D radiograms, as this technique provides axial slices of the patient.
- Rapid acquisition, allowing for dynamic studies.
- Excellent spatial resolution.
- Higher CT contrasts are achieved between very dense objects, such as bone, and low-density objects, such as air in the lungs. To improve contrast resolution in soft tissue, radio-opaque contrast agents (containing iodine or barium, for example) are administered.
- Modern CT scans have isotropic resolution, i.e., equal in all three dimensions, allowing high-quality coronal and sagittal reconstructions without reduction in resolution.

Negative

- Ionizing radiation, which can increase the risk of cancer, especially with repeated scans. This is a significant consideration, particularly for younger patients.
- Less effective at differentiating between soft tissues compared to MRI. This can limit their use in certain diagnostic scenarios.
- Some CT scans require the use of contrast material, which can cause allergic reactions or kidney issues in some patients. This is a significant consideration, particularly for younger patients.
- Metallic objects commonly used in CMF such as brackets or distractors can cause artifacts on the acquired CT image.

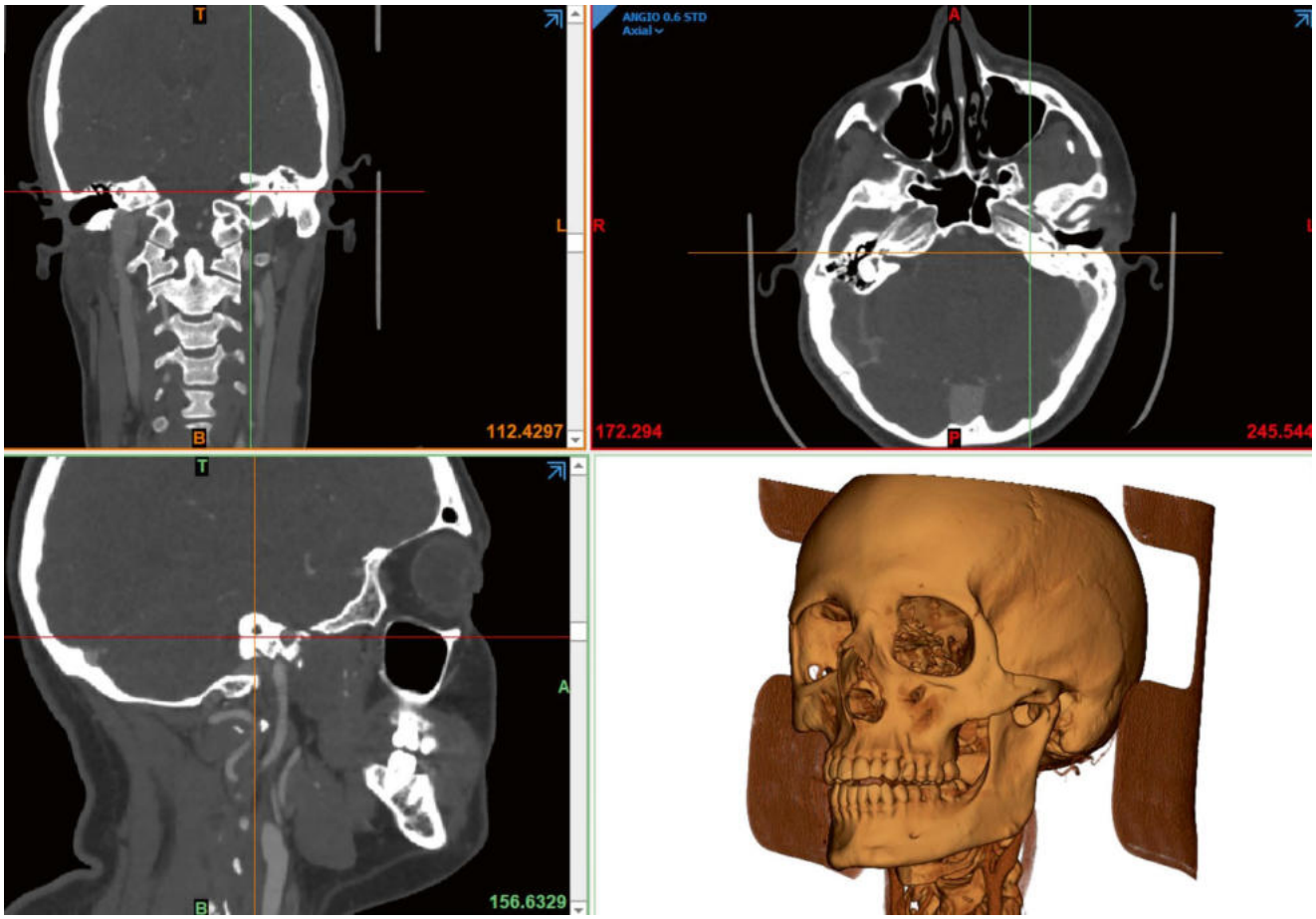


Fig. 1 Contrast-enhanced CT with optimal acquisition parameters and isotropic, thin-sliced, acquisition, as shown by multiplanar reconstructions and volume rendering

Depending on its acquisition and procedures various types of scanners exist:

- Spiral CT: Used for trauma assessment, fractures of the facial bones, detection of tumors, and evaluation of sinus diseases. Provides rapid and detailed imaging of the maxillofacial region.
- Electron Beam Tomography (EBT): Rarely used for maxillofacial imaging. Limited role but can assist in evaluating calcifications in head and neck structures.
- Dual Energy CT (or Spectral CT): Enhances tissue differentiation in maxillofacial imaging; useful for detecting bone pathology and dental materials; and helps differentiating lesions from surrounding tissues. It specifically allows the interrogation of materials with different X-ray attenuation properties.
- CT Perfusion Imaging: Limited use in maxillofacial imaging but can help assess vascularization of tumors, guiding surgical planning for excising the lesion.
- Positron Emission Tomography–Computed Tomography (PET-CT): Evaluates metabolic activity in head and neck cancers, identifies tumor staging, detects metastases, and assesses treatment response in the maxillofacial region.
- Cone-Beam Computed Tomography (CBCT): Widely used in dental and maxillofacial imaging for detailed 3D visualization of teeth, jawbones, sinus anatomy, temporomandibular joint (TMJ) evaluation, and pre-surgical planning for implants or orthodontics.

From those, the most used is the cone-beam computed tomography (CBCT) for its value in dental application, providing precise and comprehensive 3D images of the teeth aiding in detecting conditions like periodontal disease, tooth decay, and cavities early.

2.2 Cone-Beam Computed Tomography (CBCT)

General Definition Cone-beam computed tomography (CBCT) is a type of CT that uses a cone-shaped X-ray beam that rotates around the patient to capture multiple images

from different angles to create 3D images. These images are then reconstructed into a 3D model using specialized software. CBCT is particularly useful in dental and maxillofacial imaging due to its ability to provide high-resolution images with lower radiation doses compared to conventional CT. It was developed in the late 1990s by Dr. Yoshinori Arai in Japan and Dr. Piero Mozzo in Italy. CBCT is widely used in dentistry for implant planning, orthodontics, and endodontics. It provides detailed images of the teeth, jawbone, and surrounding structures, aiding in accurate diagnosis and treatment planning.

Fact *The first commercial CBCT system, the NewTom 9000, was introduced in the European market in 1996 and in the US market in 2001.*

Specificity for CMF CBCT provides high-resolution images with lower radiation doses compared to conventional CT. In CMF surgery, CBCT is essential for evaluating bone structures, such as the jaw, teeth, and facial bones and temporomandibular joints. It is used for surgical procedures planning, assessing trauma, performing orthognathic surgery, and guiding the placement of dental implants. It is a useful tool in diagnostic imaging within the operating room (Fig. 2).

Advantages and Drawbacks CBCT offers detailed 3D images with lower radiation exposure, but it is limited to smaller areas compared to conventional CT. It is less effective for imaging soft tissues and may produce artifacts in the presence of metal objects. Another disadvantage compared to MDCT is the difference in quantitative gray values provided by CBCT, which makes the traditional Hounsfield scale non-applicable, thus making threshold-based segmentation less effective compared to MDCT [5].

2.3 Magnetic Resonance Imaging (MRI)

General Definition Magnetic resonance imaging (MRI) is a noninvasive medical imaging technique used to obtain detailed internal images of the body. MRI scanners use strong magnetic fields, magnetic field gradients, and radio waves to generate images of the organs and tissues inside the body. Unlike CT scans, MRI does not use ionizing radiation. Instead, it relies on the magnetic properties of hydrogen atoms in the body to produce high-resolution images. When a patient is placed inside the MRI machine, the magnetic field aligns the protons in the hydrogen atoms. Radiofrequency pulses are then used to disturb this align-

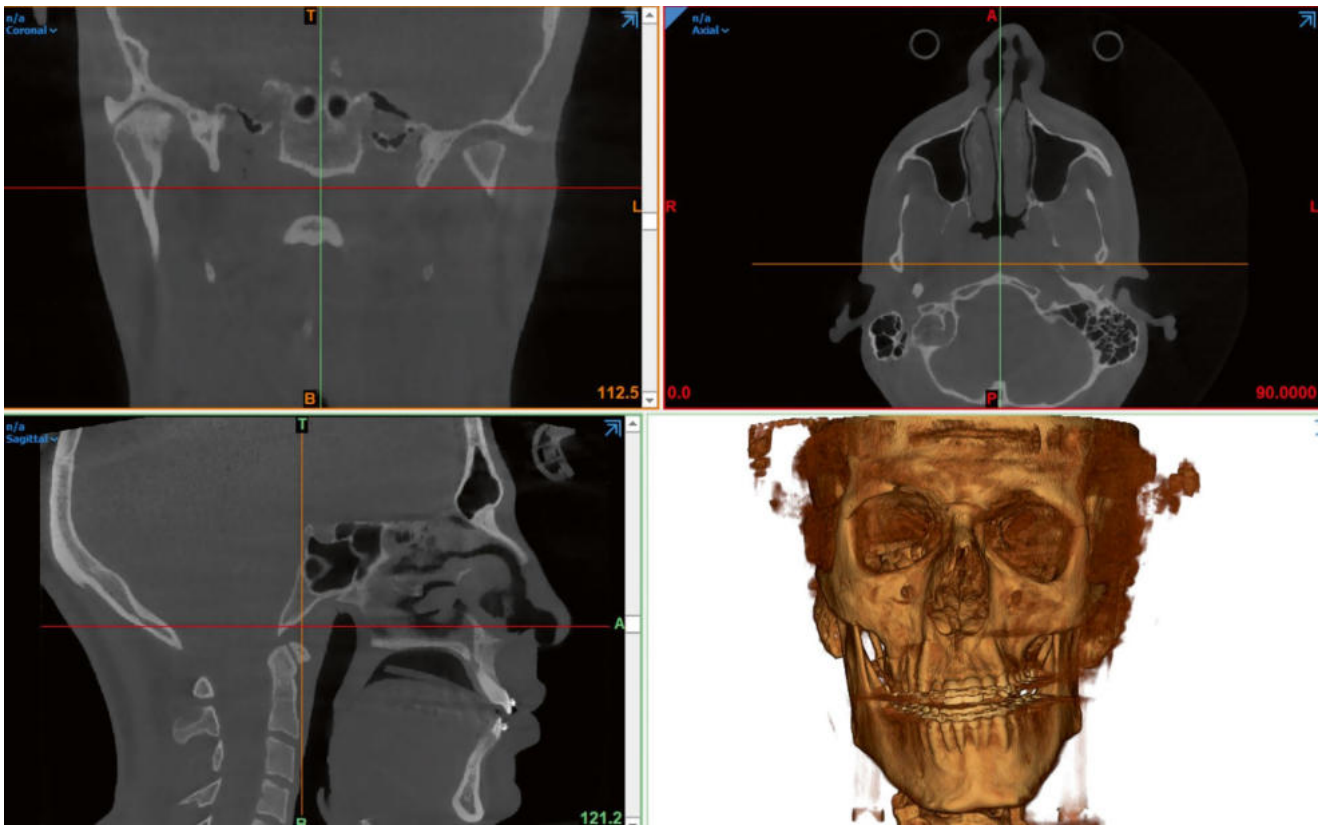


Fig. 2 High-quality CBCT used for orthognathic surgical planning. The traditional HU threshold is not applicable to CBCT, and discrimination between soft and hard tissues is less efficient, as shown in the volume rendering

ment, and as the protons return to their original state, they emit signals that are detected and converted into images by a computer [6].

The main unit of MRI is Tesla (T), which identifies the magnetic field strength. The strength of the magnetic field in an MRI scanner is crucial because it determines the quality and detail of the images produced. Based on how water and fat in tissues respond to magnetic fields different imaging sequences exist that highlight different tissue properties. T1-weighted and T2-weighted images are two common types of imaging sequences.

MRI is particularly effective for imaging soft tissues, such as the brain, spinal cord, muscles, and ligaments. It can differentiate between white matter and gray matter in the brain and is often used to diagnose conditions like tumors, arteriovenous malformations, or aneurysms. T1-weighted imaging measures longitudinal relaxation time (how fast protons realign with the magnetic field). It is effective for anatomical detail and identifying fatty structures, bone marrow or post-contrast enhancements. While T2-weighted imaging measures transverse relaxation time (how fast protons lose phase coherence after excitation). It is preferred for pathological changes related to fluid, such as inflammation, edema, infection, or cystic lesions (Table 1).

Fact *The underlying principle of nuclear magnetic resonance (NMR) was discovered by Felix Bloch and Edward Purcell in 1946, and MRI technology was developed in the early 1970s by Paul Lauterbur and Sir Peter Mansfield. Paul Lauterbur and Sir Peter Mansfield were awarded the Nobel Prize in Physiology or Medicine in 2003 for their contributions to the development of MRI* [7].

Specificity for CMF MRI is crucial for obtaining detailed images of soft tissues in the cranio-maxillofacial region, especially to visualize soft tissue structures such as muscles, nerves, and blood vessels. In CMF surgery, it is particularly useful for assessing surgeries involving soft tissue tumors, inflammatory conditions, and vascular anomalies. MRI provides high-resolution images that are essential for accurate surgical planning and the evaluation of complex anatomical structures. For VSP, it is essential that MR is acquired as a volume with isotropic voxel parameters, allowing segmentation to be performed equally in all spatial planes. Volumetric interpolated breath-hold examination (VIBE) sequences provide excellent image quality and maintain excellent contrast discrimination, which drives the effective application of algorithms for soft tissue segmentation, such as dynamic region growing, and the semi-automatic 3D interpolated brushes and smart brushes (Fig. 3).

Table 1 Key differences between MRI sequences: T1 weighted and T2 weighted

Feature	T1 weighted	T2 weighted
Fat appearance	Bright (hyperintense)	Dark (hypointense)
Water/fluid appearance	Dark (hypointense)	Bright (hyperintense)
Best use	Anatomy and structural detail	Pathology and fluid detection
Example in CMF	Soft tissue anatomy, tumors	Inflammation, cysts, effusions

Advantages and Drawbacks MRI provides excellent soft tissue contrast without ionizing radiation, but it is more expensive and time-consuming than other modalities. Additionally, MRI is less effective for imaging bone structures compared to CT scans [8].

Positive Aspects
- Superior contrast resolution for soft tissues
- No ionizing radiation, making it safer for repeated use
- Capable of producing high-resolution images in multiple planes (axial, coronal, sagittal)

Negative Aspects
- Higher cost and longer acquisition times compared to CT.
- Less effective for imaging bone structures.
- Some patients may experience discomfort or claustrophobia inside the MRI machine, especially for head and neck acquisitions due to the need for placing the head inside the machine and the high sounds produced by the machine.

Various types of MRI scanners exist depending on the magnetic field strength (with different levels of Tesla. Most common scans are between 1.5T and 3T. New scans are appearing above those magnetic fields such as 5T and 7T. The higher the T, the scans are faster, and the resolution improves. But they are more costly, tend to have more artifacts on the image, and are less safe for the patients as it increases the effects of the magnetic field such as heat. 5T and 7T scanners are less commonly used in routine clinical practice; these scanners are often used in advanced research settings to study fine anatomical details and brain function. Other techniques to enhance certain tissues:

- *Functional MRI (fMRI)*: Used to measure and map brain activity. Unlike a standard MRI, which provides static images of the brain's structure, fMRI captures dynamic changes in brain activity through blood oxygenation and flow that occur in response to neural activity by measuring the blood oxygen level dependent (BOLD) signal.

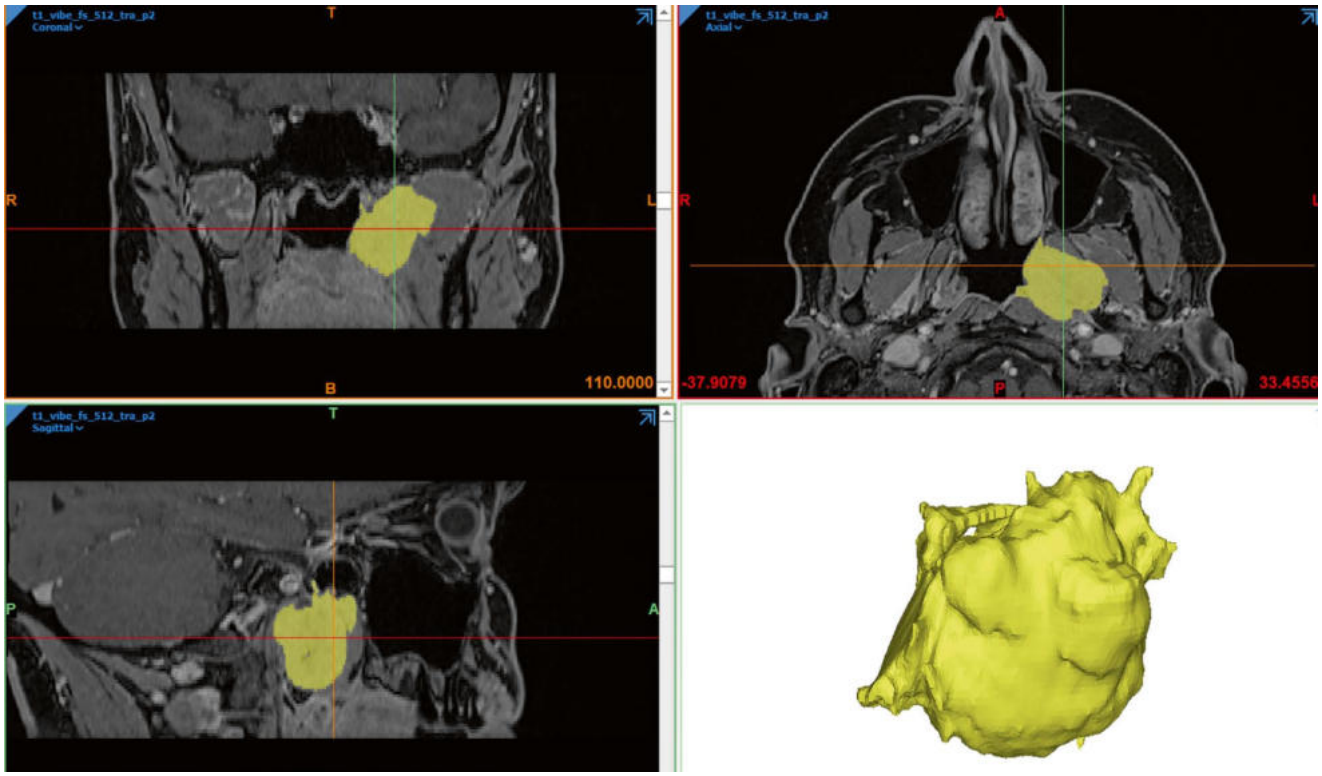


Fig. 3 Isotropic MR T1-VIBE sequence enables successful MPR reconstruction and provides a good image quality to segment soft tissue lesions, including tumors (yellow, a pterygo-palatine fossa adenoid-cystic carcinoma)

- *Magnetic Resonance Angiography (MRA)*: Used to visualize blood vessels. The technique relies on the flow of blood to generate images highlighting the vascular structures. It can be enhanced by using contrast agents.
- *Diffusion MRI*: Used to map the diffusion process of molecules, mainly water, in biological tissues, and is used to measure the random motion of water molecules within tissues. By analyzing the direction and magnitude of water diffusion, it can provide detailed images of the brain's microstructure.

2.4 Ultrasound

General Definition Ultrasound imaging, also known as sonography, is a noninvasive imaging technique that uses high-frequency sound waves to create real-time images or videos of internal organs and soft tissues. A device called a transducer or probe emits sound waves into the body, which bounce off structures and return to the probe. The returning sound waves are converted into electrical signals and processed by a computer to produce images. Ultrasound is particularly useful for imaging soft tissues and fluid-filled structures and it is widely used in various medical fields, including obstetrics, cardiology, and emergency medicine. The concept of using sound waves for imaging was first explored by Lazzaro Spallanzani in the late eighteenth century, and the first medical application was developed by Karl Dussik in 1942.

Fact *Dr. Lazzaro Spallanzani's early experiments focused on the study of bats in 1794 and they laid the groundwork for the principles of ultrasound.*

Specificity for CMF While less commonly used than CT or MRI, in CMF surgery, ultrasound is used to evaluate superficial soft tissue lesions and structures, such as salivary glands, lymph nodes, and vascular anomalies. It is also valuable for guiding needle biopsies of facial masses, providing real-time imaging to ensure accurate targeting. It is a noninvasive and real-time imaging modality.

Advantages and Drawbacks Ultrasound provides real-time imaging and is noninvasive. It does not use ionizing radiation, but it is less effective for imaging deep or dense tissues or structures that are obscured by bone or air. Ultrasound has a poor tissue to tissue contrast, which makes it difficult to segment.

2.5 Optical Scanning or 3D Photogrammetry

General Definition Optical scanning and 3D photogrammetry are noninvasive imaging techniques used to create detailed three-dimensional models of objects or anatomical structures. Optical scanning involves using laser or structured light to capture the shape and surface details of an object, while 3D photogrammetry uses multiple photographs taken from different angles to reconstruct a 3D model. Both methods are widely used in various fields, including engineering, architecture, and healthcare, to obtain precise digital representations of physical objects. On the one hand, optical scanning involves capturing reflected light using the scanner's sensors, which then process the data to generate a detailed 3D model. This technique is renowned for its high accuracy and ability to capture fine details, making it particularly well-suited for applications that demand precise measurements. On the other hand, 3D photogrammetry involves taking multiple photographs of an object from different angles. Specialized software analyzes the images to identify common points and reconstructs a 3D model based on the spatial relationships between these points. This method is particularly useful for capturing complex shapes and textures, and it is often more affordable and accessible than optical scanning.

Fact *The technology has evolved significantly since the development of early optical coherence tomography (OCT) in the early 1990s by Dr. James Fujimoto* et al. *and it was first used to image the human retina in 1993.*

Specificity for CMF In CMF surgery, both optical scanning and 3D photogrammetry are valuable tools for preoperative planning, intraoperative guidance, and postoperative assessment. These techniques provide detailed 3D models of the cranio-maxillofacial region and the facial structures, allowing surgeons to visualize and analyze the anatomical structures with high precision, superposing and integrating the 3D reconstruction of bones from CT or MRI scans with the facial reconstruction acquired with these techniques. This is particularly useful for planning complex reconstructive and plastic surgeries assessing bone deformities, and designing custom implants or prosthetics.

Advantages and Drawbacks

- *Optical scanning* offers high accuracy and detail, making it ideal for capturing intricate anatomical structures. However, it can be expensive and may require specialized equipment and training.
- *3D photogrammetry* is more affordable and accessible, and it can capture realistic textures and colors. However, it may be less accurate than optical scanning and can be affected by lighting conditions and the quality of the photographs. Both provide detailed surface images without radiation, but are limited to external structures and require integration with other imaging modalities for comprehensive planning.

The main applications of optical scanning nowadays are 1. intraoral scans and 2. 3D photogrammetry or face scans.

2.5.1 Intraoral Scan

General Definition An intraoral scan is a dental imaging technique that captures detailed digital images of the inside of the mouth. These scans are an alternative to traditional dental impressions and use a handheld scanner to create a precise 3D model of the oral cavity. The scanner emits a light source and captures the reflected light with sensors to generate the digital model. This technology is widely used in CAD/CAM dentistry for designing and manufacturing dental prosthetics (Fig. 4).

Fact *Intraoral scanners have significantly improved patient comfort by eliminating the need for messy impression materials. They also enhance the accuracy and speed of dental restorations.*

Specificity for CMF Intraoral scans are essential for creating accurate digital models of the dental arches and oral cavity, which are crucial for planning and executing complex cranio-maxillofacial surgeries. These scans provide the necessary detail to design prosthetic crowns (a process referred to as virtual wax-up, see Fig. 5), create occlusal splints, and simulate orthodontic treatment plans.



Fig. 4 Intraoral scan of a maxillary arch

Advantages and Drawbacks Intraoral scans provide high accuracy and patient comfort, but they can be expensive and require training to operate effectively.

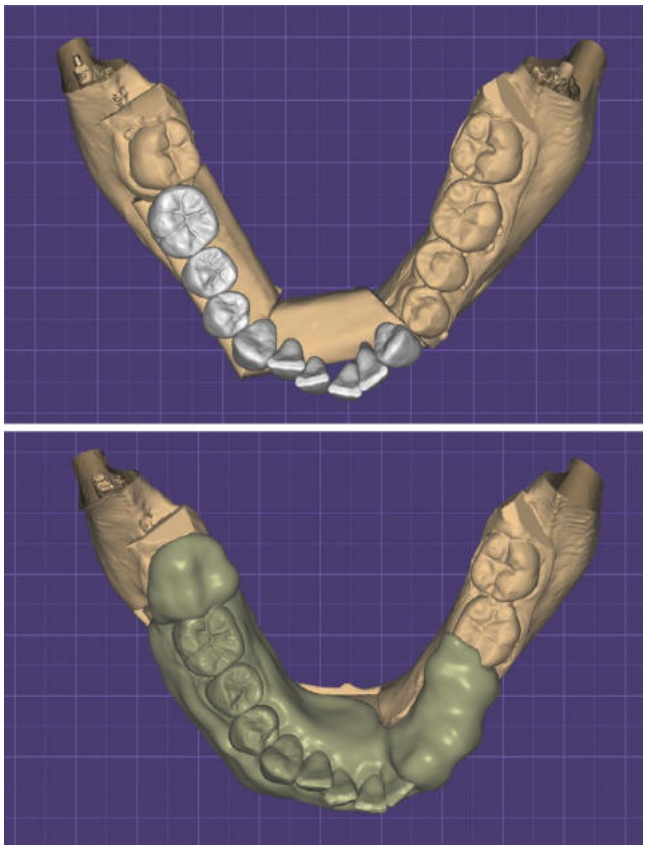


Fig. 5 Intraoral scan is used to create a diagnostic virtual wax-up to restore missing teeth (top panel) and manufacture a surgical guide for implant placement (bottom panel)

2.5.2 3D Photogrammetry or Face Scans

General Definition 3D photogrammetry, also known as face scanning, is a technique that uses multiple 2D images taken from different angles to create a detailed 3D model of an object or scene. This method combines principles of photography, mathematics, and computer vision to reconstruct the subject in a digital 3D space. It is widely used in various fields, including archaeology, film production, and medical imaging.

Fact *3D photogrammetry has been used to create realistic digital models of historical artifacts and archaeological sites, preserving them for future study and virtual exploration.*

Specificity for CMF In cranio-maxillofacial surgery, 3D photogrammetry is used to capture detailed images of the patient's face or dental models. These images are crucial for planning surgical procedures, creating custom implants, and ensuring precise alignment of facial structures. It is also used to help improve clinical-patient communication and patient comprehension of the final objective of the intervention (Fig. 6).

Advantages and Drawbacks 3D photogrammetry provides highly detailed and accurate models, but it requires multiple images and can be time-consuming to process.

2.6 Intraoperative Imaging

In cranio-maxillofacial surgery, as in other surgical specialties, several imaging techniques are commonly used in recent years in the operating room to enhance surgical precision and outcomes.

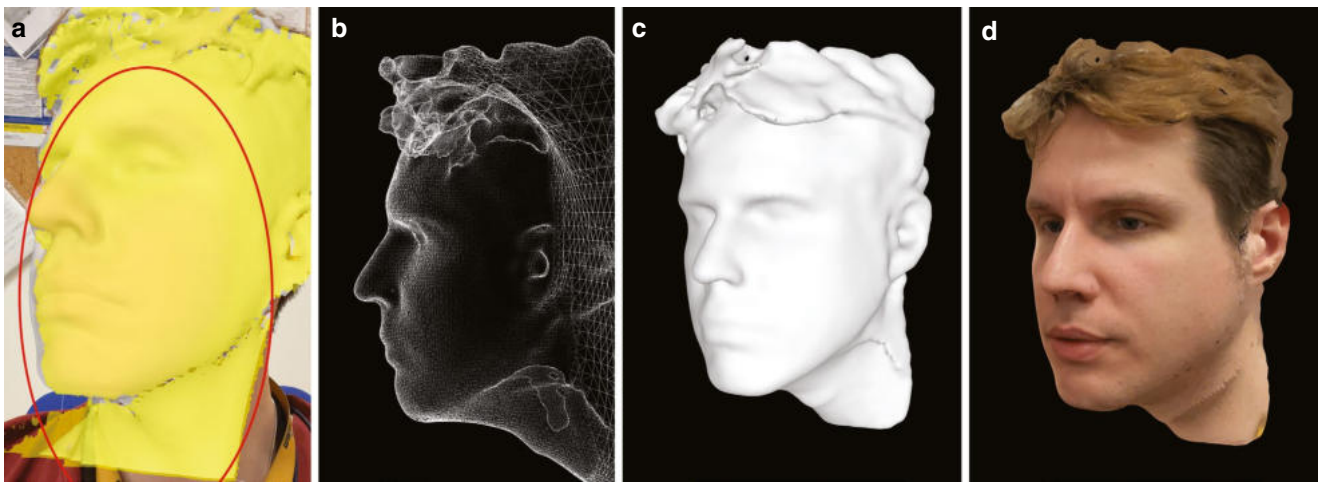


Fig. 6 Representation of the technical steps in a facial photometry: (**a**) scanned surface in yellow, (**b**) wireframe model and contours, (**c**) model surface, and (**d**) surface colorization. (Image under CC BY license [9])

In this section, the main imaging techniques and their specific characteristics and protocols for CMF diagnostic imaging in the surgical block are explored:

- *Intraoperative CT (iCT)*: Intraoperative CT scans provide real-time, high-resolution images of the surgical site, allowing surgeons to verify the success of the operation immediately while still in the operating room. This technology is particularly useful for checking implant placement and symmetry during procedures such as orthognathic surgery and trauma surgery.
- *Intraoperative CBCT (iCBCT)*: Cone-beam computed tomography (CBCT) is used intraoperatively to provide three-dimensional images with submillimeter spatial resolution and soft-tissue visibility in near real time. This technology is beneficial in procedures like zygomaticomaxillary complex fractures, orbital fractures, TMJ surgery, and orthognathic surgery [10, 11] (Fig. 7). In the Academic Hospital of Udine, the intraoperative CT scan used is SeeFactor CT3 from Imaginalis company (Imaginalis Srl, Sesto Fiorentino (FI), IT).
- *Ultrasound*: Ultrasound is used to evaluate soft tissue structures, such as salivary glands, lymph nodes, and vascular anomalies. In oncologic surgery, it has been used to some extent to map resection margins of neoplasms, especially in the tongue or salivary glands [12]. However, this 2D imaging with poor contrast is hardly usable for 3D reconstruction.
- *Intraoperative MRI (iMRI)*: Intraoperative MRI provides detailed images of soft tissues during surgery. It is particularly useful for assessing soft tissue tumors, inflammatory conditions, and vascular anomalies in the cranio-maxillofacial region.
- *Intraoperative Optical Coherence Tomography (OCT)*: OCT is a noninvasive imaging technique that uses light waves to capture high-resolution cross-sectional images of tissues. Its use in maxillofacial surgery is highly experimental, but has been tested to analyze fresh excised tissue specimens in oncologic surgery [13].
- *Fluoroscopy*: Fluorescence imaging is a real-time, intraoperative imaging technique that uses fluorescent dyes to highlight specific tissues, enhancing the surgeon's ability to visualize structures such as blood vessels, soft tissues, and tumors. A fluorescent dye, such as indocyanine green (ICG), is injected into the patient's bloodstream. A near-infrared light source is used and placed to excite the fluorescent dye in targeted tissues. Specialized cameras capture the emitted fluorescent light, generating real-time, high-contrast images. These images are displayed on surgical monitors, helping surgeons distinguish between tissues, identify critical structures, and confirm the surgical approach.
- Although fluoroscopy techniques have highly developed in oncologic surgery, in CMF surgery, fluorescence imaging has also been used to help delineate tumor margins in maxillofacial cancer surgeries, ensuring complete resection while preserving healthy tissues, and map the status of sentinel lymph-nodes [14]. In reconstructive surgeries, such as free flap transfers for jaw or face reconstruction, fluorescence imaging ensures adequate blood supply by visualizing perfusion [15]. During facial nerve preservation in procedures like parotidectomy, fluorescence helps locate and avoid critical nerves.



Fig. 7 Use of SeeFactor CT3 intraoperative CT in maxillofacial surgery to check the accuracy of alloplastic TMJ replacement in the Academic Hospital of Udine

3 Imaging Techniques and Sequences for CMF and 3D Reconstruction by Tissue/Indication

The most common medical imaging modalities for 3D printing and reconstruction are CT Scan and MRI mainly for its good tissue-tissue contrast and easy segmentation. In the following section, we describe the specific protocols for CMF conditions of MRI and CT scan:

- *Specific CT Protocols for CMF Conditions* (Table 2)
- *Advanced CT Techniques for CMF Imaging* (Table 3)
- *Specific MRI Protocols for CMF Conditions* (Table 4)
- *Advanced MRI Sequences for CMF Imaging* (Table 5)

Table 2 CT scan protocols for CMF conditions

Condition	CT protocol	Purpose/use
TMJ disorders (osteoarthritis, ankylosis)	High-resolution CT (HRCT)	Evaluate joint surfaces, bony erosion, condylar fractures, and joint ankylosis
	3D reconstruction (bone algorithm)	Provides clear visualization of joint surfaces and condylar structures
	Thin slices (≤1 mm)	
Facial fractures	CT with bone window algorithm	Detect fractures, bone displacements, and orbital trauma. For orbital fractures, ≤0.5 mm slice thickness is recommended
	Multiplanar reconstruction (MPR)	In coronal, sagittal, and oblique planes for a comprehensive fracture assessment
	3D volume rendering	To evaluate complex fractures or post-trauma deformities
Maxillofacial oncology (bone involvement)	CT with contrast (if soft tissue involved)	Assess tumor extension, bone destruction (T4a stage), and adjacent tissue invasion when soft tissue involvement is suspected
	Bone algorithm reconstruction	Assess bone destruction and invasion
	thin slices (≤0.5 mm)	
Congenital craniofacial anomalies	Low-dose CT (pediatric settings)	Evaluate craniosynostosis, maxillary or mandibular hypoplasia, and skull deformities
	Isotropic slices (submillimeter)	Precise evaluation of congenital defects
	3D CT reconstructions	For craniosynostosis or maxillofacial deformity assessment
Sinus and skull base infections	CT with soft tissue and bone window	Detect sinusitis, osteomyelitis, bone destruction, and intracranial extension
	Post-contrast CT (if indicated)	If there is a risk of intracranial extension
	Thin slices (≤1 mm)	Evaluate the full extent of sinus and skull base involvement
Facial nerve detection	High-resolution CT (HRCT)	Useful for detecting osseous abnormalities such as facial nerve canal fractures or ossicular erosion
	3D reconstruction (bone algorithm)	
	Thin slices (0.5–1 mm)	

Table 3 Advanced CT sequences for CMF surgery

CT Technique	Purpose	Use in CMF
High-resolution CT (HRCT)	Provides highly detailed images of bony structures with thin slices	Evaluate fractures, TMJ conditions, and cranial deformities
Multiplanar reconstruction (MPR)	Reconstructs axial images into coronal, sagittal, or oblique planes	Better visualization of complex fractures and bone deformities
3D volume rendering (VR) or cinematic rendering (CR)	Creates 3D models by combining multiple slices for a realistic view	Preoperative planning and anatomical modeling
Surface shaded display (SSD)	Highlights bone surfaces and boundaries	Visualizes skeletal anatomy and surgical guides
Bone algorithm reconstruction	Maximizes contrast between bones and soft tissue	Detects fractures, bone tumors, and implants
CT angiography (CTA)	Visualizes blood vessels with contrast injection	Evaluates vascular malformations, arteriovenous malformations (AVMs), and surgical planning
Low-dose CT (Pediatric Protocols)	Minimizes radiation exposure while maintaining diagnostic quality	Pediatric craniofacial imaging and congenital anomaly assessment

Table 4 MRI protocols for CMF conditions

Condition	Sequences	Purpose/use
TMJ disorders (disc displacement, arthritis)	T1-weighted (Sagittal/Coronal)	Evaluates disc position, joint anatomy
	T2-weighted (Sagittal/Coronal)	Detects effusions, joint deterioration and inflammation
	Proton density (PD)	Improves contrast of soft tissues
	Dynamic MRI (Cine MRI)	Assesses disc movement during jaw motion
Maxillofacial oncology and soft tissue lesions	T1-weighted (Pre-/Post-contrast)	Assessed tumor margins and vascularity
	T2-weighted	Detects cystic or necrotic components
	Fat suppression (STIR, T2 FS)	Enhances visibility of tumors by suppressing fat signals
	DWI (Diffusion-Weighted Imaging)	Assesses tumor aggressiveness and detect metastases

(continued)

Table 4 (continued)

Condition	Sequences	Purpose/use
Congenital craniofacial anomalies	3D T1/T2 isotropic sequences (CUBE, SPACE, VISTA)	For detailed 3D reconstructions of craniofacial anatomy
	T1/T2 coronal/sagittal	Assesses brain structures if cranial involvement is suspected
	MR angiography (MRA)	Evaluates vascular anomalies
Infections (abscesses, sinusitis, osteomyelitis)	T1-weighted	Detects bone marrow involvement
	T2-weighted & STIR	Highlights fluid, edema, and inflammatory changes
	Post-contrast T1 FS	Delineates abscess walls and sinus infections
	DWI	Differentiates abscesses from cystic lesions
Vascular abnormalities (AVMs, hemangiomas)	Time-of-flight (TOF) MRA	Visualizes vascular blood. Flows without external contrast media (Gd)
	Contrast-enhanced MRA (CE-MRA)	High-resolution vascular imaging with external contrast media (Gd)
	T2-weighted (standard or with fat-suppression: STIR o DIXON).	High anatomy and tissue information: i.e., soft tissue venous malformations
Facial nerve detection	T1-weighted (consider contrast enhancement)	Highlights nerves affected by tumors (i.e., schwannomas or paragangliomas), inflammation, or post-surgical changes
	High-resolution, thin-slice (≤1 mm) imaging	
	T2-weighted (T2W) & T2 Fat-suppressed	Detects nerve inflammation, edema, and lesions due to high fluid sensitivity
	3D-CISS (constructive interference in steady state)	Provides detailed visualization of cranial nerves in fluid-filled areas (CSF spaces) and cerebellopontine angle (CPA)

Table 5 Advanced MRI Sequences for CMF

Sequence	Purpose	Use in CMF
STIR (short time inversion recovery) or DIXON	Suppresses fat signals to highlight fluid and edema	Detects tumor, inflammation, trauma
FLAIR (fluid-attenuated inversion recovery)	Suppresses cerebrospinal fluid signals for better brain lesion visibility	Evaluates brain involvement in cranial anomalies
DWI (diffusion-weighted imaging)	Measures water molecule movement; highlights restricted diffusion	Differentiates abscesses from cysts and detect tumor metastases
Post-contrast T1-weighted with fat suppression	Enhances tissue contrast for vascular and inflamed areas	Detects tumor margins, abscess walls, facial nerve enhancement, and vascular anomalies
3D isotropic sequences (CUBE, SPACE, VISTA)	Provides high-resolution 3D reconstructions	Surgical planning, TMJ evaluation, craniofacial deformities
Diffusion tensor imaging (DTI) (nerve detection)	DTI measures the diffusion of water molecules along nerve fibers, enabling nerve tract visualization through fiber tractography	Identifying and segmenting cranial nerves, especially the facial nerve, trigeminal nerve (CN V), and optic nerve (CN II) Mapping nerve pathways in tumor surgery and post-traumatic evaluations
3D-CISS (constructive interference in steady state) (Nerve detection)	*High-resolution* imaging of structures near or within *fluid-filled spaces* (e.g., the *inner ear, internal auditory canal (IAC), cerebellopontine angle (CPA),* and *cerebrospinal fluid (CSF)*).	Highly sensitive to *soft tissues* and *fluid* (such as *nerves* and *tumors*)
FIESTA (fast imaging employing steady-state acquisition) (nerve detection)	Emphasizes imaging of fluid-filled spaces, specifically for high-contrast views of cranial nerves, blood vessels, and tumors	Particularly useful for visualizing *small nerve pathways* like the *facial nerve, trigeminal nerve,* and *vestibulocochlear nerve*

4 Protocols for VSP

4.1 CT Scan Parameters

General

Gantry tilt/oblique angle	0°
Reconstructed slice increment	≤ slice thickness
Reconstruction algorithm	Bone or high resolution

CT Scan Head

	Slice thickness	Pixel size	Patient positioning
CT parameters	Recommended: 1.00 mm Maximum: 1.25 mm	Recommended: 0.5 mm Maximum: 1.0 mm	Supine

CT Scan Bone flaps

	Slice thickness	Pixel size	Patient positioning
Fibula flap	Recommended: 1.00 mm Maximum: 3.00 mm	Recommended: 0.5 mm Maximum: 1.0 mm	Supine
Scapula, hip, rib flap	Recommended: 1.00 mm Maximum: 2.50 mm	Recommended: 0.5 mm Maximum: 1.0 mm	Supine

Field of view (FOV) Depending on the region and condition, the FOV should include the necessary regions including anatomical references (e.g., ear canal and orbits) but limited to needed structures taking into account the time and radiation:

- Ears (TMJ)
- Nose and chin (Trauma, Tumors, and Orthognatics)
- Left and right temporomandibular joint (TMJ, Orthognatics)
- Other regions of interest if required (e.g., cranium)
- For reconstruction cases, the complete tumor/defect

Current protocol At the University Hospital of Udine, all CT examinations are usually performed with or without contrast media (CM) injection from the vertex capitis to the lower margin of the mandible on a multidetector-row (64 or 128) scanner. The main technical parameters for CT include 100 kV; 120 mA; row thickness 1/4 0.625; noise index 1/4 7; rotation time 1/4 1.0 s.

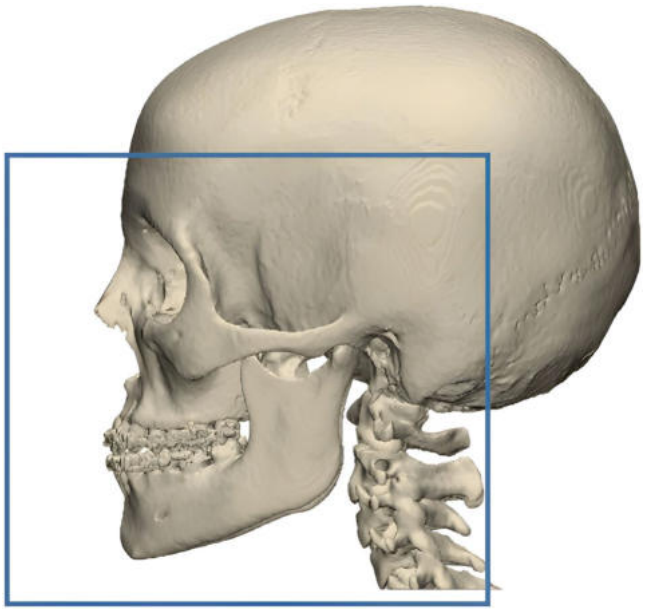


Fig. 8 Required field of view (FOV) for planning orthognathic surgery

- *CBCT Scan Parameters*

General

Field of view	Largest available
Reconstruction algorithm	Sharpest available

CBCT Scan Parameters

	Voxel size	Patient positioning
CBCT parameters	Recommended: 0.3 mm Maximum: 0.5 mm	Supine

Patient positioning for CBCT used in orthognathic and TMJ surgery Patients should be seated or standing in a natural head position with a relaxed facial expression. It's important to avoid using chin rests or mouthpieces that could affect the upper airway and distort imaging results. Although no specific guidelines exist for respiration, consistency in this area is beneficial. Figure 8 represents the ideal FOV for CBCT in orthognathic surgery.

4.2 MR Scan Parameters

There are several important aspects to consider when planning MRI acquisition. The following should be highlighted:

- A general balance must be found between the number and type of sequences and the acquisition time. There is a risk that very lengthy studies may cause the patient to move, thereby impacting the quality of the final image (motion artifacts).
- It is important to find a balance between the 3D image, which can be fused with other modalities and will maintain anatomical proportions, and the 2D image, which allows for very high resolution in the acquisition plane. In this regard, it is crucial to have good tissue resolution to enable the most precise possible segmentation.
- In general, 3D sequences should have isometric voxel size, ideally equal to or less than 1 mm in all three planes. In cases where multiple 3D studies are performed (e.g., pre- and post-contrast T1, T2, etc.), try to maintain the same angulation and voxel characteristics in all of them.
- In 2D sequences, the goal is to ensure there are no gaps between each section and that the slice thickness through the plane is not excessive to avoid excessive distortions in the 3D reconstruction.

General

Reconstructed slice	≤ slice thickness with NO GAP
	Minimal 2 different sequences (T1 and T2)

3D MRI scan (T1 pre- or post-contrast, T2, DIR or FLAIR and DIXON)

	Slice thickness	Patient positioning
3D imaging parameters	Recommended: 1 × 1 × 1 mm Maximum size voxel in 1 plane: 2.00 mm	Supine

Field of view (FOV) in MRI Depending on the region and condition, the FOV should include the necessary regions including anatomical references (e.g., ear canal and orbits) but limited to needed structures taking into account the time (higher FOV, higher acquisition time but also high signal-to-noise ratio):

- Ears (TMJ)
- Nose and chin (Trauma, Tumors, and Orthognatics)
- Left and right temporomandibular joint (TMJ, Orthognatics)
- Other regions of interest if required (e.g., cranium)
- For reconstruction cases, the complete tumor/defect

Current protocol At the University Hospital of Udine, MR examinations are generally performed on a 1.5 or on a 3.0 Tesla scanner before and after CM administration. The standard MR acquisition protocol includes non-enhanced axial and coronal turbo spin echo (TSE) T2W sequences with and without fat suppression, axial spin echo (SE) T1W sequences, axial diffusion-weighted imaging (DWI), and enhanced VIBE-T1W and 3-dimensional (3D) T2- and T1-weighted sequences.

MR 3D or volumetric sequences are essential in order to achieve a unique image containing the most relevant information of the two different techniques (CT and MR) by merging digital imaging and communication in medicine (DICOM) datasets.

The main technical parameters of the 3D-T1-weighted sequence are the following: TR 1/41400 ms; TE 1/4 3.5 ms; slice thickness 1/4 1.0 mm; number of slices 1/4240; FOV 1/4223, “255; flip angle 1/4 15.

In some cases to better delineate the anatomical relationships between the lesion and vascular structures (e.g., both extracranial portions of the internal carotid artery and external carotid artery or veins), patients undergo 3D time-of-flight (TOF) and 2D-TOF or PC (phase contrast) MR angiography and venography sequences. MR angiography is ideal to trace the course of the carotid and its bifurcation and has the appropriate resolution to identify important vessels of the splanchnocranium like the internal maxillary artery (Fig. 9). The MR venography sequence is adapted for the study of posterior cranial fossa, paying particular attention to the positioning of saturation slabs and carefully avoiding any possible inflow artifacts. It should be acquired using a 3 T magnet for more reliable reconstructions, which provides excellent segmentation of the internal jugular vein and venous sinuses (Fig. 10).

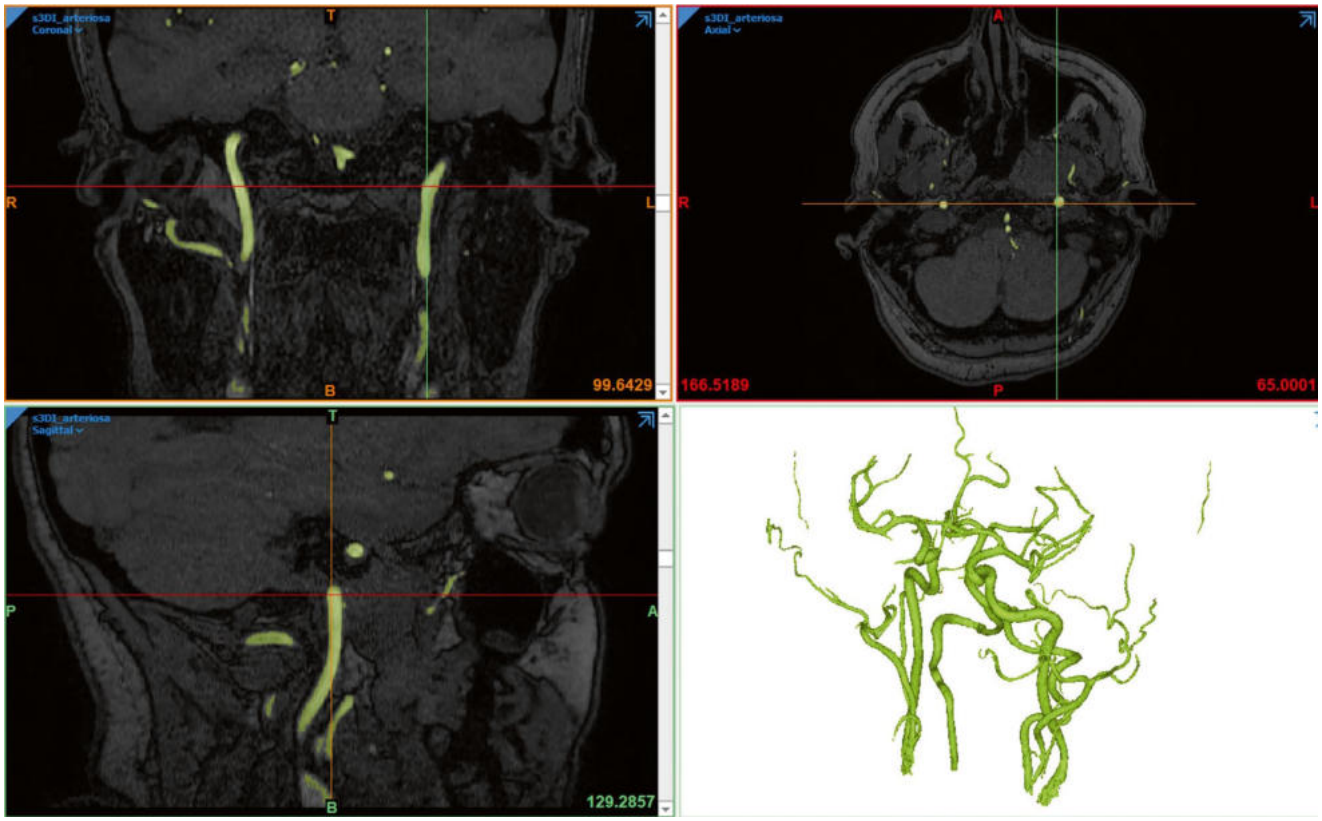


Fig. 9 TOF sequence for virtual arteriography performed with optimal standards. The internal maxillary artery is clearly visible in axial projection

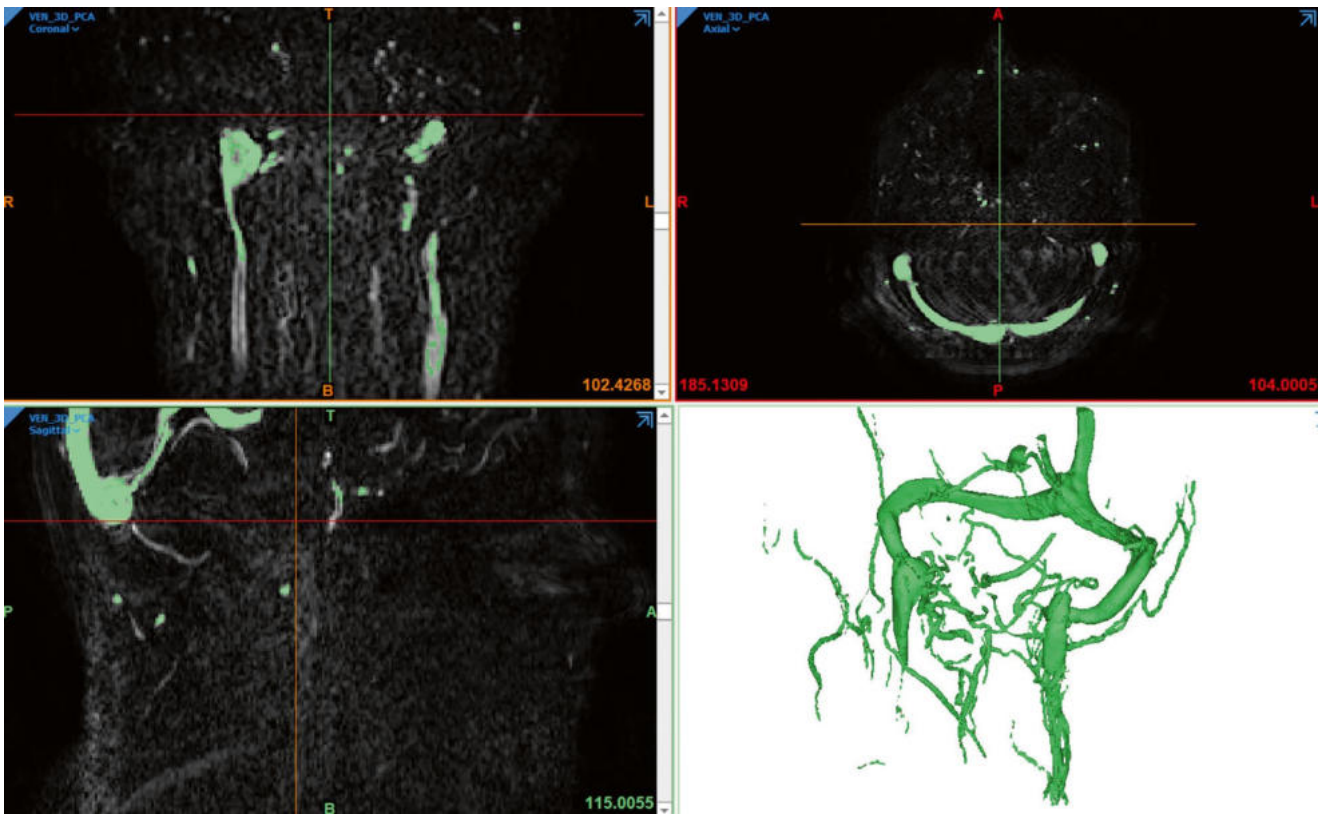


Fig. 10 VEN3D sequence for virtual venography performed with optimal standards

5 Image Reconstruction Techniques (Diagnostic Value)

CT (and CBCT) and MRI are the primary imaging tools used in diagnosing cranio-maxillofacial pathologies. In complex cases, combining both CT and MRI can significantly enhance the accuracy of imaging reconstructions and improve the visualization of both soft and hard tissues (Fig. 11).

Recent advancements in post-processing techniques, such as 3D printing (3DP), virtual reality (VR), and augmented reality (AR), have gained popularity for providing advanced 3D visualizations of anatomical structures. These innovative techniques add several steps to the digital workflow of surgical planning and require specialized software, hardware, and personnel with the required knowledge. However, most MRI and CT scan software include post-processing projection techniques and filters that facilitate 3D reconstruction visualization and enhanced imaging (Fig. 12).

Medical imaging projections or renderings are visual representations of imaging data from CT and MRI scans and

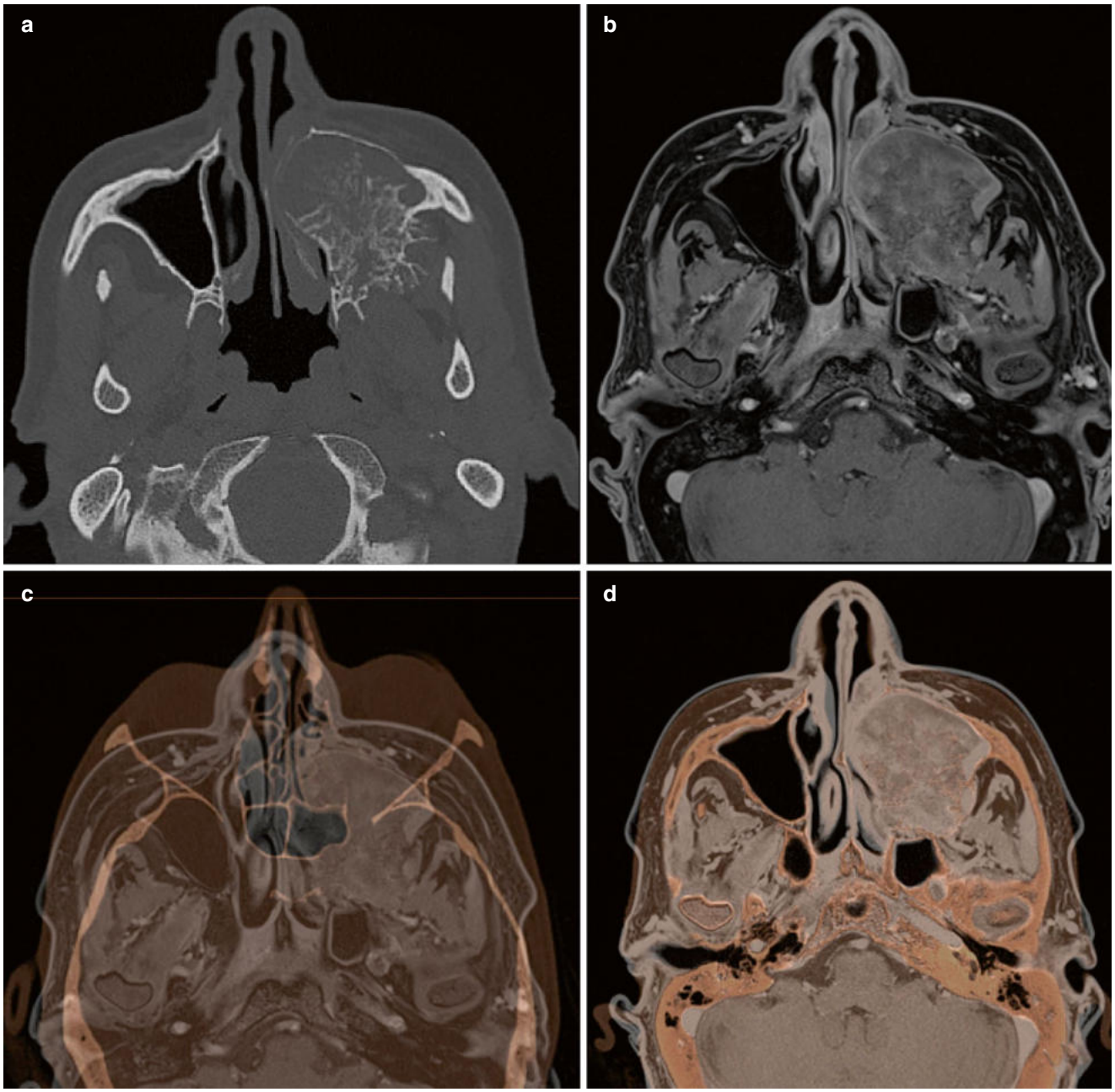


Fig. 11 Combining more imaging modalities yields the highest diagnostic accuracy. Bone CT scan (**a**) and T1 post-contrast MRI (**b**). Algorithms for imaging coregistration are highly reliable (**c** and **d**)

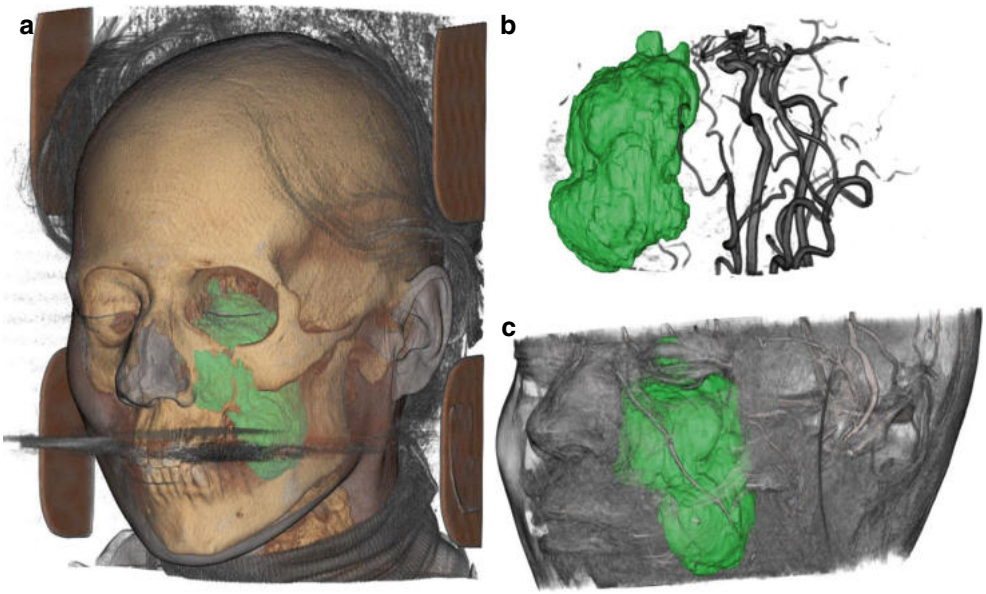


Fig. 12 Cinematic rendering (CN) associated with the segmented and tessellated STL volume of a massive odontogenic myxoma. (**a**) CT-CN; (**b**) TOF-CN; (**c**) T1-VIBE-CN

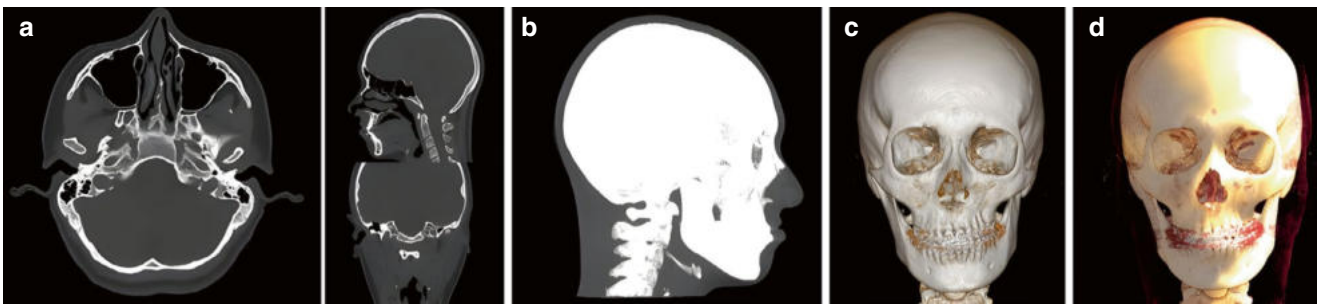


Fig. 13 (**a**) MPR, (**b**) MIP, (**c**) VolR, (**d**) CR

can be of aid in the diagnostic process by providing 3D enhanced and filtered visualizations without adding a significant cost. However, unlike fully interactive 3D reconstructions (CAD designs), these techniques have limitations. They do not allow direct manipulation, such as cutting, implant design integration, or surgical approach simulation. As a result, while projections and renderings are valuable for diagnostic interpretation, they are less suitable for detailed preoperative planning and complex surgical simulations. These projections include:

- *Multiplanar Reconstruction (MPR):* This technique allows the visualization of images in multiple planes (axial, sagittal, and coronal) from a single dataset. It helps in understanding the spatial relationships between different anatomical structures.
- *Volume Rendering (VolR):* VolR creates a 3D representation of the scanned volume by assigning colors and opacities to different tissues based on their densities. This technique provides a comprehensive view of the anatomy, making it easier to identify and analyze complex structures.
- *Maximal Intensity Projection (MIP):* MIP displays the highest intensity values within a specified volume, highlighting structures like blood vessels and bones. It is particularly useful for visualizing vascular structures and detecting abnormalities.
- *Cinematic Rendering (CR):* CR uses advanced lighting and shading techniques to produce photorealistic 3D images of anatomical structures. This method enhances the depth and detail of the images, providing a more intuitive understanding of the anatomy.

These imaging projections enhance the diagnostic process and surgical planning by providing detailed and accurate visualizations of the anatomical structures involved in CMF pathologies (Fig. 13).

6 Imaging Segmentation for 3D Reconstructions

In 3D planning, a key aspect is image segmentation. Segmentation is defined as the process of partitioning a medical (DICOM) image into multiple areas to isolate and analyze specific regions of interest [16]. This process represents the basic step before any VSP is conducted, as it enables to reconstruct specifical structures from the dataset. Such structures are defined by a segmentation mask, which is the partition corresponding to the shape of the intended target isolated across all slices in the x, y, and z axes. Segmentation masks are then converted into respective geometrical, tessellated entities, using algorithms such as the marching cube and ray casting (see previous chapter). There are several methods by which segmentation is conducted:

1. *Manual Segmentation*
   - Radiologist, surgeons, and engineers manually outline structures, ensuring precision in complex cases.
2. *Semi-Automatic Segmentation*
   - Combines human input with AI-based tools that apply algorithms like diffusion tensor imaging (DTI)-based fiber tracking to refine segmentation.
3. *Automatic Segmentation*
   - Machine learning models trained on annotated datasets perform fully automated segmentation of anatomical structures, like atlas segmentation. Such methods can be fully supervised, semi-supervised, or unsupervised [17].

Data quality is a critical factor in obtaining accurate and reliable 3D reconstructions. When deploying 3D segmentation to generate detailed models, it is essential to ensure data completeness, ensuring all relevant structures and anatomical references are included. Additionally, minimizing noise and artifacts, addressing resolution discrepancies, and maintaining consistent contrast and intensity are vital steps for producing high-quality reconstructions.

Among medical imaging modalities, CT and MRI are the most commonly used for 3D reconstructions due to their superior tissue-to-tissue contrast, which is crucial for accurately visualizing anatomical structures. Depending on the tissues of interest, these modalities offer excellent differentiation between various tissues. In contrast, ultrasound and other imaging techniques do not provide the same level of tissue contrast, which can complicate the segmentation process and reduce the accuracy of 3D reconstructions. The following paragraphs detail semi-automated segmentation methods that, owing to their reproducibility and reliability, represent the gold standard to map a given anatomical structure.

6.1 Segmentation of Bone Structure: Global Thresholding

Bones have high intensity values on CT scans due to their density, which makes it a great option to do automatic segmentation, being simple and fast. The gold-standard method is based on thresholding, which captures all the voxels above a given threshold, which is highly effective for hyperdense structures such as mineralized bone and metal. However, this method might lead to inaccuracies in CBCT owing to their quantitative gray values outside the Hounsfield range. Moreover, contrast-enhanced CT can also represent a problem, since hyperdense vessels are acquired exactly as bone structures, and subsequent separation between the bone and the convoluted course of vessels might not always be easy, especially in the splanchnocranium and the cervical spine (Fig. 14). For this reason, the authors recommend reconstructing the bone in a standard CT, coregistering an MR sequence for vessel tracking, and segmenting the vessels from sequences such as TOF and VEN3D. The application of

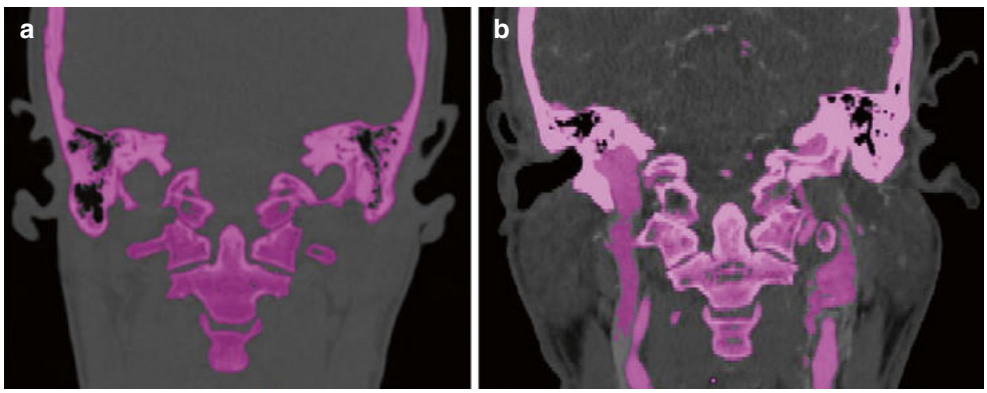


Fig. 14 Global thresholding. Left panel: bone CT. Right panel: contrast-enhanced CT. In the latter situation, the method fails in providing clean bone interfaces, as vessels cannot be isolated

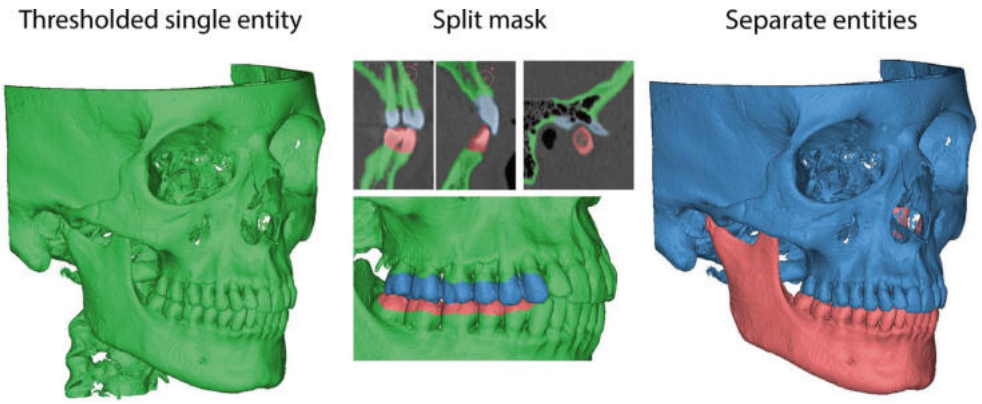


Fig. 15 Application of the split mask algorithm. Remarkably, latest releases of Mimics enable the algorithm to work also applied in 3D VolR masks

region growing to the segmented bone mask yields two separate objects in the eventuality that there is no contact point between two different areas within the segmentation mask. As this is a rare eventuality, separate bones are split along contact interfaces using the split mask algorithm, which is highly performant in Materialise Mimics (Materialise NV, Leuven, BE), as shown in Fig. 15.

6.2 Segmentation of Vessels

Segmentation of vessels can be performed either with global thresholding from suitable MR sequences (MR-TOF and VEN-3D), as illustrated in Figs. 9 and 10. Eventually, but least effectively, dynamic region growing can be implemented. Dynamic region growing is a semi-automated method in which the user places a "seed" in a target region, and the algorithm identifies neighboring isodense voxels within a predefined interval—typically around 50 Hounsfield Units (HU); moreover, voxels are selected with a proximity criteria, sampling them by spatial continuity. Thus, the algorithm is useful for vessel segmentation, especially in contrast-enhanced CT scans.

6.3 Segmentation of Soft Tissue

Segmentation of soft tissue might be indicated to outline particular anatomical structures, for instance, muscle bellies (masseter, temporalis, extraocular muscles), glands (parotid and submandibular gland), or fat compartments. However, the great importance of the following methods is undoubtedly represented by segmentation of tumors. Hereby, the authors propose the two most valuable methods as an alternative to the time-consuming and inaccurate slice-by-slice manual segmentation, which is now obsolete. However, slice-by-slice editing can be used after semi-automated methods have been applied to refine the result and detail particulars neglected by the working algorithm. The following methods, if well used, might account up to 90% of segmentation of a soft tissue lesion, assuming that the lesion is represented in the best suitable contrast phase of a CT or the most favorable gadolinium impregnation of a contrast-enhanced MR:

- Dynamic region growing: for the mathematical properties of this algorithm, it is a functional method in MR. It might fail, however, when the lesion has heterogeneous intensity components, for instance a solid mass with a colliquate, necrotic center, as the latter would appear a different entity for the algorithm. Moreover, an ROI should be assigned to avoid that far regions are included as well, resulting in inaccuracies and a dramatic increase in the computational time. The lesion can be outlined, but mask split (or mask editing) has to be applied across its boundaries (Fig. 16).
- Smart brush: brushes are user-controller that enable to outline focal parts of the image. They can be adjusted in size to be more or less fine depending on the necessary detail. Smart brushes are powered by AI algorithms that make lesion contouring highly efficient, streamlining the workflow of lesion segmentation. The smart brush introduced in Mimics can efficiently include the lesion contours in multiple planes with few user inputs. Moreover, it is also highly effective for slice-by-slice adjustments, as it interpolates its action even across few slices based on its diameter and can perform mask subtraction as well (Fig. 17).

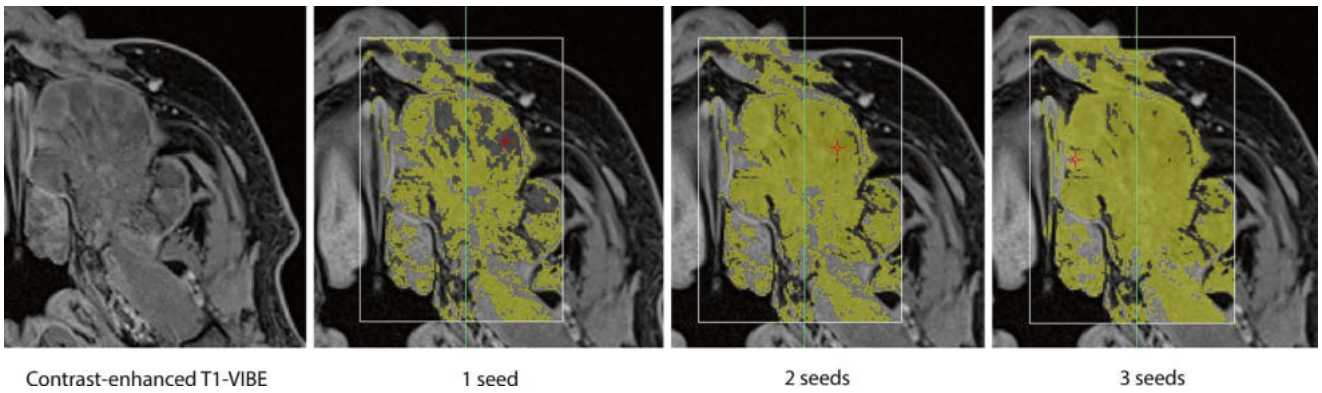


Fig. 16 Application of dynamic region growing with different seeds

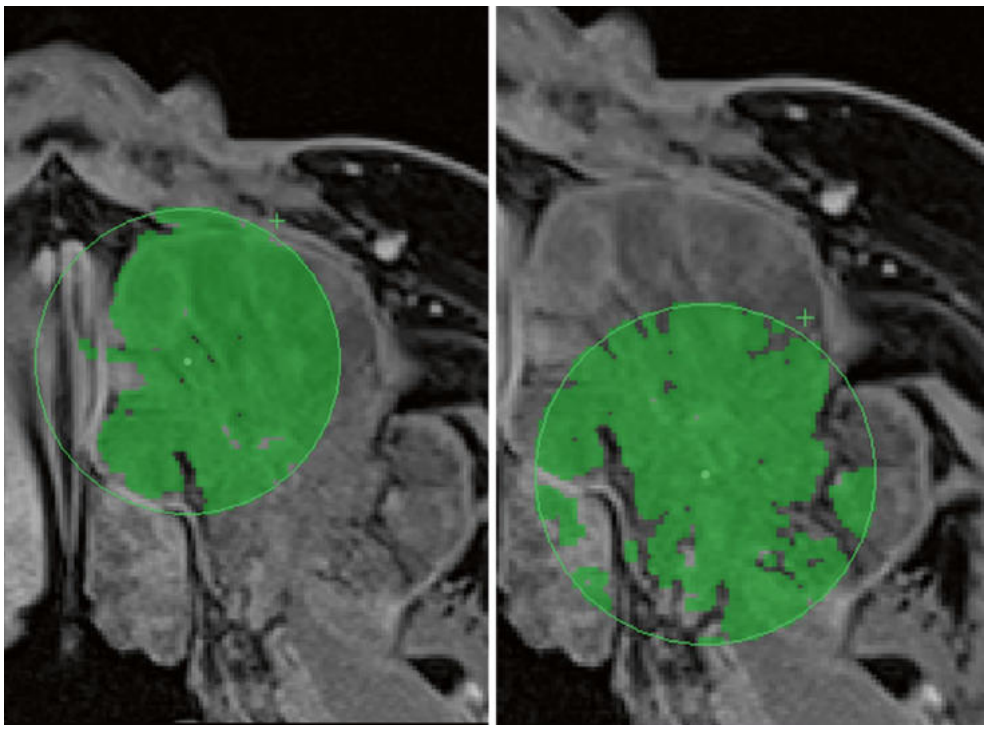


Fig. 17 Use of smart brush technology in Mimics

7 The Ten Commandments of a Good Imaging Acquisition for CMF Surgery

1. *Thou Shalt Use the Thinnest Slices Possible*
   Acquire slices as thin as clinically reasonable (≤ 1 mm) to ensure precise anatomical detail and high-quality 3D reconstructions.
2. *Thou Shalt Ensure True 3D Isotropic Models*
   Acquire at least one 3D ISO dataset with isotropic voxels, enabling accurate anatomical representations without distortion.
3. *Thou Shalt Include Anatomical Reference Points for Image Fusion*
   Use landmarks like the nose, ears, and dental occlusion to facilitate multimodal image fusion and ensure consistent anatomical alignment.
4. *Thou Shalt Not Cut Critical Structures*
   Never crop essential anatomical regions; always cover the entire face and skull when imaging the CMF area.
5. *Thou Shalt Acquire Images Close to the Date of Surgery*
   For surgical planning, especially in neonates and growing children, perform scans as near as possible to the surgery date (ideally within 1–2 weeks in neonates, infants, or oncologic cases).

6. *Thou Shalt Standardize Patient Positioning*
   Position the patient in a neutral, midline orientation to avoid head tilt or rotation, ensuring accurate 3D representations.
7. *Thou Shalt Minimize Motion Artifacts*
   Use sedation or immobilization when needed to prevent motion artifacts, ensuring the highest diagnostic quality.
8. *Thou Shalt Choose the Right Imaging Modality*
   Use *CT* for bone detail and trauma and *MRI* for soft tissue and nerve mapping.
9. *Thou Shalt Use Contrast Agents When Required*
   Apply contrast agents when necessary to enhance visibility of soft tissues, tumors, and vascular structures.
10. *Thou Shalt Document and Standardize Protocols*
    Follow established CMF imaging protocols, including field of view, slice thickness, and image orientation, ensuring reproducibility and consistency across institutions.

The software is powerful, yet not magical. It optimizes available data.

8 Safe and Appropriate Imaging

An important aspect in the use of imaging for 3D planning is to consider the reason for its use.

This type of techniques does not have only a radiological diagnostic objective but rather serves as a complement to it, especially for planning the best treatment.

Therefore, it is important that the use of this technology is based on the appropriate indication for each pathology as well as, particularly, on the safe use of the technology. This aspect is especially important when using modalities that emit radiation or exogenous contrast agents such as iodine or gadolinium.

The clinical balance of minimizing risks must, along with the clinical indication, be a crucial aspect when, for example, deciding to repeat a study or perform a new one on the patient.

8.1 Safe Imaging in the Pediatric Population

Children are not small adults; they are developing human beings undergoing a process of growth. As such, their bodies have specific needs and may present with pathologies that differ from those of adults. Therefore, diagnostic and treatment medical products must be tailored to their specific needs and age. Imaging in the pediatric population, for instance, requires special considerations to ensure the safety, comfort, and effectiveness of diagnostic procedures. Children are more sensitive to radiation and may have difficulty staying still during imaging, necessitating tailored approaches. This section will explore various aspects of pediatric imaging, including techniques to minimize radiation exposure, the use of non-ionizing methods, and strategies to create a child-friendly environment.

8.1.1 Lower Radiation Doses

Pediatric patients might be as much as 10 times more radiosensitive than adults. Thus, it is crucial to appropriately adapt the radiation doses. The most common strategies to fulfill this goal are the following:

- *ALARA Principle*: The ALARA (As Low As Reasonably Achievable) principle is a safety standard in pediatric imaging that aims to minimize radiation exposure while achieving the necessary diagnostic quality. This principle is crucial because children are more sensitive to radiation and have a longer life expectancy, increasing the potential for radiation-induced effects [18, 19].
- *TDS (Time Distance Shielding)*: Another general principle broadly used in children is the TDS. Although being applicable to all populations, it gain more importance in children. This principle mainly focus on three concepts to be applied whenever possible in any imaging acquisition:
  - Minimize the time a child is exposed to radiation source.
  - Maximize child's distance from the radiation source.
  - Maximize the shielding between the source of radiation and the child applying.
- *Size-Based Dosing*: Pediatric imaging protocols often use size-based dosing to adjust the amount of radiation according to the child's size and weight. This approach ensures that the radiation dose is appropriate for the child's body, reducing unnecessary exposure while maintaining image quality. In ionizing techniques such as X-Ray or CT Scans, it is of most important to adapt protocols. Nowadays, multiple strategies exist to lower the exposure of children to radiation without conditioning diagnostic reliability. To reduce the dose of ionizing radiation in conventional X-ray examinations, it is crucial to correctly adjust the tube voltage, utilize tube filters, ensure proper patient positioning and stabilization, selectively use a scattered-radiation grid, and employ a modern storage-plate system. In CT scans, implementing protocols tailored to the patient's age, weight, and specific medical indications can decrease radiation exposure by up to 95% [20]. The common parameters are discussed in Table 6.

Table 6 CT scan dose parameters for pediatric patients based on body weight categories

Body weight	kVP (kilovoltage peak)	mAs	Pitch	CTDI (computed tomography dose index) mGy	DLP (dose-length product) mGycm	Effective dose mSv	Dose reduction
<15 kg	120	20	1	3.6	87	1.8	
	100	20	1	2.3	85	1.1	36%
<25 kg	120	35	1	6.3	150	3.2	
	100	35	1	4.0	145	2.0	36%
<35 kg	120	55	1	9.9	237	5.1	
	100	55	1	6.3	225	3.37	36%

8.1.2 Use of Non-ionizing Techniques

Non-ionizing imaging techniques, such as ultrasound and MRI, are preferred for pediatric patients to avoid the risks associated with ionizing radiation. These techniques provide high-quality images without exposing children to radiation, making them ideal for repeated imaging and long-term monitoring. In CMF imaging, ultrasound is particularly useful for evaluating soft tissue structures, such as salivary glands, lymph nodes, and vascular anomalies. For example, ultrasound can be used to diagnose conditions like sialolithiasis (salivary gland stones) and to assess the extent of hemangiomas (benign vascular tumors) in the facial region. It is also valuable for guiding needle biopsies of facial masses, providing real-time imaging to ensure accurate targeting. As mentioned before, MRI is essential for assessing soft tissue tumors, inflammatory conditions, and congenital anomalies. For instance, MRI is used to evaluate the extent of facial tumors, such as rhabdomyosarcoma, and to plan surgical interventions and complex conditions like craniofacial dysostosis (a congenital disorder affecting the bones of the skull and face).

8.1.3 Sedation and Anesthesia

Sedation and anesthesia are often required to ensure that pediatric patients remain still during imaging procedures, which is essential for obtaining clear images. This is particularly important in pre-term babies, newborns, and patients with mental health conditions. The most common administered drugs for sedation during radiological procedures in children are midazolam by intravenous, intramuscular, or rectal routes and oral temazepam [21]. Safe sedation practices involve careful pre-procedural evaluation; obtaining parental consent; following appropriate fasting; monitoring patients closely before, during, and after the procedure; and monitoring during and after the procedure. The goal is to balance the depth of sedation with the risk, ensuring the child's safety and comfort. It is important to note that sedation agents also impact the health of patients, particularly children, who are more sensitive than adults to the effects of anesthesia, especially on organs such as the brain or kidneys [22].



Fig. 18 Example of Hospital Sant Joan de Déu Barcelona diagnostic imaging equipment designed for improved patient experience

8.1.4 Child-Friendly Environment

Creating a child-friendly environment in imaging centers can significantly reduce anxiety and improve cooperation. This includes using colorful and engaging decor, providing distractions such as toys or videos, and having trained pediatric radiographers who can communicate effectively with children. A welcoming environment helps children feel more at ease, leading to better imaging outcomes (Fig. 18).

8.2 Rapid Imaging Techniques

Rapid imaging techniques are essential in pediatric imaging to minimize the time children need to stay still. Advances in technology have led to faster imaging protocols, reducing the need for sedation and improving the overall experience for young patients. Techniques such as fast MRI sequences and low-dose CT scans are examples of rapid imaging methods used in pediatrics. Those technologies when combined with advanced post-processing techniques using AI can improve efficiency and accuracy. This improvements not only help enhance the patient experience but also impact cost-effectiveness.

8.3 Communication and Explanation

Effective communication and explanation are vital in pediatric imaging. Radiographers and healthcare providers should use age-appropriate language to explain the procedure to both the child and their parents. Clear communication helps alleviate fear and ensures that the child understands what to expect, which can improve cooperation during the imaging process. Parental presence and participation are recommended and may play a key role in improving patient experience. The use of playful techniques to help explain and comprehend the procedure may help, as well as the use of new products such as VR systems to know the procedure before coming to the radiology room.

8.4 Protocols for Contrast Use

Current radiological literature is heavily focused on the risks associated with radiation imaging. While there is a small but real increase in cancer risk from exposure to ionizing radiation in children, it is also important to recognize that alternative imaging techniques can also pose risks to patients. One such risk involves the use of contrast agents, particularly gadolinium-based contrast agents, which are among the most commonly used [23]. Although generally considered safe, gadolinium deposits have been observed in the brain and bones of patients, a condition known as "gadolinium storage condition" [24]. The long-term and cumulative effects of retained gadolinium and other agents in the brain and other tissues are described but not yet fully understood. Given the sensitivity of pediatric patients, it is crucial to protect them from potential harm. Therefore, it is recommended to use low-dose contrast systems only when necessary and to consider alternative imaging techniques whenever possible. However, when used, specific protocols for contrast use in pediatric imaging are carefully designed to ensure safety and efficacy. The selection and dosing of contrast agents need to be tailored to the child's size and medical condition. Non-ionic contrast agents are often preferred due to their lower risk of adverse reactions. Additionally, protocols include guidelines for monitoring and managing potential side effects. In all of them it is important to take into account the following contraindications: allergies and reactions to the agents, previous reactions to iodinated contrast media, history of diabetes, kidney disease, solitary kidney, or prior kidney or other organs transplant and the potential interaction with other medication such as oral hypoglycemic agents.

9 The Ecological Impact of Imaging Acquisition Techniques

To conclude this section, we would like to emphasize the significant ecological impact that imaging acquisition technologies have on the planet. It is estimated that the healthcare sector contributes 4.0–8.5% of total global CO_2 emissions, with medical imaging being a significant energy-intensive component [25]. It is crucial to be informed and conscious of this impact because, like many new technologies we use, their highly beneficial health impacts come with a caveat that all users must know to make a proper use of the technology [26]. The production and disposal of imaging equipment, such as CT scanners, MRI machines, and X-ray devices, contribute to environmental pollution and resource depletion. These machines require significant amounts of energy to operate, leading to increased carbon emissions. Additionally, the use of contrast agents and other chemicals in imaging procedures can result in hazardous waste that needs to be carefully managed to prevent environmental contamination. The manufacturing process of these devices also involves the extraction and use of rare earth metals, which can have detrimental effects on ecosystems. Furthermore, the frequent updates and replacements of imaging equipment generate electronic waste, which poses a challenge for sustainable disposal and recycling. To mitigate these impacts, the medical community is exploring the use of more energy-efficient technologies, implementing recycling programs for electronic waste, and developing eco-friendly contrast agents. By adopting these measures, the healthcare industry can reduce its ecological footprint while continuing to provide essential diagnostic services.

Bibliography

1. AI in diagnostic imaging: revolutionising accuracy and efficiency – ScienceDirect. https://www.sciencedirect.com/science/article/pii/S2666990024000132?via%3Dihub. Accessed 29 Dec 2024.
2. Health C for D and R. Artificial Intelligence and Machine Learning (AI/ML)-Enabled Medical Devices. FDA; 2024.
3. The Nobel Prize in Physiology or Medicine 1979. In: NobelPrize.org. https://www.nobelprize.org/prizes/medicine/1979/summary/. Accessed 29 Dec 2024.
4. MRI vs CT Scan: Which is Better for Brain Imaging? | UCSF Radiology. https://radiology.ucsf.edu/blog/neuroradiology/exploring-the-brain-is-ct-or-mri-better-for-brain-imaging. Accessed 29 Dec 2024.
5. Pauwels R, Jacobs R, Singer SR, Mupparapu M. CBCT-based bone quality assessment: are Hounsfield units applicable? Dentomaxillofac Radiol. 2015;44:20140238.

6. MRI – Mayo Clinic. https://www.mayoclinic.org/tests-procedures/mri/about/pac-20384768. Accessed 29 Dec 2024.
7. The Nobel Prize in Physiology or Medicine 2003. In: NobelPrize.org. https://www.nobelprize.org/prizes/medicine/2003/summary/. Accessed 29 Dec 2024.
8. Magnetic Resonance Imaging (MRI). In: National Institute of Biomedical Imaging and Bioengineering. https://www.nibib.nih.gov/science-education/science-topics/magnetic-resonance-imaging-mri. Accessed 29 Dec 2024.
9. Rubio-Palau J, Prieto-Gundin A, Cazalla AA, Serrano MB, Fructuoso GG, Ferrandis FP, Baró AR. Three-dimensional planning in craniomaxillofacial surgery. Ann Maxillofac Surg. 2016;6:281–6.
10. Adell-Gómez N, Valls-Ontañón A, Malet-Contreras A, García-Piñeiro A, Gómez-Chiari M, Valls-Esteve A, Krauel L, Rubio-Palau J. Analysis of the implementation of a circuit for intra-operative superposition and comparison of the surgical outcomes using ICBCT in maxillofacial surgery. Int J CARS. 2024;19:2463–70.
11. Rubio-Palau J, García-Piñeiro A, Malet-Contreras A, Adell-Gómez N, Valls-Esteve A, Gómez-Chiari M, Munuera-Cerro J, Muchart-López J, Valls-Ontañón A. Use of intraoperative cone beam computed tomography and superposition of preoperative data in pediatric maxillofacial surgery. 2024. https://doi.org/10.21203/rs.3.rs-4787356/v1.
12. Au VH, Yoon BC, Juliano A, Sadow PM, Faquin WC, Varvares MA. Correlation of intraoperative ultrasonographic oral tongue shape and border and risk of close margins. Otolaryngol Head Neck Surg. 2023;168:1576–9.
13. Yang Z, Shang J, Liu C, Zhang J, Hou F, Liang Y. Intraoperative imaging of oral-maxillofacial lesions using optical coherence tomography. J Innov Opt Health Sci. 2020;13:2050010.
14. Hotchkies A, Saiyed S, Palaniappan S, Koroma P, Sarsam T, Falls D, Hanif S, Rahman S, ElBatawy A. Efficacy of indocyanine green fluoroscopy for sentinel node biopsy in head and neck melanoma: a systematic review and meta-analysis. Br J Oral Maxillofac Surg. 2024;62:595–603.
15. Galli A, Salerno E, Bramati C, et al. Indocyanine green fluorescence video-angiography for flap perfusion assessment in head and neck reconstruction: a prospective study. Eur Arch Otorrinolaringol. 2024; https://doi.org/10.1007/s00405-024-08959-5.
16. Zambrano-Vizuete M, Botto-Tobar M, Huerta-Suárez C, Paredes-Parada W, Patiño Pérez D, Ahanger TA, Gonzalez N. Segmentation of medical image using novel dilated ghost deep learning model. Comput Intell Neurosci. 2022;2022:6872045.
17. Konuthula N, Perez FA, Maga AM, Abuzeid WM, Moe K, Hannaford B, Bly RA. Automated atlas-based segmentation for skull base surgical planning. Int J Comput Assist Radiol Surg. 2021;16:933–41.
18. Strauss KJ, Kaste SC. ALARA in pediatric interventional and fluoroscopic imaging: striving to keep radiation doses as low as possible during fluoroscopy of pediatric patients--a white paper executive summary. J Am Coll Radiol. 2006;3:686–8.
19. Musolino SV, DeFranco J, Schlueck R. The ALARA principle in the context of a radiological or nuclear emergency. Health Phys. 2008;94:109–11.
20. Alzen G, Benz-Bohm G. Radiation protection in pediatric radiology. Dtsch Arztebl Int. 2011;108:407–14.
21. Starkey E, Sammons HM. Sedation for radiological imaging. Arch Dis Child Educ Pract Ed. 2011;96:101–6.
22. Arlachov Y, Ganatra RH. Sedation/anaesthesia in paediatric radiology. Br J Radiol. 2012;85:e1018–31.
23. Ramalho J, Ramalho M, Jay M, Burke LM, Semelka RC. Gadolinium toxicity and treatment. Magn Reson Imaging. 2016;34:1394–8.
24. Guo BJ, Yang ZL, Zhang LJ. Gadolinium deposition in brain: current scientific evidence and future perspectives. Front Mol Neurosci. 2018;11:335.
25. Merkle EM, Bamberg F, Vosshenrich J. The impact of modern imaging techniques on carbon footprints: relevance and outlook. Eur Urol Focus. 2023;9:891–3.
26. Roletto A, Zanardo M, Bonfitto GR, Catania D, Sardanelli F, Zanoni S. The environmental impact of energy consumption and carbon emissions in radiology departments: a systematic review. Eur Radiol Exp. 2024;8:35.

Overview of 3D Printing Technologies

Erik Kornfellner and Francesco Moscato

1 Generalities

The 3D printing technology has come a long way since it was first introduced in the 1980s, and today numerous 3D printing methods are available. Each method has its own unique advantages and disadvantages, and the right method for a particular application will depend on the materials being used, the size and complexity of the object, and other factors. Therefore, it is necessary to have knowledge of all the different 3D printing methods to make the right choice for clinical applications. The section will discuss the most common 3D printing methods, how they work, and what their advantages are.

Classifying the various types of 3D printing methods is not entirely straightforward. In ISO/ASTM 52900 [1], an attempt was made to clarify the terms related to 3D printing. However, there are still numerous classification possibilities. The essential ones can categorize 3D printing methods into seven classes, which share similarities in terms of base material or manufacturing technique. A well-arranged classification is shown in Fig. 1.

Furthermore, it is possible to differentiate the manner in which the 3D structure is created. One approach is solidification, in which a typically liquid raw material is transformed into a solid. An example of this is Stereolithography (SLA) printers, which cure a resin using UV light. When the printer operates through deposition, the three-dimensional geometry grows as material is continuously added. Examples of this include material jetting, where polymer droplets are deposited and cured voxel-wise, or fused deposition modeling, where heated plastic is extruded. Lastly, there are methods that operate through binding. In this process, prepared material, often a powder, is consolidated, either through thermal fusion or by the deliberate addition of an adhesive.

Before printing can commence, the digital design must be prepared accordingly for each printer. Since most 3D printers operate layer by layer, the term "slicer" has become established for the software that slices the design into printable layers. As not every 3D printer functions the same way, there are various slicers and settings available for different devices. The slicer software generates individual layers from the 3D model, depending on the chosen layer thickness. Additionally, in the slicer software, various parameters such as print temperatures, material feed rates, or exposure times can usually be selected to match the specific 3D printer and material being used. Ultimately, machine code can be exported from this software, which the printers can interpret to produce the desired component.

E. Kornfellner
Center for Medical Physics and Biomedical Engineering, Medical University of Vienna, Vienna, Austria
e-mail: erik.kornfellner@meduniwien.ac.at

F. Moscato (✉)
Center for Medical Physics and Biomedical Engineering, Medical University of Vienna, Vienna, Austria

Ludwig Boltzmann Institute for Cardiovascular Research, Vienna, Austria

Austrian Cluster for Tissue Regeneration, Vienna, Austria
e-mail: francesco.moscato@meduniwien.ac.at

© The Author(s), under exclusive license to Springer Nature Switzerland AG 2025

A. Tel, M. Robiony (eds.), *Atlas of Virtual Surgical Planning and 3D Printing for Cranio-Maxillo-Facial Surgery*,
https://doi.org/10.1007/978-3-031-94495-6_3

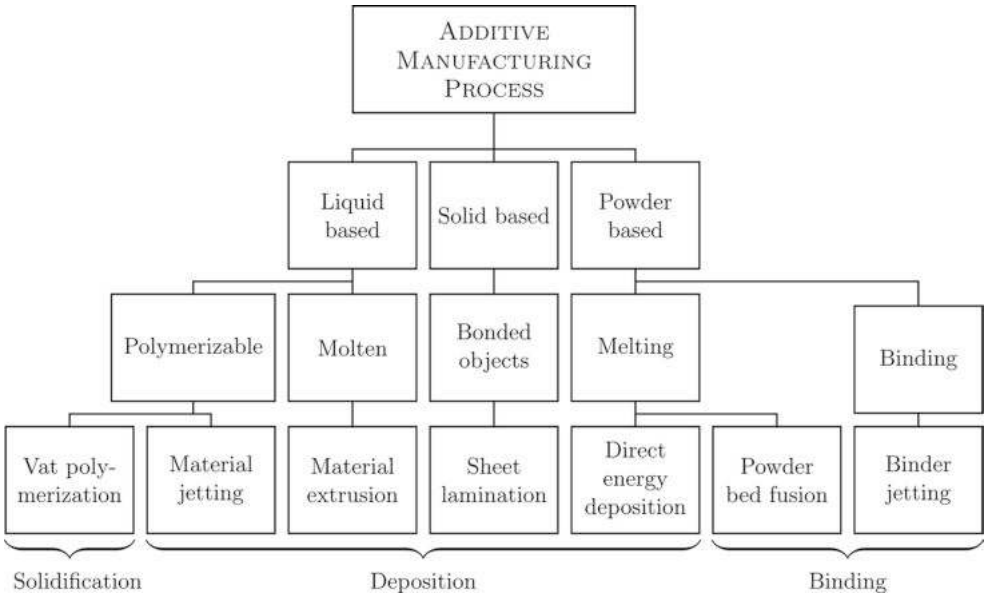


Fig. 1 Classification of additive manufacturing methods and processes. (Adapted from Godec et al. [2])

2 Material Extrusion

Material extrusion comprises the method of fused deposition modeling (FDM) also known as fused filament fabrication (FFF). Fused filament fabrication is a very popular 3D printing method, widely used in the consumer market. The concept of this 3D printer is relatively simple, which is why the devices and materials are affordable. Undoubtedly, it is the ease of use that contributes to the popularity of this type of printer (Fig. 2).

It involves melting a plastic and extruding it through a nozzle to create a three-dimensional object layer by layer. Typically, plastics such as polylactic acid (PLA) or acrylonitrile butadiene styrene (ABS) copolymer are used for this purpose. The raw material usually comes in the form of filament, occasionally as pellets, which is melted in order to extrude it.

Gels or inks can also be printed using a material extrusion method. Typically, the printing material is loaded into a cartridge and then extruded through the nozzle using a plunger or compressed air. This method is particularly popular in the field of bioprinting, as it allows for the printing of living cells within bioinks.

Most extrusion printers are designed to move along three axes. A printing layer is placed in a plane defined by two axes, and the third axis is adjusted once a layer is completed. Each layer can only be printed on top of another, making it necessary to print supports for overhanging structures, which must be removed after printing. There are also specialized

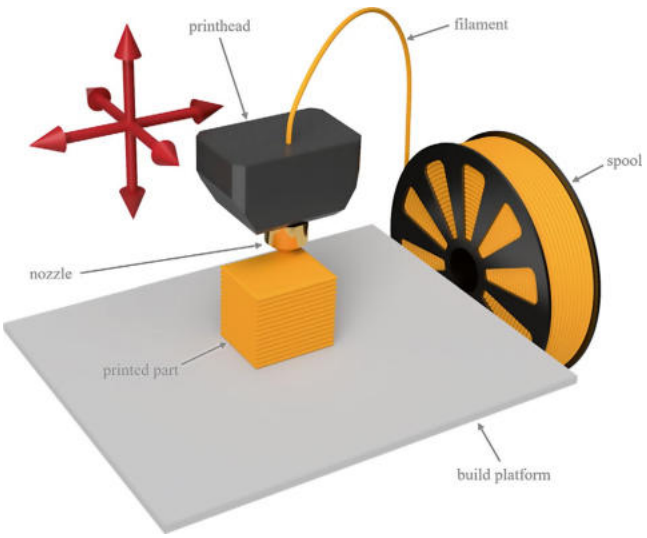


Fig. 2 Schema of an FFF printer, showing a movable printhead fed by a filament

forms, such as 5-axis printers. These can be used to save support material or to print on uneven surfaces.

In most applications involving plastics, printing is done on a flat printing bed. However, for applications using bioinks, it may be advisable to print into a gel matrix. To achieve this, a container with a gel is prepared and extruded into the gel with a long nozzle, such as the tip of a syringe. This approach allows the creation of three-dimensional structures with soft printing materials without the need for support material.

3 Vat Polymerization

Vat polymerization typically refers to the manufacturing of a three-dimensional object from a tank (the vat) filled with liquid resin. This is achieved by using a laser for the polymerization of the resin, causing it to harden. Stereolithography (SLA) is one of the earliest 3D printing methods, which uses a liquid resin and a UV laser to solidify it into a three-dimensional object. There are many variations of stereolithography printers, primarily differing in the type of UV light source used.

The laser beam selectively cures the resin layer by layer, creating a precise and accurate object. The different layers are created by submerging the already printed object further into the vat and then having another layer of liquid resin on the surface of the vat above the printed piece.

"Bottom-up" stereolithography, which has gained greater popularity, involves exposing the resin through a transparent bottom in the resin filled vat. The build platform, on which the parts are printed, gradually moves out of the vat (Fig. 3).

Instead of scanning the layer with a laser, an entire layer can be exposed at once by projecting the desired structure onto the resin. This form of stereolithography is commonly referred to as digital light processing (DLP). The quality of the parts in DLP is naturally dependent on the resolution of the projector or respectively the light mask. This type of printer is typically faster than laser-operated SLA printers because the entire layer is printed all at once.

After the printing process, any remaining resin must be washed off the components. This is often done using isopropyl alcohol, which rapidly dissolves the liquid photopolymer. To ensure that the material is fully polymerized, post-curing can be performed. In this process, the component is exposed to UV light on all sides at the frequency that initiates polymerization. This makes the material stiffer and, in most cases, more brittle. Articles embedded in this work will provide further insight into this topic.

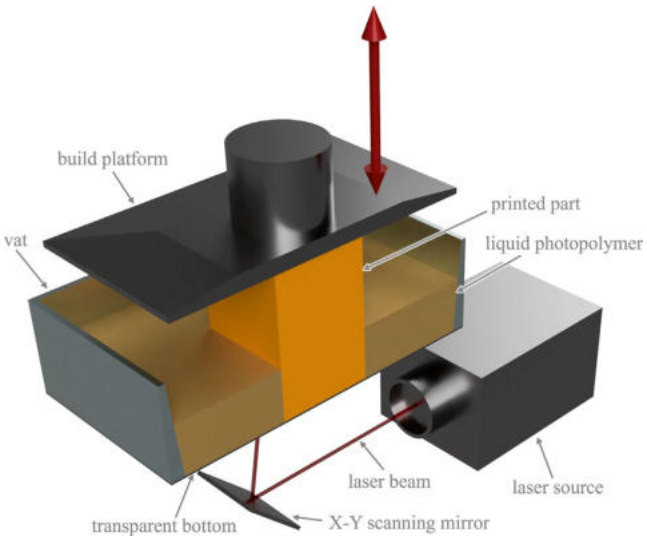


Fig. 3 Bottom-Up vat polymerization printer using a laser. The laser cures the liquid photopolymer to create a layer of the 3d printed part

SLA is known for its high accuracy and resolution, which makes it suitable for printing small parts with intricate details. Therefore, SLA is used in the manufacturing industry, especially for high-precision and high-quality prototypes. Nevertheless, it is often necessary to post-process the surface, especially in areas where support structures were attached.

Exceptionally high resolutions can be achieved with two-photon polymerization (2PP). In this process, a resin is used with a photoinitiator that requires multiphoton absorption to enter an excited state and initiate polymerization. This results in a quadratic dependence of absorption on intensity, allowing for the 3D printing of smaller structures below Ernst Abbe's diffraction limit. 2PP printers are particularly interesting for creating surface structures that can alter properties such as wettability and cell adhesion [3–6].

Photoinitiators that require more than one photon to trigger polymerization offer even more possibilities. In Xolography, two different wavelengths are used to polymerize the resin. The resin-filled tank is illuminated on one plane with the first wavelength, while the desired printing pattern is projected onto this plane with the second wavelength, orthogonal to it. Polymerization occurs where both wavelengths intersect with the resin. Naturally, the photoinitiator must be sufficiently transparent so that a layer can be exposed from the side. Accordingly, this method is currently only applicable to limited build volumes. However, this approach has the distinct advantage that the part being printed does not need to be mechanically moved during the printing process. As a result, this method is significantly faster than other SLA techniques. Furthermore, the printed part remains submerged in the resin until completion, eliminating the need for support structures. Since this method can also be used within a closed container, provided it is transparent, gravitational forces are not required for the printing process [7].

4 Powder Bed Fusion

Powder bed fusion is known by many names, with selective laser sintering (SLS) being the most common, but selective laser melting is also used. The name itself describes what happens in this 3D printing process. This method employs a high-powered laser to selectively fuse powdered material into a solid object. The powder is heated and melted layer by layer, with each layer fusing to the previous one. After each layer is completed, the build platform is lowered, and a fresh layer of powder is spread atop the previous one (Fig. 4).

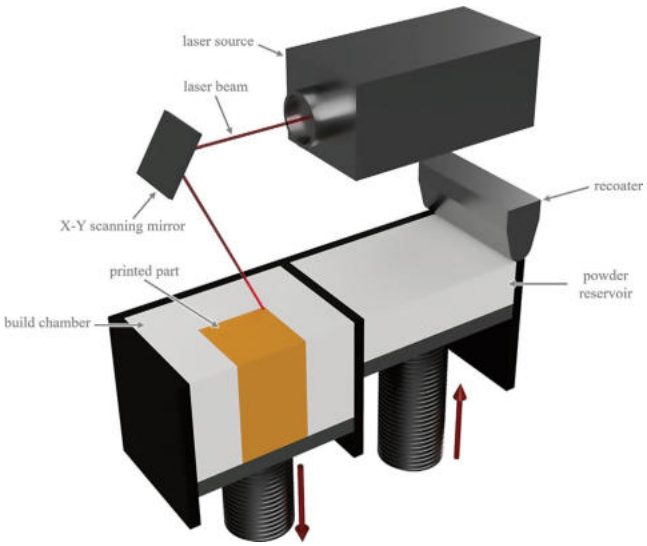


Fig. 4 Scheme of a powder bed fusion printer. The laser is melting the powder and fusing the particles together to form a part. After the layer is finished, the build chamber is moved down, the powder reservoir is moved up and the recoated distributes the powder for the next layer evenly

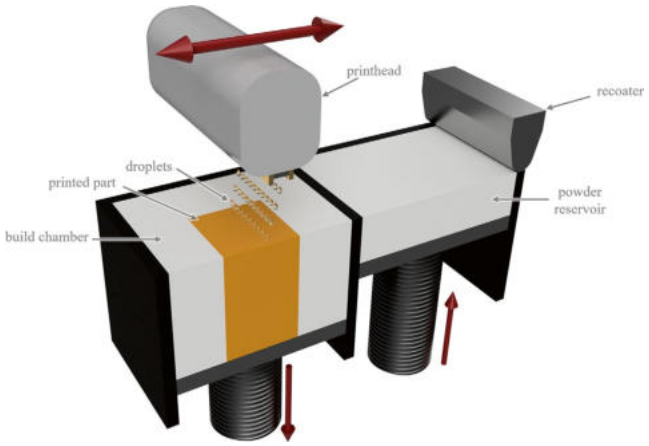


Fig. 5 Scheme of a binder jetting printer. The powder is glued together by a binder, which is applied as droplets from the printhead

Typical materials used for this process include metal powders like steel or titanium, as well as polymers like polyamide.

After the printing process, any unused, unfused powder is removed and can typically be reused. The advantage of printing in a powder bed is that there's no need for support structures to stabilize the object being printed. However, not all SLS prints can do without support structures, especially with metals, as the heat cannot dissipate quickly enough across the surface but is directed through support structures into the cooled base of the powder bed.

Support structures need to be removed in the post-processing stage. The surface roughness depends on the type of powder used and laser power and is typically rougher than SLA prints. Therefore, surface finishing is also common. By using different laser power at the edges and in the center of the object, better surface quality can be achieved without significant compromises in print speed. If higher surface quality is still required, especially for metallic SLS products, polishing, sandblasting, or hirtisation are not uncommon. To achieve even higher printing speeds, some printers use multiple lasers simultaneously.

Most SLS devices are relatively more expensive to acquire compared to similar SLA or FFF printers. Additionally, many of them operate with vacuum or require a supply of inert gas to prevent powder ignition and corrosion during operation [8]. Adequate ventilation systems are also necessary due to potential safety concerns and might require corresponding architectural measures.

Another variant of powder bed fusion is electron beam melting. The basic concept is the same as in SLS, but an electron beam is used instead. It has a higher energy density and can be employed for higher build rates or to achieve different phase formations during solidification.

5 Binder Jetting

Binder Jetting is a process similar to selective laser sintering (SLS), but it does not melt the powder. Instead, it binds the powder using a binding agent. This adhesive then cures by itself or, for example, through UV light exposure. Various materials can be bonded using this method, including sand, which is popular in the steel industry. This allows for the production of custom casting cores that can withstand high temperatures and can be easily crumbled after casting (Fig. 5).

The process does not generate as much heat as SLS because the powder is not melted. Since the entire printing process occurs within the powder bed, no support material is required, saving post-processing time and reducing material waste. Moreover, because only a relatively small amount of binding agent needs to be applied to the powder, high printing speeds with a large build volume can be achieved.

6 Material Jetting

Material jetting is similar in procedure to binder jetting, with the key difference being the way material is deposited. Just like an inkjet printer for paper, material is jetted out of fine nozzles. However, instead of saturating a powder bed or paper, the liquid forms a layer with a specific thickness due to the drop volume (Fig. 6). Photopolymers are commonly used for this method. Right after the droplets are deposited, the printed layer is cured with a UV lamp. The printer's resolution depends on the layer thickness and the nozzle resolution. These printed volumetric units are referred to as voxels.

This printing process crucially requires full-area support material for overhangs. Frequently, the entire printed object is enveloped in support material to achieve a uniform surface finish. After the printing process, the support material can be removed, and the component can be washed, as, in most polymer applications, water-soluble support materials are used.

7 Direct Energy Deposition

Direct energy deposition shares certain similarities with material extrusion. In this process, material is deposited at the desired location and melted directly at that point, allowing it to fuse with the 3D printed part. A laser or electron beam is commonly used as the energy source, similar to SLS. Upon cooling, the deposited material solidifies again. The material conditioning and microstructure depend on the cooling rate (Fig. 7).

Both powder and wire/filament can serve as material sources. This method is particularly interesting for metals since they, unlike polymers in material extrusion, are not as easily melted. Therefore, this method is occasionally referred to as laser deposition welding or laser metal deposition. When used for surface coatings, it is commonly marketed as laser cladding. Similar to SLS, the process is typically carried out in an inert atmosphere to protect metals from corrosion and contamination.

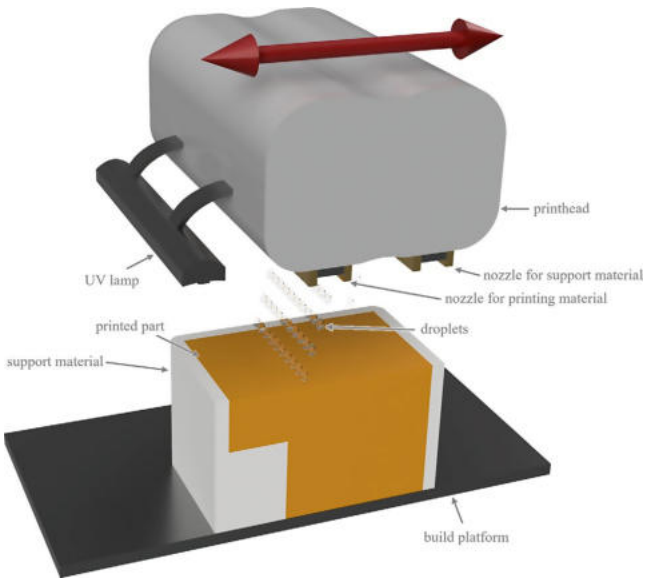


Fig. 6 Scheme of a material jetting printer. Photopolymer is applied as droplets and cured as soon as it is deposited

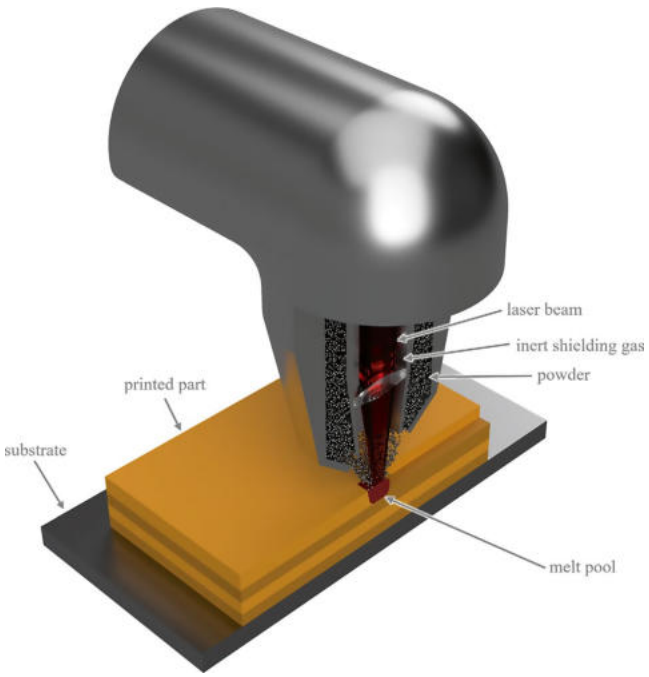


Fig. 7 Scheme of direct energy deposition. A laser is melting the substrate and the applied powder at the position where the new material is added. The material connects and solidifies when cooling down

8 Sheet Lamination

Most 3D printing processes work layer by layer, and sheet lamination is a method where individual sheets are layered and bonded together. Commonly used materials for this process include paper, cardboard, polymer, or metal sheets.

It is distinguished by whether the next layer is shaped first and then applied, or if an entire sheet is applied on the printing object and then the layer is shaped afterward [9]. If the material is applied first and then cut, a crosshatched cut is usually made on the remaining material to make it easier to remove after printing.

The shape of each layer is cut using a tool suitable for the material. For example, a laser cutter can be used for paper and polymers, while machine-controlled milling is suitable for metal sheets (Fig. 8).

There are various methods for assembling the layers. Particularly popular with paper is the application of adhesive, or glue, to hold the individual layers together. Thermal methods are also common, typically involving pressing and heating the part to bond the individual sheets together.

Ultrasonic additive manufacturing, especially for metals, presents an interesting option. In this process, sheets are compressed with significant force and rubbed against each other using ultrasonic vibrations. Modern devices typically use a frequency of around 20 kHz, transmitted to the components through a sonotrode.

The compression and rubbing lead to plastic deformation of the surfaces, where inert oxide layers on the sheets are ground away and displaced. This brings pure phases of the two metal sheets into contact, allowing them to bond. An essential feature is that, while there is a local temperature increase at the joining point, the overall process and the entire structure remain essentially cold [10–12]. In this regard, this 3D printing process resembles ultrasonic welding but is focused on two-dimensional sheets.

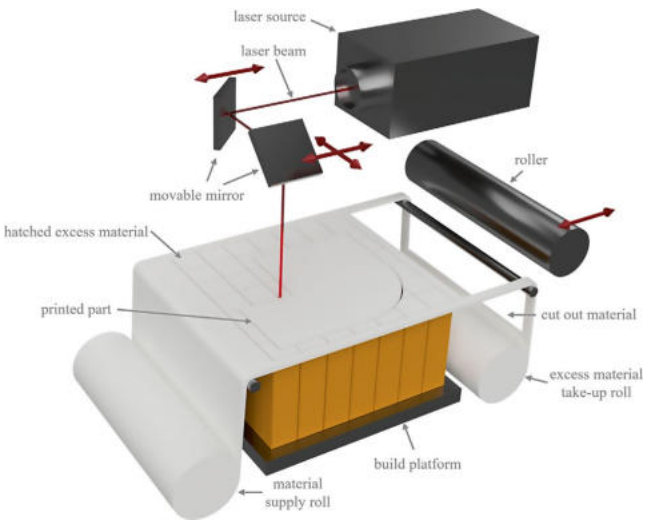


Fig. 8 Scheme of a sheet lamination printer, where the material is cut after the new layer is attached. A roll supplies the sheet which is fixed with a roller. The laser cuts out the part and crosshatches the excess material, so that it can be removed easily after the printing process.

9 Multimaterial 3D Printing

We rarely encounter materials that are truly pure and exist in a single material phase. The field of multimaterial homogenization delves into how individual materials are composed and how the formation of a multimaterial can be analytically described [13, 14]. In 3D printing, however, it is common to refer to anything consisting of more than one primary printing material, as typically bought and loaded into the printer, as multimaterial print.

Multimaterial printing can occur at various size scales. An example of very small single-phase prints is obtained using stereolithography, where at least two different resins were well mixed before the printing process. In the resulting print, the individual materials cannot be distinguished from each other. Therefore, this form of multimaterial is also referred to as mixmaterial [15].

Typical composites can also be manufactured, for example, using material jetting. For this, multiple printheads are usually employed, each loaded with a different material. Each material phase is thus at least one voxel in size. This enables the production of multimaterials in almost all size ranges, from very small phases that almost merge to very large parts that are clearly distinguishable. When creating composites in this manner, there is almost no limit to the shape of the inclusions [16] .

Three of the typical multimaterial composites manufacturable using material jetting are shown in Fig. 9. Each of these multimaterials consists of two primary materials. The more different material phases there are, the more possibilities there are to produce a composite material.

Also popular in material jetting printers is the mixing of several primary materials in the printhead before the drop is jetted onto the build platform. This again results in a mixmaterial that appears homogeneous. Since the mixing ratio can be finely controlled, a wide variety of individual materials is possible, as well as the creation of smooth material transitions.

Another simple method to produce composites is, for example, sheet lamination. Different materials just need to be stacked on top of each other. This is suitable, for example, for making circuit boards by alternating conductive and nonconductive layers. Introducing other materials between the layers is also possible, such as optical fibers [17].

Multimaterial 3D printing also works when some larger parts should be printed together. The advantage of simultaneous production is that the parts can be nested or intertwined,

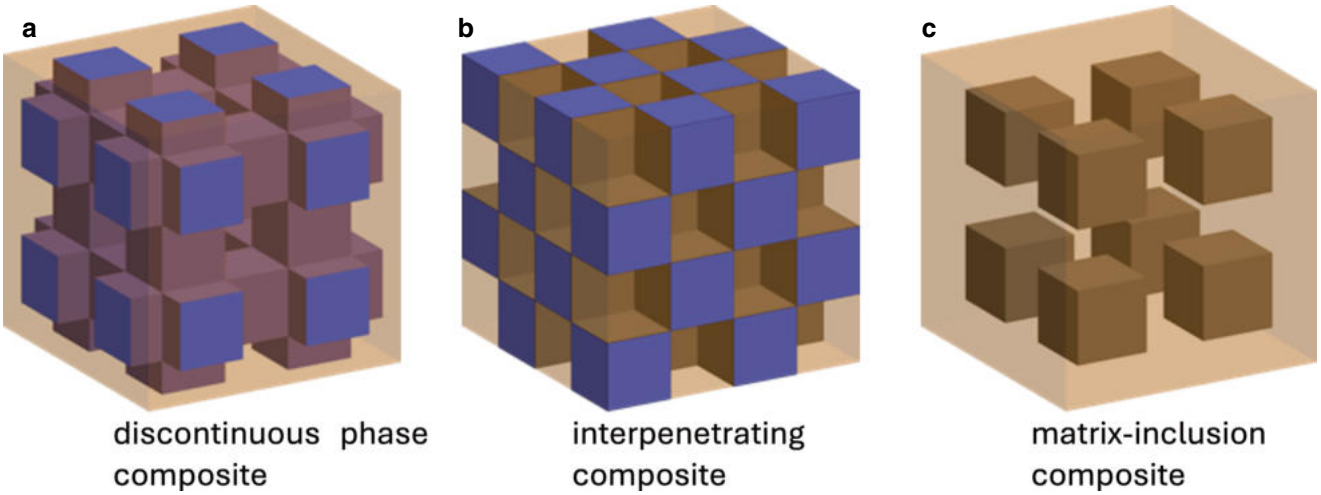


Fig. 9 Representation of three typical multimaterials forming composites from two primary materials (blue and orange) (**a**) discontinuous phase composite (**b**) interpenetrating composite (**c**) matrix-inclusion composite

which would not be possible if one were to build and assemble them individually. The term co-fabrication or co-processing is often used for this, as multiple parts from different materials with at least one contact surface are simultaneously produced.

An example of this is the previously mentioned material jetting, but material extrusion is also becoming increasingly popular for multimaterial printing to create multicolored objects, for instance. The significant advantage of multimaterials is that different properties can be obtained. This pertains not only to color but, more importantly, to mechanical properties, thermal or electrical conductivity, as well as biocompatibility. For instance, co-processing two different bioceramics can be used to manufacture an implant with excellent osseointegrative properties on one side and outstanding mechanical stability on the other.

Furthermore, in the printing process, additional foreign components can be added. A focus of current research activities is on so-called nanoparticles that are included in the printed object. These nanoparticles can be mixed into the resin before 3D printing or included in the filament. The challenge here lies in achieving the distribution and orientation of nanoparticles in a way that imparts the desired properties to the printed part [18, 19].

Thus, it is possible to 3D print different materials and create transitions between them. The key challenge is to determine mixtures and gradients of these materials in such a way that a certain geometry with the processed materials has specific properties. Functionally graded materials involve such a material transition to fulfill a certain purpose. This may involve mixing a harder and a softer material to be stiffer on one side of a beam than the other, without altering the geometry of the beam. Or to achieve a certain spring stiffness in a component that would otherwise be unattainable with the given geometry. Already now there are countless possibilities for 3D printing components with functionally graded materials. However, the way the materials are mixed will ultimately depend on the intended application.

References

1. ISO/ASTM 52900:2015 SDE. Standard Terminology for Additive Manufacturing—General Principles—Terminology. ISOASTM 52900; 2015.
2. Godec D, Gonzalez-Gutierrez J, Nordin A, Pei E, Ureña J. A guide to additive manufacturing. Springer Cham; 2022. 324 p. Available from: https://doi.org/10.1007/978-3-031-05863-9.
3. Gittard SD, Koroleva A, Nguyen A, Fadeeva E, Gaidukeviciute A, Schlie S, et al. Two-photon polymerization microstructuring in regenerative medicine. Front Biosci-Elite. 2013;5(2):602–9.
4. Fischer J, Wegener M. Three-dimensional optical laser lithography beyond the diffraction limit. Laser Photonics Rev. 2013;7(1):22–44.
5. Lee KS, Kim RH, Yang DY, Park SH. Advances in 3D nano/microfabrication using two-photon initiated polymerization. Prog Polym Sci. 2008;33(6):631–81.
6. Bunea AI, del Castillo Iniesta N, Droumpali A, Wetzel AE, Engay E, Taboryski R. Micro 3D printing by two-photon polymerization: configurations and parameters for the nanoscribe system. Micro. 2021;1(2):164–80.
7. Regehly M, Garmshausen Y, Reuter M, König NF, Israel E, Kelly DP, et al. Xolography for linear volumetric 3D printing. Nature. 2020;588(7839):620–4.
8. Das S. Physical aspects of process control in selective laser sintering of metals. Adv Eng Mater. 2003;5(10):701–11.
9. Gibson I, Rosen DW, Stucker B. Sheet lamination processes. In: Additive manufacturing technologies: rapid prototyping to direct digital manufacturing. Boston: Springer US; 2010. p. 223–52. Available from: https://doi.org/10.1007/978-1-4419-1120-9_8.
10. Hehr A, Norfolk M. A comprehensive review of ultrasonic additive manufacturing. Rapid Prototyp J. 2020;26(3):445–58.
11. Shimizu S, Fujii HT, Sato YS, Kokawa H, Sriraman MR, Babu SS. Mechanism of weld formation during very-high-power ultra-

sonic additive manufacturing of Al alloy 6061. Acta Mater. 2014;74:234–43.
12. Friel RJ, Harris RA. Ultrasonic additive manufacturing—a hybrid production process for novel functional products. Procedia CIRP. 2013;6:35–40.
13. Zaoui A. Continuum micromechanics: survey. J Eng Mech. 2002;128(8):808–16.
14. Eshelby JD, Peierls RE. The elastic field outside an ellipsoidal inclusion. Proc R Soc Lond Ser Math Phys Sci. 1959;252(1271):561–9.
15. Kornfellner E, Königshofer M, Unger E, Moscato F. Elastic and dimensional properties of newly combined 3D-printed multimaterials fabricated by DLP stereolithography. Front Mater. 2023;10:127214.
16. Kornfellner E, Königshofer M, Krainz L, Krause A, Unger E, Moscato F. Measured and simulated mechanical properties of additively manufactured matrix-inclusion multimaterials fabricated by material jetting. 3D Print Med. 2024;10(1):4.
17. Friel RJ. 13 - Power ultrasonics for additive manufacturing and consolidating of materials. In: Gallego-Juárez JA, Graff KF, editors. Power ultrasonics [Internet]. Oxford: Woodhead Publishing; 2015. p. 313–35. Available from: https://www.sciencedirect.com/science/article/pii/B9781782420286000132.
18. Xu W, Jambhulkar S, Zhu Y, Ravichandran D, Kakarla M, Vernon B, et al. 3D printing for polymer/particle-based processing: a review. Compos Part B Eng. 2021;223:109102.
19. Xu W, Jambhulkar S, Ravichandran D, Zhu Y, Kakarla M, Nian Q, et al. 3D printing-enabled nanoparticle alignment: a review of mechanisms and applications. Small. 2021;17(45):2100817.

Virtual Surgical Planning and 3D Printing at the Point-of-Care Lab for Cranio-Maxillo-Facial Surgery

Shadi Daoud, Amjad Shhadeh, Idan Redenski, Adeeb Zoabi, and Samer Srouji

1 Introduction

1.1 3D Printing in Medicine and Surgery

Three-dimensional (3D) printing, also known as additive manufacturing (AM) or rapid prototyping (RP), has revolutionized several industries, particularly healthcare. Introduced in 1986 [1], 3D printing works by building models layer by layer, converting digital designs into physical objects made from liquid, powder, or molten materials [2]. Although initially restricted to industrial use, the technology has rapidly expanded, especially within medicine and surgery [3]. The breakthrough in medical and surgical technology has been propelled by the development of affordable, user-friendly 3D printers, improved software solutions, and enhanced radiological imaging, allowing for the creation of highly realistic anatomical models [4]. What was once a complex and costly process is now more accessible, as compact 3D printers have revolutionized AM in medicine, significantly improving precision and personalized patient care [5]. Table 1 presents an overview of the 3D printing techniques used in healthcare.

Several traditional techniques, such as solvent casting, particle leaching, electrospinning, gas foaming, and phase separation, have long been used to fabricate devices and scaffolds. However, these methods are limited by the need for organic solvents, leading to lengthy production times, labor-intensive processes, and inconsistent results. Additionally, irregular pore shapes and poor interconnectivity reduce scaffold effectiveness [6, 7]. In contrast, rapid prototyping, mainly 3D printing, offers improved design flexibility, reproducibility, and customization, making it a more practical alternative for producing complex scaffolds and devices [6, 7]. Depending on the material and technology used, printed objects may require additional steps such as post-curing to improve mechanical stability, alcohol rinses, powder cleaning and sanitization, or manual removal of support structures.

Surgical 3D printing employs a wide range of materials, each with distinct properties and applications. A summary of different materials, their advantages, and disadvantages, is provided in Table 2.

The benefits of 3D printing in medicine include enhanced customization, minimized material waste, increased cost efficiency, and more precise patient-specific solutions. It also improves surgical training and practice, enhances communication with patients and colleagues, and leads to better surgical outcomes.

An important distinction in 3D printing within healthcare is whether these services are provided in-house or outsourced to external providers. In-house 3D printing facilities, or 3D Printing Point-of-Care (3DP PoC) centers, mean that the 3D printers are located near the hospital or the treatment site, which facilitates patient-specific care and adds an extra dimension to image-based diagnosis and treatment. However, setting up and maintaining an in-house facility requires significant investment in equipment, training, and data management systems. External services, though typically more costly and time-consuming due to shipping and consultation delays, provide access to specialized expertise and resources that smaller institutions may be unable to afford or maintain in-house.

The CMF field benefits from 3D printing in multiple ways. It enables the creation of anatomical models for education, training, and surgical preplanning. It also allows for the creation of occlusal splints, cutting and repositioning guides, and patient-specific implants, all of which enhance precision in treatment. Materials used for devices in the operating room must be capable of being sterilized, while those that

S. Daoud (✉) · A. Shhadeh · I. Redenski · A. Zoabi · S. Srouji
Department of Oral and Maxillofacial Surgery, Galilee College of Dental Sciences, Galilee Medical Center, Nahariya, Israel

The Azrieli Faculty of Medicine, Bar-Ilan University, Safed, Israel
e-mail: shadi.daoud@mail.huji.ac.il; amjad.shhadeh@mail.huji.ac.il; idan.redenski@gmail.com; dr.adeebz@gmail.com; dr.samersrouji@gmail.com

© The Author(s), under exclusive license to Springer Nature Switzerland AG 2025

A. Tel, M. Robiony (eds.), *Atlas of Virtual Surgical Planning and 3D Printing for Cranio-Maxillo-Facial Surgery*,
https://doi.org/10.1007/978-3-031-94495-6_4

Table 1 Overview of additive manufacturing technologies in healthcare

Technology	Description	Primary applications	Key limitations
Stereolithography (SLA)	Photopolymerization of liquid resin to build detailed models.	Dental models, surgical guides, temporary and permanent restorations.	Messy resins, poor mechanical properties, limited shelf life and may require additional post-processing.
Fused Deposition Modeling (FDM)	Extrudes thermoplastic filaments layer-by-layer to form parts.	Anatomical models, provisional prosthodontics, and restorations.	Limited material diversity, poor interlayer bonding, and manual removal of supports.
Selective Laser Sintering (SLS)	Fuses powdered materials with lasers to create durable structures.	Dental prostheses, dentures, and patient-specific implants.	Expensive infrastructure, elaborate post-processing are needed.
Direct Metal Laser Sintering (DMLS)	A high-precision laser selectively fuses metal powder into metal layered structures.	Titanium cranioplasty plates, mandibular reconstruction.	High cost, relatively slow, and post-processing.
Binder Jetting (BJ)	Liquid binders are deposited on powdered media to form models layer-by-layer.	Anatomical study models, dentures.	Low resolution, low compressive strength, handling of loose powder.
Directed Energy Deposition (DED)	Uses a high-energy electron beam or laser to melt and deposit metal powder.	Custom titanium plates, cranioplasty models, mandibular reconstruction.	High material cost, airborne particle, rough surfaces, and low resolution.
Material Jetting/ PolyJet	Jets curable polymers in layers to form precise surfaces.	Dental models, provisional prosthetics.	Expensive materials, messy and may cause irritation to living tissues.

Table 2 Summary of 3D printing of different materials and their primary advantages and limitations in surgical applications

Material	Advantages	Limitations
Titanium	Biocompatible, high strength-to-weight ratio, ideal for load-bearing applications, used for cranioplasty plates and patient-specific implants.	High cost, requires specialized equipment, relatively slow printing speed and post-processing needed.
Poly-ether-ether-ketone (PEEK)	High-performance thermoplastic with excellent dimensional stability and biocompatibility; widely used in custom implants and cranioplasty.	Typically milled from solid material and expensive.
Poly-ether-ketone-ketone (PEKK)	Similar to PEEK but allows 3D printing for more porous structures.	Requires specialized equipment and expensive.
Porous Polyethylene	Suitable for CMF reconstructions; can be customized using powder sintering for pre-shaped implants.	Limited mechanical strength compared to metal implants; requires specific molding equipment.
Vinyl Polymers	Versatile and effective for dental and surgical applications.	Not ideal for load-bearing or high-stress regions.
Polystyrene (PS) and Acrylonitrile Butadiene Styrene (ABS)	Offer high transparency and mechanical durability.	Limited biocompatibility; not ideal for long-term biomedical use.
Polyester Polymers	Biocompatible with adjustable properties, making them valuable for implants and bone tissue regeneration.	Can have reduced mechanical strength and may degrade over time within the body.

come into contact with human tissue, such as skin or mucous membranes, must be printed from biocompatible materials.

A recent advancement in 3D printing for healthcare is the development of printers capable of using multiple materials and colors. These materials can be applied across various uses, from simple and complex anatomical models to surgical and cutting guides that require high-strength materials for durability. Different materials and colors can be combined to replicate body tissues such as skin, vessels, and bones, both in form and texture for more detailed models. Radiopaque materials are also available, enabling the production of models that display realistic radiographic features under X-rays and CT scans. The combination of materials with varying biomechanical properties, colors, and radiopacity allows for creating medical models that closely resemble human tissue's appearance and behavior.

Beyond clinical applications, advancements in 3D printing hold significant potential for ex vivo research in CMF surgery. Currently, much of the data in this field has been derived from observational studies. However, the ability to produce highly detailed and realistic anatomical models through 3D printing offers researchers a new level of precision. These models can replicate the texture, structure, and biomechanical properties of human tissues, making them invaluable for testing and refining complex surgical techniques.

In ex vivo research, these 3D-printed models allow surgeons and researchers to simulate procedures on accurate anatomical replicas, reducing the risks associated with direct patient experimentation. This capability is crucial for testing new surgical approaches or devices before clinical application. Additionally, the repeatability of these models enables

consistent experimentation, allowing researchers to conduct trials under controlled conditions and compare outcomes reliably.

Moreover, these advanced models benefit staff education by providing a realistic platform for surgical training, enhancing the learning experience without exposing patients to unnecessary risk. Ultimately, the integration of these advanced 3D printing technologies supports more effective ex vivo research, leading to improved surgical techniques, safer outcomes, and faster innovation in CMF surgery.

1.2 Virtual Surgical Planning (VSP) in Cranio-Maxillo-Facial Surgery

Cranio-maxillo-facial surgery poses considerable challenges due to the complex anatomy of the facial region, which contains many vital structures and organs. Essential functions such as mastication, speech, eye movement, and facial expression are highly susceptible to disruptions from trauma, tumor resections, temporomandibular joint (TMJ) disorders, and other facial or oral diseases. Successfully treating these conditions requires a deep understanding of new technologies, particularly the use of virtual surgical planning (VSP) and 3D printing, to improve CMF surgery outcomes.

VSP is a preoperative planning method that uses 3D imaging computer software to visualize a surgical procedure and enables surgeons to predefine the steps in a surgical procedure.

Initially, VSP has been carried out by biomedical engineers due to the complexity of the software, but as the software becomes more user-friendly and accessible, it is increasingly being adopted by surgeons themselves. This shift empowers surgeons to take direct control over the planning process, further streamlining workflow and improving integration between planning and execution.

Following VSP, the next step is Virtual Surgical Designing (VSD). VSD involves the creation of patient-specific tools and implants based on the 3D models generated during the planning phase. Using advanced design software, surgeons or biomedical engineers can digitally design custom cutting guides, fixation plates, occlusal splints, and implants tailored to the patient's unique anatomy. These designs are then manufactured using 3D printing technology to ensure a precise fit during surgery. VSD not only enhances the accuracy of surgical interventions but also streamlines the intraoperative process by providing ready-to-use, customized devices that reduce variability and operation time and improve overall outcomes.

At present, a variety of tools and techniques are utilized to manage better and control the 3D printing process and achieve desired outcomes. 3D models can be readily generated using specialized software, such as Mimics In-print (Materialise), Mimics Medical (Materialise), Romexis 6 (Planmeca), and D2P (3D Systems). A crucial step in this process is segmentation, where the region of interest is extracted from imaging data to create an accurate 3D model. Such models can be used directly for anatomical model printing or to further proceed with the VSP.

For more complex surgical planning, advanced manipulation of digital models is often required to achieve the desired anatomical structures or geometric configurations. This necessitates the use of more complicated and feature-rich software, such as 3-matic Medical (Materialise), Proplan CMF (Materialise), and FreeForm Plus (3D Systems), which offer a broader range of features for detailed adjustments.

These platforms support several digital manipulation techniques. For instance, the mirroring function allows the unaffected side of a patient's anatomy to be replicated and applied to the affected side, especially useful in cases involving unilateral defects. In situations where both sides are affected or no normal reference exists, surgeons can import normative anatomical data, accessing 3D models from a database of standard anatomical features scaled to fit the patient's anatomy. Virtual fracture reduction is another critical tool, where the software enables precise segmentation of fractured bones. The fragments are then aligned by setting a pivot point and digitally repositioning them into their original state. Bone contouring tools allow surgeons to modify the model by adding or subtracting material, similar to using a paintbrush or eraser, helping to achieve the desired shape of the bone. Furthermore, osteotomy simulations digitally mimic bone cuts and subsequent movements in 3D, making them invaluable in procedures like orthognathic surgery. Additional tools, such as analysis functions and heat maps, provide various analysis options, including wall thickness measurements and comparative assessments between different models. These functionalities collectively enhance the precision and planning capabilities of complex surgical procedures.

Once the VSP is complete, the final outcome is used to guide VSD, which involves creating PSIs. These implants are designed and fabricated based on the customized model generated during the planning phase.

3D PoC planning and designing workflow is illustrated in Fig. 1. It begins with the acquisition of imaging data in Digital Imaging and Communications in Medicine (DICOM) format, typically using high-resolution computed tomography (CT) or cone beam computed tomography (CBCT) to capture the complex anatomy of the head and neck. To ensure precise 3D modeling, 2D slice thicknesses greater than 1.0 mm can compromise the accuracy of the design and should be avoided. In some instances, additional imaging modalities, such as intraoral or facial scanning, may be required to obtain detailed representations of dental arches, soft tissue, or other specific anatomical features.

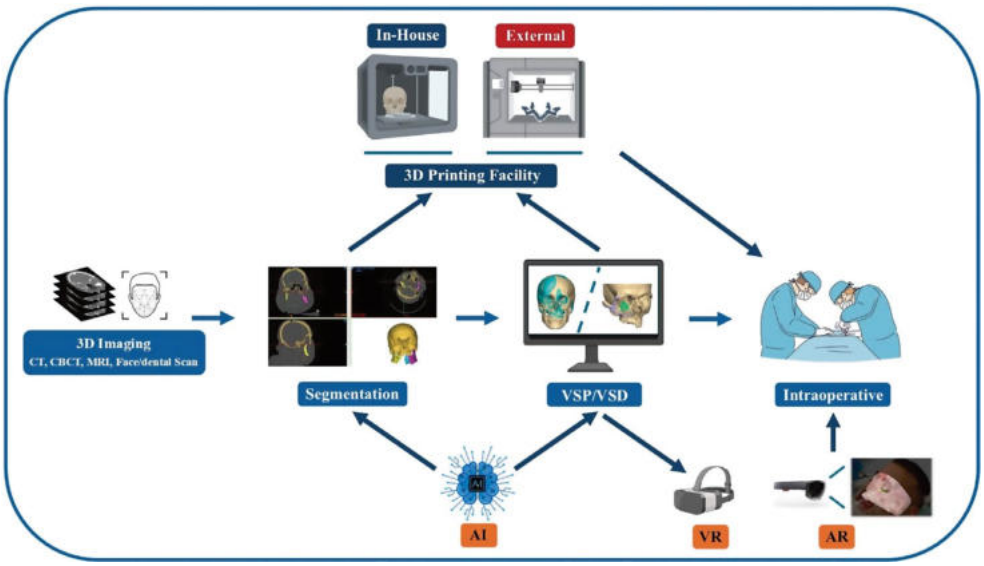


Fig. 1 3D PoC planning and designing workflow in CMF surgery

Once the imaging is acquired, segmentation is conducted using FDA-approved software to isolate and extract the patient's relevant anatomical structures. This segmentation process involves delineating the region of interest from imaging 2D slices, which are then reconstructed into a 3D object. Segmentation can be performed automatically, manually, or semi-manually, depending on image contrast and clarity. Further processing steps, such as noise reduction and defect correction, are applied to refine the model. The resulting 3D model, typically in STL format, can be sent to a 3D printing facility, which can either be in-house or external, depending on the available resources of the institution. These virtual models also serve as a foundation for VSP and VSD. In this stage, the surgeon or engineer can manipulate the model to predefine surgical steps, design PSIs, and create custom surgical guides. These digitally designed models can be printed either in an in-house or external 3D printing facility. PSIs are often produced externally when in-house capabilities are limited, regulatory standards must be met, or the case requires advanced materials or specialized techniques, such as metal printing. These 3D-printed models or guides can then be used in the operative theater providing high precision and improving intraoperative outcomes [8].

Additionally, the developing artificial intelligence (AI) technologies can assist in the segmentation and design processes by automating certain tasks and making procedures more accurate, time-efficient, and user-friendly for the surgical team [9]. Virtual Reality (VR) and Augmented Reality (AR) can also be part of the PoC workflow, since they have the potential to further enhance surgical planning and intraoperative guidance by offering interactive environments, improving communication among staff, facilitating case education, and providing real-time support during surgery [10]. However, AI and XR technologies are still evolving and face some limitations that need further research and consideration.

1.3 3D Point-of-Care (PoC) Applications in Healthcare

A 3D point-of-care facility, as defined by the FDA, refers to an infrastructure located at or near the treatment site, such as hospitals, outpatient clinics, or dental laboratories, which enables the custom fabrication of patient-specific implants and devices. In recent years, the integration of 3D PoC laboratories has grown significantly, particularly within leading healthcare institutions worldwide. These facilities are equipped with 3D printers, post-processing tools, and advanced software designed to convert medical imaging data into personalized 3D models and implants. The establishment of 3D PoC facilities brings these cutting-edge technologies closer to surgeons, facilitating their incorporation into routine practice and enhancing clinical outcomes across a wide range of cases [8, 11].

At present, many medical institutions outsource VSP and 3D printing of models/implants to private companies, which poses challenges such as potential risks to patient data confidentiality, elevated processing costs, prolonged pre-surgical delivery times, and time-consuming meetings with the external provider to finalize the surgical plan [12].

Unlike external VSP, in-house 3D PoC facilities streamline the process, allowing surgeons to integrate their expertise directly into the design of accurate patient-specific tools, such as cutting guides and implants. This approach offers more control and minimizes delays, particularly for urgent cases [13]. However, establishing a PoC center requires sub-

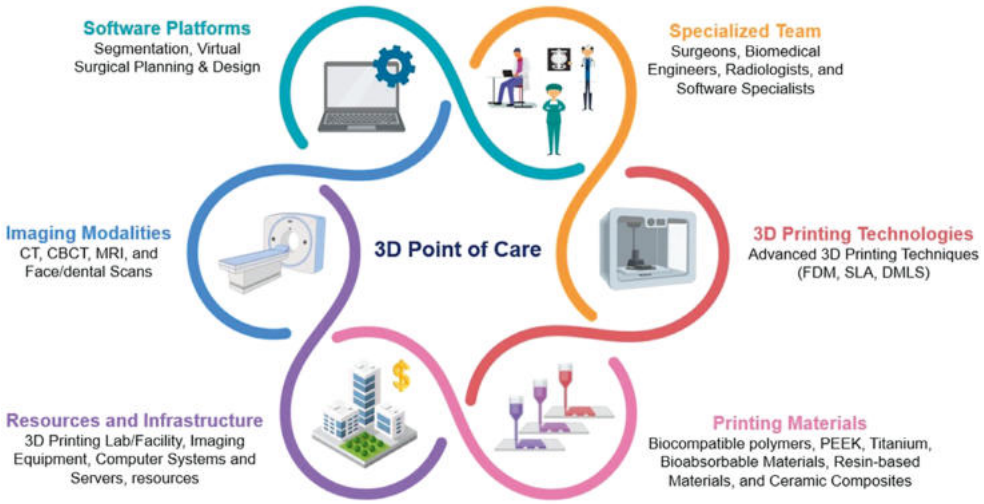


Fig. 2 Key Components of a 3D Point-of-Care Facility

stantial investment in equipment and staff training, as well as robust data management to ensure security [14].

As VSP is becoming more popular and design software and 3D printing technologies advance, the widespread adoption of PoC centers is expected to increase, facilitating greater collaboration between surgical teams and engineers and improving overall treatment outcomes.

Moreover, 3D PoC facilities can integrate cutting-edge innovations such as artificial intelligence (AI) and extended reality (XR), which further enhance personalized treatments by optimizing surgical planning, increasing precision, and reducing intraoperative risks. Figure 2 illustrates the essential elements of a 3D PoC facility, including imaging modalities, specialized teams, software platforms, 3D printing technologies, materials, and the necessary infrastructure to support personalized surgical treatment.

2 Steps in 3D Point-of-Care Capability and Development

3D point-of-care units can vary in their capabilities and evolve over time through continued training, improvements in VSP, VSD, and enhanced printing capabilities. As additional resources and expertise are acquired, the unit's ability to cope with increasingly sophisticated and complex cases improves. The progression in functionality can be categorized into distinct levels, with each level representing a higher degree of technological sophistication and clinical utility (Fig. 3).

Level 1

It is a basic facility for producing anatomical models primarily used for educational purposes and surgical preparation. This level involves fundamental imaging, segmentation, and 3D printing processes using standard materials. It is particularly suitable for handling basic surgical cases, such as simple fractures. Additionally, virtual case evaluation and assessment can be performed after segmentation. The setup at this level is characterized by its low cost and efficient processing time, making it accessible and not time-consuming overall. It is ideal for institutions seeking to introduce 3D printing capabilities without significant financial or time investments.

Level 2

The next level introduces basic VSP, allowing for enhanced surgical preparation. At this level, basic VSP involves techniques such as mirroring or virtual reduction, which enable the surgeon to visualize the desired final surgical outcome virtually. The resulting 3D models can then be printed and used for surgical preparation such as plate prebinding, hybrid plate adaptation, or fabrication of wafers. For the institute, this level is more demanding, as VSP requires educated staff, dedicated time, and specialized software, but it remains a cost-effective option and is not overly time-consuming.

Level 3

Advanced VSP is incorporated, allowing for more sophisticated techniques such as simulated osteotomies, controlled alignment, and superimposition with older scans or normative data. This level also introduces basic VSD capabilities, enabling simple guides and plates to be produced. These advancements enable handling of more complex cases, such as complex fractures and reconstructive surgery, and producing patient-specific implants. As a result, this level demands more specialized staff, extended time, and increased resources.

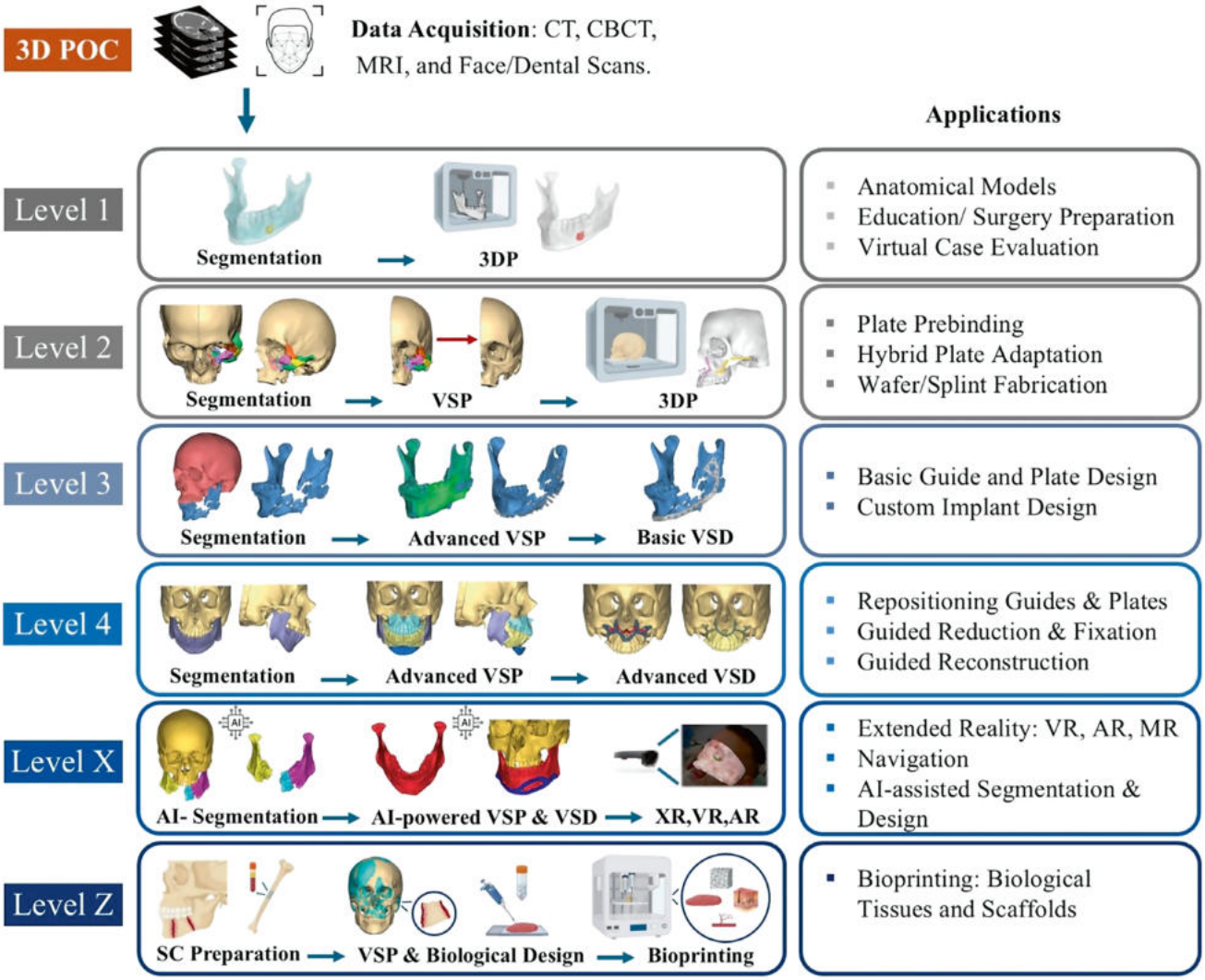


Fig. 3 3D point-of-care capabilities categorized by levels, each representing a stage of technological advancement, facility resources, and clinical applications

Level 4

This level includes advanced design capabilities such as creating multifunctional designs, and guides containing predrilled holes for repositioning, along with guided reduction and fixation plates. These features significantly improve surgical efficiency and enhance outcomes, particularly for more intricate and complex procedures like orthognathic surgery or secondary correction of facial trauma. Additionally, this level incorporates advanced printing capacities for complex anatomical model fabrication. From this level onward, the requirements for resources, skilled personnel, and time commitment increase significantly, as these advanced capabilities demand today's cutting-edge technology and well-trained teams to execute effectively.

Level X

This level incorporates AI-driven segmentation, virtual planning, and design, alongside extended reality (XR) technologies, including virtual reality (VR), augmented reality (AR), and mixed reality (MR), as adjuncts to the functionalities of Levels 1–4. AI-related technologies allow for automated procedures, making them more accurate, time-efficient, and user-friendly for the entire team. By providing immersive and interactive environments, XR technologies further enhance staff communication, case education, surgical planning, and intraoperative assistance. While these technologies are still under development and present certain limitations, they hold tremendous potential for improving surgical outcomes and increasing efficiency in the clinical setting.

Level Z

At the pinnacle of 3D PoC, Level Z integrates bioprinting capabilities for reconstructing human tissues or organs by combining 3D printing of organic tissue with the patient's own stem cells. The process begins with VSP for the defect, followed by a 3D reconstruction of the deformity to be restored. Blood or tissue samples are harvested to extract stem cells, which are then cultured and prepared for bioprinting, along with organic materials, into the precise shape of the defect. This creates 3D biological patient-specific implants for tissue regeneration and implantation. While this capability is currently beyond reach, it represents a future hope for revolutionizing cranio-maxillo-facial surgery. Only a few elite institutions are exploring this advanced technology, which holds immense promise for personalized medicine.

3 Clinical Applications of 3D Point-of-Care in Cranio-Maxillo-Facial Surgery

The complex anatomy of the maxillofacial region presents significant challenges in achieving satisfactory surgical outcomes. However, 3D printing and VSP technologies have transformed how complex surgical cases are approached, particularly in facial skeleton reconstruction, facial asymmetry correction, and comminuted fracture treatment. Achieving both functional and aesthetic improvements in these complex cases can be particularly challenging, but 3D point-of-care has made significant contributions to overcoming these obstacles.

Different fields within cranio-maxillo-facial surgery present their unique challenges. The applications of 3D PoC extend across various domains in maxillofacial surgery, including trauma, orthognathic surgery, reconstructive procedures, TMJ surgery, and implant surgery, offering tailored solutions to address each patient's specific needs.

3.1 3D Point-of-Care Solutions for the Management of Facial Trauma

The wide variety of trauma injuries encountered by the CMF surgery team, combined with the need to minimize the time between pre-operative assessment and treatment, necessitates a flexible approach to both design and additive manufacturing technologies. The establishment of 3D PoC facilities within healthcare centers significantly accelerates the guided reduction and fixation process. By streamlining the workflow, these facilities can reduce the time required for 3D-based instrument fabrication and treatment preparation to approximately 1 week—an acceptable timeframe for managing most CMF trauma cases.

In managing facial trauma, several key factors must be carefully considered, including occlusion, restoring facial buttresses, reestablishing the original anatomy, and preserving critical landmarks and anatomical relationships. These elements should be integrated into VSP phase to achieve both aesthetic and functional outcomes.

Facial trauma can be categorized into three regions: lower, middle, and upper thirds. Each region presents unique management approaches, biomechanical considerations, and critical anatomical features. In the VSP phase, these factors must be carefully considered, along with VSD elements such as plate design, borders, contouring, and thickness, to achieve optimal outcomes, ensuring they can withstand the forces in each area and adapt to the region's specific demands.

Trauma treatment can be categorized into conservative, closed, and open surgical approaches. For closed treatment, intermaxillary fixation and splints are commonly used. Patient-specific arch bars for maxillomandibular fixation and splints can be created to minimize teeth and soft tissue injuries during closed treatment. However, this approach is not widely adopted, as it is typically needed in emergency settings and is not considered cost-effective. For open surgery, screws, guides, and plates are used for reduction and fixation.

3D PoC offers several levels for managing facial trauma. The first level involves segmenting CT images and printing 3D models, which are used for surgeon education, surgical preparation, and both perioperative and intraoperative applications. The next level includes basic VSP, where techniques such as mirroring or virtual surgical reduction are applied to achieve the desired surgical outcomes. A model can be fabricated at this stage for plate prebinding, wafer fabrication, and hybrid plate adaptation. This level is particularly beneficial in managing fractures with severe displacement. The most commonly used technologies for 3D printing in this context include FDM, SLA, and Binder Jet.

Level 3 enables the surgeon to design and fabricate custom implants, such as for orbital floor fracture reconstruction. At the most advanced level, repositioning guides and plates are planned, designed, and fabricated, typically used in secondary corrections and reconstruction of severe deformities following trauma (Fig. 4).

3.2 3D Planning Platforms in Orthognathic Surgery

In orthognathic surgery, once 3D models of the patient's anatomy are generated from CT or CBCT imaging, they are transferred into specialized surgical planning platforms. These platforms play a critical role in aligning and manipulating the patient's skeletal and dental structures, enabling

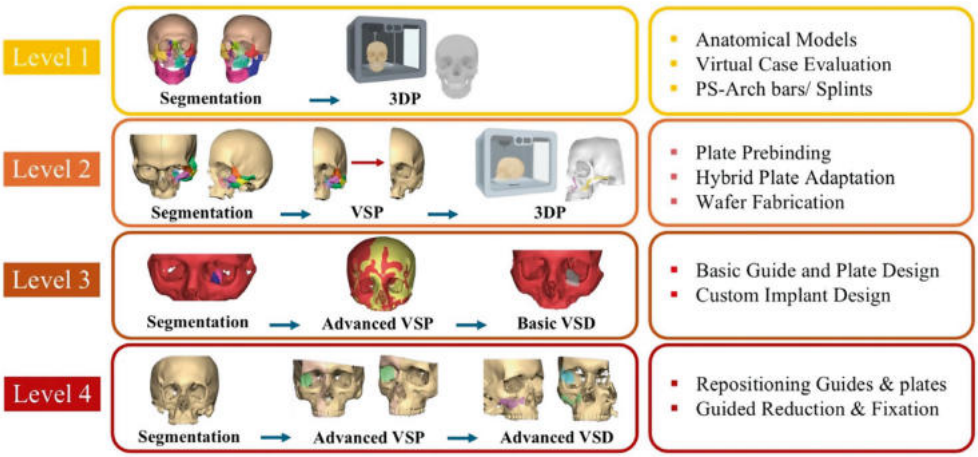


Fig. 4 The various levels of 3D point-of-care solutions in managing facial trauma, illustrating the progression from basic to advanced capabilities

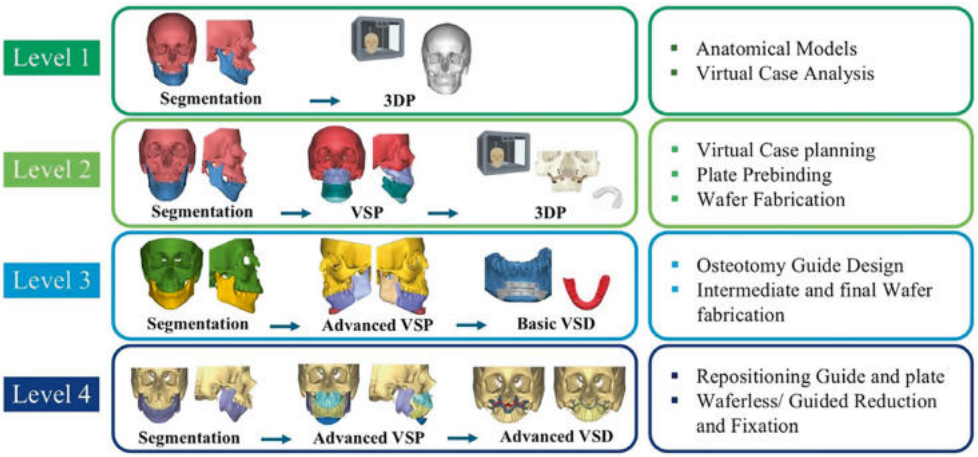


Fig. 5 The different levels of 3D point-of-care solutions in orthognathic surgery, demonstrating the progression from foundational to more advanced capabilities

surgeons to plan complex procedures with a high degree of accuracy and predictability.

VSP in orthognathic surgery must consider several key factors, including the airway, the severity of jaw malposition, soft tissue analysis, occlusion, and anatomical landmarks. After analyzing these factors, specialized software platforms allow the surgeon to simulate osteotomies, reposition skeletal components, and plan for proper occlusion. These platforms also provide digital tools to simulate the impact of jaw repositioning on soft tissue and the airway, which is crucial for achieving optimal outcomes in this domain.

From a 3D PoC perspective, Level 1, which involves segmenting and printing a 3D model of the patient without any VSP, is no longer considered sufficient for orthognathic surgery preparation, although it remains useful for case learning and virtual case analysis. At Level 2, after completing VSP and repositioning the jaws in their final position, wafer/splint fabrication can be performed for intraoperative use, and models can be printed for plate prebinding. Level 3 introduces the design of surgical guides that ensure the planned osteotomy is executed accurately, followed by jaw repositioning using wafers. At Level 4, patient-specific guides with pre-drilled holes are designed to ensure precise surgical osteotomies and jaw movements, followed by the use of patient-specific plates for fixation in the final jaw position (Fig. 5).

As orthognathic surgery is an elective procedure aimed at improving both functional and aesthetic deformities, achieving accuracy with minimal complications has become the standard of care. Today, most departments strive to reach Level 4 to ensure that planned surgical movements are executed with high precision, ultimately leading to better patient outcomes.

3.3 3D PoC Applications in Reconstruction Surgery

Reconstruction surgery is highly complex due to the intricate nature of facial anatomy, the precise adaptation required for the recipient implant, and the meticulous harvesting from the donor sites in cases of autografts. Performing procedures such as osteotomies, resections, or contouring without precise guidance is difficult, as it requires accurately adapting the graft tissue to achieve both functional and aesthetic out-

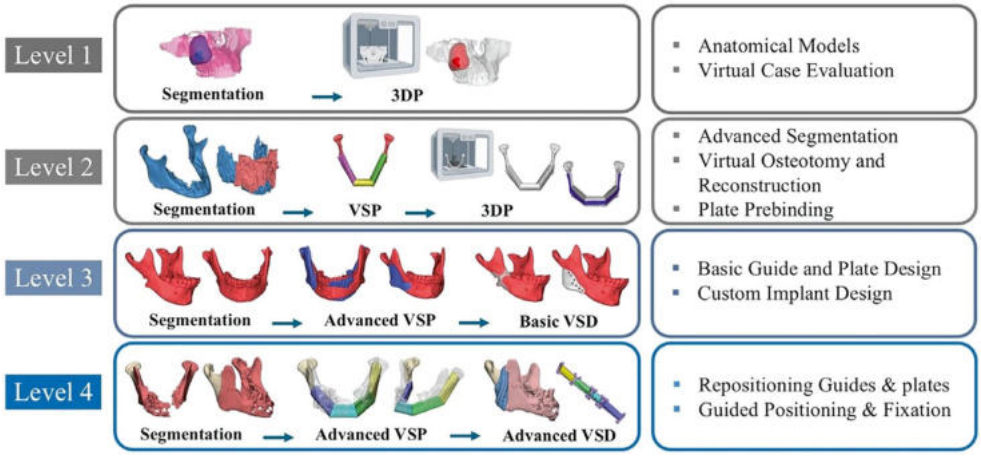


Fig. 6 Levels of 3D point-of-care solutions in reconstruction surgery, showcasing the progression from basic techniques to more advanced capabilities

comes. Achieving these results through freehand techniques alone often presents significant challenges, but the new technologies offered by 3D PoC provide a shift from surgeon-dependent resections toward more precise, technology-assisted procedures.

Facial reconstruction is typically performed after tumor or pathology resection, to correct congenital deformities, or to repair severe tissue damage resulting from trauma, among other causes. Reconstruction materials can vary and include alloplastic, allograft, xenograft, and autograft options. Alloplastic materials, such as titanium, PEEK, and polyethylene, are typically designed to fit the defect area and are often manufactured using additive manufacturing following VSP and VSD. Allografts and xenografts, including collagen, hydroxyapatite, and bone substitutes, can be used alone or in combination with autografts and are typically implanted using specialized templates such as a basket or mesh, which require customized virtual planning.

Despite advancements in materials, autografts remain the gold standard, with various donor sites available and selected based on the case's specific needs. Autografts must be carefully contoured to fit the deformity site, a process made easier through VSP, which allows for the design of cutting guides. These guides ensure accurate transfer of the positions and angulations of the osteotomies, and the fragments are then repositioned to the final location, where they are fixated using patient-specific plates.

VSP in this domain must take into account key factors such as restoring symmetry, biomechanical considerations, mastication, function, and aesthetics.

In addition to general key factors, VSP for tumor resection and reconstruction surgery must consider specific elements, including ensuring adequate surgical margins and performing the resection with precision. VSP should also be prepared to adapt to potential positive margins and the need for extended resection.

From a PoC perspective, Level 1 involves segmenting and printing a 3D model representing the tumor or deformity, primarily used for surgery preparation and performing virtual case evaluation. The next level involves advanced segmentation, including the superimposition of MRI and CT images in tumor cases, as well as performing VSP for osteotomy simulation and aligning the graft with the deformity to achieve the final reconstruction outcome. The model can then be printed, and plate prebinding can be performed. However, this level is limited in its accuracy since the osteotomy and contouring are done freehand. Level 3 offers more advanced design capabilities, allowing for the design and printing of alloplastic-custom implant reconstruction, creating guides for osteotomy and contouring, and the fabrication of the final implant.

At the most advanced level today, resection is performed using surgical guides and controlled contouring osteotomy for the graft. A custom plate is then used to reposition the bone fragments and securely fixate them (Fig. 6).

3.4 Managing Temporomandibular Joint Surgery in PoC

Temporomandibular joint (TMJ) disorders can arise from both intra-articular and extra-articular pathologies, manifesting in symptoms such as pain, limited mouth opening, malocclusion, and jaw deformity. Treatment options range from conservative management to minimally invasive endoscopic procedures or open surgeries, which may involve techniques such as discectomy, condylectomy, and other surgical interventions.

In cases of end-stage TMJ disorders, where severe degenerative joint disease or other pathologies render the joint unresponsive to conservative or minimal surgical therapies,

total joint replacement is indicated, as the joint components can no longer be salvaged.

The advent of AM technology has enabled the fabrication of both stock and custom TMJ replacements, providing more precision and better surgical outcomes.

Several key components must be considered in TMJ surgery planning, including the bony evaluation of the condyle and fossa, the assessment of pathological lesions, and the evaluation of disc position and integrity based on MRI. Additionally, the superimposition of CT and MRI scans can be applied for more accurate diagnostic purposes.

From a 3D PoC perspective, Level 1 involves printing educational 3D models, fabricating night guards for conservative treatment, and conducting virtual assessments. Level 2 includes advanced segmentation and superimposition between imaging modalities, providing critical information about the relationship between the condyle and disc, which is essential for minimally invasive surgeries such as arthroscopy and discopexy.

At Level 3, advanced guide design and fabrication are utilized to perform controlled osteotomies, such as condylectomy and coronoidectomy.

Level 4 represents the most advanced stage, involving total joint replacement using either an alloplastic implant or autograft, guided by custom templates for fossa preparation and controlled condylectomy. These guides enable the precise placement of patient-specific implants, ensuring accurate fixation of the fossa and condyle implant in their exact positions (Fig. 7).

3.5 Patient-Specific Guided Intervention and Implant Surgery in 3D PoC

Different maxillofacial applications require precise interventions to avoid damage to vital anatomical structures, such as during implant insertion, biopsies, and precise injections, among other procedures. For guided intervention, VSP must carefully consider key anatomical landmarks, including nerves, sinuses, and other critical structures. In these interventions, the goal of VSP and VSD is to ensure minimally invasive procedures with minimal risk of uncontrolled injuries to adjacent tissues.

3D PoC offers several solutions in this domain. At Level 1, the process begins with segmenting and 3D printing a model, which allows for virtual case evaluation and helps determine factors such as thickness, depth, and angulation of the planned intervention.

Level 2 involves virtual planning for guides designed for specific interventions such as injections, biopsies, and implant surgery.

At Level 3, more advanced VSP and VSD enable the fabrication of specialized guides, such as soft tissue-borne guides for the removal of foreign bodies.

Level 4 offers even more sophisticated VSD capabilities, allowing for the use of guides in both contouring procedures and implant surgery, providing comprehensive solutions for complex cases (Fig. 8).

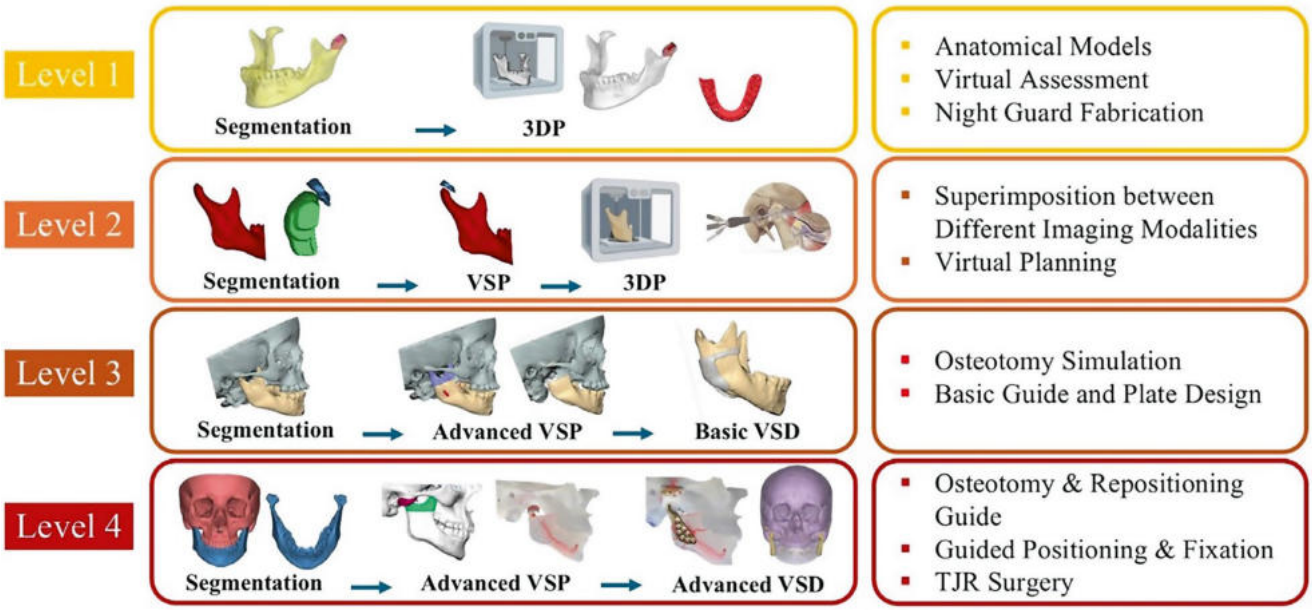


Fig. 7 The different levels of 3D PoC solutions for managing TMJ surgery, illustrating the progression from basic to advanced technique

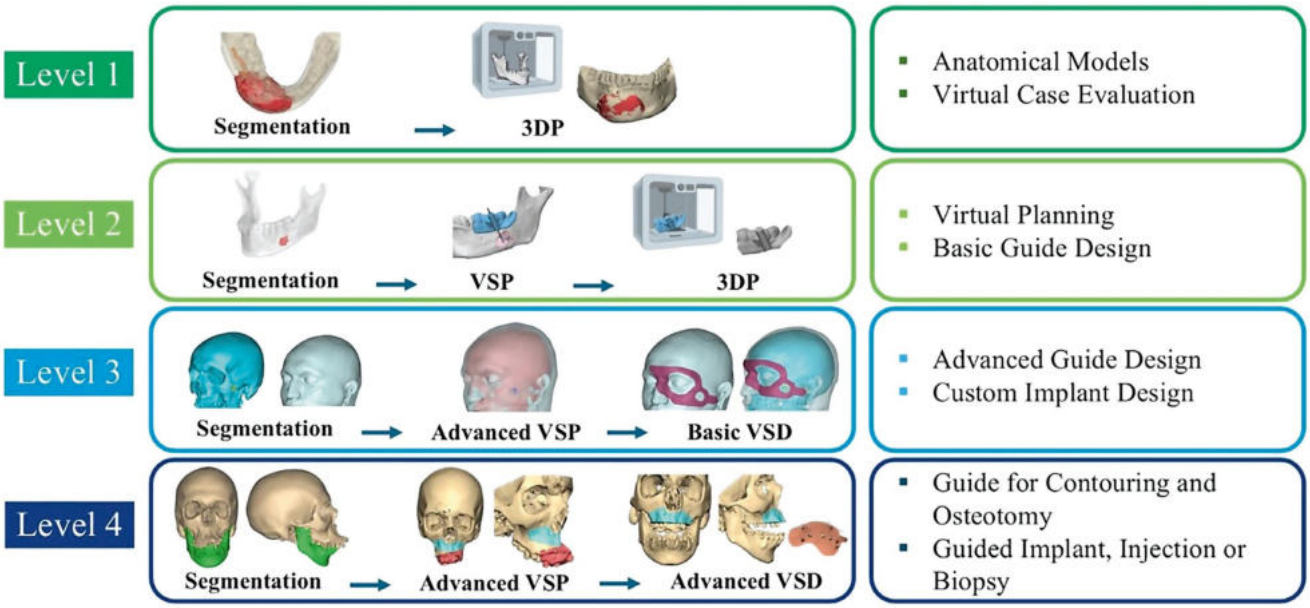


Fig. 8 The various levels of 3D PoC solutions for Patient-Specific Guided Intervention and Implant Surgery, outlining the evolution from basic methods to cutting-edge techniques

References

1. Hull CW. Apparatus for production of three dimensional objects by stereolithography. US Patent 4,575,330. 1986.
2. McGurk M, Amis AA, Potamianos P, Goodger NM. Rapid prototyping techniques for anatomical modelling in medicine. Ann R Coll Surg Engl. 1997;79:169–74.
3. Brooks M. The day the world became 3D. New Sci. 2016;232:40–1.
4. Hatz CR, Msallem B, Aghlmandi S, Brantner P, Thieringer FM. Can an entry-level 3D printer create high-quality anatomical models? Accuracy assessment of mandibular models printed by a desktop 3D printer and a professional device. Int J Oral Maxillofac Surg. 2020;49:143–8.
5. Shafiee A, Atala A. Printing technologies for medical applications. Trends Mol Med. 2016;22:254–65.
6. Wubneh A, Tsekoura EK, Ayranci C, Uludağ H. Current state of fabrication technologies and materials for bone tissue engineering. Acta Biomater. 2018;80:1–30.
7. Thieringer FM, Honigmann P, Sharma N. Medical additive manufacturing in surgery: translating innovation to the point of care. In: The future circle of healthcare. Cham: Springer; 2022. p. 359–76.
8. Zoabi A, Redenski I, Oren D, Kasem A, Zigron A, Daoud S, Moskovich L, Kablan F, Srouji S. 3D printing and virtual surgical planning in oral and maxillofacial surgery. J Clin Med. 2022; https://doi.org/10.3390/jcm11092385.
9. Abdul NS, Shivakumar GC, Sangappa SB, Di Blasio M, Crimi S, Cicciù M, Minervini G. Applications of artificial intelligence in the field of oral and maxillofacial pathology: a systematic review and meta-analysis. BMC Oral Health. 2024;24:122.
10. Stucki J, Dastgir R, Baur DA, Quereshy FA. The use of virtual reality and augmented reality in oral and maxillofacial surgery: a narrative review. Oral Surg Oral Med Oral Pathol Oral Radiol. 2024;137:12–8.
11. Numajiri T, Morita D, Yamochi R, Nakamura H, Tsujiko S, Sowa Y, Toyoda K, Tsujikawa T, Arai A, Hirano S. Does an In-House computer-aided design/computer-aided manufacturing approach contribute to accuracy and time shortening in mandibular reconstruction? J Craniofac Surg. 2020;31:1928–32.
12. Kwon T-G, Lee S-T, Choi S-Y, Kim J-W. Considerations for virtual surgical planning and simulation in orthognathic surgery—a narrative review. Front Oral Maxillofac Med. 2020;2:27.
13. Marschall JS, Dutra V, Flint RL, Kushner GM, Alpert B, Scarfe W, Azevedo B. In-house digital workflow for the management of acute mandible fractures. J Oral Maxillofac Surg. 2019;77:2084.e1–9.
14. Efanov JI, Roy A-A, Huang KN, Borsuk DE. Virtual surgical planning: the pearls and pitfalls. Plast Reconstr Surg Glob Open. 2018;6:e1443.

Regulation Perspectives for Point-of-Care Lab in Cranio-Maxillo-Facial Surgery

María Gloria Álvarez Caballero

1 Change of Paradigm in Hospitals: from Users to Manufacturers

Several studies demonstrate the benefits of virtual surgical planning (VSP) and 3D printing in the medical field [1–3]. Through the implementation of these technological innovations to support diagnostic and treatment processes, hospitals are thus beginning to actively promote:

- Accelerated training of healthcare professionals. By enhancing access to surgical training in safe environments, surgeons are allowed to develop their initial learning curve using artificial models that replicate reality, ideally before moving to clinical practice. This is especially beneficial in case of complex pathologies and low-incidence pathologies at the healthcare centre itself. Likewise, VSP and 3D printing support continuous training in the innovative and rapidly evolving field of healthcare, with the ongoing development of new techniques and surgical approaches, as well as continuous technological advances and improvements.
- Accelerated diagnoses. Advanced data processing for the development of 3D models provides additional information to surgeons in comparison to conventional DICOM (Digital Imaging and Communication in Medicine) studies.
- Personalised treatments. Surgical planning allows for a more precise approach to the pathology, which in turn leads to greater safety during the procedure. This planning also enables a more agile and effective intraoperative treatment, resulting in a reduction of re-interventions and surgical complications. Furthermore, this reduction in time and adverse incidents directly leads to a reduction in hospital stay, reporting benefits to the economy of the healthcare system and helping to streamline patient waiting lists.
- Empowering patients. 3D models provide them with a deeper understanding of their own illness and thus motivate them to become an active part in their treatment and recovery.

To optimise these benefits, it is essential to ensure an effective, transparent, and continuous management and communication between user and manufacturer. In this regard, limited time margins, the data protection regulatory framework in each region, and limited reimbursement capabilities for such procedures represent three determining factors in the evolution of hospital behaviour. This is translated into the paradigm shift that has been experienced by healthcare institutions in the recent years, where hospitals are no longer positioned solely as users and consumers of healthcare products, but also as manufacturers of these products.

This transformation aligns both in timing and in form with another paradigm shift currently taking place in healthcare: moving towards 5P medicine (Personalised, Predictive, Preventive, Participatory, and Populational). In 5P medicine, the patient becomes the centre of the healthcare system [4]. Figure 1 presents relevant examples of VSP and 3D printing, along with their application to 5P medicine.

Any significant change or transformation within the hospital setting must be accompanied by a series of adaptations. When prioritising the benefit of their patients, healthcare professionals will provide, if possible, the necessary infrastructure and human resources for the in-house implementation of VSP and 3D printing. However, true implementation and integration within hospitals would imply incorporating these technologies into the daily responsibilities of healthcare professionals as additional medical care processes. Even more crucially, it would imply training healthcare professionals specifically in this kind of technical tasks, historically outside their specialty capabilities. Therefore, it is

M. G. Á. Caballero (✉)
Coruña and Cee Health Area. Galician Health Service (SERGAS), A Coruña, Spain
e-mail: maria.gloria.alvarez.caballero@sergas.es

© The Author(s), under exclusive license to Springer Nature Switzerland AG 2025

A. Tel, M. Robiony (eds.), *Atlas of Virtual Surgical Planning and 3D Printing for Cranio-Maxillo-Facial Surgery*,
https://doi.org/10.1007/978-3-031-94495-6_5

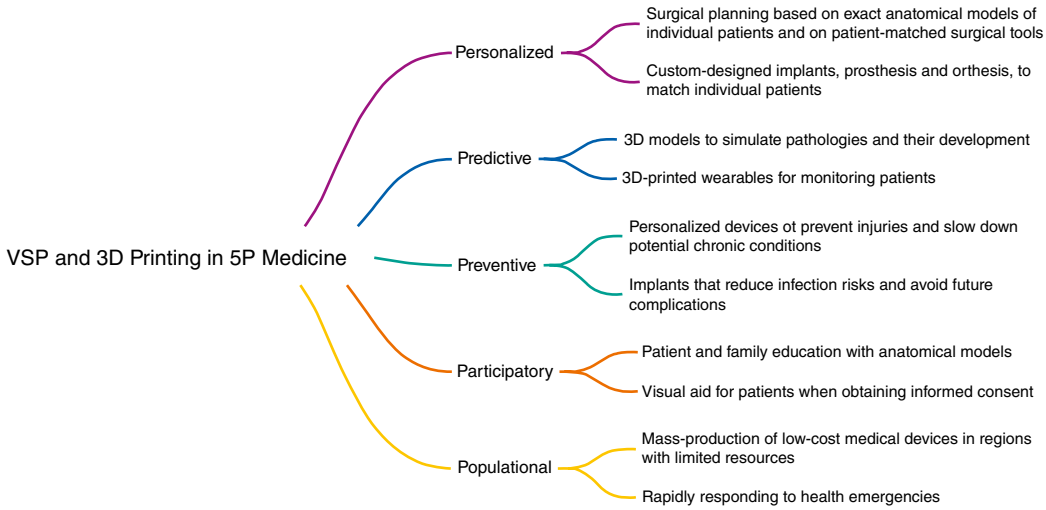


Fig. 1 Relevant VSP and 3D printing applications to enhance 5P Medicine

essential to realistically assess the workload that the incorporation of these new competencies might place on surgeons and radiologists, among others, in their daily clinical practice.

This is the reason why the clinical engineer role and its incorporation in healthcare settings is expanding and becoming more widespread. Through medical image processing and hospital technologies expertise, as well as the understanding of a common language shared with healthcare professionals, the clinical engineer is increasingly becoming a fundamental support figure in hospitals [5]. Especially, when intending the true implementation and integration of in-house VSP and 3D printing. This role is not intended to replace the work of healthcare professionals, the real specialists in anatomy, pathology, and medical imaging, but to serve as a means of maximising and optimising the information available to them. Consequently, the conjunction of clinical and technical roles is becoming the key to implementing and consolidating a new multidisciplinary hospital service: the 3DPOC.

2 Visualisation of a 3DPOC: Initial Considerations

For the implementation of a 3DPOC, it is essential to identify the healthcare institution's own capabilities:

- Available infrastructure dedicated exclusively to the development of 3D models, including facilities, technologies and IT (information technology) systems
- Human technical capabilities for the development of digital or physical 3D models
- Hospital needs that are intended to be addressed in-house with these types of technologies

This will allow us to establish the scope of the 3DPOC and define its initial product catalogue. However, to implement this scope and begin developing models, it is crucial to understand the applicable regulatory frameworks, depending on the type of product developed and the regional legislation [6–9].

Generally, any device that may affect or influence diagnostic or treatment processes is considered a medical device. In other words, 3D models that provide information about a disease, injury, or condition are considered medical devices. Likewise, 3D-printed surgical guides and implants intended to treat a disease, injury, or condition are also medical devices.

In contrast, 3D models intended to increase the capabilities of healthcare professionals in general terms, i.e. not to plan a specific surgery for an individual patient, are not considered medical products [10].

Once medical devices are identified within the 3DPOC catalogue, they need to be classified. To support this process, the following subsections provide an overview of essential concepts and boundaries. It is important to assess their application to the circumstances of the 3DPOC, considering the specific regulatory framework in each country[1]. In this context, understanding and complying with the regulatory framework is essential to promote the development of safe and effective 3D models. Building a 3DPOC based on these principles is a foundational step towards the future consolidation, scalability, and funding of the 3D lab.

[1]It is important to consider that regulations focus on the resulting products, i.e. on 3D medical devices, not on the manufacturing processes and their particularities.

2.1 Custom-Made Medical Devices

Medical devices that often require a prescription from an authorised healthcare professional, in accordance with national legislation and under their responsibility. This prescription must include, among other things, specific design requirements and the intended use of the device.

Through this prescription, custom-made medical devices are developed for the sole use of a particular patient8. In countries like the United States (US), Australia, and Canada, they can also be intended to meet the special needs arising in the course of such healthcare professional practice, or a designated one [6, 7, 9].

It is important to note that the personalisation of custom-made medical devices starts at the very beginning of the design process. That is, the adaptation of mass-produced medical devices cannot be considered custom-made medical devices.

Similarly, mass-produced devices cannot be considered as custom-made medical devices. In fact, in countries such as the USA, Australia, or Canada, the production of custom-made medical devices is regulated exclusively for the treatment of rare diseases or conditions, for which no commercial alternatives are available [7, 9, 11, 12]. In these cases, it would not be feasible to gather sufficient non-biased clinical evidence.

The regulation of custom-made medical devices is generally less stringent in comparison to standard medical devices. They are exempt from CE marking (European Union, EU), Food and Drug Administration (FDA) 510(k) clearance for equivalent devices or FDA Premarket Approval (PMA) for high-risk devices, among others [8, 9]. Additionally, manufacturers of custom-made devices are generally not required to register their developments in formal regional registers, as may be required for other types of commercial medical devices. However, they must demonstrate the safety and effectiveness of each product, and a series of Good Manufacturing Practices (GMP) must be met. This includes, among other things, documentation ensuring the traceability and safety of processes, quality controls, and post-market surveillance, where applicable.

To this end, hospitals must notify and/or register the production of custom-made medical devices to the corresponding health authorities and comply with the applicable inspections, audits, and reporting requirements.

It is recommended to consult the regulations in force in each country, as regulatory agencies may, in some cases, set or recommend limits on the number of custom-made medical devices that can be produced within a specified period [13].

2.2 Patient-Matched Medical Devices

Medical devices that may be prescribed or requested by a healthcare professional for a specific patient [12].

Unlike custom-made medical devices, these devices are based on a standard design that is personalised according to each patient, regarding specific measurements or characteristics. To this end, hospitals acting as manufacturers of personalised medical devices need to define and implement validated and reproducible processes based on design envelopes. A design envelope could be defined as a conjunction of ranges of minimum and maximum measurements or dimensions, performance limits, materials, and other relevant characteristics in terms of production [11, 12]. Once defined, these envelopes can be adapted to fit the anatomical features of a particular patient, thus meeting the accuracy required for a geometrical 3D reconstruction.

Hospital manufacturers must ensure and provide objective evidence in relation to the safety and efficacy of patient-matched medical devices, according to their intended uses. Design envelopes may be determined by clinical research, industry standards, clinical practice guidelines, specialised education or training, and practical experience in producing or using medical devices [12].

Based on the above, the design of patient-matched medical devices is responsibility of the hospital manufacturer, regardless of whether the development is advised or agreed with a healthcare professional.

The concept of patient-matched medical devices has been described in numerous harmonisation documents and regulatory guidance on personalised medical devices [14–16]. Despite most of them not being legally binding, they intend to align manufacturers with regulatory expectations. This suggests that future global regulatory trends are likely to focus on this concept. Custom-made medical devices may result from non-validated, non-verified, or non-reproducible manufacturing methods, unlike patient-matched medical devices. If custom-made medical devices are only produced in rare cases where no suitable patient-matched alternatives are available, the expansion of personalised medicine would not compromise the safety of the resulting medical devices. According to the Therapeutic Goods Administration (TGA) of Australia, one of the countries already implementing this regulation, most medical devices that previously fell under the definition of custom-made would now be considered patient-matched [12].

In markets that have not yet incorporated this concept, patient-matched medical devices are regulated as standard medical devices as they are modified commercial products customised for individual needs, with the certifications this requires. It is recommended to consult the regulatory framework in each country to assess its applicability.

Regulatory agencies, such as the TGA, may set limits on the number of patient-matched medical devices that can be produced within a given period of time under less stringent regulatory conditions. This would be the case for the

Australian Register for Therapeutic Goods (ARTG) low-volume exemption [12].

2.3 In-House Medical Devices

Medical devices exempt from certification that are manufactured on a non-industrial scale within the hospital for use solely within the same healthcare institution, meaning they are not distributed to other hospitals or legal entities. In-house medical devices must meet certain requirements, depending on the regulatory framework. Therefore, it is recommended to review the current regulations in each country to assess their applicability and the specific method for registering the production of in-house medical devices to ensure their compliance.

In the EU, in-house medical devices are regulated through Article 5 (5) of the European Medical Device Regulation (MDR) [8]. This chapter establishes that in-house manufacturing is justified when it addresses needs that cannot be met at the appropriate level of performance by an equivalent device available on the market. However, some interpretations may consider the application of in-house medical devices to be restricted to the needs of a patient group with similar characteristics, instead of personalised applications for each individual patient.

In-house manufacturing allows hospitals to produce and consume medical devices tailored to specific needs that are not covered by commercial products. These exemptions do not imply an absence of regulation, as it is still necessary to ensure the safety and efficacy of the medical devices [17]. Nevertheless, they do offer significant bureaucratic and administrative incentives to encourage in-hospital innovation and generate value that directly benefits the patient.

2.4 Risk Classification

Each regulatory agency establishes its own risk classification, regardless of whether the medical device is custom-made, patient-matched, in-house, etc. As the risk to patients increases, greater regulatory requirements and demands will be set to ensure proper identification, elimination or reduction, and control of those risks.

Based on common trends across different regulatory agencies, four levels of distinction could be established, as outlined in Table 1. It is recommended to review the current regulations in each country to understand the applicability and specific nomenclature of the risk classification.

Table 1 Risk classification and examples of the main VSP and 3D printing products developed in a 3DPOC

No risk	3D models for education: healthcare professionals, patients, or family members
	3D models for informed consent
Lower risk	3D models for surgical planning: VSP, 3D-printed
	3D-printed non-invasive medical devices
Medium risk	3D-printed invasive surgical tools. e.g. cutting/drilling guides
Higher risk	3D-printed implants

3 Integration Within the Healthcare Institution: Key to Success and Sustainability

There are three fundamental operational models for the in-hospital production of medical devices that allow the appropriate implementation of the predefined scope at the 3DPOC and the applicable regulatory framework [18]:

- Health care facility assuming all manufacturer responsibilities, including risk management and adverse event reporting. According to the specifications of the corresponding health authorities, it may be necessary to obtain the appropriate medical device manufacturer licence, register the facility with the applicable certification, etc. By assuming all manufacturing tasks and quality controls, the hospital gains greater autonomy and speed in the development of personalised medical devices, in exchange for a significant commitment of resources and technical training.
- Health care facility using a Medical Device Production System (MDPS). MDPS is commonly defined as a collection of raw materials, software, main production equipment, and post-processing equipment, to be used by a health care provider or facility to manufacture a specific type of medical device at the 3DPOC [12, 18]. MDPS systems are validated and certified according to the corresponding regulatory standards, and their conformity assessment also covers the resulting medical devices produced at the 3DPOC, considering the scope defined by the manufacturer is met. Therefore, this model simplifies regulatory compliance. However, the health care facility may need to undertake additional post-processing tasks not covered by the MDPS, such as the sterilisation of invasive devices. The responsibilities assigned to the manufacturer and the hospital user are not clearly defined



Fig. 2 Representation of the most relevant cross-disciplinary hospital departments involved in 3D models development

in all regulatory frameworks and will be subject to clarifications in the near future.

- Contract manufacturer co-located at or near the health care facility site. In this case, the company, assuming all manufacturer responsibilities, provides the necessary equipment and qualified personnel. While this model ensures regulatory compliance without requiring so many internal resources, it may reduce flexibility to accomplish last-minute modifications or developments of medical devices.

The implementation of any of the three scenarios described above requires institutional support for success. The guidelines established by the hospital management are essential to identify priority needs, align expectations, and coordinate the implementation of a 3DPOC, especially when seeking to be scalable, fundable, and sustainable in the medium to long term.

The creation of a fully integrated 3DPOC within the healthcare institution requires the modification and adaptation of clinical processes and, therefore, the coordination and collaboration with other healthcare support services. Figure 2 outlines the most relevant services to consider as stakeholders.

4 Implementation of a 3DPOC

To comply with the current regulatory framework and, as part of the responsibilities assigned as a medical device manufacturer, i.e. ensuring the safety and efficacy of the developed 3D models, it is essential to implement a QMS in the 3DPOC. The complexity of this system will depend primarily on:

- The types of medical devices to be developed
- Their classification based on patient risk
- The scope of manufacturing responsibilities assumed

This QMS must comply with the ISO 13485 standard [19], which establishes the essential quality and documentation requirements for ensuring consistency in the outcome of medical devices. Other documents to be taken into account emphasise the importance of rigorous controls, testing, and validation in a more specific manner for VSP and the additive manufacturing process [20–22].

While the cited documentation includes an interesting compilation of technical recommendations regarding design, materials, and manufacturing processes, only logistical and procedural issues will be addressed in the following paragraphs. Considering this, outlined below are the key aspects to take into account when initially building a QMS in a 3DPOC.

4.1 Facilities

Ideally, it is recommended to divide the layout of a 3DPOC facility into at least two distinct areas to meet the quality and safety requirements established in the ISO 14644 series of standards [23, 24].

1. Office area: designated for documentation and computer-assisted design procedures.
2. Workshop area: designated for manufacturing and post-processing procedures. This area should also be suitable for pre-sterilisation tasks (if applicable) and storage.

As different activities are developed in each environment, the appropriate cleanliness will vary depending on the required air quality for each intended activity.

To minimise risks in the 3D workshop, it is recommended to follow applicable regulations for clinical laboratories and controlled environments in hospitals, as well as their conditions and technical requirements. Specifically, attention should be paid to:

- Classifying relevant facilities based on air quality and biocontamination according to the activities performed [23–27]. This classification will determine the cleaning and accommodation requirements for producing medical devices. Requirements will be stricter for 3D models classified as higher risk.
- Ensuring electrical safety of the facility and arranging it to prevent unexpected power cuts during manufacturing, which could affect the production process or even the integrity of the equipment. It is advisable to connect all key production equipment to power outlets with a network protection system, backup generator, or uninterruptible power supply [28].
- Ensuring proper ventilation of the facility and providing it where necessary [29]. Certain substances typically handled in a 3DPOC, such as isopropyl alcohol or acrylonitrile butadiene styrene (ABS) in its melting phase, may pose risks to personnel if they are exposed for prolonged periods of time without the adequate precautions. If adequate natural ventilation is not possible, a forced extraction system with an appropriate renewal rate should be installed. It is recommended to consult and follow manufacturers' guidelines in this regard.
- Monitoring the cooling and heating of the facility and providing control where necessary [29]. Attention should be paid to the operating conditions required for each type of technology and to the storage conditions recommended by manufacturers. Generally, these recommendations involve maintaining ambient temperature, low light levels, and either absence or control of relative humidity.

The 3D workshop can, in turn, be divided into several spaces to optimise the 3DPOC workflow:

1. 3D printing area. For desktop equipment, it is recommended to place printers on sealed countertops to avoid vibrations that may impact the manufacturing process and printing quality. Additionally, in 3DPOCs with a large number of printers, isolating this space may be considered to control ambient noise and reduce acoustic contamination [30].
2. Post-processing area. This space must be equipped with the personal protective equipment (PPE) needed to ensure the safety and health of operators. It is recommended to review the safety data sheet for each material as well as the manufacturers' guidelines to identify and quantify the required PPE, considering the risks associated with both acute and prolonged exposure.
3. Washing area. It is important to have a sink for washing auxiliary components of the printing equipment and for performing the macroscopic cleaning of products that will later undergo sterilisation.
4. Pre-sterilisation area. 3D models intended to be in contact with the patient (tissues, mucous membranes, non-intact skin) or with invasive instruments require sterilisation and may need some previous preparation within the 3DPOC itself. In such cases, it is essential to maintain optimal aseptic conditions, free from contamination [23, 24].
5. Storage area. Storage requirements, primarily determined by environmental conditions, vary for each type of material, as outlined in the materials specification sheets. To prevent accidents and ensure compatibility between different materials, a safety cabinet is recommended for storing flammable and corrosive chemicals [30]. These cabinets are designed to minimise risks of fire, explosions, or spills and help ensure safe storage in compliance with applicable regulations for both worker and environ-

mental protection. Other key recommendations include establishing an independent storage area specifically for biocompatible materials, facilitating their identification, and implementing stock control with expiration date monitoring. In 3D printing, it is also crucial to understand factors beyond expiration dates that may influence material degradation, to set specific plans for action, prioritisation, reallocation, and disposal. Technical and safety data sheets for each material should be readily accessible to operators for consultation, in both digital and physical formats.

6. Waste area. Separate and differentiated containers are required for products that need a special waste disposal, such as flammable items. Environmental Services commonly implement environmental management systems based on the UNE-EN ISO 14001 standard [30]. It is recommended to consult the Environmental Service of each hospital for specific guidelines on storage and labelling to ensure proper disposal and subsequent destruction of waste generated in the 3DPOC. Other key considerations include neutralising absorbable or absorbed toxic materials and avoiding the storage of uncovered bottles and containers.

4.2 Resources: Equipment, Software, Raw Materials, and Fungible Goods

Within the resources available in a 3DPOC, it is important to identify those that are considered and regulated as medical devices per se, as opposed to those that are not.

Hardware devices used in a 3DPOC (3D printers, virtual/augmented reality glasses, 3D scanners, etc.) would only be considered medical devices if they are designed and marketed for specific medical purposes, which is not the usual case. On a regular basis, 3D printers, for example, are regulated as machinery, which significantly reduces the considerations and certifications required for their use in a 3DPOC. However, the 3DPOC must comply with the manufacturers' recommendations regarding maintenance and cleaning, which is essential to ensure the precision in the manufacture of medical devices.

In contrast, software that meets the definition of a medical device, Software as a Medical Device (SaMD), or a Medical Device Data System (MDDS) must be certified. This implies all solutions that directly affect or influence the diagnosis or treatment of conditions or diseases. In this regard, medical image processing and segmentation software is especially notable, regardless of its modality: manual, semi-automated, or automated using artificial intelligence (AI). This is due to the diagnostic reliability required in this type of software to ensure the correct design and development of 3D medical devices based on accurate representations of each patient's anatomy.

Particular attention is also required for raw materials used during the manufacture of 3D models that are part of a medical device or intended for medical use. Depending on the applicable regulations in each country, these materials may require the same certification as a medical device or, at the very least, must comply with the safety requirements for medical products. All materials intended to be in contact with the human body or implanted in it must meet biocompatibility requirements according to the ISO 10993 series of standards [31]. Regulatory compliance will increase in stringency depending on the type of tissue, the duration of the contact, and the subsequent risk posed to the patient.

Besides certifications, technologies such as augmented reality or mixed reality require real-time or near-real-time data processing and low latency to provide instant feedback to the surgeon. Any delay in updating 3D overlays based on changes in the patient position or the surgeon actions can lead to inaccuracies in the operating room. For this purpose, the 3DPOC should ensure seamless connectivity for the wearable hardware and sufficient computational power to handle large datasets quickly. Additionally, high-resolution systems are required to allow the visualisation of anatomical structures with diagnostic precision.

The quality of the 3D models depends on the manufacturing conditions and the maintenance of the equipment within the 3DPOC. In this regard, it is advisable to comprehend and implement the manufacturers' recommendations to ensure optimal technological conditions, thereby securing the availability of the equipment and extending its useful life. Different types of maintenance are identified:

- First-level maintenance. Cleaning and maintenance of reusable components after using a particular equipment
- Preventive maintenance. Scheduled, periodic actions to prevent potential issues
- Corrective maintenance. Unplanned interventions, typically due to equipment malfunctions or failure to meet predefined end-product requirements

The responsibility for performing these tasks is determined according to the existing maintenance contracts and the technical competencies of the 3DPOC staff. Another medium-to-long-term need for any 3DPOC is the sustainability of the lab. To achieve this, different circular economy strategies can be implemented to reduce environmental impact and optimise resources, including the following:

- Integrating material recycling into the lifecycle of 3D-printed products, which is especially interesting in the reuse of plastic filaments

- Selecting low-environmental-impact materials, such as biodegradable or recyclable options, which is especially important in healthcare settings with high-resource consumption
- Reusing failed prints as exhibition or educational models
- Repurposing expired or defective materials for non-clinical applications that do not require the same quality and safety standards, such as for exhibition or educational purposes

4.3 Human Resources

As mentioned earlier in the chapter, the professional profiles involved in supporting healthcare processes have evolved significantly in recent years, particularly with the introduction of the clinical engineer role. The ideal setup for a 3DPOC would involve the collaboration between:

(a) Technical profiles, working full-time to handle daily operations, infrastructure management, and maintenance of equipment.
(b) Healthcare professionals, who act as knowledge experts, with a more consultative role in the design, verification, and validation of medical devices. Especially surgeons, however, are becoming increasingly proficient in VSP modelling and 3D printing and can actively collaborate.

Given the importance of implementing and maintaining an appropriate QMS to comply with the applicable regulatory framework, it is also recommended to have a designated quality and compliance manager within the 3DPOC. This role would be responsible for ensuring the quality of the final products and optimising workflow processes. In some regulatory environments, appointing such a role is mandatory, especially under ISO 13485 certification [19]. Therefore, it is advisable to review the current regulations in each country to ensure compliance.

On the other hand, some regulatory frameworks define one or more similar and sometimes complementary roles to ensure that medical devices meet the corresponding regulatory requirements [6–9, 32]. These roles cover safety and performance requirements, documentation and compliance of products, post-market surveillance, and the notification and handling of incidents and adverse events. The designation and specific responsibilities of these roles vary depending on the regulatory framework, although the requirements are generally similar:

- University-level education in a related field, such as health sciences or engineering, that proves adequate qualification for the development of products within the scope of the 3DPOC
- Experience in medical devices and/or regulatory and quality aspects
- Understanding of the applicable regulatory framework, both legislatively and regarding quality harmonisation standards

4.4 Standardisation of Operational Procedures

To harmonise the development of different types of medical devices and simplify workflows, it is recommended to standardise the procedures implemented in a 3DPOC, which in turn will promote the consistency and safety of the end-products.

The following points should be considered [19–22], particularly in relation to the management and logistics of medical devices development:

- *Suitability of medical image acquisition*. To obtain accurate 3D models, the starting isotropic medical image needs to possess sufficient diagnostic quality. This may be influenced by several factors, such as the slice thickness, the pixel size, the reconstruction algorithm, or the presence of artefacts. Therefore, it is recommended to involve medical imaging specialists, i.e. radiologists, if not to directly process and segment the area of interest, at least to verify the adequacy of the image in order to obtain reliable and high-quality 3D models. Based on these criteria, the acceptance of certain cases may be compromised, especially in clinical-intended 3D models where image acquisition cannot be repeated due to radiation dosage, processing times, or available hospital resources.
- *Medical images used for VSP and 3D printing*. These correspond to personal data of patients, both identifiable and clinical-assistive, so they must be accessible and managed as such, in accordance with the current regulations of each country [33–35].
- *Changes traceability to ensure user satisfaction*. Any changes in operational and user requirements that differ from the initial request need to be registered and agreed upon between the 3DPOC and the corresponding healthcare professional.
- *Input elements*. Before designing a new kind of medical device, ISO 13485 standard [19] establishes that all clinical and technical parties involved in its development need to identify, analyse, comprehend, and agree upon the following input elements:
  - Functional, operational, usability, and safety requirements in accordance with the intended use
  - Applicable regulatory requirements and standards
  - Preliminary risk analysis according to the ISO 14971 standard [36]

  - When applicable, information derived from similar previous designs and other essential requirements to be considered
  - Project planning, including work schedule and process controls, with the corresponding tasks and responsibilities at each step
- *Risk management*. As referenced in the previous point, risk management is a crucial aspect in the development of a medical device. It is important to consider:
  - Operational risks from the 3DPOC processes that could compromise the safety, traceability, and effectiveness of the different workflows, with direct impact on 3DPOC professionals, healthcare professionals (users), and patients. Such risks must be eliminated immediately, or otherwise, minimised and controlled as efficiently as possible.
  - Potential and actual risks and hazards associated with each type of product, which could compromise user or patient safety, as well as the correct functioning of the product.

Annex I of the MDR "General safety and performance requirements" [8] and the ISO 14971 standard [36] are good references to help identifying, analysing, eliminating/reducing, re-evaluating, treating, and accepting such risks and hazards.

- *Medical devices traceability*. Another key aspect, especially for those manufactured simultaneously or in batches. Traceability can be ensured through the implementation of a coding system with the assignment of a unique identifier that can even be engraved on the model itself. This grants that each device or part can be identified and traced from its digital design to the final printed product, which is especially crucial during adverse events management.
- *Validated processes*. Traceability and efficiency of processes is not only achieved by standardising them; validation is also required. Companies can validate their certified software solutions with hardware solutions from related companies in the sector. However, each 3DPOC is responsible for validating the combined use of resources within its own hospital context. Other necessary validations would apply to, for example, IT applications developed in-house for the management of requests and their integration into the EHR, or the traceability and efficiency of the sterilisation and delivery process. Furthermore, in the event of critical changes that may affect the process's ability to achieve the expected results or may introduce new potential or actual risks, the affected processes would need to be reassessed and revalidated.
- *Sterilisation*. A key support process in the development of medical devices, given its implications. Therefore, its integration and control by the 3DPOC is recommended. Despite the manufacturers' indications, it is advisable to conduct a prior study before implementation to test and confirm the influence of the different sterilisation methods and their parametrisation on the various materials used in the 3DPOC.
- *Quality controls*. Implementation of process and end-product controls ensure the conformity of the medical device, according to the ISO 13485 standard [19]:

1. Design controls, distinguishing between:
   - Verification of medical image processing based on the anatomical adequacy of a 3D model, i.e. its morphology and dimensions. This type of verification needs to be carried out by qualified healthcare professionals. For the case of study, this would imply radiologists as experts in medical imaging, and CMF surgeons as specialists in the anatomy and pathologies, also aware of the operational and user requirements for the end-products.
   - Verification of the 3D design or prototyping based on technical feasibility and clinical suitability. On one hand, a technical profile should confirm the absence of very fine or even infinitesimal geometries, as well as peaks or an incorrect meshing, to prevent subsequent incidents. On the other hand, the requesting CMF surgeon should be actively involved in controlling this design phase. Feedback from a clinical expert helps ensuring the clinical adequacy of the model and its alignment with the predefined operational and user requirements.
2. VSP validation. Developed by CMF surgeons in a safe, controlled environment, without patient involvement, unless the purpose of the study is to conduct a prospective clinical trial. This validation is fundamental before incorporating a new family of digital or virtual medical devices into the 3DPOC product catalogue, ensuring that they meet their intended use and are safe for clinical use. It can be implemented through comparative analysis with similar clinical cases.
3. Manufacturing controls. Only applicable for 3D-printed products. This should include biocompatibility [31] and material expiration [19] checks, alongside the adequacy of printing parameters [20, 22].
4. End-product control. The aim of this control is to confirm that the integrity and properties of the 3D-printed end-product will allow the corresponding 3D model to meet its intended use. For VSP, the design verification itself is considered sufficient as end-product control, i.e. anatomical adequacy and diagnostic precision. For other families of 3D-printed products, a technical profile needs to unequivocally verify the adequacy of the

model. This implies assessing anatomical and dimensional fitting, assemblies if present, as well as the critical properties identified, e.g. mechanical properties [20, 22].

5. 3D-printed product validation. Developed by CMF surgeons in a safe, controlled environment, without patient involvement, unless the purpose of the study is to conduct a prospective clinical trial. This validation is essential before adding a new family of 3D-printed medical devices to the 3DPOC product catalogue, ensuring they meet their intended use and are safe for clinical use. It can be implemented through:
   - Comparison with similar clinical cases, preferably in anatomical models for surgical planning.
   - Skills simulation in an environment that replicates reality, preferably in surgical guides, simulators, prototypes, and other medical devices.
   - Justified testing with an experimental model (ex vivo or in vivo), for certain prototypes and medical devices.
6. Sterilisation control. To assess the conformity of sterilised medical devices, the following aspects need to be verified:
   - The integrity of the container and sterile barriers of the products it contains, ensuring no adverse incidents occurred during transportation
   - Visual and haptic inspection, without damaging the sterilisation bag, to verify the mechanical properties of the product, ensuring they have not been altered during the sterilisation process
   - Verification of colour change in chemical indicators, to ensure the sterilisation process has been carried out correctly
   - Verification of the results obtained in microbiological control tests, to rule out possible sources of contamination [37]

Design or manufacturing modifications and the repetition of the relevant controls will be necessary until approval is obtained for each of the previously described aspects.

- *Associated documentation*. Every medical device must be delivered with the documentation required according to the corresponding legislation. In general terms, the following are notable:
  - Instructions for use. Preferably a concise document, clarifying especially storage, use, and disposal conditions of the products. It also includes clinical indications, contraindications, residual risks if any, and contact details in case of reporting an incident.
  - Labelling. It ensures product identification and traceability, and it also includes essential visual instructions so the surgeon knows, for example, the expiration date of the sterile product, if the product can be re-used, storage conditions, etc. The use of standardised and harmonised iconography according to the ISO 15223-1 standard is recommended to facilitate the understanding of critical symbols for clinical users [38].
  - Technical datasheet. A compilation of tasks performed, parameters, and responsibilities assigned during product design and development. It also describes the several controls implemented during the process and their results.
- *Post-market surveillance*. Another key area in the daily operations of a 3DPOC that is often overlooked. Along the operational procedures, a communication channel with CMF surgeons allows the reporting of claims and non-compliant products. For regulatory compliance, it is recommended to also maintain close contact with CMF surgeons after using the corresponding 3D models, thus performing additional clinical monitoring of patients from the 3DPOC. This enables the identification of:
  - Alternative uses not initially foreseen.
  - Patient prognosis and the influence of the 3D model on that prognosis.
  - Potential or actual risks.
  - Adverse events.
  - Utility and ease-of-use of the 3D model in relation to its intended use.
  - Utility of the associated documentation provided with the 3D model.

All this information enables risk management updates and the improvement in the development of future similar medical devices [36]. It is also useful for reporting health alerts and preparing reports for the corresponding health authorities.

Conversely, health authorities may notify health alerts related to the printing materials used as raw materials in 3DPOCs, presumably associated with a specific batch [39]. In such cases, the 3DPOC personnel should immediately identify the referenced products or batches within their lab. Depending on the cause and scope of each health alert, it may be necessary to prevent their use in the manufacture of medical devices, retaining or recalling already manufactured medical devices to minimise the risks for patients.

- *Data storage and backup*. It is recommended for all documentation and process management of a 3DPOC to be integrated into the hospital IT systems and the EHR. This approach will make it easier to ensure data protection and interoperability, regulating its access and allowing its retrieval if needed [40].

The standardisation of procedures in a 3DPOC, although potentially laborious in the initial stages of implementation,

represents an important step in consolidating any 3DPOC. Standardised records and the continuous establishment of corrective actions and quality objectives will improve the efficiency of VSP and 3D printing processes, allowing the scaling of in-hospital production and enhancing the sustainability of the lab.

5 Conclusions

The implementation of a well-structured 3DPOC represents a significant advancement in the personalisation and precision of surgical treatments, especially in CMF surgery. By integrating 3D manufacturing practices within the hospital, professionals can enhance surgical planning, reduce intraoperative risks, and shorten patient recovery times. Through a robust QMS and sustainable practices, a 3DPOC not only adds value to clinical outcomes but also optimises hospital resources and minimises environmental impact by aligning with current quality and sustainability standards. These laboratories ultimately represent a transformation in the hospital paradigm, where healthcare centres evolve from being merely consumers to becoming manufacturers of personalised medical devices.

References

1. Kim JY, Lee YC, Kim SG, Garagiola U. Advancements in oral maxillofacial surgery: a comprehensive review on 3D printing and virtual surgical planning. Appl Sci. 2023;13(17):9907. https://doi.org/10.3390/app13179907.
2. Ostas D, Almasan O, Ilesan RR, Andrei V, Thieringer FM, Hedesiu M, et al. Point-of-Care virtual surgical planning and 3D printing in oral and cranio-maxillofacial surgery: a narrative review. J Clin Med. 2022;11(22):6625. https://doi.org/10.3390/jcm11226625.
3. Ganguli A, Pagan-Diaz GJ, Grant L, Cvetkovic C, Bramlet M, Vozenilek J, et al. 3D printing for preoperative planning and surgical training: a review. Biomed Microdevices. 2018;20:65. https://doi.org/10.1007/s10544-018-0301-9.
4. Shcherbo SN, Shcherbo DS. Laboratory diagnostics as a basis for 5P medicine. Bull RSMU. 2019;1:5–12. https://doi.org/10.24075/brsmu.2018.095.
5. David Y, Judd T. Evidence-based impact by clinical engineers on global patients outcomes. Health Technol. 2020;10(2):517–35. https://doi.org/10.1007/s12553-019-00345-0.
6. Australian Government Therapeutic Goods (Medical Devices) Regulations 2002. Australian Government; 2002. https://www.legislation.gov.au/F2002B00237/latest/text.
7. Government of Canada Medical Devices Regulations (SOR/98-282). Government of Canada; 1998. https://laws-lois.justice.gc.ca/eng/regulations/sor-98-282/.
8. European Parliament, Council of the EU. Regulation (EU) 2017/745 of the European Parliament and of the Council of 5 April 2017 on medical devices, amending Directive 2001/83/EC, Regulation (EC) No 178/2002 and Regulation (EC) No 1223/2009 and repealing Council Directives 90/385/EEC and 93/42/EEC. Official Journal of the EU; 2017. https://eur-lex.europa.eu/legal-content/EN/TXT/PDF/?uri=CELEX:32017R0745.
9. U.S. Government. Federal Food, Drug, and Cosmetic Act. FDA; 2020. https://www.govinfo.gov/content/pkg/COMPS-973/pdf/COMPS-973.pdf.
10. TGA. Regulatory basics on medical devices for health practitioners. Guidance. Version 1.0. TGA; 2024. https://www.tga.gov.au/sites/default/files/2023-12/personalised-medical-devices-including-3d-printed-devices.pdf.
11. TGA. Frequently asked questions. Regulatory framework for personalized medical devices. Version 5.1. TGA; 2023. https://www.tga.gov.au/sites/default/files/regulatory-framework-personalised-medical-devices-frequently-asked-questions.pdf.
12. TGA. Personalised medical devices (including 3D-printed devices). Regulatory changes for custom-made medical devices. Version 6.0. TGA; 2023. https://www.tga.gov.au/sites/default/files/2023-12/personalised-medical-devices-including-3d-printed-devices.pdf.
13. U.S. Department of Health and Human Services, FDA, Center for Devices and Radiological Health. Custom device exemption. Guidance for industry and FDA staff. FDA; 2014. https://www.fda.gov/media/89897/download.
14. International Medical Device Regulators Forum (IMDRF) Personalized Medical Devices (PMD) Working Group. IMDRF/PMD WG/N49 FINAL:2018. Definitions for personalized medical devices. IMDRF; 2018. https://www.imdrf.org/sites/default/files/docs/imdrf/final/technical/imdrf-tech-181018-pmd-definitions-n49.pdf.
15. IMDRF PMD Working Group. IMDRF/PMD WG/N58 FINAL:2023 (Edition 2). Personalized medical devices—Regulatory pathways. IMDRF; 2023. https://www.imdrf.org/sites/default/files/2023-09/IMDRF_PMD%20WG_N58%20FINAL_2023%20%28Edition%202%29_0.pdf.
16. Medical Devices Coordination Group (MDCG). MDCG 2021-3. Questions and answers on custom-made devices & considerations on adaptable medical devices and patient-matched medical devices. MDCG; 2021. https://health.ec.europa.eu/system/files/2021-03/mdcg_2021-3_en_0.pdf.
17. MDCG. MDCG 2023–1. Guidance on the health institution exemption under article 5(5) of Regulation (EU) 2017/745 and Regulation (EU) 2017/746. MDCG; 2023. https://health.ec.europa.eu/system/files/2023-01/mdcg_2023-1_en.pdf.
18. FDA Center for Devices and Radiological Health (CDRH). Discussion paper: 3D printing medical devices at the point of care. CDRH; 2021. https://www.fda.gov/media/154729/download.
19. International Organization for Standardization. ISO 13485:2016. Medical devices—Quality management systems—Requirements for regulatory purposes. ISO; 2016. https://www.iso.org/standard/59752.html.
20. U.S. Department of Health and Human Services, FDA, CDRH, Center for Biologics Evaluation and Research. Technical considerations for additive manufactured medical devices. Guidance for industry and FDA staff FDA; 2017. https://www.fda.gov/media/97633/download.
21. Chepelev L, Wake N, Ryan J, Althobaity W, Gupta A, Arribas E, et al. Radiological Society of North America (RSNA) 3D printing Special Interest Group (SIG): guidelines for medical 3D printing and appropriateness for clinical scenarios. 3D Print Med. 2018;4:11. https://doi.org/10.1186/s41205-018-0030-y.
22. International Organization for Standardization, American Society for Testing and Materials. ISO/ASTM 52920:2020. Additive Manufacturing—Qualification principles—Requirements for industrial additive manufacturing processes and production sites. ISO/ASTM; 2020. https://www.iso.org/standard/76911.html.
23. International Organization for Standardization. ISO 14644-1:2015. Cleanrooms and associated controlled environments—Part 1: classification of air cleanliness by particle concentration. ISO; 2015. https://iso.org/standard/53394.html.

24. International Organization for Standardization. ISO 14644-4:2022. Cleanrooms and associated controlled environments—Part 4: design, construction and start-up. ISO; 2022. https://www.iso.org/standard/72379.html.
25. International Organization for Standardization. ISO 14644-2:2015. Cleanrooms and associated controlled environments—Part 2: monitoring to provide evidence of cleanroom performance related to air cleanliness by particle concentration. ISO; 2015. https://www.iso.org/standard/53393.html.
26. International Organization for Standardization. ISO 14698-1:2003. Cleanrooms and associated controlled environments—Biocontamination control—Part 1: general principles and methods. ISO; 2003. https://www.iso.org/standard/25015.html.
27. International Organization for Standardization. ISO 14698-2:2003. Cleanrooms and associated controlled environments—Biocontamination control—Part 2: evaluation and interpretation of biocontamination data. ISO; 2003. https://www.iso.org/standard/25014.html.
28. International Electrotechnical Commission (IEC). IEC 60364-7-710:2021. Low-voltage electrical installations—Part 7–710: requirements for special installations or locations—Medical locations. IEC; 2021. https://webstore.iec.ch/en/publication/29393.
29. European Committee for Standardization (CNE). EN 16798–3:2017. Energy performance of buildings—Ventilation for buildings—Part 3: for non-residential buildings—Performance requirements for ventilation and room-conditioning systems. CNE; 2017. https://www.en-standard.eu/bs-en-16798-3-2017-energy-performance-of-buildings-ventilation-for-buildings-for-non-residential-buildings-performance-requirements-for-ventilation-and-room-conditioning-systems-modules-m5-1-m5-4/.
30. International Organization for Standardization. ISO 14001:2015. Environmental management systems—Requirements with guidance for use. ISO; 2015. https://www.iso.org/standard/60857.html.
31. International Organization for Standardization. ISO 10993-1:2018. Biological evaluation of medical devices—Part 1: evaluation and testing within a risk management process. ISO; 2018. https://www.iso.org/standard/68936.html.
32. MDCG. MDCG 2019–07 Rev 1. Guidance on article 15 of the medical device regulation (MDR) and in vitro diagnostic device regulation (IVDR) on a person responsible for regulatory compliance (PRRC). MDCG; 2023. https://health.ec.europa.eu/system/files/2023-02/mdcg_2023-3_en_0.pdf.
33. European Parliament, Council of the EU. Regulation (EU) 2016/679 of the European Parliament and of the Council of 27 April 2016 on the protection of natural persons with regard to the processing of personal data and on the free movement of such data (General Data Protection Regulation, GDPR). Official Journal of the European Union; 2016. https://eur-lex.europa.eu/eli/reg/2016/679/oj.
34. U.S. Department of Health and Human Services. Health Insurance Portability and Accountability Act of 1996 (HIPAA). https://www.hhs.gov/hipaa/for-professionals/privacy/index.html.
35. Australian Government. Privacy Act 1988. https://www.legislation.gov.au/C2004A03712/latest/text.
36. International Organization for Standardization. ISO 14971:2019. Medical devices—application of risk management to medical devices. ISO; 2019. https://www.iso.org/standard/72704.html.
37. International Organization for Standardization. ISO 11737-1:2018. Sterilization of health care products—Microbiological methods—Part 1: determination of a population of microorganisms on products. ISO; 2018. https://www.iso.org/standard/66451.html.
38. International Organization for Standardization. ISO 15223-1:2021. Medical devices—symbols to be used with information to be supplied by the manufacturer—Part 1: general requirements. ISO; 2021. https://www.iso.org/standard/77326.html.
39. MDCG. MDCG 2023-3. Questions and answers on vigilance terms and concept as outlined in the Regulation (EU) 2017/745 on medical devices. MDCG; Feb 2023. https://health.ec.europa.eu/document/download/463b4f08-44a2-4018-9957-488bf386fc3a_en?filename=md_mdcg_2019_7_guidance_art15_mdr_ivdr_en.pdf.
40. International Organization for Standardization. ISO 27799:2016. Health informatics –Information security management in health using ISO/IEC 27002. ISO, 2016. https://www.iso.org/standard/62777.html.

Personalized Implant Design in Cranio-Maxillo-Facial Surgery

Maarten Zandbergen

1 Introduction to Personalized Implant Design in CMF Surgery

The field of cranio-maxillo-facial (CMF) surgery has experienced transformative advancements with the rise of personalized implant design, largely driven by virtual surgical planning and computer-aided design/manufacturing (CAD/CAM) technology. Unlike traditional, prefabricated implants, personalized implants are custom designed to match each patient's unique anatomy, enabling surgeons to achieve a high level of precision and improve functional and aesthetic outcomes. This approach has particular value in complex cases, such as reconstructive surgeries following trauma, congenital abnormalities, or oncological resections, where traditional methods often face limitations in accuracy, stability, and long-term integration.

The integration of personalized implants in CMF surgery has been supported by experimental and computational research, which has helped establish their mechanical and biological advantages. Studies have highlighted the benefits of customized porous titanium structures, which enhance both biomechanical stability and osseointegration by mimicking the natural architecture of bone [1–3]. Barbas's research on multi-scale modeling CMF implants emphasizes the role of personalized implant design in achieving load distribution that aligns with the patient's natural biomechanics, reducing the risk of stress shielding and implant failure. Schouman's work in mandibular reconstruction with porous titanium scaffolds has further validated that custom-designed implants promote better tissue integration and support long-term stability, especially in load-bearing areas.

Other studies have reinforced these benefits by demonstrating the accuracy and efficiency of patient-specific implants. Jones et al. [4] compared maxillary positioning accuracy using patient-specific guides and plates versus interim splints and found that personalized guides and plates yielded more precise positioning and alignment, contributing to improved surgical accuracy. This level of precision in bone alignment minimizes postoperative complications and improves the predictability of surgical outcomes, which is essential for the functional and aesthetic success of CMF procedures.

Similarly, in a study on fibula free flap mandibular reconstructions, Blanc et al. [5] showed that personalized surgical guides and implants not only achieved highly accurate reconstructions but also significantly reduced operative and ischemia time. This time efficiency translates to better patient outcomes by minimizing intraoperative blood loss and reducing risks associated with extended surgery times. Zavattero et al. [6] conducted a multicenter study that further demonstrated the high accuracy of CAD/CAM-assisted mandibular reconstructions, with an error range between 0.5 mm and 3 mm, highlighting the reproducibility and precision that CAD/CAM-guided, patient-specific plates bring to complex CMF surgeries.

Personalized implant design thus represents a paradigm shift in CMF surgery. By translating virtual surgical plans into precise, intraoperative actions, these advancements enable surgeons to achieve complex reconstructions with high accuracy, reproducibility, and efficiency. These benefits result in reduced surgery times, enhanced anatomical alignment, and improved functional outcomes. Research by Schouman and Schmitt on implant fixation and bone integration further underscores the importance of using personalized implants to optimize both mechanical properties and biological compatibility, offering patients better surgical results and long-term quality of life. The continuous development of these technologies and materials is paving the way for more reliable, patient-centered approaches in reconstructive surgery (Fig. 1).

M. Zandbergen (✉)
Materialise, Leuven, Belgium
e-mail: maarten.zandbergen@materialise.be

© The Author(s), under exclusive license to Springer Nature Switzerland AG 2025

A. Tel, M. Robiony (eds.), *Atlas of Virtual Surgical Planning and 3D Printing for Cranio-Maxillo-Facial Surgery*,
https://doi.org/10.1007/978-3-031-94495-6_6



Fig. 1 Personalized guides and plates for complex reconstructive surgery

2 Design and Manufacturing Process for Personalized CMF Implants

2.1 Patient-Specific Data Acquisition and 3D Design

The foundation of personalized implant design lies in its patient-centered approach, where each implant is tailored to the anatomical, functional, and aesthetic requirements of the individual patient. This principle of personalized design is crucial in CMF surgery, where even minor inaccuracies can significantly affect functional outcomes and facial symmetry. Personalized implant design involves precise three-dimensional data acquisition, through high-resolution imaging, which forms the basis of a virtual model of the patient's unique anatomy. This model serves as the blueprint for developing an implant that aligns perfectly with the contours of the affected bone structures.

The design process begins with acquiring detailed patient-specific anatomical data through (CB)CT scans. These imaging modalities capture not only the structural integrity of the bone but also variations in bone density and critical soft tissue boundaries. By integrating these aspects into a 3D model, surgeons and engineers can virtually plan and design an implant that conforms precisely to the defect site, minimizing the need for intraoperative adjustments. This 3D modeling approach enhances both the precision and predictability of surgical outcomes, aligning with the overarching principle of creating implants that restore function while preserving natural aesthetics [2, 3].

Digital surgical planning software plays a key role in translating imaging data into a detailed digital representation of the patient's anatomy. Surgical planning software allows for extensive preoperative planning, where surgeons can simulate different surgical plans to identify the most effective approach before entering the operating room. This planning process provides significant insights into potential challenges and allows surgeons to anticipate and address anatomical variations in advance. Studies such as those by Jones et al. [4] and Blanc et al. [5] have demonstrated that the use of digital surgical planning, in combination with personalized surgical guides, significantly enhances implant placement accuracy, reducing operative time and improving postoperative outcomes [4–6] (Fig. 2).



Fig. 2 Titanium 3D printed surgical guides for orthognathic bimaxillary surgery

Computer-aided design and computer-aided manufacturing technologies convert this virtual surgical plan into a digital implant design (Fig. 3) and afterwards a fully personalized implant, precisely manufactured to fit the patient's anatomi-

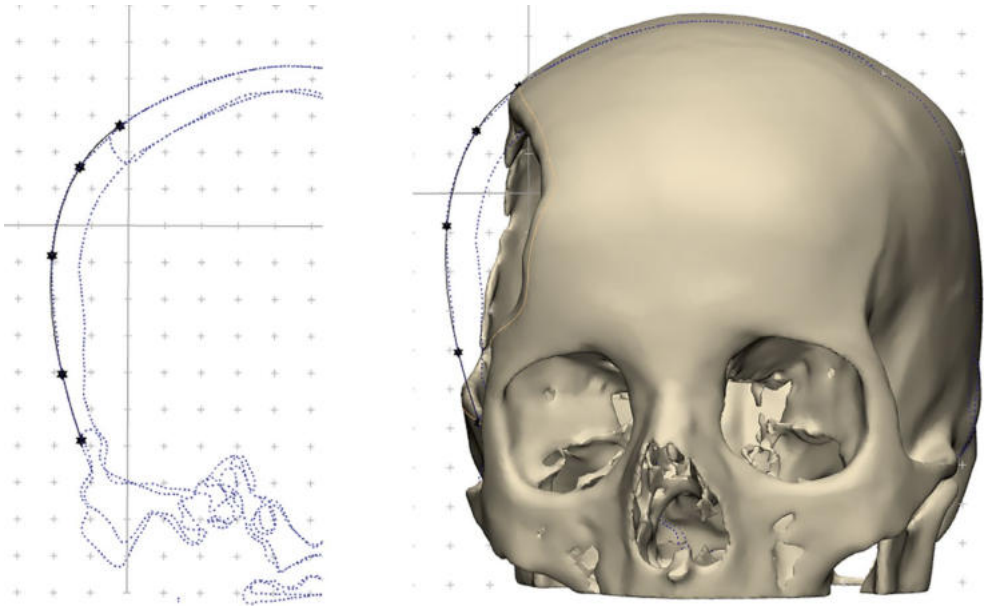


Fig. 3 Cranial implant design

cal structure. CAD software enables modifications to implant geometry, pore size, and surface topography, allowing the design to be optimized for osseointegration, load distribution, and long-term stability. This is particularly important in CMF surgeries where complex contours and high load-bearing requirements demand a balance between structural strength and biological compatibility. By adjusting parameters such as pore size and implant density based on the specific requirements of the bone and surrounding tissue, CAD/CAM facilitates the creation of implants that integrate naturally with the patient's anatomy [2, 3].

The principle of personalized implant design is grounded in the concept of anatomical and functional customization, ensuring that the implant not only reconstructs the physical structure but also supports the dynamic physiological needs of the patient. With each implant crafted to align with the patient's unique bone structure, load-bearing capacity, and aesthetic considerations, personalized implant design enhances both the surgical workflow and patient outcomes. This approach underscores the goal of personalized CMF implant design: to provide a tailored solution that minimizes postoperative complications, enhances integration with surrounding tissues, and optimally restores both form and function.

2.2 Finite Element Analysis for Mechanical Optimization

Finite Element Analysis (FEA) can be applied to optimize CMF implant design for mechanical performance. By simulating various loading conditions, FEA allows engineers to identify potential stress concentrations, predict implant behavior under physiological loads, and make necessary adjustments to the design. Schmitt's thesis incorporated FEA to model osteogenesis within porous titanium scaffolds, finding that specific pore arrangements could enhance bone ingrowth and reduce stress shielding. This computational approach has since become a standard practice in personalized CMF implant design and development, allowing for refined implant configurations tailored to patient-specific needs [3].

Schouman's work further demonstrated the use of FEA to predict stress distribution and assess implant stability in load-bearing applications. By integrating patient-specific data, Schouman's models provided a realistic depiction of bone-implant interaction under various masticatory forces, highlighting the importance of mechanical compatibility in achieving successful osseointegration [1].

FEA is also widely used to optimize the design of personalized temporomandibular joint (TMJ) prostheses. This tool helps engineers predict how the implant will behave under real-life conditions, such as chewing or speaking, and identify stress concentrations (Fig. 4). FEA can evaluate the interaction between a TMJ implant and the surrounding bone, helping to create designs that are both functional and strong. Research has highlighted how patient-specific modeling, combined with FEA, improves implant fit and reduces the risk of complications like stress buildup or implant failure designs; FEA ensures that the prostheses not only restore function but also last longer and are safer for patients.

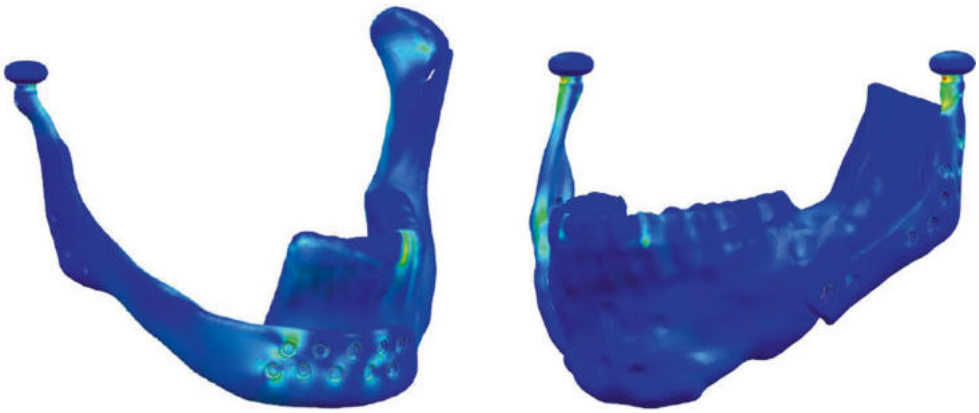


Fig. 4 Finite Element Analyses with color maps highlighting stress concentrations under loading conditions

2.3 Additive Manufacturing and Implant Fabrication

Additive manufacturing (AM), commonly known as 3D printing, has revolutionized the fabrication of patient-specific CMF implants by enabling the precise creation of complex structures that closely mimic the patient's anatomy. In CMF surgery, AM allows for the production of highly detailed implants that align with both functional and aesthetic needs. However, the production of AM-based implants must be carried out within a robust, compliant framework that adheres to medical device regulations, ensuring both patient safety and product efficacy.

2.4 Importance of Regulatory Compliance in the AM Process

Producing medical implants through AM necessitates a validated, regulatory-compliant process, as defined by regulatory agencies such as the FDA and European Medical Device Regulation (MDR). Compliance with these regulations ensures that every step of the AM process—from design to final sterilization—is carried out within a strict framework designed to minimize patient risk. Regulatory bodies emphasize that every AM implant undergoes stringent testing and documentation, covering aspects such as material quality, build consistency, and post-processing methods to maintain a high level of reliability and patient safety [7, 8].

Regulatory compliance also involves process validation at multiple levels: installation qualification (IQ), operational qualification (OQ), and performance qualification (PQ). These stages validate that the manufacturing equipment is properly set up, that the manufacturing parameters are within defined limits, and that the final product consistently meets the required specifications. By adhering to a validated process, manufacturers ensure that each implant is produced to a high standard of precision, strength, and biocompatibility, aligning with regulatory expectations.

2.5 Key Considerations in AM Regulatory Compliance

Additive manufacturing of medical devices introduces complexities that require specific regulatory attention. Unlike traditional manufacturing processes, AM allows for flexible, patient-specific design adjustments without the need for custom molds or dies. However, this flexibility also means that each implant must be individually validated, with stringent documentation of each manufacturing variable—such as layer thickness, material composition, and build orientation. Regulatory guidelines from the FDA stress the need for manufacturers to implement quality control measures for every AM stage, from material input to post-processing.

Additionally, AM implants undergo thorough post-processing treatments to ensure accuracy, biocompatibility, and mechanical stability. Because AM-based CMF implants often have intricate internal structures or porous features, achieving adequate cleaning and sterilization poses unique challenges. Therefore, each post-processing step must be validated and closely monitored to ensure that the final implant is free from contaminants and biocompatible.

2.6 Role of Quality Control in Ensuring Implant Safety and Effectiveness

In addition to regulatory compliance, rigorous quality control is crucial for ensuring the safety, functionality, and longevity of personalized implants. Given the patient-specific nature of these implants, each device must undergo comprehensive quality assessments to ensure it meets design and performance requirements. Quality control in AM-based CMF implants includes, but is not limited to material verification, layer consistency checks, and dimensional accuracy analysis, as any deviation could compromise the implant's fit, structural integrity, or integration with the patient's bone.

Several international standards, such as ISO 13485, establish quality management system requirements specific to

medical devices, mandating that each production stage is carefully controlled and documented. Quality systems ensure that all aspects of the AM process—from raw material selection to post-processing—are tracked and verified. This traceability is particularly important in AM, where small variations in build parameters, such as laser power or layer thickness, can significantly impact the mechanical properties of the final implant.

A comprehensive quality management system that encompasses all aspects of the AM process has a direct impact on patient outcomes. High-quality, patient-specific CMF implants can improve surgical precision and reduce the likelihood of postoperative complications.

As additive manufacturing techniques continue to evolve, maintaining rigorous quality control and regulatory compliance is crucial to ensuring that patient-specific CMF implants meet the highest standards of safety, reliability, and performance. Adhering to these principles helps translate the advantages of personalized implants into real-world clinical success, providing patients with safer, more effective, and longer-lasting solutions for cranio-maxillo-facial reconstruction.

3 Experimental Insights into Personalized Implant Performance

Through experimental studies and animal models, Barbas, Schmitt, and Schouman [1–3] have explored the mechanical stability, osteoconductivity, and in vivo integration of personalized implants. These experimental insights not only validate the efficacy of these implants but also provide invaluable insights into the design and development of personalized implants, tailored to specific anatomical and biomechanical needs.

3.1 Biological Integration and Osteogenesis in Porous Implants

A major focus of personalized implant research is understanding how implant structure influences biological integration, particularly osteogenesis, within porous scaffolds. Schmitt's study centered on the osteoconductive properties of porous titanium implants. Using a sheep model, Schmitt implanted titanium scaffolds with a porosity of approximately 53% and pore sizes ranging from 860 to 1500 μm in mandibular defects to observe bone ingrowth and vascularization over a 12-week period. The study employed micro-computed tomography (micro-CT) and histological analysis to quantify new bone formation and vascular penetration within the implant structure. Findings revealed substantial bone ingrowth within the porous architecture, with increased bone density in regions of optimal pore distribution, underscoring the importance of pore size and interconnectivity for successful osseointegration [3].

Schouman's research further examined the relationship between implant porosity and osseointegration in mandibular reconstructions. His experiments utilized titanium scaffolds in load-bearing regions to assess the impact of pore structure on stability and integration. Through histological assessments and mechanical testing, Schouman's study demonstrated that porous titanium implants supported substantial vascularization and bone ingrowth, creating a stable bone-implant interface. His findings align with Schmitt's observations, suggesting that controlled porosity in titanium scaffolds enhances biological integration by facilitating cell migration, tissue infiltration, and nutrient transfer, all essential for stable osseointegration in CMF applications [1].

3.2 Mechanical Stability and Load Distribution

Mechanical stability is critical for CMF implants, as they are often placed in regions subjected to dynamic forces, such as the mandible bone. Barbas's research utilized multi-scale modeling techniques to assess the load distribution and mechanical stability of porous titanium implants. His thesis employed FEA to simulate the mechanical behavior of implants with varying pore sizes and distribution under masticatory forces. Barbas's FEA simulations showed that implants with pore sizes optimized to match cortical bone properties exhibited a balanced load distribution, reducing localized stress and mitigating stress shielding effects. This finding underscores the importance of tailoring implant porosity to minimize stiffness mismatches, which can lead to bone resorption and implant loosening [2].

In addition to simulations, Barbas conducted physical mechanical testing on titanium specimens to validate FEA predictions. By applying cyclical loads that mimic jaw movements, Barbas assessed the endurance and deformation characteristics of the implants. Results indicated that implants with strategically designed porous regions distributed mechanical forces evenly, minimizing stress on surrounding bone. This balance between porosity and mechanical strength is crucial in CMF applications, where implants must withstand considerable masticatory loads without compromising bone health [2].

Schouman's research complemented these findings with an experimental approach that tested the load-bearing capabilities of titanium implants in mandibular defects. Schouman's use of in vivo loading models demonstrated that implant stability correlated strongly with pore size and arrangement, where implants with non-uniform pores showed increased susceptibility to deformation under high stress. His

work highlights the need for specifically engineered pore structures to address specific loading requirements, especially in high-stress regions like the mandible [1].

3.3 Thermal Behavior and Patient Comfort

An aspect less commonly examined in implant performance but highly relevant to patient comfort is thermal behavior. Barbas's thesis explored the thermal properties of titanium compared to alternative materials such as polyetheretherketone (PEEK) and calcium phosphate, using both thermal conductivity experiments and in silico simulations. His research demonstrated that titanium's thermal conductivity aligns well with that of natural bone, maintaining stable temperatures even in response to environmental changes. By contrast, PEEK showed lower thermal conductivity, leading to localized temperature variations, which could cause discomfort in patients, particularly in exposed facial regions (Fig. 5).

Barbas's findings underscore the importance of thermal compatibility in personalized implants, especially in regions sensitive to temperature fluctuations. His experiments confirmed that titanium implants provide a more consistent temperature profile, reducing the likelihood of patient discomfort and enhancing overall tolerance of the implant in daily life [2].

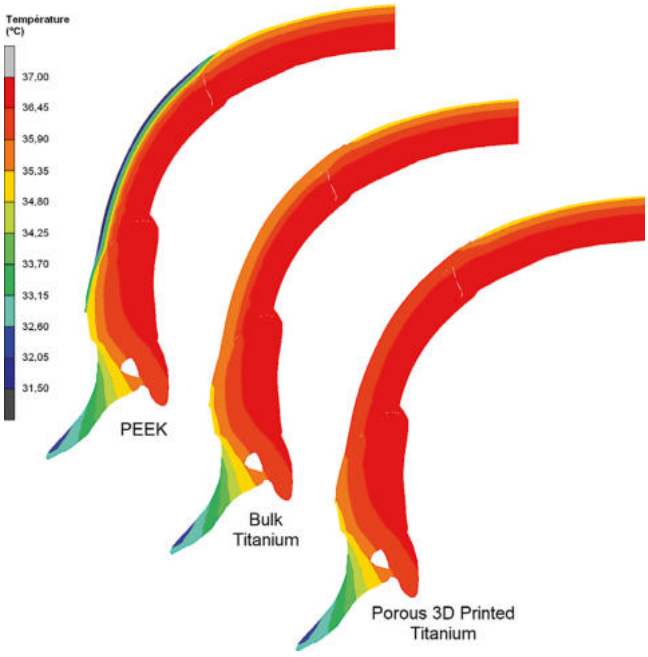


Fig. 5 Thermal conductivity simulation after a sudden temperature change for different materials in a cranial implant design

3.4 Experimental Setup and In Vivo Models for Clinical Simulation

The experimental setups used by Schmitt, Schouman, and Barbas emphasize rigorous methodologies that bridge preclinical research and real-world clinical applications. Schmitt's animal model study involved implanting porous titanium scaffolds in live sheep mandibles, allowing for a controlled observation of bone healing, vascularization, and integration in an environment mimicking human mandibular conditions. By using micro-CT and histology, Schmitt quantified new bone formation and vascular density, providing quantitative metrics on implant performance that inform both design and material selection for future implants [3].

Similarly, Schouman's work employed in vivo models to simulate the functional stresses that implants endure in mandibular reconstructions. The use of controlled loading experiments on animals with customized mandibular defects allowed for the examination of both mechanical stability and biological integration over time. This dual approach—mechanical and biological—highlighted the interplay between implant structure and surrounding bone, reinforcing the need for a design that supports both stability and tissue compatibility [1].

Barbas took a multi-modal approach, combining FEA simulations with mechanical testing of implants under cyclic loads to replicate functional conditions. This approach allowed Barbas to identify optimal pore arrangements that provide structural integrity without sacrificing flexibility or load distribution. By integrating FEA with physical testing, Barbas's work offers a comprehensive view of how personalized implants can be fine-tuned for different load-bearing requirements in the craniofacial region [2].

3.5 Clinical Implications

The findings from these experimental studies have direct implications for clinical practice. The insights into porous titanium's osteoconductive properties and load-bearing capacity have led to the definition of parameters now utilized in the designs of personalized porous implants with a controlled porosity (Fig. 6). Schmitt's and Schouman's studies underscore the benefits of a well-designed pore architecture for both stability and integration, advocating for implant designs that can withstand dynamic forces while promoting biological integration [1, 3].



Fig. 6 Personalized porous cranial implant design

4 Material Selection for Personalized Implants

4.1 Porous Titanium: Structure, Biomechanics, and Biological Compatibility

Porous titanium has gained prominence as an implant material for CMF applications due to its favorable mechanical and biological properties. The PorousiTi implants developed by Materialise use selective laser melting (SLM) to create a porous structure that mimics the characteristics of cortical bone. With a porosity rate of around 53% and pore sizes ranging from 860 to 1500 µm, PorousiTi implants allow for cellular infiltration, vascularization, and effective load distribution.

The benefits of porous titanium go beyond biocompatibility. By adjusting the pore size and density, engineers can control the mechanical strength of the implant to match the patient's bone properties, thereby reducing the risk of stress shielding—a phenomenon where differences in stiffness between bone and implant lead to bone resorption. Schouman's modeling studies demonstrated that optimized porous structures support osseointegration and stabilize the implant, even in challenging load-bearing regions like the mandible [1].

4.2 Comparison of Implant Materials: Titanium, PEEK, and Calcium Phosphate

In selecting materials for CMF implants, it is essential to consider multiple factors, including mechanical strength, biocompatibility, osseointegration potential, adaptability, and thermal behavior. Each material commonly used in (personalized) CMF implants—titanium, PEEK, and calcium phosphate—offers a unique balance of these properties, making it suitable for specific applications and surgical needs.

4.2.1 Titanium Implants: Strength, Osseointegration, and Thermal Stability

Titanium has become the standard material in CMF surgery due to its high strength-to-weight ratio, corrosion resistance, and exceptional biocompatibility. Titanium, particularly in a porous form, supports osseointegration effectively by allowing cellular migration and vascularization within its structure, which is crucial for the long-term stability of load-bearing implants. Additionally, titanium's stiffness and strength make it suitable for cases where significant mechanical support is needed, such as in mandibular reconstructions. Studies confirm titanium's excellent osteoconductive properties, which further stimulate bone growth and integration with the surrounding tissue [2, 3].

In addition to its mechanical benefits, titanium's thermal stability sets it apart from other materials. Barbas's research highlights the favorable thermal conductivity and low thermal expansion of porous titanium, which allows it to remain stable under various temperature conditions. This stability aligns well with the thermal behavior of human bone, which generally maintains a consistent temperature.

4.2.2 PEEK Implants: Flexibility, Intraoperative Adaptability, and Patient Comfort

PEEK has gained popularity as an alternative to titanium in specific CMF applications due to its flexibility, biocompatibility, and ease of intraoperative adaptability. Unlike titanium, PEEK can be modified during surgery to fit the patient's anatomy more precisely if adjustments are required, which can be especially valuable in cases where bone structures are complex or in regions requiring customized intraoperative reshaping. PEEK's lower mechanical strength

limits its use in load-bearing areas; it is often chosen for reconstructions and augmentations in non-load-bearing applications.

PEEK's low thermal conductivity, while potentially advantageous in avoiding abrupt thermal shifts, can also lead to temperature-related discomfort. As Barbas's findings suggest, its poor temperature adaptability can cause localized warmth or cooling in response to external temperature changes, which may limit its desirability in patients sensitive to temperature fluctuations [2].

4.2.3 Calcium Phosphate Implants: Bioactivity and Osteoconductive Potential

Calcium phosphate, often used in coatings or standalone scaffolds, offers the closest mimicry to natural bone mineral content, making it highly osteoconductive. Its bioactivity encourages bone tissue to grow onto and around the implant, fostering a strong bond with native bone. Because of these osteoconductive properties, calcium phosphate is commonly used as a coating material on implants to enhance their bone integration and compatibility.

Despite its bioactivity, calcium phosphate has limitations when it comes to mechanical stability. It is generally brittle and unsuitable for high-stress applications, restricting its use to coatings on more durable substrates like titanium. Additionally, calcium phosphate implants have less favorable thermal properties, and their low resistance to wear under mechanical stress makes them less appropriate for areas in CMF surgery where significant forces are anticipated, such as in mandibular or orbital reconstructions. As such, calcium phosphate is typically employed as a surface treatment on titanium implants rather than a primary implant material in load-bearing reconstructions [2, 3].

4.2.4 Comparative Summary and Advantages of Titanium

In summary, titanium remains an excellent choice for personalized CMF implants due to its comprehensive balance of strength, osseointegration potential, and thermal stability. While PEEK offers intraoperative adaptability, its limitations in thermal behavior and load-bearing capacity make it less versatile than titanium. Calcium phosphate's high osteoconductivity complements titanium well as a coating but does not have the mechanical resilience needed for standalone use in most CMF applications.

The clinical advantages of porous titanium in particular, which combine structural stability, bone compatibility, and thermal resilience, make it uniquely suited for CMF applications that require robust, durable, and biocompatible solutions. This blend of properties ensures that titanium implants can effectively withstand the diverse functional and environmental stresses encountered in cranio-maxillo-facial reconstructive surgery, resulting in improved patient comfort, long-term stability, and overall surgical success.

5 Clinical Experience with Personalized Implants

The adoption of personalized implants in CMF surgery has been transformative, significantly enhancing the accuracy of anatomical reconstruction, reducing surgical times, and improving functional and aesthetic outcomes. Clinical experiences, as documented in several studies [4–6, 9–12], offer an in-depth look at the benefits, challenges, and considerations of using patient-specific implants in complex CMF reconstructive procedures. These studies highlight how advances in digital surgical planning, computer-aided design, and additive manufacturing have contributed to the evolving landscape of CMF surgery, demonstrating clear improvements in both patient outcomes and procedural efficiency.

5.1 Enhanced Precision and Accuracy

Achieving precise anatomical alignment is critical in CMF surgery, where minor deviations can impact facial symmetry, functional recovery, and long-term implant stability. The precision afforded by personalized implants is underscored in the study by Jones et al., who compared maxillary positioning using traditional interim splints with patient-specific surgical guides and plates in bimaxillary orthognathic surgery. Their findings revealed that patient-specific guides and plates significantly reduced deviations in maxillary positioning, leading to improved surgical accuracy (Fig. 7). The patient-specific approach also provided greater control over

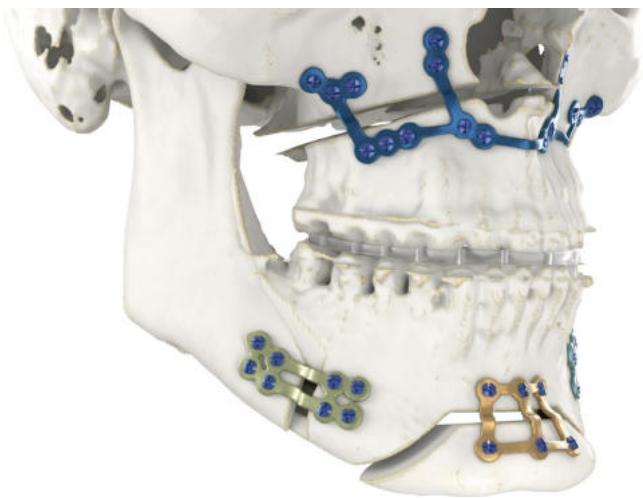


Fig. 7 Personalized implant designs for orthognathic surgery



Fig. 8 Personalized implant for mandibular reconstruction

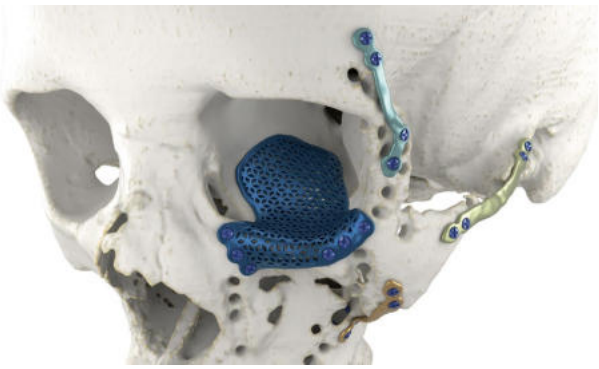


Fig. 9 Personalized implants for trauma revision surgery

the final alignment, which is essential in cases where facial symmetry and jaw function are closely linked [5].

In a multicenter study on CAD/CAM-assisted mandibular reconstructions, Zavattero et al. found that patient-specific implants achieved an accuracy range between 0.5 mm and 3 mm, which was consistent across various cases and surgical teams. This level of precision is particularly beneficial in mandibular reconstructions, where maintaining the correct angle and position of the jaw is crucial for both aesthetics and functionality (Fig. 8). The reproducibility of these results across different surgical settings further underscores the reliability of patient-specific implants, suggesting that even complex cases can achieve optimal outcomes with the use of CAD/CAM-guided surgical guides and plates [6].

Similarly, Sesqué et al. illustrated the utility of personalized implants in complex cases involving orbitofrontal reconstruction following intraosseous hemangioma resection. The personalized titanium 3D printed implant provided precise anatomical fit, facilitating symmetry restoration and achieving satisfactory aesthetic outcomes without complications. This study highlights the importance of personalized implants in addressing unique anatomical challenges presented by individual patients and underscores the role of virtual planning in preemptively tackling difficulties in cases with complex craniofacial structures [11].

5.2 Reduction in Operative Time and Complexity

The use of personalized implants is associated with significant reductions in operative time, contributing to lower intraoperative blood loss, minimized risk of infection, and overall improved patient safety. In their study on fibula free flap mandibular reconstructions, Blanc et al. reported that digital surgical planning combined with surgical guides and personalized implants substantially reduced both operative and ischemia times. The streamlined nature of these procedures, made possible by preoperative planning, reduced the complexity of reconstructive steps, which is especially important in lengthy procedures involving multiple osteotomies. Blanc et al. concluded that shorter operative times positively impact patient outcomes by reducing anesthesia exposure and promoting faster postoperative recovery [5].

Similarly, Champeaux et al., in their study of titanium 3D-printed cranioplasty implants, noted that the accuracy and pre-contoured fit of these implants greatly simplified the reconstruction process, effectively reducing operative times and decreasing intraoperative adjustments. This efficiency benefit is crucial in cases of cranial reconstruction following trauma or tumor resection, where immediate, precise contouring is needed (Fig. 9). By reducing operative time and complexity, personalized implants allow surgeons to achieve desired results more predictably and with fewer intraoperative challenges [10].

5.3 Improved Aesthetic and Functional Outcomes

The high level of anatomical accuracy achievable with personalized implants contributes directly to improved aesthetic outcomes, which are a primary concern for many CMF patients. Le Clerc et al. reported on the use of a 3D-printed titanium orbital implant for a maxillectomy reconstruction, emphasizing that the personalized implant preserved facial symmetry, facilitated smooth nasal airflow, and enabled the restoration of masticatory function. The implant provided sufficient support for functional outcomes, such as chewing, breathing, and speaking, while also restoring the natural contours of the midface. A high level of satisfaction with the aesthetic result, indicating that personalized implants can

provide life-changing improvements in facial reconstruction quality, was reported in that study [9].

Champeaux et al. also explored the impact of personalized titanium cranioplasty implants on patient aesthetics and psychological well-being, noting that the implants not only restored craniofacial structure but also significantly enhanced patients' confidence and quality of life. The study highlighted that patients experienced improvements in self-perception and social engagement, underscoring the psychological impact of achieving a visually appealing reconstruction. This is particularly important for patients who have suffered traumatic injuries or undergone extensive tumor resection, where personalized implants provide a pathway to restoring facial symmetry and achieving functional as well as aesthetic recovery [10].

5.4 Minimization of Postoperative Complications

Personalized implants have shown potential in reducing postoperative complications commonly associated with CMF reconstructions, such as infection, implant migration, and skin irritation. Sesqué et al. reported no perioperative or postoperative complications in a case study involving orbitofrontal reconstruction with a personalized porous titanium 3D printed implant. This finding supports the hypothesis that patient-specific implants, designed to achieve precise anatomical fit and stability, reduce the likelihood of complications such as implant shifting or infection, as they minimize unnecessary stress on surrounding tissues and promote better integration [11].

Le Clerc et al. highlighted the effectiveness of titanium implants in orbital reconstructions, noting low incidences of infection and minimal cases of skin extrusion, even among patients receiving postoperative radiotherapy. The use of porous titanium allowed for tissue integration, which reduces the risk of implant exposure and subsequent infection. However, two cases of extrusion did occur in irradiated patients, suggesting that clinicians may need to consider additional protective measures, such as soft tissue grafts, to prevent complications in patients receiving adjuvant therapies [9].

5.5 Improved Patient Outcomes

The use of personalized implants not only enhances functional outcomes but also has a positive impact on aesthetic results, which is especially relevant in CMF surgery. Zavattero et al.'s study reported high levels of patient satisfaction due to the precise anatomical restoration achieved with personalized mandible reconstruction plates. The tailored fit of these plates ensures that facial symmetry is restored more accurately than with traditional plates, leading to a more natural postoperative appearance [6].

Clinical experiences, as documented by Jones et al., confirm that personalized guides and implants help maintain facial aesthetics by aligning the bone structures closely with the patient's original anatomy. This close alignment is crucial in CMF surgery, where even minor deviations can affect the patient's appearance and facial harmony. The customized fit also supports improved functional recovery, allowing patients to regain normal oral and maxillofacial function more quickly [4].

6 Future Perspectives for Personalized Implants

The field of personalized implants is poised for significant advancements, driven by technological innovation, material science, and data-driven processes. As demand for patient-specific solutions in CMF and other surgical fields grows, new developments are expected to improve delivery timeline optimization and diversify material options (including bioresorbable materials). These advances aim not only to enhance patient outcomes but also to make personalized implants more accessible and efficient.

6.1 Accelerating Personalized Implant Lead Times

A challenge for personalized implants remains the lead time from initial patient data acquisition to final implant delivery. Accelerating this process requires advances across multiple fronts, including data acquisition and imaging, surgical planning and design automation, and additive manufacturing. By integrating artificial intelligence into the workflow, data from previous cases can be analyzed to streamline the surgical planning process and even the design of personalized implants, reducing the overall lead-time. Techniques such as field driven design as described by Tel et al. [13] show initial results that can lead to a more automated and faster design workflow for personalized implants. Today, the result of automated workflows is already leading to faster delivery times for personalized implants, making this a viable option for time-critical surgeries such as oncologic reconstructions or primary trauma surgery.

6.2 New Materials

Advancements in material science are set to expand the range of available materials for personalized implants, with new

options like bioresorbable and bioceramic materials. Each material brings unique mechanical and biological characteristics, prompting the need for tailored design strategies to maximize their effectiveness in CMF surgery.

Bioresorbable materials can offer both temporary structural support and enhanced regenerative capabilities, encouraging natural bone growth before gradually dissolving, thus minimizing the need for future surgeries to remove implants. Polycaprolactone (PCL) has gained popularity as a scaffold material due to its degradation rate, manufacturability, and biocompatibility. PCL-based scaffolds show osteoconductive and osteogenic capacities, making it ideal for implants intended to promote bone growth over extended periods. Given its mechanical properties, PCL is suitable for 3D printing, allowing for the fabrication of anatomically precise, patient-specific implants that can support gradual osteogenesis [14]. However, because PCL has lower load-bearing strength compared to traditional implant materials like titanium, implants made from PCL require designs that distribute mechanical loads efficiently, utilizing strategically placed porosity and thickness to balance strength and flexibility.

Magnesium, another bioresorbable material, has emerged as a promising bioresorbable material for CMF implants due to its mechanical properties and ability to degrade within the human body. Compared to bioresorbable polymers, magnesium has an increased mechanical stability, making it a better candidate for load-bearing applications. Despite its advantages, the degradation behavior of magnesium poses challenges for clinical application. Magnesium's natural corrosion in physiological environments releases hydrogen gas, which, if uncontrolled, can accumulate and impair osseointegration or lead to implant instability. Recent advancements, including the use of surface modifications, have significantly mitigated these challenges [15]. The distinct properties of magnesium, including its gradual degradation and bioactivity, necessitate innovative implant designs to optimize performance. Implants must balance initial mechanical support with predictable degradation, ensuring structural stability throughout the healing process. The integration of computational modeling techniques, such as FEA, can aid in tailoring porosity and surface characteristics to meet patient-specific anatomical and biomechanical requirements.

In parallel, bioceramic materials like hydroxyapatite (HA) offer substantial advantages in osteoconductivity and biocompatibility. Hydroxyapatite's chemical composition closely resembles natural bone, making it highly effective in supporting bone cell attachment and growth. As evidenced by Systermans et al. [16] on 3D-printed porous HA implants, bioceramics can foster robust osteointegration, with interconnected porosity enhancing vascularization and bone ingrowth. The study further demonstrated that hydroxyapatite implants, once integrated, offer substantial mechanical stability and can even support complex reconstructions in maxillofacial applications. However, HA's brittle nature compared to metals or polymers requires careful design considerations, particularly in load-bearing regions.

As these materials evolve, innovative implant design strategies are essential to accommodate their distinct biomechanical and degradation properties. Personalized implant designs will also need to account for dynamic load distribution as materials degrade, integrating strategic reinforcements in areas with higher mechanical demands. The use of composite materials represents a promising direction for implants that can adapt to physiological changes, ensuring both structural stability and biological compatibility over time.

References

1. Schouman T. Modélisation biomécanique et étude de la fonctionnalisation d'un implant personnalisé de reconstruction mandibulaire en titane poreux. Biomécanique [physics.med-ph]. Ecole nationale supérieure d'arts et métiers – ENSAM, 2016. Français. NNT: 2016ENAM0065.
2. Barbas A. Etude biomécanique de substituts osseux en titane poreux destinés à la chirurgie maxillo-faciale. Autre UniversitéPaulVerlaine-Metz, 2011. Français. NNT:2011METZ030S.
3. Schmitt M. Analyses expérimentales et modélisation numérique de l'ostéogenèse au sein d'un implant poreux en titane. Biomécanique [physics.med-ph]. Ecole nationale supérieure d'arts et métiers – ENSAM, 2015. Français. NNT: 2015ENAM0011.
4. Jones JP, et al. Comparison of the accuracy of maxillary positioning with interim splints versus patient-specific guides and plates in executing a virtual bimaxillary surgical plan. J Oral Maxillofac Surg. 2021;80(5):827–37.
5. Blanc J, Fuchsmann C, Nistiriuc-Muntean V, et al. Evaluation of virtual surgical planning systems and customized devices in fibula free flap mandibular reconstruction. Eur Arch Otorrinolaringol. 2019;276:3477–86. https://doi.org/10.1007/s00405-019-05625-z.
6. Zavattero E, Bolzoni A, Dell'Aversana G. Accuracy of fibula reconstruction using patient-specific CAD/CAM plates: a multicenter study on 47 patients. Laryngoscope. 2021;131:E2169–75. https://doi.org/10.1002/lary.29379.
7. Technical Considerations for Additive Manufactured Medical Devices, FDA. https://www.fda.gov/regulatory-information/search-fda-guidance-documents/technical-considerations-additive-manufactured-medical-devices.
8. ASME (The American Society of Mechanical Engineers). https://resources.asme.org/hubfs/TABD/Verification%20and%20Validation/ASME%20AM%20for%20Med%20Device%20Verification%20and%20Validation%20-%20FINAL.pdf?hsLang=en-us.
9. Le Clerc N, et al. 3D titanium implant for orbital reconstruction after maxillectomy. J Plast Reconstr Aesthet Surg. 73(4):732–9.
10. Charles C, Sébastien F, Yohan C. Titanium three-dimensional printed cranioplasty for fronto-nasal bone defect. J Craniofac Surg. 2019;30(6):1802–5. https://doi.org/10.1097/SCS.0000000000005493.

11. Alexandre S, Nathalie D, Aurélien C, Isabelle B, Arnaud D. Orbitofrontal reconstruction with a three-dimensional titanium patient-specific implant after intraosseous haemangioma resection. J Craniofac Surg. 2021;32(1):e69–72. https://doi.org/10.1097/SCS.0000000000006935.
12. Bachelet J-T, et al. Orbital reconstruction by patient-specific implant printed in porous titanium: a retrospective case series of 12 patients. J Oral Maxillofac Surg. 76(10):2161–7.
13. Tel A, Kornfellner E, Moscato F, Vinayahalingam S, Xi T, Arboit L, Robiony M. Optimizing efficiency in the creation of patient-specific plates through field-driven generative design in maxillofacial surgery. Sci Rep. 2023;13(1):12082. PMID: 37495645; PMCID: PMC10371983. https://doi.org/10.1038/s41598-023-39327-8.
14. Laubach M, Hildebrand F, Suresh S, Wagels M, Kobbe P, Gilbert F, Kneser U, Holzapfel BM, Hutmacher DW. The concept of scaffold-guided bone regeneration for the treatment of long bone defects: current clinical application and future perspective. J Funct Biomater. 2023;14:341. https://doi.org/10.3390/jfb14070341.
15. Rendenbach C, Fischer H, Kopp A, Schmidt-Bleek K, Kreiker H, Stumpp S, Thiele M, Duda G, Hanken H, Beck-Broichsitter B, Jung O, Kröger N, Smeets R, Heiland M. Improved in vivo osseointegration and degradation behavior of PEO surface-modified WE43 magnesium plates and screws after 6 and 12 months. Mater Sci Eng: C. 2021;129:112380. ISSN 0928-4931. https://doi.org/10.1016/j.msec.2021.112380.
16. Systermans S, Cobraiville E, Camby S, Meyer C, Louvrier A, Lie SAN, Schouman T, Siciliano S, Beckers O, Poulet V, Ullmann N, Nolens G, Biscaccianti V, Nizet J-L, Hascoët J-Y, Gilon Y, Vidal L. An innovative 3D hydroxyapatite patient-specific implant for maxillofacial bone reconstruction: a case series of 13 patients. J Cranio-Maxillofacial Surg. 2024;52(4):420–31. ISSN 1010-5182. https://doi.org/10.1016/j.jcms.2024.02.026.

Augmented Reality in Cranio-Maxillo-Facial Surgery

Thomas J. J. Maal, Jene M. Meulstee, Dylan Duits, and Ruud Schreurs

1 Introduction

Augmented reality (AR) is a rapidly evolving technology that blends the digital world into the physical reality, transforming the possibilities of perception of our environment and interaction with it. It is a collective term that constitutes many different methods and applications, but, at its core, AR technology overlays digital content—visually, but also other sensory information—onto the real world and presents the combined form to its user. Mixed reality (MR) is the interactive variant of AR, where the user can interact with the digital information located in the real world. While AR and MR are often associated with consumer applications like Snapchat filters or interactive gaming applications such as Pokémon GO, their potential stretches far beyond entertainment purposes. Head-up display systems in aircrafts and cars project navigation information onto the windscreen ahead of the driver or pilot. This ensures that essential information can be obtained while maintaining full awareness of the surroundings. The integration of AR technology into a head-mounted display (HMD) has greatly increased flexibility for the environments in which applications could be used. AR and MR show significant promise and a transformative potential for application in healthcare, benefitting patients and doctors. However, despite their potential, AR and MR applications in professional fields like healthcare are still in the early stages of development. The technology requires further refinement to ensure reliability, accuracy, and ease of use in real-world scenarios. While initial results are promising, AR and MR must overcome technical and practical challenges before they can achieve widespread clinical adoption. In Cranio-Maxillo-Facial (CMF) surgery, they could potentially enhance surgical precision, aid in virtual surgery planning (VSP), and impact the effectiveness and outcomes of surgical procedures. This chapter explores the evolution of AR and MR, delves deeper in current applications in CMF surgery, and describes the future potential of this technology in transforming surgical practices.

2 Historical Background and Evolution

The concept of augmented reality dates back to the 1960s, when Ivan Sutherland from Harvard University, considered the founder of AR technology and invented the first head-mounted display (HMD) that could visualize digital data in the real environment. His device, named "the sword of Damocles," was attached to the ceiling of his laboratory and used a flexible mechanical structure to measure the user's head position. By leveraging a special NASA computer,

T. J. J. Maal (✉) · R. Schreurs
Department of Oral and Maxillofacial Surgery, Radboud University Medical Centre, Nijmegen, The Netherlands

Department of Oral and Maxillofacial Surgery, Amsterdam University Medical Centre, Amsterdam, The Netherlands

Radboudumc 3D Lab, Radboud University Medical Centre, Nijmegen, The Netherlands
e-mail: Thomas.Maal@radboudumc.nl; r.schreurs@amsterdamumc.nl

J. M. Meulstee · D. Duits
Department of Oral and Maxillofacial Surgery, Radboud University Medical Centre, Nijmegen, The Netherlands

Radboudumc 3D Lab, Radboud University Medical Centre, Nijmegen, The Netherlands
e-mail: Jene.Meulstee@radboudumc.nl; dylan.duits@radboudumc.nl

© The Author(s), under exclusive license to Springer Nature Switzerland AG 2025

A. Tel, M. Robiony (eds.), *Atlas of Virtual Surgical Planning and 3D Printing for Cranio-Maxillo-Facial Surgery*,
https://doi.org/10.1007/978-3-031-94495-6_7

Sutherland displayed wire-frame images of 3D objects at a rate of 30 frames per second. Although this was only half the speed of today's modern AR devices, it marked a significant milestone in AR development [1, 2]. The 1980s and 1990s saw further technological advancements that contributed to the evolution of AR.

In the early 1990s, AR saw practical applications in various industries. Tom Caudell, an engineer at Boeing, sought to improve the complex process of aircraft manufacturing. He developed an HMD to virtually display wiring instructions, coining the term "Augmented Reality." His innovation sped up the manufacturing process by replacing physical templates with modifiable virtual instructions. This early implementation demonstrated the potential of AR to streamline workflows and reduce errors in complex tasks [3]. In the same time period, Louis Rosenburg created an MR system that allowed physical objects to interact with virtual objects. His system used an exoskeleton to control two robotic hands, enabling users to manipulate virtual content as if it were real. This system was utilized by the United States Air Force to train pilots, marking AR and MR's initial foray into aviation and defense. The ability to merge physical and virtual worlds in real time opened new possibilities for training and simulation [4]. Another notable example from the 90s was the introduction of virtual yard markers in American football games by the company SportVision. Using real-time camera feeds, SportVision projected a virtual yellow yard line onto the field that appeared perfectly aligned with the real environment. This innovation not only enhanced the viewer experience but also demonstrated how AR could seamlessly blend virtual elements with live action, paving the way for further developments in AR visualization techniques.

3 The Rise of AR in Healthcare

The healthcare sector began to explore AR's potential in the early 2010s. Initially, AR was utilized in surgical navigation and medical training. Wearable devices like Google Glass, introduced in 2013, allowed healthcare professionals to access digital information hands-free. In the early days, the Google Glass was used during surgery to broadcast procedures from the surgeon's perspective for educational purposes. However, limitations such as low display quality, short battery life, and limited functionality hindered its widespread adoption. Despite these early challenges, the potential of the technique was recognized by medical researchers and clinicians, and interest on AR continued to surge.

In 2014, Meta Glass introduced the first stereoscopic HMD, capable of visualizing 3D objects, tracking user movements, and enabling interaction with virtual models. Despite offering an authentic MR experience, practical issues such as low resolution and cumbersome cables reduced its usability in medical settings. Nonetheless, the concept of using AR for interactive 3D visualization laid the groundwork for more advanced devices. The introduction of the Microsoft HoloLens in 2016 marked a significant leap forward. The HoloLens offered a wireless design with a high-quality display and an improved field of view. Its stereoscopic visualization capabilities allowed users to inspect virtual 3D models from different angles, making it a promising tool for VSP applications and intraoperative navigation, where the VSP of the patient could be aligned with the physical position of the patient in the operating room. Figure 1 illustrates various head mounted AR devices that allow users to visualize 3D content in a real environment.

In CMFS, AR is still in its early stages of adoption within operating rooms, and notable issues regarding accuracy hamper widespread implementation during surgery. Current systems are also prone to drift resulting in misalignment of the virtual and real-world information over time. Technological advancements (both hardware and software) are needed to improve both the precision of overlays and the robustness of tracking systems to ensure reliable performance in complex surgical environments. Nevertheless, ongoing research and development are demonstrating the technology's potential to improve patient outcomes by increasing surgical accuracy and reducing procedure times. Researchers are exploring ways to integrate AR with other technologies, such as robotics and artificial intelligence, to further enhance surgical workflows and improve patient care. In the subsequent subsections, an overview of the technological foundation for AR in surgery is provided first, followed by an overview of innovative present-day uses in CMF subspecialties.



Fig. 1 Various AR devices that allow users to visualize 3D content in a real environment. Left: the Google Glass used during orthognathic surgery in the Radboudumc (2013). Middle: the META glasses provided a real 3D visualization by using stereoscopic, semi-transparent displays (Radboudumc 2014). Right: the surgeon uses the Microsoft HoloLens to demarcate the course of blood vessels on a patient's abdomen as preparation for a free flap raising procedure

4 Technological Foundation of AR in Surgery

4.1 Hardware Components

AR hardware plays a critical role in delivering accurate, real-time augmented visuals to surgeons. The primary hardware components include head-mounted displays (HMDs), depth sensors, cameras, and software components. Each of these components serves a specific function in enhancing the surgical experience.

4.2 Head-Mounted Displays (HMDs)

Wearable devices, such as smart glasses and surgical head-mounted displays (HMDs), are becoming increasingly popular in AR-assisted surgeries due to their ability to enhance the surgeon's situational awareness without disrupting the workflow. These devices are essential for delivering AR content directly in the area of interest to the surgeon, minimizing the need to shift focus away from the patient. Devices like Microsoft HoloLens and Magic Leap provide an immersive experience that allows surgeons to view anatomical overlays or other patient information while performing procedures. These devices are often equipped with voice control and gesture recognition to ensure that they can be controlled in a hands-free fashion, maintaining sterility throughout the procedure.

Nowadays, HMDs are equipped with advanced optics and sensors that track head movements and adjust the overlay to maintain alignment with the patient's anatomy. This capability ensures that virtual overlays and instructions remain accurate throughout the procedure; as mentioned, achieving high accuracy and stability remains a challenge. The weight and comfort of HMDs also leave room for improvement for reducing fatigue during lengthy surgeries. However, wearable devices continue to evolve in terms of display quality, tracking accuracy, and integration with other surgical systems, paving the way for more seamless AR adoption in surgery.

4.3 Depth Sensors and Cameras

Depth sensors and cameras integrated in the mount of the HMD capture the surgical environment and provide essential data for aligning virtual models with real-world anatomy. Depth sensors measure the distance between the device and various points in the surgical field, creating a 3D map that the AR system uses to position holographic overlays. Cameras capture real-time images that are processed by AR algorithms to ensure that virtual models remain in their original position. Some more advanced AR systems use stereo-cameras to provide a more detailed, three-dimensional view of the surgical area, improving the accuracy of virtual overlays.

4.4 Software Components

The software infrastructure of AR systems is responsible for processing visual data and generating virtual overlays. The primary software components include AR algorithms, the user interface, and cloud-based data storage solutions. AR algorithms are at the core of any AR system. These algorithms process visual data from cameras and depth sensors to identify anatomical landmarks and adjust virtual overlays in real time. The accuracy of these algorithms is crucial for ensuring that virtual models remain aligned with the patient's

anatomy throughout the surgical procedure. Advanced AR algorithms use computer vision techniques to recognize and track anatomical structures.

The user interface (UI) of an AR system is a critical factor in its usability. Modern AR systems use intuitive UIs that allow surgeons to interact with virtual overlays using voice commands, gestures, or touch inputs. Gesture recognition technology enables surgeons to manipulate virtual models, such as rotating or zooming in on specific areas, without breaking sterility. The UI must be designed to provide clear and concise information without overwhelming the surgeon with too many details. Achieving this balance is essential to ensure that AR systems enhance surgical performance rather than distract from the procedure.

Cloud-based solutions play a vital role in managing the large volumes of data generated by AR systems. Patient imaging data, surgical plans, and AR overlays are stored in the cloud, allowing surgeons to access this information from any device with an internet connection. Cloud-based processing enables real-time collaboration between surgical teams, even if they are in different locations. This capability is particularly valuable for remote consultations and surgical planning sessions. Additionally, cloud storage ensures that patient data remains secure and can be easily updated as new information becomes available.



Fig. 2 While the HoloLens tracks the patient position by the quick response marker above the navel, the anatomy hologram is visualized. The green cylinders indicate perforator locations on the skin. The user can switch between visualizations of different anatomical structures

5 The Role of AR in CMF Surgery

Studies have highlighted the potential of AR visualization tools, such as 3D computer screens, holographic projectors, and stereoscopic AR glasses, in improving surgical outcomes. Historically, concerns about the high costs, cumbersome setup, and lack of comparative studies have hindered widespread adoption. However, the latest AR devices, such as the HoloLens 2 and Apple Vision Pro, address many of these concerns by offering a user-friendly, cost-effective, and widely available solution. These advances make AR an increasingly viable option for use in every operating room. Future research should focus on the usability of AR glasses during surgery and on reducing factors that may hinder their practical application.

5.1 Surgical Guidance

One of the transformative aspects of AR is its ability to shift medical imaging from purely diagnostic purposes to direct intraoperative use. For example, in free flap surgeries such as Deep Inferior Epigastric Perforator (DIEP) flap procedures, preoperative CT-angiograms are used to identify and assess perforators. Traditionally, this information is reviewed in the planning phase, but AR technology can bring these images into the operating room. By converting the diagnostic scans into 3D models and overlaying them onto the patient's body using AR glasses, surgeons can see the precise location of blood vessels in real time.

This capability was demonstrated in a DIEP flap breast reconstruction case, where a preoperative CT-angiogram was segmented and transformed into a 3D visualization using the HoloLens (Fig. 2). By employing real-time tracking and patient-specific registration, the surgeon could view the anatomy directly on the patient's body. In follow-up research involving ten patients, this workflow showed that AR guidance could pinpoint perforator locations within a clinical margin of 10 mm, which is sufficient for practical use in surgery. This example underscores the potential of AR to bridge the gap between diagnostic imaging and image-guided surgery, facilitating better outcomes and more efficient workflows [5].

5.2 Dynamic Guidance Systems with AR

AR offers the potential to create dynamic guidance systems that can adapt in real time to the surgeon's actions. In traditional navigation systems, if a surgeon makes an error during the first cut, subsequent steps may need to be adjusted manually, leading

to delays and complications. AR systems, on the other hand, can track surgical tools and adjust the virtual plan automatically. For example, if the initial osteotomy in a fibula segment is off by a few millimeters, the AR system can recalibrate subsequent cuts to ensure that the final reconstruction fits perfectly. This capability could greatly enhance surgical outcomes by providing a more flexible and adaptive guidance system.

In addition to improving accuracy, AR guidance systems can replace expensive navigation tools that are currently used in surgical settings. Conventional surgical navigation systems can cost upwards of 50,000 euros, whereas AR glasses provide a more affordable alternative. By enabling surgeons to remain focused on the operative site while receiving real-time feedback, AR glasses offer a practical solution for transferring virtual plans to a physical surgical setting.

AR also simplifies the execution of complex surgical plans by providing intuitive, step-by-step visual guidance. For example, during cranial reconstructions or orbital implant placements, the presence of a technical physician is often necessary to help interpret the surgical plan and ensure accurate execution. AR can reduce this dependency by providing clear, real-time visual instructions directly in the surgeon's field of view.

This capability could lead to the creation of more advanced virtual surgical plans. As AR makes the execution of these plans easier, surgeons will be able to tackle more complex procedures with greater confidence. Existing image-guided surgery systems, such as the X-Guide® d-CAIS system (X-Guide®, X-Nav Technologies®, LLC, Lansdale, PA, USA) for dental implants or specialized intraoperative navigation systems for orthopedic screws and orbital implants, demonstrate the value of image-guided surgery. However, these systems often require dedicated tools and tracking setups. AR, by contrast, can display virtual content in the real environment without the need for specialized hardware, making it a versatile and scalable solution for various surgical applications.

6 Current AR Applications in CMF Surgery

6.1 Dental Implantology

One of the primary challenges in dental implantology is ensuring precise implant placement to avoid complications and maximize long-term success. AR addresses this challenge by overlaying 3D virtual models of the patient's jaw onto their physical anatomy, allowing clinicians to visualize bone density, nerve pathways, and optimal implant sites before surgery.

6.1.1 Surgical Guidance

Intraoperative navigation is one of the most significant applications of AR in dental implantology. One of the primary challenges in dental implantology is ensuring precise implant placement to avoid complications and maximize long-term success. AR addresses this challenge by overlaying 3D virtual models of the patient's jaw onto their physical anatomy, allowing clinicians to visualize bone density, nerve pathways, and optimal implant sites before surgery. By providing real-time guidance during surgery, AR systems help clinicians accurately place implants in the correct position, angle, and depth.

Ma et al. developed an AR-based navigation system that integrates accurate cone beam computed tomography (CBCT)-patient registration [6]. The system allows for the projection of 3D virtual images of the mandibular nerve and implant path onto the patient in real-time, improving accuracy during implant placement and reducing the risk of nerve damage. The developed AR navigation system consists of a computer, an optical tracker, a registration device, and a 3D image overlay device employing immersive visualization technology. The custom registration device was used to align preoperative CBCT data with the patient. During the procedure, this device is worn on the patient's teeth for real-time tracking. Naked-eye 3D images of the planned implant path and the mandibular nerve are overlaid directly onto the patient, forming an AR scene. The drill's 3D position is also superimposed on the real one to guide the procedure. Their study demonstrated that AR-guided implant placement achieved better accuracy compared to traditional methods, with a mean target error of 1.25 mm and a mean angular deviation of 4.03°.

Pellegrino et al. conducted a pilot clinical study using AR for dynamic navigation in dental implantology [7]. Their research involved two cases where implants were placed using AR glasses combined with a navigation system (ImplaNav, BresMedical, Sydney, Australia) for real-time navigation. The study found that AR-assisted navigation resulted in a deviation of less than 0.5 mm from the planned implant position, indicating that AR can enhance precision and reduce surgical errors.

Zygomatic implant placement is challenging due to limited bone mass, long drilling paths, and proximity to vital structures. Especially in Zygomatic implant augmented reality (AR) navigation has the potential to enhance surgical visualization and could offer a potential alternative to traditional guides. Tabernée Heijtmeijer et al. performed a cadaver study in which 20 implants were placed using an AR system integrating a commercial navigation platform with Microsoft HoloLens [8]. Postoperative scans were compared to preoperative 3D planning to assess accuracy. The mean entry point deviation was 2.43 mm, exit point 3.28 mm, and angular deviation 5.80°.

Although surgical guides showed higher precision in entry points and angles, AR navigation achieved acceptable accuracy, particularly at the exit point and demonstrates the feasibility of AR navigation for zygomatic implants and its potential for further refinement.

Although several studies have highlighted the potential benefits of combining AR with navigation systems in dental implantology, the real value lies in optimizing the integration between AR hardware and tracking technology. Current set-ups rely on external navigation systems, which increase complexity and cost. The real benefits lie in a set-up where AR is used for visualization and tracking, obviating the need for an additional surgical navigation system that is associated with burdensome intraoperative logistics and high cost. In this situation, AR-guided implant surgery has the potential to become a practical and accessible tool in clinical practice, reducing reliance on physical guides while maintaining precision in implant placement.

6.2 Craniomaxillofacial Trauma

6.2.1 Diagnostics

In the diagnostic process of craniofacial fractures, accurate detection and spatial recognition of fractures are vital for virtual surgical planning and the surgical intervention itself. Lee et al. devised a software application that utilized AR to visualize 3D skull models of six patients with craniomaxillofacial trauma [9]. The diagnostic accuracy was tested by 30 surgeons and compared to diagnosis with a conventional 3D visualization on screen. No significant differences in diagnostic accuracy were found, but a significant reduction in task load index for surgeons with less experience was seen. Subjectively, AR was preferred over the standard 3D model as an accessory to the multiplanar slices for providing a global overview by 83% of surgeons because of the improved ease of manipulation of the model.

6.2.2 Education

Colback et al. continued on the global overview of facial trauma that AR is able to provide and investigated its use as a tool for patient education. Participants were given two tutorials concerning treatment of zygomaticomaxillary complex fractures: one group started with the conventional CT-based explanation, while the other group saw an immersive MR explanation on the magic leap [10]. While there was no objective difference in patients' knowledge of the procedure, patients who got to experience the immersive explanation first self-reported significantly higher understanding. This self-perceived understanding may yield improved patient confidence about the procedure and might lead to enhanced patient satisfaction.

The Magic Leap was also used for patient education by Wilkat et al. [11]. They demonstrated the fracture pattern, defect size, and reconstruction possibilities with conventional preformed implants and a patient-specific implant (PSI). They reported that the MR experience aided in facilitating the informed consent process and hypothesized on the advantages in training medical students and training craniomaxillofacial surgeons. These effects on education of craniomaxillofacial trauma on medical students were investigated in greater detail by Bouaoud et al., who assessed student understanding through the use of their DIVA (Data Integration and Visualization in Augmented and Virtual Environments) software; in this specific application, VR was used [12]. Overall, students reported high satisfaction and improved understanding of craniomaxillofacial trauma through the experience, which demonstrates the potential of XR technology in education.

6.2.3 Surgical Guidance

Similar to other CMF subspecialties, surgical guidance has been one of the main focus points in application of AR technology. The main focus was utilization in ZMC surgery as an alternative to freehand reduction. Chen et al. and Lin et al. both described a standalone AR system for reduction of zygomaticomaxillary complex (ZMC) fractures [13, 14]. Their systems utilized QR codes on unaffected anatomy; Lin et al. also tracked the ZMC segment(s) by QR codes and showed visual cues on repositioning during reduction of the segment(s). Chen et al. described an average discrepancy between planning and postoperative result of 0.4 mm in nine patients. Lin et al. found a significant improvement in the time needed for fracture reduction (15.4 min with AR vs 20.4 min conventional, $p = 0.03$) and a significant improvement in reduction accuracy (1.35 mm vs 1.61 mm, $p = 0.02$). Despite these promising results, both articles recognize known drawbacks of the technology (image drift, depth perception, tracking stability, and weight of the HMD) that need to be optimized to enable widespread clinical implementation. Machine-learning approaches, like the one described by Kim et al., may alleviate the stability and image drift concerns: in 19 patients treated with the AR approach, the RMS symmetry error reduced from 1.7 mm preoperatively to 1.0 mm postoperatively [15].

6.3 Orthognathic Surgery

6.3.1 Diagnostics

Clinical assessment of TMJ movement and function is of paramount importance in diagnostics for orthognathic surgery. Cercenelli et al. provided an AR-based solution to visualize the movement of the mandible and condyles in

relation to the cranium [16]. The fossa and mandibular components were individually tracked with pose estimation and a QR code to capture movements between the two. In one test subject, the AR tracking showed deviations from kinesiography tracking in the range of 0.5 mm to 3 mm) in the sagittal view (<1 mm) but more significant deviations in the frontal view (2–6.5 mm), but with the advantage of simultaneous visualization of joint anatomy during movement of the jaw.

Wilkat et al. focused on the implementation of MR in the virtual surgical planning process [17]. Specifically, they introduced an MR tool for establishing the virtual occlusion in the planning process and compared the resulting occlusion to the occlusion established by a conventional (plaster cast) method and a virtual occlusion through IPS Case Designer's occlusion tool. While the overall occlusions were comparable between all methods, both virtual methods showed a slight tendency to position the maxilla more anteriorly, with a higher overjet and less occlusal contact. The authors suggested a superior visualization for the MR method, with possibilities that are not achievable with conventional models or virtual occlusion tools in 2D, and postulated that integration with automatic alignment algorithms or haptic feedback could add the functionality of the other methods to the MR method.

6.3.2 Education

Similar to other education applications, the focus for orthognathic surgery has been on VR rather than AR or MR applications for education. The effectiveness of virtual reality in surgical training for Le Fort I osteotomy was investigated in a randomized controlled trial by Pulijala et al. [18]. The study group used a VR surgical application for training, while the control group received training from a PowerPoint presentation featuring the same content. The results revealed significantly higher self-confidence levels for the XR study group ($p = 0.034$), with first-year trainees demonstrating the largest confidence improvement. Medellin-Castillo et al. integrated haptic feedback in their comprehensive VR training solution [19]. In an experiment with nine OMF postgraduate students, their results showed that students who received VR training had improved speed and accuracy in performing an osteotomy on a 3D printed model and that the addition of haptic feedback to the VR systems yielded further improvement.

6.3.3 Surgical Guidance

Intraoperative application of AR in orthognathic surgery has a long history: more than a decade ago, Zinser et al. tried intraoperative use of an AR application. Their solution used a tablet-like device that could augment the camera view with the planned position of the maxilla; the tracking solution was based on optical surgical navigation [20].

Most AR tracking systems utilize a splint that is equipped with a QR code, either for registration of the VSP to the patient position or for tracking of the maxilla (in case of maxillary orthognathic surgery). Ahn et al. describe an in vitro testing of a system for repositioning the maxilla after a Le Fort I osteotomy, with remarkable measurement accuracy for movement of the segment [21]. Sugahara et al. described a secondary reconstruction of a maxillary non-union after a Le Fort osteotomy, while Huang et al. presented a case report for a BSSO and genioplasty [22, 23]. The virtual surgical plannings of both were projected on the patient using the Microsoft Hololens, with QR code registration markers attached to an occlusal plate. Koyashi et al. used the Hololens in a larger cohort of patients ($n = 26$) for repositioning of the maxilla and described high accuracy of repositioning in all dimensions. However, in nearly all these studies, AR was used as an addition to other guidance tools, such as 3D models, prebent plates, occlusal splints, or resection guides, which makes isolation of the effect of AR on surgical outcome infeasible [24].

Remarkably, AR has also found its way to applications in surgery of the mandible, while—or because—conventional surgical navigation technology is lacking in this region. In a case report on TMJ reconstruction, Niloy et al. used an external tracking camera and surgical guides that were equipped with reflective marker spheres to track the position of the guide; AR feedback was provided to the surgeon once the guide was positioned on the mandible or fossa [25]. A high accuracy was demonstrated in two patients, with a mean error of 1.252 mm and 1.393 mm for the mandible and fossa respectively, but the authors describe significant challenges regarding a steep learning curve, technical difficulties, surgical time, and added cost.

Zhu et al. measured surgery time, preparation time, and surgical accuracy of mandibular angle osteotomies with AR in 31 patients, and compared this to a 3D printed guide group and a conventional freehand group [26]. While preparation time was significantly longer for both AR and 3D guides, there were no significant differences in operating time. AR was found to have comparable accuracy to 3D printed guides (mean 1.18 mm AR vs 0.96 mm 3D guides); both technologies outperformed the freehand technology significantly (mean 3.64 mm). The same group demonstrated the use of AR in a variety of interventions, in which osteotomy planning and critical structures such as the inferior alveolar nerve were projected.

Accurate osteotomy (≤1 mm) for proportionate condylectomy using AR surgical guidance was also described by Bussink et al. [27] (Fig. 3). Similar findings on positioning accuracy and rotational deviation of the osteotomy plane were seen in distraction osteogenesis for hemifacial micro-

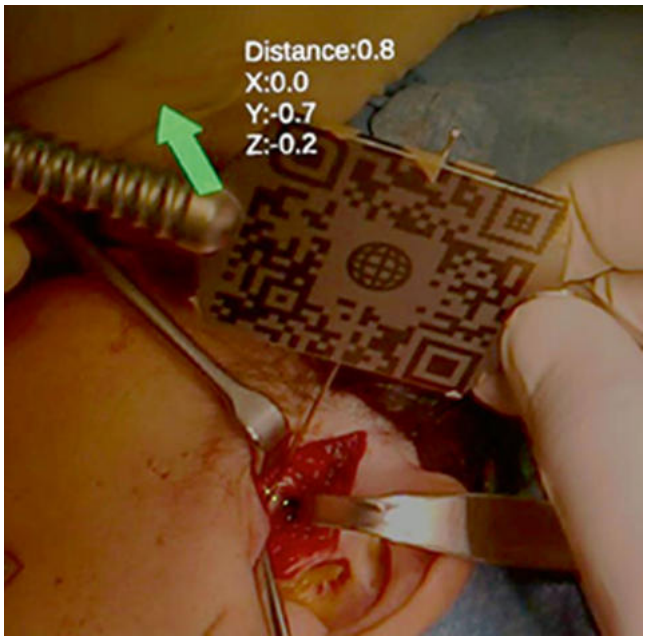


Fig. 3 Visualization of landmarks from the virtual surgery plan of a proportional condylectomy in the Microsoft HoloLens 2: the green arrow indicates how the tip of the pointer should be manipulated to target the planned osteotomy position

somia: compared to the freehand method, the accuracy using AR guidance was significantly improved for position of the osteotomy (1.45 mm vs 2.37 mm), but not for rotational deviation of the plane (9.39° vs 10.48°) [28, 29]. Bussink et al. concluded in light of their results that AR was a low-cost alternative to conventional surgical navigation systems, but the rotational deviations seen in both studies warrant more extensive evaluation of all degrees of freedom.

6.4 Craniofacial Surgery

Complex craniofacial procedures, such as craniosynostosis correction and cranial vault reconstruction, often require precise anatomical navigation to achieve optimal outcomes. Traditional methods, such as manual palpation and physical surgical guides, can be prone to error or time-consuming to manufacture. AR offers a promising alternative by projecting virtual models directly onto real-world anatomy, improving accuracy, efficiency, and surgeon confidence throughout the surgical process.

6.4.1 Education

One of the earliest applications of AR in craniofacial surgery involves the use of hybrid models that combine physical 3D-printed anatomical structures with virtual overlays. Coelho et al. demonstrated this approach in the preoperative planning of metopic craniosynostosis surgery [30]. Using diagnostic CT scans, patient-specific skull replicas were created with various silicone materials to mimic the actual anatomy. An AR mobile application further enhanced these models by projecting virtual anatomical landmarks onto the physical replica. This allowed surgeons to practice critical steps such as skin incisions, subperiosteal dissection, and cranial remodeling before the actual procedure. Surgeons who tested the hybrid model reported improved understanding of 3D anatomy and increased precision in surgical planning, leading to a reduction in potential intraoperative errors.

6.4.2 Surgical Guidance

Building on the surgical education concept of Coehlho, Thabit et al. developed an AR navigation system that integrates an electromagnetic tracking device with the Microsoft HoloLens to visualize cranial sutures in real time [31]. Accurate localization of cranial sutures is essential for minimally invasive spring-assisted craniectomy, but manual palpation can be error-prone. In this study, the AR system was tested on two skull phantoms, with participants visualizing and delineating five cranial sutures. The system achieved an average accuracy of 2.4 mm when compared to preoperative CT scans, and users reported a usability score of 73 on the System Usability Scale. The study demonstrated that AR navigation could reduce reliance on manual palpation, potentially improving surgical accuracy and reducing errors in suture identification. However, the authors noted that further clinical validation is needed to confirm the system's efficacy in real surgical settings.

Additionally, AR navigation has been explored in more complex craniofacial corrections, such as orbital hypertelorism, a condition that requires precise osteotomies and repositioning of the orbits. Zhu et al. developed an AR-based navigation system that guided surgeons through these challenging procedures [32]. Using preoperative CT data, a virtual surgical plan was created and superimposed onto the patient's anatomy during surgery. The system displayed 3D navigational information directly onto the surgical field, helping surgeons perform precise bone cuts and achieve better aesthetic outcomes. In a study of 12 patients, postoperative evaluations showed minimal differences between the preoperative plans and actual outcomes, demonstrating the accuracy and reliability of AR-guided navigation in these complex cases.

Another critical application of AR in craniofacial surgery is cranial vault reconstruction for patients with synostotic plagiocephaly. Han et al. introduced an AR navigation system that provided real-time images during open calvarial reconstruction [33]. The system guided

surgeons through precise osteotomies, ensuring accurate corrections and reducing intracranial volume asymmetry. In a study of seven patients, the AR system achieved significant improvements in surgical accuracy and postoperative outcomes. By overlaying preoperative design data onto the surgical field, surgeons were able to achieve their planned corrections with high precision, leading to more symmetrical cranial vaults and improved cosmetic results.

AR is also becoming more accessible through smartphone-based applications, making it a practical solution for a wider range of surgeons and institutions. Alshomer et al. explored the use of a low-cost, smartphone-assisted AR tool for craniofacial surgical planning [34]. The app, Camera Lucida, allowed surgeons to superimpose 3D CT scans onto the surgical field during fronto-orbital advancement procedures. This approach provided a cost-effective solution for visualizing complex cranial anatomy in real time without requiring expensive equipment. Two case studies involving fronto-orbital advancement and craniosynostosis surgery highlighted the tool's effectiveness in guiding bone cuts and prioritizing soft tissue reconstruction. The AR app allowed surgeons to better plan their osteotomies and improve surgical precision, particularly in resource-limited settings where traditional navigation systems may not be available [13].

García-Mato et al. further explored smartphone-based AR visualization systems for fronto-orbital advancement surgeries [35]. Their system used intraoperative markers and 3D photography to ensure accurate alignment between virtual models and patient anatomy during surgery. Tested on patient-specific phantoms and in two live surgeries, the AR system was used in guiding osteotomies and cranial remodeling. This research highlights the potential of AR to be integrated into routine craniofacial surgeries, providing real-time guidance that enhances both precision and patient safety.

Overall, AR technology in craniofacial surgery offers significant potential to enhance accuracy, improve surgical planning, and reduce intraoperative errors. By providing real-time visualization of critical anatomical landmarks, AR helps surgeons bridge the gap between virtual planning and real-life execution. The development of smartphone-based AR applications and hybrid models makes this technology more accessible and affordable, broadening its applicability to various surgical settings. While AR has demonstrated promising results in phantom studies and proof-of-concept clinical studies, further research involving larger patient groups and more diverse surgical teams is essential to validate its clinical effectiveness fully. As AR systems continue to evolve, they have the potential to revolutionize craniofacial surgery, making procedures safer, more efficient, and more precise.

6.5 Head and Neck Oncology

The integration of augmented reality (AR) technology into head and neck oncology has shown significant potential in improving surgical precision and patient outcomes. AR enables surgeons to visualize critical anatomical structures and tumor margins in real time, reducing risks and enhancing the accuracy of complex procedures. This innovative technology has been explored across various otolaryngology subspecialties, demonstrating its utility in tumor localization, surgical navigation, and reconstructive planning.

One of the key challenges in head and neck cancer surgery is achieving clear margins while avoiding damage to critical structures. AR addresses this challenge by overlaying 3D virtual models of tumors and anatomical landmarks onto the surgical field. For instance, Chan et al. conducted a cadaveric study using AR within transoral robotic surgery (TORS) to overlay the internal carotid artery during tumor resection. This approach facilitated the identification of critical structures, reducing the risk of accidental damage [36, 37].

Similarly, Taboni et al. demonstrated the use of AR for transnasal tumor delineation in maxillary cancer. By integrating 3D-rendered surgical navigation with virtual endoscopy, they showed that AR-guided simulations significantly improved margin-negative resections and reduced the risk of carotid artery injury compared to unguided procedures. The inclusion of a 2-mm alert cloud around the carotid artery further enhanced the safety and precision of these procedures [37, 38].

Preclinical studies have also validated the role of AR in open sinonasal tumor resections. Sahovaler et al. found that AR-guided cuts improved tumor margin delineation, with intratumoral cuts dropping from 20.7% in unguided cuts to 0% in AR-guided procedures [39]. These findings underscore the potential of AR in achieving precise resections and minimizing the risk of recurrence.

6.5.1 Surgical Guidance

Building on cadaveric studies, AR has been applied in live surgeries through the use of holographic models. Scherl et al. utilized the Microsoft HoloLens to project 2D and 3D holographic images derived from preoperative MRI data onto patients undergoing parotid surgery. Despite a mean alignment error of 10.06 mm, the study demonstrated the feasibility of AR in improving anatomical visualization during surgery [37, 40].

Chand et al. explored AR's application in sentinel node localization for oral squamous cell carcinoma. They used a handheld AR scanning device to align sentinel nodes with preoperative single-photon emission computed tomography

(SPECT) images. The accuracy of this approach was validated through the alignment of fluorescence tracers with both SPECT-CT and handheld AR probes, paving the way for more precise lymph node mapping during cancer surgeries [37, 41].

Prasad et al. took a different approach by using 3D holograms to guide reresections in head and neck cancer surgeries. The holograms, projected using the Microsoft HoloLens 2, allowed surgeons to manipulate and annotate the virtual models hands-free, maintaining sterility in the operating room. The study reported a mean relocation error of 4 mm, suggesting that AR can enhance the accuracy of reresections and improve patient outcomes [37, 42].

Augmented Reality (AR) holds significant potential to improve reconstructive surgery by enhancing surgical planning and execution. Recent exploratory studies have demonstrated how AR can assist in aligning virtual models with real-world anatomy. Necker et al. used AR to project annotated holograms of anatomical structures onto free flap harvest sites. The color-coded holograms helped surgeons align virtual 3D models with the resection bed, reducing time spent on flap orientation and providing a more intuitive understanding of the surgical site. However, the use of AR in reconstructive procedures is still in its early stages, and its clinical utility requires further validation [37, 43].

AR technology has also been tested in microvascular reconstructions to align donor and recipient sites more precisely. By projecting virtual templates directly onto the patient's anatomy, AR showed potential to improve the accuracy of bone cutting and tissue placement. This approach may reduce reliance on static, pre-made cutting guides, offering the possibility of more dynamic surgical adjustments. Despite these promising results, current AR systems still face challenges in terms of ease of use, accuracy, and real-time adaptability in clinical settings.

One of the most recent developments in maxillomandibular reconstruction is an AR-guided technique using the Microsoft HoloLens 2. Unlike physical cutting guides, which lack flexibility for intraoperative adjustments, this AR application projects virtual osteotomy planes onto the fibular bone and provides real-time feedback on the saw's position (Fig. 4). In a validation study using 3D-printed fibular models, the system achieved mean angular deviations of 4.1° and 3.1°, and segment length deviations of 2.0 mm and 2.3 mm across two sessions. These results suggest that AR could offer valuable real-time guidance for surgeons, allowing for intraoperative adjustments without compromising precision.

Although these initial studies highlight the potential of AR in reconstructive surgery, the technology is not yet ready for widespread clinical use. The accuracy, usability, and reliability of AR systems need to be further improved, and more clinical validation is essential to determine their effectiveness in real-world surgical scenarios.

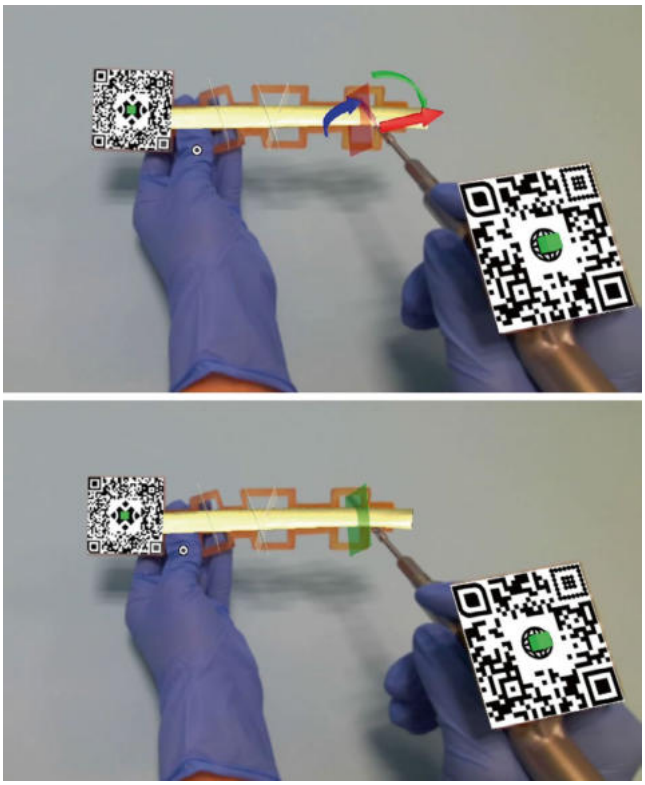


Fig. 4 Visual feedback mechanisms to provide information about the difference between the tracked saw blade plane and the planned osteotomy plane. The osteotomy plane switched from red to green when the user moved the saw blade closer to the osteotomy plane. The arrows indicated the left/right translation (red), pitch (green), and yaw (blue) and disappeared when the left/right translation and the value for pitch and yaw were below a predetermined threshold with respect to the planned osteotomy plane

7 Challenges and Future Directions

Although AR holds significant promise in the fields of craniomaxillofacial surgery and dental implantology, its implementation still faces several hurdles. Technical limitations, such as alignment inaccuracies and the transition from cadaveric models to live surgeries, introduce challenges that must be overcome to ensure reliable clinical use. Additionally, the costs associated with AR systems, along with the need for specialized training, can hinder widespread adoption in surgical practice.

Despite these obstacles, future advancements in AR technology and its integration with artificial intelligence (AI) offer exciting possibilities. Improvements in holographic projections, real-time tracking, and robotic system integration will likely enhance AR's accuracy, usability, and relevance in CMFS. AI-driven patient-specific AR models could further personalize surgical planning, providing more predictive and precise outcomes.

As AR technology continues to evolve, its transformative potential in surgical care becomes increasingly evident. In

particular, the use of AR in CMFS holds the promise of improving patient outcomes through enhanced visualization and navigation. However, realizing this potential requires ongoing research, clinical trials, and close collaboration between surgeons, engineers, and software developers.

Ultimately, addressing current limitations and driving innovation in AR will shape the future of surgical care. By improving precision, reducing risks, and enhancing efficiency, AR technology has the capacity to revolutionize CMF surgery and beyond, making it an indispensable tool in modern healthcare practices.

References

1. Sutherland IE. A head-mounted three dimensional display. In: Proceedings of the December 9–11, 1968, Fall Joint Computer Conference, Part I on – AFIPS '68 (Fall, Part I), vol. 33. ACM Press; 1968. p. 757.
2. Van Krevelen DWF, Poelman R. A survey of augmented reality technologies, applications and limitations. Int J Virtual Real. 2010;9(2):1–20.
3. Caudell TP, Mizell DW. Augmented reality: an application of heads-up display technology to manual manufacturing processes, vol. 2. Institute of Electrical and Electronics Engineers (IEEE); 2003. p. 659–69.
4. Rosenberg LB. The use of virtual fixtures as perceptual overlays to enhance operator performance in remote environments; Technical Report AL-TR-0089. USAF. 1992.
5. Wesselius TS, Meulstee JW, Luijten G, Xi T, Maal TJJ, Ulrich DJO. Holographic augmented reality for DIEP flap harvest. Plast Reconstr Surg. 2021;147(1):25e–9e.
6. Ma L, Jiang W, Zhang B, Qu X, Ning G, Zhang X, Liao H. Augmented reality surgical navigation with accurate CBCT-patient registration for dental implant placement. Med Biol Eng Comput. 2019;57(1):47–57.
7. Pellegrino G, Mangano C, Mangano R, Ferri A, Taraschi V, Marchetti C. Augmented reality for dental implantology: a pilot clinical report of two cases. BMC Oral Health. 2019;19(1):158.
8. Tabernée Heijtmeijer S, Glas H, Janssen N, Vosselman N, de Visscher S, Spijkervet F, Raghoebar G, de Bree R, Rosenberg A, Witjes M, Kraeima J. Accuracy of augmented reality navigated surgery for placement of zygomatic implants: a human cadaver study. PeerJ. 2024;12:e18468.
9. Lee S, Panchal N, Hoffman W, Pomerantz J, Laguna B, Courtier J. An augmented reality model for evaluating traumatic craniofacial fractures. FACE. 2024;5(3):525–32.
10. Colback A, Velazquez-Castro O, Agarrado M, Reddy R, Strong E, Wilson M, Bradley. Evaluating mixed reality as a tool for patient education of facial fractures. Facial Plast Surg Aesthet Med. 2024;26(5):646–51.
11. Wilkat M, Karnatz N, Schrader F, Schorn L, Lommen J, Parviz A, Möllmann HL, Rana M. Usage of object matching algorithms combined with mixed reality for enhanced decision making in orbital reconstruction-a technical note. J Pers Med. 2023;13(6):922.
12. Bouaoud J, El Beheiry M, Jablon E, Schouman T, Bertolus C, Picard A, Masson JB, Khonsari RH. DIVA, a 3D virtual reality platform, improves undergraduate craniofacial trauma education. J Stomatol Oral Maxillofac Surg. 2021;122(4):367–71.
13. Chen G, Zeng W, Yin H, Yu Y, Ju R, Tang W. The preliminary application of augmented reality in unilateral orbitozygomatic maxillary complex fractures treatment. J Craniofac Surg. 2020;31(2):542–8.
14. Lin L, Gao Y, Aung ZM, Xu H, Wang B, Yang X. Preliminary reports of augmented-reality assisted craniofacial bone fracture reduction. J Plast Reconstr Aesthet Surg. 2022;75(11):4328–33.
15. Kim TH, Kim YC, Jeong WS, Choi JW. Enhancing surgical approach: breakthrough markerless surface registration with augmented reality for zygomatic complex fracture surgeries. Ann Plast Surg. 2024;93(1):70–3.
16. Cercenelli L, Emiliani N, Gulotta C, Bevini M, Badiali G, Marcelli E. Augmented reality to assist in the diagnosis of temporomandibular joint alterations. Inf Syst Front. 2024:1572–9419.
17. Wilkat M, Liu S, Schwerter M, Schrader F, Saigo L, Karnatz N, Kübler NR, Rana M. A new approach to virtual occlusion in orthognathic surgery planning using mixed reality-a technical note and review of the literature. J Pers Med. 2023;13(12):1709.
18. Pulijala Y, Ma M, Pears M, Peebles D, Ayoub A. Effectiveness of immersive virtual reality in surgical training-a randomized control trial. J Oral Maxillofac Surg. 2018;76(5):1065–72.
19. Medellin Castillo HI, Zaragoza-Siqueiros J, Govea-Valladares EH, de la Garza-Camargo H, Lim T, Ritchie JM. Haptic-enabled virtual training in orthognathic surgery. Virtual Real. 2021;25(1):53–67.
20. Zinser MJ, Mischkowski RA, Dreiseidler T, Thamm OC, Rothamel D, Zöller JE. Computer-assisted orthognathic surgery: waferless maxillary positioning, versatility, and accuracy of an image-guided visualisation display. Br J Oral Maxillofac Surg. 2013;51(8):827–33.
21. Ahn J, Choi H, Hong J, Hong J. Tracking accuracy of a stereo camera-based augmented reality navigation system for orthognathic surgery. J Oral Maxillofac Surg. 2019;77(5):1070.e1–1070.e11.
22. Sugahara K, Koyachi M, Tachizawa K, Iwasaki A, Matsunaga S, Odaka K, Sugimoto M, Abe S, Nishii Y, Katakura A. Using mixed reality and CAD/CAM technology for treatment of maxillary nonunion after Le Fort I osteotomy: a case description. Quant Imaging Med Surg. 2023;13(2):1190–9.
23. Huang L, Liu Y, Zhu Z, Luo E. Application of mixed reality bone registration and positioning technology in orthognathic surgery. Int J Oral Maxillofac Surg. 2024;S0901-5027(24):00372.
24. Koyachi M, Sugahara K, Odaka K, Matsunaga S, Abe S, Sugimoto M, Katakura A. Accuracy of Le Fort I osteotomy with combined computer-aided design/computer-aided manufacturing technology and mixed reality. Int J Oral Maxillofac Surg. 2021;50(6):782–90.
25. Niloy I, Liu RH, Pham NM, Yim CMR. Novel use of virtual reality and augmented reality in temporomandibular total joint replacement using stock prosthesis. J Oral Maxillofac Surg. 2024;82(6):632–40.
26. Zhu M, Liu F, Zhou C, Lin L, Zhang Y, Chai G, Xie L, Qi F, Li Q. Does intraoperative navigation improve the accuracy of mandibular angle osteotomy: comparison between augmented reality navigation, individualised templates and free-hand techniques. J Plast Reconstr Aesthet Surg. 2018;71(8):1188–95.
27. Bussink T, Maal T, Meulstee J, Xi T. Augmented reality guided condylectomy. Br J Oral Maxillofac Surg. 2022;60(7):991–3.
28. Qu M, Hou Y, Xu Y, Shen C, Zhu M, Xie L, Wang H, Zhang Y, Chai G. Precise positioning of an intraoral distractor using augmented reality in patients with hemifacial microsomia. J Craniomaxillofac Surg. 2015;43(1):106–12.
29. He SX, Ma C, Yuan ZY, Xu TF, Xie QT, Wang YX, Huang XP. Feasibility of augmented reality using dental arch-based registration applied to navigation in mandibular distraction osteogenesis: a phantom experiment. BMC Oral Health. 2024;24(1):1321.
30. Coelho G, Rabelo N, Vieira E, Mendes K, Zagatto G, De Oliveira R, Raposo-Amaral C, Yoshida M, De Souza M, Fagundes C, Teixeira M, Figueiredo E. Augmented reality and physical hybrid model simulation for preoperative planning of metopic craniosynostosis surgery. Neurosurg Focus. 2020;48(3):E19.
31. Thabit A, Benmahdjoub M, van Veelen MC, Niessen WJ, Wolvius EB, van Walsum T. Augmented reality navigation for minimally

invasive craniosynostosis surgery: a phantom study. Int J Comput Assist Radiol Surg. 2022;17(8):1453–60.
32. Zhu M, Chai G, Lin L, Xin Y, Tan A, Bogari M, Zhang Y, Li Q. Effectiveness of a novel augmented reality-based navigation system in treatment of orbital hypertelorism. Ann Plast Surg. 2016;77(6):662–8.
33. Han W, Yang X, Wu S, Fan S, Chen X, Aung Z, Liu T, Zhang Y, Gu S, Chai G. A new method for cranial vault reconstruction: augmented reality in synostotic plagiocephaly surgery. J Craniomaxillofac Surg. 2019;47(8):1280–4.
34. Alshomer F, Alazzam A, AlTurki A, Almeshal O, Alhusainan H. Smartphone-assisted augmented reality in craniofacial surgery. Plast Reconstr Surg Glob Open. 2021;9(8):e3743.
35. García-Mato D, Moreta-Martínez R, García-Sevilla M, Ochandiano S, García-Leal R, Pérez-Mañanes R, Pascau J. Augmented reality visualization for craniosynostosis surgery. Comput Methods Biomech Biomed Eng Imaging Vis. 2020;9(4):392–9.
36. Chan JYK, Holsinger FC, Liu S, et al. Augmented reality for image guidance in transoral robotic surgery. J Robot Surg. 2020;14:579–83.
37. Aweeda M, Adegboye F, Yang SF, Topf MC. Enhancing surgical vision: augmented reality in otolaryngology-head and neck surgery. J Med Ext Real. 2024;1(1):124–36.
38. Taboni S, Ferrari M, Daly MJ, Chan HHL, Eu D, Gualtieri T, Jethwa AR, Sahovaler A, Sewell A, Hasan W, Berania I, Qiu J, de Almeida J, Nicolai P, Gilbert RW, Irish JC. Navigation-guided transnasal endoscopic delineation of the posterior margin for maxillary sinus cancers: a preclinical study. Front Oncol. 2021;11:747227.
39. Sahovaler A, Chan HHL, Gualtieri T, Daly M, Ferrari M, Vannelli C, Eu D, Manojlovic-Kolarski M, Orzell S, Taboni S, de Almeida JR, Goldstein DP, Deganello A, Nicolai P, Gilbert RW, Irish JC. Augmented reality and intraoperative navigation in sinonasal malignancies: a preclinical study. Front Oncol. 2021;11:723509.
40. Scherl C, Stratemeier J, Rotter N, Hesser J, Schönberg SO, Servais JJ, Männle D, Lammert A. Augmented reality with HoloLens® in parotid tumor surgery: a prospective feasibility study. ORL J Otorhinolaryngol Relat Spec. 2021;83(6):439–48.
41. Chand M, Keller DS, Devoto L, McGurk M. Furthering precision in sentinel node navigational surgery for oral cancer: a novel triple targeting system. J Fluoresc. 2018;28(2):483–6.
42. Prasad K, Miller A, Sharif K, Colazo JM, Ye W, Necker F, Baik F, Lewis JS Jr, Rosenthal E, Wu JY, Topf MC. Augmented-reality surgery to guide head and neck cancer re-resection: a feasibility and accuracy study. Ann Surg Oncol. 2023;30(8):4994–5000.
43. Necker FN, Chang M, Leuze C, Topf MC, Daniel BL, Baik FM. Virtual resection specimen interaction using augmented reality holograms to guide margin communication and flap sizing. Otolaryngol Head Neck Surg. 2023;169(4):1083–5.

Artificial Intelligence in Cranio-Maxillo-Facial Surgery

Stefanie van den Bosch, Niels van Nistelrooij, Michel Beyer, Wesley Do, Stefaan Bergé, and Shankeeth Vinayahalingam

1 Evolution of Medical Imaging

Medical imaging has transformed the landscape of healthcare, offering non-invasive methods to visualize the internal structures of the body. The evolution of this field can be traced back to the late nineteenth century, when Wilhelm Röntgen discovered X-rays in 1895, revolutionizing medical diagnostics [1]. This marked the birth of medical imaging, which rapidly developed over the years with the invention of new technologies like ultrasound, computed tomography (CT), and magnetic resonance imaging (MRI) [2]. These modalities have progressively advanced, giving healthcare providers more precise diagnostic tools.

The real boom in medical imaging occurred during the 1980s, driven by the development of digital imaging technologies and the widespread use of MRI and CT scans. In this period remarkable improvements in the speed, quality, and accessibility of imaging technologies developed. The transition from analog to digital systems allowed faster image processing, easier storage, and broader distribution of images among healthcare professionals, which significantly improved diagnostic [3]. Radiologists could now assess intricate details of tissues and organs, enabling earlier disease detection and more effective treatment planning.

Since the 1980s, medical imaging has continued to evolve rapidly. Innovations such as 3D and 4D imaging have further enhanced diagnostic capabilities, allowing for better visualization of complex anatomical structures [4]. Real-time imaging technologies now play a crucial role in guiding surgeries and other medical procedures, making healthcare safer and more efficient [4].

In the context of cranio-maxillofacial (CMF) imaging, the evolution of medical imaging has been particularly impactful. Early imaging techniques like X-rays provided basic views of the CMF region, but advancements in CT and MRI revolutionized the ability to visualize complex structures in this area. The development of cone beam computed tomography (CBCT) in the twenty-first century has further refined imaging in the CMF field, offering high-resolution, 3D images with lower radiation doses and lower costs compared to conventional CT. These advancements have improved preoperative (3D) planning, postoperative assessments, and overall outcomes in CMF surgery, contributing to more precise and less invasive interventions [5].

2 Evolution of Artificial Intelligence

Artificial intelligence (AI) has experienced a transformative journey, much like medical imaging. The term "artificial intelligence" was introduced by John McCarthy in 1956 during the Dartmouth Conference [6]. Early AI research focused on symbolic reasoning and problem-solving, but progress was limited due to technological constraints. However, in the

S. van den Bosch · W. Do · S. Bergé · S. Vinayahalingam (✉)
Radboud University Medical Center, Department of Oral and Maxillofacial Surgery, Nijmegen, The Netherland
e-mail: Stefanie.vandenBosch@radboudumc.nl; wesley.do@radboudumc.nl; Stefaan.Berge@radboudumc.nl; Shankeeth.Vinayahalingam@radboudumc.nl

N. van Nistelrooij
Radboud University Medical Center, Department of Oral and Maxillofacial Surgery, Nijmegen, The Netherland

Charité—Universitätsmedizin Berlin, Corporate Member of Freie Universität Berlin and HumboldtUniversität zu Berlin, Department of Oral and Maxillofacial Surgery, Berlin, Germany
e-mail: Niels.vanNistelrooij@radboudumc.nl

M. Beyer
University Hospital Basel, Department of Oral and Cranio-Maxillofacial Surgery, Basel, Switzerland

University of Basel, Department of Biomedical Engineering, Medical Additive Manufacturing Research Group (Swiss MAM), Allschwil, Switzerland
e-mail: michel.beyer@usb.ch

© The Author(s), under exclusive license to Springer Nature Switzerland AG 2025

A. Tel, M. Robiony (eds.), *Atlas of Virtual Surgical Planning and 3D Printing for Cranio-Maxillo-Facial Surgery*,
https://doi.org/10.1007/978-3-031-94495-6_8

1980s, a significant boom was seen in AI research, with the introduction of machine learning and neural networks, allowing computers to learn from data and improve over time [6].

One of the key milestones in AI development was the creation of deep learning algorithms in the early 2000s. These algorithms mimicked the structure of the human brain through artificial neural networks, enabling computers to recognize patterns in large datasets with unprecedented accuracy and marking a turning point in AI's evolution [7]. More recently, the development of large language models (LLMs), such as GPT-3 and GPT-4, has revolutionized AI and natural language processing (NLP). These models have demonstrated remarkable capabilities, including understanding and generating human-like text, translating languages, writing code, and passing professional exams [8]. In the following sections, the basics of deep learning and the higher-level concepts of AI will be explained.

3 Neural Networks

Neural networks (NNs) are computational models inspired by the structure and function of the human brain [7]. NNs consist of interconnected nodes called neurons organized in layers. Each neuron receives inputs, performs a mathematical operation on them, and produces an output [9].

In mathematical terms, let x_i denote the input vector to a neuron, w_i represent the weights associated with each input, and b represent the bias. The output of the neuron, denoted y, is calculated using an activation function, typically denoted as f, applied to the weighted sum of inputs plus the bias (Fig. 1).

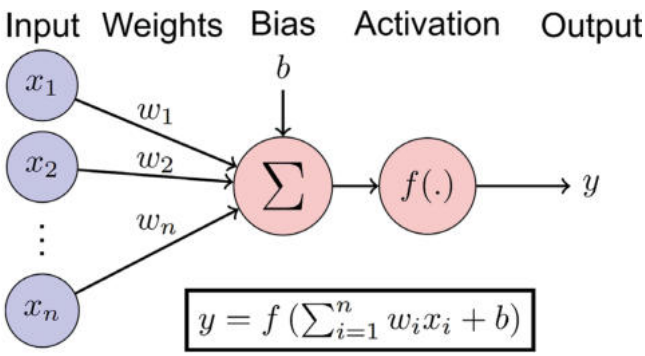


Fig. 1 Artificial neuron: to determine the output value of an artificial neuron, the neuron activation is computed as a weighted sum given the input values and connection weights. The artificial neuron applies a nonlinear activation function to determine the final output

Common activation functions include the sigmoid function, hyperbolic tangent (tanh) function, and rectified linear unit (ReLU) function [6]. These functions introduce nonlinearity into the neural network, allowing it to learn complex patterns in the data [9].

Neural networks learn by adjusting the weights and biases during a process called training. This is typically done using optimization algorithms like gradient descent, which minimizes a loss function that measures the difference between the predicted outputs and the true outputs [9, 10].

4 Convolutional Neural Network

Convolutional neural networks (CNNs) are deep learning models specifically designed for processing grid-like data, such as images. They consist of multiple layers, including convolutional layers, pooling layers, and fully connected layers [9]. The convolutional layer is the core building block of a CNN. It applies filters to input images, extracting features such as edges, textures, and shapes [11]. Mathematically, the convolution operation in a CNN layer is represented as:

$$Z^{[l]} = W^{[l]} * A^{[l-1]} + b^{[l]},$$

where $Z^{[l]}$ is the output of the lth layer, $W^{[l]}$ and $b^{[l]}$ are the weights and bias of the layer, $A^{[l-1]}$ is the activation of the previous layer, and $*$ denotes the convolution operation [7, 9].

Pooling layers are used to reduce the spatial dimensions of feature maps while retaining the most important information. They downsample feature maps by applying operations such as max-pooling or average-pooling [9] (Fig. 2).

Finally, fully connected layers integrate the extracted features and perform classification or regression tasks. Through the combination of these layers, CNNs can automatically learn hierarchical representations of input data, making them effective for tasks such as image classification, object detection, and image segmentation [9].

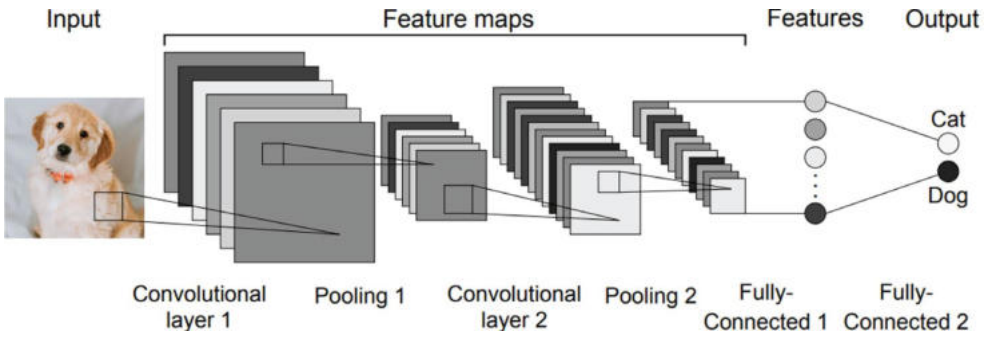


Fig. 2 Convolutional neural network: an input image is processed by computing a feature value for each image patch to create a feature map. These feature maps are processed by additional convolutional and pooling layers to learn increasingly more complex features while reducing the spatial resolution. The final feature maps are converted to a vector of features and two fully-connected layers determine the final output: classifying whether the input image contains a cat or dog

5 Classification

Classification is a machine learning task where the goal is to categorize data points into predefined classes or categories based on their features. Mathematically, this can be represented as follows:

Let X be the input features, Y be the output class labels, and $f(X)$ be the mapping function that predicts the class label for each input data point X. The classification task involves learning this mapping function $f(X)$ from labeled training data. Formally, the goal is to learn a classifier $h(X)$ that maps input features to class labels. In binary classification, where there are only two classes, the classifier can be represented as:

$$h(X) = \begin{cases} 1, \text{if } P(Y = 1|X) \geq 0.5 \\ 0, \text{if } P(Y = 1|X) < 0.5 \end{cases}$$

where $P(Y = 1|X)$ represents the probability that the output class Y is equal to 1 given the input features X [12].

For multi-class classification, the classifier $h(X)$ can be represented using the softmax function:

$$P(Y = k|X) = \frac{e^{f_k(X)}}{\sum_{j=1}^{K} e^{f_j(X)}}$$

where $f_k(X)$ represents the score or output of the classifier for class k, and K is the total number of classes [12]. The class with the highest probability is predicted as the output class label (Fig. 3).

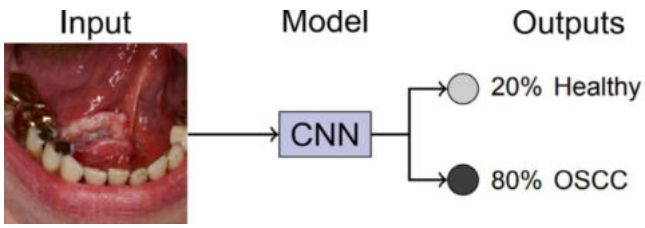


Fig. 3 Classification task. Classification categorizes an input image as one class from a pre-defined set of classes. The model's uncertainty about its prediction is provided as a score between 0 and 100

6 Object Detection

Object detection is a computer vision task that involves identifying and localizing objects within images or videos. Unlike image classification, which assigns a single label to an entire image, object detection aims to detect multiple objects of interest and precisely locate them within the image by drawing bounding boxes around them (Fig. 4).

Object detection typically involves several steps. Firstly, the image is processed to extract features using CNNs or other feature extraction methods [13]. Then, a detection algorithm identifies regions of interest (ROI) likely to contain objects using techniques like selective search or region proposal networks (RPNs) [13]. These regions are further refined and classified to determine the presence of objects and assign class labels using classification models. Finally, the detected objects' bounding boxes are adjusted to accurately localize them within the image [13].

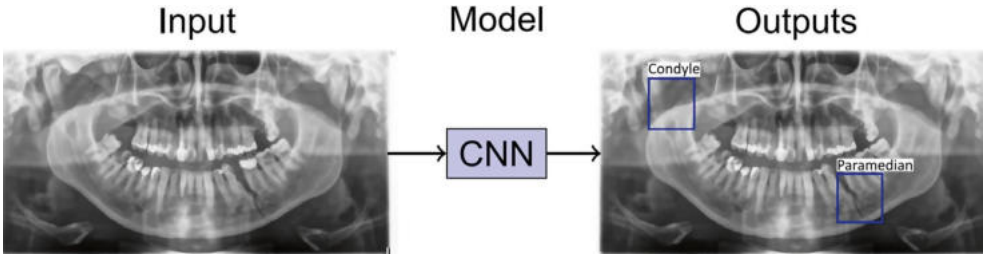


Fig. 4 Object detection task: object detection processes an input image to predict the location and category of objects of interest with bounding boxes and classes, respectively. This illustrative example shows fracture detection on an orthopantomogram (OPG) with the subregion of each fracture predicted as category

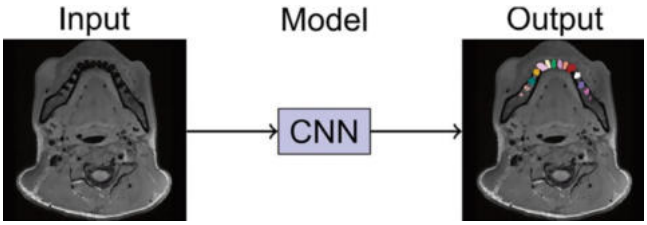


Fig. 5 Segmentation task: segmentation processes an input image to predict a class for each pixel of the image. The illustrative example shows a slice from an MRI scan with the model predicting pixel-level segmentations of the individual mandibular teeth

7 Segmentation

Segmentation is the process of partitioning an image into multiple segments or regions to simplify its representation and facilitate analysis. It aims to identify and delineate objects or regions of interest within an image (Fig. 5). In medical image analysis, segmentation is particularly valuable for identifying structures like organs, tissues, or abnormalities [14]. Common techniques include thresholding, region-based methods, and CNNs. These methods use mathematical functions to assign each pixel in the image to a specific class or label, enabling accurate and precise delineation of structures for further analysis or diagnosis.

8 The Role of AI in Craniomaxillofacial Surgery

The integration of advanced imaging technologies and artificial intelligence (AI) will revolutionize the field of oral and craniomaxillofacial (CMF) surgery, which involves highly complex procedures aimed at treating conditions such as congenital deformities, trauma, and head and neck oncology affecting the facial skeleton and soft tissues [15]. Precise preoperative planning and real-time intraoperative guidance are critical to the success of these surgeries, and the combination of medical imaging and AI plays a pivotal role in improving these processes [16].

Moreover, AI-driven simulations are increasingly used to model various surgical scenarios, allowing surgeons to anticipate potential challenges, such as the soft tissue simulation in orthognathic surgery. These simulations offer insights into how a patient's anatomy may respond to different interventions, enabling surgeries to be tailored to the patient's unique physiological features. This approach not only improves surgical outcomes but also reduces the likelihood of complications, leading to faster recovery times and overall better patient care [9].

Building on the profound impact that AI has had in craniomaxillofacial surgery, its applications extend across multiple subspecialties within the field. The integration of AI into surgical workflows is enhancing precision, improving outcomes, and transforming preoperative planning in several key areas:

- Dentoalveolar surgery
- Implantology
- Traumatology
- Oncology
- Craniofacial surgery
- Orthognathic and feminization surgery

8.1 Dentoalveolar Surgery

One of the intriguing challenges in dentistry and oral surgery is to determine whether a wisdom tooth should be removed or not. In cases of diseased wisdom teeth, where pain or pathology is obvious, there is a general consensus that surgical removal is indicated. However, most of the removed wisdom teeth are asymptomatic [17]. In the Netherlands, more than 200.000 wisdom teeth are removed annually [18], which is associated with a large societal and financial burden (over €40.000.000/per year). Nevertheless, it is a well-hidden public secret that millions of unnecessary wisdom teeth surger-

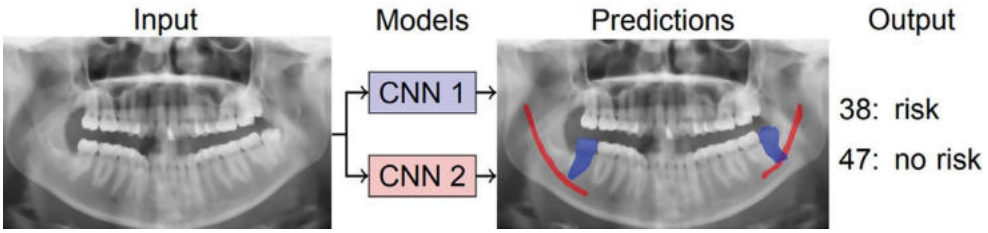


Fig. 6 Automated assessment of tooth extraction risk. One application of AI for dentoalveolar surgery is the automated assessment of risk to damage the inferior alveolar nerve during tooth extraction. Deep learning models are used to predict segmentations of teeth and the mandibular canal, which are used to determine the overlap between the teeth and the nerve

ies are performed worldwide per annum [17]. A 25% to 50% reduction of unnecessary wisdom teeth removals would result in a cost reduction of up to € 20.000.000 annually in the Netherlands only.

Nowadays, the decision flowchart for wisdom tooth removal is based on the experience of the surgeon as well as on considerations of a wide range of risk versus benefit factors, including the anatomy, general health, age, dental status (pericoronitis, unrestorable caries, odontogenic infection, periapical pathology, periodontitis, root resorption, food trapping, or other oral pathology (cysts, tumors, etc.), drug history, and other specific patient-, surgeon-, and financial-related factors [19].

The decision whether to remove a wisdom tooth or not can only be made by combining all this clinical data with necessary radiological information. Therefore, removal of wisdom teeth necessitates a high-quality pre-operative orthopantogram (OPG) radiograph. In certain circumstances, radiological abnormalities detected on an OPG may require further investigation with a cone beam computed tomography (CBCT). The proximity of the inferior alveolar nerve (IAN) to the roots of lower wisdom teeth is a risk factor for the occurrence of nerve damage and subsequent sensory disturbances of the lower lip and chin following the removal of wisdom teeth [18, 20]. CBCT supports the decision-making process by imaging this proximity so that the patient can be appropriately and accurately counseled regarding the potential risks and associated complications during the consent process for this procedure.

Taking the numerous interactions between all those clinical and radiological factors into account, it is very challenging to make the correct decision. It is hypothesized that an AI-based decision flowchart for wisdom teeth removal may have a huge potential to aid patients and surgeons to make the right choice, thereby inducing health improvement to patients, whose wisdom teeth will pose a significant health risk to them, while protecting those who will not benefit from surgery.

Recent studies have explored the application of AI in diagnosing, predicting, and managing third molar impactions [21]. AI's role in predicting third molar eruption has also been investigated, with mixed results. While AI models show promise in predicting molar uprighting, studies like Chopra et al.'s suggest challenges in accurately predicting eruption [22].

In assessing the relationship between third molars and the inferior alveolar nerve, AI models help identify positional relationships, aiding safer surgeries (Fig. 6). Furthermore, AI tools have been developed to predict removal difficulties and potential complications, enhancing preoperative preparation and decision-making, although more comprehensive databases are needed to improve accuracy and reliability.

8.2 Implantology

Dental implantology is a continuously growing working area for dental surgeons. Implants are an often used treatment modality for single tooth replacement, but also in traumatology and oncology, implants have an important role. Many dental surgeons are still working without implant guides from computer-assisted implant planning (CAI). This software enables the accurate planning of the implant structure, combining functional and esthetic planning of the suprastructure for the future prostheses. Also critical anatomical structures, like the inferior alveolar nerve and the maxillary sinus, are visualized. During surgery, the planned implant positions are accurately transferred to the surgical site using guided or navigated systems. However, despite its advanced capabilities, the diagnostic and planning phases in CAI are still more time-consuming and expensive than traditional workflows [23]. The integration of AI is set to revolutionize CAI, where speed and cost-efficiency will be greatly improved. AI has the potential to streamline these stages, thus reducing costs and improving efficiency, ultimately making CAI more accessible for widespread clinical use [24].

8.2.1 Treatment Planning: Toward Automation

In the current implant planning systems, the user has to assess the intended implant site. This is usually the technical physician. The implant type and system are given by the performing surgeon, which is a maxillofacial surgeon or a specialized dentist. The anatomical structures near the implant site are evaluated by the technician and risk for damage needs to be estimated. If the risk is considered to be low, the location, angulation, and depth are determined, while considering the function and esthetic of the coming suprastructure.

Recent studies have shown the potential of AI in analyzing CBCT scans for detailed implant planning. Bayrakdar et al. applied deep learning to dental implant planning with CBCT images but found limited success, suggesting more training is needed for accurate bone height and width measurements [25]. Moufti et al. compared AI-based segmentation with human evaluations for edentulous areas, showing that AI offers acceptable accuracy and significantly reduces time and cost in implant planning [26].

While AI's performance in measuring bone height and width for implant placement has been moderate, it has proven valuable in detecting anatomical landmarks. Studies by Kwak et al. and Oliveira-Santos et al. demonstrated AI's accuracy in identifying the mandibular canal and its variations, which are critical for implant planning [27, 28]. AI models have also shown consistency in segmenting the maxillary sinus, aiding 3D model creation for diagnosis and treatment planning [29].

AI-powered surgical navigation systems are being increasingly used to guide clinicians in implant placement. These systems provide real-time guidance based on presurgical planning. These systems visualize the position of the implant within the anatomy of the patient using augmented reality (AR). By doing so, surgeons will be able to place the implants with higher precision, reducing the risk of errors such as perforation of vital structures or misalignment of the implant. A case report by Mangano et al. showcased how this combination enhances surgical efficiency and accuracy [30].

Furthermore, AI can enhance robotic systems for implant placement with the ability to make automated adjustments intraoperatively. This automation improves accuracy and consistency, therefore improving outcomes with less manual intervention. For instance, AI-based robotic systems can adapt in real time to optimize implant placement based on the patient's unique anatomy.

8.2.2 Predicting Treatment Outcomes

Dental implants are the preferred treatment for tooth replacement, but complications and implant failures are rising, leading to increased costs and additional procedures for patients and clinicians. Predicting implant loss or complications is challenging due to various risk factors, including patient characteristics, bone quality, implant type, and surgical plan. Currently, implant failure predictions rely on clinicians' expertise, but AI shows promise in improving treatment outcome predictions [24]. Machine learning algorithms can analyze patient data, such as medical history, bone condition, and previous dental procedures, to predict outcomes and recommend personalized implant placement strategies. For example, AI can help in identifying potential complications, such as insufficient bone volume or proximity to vital structures like the inferior alveolar nerve, thus allowing clinicians to adjust their approach in advance.

Research in this field is limited, with few studies and no comprehensive systematic reviews. Lyakhov et al. developed a neural network model that predicted single implant survival with 94.48% accuracy based on patient case histories but concluded that AI should assist, not replace, clinical decision-making [31]. Oh et al. demonstrated AI's potential in predicting osseointegration using radiographs, and Cha et al. applied AI to measure peri-implant bone loss, finding no significant difference between AI and clinician measurements [32, 33].

Huang et al. introduced AI models to predict implant loss over 5 years, suggesting AI could help identify high-risk patients and adjust treatment plans [34].

8.2.3 Post-surgical Monitoring and Predictive Analytics

AI is also of great value in the post-surgical phase by monitoring the healing process and detecting potential complications. AI systems can analyze postoperative images, such as dental single-tooth x-rays, OPGs or CBCTs, to identify signs of infection, implant failure, or bone loss around the implant. The ability of machine learning models to predict the complication rate allows for early intervention if necessary. A large dataset is, however, needed to build such a prediction model.

Moreover, AI can assist in predicting long-term outcomes by analyzing the patient's response to the implant over time. These predictive models can help clinicians adjust treatment plans, whether through early interventions, additional procedures, or customized follow-up schedules, to ensure the long-term success of implants.

8.2.4 Implant Type Detection

With the increasing number of dental implant brands and prosthetic components on the market, identifying the correct implant system can be challenging, particularly when complications arise or when treatment was performed at another clinic. AI can automate the identification and classification of different dental implant systems (DIS) based on radiographic images [35]. This reduces time and complexity involved in manual identification, providing clinicians with a more efficient way to determine the correct implant system.

Recent literature supports AI's potential in dental implant system (DIS) detection, with studies showing high accuracy (93.8–98%) in AI models using 2D radiographs, like periapical or panoramic images. However, CBCT has not yet been widely used for AI model training due to lower resolution concerns. Larger and more diverse datasets are needed to improve AI accuracy and global applicability [35].

8.2.5 Challenges and Future Directions

Despite the numerous advantages, there are a variety of challenges that exist in integrating AI into implantology. The first limitation involves large and high-quality data for the training of AI algorithms. Ensuring that AI systems are accurate across a diverse range of patients and anatomical variations is crucial. In addition, clinicians must have confidence in the recommendations made by AI, which requires transparent and explainable AI models that provide clear justifications for their decisions.

Future development of AI in implantology will be the further integration of CBCT with MRI and other diagnostic tools to create of more comprehensive treatment plans. AI-driven technologies may evolve further to take into consideration patient-specific factors in real-time, that might alter the proposed treatment during surgery for an even more optimized outcome. In conclusion, AI will revolutionize implantology by improving the accuracy, efficiency, and predictability of dental implant procedures. Further evolution of AI holds great promise for better patient outcomes, smoother clinical workflows, and more personalized care in dental implantology.

8.3 Traumatology

8.3.1 Fracture Detection

AI is increasingly being integrated into craniofacial traumatology, offering significant advancements in the diagnosis, treatment planning, and management of facial injuries. One of the primary applications of AI in this field is in the detection and classification of facial fractures, which are often complex and challenging to diagnose manually due to their intricate patterns and the overlapping structures in craniofacial imaging.

AI algorithms, particularly deep learning models, have shown great promise in automating the detection of various craniofacial fractures, such as those in the zygoma, mandible, and nasal bones. Convolutional neural networks (CNNs) have been employed to analyze CT and CBCT scans, significantly reducing diagnostic time while maintaining high accuracy levels. These AI models can identify fractures that may be missed by human observers, especially in cases involving subtle or complex fracture patterns, such as those with both horizontal and vertical components. This automation not only improves diagnostic efficiency but also allows clinicians to focus on more complex aspects of patient care, such as treatment planning and surgical intervention (Fig. 7).

For example, Tong et al. developed a CNN algorithm that automatically detects zygomatic fractures using CT imaging, demonstrating comparable performance to manual diagnosis and highlighting its potential for clinical use [36]. Similarly, other studies have implemented CNN-based models to detect mandibular fractures in panoramic radiographs, achieving success rates that surpass expert-level human performance, with AUC values exceeding 90% [37, 38]. AI has also proven to be a reliable tool in diagnosing orbital blow-out, mandibular, and nasal bone fractures from (CB)CT scans, enhancing both accuracy and efficiency in facial trauma diagnosis [39–41]. These advancements hold promise for improving patient care, expediting clinical workflows, and contributing to resident training.

8.3.2 Prognosis Prediction

In addition to fracture detection, AI has the potential to assist in predicting the severity and prognosis of craniofacial trauma. By analyzing large datasets of patient images, clinical information, and outcomes, AI models can help predict the likelihood of complications, recovery times, and the best course of treatment. These predictive capabilities could be especially valuable in determining whether non-surgical management is appropriate or if surgical intervention is necessary.

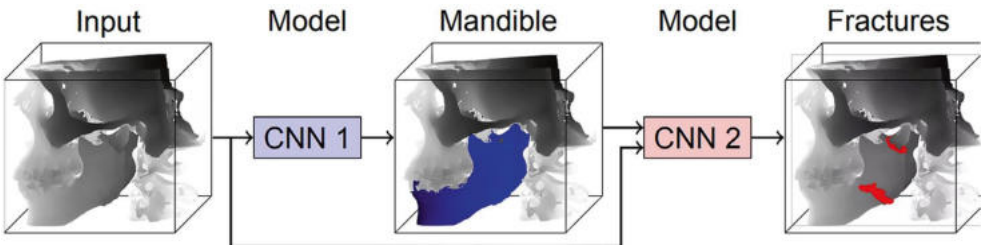


Fig. 7 Automated detection of mandibular fractures. AI has been applied to automatically detect fractures of the mandible in CBCT scans. The method uses an intermediate segmentation of the mandible to improve the robustness of fracture segmentation

8.3.3 Image Quality

AI is also helping to optimize image quality in craniofacial imaging. Advanced deep learning algorithms, such as those used in low-dose CT imaging, improve the quality of scans while reducing radiation exposure, which is a significant benefit for patients, especially in pediatric and trauma cases. By enhancing image resolution and clarity, AI aids in more accurate detection and better visualization of fractures and soft tissue injuries.

Rozema et al. demonstrated the effectiveness of advanced modeled iterative reconstruction (ADMIRE) and the PixelShine DL algorithms in low-dose CT protocols for midfacial trauma. These algorithms significantly improved image quality while reducing radiation exposure by 61.7% [42].

8.3.4 Further Prospects

Despite these advancements, challenges remain in the implementation of AI in craniofacial traumatology. One major hurdle is the variability in image quality, especially in emergency situations where imaging may be suboptimal due to the patient's condition or limited access to advanced imaging technology. Additionally, AI models must be able to handle the complexity of the craniofacial anatomy, where fractures can sometimes be hidden by overlapping structures or may be missed due to the presence of artifacts.

Looking ahead, future directions in AI for craniofacial traumatology include the development of multimodal AI systems that can integrate different imaging modalities (such as CT, MRI, and X-rays) to provide a more comprehensive view of the injury. These systems could offer enhanced accuracy in fracture detection, soft tissue injury assessment, and treatment planning. Furthermore, AI could be used to assist in personalized treatment strategies by combining imaging data with clinical factors, allowing for more tailored care and better outcomes.

8.4 Oncology

8.4.1 Histology Whole-Slide Imaging

AI is transforming the field of histology, mainly in whole slide imaging (WSI). This process involves digitizing histological slides to generate high-resolution images that can be analyzed by pathologists and researchers without losing the rich morphology of the slides. The shift from traditional microscopy to digital platforms enhances the capacity to store, share, and analyze pathological data without the need for a microscope, making it a valuable resource for both research and clinical diagnostics [43].

Deep learning models are increasingly being applied to WSI to assist in the interpretation of histological images. These algorithms are shown to be successful in tasks like the identification and classification of various tissue types and pathological features, significantly speeding up the diagnostic process. The models can detect malignant cells, quantify tumor characteristics, and even predict patient outcomes based on histological patterns. This automation not only improves accuracy but also reduces the workload on pathologists, allowing them to focus their labor on more complex cases that require expert analysis [9].

Furthermore, the integration of AI into WSI facilitates standardization and objective assessments. Traditional histological evaluations are prone to subjective interpretations, whereas AI models trained on large datasets give more consistent results, making the results more reproducible. Also, the capability to analyze large volumes of imaging data can reveal patterns and insights that might be missed in manual reviews, potentially leading to new understandings of disease mechanisms and the development of personalized treatment strategies [44].

Despite these advantages, the implementation of AI in digital histology does come with challenges. The necessity for a high amount of high-quality annotated datasets to train AI models is a hurdle to overcome, especially the need for computing power to train and employ such a model [44]. It is also important to ensure that AI serves to complement the expertise of pathologists to maintain diagnostic quality, rather than replacing the latter. As this technology continues to evolve, collaboration between AI developers and histopathologists will be essential in harnessing the potential of AI in WSI, ultimately improving patient care and advancing the field of pathology [44].

8.4.2 Radiological Imaging

Radiological imaging plays a crucial role in the diagnosis, treatment planning, and monitoring of head and neck oncology. Techniques such as ultrasound, CT, MRI, and positron emission tomography (PET) provide detailed insights into the anatomy and pathology of tumors in this complex region. These imaging modalities help clinicians identify the extent of disease, evaluate lymph node involvement, and assess potential treatment responses, ultimately guiding therapeutic decisions.

The integration of AI into radiological imaging will be transforming the approach of head and neck oncology. Deep learning AI algorithms can analyze large volumes of imaging data with remarkable speed and accuracy. These technologies are shown to assist radiologists in detecting tumors, characterizing lesions, and predicting treatment outcomes by recognizing patterns that may be hard to notice for human observers. For instance, AI can enhance the detection of early-stage cancers, allowing for timely intervention and improved patient prognosis [45].

Also, AI-driven tools will facilitate the standardization of imaging interpretations, reducing variability among radiolo-

gists. This is particularly important in head and neck oncology, where the complex anatomy and overlapping structures can complicate assessments. By providing consistent and objective analyses, AI algorithms help to ensure that patients receive appropriate and effective treatment plans based on imaging data. Additionally, machine learning models can be trained to integrate clinical information with imaging findings, offering more comprehensive insights into patient management.

8.4.3 Clinical Imaging

In head and neck oncology, physical examination plays the most important role, where radiological imaging only adds to the clinical view. The golden standard for diagnosing head and neck cancers remains clinical examination and biopsy. When diagnosed in early stages, less invasive treatment is necessary for these tumors. Here, the diagnostic challenge arises since not every mucosal lesion is (potentially) malignant and not every mucosal lesion requires biopsy. It is also shown before that primary healthcare workers have good, but not perfect detection rates for oral potentially malignant disorder (OPMD) and oral cancer, with sensitivities ranging from 0.59 to 0.99 and specificities ranging from 0.64 to 0.99 [46]. It has been reported that an AI model using a visual transformer gives a sensitivity and specificity of 0.99 in detecting head and neck cancers in digital clinical photographs (Fig. 8). When used in conjunction with the visual inspection of a primary healthcare worker, a near-perfect accuracy is to be expected. This will result in less doctors delaying and diagnosing in early stages, meaning less invasive treatment and higher survival rates.

Another clinical imaging modality where AI models are applied is in nasal endoscopic images. A real-time augmentation during the endoscopy can be applied, for example [47]. The accuracy of the AI model is comparable to trained otolaryngologists for certain diagnosis, such as sinonasal inverted papilloma [48]. Research on AI models predicting the HPV state and assessing prognosis of tumors is to be expected sooner rather than later.

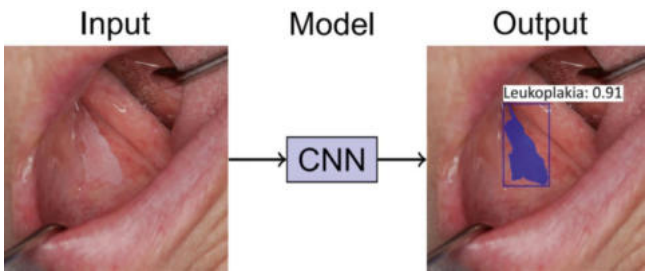


Fig. 8 Automated detection and segmentation of potentially malignant oral disorders. The model implemented the instance segmentation task, which includes bounding box detection, classification, and segmentation. The score above the bounding box represents the confidence of the model

Despite these advancements, challenges remain in the implementation of AI in clinical practice. The quality and quantity of data needed to train AI models can be limiting, especially for rare cancers. Furthermore, the interpretability of AI outputs is crucial; clinicians must understand the rationale behind AI recommendations to make accurate informed decisions.

8.5 Craniofacial Surgery

Craniofacial surgery, which encompasses the diagnosis, treatment, and surgical management of congenital and acquired deformities of the skull, face, and jaw, can benefit greatly from AI-driven advancements. From preoperative planning to post-surgical care, AI promises to enhance precision, improve patient outcomes, and streamline complex workflows in craniofacial procedures.

8.5.1 Detection of Craniofacial Abnormalities

AI algorithms have demonstrated the ability to detect subtle craniofacial patterns that may elude even experienced clinicians [49]. Han et al. developed a deep learning model using U-Net to segment and evaluate the masseter muscle in patients with hemifacial microsomia, achieving high efficiency compared to manual segmentation by radiologists [50]. Geisler et al. achieved a 90.6% accuracy rate using a pre-trained AI model to screen, detect, and classify non-syndromic craniosynostosis from 2D clinical photographs [51]. Similarly, Mizutani et al. developed an AI system using skull X-rays, which reached 100% accuracy, sensitivity, and specificity for non-syndromic craniosynostosis compared to CT scans [52] (Fig. 9).

Further advancements include Blum et al.'s machine learning algorithm for rating the severity of metopic synostosis in CT images [53]. Xu et al. developed a 3D point cloud graph CNN for predicting and locating landmarks in patients with cleft lip and palate, achieving results comparable to expert annotations [54]. Arjmand et al. utilized a modified 3D U-Net to predict facial shape from CT images, improving understanding of the link between craniofacial deformities and bone structure [55].

However, limitations remain. AI models have struggled to classify rare craniofacial conditions, such as lambdoid cra-

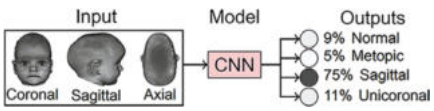


Fig. 9 Automated classification of craniosynostosis. A three-dimensional stereophotogrammetry scan of a baby's head is used to automatically classify the type of skull deformity

niosynostosis, and to distinguish between different causes of craniofacial abnormalities, including trauma, genetics, and muscle-related deformities [49].

8.5.2 Preoperative Planning

Preoperative planning is critical in open craniofacial surgery, where even small errors can lead to significant functional and aesthetic challenges. An AI system can help surgeons by analyzing patient data, including 3D photographic imaging and CT scans, to create highly detailed, personalized surgical plans. AI can automatically segment different structures, such as bones, soft tissues, and blood vessels, from these images, helping surgeons visualize critical anatomical features in greater detail.

AI-powered virtual surgery platforms allow surgeons to "practice" complex procedures virtually. These systems can simulate tissue movement, bone cutting, and the placement of implants, ensuring that the surgical team is well-prepared for the actual operation. Surgeons can explore these 3D models interactively, adjusting angles, observing potential risks, and determining the best surgical approaches before performing any incisions.

8.5.3 Further Considerations

In the future, a role is reserved for AI to assist in forecasting long-term outcomes, such as the potential for facial growth in pediatric patients or the durability of skull implants in adult patients. By predicting how a patient's face will evolve over time, AI helps in planning not only the immediate surgical intervention but also future corrective surgeries if necessary. Some research on cephalometric measurements in healthy adolescent patients are conducted, showing promising results.

The integration of AI into clinical practice requires careful training for healthcare professionals. Surgeons and medical staff must be adequately prepared to work with AI tools, interpreting the insights provided by AI while maintaining clinical judgment. AI should be seen as a tool that enhances human expertise, not as a replacement for it.

8.6 Orthognathic and Feminization Surgery

Orthognathic surgery, which corrects jaw and facial bone irregularities, is often required to address functional issues such as bite problems, malocclusion, and facial asymmetry. Virtual surgical planning (VSP), particularly three-dimensional (3D) preoperative treatment planning and surgical outcome simulation, has become the gold standard in orthognathic surgery. A key step in successful VSP is the accurate segmentation of skeletal structures from CT or CBCT scans. However, manual segmentation is time-consuming, often requiring several hours of effort. Once 3D models are generated, cephalometric landmarks must also be identified manually, further adding to the time burden. AI is revolutionizing orthognathic surgery by improving precision, streamlining planning processes, and enhancing surgical outcomes. With the integration of AI technologies, the field is experiencing significant advancements that improve both the efficiency and effectiveness of these complex procedures.

8.6.1 Segmentation

Recent advances in AI have significantly improved the segmentation of skeletal structures and the identification of cephalometric landmarks in CT and CBCT images. Studies over the past 3 years have increasingly focused on training CNNs for these tasks, with accuracy comparable to that of trained clinicians [49]. AI-driven tools provide a substantial time-saving advantage, with some CNN-based processes completing tasks up to 100 times faster than manual approaches. Even when manual touch-ups are necessary, AI significantly reduces overall processing time [56].

For example, Menezes et al. demonstrated that AI models could accurately detect cephalometric landmarks under varying conditions of brightness and contrast, illustrating continuous improvements in AI-based image analysis [57]. Choi et al. developed an AI model with a 96% success rate in determining whether surgery was required and a 91% accuracy in choosing the appropriate osteotomy or deciding on dental extractions [58]. AI tools have also been developed to predict postoperative soft tissue profiles and the effects of surgery on facial appearance relative to age (Fig. 10). In one study by Ter Horst et al., a deep learning algorithm was trained using 3D and CBCT images to simulate soft tissue outcomes, which were compared to actual postoperative photographs, showing a clinically acceptable margin of error (mean absolute error of 1.0 ± 0.6 mm) [59].

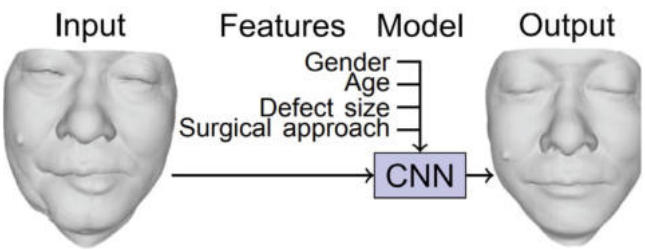


Fig. 10 Prediction of soft-tissue changes following orthognathic surgery. Three-dimensional stereophotogrammetry scans are used to predict the post-operative facial profile following orthognathic surgery to correct a mandibular deformity. Clinical features such as gender, age, defect size, and the surgical approach are provided as additional features to the model to evaluate the soft-tissue changes for different surgical plans

8.6.2 Predictive Analytics and Outcome Modeling

The role for AI in orthognathic surgery extends beyond preoperative planning into predicting postoperative results. Machine learning models can analyze vast datasets of patient outcomes to identify patterns and predict how specific patients will respond to surgery. By considering factors like age, bone density, and previous treatments, AI can estimate the likelihood of complications or predict recovery times, providing surgeons with invaluable information for personalized treatment plans.

In addition, AI can help optimize the positioning of the jaws, facial bones, and implants during surgery. Algorithms can simulate different surgical approaches and predict how each one will affect the patient's bite, facial symmetry, and long-term outcomes, ensuring that the most appropriate plan is chosen before the procedure begins.

8.6.3 Surgical Assistance and Navigation

During surgery, AI-based technologies, such as robotic systems and augmented reality (AR), provide real-time guidance, improving surgical precision and reducing the risk of errors. AI algorithms integrated into robotic surgical systems can assist with tasks like bone cutting, aligning the jaw, and securing implants with exceptional accuracy. These systems can also adapt to changes during the surgery, ensuring the procedure is tailored to the patient's real-time anatomy.

Additionally, augmented reality (AR) tools can overlay digital images onto the patient's anatomy during surgery, providing the surgeon with visual cues and guiding them in making the right incisions and adjustments. This technology can reduce surgical time and improve the accuracy of the procedure, ultimately leading to better functional and aesthetic outcomes for patients.

AI's potential extends beyond surgical planning. AI accurately predicted perioperative blood loss in 950 patients undergoing orthognathic surgery, showing a strong correlation between predicted and actual blood loss [60].

8.6.4 Postoperative Monitoring and Recovery

The role for AI in orthognathic surgery does not end with the procedure itself. Postoperative monitoring is crucial for detecting complications, such as infection, malunion of bones, or issues with the positioning of osteosynthesis material. AI-driven systems can automatically analyze a postoperative CBCT scan to detect early signs of future problems that may require intervention.

Machine learning models can also predict recovery trajectories, enabling clinicians to personalize follow-up care plans. By analyzing historical data, AI can help estimate the patient's healing process and suggest appropriate adjustments to the treatment plan to minimize the risk of complications and enhance recovery.

8.6.5 Patient-Specific Customization

One of the most significant benefits of AI in orthognathic surgery is its ability to facilitate patient-specific customization. AI can help design custom osteosynthesis implants or surgical guides based on the patient's unique anatomy, reducing the risk of plate misplacement and improving the overall fit and function of the surgical outcome. 3D printing, combined with AI, allows for the creation of highly personalized surgical tools and implants that match the patient's bone structure precisely, optimizing both the functional and aesthetic aspects of the surgery.

8.6.6 Challenges and Future Directions

While AI is proving to be a powerful tool in orthognathic surgery, there are still challenges to overcome. One major obstacle is the need for large, high-quality datasets to train AI algorithms effectively. Since each patient's anatomy is unique, AI models must be trained on diverse and comprehensive datasets to ensure accurate predictions and treatment recommendations. Additionally, there is a need for AI systems that can explain their decision-making processes in a way that is understandable to surgeons, ensuring transparency and trust in the technology.

Looking ahead, the future of AI in orthognathic surgery is exciting. As AI models become more sophisticated, they will likely play an even greater role in refining surgical techniques, improving patient outcomes, and reducing recovery times. The integration of AI with other technologies, such as robotic surgery and virtual reality, could further enhance surgical precision and the customization of treatments for individual patients.

In conclusion, AI is transforming orthognathic surgery by improving diagnostic accuracy, refining treatment planning, and enhancing surgical precision. As technology continues to evolve, AI will likely play an even more central role in personalizing care, optimizing outcomes, and advancing the field of craniofacial surgery.

References

1. Nusslin F. Wilhelm Conrad Rontgen: the scientist and his discovery. Phys Med. 2020;79:65–8.
2. Tempany CM, McNeil BJ. Advances in biomedical imaging. JAMA. 2001;285(5):562–7.
3. Bercovich E, Javitt MC. Medical imaging: from roentgen to the digital revolution, and beyond. Rambam Maimonides Med J. 2018;9(4):e0034.
4. Li G, et al. Advances in 4D medical imaging and 4D radiation therapy. Technol Cancer Res Treat. 2008;7(1):67–81.
5. Portnoy Y, et al. Three-dimensional technologies in presurgical planning of bone surgeries: current evidence and future perspectives. Int J Surg. 2023;109(1):3–10.
6. Goodfellow I. Deep learning. MIT press; 2016.
7. LeCun Y, Bengio Y, Hinton G. Deep learning. Nature. 2015;521(7553):436–44.

8. Raiaan MAK, et al. A review on large language models: architectures, applications, taxonomies, open issues and challenges. IEEE Access. 2024; https://doi.org/10.1109/ACCESS.2024.3365742.
9. Litjens G, et al. A survey on deep learning in medical image analysis. Med Image Anal. 2017;42:60–88.
10. Rumelhart DE, Hinton GE, Williams RJ. Learning representations by back-propagating errors. Nature. 1986;323(6088):533–6.
11. Krizhevsky A, Sutskever I, Hinton GE. Imagenet classification with deep convolutional neural networks. Adv Neural Inf Proces Syst. 2012;25. https://doi.org/10.1145/3065386.
12. Bishop CM, Nasrabadi NM. Pattern recognition and machine learning, vol. 4. New York: Springer; 2006.
13. Ren SQ, et al. Faster R-CNN: towards real-time object detection with region proposal networks. IEEE Trans Pattern Anal Mach Intell. 2017;39(6):1137–49.
14. Ronneberger O, Fischer P, Brox T. U-Net: convolutional networks for biomedical image segmentation. In: Medical image computing and computer-assisted intervention, Pt Iii, vol. 9351; 2015. p. 234–41.
15. Miragall MF, et al. Face the future-artificial intelligence in oral and maxillofacial surgery. J Clin Med. 2023;12(21):6843.
16. Dell'Oglio P, et al. Precision surgery: the role of intra-operative real-time image guidance - outcomes from a multidisciplinary European consensus conference. Am J Nucl Med Mol Imaging. 2022;12(2):74–80.
17. Friedman JW. The prophylactic extraction of third molars: a public health hazard. Am J Public Health. 2007;97(9):1554–9.
18. Ghaeminia H, et al. Clinical relevance of cone beam computed. tomography in mandibular third molar removal: a multicentre, randomised, controlled trial. J Craniofac Surg. 2015;43(10):2158–67.
19. Ghaeminia H, et al. Surgical removal versus retention for the management of asymptomatic disease-free impacted wisdom teeth. Cochrane Database Syst Rev. 2020;5:CD003879.
20. Ghaeminia H, et al. The use of cone beam CT for the removal of wisdom teeth changes the surgical approach compared with panoramic radiography: a pilot study. Int J Oral Maxillofac Surg. 2011;40(8):834–9.
21. Assiri HA, et al. Artificial intelligence application in a case of mandibular third molar impaction: a systematic review of the literature. J Clin Med. 2024;13(15):4431.
22. Chopra S, et al. A retrospective longitudinal assessment of artificial intelligence-assisted radiographic prediction of lower third molar eruption. Sci Rep. 2024;14(1):994.
23. Colombo M, et al. Clinical applications and effectiveness of guided implant surgery: a critical review based on randomized controlled trials. BMC Oral Health. 2017;17(1):150.
24. Altalhi AM, et al. The impact of artificial intelligence on dental implantology: a narrative review. Cureus. 2023;15(10):e47941.
25. Kurt Bayrakdar S, et al. A deep learning approach for dental implant planning in cone-beam computed tomography images. BMC Med Imaging. 2021;21(1):86.
26. Moufti MA, et al. Developing an artificial intelligence solution to autosegment the edentulous mandibular bone for implant planning. Eur J Dent. 2023;17(4):1330–7.
27. Kwak GH, et al. Automatic mandibular canal detection using a deep convolutional neural network. Sci Rep. 2020;10(1):5711.
28. Oliveira-Santos N, et al. Automated segmentation of the mandibular canal and its anterior loop by deep learning. Sci Rep. 2023;13(1):10819.
29. Fontenele RC, et al. Convolutional neural network-based automated maxillary alveolar bone segmentation on cone-beam computed tomography images. Clin Oral Implants Res. 2023;34(6):565–74.
30. Mangano FG, et al. Artificial intelligence and augmented reality for guided implant surgery planning: a proof of concept. J Dent. 2023;133:104485.
31. Lyakhov PA, et al. Neural network system for analyzing statistical factors of patients for predicting the survival of dental implants. Front Neuroinform. 2022;16:1067040.
32. Oh S, et al. Deep learning-based prediction of osseointegration for dental implant using plain radiography. BMC Oral Health. 2023;23(1):208.
33. Cha JY, et al. Peri-implant bone loss measurement using a region-based convolutional neural network on dental periapical radiographs. J Clin Med. 2021;10(5):1009.
34. Huang N, et al. Predicting the risk of dental implant loss using deep learning. J Clin Periodontol. 2022;49(9):872–83.
35. Chaurasia A, et al. Deep-learning performance in identifying and classifying dental implant systems from dental imaging: a systematic review and meta-analysis. J Periodontal Implant Sci. 2024;54(1):3–12.
36. Tong Y, et al. Is convolutional neural network accurate for automatic detection of zygomatic fractures on computed tomography? J Oral Maxillofac Surg. 2023;81(8):1011–20.
37. Vinayahalingam S, et al. Detection of mandibular fractures on panoramic radiographs using deep learning. Sci Rep. 2022;12(1):19596.
38. Warin K, et al. Assessment of deep convolutional neural network models for mandibular fracture detection in panoramic radiographs. Int J Oral Maxillofac Surg. 2022;51(11):1488–94.
39. van Nistelrooij N, et al. Detecting mandible fractures in CBCT scans using a 3-Stage neural network. J Dent Res. 2024;103(13):1384–91.
40. Li L, et al. Deep convolutional neural networks for automatic detection of orbital blowout fractures. J Craniofac Surg. 2020;31(2):400–3.
41. Jeong Y, et al. Development of AI-Based diagnostic algorithm for nasal bone fracture using deep learning. J Craniofac Surg. 2024;35(1):29–32.
42. Rozema R, et al. Iterative reconstruction and deep learning algorithms for enabling low-dose computed tomography in midfacial trauma. Oral Surg Oral Med Oral Pathol Oral Radiol. 2021;132(2):247–54.
43. Kiran N, et al. Digital pathology: transforming diagnosis in the digital age. Cureus. 2023;15(9):e44620.
44. Basak K, Ozyoruk KB, Demir D. Whole slide images in artificial intelligence applications in digital pathology: challenges and pitfalls. Turk Patoloji Derg. 2023;39(2):101–8.
45. Mahmood H, et al. Artificial Intelligence-based methods in head and neck cancer diagnosis: an overview. Br J Cancer. 2021;124(12):1934–40.
46. Warnakulasuriya S, et al. Oral potentially malignant disorders: a consensus report from an international seminar on nomenclature and classification, convened by the WHO Collaborating Centre for Oral Cancer. Oral Dis. 2021;27(8):1862–80.
47. Bidwell J, et al. Real-time augmentation of diagnostic nasal endoscopy video using AI-enabled edge computing. Int Forum Allergy Rhinol. 2024;15(2):191–4.
48. Yui R, et al. Preoperative prediction of sinonasal papilloma by artificial intelligence using nasal video endoscopy: a retrospective study. Sci Rep. 2023;13(1):12439.
49. Sillmann YM, et al. Empowering surgeons: will artificial intelligence change oral and maxillofacial surgery? Int J Oral Maxillofac Surg. 2025;54(2):179–90.
50. Han W, et al. Radiomics and artificial intelligence study of masseter muscle segmentation in patients with hemifacial microsomia. J Craniofac Surg. 2023;34(2):809–12.
51. Geisler EL, et al. A role for artificial intelligence in the classification of craniofacial anomalies. J Craniofac Surg. 2021;32(3):967–9.
52. Mizutani K, et al. Application of deep learning techniques for automated diagnosis of non-syndromic craniosynostosis using skull. J Craniofac Surg. 2022;33(6):1843–6.

53. Blum JD, et al. Machine learning in metopic craniosynostosis: does phenotypic severity predict long-term esthetic outcome? J Craniofac Surg. 2023;34(1):58–64.
54. Xu M, et al. Using a new deep learning method for 3D cephalometry in patients with cleft lip and palate. J Craniofac Surg. 2023;34(5):1485–8.
55. Arjmand H, et al. Artificial intelligence–based modeling can predict face shape based on underlying craniomaxillofacial bone. J Craniofac Surg. 2023;34(7):1915–21.
56. Schwendicke F, Samek W, Krois J. Artificial intelligence in dentistry: chances and challenges. J Dent Res. 2020;99(7):769–74.
57. Menezes LDS, et al. Assessment of landmark detection in cephalometric radiographs with different conditions of brightness and contrast using the an artificial intelligence software. Dentomaxillofac Radiol. 2023;52(8):20230065.
58. Choi H-I, et al. Artificial intelligent model with neural network machine learning for the diagnosis of orthognathic surgery. J Craniofac Surg. 2019;30(7):1986–9.
59. Ter Horst R, et al. Three-dimensional virtual planning in mandibular advancement surgery: soft tissue prediction based on deep learning. J Craniomaxillofac Surg. 2021;49(9):775–82.
60. Stehrer R, et al. Machine learning based prediction of perioperative blood loss in orthognathic surgery. J Craniomaxillofac Surg. 2019;47(11):1676–81.

Applications of VSP for Customized Subperiosteal Implants for the Rehabilitation of the Atrophic Jaws

Luigi Angelo Vaira and Giacomo De Riu

1 History

The concept of subperiosteal implants was first introduced by Dahl in the 1940s as a solution for the rehabilitation of severely atrophic mandibles [1, 2]. These early implants were composed of cobalt-chromium bars meticulously shaped to rest directly on the crestal bone, with the gingiva sutured back over them. The stability of the implant relied on the scar contraction of the periosteum. However, because these implants were positioned just beneath the mucosa, they often lost stability and became exposed in a significant number of cases, leading to complications.

Inspired by Dahl's work, Gershoff and Goldberg, in the late 1940s, sought to enhance implant performance [3]. They aimed to increase the implant's support base, distance the structure from the surgical wound, and improve its fit. To achieve this, they crafted the implants based on plaster models of the arch, estimating the underlying bone surface using intraoral radiographs and gingival probing. This allowed for a broader implant base that extended beyond the narrow crestal portion.

A major breakthrough came in 1950 when Lew and Berman [4, 5] proposed a two-step rehabilitation process. In the first surgical phase, the target bone segments were exposed, and an impression of the bone was taken. This enabled the creation of an accurate bone model, which was used to design a custom implant. The new implant design leveraged a broader base and utilized mandibular and maxillary undercuts to improve stability. To further enhance stability and reduce exposure risks, Berman introduced bone cerclage techniques to secure the implants. These innovations resulted in short- and medium-term success rates exceeding 95% [6]. However, long-term outcomes were compromised due to the implants' reliance on the resorbing alveolar bone, often leading to exposure over time [6].

The advent of endosseous implants led to the decline of subperiosteal implantology. However, in the late 1970s, the technique was revived by Linkow [7], who adapted subperiosteal implants for severe mandibular atrophy. He proposed the use of more biocompatible titanium implants and identified regions of the mandible less prone to resorption, such as the symphysis and the base of the mandibular rami. Linkow developed a tripodic implant design with three support points in these areas, connected by a bar system for prosthesis fixation. Despite these advances, the historical challenges of subperiosteal implants—requiring two surgeries, issues with fitting, and long-term stability—persisted.

In 2017, Mommaerts [8] introduced a new generation of subperiosteal implants, leveraging technological advancements in CAD/CAM and laser melting. These innovations eliminated the need for the initial surgical phase and allowed for the creation of implants with highly customized designs and extensive coverage, targeting areas of maximum bone solidity. The design process incorporated finite element analysis, principles of force transmission through maxillary and mandibular resistance pillars as described by Le Fort and Champy, and rigid fixation techniques adapted from maxillofacial trauma management. These developments have reignited interest in subperiosteal implants, offering a single-surgery solution with immediate loading for severe maxillary and mandibular atrophies.

L. A. Vaira (✉) · G. De Riu
Maxillo-Facial Surgery Unit, Department of Medicine, Surgery and Pharmacy, University of Sassari, Sassari, Italy
e-mail: lavaira@uniss.it; gderiu@uniss.it

© The Author(s), under exclusive license to Springer Nature Switzerland AG 2025

A. Tel, M. Robiony (eds.), *Atlas of Virtual Surgical Planning and 3D Printing for Cranio-Maxillo-Facial Surgery*,
https://doi.org/10.1007/978-3-031-94495-6_9

2 Implant Planning Process

Patients selected for subperiosteal implant rehabilitation underwent a thorough diagnostic and planning process tailored to the specific anatomy of the mandible or maxilla. For mandibular rehabilitation, cone beam computed tomography (CBCT) was performed with a slice thickness of 0.1–0.3 mm and a field of view sufficient to encompass the entire mandible, including the mandibular angles. For maxillary rehabilitation, the CBCT scans similarly employed high-resolution settings, but with a field of view wide enough to include the entire maxilla and the zygomatic buttresses.

In addition to CBCT imaging, all cases required digital scans of both dental arches and a diagnostic wax-up of the planned prosthetic restoration. The wax-up played a critical role in determining the optimal orientation and length of the implant abutments.

The planning process began with exporting the DICOM files from the CBCT scans and STL files from the dental arch scans. These files were sent to the implant manufacturer. Using the B&B Dental GS software (B&B Dental, San Pietro in Casale, Italy), the DICOM data was reconstructed into a 3D model of the bony anatomy. This model was cleaned of scattering artifacts and other inaccuracies, producing and augmented model (Fig. 1). For mandibular cases, the inferior alveolar nerve was identified and carefully marked.

The STL files of the dental arches and the diagnostic wax-up (Fig. 2) were then aligned with the 3D jaw model, creating an integrated representation of the patient's anatomy and prosthetic needs. This composite model was imported into Meshmixer software (Autodesk, San Rafael, CA, USA), where the implant design was finalized in collaboration with the surgeon (Fig. 3).

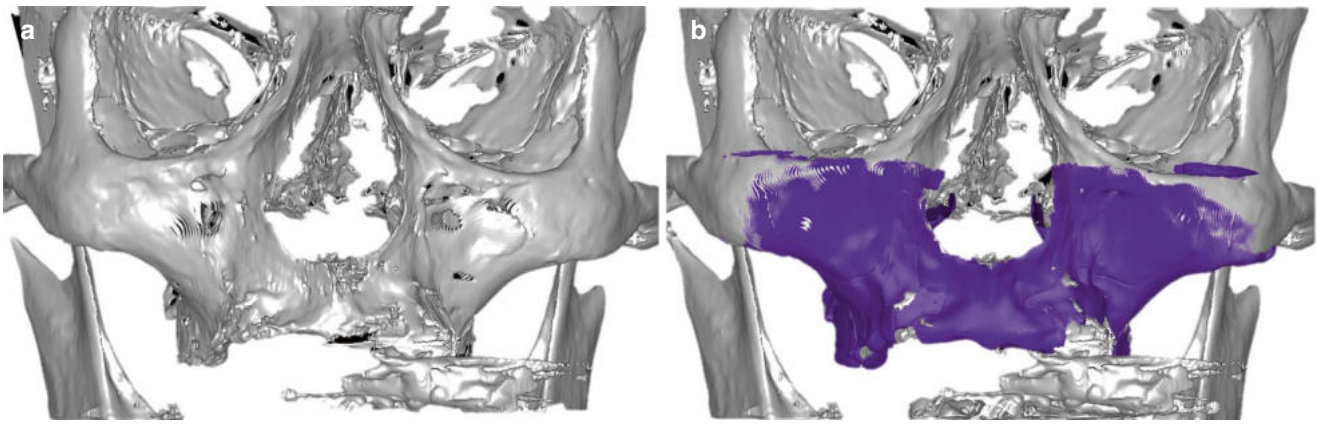


Fig. 1 (**a**) 3D CBCT scan. (**b**) augmented model of the maxilla

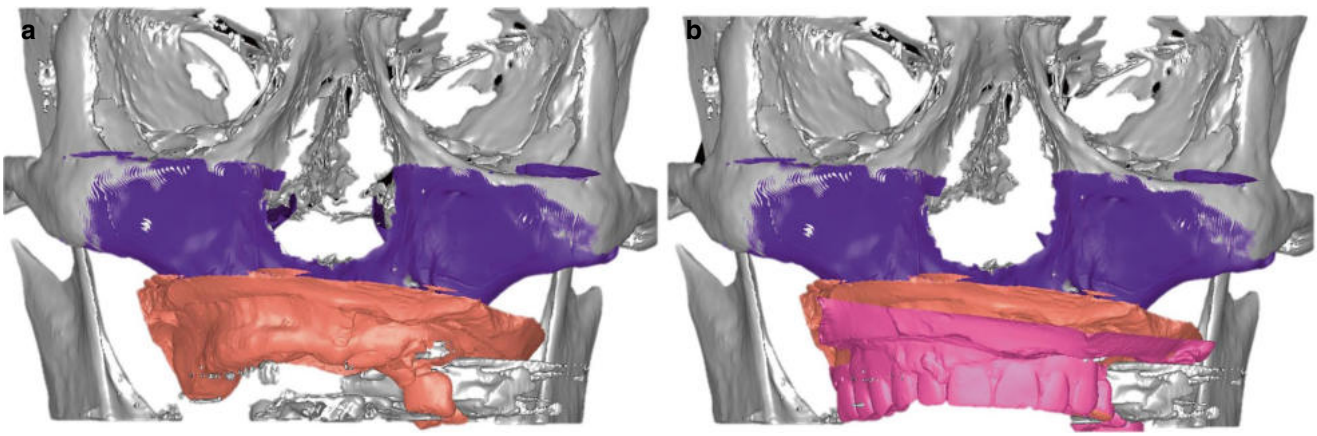


Fig. 2 (**a**) Superimposition of the soft tissue scan. (**b**) Superimposition of the diagnostic wax up

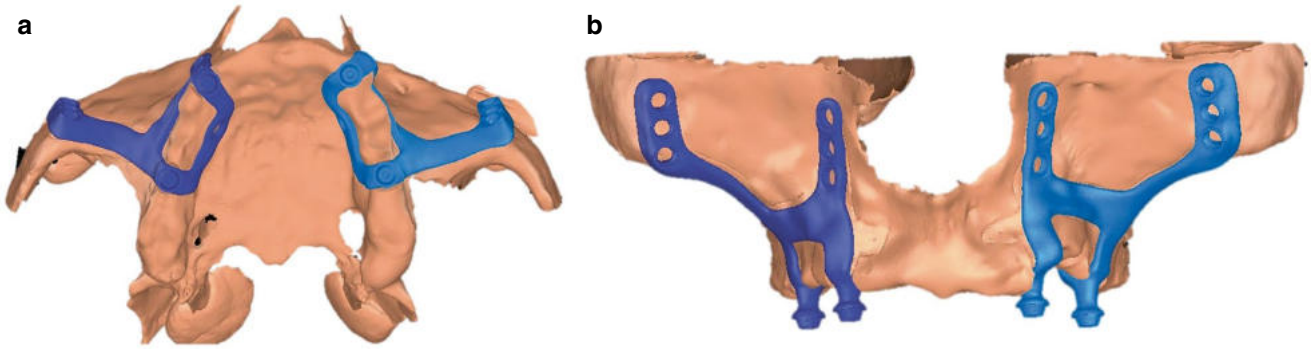


Fig. 3 Final implant design for surgeon's evaluation (**a**) Bottom view. (**b**) Frontal view

Abutments were custom-designed to rest in preprepared slots along the alveolar crest ensuring support on basal bone less prone to resorption. This requires the removal of all residual alveolar bone, allowing the implant to rest on a uniform layer of stable basal bone. Embedding the implant within the basal bone also facilitates improved coverage of its superficial portions by soft tissues, which are often deficient in atrophic cases. This enhanced tissue coverage minimizes the risk of implant exposure, contributing to better long-term outcomes [9–11]. The abutments' length and orientation were determined based on the diagnostic wax-up and the gingival thickness obtained from the dental scans. To prepare the slots for the abutments in the crest, a cutting guide is planned and provided. This guide ensures precise preparation of the bone to accommodate the abutments, optimizing their fit and stability on the basal bone (Fig. 4). Finally, the complete 3D models of the bone, soft tissue, prosthesis, and implant were reimported into the B&B Dental GS software for final review and approval by the surgeon.

2.1 Maxillary Implants Planning

The design of subperiosteal implants for maxillary rehabilitations is rooted in finite element analysis and studies of masticatory force distribution on the maxillary resistance pillars [12–16]. This ensures optimal biomechanical stability and effective load transfer during function.

The implant consists of abutments, which can be cementable or multiunit abutments (Fig. 5). Two vertical arms extend from the abutments, connected by a horizontal vestibular bridge that solidifies the structure (Fig. 6). Two arms branch off from this horizontal connection, following two of the maxillary resistance pillars, each containing screw holes for fixation. The anterior arm secures the implant to the nasomaxillary pillar, while the posterior arm extends along the maxillo-zygomatic pillar, allowing fixa-

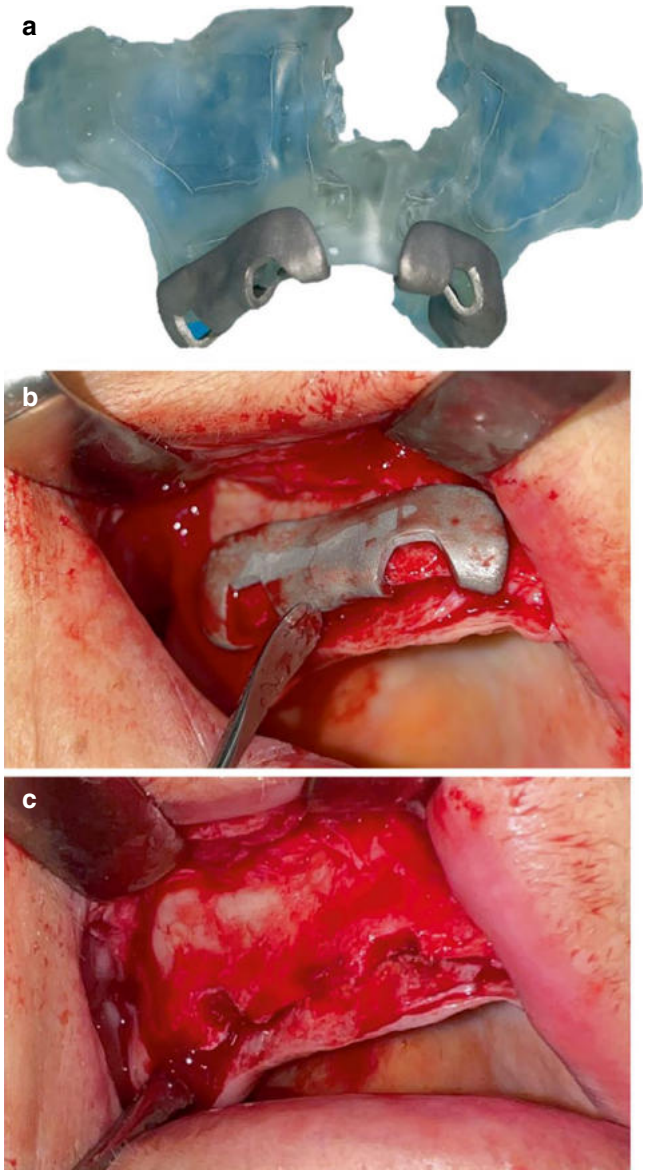


Fig. 4 (**a**) Surgical guide for the preparation of the alveolar housings. (**b**) Surgical guide positioned on the alveolar crest. (**c**) Alveolar crest after alveolar preparation

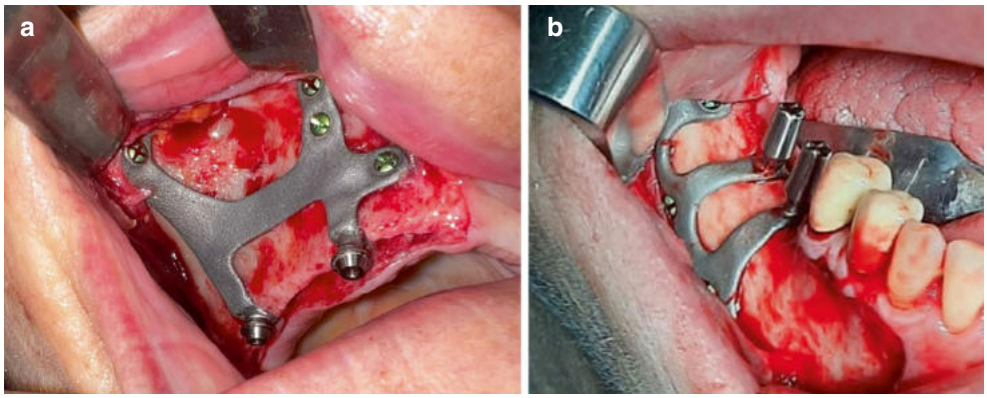


Fig. 5 (**a**) Subperiosteal implant with multi-unit abutments. (**b**) Subperiosteal implant with cementable abutments

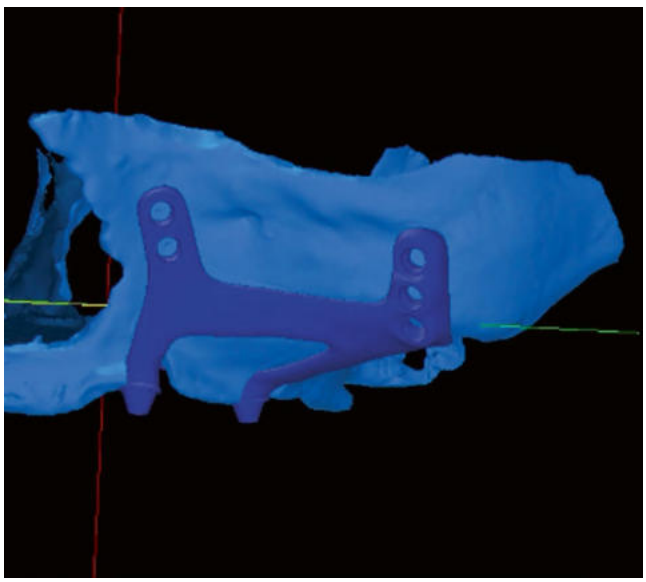


Fig. 6 Subperiosteal maxillary implant design

tion to the zygomatic buttress. Additionally, a palatal connection between the two abutments is typically included, providing enhanced structural integrity. This design has demonstrated superior distribution of masticatory forces across the maxilla [12–16].

Simpler surgical designs, particularly those relying on unreliable rigid fixation (e.g., on the sinus walls) or placing screws along the alveolar crest close to the surgical wound, should be avoided due to higher risks of contamination and failure [9, 10, 17].

2.1.1 Full-Arch Rehabilitation Considerations

For full-arch rehabilitations, it is advisable to use separate implants for each side of the maxilla [10]. Attempting to rehabilitate the entire arch with a single subperiosteal implant presents significant challenges:

1. Managing a larger surgical field increases anesthetic spread and bleeding.
2. A larger implant requires a wider surgical opening, more extensive detachment of the upper maxilla, the sacrifice of the nasopalatine nerve, and significant dissection of the palatal fibromucosa.
3. Minor imperfections in fitting on one side may cause significant and intolerable mismatches on the other.
4. Infection in one region of the implant could necessitate removal of the entire structure, resulting in the failure of the entire rehabilitation.

2.1.2 Screw Placement and Fitting Precision

When designing the implant on the virtual model, it is critical to account for the potential obstruction of screw insertion angles by soft tissues within the oral cavity. This consideration helps minimize surgical challenges. For example, screws for the zygomatic buttress should be inserted on the anterior surface of the zygoma, rather than its lateral surface, where soft tissue can obstruct access (Fig. 7). Anterior placement also aligns screws with the major axis of the zygoma, allowing for the use of longer screws, which improve fixation (Fig. 8).

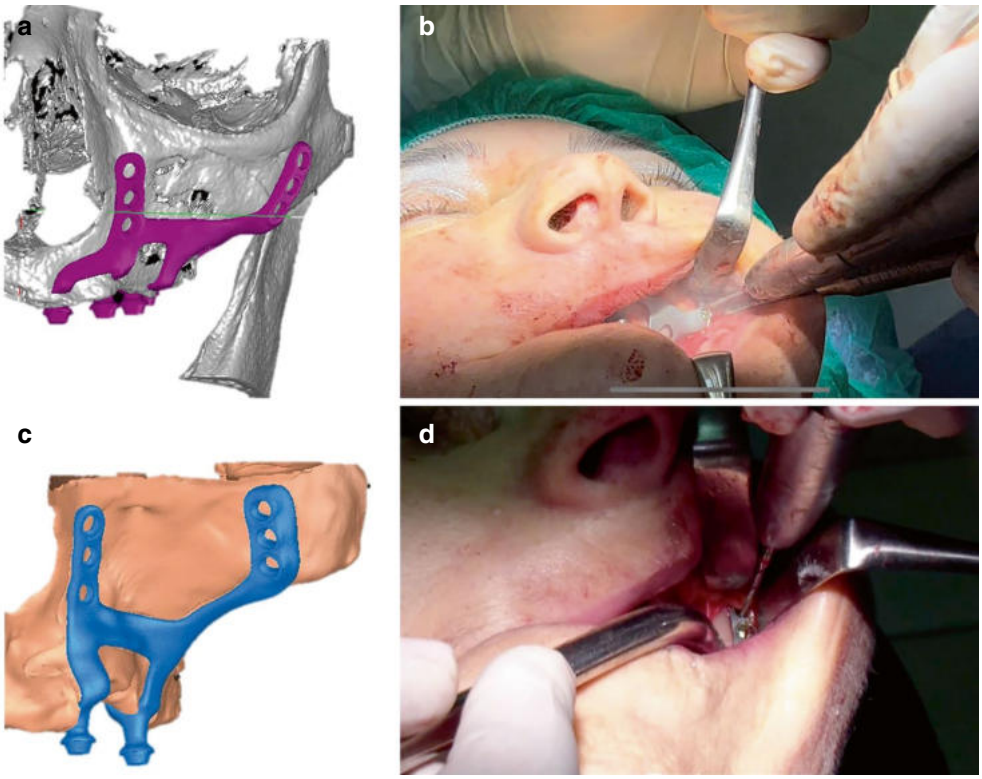


Fig. 7 (**a**) Implant design with screws positioned on the lateral surface of the zygoma. (**b**) Screw insertion requires extensive zygomatic dissection and greater retraction of soft tissues to achieve perpendicular screw placement. (**c**) Implant design with screws positioned on the anterior surface of the zygoma. (**d**) Screw insertion is simplified, requiring less zygomatic dissection and softer tissue retraction

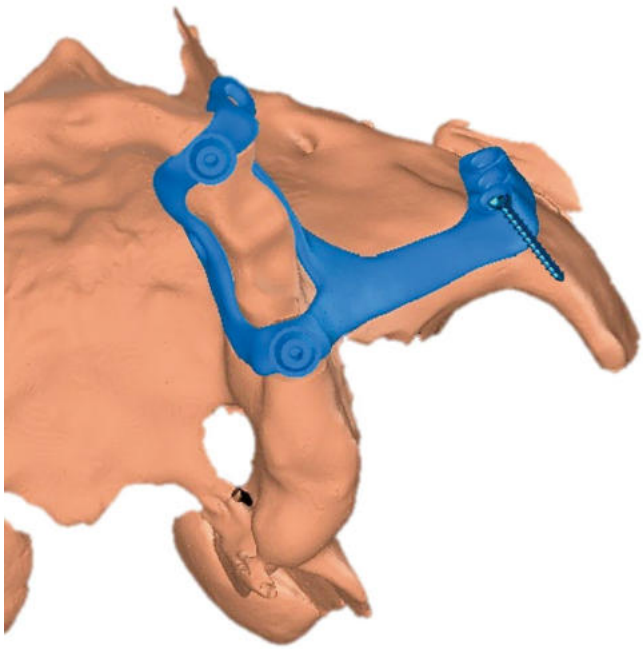


Fig. 8 Screw orientation along the major axis of the zygoma

2.1.3 Managing Post-extraction Sites

If abutments are placed in post-extraction sites, alveolar bone loss during extractions can compromise the implant's fitting (Fig. 9). To address this, extractions should either be completed before the case is planned, or the abutment should be positioned to the bottom of the dental socket to mitigate the risk of misfitting.

2.2 Mandibular Implants Planning

The buccal portion of the mandibular implant is designed to run as far as possible from the surgical wound to minimize the risk of bacterial colonization and implant exposure [18]. This approach mirrors established practices in mandibular fracture fixation, where complication rates drop dramatically when plates are positioned inferiorly rather than superiorly [19]. Additionally, this design ensures the osteosynthesis screws can be placed in the strongest regions of the mandible, aligning with the physiological force distribution pathways codified by Le Fort and Champy. When

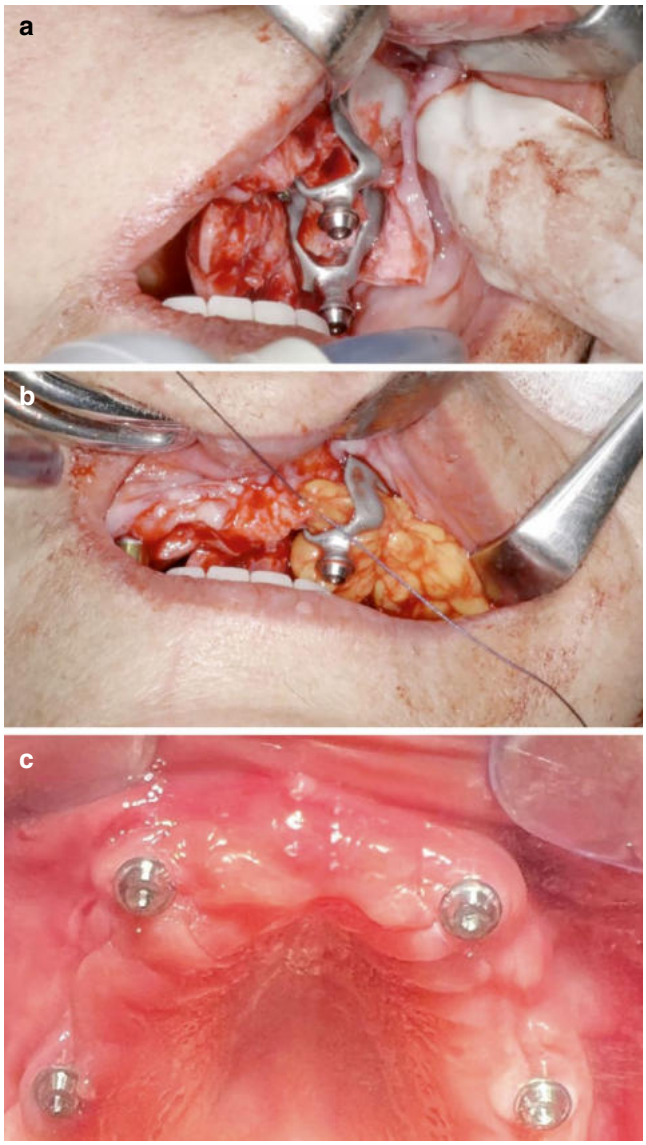


Fig. 9 (**a**) Mis-fitting of the implant in a post-extraction site due to loss of buccal alveolar bone during tooth extraction. (**b**) Bichat's fat pad transposed to fill the gap. (**c**) Soft tissue healing at 12 months post-procedure

the positioning of the abutments permits, the implant should extend below the emergence of the mental nerve, offering better protection and isolation for the nerve (Fig. 10).

2.2.1 Planning for Screw Hole Placement

When planning the implant, it is critical to consider that the mandible is covered by soft tissues, which must be retracted during placement. Screw holes should be positioned at least 8 mm away from the mental foramen to avoid undue stress on the nerve during insertion and reduce the risk of traction injuries (Fig. 11). The implant design must ensure that all screw holes are accessible during surgery while remaining sufficiently protected by soft tissues postoperatively, reducing the risk of exposure and infection.

2.2.2 Evaluating Nerve Position and Screw Length

A thorough assessment of the distance between the inferior alveolar nerve and each planned screw hole is essential to determine the appropriate screw length (Fig. 12). This is particularly critical in cases where the implant extends deeply and approaches the inferior border of the mandible. In such scenarios, it may not be possible to insert screws perpendicularly to the implant surface. The nerve's position must be evaluated accordingly to ensure safe screw angulation and prevent neurological complications.

2.2.3 Lingual Design

On the lingual side of the mandible, the connection of the abutments is not feasible if the mylohyoid line is too superficial (Fig. 13). Attempting to place the implant in this region would require significant dissection of the mylohyoid muscle, creating an undercut that cannot be effectively crossed by the implant. This anatomical constraint must be carefully considered during the planning phase to ensure the implant's design is compatible with the patient's specific anatomy and avoids unnecessary surgical complexity.

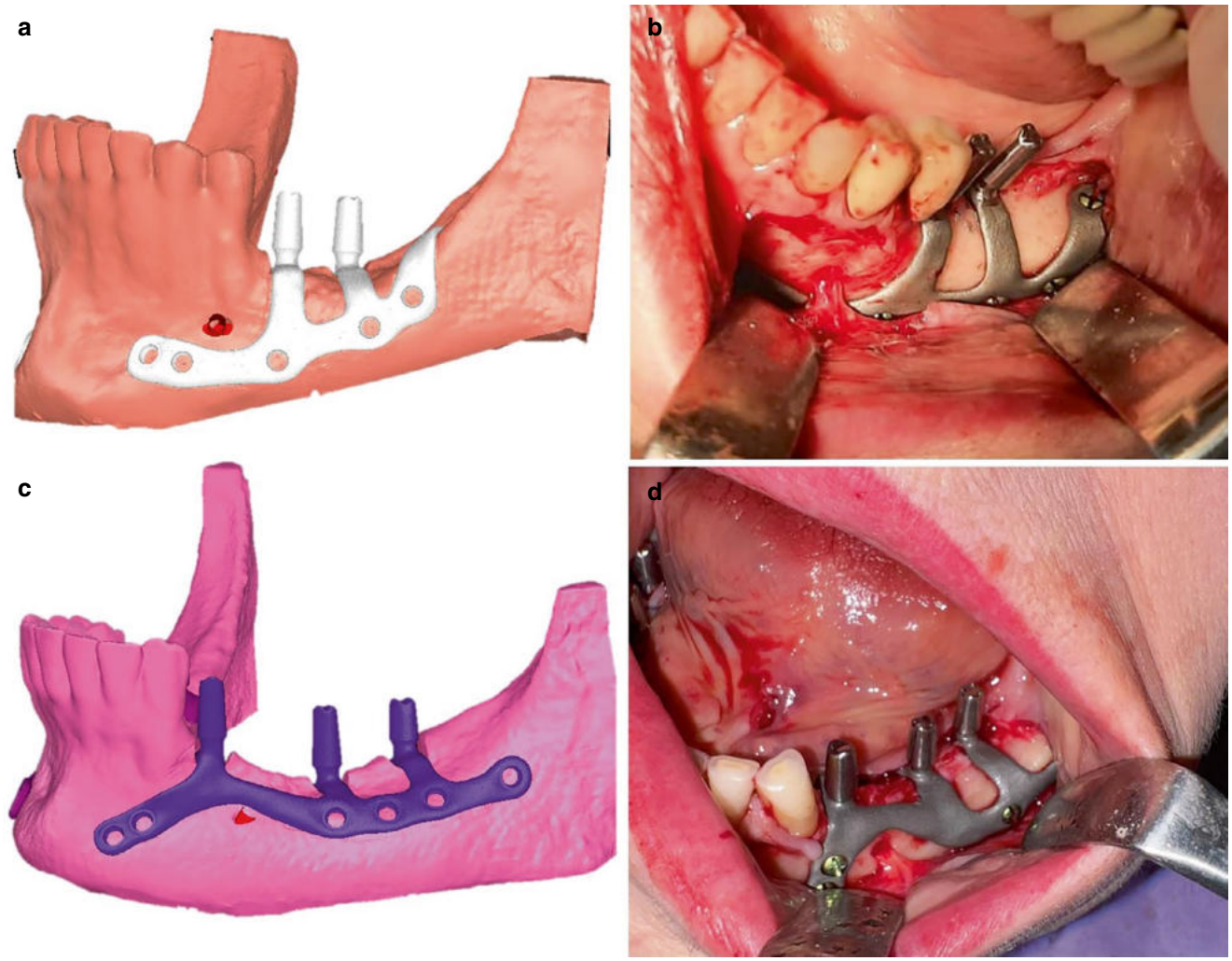


Fig. 10 Implant passing under the nerve for the rehabilitation of the molar area. (**a**) Digital planning. (**b**) Intraoperative view. Implant passing above the nerve for the rehabilitation of the premolar and molar area. (**c**) Digital planning. (**d**) Intraoperative view

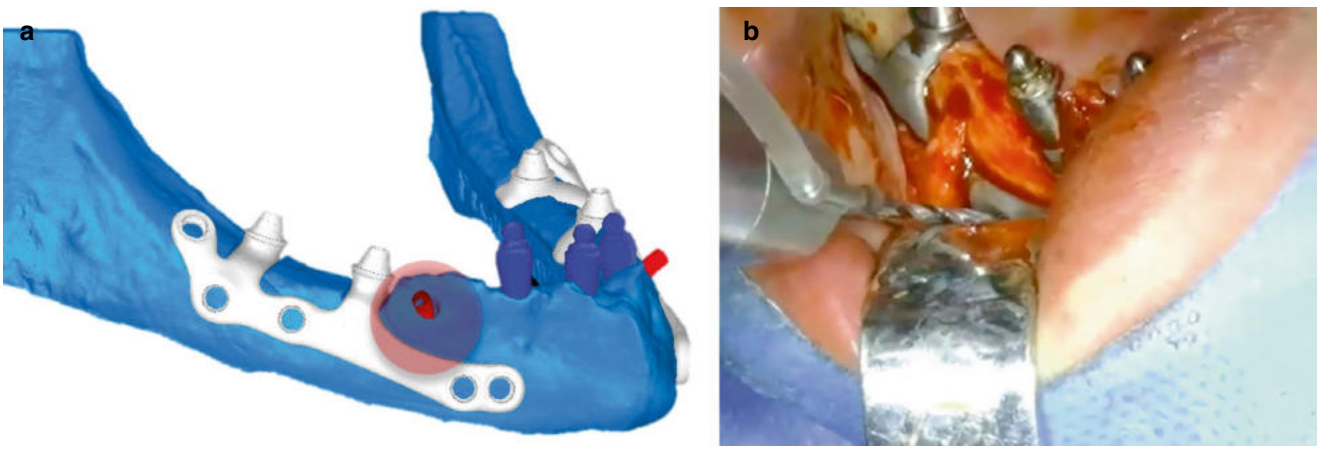


Fig. 11 (**a**) Area surrounding the emergence of the mental nerve where screws should not be placed to avoid nerve compression or damage. (**b**) Intraoperative view showing the relationship between the implant and screws, highlighting how the proximity of the nerve emergence prevents the placement of screws too close to it

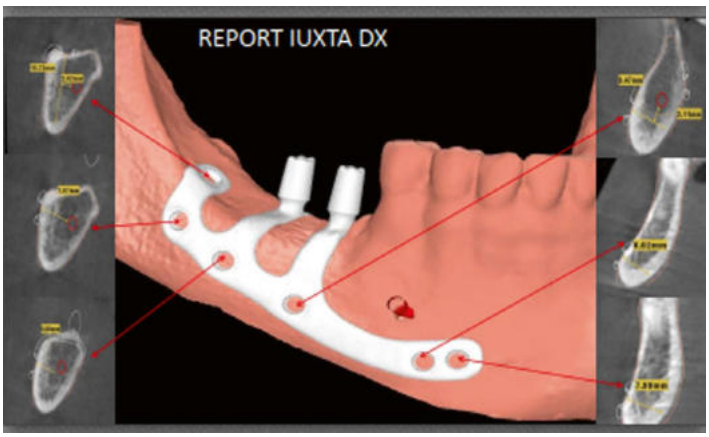


Fig. 12 Report detailing the distances between the implant and the inferior alveolar nerve at each screw hole

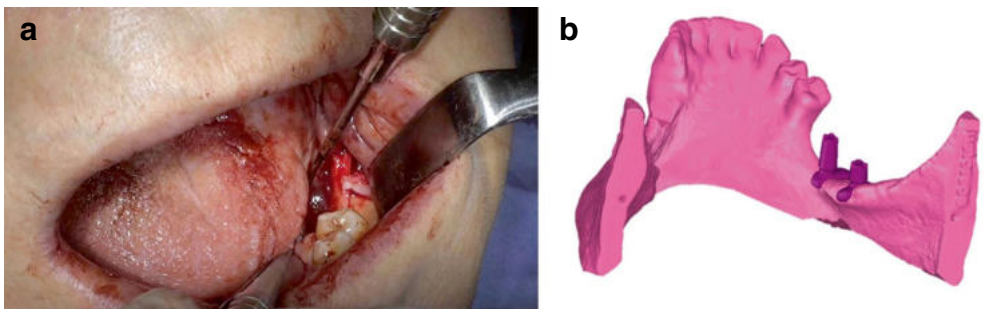


Fig. 13 (**a**) Mylohyoid muscle exposed after dissection of the lingual surface of the mandible. (**b**) A superficial mylohyoid line prevents the lingual connection of the abutments

3 Implant Manufacturing

After the project received the surgeon's approval, the implant was fabricated from grade V titanium using double laser melting technology (MYSINT100, Sisma, Piovene Rocchette, Italy). To ensure the metal's stability and eliminate porosity, the implant underwent a sintering process in a specialized oven (Nabertherm GMBH, Lilienthal, Germany) at 840 °C for 4 hours, followed by an additional 2 hours at 500 °C. This heat treatment process was carefully controlled to prevent any dimensional changes to the implant.

The abutments were then refined using a 5-axis milling machine (Datron D5, Datron, Milford, NH, USA), and, where applicable, the internal threads of the multi-unit or conometric abutment were machined with precision. The subperiosteal implant was subsequently cleaned in the organic acid solution DOWCLENE 1601 (Dow Chemicals Corporation, Midland, MI, USA) to remove any residual impurities and then sterilized to ensure surgical readiness.

Templates for preparing the alveolar crest slots to house the abutments were milled from cobalt-chrome alloy using the same 5-axis milling machine. This material was chosen for its strength, thin profile, and ease of placement. Additionally, a stereolithographic model of the jaw was 3D printed in resin (Stratasys Objet 30, Stratasys, Eden Prairie, MN, USA) and provided to the surgeon to aid in preoperative planning.

4 Surgical Procedure

4.1 Maxillary Rehabilitation

Maxillary subperiosteal implant placement is performed under local anesthesia, complemented by superficial intravenous sedation with diazepam. Local anesthesia is administered using articaine with 1:100,000 adrenaline. Extraoral nerve blocks are used for the infraorbital and zygomatic nerves to ensure anesthesia of the anterior and lateral maxillary regions. Intraorally, the vestibular fornix is anesthetized, followed by palatal anesthesia with blocks of the greater palatine and nasopalatine nerves.

For each procedure, two separate implants are used, allowing one surgical field to be managed at a time. On each side, a full-thickness mucosal incision is made along the alveolar crest with two vestibular releases: one at the midline and the other posteriorly, positioned at least 5 mm distal to the most posterior abutment. The incision is offset 2–3 mm palatally to ensure repositioning of a sufficient layer of kera-

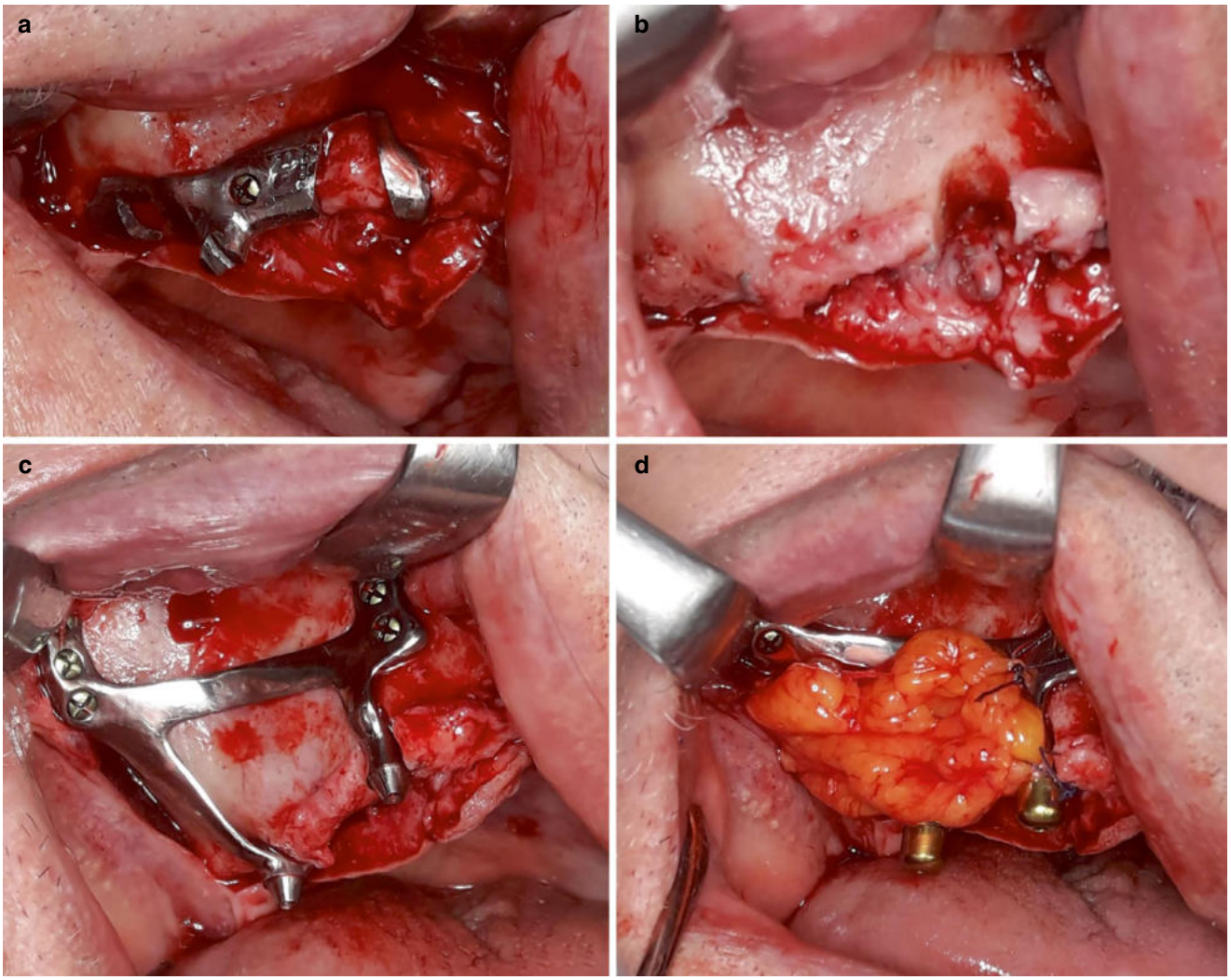


Fig. 14 (**a**) Surgical guide in position for crestal preparation. (**b**) Crestal preparation showing the slots created for abutment housing. (**c**) Implant placed in position. (**d**) Transposed Bichat's fat pad to augment soft tissue thickness over the implant

tinized gingiva on the buccal side of the abutments. Full-thickness flaps are then elevated on both the palatal and buccal sides.

In the initial phase, the dissection is limited to the alveolar crest to accommodate the crestal preparation guide. Using the template, slots for the abutments are prepared, extending deep enough to reach the basal bone (Fig. 14a, b). In distal sites, preparation may approach the sinus membrane, which must be carefully preserved and detached when necessary. If perforations occur, a resorbable membrane is placed beneath the abutment to protect the area. After completing the crest preparation, skeletonization of the upper maxilla is extended upward to identify and preserve the infraorbital nerve while fully detaching the nasomaxillary pillar and zygomatic buttress. In some cases, releasing the anterior masseter muscle insertions may facilitate this maneuver.

The subperiosteal implant is then inserted, and its fit meticulously checked. Fixation is achieved using 2 mm diameter grade V titanium osteosynthesis screws. Screw lengths are determined based on the underlying bone thickness: 10–14 mm at the zygomatic buttress, 4–6 mm at the nasomaxillary pillar, and 4–8 mm at the palate. If a screw fails to achieve sufficient torque, a 2.3 mm diameter safety screw is used. Each implant is secured with at least two screws per pillar to ensure primary stability adequate for immediate loading (Fig. 14c).

Following fixation, the implant structure is covered with resorbable membranes, cortical laminae, or by transposing Bichat's fat pad to ensure soft tissue coverage (Fig. 14d). The mucosa is passivated using periosteal releases and sutured to achieve tension-free closure.

Postoperative care includes a six-day course of antibiotics (amoxicillin with clavulanic acid, 1 g twice daily) and analgesics as needed. Immediate loading is performed with a fixed provisional prosthesis (Fig. 15). Patients are instructed to follow a soft diet for the first 15 days post-surgery and to



Fig. 15 Immediate loading of the prosthesis

avoid hard foods until the delivery of the definitive prosthesis.

The definitive prosthesis is provided 6 months after surgery, once the soft tissues have healed and been conditioned. Adjustments are made as needed to ensure optimal fit and function.

4.2 Mandibular Rehabilitation

Subperiosteal implant placement is performed under local anesthesia without the need for intravenous sedation. Local anesthesia is administered using articaine with 1:100,000 epinephrine. Inferior alveolar nerve blocks are not routinely performed, as is typical in posterior jaw implant surgeries. The vestibular fornix is infiltrated from the retromolar trigone to the incisor region, both superficially and deeply, reaching the inferior border of the mandible. Lingual infiltration is also completed to fully anesthetize the surgical site.

A full-thickness mucosal incision is made along the edentulous crest, extending mesially intrasulcularly or paramarginally on residual teeth. Along the edentulous crest, the incision ensures that at least 2 mm of keratinized mucosa remains on the buccal side to provide sufficient lining for the abutments. Two vestibular release incisions are made: the posterior release is located at least 5 mm distal to the last abutment to promote optimal mucosal healing around it, while the anterior release is placed more mesial than the nearest screw hole to reduce the risk of exposure during healing.

Following the mucosal incision, a full-thickness buccal flap is elevated to skeletonize the mandible from the retromolar trigone to the parasymphyseal region, extending inferiorly below the external oblique ridge to the lower border of the mandible. If required by the implant design, the mental nerve is isolated circumferentially with a curved dissector. On the lingual side, the periosteum is elevated to the mylohyoid crest, which serves as the anatomical limit of dissection.

A cutting guide is used to prepare the alveolar ridge for the abutment slots. The guide is seated firmly on the bone, and the slots are created with a cylindrical diamond bur matching the planned slot width (Fig. 16a, b). During this phase, if the inferior alveolar nerve is superficial, patients may require additional anesthesia with a nerve block.

Once the slots are prepared, the subperiosteal implant is inserted. For implants running above the mental nerve, placement is straightforward and does not require full nerve isolation. When the implant runs below the nerve, the anterior arm is inserted vertically beneath the nerve and gently advanced with forceps. After passing the nerve, the implant is rotated horizontally into its final position.

The implant fit is meticulously evaluated, and any misfits are corrected by refining the prepared slots before fixation. Once the fit is satisfactory, the implant is pressed firmly into place. Fixation is achieved using 2 mm diameter grade V titanium osteosynthesis screws. Screw length, determined during surgical planning, ranges from 4 to 10 mm and is selected based on the thickness of the underlying bone. To avoid nerve damage, a surgical bur with a pre-calibrated stop is used to prepare the screw holes. If sufficient tightening torque is not achieved, 2.3 mm diameter safety screws are employed. Each implant is secured with at least four osteosynthesis screws (Fig. 16c).

Following fixation, the periosteum is released, and the mucosa is sutured to achieve tension-free closure (Fig. 16d). Postoperative care includes antibiotic therapy (amoxicillin + clavulanic acid 1 g twice daily for 6 days) and analgesics as needed.

Ten days post-surgery, after suture removal, a provisional prosthesis is delivered. The provisional prosthesis is fabricated using a conventional precision impression and is adjusted over subsequent months to facilitate soft tissue conditioning and healing. The final prosthesis is delivered 6 months after surgery, once the soft tissues have stabilized and adapted (Fig. 17).

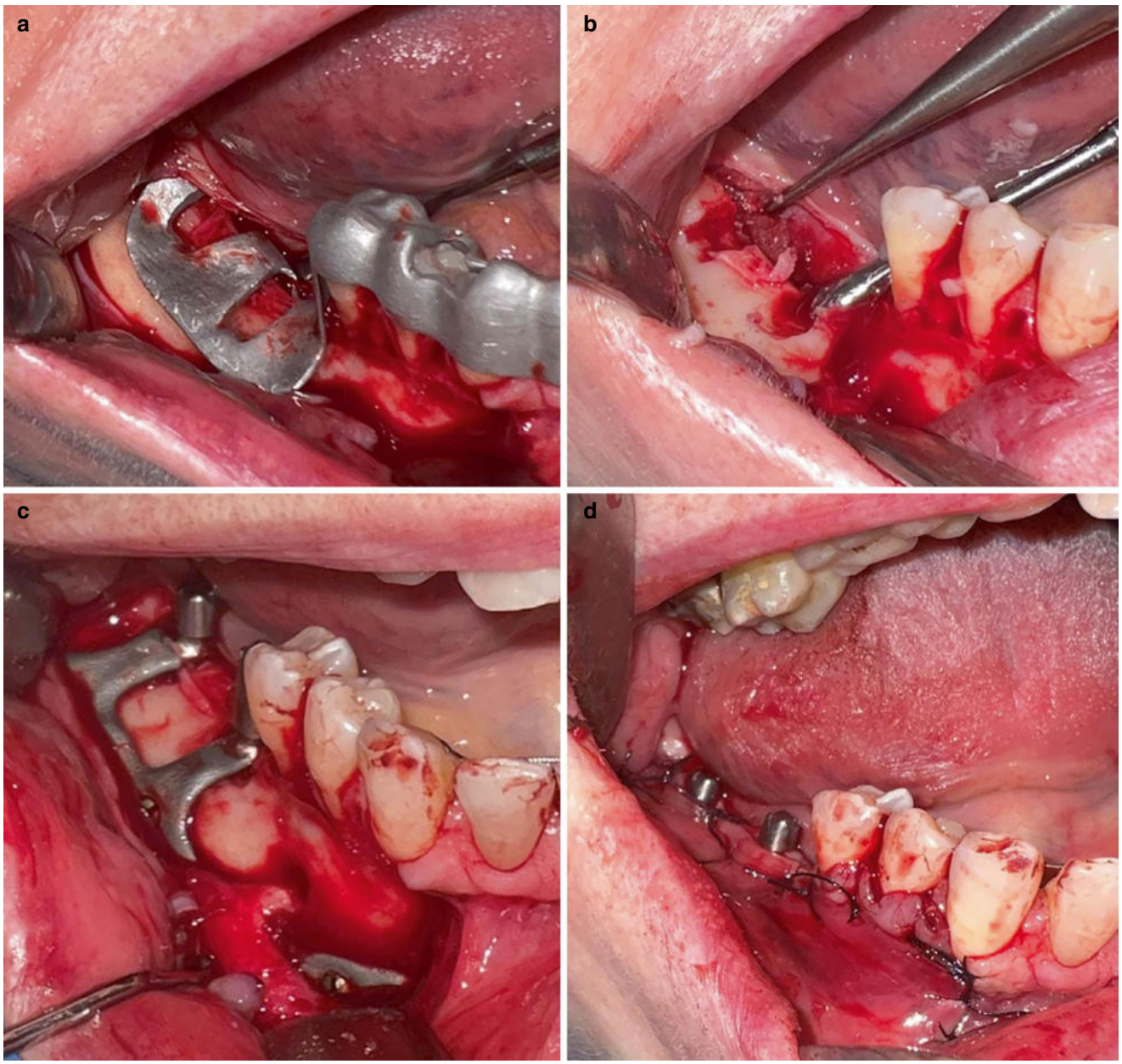


Fig. 16 (**a**) Placement of the surgical guide for the preparation of the alveolar ridge. (**b**) Housings for abutments milled into the alveolar bone. (**c**) Subperiosteal implant placed and fixed. (**d**) Surgical access sutured

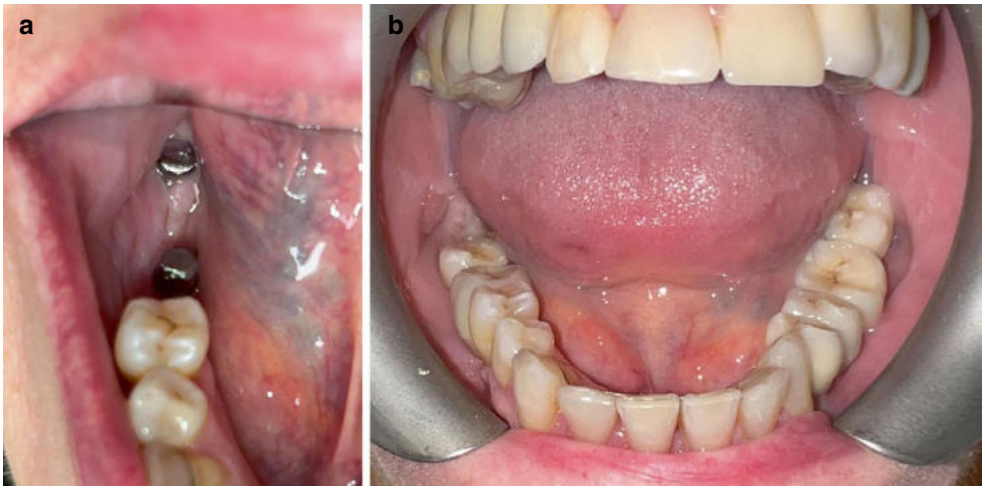


Fig. 17 (**a**) Soft tissue healing 6 months after the surgery (**b**) Final prosthesis

References

1. Łoginoff J, Majos A, Elgalal M. The evolution of custom subperiosteal implants for treatment of partial or complete edentulism in patients with severe alveolar ridge atrophy. J Clin Med. 2024;13(12):3582. https://doi.org/10.3390/jcm13123582.
2. Dahl GJA. Om Mojligheten for Implantation i de Kaken an Metallskelett Som Bas Eller Retention for Fosta Eller Aotaglosa Protester. 1943. Available online: https://api.semanticscholar.org/CorpusID:151979266. Accessed 4 Dec 2024.
3. Goldberg NI, Gershkoff A. The implant lower denture. Dent Dig. 1949;55:490–4.
4. Berman N. Implant technique for full lower denture. Washington Dent J. 1950;19:15–7.
5. Lew I. Progress in implant dentistry—an evaluation. JADA. 1959;59:478–92.
6. Schou S, Pallesen L, Hjørting-Hansen E, Pedersen CS, Fibaek B. A 41-year history of a mandibular subperiosteal implant. Clin Oral Implants Res. 2000;11:171–8.
7. Linkow LI. Evolutionary design trends in the mandibular subperiosteal implant. J Oral Implantol. 1984;11:402–38.
8. Mommaerts MY. Additively manufactured sub-periosteal jaw implants. Int J Oral Maxillofac Surg. 2017;46:938–40.
9. Mommaerts MY. Evolutionary steps in the design and biofunctionalization of the additively manufactured sub-periosteal jaw implant "AMSJI" for the maxilla. Int J Oral Maxillofac Surg. 2019;48:108–14.
10. Vaira LA, Biglio A, Roy M, Salzano G, Troise S, Abbate V, Mayo-Yanez M, Lechien JR, Piombino P, De Riu G. Full-arch rehabilitation of severely atrophic maxilla with additively manufactured custom-made subperiosteal implants: a multicenter retrospective study. J Craniomaxillofac Surg. 2024;52:991–8. https://doi.org/10.1016/j.jcms.2024.06.016.
11. Vaira LA, Biglio A, Salzano G, Lechien JR, De Riu G. Additively manufactured custom-made subperiosteal implant rehabilitation for severely atrophic maxillary molar area: a technical note. J Stomatol Oral Maxillofac Surg. 2024;125:101917. https://doi.org/10.1016/j.jormas.2024.101917.
12. De Moor E, Huys SEF, van Lenthe GH, Mommaerts MY, Vander Sloten J. Mechanical evaluation of a patient-specific additively manufactured subperiosteal jaw implant (AMSJI) using finite-element analysis. Int J Oral Maxillofac Surg. 2022;51:405–11. https://doi.org/10.1016/j.ijom.2021.05.011.
13. Altıparmak N, Polat S, Onat S. Finite element analysis of the biomechanical effects of titanium and Cfr-peek additively manufactured subperiosteal jaw implant (AMSJI) on maxilla. J Stomatol Oral Maxillofac Surg. 2023;124:101290. https://doi.org/10.1016/j.jormas.2022.09.011.
14. Zielinski R, Sowinski J, Piechaczek M, Okulski J, Kozakiewicz M. Finite element analysis of subperiosteal implants in edentulism-on the basis of the MaI implant® by integra implants®. Materials (Basel). 2023;16:7466. https://doi.org/10.3390/ma16237466.
15. Kundakcioglu A, Ayhan M. Evaluation of different subperiosteal implant thicknesses on mechanical strength and stress on bone by finite element analysis. Int J Med Sci. 2024;21:1672–80. https://doi.org/10.7150/ijms.91620.
16. Parhiz A, Nourishirazi R, Asadi A, Karimpour M. Finite element assessment of a novel patient-specific mandibular implant for severely atrophic ridge. Biomed Res Int. 2024;2024:9735427. https://doi.org/10.1155/2024/9735427.
17. Herce-López J, Pingarrón MDC, Tofé-Povedano Á, García-Arana L, Espino-Segura-Illa M, Sieira-Gil R, Rodado-Alonso C, Sánchez-Torres A, Figueiredo R. Customized subperiosteal implants for the rehabilitation of atrophic jaws: a consensus report and literature review. Biomimetics (Basel). 2024;9:61. https://doi.org/10.3390/biomimetics9010061.
18. Vaira LA, Biglio A, Favro A, Salzano G, Abbate V, Lechien JR, De Riu G. Implant-prosthetic rehabilitation of the atrophic posterior mandible with additively manufactured custom-made subperiosteal implants: a cohort study. Int J Oral Maxillofac Surg. 2024;53:533–40. https://doi.org/10.1016/j.ijom.2024.01.003.
19. Falci SGM, de Souza GM, Fernandes IA, Galvao EL, Al-Moraissi EA. Complications after different methods for fixation of mandibular angle fractures: network meta-analysis of randomized controlled trials. Int J Oral Maxillofac Surg. 2021;50:1450–63.

Principles of Cranial Reconstruction

Alessandro Tel, Francesco Tuniz, and Massimo Robiony

1 Types of Skull Vault Defect

For virtual planning purposes, two types of defects of the cranial vault must be acknowledged:

- *Defect created during surgical planning to simulate a simultaneous craniotomy*: The presence of a lesion arising primarily from the bone or involving it as a spreading of a nearby pathological process requires. Examples of pathological processes arising primarily from the bone include benignant lesions (the most common of which is cranial osteoma) and malignant lesions, often aggressive bone lesions that require margin-free surgical resection and include osteosarcomas. Other examples of lesions localized within the bone include intraosseous metastases, multiple myeloma, Langerhans histiocytosis, osseous hemangioma, fibrous dysplasia, and the rare intraosseous meningioma. Lesions invading the skull as a sequela of nearby processes basically include meningiomas, which often involve the bone and are firmly attached, requiring resection of an overlaying cranial flap. In such cases, the virtual planning must take into account a wide bone resection including the whole lesion (if intraosseous), or its underlying attachment (for instance, in case of meningiomas). Resection is planned by applying a transparent shader to the bone, allowing to inspect the associated lesions, and by contouring the area targeted for excision by drawing the corresponding curve. We commonly design two curves, the first one on the inner skull surface and the second, slightly larger, on the outer surface, allowing to create a tapered bone defect that also provides support for the cranial plate, as the bone section is conic and not straight. The result of virtual craniotomy is a geometrical hole, well defined, with an identifiable profile curve, requiring a specular cranial plate (Fig. 1).
- *Pre-existing defect (craniolacunia)*: This is the case of secondary cranial reconstruction, often a sequela of a previous trauma with loss of bone substance sustained by the patient time before, or a previous neurosurgical procedure in which the repositioned cranial operculum underwent resorption process. Although apparently more easier to deal with, the design of a cranial plate over an irregularly shaped geometry, compared to the well-defined margin of a craniotomy, poses more challenges. In order to minimize bone loss, it is important to take advantage of irregular bone spikes around the defects, representing the combined effect of both substance loss and bone resorption, which are element of support for the cranial implant. A careful evaluation of undercut is mandatory to avoid fitting incompatibilities. In cases of bone resorption involving a repositioned skull operculum after a previous neurosurgical procedure, it is usual that the bone flap is positioned centrally to the defect, as resorption starts from the margins. In such cases, it must be removed, and the cranial plate must be shaped around healthy bone margins. During planning, removal of the interfering bone has the same importance, as it allows to free the area used for the design of the cranial implant (Fig. 2).

A. Tel (✉)
Lead Specialist for VSP and 3DP, Maxillofacial Surgery Clinic, Head & Neck and Neuroscience Department, Academic Hospital of Udine, Udine, Italy
e-mail: alessandro.tel@uniud.it

F. Tuniz
Neurosurgery Unit, Department of Head & Neck and Neuroscience, Academic Hospital of Udine, Udine, Italy
e-mail: francesco.tuniz@asufc.sanita.fvg.it

M. Robiony
Chief of Maxillofacial Surgery Clinic, Director of the Postgraduate School in Maxillofacial Surgery, Chief of Head & Neck and Neuroscience Department, Academic Hospital - University of Udine, Udine, Italy
e-mail: massimo.robiony@uniud.it

© The Author(s), under exclusive license to Springer Nature Switzerland AG 2025

A. Tel, M. Robiony (eds.), *Atlas of Virtual Surgical Planning and 3D Printing for Cranio-Maxillo-Facial Surgery*,
https://doi.org/10.1007/978-3-031-94495-6_10



Fig. 1 Defect created during surgical planning to excise a bone osteosarcoma. As the defect is geometrically determined, it has clean edges and tapered margins

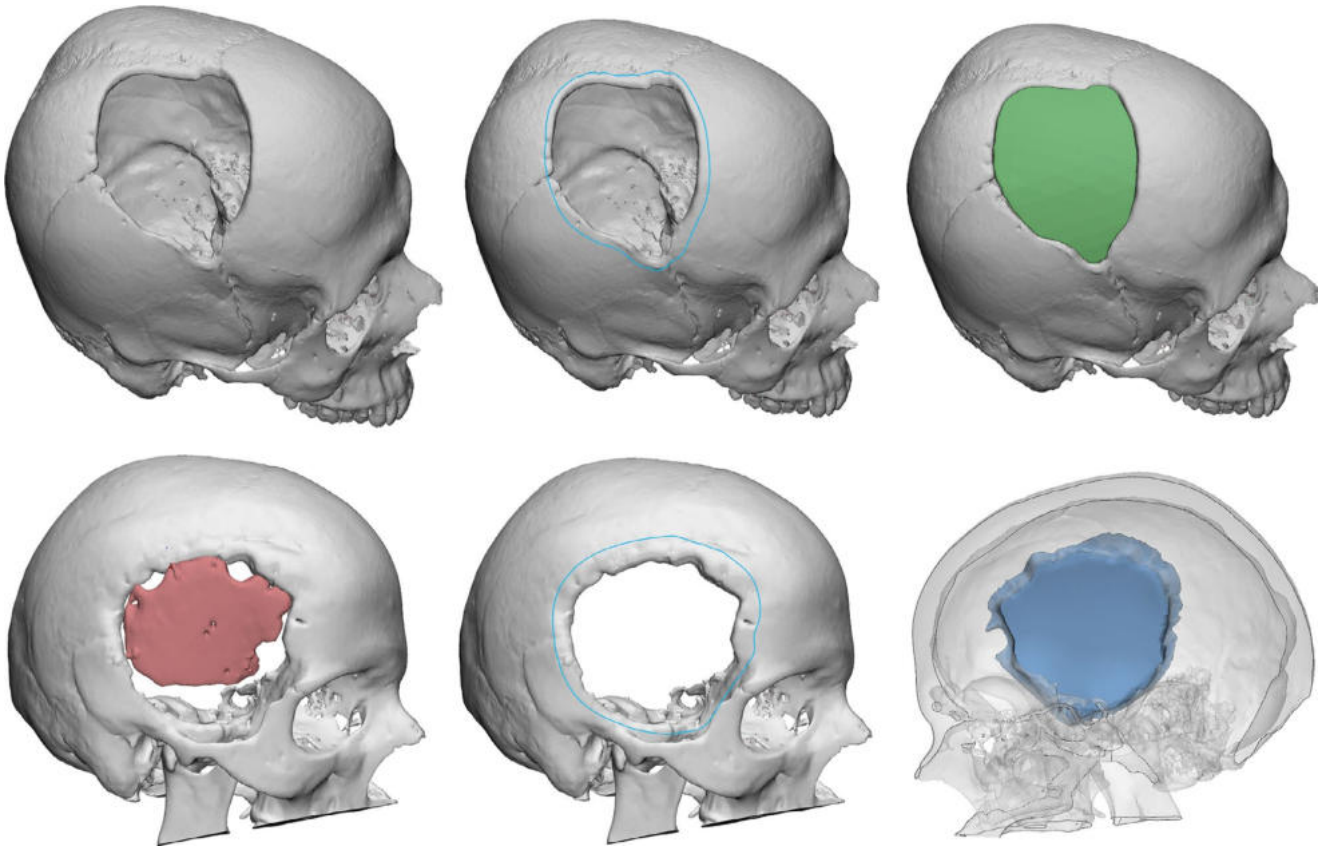


Fig. 2 Preexisting defects (craniolacunia), with rugged edges due to bone remodeling and resorption. The resulting implant takes into account the irregular margins and fits the boundaries of the defect

2 Technical Approaches to Reconstruct a Skull Vault Defect

Based on the typology of defect, its location, extension, and morphology, we acknowledge different approaches to restore cranial vault continuity:

- *Mirroring:* It probably the most well-known method to efficiently restore symmetry. As such, it is suitable to reconstruct even very large defects using contralateral geometry, on the condition that the lesion is sided and that there is a contralateral healthy anatomy to replicate [1]. The most important step is the correct placement of a symmetry midplane, which has to be performed by the operator through a careful observation of skeletal anatomy and taking into account the individual morphology of the patient. Once the symmetry plane is positioned, a replica of the skull is cloned with reversed symmetry. The procedure is finalized by applying a registration algorithm to fine-tune the correspondence of the mirrored skull over its original, taking care to maximize the correspondence around the margins of the defect (Fig. 3).
- *Anatomical CAD reconstruction (spline method):* It is a powerful feature of the software 3-Matic, which allows to create a corresponding anatomical shape starting from two basic inputs: the contour curve of the defect, similar to that identified in Fig. 2, and one, or multiple, splines, which provide the software with the arch and the curvature of the cranial implant [2]. We advise creating multiple splines in an anterior-posterior direction, although for some cases also an axial top-bottom direction might be useful. Once both inputs are given, the software interpolates data to generate a rough cranial plate fitting the margins of the defect (Fig. 4). The basic advantage of this technique is that it allows the surgeon-designer to save a significant amount of time, although the largely automatic process might lead to unexpected results, especially in presence of an irregular shape represented by bone spikes and holes. Additionally, we recommend this technique for simple defects located in the skull vault not impacting in

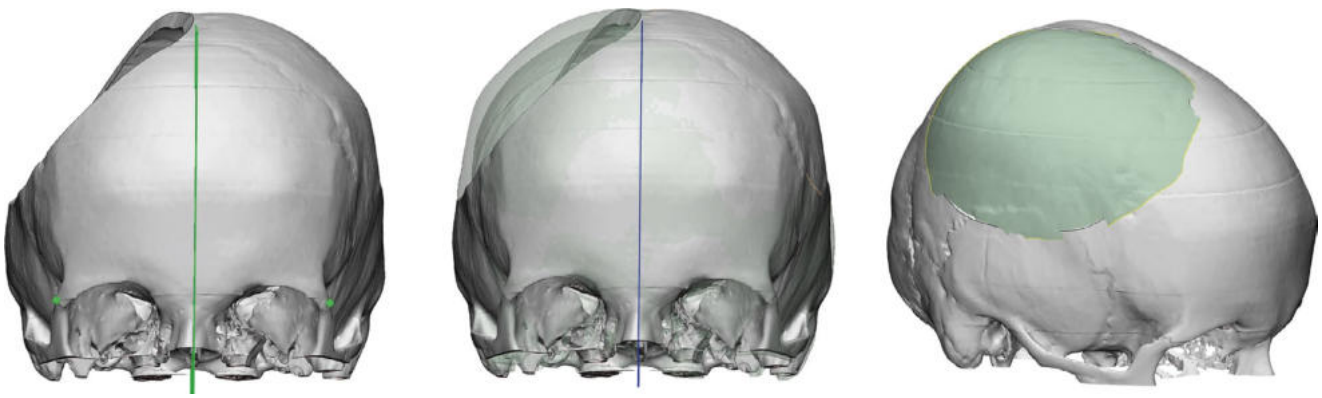


Fig. 3 Application of the mirroring method using a symmetry midplane

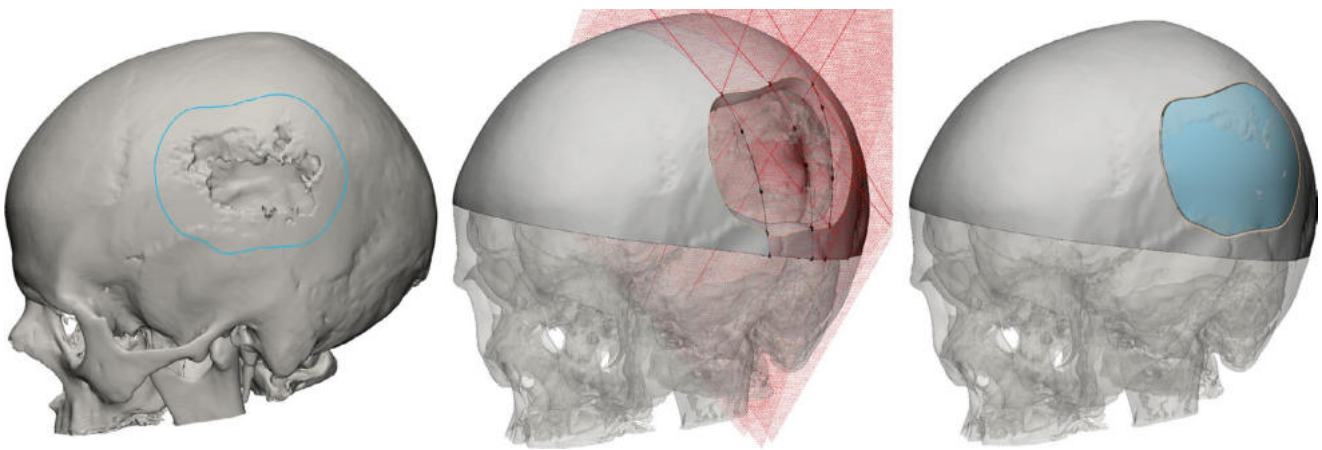


Fig. 4 Application of the anatomical CAD method using spline interpolation

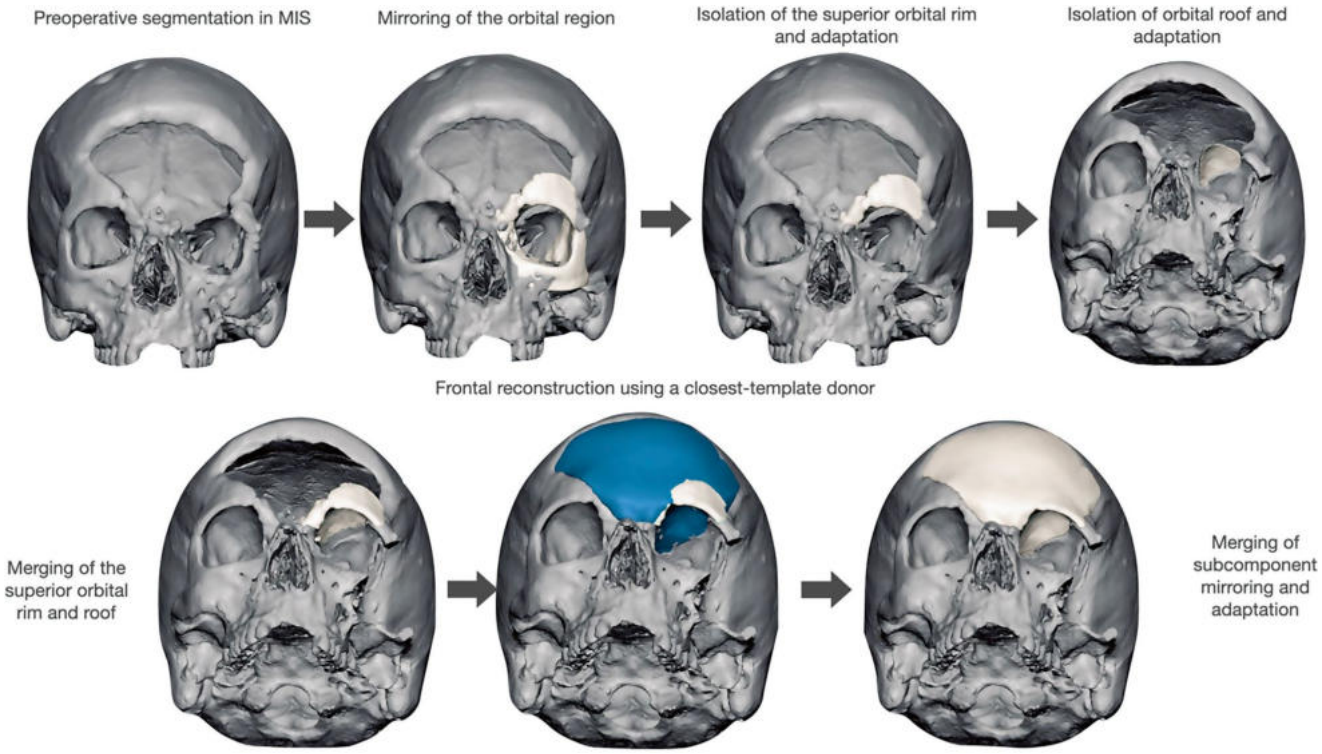


Fig. 5 Application of the subunit composition method

esthetics: as the shape generated by the algorithm is simple, it fails to represent the natural bone prominences located in esthetic areas, such as in the forehead around the glabellar region, and the contours of the orbital rims.

- *Subunit composition (mirroring + polysculpt):* This approach is most suitable when only part of the contralateral healthy anatomy is available due to a high-energy trauma with considerable bone disruption or a massive resorption. For instance, in case of a frontal bone loss with partial unilateral orbital involvement, it is possible to selectively identify contralateral healthy orbital subunits that can be included in the final reconstruction. Such subunits are mirrored using a reference midsagittal plane and are fused together until the desired orbital shape is achieved. This method has the advantage to maximize the information that can be extracted by the patient himself, without resorting to external sources of geometry. Intuitively, in the same example, the frontal bone loss represents a central defect and has to be reconstructed using different methods. Subunit composition works best when coupled with other methods, because it allows to include specific anatomical regions within a composite reconstruction (Fig. 5).
- *Closest-template donor:* It represents the traditional method to reconstruct a defect in the absence of any other sources. The typical scenario is represented by a median defect, with no mirroring options available, or an exceedingly large defect that makes any mirroring approaches unsuitable [3]. This method is strongly dependent on the sensibility of the operator, as the choice of the donor source might show interobserver variability. In addition, once the donor geometry is identified, it requires adaptation onto the receiving margins to suit the recipient anatomy; thus, polysculpt is an essential implementation (Fig. 6).
- *Statistical shape modeling (SSM):* It represents a recent, highly innovative method to reconstruct anatomical geometries in the absence of any other reference. Compared to closest-template donor method, of which it represents an evolution, SSM can bring multiple geometries, each of which should be chosen in accordance with the desired properties, into an averaged dynamic model. In fact, SSM model is made of several modes, which represent the same number of models computed by the algorithm. By varying coefficients of single modes, the operator can achieve modifications of the averaged models where one or multiple modes can have a higher influence compared to the other. If multiple geometries are candidates to become the source for another patients, they can be averaged together, and they can all contribute, with different thresholds, to the final result [4].

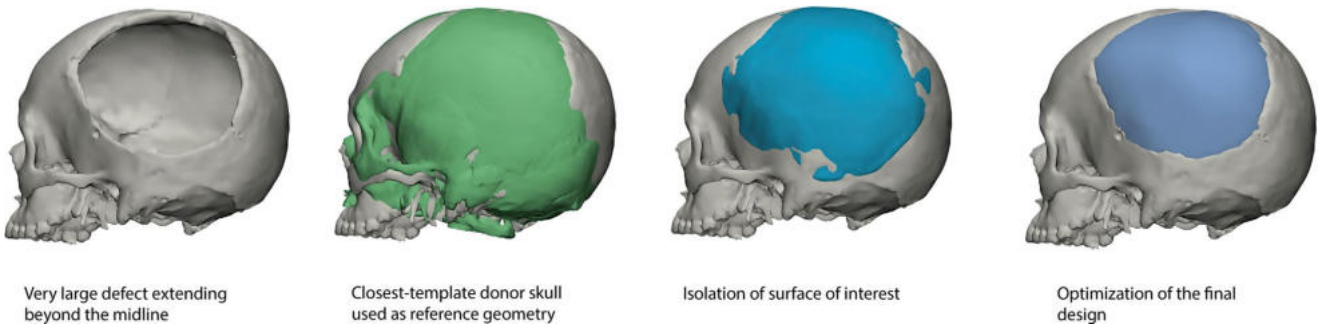


Fig. 6 Application of the closest-template donor method

- *Neural completion networks:* Yet currently immature, this method is based on deep learning and generative adversarial networks. Through multiple training set, the algorithm is able to complete the missing skull shape with substantial accuracy [5].

3 Computer-Guided Cranial Autograft: From Planning to the All-in-One Surgical Guide

3.1 Indications

A variety of lesions does not require extended skull vault resection, owing to location and size, and the resulting skull vault defect might be small. For this typology of defects, cranial autografts offer a superior alternative compared to excessively small alloplastic implants. The typical indication includes small, isolated lesions of the cranial vault causing deformity or accidentally diagnosed, such as osteomas, cavernous hemangiomas, Langerhans histiocytosis, and isolated bone metastases. Compared with any type of prosthesis, autogenous bone grafts integrate with the surrounding calvaria, and the harvest of bone graft dowel can be performed using the split-thickness technique, which includes solely the outer calvarial layer. Additionally, the harvest phase is performed in proximity of the recipient site after resection, using the same surgical access. To maximize the result, computer-aided techniques can provide the correct geometry of the donor site in relation to the recipient site, the appropriate curvature, as well as match the donor size with the recipient site. Computer modelling and 3D printing allow to design and manufacture specific surgical guides that assist the clinician in each surgical step, providing a predictable and accurate result.

Phases of virtual surgical planning can be defined as follows:

- *Osteotomy:* As a first approach, the lesion is segmented and reconstructed within the skull wall. This step enhances visualization, allowing to inspect the lesion by turning on transparency over the skull model. A quadrangular area is marked around the lesion by drawing an osteotomy template, paying attention not to be tangent to the lesion with its edges, but rather distant, to increase radicality of resection (Fig. 7).
- *Identification of the appropriate skull curvature area for harvest:* A curvature analysis is performed on the skull to identify areas with similar geometrical properties. As integration, the skull can be duplicated and the calvaria can be rotated over the resection area to identify the most suitable curvature radius to restore the continuity of the skull. Before simulating osteotomies, a wall-thickness analysis is also required, possibly to harvest the graft with ideal geometrical features in the thickest region of the skull, facilitating the separation of the outer calvarial layer (Fig. 8). Once identified, the previously created osteotomy template is cloned and dragged over the area marked for harvesting based on the analyses.
- *Repositioning of the graft over the resection site:* The graft is then repositioned over the resection site to verify compatibility in terms of size and curvature and to establish contact points. In addition, osteosynthesis plates can be designed in additional CAD packages and placed to establish their position directly within the virtual plan (Fig. 9).

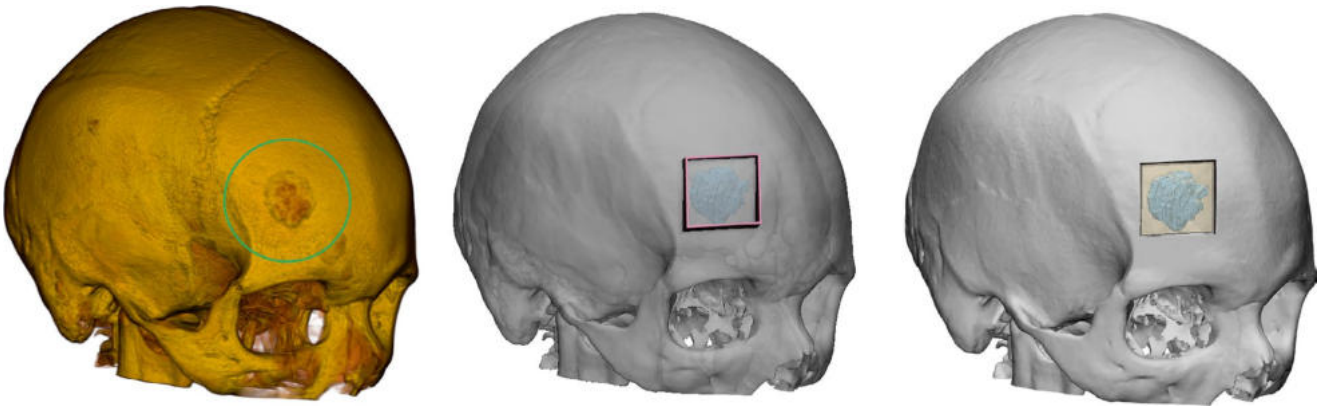


Fig. 7 Virtual surgical planning of the bone dowel to excise with the lesion inside

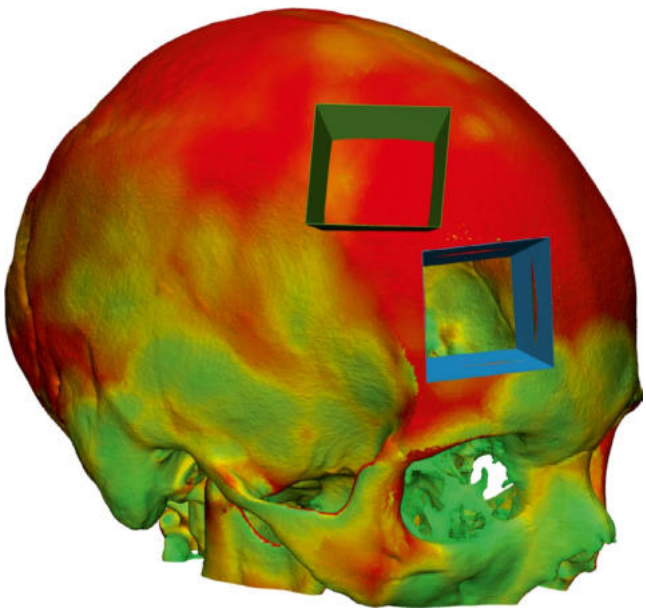


Fig. 8 Wall-thickness analysis to assess the most appropriate donor site over the calvaria

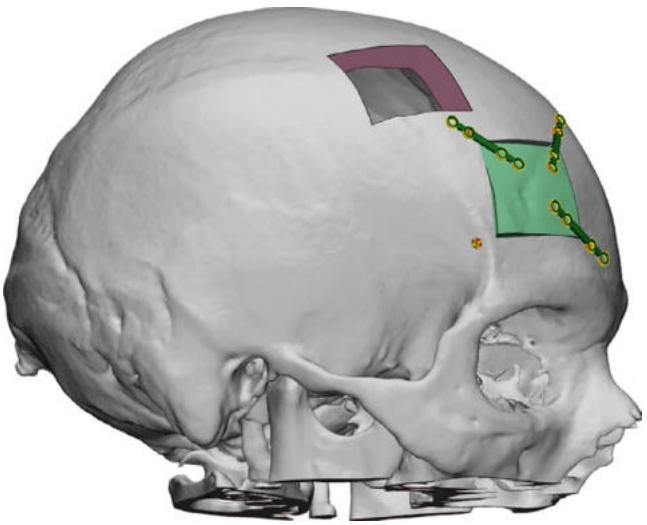


Fig. 9 Located graft is repositioned over the recipient site to assess its compatibility

3.2 All-in-One Surgical Guide

In order to maximize accuracy and shorten operative times, the author proposed an innovative device that can assist surgeons in all phases of surgery, including osteotomy for excision of the bone dowel containing the lesion; osteotomy in the donor site to harvest the graft; transfer of the graft to the recipient area; and plating and synthesis of the bone graft. As the graft is a partial thickness, outer calvaria, dowel, it's fragile and it should be handled with an adequate device. For this reason, the author developed an all-inclusive device called "all-in-one" surgical guide, which includes all such features [6]. The all-in-one surgical guide is composed of an outer rim and a core component (Fig. 10):

- The outer rim is primarily responsible for fitting properties and includes at its corners four holes for fixing the guide. The same holes are calculated to be coincident with the holes necessary to fix osteosynthesis plates. The inner edges of the outer rim are 45° bent, guiding the blade of the piezosurgical device to cut the bone not perpendicularly, but rather quite tangent to the calvaria, facilitating the separation of the diploic layer from the outer cortical bone.
- The inner component includes a handle for a more comfortable surgeon's experience and the holes and sockets for drilling holes and harboring osteosynthesis plates. Two central holes, with a locking mechanism, are needed to fix and tighten the graft to the guide, while the four peripheral holes placed at the corners enable osteosynthesis. In addition, the bottom surface of the guide has four sockets that contain the plates fixed to the graft. In this

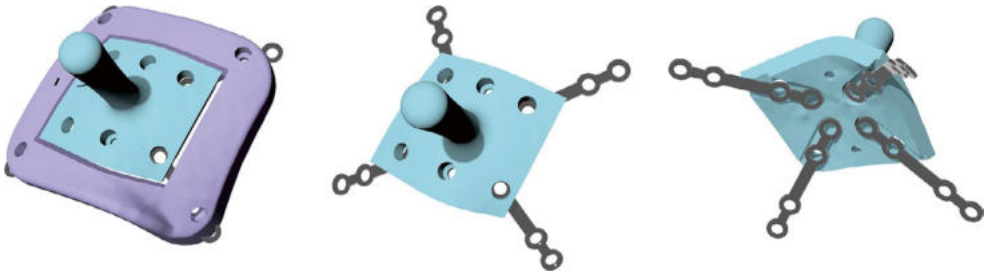


Fig. 10 Design of the all-in-one surgical guide

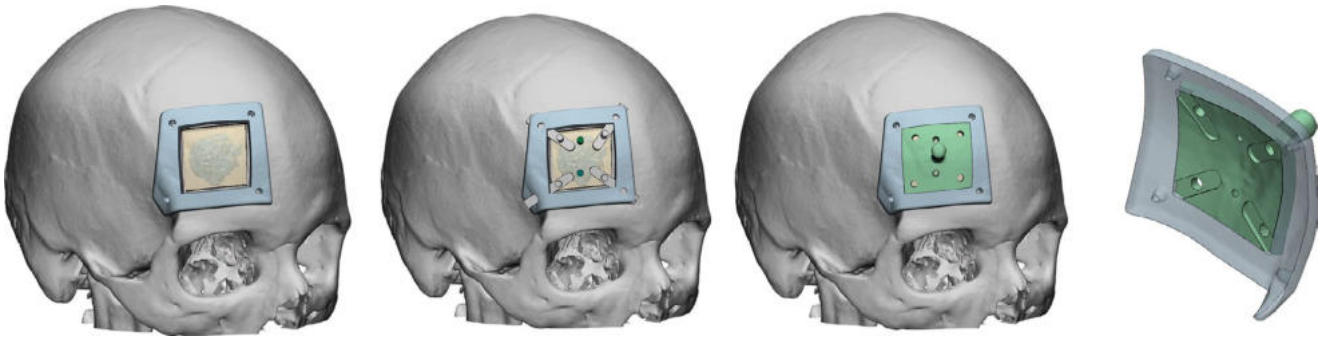


Fig. 11 Virtual surgical positioning of the all-in-one guide on the patient's skull and overview of sockets for plates on its inferior surface

way, the surgeon can manipulate the guide and transfer the calvarial graft with plates and screws already in place to the recipient site, where predrilled holes are located already in the right position using the outer rim component.

To optimize design of the guide, it would be ideal to already have in mind which plates and screws are going to be used. The same fixation devices should be transferred to the surgical planning by CAD design or high-resolution optical scanning and reverse engineering. As a result of the precise fitting mechanism between the outer rim and the core component, and considering the congruence between the base of the core component and the harvested graft, the result is the precise correspondence between the repositioned graft and the osteotomy site.

3.3 Clinical Case

A young woman presented to our attention for dumb pain located in the left fronto-temporal area of the skull. CT scan revealed a lesion with well-defined margins located within the bone thickness, which resulted to be an eosinophil granuloma. VSP with segmentation of the intraosseous lesion and design of the all-in-one surgical guide was accomplished (Fig. 11).

The hemicoronal access is the most favorite way to simultaneously expose both the lesion and the donor area. The incision must be carefully planned based on the location of the donor area observed at the surgical planning. Intuitively, it is preferrable to identify an ipsilateral donor area to use a single surgical access. The space between the galea and the pericranium, containing the areolar loose tissue, is dissected to facilitate mobilization of the flap. An incision is made within the pericranium, continuing to the deep temporal fascia, a prosecution of the pericranium itself, to increase the rotation arch of the flap and hence the exposure. Subperiosteal dissection is carried until the desired areas are exposed. The assembled surgical guide including both components in positioned as a whole to maximize the fitting surface and avoid malpositions. The outer rim component of the guide is then fixed using the four holes provided at its corners (Fig. 12). Due to the thinness of the splint calvarial graft and the presence of the underlying dura mater, the use of a piezosurgical handle is mandatory. The lesion is excised within a bone dowel corresponding to the osteotomy in the surgical planning.

Concerning reconstruction, the core component is positioned in the site identified during surgical planning. The two locking holes of the guide are used to fix the central component to the calvarial bone. The piezo-osteotomy is drawn all around the core component, which is then removed. Using a chisel and changing the inclination of the piezosurgical

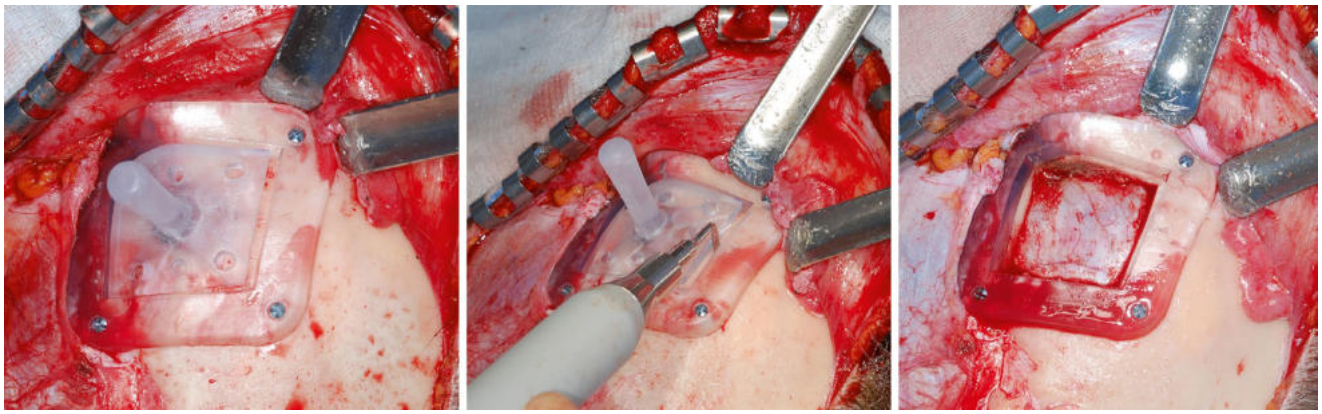


Fig. 12 Surgical positioning of the guide and excision of the lesion using its ring component, leaving exposed the underlying dural layer

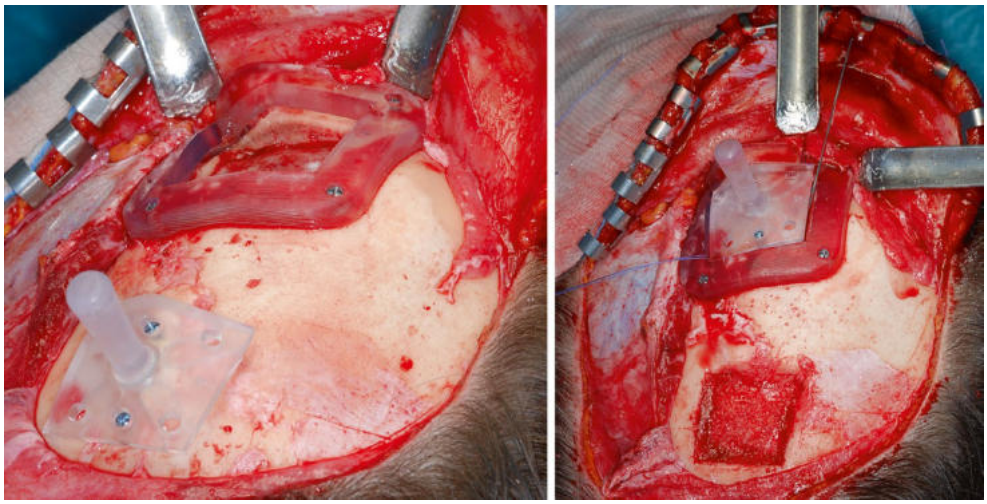


Fig. 13 Positioning of the internal core component on the donor site to perform the split-thickness grafting procedure

blade, the separation of the outer calvaria through the diploid layer is meticulously performed, and the partial-thickness graft is harvested (Fig. 13).

The split graft is then fixed to the core component, and plates are inserted between the graft and the guide itself using the appropriately designed sockets, which allow to already stabilize the plates to the graft using screws inserted through the holes within the sockets. Like a shuttle, the graft is transferred to its recipient site with plates already in the correct place, and, once in place, the distal hole of the plate will match the predrilled hole achieved using the outer rim guide (Fig. 14). Notably, the whole process is assisted by a unique, all-in-one, surgical guide to match not just the size and orientation of the graft with the recipient site, but also the correspondence of each hole with its screw (Fig. 15).

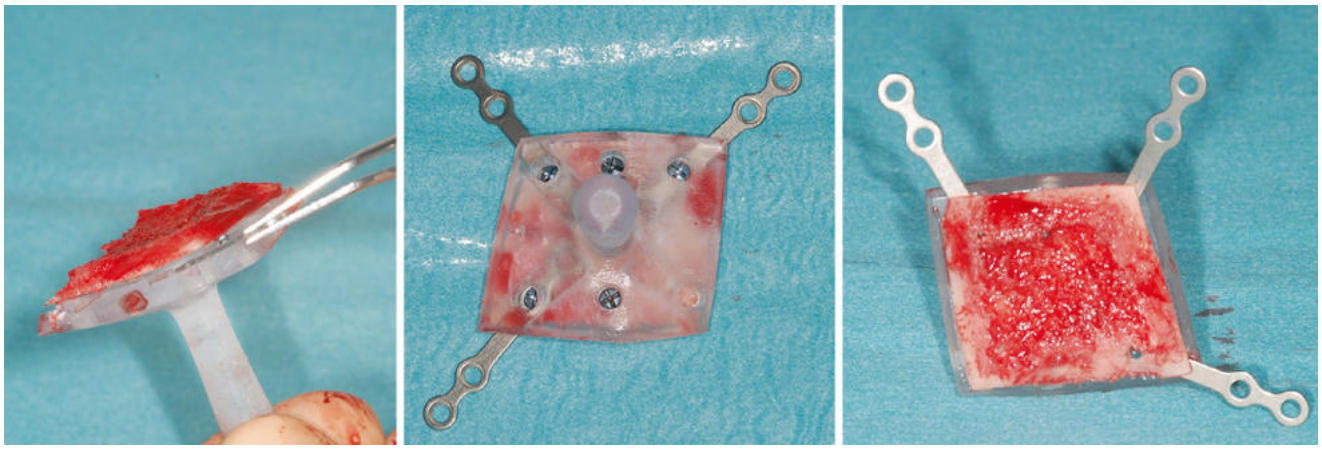


Fig. 14 Loading of the graft onto the core component, which represents a sort of "assembly platform" where the split graft is plated and prepared to be transferred on the recipient site

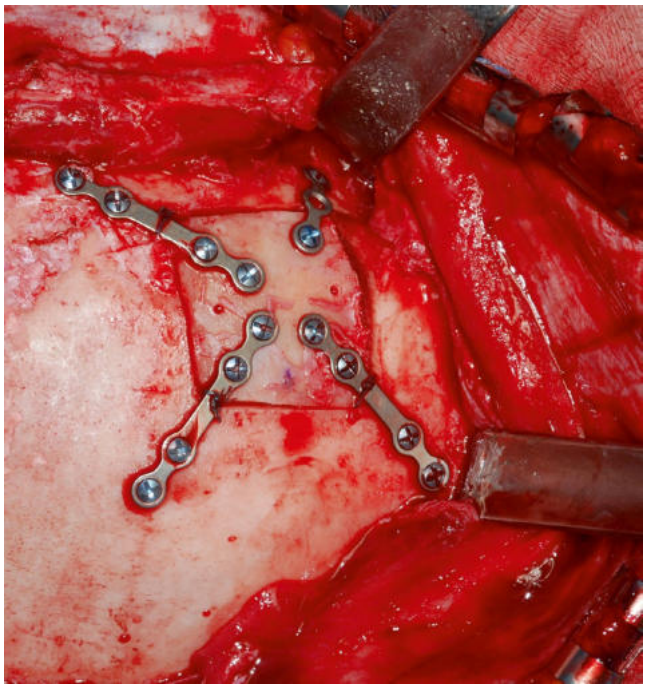


Fig. 15 Final appearance of the reconstruction. The graft has perfect adherence with the argins of the resection site, congruence is maximal and gaps are minimal, allowing for improved integration

4 CAD-CAM Molds for Cranial Vault Reconstruction

Skull vault defects can significantly vary in terms of size, location, and shape. In addition, they can result from loss of substance due to traumatic injuries, resorption of cranial flaps after a craniotomy procedure, or they can be created during surgery to excise lesions with bone involvement. Although it is not possible to objectively differentiate between small and large defects using a numerical threshold, for the purposes of virtual surgical planning the author suggests the following criteria:

- Reconstruction of small defects can be easily performed by the spline method and always using the patient's anatomy without resorting to input geometries, including closest-template donors and statistical shape modeling. Even when they are located in a median area, the algorithm for spline interpolation is effective in reconstructing an accurate shape.
- Large defects often require an input geometry, consisting of a mirrored counterpart for sided defects and a closest-template donor geometry or a statistical shape model for median or extremely large defects extending beyond one half.

Cranial molds represent an excellent solution for the intraoperative conformation of implantable prostheses, enabling hospitals to self-fabricate cranial implants during surgery in a considerably short amount of time, using commonly available polymethyl-methacrylate, which has been used for decades to restore cranial vault defect. Although some authors have reported a manual fabrication of cranial molds using a 3D printed template to create a negative impression on the mold material, commonly silicone [7], our philosophy is to make the whole process digital by designing the molds within the CAD software. In this way, the operator can increase his control over the features of the molds, including creation of pin-holes structures, drainage channels, undercut removal, and written impressions [8].

The basic prerequisite to successfully reproduce a cranial implant using a pair of molds is that the planar projection on

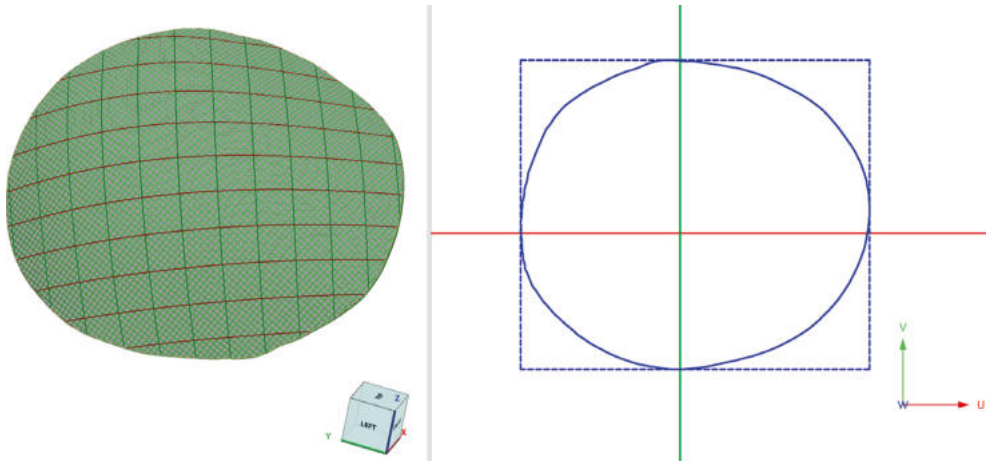


Fig. 16 UV planar projection of a traditional cranial plate for skull convexity. Checker map is correctly represented without any distortions, thus confirming that a planar mold can represent both surfaces of the implant

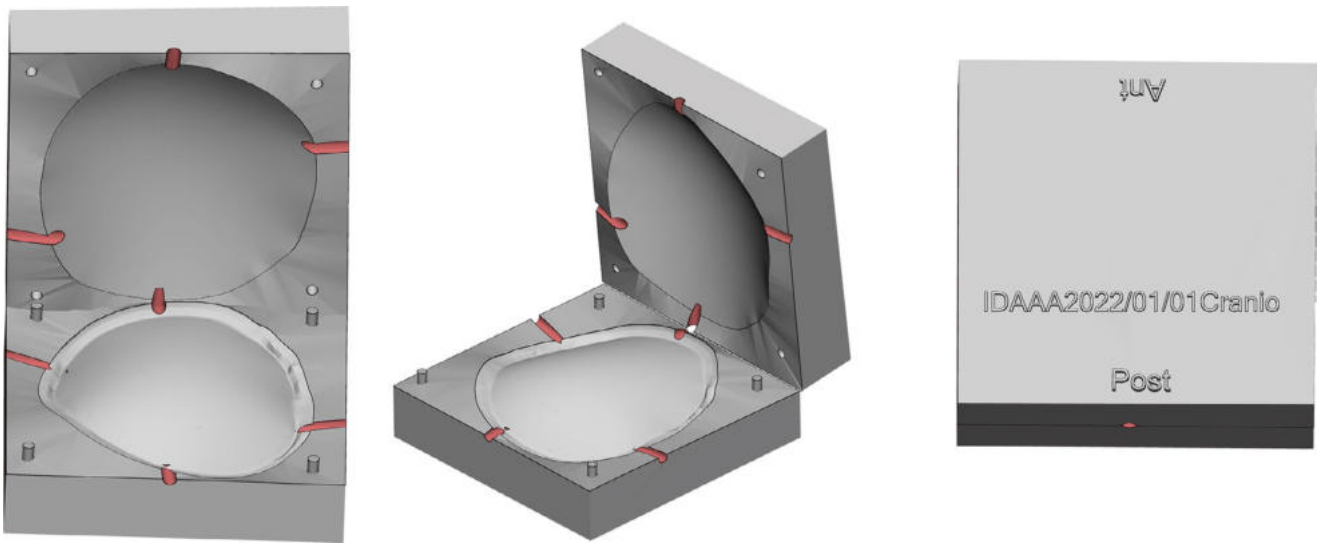


Fig. 17 Molding system for cranial implants designed using 3-matic. Salient features are extrusion channels to improve filling of the molding chamber, pins and holes at its corners for maximal correspondence, and ID and coding of the patient for univocal identification

the U-V plane of the simulated implant across its upper and lower face originates two separate, non-intersecting entities [9]. The UV seam must be chosen so that it divides the implant into two halves, the convexity and the concavity; the thickness of the plate can be associated with any of them independently. Basically, one projection for each face is able to unfold the geometry into a planar representation. Satisfying this criterion ensures that the three-dimensional geometry of the implant can be successfully reproduced by two stacked molds (Fig. 16). Once the convexity and the concavity have been identified, they provide the core to construct the mold. Basically, a box is built around the implant, which represents the cage of the mold, and is then split in two halves across the selected seam between the concave and the convex surface (Fig. 17).

4.1 Small Convexity Defects

As mentioned, describing the general features of cranial vault defects, small defects of the skull convexity, or vault, can originate both for loss of substance caused by trauma, resorption of bone flaps after a craniotomy procedure, or resection performed for oncological purposes. In the first two cases, reconstruction is delayed, while in the latter circumstance, it is simultaneous with the reconstruction. From a practical point of view, the clinician dealing with the surgical planning of small defects will be able to adopt automated algorithms for skull vault filling without the need to resort to external input geometries, including self-mirroring, closest-template donor, statistical shape modeling and anatomical subunit compositing. In the first phase, the operator will circumscribe the defect

(in case of post-traumatic or post-surgical defects) or will define the boundary for craniotomy to excise a lesion within safe margins. The definition of the outline of the cranial geometry will provide the contour to build the reconstruction. Subsequently, the user will need to define an ideal contour to drive the construction of the virtual prosthesis, for instance, by placing a sketch intersecting the orthogonal projection of the skull vault around the defect. This is basically the definition of the spline method, and work with automated algorithm, including the "create cranial plate" function in 3-matic.

Hereby the Authors will present a list of cranioplasties performed for small size defects with varying locations, sizes, and features. Most importantly, all cases were treated using an in-house protocol for the intraoperative modeling of polymethylmethacrylate, using 3D printed molds. As previously described, such cranial plates can be effectively defined by an inward and an outward face, and can be successfully reproduced in the UV plane.

4.1.1 Case 1: Temporo-Parietal Excision of a Skull Vault Osteoma

A 70-year-old lady presented for neurosurgical attention for progressive onset of a hard protuberance located over the right temporal area. CT exam revealed a substantial alteration of the bone with was related to an osteoma. The patient underwent subsequent resection and simultaneous reconstruction of the defect. Resection area was planned in red color to include the full mass, and its inner surface was designed slightly smaller to achieve a bevel edge able to support the positioning of the plate. Resulting reconstruction was performed using the spline method and successfully reproduced the contours of the surrounding cranial vault (Fig. 18).

4.1.2 Case 2: Occipital Reconstruction of a Skull Vault Defect Originated from Resorption of a Craniotomy Flap

A 65-year-old gentleman came to our attention for a gross alteration located in the occipital area after a previous occipital craniotomy. In this case, the bone flap underwent almost complete resorption, and there was no contact between its edge and the outline of the defect. During virtual planning, the craniotomy flap was isolated and hidden to expose the boundaries of the skull vault defect. A customized plate was designed fitting the remaining bone spikes across the edge of the defect, which acted as a support for the overlying cranial plate. Molds were designed according to the features of the virtually planned plate (Fig. 19).

4.1.3 Case 3: Reconstruction of a Parietal Midline Defect Originating from Previous Trauma

The defect is median in this case, but an external input geometry is not necessary because of the limited size, which allows the algorithm for cranial plate reconstruction to work effectively. In the sagittal view, it is evident that the convexity around the vertex capitis has been effectively restored. Owing to the irregular margins of the pre-existing defect, it is important that the resulting cranial plate is designed with a complementary geometry, able to engage all the spikes and slots of the receiving bone. Even if the curvature radius of this prosthesis is increased compared to previously presented cases, it is perfectly reproducible using a dual-component molding systems (Fig. 20).

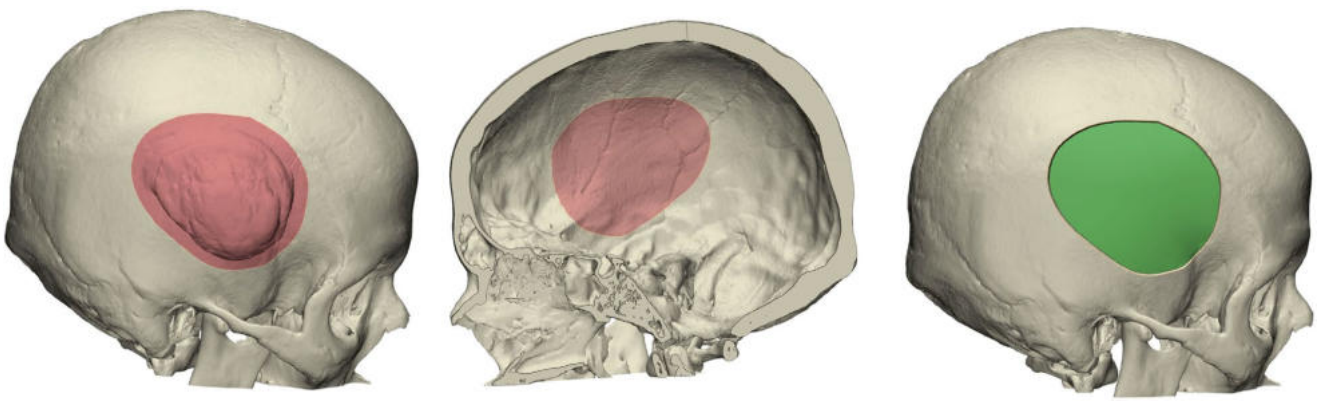


Fig. 18 Planning of a one stage resective-reconstructive procedure for a temporo-parietal osteoma. Edges are clean as the resection was computer planned

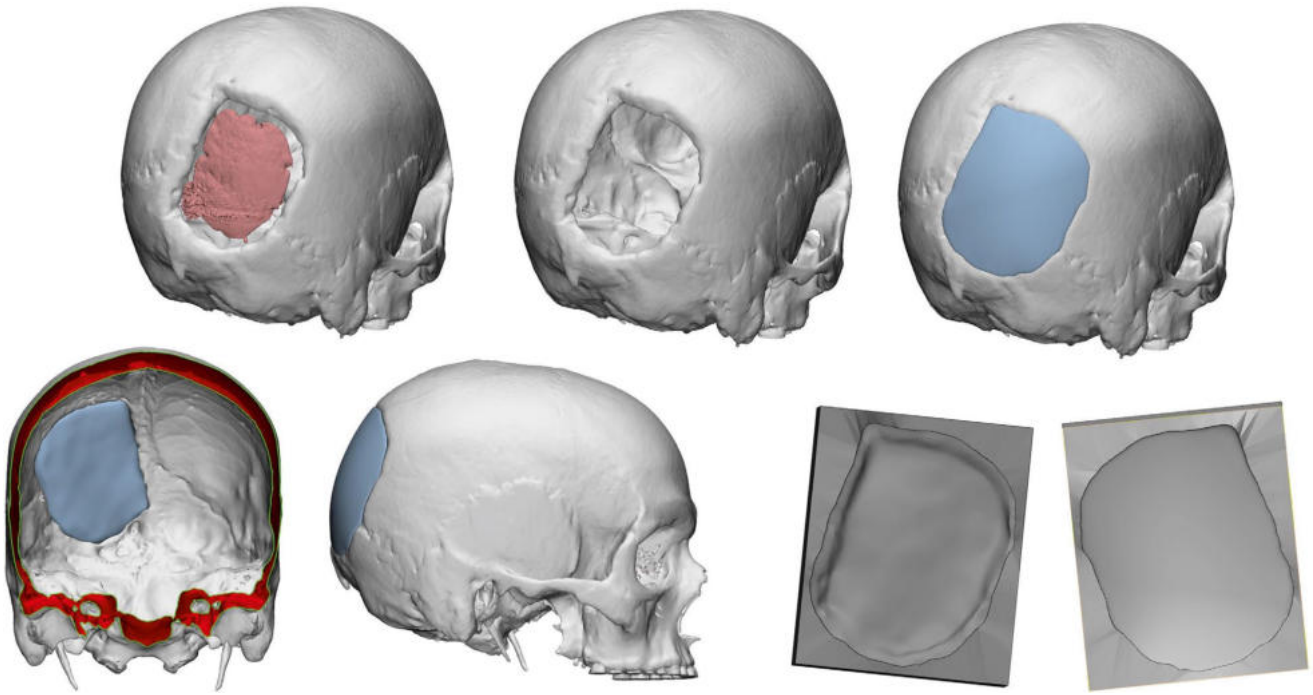


Fig. 19 Planning of reconstruction of a previous occipital skull defect. Complete resorption of the bone flap required its removal. Reconstruction was performed on a very irregular defect

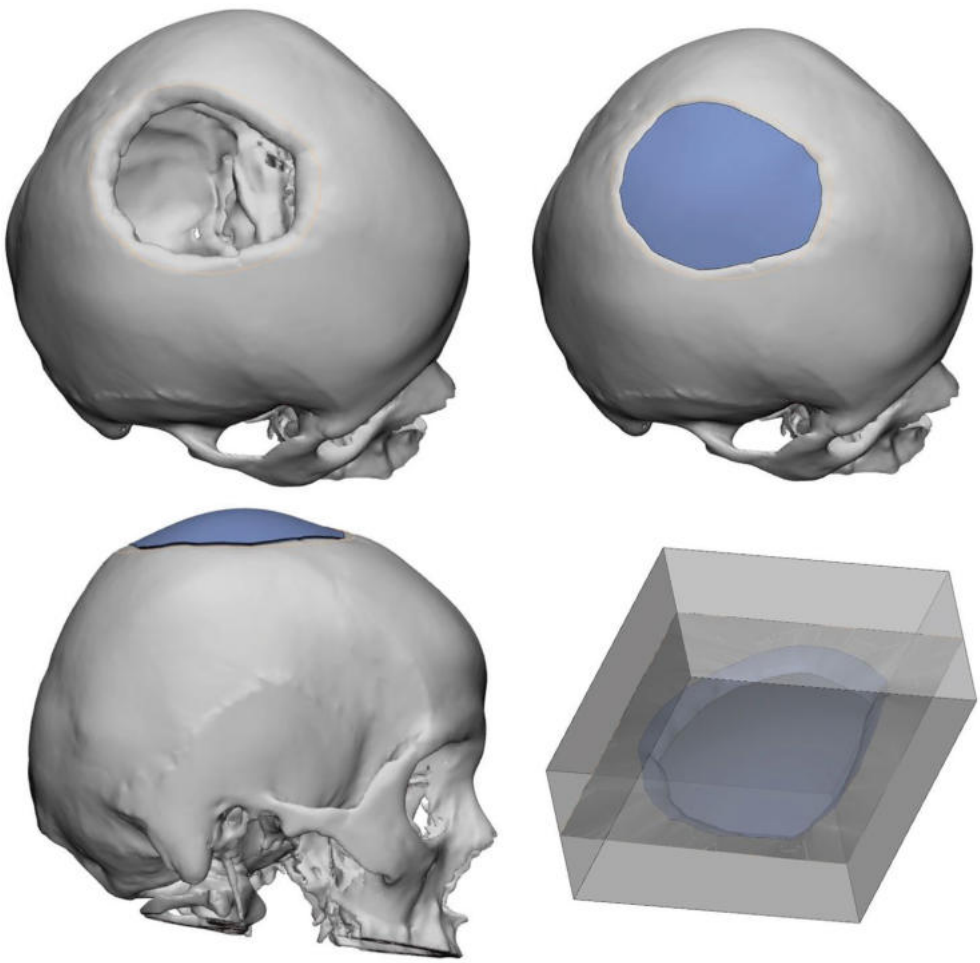


Fig. 20 Planning of reconstruction of a convexity defect around the vertex region. The plate was designed to restore the appropriate skull curvature at its maximal point and to fit the irregular margins of the defect

4.1.4 Case 4: One-Stage Resection and Reconstruction of Parietal Meningioma

In this case, a craniotomy is performed, and the virtual surgical planning itself includes a clean margin contour around the defect, which is intraoperatively replicated thanks to computer-guided methods, including intraoperative navigation or a surgical guide. As previously mentioned, the inner surface of the craniotomy is designed slightly smaller in size so that the resulting craniotomy edge is tapered, providing the necessary support to the cranial plate. In this case, the planned implant has very clear edges, which are geometrically coherent with the margins of craniotomy (Fig. 21). This method allows for immediate cranial vault reconstruction, which can be adapted to the needs of radicality during resection.

4.1.5 Surgery: One-Stage Resection and Reconstruction Using Dual Molds for Skull Vault Reconstruction for a Small Defect

A skin flap is raised, continuing down to the pericranial layer; in regions critical for the frontal branch of the facial nerve, a temporal subfascial approach is used. In case of single-step resection and reconstruction, the craniotomy is performed under navigational guidance to match the shape of the planned reconstruction. Once the lesion is excised, PMMA is intraoperatively molded in the operating room to achieve the desired implantable cranial plate. In case of slightly excess of material, PMMA implant can be refined by smoothing its margins or by flattening possible prominences responsible for undercut using a rotating bur. The preparation of the plate and the eventual remodeling are performed in a sterile operative field, which is kept separate from the surgical field to prevent possible PMMA debris contamination. Once the plate is positioned in the desired position, it is secured using titanium thin plates and screws, and holes are drilled in the implant to perform dural suspension and prevent accumulation of blood between the dura and the implant (Fig. 22). All layers are sutured, and a drainage is placed in position.

4.2 Large Convexity Defects

Large convexity defects have the same etiology of their smaller counterparts; however, they most often result from resorption of large flaps after decompressive craniotomies, extended neoplasms with vast resections and highly disrupting trauma with loss of substance. Compared with small defects, the reconstruction of large ones most often relies of external donor sources of geometry, including mirroring, closest-template donors, and statistical shape models. However, in several cases, especially when contour margins are well defined, the spline method might also work and provide excellent results, especially when the defect is located in an area of regular curvature, which the algorithm can easily interpret.

4.2.1 Case 1: Massive Relapse of Intraosseous Occipital Meningioma with Intracranial Extension

The following example refers to a relapsing meningioma with massive intracranial extension. The patient was already operated, and the previous craniotomy outline is visible. Considering the intracranial extension of the tumor, representing two-thirds of the whole bulk of disease, a very large craniotomy was planned, with a superior extension enclosing

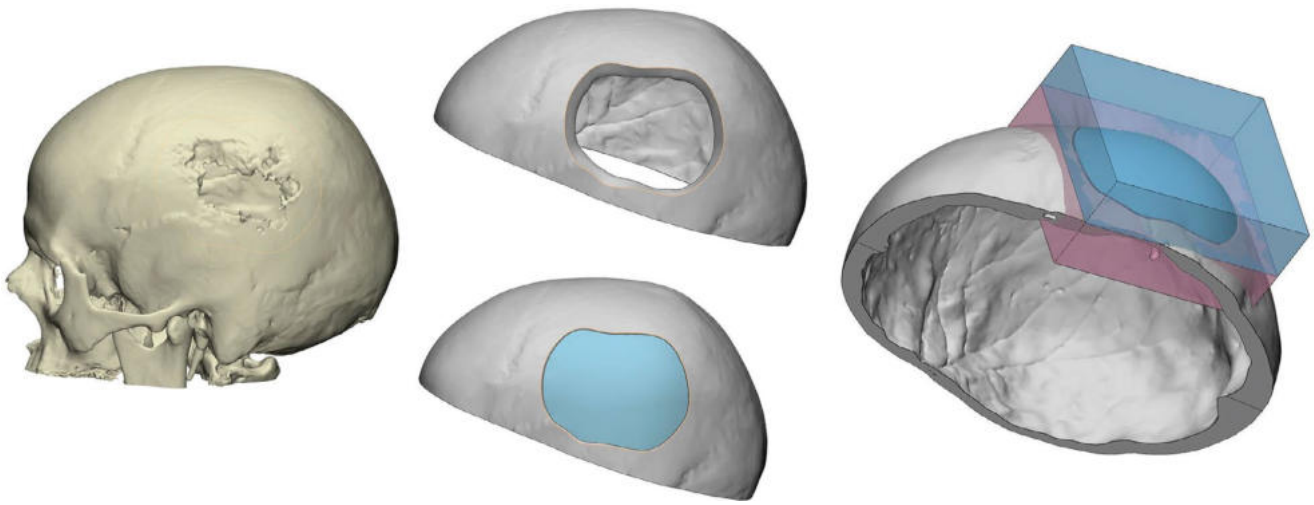


Fig. 21 Resection and reconstruction of a parietal meningioma causing bone erosion. Due to the clean margins of resection area, reconstruction was performed using the anatomical CAD method

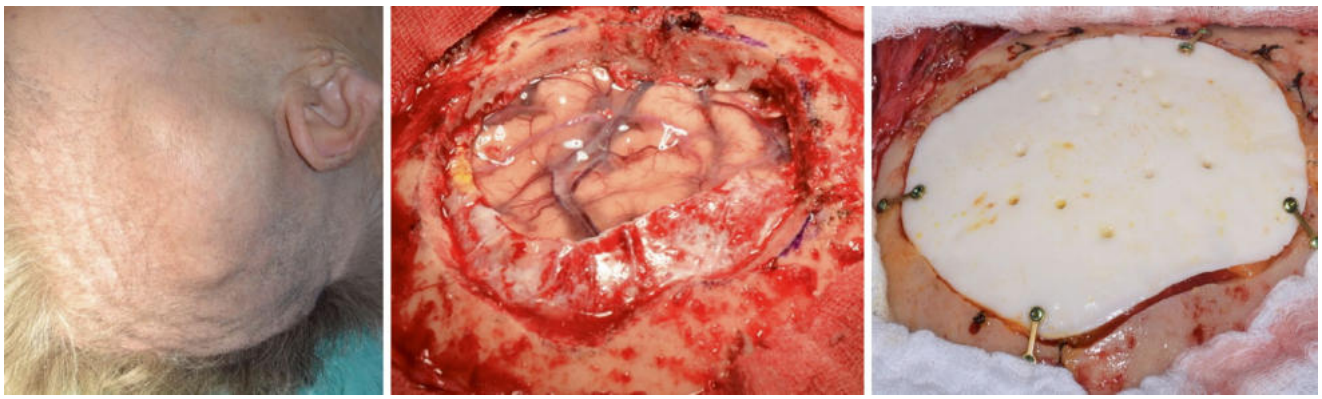


Fig. 22 Intraoperative overview of the patient in Fig. 18

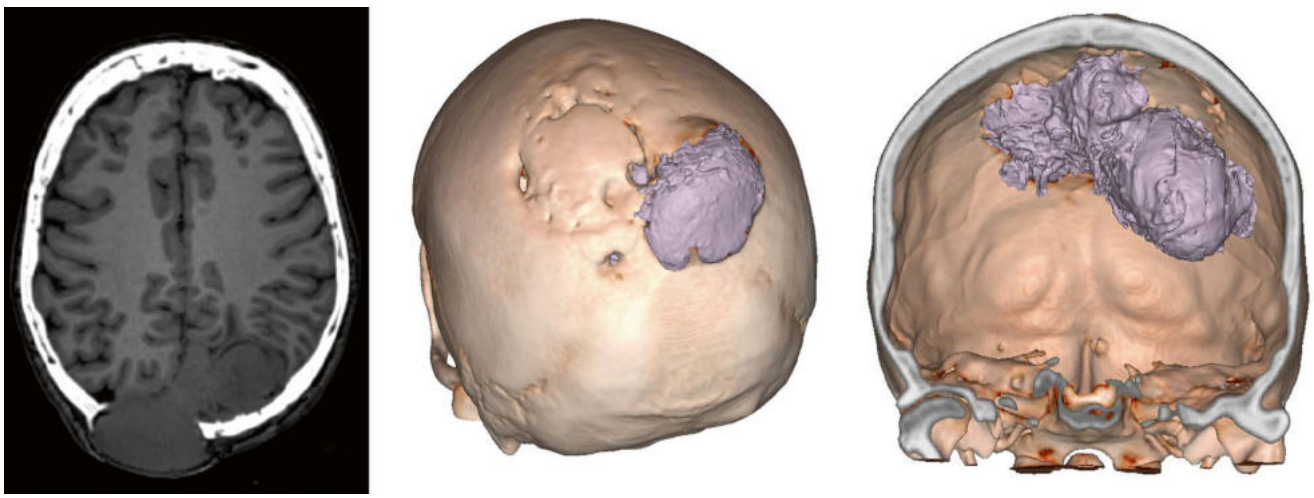


Fig. 23 Fused CT-MR image and virtual reconstruction of a large parieto-occipital meningioma

the previous craniotomy flap, which underwent partial resorption. Therefore, a trilobed craniotomy was performed to excise the disease with clean bone margins, and a simultaneous reconstruction was planned (Fig. 23).

After the craniotomy flap was planned in 3-Matic, and a geometrically precise defect outline was determined as a contour curve, the operator planned multiple splines to provide the algorithm with the ideal curvature of the cranial implant. In this case, the spline method was used and the "create cranial plate" algorithm could effectively construct the implant design, to which a 1 mm offset was applied to avoid possible interferences with intervening bone fragments. The implant shape was further refined and optimized for the intraoperative use applying a "remove undercut" command. Once the design was approved, CAD-CAM paired dual molds were modeled, including channels for exceeding material extraction, and were 3-D printed for intraoperative use (Fig. 24).

4.2.2 Case 2: Relapse of Meningioma Along the Margins of a Previous Large Craniectomy

In another case, a very large, midline-crossing defect is represented, following the excision of a very large meningioma with intraosseous infiltration. At preoperative imaging, margins of the bone defects resulted to be still infiltrated by remaining disease; thus, the operator planned an extension of the resection, performing a craniotomy around the existing border with a 3 cm safety margin. To improve the accuracy of craniotomy planning, a virtual model of the residual disease involving bone margins was simulated.

Clean margins of the simulated craniotomy were achieved by precise surgical planning, and a geometrically defined defect outline was achieved (Fig. 25). In this case, considering that the defect extended beyond the midline and included the point of maximum curvature of the skull vault (the convexity), the application of the spline method led to subopti-

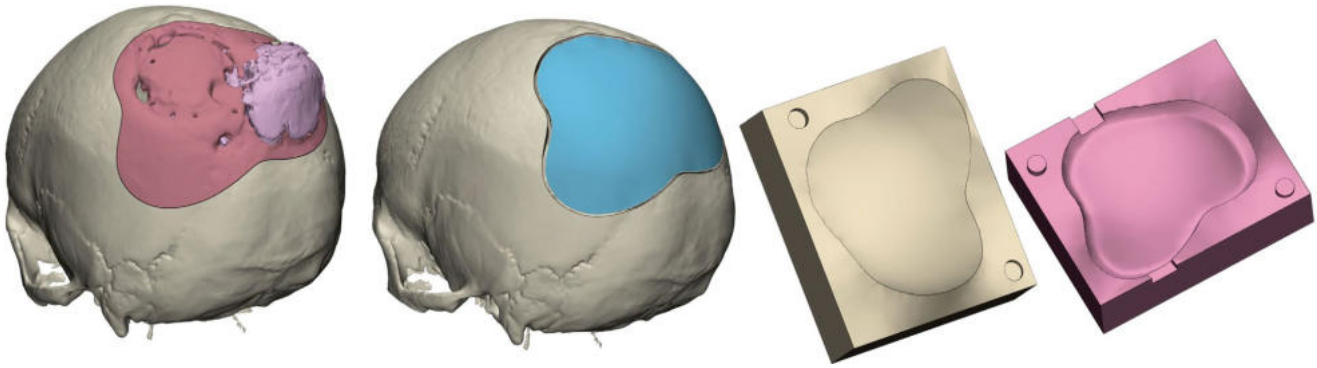


Fig. 24 Virtual surgical planning and mold creation

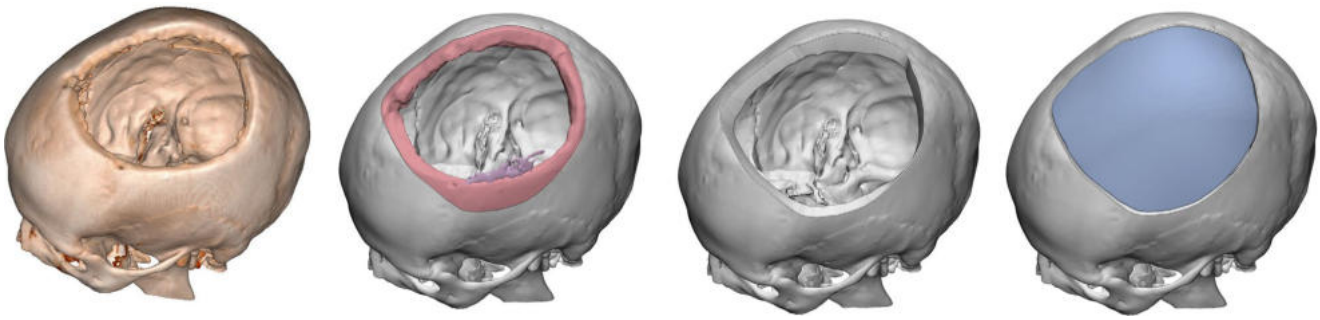


Fig. 25 Ring-resection of bone margins infiltered by intraosseous meningioma and creation of the plate. Owing to the size of the defect and the fact that it crossed the midline, reconstruction was performed using the closest-template donor method

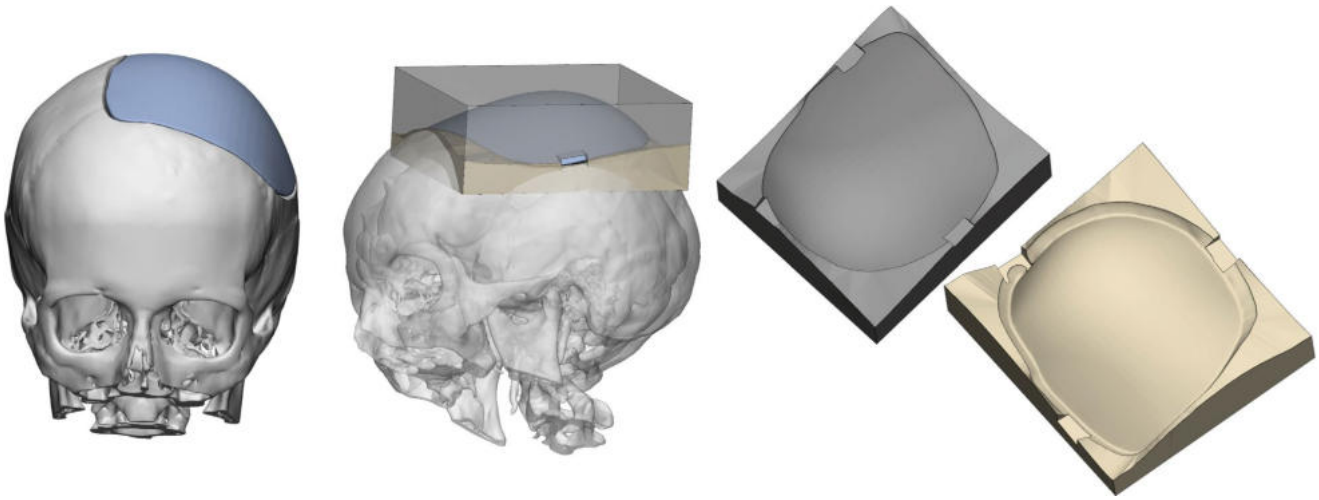


Fig. 26 Although the implant curvature was significant due to the large part of skull to reconstruct, two-component molds were successfully used to reconstruct the implant

mal results. Therefore, a closest-donor template was identified and manually fitted to the recipient skull, and the cranial plate was modeled according to the donor geometry, made suitable for the margins of the recipient skull. Also in this case, the author preferred to keep a small offset of 1.5 mm to prevent possible interferences while positioning the plate. A pair of planar molds were designed and planned for the intraoperative modeling of the plate (Fig. 26).

4.2.3 Case 3: Cranial Vault Osteosarcoma

In this example, an apparently small defect caused by bone erosion from a malignant skull vault osteosarcoma was con-

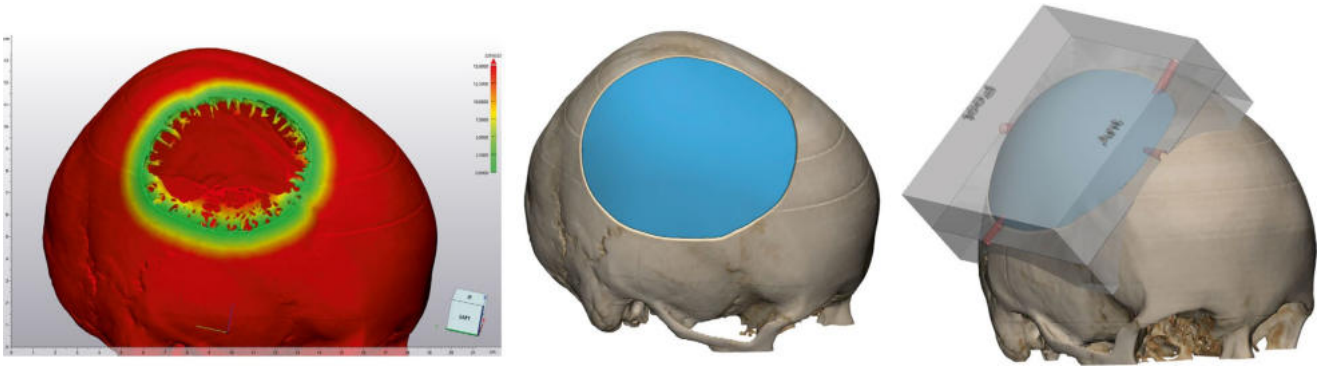


Fig. 27 Surface-to-curve analysis to assess the distance of surface points from the curve and establish the magnitude of resection margins



Fig. 28 Resorption of a bone flap after a decompressive craniectomy. Virtual removal of the remaining bone and of fixation devices (screws and plates) and design of the cranial implant performed on a highly irregular geometry with rugged edges

verted into a large-size defect by planning a craniotomy to excise the lesion within safe margins (2 cm). First, a bone-fitting curve was traced around the lesion to circumscribe it, subsequently, a distance-to-curve algorithm was applied to compute a graphical scale defining the distance from the visible lesion, providing an aid to plan a margin-free craniotomy. Following the contour indicated the color scale, a second curve was designed around the surgical bone margins to define the outline of the craniotomy. The resulting defect was far larger than it appeared on the volume-rendered 3D CT scan, posing challenges concerning the reconstruction, considering that the defect outline was tangential to the midline and the vertex (Fig. 27).

4.2.4 Case 4: Wide Defect Resulting from a Previous Decompressive Craniectomy

In this example, a very large defect was created in a previous surgery to perform an emergency decompressive craniectomy for a severe head injury. Once the flap was repositioned, it underwent massive resorption, and only little bone spikes remained covering the brain. During virtual surgical planning, the operator performed the virtual removal of all plates and screws, leaving only the skull vault to avoid any possible inaccuracies of the designed implant caused by the interposition of osteosynthesis devices. Similarly, thin bone residuals from the previous bone flap were removed to highlight bone margins of the defect. Subsequently, considering the magnitude of the defect and the unavailability of a clean craniotomy contour, owing to irregular, jagged edges of the defect, a closest-template donor method was chosen to achieve the final design of the implant. The edges of the resulting plate showed geometrical congruence with the margins of the defect, improving fitting of the implant on the recipient site anatomy (Fig. 28). As a consequence, the negative impression on the molds had the same features (Fig. 29).

4.2.5 Surgery: One-Stage Resection and Reconstruction Using Dual Molds for Skull Vault Reconstruction for a Large Defect

The surgical approach is similar to that described for small skull vault defects. In this particular case, a trilobed craniot-

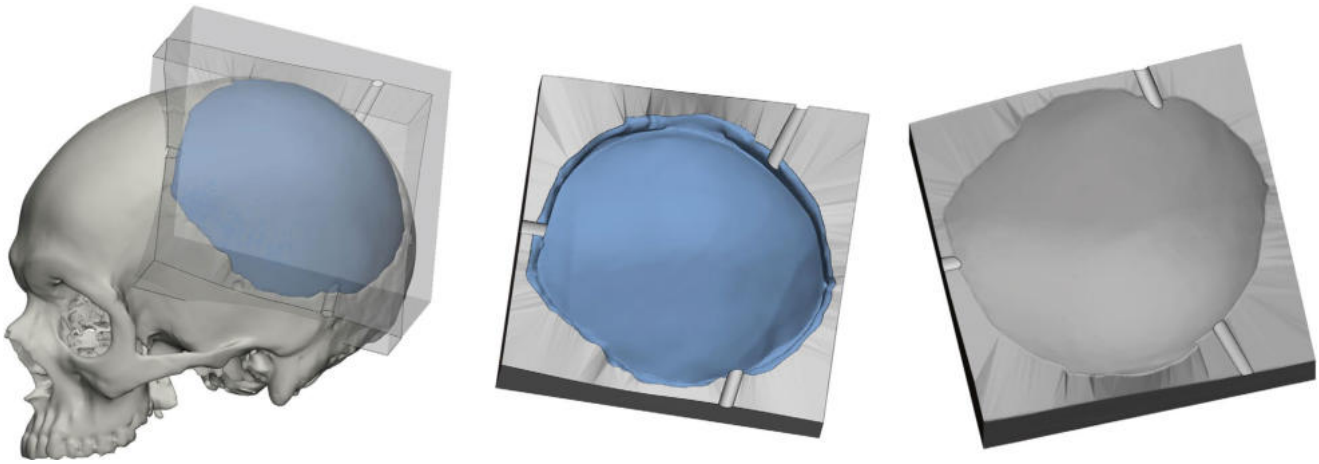


Fig. 29 Design of the two-component molding system. This method is suitable also for very large defect

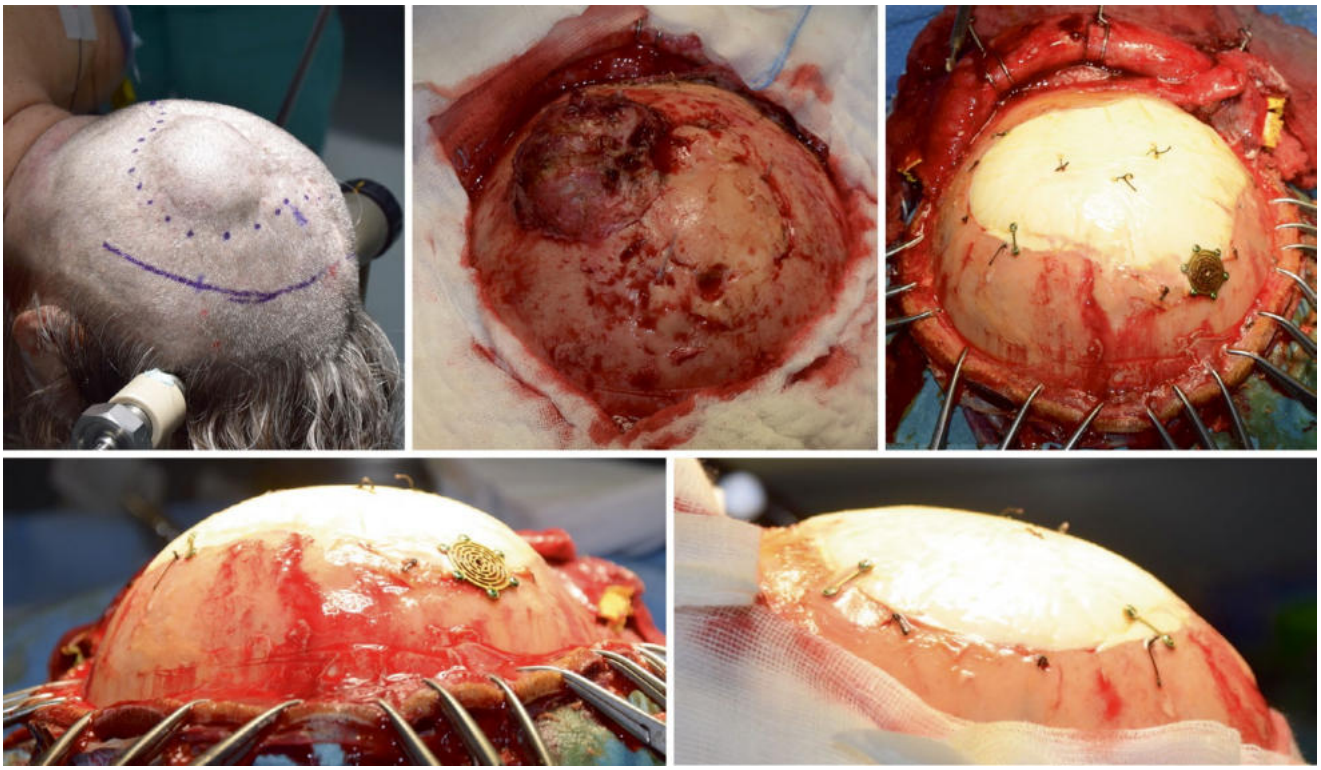


Fig. 30 Surgical phases illustrating the case presented in Figs. 22 and 23

omy was performed to include the whole meningioma beyond both sides of calvarial bone, the bone flap of a previous craniotomy, and the area overlying the intracranial extension of disease. Navigation-guided resection of bone according to the virtual surgical planning was followed by microsurgical dissection of the tumor mass from the healthy brain parenchyma, and accurate hemostasis was performed within the resection cavity. The creation of the PMMA prosthesis was performed using dual-paired molds and allowed to effectively restore the geometrical curvature of the cranial vault (Fig. 30).

4.3 Pterional Defects

Pterional defects have the peculiarity that they are not defects of the sole convexity, but they lie on the borderline with the skull base. The great sphenoid wing, whose lateral aspect

composes the outer skull wall in the pterional region, is part of the sphenoid, which is predominantly a skull base bone. Moreover, the free edge of the lesser sphenoid wing is in direct contact with the outer cranial wall, altering its curvature along its inner aspect. The result of such geometrical considerations is that the spline method less reliable for pterional defects. On the other hand, pterional defects are usually more limited in size than their counterparts over the skull vault convexity, as they are often the result of a previous pterional craniotomy, and more infrequently they result from trauma. As a consequence, they are usually sided defects, meaning that the mirroring technique can provide excellent results for surgical planning. Notably, the mirroring technique must be combined with a poly sculpting technique to adapt the mirrored volume to the recipient site on the injured side.

4.3.1 Case 1: Large Pterional Defect Resulting from Bone Resorption After a Previous Craniotomy

The bone defect extended from the pterional region to the temporal region and can be classified as a craniolacunia due to resorption of a post-craniotomy operculum. It is of prominent importance to isolate and remove the operculum to effectively visualize the margins of the defect, which are highly irregular. On the inner aspect, it can be seen that the defect involves part of the lesser sphenoid wing and proceeds inferiorly down to the root of the zygomatic arch. A mirroring approach was used to design the final implant, considering that the implant has a non-uniform curvature that is hardly recognized by the spline algorithm. In the intracranial aspect, the operator decided to avoid reconstruction of a prominence corresponding to the lesser sphenoidal wing to facilitate plate placement; however, the designed implant enables to achieve satisfactory closure of the lateral skull base (Fig. 31).

4.3.2 Case 2: Small Pterional Defect Resulting from Bone Resorption After a Previous Craniotomy

This patient underwent neurosurgical clipping of an intracranial aneurysm with a pterional access. The cranial flap was repositioned but it underwent resorption, and an infection developed on the surgical site which complicated wound healing. In this case, the defect included the lateral half of the lesser sphenoidal wing, and extended anteriorly almost at the level of the lateral orbital rim. An adaptive mirroring approach was used to mirror the contralateral healthy side, which was then polysculpted to ensure optimal fit with the recipient site. Particular care was taken during surgical planning to reconstruct the correct intracranial anatomy, which was reported in a simplified version on the cranial implant, to ensure the optimal fit. The implant was then remodeled to optimize its contours to the edge of the craniolacunia and undercut was analyzed and eliminated. A couple of molds was designed and produced for surgery (Fig. 32).

4.4 Cubik System for Complex Cranio-Orbital Reconstruction: Overcoming Limitations of Two-Component Molds

In the most complex cases, disease process is not localized entirely within the cranial vault, but it may develop in the frontal region and extend down to the orbits. The superior orbital rim is contiguous with the frontal bone and the orbital roof; therefore reconstruction of this anatomical district has to extend to orbital components as well. Orbital geometry has peculiarities in terms of shape and morphology due to the complex spatial arrangement of its subcomponents; therefore great care is needed when dealing with the reconstructive phase of virtual surgical planning. Moreover, when a cranio-orbital reconstruction is projected across the UV

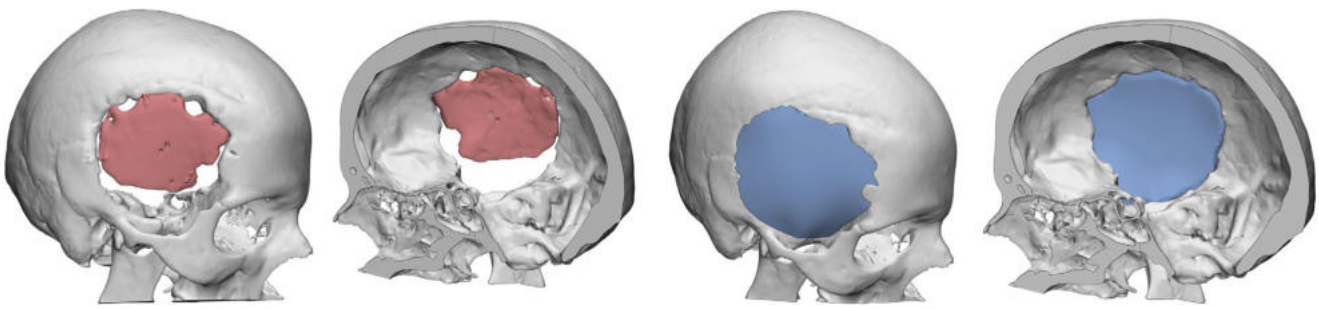


Fig. 31 Resorption of pterional bone after a craniotomy in the temporal region, with virtual removal of the bone flap to plan the cranial reconstruction. Margins are highly irregular and the plate must fit the irregular edge of the defect, at the same time providing an internal sealing

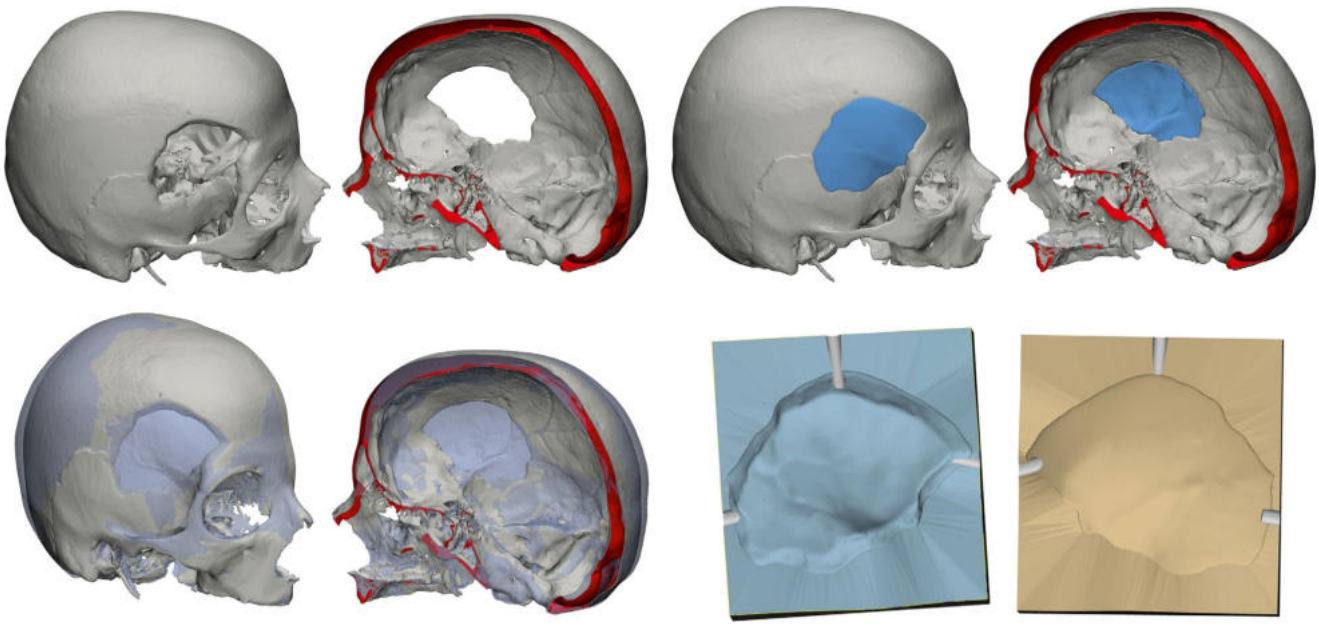


Fig. 32 Pterional defect in a case of previous neurosurgical access to treat an intracranial aneurysm. Adaptive mirroring is used to restore the skull vault paying attention to replicate the intracranial morphology as well

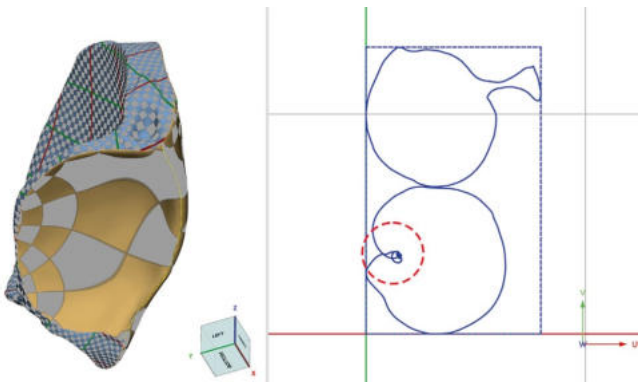


Fig. 33 UV planar projection of a cranio-orbital implant. The complex spatial morphology precludes a successful planar projection, demonstrating improper unfolding across the orbital roof. This is seen as a distortion in the checker map used and accounts for the impossibility to use two planar impressions to reproduce a cranio-orbital implant, making the dual-component molding system useless

plane, it fails to provide a planar image, resulting in distorted texture maps which do not successfully reproduce the checker map tester. In the example below, it is evident that UV distortion occurs all over the orbital roof, and this phenomenon is caused by overlapping seams within the UV plane due to the impossibility to perform a planar projection of the orbital roof and the orbital rim, as such structures show considerable twisting (Fig. 33).

The impossibility to achieve two planar projections makes the use of conventional molds useless in such cases, posing severe limitations to intraoperative fabrication of cranio-orbital prostheses. To solve this issue, the Author developed a multi-component mold system called Cubik system [10]. The name originates from the fusion of the terms "CUbe" and "ruBIK," referencing to the famous Rubik's cube. As the Rubik's cube can account for virtually unlimited combinations, the same does the Cubik system, a simple Cube-shaped mold, inside which sizes and splitting seams can combine in countless ways to replicate any desired shape. To allow the Cubik system to work, it is necessary first to define splitting seams of the desired object. The choice of seams is fundamental as it conditions the subsequent molds shape and undercut features, with a direct impact on the intraoperative ease of PMMA conformation and extraction after the molding process is complete. Although any patient and any resection type require a unique design for reconstruction, we identified a reproducible splitting pattern using three interfaces (Fig. 34):

- The external surface subdivision is assigned to the outer skull layer. This interface often includes the lateral and posterior margin of the orbital rim, which articulates with the zygoma. All anatomical prominences have to be respected as this outer part is responsible for the esthetical appearance of the implant,
- The internal surface subdivision is responsible for the definition of the intracranial space and the thickness of the final implant,

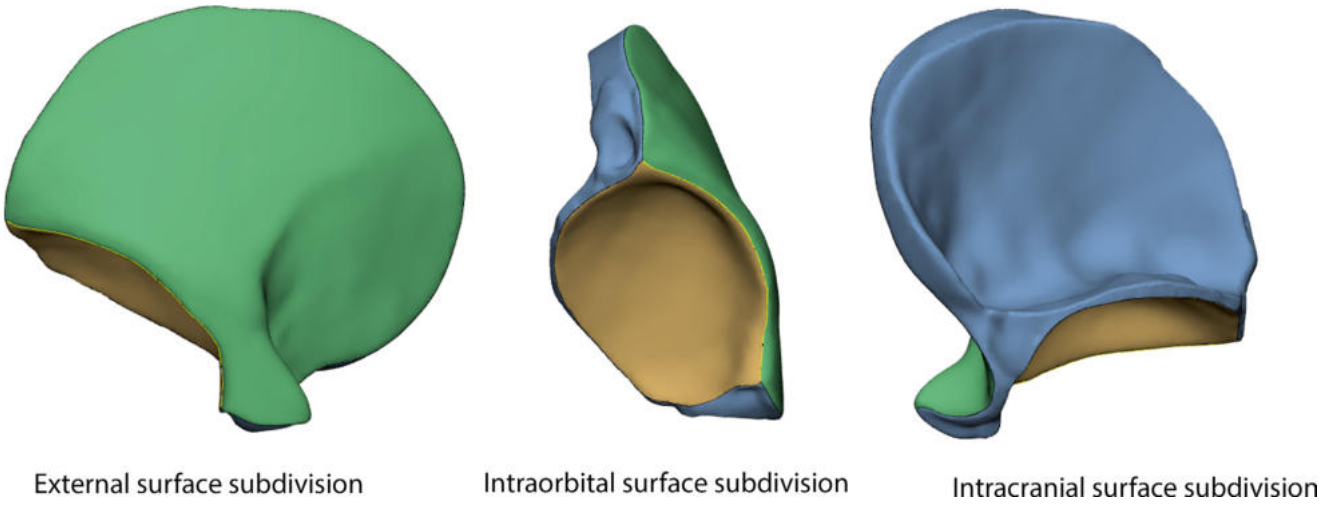


Fig. 34 Scheme for interface splitting in a cranio-orbital implant

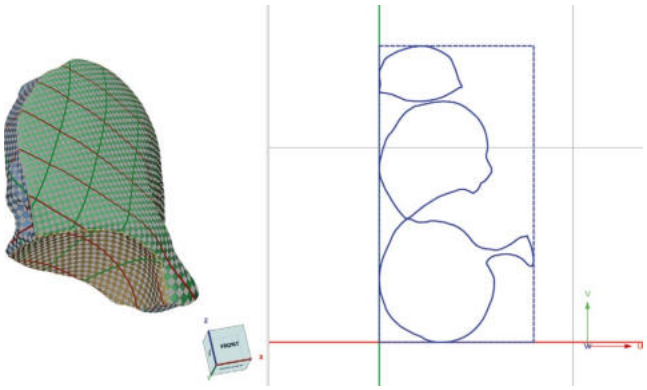


Fig. 35 Once the cranio-orbital implant is split into its three subcomponents, each of them can be successfully projected in the UV plane, and the checker map does not show any distortions. This means that three different mold components can successfully reproduce the desired implant

- The orbital roof subdivision accounts for the intraorbital surface of the orbital roof, which is defined together with its intracranial surface.

Once subdividing seams are identified and surface interfaces are defined, they are projected on the UV plane, yielding an appropriate subdivision pattern which is compatible with a planar representation and thus with a molding component. As Fig. 35 demonstrates, once the surface splitting is complete, the checker map tester is successfully projected over all subdivisions without any distortion. This means that the individual components of the future implant can be successfully replicated using a molding subunit. Intuitively, for cranio-orbital reconstruction, these considerations lead to the fact that a three-subunit molding system is required to effectively model a cranio-orbital implant in PMMA.

It is worth noting that, in contrast with traditional cranioplasties, whose effects on aesthetics are often mitigated by the presence of hair, especially in women, cranio-orbital reconstruction, if poorly performed, can have a detrimental effect on the patient's appearance, therefore great care is required when approaching such reconstruction, both in terms of virtual planning and surgery.

4.4.1 Cranio-Orbital Reconstruction for Defects Located in the Frontal Area

Clinical History

Defects involving a bone loss of the fronto-orbital region, including the superior and lateral orbital rim, can have both an iatrogenic and traumatic etiology. Most commonly, such defects are generated by the surgical excision of pathological processes developing within the bone or in nearby tissues with a bone involvement. In such cases, a virtual surgical resection is planned in the software and the defect is geometrically well-defined, accounting for a close-fitting reconstruction.

The proposed example refers to a case of intraosseous cavernous hemangioma developing within the orbital roof and the anterior skull base, the lateral orbital rim and part of the frontal bone. The patient presented with a story of slowly progressive left eye dystopia and the onset of diplopia, due to the downward displacement of the left eye globe caused by the mass developing predominantly within the orbital space (Fig. 36).

Virtual Surgical Planning

Resection area was identified while keeping a uniform 1 cm offset from the altered bone, in order to ensure a radical excision of the disease. To mark the site candidate for resection, a mark brush function was used, and the resection volume was refined by using a smooth marked borders function,

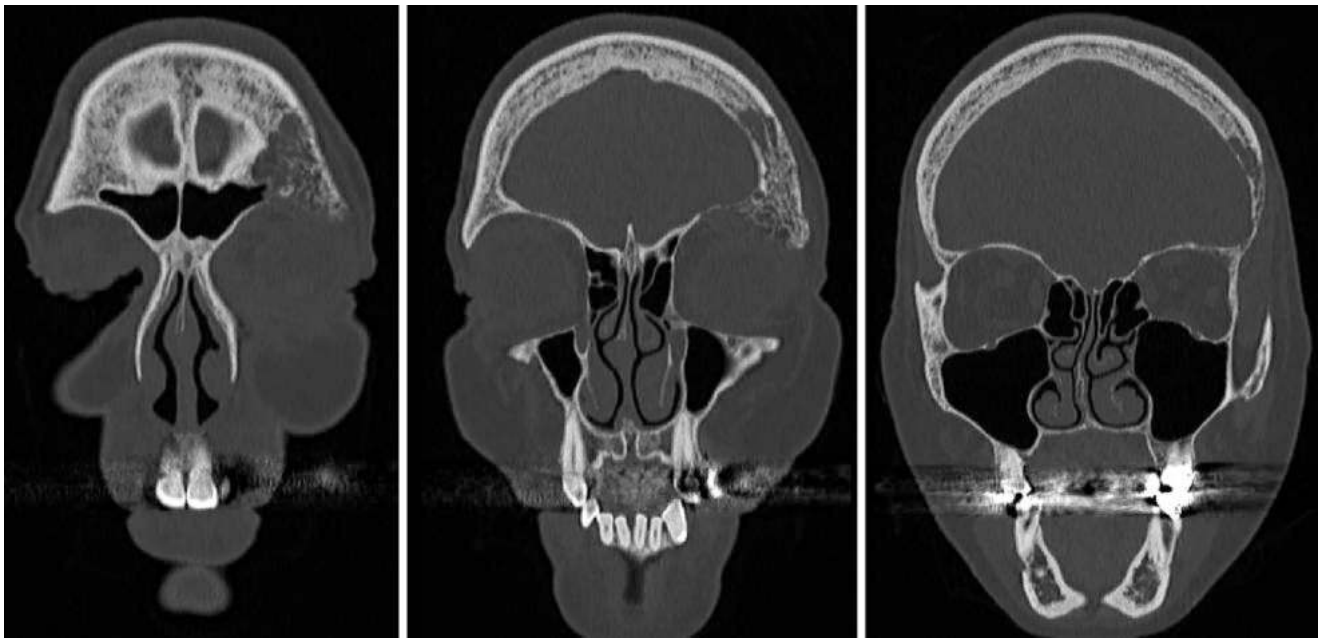


Fig. 36 CT appearance of a case of intraosseous cranio-orbital hemangioma of the fronto-orbital area

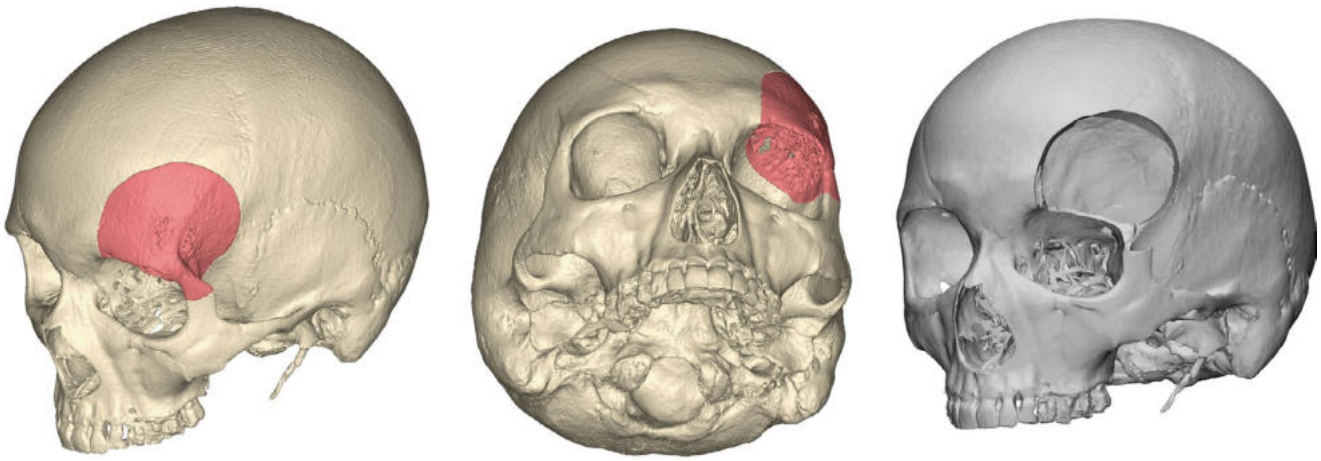


Fig. 37 Definition of resection area

yielding a well-defined surface both on the intracranial and the extracranial space corresponding to the planned resection (Fig. 37).

A mirroring operation was used to define the shape of the implant, which was subsequently refined by soft modeling to suit the mirrored anatomy with the edges of the recipient site. Once anatomical congruence was achieved between the margins of the prosthesis and the resection area, a Boolean operation was performed to maximize the fitting of the implant by subtracting the resected skull from the implant. The prosthesis was subsequently refined by smoothing unnecessary detail and removing undercut across interfering surfaces. Subsequently, the implant was split into three surfaces and seams were defined between the following subcomponents: orbital roof, lateral aspect, intracranial aspect. Each surface was defined by a mold, yielding a three-subunit Cubik system (Fig. 38).

Surgery

Intraoperative modeling of the PMMA prosthesis was performed by first applying a thin layer of liquid paraffine to the molds, to prevent sticking of the solidifying PMMA to the stereolithographic resin with subsequent failure to separate the molds from the prosthesis. PMMA was prepared by merging a powder phase with a solvent and yielding a soft paste which was poured within the molds, which were then closed and compressed, leaving the exceeding material to be extruded through apposite channels. After almost 10 minutes,

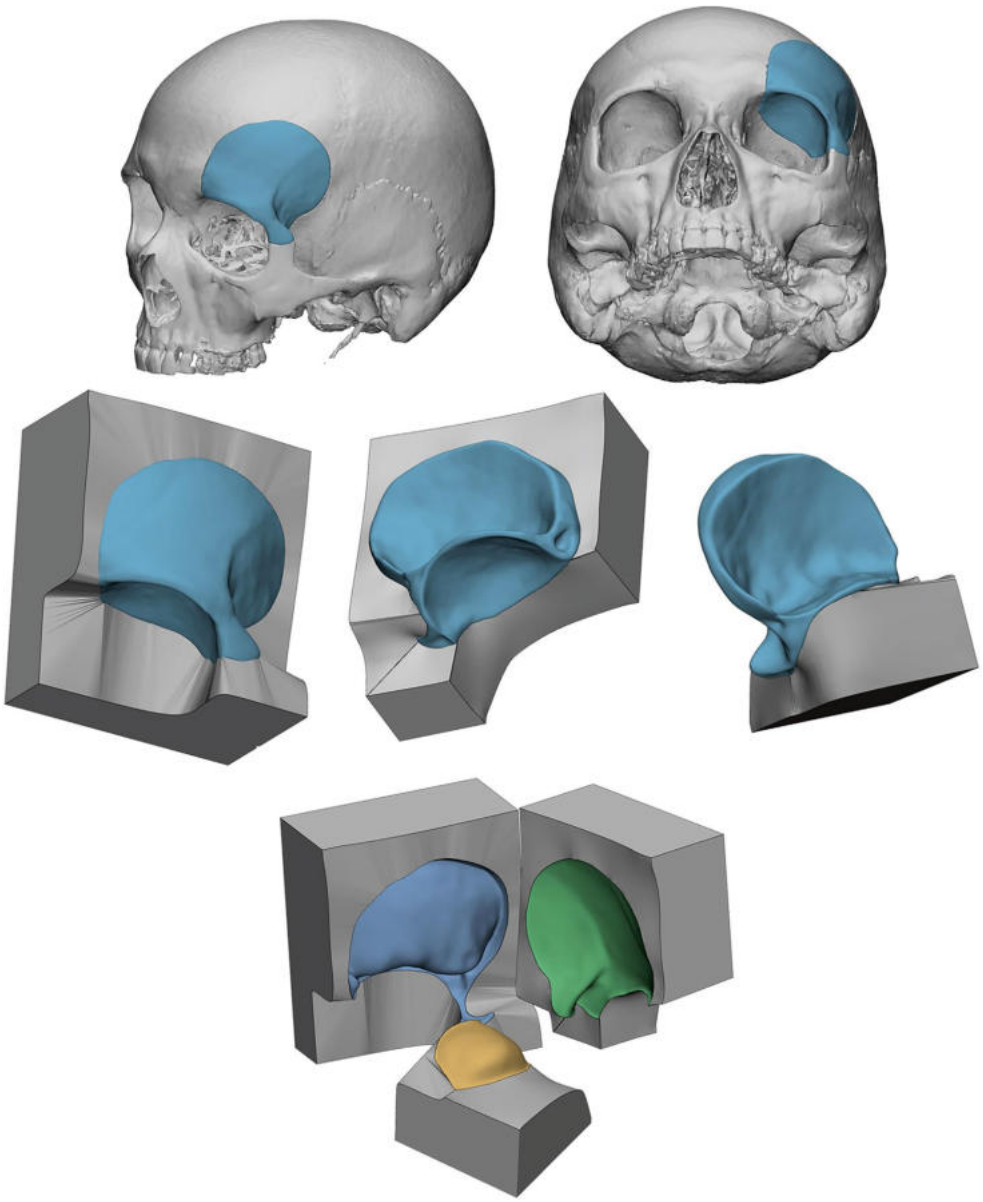


Fig. 38 Reconstruction of the cranio-orbital defect using the adaptive mirroring technique. Subsequent creation of the Cubik system based on three interfaces

the final prosthesis was extracted from the molds and slight excel of material due to PMMA leaking through mold seams was removed using a rotating bur, and the final prosthesis was ready for implantation (Fig. 39). Postoperative clinical appearance confirmed a satisfactory outcome (Fig. 40).

4.4.2 Cranio-Orbital Reconstruction for Defects Located in the Lateral Area

Defects located laterally and involving the lateral orbital rim have an inferior impact on facial esthetics, but still not neglectable, as the lateral orbital rim and its continuation with the zygomatic arch are a major prominence of the face, and even slight alterations can result in a visible defect. On the other hand, the cranial component of the reconstruction is concealed above the hairline, unless the patient is hairless. In this last circumstance, the design of the cranial implant plays a major role to balance facial symmetry. In fact, injuries in the lateral skull area involve the temporal area, and often result in soft tissue damage of the temporalis muscle, resulting in the so called "temporal hollowing". It is therefore important that the plate is designed with an increased curvature to account also for the loss of thickness of the temporalis muscle. Moreover, as seen for pterional defects, those with simultaneous involvement of the temporal area and the lateral orbital rim cross the pterional region, a crucial area between the skull convexity and the skull base, posing the same criticalities observed for pure cranial defects.

Clinical History

In the following case, a patient presented with an intraosseous meningioma causing significant deformity due to the

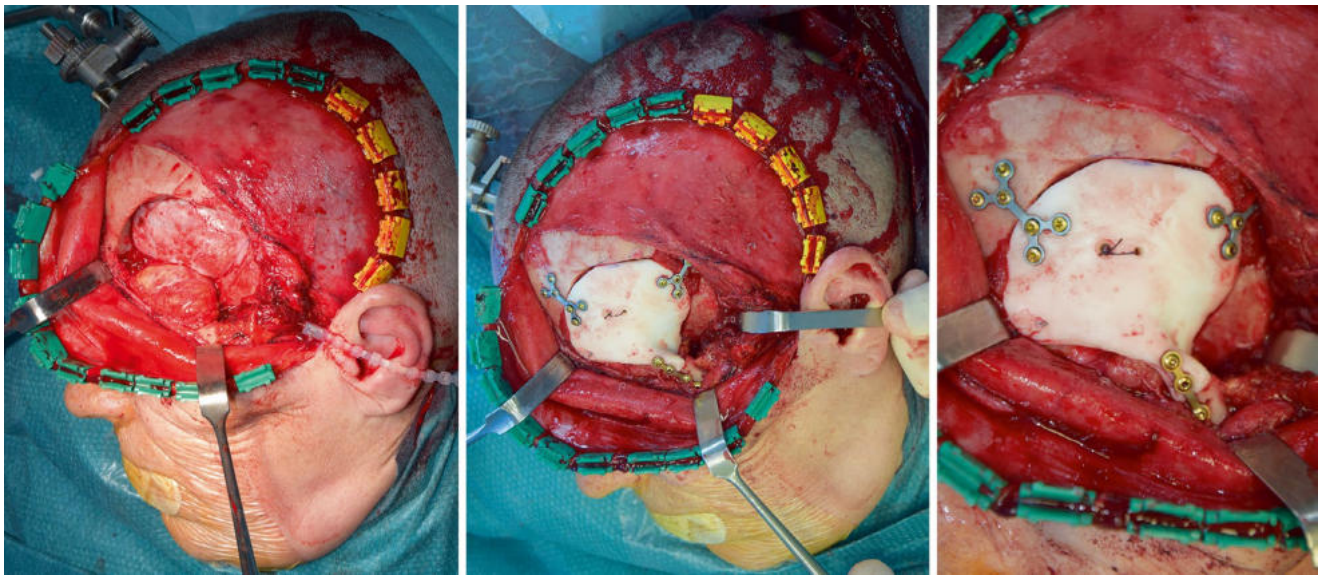


Fig. 39 Intraoperative photographs with resection and reconstruction using the PMMA implant

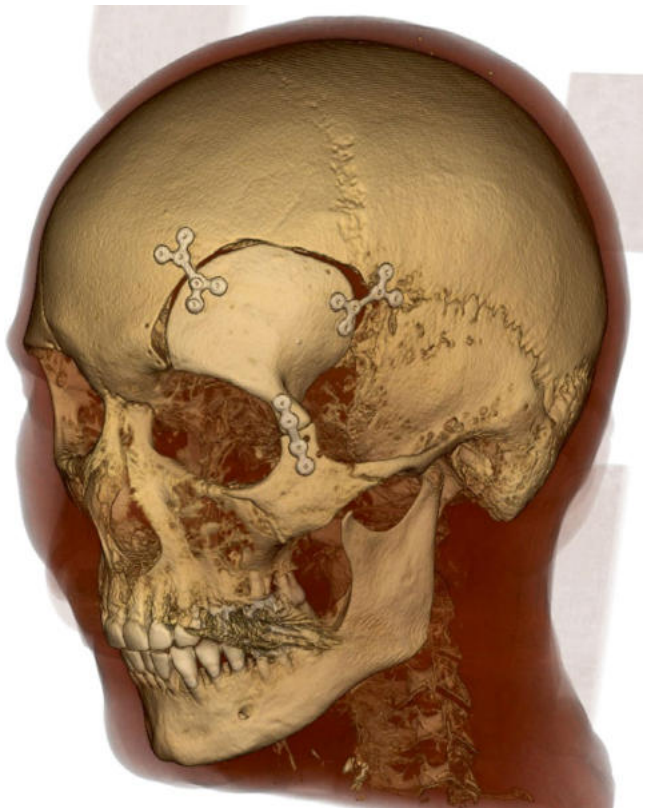


Fig. 40 Postoperative CT with optimal implant positioning

downward displacement of the eye globe and right exophthalmos. Preoperative CT scan revealed a gross alteration of bone structure in correspondence of the greater sphenoidal wing and resorption of bone in the pterional and temporal area, due to previous surgeries. Moreover, a gross thickening of the lateral orbital wall was assessed.

Virtual Surgical Planning

Virtual surgical planning simulated a wide resection including the area with bone resorption in the pterional and temporal region, as well as the entire lateral orbital wall until the supraorbital foramen, and the root of the zygomatic arch. As the defect was sided, yet extended, the cranial plate was designed using the mirroring approach with a refinement achieved by poly-sculpting to maximize the compatibility with the recipient site, particularly along the orbital contour. Subsequently, the implant was optimized in its topological characteristics and the undercut was removed, facilitating the surgical placement. For the intraoperative creation of the PMMA prosthesis, the aforementioned Cubik system was used. Seams between subunits were defined, trying to conceal them in the thickness of the plate, until the well-known tripartition into orbital, intracranial and skull convexity subunits was achieved. As usual, extrusion channels were modeled within the molds to improve the filling of the molding chamber and let the exceeding material flow outside. Molds were then 3D printed and brought in the operating room after sterilization (Fig. 41).

Surgery

An hemicoronal flap represented the most straightforward access way to the lateral skull base, orbital rim, and temporal area. First, a navigation-driven craniotomy was performed to excise the relapsed intraosseous meningioma within the thickened lateral orbital rim and around the margins of the operculum (Fig. 42). Through the breach of bone, a dural adherence had formed, which led to a laceration intraoperatively, needing a dural repair using a collagen substitute. After correct exposure of the defect and excision of the lesion, the prosthesis was implanted and checked with navigation, then fixed with three titanium plates (Fig. 43). Postoperative CT confirmed optimal implant positioning (Fig. 44).

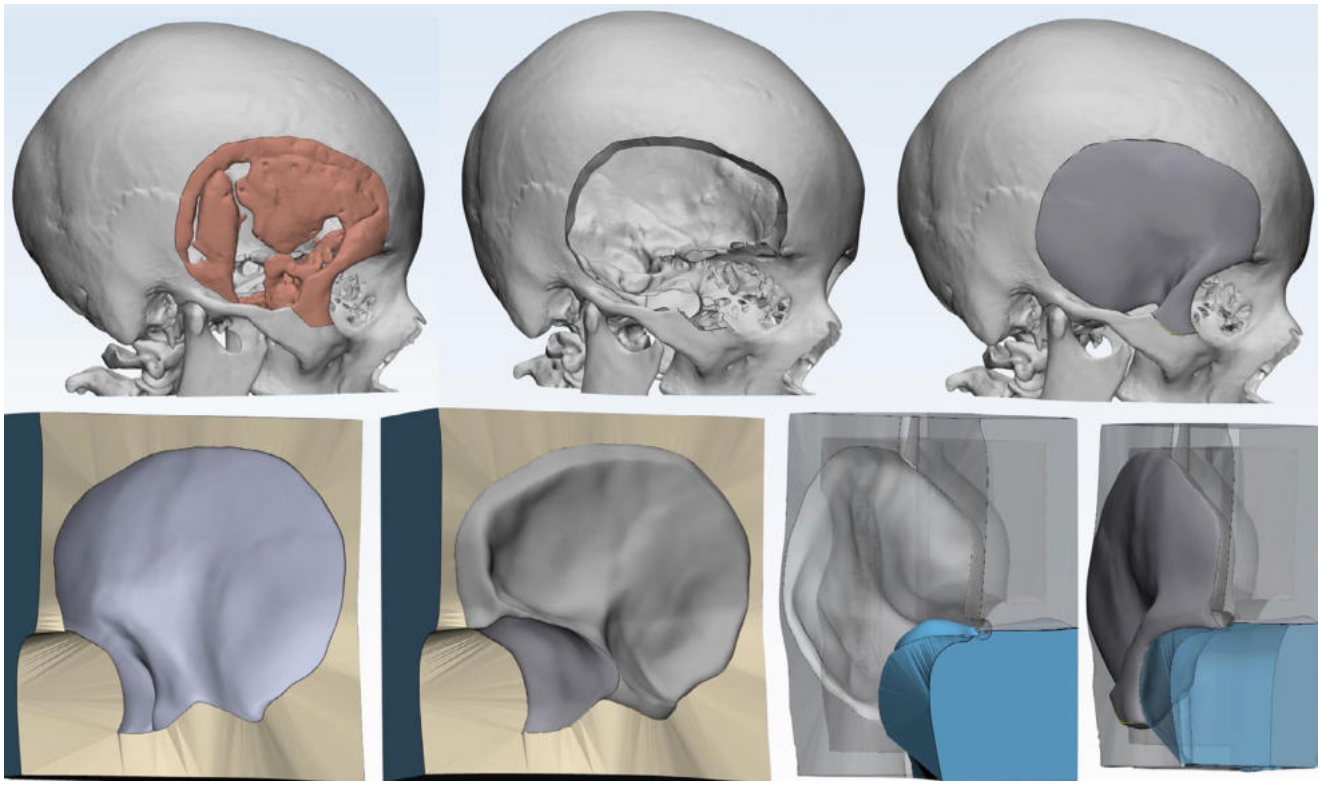


Fig. 41 Virtually simulated resection and reconstruction with creation of the Cubik molding system

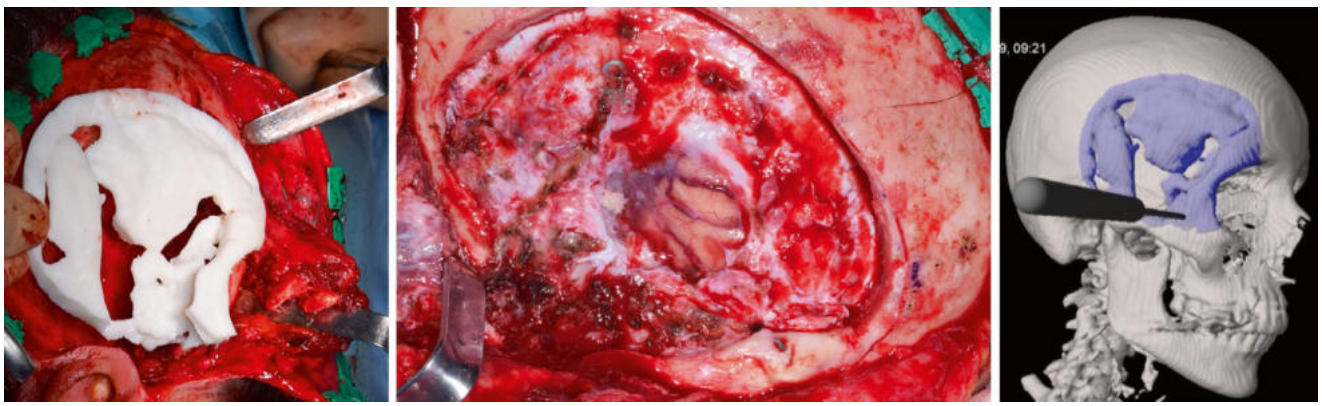


Fig. 42 Intraoperative picture showing resection guided by navigation

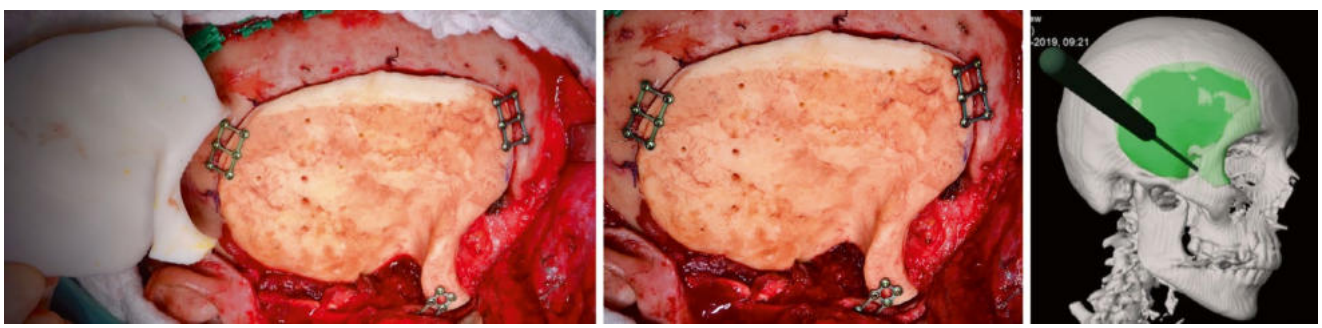


Fig. 43 Intraoperative picture showing reconstruction guided by navigation

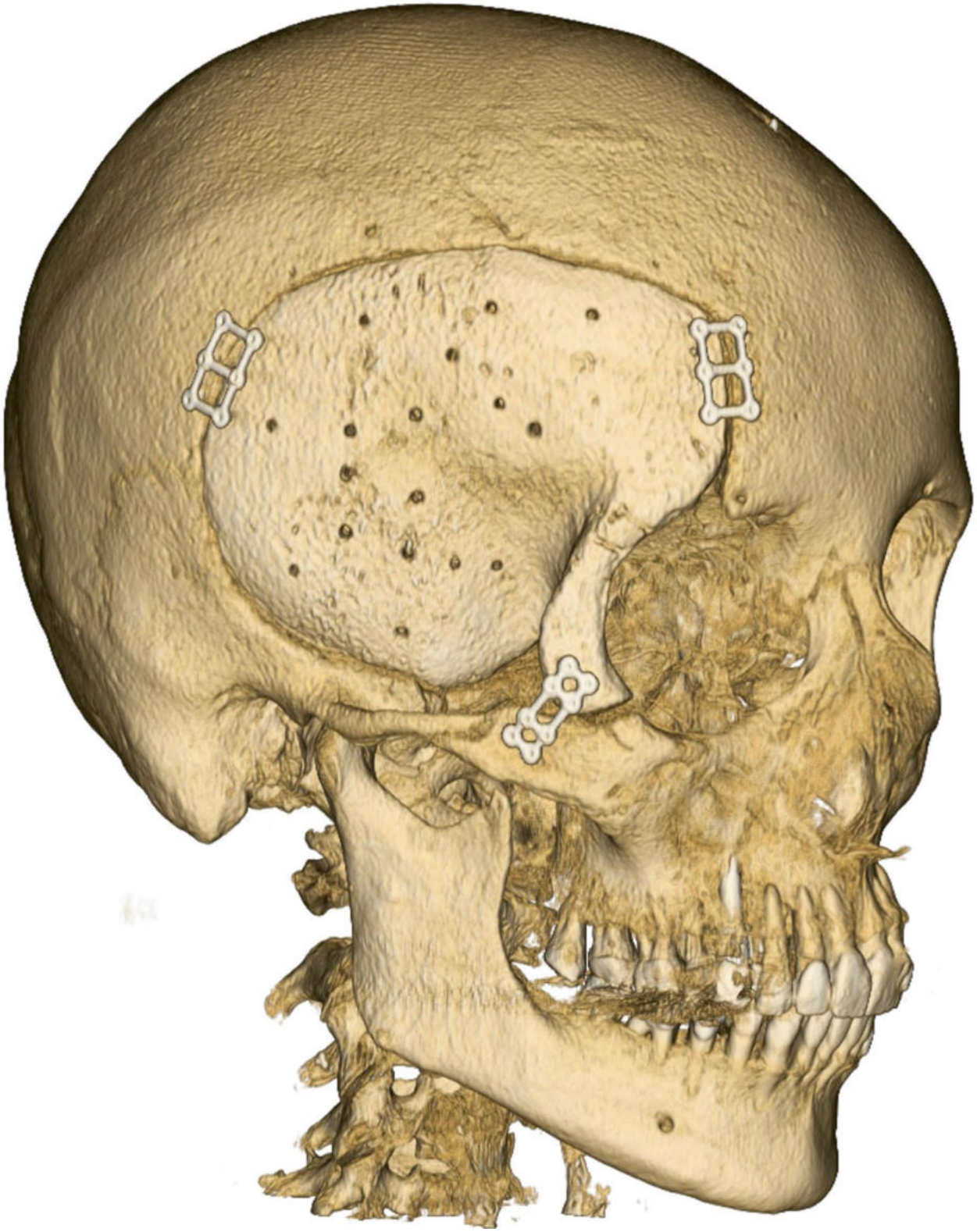


Fig. 44 Postoperative CT scan showing optimal implant positioning

References

1. Gall M, Li X, Chen X, Schmalstieg D, Egger J. Computer-aided planning and reconstruction of cranial 3D implants. Annu Int Conf IEEE Eng Med Biol Soc. 2016;2016:1179–83.
2. Marreiros FMM, Heuzé Y, Verius M, Unterhofer C, Freysinger W, Recheis W. Custom implant design for large cranial defects. Int J Comput Assist Radiol Surg. 2016;11:2217–30.
3. Jie B, Han B, Yao B, Zhang Y, Liao H, He Y. Automatic virtual reconstruction of maxillofacial bone defects assisted by ICP (iterative closest point) algorithm and normal people database. Clin Oral Investig. 2022;26:2005–14.
4. Li J, Ellis DG, Pepe A, Gsaxner C, Aizenberg MR, Kleesiek J, Egger J. Back to the roots: reconstructing large and complex cranial defects using an image-based statistical shape model. J Med Syst. 2024;48:55.
5. Mazzocchetti S, Spezialetti R, Bevini M, Badiali G, Lisanti G, Salti S, Di Stefano L. Neural shape completion for personalized maxillofacial surgery. Sci Rep. 2024;14:19810.
6. Tel A, Costa F, Sembronio S, Lazzarotto A, Robiony M. All-in-one surgical guide: a new method for cranial vault resection and reconstruction. J Craniomaxillofac Surg. 2018;46:967–73.
7. Csámer L, Csernátony Z, Novák L, Kővári VZ, Kovács ÁÉ, Soósné Horváth H, Manó S. Custom-made 3D printing-based cranioplasty using a silicone mould and PMMA. Sci Rep. 2023;13:11985.
8. Tel A. Computer-guided in-house cranioplasty: establishing a novel standard for cranial reconstruction and proposal of an updated protocol. J Oral Maxillofac Surg. 2020. https://doi.org/10.1016/j.joms.2020.08.007.
9. (2024) UV mapping. Wikipedia.
10. Tel A, Tuniz F, Sembronio S, Costa F, Bresadola V, Robiony M. Cubik system: maximizing possibilities of in-house computer-guided surgery for complex craniofacial reconstruction. Int J Oral Maxillofac Surg. 2021;50:1554–62.

Personalized Cranial Implants: Pioneering Techniques with Additive Manufacturing

Neha Sharma, Jokin Zubizarreta Oteiza, Daniel Seiler, and Florian M. Thieringer

1 Introduction

Cranial reconstruction or cranioplasty is an essential aspect of neurosurgery and craniomaxillofacial (CMF) surgery that aims to restore the shape and function of the skull. This surgical treatment has developed substantially throughout the years, owing to advances in material science, surgical techniques, and manufacturing technologies. Cranial implants have a long history, dating back to ancient cultures when simple materials were utilized to correct cranial abnormalities. Over time, techniques advanced, transitioning from handcrafted solutions to standardized implant production and, more recently, additive manufacturing (AM), also known as three-dimensional (3D) printing technologies that allow for unprecedented personalization and precision [1].

1.1 Historical Background and Evolution of Cranial Implant Techniques

Cranial reconstruction dates back to 7000 BC, with evidence like a Peruvian skull from 2000 BC showing early repairs using gold. Ancient Asian, Egyptian, Greek, and Roman civilizations mainly used materials like gourds, shells, and metals for cultural purposes. The Renaissance brought a more scientific approach, as surgeons used metal plates for skull fractures, but infections were common due to poor biocompatibility and lack of sterility [2–4]. Autologous bone grafting began in the nineteenth century, with the Dutch surgeon Job van Meekeren performing the first successful cranioplasty using canine cranial bone. Surgeons later used ribs and tibias [5]. By the mid-twentieth century, synthetic materials like polymethylmethacrylate (PMMA) and titanium meshes emerged, offering durable and aesthetic options, but they lacked the customization needed for complex cranial reconstructions [6].

The first 3D reconstruction of imaging data, achieved in 1984 [7], marked a significant milestone in medical imaging and paved the way for subsequent advancements. By the late 1990s, the introduction of computer-aided design (CAD) and computer-aided manufacturing (CAM) transformed cranial implant design and production, allowing for anatomically precise implants based on enhanced preoperative imaging data. During this time, titanium and polyetheretherketone (PEEK) became the materials of choice due to their advantageous biocompatibility material properties. However, these were still manufactured using subtractive methods such as computer numerical controlled (CNC) milling, which constrained design complexity and resulted in significant material waste [8].

Cranial implants have advanced drastically with the introduction of AM technology. Unlike traditional methods that carve implants from solid blocks, AM builds implants layer by layer, allowing for precise, patient-specific customization. Through virtual surgical planning (VSP) and AM, hospitals and the MedTech industry can offer tailored cranial implants that improve treatment outcomes over traditional off-the-shelf options. AM technology supports intricate designs, internal lattices, and bioactive material integration, enhancing fit, functionality, and clinical results [9, 10].

In summary, cranial implant techniques have advanced from basic repairs using organic materials to sophisticated, patient-specific solutions driven by additive manufacturing (AM) and digital planning. As AM and material innovations

N. Sharma (✉) · J. Z. Oteiza · F. M. Thieringer
Clinic of Oral and Cranio-Maxillofacial Surgery and 3D Print Lab, University Hospital Basel, Basel, Switzerland

Medical Additive Manufacturing Research Group (Swiss MAM), Department of Biomedical Engineering, University of Basel, Allschwil, Switzerland
e-mail: neha.sharma@usb.ch; jokin.zubizarreta@usb.ch; Florian.Thieringer@usb.ch

D. Seiler
Institute for Medical Engineering and Medical Informatics IM, University of Applied Sciences and Arts Northwestern Switzerland FHNW, Muttenz, Switzerland
e-mail: daniel.seiler@fhnw.ch

© The Author(s), under exclusive license to Springer Nature Switzerland AG 2025

A. Tel, M. Robiony (eds.), *Atlas of Virtual Surgical Planning and 3D Printing for Cranio-Maxillo-Facial Surgery*,
https://doi.org/10.1007/978-3-031-94495-6_11

continue to evolve, the future of cranial reconstruction promises more individualized, efficient, and compliant approaches, enhancing outcomes and expanding access to high-quality care.

2 Clinical Relevance of Cranial Implants

Cranial reconstruction is a complex procedure that extends beyond restoring the skull's structural integrity to encompass functional and psychological aspects of patient care. The skull influences the overall aesthetics of the face and head. As a result, a cranial defect, whether caused by trauma, tumor excision, or congenital malformations, can have a major impact on a patient's self-esteem and psychological well-being [11, 12]. Traditional manufacturing methods frequently fail to provide tailored solutions that match each patient's aesthetic and anatomical needs (Fig. 1).

In contrast, AM has changed cranial implant design and production, allowing surgeons to provide patient-specific solutions that accomplish functional restoration and aesthetic pleasure. Surgeons can now use AM to produce implants that match the various curves and shapes of a patient's skull. These implants are designed preoperatively using digital planning tools, ensuring a precise fit and smooth transition into the surrounding tissues [13–15].

From a clinical perspective, patient-specific AM implants provide several key benefits that address traditional challenges in cranial reconstruction. One of the most significant advantages is the ability to restore the natural contour and symmetry of the skull, which is crucial for both protection and aesthetics, particularly in visible regions such as the frontal and temporal areas. The precise fit of AM implants reduces the risk of complications such as implant displacement, infection, or extrusion, which are more common with conventional implants that may not fit perfectly or require extensive intraoperative adjustments [16, 17].

Furthermore, AM-based cranial implants based on VSP reduce operating time, which lowers the risk of anesthesia-related problems and blood loss during surgery. This streamlined procedure promotes faster recovery and better outcomes, increasing overall patient satisfaction. By addressing functional and aesthetic difficulties, AM-based cranial implants have improved the standard of care, resulting in better psychosocial results, increased patient confidence, and a higher quality of life. As technology advances, the use of AM in cranial reconstruction is projected to grow, providing more sophisticated solutions for complex clinical scenarios [18, 19].

3 Digital Workflow for Virtual Surgical Planning and Additive Manufacturing

The integration of AM in cranial implant production begins well before surgery, requiring a multidisciplinary approach that combines imaging, surgical planning, and precision implant design to achieve optimal results. The workflow comprises several key steps, each addressing design considerations, material selection, and regulatory requirements to ensure the implant meets clinical and functional specifications.

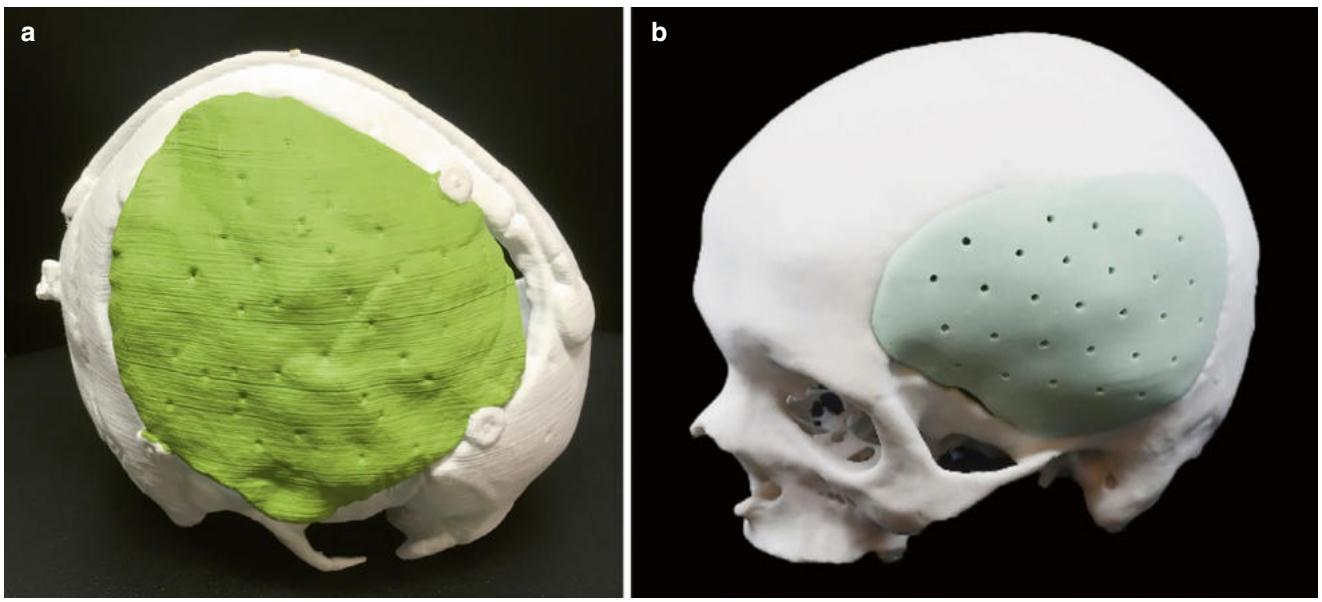


Fig. 1 Illustration of (**a**) hand-molded polymethylmethacrylate (PMMA) cranial implant versus (**b**) 3D-printing assisted fabrication of PMMA cranial implant

The process starts with comprehensive patient evaluation and high-resolution imaging, typically using thin-slice computed tomography (CT) or magnetic resonance imaging (MRI). These modalities capture detailed anatomy and defect boundaries, enabling the creation of an accurate 3D digital model. Using medical imaging software such as Materialise Mimics, D2P, 3D Slicer, or similar programs, the data is converted into a virtual 3D representation of the patient's cranial anatomy. Once the patient-specific 3D model is generated, the defect site is analyzed in a virtual environment to assess its size, shape, and location relative to critical anatomical landmarks. This stage often involves mirroring the healthy contralateral side, if applicable, to achieve symmetry and natural anatomical contours. Validation by a clinical expert is essential at this point to ensure that the defect analysis and mapping are accurate and align with the patient's clinical needs. With the defect mapped out, the implant is digitally designed to fit precisely within the boundaries of the missing bone, ensuring a seamless integration with the surrounding structures. At this stage, a second validation by the clinical expert is performed to confirm that the implant design meets both anatomical and functional requirements and is suitable for surgical application. These dual validation steps help ensure a high degree of accuracy and reliability throughout the workflow, bridging advanced technology with clinical expertise [20–22].

Further clinical factors such as implant thickness, fixation point inclusion, and potential soft tissue augmentation are considered during the design process. Surgeons and biomedical engineers collaborate to fine-tune the implant design, taking into account functional and cosmetic considerations. Advanced design optimization procedures are frequently used to reduce the implant's weight while retaining structural integrity, guaranteeing that it can bear mechanical loads without putting too much pressure on adjacent tissues. A close relationship between material selection and design optimization characterizes this phase. The material used—whether titanium, PEEK, or bioactive ceramics—directly impacts the design characteristics that can be included, such as thickness, structural support, and surface qualities. For example, if the implant is made of titanium, the design may prioritize lightweight features like lattice structures. In contrast, smooth surfaces and curves are preferred for a PEEK implant to balance strength and comfort. These 3D digital models can be further optimized to include features such as screw holes, fixation tabs, and porosity levels based on the selected material's properties and the clinical requirements of the defect [19, 20, 23, 24].

Before entering the operating room, surgeons utilize VSP to digitally plan osteotomy sites, determine optimal implant positioning, and visualize the desired surgical outcome. This detailed preoperative planning allows surgeons to test multiple surgical approaches, define screw trajectories, and identify potential challenges that may arise during the procedure, thus minimizing uncertainties and creating a smoother intraoperative experience. Anatomical models of the patient's skull can be 3D printed to facilitate pre-surgical simulations, enabling the surgical team to rehearse the procedure and make necessary adjustments to the plan if required. For more complex cases, surgical guides and skull templates can also be designed and 3D printed during this stage to provide intraoperative assistance, ensuring that the planned surgical steps are executed with high precision. These guides are handy for complex reconstructions where precise implant positioning relative to critical neuro- and vascular structures is essential [25].

After the simulation and planning phases are completed, the 3D printing and post-processing stages begin. It entails converting the 3D digital design into a physical implant using the appropriate AM technology. For cranial implants, selective laser melting (SLM) or electron beam melting (EBM) is often used for titanium [26], while material extrusion or selective laser sintering (SLS) may be used for PEEK [27, 28]. This layer-by-layer fabrication approach replicates the digital model with high precision, allowing for constructing complicated geometries that are impossible with traditional manufacturing processes. Following printing, post-processing steps—such as support structure removal, surface polishing, sterilization, and quality assurance testing—are required to meet the defined medical device specifications guaranteeing clinical safety and efficacy. In some circumstances, additional treatments, such as bioactive surface coatings, are applied to promote better integration with host bone and soft tissues [29, 30].

The final step is intraoperative guidance and placement of the pre-planned implant using the surgical guide markings produced during the planning phase. During surgery, intraoperative navigation systems or augmented reality (AR) technology can provide real-time visual feedback, improving precision and validating the correct implant positioning. This holistic strategy enhances clinical outcomes and increases patient safety in complicated craniofacial surgeries [31, 32].

In summary, the workflow for AM cranial implants is a comprehensive procedure that combines imaging, design, material selection, and production into a single plan. Each phase builds on the previous one, ensuring the final implant is anatomically correct and meets the patient's mechanical and biological needs. The combination of advanced digital planning and precise execution significantly improves clinical outcomes, reduces intraoperative risks, and enhances patient satisfaction.

4 Clinical Applications and Implementation

AM in cranial reconstruction has opened new opportunities to address complex cases with high precision and patient-specific solutions. Clinical applications often require a flexible approach, with manufacturing methods tailored to the defect's complexity, available resources, and patient-specific needs. Over time, cranial reconstruction has evolved from traditional techniques to modern technologies, offering varying degrees of precision, personalization, and efficiency. This progression can be categorized into three main strategies: hybrid PMMA manufacturing as seen in the previous chapter, milling of customized implants, and advanced 3D printing using high-performance materials like PEEK. This section explores typical clinical scenarios showcasing hybrid methods, traditional milling enhanced by digital planning and intraoperative navigation, and fully additive solutions fabricated directly in hospitals.

4.1 Point-of-Care Hybrid PMMA Manufacturing Approach: Cost-Effective Solutions for Resource-Constrained Settings

The hybrid manufacturing method combines traditional hand-crafted molding techniques with digital planning and the selective use of 3D printing to fabricate patient-specific implants. Unlike fully additive manufacturing processes, this approach involves the 3D printing of only specific components, such as an implant template or mold, which are derived from preoperative CT scans. During surgery, PMMA is manually molded into these molds—often made from silicone or 3D-printed resin/plastic material—resulting in customized implants. This method avoids the high costs and extended timelines associated with centralized manufacturing, where implants are designed and produced in specialized off-site facilities and then shipped to hospitals. Instead, this implant-manufacturing approach can be implemented in a hospital or clinical setting, aligning it with decentralized or point-of-care (POC) manufacturing practices (Fig. 2).

This method, while not as precise as fully automated manufacturing techniques, provides a cost-effective and time-efficient solution for cranial reconstructions. However, the use of manual molding introduces variability, resulting in potential inconsistencies in the implant's fit and finish due to human handling during the fabrication process. This increases reliance on the surgeon's expertise and time, as they play a critical role in shaping the implant and ensuring its proper fit during surgery. Additionally, regulatory compliance poses a challenge, as implants produced using this method may not meet the stringent quality and traceability standards typically required in centralized manufacturing processes.

Despite these limitations, the hybrid approach provides a practical and valuable alternative in situations where cost-effectiveness, accessibility, and speed are primary considerations. By combining digital planning with traditional techniques, it enables the production of patient-specific implants with acceptable clinical and aesthetic outcomes at a fraction of the cost of fully 3D-printed solutions. This method bridges the gap between high-cost, centralized manufacturing processes, and entirely manual techniques, offering a balanced option for resource-constrained settings [33–36].

4.2 Outsourced Milled Customized PEEK Implants: Precision with Conventional Manufacturing Techniques

The next step in the evolution of cranial reconstruction is milled customized PEEK implants. This approach begins with detailed preoperative planning using VSP and intraoperative navigation, ensuring precise defect mapping and optimal implant design. The implant is then produced using a subtractive CNC milling process, carving it from a solid block of PEEK. This method allows for the creation of highly durable implants that offer superior mechanical properties, precise fit, and predefined screw holes for secure and accurate fixation during surgery.

A key advantage of PEEK implants is their ability to retain excellent dimensional stability and structural integrity, making them ideal for long-term cranial reconstructions. Additionally, PEEK's radiolucency makes postoperative imaging more precise and accessible for evaluation, enhancing follow-up care. During the one-step surgical procedure, a 3D-printed surgical guide is used to ensure accurate resection of the cranial defect, facilitating the exact placement of the milled implant with minimal need for intraoperative adjustments (Fig. 3). This combination of digital planning, advanced intraoperative navigation, and precise manufacturing significantly improves surgical precision, stability, and patient outcomes compared to hybrid techniques [31, 37–39].

However, this method has limitations, including a longer turnaround time and higher cost due to the centralized manufacturing process required for milling, which often involves outsourcing to a certified Medical Device Regulation (MDR) compliant supplier to meet regulatory standards. Despite these challenges, milled PEEK implants remain a highly effective solution for complex cranial reconstructions where long-term durability and precision are critical.

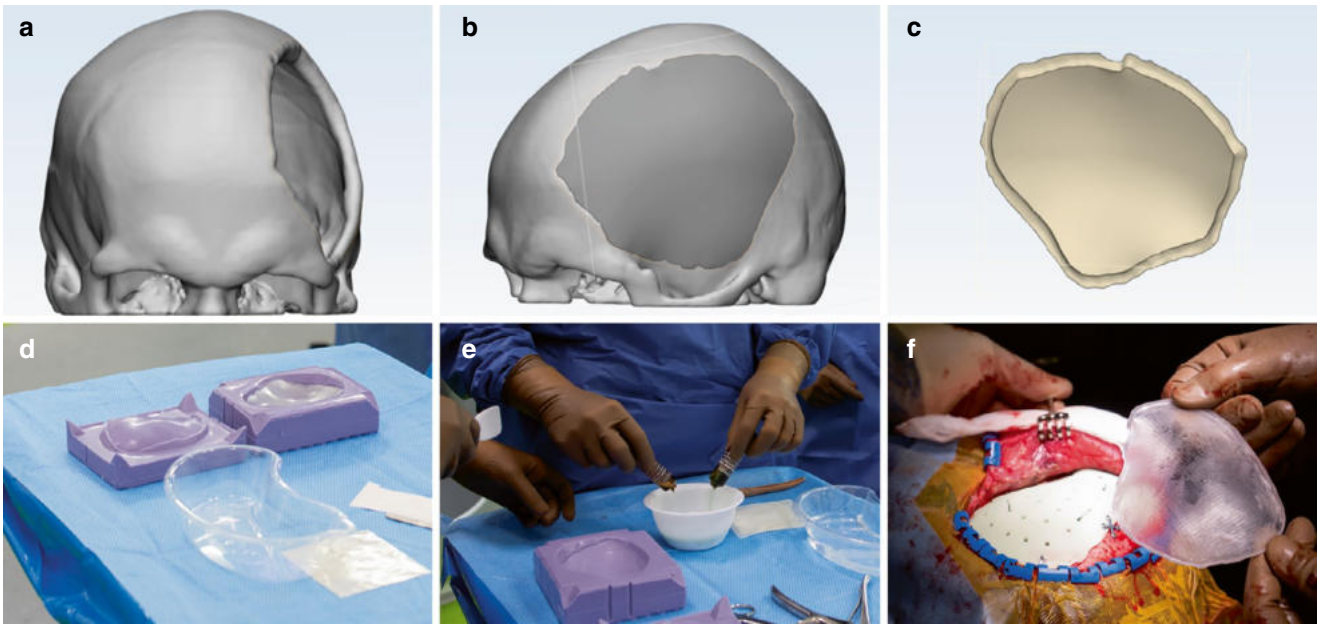


Fig. 2 Example of a hybrid manufacturing process for PMMA cranial implants, illustrating a 3D-printed implant template and silicone mold fabrication for intraoperative manual PMMA molding, providing a cost-effective solution with reasonable anatomical accuracy for cranial reconstruction

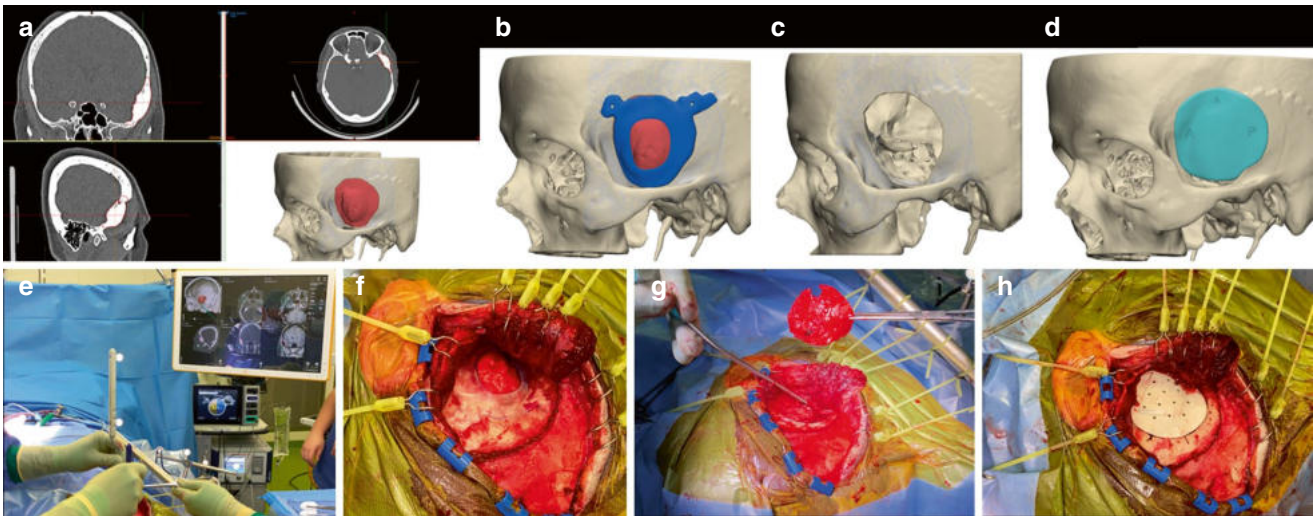


Fig. 3 Example of a milled customized PEEK cranial implant with predefined screw holes, highlighting the precision and anatomical fit achieved using conventional subtractive manufacturing methods combined with intraoperative navigation for accurate placement during surgery

4.3 Point-of-Care 3D Printing: On-Demand Fabrication for Optimal Personalization

The most advanced and efficient technique for cranial reconstruction is POC AM of PEEK cranial implants, which combines digital surgical planning with on-site, on-demand production. In this approach, patient-specific cranial implants are created using VSP and manufactured directly at the hospital's 3D printing facility using high-temperature 3D printers optimized for PEEK. This method offers unparalleled flexibility and speed, enabling real-time design modifications and rapid production within a clinical setting. POC 3D printing reduces logistical challenges, shortens wait times, and facilitates immediate surgical application, making it ideal for complex cases requiring high levels of customization and quick turnaround. Additionally, in-house production eliminates the need for outsourcing, further streamlining workflows and enhancing efficiency [19, 20, 40, 41].

Notably, the entire manufacturing process adheres to European Medical Device Regulation (EU) 2017/745 (MDR) article 5.5 compliance standards, ensuring every implant meets stringent general safety and performance require-

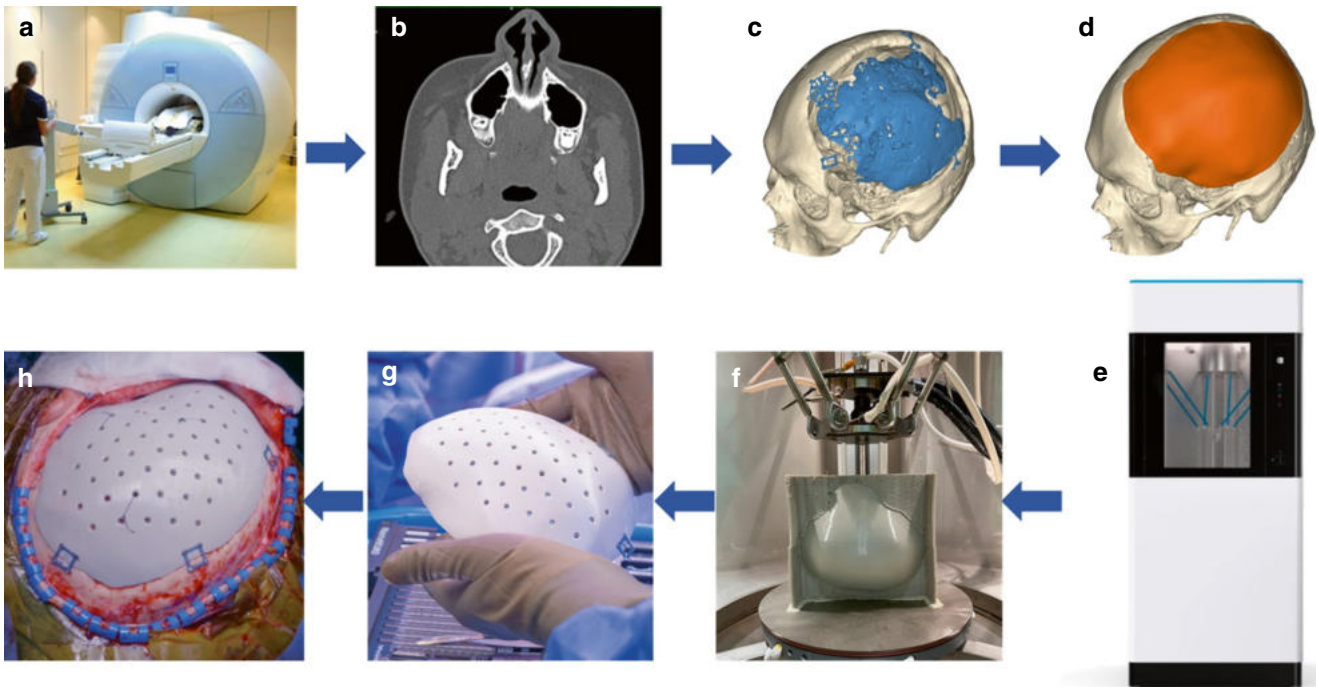


Fig. 4 An example of a 3D-printed PEEK cranial implant produced at the point-of-care highlights the stream-lined workflow from digital surgical planning to on-site fabrication, ensuring high customization and rapid implementation for cranial reconstruction

ments. The MDR-compliant production process includes material selection, digital design validation, and post-production quality checks, such as mechanical testing and sterilization, ensuring that the final implant is manufactured to meet the verified and validated specifications of the patient-matched device template. This guarantees that the final implant is tailored to the patient's anatomical requirements and is safe and efficient for long-term clinical use.

In 2023, the University Hospital Basel in Switzerland successfully implemented this POC 3D-printed cranial implant workflow, showcasing its feasibility and clinical benefits. This approach demonstrates how hospitals can combine cutting-edge technology with regulatory compliance to deliver timely, effective, and patient-specific solutions for complex cranial reconstruction (Fig. 4). By integrating POC 3D printing with MDR-compliant manufacturing processes, hospitals can set a new standard in cranial reconstruction, offering streamlined, patient-centered care that enhances safety, efficiency, and treatment outcomes [42, 43].

5 Challenges and Future Directions

AM has transformed the creation of personalized cranial implants, enabling complex, patient-specific designs with unprecedented precision. However, several challenges continue to hinder its widespread clinical acceptance. One major obstacle is navigating the intricate regulatory landscape, which is often tailored to standardized, mass-produced medical devices rather than the bespoke nature of AM. While certain university hospitals in Switzerland (e.g., Basel) and later in Austria (e.g., Salzburg) have implemented in-house AM facilities that meet MDR compliance, global adoption of similar systems remains limited. Hybrid manufacturing approaches, such as using 3D-printed templates to manually mold PMMA implants, are still prevalent but lack robust regulation, raising safety concerns.

Cost and accessibility also present significant barriers. Advanced AM methods require substantial investment in high-end 3D printers, biocompatible materials, and post-processing equipment, making them prohibitive for many low-resource settings [44]. The need for specialist expertise and sophisticated software further escalates expenses, limiting accessibility. POC manufacturing offers a promising alternative by shortening lead times and improving access. However, establishing POC facilities demands considerable upfront investment, rigorous regulatory compliance, and specialized knowledge. Hospitals often struggle with risk-based medical device development, including clinical evaluation, design verification, and process validation. These challenges necessitate external support from certified suppliers or regulatory experts to establish validated workflows and ensure compliance with international standards. The development of standardized tools and training programs is critical to empowering hospitals to implement POC manufacturing and address gaps in regulatory adherence safely.

Technical issues such as reproducibility and quality control also complicate the clinical adoption of AM. Variability in printer settings, material properties, and environmental conditions can affect implant quality, requiring stringent quality assurance protocols. Emerging technologies, such as AI-driven process monitoring, offer solutions by detecting anomalies in real-time and optimizing production parameters to ensure consistency. AI also automates implant design, reducing manual adjustments and optimizing fit and functionality [45–47].

Material innovation represents another frontier for cranial reconstruction. While titanium and PEEK remain the standard materials, research into biodegradable polymers and bioactive composites offers potential for implants that promote bone regeneration. Multi-material printing, combining materials with distinct mechanical and biological properties, could enable implants that better mimic the interactions of natural bone and soft tissue interactions. However, translating these advancements to clinical practice will require addressing long-term stability concerns and meeting regulatory approval requirements [48–51].

Personalized medicine, advanced imaging, and VSP are also shaping the future of AM in cranial implants. Mixed reality technologies, such as virtual reality (VR) and AR, are being incorporated into preoperative planning, allowing surgeons to visualize complex reconstructions and practice procedures, improving precision and reducing intraoperative risks [52].

The future also holds promise for integrating innovative advanced functionalities into cranial implants. Sensor-enabled implants capable of monitoring intracranial pressure, temperature, and infection markers could provide clinicians with real-time feedback for improved postoperative care. Additionally, advancements in bioprinting and AI may pave the way for regenerative implants incorporating living cells and bioactive components, offering revolutionary possibilities for cranial reconstruction.

Despite these advancements, economic, regulatory, and technological hurdles remain. Overcoming these challenges will require collaborative efforts among surgeons, engineers, regulatory agencies, and industry partners. As AM technologies continue to evolve, they hold the potential to enhance precision, personalization, and multifunctional in cranial implants, ultimately improving clinical outcomes and expanding access to high-quality care.

6 Conclusions

AM has revolutionized cranial reconstruction, offering new possibilities for creating precise, patient-specific implants. The technology has evolved from hybrid manufacturing techniques to advanced POC 3D-printed solutions, each suited to different clinical and resource needs. While regulatory compliance and cost remain, innovations like POC 3D-print facilities and AI-driven design and quality assurance address these barriers.

The future of AM will focus on integrating new materials, smart implants, and enhanced digital planning to further optimize cranial reconstruction. With continued interdisciplinary collaboration, AM will continue to set new standards for personalized, safe, and effective cranial implant solutions.

Acknowledgments We gratefully acknowledge the generous support of the Werner Siemens Foundation (WSS), which funded our research within the MIRACLE II (Minimally Invasive Robot-Assisted Computer-Guided LaserosteotomE) project. We also extend our thanks to the University Hospital Basel, which supported our work through the Innovation Focus—Regenerative Surgery project.

The authors declare no potential conflicts of interest.

References

1. Huggins C, Rabinovitz B, Armand M, Gordon C. 3D printing and neurotechnology in cranial reconstruction. In: 3D printing at hospitals and medical Centers: a practical guide for medical professionals. 2nd ed. Cham: Springer International Publishing; 2024.
2. Aydin S, Kucukyuruk B, Abuzayed B, Aydin S, Sanus GZ. Cranioplasty: review of materials and techniques. J Neurosci Rural Pract. 2011;02:162–7.
3. Rifkinson-Mann S. Cranial surgery in ancient Peru. Neurosurgery. 1988;23:411–6.
4. Mahapure KS, Murray DJ. The historical timeline of cranioplasty. J Plast Reconstr Aesthet Surg. 2021;74:632–3.
5. Shah AM, Jung H, Skirboll S. Materials used in cranioplasty: a history and analysis. Neurosurg Focus. 2014;36:E19.
6. Alkhaibary A, Alharbi A, Alnefaie N, Almubarak AO, Aloraidi A, Khairy S. Cranioplasty: a comprehensive review of the history, materials, surgical aspects, and complications. World Neurosurg. 2020;139:445–52.
7. Vannier MW, Marsh JL, Warren JO. Three dimensional CT reconstruction images for craniofacial surgical planning and evaluation. Radiology. 1984;150:179–84.
8. Harris DA, Fong AJ, Buchanan EP, Monson L, Khechoyan D, Lam S. History of synthetic materials in alloplastic cranioplasty. Neurosurg Focus. 2014;36:E20.
9. Thieringer FM, Honigmann P, Sharma N. Medical additive manufacturing in surgery: translating innovation to the point of care. In: The future of business and finance. 1st ed. Cham: Springer International Publishing; 2022.
10. Modgill V, Balas B, Chi M, Honigmann P, Thieringer FM, Sharma N. Knowledge domain and innovation trends concerning medical 3D printing for craniomaxillofacial surgery applications: a 30-year bibliometric and visualized analysis. Craniomaxillofac Res Innov. 2023;8:27528464231170964.
11. Maricevich JP, Cezar-Junior AB, de Oliveira-Junior EX, et al. Functional and aesthetic evaluation after cranial reconstruction with polymethyl methacrylate prostheses using low-cost 3D printing templates in patients with cranial defects secondary to decompressive craniectomies: a prospective study. Surg Neurol Int. 2019;10:1–1.

12. Johnston DT, Lohmeier SJ, Langdell HC, et al. Current concepts in cranial reconstruction: review of alloplastic materials. Plast Reconstr Surg Glob Open. 2022;10:e4466.
13. Day KM, Kelley PK, Harshbarger RJ, et al. Advanced three-dimensional technologies in craniofacial reconstruction. Plast Reconstr Surg. 2021;148:94e–108e.
14. Sharma N, Ostas D, Rotar H, Brantner P, Thieringer FM. Design and additive manufacturing of a biomimetic customized cranial implant based on Voronoi diagram. Front Physiol. 2021;12:647923.
15. Miljanovic D, Seyedmahmoudian M, Stojcevski A, Horan B. Design and fabrication of implants for mandibular and craniofacial defects using different medical-additive manufacturing technologies: a review. Ann Biomed Eng. 2020;48:2285–300.
16. Ulmeanu ME, Mateș IM, Doicin CV, et al. Bespoke implants for cranial reconstructions: preoperative to postoperative surgery management system. Bioengineering. 2023;10:544.
17. Jardini AL, Larosa MA, Maciel Filho R, et al. Cranial reconstruction: 3D biomodel and custom-built implant created using additive manufacturing. J Craniofac Surg. 2014;42:1877–84.
18. Kopačin V, Zubčić V, Mumlek I, et al. Personalized 3D-printed cranial implants for complex cranioplasty using open-source software. Surg Neurol Int. 2024;15:39.
19. Pöppe JP, Spendel M, Griessenauer CJ, Gaggl A, Wurm W, Enzinger S. Point-of-care 3-dimensional–printed polyetheretherketone customized implants for cranioplastic surgery of large skull defects. Oper Neurosurg. 2024;24:449–54.
20. Sharma N, Honigmann P, Cao S, Thieringer F. Dimensional characteristics of FDM 3D printed PEEK implant for craniofacial reconstructions. Trans Addit Manuf Meets Med. 2020;2:1.
21. Ebel F, Schön S, Sharma N, Guzman R, Mariani L, Thieringer FM, Soleman J. Clinical and patient-reported outcome after patient-specific 3D printer-assisted cranioplasty. Neurosurg Rev. 2023;46:93.
22. Msallem B, Maintz M, Halbeisen FS, et al. Biomechanical evaluation of patient-specific polymethylmethacrylate cranial implants for virtual surgical planning: an in-vitro study. Materials (Basel). 2022;15:1970.
23. Bonda DJ, Manjila S, Selman WR, Dean D. The recent revolution in the design and manufacture of cranial implants: modern advancements and future directions. Neurosurgery. 2015;77:814–24.
24. Engstrand T, Kihlström L, Lundgren K, Trobos M, Engqvist H, Thomsen P. Bioceramic implant induces bone healing of cranial defects. Plast Reconstr Surg Glob Open. 2015;3:e491.
25. Velarde K, Cafino R, Isla A Jr, et al. Virtual surgical planning in craniomaxillofacial surgery: a structured review. Comput Assist Surg (Abingdon). 2023;28:2271160.
26. Aufa AN, Hassan MZ, Ismail Z, et al. Current trends in additive manufacturing of selective laser melting for biomedical implant applications. J Mater Res Technol. 2024;31:213–43.
27. Sharma N, Aghlmandi S, Dalcanale F, et al. Quantitative assessment of point-of-care 3D-printed patient-specific polyetheretherketone (PEEK) cranial implants. Int J Mol Sci. 2021;22:8521.
28. Berretta S, Evans K, Ghita O. Additive manufacture of PEEK cranial implants: manufacturing considerations versus accuracy and mechanical performance. Mater Des. 2017;139:141–52.
29. Zhou L, Miller J, Vezza J, et al. Additive manufacturing: a comprehensive review. Sensors. 2024;24:2668.
30. Engstrand T, Kihlström L, Neovius E, et al. Development of a bioactive implant for repair and potential healing of cranial defects. J Neurosurg. 2013;120:273–7.
31. Westarp E, Thieringer FM, Roethlisberger M. Virtual surgical planning and customized CAD/CAM cranial implants: preoperative and intraoperative strategies for temporal intraosseous meningioma resection. J Craniofac Surg. 2024;35:e307–9.
32. Hobert M, Sharma N, Benzimra C, et al. Case report: One-stage craniectomy and cranioplasty digital workflow for three-dimensional printed polyetheretherketone implant for an extensive skull multilobular osteochondosarcoma in a dog. Front Vet Sci. 2024;11:1459272.
33. Obaeed NH, Hamdan WK. Reconstruction and evaluation of 3D Printing PMMA cranioplasty implants. Int J Interact Des Manuf (IJIDeM). 2024;18:4233–55.
34. Iratwar S, Roy Chowdhury S, et al. Comprehensive functional outcome analysis and importance of bone remodelling on personalized cranioplasty treatment using Poly(methyl methacrylate) bone flaps. J Biomater Appl. 2024;38:975–88.
35. Çakın H, Yildirim Y, Ozsoy U. Demonstration of cosmetic improvement after cranioplasty using a personalized 3D-printed mold for creating polymethylmethacrylate implants with a simplified process. World Neurosurg. 2023;182:100–4.
36. Oteiza JZ, Zimmermann CJ, Thieringer FM, Sharma N. Harnessing generative design algorithms in cranioplasty. Trans Addit Manuf Meets Med. 2024;6:1803.
37. Ng ZY, Nawaz I. Computer-designed PEEK implants. J Craniofacial Surg. 2014;25:e55–8.
38. Zhang J, Tian W, Chen J, Yu J, Zhang J, Chen J. The application of polyetheretherketone (PEEK) implants in cranioplasty. Brain Res Bull. 2019;153:143–9.
39. O'Reilly EB, Barnett S, Madden C, Welch B, Mickey B, Rozen S. Computed-tomography modeled polyether ether ketone (PEEK) implants in revision cranioplasty. J Plast Reconstr Aesthet Surg. 2014;68:329–38.
40. MohanaSundaram A, Kamalakannan Y, Raja V, Mofatteh M, Haque MA. The World's first 3D-printed PEEK cranial implant: a new horizon in precision and personalized neurosurgery. Neurosurg Rev. 2024;47:616.
41. Sharma N, Oteiza JZ, Tourbier C, Thieringer FM. Can steam sterilization affect the accuracy of point-of-care 3D printed Polyetheretherketone (PEEK) customized cranial implants? An investigative analysis. J Clin Med. 2023;12:2495.
42. Johnson C. 3D printing: USB patient receives first implant to be produced on-site at the hospital. In: Unispital-basel.ch. 2023. https://www.unispital-basel.ch/en/newscenter/medienmitteilungen/12-09-2023. Accessed 10 Oct 2024.
43. Osborne A. 3D systems receives FDA clearance for world's first 3D printed PEEK cranial implants. 2024. https://www.additive-manufacturing.media/news/3d-systems-receives-fda-clearance-for-worlds-first-3d-printed-peek-cranial-implants. Accessed 10 Oct 2024.
44. Jayakrishna M, Vijay M, Khan B. An overview of extensive analysis of 3D printing applications in the manufacturing sector. J Eng. 2023;2023:7465737.
45. Strelko O, Aryal MR, Zack A, et al. Early challenges in the implementation of automated CranialRebuild freeware for generation of patient-specific cranial implant using additive manufacturing: a pilot project in review. Biomimetics. 2024;9:430.
46. Li J, Von Campe G, Pepe A, et al. Automatic skull defect restoration and cranial implant generation for cranioplasty. Med Image Anal. 2021;73:102171.
47. Li J, Ellis DG, Kodym O, et al. Towards clinical applicability and computational efficiency in automatic cranial implant design: an overview of the AutoImplant 2021 cranial implant design challenge. Med Image Anal. 2023;88:102865.
48. Maintz M, Tourbier C, de Wild M, et al. Patient-specific implants made of 3D printed bioresorbable polymers at the point-of-care: material, technology, and scope of surgical application. 3D Printing Med. 2024;10:13.

49. Su Q, Qiao Y, Xiao Y, et al. Research progress of 3D printed poly (ether ether ketone) in the reconstruction of craniomaxillofacial bone defects. Front Bioeng Biotechnol. 2023;11:1259696.
50. Li N, Cui J, Chi M, Thieringer FM, Sharma N. Building a better bone: the synergy of 2D nanomaterials and 3D printing for bone tissue engineering. Mater Des. 2023;234:112362.
51. Chi M, Li N, Cui J, et al. Biomimetic, mussel-inspired surface modification of 3D-printed biodegradable polylactic acid scaffolds with nano-hydroxyapatite for bone tissue engineering. Front Bioeng Biotechnol. 2022;10:989729.
52. Vervoorn MT, Wulfse M, Van Doormaal TPC, et al. Mixed reality in modern surgical and interventional practice: narrative review of the literature. JMIR Serious Games. 2023;11:e41297.

Virtual Planning in Frontal Sinus and Anterior Skullbase

Alessandro Tel, Fabio Costa, Marc Generowitz, Robert Pellecchia, and Massimo Robiony

1 Introduction

The anterior skullbase and the frontal sinus represent an intertwined anatomical unit that shares functional implications. Its conceptualization as a unique morpho-functional unit accounts for the importance of involvement of both structures in different pathological processes and trauma. For instance, fractures of the frontal sinus, if extended to the posterior table, also require management of the anterior skullbase through cranialization. Likewise, infectious processes arising primarily within the frontal sinus can lead to anterior skullbase involvement with subsequent extradural abscess and meningitis. Therefore, it is the purpose of this chapter to present how technology can improve surgery in this region, considering the frontal sinus and anterior skullbase as a single anatomo-functional unit. This chapter will focus predominantly on indications for the use of VSP in open surgery, including infective/inflammatory lesions, benignant neoplasms, and trauma. The application of technology can make surgical accesses more conservative and respectful of the complex functional mechanisms that ensure the natural physiology of the frontal sinus. In contrast, malignant pathology arising primarily within the frontal sinus or invading it as the result of infiltrative expansion from nearby regions will be discussed in the context of craniofacial resections, as such surgeries are highly disruptive and here technology is used to ensure a radical resection, with less emphasis on morphofunctional aspects.

2 Digital Anatomy of the Frontal Sinus

Results of frontal sinus segmentation confirm traditional anatomical knowledge [1, 2], according to which the frontal sinus is a pyramid-shaped cavity extending between the anterior and posterior tables of the ascending portion of the frontal bone. The apex of the pyramid is superior, and the base lies inferiorly. The frontal sinus stretches superiorly into the superciliary region and posteriorly above the medial portion of the roof of the orbit. Its lateral extension has been reported to be well beyond the orbit and into the lateral portion of the frontal bone. The inferior extension may reach the nasal bone and the frontal process of the maxilla. There are two frontal sinuses separated completely by a bony septum. Bilateral asymmetry is a frequent anatomical finding. Each sinus is further divided into incomplete chambers by a bony intrasinus septation, which creates deep recesses of the sinus.

The frontal sinus is bounded by anterior, posterior, medial, and inferior walls. The inferior wall is the frontal sinus floor. The anterior wall of the sinus forms the forehead and is by far the thickest of all sinus walls, measuring up to 12 mm. The posterior wall is a plate of thin, compact bone (1–2 mm) and also represents the anterior wall of the anterior cranial fossa. The thin posterior wall of the frontal sinus is attached to the dura of the anterior cranial fossa; therefore, infections from the

A. Tel (✉)
Lead Specialist for VSP and 3DP, Maxillofacial Surgery Clinic, Head & Neck and Neuroscience Department, Academic Hospital of Udine, Udine, Italy
e-mail: alessandro.tel@uniud.it

F. Costa
Maxillofacial Surgery Clinic, Head & Neck and Neuroscience Department, Academic Hospital of Udine, Udine, Italy
e-mail: fabio.costa@asufc.sanita.fvg.it

M. Generowitz
Oral and Maxillofacial Surgery, New York City Health and Hospitals Corporation, Lincoln Hospital, New York, NY, USA
e-mail: generowm@nychhc.org

R. Pellecchia
OMFS and Dental Medicine, New York City Health and Hospitals Corporation, Lincoln Hospital, New York, NY, USA
e-mail: Robert.Pellecchia@nychhc.org

M. Robiony
Chief of Maxillofacial Surgery Clinic,
Director of the Postgraduate School in Maxillofacial Surgery,
Chief of Head & Neck and Neuroscience Department,
Academic Hospital - University of Udine, Udine, Italy
e-mail: massimo.robiony@uniud.it

© The Author(s), under exclusive license to Springer Nature Switzerland AG 2025

A. Tel, M. Robiony (eds.), *Atlas of Virtual Surgical Planning and 3D Printing for Cranio-Maxillo-Facial Surgery*,
https://doi.org/10.1007/978-3-031-94495-6_12

frontal sinus can spread through its posterior wall, resulting in an extradural abscess. The medial wall of the frontal sinus is represented by the intersinus septum, the thin segment of bone that may occasionally have interruptions. The most inferior portion of this intersinus septum is always located in the same plane as the nasal septum. The inferior wall of the frontal sinus is formed by the orbital roofs on the lateral side and the nasoethmoid floor on the medial side. The floor of the sinus is convex above and inward and extends laterally over the orbital cavity, depending on the size of the sinus. The floor of the frontal sinus corresponding to the nasoethmoid floor is located near the midline and overlaps, in part, the fovea ethmoidalis and overlies the anterior ethmoid sinus. At the frontal sinus floor close to the anteromedial aspect of the intersinus septum rests the frontal sinus ostium. It has a conical shape that leads to a narrow opening inferiorly called the frontal recess.

The frontal sinus can be easily reconstructed from high-resolution CT scan using a negative-segmentation method, similarly to the other paranasal sinuses. Following this approach, segmentation threshold is set to negative Hounsfield Units (HU) values, with the aim of capturing air density. This strategy enables to effectively capture the anatomical detail of the frontal sinus. A positive segmentation with threshold in bone values is then used to acquire a traditional bone mask. The final result is the possibility to have a 3D printable model of the frontal bone with the sinus inside [3]. This visualization is excellent to depict the considerable interindividual variability of the frontal sinus and of the interfrontal septum (Fig. 1).

3 Applications of VSP in Frontal Sinus Pathology

Endoscopic sinus surgery became the gold standard in inflammatory disorders of the nose and paranasal sinuses. However, there are certain limitations which make an external approach mandatory. Despite the evolution of endoscopic surgery, external approaches are still indicated. Osteoplastic flap remains an option for the refractory inflammation of the frontal sinus. Benign tumors with lateral or superior extension and duct occlusion usually require an external approach. Superior and lateral posterior wall defects of frontal sinus with cerebrospinal fluid leak may mandate an open procedure.

Despite the substantial technological improvements in endoscopic navigation, in particular with the advent of magnetic navigation, the highest benefit of VSP generally concerns external approaches. In this regard, it enables a more conservative surgery, reducing the size of the osteoplastic flap, allowing to optimize its shape as well, tailored according to the underlying disease and the sinus cells. 3D printing unifies digital planning with surgery by manufacturing a surgical guide that provides rigid boundaries to the cutting blade within the shape of computer-designed osteotomies [4]. Navigation of surgical planning as well is highly effective in providing guidance across the depth of surgical exploration, yet it has less importance in osteotomy design, where surgical guides are superior.

4 Clinical Cases

4.1 Osteoma of the Frontal Sinus

4.1.1 Clinical History

This patient was referred by emergency department colleagues following admission for rhinosinusitis treated with medical therapy. The patient had been complaining of recurrent headache and rhinosinuitis symptoms for a fortnight. On physical examination, sinus trigger points on the right side were painful with irradiation in the nuchal region. The CT scan performed was suspected for osteoma of the right frontal sinus.

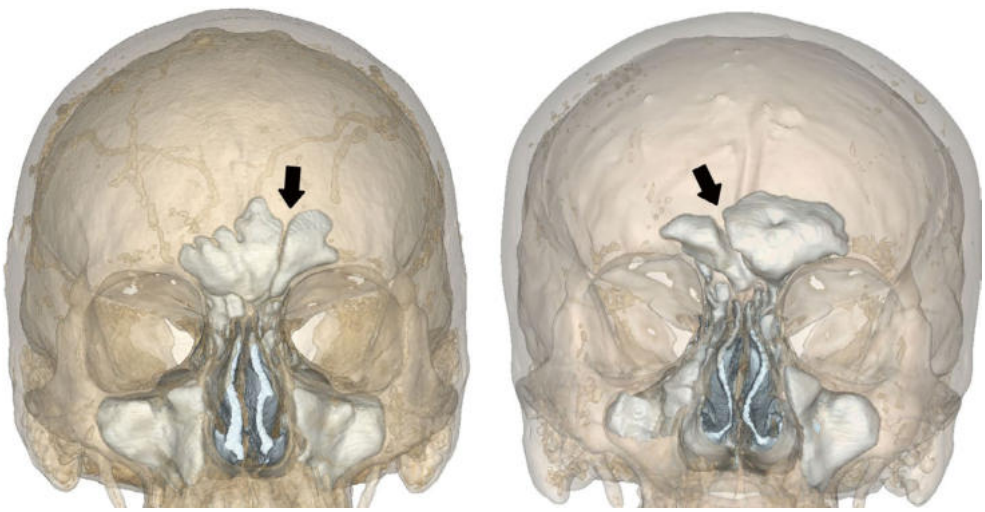


Fig. 1 Importance of virtual model reconstruction by merging a skeletal model and an airway model. In these two cases, the variability of sinus extension can be assessed, as well as the interfrontal septum (arrow)

4.1.2 Virtual Surgical Planning

The protocol for frontal sinus segmentation was applied, revealing the presence of a bone-like, bulging, mass of the right hemi-sinus, with insertion base on the right orbital roof. However, VSP analysis revealed that the lesion was confined within the right sinus, without interrupting the intermediate septum. The purpose of surgery was to decrease the bulk effect of the lesion to free the drainage path of the frontal sinus (Fig. 2). A radical excision was deemed impossible, as it would have incorporated the orbital roof in the resection area. To safely access frontal sinus, a bony operculum was simulated, with a rounded inferior margin to preserve the superior orbital rim and related neurovascular bundles, while its superior margin and sides were limited to the exact size of the lesion. In particular, care was taken not to enter the healthy left frontal sinus by preserving the intermediate septum and not to extend the osteotomy beyond the right lateral extension of the frontal sinus. To bridge such needs of surgical planning with intraoperative gestures, a surgical guide was designed with the following features: incomplete margin inferiorly, not to compress aforementioned neurovascular bundles; lateral extension to the temporal region with marked curvature across the posterior border of the superior-lateral orbital rim: this extension helps find a stable anatomical landmark for a reliable placement; three fixation slots to accommodate a screw in the thickest skull regions; a small handle to be grasped gently with a forceps to improve intraoperative ergonomics (Fig. 3).

4.1.3 Surgery

Under general anesthesia, infiltration with local anesthetic was performed in the right hemicoronal region. After inci-

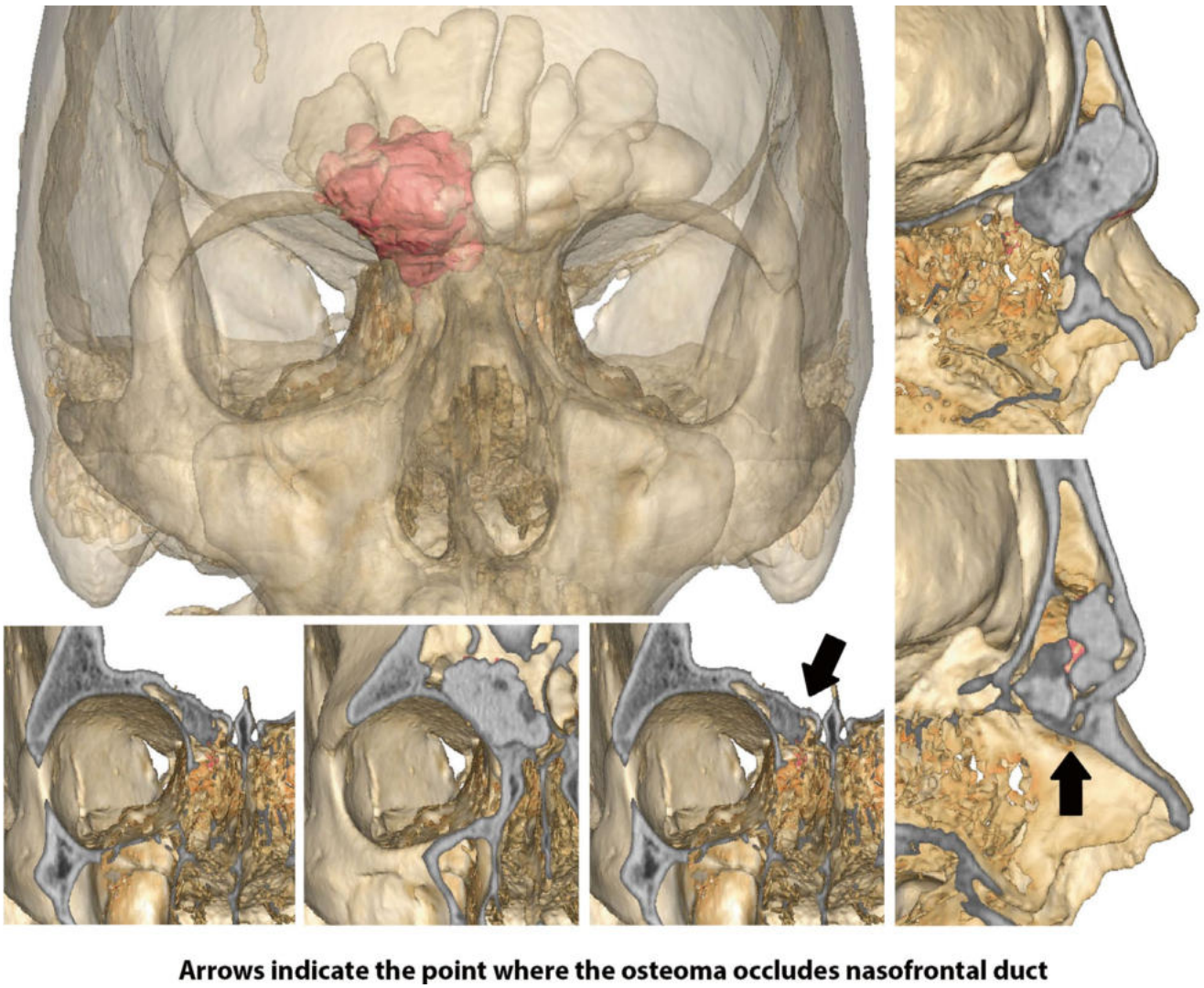


Fig. 2 Virtual model analysis of a case of intrasinusal frontal osteoma occluding the nasofrontal duct. Cross-sectional cuts of the 3D model, viewed as superimposed DICOM slices, demonstrate the osteoma bulging within the frontal sinus outflow tract (arrows)

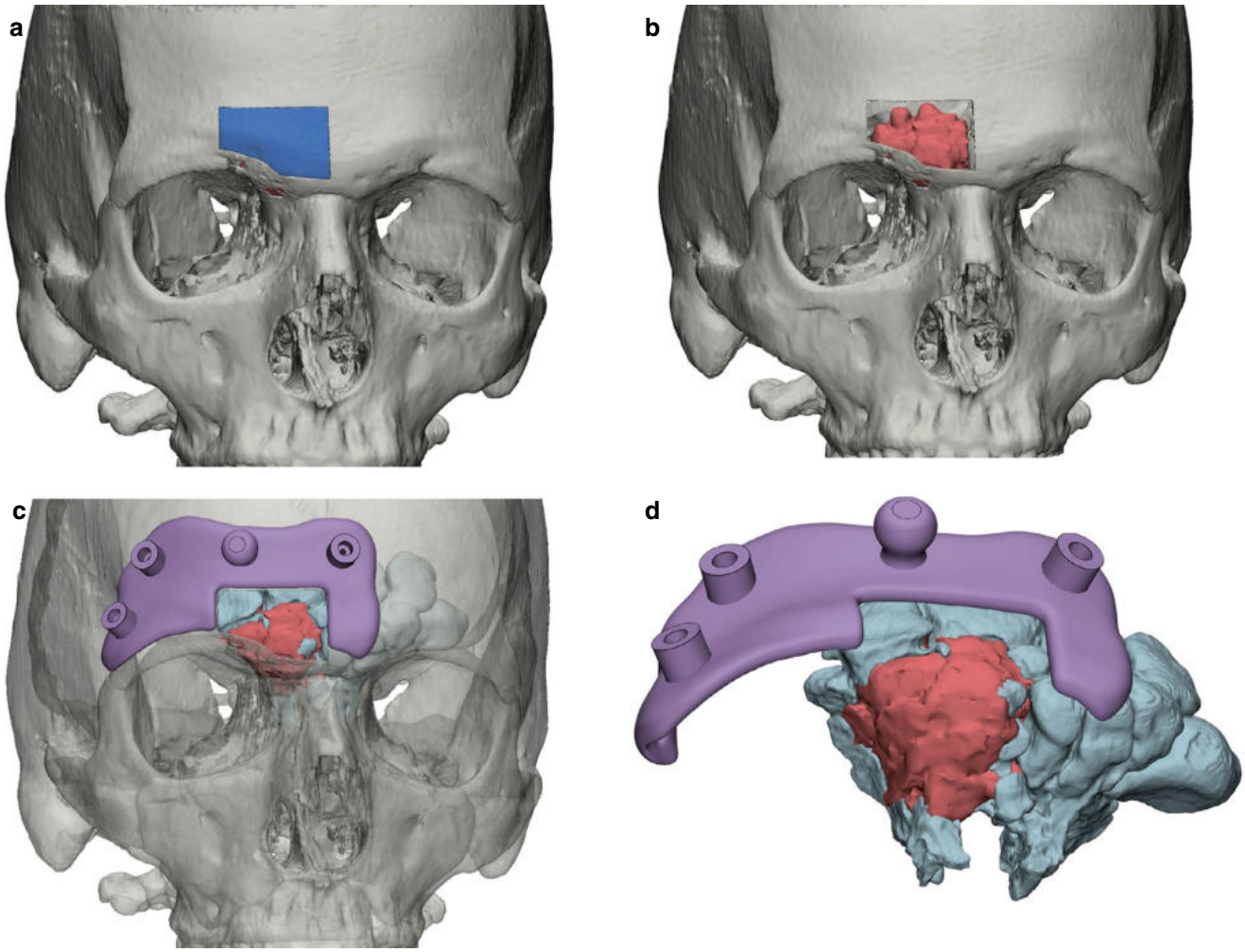


Fig. 3 Computer-guided excision of the osteoma. (**a**) Definition of a bone window to excise the lesion without violating the contralateral sinus; (**b**) small operculum is hidden showing the underlying osteoma; (**c**) a surgical guide is modeled to assist the window design. The guide finds a stable fit point over the lateral orbital rim; (**d**) particular of the relationship between the guide, airways and the osteoma

sion, a right hemicoronal flap was performed and the frontal bone and right upper orbital frame were exposed. 3D-printed surgical guide was placed paying attention to the identification of supratrochlear and supraorbital bundles. A bone osteotomy with piezoelectric handpiece was then performed to access the right frontal sinus and before removal of the bone preplating of the bone flap was performed. After removing the osteoplastic flap, no entrance in the left healthy hemisystem was assessed. Upon removal of the bony flap and creation of the planned operculum, the osteotoma was removed, leaving the remaining frontal sinus mucosa intact and preserving its insertion over the orbital roof. The opening and endoscopic calibration of the natural ostium of the right frontal sinus was then performed. The osseous flap was repositioned and fixed with plates and screws (Fig. 4).

4.2 Frontal Sinus Mucocele

4.2.1 Clinical History

This patient had been presenting with continuous pain with recurrent swelling in the right fronto-parietal region for about 2 months. Nausea and photophobia worsening with head movement were also clinically appraised. The patient acknowledged pain activation at the level of the nasal root. CT and MRI scan of the head showed a right frontal endosinusal neoformation with erosion of the posterior wall of the frontal sinus of about 4 cm in maximum size, with fluid content, which could be related to a frontal mucocele. The patient reported previous right frontal trauma 15 years earlier. Open removal of the lesion through a hemicoronal access was established as surgical indication.

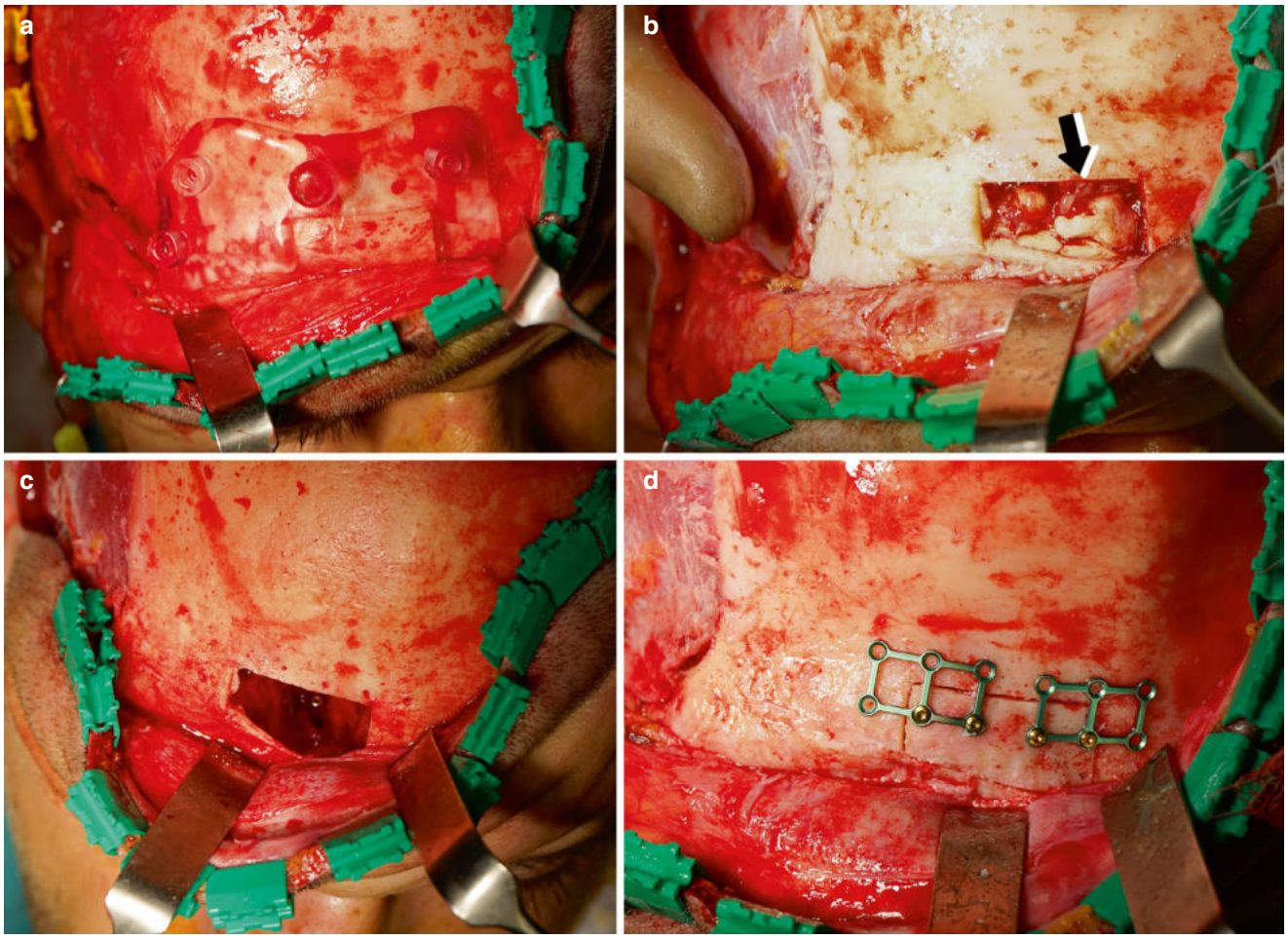


Fig. 4 From (**a**) to (**d**): corresponding surgical phases from guide placement to piecemeal excision of the osteoma

4.2.2 Virtual Surgical Planning

As in the previous case, accurate reconstruction of the frontal sinus was performed through a negative segmentation technique. However, given the mass hardly visible in CT scan, MR sequences underwent image registration with CT: this enabled to segment the soft tissue lesion, as well as surrounding hyperplastic mucosa within sinus boundaries. The importance of surgical planning here was to locate the osteotomy in correspondence of the lateral extremity of the right frontal sinus and not beyond. Design specifications for the surgical guide were similar to the previous case, hence the need of a lateral extension of the guide to stabilize it across the lateral orbital rim (where the curvature radius briskly changes compared to the surrounding flat cranial vault), a curved handle to improve ergonomics, and fixation system to stabilize it over the cranial vault once the optimal fit is found. The inferior margin was complete in this case, as it was located at enough distance compared with the underlying neurovascular bundles (Fig. 5).

4.2.3 Surgery

A coronal flap was then elevated to expose the frontal regions and the orbital rims. Part of the lateral orbital rim was carefully deperiostized to facilitate the accurate anatomical positioning of the guide through its lateral extension. After positioning and fixing the surgical template, osteotomy of the anterior wall of the right frontal bone with the aid of the template was performed. Before removal of the frontal bone, preplating was performed. Then excision of cystic neoformation of the right frontal sinus was safely accomplished without violating non-sinus bone, as the bone window was perfectly tailored over the lesion. After excision, the dura mater appeared intact. Complete removal of the sinus mucosa of the frontal sinus under endoscopic guidance was performed and the frontal sinus was plugged in multiple layers using a combination of fascia lata, fibrin glue, and fat. Histologic examination confirmed the diagnosis of mucocele (Fig. 6).

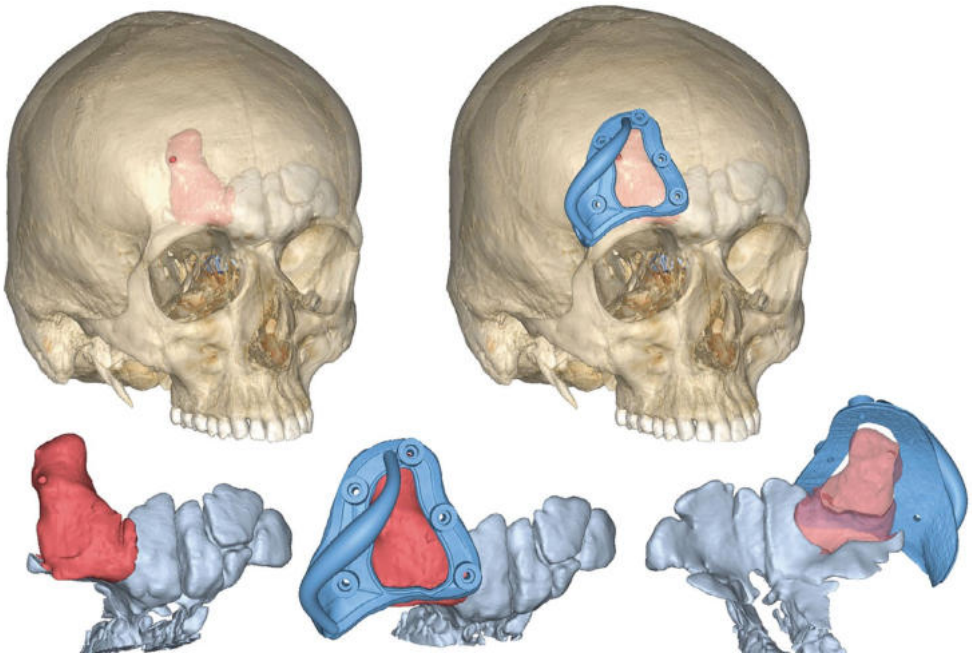


Fig. 5 Computer-guided excision of frontal sinus mucocele. Here, the main role of the guide is to avoid creating an access window outside the lesion. The bone window is exactly sized over the lesion

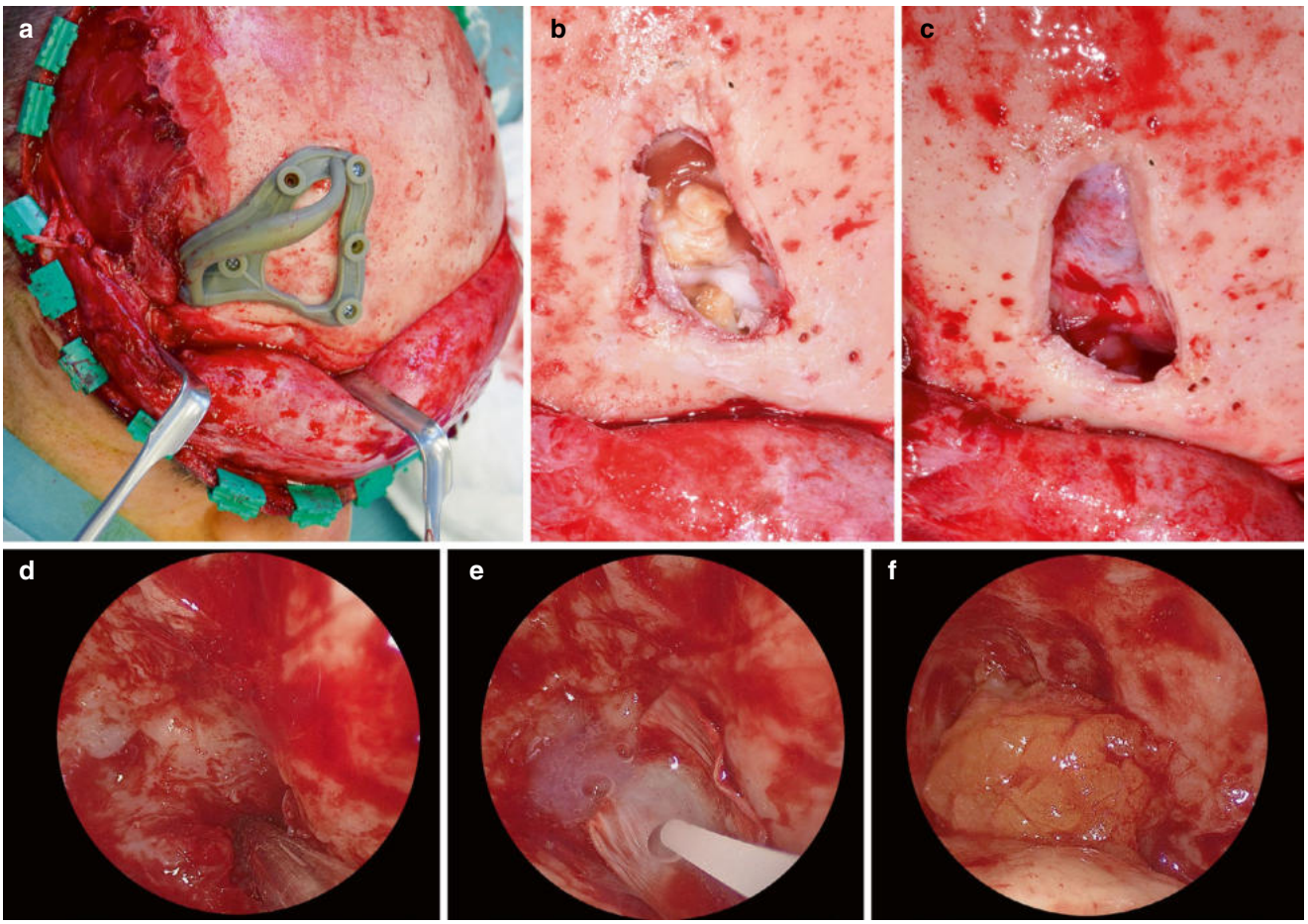


Fig. 6 From (**a**) to (**c**): surgical guide-assisted bone window creation. (**c**) The preservation of a integer dural layer. From (**d**) to (**f**): endoscopic steps to isolate the frontal sinus through nasofrontal duct occlusion using a collagen membrane, fibrin glue, and a fat graft

5 Frontal Sinus and Anterior Skullbase Traumatology Introduction

The purpose of the frontal bone and its associated frontal sinus is to act as a shock absorber for direct trauma to the brain. As a result of this, the frontal bone is able to withstand great amounts of force prior to fracture. Once superseded, blunt force to the forehead can induce frontal bone fractures. Studies show that the most common mechanisms of injury are usually secondary to motor vehicle accidents, followed by pedestrian investments, falls, and other traumatic events [5]. Adjacent structures, such as the nasal bone and orbital rims, fracture at lesser kilograms of force; thus, frontal bone fractures are usually present with concomitant fractures of adjacent bony structures. Therefore, the management of anterior skull base trauma is intertwined with management of contiguous facial subunits. Proper management of anterior skull base fractures can mitigate both early and late complications following surgical intervention, including ocular or neurological post-traumatic sequelae. Though the primary goal of treatment in frontal bone fractures is the maintenance of a healthy frontal sinus and aesthetic reconstructive outcomes, the surgeon must consider the adjacent anatomical structures and include neurosurgical and ophthalmological evaluations in treatment planning (Fig. 1).

5.1 Management of Anterior Skull Base Fractures

The anterior skull base is the anterior third of the cranial base that includes bony, vascular, neural, and soft tissue subunits. Superiorly, the anterior skull is defined by the frontal bone with both anterior and posterior tables. The septum is often parasagittal and does not form at the true midline. As seen, the frontal sinus lies between the anterior and posterior tables and includes the mucosa and ostia located posteriorly and medially on the sinus floor that allows drainage through the infundibulum to the middle meatus of the nasal cavity, either through a direct outflow tract or through the ethmoid sinus [6].

A thorough understanding of both the anatomical and functional subunits of the frontal sinus is warranted when considering surgical options for repair. As stated, the relevant subunits implicit in the reconstruction of anterior skull base fractures include the anterior table, nasofrontal outflow track, and the posterior table. High-resolution CT scan from the vertex to the upper maxilla is indicated to determine the extent of fractures. The author advises at least 1 mm slice thickness and 512 × 512 matrix acquired with a bone window. Posterior table fractures can cause dural tears, leading to pneumocephalus and intracranial hemorrhage, which are to be ruled out during diagnostic examination. Rhinorrhea may be an indication of dural tears, where a communication exists between the contents of the cranial vault and the aerodigestive tract.

5.2 Treatment Algorithm for Tailored Application of Technology

Several treatment algorithms have been used throughout the years with varying degrees of success. Although there is no universally accepted algorithm, many maxillofacial surgeons plan treatment based on the location of the fracture, presence of nasofrontal outflow tract obstruction, and presence of prolonged CSF leaks. Location of the fractures impart an important role in reconstructive management of frontal bone fractures. For example, the location of the fracture may involve the anterior table, posterior table, or a combination of both. In a study by Bell et al. in 2007, surgical intervention was based on two main criteria, which are the displacement of the fractures and nasofrontal duct patency [7].

- If the anterior or posterior table is non-displaced and the nasofrontal duct is patent, the patient can be observed with no surgical intervention indicated.
- If the patient has displacement of fracture segments, but a patent nasofrontal duct, clinical judgment must be made. The authors suggest following a rule that if the displacement is greater than the thickness of overlying soft tissues, it is assumed that the injury will create a cosmetic deformity and will benefit from repair.
- If the posterior table is comminuted or there is significant dural involvement, operative intervention with cranialization is recommended to allow for safe herniation of the brain. Furthermore, if the nasofrontal duct is obstructed, the frontal sinus must be obliterated to prevent future complications.

Understanding the sequences for frontal sinus and anterior skullbase fracture management is relevant to determine which steps can be enhanced by the application of technology, including VSP, 3D printing, and navigation.

Anatomical Outer Table Reconstruction Anterior table fractures that are displaced without involvement of the nasofrontal outflow tract can be anatomically reduced and plated with titanium plates and screws. If severe comminution exists, titanium mesh or autogenous bone grafts can be used to repair anatomic defects. Repair of these defects aids in reducing unwanted postoperative contour deformities.

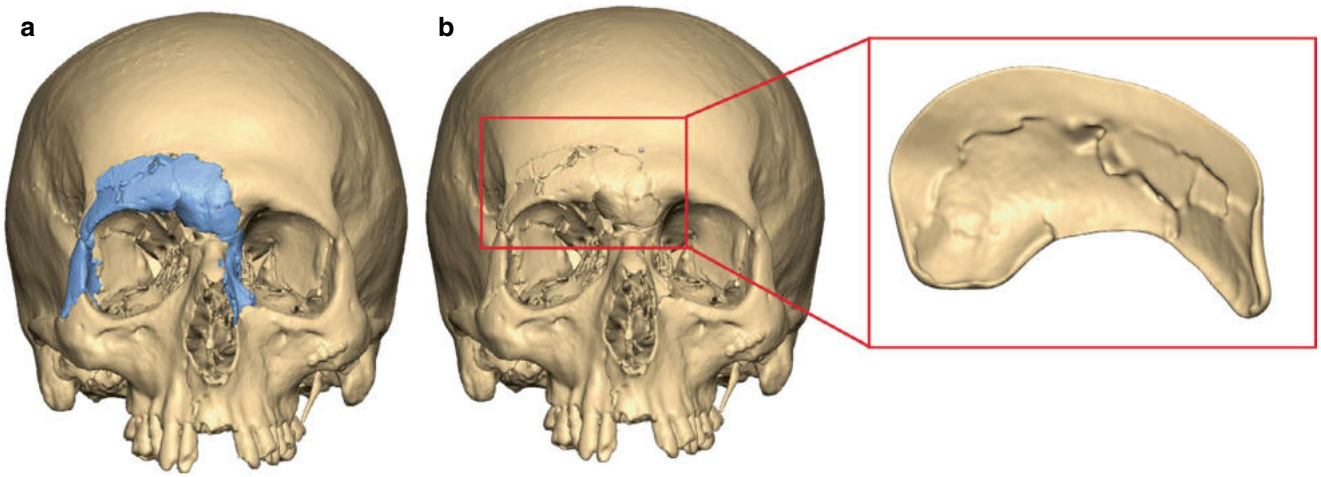


Fig. 7 Role of VSP for anatomical reconstruction of outer table fractures. (**a**) Anatomical segmentation with isolation of fractured fragments virtually repositioned in a reduced position (**b**) A negative template can be designed from the models of reduction to intraoperatively assess the correspondence of reduction

- *VSP: in this step, realigning bone fragments in the virtual project can help to establish their orientation. In addition, the use of a 3D-printed repositioning template may facilitate bench assembly of such fragments, as described for the all-in-one surgical guide (*Fig. 7*).*

Naso-Frontal Duct Evaluation For fractures involving the anterior table with obstruction of the nasofrontal duct, the initial treatment step after exposing the fracture site is elevation of the anterior table. Comminuted osseous structures of the anterior table can be placed onto the back table and placed into the correct reconstructive orientation. Mucosal remnants on the posterior aspect of the anterior table should be removed at this time. Next, the nasofrontal duct system can be evaluated. A relatively straightforward technique of evaluating the patency of the outflow track is by placing an angiocath into the nasofrontal duct ostia, located in the posteromedial aspect of the frontal sinus, introducing fluorescein or methylene blue, and observing its emergence from the medial meatus of the semilunar hiatus or its collection in the posterior pharynx.

- *VSP: at this point, VSP can be used to perform a virtual exploration of the nasofrontal duct, to determine whether bone fragments impinge within its lumen. Although the most reliable method is still based on fluorescein staining or catheterization, virtual endoscopy of the nasofrontal duct performed in a 3D model reconstructed from a high-resolution CT can provide initial clues* (Fig. 8).

Obliteration In the event that the nasofrontal duct system flow is delayed or absent, obliteration of the sinus is warranted. The sinus margins can be outlined using a Bayonet forceps by inserting it into the anterior table defect and tracing the periphery of the sinus. Alternatively, transillumination with a light source can be used to trace the boundaries of the sinus. This step is important because if obliteration is indicated, all mucosa must be removed; incomplete removal of mucosa can lead to long-term complications as described later in the chapter. The periphery is marked with a marking pen or electrocautery. After proposed osteotomy is marked, 1.0 mm plates can be placed spanning the sinus margin, predrilled, and rotated away from the sinus. This allows for accurate repositioning of the anterior table after sinus obliteration. A fissure bur is then used to outline the anterior table over the frontal sinus to allow for complete removal. Rongeurs, curettes, and round burs can be used to remove all mucosal remnants of the frontal sinus, completing sinus obliteration. Afterward, the nasofrontal duct is occluded with fibrin glue and temporal fascia. Additionally, a pedicled pericranial flap can be used to occlude the duct, which is described below. Complete obliteration of the frontal sinus is then achieved to fill the dead space with either abdominal fat, temporalis muscle, autologous bone, or bone cement. Once obliteration is complete, plating of the anterior table is indicated. The bony segments may be fixated via cranial plates, and in some cases, when comminuted, titanium mesh can be configured to restore anterior projection of the frontal bone.

- *VSP: the negative segmentation of frontal sinus can be useful to construct a 3D model that can be intraoperatively navigated to enable sinus mapping on the surface; eventually, the osteotomy can be made highly selective, as seen in case of sinus pathology, using a surgical guide, as seen in cases of frontal sinus pathology.*

Cranialization Neurosurgical evaluation and assistance are indicated if cranialization is required. Bifrontal craniotomy is usually performed which allows complete exposure of the posterior table. The posterior table is removed after the dura

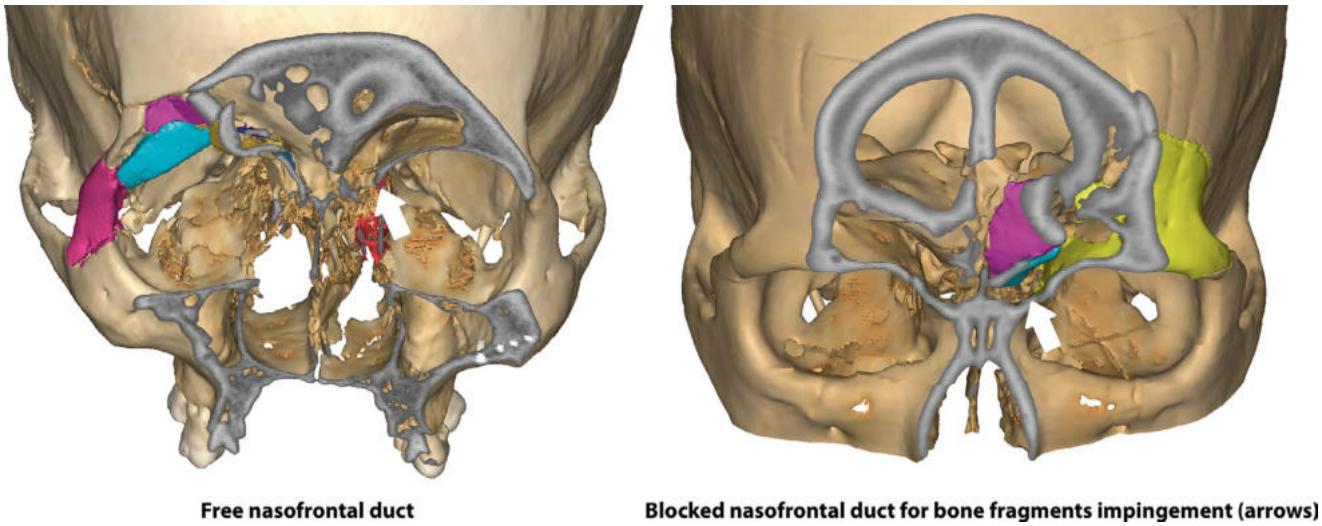


Fig. 8 Enhanced VSP visualization of fragments potentially occluding the nasofrontal duct in frontal sinus fractures

is carefully dissected. The frontal sinus mucosa is then removed as described above. Once completed, the neurosurgery team can repair any dural tears via primary repair or fibrin glue. Next, obliteration of the nasofrontal outflow tract and filling of the dead space must be completed using a pericranial flap. The flap is inserted over the supraorbital rims and into the sinus, and secured with sutures through craniectomy sites. Finally, the anterior table can be repaired in the same fashion as described above.

- *VSP: Navigation can drive the identification of fragments displaced posteriorly and provide intraoperative guidance while the posterior table is drilled* [8]. *A 3D-printed surgical guide can safely guide the anterior table osteotomy to safely access the entire posterior sinus wall without violating the boundaries of the sinus itself* [9].

Anterior Skullbase Reconstruction As stated above, localized flaps can be elevated to separate the brain from the aerodigestive tract. Pericranial flaps are vascularized flaps that can be elevated from an existing coronal incision, often used in cranialization procedures [10]. When the posterior table is fractured with resultant dural tears, a pericranial flap enables obliteration of the sinus, separates the nasofrontal ductal system from the brain, and allows the brain to safely herniate anteriorly. The pericranial flap protects the brain from the anterior table of the frontal bone, taking the place of the posterior table. Proper flap design and elevation is crucial to ensure flap vascularity and viability. To elevate a pericranial flap, an incision is made through the loose areolar tissue to pericranium in a horizontal fashion. Full thickness parasagittal incisions are then made in a superior-inferior direction. Elevation of the flap can then be achieved, and dissection is performed sharply to preserve vascularity of the flap. The most commonly used pericranial flaps are anteriorly based relying on the supraorbital and supratrochlear vessels. If any concerns in the patency of the supraorbital vessels exist, a lateral temporoparietal flap can be elevated based on the superficial temporal artery. Intraoperative doppler ultrasonography can assist in determining the patency of the vessels.

5.3 VSP Protocol

As seen, the incorporation of technology within the management workflow of anterior skull base trauma contributes to improve surgical outcomes. Primary goals of surgical management of anterior skull base fractures are the protection of cranial contents, maintenance of a healthy sinus, and achieving esthetic outcomes.

The initial planning phase involves gathering anatomical data through computed tomography (CT) scans and uploading it to a design software. Yet we advise 1 mm sliced CT scan, preferably slices should be acquired in 0.625 mm amounts to maximize the likelihood to detect thinnest bony walls at the same time minimizing partial volume effect. This is highly important when aiming to perform the evaluation of the nasofrontal duct and segmentation of tiny bone fragments. Bone geometry is acquired with threshold algorithm applied in a bone window. On the segmented mask, the application of split mask algorithm allows surgeons to separate fractured subunits from one another based on location and density, yielding distinct objects that have been separated across fracture lines. This is the base to reposition fragments postoperatively when performing the digital reduction, or, alternatively, to decide to exclude fragments from reduction and complete a mesh cleanup to isolate stable bone margins (Fig. 9).

In this case, it is possible to determine the margins for a planned custom implant. Once segmented, surgeons can use

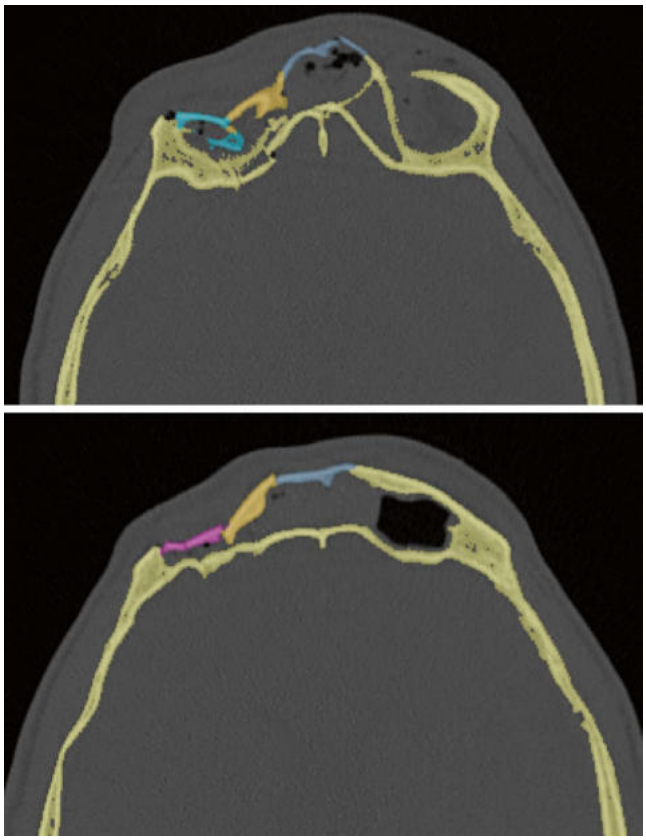


Fig. 9 Application of split mask algorithm to separate fracture fragments in a comminuted anterior table injury

mirroring tools within the software to mirror the unaffected contralateral anatomy to the affected side. For frontal bone fractures, a series of mirroring applications are performed to rebuild the contours of the frontal bone, eventually including part of the orbital rims by mirroring individual subunits that are then merged in the final implant. Whenever this is not feasible owing to a midline defect or severe comminution, alternative approaches have to be taken into account, including closest template donor and statistical shape modelling, as explained in detail in chapter "Applications of VSP for Customized Subperiosteal Implants for the Rehabilitation of the Atrophic Jaws" for cranioplasties. Another possibility in the future will be based on point completion algorithms, that take advantage of deep learning to reconstruct the most reliable filling of the defect, in an entirely generative process.

5.4 Additive Manufacturing in Anterior Skullbase Reconstruction

Once the planning phase is complete, tangible objects, whether they are molds or patient-specific implants additively manufactured, can be printed or milled. Described as the modeling phase, surgeons can use in-house laboratories (alternatively, outsource files to third-party manufacturers) to fabricate models to be used in the pre- and perioperative settings. Applications include the following:

- Printed replicas of VSP: surgeons can print models of the segmented and reconstructed skulls so that plates can be contoured and sterilized preoperatively. In addition to plates, cutting and drill guides can be designed and printed prior to entering the operating room. This is the most obvious and simple use.
- Cutting guides: For fractures involving the nasofrontal duct or posterior wall, prefabricated cutting guides can be used to outline the contours of the frontal sinus, allowing to expose the whole inner surface of the sinus. This is important as this mucosa must be entirely removed during cranialization or a mucocele can form as a late complication. The frontal sinus is irregularly shaped, and having a prefabricated cutting guide can facilitate inner surface exposure by defining the borders of the sinus more predictably (Fig. 10).
  ** Cutting guides can also play a role by predefining the site of localized calvarium grafts, as seen in chapter "Principles of Cranial Reconstruction". With the supraorbital bandeau often affected by frontal bone fracture, calvarium grafts can be harvested to aid in recreating the contour. The typical donor sites can be from the outer table of the cranium for smaller defects, as well as anterior or posterior iliac crest for larger defects. Moreover, surgeons can then use pre-fabricated drill guides to create predictive holes for plating bone grafts and patient specific implants.*
- Implants: surgeon's preference generally determines the type of implant to be used. The possibilities offered by computer guided, patient-specific reconstruction include template-shaped autologous grafts or alloplastic prostheses, such as titanium alloys and poly-ether-ketone-ketone (PEKK) implants [11].

With advances in technology and fabricated synthetic materials, as well as to avoid the morbidity associated with a second surgical site, PEEK and PEKK are viable options for the reconstruction of anterior skull base defects. Both materials are highly performing thermoplastic polymers with inert properties and additional favorable features, such as mechanical stability, high temperature resistance, and chemical resistance [12]. Such implants are designed during the modeling phase and printed prior to taking the patient to the operating room. The optimal indication includes situations where significant comminution occurs or wide fragments of bone are missing. However, the authors prefer their use in secondary reconstruction, namely, to restore the anterior-posterior dimension in a healed depressed frontal bone fracture. This is true for two essential reasons: first, manufacturing

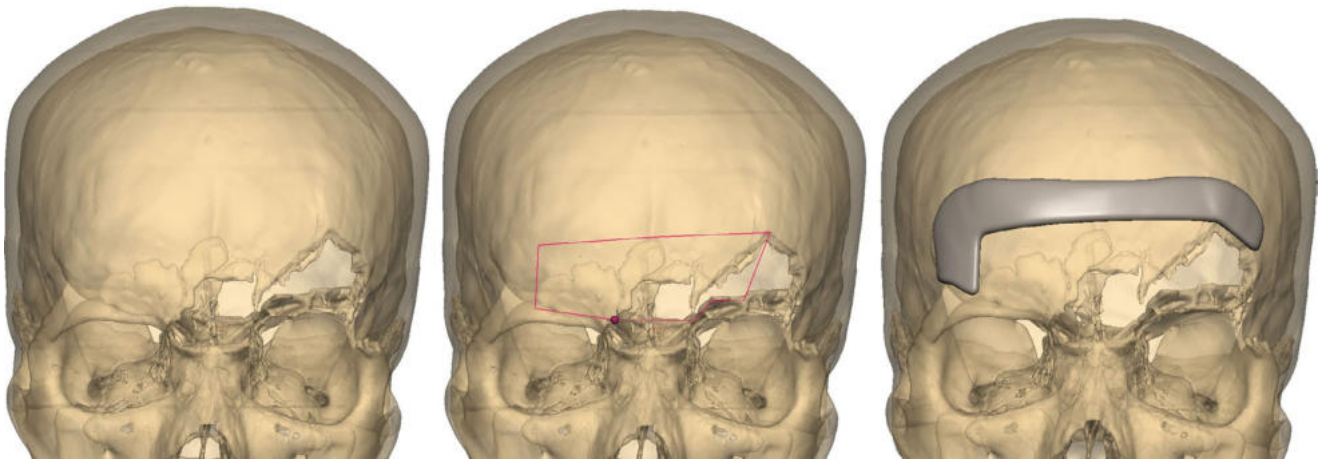


Fig. 10 Importance of VSP in cranialization procedures: osteotomy of the anterior wall is designed exactly overlapping the frontal sinus contours to limit a possible dural injury and optimally expose the posterior wall. A surgical guide can be designed to assist such osteotomy

time and delivery by a third-party producer are hardly compatible with trauma surgery performed in a urgency regimen (yet this can be partly solved if a point-of-care lab is available and cranioplasty molds are produced, as seen in chapter "Principles of Cranial Reconstruction"), but most importantly, to decrease the risk of implant contamination, which is substantially higher after trauma. In this case, it is best to remove comminuted and avascular fragments to decrease the risk of bone necrosis and put the patient in antibiotic therapy, differing reconstruction in a second stage when wounds are healed and inflammation ceased.

5.5 Intraoperative Image-Guided Technologies in Anterior Skullbase Injuries

Execution of the surgical plan is the last and most obvious phase of this process. Planning the surgery virtually using the technology described should allow for an otherwise burdensome procedure to be carried out in stepwise fashion to provide the patient with the most ideal outcome.

Intraoperative navigation is defined as, "a device that can accurately locate critical anatomical structures, the safest way to reach that target, and the orientation around which safe and reliable surgery can be carried out." Navigation allows surgeons to detect structures whose intraoperative identification is complex due to their localization and depth. Concerning anterior skullbase fractures, the use of navigation can play a critical role in predictably defining relevant surgical limits, such as the dura, nasofrontal ducts, nasofrontal recess, and other important anatomical structures. Using an optical or magnetic tracking device, intraoperative navigation combines data from imaging and VSP with a localizer fixed to the patient's head to generate real-time feedback in three dimensions. Unlike the lower facial third which is mobile, navigation in the upper and middle facial thirds is more predictable as they are fixed to the rest of the cranium. In these cases, utilizing surgical probes intraoperatively to locate and track the nasofrontal outflow tract in severely comminuted frontal bone fractures can be useful in obliteration procedures. Even more so, when coronal access is not performed, intraoperative navigation can be used in more conservative surgical approaches to obtain predictable outcomes with limited direct visibility [13].

6 Clinical Cases

6.1 Fracture of the Anterior Table of the Frontal Sinus Without Nasofrontal Duct Injury

6.1.1 Clinical History

A young patient was admitted to emergency department following a car crush with multiple fractures and spleen rupture. In his face, there was a conspicuous depression with a small laceration of the overlying skin. CT scan revealed a multifragment fracture of the anterior wall of the frontal sinus, the glabellar region, and the superior-lateral orbital rim. Moreover, a type I nasal-orbital-ethmoidal (NOE) fracture in the left canthal region was detected. Indication for surgery was established after orthopedic and abdominal surgery.

6.1.2 Virtual Surgical Planning

All fracture fragments were isolated and managed separately using the application of the split mask algorithm, then individual masks were retessellated into polymeshes. A mirroring template was simulated, as the defect in the frontal region

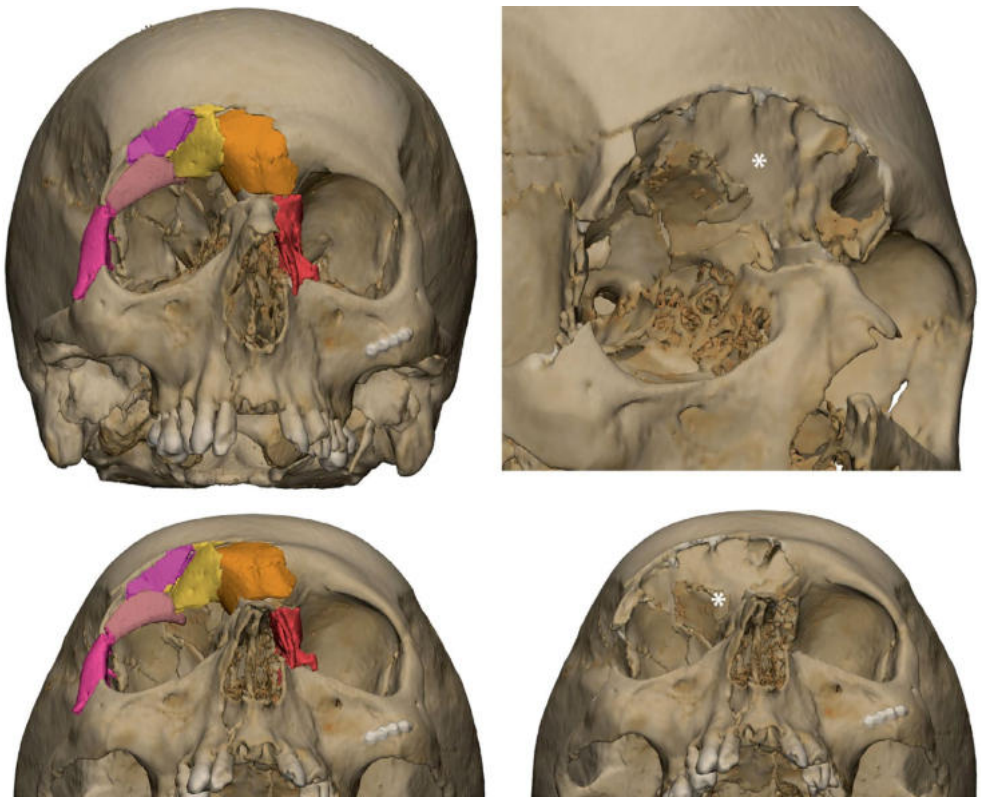


Fig. 11 Example of comminuted anterior table fracture with preservation of the integrity of the posterior table (asterisk). This is an indication for anatomical reduction only of the anterior table. The nasofrontal duct should always be checked for patency

was mostly limited to the right half. The mirroring was made coincident with the native skull using a global registration algorithm. Once displaced fragments were removed, the integrity of the posterior wall of the frontal sinus was assessed (Fig. 11). Based on the mirrored template and with manual fine-tuning, virtual reduction was performed in 3-matic software. A surgical guide for anterior wall reduction was modeled based on the planned position of the fragments, which were individually labeled to establish the order of reduction. The same labeling order was transferred to the surgical guide, which included a screw slot above each fragment to lift it and stabilize it in the proper position. The surgical guide was secured to the surrounding, integer bone, using three fixation holes and a handle was included to facilitate its positioning (Fig. 12).

6.1.3 Surgery

The fracture was exposed using a coronal flap. Fragments were first mobilized and lifted using an elevator. After the surgical guide was secured to the intact bony edges, a screw hole for fragment 1, 2, and 3 was drilled in the corresponding planned position and the screw was inserted to lift the fragment. This further facilitated reduction and alignment of bone fragments. The surgical guide was gently removed and plating was accomplished. Postoperative CT scan revealed a successful reduction in the anatomical position (Fig. 13).

- This guide can also be designed with inner slots that enable plating when the guide is still in situ.

6.2 Fracture of the Posterior Table of the Frontal Sinus with Cranialization

6.2.1 Clinical History

This patient was similar to the previously described case, but here CT scan showed a minimally injured anterior wall, but a severely fractured posterior wall with its fragments occluding the nasofrontal duct as well. Clinical examination revealed the presence of CSF leak from the nasal fossae. Surgery with a cranialization procedure and nasofrontal duct obliteration was deemed necessary.

6.2.2 Virtual Surgical Planning

As mentioned in the previous sections, for cranialization procedures, the main goal of VSP is to provide a safe access to the inner surface of the sinus, to remove all its mucosa (in case of a nasofrontal duct obliteration procedure), and to dismantle the posterior wall when cranialization is performed. The osteotomy of the anterior wall of the frontal sinus should not violate the boundaries of the sinus itself to avoid inadvertent damage to the dura. In this regard, a full cranialization procedure was simulated, from the anterior wall flap osteot-

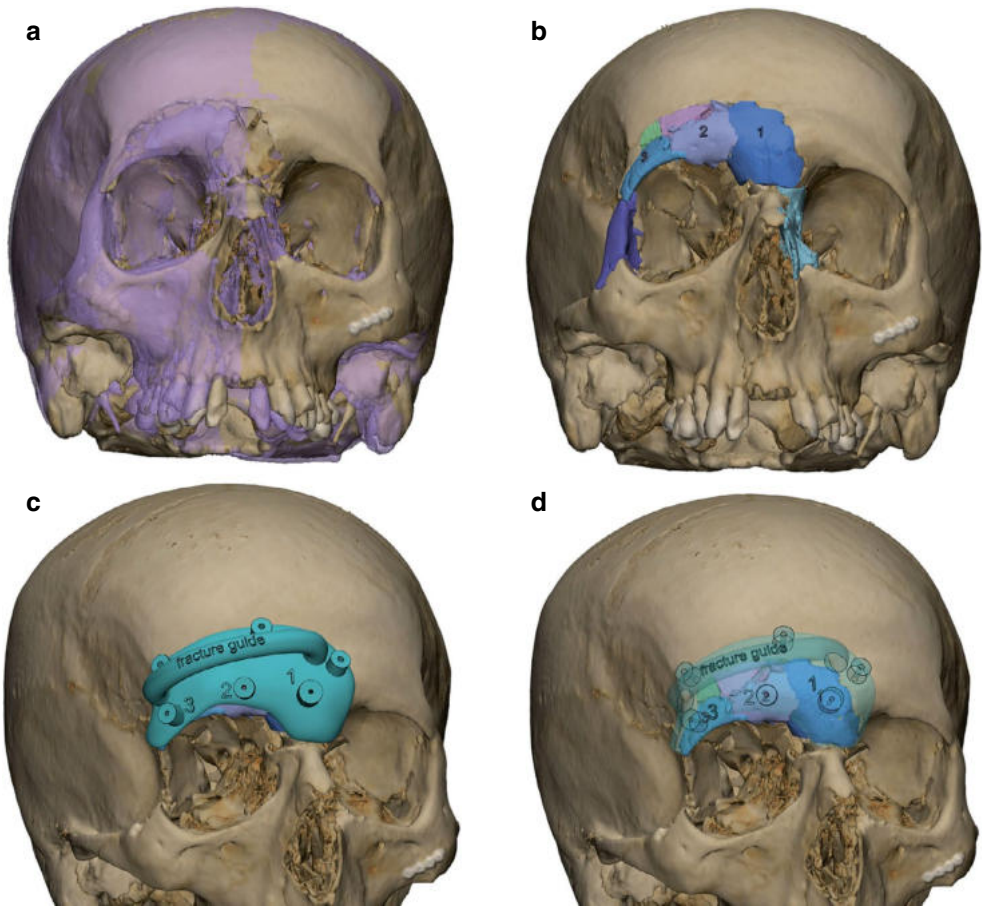


Fig. 12 A combination of mirroring-registration and anatomical landmark-based reduction is used to optimally realign fractured fragments. Here, a surgical guide has been purposely created with the aim of intraoperatively verifying the correspondence of anatomical reduction with VSP. In case some fragments are displaced downward, the surgical guide allows to elevate them by inserting a cortical screw

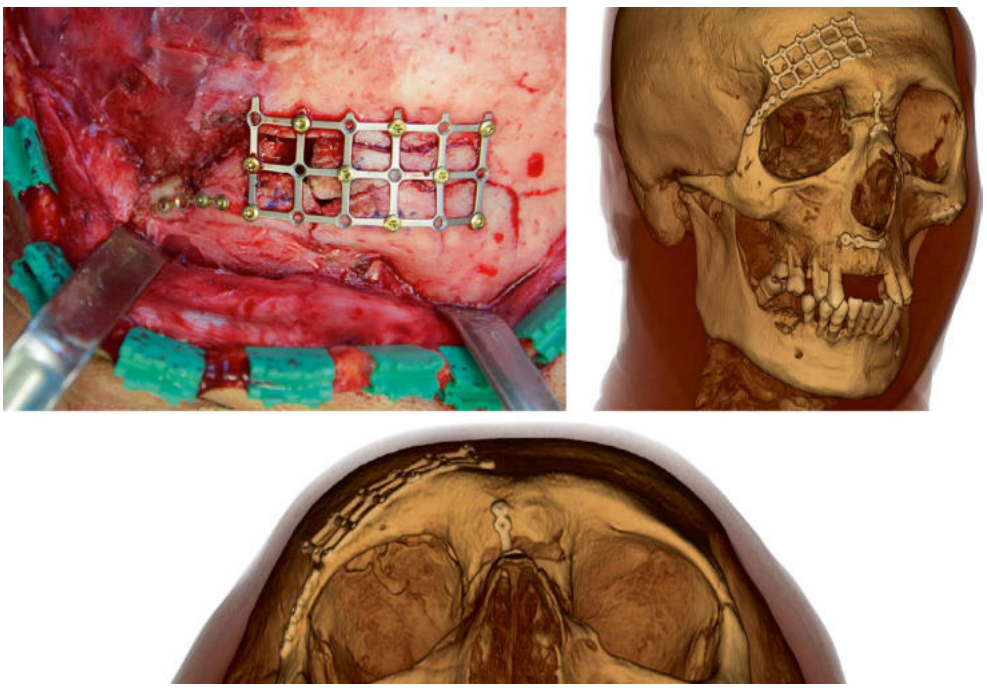


Fig. 13 Outcome of the computer-guided reduction, with overall correct realignment of fracture fragments. Intraoperative sequence and postoperative CT are shown

omy, to the posterior wall ostectomy. A surgical guide was modeled to tailor the anterior wall osteotomy exactly above the boundaries of frontal sinus, whereas a simulation of the posterior wall ostectomy was performed to define the extent of the posterior wall removal. The same coordinates could then be exported for intraoperative navigation, allowing to navigate the safe removal of the posterior wall (Fig. 14).

6.2.3 Surgery

A coronal flap was elevated to gain access to the anterior wall of the frontal sinus. Using the surgical guide, a safe anterior wall osteotomy was performed and the osteoplastic flap lifted to expose the inner sinusal surface. Accurate removal of the mucosa was accomplished and the posterior wall removal was conducted under navigational guidance to create a posterior wall window of appropriate width for brain expansion. The frontal lobe of the brain was lifted, and anterior skullbase was sealed using a multilayer reconstruction based on pericranial flap, fat, and fibrin glue. The anterior wall flap was them put back in place and fixed using plates and screws (Fig. 15).

6.3 Secondary Cranio-Orbital Reconstruction for an Extended Anterior Skullbase Defect Using Intraoperative PMMA Molding

6.3.1 Clinical History

A young lady suffered from a road accident with multiple fractures of the frontal bone and the orbit. She underwent an emergency surgery in which the left orbital roof was reconstructed using an iliac crest graft and fractured calvarial segments were treated with reduction and internal rigid fixation. She subsequently developed a massive infection with meningitis and brain empyema, which led to removal of all infected bone and a long period in intensive care unit. Once the infection was solved and the patient discharged, she presented a disfiguring depression in the frontal bone with asymmetry of the left eye globe and diplopia (Fig. 16).

6.3.2 Virtual Surgical Planning

Extended defects in the frontal area can be highly complex to reconstruct, with significant implications in aesthetical

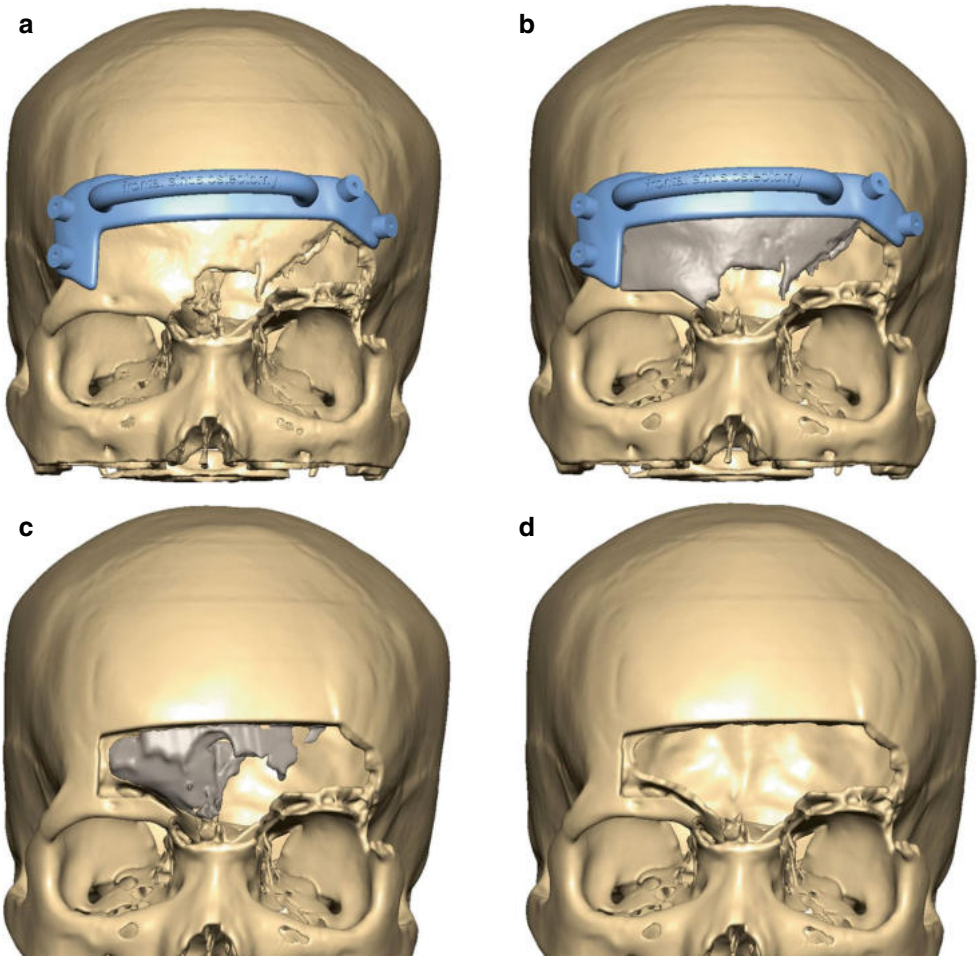


Fig. 14 VSP in case of posterior table injury requiring cranialization. (**a**, **b**) A surgical guide is used to perform a frontal craniotomy tailored over the shape of the frontal sinus. (**c**, **d**) VSP of the posterior wall ostectomy is simulated and such coordinates are delivered to the navigation system. This enables to safely remove the posterior wall to enable brain expansion

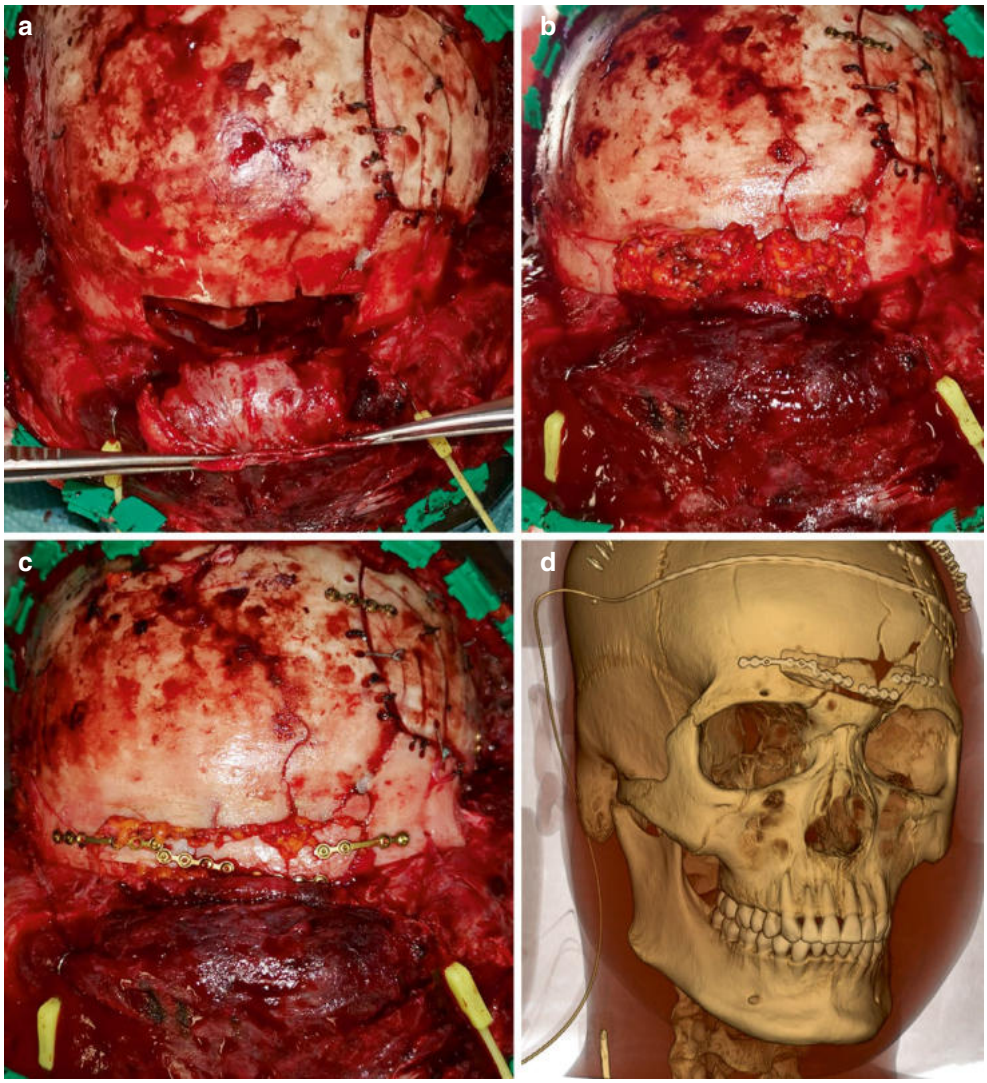


Fig. 15 Intraoperative sequences. (**a**) After cranialization, a pericranial flap is elevated. (**b**) Mucosa is removed and the flap is placed to seal anterior skullbase. Empty spaces are occluded with a fat graft. (**c**) The frontal operculum is repositioned; (**d**) postoperative CT. To be even more conservative, only the upper margin of the guide was used, and the access window was smaller than its VSP prediction



Fig. 16 Preoperative photographs of the patient, with an extended frontal bone defect involving the left superior orbital rim and roof

appearance. In many cases, such defects result from high-energy trauma with the loss of a significant part of the frontal bone, damage to the frontal sinus, and involvement of the orbital roof. In particular, the correct restoration of the orbital roof plays a central role, because of its implication on the orbital volume, whose alteration might lead to enopthalmos or dystopia. It is therefore crucial that anatomy is restored with maximal accuracy, and it is of great value to seek for photographs portraying the patient before the injury. An accurate aesthetical evaluation can provide valuable elements to plan a cranial reconstruction in accordance with the patient's original skull and can therefore influence the choice of the virtual donor, namely the closest-looking skull that is used to restore the cranial vault. In fact, large defects in the frontal region involve anatomical regions at both sides of the midline, making it impossible to use a contralateral mirroring technique. To partially solve this issue, the authors proposed the so called "subunit composition approach"; for example, any useful part from contralateral healthy anatomy is mirrored. In the following example (see "subunit composition method"), the loss of the left orbital roof and left superior and medial orbital rim, together with an extensive part of the frontal bone, is compensated by mirroring individual anatomical subunits corresponding to the right, intact, orbital roof and rim. This approach maximizes the use of the patient's own anatomy and decreases the use of an external, donor, geometry, which might alter the patient's own peculiarities, impairing the patient's self-perception after surgery. The donor geometry itself is then imported from a best-fitting template skull and overlapped to areas not replaceable with any mirrored anatomy and is carefully suited to the defect's contours, while carefully remodeling its curvature along critical areas, such as frontal prominences, taking into account pre-injury photographic documentation made available by the patient. Once the frontal defect is satisfactorily reconstructed, it is merged with the mirrored subunit (composition) using a Boolean union operation, as seen in Fig. 5 of chapter "Applications of VSP for Customized Subperiosteal Implants for the Rehabilitation of the Atrophic Jaws." Next, a Boolean operation is performed by subtracting the defect's margins from the designed implant, thus adapting the implant shape to the recipient site, and an undercut removal is performed to ensure optimal fit.

Subsequently, seams between interfaces are designed to achieve distinct and non-overlapping surfaces for the orbital roof, the intracranial surface, and the outer convexity, by splitting the mesh into three subcomponents corresponding to the mold structure (Fig. 17). Using 3-matic, the Cubik system [14] is designed paying attention to represent the whole volume of the implant and optimal closure between seams to avoid spilling of material and deformations of the implant. Extrusion channels for exceeding material are then inserted and each subcomponent is labeled with patient's ID and name of the component (Fig. 18).

Intraoperative modeling of the prosthesis was performed as previously described, by pouring PMMA within the Cubik system and awaiting its solidification. Once the material hardened, a prosthesis totally superimposable to its 3D-printed replica was extracted from the molds (Fig. 19).

6.3.3 Surgery

A coronal incision was performed. A dissection plane was created between the galea and the fibrosis overlying the dura; next, the margins of the defect were exposed and freed from intervening soft tissue (Fig. 20). Similarly, the entire rim or the orbital roof defect was exposed, using the navigator's



Fig. 17 Virtual surgical planning of defect reconstruction and subdivision into three subsurfaces

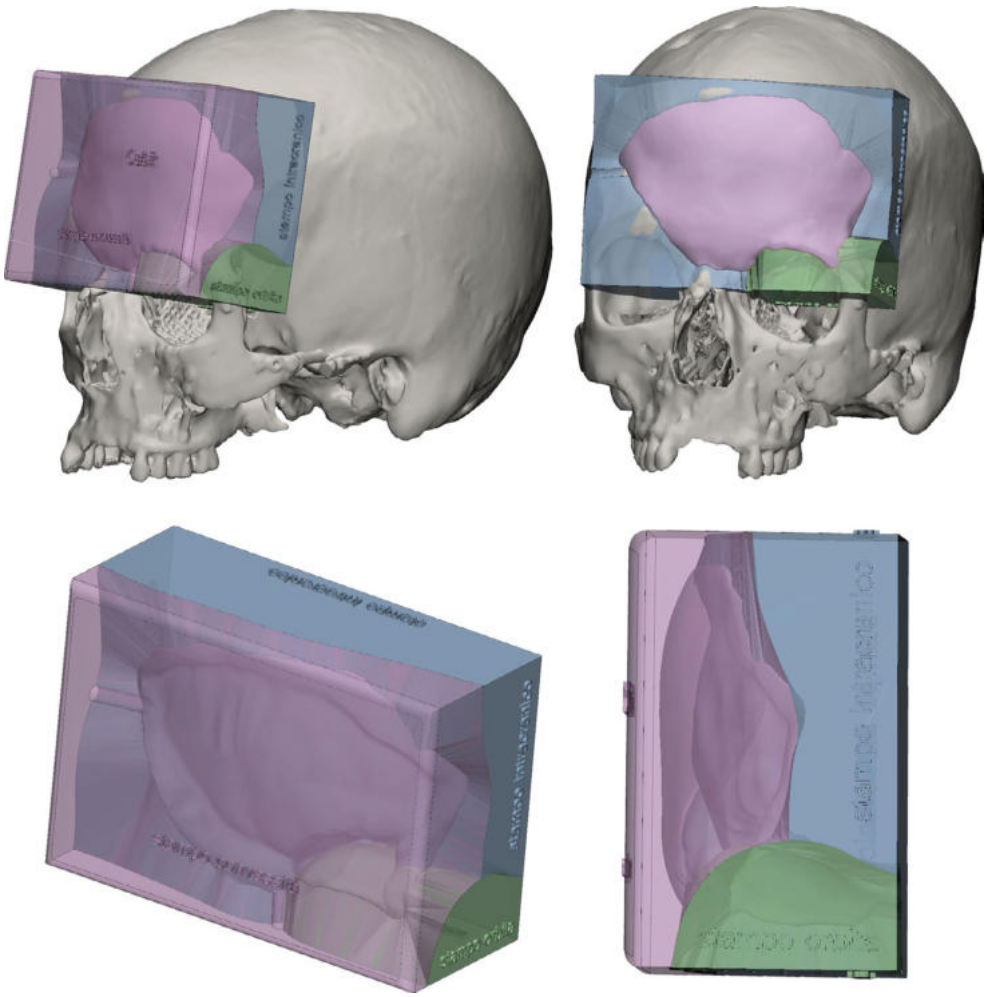


Fig. 18 Mold creation based on the implant shape and subdivision

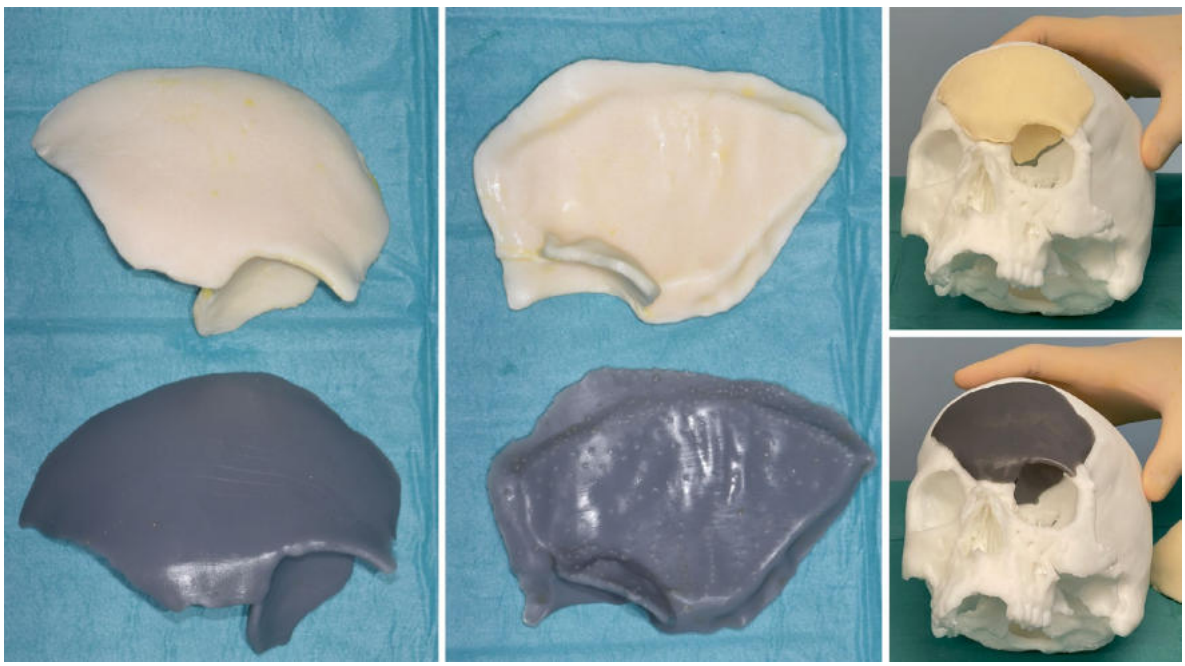


Fig. 19 Intraoperative comparison between the PMMA molded implant, implantable (white) and its 3D printed replica, template (gray), showing high resemblance



Fig. 20 Intraoperative exposure of the defect rim

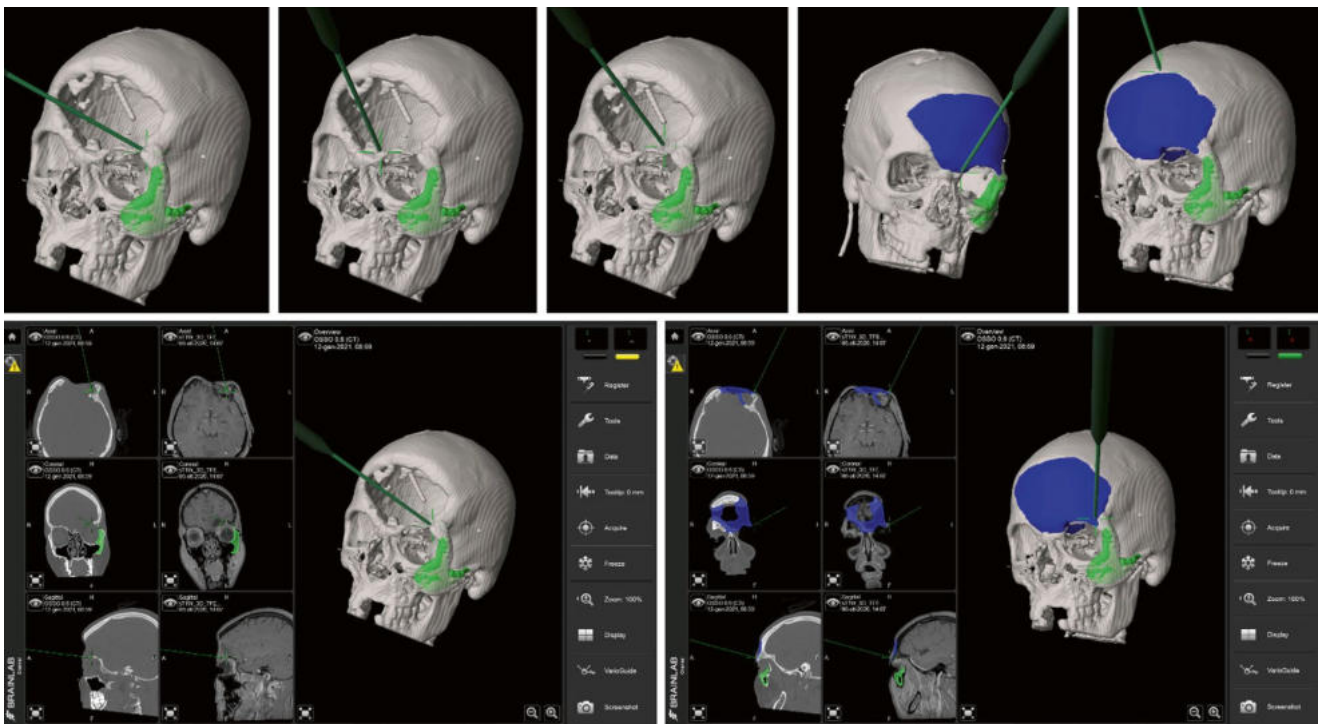


Fig. 21 Navigation of defect margins and verification of the correct implant placement (blue). Malar bone repositioning was performed to enhance orbital symmetry (green)

probe to check the deep aspect of the orbit. The final prosthesis was implanted and accurate fitting was assessed between the defect margins and the implant's contours. Again, the use of cranial navigation allowed to check for margin correspondence between the planned prosthesis and the surgically positioned one (Fig. 21). In particular, the authors emphasize the importance of reconstructing the continuity along the contour of the superior-lateral orbital rim, which is crucial both for the correct eye globe position and for the overall facial aesthetics (Fig. 22). Postoperative photographs demonstrate a satisfactory aesthetical outcome with frontal reconstruction and eyebrow symmetrization (Fig. 23).

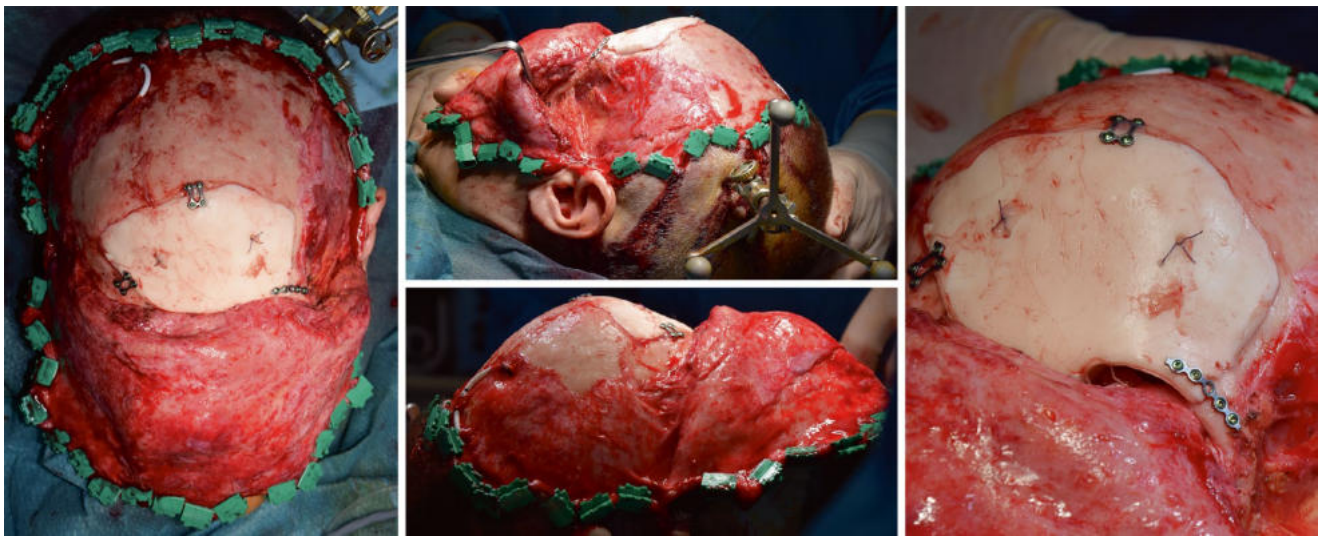


Fig. 22 Intraoperative view of implant positioning and reconstructive outcome



Fig. 23 2-month postoperative view

7 Complications of Frontal Sinus and Anterior Skullbase Surgery

The importance of technology is related to decreasing the occurrence of complications, other than decreasing surgical time and improving accuracy. The frontal sinus is an air space containing normal respiratory flora. Since the sinus communicates with the nasal aerodigestive tract, frontal sinus fractures are considered open and are prone to infections. Early or delayed complications occur in 10–20% of the patients with frontal sinus fractures. Immediate complications are those that occur within the first week of surgery. The most common immediate complications are localized wound infection or hematoma. These complications are managed by placing suction drains into the surgical site.

Postoperatively, there is always risk of developing pneumocephalus. This tends to occur without symptoms and resolve without any intervention. Tension pneumocephalus can result from increased air pressure from craniopharyngeal tract and ball valve effect which allows trapping of air [15]. If symptomatic, surgical treatment may be indicated to close the communication.

These patients are also at risk of developing frontal sinusitis in cases where sinus mucosa was left intact. These patients present with symptoms of frontal migraines and generalized tenderness to the forehead. Decongestants are

recommended for these patients to reduce mucosal inflammation.

Even without the presence of posterior table fractures, infections can travel through invaginations of the posterior table, eliciting brain abscesses and/or meningitis. While meningitis is the most common postoperative complication with a reported incidence of 0.9–6%, the cause can be multimodal [16]. For example, in addition to bacterial infections traveling posteriorly, incomplete obstruction of the nasofrontal outflow tract or remnants of sinus mucosa allows bacteria to travel into the intracranial space, increasing the risk of developing meningitis. These patients present with symptoms of severe headaches, seizures, and fevers. This serious early complication is managed via surgical intervention and intravenous antibiotic administration.

While meningitis is the most common immediate complication, the most common late complications arise in the form of mucoceles. These form as a result of continued growth of respiratory mucosa secondary to incomplete removal of pseudostratified ciliated columnar epithelium within the frontal sinus which could occur 10 years post-operatively [17]. Accumulation of produced mucus causes mucoceles to develop, increasing pressure to the frontal sinus. These mucoceles can also become secondarily infected, becoming mucopyoceles. This late complication is considered an emergency because the infected tissue can cause osteomyelitis to the adjacent structures, such as the orbit or brain. Mucoceles and mucopyoceles are most often first noticed by patients in the form of frontal headaches, diplopia, or blurry vision. Diagnosis of a mucocele is then achieved after obtaining CT imaging. The presence of a mucocele or mucopyocele warrants surgical intervention in the form of marsupialization with restoration of frontal outflow tract versus cranialization with obliteration of all mucosa within the frontal sinus.

References

1. Chen PG, McMains KC, Tewfik MA, Aden JK, Brown S, Weitzel EK. Teaching frontal sinus anatomy using the frontal sinus masterclass 3-D conceptualization model. Laryngoscope. 2018;128:1294–8.
2. Wormald P-J, Hoseman W, Callejas C, et al. The international frontal sinus anatomy classification (IFAC) and classification of the extent of endoscopic frontal sinus surgery (EFSS). Int Forum Allergy Rhinol. 2016;6:677–96.
3. Li Y, Xu C, Yu D, Xiong T, Zhao H, Xue H, Liang WB, Deng ZH, Zhang L. Computer-aided superimposition of the frontal sinus via 3D reconstruction for comparative forensic identification. Int J Legal Med. 2021;135:1993–2001.
4. Kumbla PA, Thorburn AQ, de la Torre JI, Myers RP. Correction of severe frontal bossing with coronal brow lift and osteoplastic frontal sinus setback aided by virtual surgical planning: a case report. Craniomaxillofac Trauma Reconstr Open. 2020;5:2472751220974918.
5. Al-Shami H, Alnemare AK, Mahfoz TB, Salah AM. Traumatic frontal sinus fractures management: experience from high-trauma centre. Korean J Neurotrauma. 2021;17:15–24.
6. Daniels DL, Mafee MF, Smith MM, et al. The frontal sinus drainage pathway and related structures. AJNR Am J Neuroradiol. 2003;24:1618–27.
7. Bell RB, Dierks EJ, Brar P, Potter JK, Potter BE. A protocol for the management of frontal sinus fractures emphasizing sinus preservation. J Oral Maxillofac Surg. 2007;65:825–39.
8. Bang YJ, Lim BW, Ha R, et al. Frontal sinus osteoplastic flap surgery using a surgical navigation system. J Craniofac Surg. 2018;29:e662–3.
9. Carraturo E, Germano C, Troise S, Spinelli R, Romano A, Giudice GL, Vaira LA, Piombino P. In house 3-D printed surgical guide for frontal sinus osteotomy in traumatology: a technical note. J Stomatol Oral Maxillofac Surg. 2024;126:102023.
10. Polley JW, Penney D, Cohen M. Use of pericranial flaps in the management of cranial base trauma. Skull Base Surg. 1993;3:45–53.
11. Jackson D, Obayomi T, Mir F. Reconstruction of frontal bone using patient specific implant poly-ether-ketone-ketone via a lateral nasal/lynch incision. Oral Maxillofac Surg Cases. 2023;9:100293.
12. Yuan B, Cheng Q, Zhao R, Zhu X, Yang X, Yang X, Zhang K, Song Y, Zhang X. Comparison of osteointegration property between PEKK and PEEK: effects of surface structure and chemistry. Biomaterials. 2018;170:116–26.
13. Velusamy A, Anand A, Hameed N. Navigation assisted frontal sinus osteoplastic flap surgeries - a case series. Indian J Otolaryngol Head Neck Surg. 2022;74:1232–6.
14. Tel A, Tuniz F, Sembronio S, Costa F, Bresadola V, Robiony M. Cubik system: maximizing possibilities of in-house computer-guided surgery for complex craniofacial reconstruction. Int J Oral Maxillofac Surg. 2021;50:1554–62.
15. Kankane VK, Jaiswal G, Gupta TK. Posttraumatic delayed tension pneumocephalus: rare case with review of literature. Asian J Neurosurg. 2016;11:343–7.
16. Wallis A, Donald PJ. Frontal sinus fractures: a review of 72 cases. Laryngoscope. 1988;98:593–8.
17. Jing XL, Luce E. Frontal sinus fractures: management and complications. Craniomaxillofac Trauma Reconstr. 2019;12:241–8.

Virtual Surgical Planning in Craniofacial Surgery

Federica Ruggiero, Alberto Bianchi, Emanuela Marcelli, Owase Jeelani, Mino Zucchelli, Laura Cercenelli, and Alessandro Borghi

1 Introduction

Virtual surgical planning (VSP) is gaining emerging success in pediatric craniofacial surgery, particularly for the treatment of craniosynostosis—a congenital condition in which one or more sutures in the infant's skull fuse prematurely [49]. This premature fusion restricts skull growth, leading to morphological deformities, increased intracranial pressure, and potential neurodevelopmental delays. Surgical intervention is necessary to address these deformities and restore normal cranial anatomy [80]. However, the complex three-dimensional (3D) structure of the craniofacial skeleton adds complexity to reconstructive procedures, making it challenging to achieve both optimal aesthetic and functional outcomes.

Traditionally, procedures for correction of craniosynostosis relied mostly on the surgeon's subjective judgment of form and aesthetics, both preoperatively and intraoperatively. Furthermore, it is historically considered a complete operator's dependent surgery, as every surgeon has their technique of choice [32]. Thus, decisions regarding where to make bone cuts and how to shape bone segments were largely based on this subjective assessment, resulting in significant variability between surgeons and longer operating times. While satisfactory outcomes were often achieved, this approach lacked precision and predictability [32, 49, 65, 68].

The introduction of VSP which allowed the use of computer-aided design (CAD) and computer-aided manufacturing (CAM) has changed craniofacial surgery by providing a more precise preoperative strategy, reducing intraoperative guesswork, and enabling reproducibility [30, 37, 49, 70]. Applications of VSP include virtual surgery planning preoperatively, creation of cutting guides and bone models through 3D printing, and surgical navigation systems to assist with implant placement and bone cuts. These technologies enable surgeons to simulate the entire procedure preoperatively, optimizing bone cuts and ensuring symmetrical, predictable outcomes during surgery [12, 17, 21, 22, 25, 30, 37, 46, 56, 57, 64, 65, 67, 70].

VSP is particularly beneficial in the treatment of craniosynostosis, which is categorized into single-suture and syndromic types. Single-suture craniosynostosis involves the fusion of one cranial suture, such as the sagittal or coronal suture, leading to characteristic skull deformities like scaphocephaly or plagiocephaly. Syndromic craniosynostosis, such as that seen in Apert, Crouzon, and Pfeiffer syndromes, often involves the fusion of multiple sutures and is associated with other craniofacial and systemic anomalies. Surgical correction of syndromic craniosynostosis is more complex due to the involvement of multiple sutures and craniofacial

F. Ruggiero (✉)
Oral and Maxillofacial Surgery, AUSL Bologna, Bellaria-Maggiore Hospital, Bologna, Italy

Department of Biomedical and Neuromotor Sciences (DIBINEM), Alma Mater Studiorum University of Bologna, Bologna, Italy
e-mail: federica.ruggiero6@unibo.it

A. Bianchi
Oral and Maxillo Facial Surgery, University of Catania, Catania, Italy
e-mail: alberto.bianchi@unict.it

E. Marcelli · L. Cercenelli
Laboratory of Bioengineering – eDIMES Lab, Department of Medical and Surgical Sciences (DIMEC), University of Bologna, Bologna, Italy

IRCCS Azienda Ospedaliero-Universitaria di Bologna, Bologna, Italy
e-mail: emanuela.marcelli@unibo.it; Laura.cercenelli@unibo.it

O. Jeelani
UCL Great Ormond Street Institute of Child Health and Craniofacial Unit, Great Ormond Street Hospital for Children, London, UK
e-mail: o.jeelani@ucl.ac.uk

M. Zucchelli
IRCCS Istituto delle Scienze Neurologiche di Bologna, Pediatric Neurosurgery, Bologna, Italy
e-mail: Mino.zucchelli@isnb.it

A. Borghi
Department of Engineering, Durham University, Durham, UK
e-mail: alessandro.borghi@durham.ac.uk

© The Author(s), under exclusive license to Springer Nature Switzerland AG 2025

A. Tel, M. Robiony (eds.), *Atlas of Virtual Surgical Planning and 3D Printing for Cranio-Maxillo-Facial Surgery*,
https://doi.org/10.1007/978-3-031-94495-6_13

deformities [80]. VSP has proven especially useful in these cases, allowing surgeons to plan multi-stage procedures such as cranial vault expansion and midface advancement with greater precision [4].

Although CAD/CAM technology has been available for decades, recent advancements in imaging resolution and thin-slice computed tomography (CT) have greatly enhanced its application in craniofacial surgery. These improvements have enabled the generation of highly accurate 3D models for surgical planning and manipulation. Advanced simulation tools allow surgeons to manipulate 3D craniofacial models with six degrees of freedom, enabling them to visualize osteotomies from various angles and optimize bone movements. Additionally, the rapid advancement in rapid prototyping technologies now allows for the production of detailed 3D models with intricate internal contours. This enables the creation of precise cutting guides for osteotomies, which can be followed during surgery with high accuracy [57, 68].

The integration of VSP has also reduced the need for intraoperative trial and error, leading to shorter surgical times, improved accuracy, and better postoperative outcomes. However, there are challenges associated with this technology. One of the primary concerns is the cost of implementing VSP, which can be higher than traditional methods. While VSP may reduce intraoperative time and lead to better outcomes, the upfront costs may not always be offset by these savings, particularly in routine cases. Despite this, the use of VSP in complex cases, such as syndromic craniosynostosis, where precise surgical planning is critical, justifies the added expense by ensuring safer and more predictable outcomes [34, 68, 70].

In addition to 3D modeling, VSP integrates advanced technologies like CAD/CAM cutting guides [25, 49, 68, 70], patient-specific implants (PSIs) [46, 68, 70], and augmented reality (AR) [3, 40, 65] to enhance surgical precision and clinical outcomes. CAD/CAM technology assists in fabricating customized cutting guides that replicate the virtual plan, translating it into the operating room with high fidelity. These cutting guides ensure precise and symmetrical osteotomies, which are essential in cranial vault remodeling. PSIs, made from materials such as titanium or PEEK (polyetheretherketone), are also created using 3D printing technologies, allowing for personalized reconstruction of cranial defects, especially in syndromic cases where bone abnormalities can be complex [25, 49, 65, 68, 70].

Finally, AR has gained attention for its potential to enhance intraoperative navigation by overlaying virtual models onto the patient's anatomy in real time. This technology allows surgeons to visualize underlying structures during surgery, improving accuracy in bone cuts and implant placement. The use of AR is still in its early stages but shows great promise in craniofacial surgeries, particularly those requiring complex osteotomies [3, 40, 65].

Incorporating finite element modeling (FEM) into VSP adds another layer of precision by simulating the biomechanical behavior of cranial bones during surgical interventions. FEM provides insights into how bones will react to surgical manipulations, helping to predict complications such as fractures or insufficient corrections. This is particularly important in pediatric patients, whose bones are still growing, allowing surgeons to make informed decisions that will affect long-term outcomes [21, 55, 69]. As technology continues to evolve, VSP, along with CAD/CAM, AR, and FEM, will continue to transform pediatric craniofacial surgery by improving precision, reducing surgical time, and enhancing patient outcomes.

2 Craniosynostosis: Overview and Challenges

The human skull is composed of several bones connected by fibrous joints known as cranial sutures. Normally, these sutures remain open during early childhood to accommodate brain growth and then gradually fuse over time. However, in cases where one or more sutures fuse prematurely—a condition known as craniosynostosis—the skull's natural growth pattern is disrupted. Skull growth, which typically occurs perpendicularly to the sutures, becomes restricted along the fused sutures. This restriction forces compensatory growth at the remaining open sutures, leading to abnormal head shapes, as first described by Virchow's law [73].

The primary force behind the rapid skull growth during infancy is the expansion of the brain. If the skull cannot expand sufficiently due to suture fusion, it can limit the space available for brain growth. In severe cases, this can lead to increased intracranial pressure, which, if left untreated, can cause developmental delays and other neurological complications [26].

Craniosynostosis is categorized as "simple" when a single suture is involved and "complex" when multiple sutures are affected [5]. It can present either as an isolated condition, termed nonsyndromic craniosynostosis, or as part of a broader genetic syndrome. For example, scaphocephaly arises from the premature fusion of the sagittal suture, resulting in a long, narrow skull resembling the shape of a boat. This is the most common form of craniosynostosis, and its compensatory growth at the coronal sutures produces distinctive features, such as frontal bossing and posterior cranial bulging, often referred to as "bullet" [75].

Trigonocephaly, resulting from early fusion of the metopic suture, is the second most common form of single-suture craniosynostosis. It affects 1 in 7000 to 1 in 15,000 live births [44, 76]. Trigonocephaly results in a triangular forehead [28, 76] with a ridge along the metopic suture, leading to a narrowed forehead and orbital deformities. Interestingly, genetic factors are thought to play a more prominent role in this form

of craniosynostosis than in others, with familial patterns observed in many cases [8, 35, 43].

The clinical presentation of trigonocephaly ranges from mild, involving only a subtle ridge, to severe cases marked by significant forehead narrowing and orbital anomalies [76].

Another form, plagiocephaly, can be anterior or posterior, depending on which sutures are prematurely fused. Anterior plagiocephaly typically results from unilateral coronal synostosis, leading to asymmetrical skull and facial features. The head's growth is stunted in a plane perpendicular to the fused suture, resulting in a flattened forehead on the same side and compensatory bulging on the opposite side. This deformity affects not only the skull but also facial structures, including the nose, chin, and eyes. Common complications include jaw malocclusion and strabismus [59].

Posterior plagiocephaly, on the other hand, results from lambdoid suture synostosis and primarily affects the back of the skull. It presents with asymmetry in the occipital region and may also influence the cervical spine, causing curvature [18].

In contrast, brachycephaly occurs when both coronal sutures close prematurely, resulting in a broad and flat head. This limits anterior-posterior growth and leads to the skull's sideways and upward expansion, which is observed in the sagittal and lambdoid sutures [18].

Pansynostosis, involving the closure of three or more sutures, can manifest in various forms, the most severe being kleeblattschädel or cloverleaf skull, characterized by bulging of multiple cranial bones. This condition can resemble primary microcephaly, where the head is significantly smaller than normal but remains proportionate [13].

Syndromic craniosynostosis, which is genetically driven, involves complex malformations and multisystem abnormalities. These syndromes, such as Apert, Crouzon, and Pfeiffer, are typically caused by gain-of-function mutations, most often in the fibroblast growth factor receptor (FGFR) gene family. Syndromes like Muenke, Crouzon, and Saethre-Chotzen have different incidences and are characterized by distinct craniofacial and skeletal features. A multidisciplinary approach is crucial in managing these patients, as craniofacial anomalies are often accompanied by skeletal and visceral abnormalities, especially affecting the limbs.

Though rare, these syndromic forms of craniosynostosis often require early and more complex surgical interventions due to their severe cranial and extracranial manifestations.

Historically craniosynostosis has been managed through open cranial vault techniques, which include strip craniectomies, remodeling, etc. It requires bicoronal scalp incision to expose and remove the fused suture. The bones are then reshaped to normalize the cranial structure, which is particularly important for ensuring that the brain has enough room to grow. This approach is most commonly performed in infants aged 6 to 12 months when the skull is still malleable enough to achieve optimal correction.

While open techniques (calvarial vault remodeling—CVR) allow for comprehensive correction, particularly in cases involving multiple sutures or syndromic craniosynostosis, it comes with notable limitations. The procedure is highly invasive, involving significant manipulation of the skull, which often leads to prolonged surgery times, increased blood loss, and a longer recovery period. Postoperative swelling can be extensive, and the aesthetic results may vary, as much of the surgical decision-making is reliant on the surgeon's intraoperative judgment. However, despite these challenges, open procedures continue to be a mainstay for treating complex cases where extensive cranial reshaping is required [15, 42, 74].

In contrast to CVR, the development of endoscopic strip craniectomy, introduced in the 1990s, marked a shift toward less invasive techniques. This procedure is typically performed on infants under 6 months of age and involves making small incisions through which endoscopes are used to remove the fused suture. While less invasive than CVR, this approach generally requires the use of a postoperative helmet to guide the natural reshaping of the skull as it grows. Although endoscopic strip craniectomy is less effective in treating complex, multi-suture, or syndromic cases, it significantly reduces operative time, blood loss, and recovery time, making it a preferred option for simple, single-suture craniosynostosis when diagnosed early [15, 42, 74].

3 Virtual Surgical Planning in Craniosynostosis

Cone-beam computed tomography (CBCT) and CT are regarded as the gold standard in cranio-maxillofacial surgery for preoperative imaging, primarily due to their superior ability to visualize bone structures. In pediatric craniofacial contexts, in order to have suitable images for VSP, the scans should not be older than 1–2 months prior to surgery [49]. However, recent advancements have also positioned magnetic resonance imaging (MRI) as a valuable tool for soft tissue segmentation [24, 78]. Imaging data, typically stored in Digital Imaging and Communication in Medicine (DICOM) format, allows for the segmentation and volume rendering of both bone and soft tissue. From this raw data, a 3D digital model of the patient is created, enabling virtual surgical planning to simulate bone movements and assess their impact on soft tissues [1].

As part of this virtual planning, several post-processing tools can be integrated, such as intraoperative navigation and CAD/CAM for creating surgical splints, templates, and custom implants. This approach not only aids surgical precision

but also enhances patient communication and helps evaluate postoperative outcomes [48, 50, 54]. Numerous commercial software packages are available for these purposes, including:

- Dolphin (Dolphin Imaging & Management Solutions, USA)
- Maxilim (Medicim, Belgium)
- Mimics (Materialise, Belgium)
- 3-Matic (Materialise, Belgium)
- IPS Case Designer (KLS Martin, Germany)

These software solutions can integrate also advanced mathematical models such as FEM, mass tensor models (MTM), and mass spring models (MSM) [48].

In our center, preoperative CT scan data are acquired and segmented using Mimics software (Materialise, Belgium), creating a comprehensive 3D virtual model. This model includes essential anatomical structures like bones, brain, eyes, and skin, with the final 3D meshes saved in Standard Tessellation Language (STL) format for use in surgery (Fig. 1).

One of the most significant advantages of VSP is the ability to perform surgical rehearsals in a virtual environment. This feature allows the surgeon to simulate complex osteotomies and bone movements multiple times before entering the operating room, giving them confidence in their chosen approach. By rehearsing the procedure, surgeons can anticipate potential challenges and refine their technique, reducing uncertainty during the actual surgery. This rehearsal phase is particularly critical in complex or syndromic craniosynostosis cases, where multiple sutures may be involved, or where the patient presents with significant anatomical anomalies.

The benefits of VSP in pediatric craniosynostosis surgery are numerous and well documented. First, the precision of VSP allows for more accurate bone cuts and reconstructions, improving both functional and aesthetic outcomes. The 3D models provide a comprehensive understanding of the patient's anatomy, helping to reduce intraoperative guesswork. Additionally, the use of preoperative planning and patient-specific cutting guides leads to shorter operating times, minimizing the risk of complications such as excessive blood loss and prolonged anesthesia. Studies have shown that VSP contributes to reduced complication rates and shorter hospital stays, making it a valuable tool in improving the overall safety and effectiveness of craniosynostosis surgery.

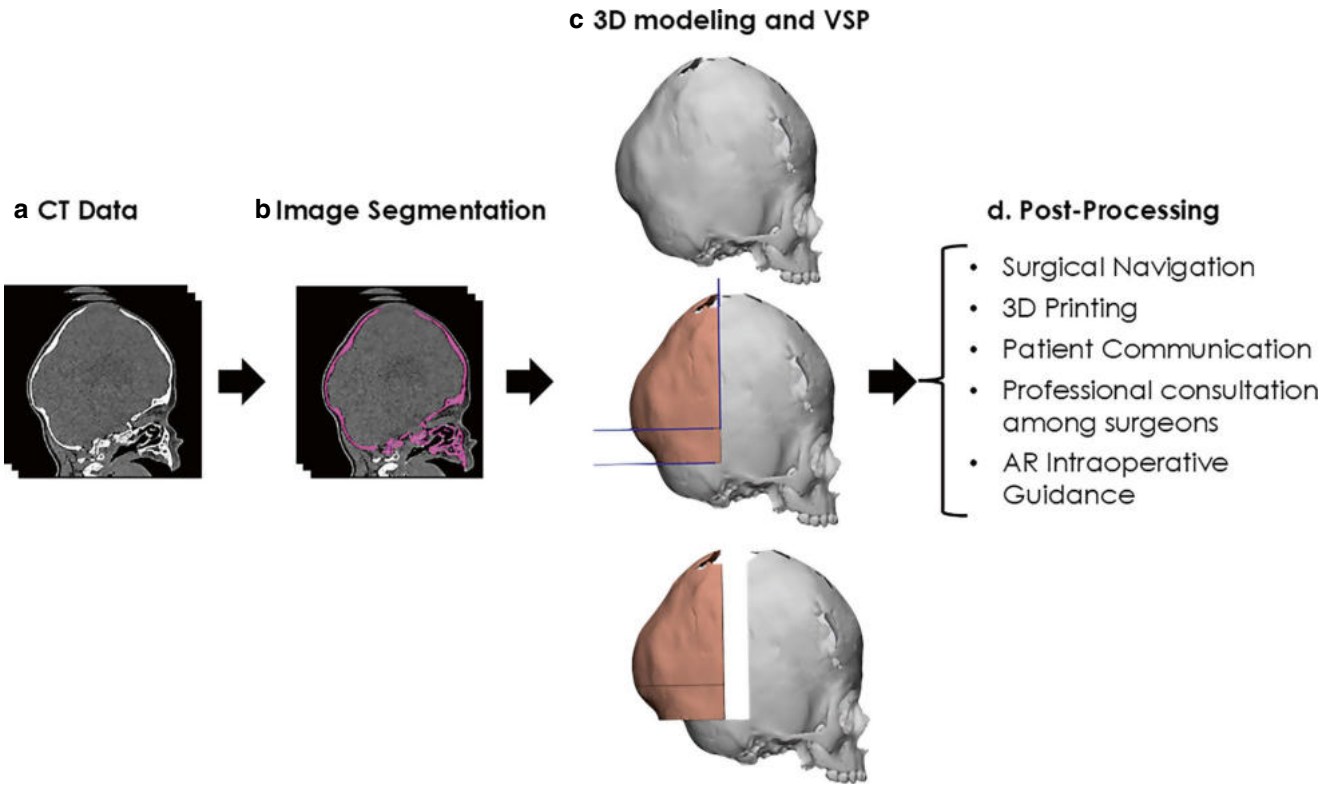


Fig. 1 Synthetic workflow for 3D modeling from DICOM CT scans data

4 FEM in Craniofacial Surgery

FEM analysis is a mathematical approach used for structural analysis. It involves breaking down a complex system into smaller, simpler units, which allows for the solving of partial differential equations [7]. Initially developed for aeronautical engineering [19, 36], FEM was introduced into surgical planning in the 1990s due to its remarkable accuracy [3, 20, 21]. This method represents a mathematically defined subdivision of continuum problems, allowing biomechanical properties to be assigned to each individual unit [41, 53].

In facial surgery, the units are typically represented as tetrahedra, as this shape provides a more accurate representation of anatomical structures [31]. Since the 1990s, the use of FEM in computer-assisted surgical planning has gained popularity [1].

Despite its advantages, FEM has limitations, including significant computational time and the requirement for extensive engineering expertise, which have hindered its widespread adoption in commercial software [16]. Over the past two decades, the accuracy of FEM has improved dramatically, incorporating more detailed anatomical features and biomechanical properties obtained from various imaging sources, including MRI [69]. Since CBCT does not capture distinct soft tissue layers, the anatomical representation of the mesh has been enhanced by creating a facial template from MRI images, which is then adapted to match the patient's specific anatomy [6, 47, 69, 79]. Another challenge is the variability of material properties both between and within patients, necessitating patient-specific parameters for accurate material assignment in complex anatomical meshes [72].

Several commercial software programs now utilize FEM or related methods, such as the Finite Difference Method (FDM), to simulate soft tissue behavior [55, 69].

The use of FEA has been explored for the preoperative planning of spring-assisted posterior vault expansion [20, 21]. The modeling framework is similar to that utilized for modeling scaphocephaly correction (Fig. 2). The main difference resides in the position and shape of the osteotomy, the position and number of the distractors (up to 6), and the use of different material properties, due to the different age of the patients [20, 22].

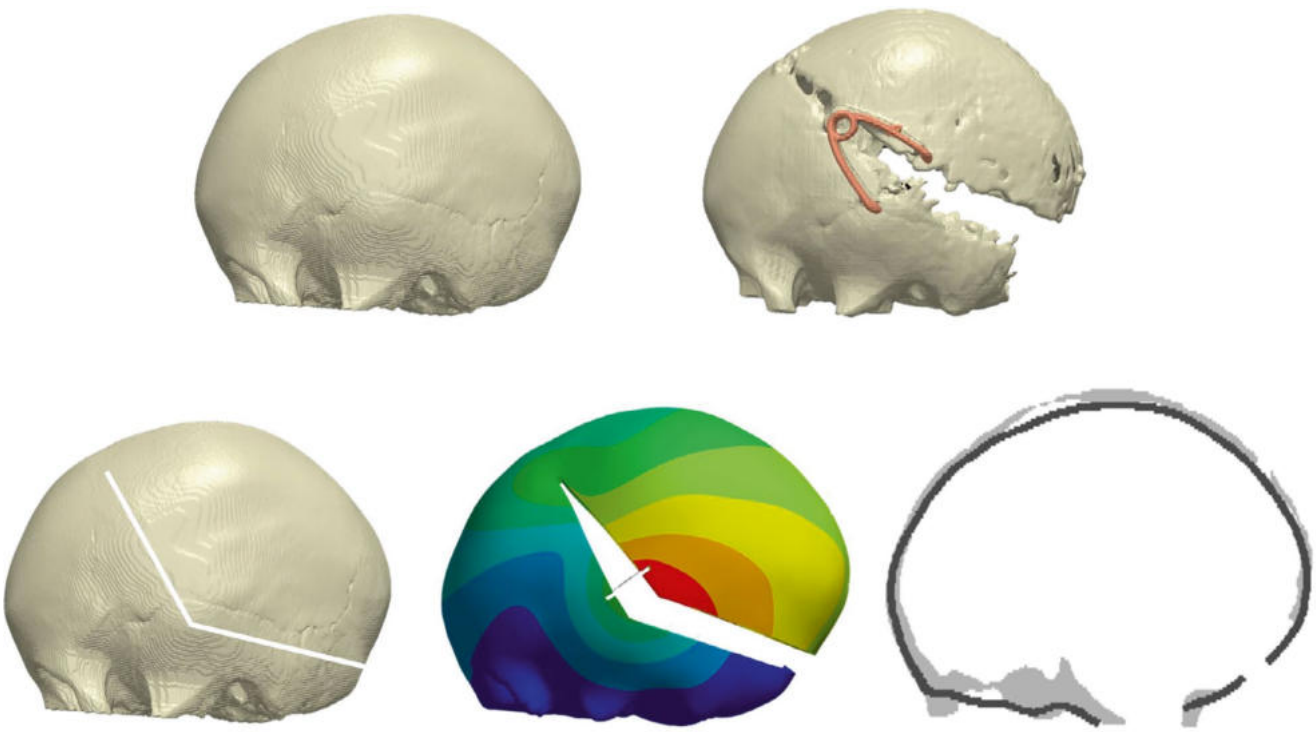


Fig. 2 Application of Finite Element Analysis to the prediction of vertical vector posterior vault expansion outcome on a patient affected by scaphocephaly. On the top, CT reconstruction of preoperative (on the left) and postoperative (on the right) anatomy. On the bottom, preoperative computational model showing the osteotomy (on the left), result of the computational simulation (in the middle), and sagittal cross-section showing a comparison between the postoperative CT reconstruction (light gray) and computational analysis (dark gray, on the left)

5 VSP in Spring-Assisted Cranioplasty

Spring cranioplasty has been introduced in 1998 by Claes Laurizen for the treatment of scaphocephaly [45]. Following the plan of the osteotomies, design for cranial expansion and reshaping, spring distractors are inserted and operate by exerting a gentle force on the calvarium and promoting localized bending [66]. Initially pre-bent in theater as patient-specific devices [61], several versions have received regulatory clearance and are currently commercialized in the Europe and the United States.

In Great Ormond Street Hospital, this technique is adopted on patients 3- to 8 month old who present with scaphocephaly due to craniosynostosis of the sagittal suture. The surgical technique requires the patient in prone position with extended neck (sphynx position): a central scalp incision is performed perpendicular to the sagittal suture, a square craniectomy (with a side 1.5–2 cm) is carried out halfway along the fused sagittal suture. Two parasagittal osteotomies are made parallel to the craniectomy, extending to the coronal suture in the front and to the lambdoid suture in the back. Notches are inserted along the parasagittal osteotomies, and spring distractors (with varying stiffness) are pre-crimped, placed into the notches, and released. The springs start expanding on table and continue expanding for the following few days, causing lateral expansion and sagittal shortening of the patient head. The skin is then closed and the patient remains under observation for 24 hours [66].

Finite Element Analysis is a powerful tool for the prediction of surgical outcome in craniofacial procedures [33]. It was tested in conjunction with VT technologies to improve the experience of parental consenting.

A 6-month-old baby presented with scaphocephaly caused by craniosynostosis of the sagittal suture, confirmed by imaging. Preoperative CT scan (age 4 months) was collected and processed using specialized image processing software (Simpleware ScanIP, Synopsys®) following a published protocol [10, 11]. Briefly, the skull was extracted by means of gray-scale thresholding. Sutures were reconstructed using a combination of morphological operations and manual segmentation (Fig. 3).

The top portion of the calvarium was separated from the skull base by means of a plane encompassing the nasion and the left and right portions. This section was used for numerical modeling. Following consultation with the operating surgeon, osteotomies and spring notches were included in the model (Fig. 4).

The 3D model was then discretized and imported into a FE solver (ANSYS 2020R2) for simulation of spring expansion. Spring action was simulated using boundary condi-

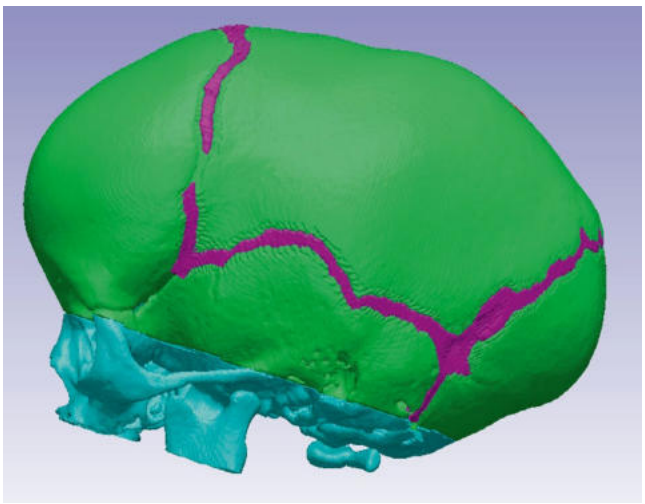


Fig. 3 3D reconstruction of a patient affected by sagittal craniosynostosis. In blue the skull base, in green the portion of the calvarium used for the computation, in purple the sutures

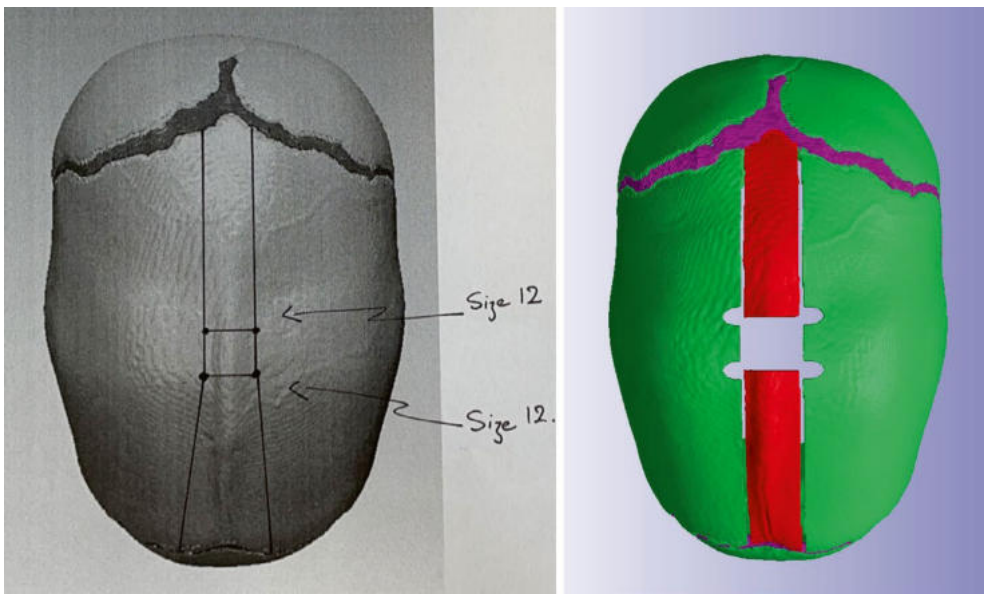


Fig. 4 On the left, planning of the bony cuts and distractor location. On the right, reproduction of the planned osteotomies and spring notches on the computational model

tions, relative to S12 springs as reported in the literature [9]. Ten-day expansion was simulated, since spring action has been reported to be completed in that timeframe [9]. Different surgical configurations (springs in central, anterior, posterior position) were tested to optimize the position of the distractors. The surgical configuration yielding the most natural head shape (central springs) post-expansion was selected as final configuration (Fig. 5).

Simulation results were extracted, processed, and uploaded in a VR system (Oculus Rift, Oculus VR) for parental information and consent (Fig. 6). The parents had chance to appreciate the overall reshaping of the baby's head

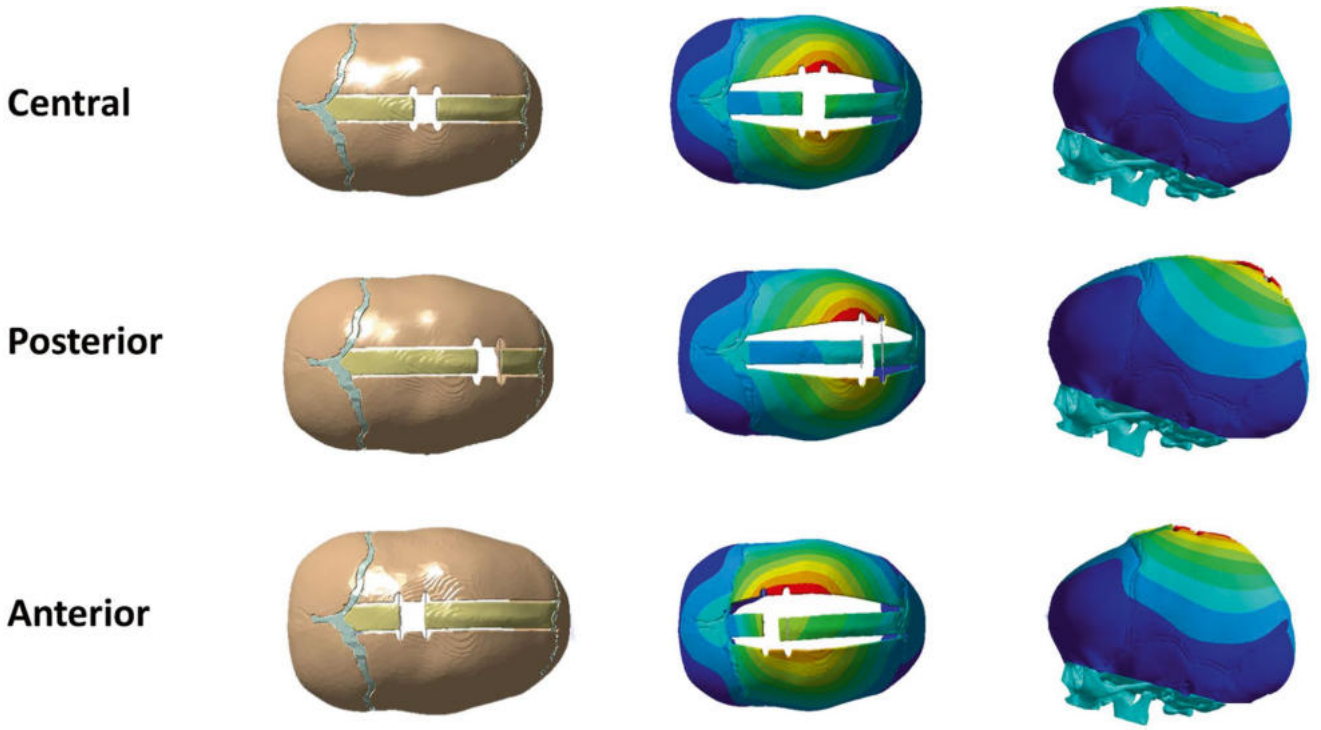


Fig. 5 Simulation of spring expansion in central (top), posterior (middle row), and anterior position (bottom). On the left, the preop model with osteotomies and spring notches; in the middle column, the top view of the post-expansion model; on the right, the lateral view of the post-expansion model



Fig. 6 On the left, comparison between the pre-expansion anatomy (gray) and predicted post-expansion skull shape (pink). On the right, parent consultation (the operating surgeon and a TV reporter are visible in the picture) based on the use of VR technology

and provided positive feedback on the usefulness of this communication method.

6 CAD/CAM Cutting Guides and Patient-Specific Implants

6.1 CAD/CAM Cutting Guides

CAD/CAM cutting guides are among the most prevalent uses of VSP in craniofacial surgery. These guides are developed from the patient's virtual 3D model, which serves as the foundation for designing the surgical plan, including osteotomies. In our practice, we use 3-Matic Medical (Materialise, Belgium) to create CAD/CAM templates that align with our planned osteotomies. After the surgeon has approved the design, the cutting guides were 3D printed in biocompatible resin using the Form 3B (Formlabs, Somerville, USA) stereolithography (SLA) printer. Then, they were steam sterilized to be ready for use in the operating room. During surgery, these templates are positioned on the patient's skull, enabling the surgeon to accurately replicate the preoperative surgical plan (Fig. 7).

6.2 Patient-Specific Implants (PSIs)

Reconstruction of bony craniofacial defects requires a precise understanding of anatomical relationships. An ideal reconstructive technique should be efficient and cost-effective, minimize donor-site morbidity, and yield durable and aesthetically pleasing results. However, there are instances where a patient's own tissue may be insufficient for effective reconstruction. The advancement of sophisticated software has paved the way for the development of PSIs, which are tailored to meet individual anatomical needs [48].

The emergence of technologies for CAD/CAM-aided surgery has led to a broad spectrum of secondary surgical options, ranging from autologous fat transfer to PSIs crafted from biocompatible materials such as polyether ether ketone (PEEK) and polymethylmethacrylate (PMMA) or other biomaterials under exploration [60]. Historically, also titanium has been described. These innovations enable surgeons to achieve optimal outcomes while addressing the specific requirements of each patient [46]. Temporal indentations represent a significant craniofacial complication that can occur following coronal flap dissection, primarily resulting from dissection of the temporal fat pad or temporalis muscle [23, 38].

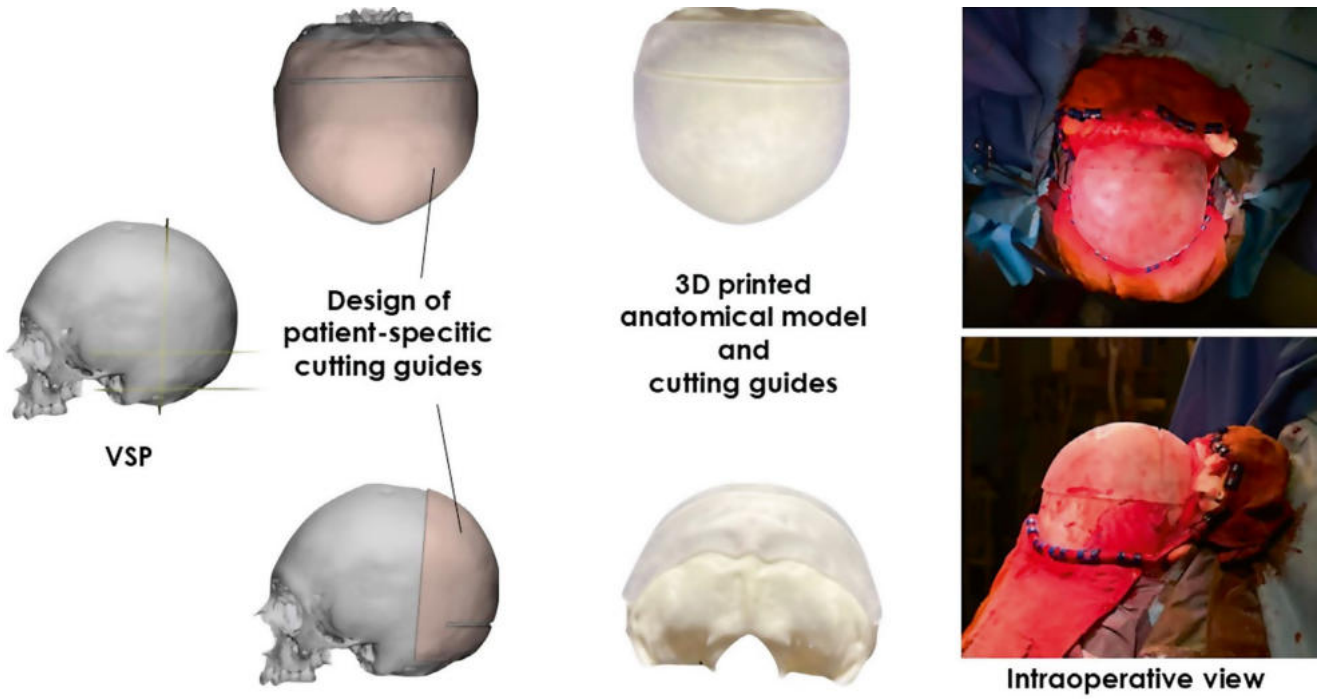


Fig. 7 workflow for producing cutting guides for supratorcular in posterior vault distraction in Crouzon syndrome



Fig. 8 Preoperative soft tissue (on the left) and skull (in the middle) reconstruction of the patient undergoing PEEK implants; on the right, post-treatment planning as designed by one of the operating surgeons

Recent advancements in CAD/CAM-assisted surgery and the capability for precise pre-surgical virtual planning have enabled a customized approach to correct these indentations. Additionally, progress in material science has allowed surgeons to utilize biocompatible materials, such as PEEK, which exhibit low rates of complications and recurrences [48], for creating patient-specific implants.

A 13-year-old boy, previously diagnosed with metopic synostosis, was admitted to the Craniofacial Unit at Great Ormond Street Hospital for Children in London for fronto-orbital remodeling (FOR) in 2005 when he was just 1 year old. Twelve years later, the patient presented again because of the occurrence of indentations in the temporal regions. To assess the soft and bony tissues preoperatively, a CT scan was performed. The scans were imported into Mimics Innovation Suite (Materialise, Belgium) for 3D reconstruction and analysis of both soft and hard tissues (see Fig. 7). An experienced plastic surgeon processed the soft tissue model using MESHMIXER (Autodesk, USA) to achieve the desired forehead shape (Fig. 8). The soft tissue was offset by a constant value of 5.6 mm, corresponding to the soft tissue thickness in the area, while the skull volume was subtracted. This process yielded two volumetric patches (implants) in the indentation region, which could effectively stretch the outer skin to achieve the intended shape (Fig. 9).

The implants were surgically inserted after reopening the preexisting coronal incision following injection of tumescent solution. The coronal flap was elevated in the sub-pericranial plane. The implants were secured to the skull using titanium mini-screws. The entire surgical procedure took 90 minutes. The patient was discharged on the first postoperative day after a smooth recovery. A qualitative comparison was made between the preoperative CT and a follow-up 3D scan was obtained 12 months after the procedure (Fig. 10).

CAD/CAM guides and PSIs significantly enhance surgical outcomes by providing precise, patient-specific tools that reduce the risk of errors, minimize unnecessary bone loss, and ensure better cosmetic and functional results. This precision leads to faster recovery, fewer complications, and more predictable long-term outcomes, improving the overall success rate of surgeries.

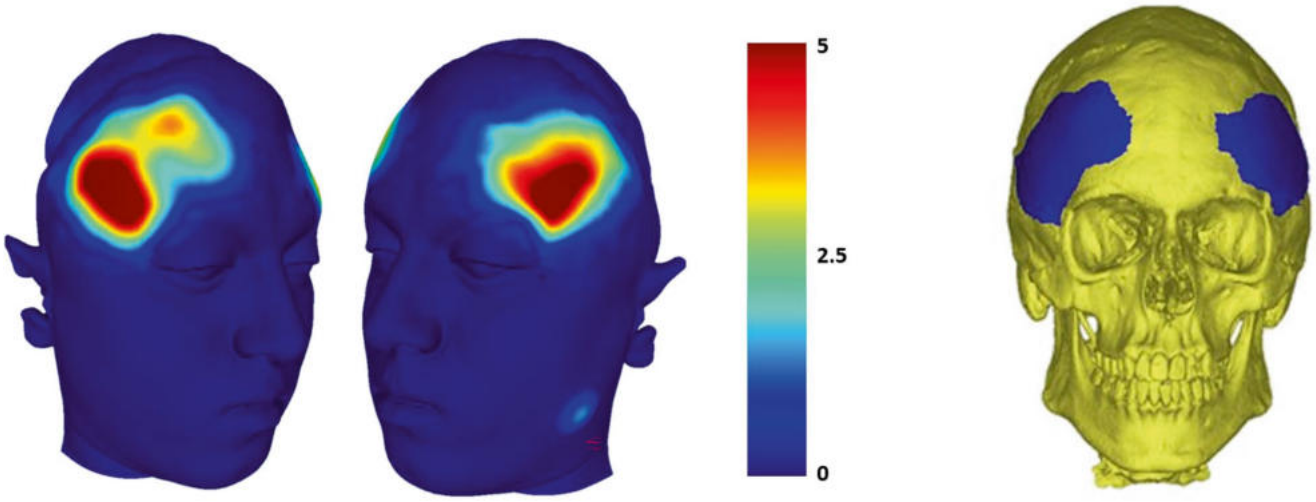


Fig. 9 On the left, surface distance between the preoperative anatomical model and the desired forehead shape; on the right, visualization of the PEEK implants designed to obtain forehead shape correction

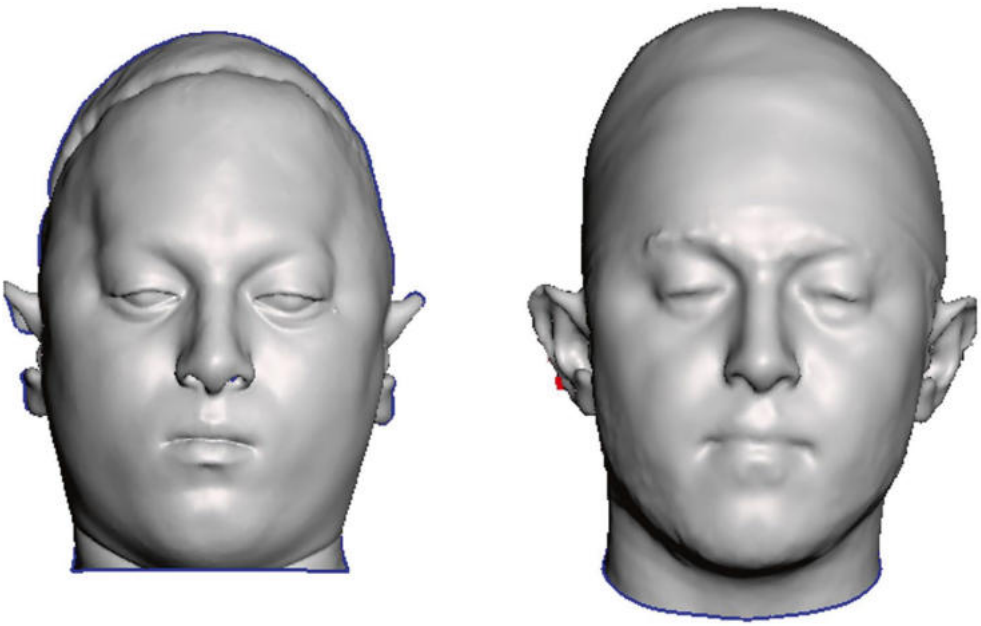


Fig. 10 On the left, CT reconstruction of the patient's face and forehead; on the right, postoperative 3D scan showing forehead shape normalization

7 AR in Craniofacial Surgery

7.1 Introduction to AR

AR is a computerized technology that merges virtual information with real-world environments, creating a composite view that enhances sensory perception. This technology operates on the principle of "onlay," where a camera captures an object within its frame, and the system recognizes it, allowing a virtual layer to be integrated seamlessly with the real-world object [65]. AR has found extensive applications in various fields, particularly in surgical navigation [2, 4, 14, 27, 29, 39, 52, 58, 62, 63, 65, 71, 72, 77]. In the medical domain, AR projects a tailored virtual layer onto the physical environment, designed specifically for each patient's unique anatomy [2, 4, 14, 27, 29, 39, 52, 58, 62, 63, 65, 71, 72, 77].

In contemporary surgical practices, AR significantly enhances navigation, especially for procedures like ventriculo-peritoneal shunt insertion, craniofacial surgeries, and neurosurgical tumor resections. These procedures often utilize advanced navigation systems [72]. Traditional surgical navigation relies on external devices that track the patient's position and project data from imaging studies, such as CT scans or MRIs, onto a screen. While this method enhances procedural safety by helping locate critical anatomical structures, it requires surgeons to frequently shift their attention between the patient and the display [62, 65].

The advent of AR head-mounted displays (HMDs), such as Microsoft HoloLens, represents a significant advancement that mitigates this limitation. These headsets feature integrated displays, allowing surgeons to access vital information while maintaining their focus on the surgical field [65]. They provide real-time visualization of critical anatomical structures, osteotomy trajectories, and incision points directly superimposed onto the patient, ensuring that the surgeon's natural field of vision remains unobstructed [29, 51].

In pediatric craniofacial surgery, which aims to correct congenital skull deformities like single-suture craniosynostosis, multiple-suture synostosis, and syndromic craniosynostosis, the precision offered by AR is particularly valuable. Accurate osteotomy designs are crucial for achieving successful morphological outcomes while avoiding damage to critical structures [29].

7.2 Application in Craniosynostosis

In our center in Bologna, we have been developing and implementing a system for intraoperative surgical navigation by means of HMD.

We initiated our process by utilizing preoperative CT scans from patients scheduled for corrective surgery related to single-suture craniosynostosis. From the DICOM data derived from each CT scan, we constructed 3D virtual models of the patients' skulls using Mimics Medical software (Materialise, Leuven, Belgium). The osteotomy lines developed during the virtual surgical planning phase were also integrated into the virtual skull model in STL format. We also designed patient-specific accuracy templates having grooves of different widths (3 mm, 2 mm) in order to evaluate two levels of achievable accuracy (±1.5 mm, ±1.0 mm).

Subsequently, we imported the complete virtual skull model, which included the bone, skin, osteotomy lines, and accuracy templates, into Unity 3D software (Unity Technologies, San Francisco, CA, USA), enhanced by the Vuforia Engine Software Development Kit (PTC Inc., Boston, MA, USA). For intraoperative patient recognition, we adopted a marker-based tracking method, using Vuforia "Image Target" tracking mode, which relies on detecting a QR-code pattern that provides enough detail for accurate identification. A specialized tracker was designed using 3-Matic software and subsequently produced through 3D printing, ensuring that the QR code could be anchored in a precise and unique position relative to the patient's skull, making it easily reproducible during surgery (please refer to Fig. 11).

The AR application was developed as a Universal Windows Platform (UWP) app and deployed on Microsoft HoloLens 2 smart glasses. We incorporated interactive features such as checkboxes for toggling virtual anatomical structures and voice commands for hands-free operation (Fig. 12). The entire workflow is depicted in Fig. 13.

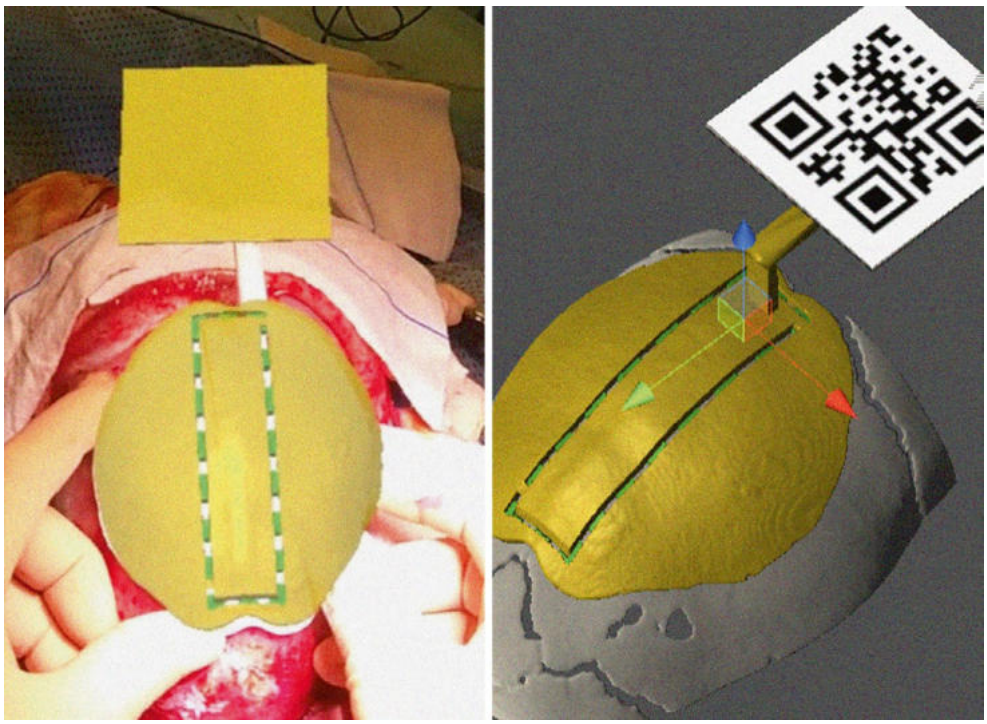


Fig. 11 Intraoperative view of the QR code-based tracking method on the left, and VSP image on the right

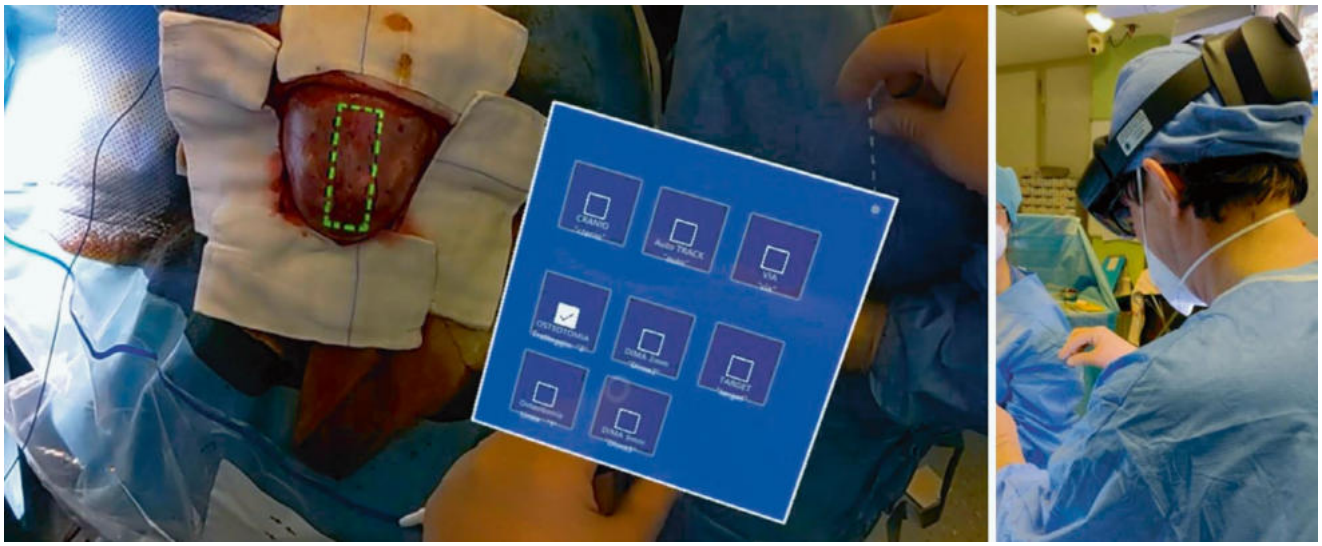


Fig. 12 Intraoperative view with interactive checkboxes for toggling virtual anatomical structures and VSP

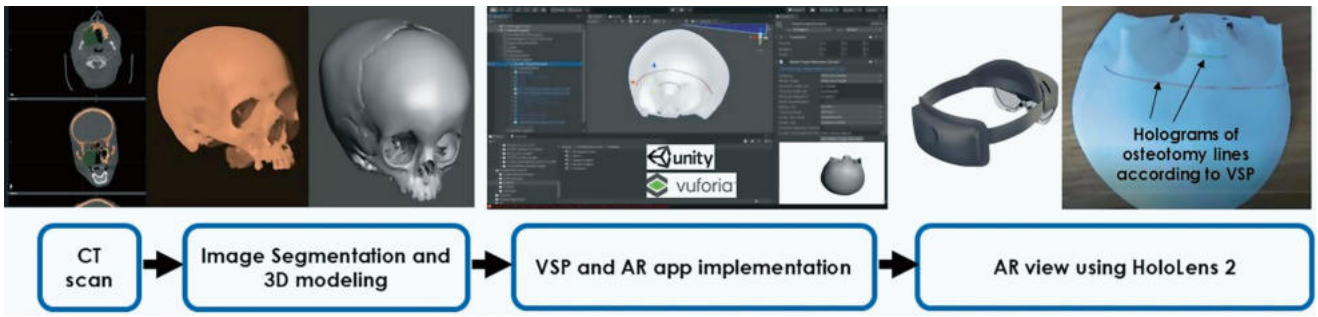


Fig. 13 Workflow for implementation of AR guidance in craniosynostosis surgery

8 Other Applications of VSP in Craniofacial Surgery

The authors hereby discuss complex cases with different applications of the VSP.

*Case 1: Example of posterior vault distraction in Apert syndrome (*Fig. 14*)*

*Case 2: Example of mandibular distraction planning and intraoperative navigation in Nager syndrome (*Fig. 15*)*

*Case 3: Example of temporo-mandibular joint prosthesis to address bilateral ankylosis in Nager syndrome (*Fig. 16*)*

*Case 4: Example of VSP of LeFort 3 distraction osteogenesis in a case of Crouzon syndrome (*Fig. 17*)*

9 Conclusions

VSP has become increasingly invaluable in pediatric craniofacial surgery, particularly in the treatment of craniosynostosis. It enhances the accuracy of preoperative planning, enabling surgeons to visualize complex anatomical structures and anticipate potential challenges before entering the operating room. VSP's help is crucial in pediatric cases, where accuracy and precision are paramount to avoid damaging delicate and developing structures and to achieve optimal functional and aesthetic outcomes for young patients.

Recent technological advancements in tools like FEM, PSI, CAD/CAM systems, and AR have collectively enhanced the precision and efficiency of craniofacial procedures. FEM, for

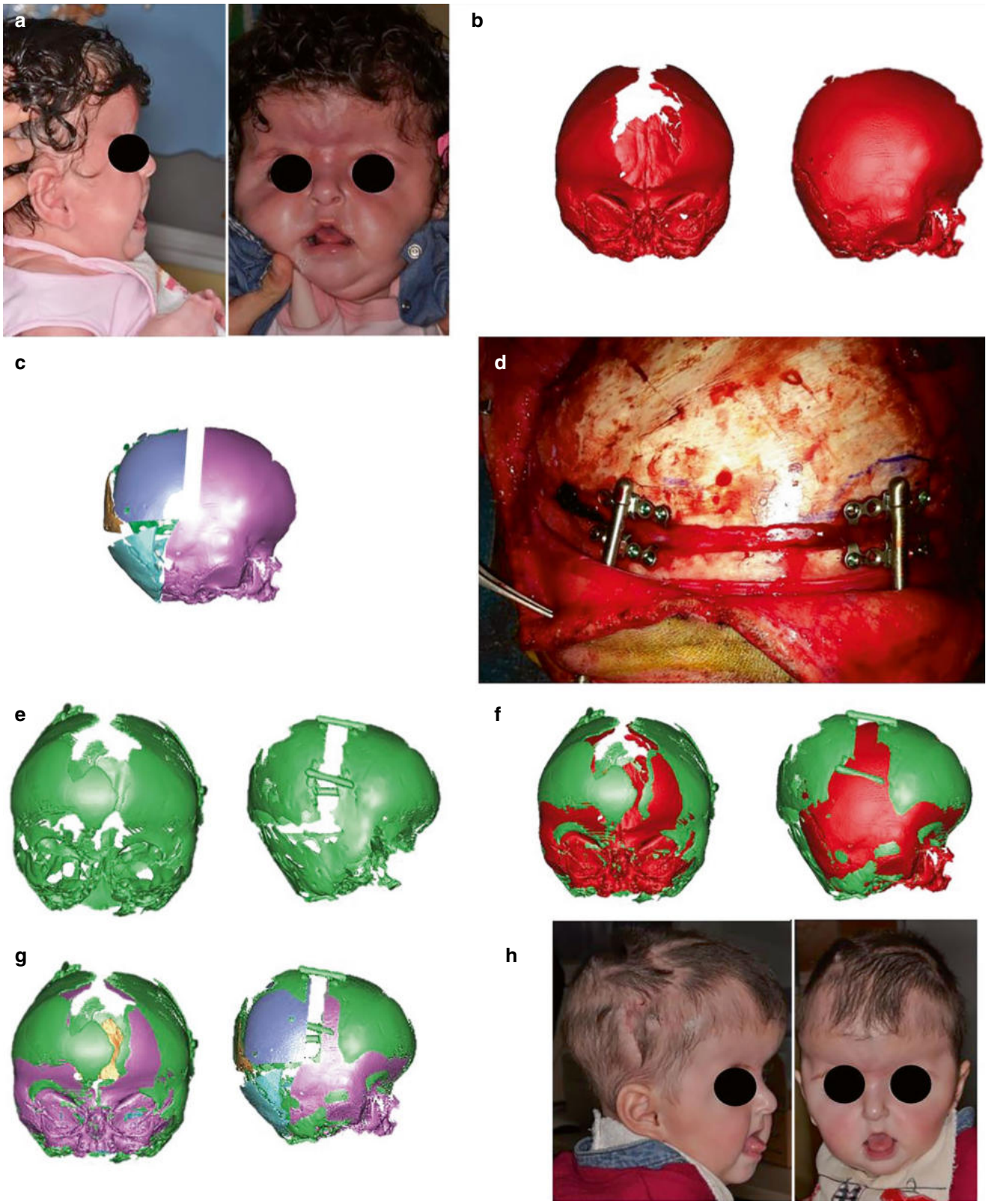


Fig. 14 (**a**) Preoperative view, (**b**) preoperative 3D reconstruction, (**c**) virtual planning of the expansion, (**d**) intraoperative view, (**e**) postoperative 3D reconstruction, (**f**) overlapping of the 3D reconstructions of both pre- and postoperative imaging, (**g**) comparison between the VSP and the postoperative imaging, (**h**) postoperative pictures

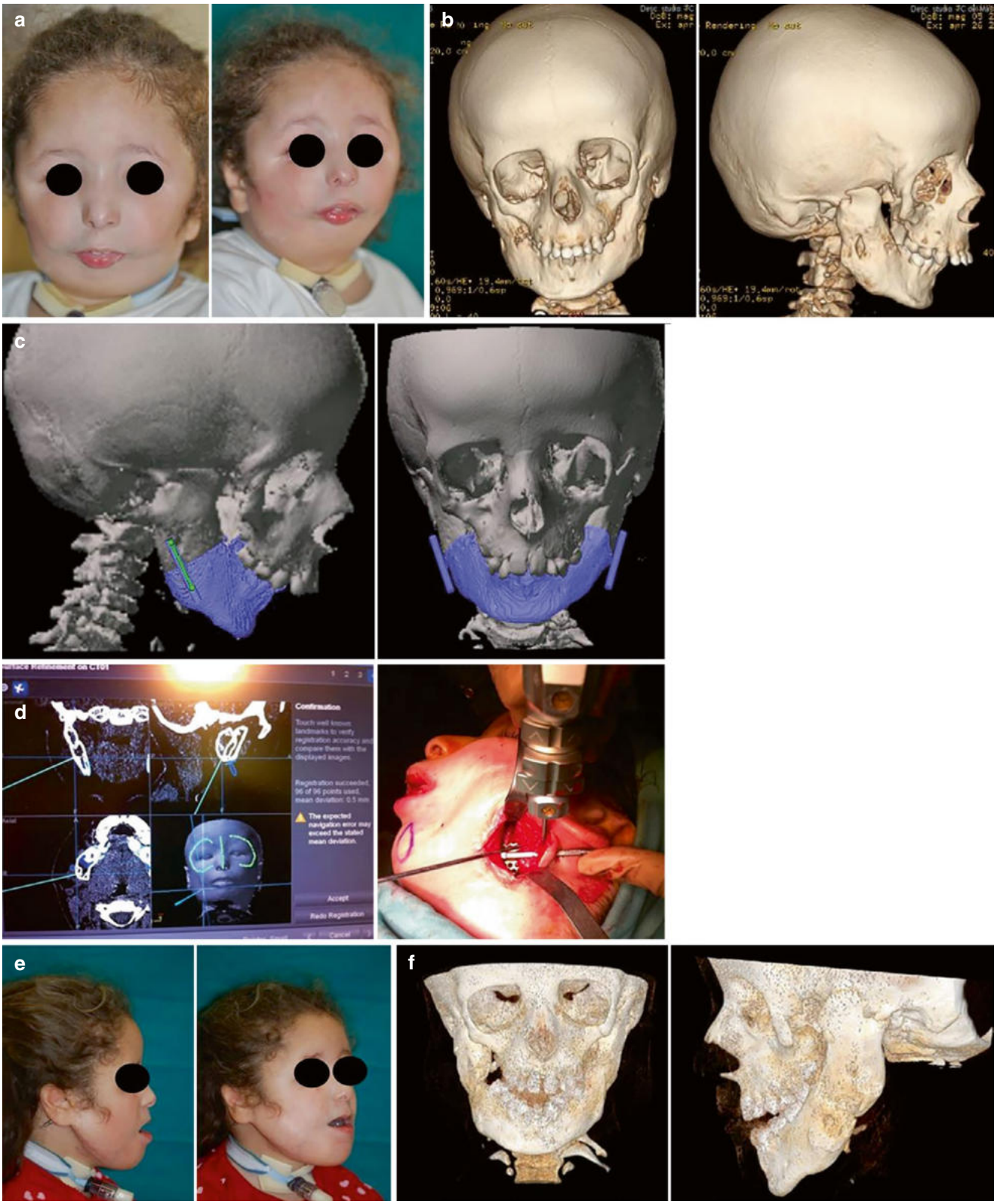


Fig. 15 (**a**) Preoperative view. The patient had already undergone a first attempt of mandibular distraction at birth. She was presenting with a recurrence of upper airways obstruction at 4 year of age and a redo distraction was required, (**b**) preoperative 3D reconstruction, (**c**) virtual planning of the distraction, both osteotomies and vectors, (**d**) intraoperative view with the aid of surgical navigation, (**e**) long-term postoperative pictures, (**f**) postoperative 3D reconstruction

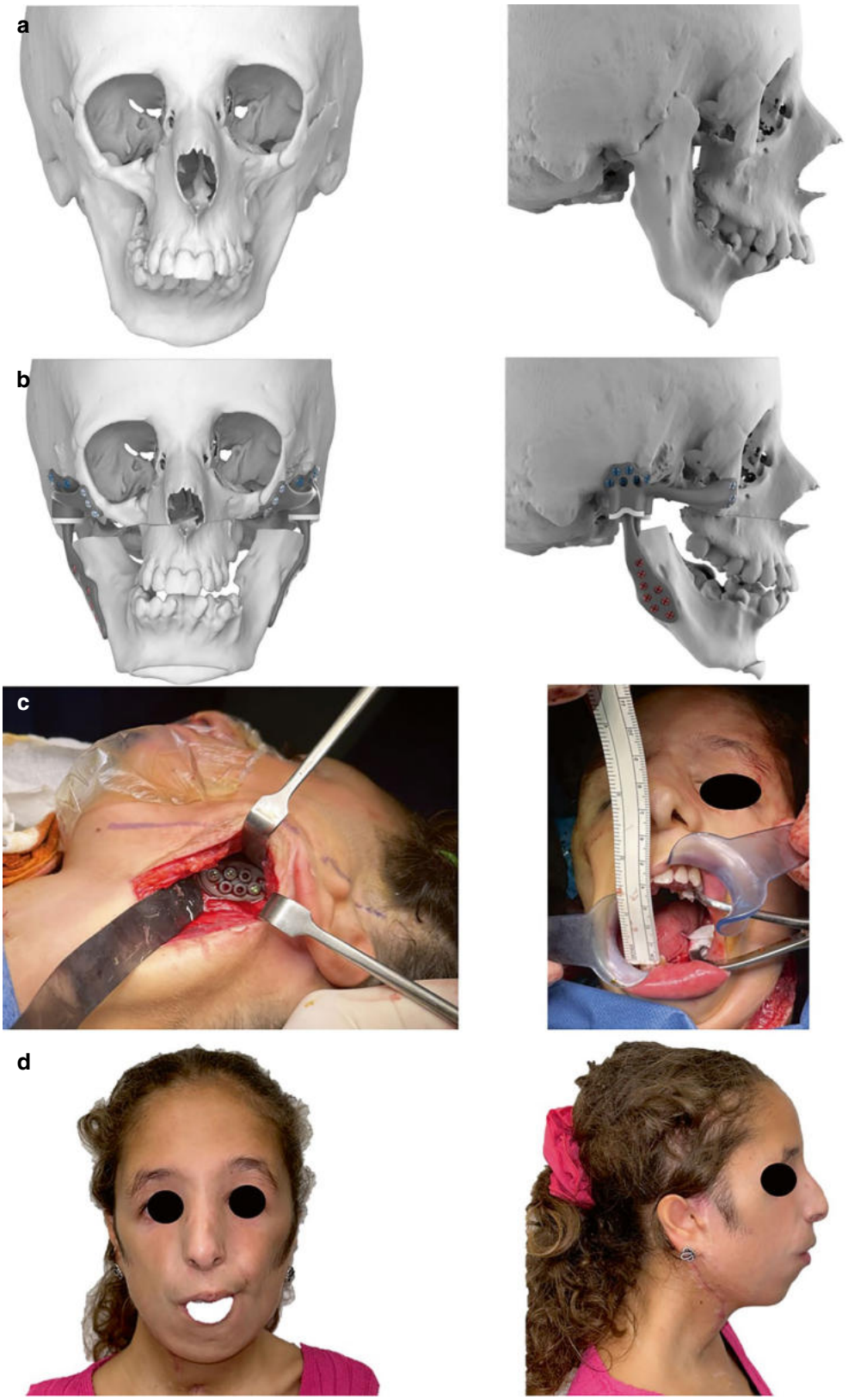


Fig. 16 (**a**) Preoperative 3D CT scan. The patient is the same of Case 2 and had already undergone several attempts of distraction osteogenesis. She was presenting with bilateral ankylosis at the end of growth. (**b**) Virtual planning and design of the PSIs for TMJ replacement surgery, (**c**) intraoperative view with immediate restoring of the mouth opening, (**d**) postoperative picture

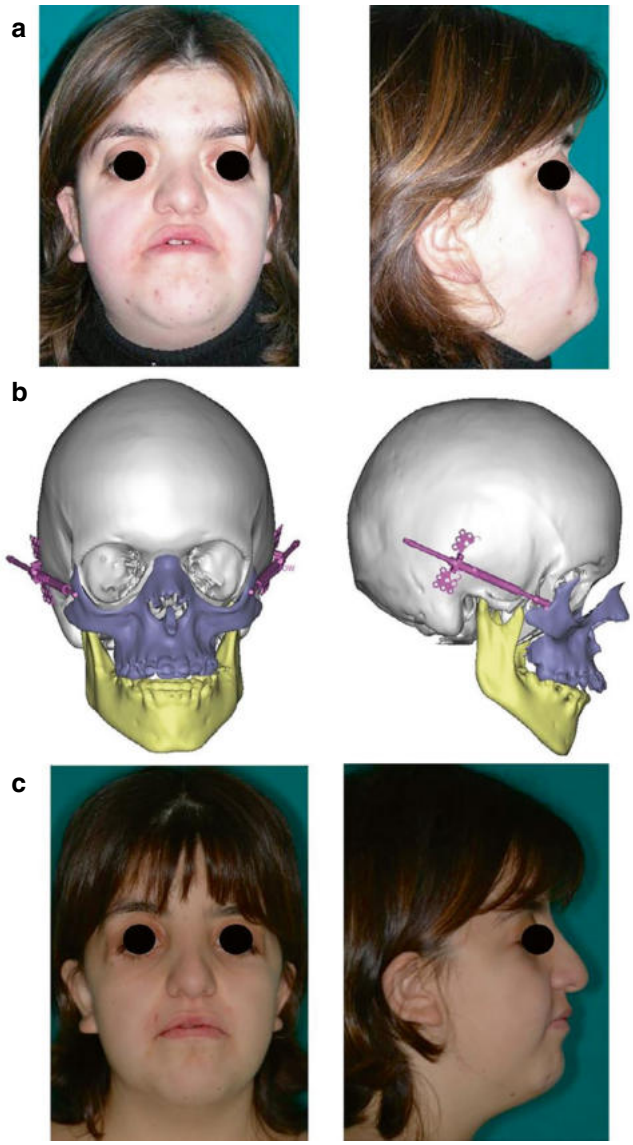


Fig. 17 (**a**) Preoperative pictures, (**b**) VSP of the distraction (length and vector), (**c**) postoperative view

instance, allows for biomechanical simulations that predict the effects of surgical interventions on cranial structures, aiding in the assessment of potential outcomes and complications. PSI, tailored to each patient's unique anatomy, provides structural support and alignment, facilitating more precise osteotomies and reconstruction. Meanwhile, CAD/CAM technology has revolutionized the fabrication of these implants and guides, ensuring a high degree of conformity to the patient's anatomy and improving the alignment of surgical cuts.

The integration of AR, particularly through HMDs, marks a transformative leap in surgical navigation. By overlaying holographic surgical plans onto the patient in real time, AR enhances intraoperative accuracy while allowing surgeons to maintain their focus on the surgical field. This reduces cognitive load and mitigates the limitations of traditional two-dimensional navigation systems.

These technologies not only improve the precision of surgical interventions but also help minimize intraoperative complications, reduce operating times, and contribute to better long-term outcomes for patients with craniosynostosis. Despite their main drawback of the costs, this is well overcome by the improvement of the overall treatment quality.

Acknowledgments We would like to thank Dr Lara Deliege, Prof. Silvia Schievano, and Dr Juling Ong from Great Ormond Street Institute of Child Health; Dr Nicolas Emiliani and Ms. Barbara Bortolani from the Laboratory of Bioengineering—eDIMES Lab, Department of Medical and Surgical Sciences (DIMEC), University of Bologna, Bologna, Italy; Dr Micol Babini, Dr Beatrice Gardenghi, Dr Mariella Lefosse, Dr Filippo Friso, Dr Emanuele La Corte, Dr Alessandro Carretta, IRCCS Istituto delle Scienze Neurologiche di Bologna, Pediatric Neurosurgery, Bologna, Italy; Lorenzo Ciarma and all the nurses of the Pediatric Operating theater of IRCCS AOU di Bologna, Policlinico Sant-Orsola Malpighi; and Prof Claudio Marchetti.

Bibliography

1. Aboul-Hosn Centenero S, Hernández-Alfaro F. 3D planning in orthognathic surgery: CAD/CAM surgical splints and prediction of the soft and hard tissues results – our experience in 16 cases. J Craniofac Surg. 2012;40(2):162–8. https://doi.org/10.1016/j.jcms.2011.03.014.
2. Aguilar-Salinas P, Gutierrez-Aguirre SF, Avila MJ, Nakaji P. Current status of augmented reality in cerebrovascular surgery: a systematic review. Neurosurg Rev. 2022;45(3):1951–64. https://doi.org/10.1007/s10143-022-01733-3.
3. Ayoub A, Pulijala Y. The application of virtual reality and augmented reality in Oral & Maxillofacial Surgery. BMC Oral Health. 2019;19(1):238. https://doi.org/10.1186/s12903-019-0937-8.
4. Badiali G, Ferrari V, Cutolo F, Freschi C, Caramella D, Bianchi A, Marchetti C. Augmented reality as an aid in maxillofacial surgery: validation of a wearable system allowing maxillary repositioning. J Craniofac Surg. 2014;42(8):1970–6. https://doi.org/10.1016/j.jcms.2014.09.001.
5. Bannink N, Nout E, Wolvius EB, Hoeve HLJ, Joosten KFM, Mathijssen IMJ. Obstructive sleep apnea in children with syndromic craniosynostosis: long-term respiratory outcome of midface advancement. Int J Oral Maxillofac Surg. 2010;39(2):115–21. https://doi.org/10.1016/j.ijom.2009.11.021.
6. Barbarino GG, Jabareen M, Mazza E. Experimental and numerical study on the mechanical behavior of the superficial layers of the face. Skin Res Technol. 2011;17(4):434–44. https://doi.org/10.1111/j.1600-0846.2011.00515.x.
7. Bathe KJ. Finite element procedures. Englewood Cliffs: Prentice Hall; 1996.
8. Birgfeld CB, Saltzman BS, Hing AV, Heike CL, Khanna PC, Gruss JS, Hopper RA. Making the diagnosis. J Craniofac Surg. 2013;24(1):178–85. https://doi.org/10.1097/SCS.0b013e31826683d1.
9. Borghi A, Schievano S, Florez NR, McNicholas R, Rodgers W, Ponniah A, James G, Hayward R, Dunaway D, Owase Jeelani NU. Assessment of spring cranioplasty biomechanics in sagittal craniosynostosis patients. J Neurosurg Pediatr. 2017;20(5):400–9. https://doi.org/10.3171/2017.1.PEDS16475.

10. Borghi A, Rodriguez-Florez N, Rodgers W, James G, Hayward R, Dunaway D, Jeelani O, Schievano S. Spring assisted cranioplasty: a patient specific computational model. Med Eng Phys. 2018;53:58–65. https://doi.org/10.1016/j.medengphy.2018.01.001.
11. Borghi A, Rodriguez Florez N, Ruggiero F, James G, O'Hara J, Ong J, Jeelani O, Dunaway D, Schievano S. A population-specific material model for sagittal craniosynostosis to predict surgical shape outcomes. Biomech Model Mechanobiol. 2020;19(4):1319–29. https://doi.org/10.1007/s10237-019-01229-y.
12. Burge J, Saber NR, Looi T, French B, Usmani Z, Anooshiravani N, Kim P, Forrest C, Phillips J. Application of CAD/CAM prefabricated age-matched templates in cranio-orbital remodeling in craniosynostosis. J Craniofac Surg. 2011;22(5):1810–3. https://doi.org/10.1097/SCS.0b013e31822e8045.
13. Cartwright CC, Jimenez DF, Barone CM, Baker L. Endoscopic strip craniectomy: a minimally invasive treatment for early correction of craniosynostosis. J Neurosci Nurs. 2003;35(3):130–8. https://doi.org/10.1097/01376517-200306000-00002.
14. Ceccariglia F, Cercenelli L, Badiali G, Marcelli E, Tarsitano A. Application of augmented reality to maxillary resections: a three-dimensional approach to maxillofacial oncologic surgery. J Pers Med. 2022;12(12):2047. https://doi.org/10.3390/jpm12122047.
15. Cevidanes LHC, Tucker S, Styner M, Kim H, Chapuis J, Reyes M, Proffit W, Turvey T, Jaskolka M. Three-dimensional surgical simulation. Am J Orthod Dentofacial Orthop. 2010;138(3):361–71. https://doi.org/10.1016/j.ajodo.2009.08.026.
16. Chabanas M, Luboz V, Payan Y. Patient specific finite element model of the face soft tissues for computer-assisted maxillofacial surgery. Med Image Anal. 2003;7(2):131–51. https://doi.org/10.1016/S1361-8415(02)00108-1.
17. Cho RS, Lopez J, Musavi L, Kachniarz B, Macmillan A, Badiei B, Bello R, Dorafshar AH. Computer-assisted design and manufacturing assists less experienced surgeons in achieving equivalent outcomes in cranial vault reconstruction. J Craniofac Surg. 2019;30(7):2034–8. https://doi.org/10.1097/SCS.0000000000005748.
18. Chumas PD, Cinalli G, Arnaud E, Marchac D, Renier D. Classification of previously unclassified cases of craniosynostosis. J Neurosurg. 1997;86(2):177–81. https://doi.org/10.3171/jns.1997.86.2.0177.
19. Courant R. Variational methods for the solution of problems of equilibrium and vibrations. Bull Am Math Soc. 1943;49(1):1–23. https://doi.org/10.1090/S0002-9904-1943-07818-4.
20. Deliège L, Misier KR, Bozkurt S, Breakey W, James G, Ong J, Dunaway D, Jeelani NUO, Schievano S, Borghi A. Validation of an in-silico modelling platform for outcome prediction in spring assisted posterior vault expansion. Clin Biomech (Bristol, Avon). 2021;88:105424. https://doi.org/10.1016/J.CLINBIOMECH.2021.105424.
21. Deliège L, Ramdat Misier K, Silva D, James G, Ong J, Dunaway D, Jeelani NUO, Schievano S, Borghi A. Spring-assisted posterior vault expansion: a parametric study to improve the intracranial volume increase prediction. Sci Rep. 2023;13(1):21371. https://doi.org/10.1038/s41598-023-48143-z.
22. Deliege L, Carriero A, Ong J, James G, Jeelani O, Dunaway D, Stoltz P, Hersh D, Martin J, Carroll K, Chamis M, Schievano S, Bookland M, Borghi A. A computational modelling tool for prediction of head reshaping following endoscopic strip craniectomy and helmet therapy for the treatment of scaphocephaly. Comput Biol Med. 2024;177:108633. https://doi.org/10.1016/j.compbiomed.2024.108633.
23. Doh G, Eo S, Hong KY. Temporal hollowing augmentation with polyetheretherketone patient-specific implant. J Craniofac Surg. 2019;30(7):2131–3.
24. Eley KA, Watt-Smith SR, Sheerin F, Golding SJ. "Black Bone" MRI: a potential alternative to CT with three-dimensional reconstruction of the craniofacial skeleton in the diagnosis of craniosynostosis. Eur Radiol. 2014;24(10):2417–26. https://doi.org/10.1007/s00330-014-3286-7.
25. García-Mato D, Ochandiano S, García-Sevilla M, Navarro-Cuéllar C, Darriba-Allés JV, García-Leal R, Calvo-Haro JA, Pérez-Mañanes R, Salmerón JI, Pascau J. Craniosynostosis surgery: workflow based on virtual surgical planning, intraoperative navigation and 3D printed patient-specific guides and templates. Sci Rep. 2019;9(1):17691. https://doi.org/10.1038/s41598-019-54148-4.
26. Gault DT, Renier D, Marchac D, Jones BM. Intracranial pressure and intracranial volume in children with craniosynostosis. Plast Reconstr Surg. 1992;90(3):377–81. https://doi.org/10.1097/00006534-199209000-00003.
27. Ghaednia H, Fourman MS, Lans A, Detels K, Dijkstra H, Lloyd S, Sweeney A, Oosterhoff JHF, Schwab JH. Augmented and virtual reality in spine surgery, current applications and future potentials. Spine J. 2021;21(10):1617–25. https://doi.org/10.1016/j.spinee.2021.03.018.
28. Greenwood J, Flodman P, Osann K, Boyadjiev SA, Kimonis V. Familial incidence and associated symptoms in a population of individuals with nonsyndromic craniosynostosis. Genet Med. 2014;16(4):302–10. https://doi.org/10.1038/gim.2013.134.
29. Guha D, Alotaibi NM, Nguyen N, Gupta S, McFaul C, Yang VXD. Augmented reality in neurosurgery: a review of current concepts and emerging applications. Can J Neurol Sci. 2017;44(3):235–45. https://doi.org/10.1017/cjn.2016.443.
30. Haber SE, Patel A, Steinbacher DM. Digital planning in pediatric craniofacial surgery. In: Digital technologies in craniomaxillofacial surgery. New York: Springer; 2018. p. 305–29. https://doi.org/10.1007/978-1-4939-1532-3_12.
31. Han W, Yang X, Wu S, Fan S, Chen X, Aung ZM, Liu T, Zhang Y, Gu S, Chai G. A new method for cranial vault reconstruction: augmented reality in synostotic plagiocephaly surgery. J Craniofac Surg. 2019;47(8):1280–4. https://doi.org/10.1016/j.jcms.2019.04.008.
32. Imahiyerobo TA, Valenti AB, Guadix S, LaValley M, Asadourian PA, Buontempo M, Souweidane M, Hoffman C. The role of virtual surgical planning in surgery for complex craniosynostosis. Plast Reconstr Surg Glob Open. 2024;12(1):e5524. https://doi.org/10.1097/GOX.0000000000005524.
33. Jeelani NUO, Borghi A, Florez NR, Bozkurt S, Dunaway D, Schievano S. The science behind the springs: using biomechanics and finite element modeling to predict outcomes in spring-assisted sagittal synostosis surgery. J Craniofac Surg. 2020;31(7):2074–8. https://doi.org/10.1097/SCS.0000000000006865.
34. Kaplan N, Marques M, Scharf I, Yang K, Alkureishi L, Purnell C, Patel P, Zhao L. Virtual reality and augmented reality in plastic and craniomaxillofacial surgery: a scoping review. Bioengineering. 2023;10(4):480. https://doi.org/10.3390/bioengineering10040480.
35. Kapp-Simon KA, Speltz ML, Cunningham ML, Patel PK, Tomita T. Neurodevelopment of children with single suture craniosynostosis: a review. Childs Nerv Syst. 2007;23(3):269–81. https://doi.org/10.1007/s00381-006-0251-z.
36. Keeve E, Girod S, Kikinis R, Girod B. Deformable modeling of facial tissue for craniofacial surgery simulation. Comput Aided Surg. 1998;3(5):228–38. https://doi.org/10.3109/10929089809149844.
37. Khechoyan DY, Saber NR, Burge J, Fattah A, Drake J, Forrest CR, Phillips JH. Surgical outcomes in craniosynostosis reconstruction: the use of prefabricated templates in cranial vault remodelling. J Plast Reconstr Aesthet Surg. 2014;67(1):9–16. https://doi.org/10.1016/j.bjps.2013.09.009.
38. Kim S, Matic DB. Anatomic study the anatomy of temporal hollowing: the superficial temporal fat pad. (C). n.d.:651–4.
39. Kim Y, Kim H, Kim YO. Virtual reality and augmented reality in plastic surgery: a review. Arch Plast Surg. 2017;44(03):179–87. https://doi.org/10.5999/aps.2017.44.3.179.

40. Knoops PGM, Borghi A, Ruggiero F, Badiali G, Bianchi A, Marchetti C, Rodriguez-Florez N, Breakey RWF, Jeelani O, Dunaway DJ, Schievano S. A novel soft tissue prediction methodology for orthognathic surgery based on probabilistic finite element modelling. PLoS One. 2018;13(5):e0197209. https://doi.org/10.1371/journal.pone.0197209.
41. Koch RM, Gross MH, Carls FR, von Büren DF, Fankhauser G, Parish YIH. Simulating facial surgery using finite element models. In: Proceedings of the 23rd annual conference on computer graphics and interactive techniques; 1996. p. 421–8. https://doi.org/10.1145/237170.237281.
42. Kung TA, Vercler CJ, Muraszko KM, Buchman SR. Endoscopic strip craniectomy for craniosynostosis: do we really understand the indications, outcomes, and risks? J Craniofac Surg. 2016;27(2):293–8. https://doi.org/10.1097/SCS.0000000000002364.
43. Lajeunie E, Crimmins DW, Arnaud E, Renier D. Genetic considerations in nonsyndromic midline craniosynostoses: a study of twins and their families. J Neurosurg Pediatr. 2005;103(4):353–6. https://doi.org/10.3171/ped.2005.103.4.0353.
44. Lattanzi W, Barba M, Di Pietro L, Boyadjiev SA. Genetic advances in craniosynostosis. Am J Med Genet A. 2017;173(5):1406–29. https://doi.org/10.1002/ajmg.a.38159.
45. Lauritzen C, Sugawara Y, Kocabalkan O, Olsson R. Spring mediated dynamic craniofacial reshaping. Case report. Scand J Plast Reconstr Surg Hand Surg. 1998;32(3):331–8. http://www.ncbi.nlm.nih.gov/pubmed/9785439.
46. LoPresti M, Daniels B, Buchanan EP, Monson L, Lam S. Virtual surgical planning and 3D printing in repeat calvarial vault reconstruction for craniosynostosis: technical note. J Neurosurg Pediatr. 2017;19(4):490–4. https://doi.org/10.3171/2016.10.PEDS16301.
47. Luboz V, Chabanas M, Swider P, Payan Y. Orbital and maxillofacial computer aided surgery: patient-specific finite element models to predict surgical outcomes. Comput Methods Biomech Biomed Engin. 2005;8(4):259–65. https://doi.org/10.1080/10255840500289921.
48. Manrique OJ, Lalezarzadeh F, Dayan E, Shin J, Buchbinder D, Smith M. Craniofacial reconstruction using patient-specific implants polyether ether ketone with computer-assisted planning. J Craniofac Surg. 2015;26(3):663–6. https://doi.org/10.1097/SCS.0000000000001443.
49. Mathijssen IMJ. Updated guideline on treatment and management of craniosynostosis. J Craniofac Surg. 2021;32(1):371–450. https://doi.org/10.1097/SCS.0000000000007035.
50. Mazzoni S, Bianchi A, Schiariti G, Badiali G, Marchetti C. Computer-aided design and computer-aided manufacturing cutting guides and customized titanium plates are useful in upper maxilla waferless repositioning. J Oral Maxillofac Surg. 2015;73(4):701–7. https://doi.org/10.1016/j.joms.2014.10.028.
51. McHenry D. Discussion: "Solution of problems of elasticity by the framework method" (Hrennikoff, A., 1941, ASME J. Appl. Mech., 8, pp. A169–A175). J Appl Mech. 1942;9(3):A144–5. https://doi.org/10.1115/1.4009210.
52. Milgram P, Takemura H, Utsumi A, Kishino F. Mixed reality (MR) reality-virtuality (RV) continuum. Syst Res. 1994;2351:282–92.
53. Mollemans W, Schutyser F, Van Cleynenbreugel J, Suetens P. Tetrahedral mass spring model for fast soft tissue deformation; 2003. p. 145–54. https://doi.org/10.1007/3-540-45015-7_14.
54. Mollemans W, Schutyser F, Nadjmi N, Maes F, Suetens P. Predicting soft tissue deformations for a maxillofacial surgery planning system: from computational strategies to a complete clinical validation. Med Image Anal. 2007;11(3):282–301. https://doi.org/10.1016/j.media.2007.02.003.
55. Moss ML. Functional anatomy of cranial synostosis. Pediatr Neurosurg. 1975;1(1):22–33. https://doi.org/10.1159/000119554.
56. Ni J, Yang B, Li B. Reconstructive operation of nonsyndromic multiple-suture craniosynostosis based on precise virtual plan and prefabricated template. J Craniofac Surg. 2017;28(6):1541–2. https://doi.org/10.1097/SCS.0000000000003784.
57. O'Hara J, Ruggiero F, Wilson L, James G, Glass G, Jeelani O, Ong J, Bowman R, Wyatt M, Evans R, Samuels M, Hayward R, Dunaway DJ. Syndromic craniosynostosis: complexities of clinical care. Mol Syndromol. 2019;10(1–2):83–97. https://doi.org/10.1159/000495739.
58. Okamoto T, Onda S, Yanaga K, Suzuki N, Hattori A. Clinical application of navigation surgery using augmented reality in the abdominal field. Surg Today. 2015;45(4):397–406. https://doi.org/10.1007/s00595-014-0946-9.
59. Persing JA. MOC-PS(SM) CME article: management considerations in the treatment of craniosynostosis. Plast Reconstr Surg. 2008;121(Supplement):1–11. https://doi.org/10.1097/01.prs.0000305929.40363.bf.
60. Pisaneschi G, Mele M, Zucchelli A, Fiorini M, Campana G, Marcelli E, Tarsitano A, Lucchi E, Cercenelli L. Numerical and experimental investigation of a 3D-printed PCU patient-specific cranial implant. Prog Addit Manuf. 2024;9(2):299–313. https://doi.org/10.1007/s40964-023-00452-5.
61. Pyle J, Glazier S, Couture D, Sanger C, Gordon S, David L. Spring-assisted surgery-a surgeon's manual for the manufacture and utilization of springs in craniofacial surgery. J Craniofac Surg. 2009;20(6):1962–8. https://doi.org/10.1097/SCS.0b013e3181bd2cb2.
62. Qu M, Hou Y, Xu Y, Shen C, Zhu M, Xie L, Wang H, Zhang Y, Chai G. Precise positioning of an intraoral distractor using augmented reality in patients with hemifacial microsomia. J Craniofac Surg. 2015;43(1):106–12. https://doi.org/10.1016/j.jcms.2014.10.019.
63. Quero G, Lapergola A, Soler L, Shahbaz M, Hostettler A, Collins T, Marescaux J, Mutter D, Diana M, Pessaux P. Virtual and augmented reality in oncologic liver surgery. Surg Oncol Clin N Am. 2019;28(1):31–44. https://doi.org/10.1016/j.soc.2018.08.002.
64. Rahimov C, Asadov R, Hajiyeva G, Verdiyev N, Novruzov Z, Farzaliyev I. Crouzon syndrome: virtual planning of surgical treatment by application of internal distractors. Ann Maxillofac Surg. 2016;6(1):135. https://doi.org/10.4103/2231-0746.186144.
65. Robiony M, Salvo I, Costa F, Zerman N, Bandera C, Filippi S, Felice M, Politi M. Accuracy of virtual reality and stereolithographic models in maxillo-facial surgical planning. J Craniofac Surg. 2008;19(2):482–9. https://doi.org/10.1097/SCS.0b013e31814fb5c1.
66. Rodgers W, Glass GE, Schievano S, Borghi A, Rodriguez-Florez N, Tahim A, Angullia F, Breakey W, Knoops P, Tenhagen M, O'Hara J, Ponniah A, James G, Dunaway DJ, Jeelani NUO. Spring-assisted cranioplasty for the correction of nonsyndromic scaphocephaly: a quantitative analysis of 100 consecutive cases. Plast Reconstr Surg. 2017;140(1):125–34. https://doi.org/10.1097/PRS.0000000000003465.
67. Ruggiero F, Borghi A, Bevini M, Badiali G, Lunari O, Dunaway D, Marchetti C. Soft tissue prediction in orthognathic surgery: improving accuracy by means of anatomical details. PLoS One. 2023a;18(11):e0294640. https://doi.org/10.1371/journal.pone.0294640.
68. Ruggiero F, Cercenelli L, Emiliani N, Badiali G, Bevini M, Zucchelli M, Marcelli E, Tarsitano A. Preclinical application of augmented reality in pediatric craniofacial surgery: an accuracy study. J Clin Med. 2023b;12(7):2693. https://doi.org/10.3390/jcm12072693.
69. Ruggiero F, Budden C, Ong J, Dunaway D, Borghi A. Finite element method for the design of implants for temporal hollowing. Br J Oral Maxillofac Surg. n.d.
70. Schendel S, Hazan-Molina H, Rachmiel A, Aizenbud D. The future in craniofacial surgery: computer-assisted planning. Rambam

Maimonides Med J. 2012;3(2):e0012. https://doi.org/10.5041/RMMJ.10079.
71. Scherl C, Stratemeier J, Rotter N, Hesser J, Schönberg SO, Servais JJ, Männle D, Lammert A. Augmented reality with HoloLens® in parotid tumor surgery: a prospective feasibility study. ORL. 2021;83(6):439–48. https://doi.org/10.1159/000514640.
72. Schiavina R, Bianchi L, Chessa F, Barbaresi U, Cercenelli L, Lodi S, Gaudiano C, Bortolani B, Angiolini A, Bianchi FM, Ercolino A, Casablanca C, Molinaroli E, Porreca A, Golfieri R, Diciotti S, Marcelli E, Brunocilla E. Augmented reality to guide selective clamping and tumor dissection during robot-assisted partial nephrectomy: a preliminary experience. Clin Genitourin Cancer. 2021;19(3):e149–55. https://doi.org/10.1016/j.clgc.2020.09.005.
73. Slater BJ, Lenton KA, Kwan MD, Gupta DM, Wan DC, Longaker MT. Cranial sutures: a brief review. Plast Reconstr Surg. 2008;121(4):170e–8e. https://doi.org/10.1097/01.prs.0000304441.99483.97.
74. Tarsitano A, Battaglia S, Crimi S, Ciocca L, Scotti R, Marchetti C. Is a computer-assisted design and computer-assisted manufacturing method for mandibular reconstruction economically viable? J Craniofac Surg. 2016;44(7):795–9. https://doi.org/10.1016/j.jcms.2016.04.003.
75. van der Meulen J. Metopic synostosis. Child's Nerv Syst. 2012;28(9):1359–67. https://doi.org/10.1007/s00381-012-1803-z.
76. van der Meulen J, van der Hulst R, van Adrichem L, Arnaud E, Chin-Shong D, Duncan C, Habets E, Hinojosa J, Mathijssen I, May P, Morritt D, Nishikawa H, Noons P, Richardson D, Wall S, van der Vlugt J, Renier D. The increase of metopic synostosis. J Craniofac Surg. 2009;20(2):283–6. https://doi.org/10.1097/SCS.0b013e31818436be.
77. Verhey JT, Haglin JM, Verhey EM, Hartigan DE. Virtual, augmented, and mixed reality applications in orthopedic surgery. Int J Med Robot Comput Assist Surg. 2020;16(2):e2067. https://doi.org/10.1002/rcs.2067.
78. Zachow S. Computational planning in facial surgery. Facial Plast Surg. 2015;31(05):446–62. https://doi.org/10.1055/s-0035-1564717.
79. Zhang X, Tang Z, Liebschner MAK, Kim D, Shen S, Chang C-M, Yuan P, Zhang G, Gateno J, Zhou X, Zhang S-X, Xia JJ. An eFace-template method for efficiently generating patient-specific anatomically-detailed facial soft tissue FE models for craniomaxillofacial surgery simulation. Ann Biomed Eng. 2016;44(5):1656–71. https://doi.org/10.1007/s10439-015-1480-7.
80. Zucchelli M, Ruggiero F, Babini M, Lefosse M, Borghi A, Rodriguez-Florez N, Tarsitano A, Nicolini F, Galassi E. Surgical strategy in treatment of metopic synostosis in a single centre experience: technical note and quantitative analysis of the outcomes. Childs Nerv Syst. 2024;40(12):3963–70. https://doi.org/10.1007/s00381-024-06520-7.

Introduction to Virtual Planning in Orbital Region and Applications in Orbital Trauma

Alessandro Tel and Massimo Robiony

1 Anatomical Peculiarities for the Virtual Reconstruction of the Orbit

1.1 Hard Structure and Framework: Common Issues

The orbit is a cone shaped cavity, with its apex directed posteriorly and medially, which poses significant challenges to virtual planning. First, orbital morphology is complex, as this cavity opens into the superior orbital fissure, bordered by the greater and the lesser sphenoidal wing, the inferior orbital fissure, delimited by the posterior wall of the maxillary bone and the inferior margin of the greater sphenoid wing, and the optic foramen, which is entirely within the sphenoid body.

However, beyond anatomical complexity, the orbit has some intrinsic characteristics that render it one of the most complex regions of the craniofacial skeleton to be reconstructed in a virtual model: extreme thinness of the inferior and medial wall, a slight thicker roof, and a thick, well defined, lateral wall.

- The extreme thinness of the inferior wall of the orbit (the orbital floor) makes radiological image subject to the partial volume effect, which is due to the relatively low resolution of CT imaging, and hence the size of the voxel, compared to the thickness of bone. This is due to the presence of a pneumatized cavity underlying the orbital space, represented by the maxillary sinus. In this setting, the thresholding algorithm might interpret voxels of mixed value (bone and air occurring in the same voxel) as very low Hounsfield Unit (HU) value, thus creating voids in the orbital floor, which in reality is a solid, although extremely thin, structure. The results are virtual models with hollow orbits, not defined by walls.
- The same issue affects the medial orbital wall, which is contiguous with many pneumatized ethmoidal cells. It is called "lamina papyracea," owing to its extreme thinness.
- The orbital roof, representing the inferior limit of the anterior skullbase, is slightly less subject to hollowing artifacts, yet it is still a very thin structure and may potentially result altered if CT scan does not meet optimal requirements, or if segmentation was poorly performed.
- In addition, another significant limit of the orbital space for the purpose of a 3D reconstruction, and especially for volume calculations and mirroring, is the absence of an anatomically defined anterior limit, representing the base of the cone. Thus, it is always established arbitrarily, as the orbital septum, making its anatomical boundary, is not visible in CT or MR.

1.2 Soft Structure and Content

Within the orbital space, several crucial structures are hosted. The orbit is an extremely complex environment, with a high number of densely packed contents, including:

- Eye globe
- Nervous structures: the most important is the optic nerve, although smaller are represented by the first branch of trigeminal nerve (ophthalmic), and short and long ciliary nerves
- Arterial vessels: the ophthalmic artery along with its branches, including the central retinal artery, ciliary arteries, ethmoidal arteries

A. Tel (✉)
Lead Specialist for VSP and 3DP, Maxillofacial Surgery Clinic, Head & Neck and Neuroscience Department, Academic Hospital of Udine, Udine, Italy
e-mail: alessandro.tel@uniud.it

M. Robiony
Chief of Maxillofacial Surgery Clinic, Director of the Postgraduate School in Maxillofacial Surgery, Chief of Head & Neck and Neuroscience Department, Academic Hospital - University of Udine, Udine, Italy
e-mail: massimo.robiony@uniud.it

© The Author(s), under exclusive license to Springer Nature Switzerland AG 2025

A. Tel, M. Robiony (eds.), *Atlas of Virtual Surgical Planning and 3D Printing for Cranio-Maxillo-Facial Surgery*,
https://doi.org/10.1007/978-3-031-94495-6_14

- Venous vessels: superior and inferior ophthalmic veins, vorticose veins
- Glandular structures: the lacrimal gland
- Muscles: superior, inferior, medial and lateral recti, as well as superior and inferior obliqui
- Tendons: annulus of Zinn
- Fat tissue, which surrounds all noble structures
- An external envelope, the periorbit, which includes all the aforementioned

All such structures cannot generally be recognized in a standard MR imaging; therefore, it is intuitive that not all of them are suitable for the 3D reconstruction, but some simplifications and assumptions are mandatory. Therefore, a model for orbital virtualization must be conceptually defined.

1.3 A Model for Orbital Visualization

This model provides a simplified, yet trustful, virtual reconstruction of the patient's anatomy and is based upon the following components:

- The skeletal framework: CT allows for an accurate reconstruction of the orbital boundaries. There are some intrinsic limitations that are due to artifacts occurring in highly thin regions [1].
- The eye globe: It can be reconstructed both in the CT, where the spatial resolution is higher, and in the MR, where, especially in T2-weighted sequences, the vitreous body is easily identifiable. The drawback of using T2 sequence for eye globe segmentation is that this MR sequence will certainly underestimate the globe size, as it is based exclusively on the vitreous body and does not consider the Tenon's capsule. Some sequences designed for volumetric acquisition, like the Volumetric Interpolated Breath-hold Examination (VIBE) sequence, also allow an accurate eye globe definition [2].
- The optic nerve: It has a consistent diameter, ranging between 3.5 and 4.5 mm; therefore, it can be easily identified. It has an inherent contrast that differentiates it from the surrounding intraconal fat. It can be easily seen in T1-weighted sequences and can be reliably segmented by using a threshold and proximity-based algorithm in Short-TI Inversion Recovery (STIR) sequence [3].
- Extraocular muscles: Concerning the four recti (superior, medialis, inferior, and lateralis), they can be segmented from CT scan taking benefit of the higher spatial resolution compared to MR, as slices can be only 0.6 mm thick, compared to MR that generally has the limit of 1 mm slices. 1 mm for structures as small as extraocular muscles is a considerable size, which may result in a stair-like 3D model, if segmentation is not carefully performed. Actually, using T1-w or STIR sequences is the best way to define the muscles by contrast and ensure that they are segmented along their correct anatomical margins. To further lower the possible stair-like artifact, the author suggests to reslice the DICOM stack by applying an interpolation method that virtually lowers slice thickness. As for obliqui muscles, the same principles apply, with additional difficulties due to the even thinner appearance and ribbon-like shape, especially of the obliquus inferior. Thus, obliqui are generally less visible and pose stricter limits to segmentation [4].
- Arteries: Using 3D-Time-of-Flight (TOF) sequences, the most accurate imaging might allow to segment the ophthalmic artery up to the point where it becomes intraconal.
- Intraconal fat: It does not generally have importance as it does not represent a noble functional structure, but it fills the intraconal space between nerves, arteries, and muscles. However, its study might play a key role in Graves' orbitopathy.

Figure 1 The orbital virtual model and its components.

1.4 Strategies to Compensate for Bone Loss of Thin Walls

The skeletal framework that defines the orbital cavity and is made of the orbital walls is notably very thin; therefore, a proper knowledge on how to compensate for the loss of bone caused by the partial volume effect is mandatory. As mentioned, the orbital floor, the lamina papyracea, and the orbital roof are extremely thin, and their segmentation tends to provide hollowed structures that might impair the virtual reconstruction process, especially for procedures that require a detailed visualization of the orbital walls, including the creation of models for prebending of implants, the design itself of orbital implants, and simulations involving orbital osteotomies.

There are basically two methods that enable to trustfully repair holes in models. It is of prominent importance that the repairing of hollowed structures does not alter the true anatomical morphology of the orbital floor:

- Using the "Segment thin bone" plugin: It is a novel plugin introduced in Materialise Mimics since version 24.0. Upon the operator's input to generate a Region of Interest (ROI) over the structure to segment, the plugin elaborates a script that enables to segment the structure as a continuous surface, without the hollows that are typical of very thin bones. According to the author's experience, it works with maximal precision in some anatomical regions, including orbital floor, medial wall, and ethmoidal cells. This is the method recommended by the Author (Fig. 2).



Fig. 1 Construction of the virtual orbital anatomical atlas. It enables for patient-specific visualization with the progressive addition of anatomical layers, starting from the bone frame, recti and obliqui extraocular muscles, optic nerve, intraconal fat, and eye globe. These are the basic structures for orbital VSP

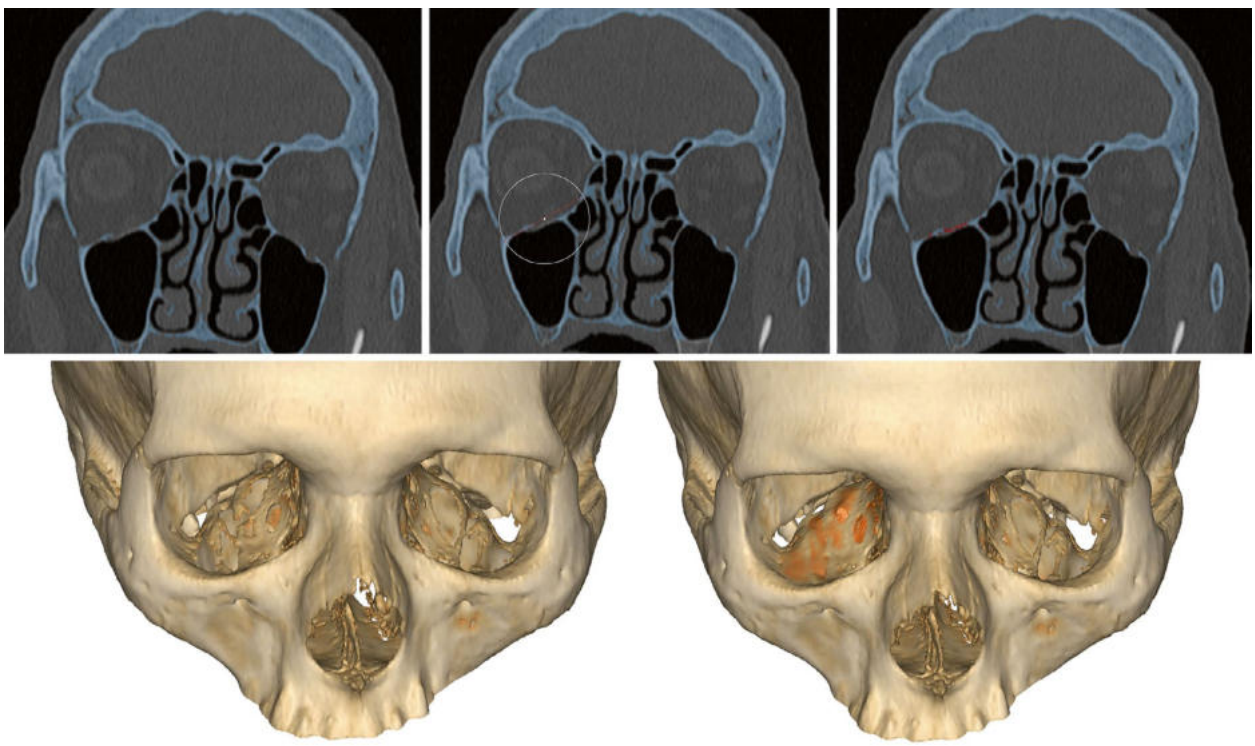


Fig. 2 Correction of partial volume effect is essential to reconstruct the orbital floor, both fractured and normal (to be used in mirroring). Here an application of the segment thin structure plugin of Materialise Mimics is shown in the right orbital floor

- Orbital wall segmentation using paranasal sinuses anatomy as template [5]: This method can be performed using a visual interface or by applying a script, as its phases are very sequential. Basically, paranasal sinuses are segmented using an air thresholding value, appearing as solid structures. They are then used to fill the gaps in the orbital floor, where the HU value is below the bone range.
- Modifying threshold locally within the same segmentation mask, applying a lower threshold value in correspondence of thin orbital walls to maximize voxels captured.

These are the most accurate methods, although other options are possible:

- Manual segmentation in areas where there is a discontinuity of the mask in regions affected by hollowing: highly time consuming and might lead to inaccurate results in non-expert hands
- Filling hollowed regions directly on the STL file in a CAD editing software: This method is performed without DICOM images as reference and might lead to inaccurate results without the proper experience.

2 Orbital Traumatology: Principles of VSP

2.1 Generalities

Trauma in the orbital region is very common in maxillofacial surgery practice. It can result from various mechanisms and can affect different regions of the orbit. As seen concerning anatomy and its implications for segmentation and creation of 3D models, there are two functionally separate divisions that account for different trauma mechanisms:

- The orbital rim, and especially the lateral orbital rim, is a thick, cortical bone, with the purpose of creating protective cage around the eye, acting like a "bumper" against injuries. It breaks for generally high-energy traumas occurring directly in the point of application of a force. The lateral orbital rim is contiguous with the zygomatic arch and represents a robust buttress that protects the lateral part of the orbital space. The superior orbital rim, which includes the supraorbital and supratrochlear nerves, is thinner and separates the orbital space from the frontal sinus. The medial orbital rim is the thinnest and is a vulnerable structure, as it contains the lacrimal notch with the lacrimal sac and is contiguous with the lamina papyracea; fractures of the medial orbital rim almost never occur isolated, but in conjunction with a centrofacial injury involving the ethmoid. The inferior orbital rim is a robust, thick structure and represents one of the roots of the zygomatic bone, as its fracture usually occurs in association with a zygomatic-maxillary complex (ZMC) fracture. Underneath the inferior orbital rim, there is the emergence of the infraorbital nerve. Given the strong association between fractures of the inferior orbital rim and ZMC fractures, they will be described in the context of ZMC fractures.
- Orbital walls, as mentioned, are very thin structures, except for the lateral orbital wall. The mechanism of injury is generally indirect, as the walls tend to collapse under the effect of a force applied on the eye globe, which dissipates to protect the globe. This is the etiology of blow-out orbital fractures, as the force distribution across orbital walls immediately overcomes the resistance of the orbital floor, causing its fracture. In many cases, depending on the magnitude of the force applied, also the medial wall might collapse, as it is anatomically contiguous, in terms of proximity and curvature, with the orbital floor. The mechanism of action of fractures involving the orbital roof is slightly different, as the roof might rupture as a consequence of head trauma. Depending on the direction of displacement of fractured bone segments, orbital wall fractures might additionally be subclassified as blow-out (the paradigm is the orbital floor) and blow-in, the latter occurring with a higher frequency across the orbital roof [6].

Orbital fractures, especially when involving the walls, can have detrimental functional consequences on the patient. The collapse of the orbital floor allows for a downward displacement of the eye globe, altering its horizontal symmetry with the contralateral. The most common and disturbing clinical symptom referred by the patient is diplopia, and in several cases the dislocation of the eye globe leads to unpleasant esthetical appearance due to enophthalmos and dystopia. In some cases, the fracture of the thin bone lamina might pinch the inferior rectus muscle, causing its entrapment with its complete functional impairment, generally manifest as a limitation of ocular infraduction [7].

2.2 The Role of Virtual Surgical Planning in Orbital Traumatology

Given the anatomical complexity of the orbital region, it is largely acknowledged that virtual surgical planning plays a key role to restore the correct anatomical shape, which is crucial for the appropriate functional outcomes. In particular, the computation of orbital volume is an essential element to evaluate since it conditions the eye globe projection. One major issue is to be mentioned when trying to define the orbital volume, and it consists in the definition of the anterior limit of the orbital cone. Several works report the anterior

limit of the cone (i.e., the base) as a planar surface passing through the superior, inferior, medial, and lateral orbital rim. In other circumstances, soft tissue may account for this evaluation, and even in presence of an intraconal volume comparable to the healthy orbit (in unilateral disease), there might be evident bulbar proptosis for accumulation of tissue beyond the base of the cone, in the peribulbar space, or even within the eyelids, such as in soft tissue thickening occurring in Graves' orbitopathy. Another complex scenario is defined by bilateral orbital involvement, a condition that makes the mirroring technique unsuitable, and requires to implement more advanced methods, for instance, the statistical shape modeling and deep learning.

Concerning methods of virtual planning useful for orbital trauma, the following are the most frequently used:

- Mirroring: Upon definition of a sagittal symmetry midplane, the healthy orbit is mirrored and superimposed to the contralateral to ascertain parameters of normality useful for reconstruction (Fig. 3). It is worth mentioning that this approach is never perfect, as there is a minimal slight asymmetry in all subjects; thus, further realignment using a vertex-to-vertex alignment by the iterative closest point algorithm is advised. Obviously, this technique requires one side to be unaltered and is precluded in cases of bilateral orbital involvement. Mirroring can be highly useful to create a digital template that enables repositioning of fractured segments, which are aligned point-by-point with the mirrored replica to facilitate resymmetrization of the orbit [8, 9].
- Anatomical reconstruction: Similar to cranial defects, it requires to identify the edge of the orbital defect, then project the altered geometry across a two-dimension plane where splines are constructed to reconstruct an ideal shape of the 3D object (Fig. 4). In the author's experience, this method is particularly suitable to reconstruct defects surrounded by a normal geometry, and internal orbital floor fractures are paradigmatic. This is an example of "context-driven reconstruction," as no external geometry is used to complete the reconstruction of the orbital floor, but all the information is drawn from the context, which is the surrounding healthy anatomy. The creation of a digital reconstruction is useful to fill gaps in the orbital floor both because of trauma or excessive bone loss if CT scan was not appropriately performed and to conform devices which are designed to fit the orbital floor, for instance, in case of alloplastic implants for an orbital floor fracture, or a surgical guide to harvest a bone graft with the optimal size and shape for the orbital floor [10].

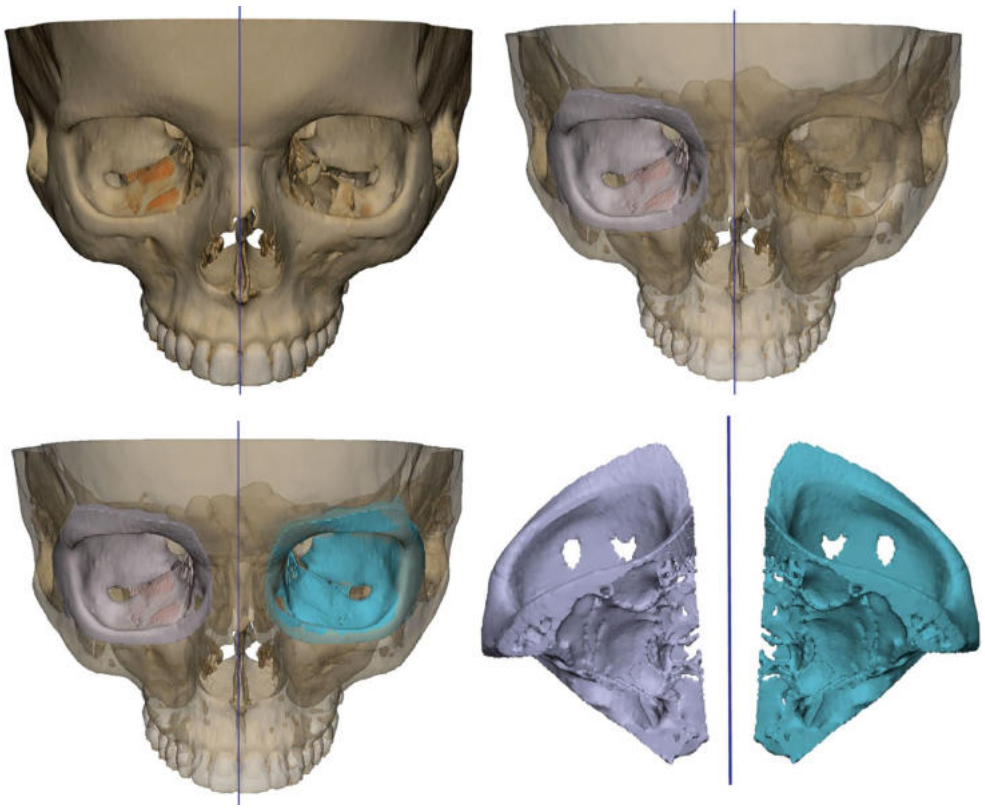


Fig. 3 Mirroring process of the orbital cone starts from accurate definition of the symmetry plane. Mirroring the cone means to mirror all the walls of the orbit, depending on the defect to be addressed



Fig. 4 Context-driven reconstruction is performed by outlining the orbital defect and applying a spline in an orthogonal plane to define the ideal course of the filled defect. Reconstruction is highly accurate and can overcome the need of mirroring

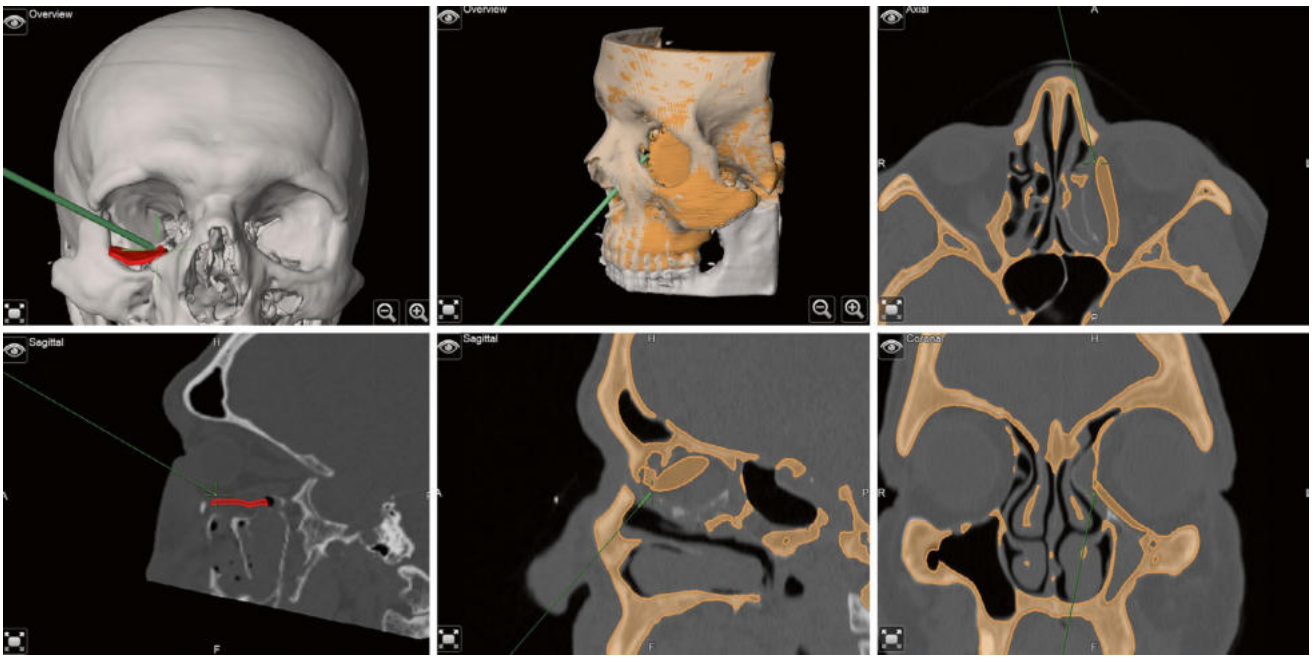


Fig. 5 Image guided surgery in orbital traumatology. In this case, navigation is used to reposition an autograft over the fractured orbital floor

2.3 Image-Guided Surgery in Orbital Traumatology

In orbital trauma, navigation can be helpful in internal orbital floor fractures to establish the posterior margin of the fracture, especially in open transcutaneous or transconjuntival approaches, where it is not so clearly visible as it is with transantral endoscopy. Moreover, a navigated surgical planning including the established position of the implant can be used as reference, allowing the surgeon to check for the correct placement of the implant as well, avoiding re-operations due to unsatisfactory implant placement with persistence of orbital enlargement and enophthalmos [11, 12]. Likewise, navigation of surgical planning can be used in traumas of the lateral orbital rim to evaluate the correct alignment of fragments and the coherence with computer-planned reduction (Fig. 5).

3 Fractures Involving the Lateral Orbital Rim

In fractures of the lateral orbital rim, it is crucial to reestablish both the anatomical integrity of displaced anatomical segments and the esthetic contour of the orbit. Such fractures often result from direct trauma over the lateral orbital rim and in the majority of cases are lateralized, thus making the mirroring technique ideal to reconstruct anatomy. The mir-

roring replica works as a *digital repositioning template*, because it can drive the optimal alignment of displaced bone segments to restore symmetry in a fast and accurate way. Additionally, this template can be exported as an overlay mask within the navigation project, and it can be intraoperatively navigated to maximize the accuracy in bone repositioning [13].

3.1 Single Fragment Fracture of the Lateral Orbital Rim

3.1.1 Clinical History

In this case, a 20-year-old boy had fallen at work hitting a blunt surface, causing an inward displacement of the lateral orbital rim which had broken in two points, leaving a conspicuous bone fragment mobile. The patient presented with marked swelling and periorbital ecchymosis. Eye globe projection was mildly affected. Ocular motility was preserved.

3.1.2 Virtual Surgical Planning

In this case, the mirroring of the unaffected side was used as a digital template for bone repositioning, facilitating the optimal alignment of the displaced segment. After fracture reduction in the virtual surgical planning resulting from the alignment with the mirroring template, the displaced segment resulted in the correct anatomical reduction relationship (Fig. 6). This was useful to understand the orientation and the feasibility of anatomical reduction; however, as the fracture was a single piece, image-guided surgery techniques or surgical guides were not deemed to add value to simplify the procedure.

3.1.3 Surgery

A subciliary incision with a lateral "lazy S" design was used to access the lateral orbital wall. Orbicularis oculi muscle was sectioned and periosteum elevated to uncover the fracture. Reduction was performed by gently elevating the inward displaced fragment using a bone hook and a traditional periosteal elevator. Fixation was achieved with two linear plates placed and a single L-shaped plate placed at the extremities of the fracture boundaries (Fig. 7).

3.2 Multi-fragment Fracture of the Lateral Orbital Rim

3.2.1 Clinical History

This patient was kicked by a horse during the preparation for a competition. The impact caused an eyeball rupture associated with an inward displaced, multifragmented, fracture of the right lateral orbital wall in association with the ipsilateral ZMC. The patient underwent urgent ophthalmologic surgery with corneal suture and maxillofacial surgery was differed to optimize a personalized treatment planning.

3.2.2 Virtual Surgical Planning

Especially in high energy trauma or falls, lateral orbital rim fracture is often associated with a zygomatic-maxillary complex fracture (ZMC). In such cases, when the injury is well sided, the digital reduction template offered by the mirroring still represents a validated method to align even multiple fragments. In this case, the midsagittal plane is identified as usual, then the mirroring operation is performed to generate a specular image used as a digital repositioning template.

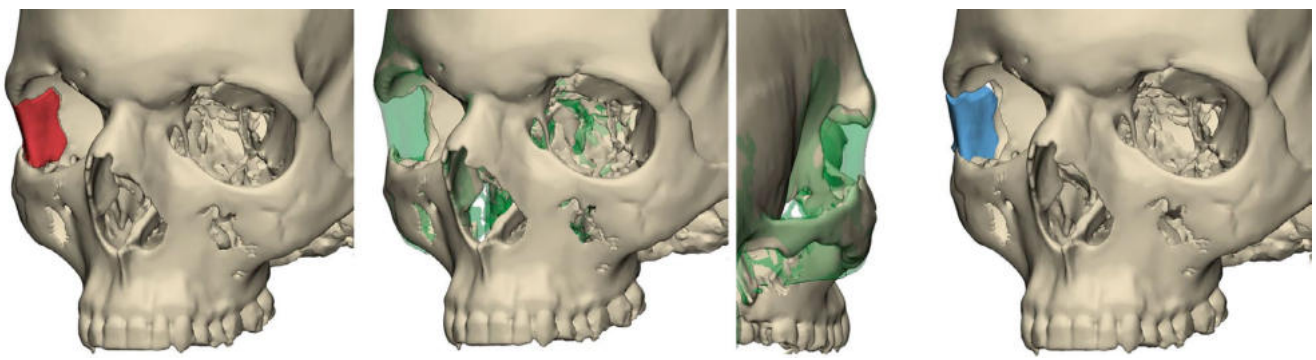


Fig. 6 VSP in reduction of a single fragment lateral wall fracture. In a sided injury, mirroring is ideal to define a virtual reduction mask

The mirrored image is then optimally aligned with the contralateral side, a procedure that usually has a favorable outcome unless there is manifest asymmetry between both halves of the facial skeleton. Once the alignment process is complete, it is important to verify that the mirrored replica ensures continuity of rims and buttresses and, if reliable, it is used to automatically reposition fragments. Instead of aligning each fragment manually, the use of the mirrored repositioning template fastens the workflow, as each individual fragment can be instantaneously aligned with the template (Fig. 8). STL files of repositioned orbital and zygomatic segments were imported in Brainlab Elements (Brainlab AG, Munich, DE) to create a navigation plan.

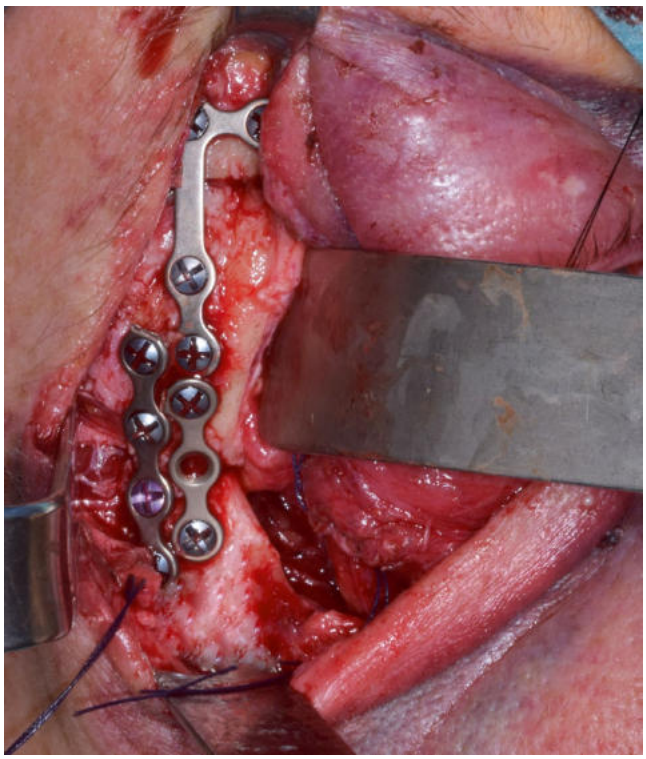


Fig. 7 Bone fragment fixation using multiple osteosynthesis plates

3.2.3 Surgery

A subciliary incision extended laterally across a lateral canthal skin fold was used to access the inferior and lateral orbital rim. Anatomical reduction was performed under navigational guidance, where virtual templates of repositioned STL files of virtual surgical planning were interactively checked as digital repositioning templates (Fig. 9). Navigation masks represented the planned position of each skeletal segment, allowing surgeons to visualize the correct position for a satisfactory reduction, respectful of orbital symmetry. Curved titanium plates were used for osteosynthesis. ZMC fracture plating required an intraoral access as well to reconstruct the maxillo-malar buttress (Fig. 10).

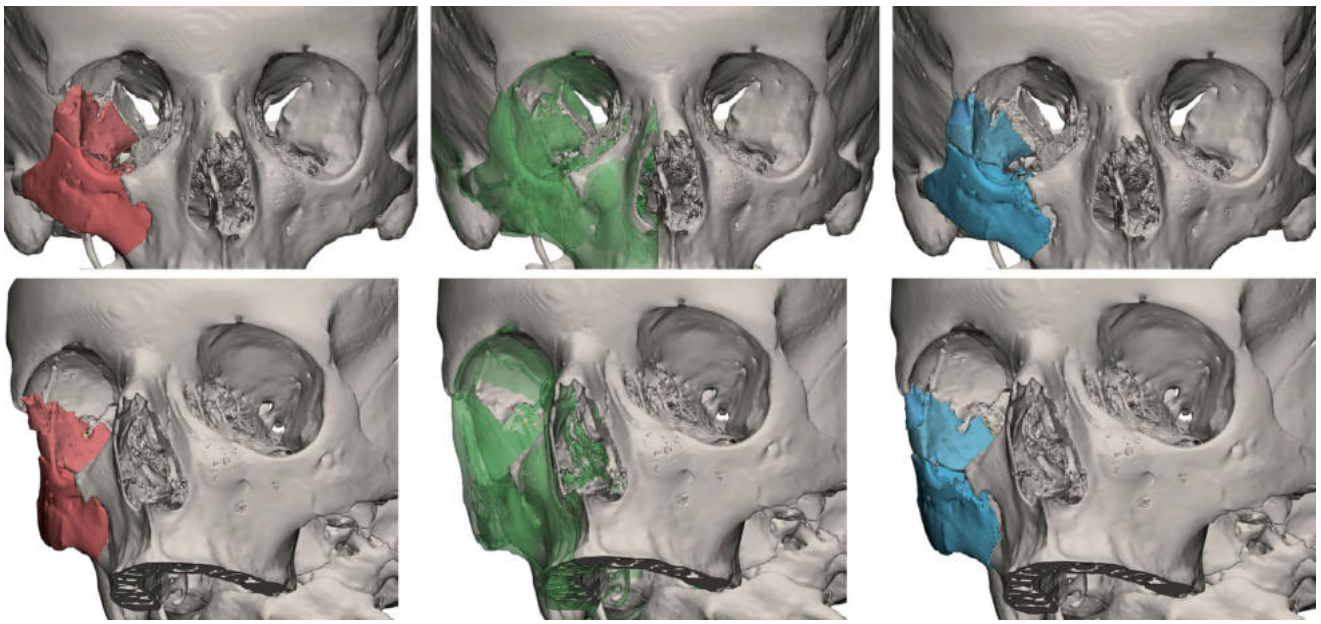


Fig. 8 VSP in a multiple fragment orbital rim fracture, which is often associated with concurrent ZMC fracture (red). In a sided injury, mirroring creates a useful reduction mask (green) to realign fragments in the most accurate relationship (blue)

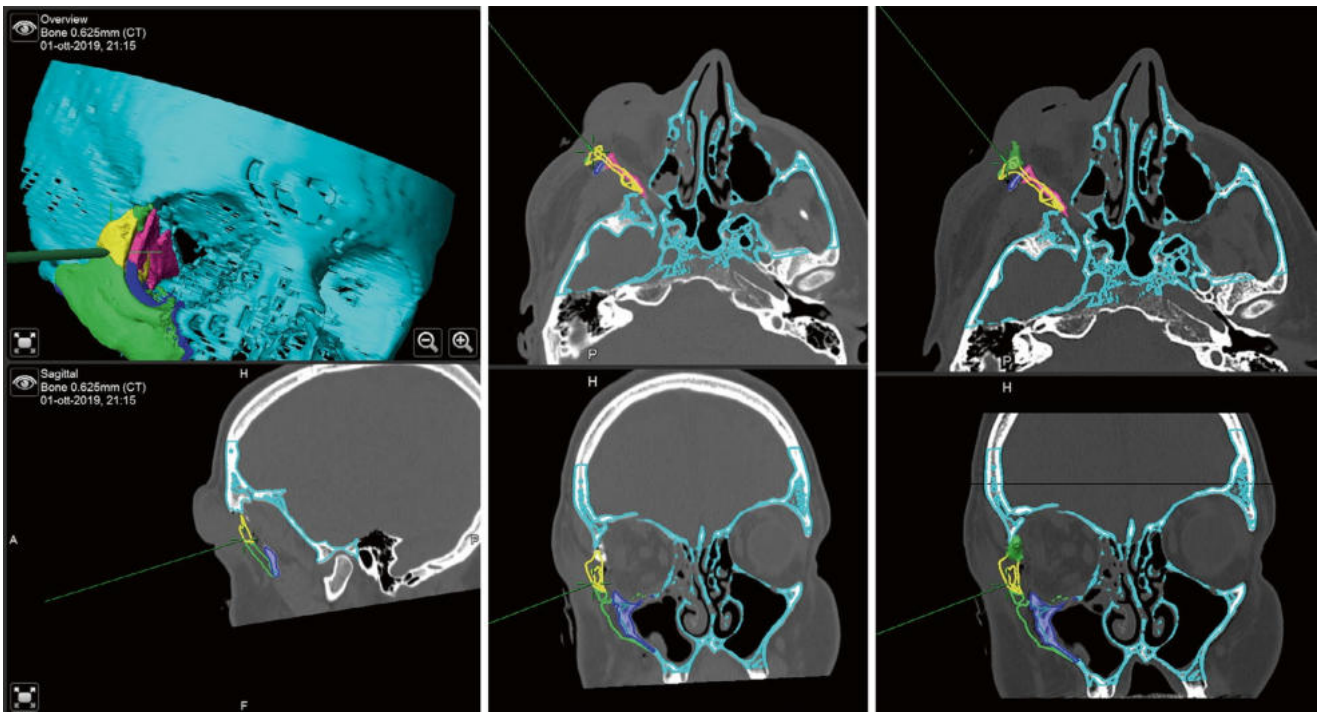


Fig. 9 Navigation of repositioned fragments allows to intraoperatively determine the most optimal projection

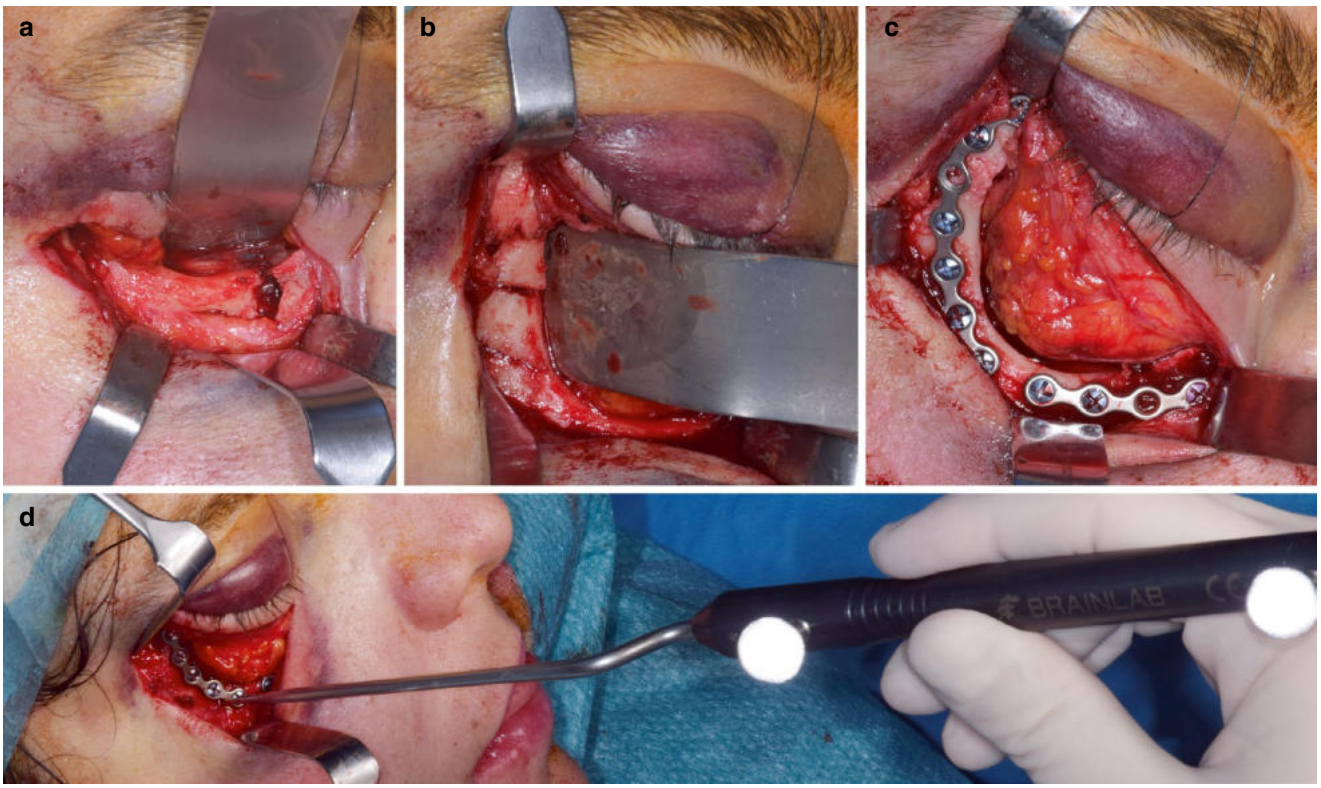


Fig. 10 Navigation drives reduction process and once the correct fragment positioning is verified, osteosynthesis can be performed

4 Internal Orbital Floor Fractures

Internal orbital floor fractures often result from an indirect trauma. As previously mentioned, the force is applied to the eye globe, which transfers the energy to the intraconal volume, which undergoes an abrupt increase. As a result, to prevent the eye from rupturing, the limiting walls of the orbit absorb the force and break, thus dissipating the energy of trauma. This mechanism is vital to prevent injuries to the most noble structures within the orbit, mainly the eye globe, extraocular muscles, and the optic nerve, but the fracture of the inferior orbital wall is not exempt from adverse clinical consequences. The breach determined on the orbital floor, and, in several cases, involving the medial walls as well, widens the intraorbital volume, allowing tissues to expand beyond measure; moreover, the eye globe loses its support. The clinical consequences are enophthalmos and diplopia. Therefore, reconstruction of the orbit must consider repairing the breach determined on the orbital walls and restoring the correct volume to allow symmetrization of the eye globe.

4.1 Virtual Reconstruction of the Fractured Orbital Wall

Independent of which method for reconstructing the orbital floor the surgeon may choose (transcutaneous/transconjunctival open or transantral endoscopic), the surgical planning for internal orbital floor fractures shares some common principles [14].

1. The first necessary step is to define the contour defect eliminating collapsed bone fragments. The clear identification of fracture margins has a prominent importance to position an orbital implant via both approaches, as bone margins are a fundamental element that supports the stability of the implant itself and its correct positioning over stable anatomical landmarks. This can be done both in segmentation masks and the final segmented STL, but the author prefers to work on segmentation masks as they offer more versatility and are not hampered by tessellation and mesh issues that affect geometrical models (Fig. 11).
2. The second step is to recreate the continuity of the orbital floor according to its natural curvature. This means that a simple geometrical method to "fill the hole" is unsuitable, as the reconstruction of the defect needs to be performed respecting well-defined anatomical principles. The first step consists in drawing a curve to outline the margins of the bone defect, thus circumscribing the floor breach. Subsequently, the mirrored orbital floor can be mirrored and superimposed to the injured side using a best-fit algorithm (iterative closest point), allowing to assess the difference in orbital volume. This step can be performed only when there is a viable contralateral anatomy; in other words, there is no evident asymmetry between sides and the contralateral side is integer, otherwise it is necessarily avoided. After mirroring, a sketch is created, namely, a two dimension plane which intersects at a given section the three-dimensional model. The sketch will represent the intersection of models (the fractured orbital floor and the contralateral integer replica). A spline is designed to restore the closest-looking possible orbital floor and maximize the symmetry between two orbits. This spline and the contour curve of the fracture margins are interpolated using a sophisticated algorithm to reconstruct a surface, which is made correspondent to the missing part of the orbital floor and which represents the substrate to design a customized implant or to simulate a bone graft. Moreover, to assess the correspondence between the reconstructed surface and the mirrored image of the orbital floor, the author suggests to perform a part comparison analysis to map the surface over the mirrored replica using a colorimetric map which highlights the deviation. Generally, only an error between 1 and 2 mm is

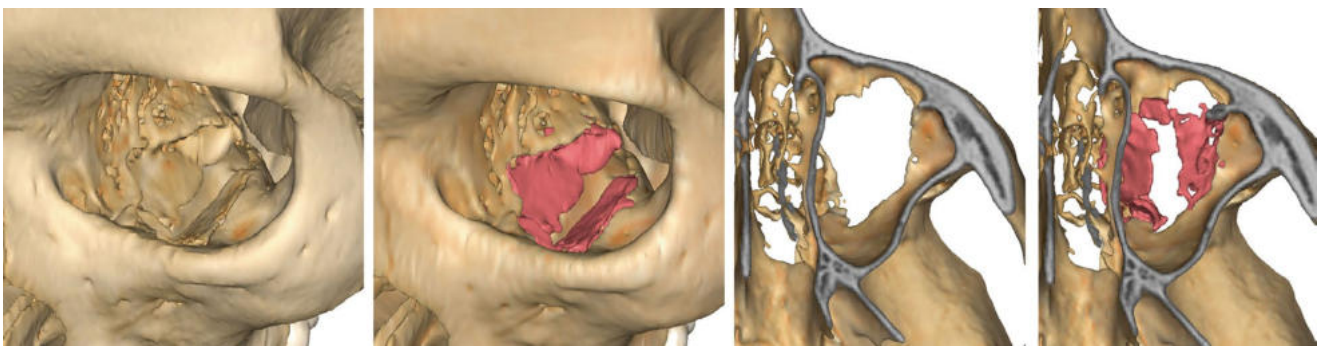


Fig. 11 VSP setup for orbital floor fractures. The first step is separation of collapsed fragments (red), which can be hidden to outline the orbital floor defect

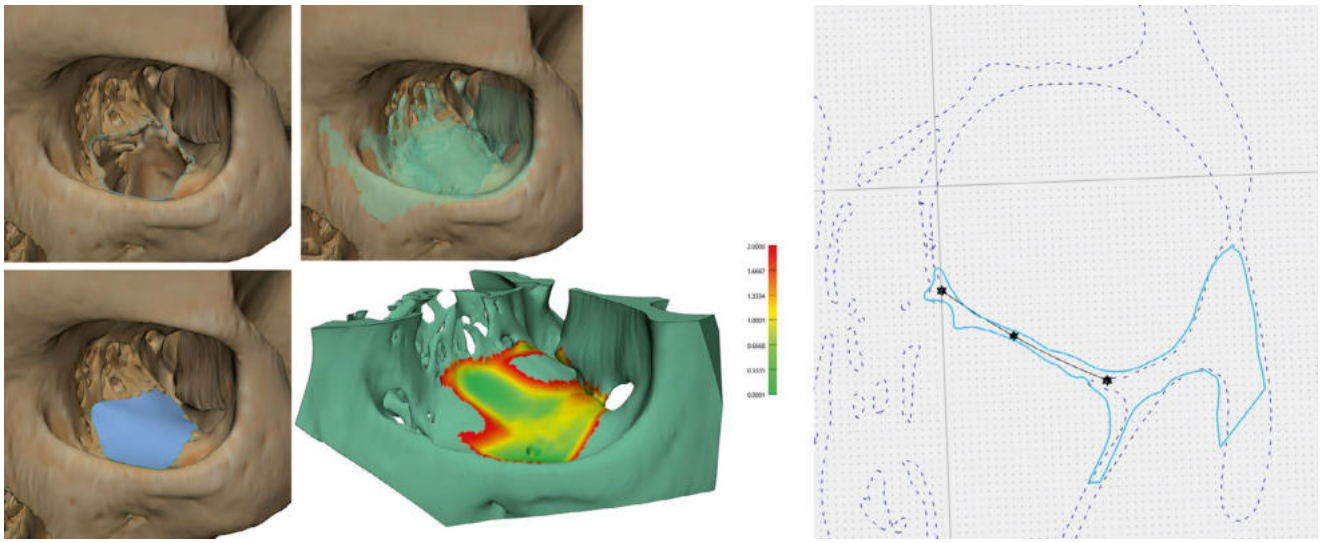


Fig. 12 As mentioned, context-driven reconstruction is essential when a contralateral healthy (or symmetrical) anatomy is not viable. In this case, the theoretical spline yields an accurate reconstruction which is mapped over the mirrored floor and undergoes part-comparison analysis, demonstrating an optimal correspondence, thus supporting this method

tolerated. This step is essential to control whether the algorithm generated any undesired shape which might alter the final orbital floor (Fig. 12).

3. The third step is planning the strategy for surgical reconstruction of the orbital floor and simulating it in the virtual surgical planning. This can be accomplished both by a customized orbital implant, which is best positioned using a transcutaneous incision, and by an autogenous maxillary graft, which is best positioned using the endoscopic transantral approach. The first initial step is to measure the diameter of the defect: very large defects are generally poor candidates to reconstruction using the autogenous bone graft, due to the wide breach that it would determine on the anterior wall of the maxillary sinus, with potential damage to the root apices in the molar region, as well as the high risk of injuring the infraorbital nerve (Fig. 13). On the other hand, the transantral endoscopic approach provides a superior and direct vision of the orbital floor from above, allowing to easily remove the collapsed bone fragments, to reduce the herniated intraconal fat and eventually to free the inferior rectus muscle [15]. Inspection of defect rim is superior with the transantral endoscopic approach, and it is essential to clearly expose the margins of the breach to engage the bone graft, whose stability exclusively depends on the support given by the margins.

   A customized implant is placed using transcutaneous or transconjunctival incisions, which may undergo an unfavorable scarring process with resulting ectropion and entropion, but is unavoidable in the presence of large defects. As trauma of the orbit is best treated with elective surgery, a customized implant can be compatible with a primary reconstruction, yet it offers unquestionable superiority in secondary reconstruction, where a traditional surgery failed. In addition, a customized implant is the only solution for very extended defects, for instance, those involving both the orbital floor and the medial wall [16] (Fig. 14).

In summary, the core concept is that to plan both reconstructions, steps 1 and 2 are essential prerequisites, as both the design of a customized implant and the simulation using a graft require excellent definition of fracture margins and reestablishing the continuity of the orbital floor.

4.2 Modified Classification of Jaquiéry for the Virtual Reconstruction of the Orbit

Jaquiéry's classification is commonly used to describe defects of the orbital floor both from an anatomical perspective and from a functional point of view [17]. It is a five-item classification that can be modernized by associating to each class the most appropriate indications for the preferred computer-guided method to repair the defect.

1. Class 1: Defects of class one are limited to the orbital floor or medial wall with an extension inferior to 1 or 2 cm^2. In several cases, such defects do not involve functional consequences for the eye globe and patients can be managed conservatively. Hence, virtual surgical planning is not indicated for this typology of defects.
2. Class 2: Defects of class 2 involve the orbital floor and/or the medial wall with an extension superior to 2 cm^2.

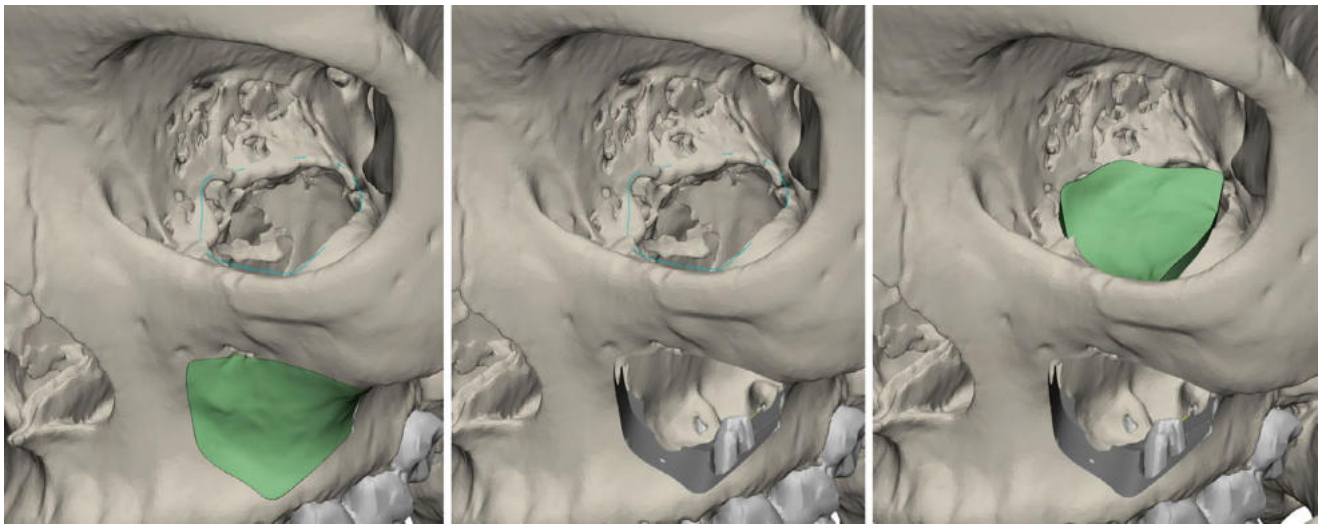


Fig. 13 Defect is circumferentially designed with a spline and assessed to define whether it should be treated with an alloplastic implant or using an autogenous graft through the transantral approach. In the latter option, the defect's size must be mapped on the maxillary sinus to determine feasibility

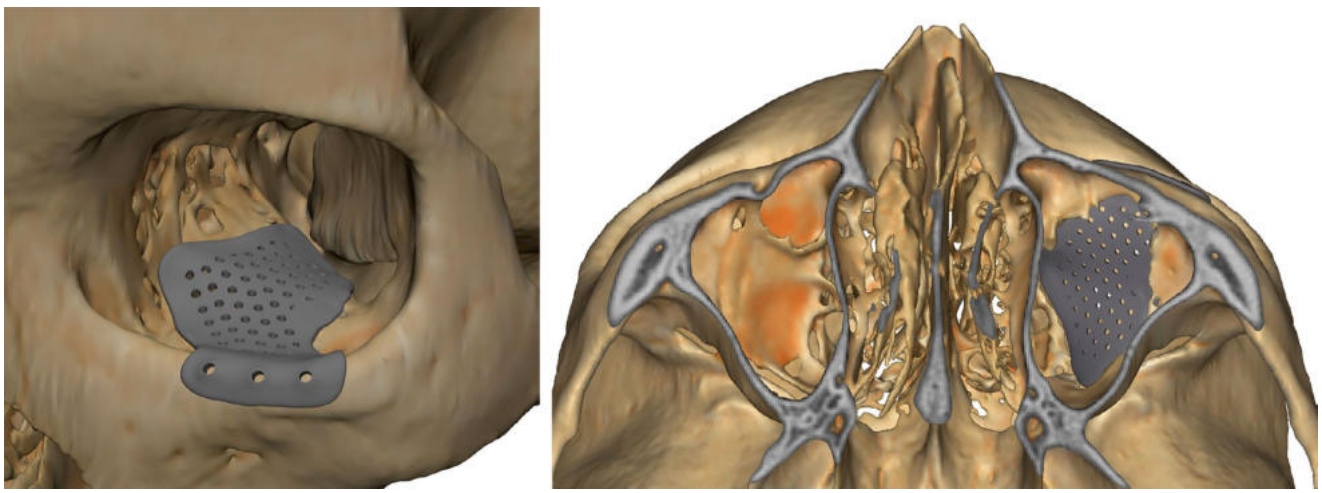


Fig. 14 If the defect is oversized, a customized alloplastic implant is the preferred choice and can be designed in software packages such as Materialise, 3-matic, or Geomagic Freeform Plus

Typical of such defects is the preservation of the thin bony ledge that separates the posterior margin of the defect from the anterior margin of the inferior orbital fissure and that represents a crucial element for the stability of the graft or the implant (Fig. 15). As such defects are not exceedingly extended and are surrounded by an integer bone edge, appearing as "holes" on the orbital floor, they are ideal candidates to repair using the endoscopic transantral approach that involves an autogenous bone graft using the anterior wall of maxillary sinus as a donor source, as described by the Author.

3. Class 3: Defects of class 3 involve the orbital floor and/or the medial wall with an extension superior to 2 cm^2. In contrast with class 2 defects, typical of class 3 is the loss of the bony ledge which separates the fracture border from the inferior orbital fissure, as such defects are more extended posteriorly (Fig. 16). This ledge represents a strut which is fundamental to engage the graft or the implant, especially when using the transantral endoscopic approach, and its loss makes the procedure more complex. It is still possible to use an autogenous bone graft harvested from the anterior wall of the maxillary sinus in this case in selected cases, but the use of a titanium mesh which allows to cover the defect without excessively dismantling the anterior maxillary sinus wall is a valuable alternative. Considering a transcutaneous or a transconjunctival access, a customized titanium implant provides the most effective restoration of the orbital wall, and its

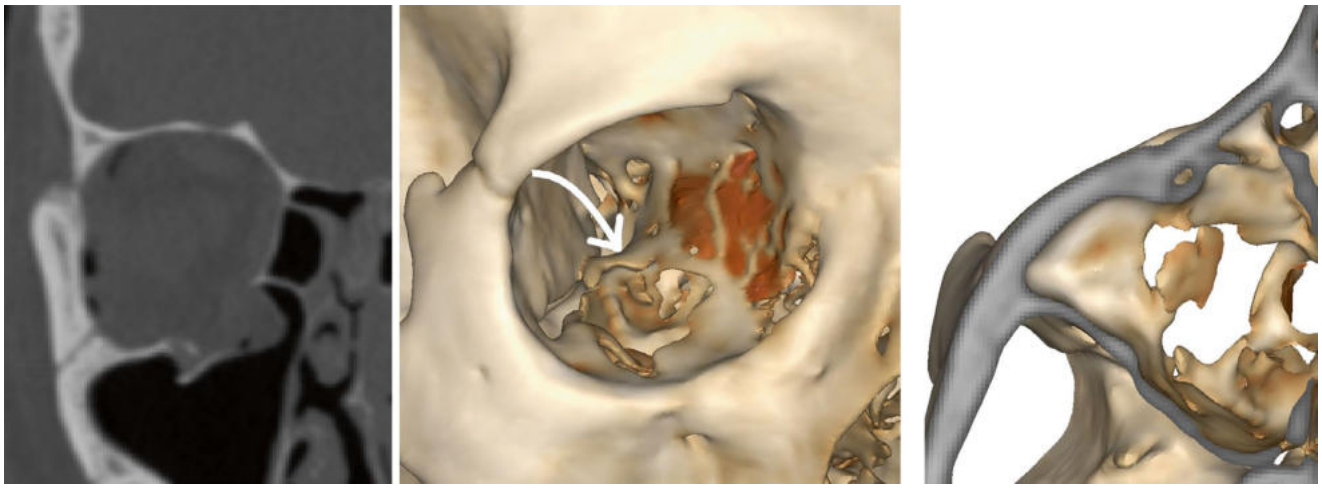


Fig. 15 Example of Jaquiéry's class II defect

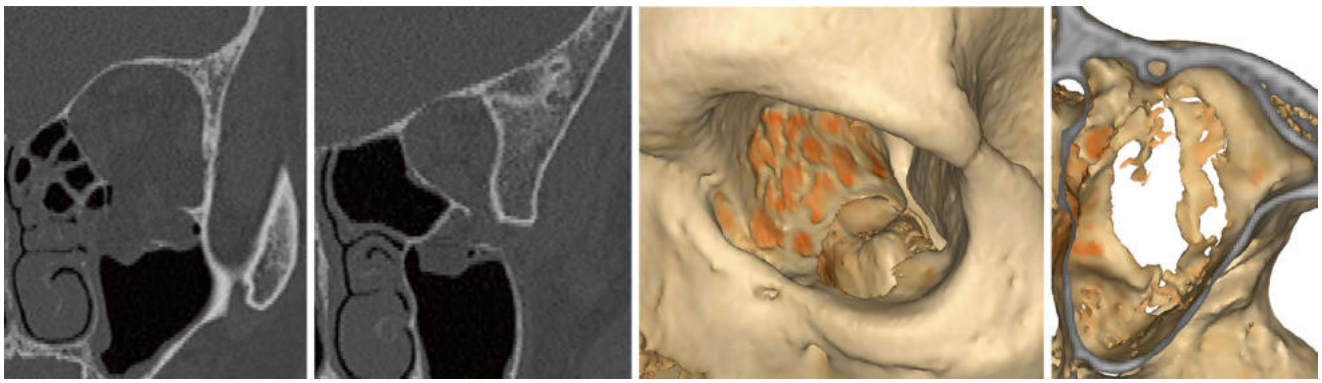


Fig. 16 Example of Jaquiéry's class III defect

anterior fixation on the inferior orbital rim compensates for the loss of the posterior bone support.

4. Class 4: Defects of class 4 involve the entire orbital floor and the medial wall. As mentioned previously, the medial wall is in close continuity with the orbital floor; thus, high energy injuries can cause the rupture of the medial orbital wall as well. In these cases, the bone defect is too extended to be filled using a bone graft; moreover, it is not planar, but it simultaneously involves the floor and the lamina papyracea (Fig. 17). The recommended method is based on the use of a customized implant, and a wide exposure is necessary.
5. Class 5: Class 5 defects add to class 4 the involvement of the orbital roof. Such defects are very complex and require a careful virtual reconstruction of the orbital walls during virtual surgical planning, as even slight asymmetries might result in alterations in the orbital volume. Although such defects can be approached in multiple ways and several surgical "freehand" methods can be used, including grafts for the orbital roof, Medpor® inserts for the orbital wall, and stock titanium meshes or plates for the orbital floor, the most accurate reconstruction would require patient-specific implants.

4.3 Clinical Cases

4.3.1 Class II Defect: Transantral Approach

Clinical History

A 48-years-old woman fell from stairs at home, hitting his face at the ground. He presented to emergency department with conspicuous swelling and ecchymosis in the orbital region and he referred diplopia in all directions of gaze. He underwent CT scan that revealed a class 2 fracture of the left orbital floor with herniation of the intraconal fat and entrapment of the inferior rectus muscle.

Virtual Surgical Planning

Virtual surgical planning was performed according to the sequences previously defined: removal of bone fragments and clearance of the fracture border, digital reconstruction of

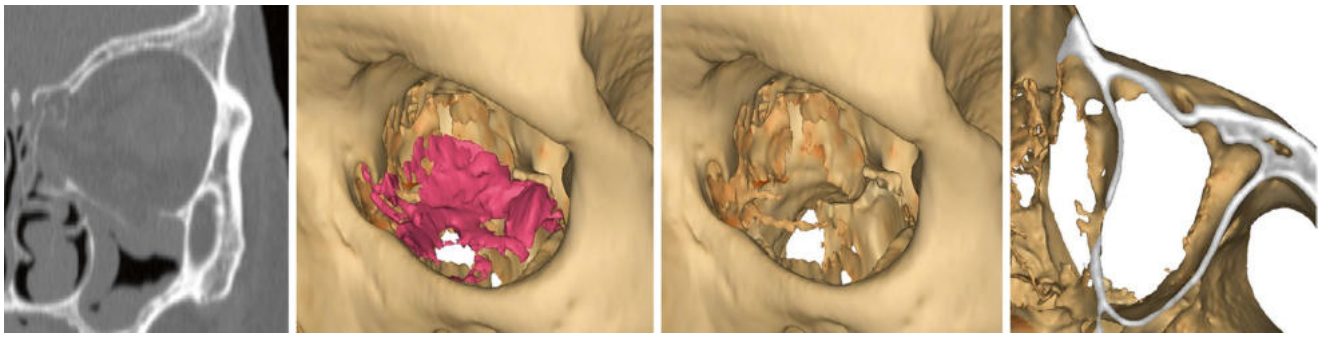


Fig. 17 Example of Jaquiéry's class IV defect

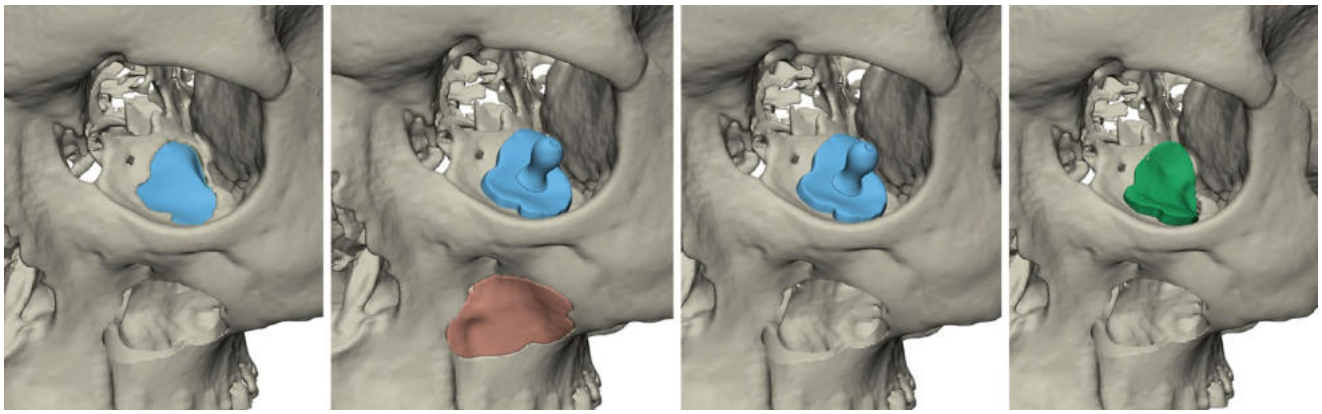


Fig. 18 VSP for a transantral endoscopic repair in a class II orbital floor fracture. A surgical guide, sized on the orbital defect, is used to harvest a correspondent antral autograft matching the orbital floor defect

the floor, and computer-guided strategy. Specifically, in the latter phase, a surgical guide was designed and sized on the orbital floor defect, with the aim of assisting the harvest of the same size and shape graft taken from the anterior maxillary wall. Subsequently, the removal of the graft from the anterior maxillary wall was simulated to avoid any possible pitfall related to teeth apices and damage of the intraorbital nerve. Finally, the graft was digitally extracted from the anterior antral wall using Boolean operations and superimposed over the orbital floor defect, to evaluate its full compatibility to restore the defect. The surgical guide was printed and taken to the operating room after sterilization (Fig. 18).

Surgery

VSP allowed to establish that type of defect was appropriate for a transantral endoscopic approach using a maxillary wall autograft. A maxillary vestibular incision from the canine to the second molar area was performed and the anterior-lateral maxillary surface was exposed. The corresponding surgical guide, tailored on the orbital defect whose size was digitally transferred to the antral wall, was applied and used to shape a bone window optimized for the defect size. Using transantral endoscopy, the prolapsed intrasinusal orbital fat was assessed with a 30° optics, and it was pushed back into the orbital compartments using blunt instruments. Likewise, margins of the fracture were undermined to circumscribe the orbital floor defect. The graft was inserted and oriented and successfully stabilized over fracture margins thanks to its predetermined shape (Fig. 19). Gingival mucoperiosteum was sutured to cover the resulting antral defect.

4.3.2 Class III Defect: Transantral Approach

Clinical History

A 35-years-old man was the victim of assault. He remembered being punched in his left eye before falling unconscious. At clinical examination, he revealed gross swelling and ecchymosis of the periorbital skin with subcutaneous emphysema and frank diplopia in all gaze directions, with the complete loss of sensation of sensitivity in the anterior cheek area. A CT scan was performed with aforementioned parameters, revealing a conspicuous orbital floor defect classified as class 3, due to the loss of the bone ledge anterior to the inferior orbital fissure.

Virtual Surgical Planning

Data were imported in the Mimics Innovation Suite for virtual surgical planning and all the steps for planning setup

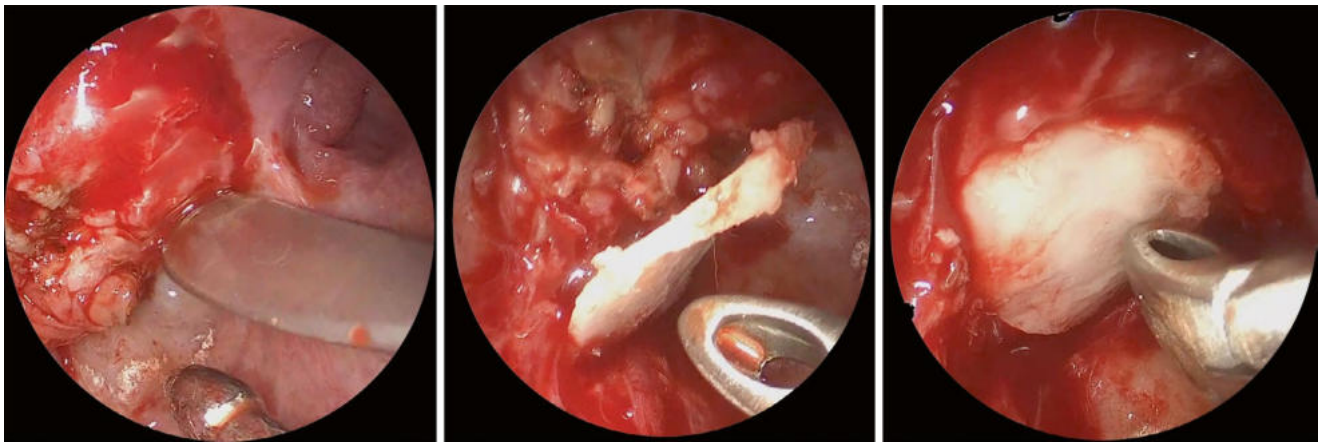


Fig. 19 Phases of endoscopic repair. Left: visualization of prolapsed orbital fat through the orbital floor breach. Center: autograft inset. Right: the graft is stabilized in place by engaging fracture margins

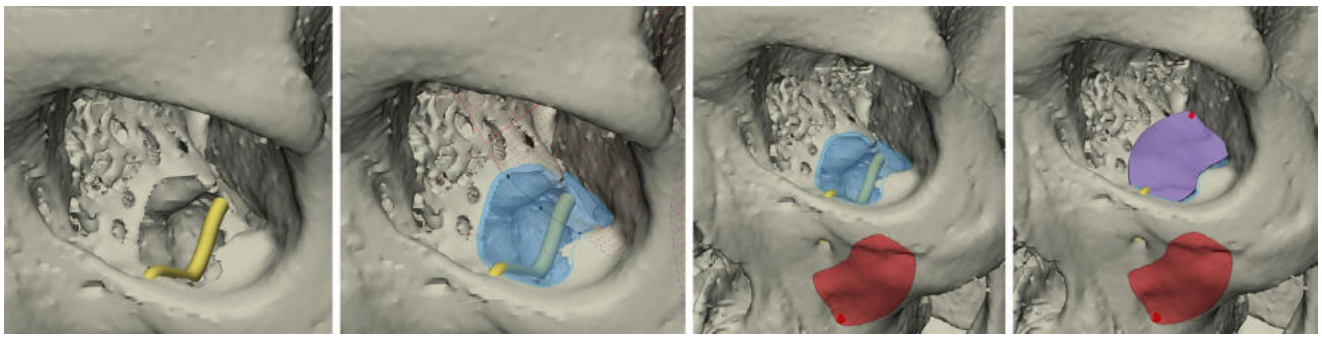


Fig. 20 VSP for a transantral endoscopic repair in a class III orbital floor fracture. An infraorbital nerve model is also represented to account its finding when performing the transantral procedure. Likewise, the floor defect is outlined and transposed on the antral wall to study the most correct harvesting site for the autograft

were accomplished as usual. Moreover, the author performed the reconstruction of the infraorbital nerve, which was injured due to the collapse of the orbital floor. Although the nerve is not directly visible in a CT scan, its course can be trustfully reconstructed by identifying the hollow structure of its canal. Although it was a class 3 defect, its shape and the wide maxillary sinus anatomy allowed to plan a transantral endoscopic reconstruction of the orbital floor using a maxillary wall autograft. Also in this case, a surgical guide was modelled to assist the harvest of the antral wall graft, which was optimized on the basis of the recipient defect. Moreover, the infraorbital nerve was reproduced as well to simulate its relationship with the orbital floor fracture. The design of the maxillary wall graft allowed to avoid the emergence of the infraorbital nerve and teeth apices (Fig. 20).

Surgery

The procedure is exactly the same described for the previous case. However, as class III is characterized by the loss of the posterior bony ledge between the fracture and the inferior orbital fissure, the substantial support for the graft was offered by the lateral margins of the fracture. The graft was designed wider as well to fill a larger defect size (Fig. 21).

4.3.3 Class IV Defect

Clinical History

A 72-year-old man fell from a height of two meters while climbing a tree and hitting violently his face to the ground. He was admitted to emergency department and a CT scan was immediately performed on the head and face to rule out any intracranial hemorrhage. After excluding any neurosurgical priority, the patient was admitted in Maxillofacial Surgery department to be operated.

Virtual Surgical Planning

Segmentation of the orbits was performed in Mimics and revealed a massive class 4 defect, involving the entire orbital floor and medial wall. The extension of the breach over two walls and its size made inapplicable the choice of an antral graft and also the endoscopic approach using a titanium mesh, as it would provide good control for the orbital floor

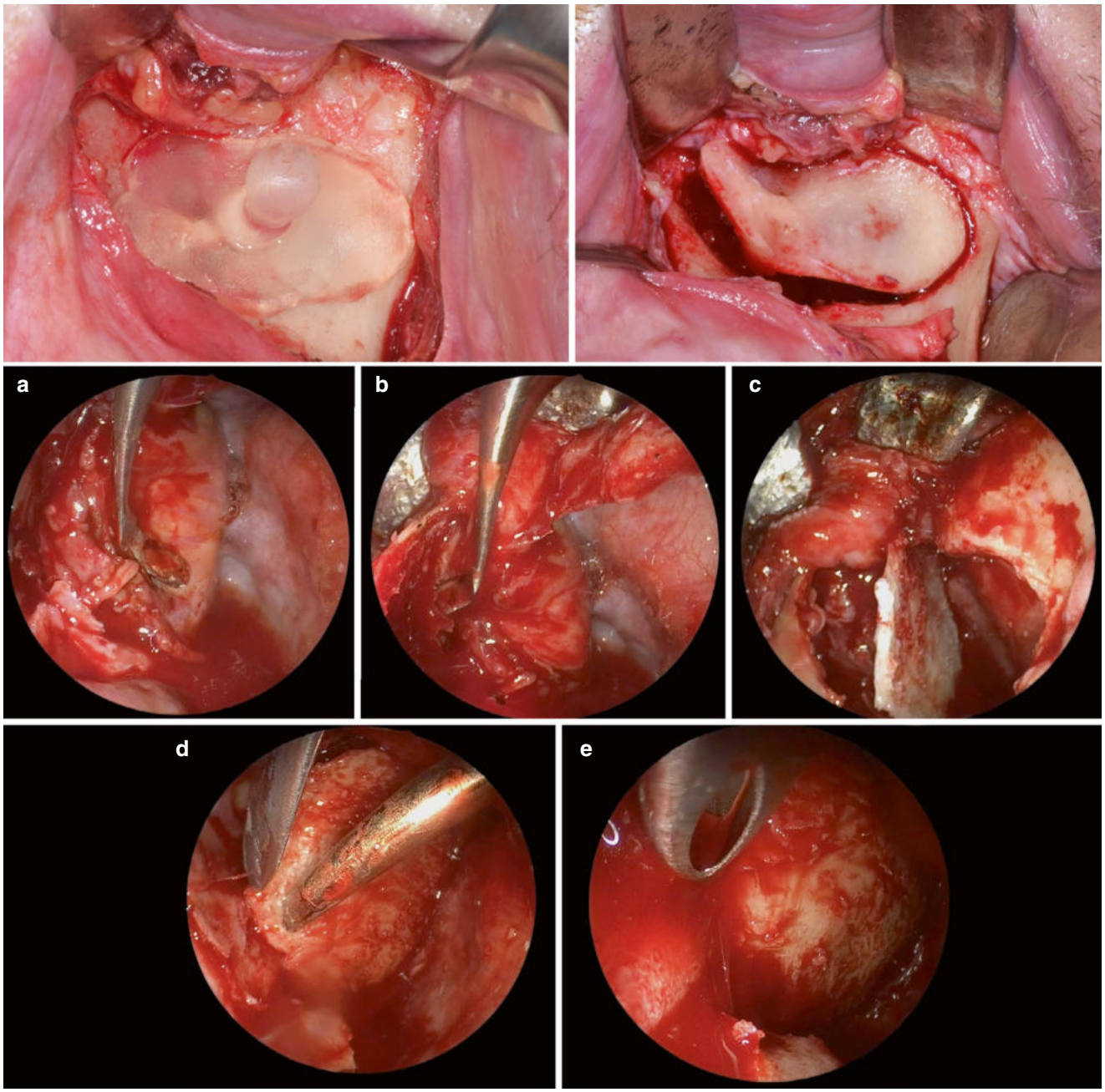


Fig. 21 Phases of endoscopic repair. The antral graft is harvested using the surgical guide, which is sized and placed over the orbital floor. The graft is inserted through the same opening and, once prolapsed orbital content is pushed back into the orbit, it is stabilized to the fracture margins

but not on the medial wall. A simulation was performed by the author, designing a customized implant on the mirrored contralateral wall to maximize symmetrization, which made the adoption of a customized orbital implant the most suitable approach (Fig. 22). This surgery was performed using a traditional transconjunctival approach.

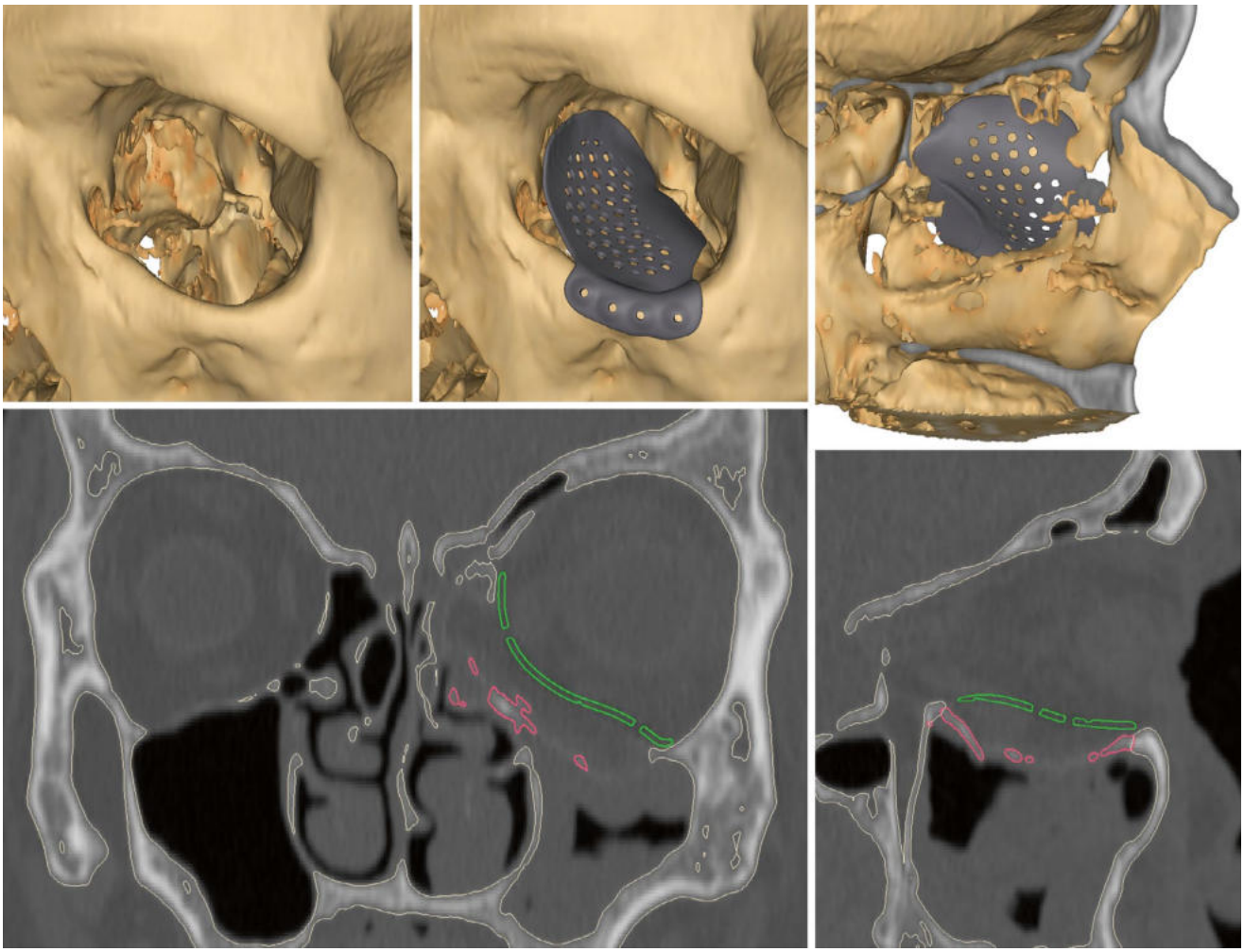


Fig. 22 VSP for a class IV defect, in which both the inferior and medial walls are involved. The implant (green in cross-sectional cuts) enables to restore the optimal orbital volume. In red, fractured fragments are visible

4.3.4 Class V Defect

Clinical History

An 18-year-old lady was urgently referred by ophthalmologist for a close-range firework explosion on New Year's Eve. She presented with a complex bulbar trauma with multiple eyelid lacerations and scleral rupture with vitreal herniation. The eye glob was lost. On CT examination, she revealed multiple fractures across all the orbital walls, with involvement of the inferior orbital margin, the lateral and medial orbital wall, as well as the orbital roof and the superior orbital rim. The patient was urgently admitted to hospital and VSP was started.

Virtual Surgical Planning

The selective application of the split mask algorithm in Mimics yielded the separation of fractured fragments into

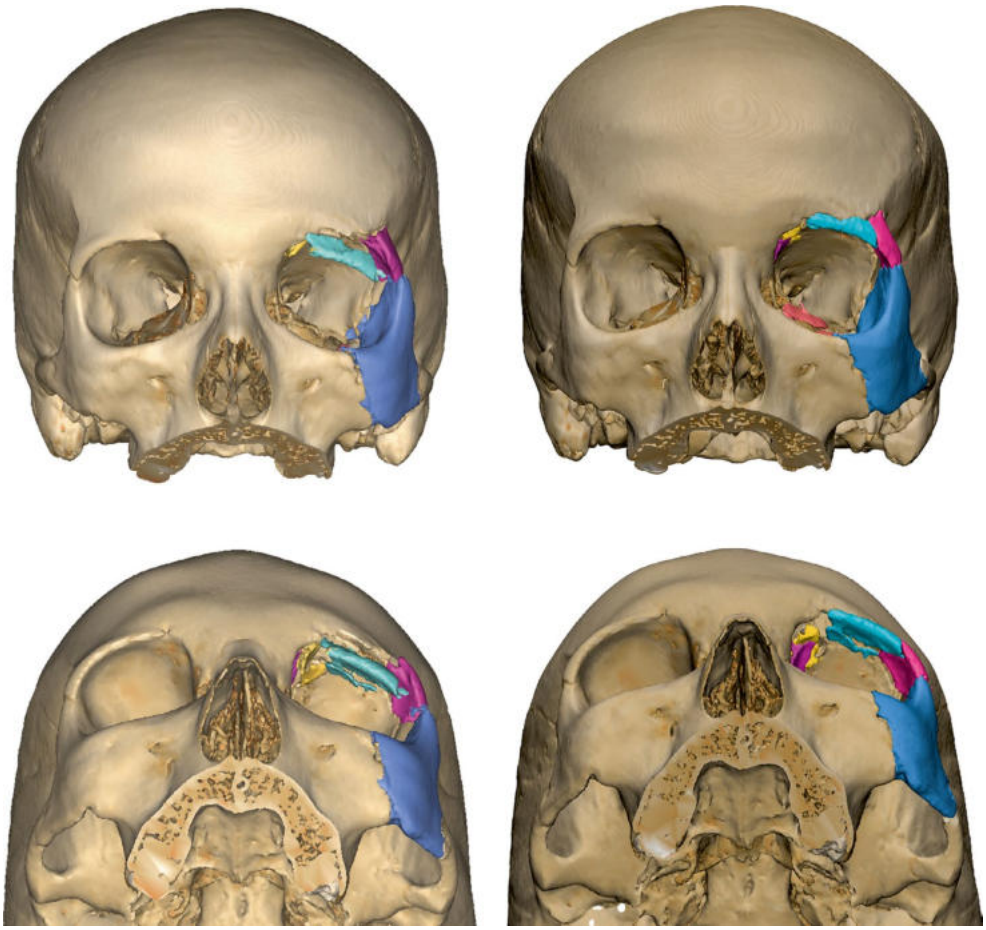


Fig. 23 VSP for a multifragment, class V, fracture of the left orbit. Left: displaced; right: reduced

separate entities, which were reconstructed selectively as distinct STL files. A mirrored template was defined to drive realignment of displaced fragments in the symmetrical reconstruction of the orbit, with subsequent manual readjustment to refine anatomical reduction (Fig. 23). This process was entirely performed in 3-matic. Subsequently, Brainlab Elements software was used to create the navigation plan, allowing to import STL files form virtual reduction as digital templates for intraoperative feedback (Fig. 24).

Surgery

The exploration of the conjunctival fornix revealed an extensive laceration in the superior-temporal region extending down to the pterygo-zygomatic suture. This laceration was

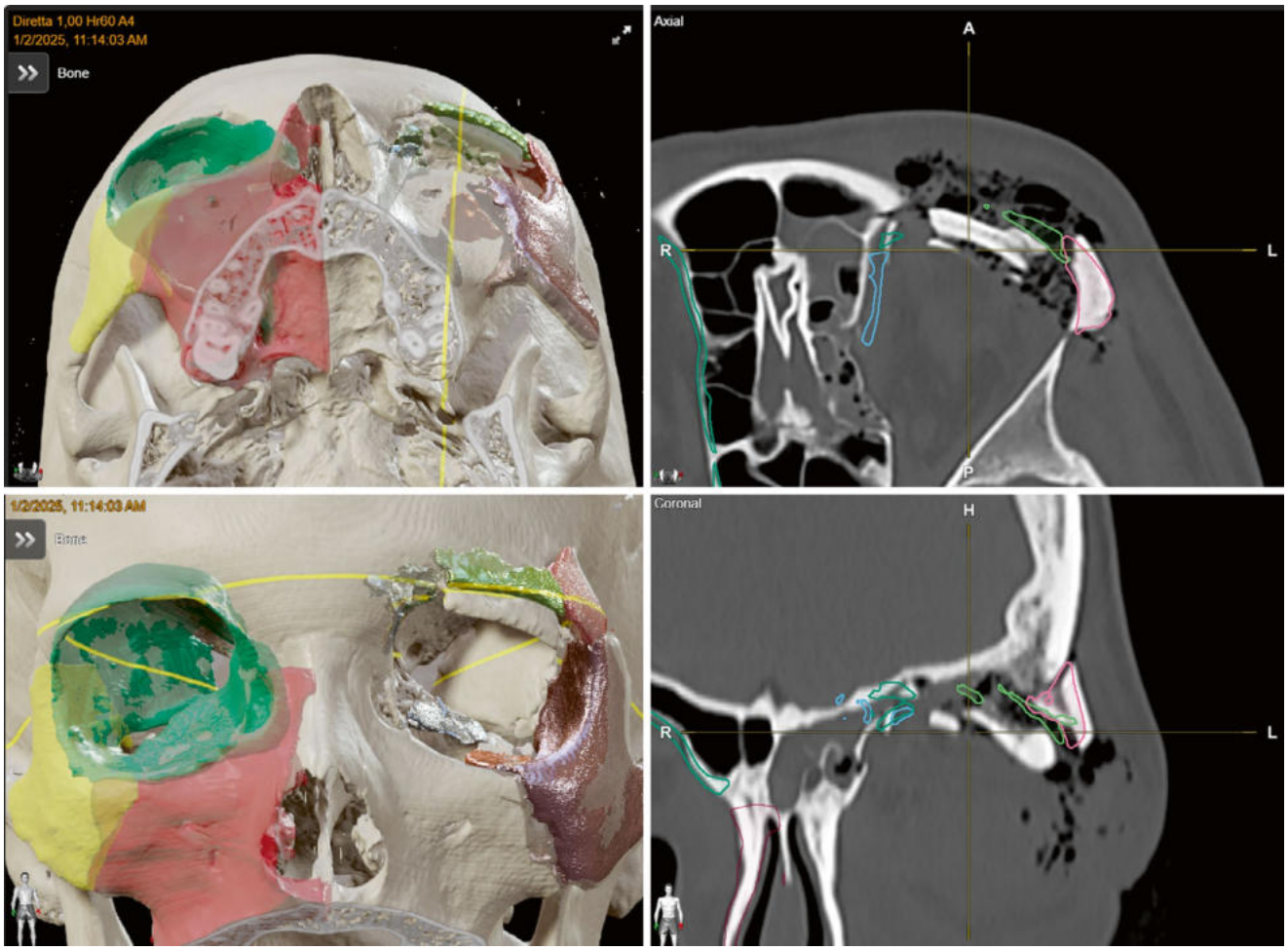


Fig. 24 Definition of the navigation plan in Brainlab Elements software importing repositioned STL files in 3-matic

used to explore the lateral orbital rim and was slightly extended up to the superior orbital margin and roof. Inferiorly, a traditional transconjunctival approach was created to dominate the orbit. After iridectomy, a limbar conjunctival flap was raised allowing to dissect subconjunctivally superficial to the scleral layer and isolate the insertions of extraocular muscles. Ocular contents were removed to complete a bulb evisceration and scleral lacerations repaired. A hydroxyapatite sphere was positioned within the scleral shell [18] (Fig. 25). Subsequently, from the conjunctival accesses reduction of bone fractures was accomplished under navigational guidance (Fig. 26). Final suturing of the conjunctival layer and eyelid reconstruction was accomplished. Postoperative CT confirmed the correct reduction of fractures based on the VSP (Fig. 27).

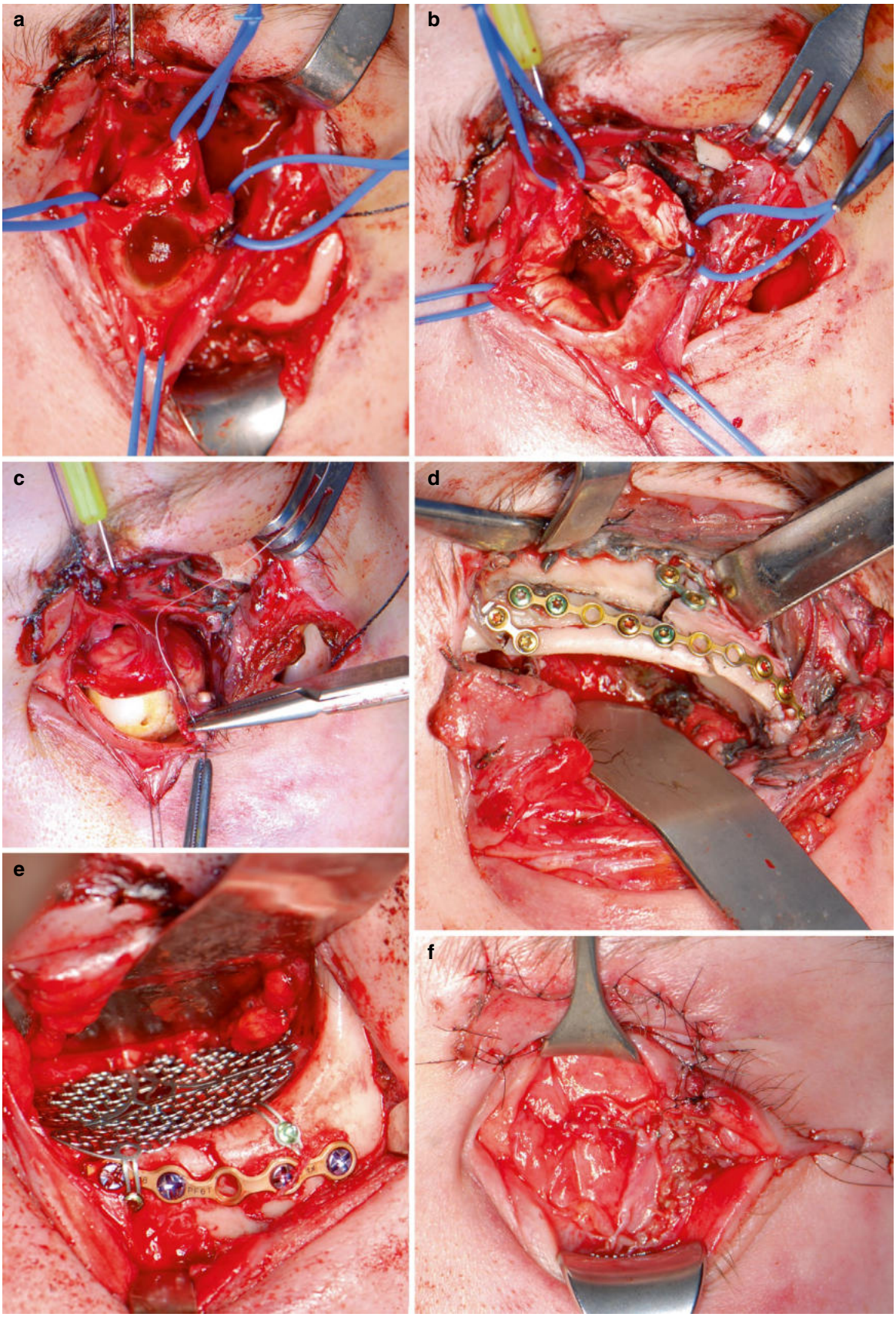


Fig. 25 Intraoperative sequences: (**a**) mobilization of the Tenon's capsule after peritomy and subconjunctival dissection with isolation of extraocular muscles; (**b**) after iridectomy and evisceration; (**c**) positioning of the hydroxyapatite ball; (**d**) reduction and fixation of fractures of the superior and lateral orbit; (**e**) reduction and fixation of inferior orbit fractures and orbital floor; (**f**) final soft tissue reconstruction

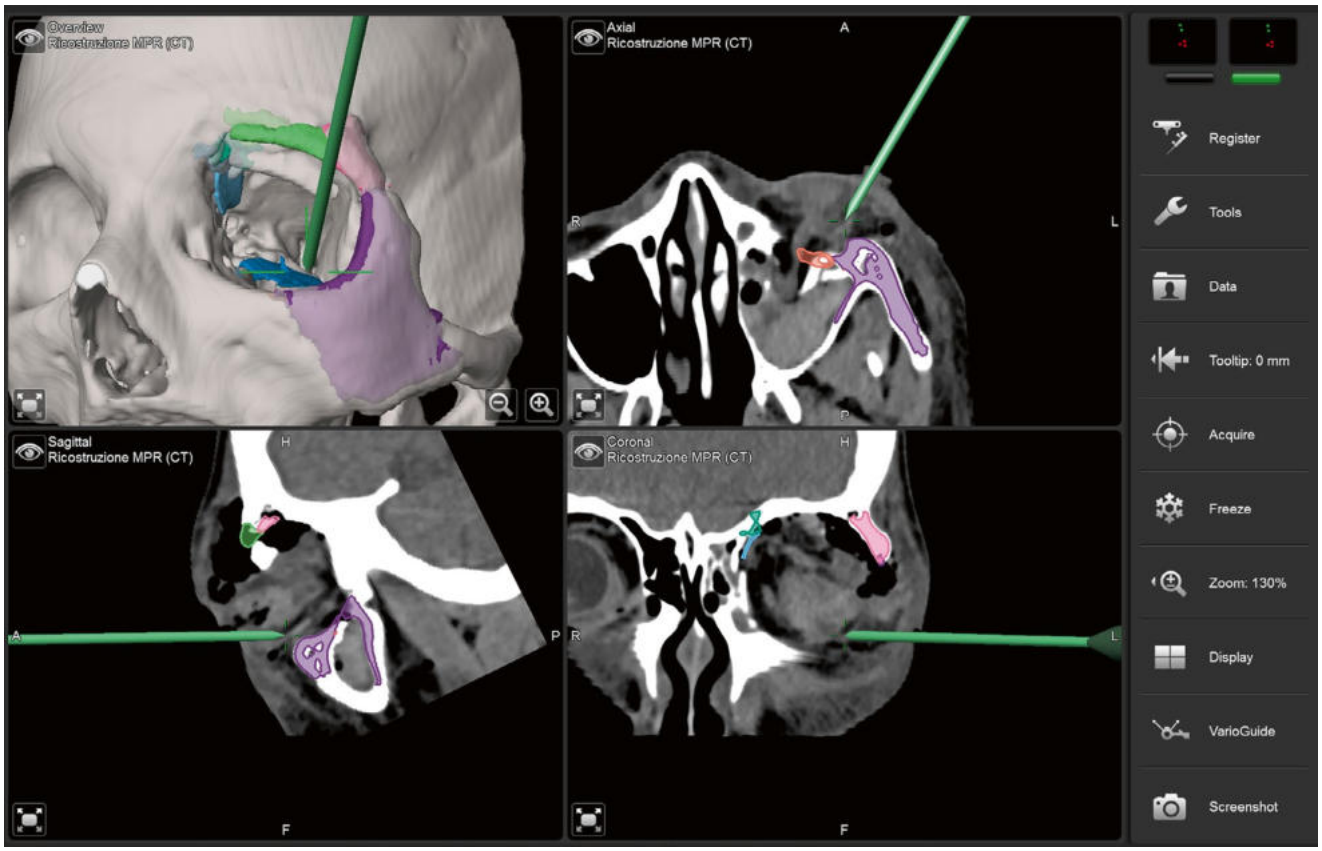


Fig. 26 VSP navigation for the inferior orbital margin

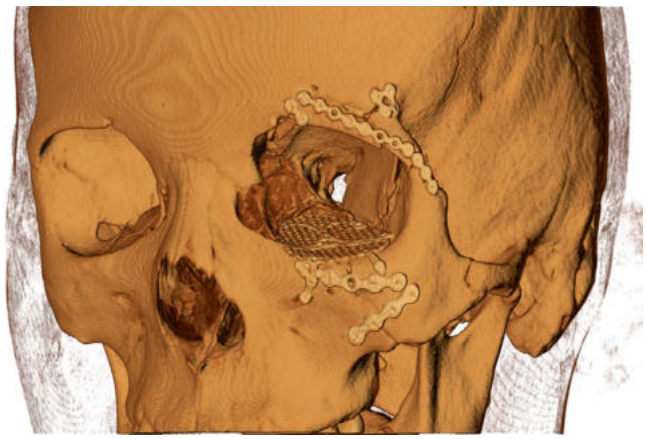


Fig. 27 Postoperative CT showing satisfactory reconstruction

4.4 Additional Concepts About the Transantral Endoscopic Repair of Orbital Floor Fractures

The transantral endoscopic approach is a versatile technique, ideal to reconstruct class II defects, but it can be extended also to class III defects. Moreover, it might be employed also in cases of more complex trauma, not in exclusive internal orbital floor fractures. If a patient presents with a ZMC fracture and a maxillary fracture associated with an internal orbital floor fracture, the harvesting site for the graft should be the contralateral side, where the antral wall is intact (Fig. 28).

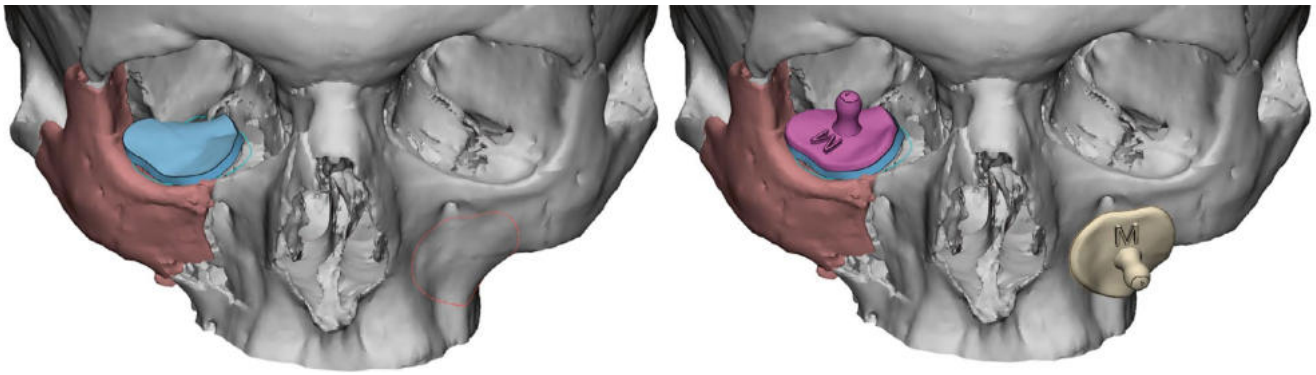


Fig. 28 Transantral endoscopic repair in cases of associated maxillo-malar trauma needs to consider the contralateral, integer, antral wall as donor site

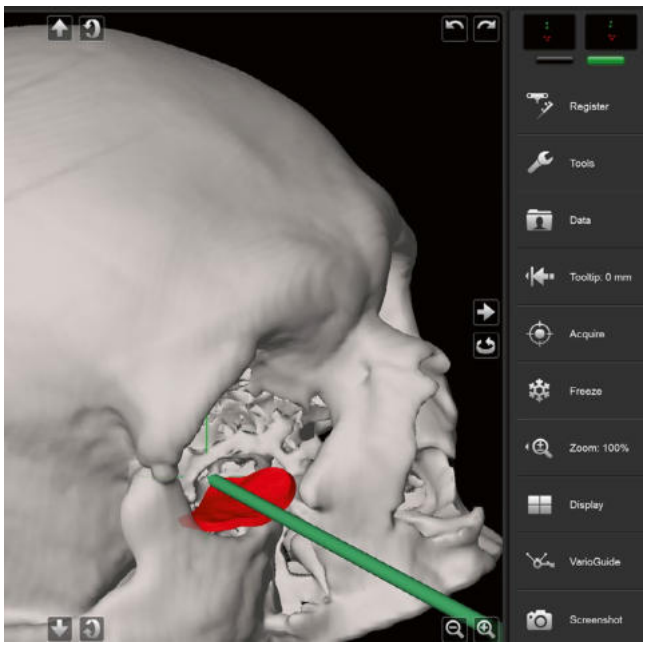


Fig. 29 Navigation of transantral approach to check the posterior fracture limit

In addition, to increase the accuracy in antral graft repositioning, the whole procedure can be performed under navigational assistance, enabling a more precise detection of fracture margins and checking the correspondence of graft placing compared with the VSP (Fig. 29).

Figure 30 Postoperative CT outcomes for orbital floor reconstructions in different classes performed using the transantral endoscopic technique with the maxillary wall autograft.

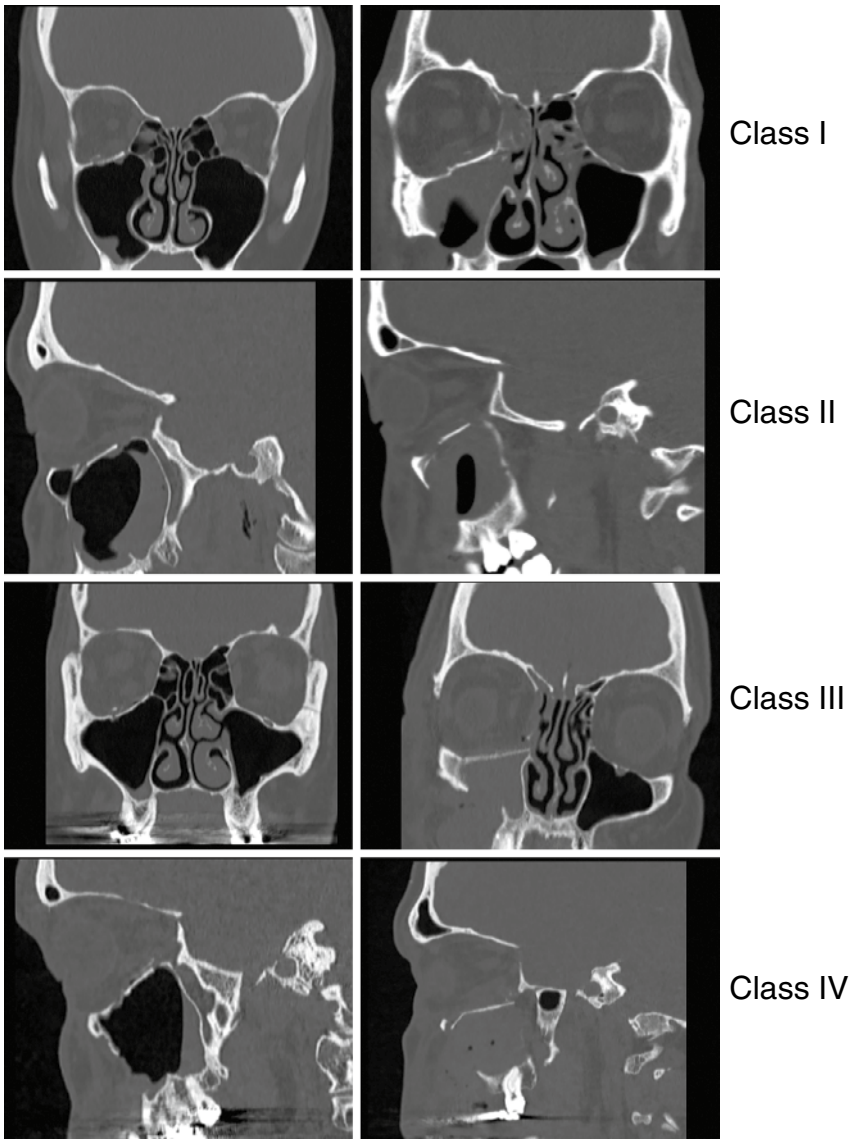


Fig. 30 Postoperative CT results for orbital floor fractures of classes II, III, and IV reconstructed with the endoscopic transantral approach. Management of class IV defects with an entirely transantral approach is not frequent and occurs in presence of minimally injured medial wall

5 Secondary Reconstruction of Orbital Trauma

Secondary reconstruction of the orbital floor poses different challenges compared to immediate or differed surgery. The fracture already healed, and its margins are ossified; moreover, there is often associated longstanding deformity including enophthalmos and vertical dystopia, possibly associated with diplopia. Since fracture margins cannot be identified and there is no loss of continuity of the orbital floor, the endoscopic transantral approach is not an option for such cases. The aim of surgery is to restore symmetry between eye projection and reconstruct the orbital floor. In contrast with a traditional repair, which involves a manual bending of the implant, which is not controlled, or the more reliable implant conformed over a 3D printed template, which still is flexible and might deform during insertion, customized 3D printed implants are the optimal choice for secondary orbital reconstruction [19]. Advantages include their easy adaptability on the recipient site and stiffness, which ensure the reliability of the VSP. Additionally, accuracy of placement can be improved using image-guided techniques, like navigation.

5.1 Secondary Orbital Floor Reconstruction Using a Patient-Specific 3D Printed Implant

5.1.1 Clinical History

A 33-year-old patient had a history of long standing diplopia, anisocoria, and enophthalmos following a working accident which conditioned an orbital floor fracture. The patient chose not to undergo surgery at that time. He then presented for secondary reconstruction as diplopia had significantly worsened his daily life. CT scan was performed showing a deformed orbital floor, with ossified collapsed fragments resulting in a depression of the orbital floor and a substantial increase of orbital volume compared with the contralateral side.

5.1.2 Virtual Surgical Planning

Segmentation of high-resolution CT with appropriate matrix resolution and slicing parameters yielded an optimal reconstruction of the orbital cavity, with minimal need to fill the voids of partial volume effect. Mirroring operation was considered the optimal method to provide a correctly shaped reconstruction of the orbital floor: midsagittal plane was carefully positioned and the resulting mirrored replica was aligned with the fractured orbital floor. A raw implant shape was designed using the mirrored replica to define the optimal shape, and the fractured original to outline the fracture contours and thus model the implant boundaries. The implant was extruded and sites for screw insertion were added. This process was managed entirely in-house. Subsequently, the resulting plan was sent to the manufacturer (Materialise NV, Leuven, BE) which modified the raw implant shape including necessary optimization to comply with regulation rules. The project was sent back to surgeons for approval and the customized implant was 3D printed using SLS technology with anodization (Fig. 31).

5.1.3 Surgery

A subciliary incision with preseptal dissection was used to access the orbital floor. Accurate periosteal elevation was gently accomplished with a Freer elevator up to the Zinn's anulus. The fractured floor was exposed, and undermining was conducted in the sites planned to fit the implant. The implant was inserted under navigational guidance, until perfect correspondence was assessed with the VSP (Fig. 32). Suture of the cutaneous layer was accurately performed with 6.0 Ethilon sutures. Postoperative CT scan showed the perfect correspondence of the implant with VSP and the correctly shaped orbital floor (Fig. 33).

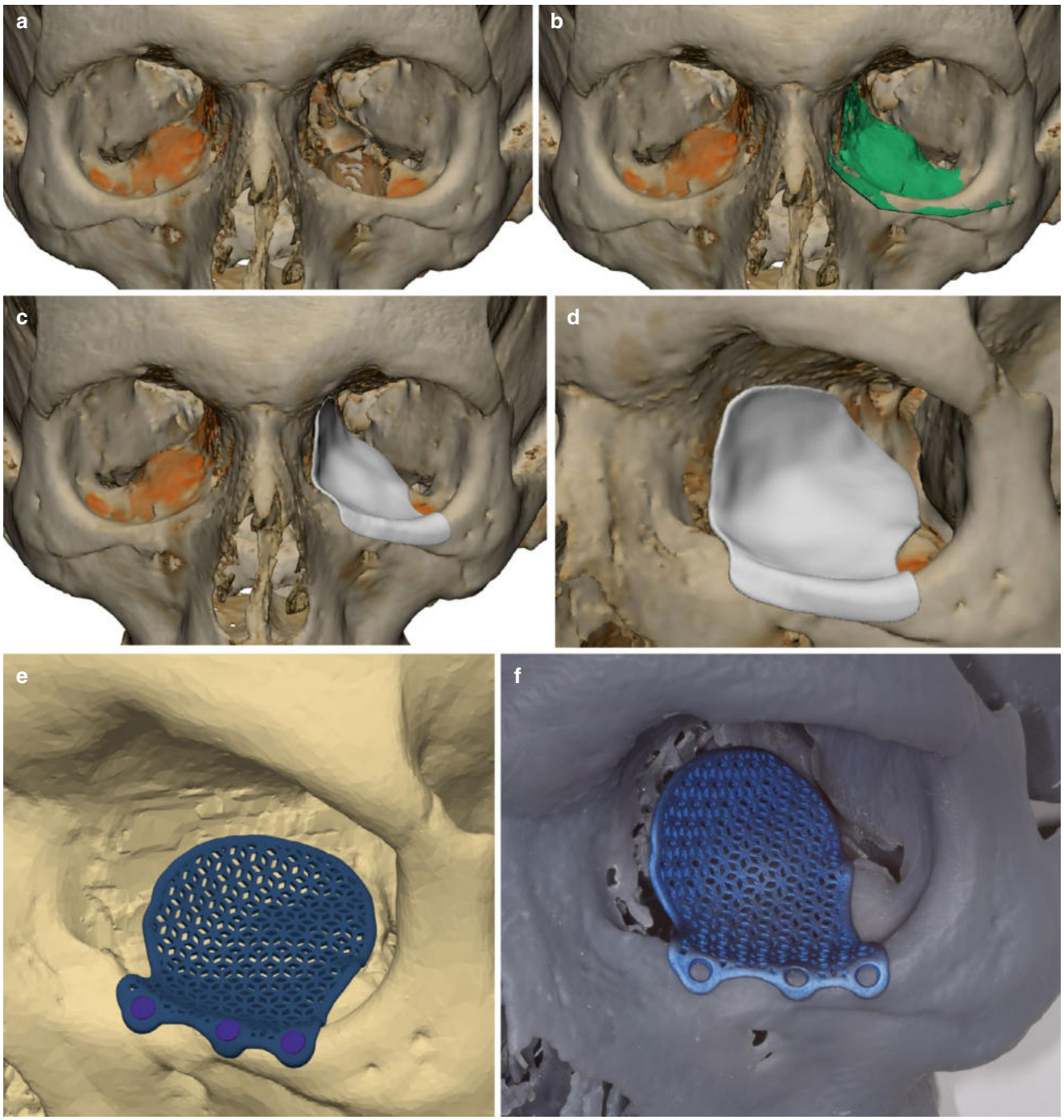


Fig. 31 Customized orbital implants in secondary trauma management. (**a**) segmentation and partial volume effect correction using segment thin walls plugin; (**b**) mirroring of the contralateral side; (**c**) design of a correspondent rough implant shape that is shared with the manufacturer (advanced hybrid workflow); (**d**) close look; (**e**) implant design provided by the manufacturer (Materialise NV); (**f**) customized implant fits PoC 3D printed model

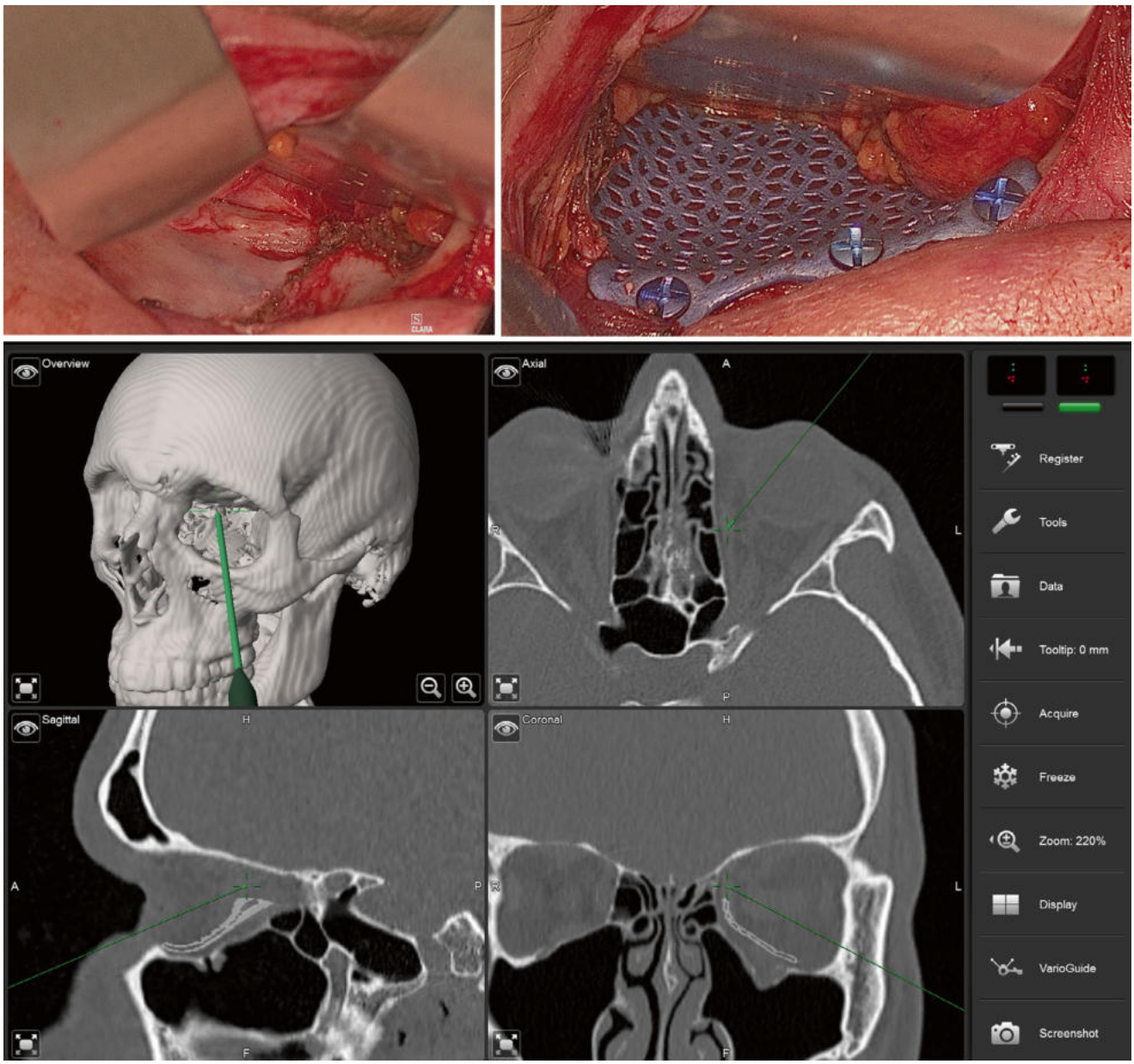


Fig. 32 Surgical sequences: left, defect exposure; right, implant positioning. Bottom: implant position check using intraoperative navigation

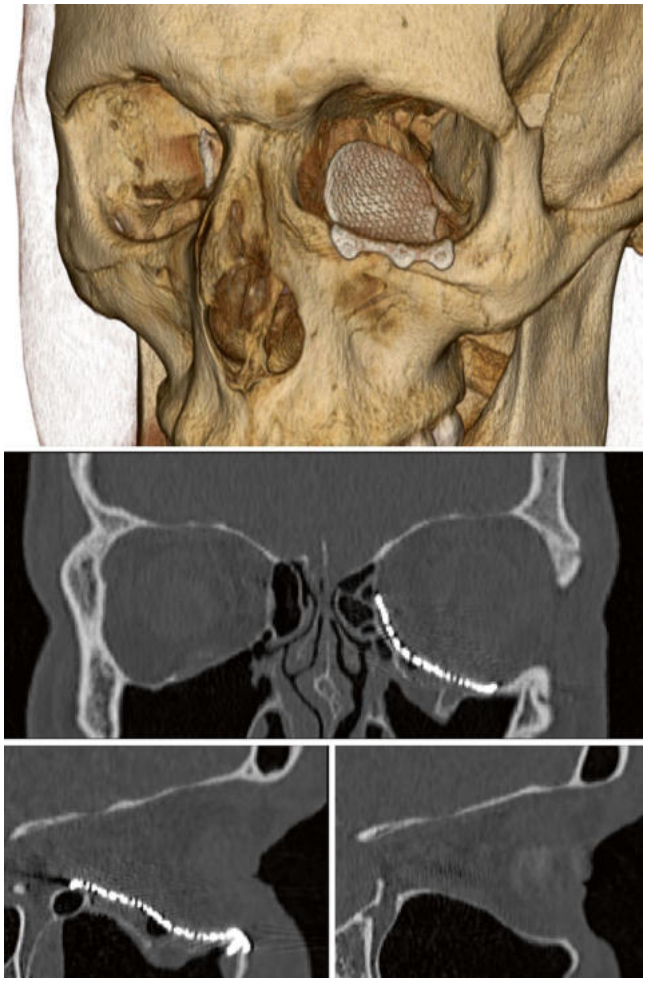


Fig. 33 Postoperative CT and comparison with healthy side

References

1. Chepurnyi Y, Zhukovtseva O, Kopchak A, Kanura O. Clinical application of automated virtual orbital reconstruction for orbital fracture management with patient-specific implants: a prospective comparative study. J Craniofac Surg. 2022;50:686–91.
2. Wei L, Hu M. A review of medical ocular image segmentation. Virtual Real Intell Hardw. 2024;6:181–202.
3. Marques R, Andrade De Jesus D, Barbosa-Breda J, Van Eijgen J, Stalmans I, van Walsum T, Klein S, Vaz PG, Sánchez Brea L. Automatic segmentation of the optic nerve head region in optical coherence tomography: a methodological review. Comput Methods Prog Biomed. 2022;220:106801.
4. Qureshi A, Lim S, Suh SY, Mutawak B, Chitnis PV, Demer JL, Wei Q. Deep-learning-based segmentation of extraocular muscles from magnetic resonance images. Bioengineering. 2023;10:699.
5. Kim H, Son T, Lee J, Kim HA, Cho H, Jeong WS, Choi JW, Kim Y. Three-dimensional orbital wall modeling using paranasal sinus segmentation. J Craniofac Surg. 2019;47:959–67.
6. Darwich A, Attieh A, Khalil A, Szávai S, Nazha H. Biomechanical assessment of orbital fractures using patient-specific models and clinical matching. J Stomatol Oral Maxillofac Surg. 2021;122:e51–7.
7. Orbit, orbital floor fracture. In: site name. https://surgeryreference.aofoundation.org/cmf/trauma/midface/orbital-floor/definition. Accessed 18 Jan 2025.
8. D'Alpaos D, Badiali G, Ceccariglia F, Tarsitano A. Delayed orbital floor reconstruction using mirroring technique and patient-specific implants: proof of concept. J Pers Med. 2024;14:459.
9. Tarsitano A, Badiali G, Pizzigallo A, Marchetti C. Orbital reconstruction: patient-specific orbital floor reconstruction using a mirroring technique and a customized titanium mesh. J Craniofac Surg. 2016;27:1822–5.
10. Gass M, Füßinger MA, Metzger MC, Schwarz S, Bähr JD, Brandenburg L, Weingart J, Schlager S. Virtual reconstruction of orbital floor defects using a statistical shape model. J Anat. 2022;240:323–9.
11. Park TH. The usefulness of the navigation system to reconstruct orbital wall fractures involving inferomedial orbital strut. J Clin Med. 2023;12:4968.
12. Verbist M, Dubron K, Bila M, Jacobs R, Shaheen E, Willaert R. Accuracy of surgical navigation for patient-specific reconstructions of orbital fractures: a systematic review and meta-analysis. J Stomatol Oral Maxillofac Surg. 2024;125:101683.
13. González LV, López JP, Orjuela MP, Díaz-Báez D. Technology guided management of orbital trauma: a systematic review. J Maxillofac Oral Surg. 2024. https://doi.org/10.1007/s12663-024-02255-9.
14. Seifert LB, Mainka T, Herrera-Vizcaino C, Verboket R, Sader R. Orbital floor fractures: epidemiology and outcomes of 1594 reconstructions. Eur J Trauma Emerg Surg. 2022;48:1427–36.
15. Tel A, Sembronio S, Costa F, Stenico AS, Bagatto D, D'Agostini S, Robiony M. Endoscopically assisted computer-guided repair of internal orbital floor fractures: an updated protocol for minimally invasive management. J Craniofac Surg. 2019;47:1943–51.
16. Consorti G, Betti E, Catarzi L. Customized orbital implant versus 3D preformed titanium mesh for orbital fracture repair: a retrospective comparative analysis of orbital reconstruction accuracy. J Craniomaxillofac Surg. 2024;52:532–7.
17. Jaquiéry C, Aeppli C, Cornelius P, Palmowsky A, Kunz C, Hammer B. Reconstruction of orbital wall defects: critical review of 72 patients. Int J Oral Maxillofac Surg. 2007;36:193–9.
18. Quaranta-Leoni FM, Sposato S, Lorenzano D. Secondary orbital ball implants after enucleation and evisceration: surgical management, morbidity, and long-term outcome. Ophthalmic Plast Reconstr Surg. 2015;31:115–8.
19. Manmadhachary A, Mohan AA, Reddy MH. Manufacturing of customized implants for orbital fractures using 3D printing. Bioprinting. 2021;21:e00118.

Virtual Surgical Planning in Orbital Oncology

Alessandro Tel and Massimo Robiony

1 Generalities

Masses arising within the orbit represent a heterogeneous group that includes both neoplastic and non-neoplastic disease processes. Among neoplasms, several lesions with different origins can be classified, including metastases, lacrimal gland carcinomas, soft tissue sarcomas, meningiomas and schwannomas, neurofibromas, congenital cysts (dermoid or epidermoid) and, concerning vascular lesions, which represent the most frequent subgroup, cavernous and capillary hemangiomas, lymphangiomas, and orbital varices. Other possible conditions that manifest as orbital masses but for which surgery is contraindicated are lymphomas, pseudotumors, sarcoidosis, and IgG4-related disease. The orbit can be invaded by nearby aggressive processes, such as malignant neoplasms of epithelial and bone tissue.

From a surgical perspective, there are two major categories:

- Intraorbital, well-defined masses that occupy the orbital space and appear as circumscribed lesions, susceptible to precision surgery for minimal invasiveness (ISOLs, intraorbital space-occupying lesions) [1].
- Extensive, infiltrating lesions that invade the orbit from nearby structures, which require an orbital exenteration and/or an associated resection of broad parts of the orbit in combination with other anatomical parts (for instance, paranasal sinuses, maxilla, zygoma). In contrast with ISOLs, such lesions will not be selectively excided, although virtual planning is very useful to define the whole resection for oncological purposes. This latter group will be discussed in the chapter dedicated to maxillectomies and craniofacial resection [2].

2 Virtual Surgical Planning for the Excision of Intraorbital Space Occupying Lesions

Virtual surgical planning for the excision of ISOLs requires the adoption of all the components of the model for orbital virtualization, described in the previous chapter, in contrast with orbital traumatology, which only relies on the reconstruction of the skeletal anatomy. In addition to the eye globe, it is of prominent importance to reconstruct the noble elements of the intraconal space, namely the extraocular muscles and the optical nerve, as many masses develop posterior to the globe and contract crucial relationships with such structures. As previously mentioned, in a perspective of precision surgery, virtual surgical planning specific for ISOLs conceptually differs from planning related to malignant disease, which requires broad resections with sacrifice of nearby structures and will be discussed in the context of craniofacial resection. In the case of ISOLs, virtual planning has multiple roles that enable the surgeon to conduct minimally invasive procedures, taking benefit of:

- Definition of the surgical approach: depending on the localization of the lesion within the orbit, the approach can significantly differ in terms of incisions, use of osteotomies, and endoscopic assistance
- Three-dimensional (and 3D printable) representation of the anatomical relationships between the orbital mass and the noble structures, allowing to visualize cleavage planes
- Creation of a preoperative virtual endoscopy to anticipatorily simulate the endoscopic surgery

A. Tel (✉)
Lead Specialist for VSP and 3DP, Maxillofacial Surgery Clinic, Head & Neck and Neuroscience Department, Academic Hospital of Udine, Udine, Italy
e-mail: alessandro.tel@uniud.it

M. Robiony
Chief of Maxillofacial Surgery Clinic, Director of the Postgraduate School in Maxillofacial Surgery, Chief of Head & Neck and Neuroscience Department, Academic Hospital - University of Udine, Udine, Italy
e-mail: massimo.robiony@uniud.it

© The Author(s), under exclusive license to Springer Nature Switzerland AG 2025

A. Tel, M. Robiony (eds.), *Atlas of Virtual Surgical Planning and 3D Printing for Cranio-Maxillo-Facial Surgery*,
https://doi.org/10.1007/978-3-031-94495-6_15

- Drawing of osteotomies and modeling of surgical guides
- Creation of a navigation plan available during surgery or an augmented reality plan

2.1 Localizing Lesions in the Orbit: A Key Step for Approach Definition

The orbit can be subdivided into two halves, or divisions, respectively superior and inferior, by drawing an imaginary line conjoining the Whitnall tubercle and the superior margin of the anterior lacrimal crest. Each half can be further subdivided into three equal subcompartments using an imaginary line passing through the centerpoint of the first line [1]. According to this model, two halves are defined that play a significant clinical importance: the superior-lateral division and the inferior-medial division. The superior-lateral division can be approached via a lateral orbital rim marginotomy, which exposes all the intraconal space between the superior and the inferior recti muscles, while the inferior-medial subdivision is well dominated through both transcaruncular/retrocaruncular/Lynch open approaches and by transnasal and transantral endoscopic approaches. This classification based on compartments is a suitable tool for the surgeon to choose the most appropriate surgical approach (Fig. 1). In addition, there are lesions that may involve multiple compartments at once, owing to their size or their multifocal behavior. A further compartment should be identified in the deep retrobulbar space, which is mostly critical due to the presence of the optic nerve.

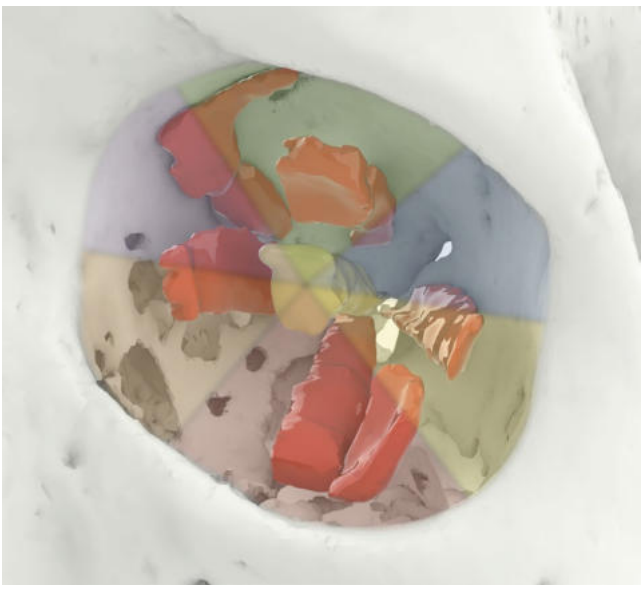


Fig. 1 Subdivision of the orbital space in multiple compartments. The most important subdivision accounts for a superior-lateral division and an inferior-medial division

3 Image-Guided Surgery in Orbital Oncology

As mentioned, the orbit can be considered a cone-shaped space in which only the most superficial parts uncovered by surgical approaches are directly explorable under direct vision, while the deeper parts are difficult to reach. One of the most complex issues is to precisely evaluate the depth as dissection proceeds and the anatomical structures that intervene at each point, such as ethmoidal arteries and the optic nerve. Surgical navigation allows for a real-time anatomical tracking by univocally associating the real patient with imaging loaded in the navigator. The so-called "image-to-patient registration" is a rigid body alignment between the surface mapping of the real patient, defined using point clouds sampled using a registration pointer, and the volumetric rendering of the virtual patient, or some predefined points made coincident with specific anatomical landmarks.

The author prefers using an optical navigation system, which enables navigation to be performed even in the presence of metal objects within the operating field. The optic navigation system is dependent on the presence of an infrared stereocamera, which uses diodes to emit light impulses reflected on the surface of photoreflective spheres positioned respectively in the reference frame attached to the patient and in the probe. In contrast with neurosurgery, where the head is in a fixed position and kept stable by the Mayfield headset, in orbital surgery the head should freely move to allow working from different perspectives, or at least to give more freedom to the operator. This is made possible by attaching to the patient's head a reference frame whose movement is solidary with the movements of the head, therefore not altering the spatial relationship defined between the stereocamera and the photoreflective spheres mounted on the reference frame (dynamic reference frame, DRF). The author uses a special system consisting of a metal tripod that engages a screw fixed to the patient's skull using a miniscrew and is then tightened with a locking mechanism [3, 4].

Before starting calibration of the navigator, when multiple imaging datasets are navigated, it is important to perform their coregistration within the same coordinate system, a key step required also for segmentation of multiple structures from different imaging sequences. In this way, it is possible to simultaneously navigate all datasets loaded within the navigator, regardless of their different orientation and acquisition field. This can be either performed within Brainlab Elements (Brainlab, Munich, DE) or Mimics (Materialise, Leuven, BE) (Fig. 2). However, the navigation software is essential to import STL files from the VSP to the navigation system. The navigation of VSP is a crucial concept, as it

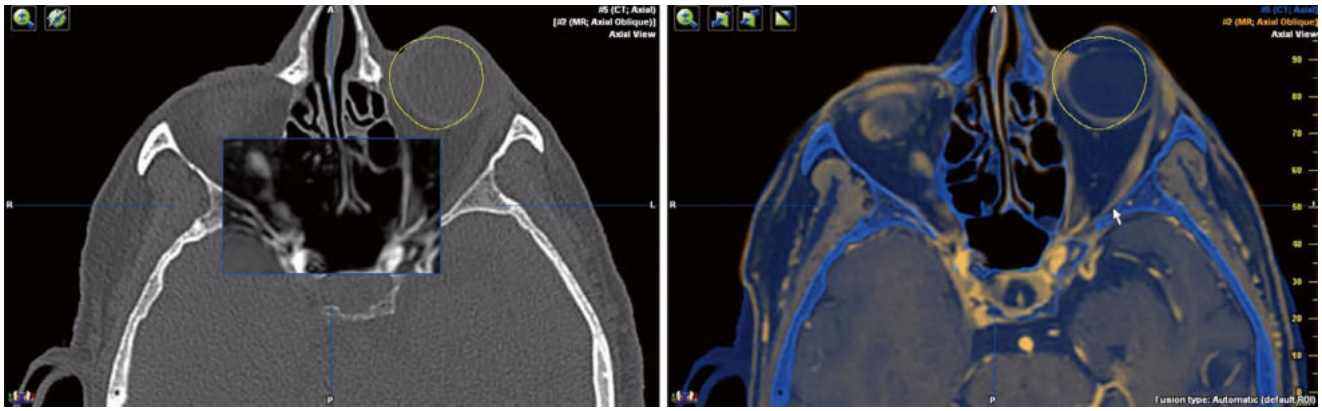


Fig. 2 Before navigation, CT and MR have to be merged either in the navigator or in a dedicated software. Brainlab Elements CMF was used in this case

extensively overcomes navigation of basic DICOM datasets and enriches the possibilities of image-guided surgery to assist osteotomy design and locate the tumor margins [5].

3.1 The Importance of Navigation in Orbital Oncology

Intraoperative navigation represents the trait d'union between computer planning and the real patient: it is a powerful tool that facilitates dissection as it dynamically identifies the depth and the proximity to vulnerable structures. In the orbital area, navigation offers unquestionable benefits compared to surgical guides: Theoretically, surgical guides are more effective in translating precise osteotomies, but they require more aggressive periosteal elevations and wider incisions to be securely positioned and therefore increase the invasiveness of surgery [6].

**VSP and technology should not just facilitate osteotomy design, but also reduce invasiveness of a procedure. A computer-guided approach where surgical guide placement makes surgical access more invasive is a misuse of technology, which has to lead to more favorable clinical outcomes, less bleeding, less swelling and less pain.*

Concerning orbital oncology, the concept of targeting ISOLs can not prescind from navigation, as the intraoperative target mode, and its role is presented for each analyzed group:

- In case of masses arising in the superior-lateral division, navigation is essential to guide piezosurgical lateral marginotomy in order that the resulting bone opening maximizes the exposure of the lesions and avoids harmful regions. Once the lateral orbital rim is removed, navigation is used to check in depth the vulnerable structures as dissection proceeds, especially the extraocular muscles and the optic nerve (Fig. 3).
- For lesions of the inferior and medial compartment, navigation is useful to check the depth of the lesion during endoscopic exploration, allowing to locate the ideal point on bone walls where osteotomies should be performed to expose the tumor. For masses of the medial orbital wall, during transnasal endoscopy navigation facilitates the identification of the most appropriate site to conduct the osteotomy on the lamina papyracea. In case of a lesion overlying the orbital floor for whose excision the transantral endoscopic approach is advocated, navigation can also be performed within the maxillary sinus, leading to similar advantages (Fig. 4).
- For extended lesions involving a conspicuous part of the orbital volume, extending profoundly and eventually within the intracranial space, navigation is essential to progressively check the depth, which might be more difficult to assess due to the anatomical alteration that such cases present. Moreover, navigation allows to target critical structures, especially the internal carotid artery, the cavernous sinus as well as crucial functional structures, such as the extraocular muscles and the optical nerve. In cases of intracranial extension, it provides orientation in the anterior and middle skull base (Fig. 5).
- In case of multifocal lesions, intraoperative navigation is essential to target each nodule segmented in the virtual surgical planning and to ensure that surgery is radical. This is of prominent importance, especially in case of lesions that are at high risk of relapsing, for instance, pleomorphic adenomas. Even if the largest disease localization is successfully excised, it is of prominent importance that each nodule is resected to consider the surgery radical. A skin mapping of lesions before incising can be useful to have a general view of the sites of lesions (Fig. 6).

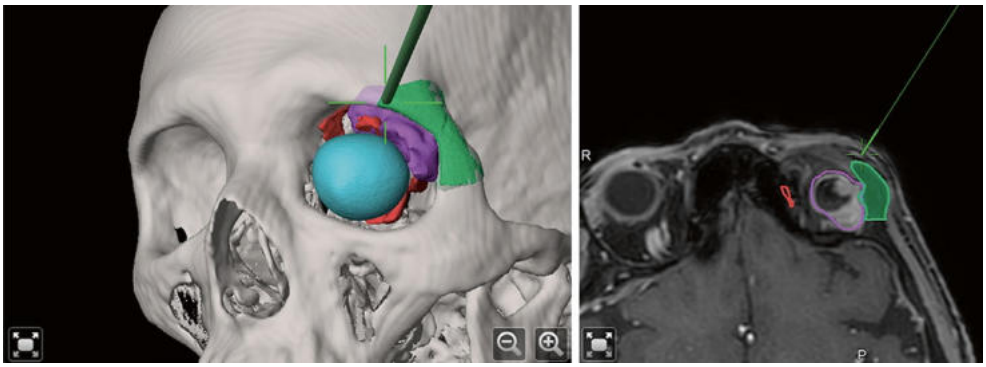


Fig. 3 Navigation-guided lateral marginotomy to expose the underlying tumor model. The probe allows to check where the osteotomy starts

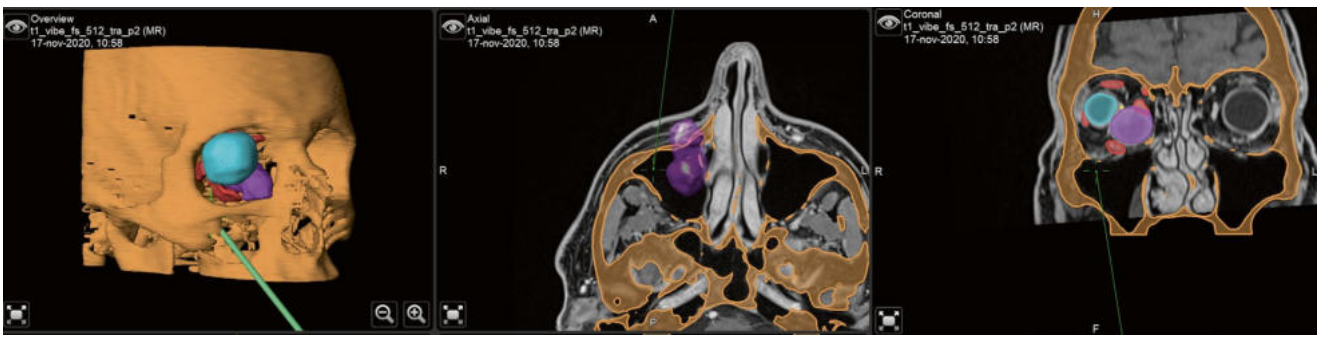


Fig. 4 Navigation applied in the transantral endoscopic excision of masses of the inferior-medial division

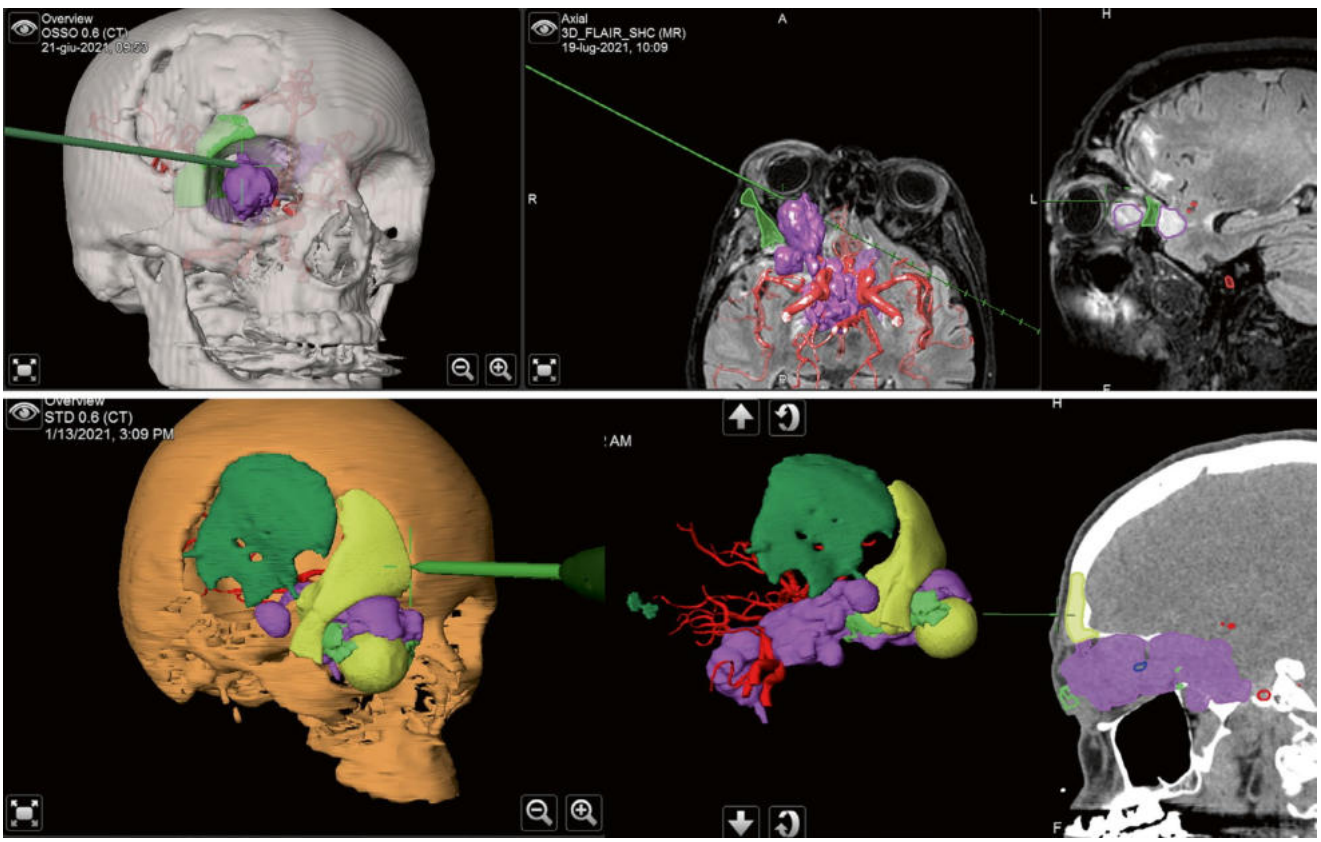


Fig. 5 Navigation for lesions extending in depth up to the intracranial space guides neurosurgical dissection as well

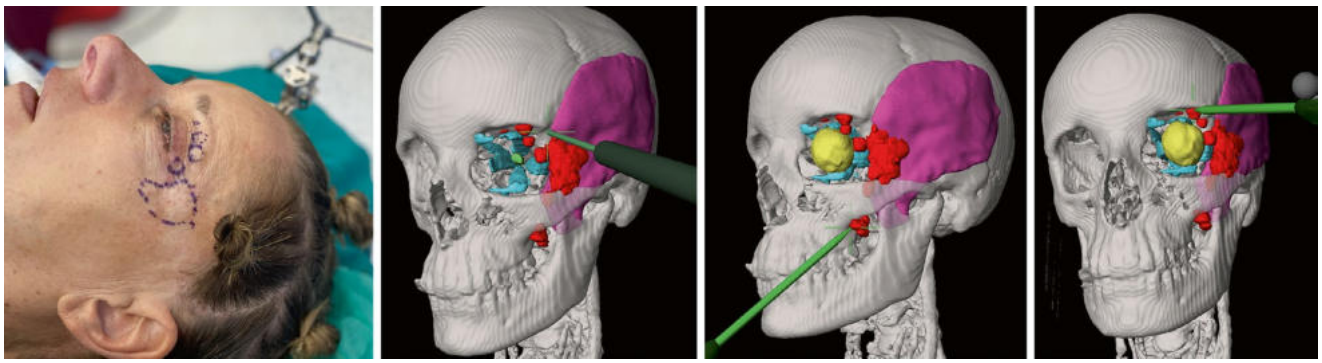


Fig. 6 Navigation in multifocal masses enables nodule mapping to identify disseminated disease localizations

4 Lesions Arising in the Superior-Lateral Division

Masses arising in the superior-lateral division develop in a space between the superior and the inferior rectus muscle. Due to their localization, in several cases such masses originate from the lacrimal gland, but a number of non-glandular tumors, including hemangiomas, nerve-sheath tumors, and other neoplasms, may develop in this space. The superior-lateral division is best exposed through a bone osteotomy directed to the lateral orbital rim. Virtual surgical planning with virtual reconstruction of orbital structures provides significant advantages in defining the optimal size and shape of the orbital marginotomy, avoiding to expose the desired amount of periorbita without exceeding beyond what is strictly necessary [7]. If accessed through a Stallard incision, this approach allows to expose a significant amount of orbital volume with minimal esthetical scarring. The most effective design of the virtual marginotomy, which is the key virtual planning procedure to ensure optimal surgical exposure, relies on freehand polygon marking and polysculpting instead of planes, owing to the complex geometry of the lateral orbital rim. This detail can be translated intraoperatively by navigation or 3D printing of a surgical guide, which the author personally does not advise due to the additional periosteal elevation and exposure required.

4.1 Pleomorphic Adenoma of the Lacrimal Gland

4.1.1 Clinical History

A 73-year-old woman complained of the progressive onset of diplopia. Clinical examination revealed a vertical dystopia of the left eye globe with downward displacement of the eye globe and marked proptosis of the eye. The patient was sent to ophthalmologist where Hess-Lancaster test was conducted, confirming diplopia especially in up-left gaze. The patient underwent both a CT scan and an MR, which were requested according to the aforementioned parameters for the virtual orbital reconstruction.

4.1.2 Virtual Surgical Planning

DICOM data were imported into Materialise Mimics, and anatomical structures were segmented to simulate a complete orbital model, including the skeletal framework, the tumor, the eye globe, extraocular muscles, and the optic nerve. A lateral marginotomy was designed through freehand modeling, with a size tailored for the surgical needs, to uncover the exact amount of periorbita needed to perform its incision and expose the neoplasm, which was located in the region of the lacrimal gland, not definable anymore (Fig. 7). STLs of VSP were imported into the software Brainlab Elements (Brainlab, Munich, DE) to create the navigation plan.

4.1.3 Surgery

Such cases all share the same surgical approach, thus described only for this first case. A Stallard sovrapalpebral incision with lateral extension is generally performed, the orbicularis oculi sectioned, and the periosteum of the lateral orbital rim incised and elevated to yield optimal bone exposure. Alternatively, a hemicoronal flap can be raised to uncover a wider bone area. Under navigational guidance, the marginotomy is conducted with a piezosurgical handle to minimize soft tissue damage (Fig. 3). Before removing the bone dowel, two linear 4-hole plates are preliminarily conformed over the native orbital rim, and holes are made using a bur in the optimal place for fixation. The bone dowel is removed, and a meticulous detachment of the bone from the underlying periorbital layer is performed. The intact periorbita is incised and the orbital content is revealed. By blunt dissecting the intraconal fat, the lateral and superior recti muscles are identified and gently tractioned using a lace. The mass is exposed, and its deep and medial margins are checked with the navigator probe to assess the relationship and distance from the optic nerve. Using dissection blunt-tipped scissors, accurate sectioning of all adhesions around the mass is performed, and the mass is removed

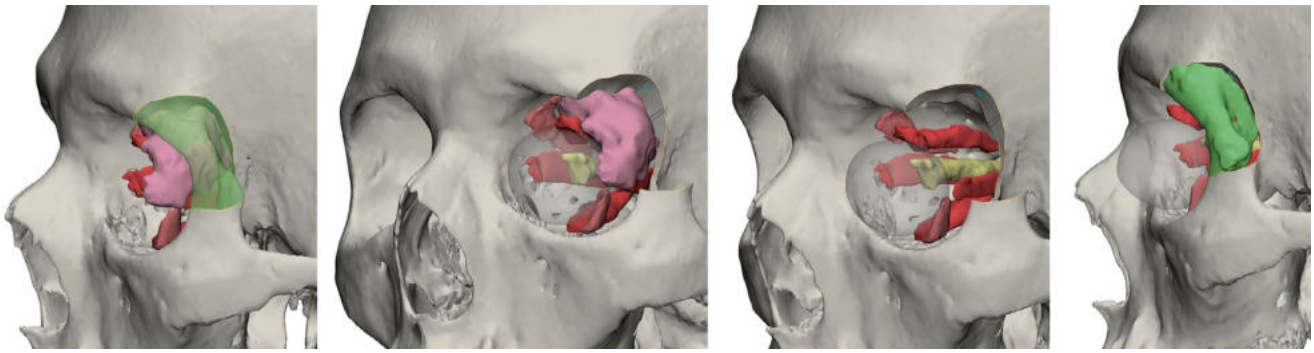


Fig. 7 VSP for masses of the superior-lateral subdivision. The aim is to tailor lateral marginotomy to the underlying disease to maximize exposure with a more conservative osteotomy

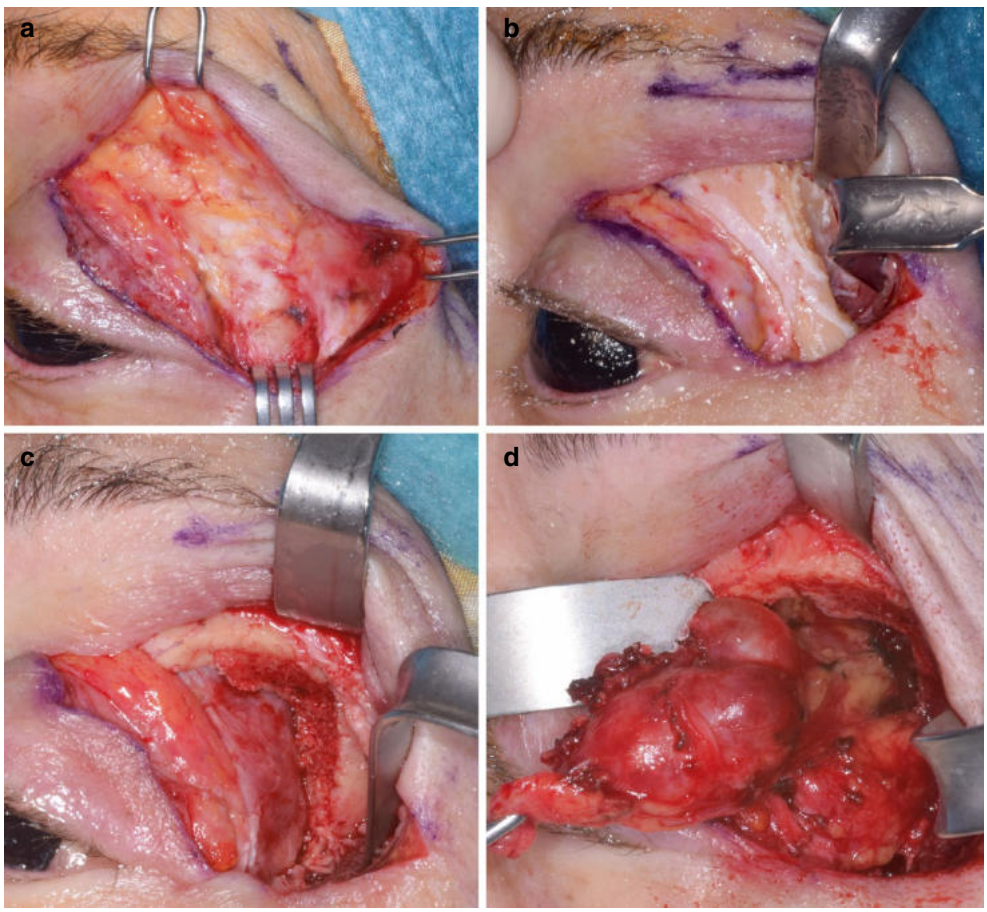


Fig. 8 Surgical steps with a Stallard incision: (**a**) suborbicolaris dissection; (**b**) periosteal incision and bone exposure; (**c**) lateral marginotomy; (**d**) tumor excision

(Fig. 8). Accurate hemostasis is accomplished, and the segment of lateral orbital rim is fixed in its correct place using previously drilled holes. Suturing of the orbicularis oculi muscle and of the overlying skin is performed. Histopathology confirmed that the lesion was consistent with the diagnosis of a pleomorphic adenoma of the lacrimal gland.

4.2 Cavernous Hemangioma

4.2.1 Clinical History

A 38-year-old woman presented to her ophthalmologist's attention complaining of metamorphopsia, blurring of vision, and headache. An MR was required, revealing the presence of a lesion of the superior orbital compartment with

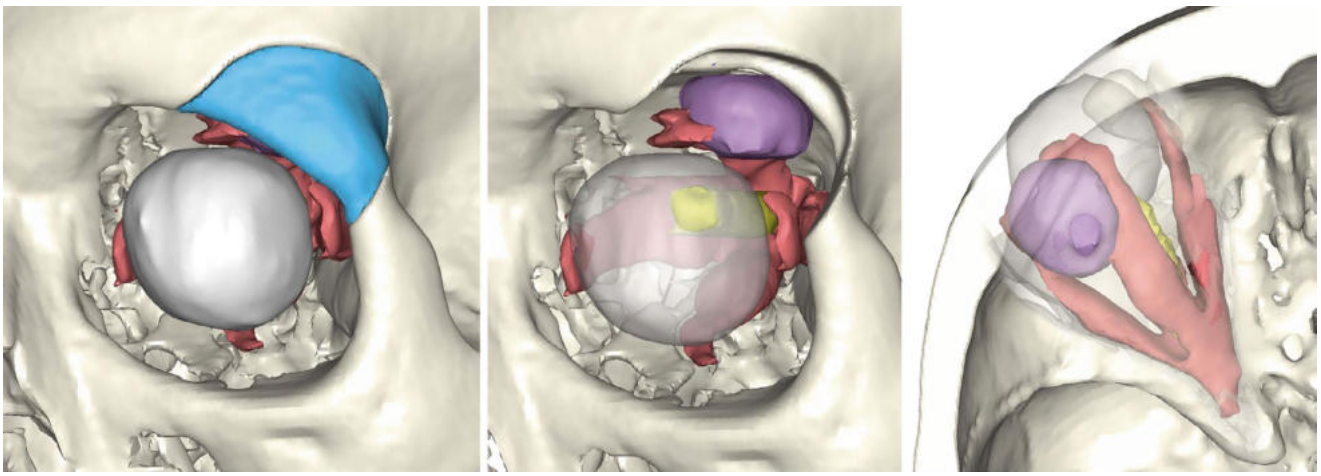


Fig. 9 VSP for a cavernous hemangioma of the orbital roof. Left: virtual marginotomy. Center: bone removal and localization of the lesion in depth. Right: top view. The lesion has determined a focal erosion of the orbital roof

dislocation of superior rectus muscle. CT was also performed to evaluate the bony orbital frame.

4.2.2 Virtual Surgical Planning

CT and MR were co-registered before the segmentation procedures, then a three-dimensional model was created with all orbital structures being represented in their relationship with the tumor. In particular, the application of smart brushes and dynamic region growing was a successful method to segment the lesion from MR. In 3-matic (Materialise, Leuven, BE), a lateral marginotomy was performed with a more superior and posterior orientation, due to the location of the tumor. 3D model analysis allowed to appraise the intimate relationship between the lesion and the anterior skull base, which presented a tiny fenestration above the lesion (Fig. 9).

4.2.3 Surgery

Due to the deeper localization of the lesion, hidden beneath the orbital roof, and the subsequent more superior design of the marginotomy, an hemicoronal access was chosen. The lesion was located within the orbital fat by checking its depth and margins under virtual surgical plan navigation, at the same time allowing to track distance from the optic nerve (Fig. 10). The navigated marginotomy allowed the optimal exposure of the lesion for its size, location, and design, confirming the presurgical VSP study. After the lesion was excised with preservation of the lateral rectus, the orbital rim was fixed back in its position (Fig. 11). The histopathological analysis of the specimen confirmed the diagnosis of cavernous hemangioma.

4.3 Mesenchymal Chondrosarcoma

4.3.1 Clinical History

A 33-year-old woman presented to our attention complaining of diplopia and a clinically manifest exophthalmos. She underwent CT scan showing a round, clear margins, isodense mass compressing the eye globe with coarse core calcifications. The patient underwent additional MR scan confirming the same findings, aiding 3D reconstruction of soft structures.

4.3.2 Virtual Surgical Planning

The orbital virtual model was constructed with the mass, elucidating its three-dimensional relationship and allowing to tailor the most appropriate design for the bone window created by the marginotomy. In particular, VSP emphasized the close relationship between the superior and lateral rectus muscle and the lesion, which reached at its apex the optic nerve as well (Fig. 12).

4.3.3 Surgery

Owing to the amplitude of the bone window required, a hemicoronal approach was preferred to the Stallard incision, also considering the young age of the patient and the relatively stiff tissues compared with the laxer skin of the elderly. The mass was removed under navigational guidance, checking its crucial relationship with the optic nerve (Fig. 13). Histopathological analysis revealed a mesenchymal chondrosarcoma, and the patient was followed in an oncology center and underwent protontherapy, resulting negative at subsequent follow-up.

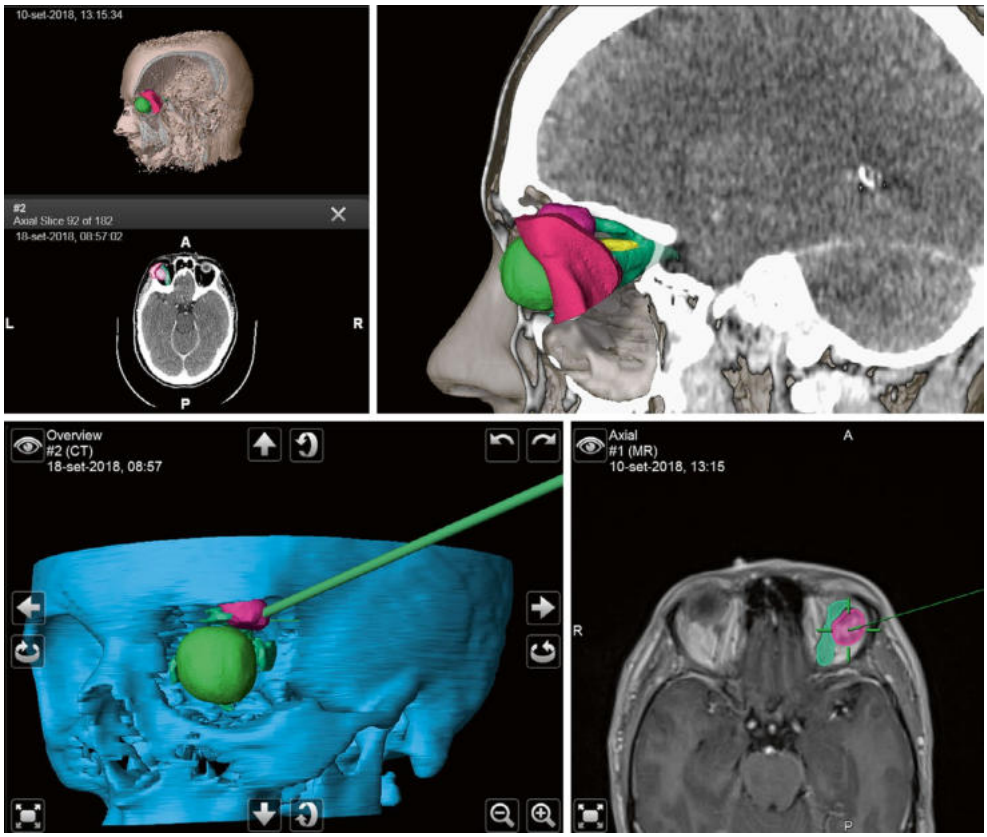


Fig. 10 Intraoperative navigation with lesion targeting

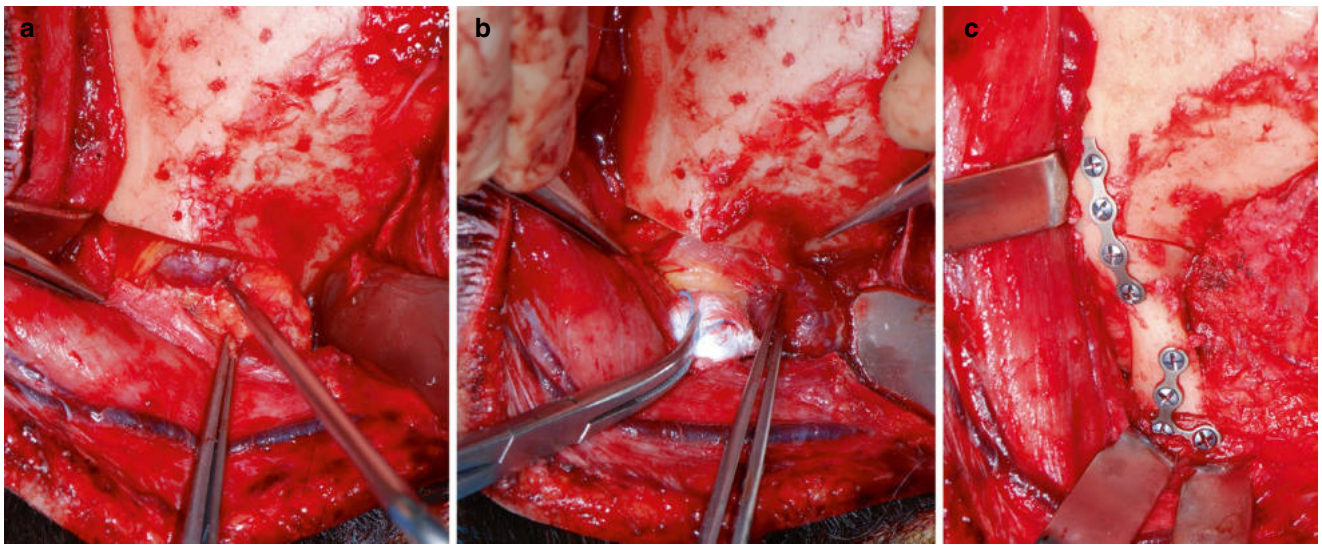


Fig. 11 (**a**) the probe localizes the lesion; (**b**) the lesion is separated from the superior rectus; (**c**) osteosynthesis is complete

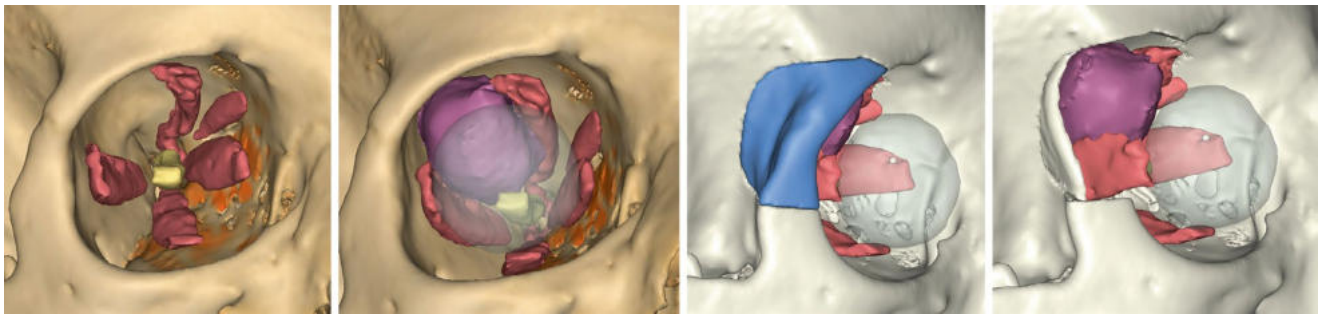


Fig. 12 VSP for the excision of a deep chondrosarcoma in close relationship with the optic nerve. Customized lateral marginotomy enables to expose successfully the lesion while minimizing the extent of orbital rim removal

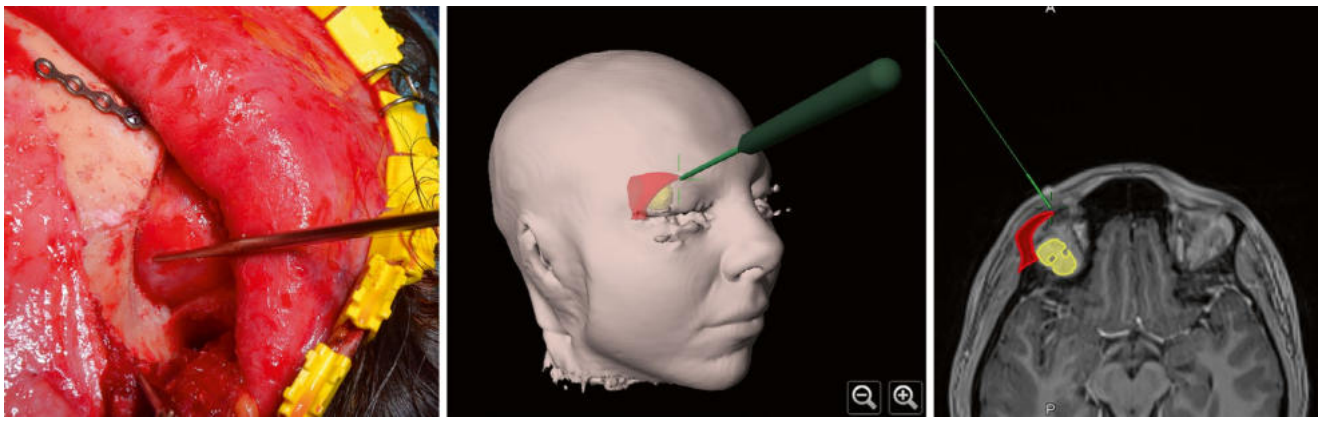


Fig. 13 Navigation guided localization of the lesion (navigation of VSP)

5 Lesions Arising in the Inferior-Medial Division

ISOLs arising in the inferior-medial division are often more challenging due to a variety of reasons: first, while the lateral orbital rim allows to open a wide portal exposing a broad part of the orbital contents, there is not any specular option available for the inferior-medial division. Moreover, this anatomical space is narrower and more risky to approach due to the presence of a number of vulnerable structures, including the inferior obliquus muscle, arising from the lacrimal crest, the lacrimal sac, the medial rectus, anterior and posterior ethmoidal arteries. Most of all, the orbital apex containing the optic foramen for the optic nerve converges medially and is found briefly after the posterior ethmoidal artery along the lamina papyracea. Among the open approaches for masses located in this compartment, the Lynch incision allows to skeletonize and expose the medial orbital wall in a subperiosteal plane, whereas the trans and retrocaruncular approaches allow to enter the periorbital space and excising masses located within the orbital cone.

Endoscopic approaches have revolutionized the surgery of the inferior-medial orbit, exploiting the very thin walls represented by the orbital floor and the lamina papyracea as potential corridors to access the orbital space. Transnasal endoscopy allows for an optimal visualization of the lamina papyracea, which can be found immediately above the middle turbinate in the lateral wall of the nasal cavity, while the orbital floor, similarly to what is performed for orbital floor fractures, can be optimally scoped using the transantral pathway as portal to remove the orbital floor and uncover any lesion arising within this space. A very important acquisition for endoscopic surgery is the entire simulation of the camera view, a concept referred to by the author as "virtual endoscopy," namely, the possibility to anticipately visualize an anatomical scenario similar to the real endoscopic view, including optics parameters, which can be set as desired [8].

5.1 Cavernous Hemangioma Located in the Deep Medial Wall, Close to the Apex

5.1.1 Clinical History

A 45-year-old lady came to our attention after undergoing a MR prescribed by the neurologists for persistent headache with irradiation to the right orbit irresponsive to any medica-

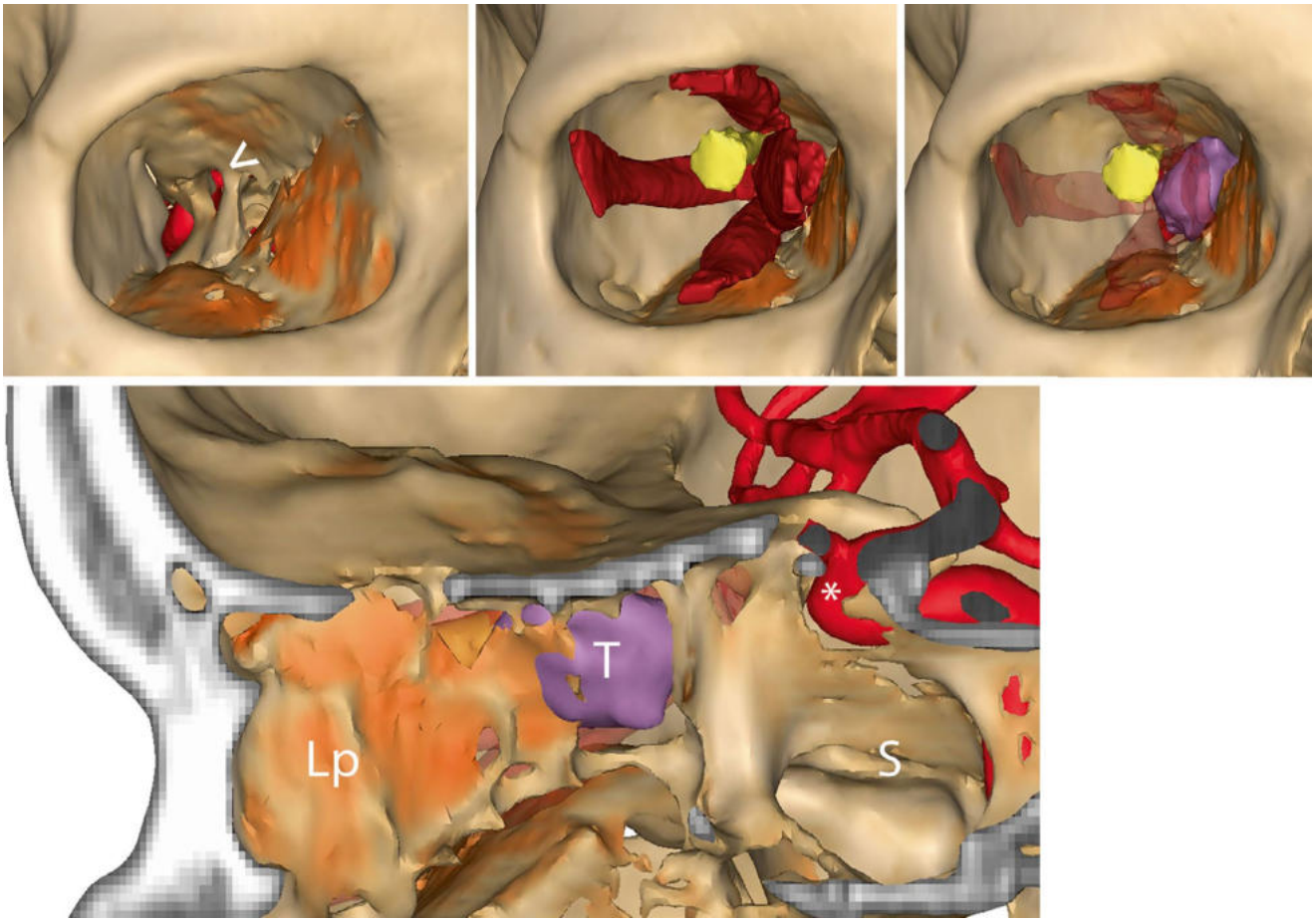


Fig. 14 VSP of a lesion localized in close relationship with the optic foramen (arrow tip). The lesion (T) is enclosed between the lamina papyracea (Lp) and the medial rectus, causing its displacement. S is the location of the carotid siphon. The bottom panel shows a medial view from the lamina papyracea perspective, showing its focal erosion

tion. MR showed a well-circumscribed mass, located in depth, 5 mm distant from the optic foramen, causing a deformation of the lamina papyracea within the nasal cavity with partial bone erosion. The patient underwent an additional CT scan according to the 3D visualization protocol to define the relationships of bone surfaces with soft tissues, according to the components of the virtual model.

5.1.2 Virtual Surgical Planning

After proper segmentation and 3D reconstruction, a clipping plane was positioned medially to the lamina papyracea to scope the lateral aspect of the nasal cavity, which revealed its perforation due to the presence of the orbital mass. Unfortunately, as mentioned, current TOF MR sequences do not have enough resolution to capture the course of ethmoidal arteries, tiny but surgically important vessels that are intercepted in open approaches to the medial orbit. STL files for each mesh were exported and used to create the navigation plan. This enabled to drive the depth of the transcaruncular approach exactly in correspondence with the fenestration of the lamina papyracea (Fig. 14).

5.1.3 Surgical Technique

A retrocaruncular approach was used to access the medial orbital division, being tangential to the lamina papyracea. Moreover, this approach was coupled with a conventional, non-computer-guided, lateral marginotomy, which enabled to decompress the orbital content, allowing the bulb to shift laterally, thus widening the corridor for the retrocaruncular access. A blunt dissection was performed posteriorly to Horner's muscle, and the periosteum was incised and elevated. The medial rectus muscle was isolated and identified with a loop, anterior and posterior ethmoidal vascular bundles were cauterized and sectioned, and the full medial wall was exposed until the mass was visualized, checking the correct depth of dissection under navigational guidance (Fig. 15). Using endoscopic vision both through the transcaruncular approach and within the nasal cavity to scope the medial wall, the mass was gently dissected and excised.

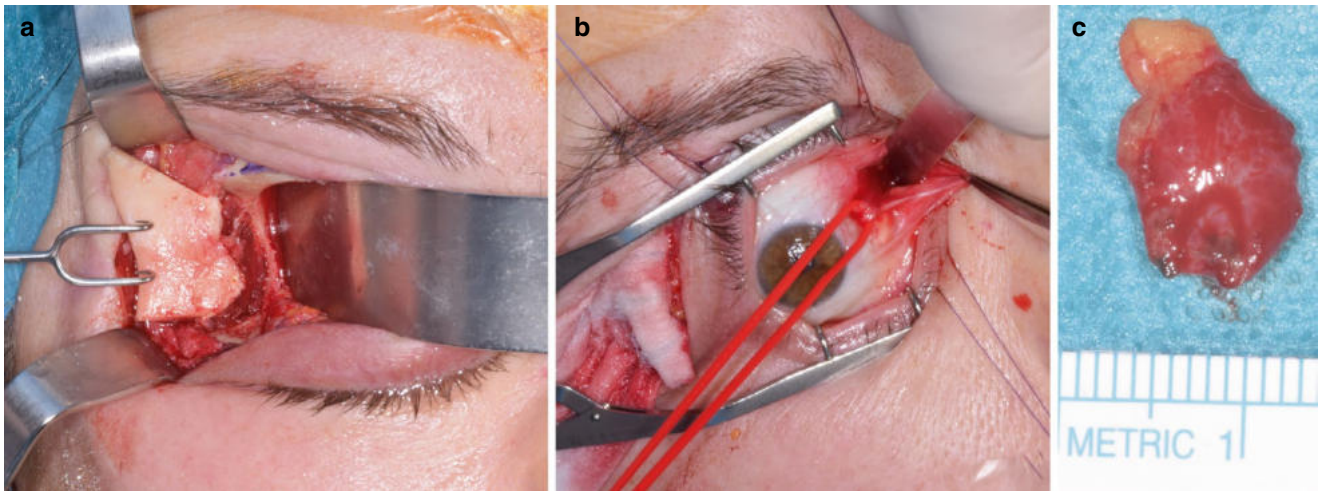


Fig. 15 (**a**) a strategic lateral marginotomy is performed to enable lateral decompression and (**b**) widen the medial corridor through the transcaruncular approach to expose the lesion (**c**)

5.2 Cavernous Hemangioma Excised Endoscopically: Reconstructing the Orbit for Virtual Endoscopic Simulation

5.2.1 Clinical History

A 41-year-old patient presented for clinical attention for the progressive onset of a palpable tumefaction underneath the inferior eyelid, associated with diplopia, especially in inferior and superior gaze positions, and a significant vertical dystopia of the globe. The patient underwent MR scan according to volumetric acquisition, which was highly suggestive of a mass of vascular origin; moreover, a CT scan with thin slices according to the aforementioned imaging protocol was performed.

5.2.2 Virtual Surgical Planning

3D-reconstruction emphasized the proximity of the orbital mass to the orbital floor, a condition sufficient to define the indication for a transantral endoscopic approach to the orbital floor. This approach has to be carefully planned, taking care to minimize anatomical distortions, especially across the very thin orbital floor, which is critical. Although the CT imaging was satisfactorily acquired with sub-millimeter slices (0.625 mm), the orbital floor presented multiple hollows, especially in areas corresponding to the overlying mass. The careful use of contralateral orbital mirroring, coupled with a meticulous use of the segment thin bone plugin and the selection of the optimal local threshold range, proved to be essential to achieve the integrity of the orbital floor in the virtual model. Subsequently, the mass was segmented using a combination of dynamic region growing methods and smartbrush contouring until its shape faithfully replicated the MR image (Fig. 16).

Subsequently, the implemented workflow was similar to that described for internal orbital floor fractures, with one essential difference: the osteotomy on the orbital floor was designed to configure a portal allowing to excise the mass from the maxillary sinus. Once the orbital floor access portal was defined, a specular, size-comparable, opening was planned on the maxillary sinus, enabling to insert instrumentation functional to perform the osteotomy on the orbital floor under endoscopic vision from the maxillary sinus. The definition of the access portals both on the maxillary sinus and the orbital floor, satisfying specific requirements of reciprocal compatibility, was essential to create the backbone of surgical planning, as the novel technique of virtual endoscopy was implemented to enhance simulation [8] (Fig. 17).

5.2.3 Setup for Virtual Endoscopy

Once all three-dimensional elements were defined, they were exported as individual STLs to a 3D animation software, Autodesk Maya (Autodesk Inc., San Francisco, CA, USA). In Maya, a cylinder was created with the same diameter and length as the optics for endoscopy, and a virtual camera was parented on the tip of the cylinder, defining the optical windows through which anatomy is scoped under endoscopic vision. Optic parameters were readapted from the manufacturer (KARL STORZ SE & Co KG, Tuttlingen, Germany), including an imaging refreshing rate of 50 fps and a focal distance of 18 mm. In Maya, one view was dedicated to camera see-through vision, through which the optics were moved to explore the orbital floor under simulated endoscopic vision from the maxillary sinus.

After the correct operational sequence for endoscopic vision was established, each movement of the camera was marked in the animation timeline with a keyframe, allowing

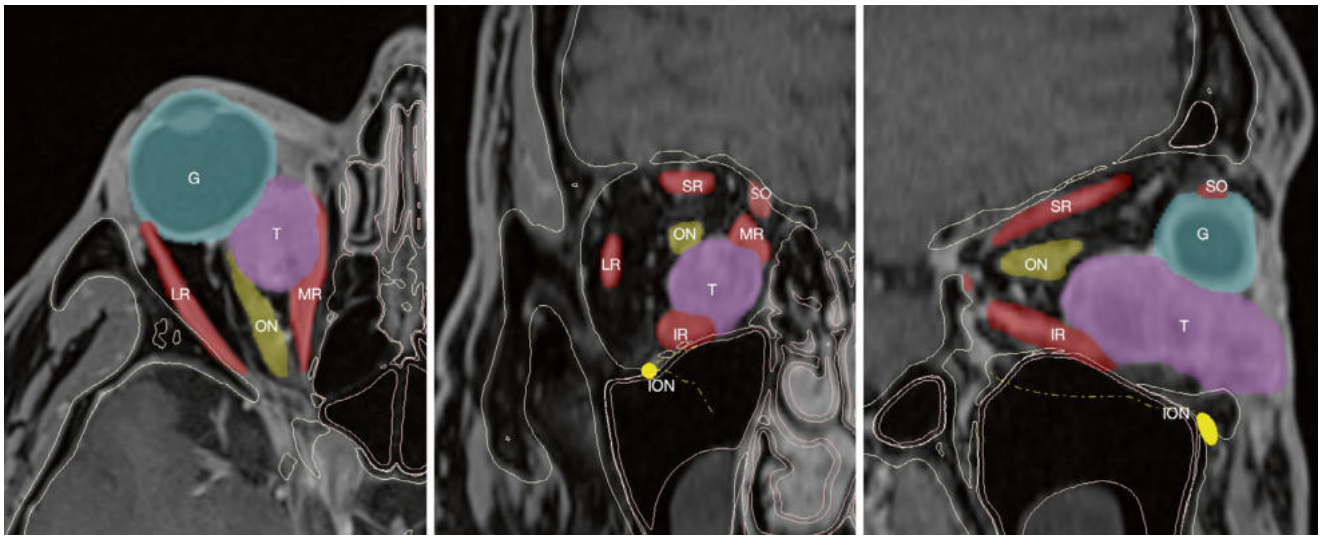


Fig. 16 Preoperative segmentation of a mass of the inferior-medial division developing underneath the eye globe. CT was already registered to MR and segmented; the skeletal model appears as a continuous line matching the bone in MR. Individual masks are created for the eye globe (G), tumor (T), medial rectus (MR), lateral rectus (LR), superior rectus (SR), inferior rectus (IR), superior obliquus (SO), optic nerve (ON)

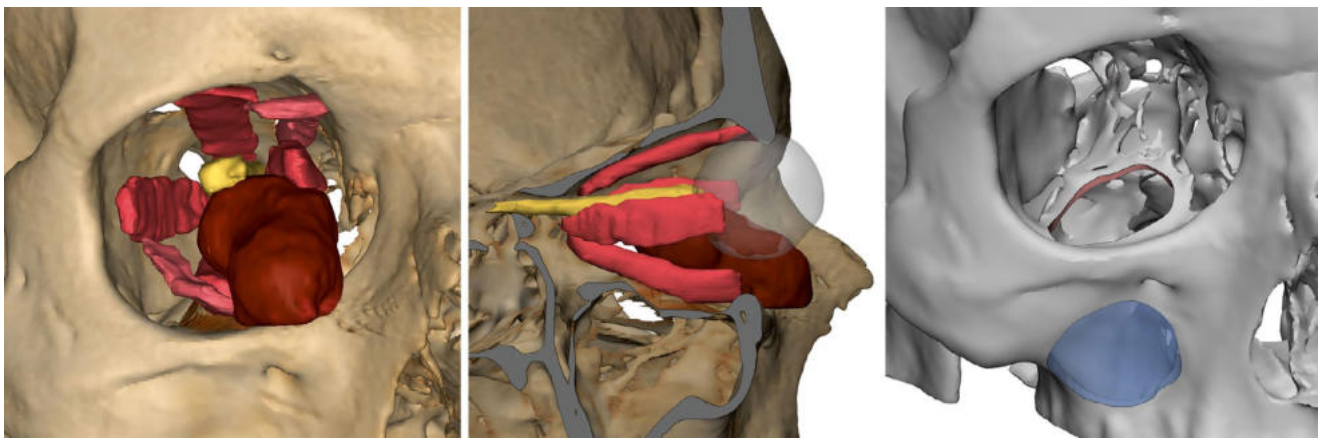


Fig. 17 Anatomical reconstruction and, right, creation of a transantral and orbital portal to complete mass excision

to keep track of the endoscope movements to reproduce the desired sequence. Following the animation of the endoscope, other sequences valuable for virtual surgical planning were animated, including orbital floor osteotomy to remove the thin bone window from the orbital floor, isolation and traction of the infraorbital nerve, tumor excision, and orbital floor reconstruction. In the operating room, the whole sequence was observed during endoscopy to enhance the orientation of the operator (Fig. 18).

5.2.4 Surgery

Incision was practiced in the oral mucosa underneath the superior lip in depth to the periosteal layer. Accurate elevation of periosteum was conducted, and the anterior-lateral maxillary wall was exposed. Under navigational guidance, a piezosurgical osteotomy was performed on the anterior antral wall to define the maxillary access portal. The bone flap was removed, and the endoscope was inserted within the maxillary sinus, scoping the orbital floor with a 30° optics.

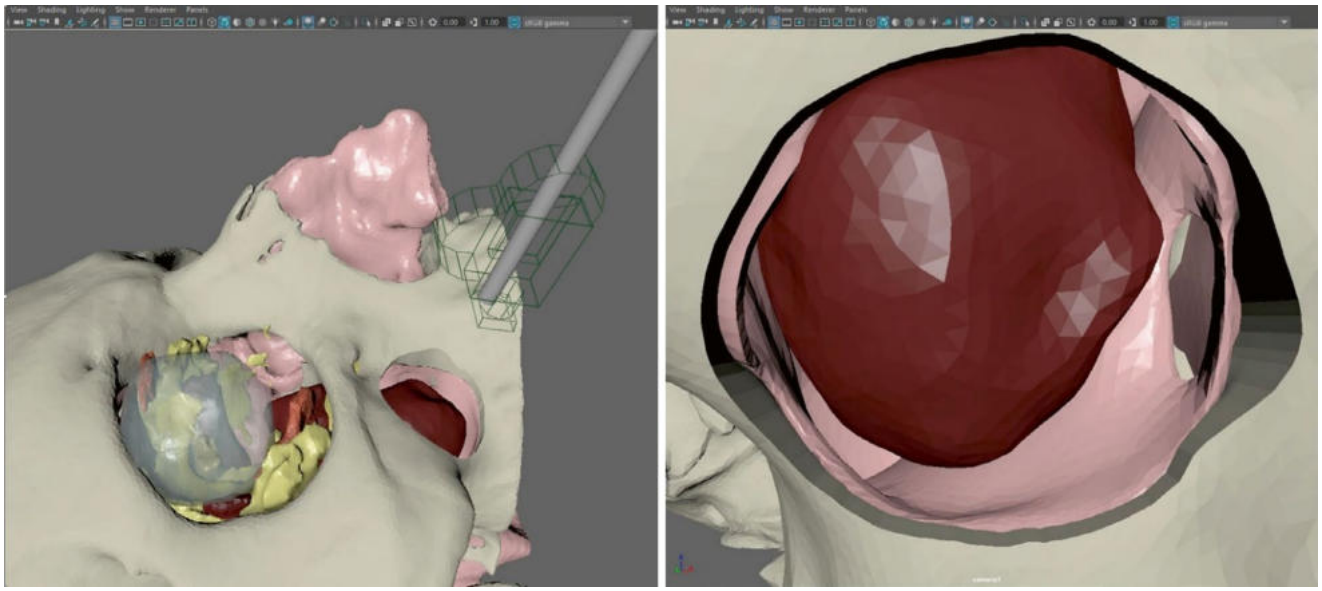


Fig. 18 Creation of the virtual camera associated with the endoscope. Optic parameters associated with the camera match those of a surgical optics. Right panel shows the view from the camera perspective with the focal distance associated with the optics

Under endoscopic vision, the osteotomy was reproduced on the orbital floor as well, defining the orbital access portal. The periorbita was exposed and incised, revealing the intraorbital content. Blunt dissection through intraconal fat was carried out, leading to visualize and isolate two critical structures: the infraorbital nerve, exposed during orbital floor osteotomy given its course within the infraorbital canal located within the orbital floor, and the inferior rectus muscle; both structures were identified by applying a flexible loop around them, and were tractioned to avoid their accidental lesion during maneuvers related to dissection. Once the mass was identified, it was dissected all around its capsule, checking the location of its deepest pole using the navigation probe. Using a Blakesley-Wilde forceps, the lesion was grasped and progressively mobilized through the orbital portal, where it was extracted from the maxillary sinus. The whole sequence of steps simulated in virtual endoscopy and related to actual surgery is shown in Fig. 19. The orbital floor was reconstructed alternatively by repositioning the original bone flap, but also the anterior antral wall is a possibility, exactly as internal orbital floor fractures.

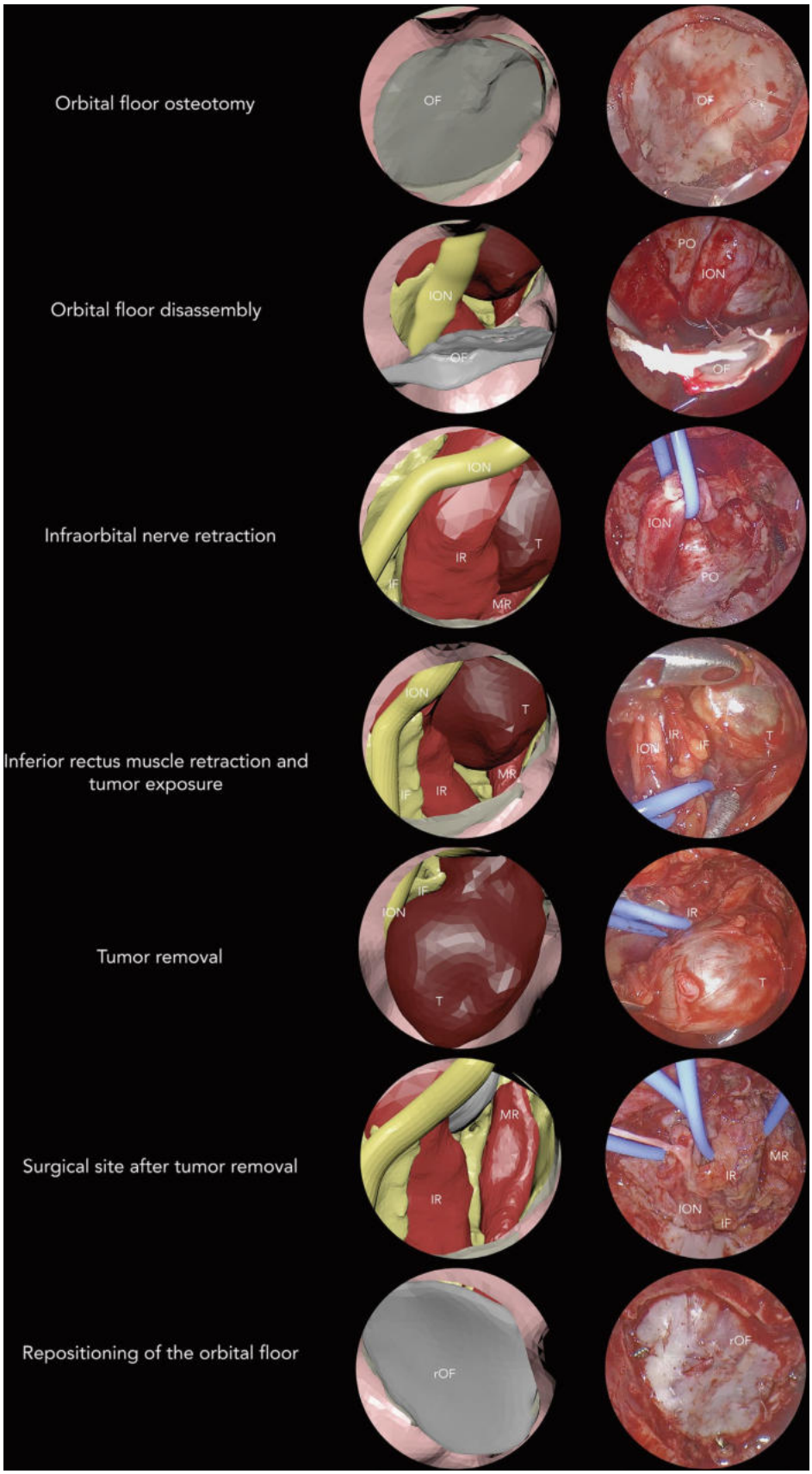


Fig. 19 Phases of VSP simulation associated with the real endoscopic correlated image in the transantral transorbital approach. Interesting is the isolation and displacement of infraorbital nerve, which is located in the path straightforward to the orbit

6 Orbital Masses with Deep Intracranial Extension

In some circumstances, the surgeon may intervene on orbital lesions that represent the extension of advanced disease processes that go beyond the orbit and enter the intracranial space, requiring a combined neurosurgical procedure. In several cases, the extension of disease poses a limit to surgeries with radical intent; nevertheless, patients may seek surgery to improve their quality of life, avoiding complications related to eye proptosis and diplopia. In these cases, the aim of surgery is to perform a debulking of the lesion, trying to excise the most of the pathologic tissue, at the same time balancing the risks of injuring nearby structures whose lesion may worsen the life of the patient.

6.1 Massive Plexiform Schwannoma with Orbital Involvement

6.1.1 Clinical History

This patient had a diagnosis of Von Recklinghausen disease and underwent two previous surgeries to excise intracranial and orbital schwannomas. In such surgeries, neurosurgeons approached the disease with an extended pterional approach. After a few years, the lesion relapsed in the anterior skull base, invading a corridor from the posterior fossa to the orbit and involving the crucial vessels of the Willis polygon. However, although esteemed not operable from a neurosurgical point of view, the patient presented to clinical attention requesting an intervention in the orbital space to decrease proptosis and overall improve her quality of life, given the eye dryness and diplopia related to the abnormal position of the eye globe [9].

6.1.2 Virtual Surgical Planning

A detailed segmentation and 3D reconstruction study was performed to ascertain the global extension of disease, including reconstruction of the intracranial arterial vasculature and the functional components of the orbital space, namely the extraocular muscles and the optical nerve, entirely concealed within the tumor mass. In this specific case, considering the entity of the intracranial involvement, the author decided to perform the segmentation of the brain as well, to define the depth of the tumor mass in relation to neurosurgical anatomy (Fig. 20). Concerning virtual surgical planning approaches, the planned strategy consisted of creating a wide lateral marginotomy (to be approached through an extended hemicoronal access) in continuity with the previous pterional operculum, which was removed in case the orbital access was not sufficient [10] (Fig. 21).

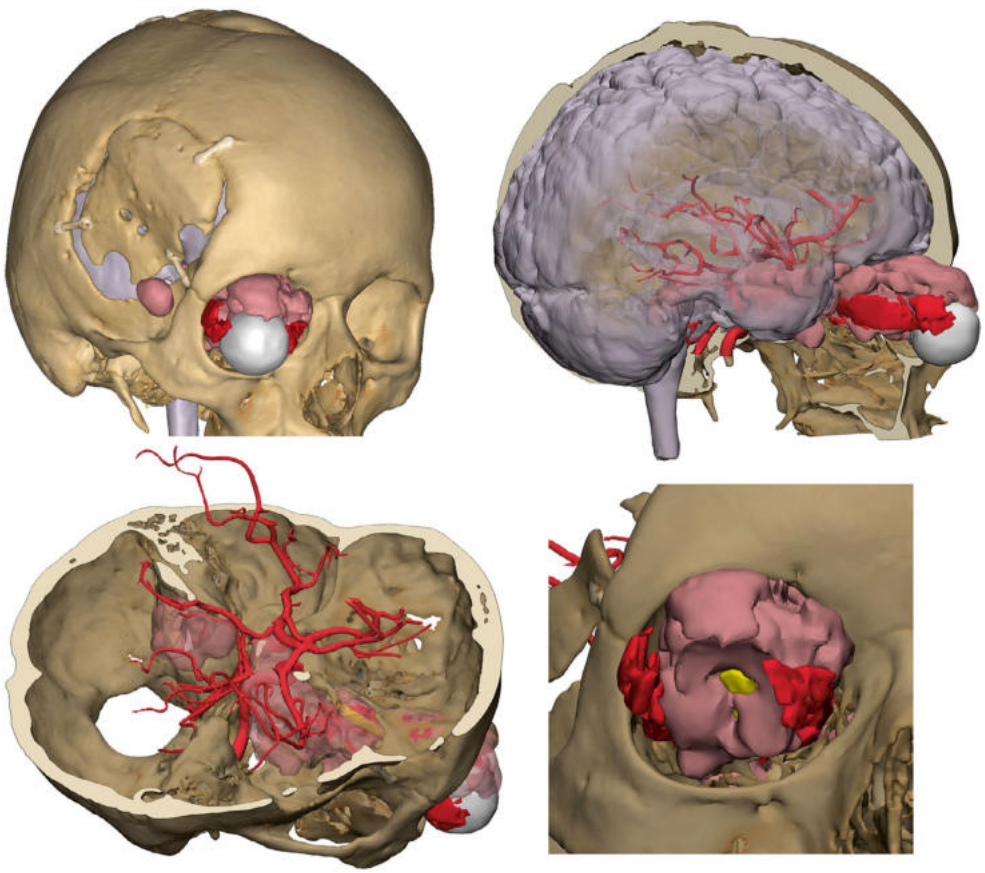


Fig. 20 VSP enlights the extension of a plexiform schwannoma of the orbit invading the intracranial space. Relationships with the optic nerve and the intracranial vasculature are elucidated

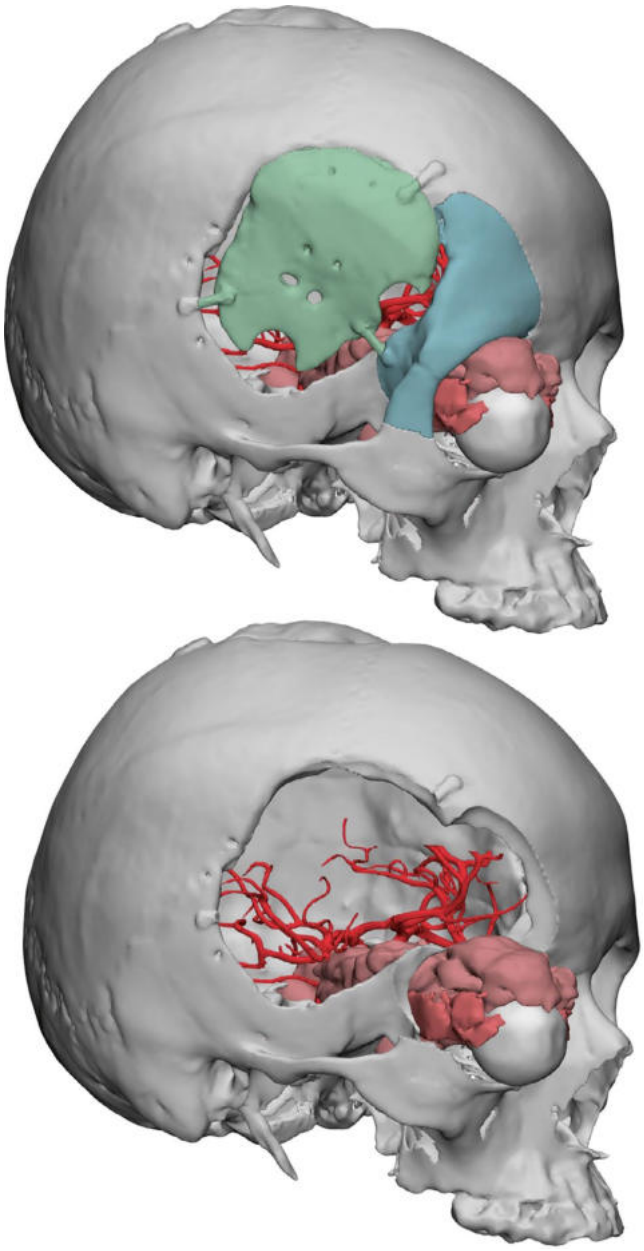


Fig. 21 As the lesion was originally approached through a pterional approach, an extended fronto-lateral marginotomy joining to the pterional operculum was planned and the resulting field was wide enough to satisfactorily expose the lesion. Radical excision was not possible as the lesion grew around the Willis polygon

6.1.3 Surgery

A hemicoronal access was used to approach the superior-lateral orbital rim, including the region of the previous skull flap in the temporal region. The periosteum was incised, and bone surfaces were exposed. Under navigational guidance (Fig. 5), a piezosurgical osteotomy of the lateral orbital rim, extending more upwards in the lateral part of the frontal bone, was performed. The most anterior part of the calvarial bone flap was cut and excised to enhance visibility. The orbital roof was disassembled from the orbital rim and removed. Superior and medial rectus muscles were isolated using a surgical loop. The mass was excised in a piecemeal fashion within all the intraorbital space until the desired debulking was achieved. After orbital mass resection, the wide corridor between the orbit and the middle skull base was used by the neurosurgeon to dissect the intracranial component. The orbital roof was reconstructed using a titanium mesh fixed to the lateral orbital rim and repositioned together with the lateral marginotomy (Fig. 22).

6.2 Case 2: Atypical Meningioma of the Orbit with Intracranial Involvement

6.2.1 Clinical History

A very similar case presented to our clinical attention for deforming bulbar proptosis. The patient had already undergone a previous neurosurgical operation to excise brain tumor, followed by a relapse. In this case, the patient had lost sight in the right eye and required a debulking surgery to improve her quality of life. Due to the histology of the tumor, in this case an additional neurosurgical procedure was not indicated, but only the maxillofacial intervention aiming to decrease the pathological tissue within the orbital space [11]. Virtual surgical planning workflow was exactly the same as the previous case (Fig. 23).

6.2.2 Surgery

A Stallard incision starts as a superior eyelid approach and continues as a “lazy S” curve in a skin fold in the lateral eye region. Dissection underneath the orbicularis oculi muscle

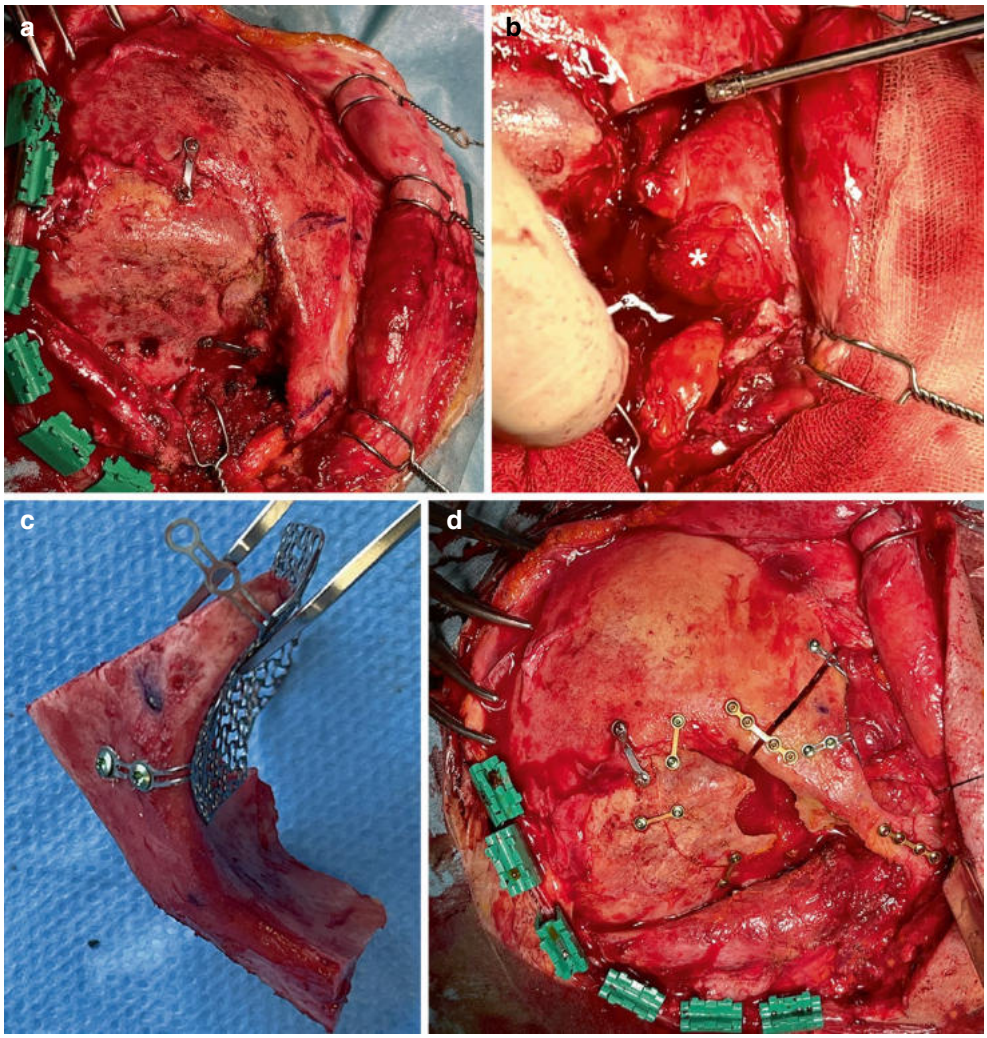


Fig. 22 (**a**) exposure through a coronal approach; (**b**) fronto-lateral marginotomy is removed and plexiform schwannomas are seen; (**c**) repositioning of the fronto-lateral orbital rim is associated with an orbital roof reconstruction; (**d**) bone flaps are repositioned back in place

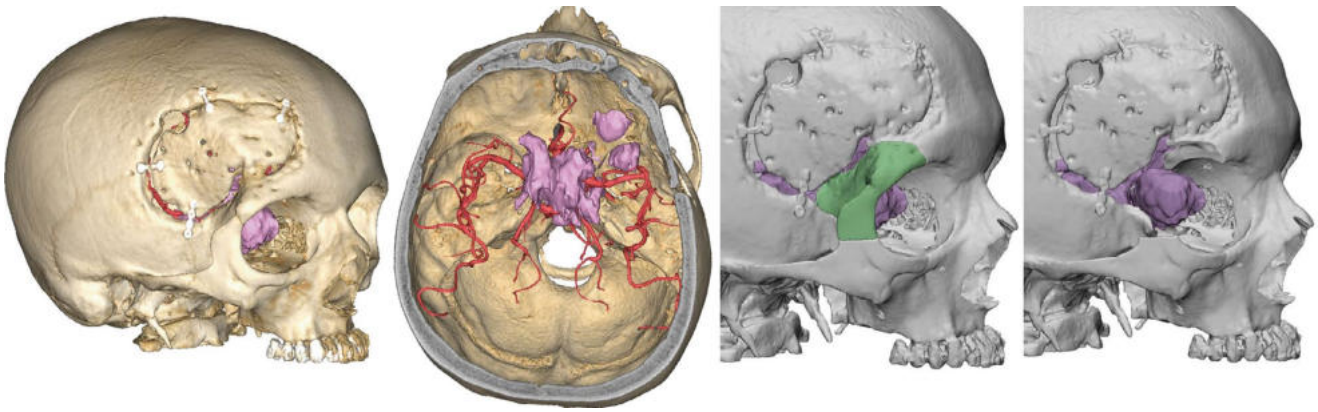


Fig. 23 A similar case showing an atypical meningioma causing the posterior invasion of the orbit with significant exophthalmos. As it was a palliative surgery, the extent of decompression was limited to the orbital disease. The Willis polygon was circumferentially invaded. A lateral marginotomy enabled to uncover the lesion located at the orbital apex

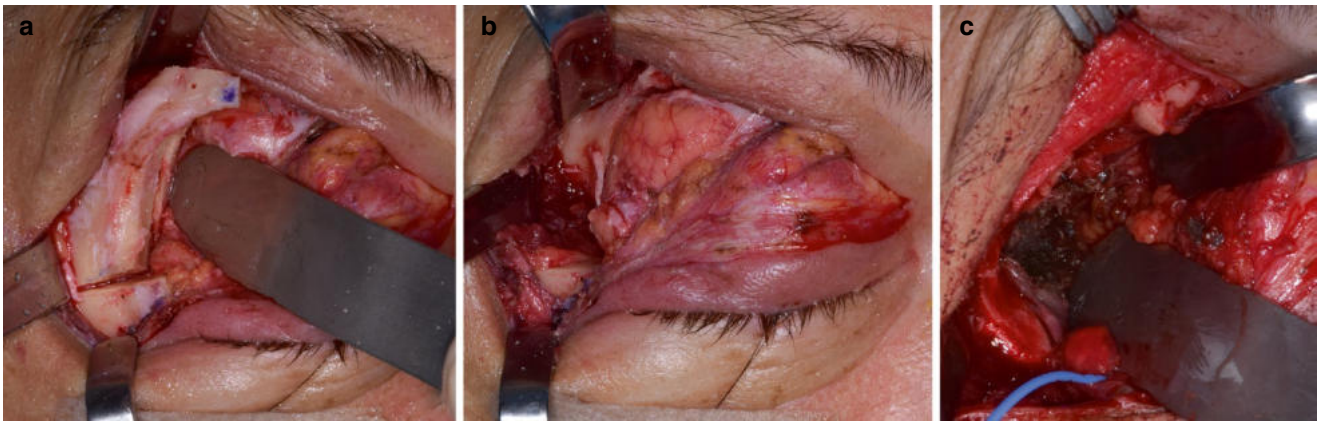


Fig. 24 A minimal invasive approach was used to expose the lateral orbital rim and perform a lateral marginotomy to excise the lesion

was performed, and the periorbital space was entered, revealing exuberant tissue of fleshy consistency spreading behind the eye globe. A navigated lateral marginotomy with plate prebending was performed, uncovering the prolapsing tumor tissue. The eye globe was gently retracted, and the optical nerve clamped and sectioned due to the preexisting blindness of the patient. This maneuver enabled to expose all the posterior orbit around the apex, maximizing tumor excision (Fig. 24). The lateral orbital rim was repositioned with prebent plates.

7 Multifocal Orbital Masses

In general, ISOLs present as unique, well-defined lesions, which can be distinctly localized within the orbital space and targeted for excision using a single orbital approach. In rare circumstances, due to the biology of disease or previously failed attempts of surgical excision, the mass might present as multiple nodules localized in multiple orbital compartments, which require combination of several surgical approaches while maintaining at the same time a radical intent with reduced invasiveness. In such cases, targeting the disease spots makes it indispensable the use of navigated virtual surgical planning [12].

7.1 Relapsed Pleomorphic Adenoma of the Lacrimal Gland

7.1.1 Clinical History

A 49-year-old lady presented for clinical attention following multiple excisions of a lacrimal gland pleomorphic adenoma. During yearly follow-up MR scans, a multifocal relapse of the disease was intercepted, with localizations in the superior-lateral orbit, corresponding to the site of the lacrimal gland, as well as in multiple nodules in the superior eyelid and the lateral canthal region; moreover, a localization was found in the infratemporal fossa medial to the coronoid process of the mandible.

7.1.2 Virtual Surgical Planning

The patient underwent a novel MR and CT with parameters suitable for the reconstruction of a virtual anatomical model of the orbit, and the following structures were reconstructed: adenomatous nodules, each one being numbered to be easily targeted during surgery; extraocular muscles, including recti and obliqui; optic nerve; eye globe, and temporalis muscle, in whose thickness the nodules located in the infratemporal fossa (5) were partly included. Given the complexity of anatomical reconstruction and the high number of nodules to be identified, coregistration proce-

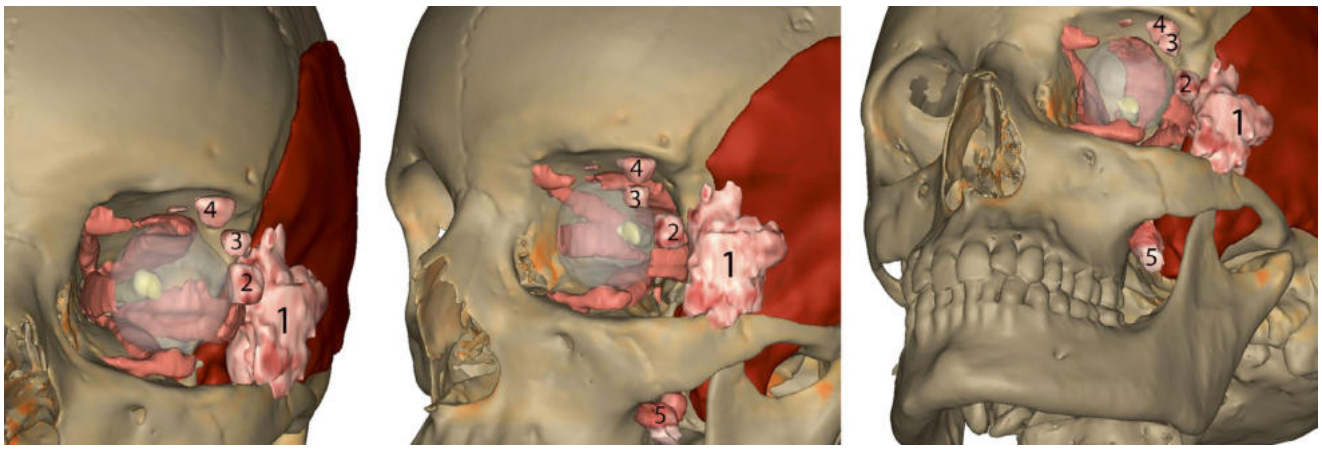


Fig. 25 Multifocal disease with multiple disease nodules in a case of relapsed pleomorphic adenoma of the left lacrimal gland. Nodule 1 is the largest and localized in the infratemporal fossa, nodules from 2 to 3 are in the orbital pre and retroseptal space, nodule 5 is in the pterygo-maxillopalatine fossa

dures between CT and MR were crucial (Fig. 25). As the lateral orbital rim presented interrupted owing to previous surgery with a lateral marginotomy, without repositioning of the bone segment, in this case there was no need to simulate any osteotomy. All nodules, whose localization was thoroughly studied in the virtual plan, were exported, together with virtual anatomy, in the navigation plan to be easily targeted during surgery.

7.1.3 Surgery

All multifocal localizations of disease were preoperatively marked by navigating over the skin and contouring the area using a dermographic pen. To excise the five nodules, multiple approaches were planned:

- A hemicoronal approach to excise the most conspicuous nodule in the infratemporal fossa.
- Conjunctival limbus approaches, performed by the ophthalmologist, for nodules in contact with the eye globe.
- A superior eyelid crease approach was adopted to excise the nodules located just beyond the plane of the orbicularis oculi muscle.
- An intraoral approach to the mandibular ramus and coronoid process was used to remove the nodule in the retromaxillary space.

For each surgical step, navigation proved to be essential in localizing the nodules and allowing for effective excision of nodules involving the minor morbidity possible (Fig. 6). The resection was performed as a unique block specimen (Fig. 26).

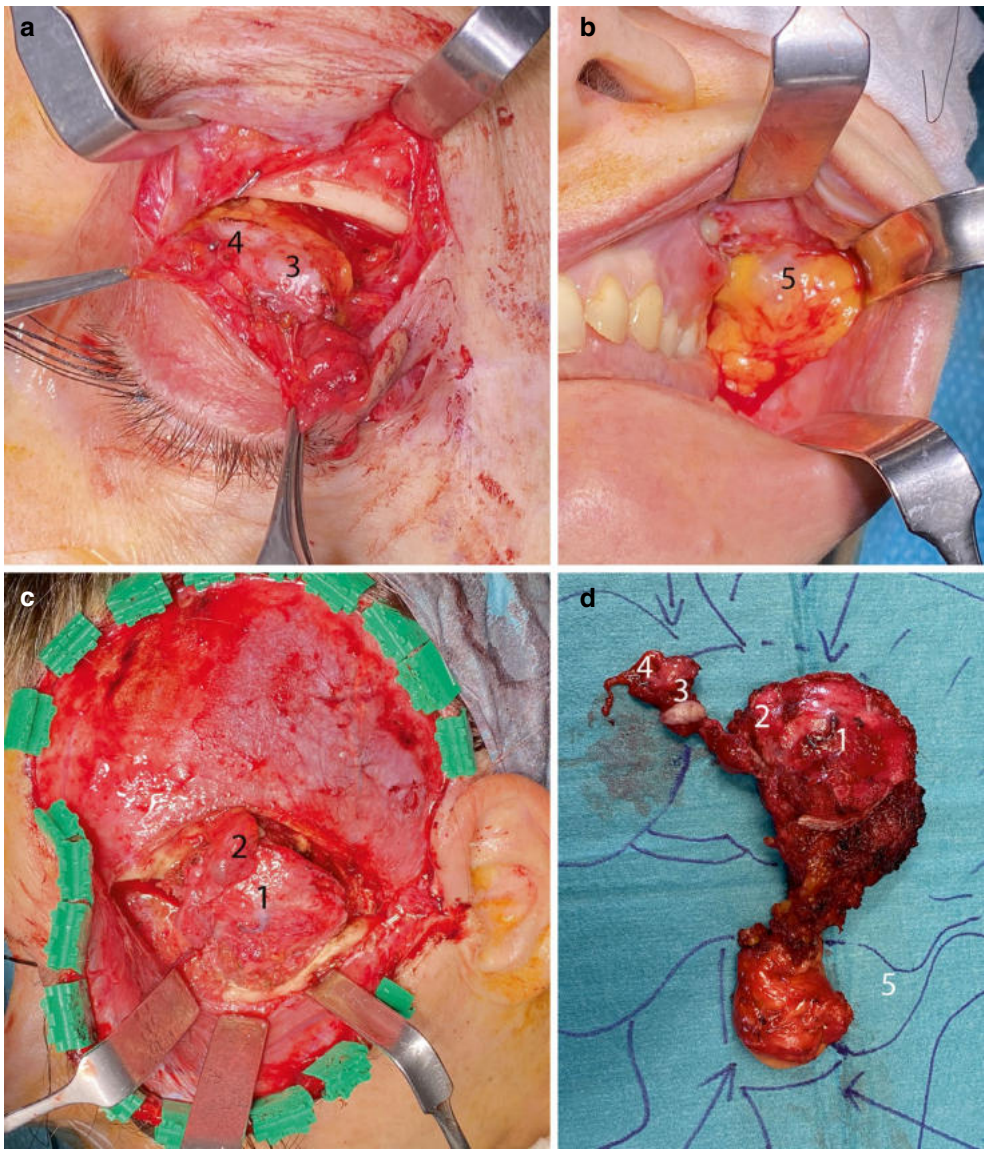


Fig. 26 (**a**) superior eyelid approach to intraorbital nodules; (**b**) intraoral approach to retromaxillary nodule; (**c**) hemicoronal approach to infratemporal fossa; (**d**) en bloc resected specimen for radical resection

8 Orbitofacial Resection

Orbitofacial resection is a particular subtype of craniofacial resection performed for advanced-stage malignant disease invading the orbit. This approach involves resecting facial parts contiguous to the orbital region, which may include maxillary bone, anterior skull base, zygomatic bone, and nasal vault. Compared with a classical craniofacial resection, it lacks traditional transfacial approaches and is more confined to the orbital region. This surgical procedure can be significantly improved in its accuracy with a virtual model corresponding to the clinical case and brought to the OR through navigation.

8.1 Squamocellular Carcinoma Invading the Anterior Skull Base and Extending Through the Orbit to the Apex

8.1.1 Clinical History

A 67-year-old patient complained the progressive onset of diplopia, followed by a loss of visual acuity. After several weeks, his sight was dramatically compromised, and his ophthalmologist prescribed MR examination, revealing the presence of heterotopic tissue, with pathological enhancement, from the skin of eyelids up to the optic nerve. The patient was studied with an additional CT, which confirmed the bony erosion on the medial wall and orbital roof of the

orbit, highly suspicious for a malignant process. An incisional biopsy conducted transconjunctivally confirmed the diagnosis of squamocellular carcinoma of the orbit, for which orbital exenteration with selective wall resection was planned [13, 14].

8.1.2 Virtual Surgical Planning

Coregistration between CT and MR was carefully accomplished, including an isotropic VIBE sequence and 0.3 mm-sliced TOF sequence. This enabled to segment all structures concurring to represent the patient-specific virtual replica. In particular, a highly detailed model including skin, subcutis, craniofacial skeleton, eye globe, extraocular muscles, optic nerve, and tumor was constructed in Mimics v.26. In this case, care was taken to reconstruct the skin as well as the anterior margin of the tumor showed its infiltration; thus, simulated resection had to take into account part of the skin in the final surgical specimen (Fig. 27). The tumor showed deep invasion up to the orbital roof and down to the orbital floor and medially, the lamina papyracea: these features were important to highlight simulated marginotomies, which were simulated as follows (Fig. 28):

- A strategic lateral marginotomy was simulated, as shown previously, with the intent to enable the outward shift of the eye globe and provide the necessary space for surgical maneuvers in the medial wall;
- A superior marginotomy enabled access to the orbital roof, which had to be included in the resection specimen owing to its infiltration;
- An inferior marginotomy, combined with a medial wall resection including the lacrimal crest, represented the inner limit of resection of the tumor that lied over the lamina papyracea.

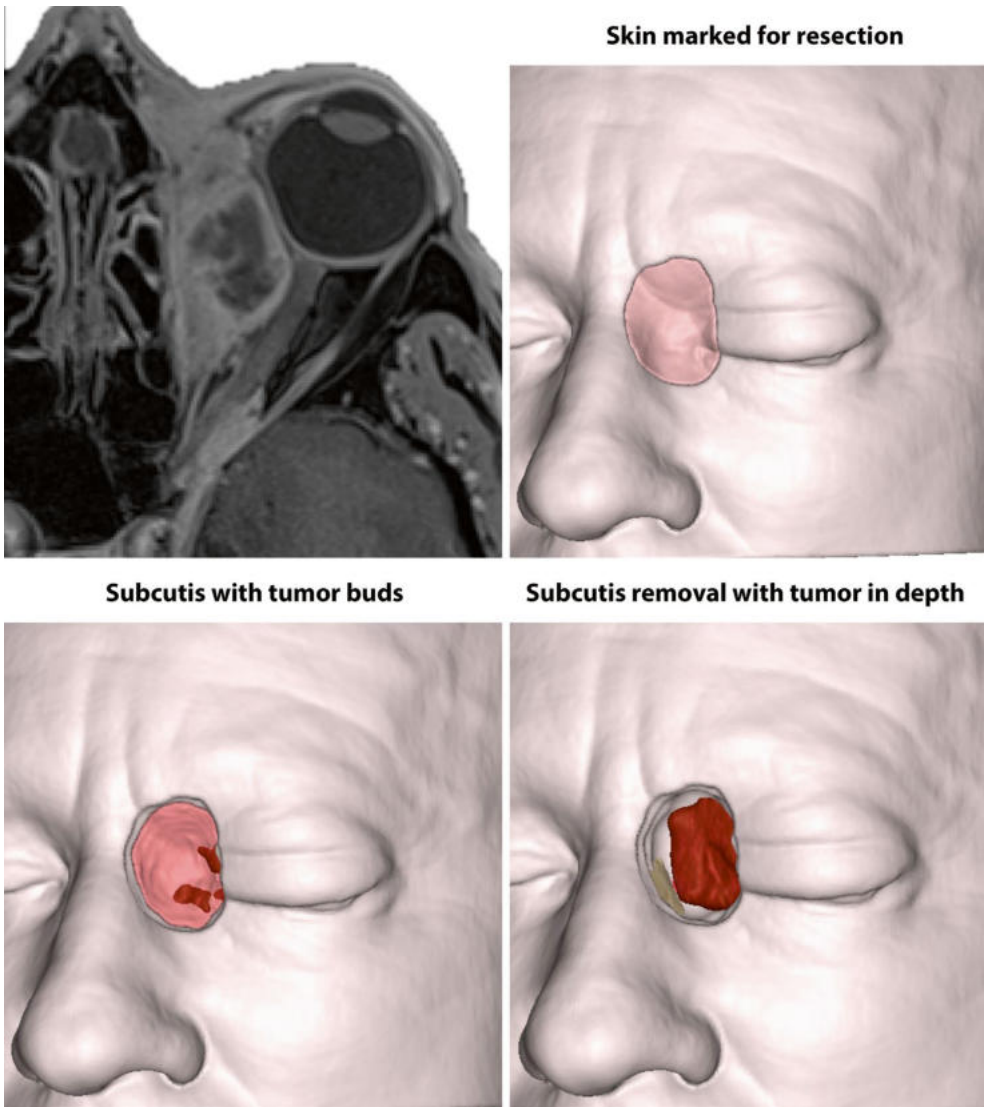


Fig. 27 Case of squamous cell carcinoma of the left orbit invading the skin. VSP panels show a skin resection planning, including the subcutis. Tumor buds are visible in depth beyond skin resection

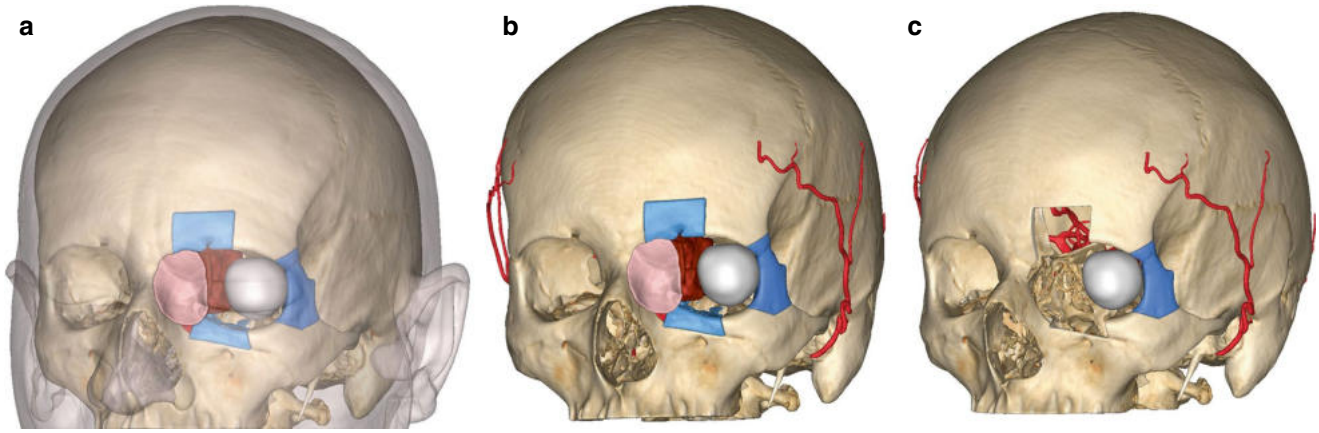


Fig. 28 VSP of skin resection associated to bone resection for the orbital roof, the medial wall, and the inferior orbital rim. A strategic lateral marginotomy is performed to widen the operative space

8.1.3 Surgery

Surgery was performed gaining exposure of the superior and lateral orbital wall using a hemicoronal approach and surrounding the eye globe to resect with a superior and inferior transconjunctival access. Bone marginotomies were performed under navigational guidance to access deep compartments, including the lateral marginotomy, first performed, to luxate laterally the eye globe and perform the medial wall osteotomy, extending from the nasal bones to the midpoint between anterior and posterior ethmoidal artery. From the superior ostectomy, the roof osteotomy was performed and conjoined with the medial wall resection. The intraconal compartment, enclosed within the periorbita, was mobilized, and the optic nerve was transected. The full specimen was delivered to histopathological assessment, and its boundaries were compared with those defined in the VSP (Fig. 29). The orbito-cranial communication was sealed using a dural substitute and fibrin glue to prevent leakage of CSF (Fig. 30). Tarsal plates were sutured to close the anophtalmic cavity. After surgery, the patient underwent adjuvant proton therapy to sterilize the surgical field.

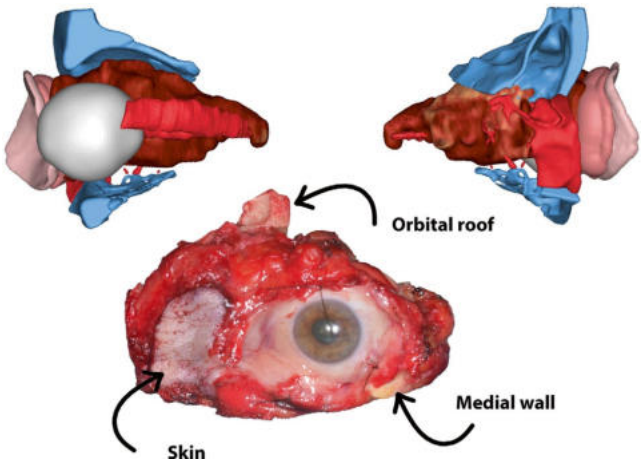


Fig. 29 VSP specimen compared to the intraoperative specimen including eye, superior rim and roof, inferior rim, and medial wall

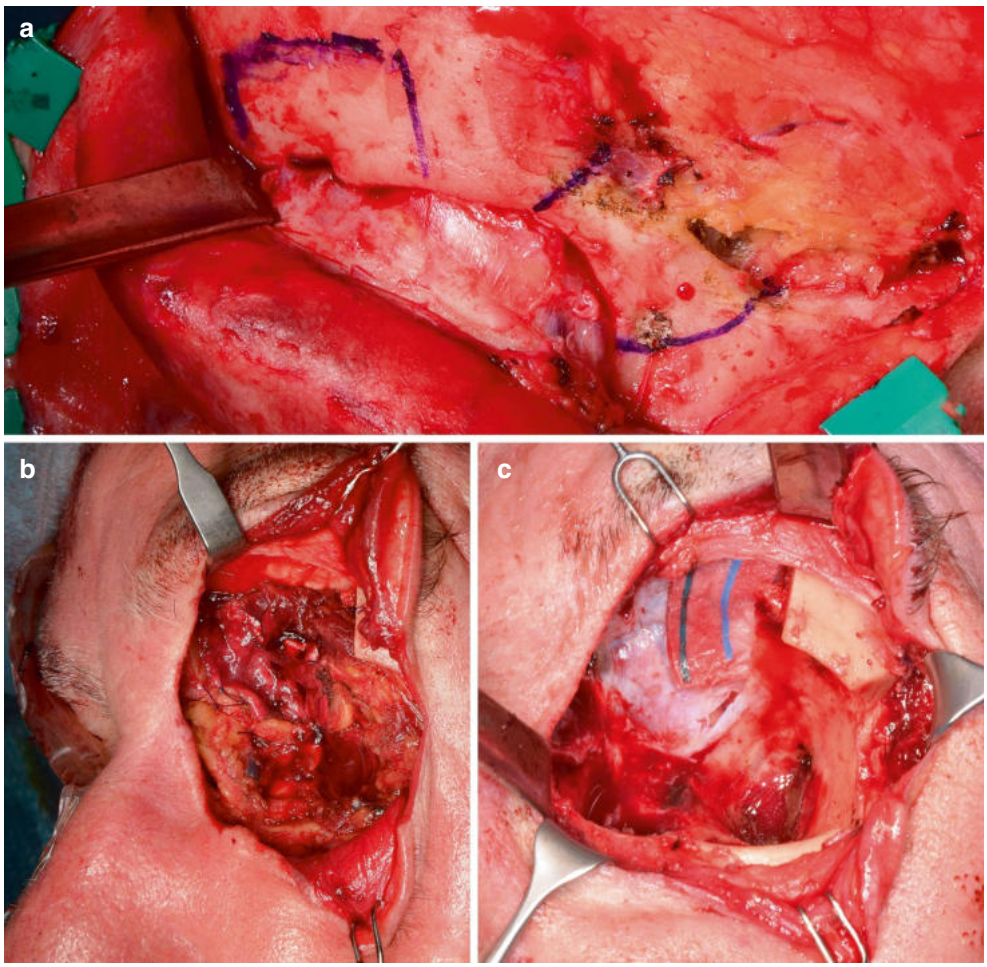


Fig. 30 (**a**) osteotomies are designed under navigation guidance; (**b**) post resection cavity with wide breach over the orbital roof; (**c**) anterior skull base reconstruction using a dural substitute

References

1. Tel A, Murta F, Sembronio S, Costa F, Robiony M. Virtual planning and navigation for targeted excision of intraorbital space-occupying lesions: proposal of a computer-guided protocol. Int J Oral Maxillofac Surg. 2022;51:269–78.
2. Kim Y-S, Moon K-S, Kim G-W, Lim SC, Lee K-H, Jang W-Y, Jung T-Y, Kim I-Y, Jung S. Role of craniofacial resection for malignant tumors involving the anterior skull base: surgical experience in a single institution. Brain Tumor Res Treat. 2015;3:81.
3. Schreurs R, Baan F, Klop C, Dubois L, Beenen LFM, Habets PEMH, Becking AG, Maal TJJ. Registration-free workflow for electromagnetic and optical navigation in orbital and craniofacial surgery. Sci Rep. 2021;11:18080.
4. Campbell AA, Mahoney NR. Use of computer-assisted surgery in the orbit. Orbit. 2022;41:226–34.
5. Khan RI, Golahmadi AK, Killeen RP, O'Brien DF, Murphy C. Image-guided navigation in posterior orbital tumour surgery: a comparative cohort study. Orbit. 2024;43:566–75.
6. Ali MJ, Naik MN, Kaliki S, Dave TV, Dendukuri G. Interactive navigation-guided ophthalmic plastic surgery: the techniques and utility of 3-dimensional navigation. Can J Ophthalmol. 2017;52:250–7.
7. Sullivan WG, Kawamoto HK. Periorbital marginotomies: anatomy and applications. J Craniomaxillofac Surg. 1989;17:206–9.
8. Tel A, Arboit L, Sembronio S, Costa F, Nocini R, Robiony M. The transantral endoscopic approach: a portal for masses of the inferior orbit—improving surgeons' experience through virtual endoscopy and augmented reality. Front Surg. 2021;8:715262.
9. Shapira Y, Juniat V, Dave T, et al. Orbito-cranial schwannoma-a multicentre experience. Eye (Lond). 2023;37:48–53.
10. Strianese D, Mariniello G, Lorenzetti M, Maiuri F. The lateral orbito-cranial approach. In: Bonavolontà G, Maiuri F, Mariniello G, editors. Cranio-orbital mass lesions: diagnosis and management. Cham: Springer International Publishing; 2023. p. 83–7.
11. Agosti E, Zeppieri M, De Maria L, et al. Surgical treatment of spheno-orbital meningiomas: a systematic review and meta-analysis of surgical techniques and outcomes. J Clin Med. 2023;12:5840.
12. Orbital Tumors—Clinical, Radiologic and Histopathologic Correlation. https://www.mdpi.com/2075-4418/12/10/2376. Accessed 19 Jan 2025.
13. Martel A, Baillif S, Nahon-Esteve S, Gastaud L, Bertolotto C, Lassalle S, Lagier J, Hamedani M, Poissonnet G. Orbital exenteration: an updated review with perspectives. Surv Ophthalmol. 2021;66:856–76.
14. Malik M, Vahdani K, Rose GE, Daniel C, Uddin JM, Verity DH, Collin JRO. Orbital exenteration for advanced periocular adnexal malignancies: curative versus palliative surgical intent. Ophthalmic Plast Reconstr Surg. 2022;38:387–92.

Computer-Guided Orthognathic Surgery: State of the Art and Innovation

Alessandro Tel, Tong Xi, and Massimo Robiony

1 Introduction

Orthognathic surgery represents perhaps the most characterizing surgery in the field of maxillofacial surgery. Moreover, it includes the most standardized workflow that has brought orthognathic surgery virtual surgical planning (VSP) also among the less experienced users [1]. This is due to the following reasons:

- Highly sequential surgery with reproducible osteotomies
- Easy, threshold-based segmentation of skeletal bases, and no need to reconstruct soft-tissue volumes except for the facial soft tissue, which can be easily acquired from CT itself of facial scanning
- Need for high precision in reproducing the desired occlusion with planned movements, as each millimeter can have a substantial impact on both functional and esthetic outcomes
- Very easy and scalable surgical planning: osteotomies are linear and can be performed by joining points placed by the user; movements can be chosen from a visual interface implementing simple commands for each spatial direction
- Creation of surgical splints that can be manufactured in-house using commercially available 3D printers
- Entirely incorporated within single software packages available for clinicians and which do not require any prior engineering or CAD knowledge background. This is not the case with other complex simulations including cranial reconstruction, orbital surgery and trauma.

This chapter will focus on the methodology of virtual surgical planning in orthognathic surgery, describing the key sequence ideal to achieve a predictable and reproducible VSP. Emphasis will be placed in reinforcing the connections between virtual actions and their impact on the final outcome of the patient, through a sophisticated cephalometric analysis. The following chapter will demonstrate the application of this methodology in a multitude of clinical scenarios.

2 Prerequisites for Computer-Guided Orthognathic Surgery

Compared with other simulated surgical procedures that traditionally require exclusively to import DICOM data of volumetric imaging, orthognathic surgery needs the following items in order to be performed:

- CT scan: Differently from other surgeries, for orthognathic surgery the patient often undergoes a cone beam CT scan (CBCT). Cone beam CT scan is a volumetric imaging, but it is performed using a low voltage, which is particularly suitable for younger patients. However, compared with traditional multidetector CT (MDCT) usually performed in a hospital setting, CBCT provides a slightly inferior image quality, often presenting a "patchy" texture in the background, as the result of the different features of the x-ray beam implemented. Moreover, traditional Hounsfield Units (HU)-based thresholding intervals for segmentation of bone in MDCT are not applicable to CBCT. Thus, discrimination between bone and nearby tissues is less efficient; moreover, thin or cancellous-bone

A. Tel (✉)
Lead Specialist for VSP and 3DP, Maxillofacial Surgery Clinic, Head & Neck and Neuroscience Department, Academic Hospital of Udine, Udine, Italy
e-mail: alessandro.tel@uniud.it

T. Xi
Oral & Maxillofacial Surgery, Radboud university medical center, Nijmegen, The Netherlands
e-mail: Tong.Xi@radboudumc.nl

M. Robiony
Chief of Maxillofacial Surgery Clinic, Director of the Postgraduate School in Maxillofacial Surgery, Chief of Head & Neck and Neuroscience Department, Academic Hospital - University of Udine, Udine, Italy
e-mail: massimo.robiony@uniud.it

© The Author(s), under exclusive license to Springer Nature Switzerland AG 2025

A. Tel, M. Robiony (eds.), *Atlas of Virtual Surgical Planning and 3D Printing for Cranio-Maxillo-Facial Surgery*,
https://doi.org/10.1007/978-3-031-94495-6_16

structures, such as orbital walls, condyles and the posterior regions of the maxilla, are often inadequately captured by the thresholding because the intrinsic contrast of voxels is overall inferior. CBCT should include in its acquisition field the orbital region down to the menton (ME) point, extending posteriorly to include both temporomandibular joints. The protocol for CBCT scan should include a 512 × 512 px matrix and a 0.6 mm slice thickness. The CT has to be performed while keeping the condyle in centric relationship, preferably with closed mouth and maximized intercuspation or eventually by interposing a thin wax layer to create a minimal intercuspal disclusion, which does not affect significantly centric relationship and facilitates the separation of dental arches in VSP.

- Dental models: The second essential prerequisite to perform an orthognathic surgical planning is the availability of models of dental arches. Depending on the orthodontist, the patient might arrive to the surgeon with physical plaster models or an intraoral scan.
  - Physical plaster models are yielded by pouring plaster within an alginate impression taken from the patient. They have the advantage to convey the sensation of occlusal stability by placing dental cusps into optimal engagement (intercuspation). The drawback is that such models need to be digitized, can be lost or subject to rupture. Their overall quality is inferior to acquisition using a dental scanner (Fig. 1). Moreover, to replicate the preoperative occlusion, the acquisition of an occlusion wax is necessary.
  - Intraoral scanning is performed using a scanner whose tip can be easily inserted within the oral cavity, and it contains a system of deflection mirrors to capture the shape of each dental cusp from different angulations. Intraoral scanners are based on pulses of a structured light beam, which is reflected and captured by a sensor. The time of reflection of light across each point of the surface is converted into a geometrical output, retessellated and rendered as an STL file compatible with design software. This method can prescind from an occlusion wax because the software is able to acquire the digital landmarks for habitual occlusion and transfer them to the dental arches STLs (Fig. 2). Before the advent of automatic surgical occlusion algorithms, it was hazardous to search for a stable occlusion using only digital models.
  - A mixed solution consists in taking the digital teeth impressions using an intraoral scanner, 3D printing the models and put them manually in the desired surgical occlusion (Fig. 3). This method combines the versatility and safety of an entirely digital workflow with the tactile sensation and the perception of occlusal stability that the intercuspation of plaster models provides. Once the physical occlusion is determined, the intraoral scanner can be used to acquire a registration mask on the plaster models, which is then imported in the virtual project and used to align the intraoral scans of the superior and inferior arched previously acquired. This third solution is useless if virtual occlusion is used.

Additional data can be imported in the virtual project to improve the final virtual plan:

- Soft tissue model: A full volumetric reproduction of soft tissues, yet static, is essential for certain phases of VSP, including natural head positioning, midline evaluation and postsimulation morphing. It is generally achieved through segmentation of CT scan, but it can be substantially improved using a facial scanner. Using a structured light beam, it collects a point cloud, which can then be tessellated into a geometrical triangulated file stored as an STL or OBJ files, or in the more advanced PLY format, which can store information about colors, surface normals and texture coordinates.



Fig. 1 Scanned plaster models taken through alginate impressions are used to determine the most stable intercuspation. Occlusion is scanned and imported in the VSP software

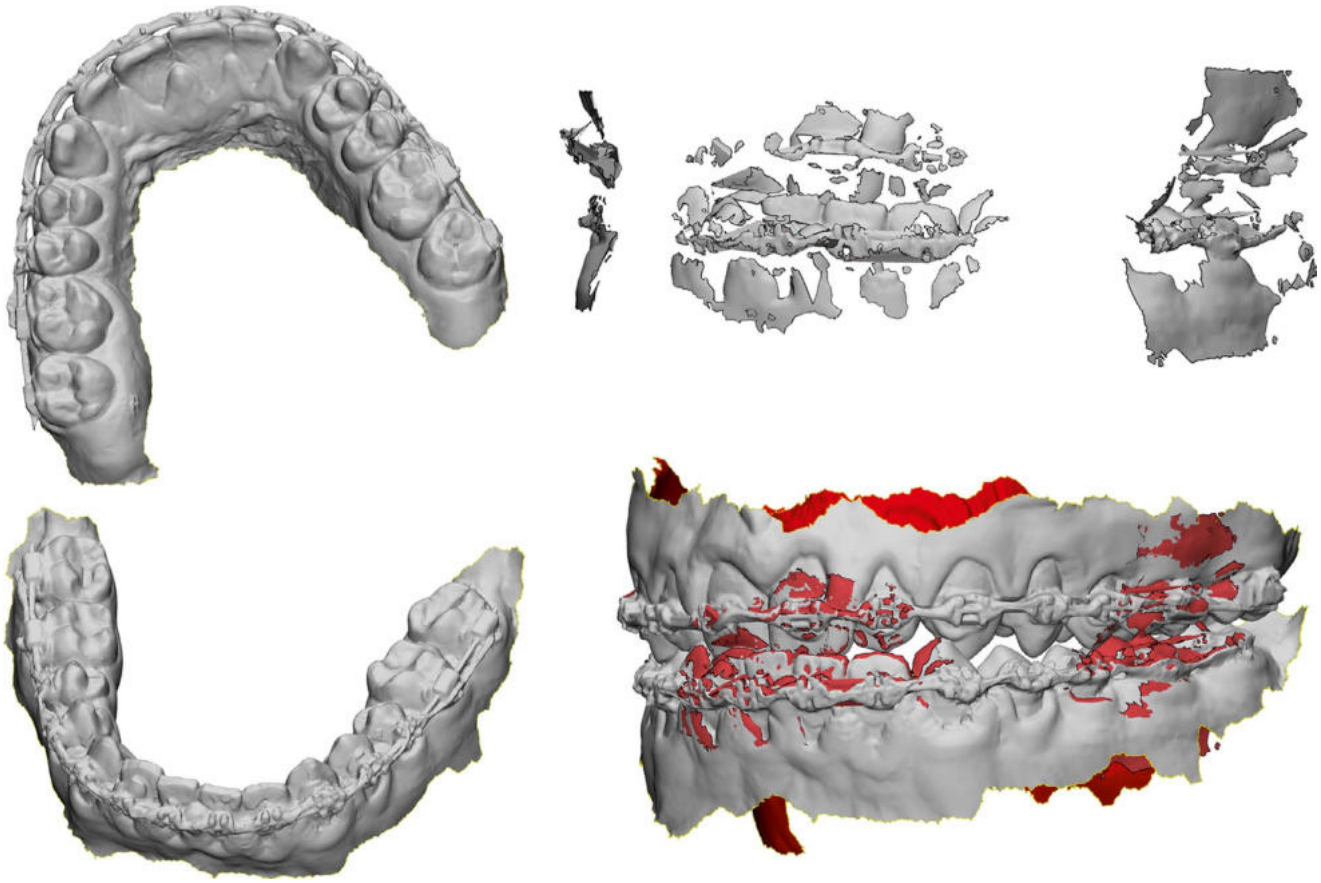


Fig. 2 Intraoral scan shows a consistently higher detail. A registration mask can define the reciprocal alignment of scanned arches



Fig. 3 3D printing of scanned impressions is used to manually determine the most stable occlusion, which is then rescanned and imported in the VSP

Similar sources can be represented by 3D photography or stereophotogrammetry. However, in the majority of cases, a satisfactory CT scan, both MDCT or CBCT, can provide a trustful representation of soft tissue anatomy.
- Airway model: The posterior air space is reconstructed in case a functional evaluation is needed. This is most often performed in cases of severe micrognathia or obstructive sleep apnea.

3 Sequences of Phases for Orthognathic Surgical Planning (Simple Bimaxillary Surgery)

Although the sequence of phases for virtual surgical planning can slightly vary between different software, considering the tendency of newer software to be more "clinician friendly", it is possible to identify a uniform workflow. Due to its widespread presence in hospitals and mentions in scientific literature, in this chapter the Author will describe the basic workflow in the software ProPlan CMF v.3, and its successor, Mimics Enlight (Materialise NV, Leuven, BE).

3.1 Segmentation, Mask Cleanup and Refinement

As previously explained, CBCT are suboptimal compared to MDCT, and a basic segmentation using a single thresholding algorithm would yield models unsuitable for virtual surgical planning (Fig. 4). Starting from the concept that average threshold values for Hounsfield Units are not applicable to CBCTs, and that the intrinsic contrast is lower due to an increased partial volume effect in CBCTs, there are several problems generally encountered [2]:

- CBCT underestimates regions with a predominance of cancellous or rarefied bone, typically in the mandibular condyle and in the posterior sectors of the maxilla, in the tuber region.
- CBCT underestimates regions with thin bone, in particular the nasal cavity, the orbital walls and the palatine bones and pterygoid plate regions due to an increased partial volume effect. This underestimation is much more evident than in MDCT where likewise orbital walls often present interrupted.
- Radiological density of bone and certain regions of soft tissues might overlap: increasing threshold to reduce soft tissue interposition leads to a conspicuous loss of bone, while decreasing it to acquire thinner bone involves conspicuous overlap of non-skeletal voxels.
- Metal artifact is always present in orthognathic patients due to metal appliances used for orthodontic treatment.

Manual mask editing remains the mainstay of image processing to remove unwanted parts. Unfortunately, very few semiautomated tools can assist in this process, which is entirely user-dependent. A solution for loss of bone might be to apply different local thresholds, enabling diverse regions to be captured with different values. This is highly useful in the condylar region, given the importance in orthognathic surgery to visualize the condylar morphology and position. In this case, special segmentation brushes can assist the filling of voids in less radiopaque regions (Fig. 5).

Metal artifact is an always present issue in orthognathic surgical planning, as patients perform the preoperative CT for surgical planning at the end of orthodontic treatment with orthodontic appliances, whose metal component is responsible for X-ray scattering, evident on images as hyperdense beams producing disruptive artifacts on segmentation. Multiple solutions are available to solve this issue, including:

- use of a dual-energy CT machine with modulation of the X-ray energy over metal surfaces [3, 4]
- application of a metal artifact compensation filter, an image-editing feature available in Mimics software, which enables to process the DICOM dataset by applying a given algorithm to reduce the effect of artifact on surrounding anatomy

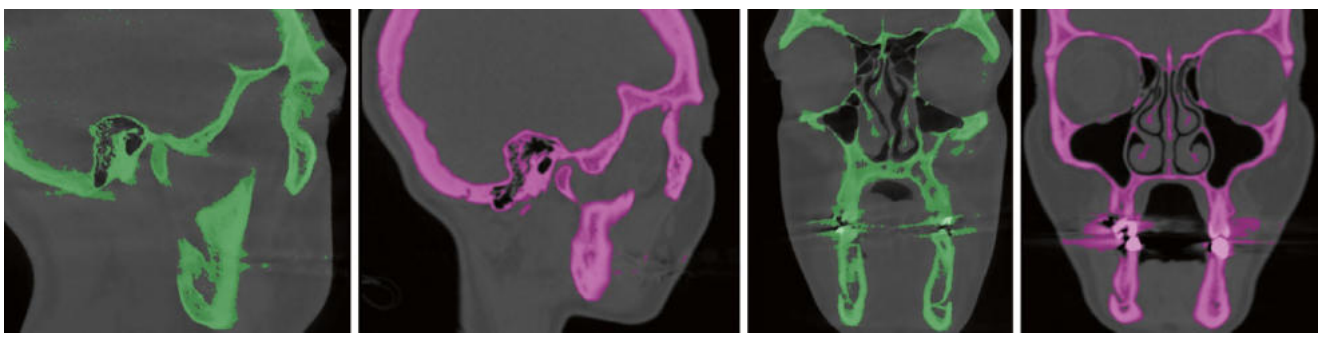


Fig. 4 Differences in bone segmentation by thresholding from a CBCT (green, suboptimal) and a MDCT (purple, optimal)

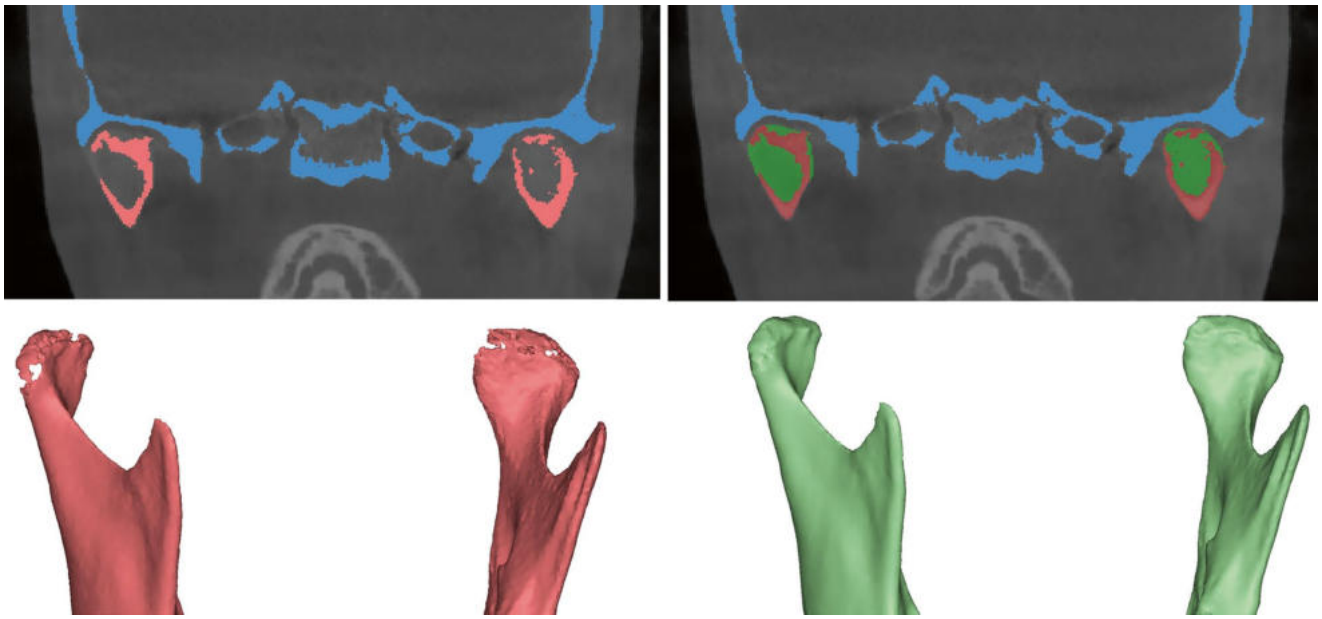


Fig. 5 Smart filling technique used to reconstruct voids in condylar morphology due to the predominantly cancellous structure of the mandibular condyle

- mask editing in correspondence of scattered beams, trying to eliminate them from the 3D models and preserving as much as possible the dental anatomy
- sculpting of the reconstructed polymesh with cleaning of geometry correspondent to scattering areas

It can be noted that the four methods intervene in sequential steps of the process (image acquisition, image editing, mask editing, polymesh editing).

In addition to skeletal model creation, it is advisable to create a segmentation mask for soft tissues. This is generally well achieved by setting a comprehensive threshold that captures the soft tissues and everything inside, except for the airways.

3.2 Separation of the Mandible from the Skull Base

The reconstruction of the 3D model yields a unique solid object, whether it is a segmentation mask or a polymesh, representing the skeletal anatomy of the patient. However, for orthognathic surgery to be simulated, it is essential to provide two distinct models for the skull/maxilla and for the mandible. As the software is unable to distinguish between each of them, it is essential that the user splits the geometrical entities across their reciprocal fusion points: temporomandibular joint and occlusal contacts.

The author suggests that the separation process is accomplished using segmentation masks and not polymeshes, yet it is theoretically feasible for both. Segmentation masks provide a much more flexible environment, where editing operations are easier and not linked to vertex separation. In particular, the splint mask tool designed in Mimics provides the fastest and most accurate solution, as the user defines few splitting interfaces in regions of anatomical contact (in this case, TMJ and dental cusps) and the software is able to interpolate very accurately the input over all slices of the DICOM stack, by recognition of anatomically distinct regions across radiotransparent lines (cusp-to-cusp contact, joint, suture between two bones). The result is the original mask being split in two, one for the mandible and one for the skull/maxilla, and the two masks can be tessellated into different polymeshes (Fig. 6).

3.3 Alignment and Merging of Dental Casts over Skeletal 3D Models

This step is essential because CT scan is not accurate enough to trustfully reproduce the detailed anatomy of dental cusps, in which even submillimeter particulars might have a clinically relevant outcome on the final occlusion. The solution for this problem is to use scanned dental anatomy and register it over the CT-derived 3D model. Scanned dental anatomy, as previously explained, can originate either from optical scanning of a plaster model taken from alginate impressions or can be the result of intraoral scanning, this latter method being the most accurate. Digital impressions are imported into the virtual planning software as STL files, and cusps are aligned with the teeth visible in the CT model using a point-to-point registration, which is then refined

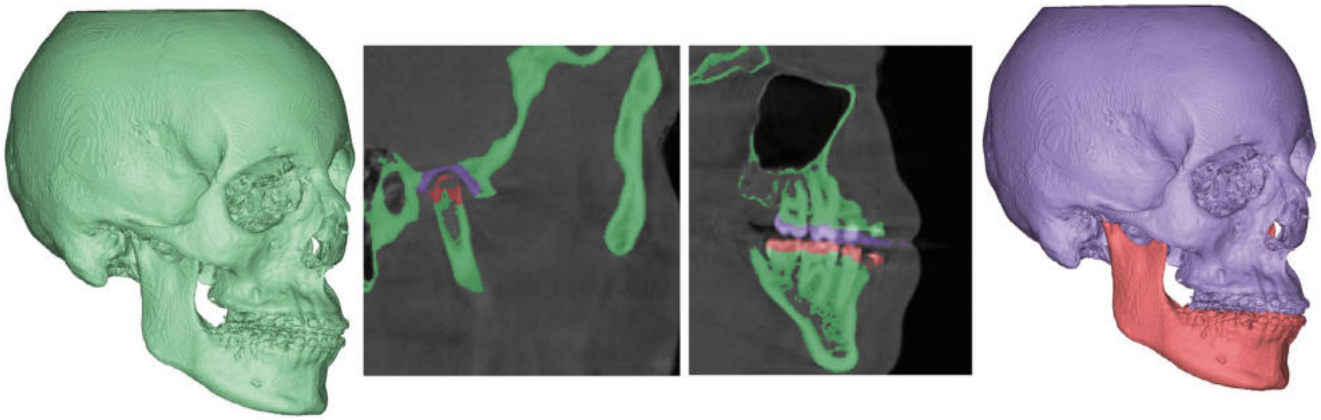


Fig. 6 Mandible separation using the mask split technique applied to contact points: the TMJ and occlusal surfaces

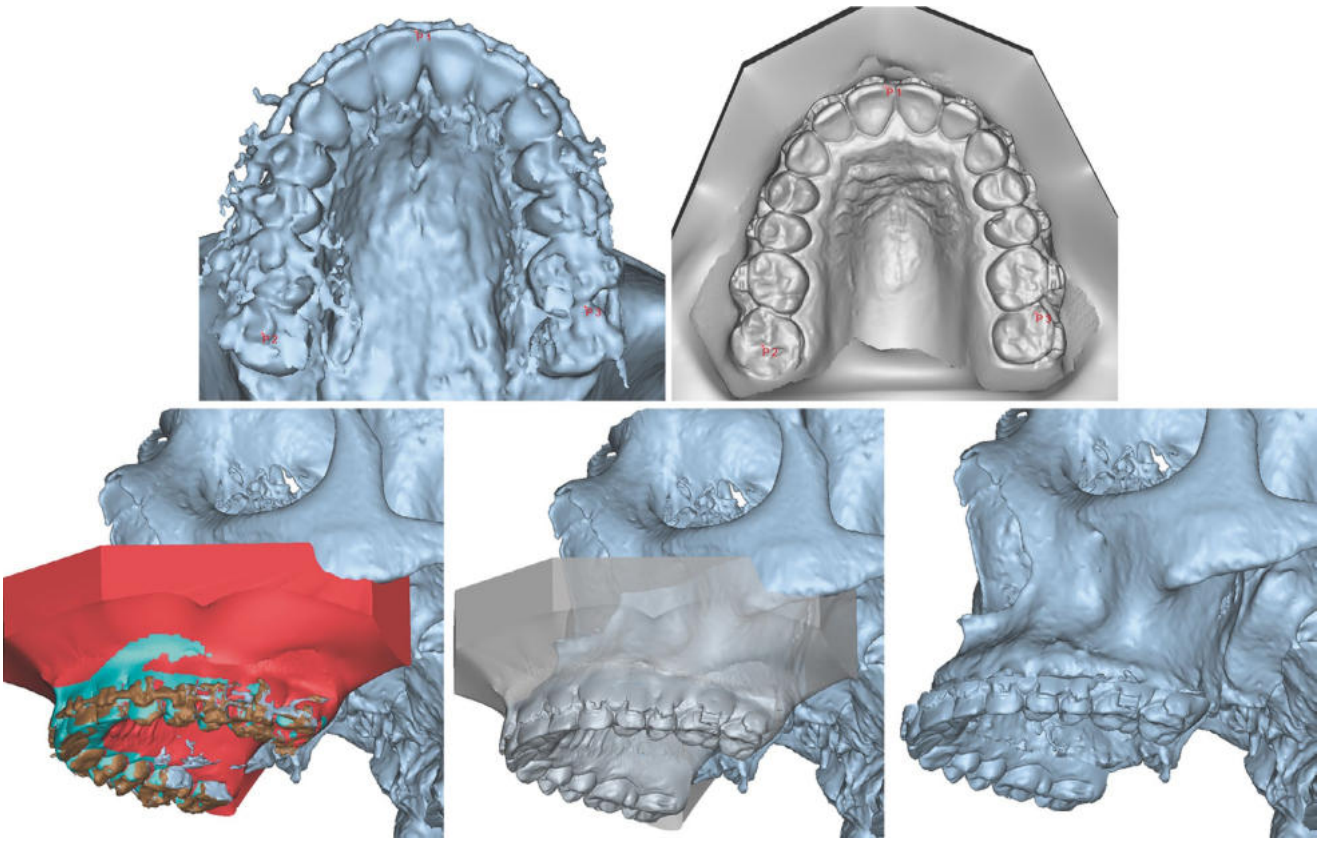


Fig. 7 Registration and fusion between skeletal model reconstructed from CT and scanned impressions (in this example, from plaster models). The less accurate the dental arch in the native CT model, the less performing the alignment process

using a global registration function based on the iterative closest point algorithm.

It is worth mentioning that the registration is performed between two geometrically very different objects, because dental arches reconstructed from CT are much rougher, often not all cusps are visible, and are impaired by the effect of metal artifact. Thus, the quality of the CBCT image is of prominent importance to find the exact matching points between CT cusps and their correspondent cusps on the scanned STL. Once the registration is complete, the software elaborates the merging of geometries, yielding a compound model, which reproduces skeletal surfaces but bears the teeth detail of scanned cusps (Fig. 7).

3.4 Head Orientation

Determining the correct natural head position (NHP) is still an unsolved issue [5–7]. NHP is highly variable between individuals due to a multitude of factors, including postural, proprioceptive, anatomical and psychological. Several methods are documented in the literature to replicate reliably the NHP within the VSP, including the acquisition of CT scan with fiducial markers and a laser to record the horizontal plane or the use of a digital gyroscope attached to a bite fork and a face bow, which provides the quantification of Eulerian angles (pitch, roll, yaw), which can then be transferred to the models.

In the absence of such technologies, NHP can be assessed through accurate photographic documentation. The most effective method to transfer it in the VSP includes the definition of a grid with a vertical axis and a horizontal axis. The horizontal axis should be maintained parallel to a less variable anatomical landmark. For this purpose, the author of this chapter adopts the supraorbital line, rather than the inferior orbital line, which can be more subject to variation especially in cases of skeletal asymmetry. However, it should be noted that severe asymmetries, especially craniofacial malformations requiring orthognathic surgery, might present considerable orbital dystopia affecting the supraorbital line as well. In such cases, more posteriorly placed landmarks should be considered, for instance, a line joining both mastoids. The alignment over the horizontal line accounts for the correction of the roll.

Pitch rotation can be defined by careful assessment of side photographs. Some postural behaviors might conceal the true NHP; for instance, it is common for III class patients with marked mandibular prognathism to elevate the chin in side view. The use of Frankfurt plane has the benefit of standardizing pitch angle but does not correspond to the truth. Therefore, it is advisable to manually remodulate head pitch with careful soft tissue model rotation searching the highest correspondence with clinical photographs.

Concerning yaw, this is probably the most difficult angle. Once roll is corrected, the vertical midline should be made coincident with the true soft tissue midline to evaluate the deviation of the superior interincisal line. This is achieved by correcting the yaw from the bottom view, ideally placing the vertical line as symmetry plane. This should in turn entail that the grid midline, shown in pink in the following illustrations, coincides with the facial midline. In cases in which a mismatch between the position of the soft tissue nasion and the midpoint of the superior labial philtrum, such as in cases of asymmetry, the latter should be preferred owing to its major impact on the patient's smile. In other circumstances, where a considerable lateral repositioning of the maxillo-mandibular complex is planned, the true facial midline might be considered the average between the soft tissue nasion and the midpoint of the superior labial philtrum.

Figure 8 shows the process of reorienting both the skeletal models and the soft tissue according to the NHP.

3.5 Creation of 3D Cephalometry

Once skeletal models with the detail of scanned dental anatomy are available as 3D polymeshes, it is important to determine three-dimensional cephalometric points at their $x_0y_0z_0$ values, which will be modified based upon the planned movements [8]. Software for orthognathic surgical planning generally facilitates this task (Fig. 9) and may incorporate a variety of cephalometric models that can be applied to the project, but the author of this chapter advises the following to be strictly taken into account in an orthognathic VSP:

- Points for dental exposure evaluation: UIL, UIR, UIM (Upper Incisor left, Right and Midline), UCL, UCR (Upper Canine Left and Right). Such points have a critical impact in determining the smile exposure of crowns and are primarily assessed for the esthetic evaluation.
- Points to determine posterior dental movements: 2UML, 1UML, 2UMR, 1UMR (Second and First Molar Left and Right). Such points enable to understand the effect of rotational movements over teeth, such as roll (cant) correction. They can be useful to assess the esthethics as well in the buccal corridors.
- Points to evaluate the skeletal movements of the anterior maxilla: A, ANS (Anterior Nasal Spine). They are useful to assess the effect of vertical movements (impaction) and pitch correction. Their values can be different from dental movements in case of clockwise/counterclockwise rotation.
- Points to evaluate the skeletal movements of the posterior maxilla: PNS (Posterior Nasal Spine). In case of pitch corrections, they provide values opposite from ANS and A.
- Points to evaluate the effect of sagittal mandibular repositioning: B and Pog (Pogonion). They provide the magnitude of advancement/setback.
- Points to evaluate the effect of mandibular asymmetry correction: GoL and GoR (Gonion Left and Right). Such points are especially important if a simultaneous condylectomy is planned.

Mandibular dental points are not included because they depend on the maxillary repositioning. In the VSP phase of skeletal repositioning, the maxillo-mandibular complex in occlusion is considered a unique entity, and esthetical considerations are based upon upper dental points. However, at

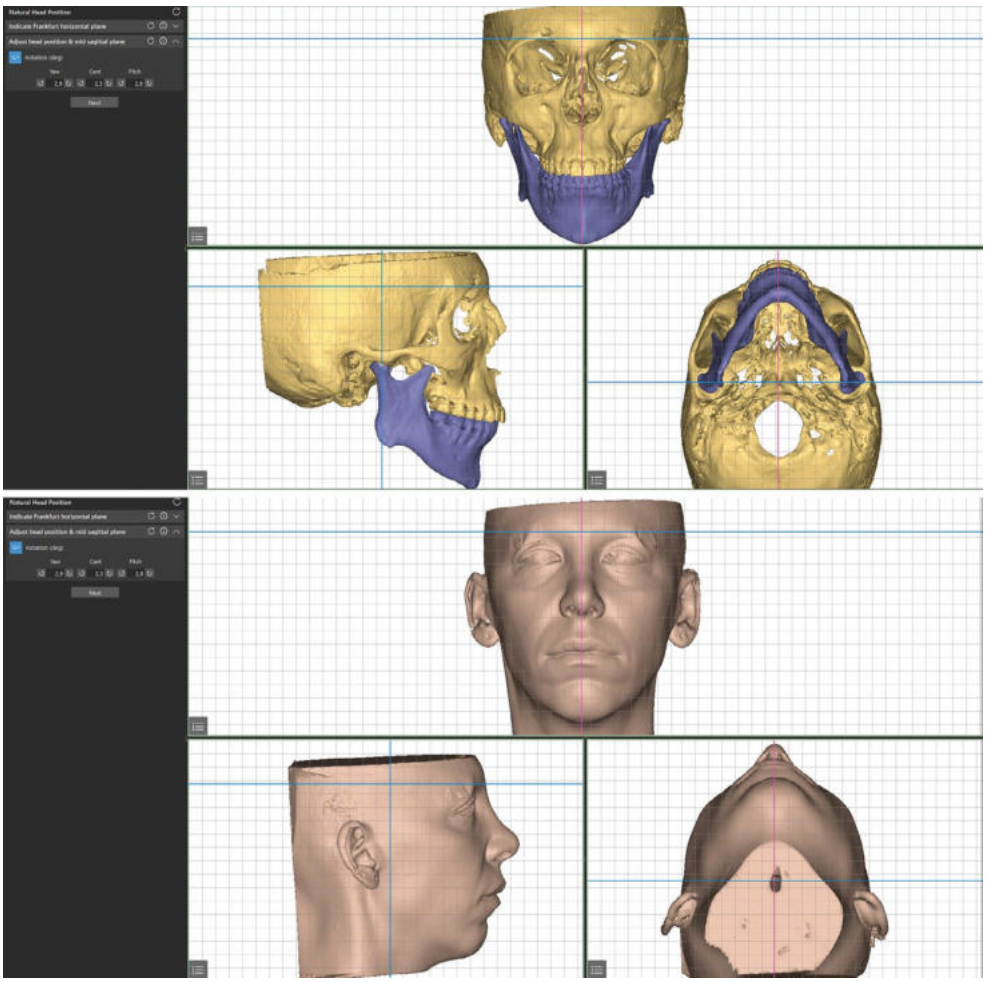


Fig. 8 Natural head position (NHP) adjustment in the software Enlight CMF. Angular degrees are provided. Evaluation should be performed both for the skeletal and the soft tissue model

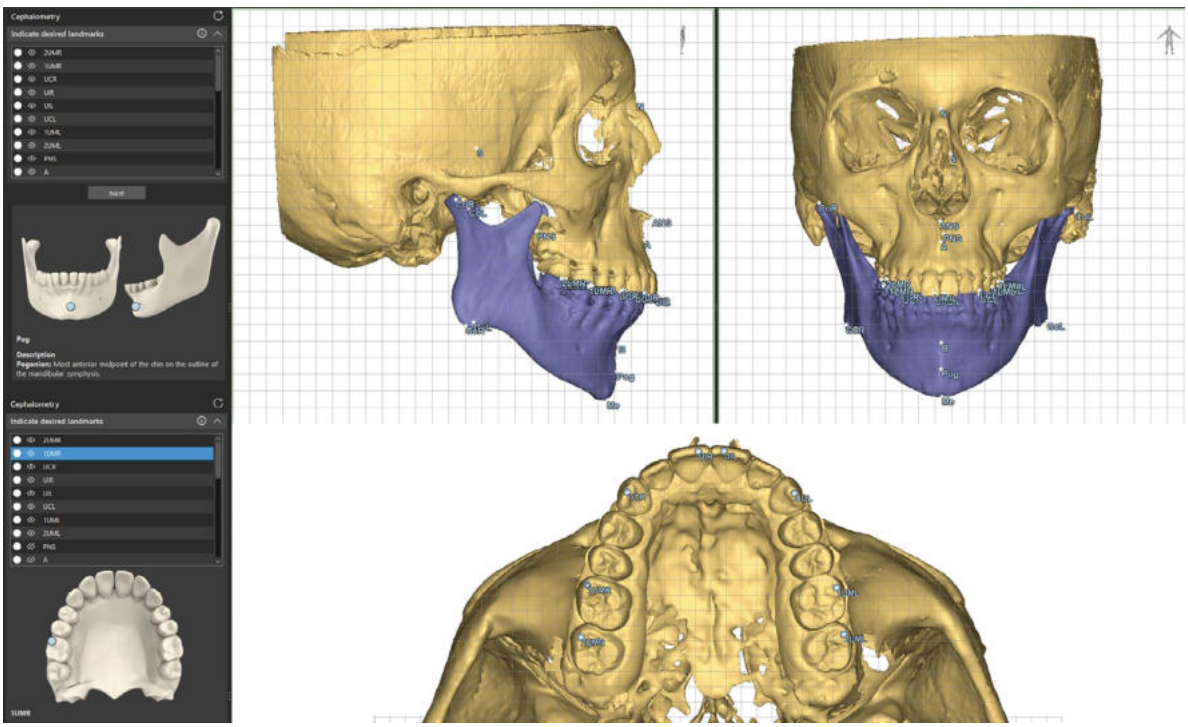


Fig. 9 3D cephalometry guided by visual landmarks in Enlight CMF

the end of VSP, also mandibular dental points values can be inspected to verify the movements of the inferior incisors and canines.

3.6 Osteotomies

Software designed for orthognathic surgical planning, as mentioned, is clinical friendly, and this translates on the fact that designing osteotomies is an easy and fast process, as orthognathic surgery software already provides specific cursors which can be placed over anatomical landmarks to achieved standardized cutting planes.

During segmentation, definition of dental anatomy and teeth roots should be preliminarily accomplished, to establish the osteotomy line far from root apices to avoid their damage. Recent software can make this step automatic, as a volume-rendering algorithm is applied during the creation of the osteotomy plane to emphasize the position of roots, which are typically hyperdense compared to surrounding alveolar bone. The polyplane for osteotomies is designed by defining its origin points and is assigned a thickness, which should generally correspond to the magnitude of the cutting instrument. First, Le Fort I osteotomy plane is defined taking care to cut through all the maxillary bone, especially in the area of the pterygo-maxillary junction. Its osteotomy planes do not pass through the entire geometry, the Boolean operation applied to separate the cut part will result ineffective. Second, before performing the bilateral sagittal split osteotomy of the mandible (BSSO), it is useful to simulate the course of the inferior alveolar nerve, although it can be easily inferred from CT in coronal section (Fig. 10).

After creating osteotomies, the object list will include the following parts: skull, Le Fort I maxilla, both mandibular

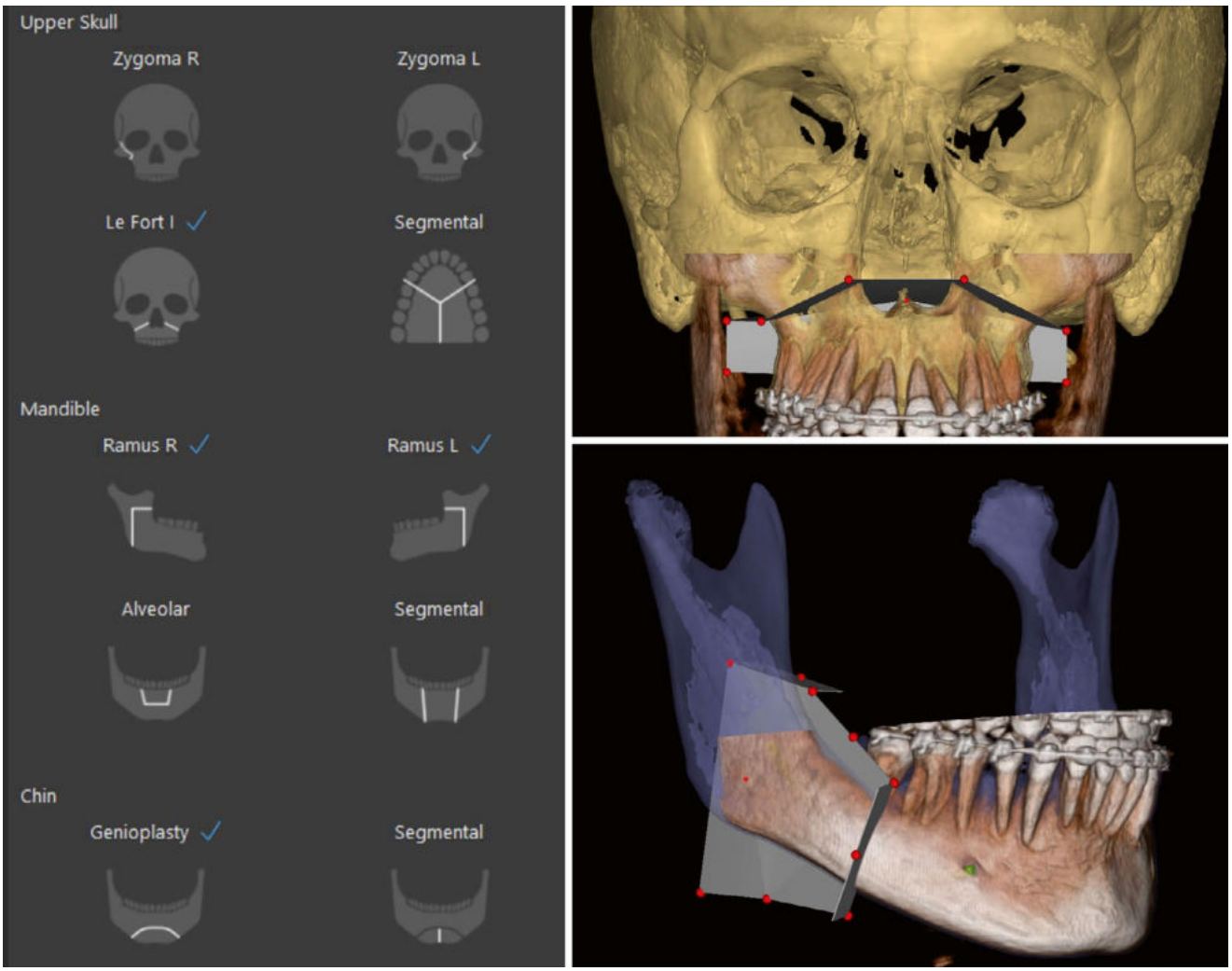


Fig. 10 Le Fort I and BSSO osteotomies with volume-rendered dental roots

rami (proximal mandibular segments), and the distal tooth-bearing segment. Each segment should be assigned a different color and an univocal nomenclature. The same applies to any additional osteotomy performed, including genioplasty, border contouring, multipiece maxilla. Once osteotomies are performed and children's parts are generated, each cephalometric point belonging to the entire geometry will link to the children segments always in the position $x_0y_0z_0$.

3.7 Surgical Occlusion

A crucial step in orthognathic surgical planning is the reproduction of surgical occlusion. There are basically two approaches, yet they are conceptually very different:

- Import occlusion cast: in this method, the occlusion determined by the clinician based on plaster models physical intercuspation (Fig. 11). Occlusion is scanned and is used as template to realign the superior and the inferior dental arch in the correct occlusal relationship within the software. It is a trusted method because it still relies on the traditional approach in which the surgeon determines by his hands the correct occlusal relationship, however its reproducibility in the virtual environment depends on the accuracy of registration, therefore it is not exempt from errors. Moreover, it entails a further scanning of plaster models, which can introduce inaccuracies.
- Automatic virtual occlusion: newer software being developed is increasingly incorporating this function. In this approach, a computational algorithm determines the optimal intercuspation between the superior and the inferior scanned models. The algorithm can apply three contact points, to enhance the automatic intercuspation of dental arches in a tripodic occlusion, or a single dental contact to improve user freedom and decide, for instance, the amount of posterior disclusion. Then, the surgeon can modify the virtual occlusion according to his preferences by acting on specific features, including correction of midline deviation, axial rotation and over-

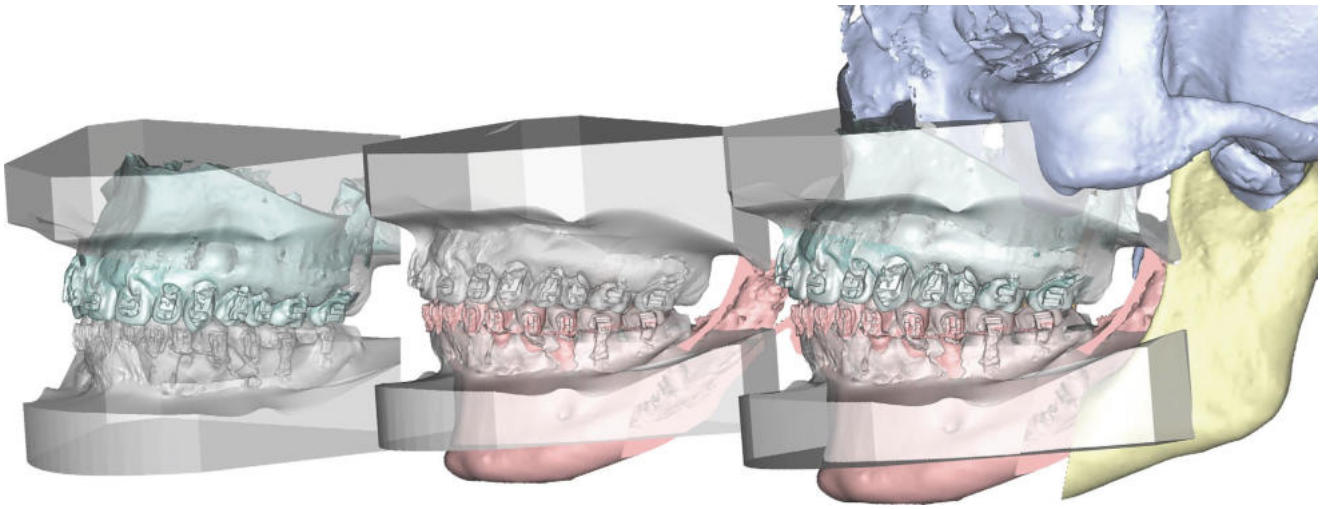


Fig. 11 Sequence of alignment for the maxillo-mandibular complex: left: occlusion aligned to the maxilla (UIM = 0); center: distal segment aligned to occlusion; right: effect of mandibular repositioning with native position of the Le Fort I segment

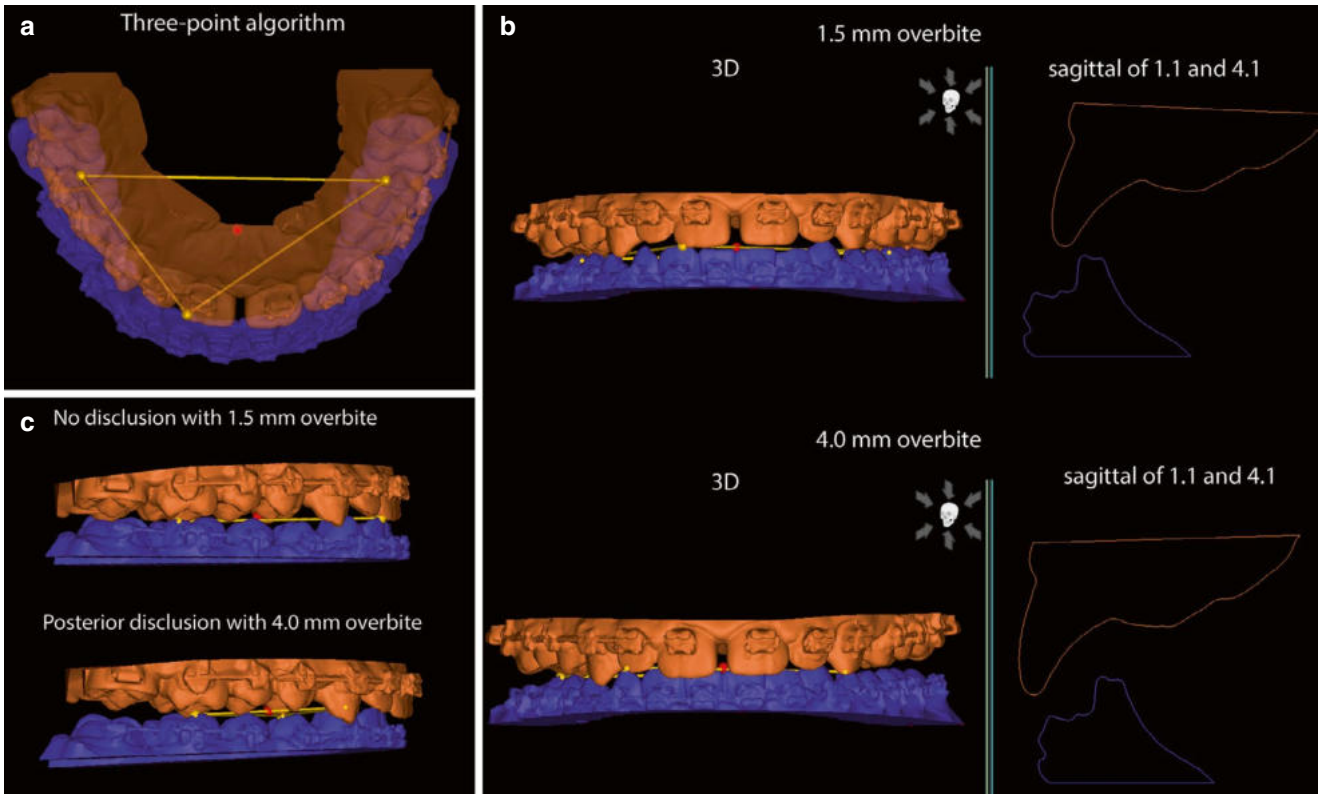


Fig. 12 Virtual occlusion with fine variation of parameters and three-points contact scheme

jet (Fig. 12). Although this method is becoming more robust and validated [9, 10], showing comparable results with the traditional method (Fig. 13), many surgeons are resistant to its adoption. Virtual occlusion provides the most accurate prediction of the final occlusion as it does not involve intermediate scans of alginate impressions and can be immediately applied starting from intraoral scans.

Once the surgical occlusion is determined, both using a scanned or an entirely automated method, it is imported in the virtual surgical plan and is used to register the mandibular distal segment into correct occlusion with the superior antagonist. For the occlusion cast method, the occlusion cast is imported, its superior component is aligned with the Le Fort I segment and is made coincident using a global alignment method; subsequently, its inferior arch provides the template to register the teeth of the mandibular distal segment in correct occlusion. This step is automatically performed by the software when the virtual occlusion algorithm is implemented.

The result of this method is the mandible registered in the correct occlusal relationship with the superior antagonist: a mandibular setback will result in III class, while a mandibular advancement will result in II class. Notably, cephalometric points linked to the mandibular distal segment will now show modifications proportional to the entity of mandible repositioning; for instance, the Δx component of LIM (Lower Incisor Midline) will reflect the entity of overjet correction.

3.8 10-Step Flowchart for Skeletal Repositioning in Orthognathic Virtual Surgical Planning

During surgical movements, the maxillo-mandibular complex in the desired occlusal relationship should be considered a unique entity. Therefore, Le Fort I segment and mandibular distal segment are treated as a single part and not separately, taking as reference cephalometric points applied to the Le Fort I segment that are still in the position $x_0y_0z_0$. From this step onwards, the correction of the dentofacial deformity is planned using a predefined stepwise approach:

1. Cant adjustments (*roll*): an invariable horizontal plane is taken as reference, generally based on the Frankfurt plane (see Sect 3.4). From this reference, perpendicular measurements are drawn to the cusps of canines and first molars, thus measuring their vertical discrepancy that accounts for cant correction. If needed, correction of canting is performed by placing the rotation pivot at the

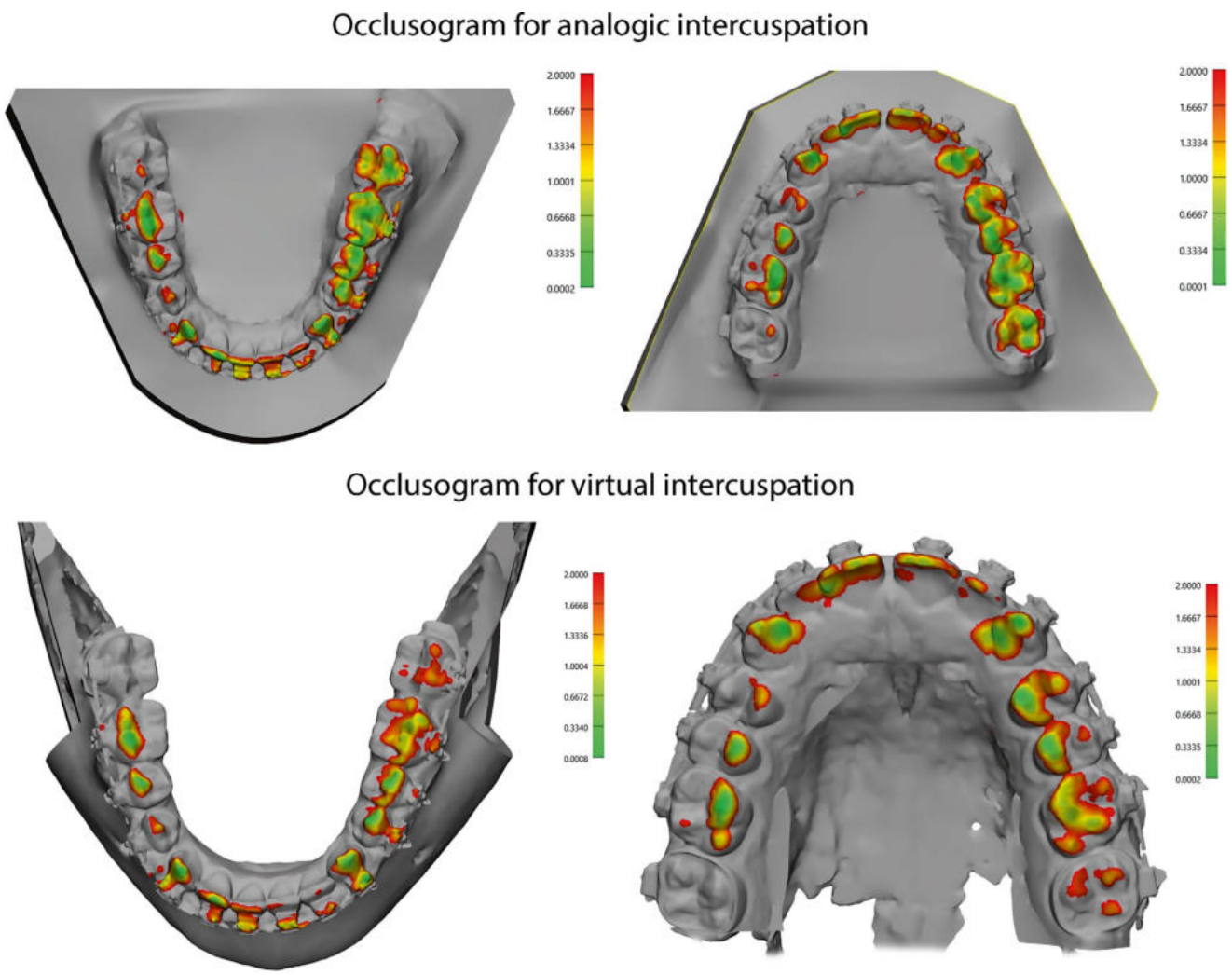


Fig. 13 Occlusograms between analogic and fully virtual intercuspation

lateral extremity of the osteotomy line in the contralateral side. To facilitate this step, the mandible object can be selectively hidden while remaining still selected and affected by correction (Fig. 14).

2. Midline adjustments: we consider as reference midline a vertical line passing through the labialis superior point and subdividing the Cupid's arch into two symmetrical halves. If the superior interincisal line is deviated from the midline, a translation movement is applied to center it. The inferior interincisal line is already aligned with the superior because the mandible is in occlusion (Fig. 15).
3. Anterior-Posterior correction: depending on the profile and dental exposure during smile, as assessed from preoperative clinical analysis, anterior-posterior movements of the maxillo-mandibular complex are performed. This step is crucial to correct maxillary retrusion, as the advancement should be proportional to the increase of volume around the middle third region. Maxillary

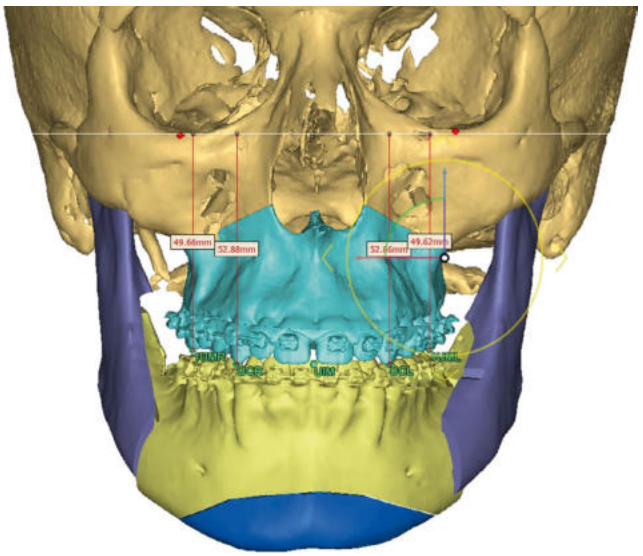


Fig. 14 Evaluation of maxillary coronal symmetry calculated on canines and first molars to ascertain the presence of maxillary cant

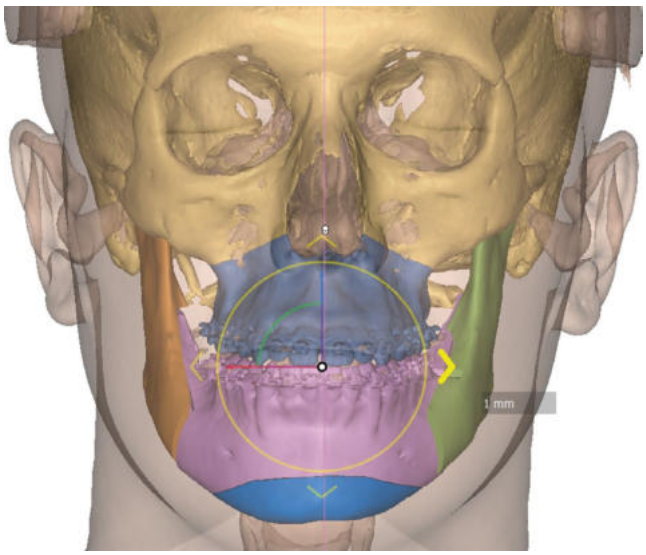


Fig. 15 Midline centering. The soft tissue reference is placed in the midpoint of the columella-Cupid's bow

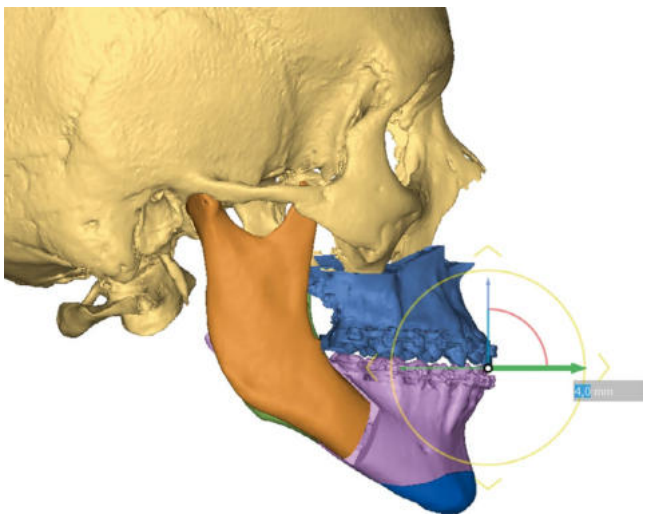
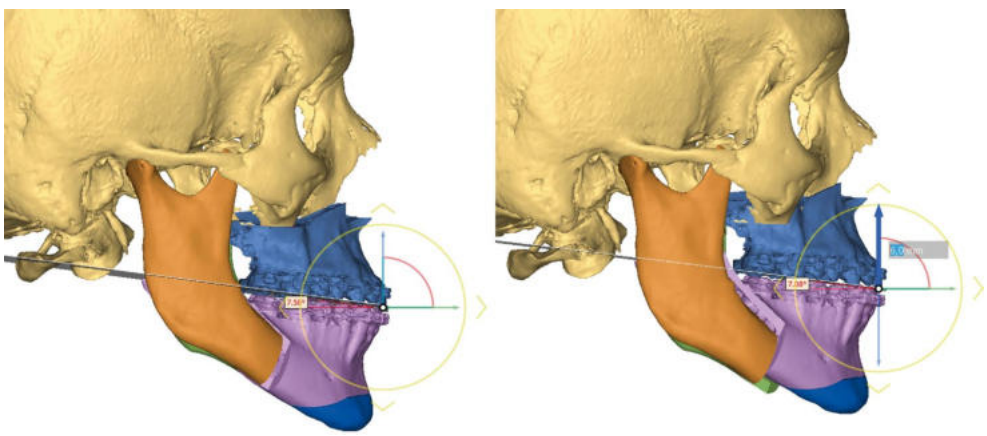


Fig. 16 Sagittal repositioning of the maxillomandibular complex

advancement also impacts on dental exposure; thus, its amount should be balanced between the correction of a gummy smile (or a reduced crown exposure) and the need for vertical correction (Fig. 16). As mentioned, the mandible is automatically repositioned in its correct occlusal relationship. The main concept of modern computerized VSP is that skeletal repositioning should be based on a comprehensive, holistic, facial analysis and not on the separate evaluation of the upper and lower jaw.

4. Vertical correction: it mostly impacts the dental exposure during smile accounts also for the height of the occlusal plane. Typically, long face phenotype is hyperdivergent, whereas short face phenotype is hypodivergent. Maxillo-mandibular impaction lifts the occlusal plane, decreases the occlusal angle between Frankfurt plane (FHP) and occlusal plane (OcP), and decreases hyperdivergence (Fig. 17). In addition, linear maxillo-mandibular impaction ("in toto"), compared with counterclockwise rotation alone, decreases the amount of lateral gummy smile, acting on the so-called "buccal corridors". Differential maxillo-mandibular impaction refers to the combination of linear impaction with pitch correction.
5. Occlusal plane rotation (*pitch*): this rotational movement acts specifically on the occlusal angle (FHP-OcP). This angle measures on average 8° ± 4° [11]. High occlusal plane phenotypes, which are typically associated with hyperdivergence and increased verticality, require a correction through an anterior rotation (counterclockwise rotation, CCW). Low occlusal plane phenotypes, generally associated with hypodivergence, II class and reduced verticality, require FHP-OcP augmentation through a posterior rotation (clockwise rotation, CW). Figure 18 illustrates the effect of CW and CCW on occlusal plane pitch.

Fig. 17 Pitch modifications



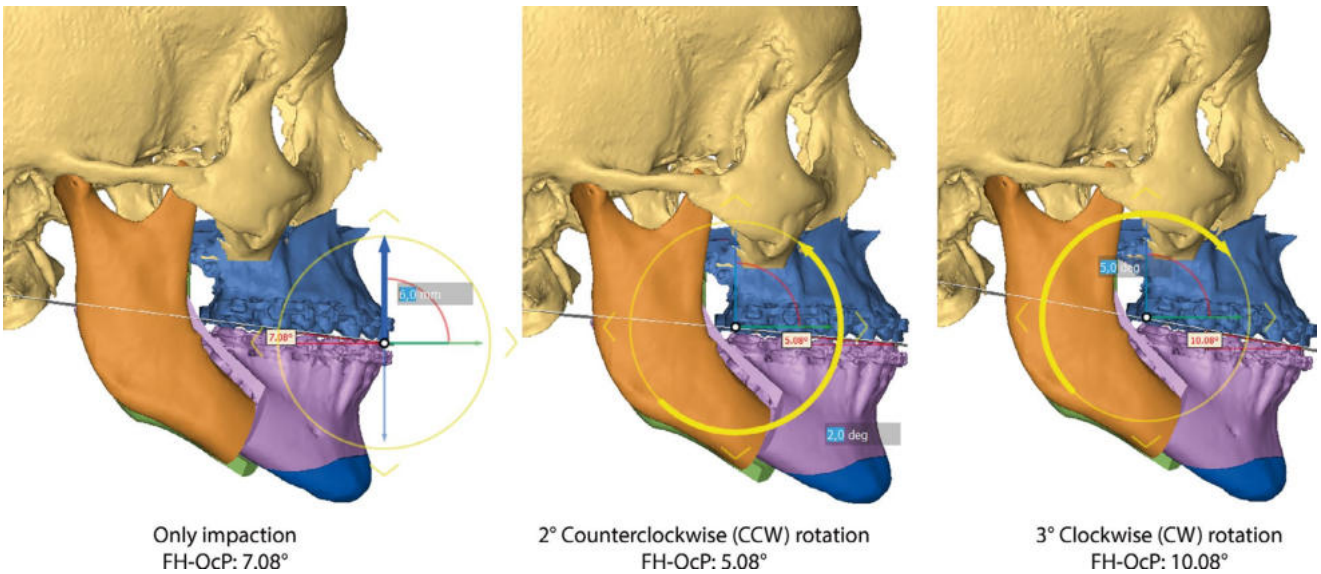


Fig. 18 Effect of CW and CCW on the slope of occlusal plane and the FHP-OcP angle

6. Axial maxillo-mandibular rotation (*yaw*): this movement enables the correction of rotational discrepancies in the axial plane. Axial mismatches must be fist corrected when assessing the natural head orientation. First, a reference grid should be enabled in the software to evaluate whether each tooth lies on the same horizontal line as its contralateral; if not, the axial discrepancy must be corrected to symmetrize. Moreover, this movement is strategical to minimize the bone interference between the proximal and distal segments of the mandible. As this movement affects the interincisal line, already centered, the Author advises to position the rotational fulcrum in correspondence of the interincisal line itself to preserve its alignment with the dental midline (Fig. 19).
7. Genioplasty: the three-dimensional repositioning of the chin completes the VSP in cases where a genioplasty has been planned to further correct the lower third if mandibular repositioning was not sufficient (Fig. 20).

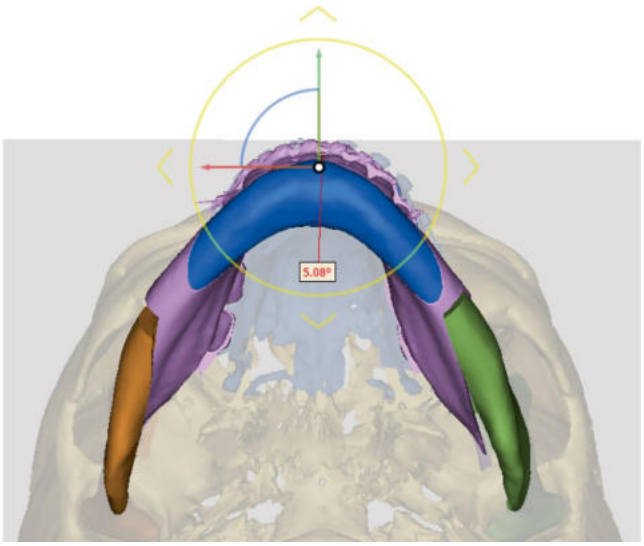


Fig. 19 Yaw correction

8. Assessment of mandibular rami: after placing the rotational pivot in the center of the mandibular condyle, the position of each mandibular ramus is optimized for the new orthognathic setup (Fig. 21). This is particularly important for fully-custom surgery with patient-specific plates. In such specific circumstances, care should be taken to avoid geometrical compenetrating of ramus and distal segment geometries to increase predictability of surgery. If a suboptimal correspondence of mandibular rami with the distal segment is seen, yaw correction should be inspected to ensure that no further improvements are possible. Moreover, excessive correction in the coronal plane should be avoided for its implications in introducing a condylar torque, with detrimental effects on the joint.
9. Visualization of bony interferences and eventual trimming: the assessment of bone intersection is essential to evaluate the necessary ostectomy around the Le Fort I osteotomy to surgically achieve the planned movements. The same is true in case a reduction genioplasty is planned. In addition, it enables to define hindrances between the distal and proximal mandibular segments, which can be solved using a trimming procedure, correspondent to a selective ostectomy during surgery (Fig. 22).
10. Soft tissue simulation: once bone segment repositioning is complete, modern software enables to perform the soft tissue simulation to visualize the effects of skeletal change on soft tissue volumes. Yet this technology has several limitations, it provides a gross idea of the final surgical aspect (Fig. 23). More sophisticated studies in the future will substantially improve this aspect, for instance using finite element analysis (FEA) to regionally determine the resilience of any tissue to the skeletal movement in terms of skin thickness, fat volumes, muscle involvement.

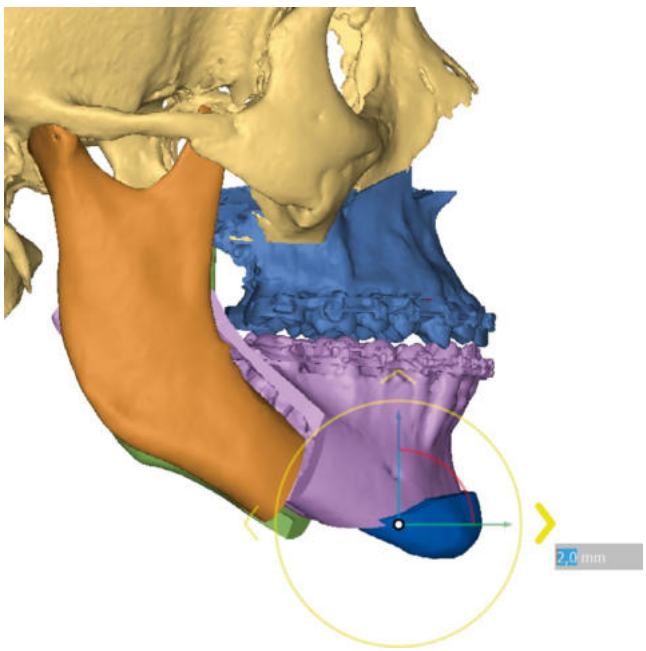


Fig. 20 Genioplasty

3.9 Cephalometry Inspection

After repositioning of the bone segments, it is crucial that each cephalometric points previously placed is carefully inspected to determine its position in relation to the surgical plan (Fig. 24). As mentioned in Sect. 3.5, the most esthetically impactful evaluation is played by the vertical and anterior-posterior values of UIM. Moreover, four angles are crucial as their change is directly related to the corrective orthognathic movements:

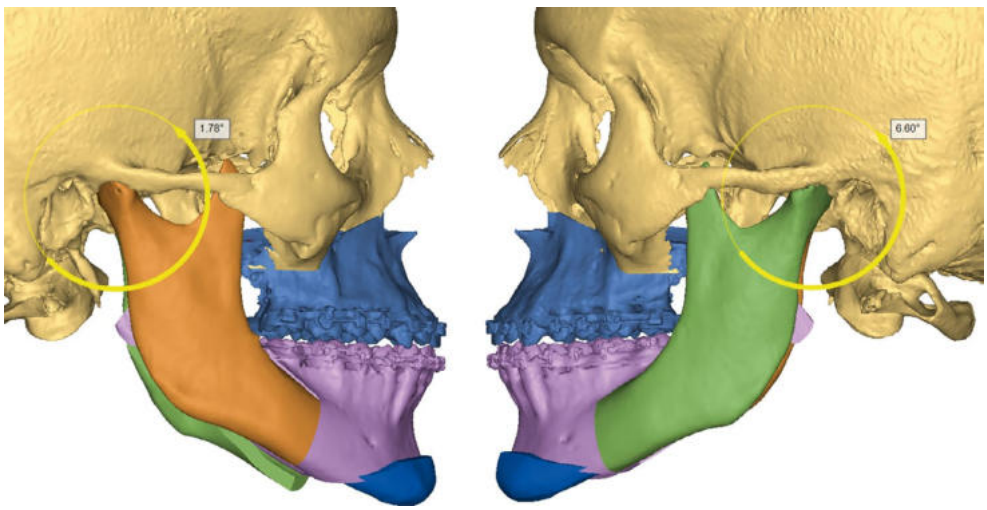


Fig. 21 Mandibular rami assessment

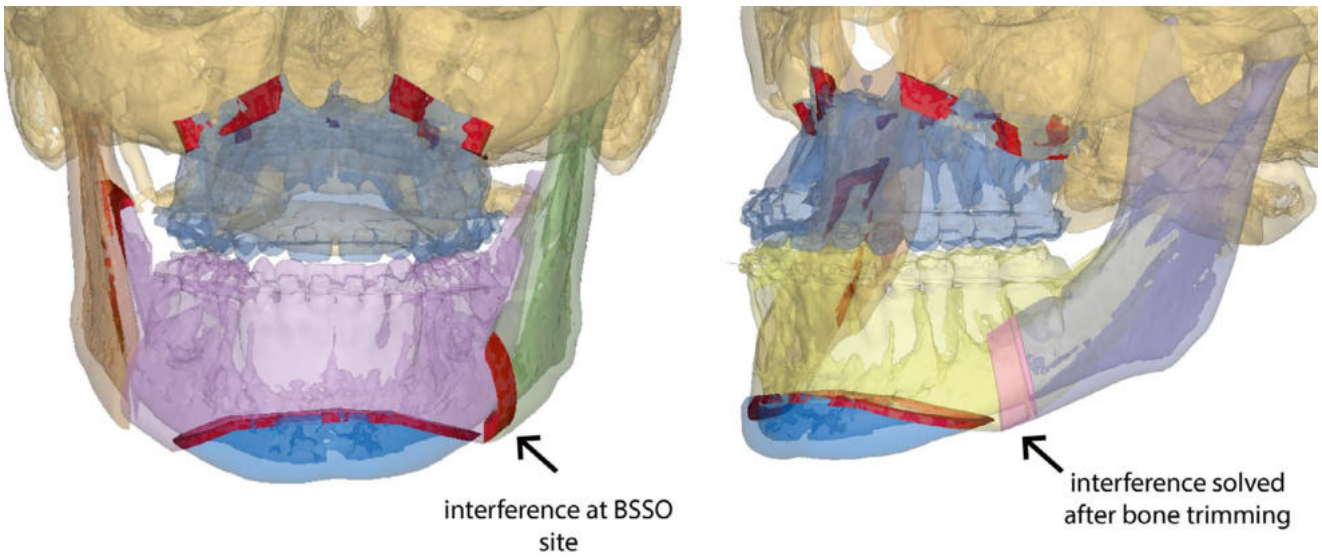


Fig. 22 Evaluation of interferences at osteotomy sites

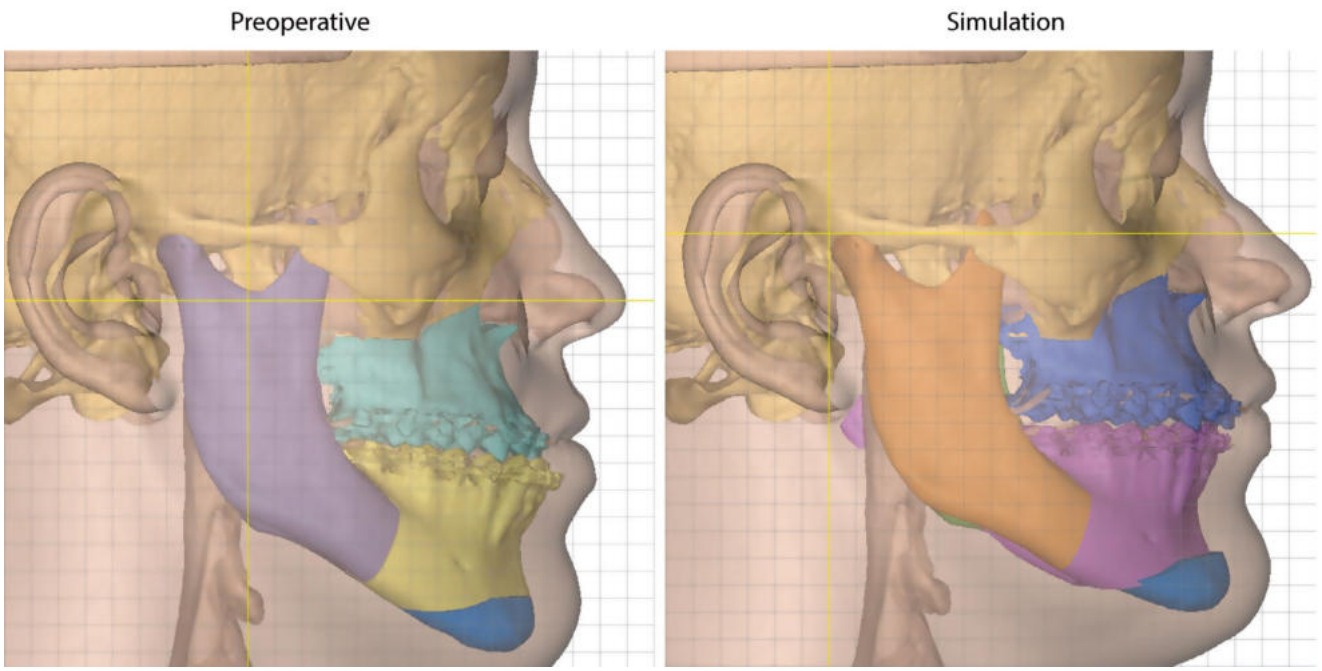


Fig. 23 Simulation of orthognathic surgery on soft tissues

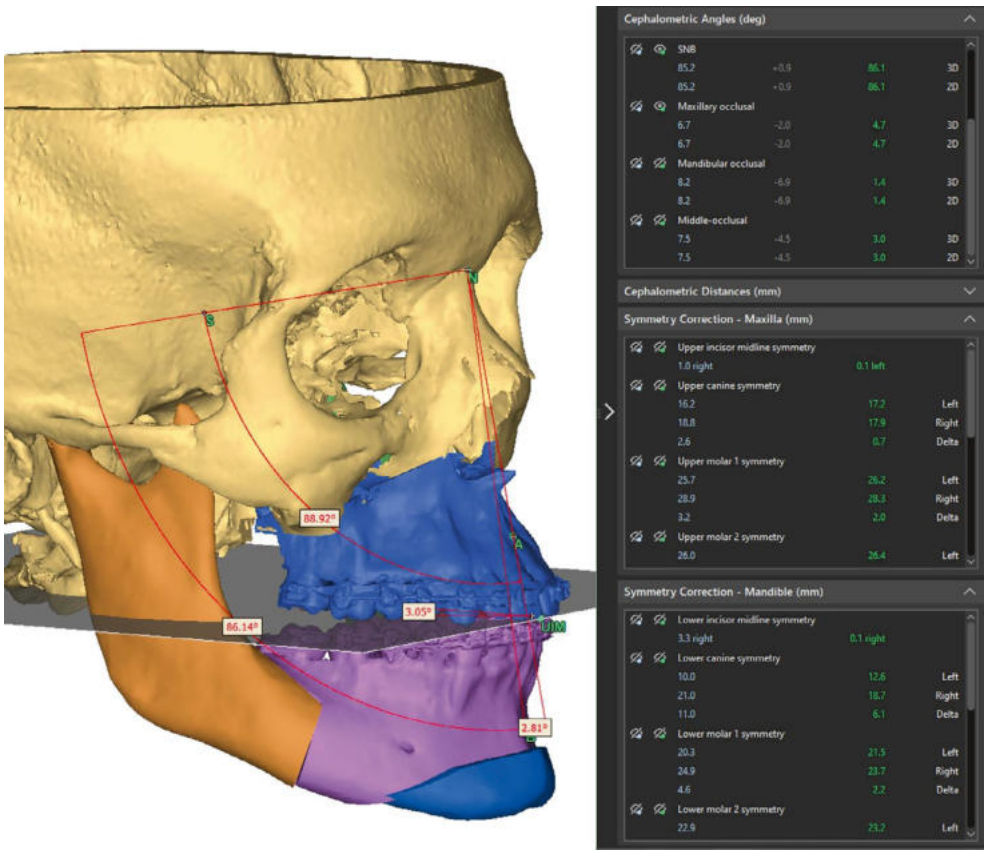


Fig. 24 Cephalometry interactive modification is used to verify the effect of skeletal repositioning across the cephalometric points

- ANB: it defines the entity of the maxillomandibular discrepancy and its slight variations are related with mandible repositioning. Used at first for 2D cephalometric evaluation at its earliest, its implications are less relevant with automatic occlusion. It can be affected and normalized by pitch variations.
- SNA: it defines the sagittal position of the maxilla. Its normalization accounts for the appropriate anterior-posterior repositioning of the upper skeletal base.
- SNB: it represents the SNA lower counterpart.
- Occlusal plane (FHP-OcP): its correction is particularly important when related to the high/low occlusal plane phenotypes, as described in Sect 3.8.

3.10 Ancillary Procedures

Any additional procedure, including mandible contouring ostectomies or malar augmentation, should be planned on the final orthognathic setup. The software already provides the appropriate tools to perform such basic osteotomies and there is no need to shift to other more advanced software.

3.11 Measurements

Once the final plan is validated, is important to produce a report with the following data:

- Planned cephalometry, displaying the ($\Delta x,y,z$) for each cephalometric points related to skeletal movements.
- Maxillary bone intersection quantification: in the absence of a surgical guide, not routinely used for orthognathic surgery, it is important that, in case of a maxillary impaction movement, the surgeon knows the exact quantity of bone to excise to achieve the desired movement. This is even more important when a pitch or roll correction is planned owing to a differential osteotomy design (the ostectomy differs between posterior and anterior, and/or left and right). Measurements are calculated on the bone interference model and taken lateral to the piriform notch and the zygomatic buttresses bilaterally.
- Similarly, it is important to know the amount of bone to excise in the proximal mandibular segment (the ramus) to avoid undesired interferences with the proximal segment which would hinder osteosynthesis. This quantity of bone

is optimally determined during trimming of interferences (see Sect. 3.8, point 8).
- If a reduction genioplasty is planned, likewise the surgeon has to know the exact quantity of bone to excise.
- Maxillary advancement: especially in case of combined, nonlinear movement, including not only translations but a pitch and roll correction, a three-dimensional measurement should be conducted to quantify the magnitude of the "step" between the advanced Le Fort I segment and the skull model.

3.12 Choosing the Surgical Sequence (Intermediate Position) and Designing Splints

Depending on the clinical case, there are two possible surgical sequences [12]:

- Maxilla first: in the splint creation phase, the intermediate position is defined by the final position of Le Fort I segment (upper maxillary) and the preoperative position of the mandibular distal segment (lower maxillary). Especially in second classes with marked overjet which require a simultaneous maxillary advancement, the maxillary-first intermediate position might lead to the creation of a surgical splint with very distant dental arches, thus hindering the application of metal wires for intermaxillary block creation. Such cases might be strategically approached with a mandibular first sequence to facilitate intermaxillary block (Fig. 25a).
- Mandible first: in the splint creation phase, the intermediate position is defined by the final position of the inferior maxillary and the preoperative position of the superior maxillary. This choice, yet preferrable for several aspects [13], raises some concerns during the virtual surgical planning in case a maxillary impaction is planned, because this movement causes an upward displacement of the occlusal plane. As a consequence, the preoperative maxilla will be lower than the final occlusal plane of the mandibular distal segment, and the two will compenetrate each other. The solution is to simulate ad additional disclusion of the final mandible, placing the rotation fulcrum over the TMJ and increasing the rotation of the mandible distal segment to avoid the compenetration with the preoperative upper maxillary, making the creation of the splint possible [14]. This maneuver, however, introduces a slight inaccuracy, even if correctly performed, because it is based on a fictitious movement, as a normal TMJ exhibits a complex combined rotation and translation movement. For small rotations, however, the error can be considered negligible (Fig. 25b).

Based on such principles, splint design can be performed entirely within the orthognathic surgical planning software through a dedicated module by placing marker points across the upper and lower dental arches. Points should be placed lower than the center of brackets to avoid bracket interference; in other words, the negative impression on the splint should take into account the volume of the bracket. Last, it is of prominent importance that undercut removal is applied before the creation of any splint.

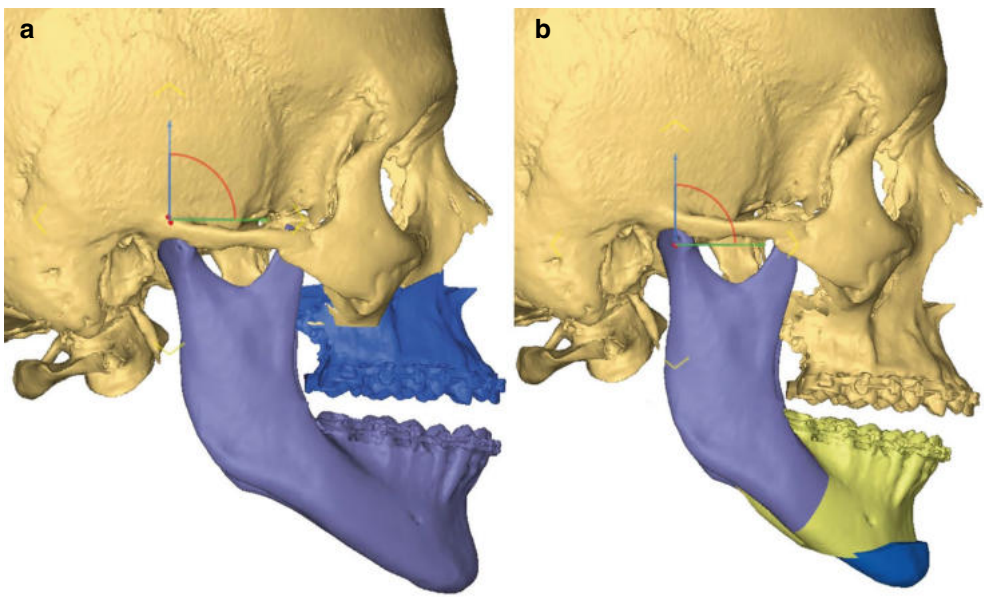


Fig. 25 Establishing the surgical sequence: maxilla first (left) or mandible first (right)

4 Sequences of Phases for Bimaxillary Orthognathic Surgery with Multipiece Maxillary Segmentation

Multipiece orthognathic surgery is generally required to correct transversal defects or severe discrepancies of the Spee curve, which can not be compensated exclusively orthodontically. Compared with a two-stage process that involves surgically assisted rapid palatal expansion (SARPE), two-piece or three-piece maxillary segmentation has the benefit of addressing severe transversal defects in the same surgical time and is particularly indicated in a variety of situations, including posterior crossbite and anterior open bite. Moreover, three-segment maxilla has several additional advantages over SARPE, including avoidance of maxillary fibrosis and scarring due to a previous operation; less esthetic impact, because the space created by the expansion is divided between right and left interproximal spaces between laterals and canines (or canines and premolars) instead of causing a disfiguring midline diastema; prevention of damage to the midline dental papilla; preservation of the nasopalatine bundle; and possibility for an asymmetric expansion [15].

Segmentation of the maxilla in orthognathic surgery introduces several elements of complexity compared to the workflow described for basic bimaxillary orthognathic surgery. For multipiece maxillary surgery, many surgeons still prefer the physical setup performed on plaster models and articulator ("model surgery"). However, virtual occlusion for multipiece maxillary surgery is providing interesting clues for a faster, fully-digital, workflow, which can eliminate the tedious and costly processes of model surgery.

4.1 Traditional Model Surgery

Analogic setup often requires the availability of a dental technician, and involves cutting plaster models with a saw, with possible damages to the models themselves. Cut maxillary segments are positioned in the optimal setup within the desired occlusal relationship using the articulator, and separate pieces are then sticked together using hot glue or wax (Fig. 26). The setup needs to be rescanned to provide the final occlusion for the VSP, thus adding another analogical-to-digital transition, which might introduce further inaccuracies. Both pre-setup, native, dental arches scans and post-setup occlusion need to be provided to the software.

4.2 Osteotomies for Maxillary Partition

Osteotomies for maxillary partition have to be simulated on the native maxilla with the preoperative intraoral scan aligned and superimposed, cut through the Le Fort I plane. Given the importance of performing such osteotomies without violating teeth apices, it is of prominent importance to visualize a volume rendering of dental roots when positioning cutting planes for segmental osteotomies. Moreover, the orthodontist should have created a gap when the osteotomy is planned to decrease this risk. For a three-piece partition setup, virtual osteotomies can be performed using two design subtypes (Fig. 27):

- A "Y-shaped" cut is the easiest to perform using planar cuts and yield a configuration much similar to that of the model surgery, allowing to compare the virtual setup to the physical one in the surgical planning.
- On the contrary, a "central island" design is more difficult to achieve, but it mirrors the intraoperative expansion, allowing to reproduce a configuration to assess the intraoperative situation.

The same principles apply to maxillary bipartition where both a single midplane splitting the maxilla in two symmetric halves and a midplane crossing the H-shaped design can be simulated.



Fig. 26 Model surgery performed on plaster models to simulate three-piece maxillary partition

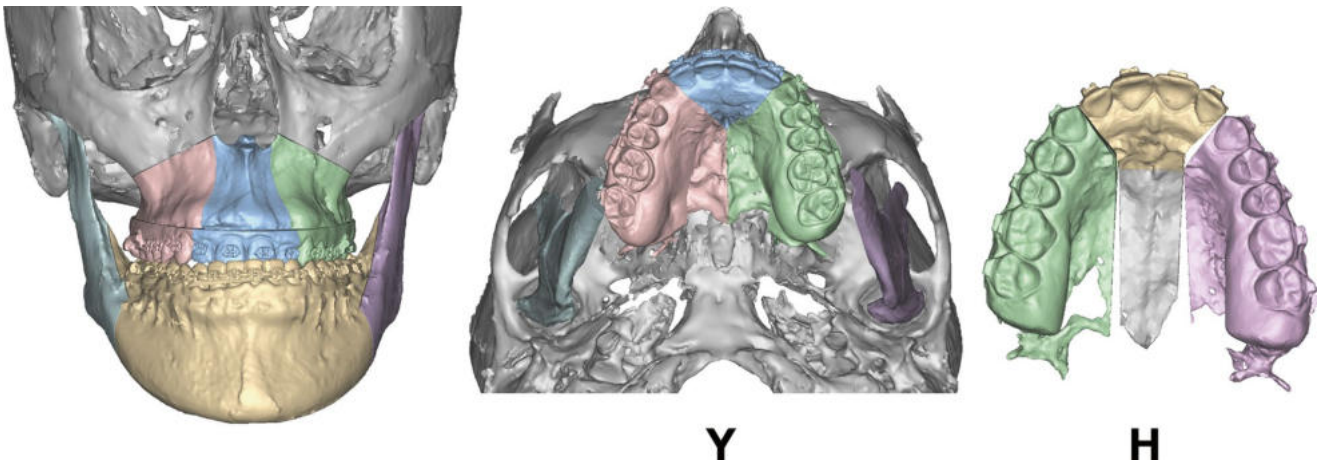


Fig. 27 Comparison of two design methods for maxillary tripartition in VSP: Y-shaped (more practical), or H-shaped (mimics what happens during surgery)

4.3 Virtual Multipiece Occlusion

Virtual multipiece occlusion is a new and highly promising frontier. It involves a complete, digital, setup, avoiding the time and resources spent in performing the analogical articulation of sawed plaster models. Moreover, it works using exclusively native intraoral scans, and the quality is not worsened by subsequent, additional rescans of analogical setup. After segmental osteotomies have been simulated in the VSP, left and right hemimaxillary parts (for bipartite setup) or left, right posterior sectors and premaxilla (for tripartition) can be handled by the software, which detects the most suitable configuration. In contrast with automatic setup for a full-arch maxilla, for segments the algorithm can adopt maximum two contact points, where the user is allowed to modify coefficients that include buccal-lingual translation, mesial-distal translation, axial rotation and buccal-lingual tilt (for lateral segments), or midline deviation, overjet, axial rotation and sagittal rotation (overbite) for the premaxilla. This approach holds great value as it allows to predict if a conventional bimaxillary surgery, planned as such, could benefit from a multipiece setup, in the eventuality that this was not considered both from the surgeon and the orthodontist. The surgeon can make countless simulations in the VSP to find the best arrangements and understand whether a single arch preparation is sufficient or if a multipiece maxillary partition is needed, both in the presurgical VSP, as well as during the orthodontic preparation, which can drive the orthodontist to shift toward a preparation for multipiece osteotomies by widening interdental spaces where osteotomies are planned (Fig. 28).

4.4 Transferring the Physical Setup in the VSP (Not Needed for Virtual Occlusion)

Subsequently, the setup model is imported in the virtual planning and is used as template to rearrange the virtual segments exactly as the physical setup. In a three-piece maxillary surgery, the alignment chain proceeds as follows:

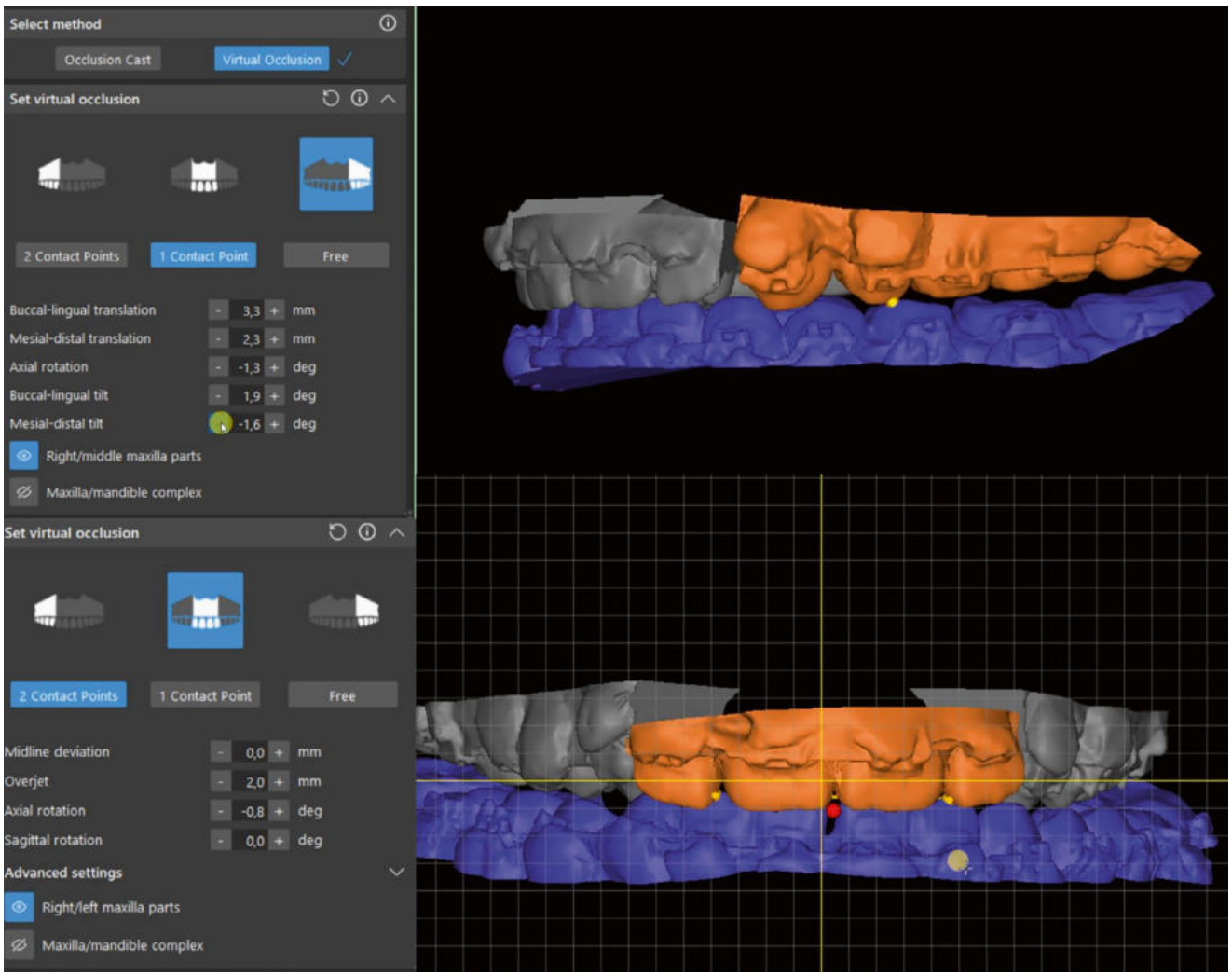


Fig. 28 Virtual occlusion applied to multipiece maxillary setup. Each individual segment is managed separately, allowing to correct Spee curve and transverse diameter

- First, the premaxilla of the model setup (moving) is aligned to the premaxilla of the native patient (fixed) in order not to alter the sagittal position of the superior incisor, which remains in the position $x_0y_0z_0$. The superior incisal point (UIM) is the most important parameter to monitor when assessing surgical movements, because it has a direct implication on the patient's smile. This step ensures that premaxilla is in a neutral position, and subsequent registration phases will define the transversal expansion of the lateral segments, which are taken into account also in the cephalometric points in the molars.
- Second, once the premaxilla of the plaster model setup is coincident with that of its virtual homologue, both lateral sectors are aligned with the molars of the analogic setup. This step enables the correct expansion of the maxilla exactly as planned in plaster models (Fig. 29).

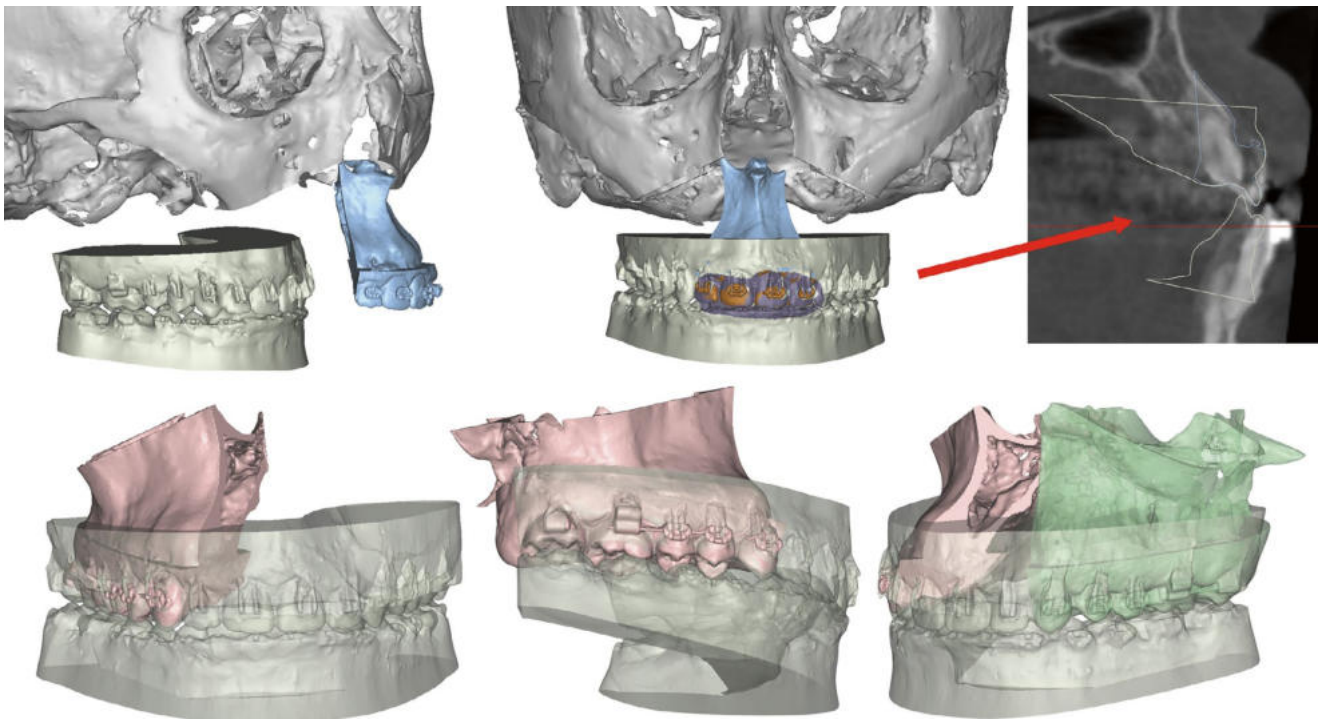


Fig. 29 Multipiece maxilla VSP using plaster model setup. The first step is alignment of the setup with the premaxilla, maintaining UIM at 0 value. Then, lateral segments are expanded according to the setup

- Verification of the plaster model setup with the expansion achieved in the virtual surgical plan: this step is essential to assess that dental cusps of the expanded segments match the cusps of the imported setup. For Y-based osteotomy design in tripartitions and for the simple midplane in bipartitions, the movement of bone segments can be specular and more intuitive to demonstrate (Fig. 30).
- Following the scanned plaster model setup, the maxillo-mandibular occlusion is established by repositioning the mandible according to the model surgery occlusion. At this point, the maxillo-mandibular complex in the correct occlusal relationship can be repositioned to achieve required facial movements and the desirable occlusal plane tilting (Fig. 31).

In case of maxillary splitting across the midline, the procedure is the same, with the difference that there are only two segments to realign rather than three. The model surgery setup will be realigned to the less expanded segments and, once in position, will drive the contralateral half in the correct occlusal relationship.

From the analysis of both workflows, fully virtual and half-analogic with model surgery, it is clear that the fully virtual workflow excels in terms of intuitiveness and decreased number of steps, which translates into decreased possibility of introducing errors.

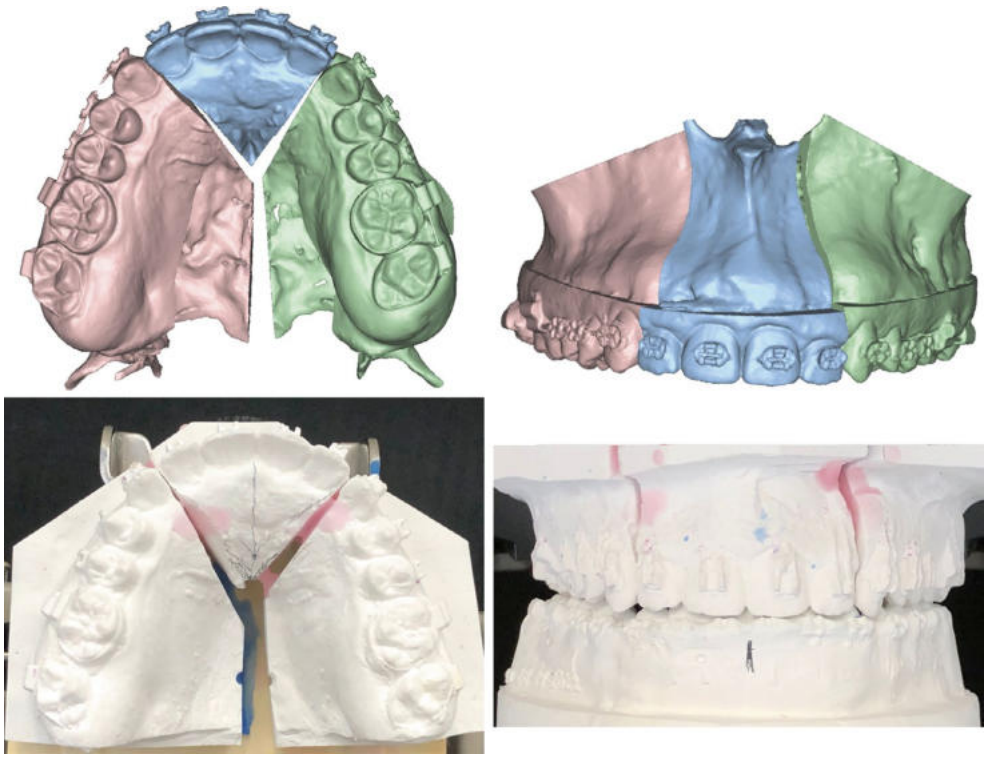


Fig. 30 Expected modifications in plaster model surgery are reliably mirrored by VSP alignment, confirming the correct expansion of the Le Fort I segment

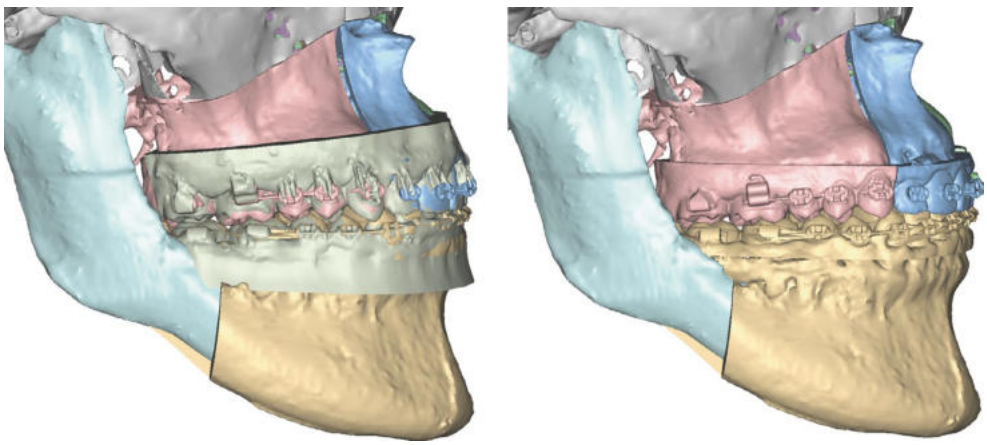


Fig. 31 Mandibular repositioning in relation to the expanded Le Fort I

5 Fully Custom Orthognathic Surgery

Fully custom orthognathic surgery refers to the process of establishing a VSP, as seen so far, and designing patient-specific surgical guides for computer-guided osteotomies, as well as personalized osteosynthesis plates [16]. This process aims at creating automation in surgery, decreasing variability and achieving an overall more standardized and accurate workflow according to the preoperative virtual plan. As the final osteosynthesis plates are designed on the provisional, final configuration after skeletal repositioning, they already incorporate the necessary skeletal movements, allowing to discard the use of traditional dental splints. For this reason, fully custom orthognathic surgery is also referred to as "splintless" surgery.

The fact that surgical guides allow to predrill holes in the correct final positions and that plates bridge skeletal segments in the planned arrangement overcomes the traditional sequencing (maxilla or mandible first) as well. The sequence is fully interchangeable based on surgeon's preferences, as it does not rely upon a specific splint [17].

Plates are designed as wrapping envelopes around the final skeletal position, after defining the most appropriate sites for screw insertion, which can be placed based on considerations of bone wall-thickness, anatomical variations and accessibility. Once screws are placed, the final skeletal configuration, along with the screws themselves, is brought back

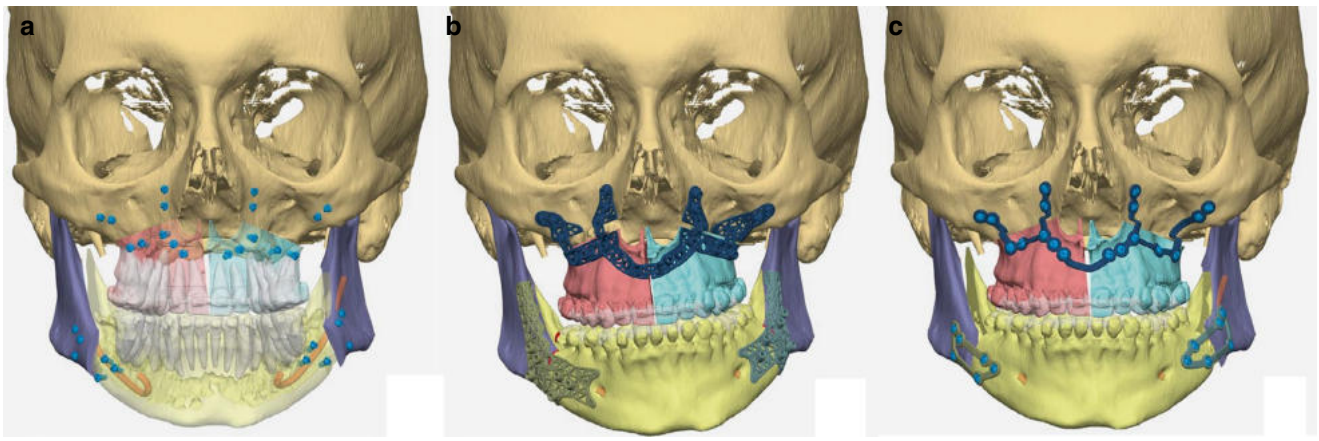


Fig. 32 Sequence of planning in fully custom orthognathic surgery. (**a**) Screw placement; (**b**) realignment of screws with the initial position and creation of the surgical guides; (**c**) final custom plates

to the preoperative configurations, where the same holes are used to fix surgical guides. Cutting planes used to simulate osteotomies in the VSP are taken as reference to define the cutting path within the surgical guide (Fig. 32).

5.1 Workflow for Fully Custom Orthognathic Surgery

The workflow for fully custom orthognathic surgery necessarily involves a medical device company that has the technology to manufacture customized plates, which are implantable devices. There are several steps of increasing complexity that can be used:

- Outsourcing to the external company both the VSP and the manufacturing: it is the oldest and less proficient workflow. It is the preferred choice for centers that do not have the clinical and technological expertise to perform the VSP. As such software is widely available and consistently clinically friendly, the traditional "on-call" VSP performed in teleconference, where the company performs the VSP under the surgeon's supervision, is declining.
- Clinicians performing VSP outsource the final plan to the company for manufacturing (hybrid workflow): it represents the most robust workflow. Using VSP software, surgeons are able to plan the case by themselves, and, once the plan is complete, they deliver it to the company for splint creation. Intermediate stages may involve additional meetings to establish if the position of the screws is correct and solve other issues that may arise. However, this workflow fastens the whole process and is not prone to misunderstandings in the VSP.
- Clinicians performing VSP and designing surgical guides, the company manufactures the plate (advanced hybrid workflow): it is the most advanced stage. For clinicians wishing the highest control and having the right expertise, not just the VSP is performed in hospital, but also the design and production of the surgical guides. In some cases, experienced surgeons might wish to draft plates as well and share their design with the manufacturer, which modifies it according to the regulation criteria established in the company. This has utility especially in case surgeons wish to experiment design variations or prototypes for fixation plates or other implants.

5.2 Precautions in VSP for Fully Custom Surgery

The most impactful maneuver in orthognathic VSP for fully custom procedures is the assessment of bone interferences. This is true in particular for the mandible: after the maxillo-mandibular complex in occlusion has been repositioned, mandibular rami be still in their preoperative position. The final position requires that rami are placed in the most optimal arrangement with the repositioned distal segment by placing their fulcrum of rotation in the center of the mandibular condyle. Any compenetration between the repositioned distal segment and mandibular rami should be minimized by accurately addressing yaw correction, if possible. As the BSSO customized plates are designed in the final position, the final VSP must clearly locate and indicate areas of bone interference to be removed, avoiding to fixate customized plates against a tension caused by posterior inferences.

6 AI-Assisted Digital Workflow in Orthognathic Surgery

The full-digital workflow in virtual surgical planning (VSP) of orthognathic surgery requires meticulous planning to achieve satisfactory clinical outcomes. Various steps in VSP, such as segmentation of anatomic structures, rendering of 3D augmented head models, cephalometry, establishment of the final occlusion, and determining optimal virtual jaw displacements, involve multiple, complex manual operations that are time-consuming and prone to operator-dependent errors. In recent years, the integration of artificial intelligence (AI) into VSP is enhancing the accuracy and efficiency of this process, providing surgeons with advanced (semi) automated tools for image analysis, predictive modeling, and treatment simulations.

6.1 AI-Assisted Segmentation and Rendering of 3D Augmented Models

Recent developments in deep learning have facilitated the traditionally labor-intensive identification and segmentation of various anatomical structures that are required for VSP in orthognathic surgery, such as teeth, jaws, the temporomandibular joint (TMJ), and the mandibular canal.

Automated segmentation of jaws from CBCT scans has been achieved using a mixed-scale dense (MS-D) convolutional neural network. In this way, simultaneous segmentation of the jaw and teeth can be carried out accurately, within approximately 25 s for each CBCT scan [18]. By using convolutional neural network (CNN), combining PointCNN and 3D U-net, teeth on intraoral scans (IOSs) can be segmented and labelled automatically, with clinically acceptable accuracy [19]. The segmented and labeled teeth data from IOS can subsequently be superimposed on the segmented jaws from CBCT through AI-driven registration. A recent randomized clinical study has demonstrated that in the absence of imaging artifacts, the accuracy of this multimodal AI-driven registration is similar to conventional superimposition methods [20]. By combining different AI-based approaches, a 3D augmented head model with accurate image data of the dentition, jaws and facial soft tissues can be created, upon which VSP can be performed.

6.2 AI-Assisted Diagnostics in VSP

Conventional presurgical diagnostics in orthognathic surgery include hard tissue and soft tissue cephalometry. Furthermore, it is important to evaluate the morphology and seating of the condyles to determine the appropriate sequencing of double-jaw surgery and to assess the risk of postoperative condylar resorption and skeletal relapse. Accurate assessment of the location of the mandibular canal with regard to the mandibular buccal cortex and lower border is important to minimize the risk of direct injury to the alveolar nerve during osteotomies. Latest advancements in AI-assisted techniques have improved all these diagnostic steps in VSP.

AI-assisted cephalometry uses deep learning models to automatically identify cephalometric landmarks on CBCT images and perform automated linear and angular measurements. CEFBOT is a deep learning-based method, which applied convolutional neural networks (CNNs), to identify skeletal and soft tissue landmarks on 2D cephalograms. The accuracy of Arnett's cephalometric measurements obtained by CEFBOT was comparable to that of experienced clinicians [21]. By using deep learning approaches, automated systems for cephalometric landmarking on 3D CBCT images can also be achieved with a mean localization error of 1.0 mm, with a reliability for skeletal measurements on par with what clinicians obtain. However, dentoalveolar measurements are less accurate, though satisfactory for hard and soft tissue cephalometry in VSP [22]. .

In assessing the condyles' morphology and seating, deep learning-based image segmentation methods have demonstrated high accuracy in segmenting the TMJ, both the condyles and glenoid fossa from CBCT images [23]. Subsequently, by using integration of multistep segmentation, ray-casting and a feed-forward neural network, an automated evaluation of the condylar seating can be performed in VSP [24]. In this way, incorrectly seated condyles can be identified so that adequate actions can be taken by the surgeon prior to surgery to ensure predictable outcome, such as re-scanning of the patient or adopting a mandible-first sequencing in bimaxillary surgery.

Additionally, the location of the mandibular canal, important for a safe osteotomy, can be identified automatically using AI-driven image analysis. A recent study presented a robust and clinically applicable AI system capable of fully automated segmentation of the mandibular canal on CBCT scans obtained from multiple centers [25]. Compression of the main trunk of the mandibular canal by third molar roots can even be visualized in 3D. This high accuracy supports precise surgical planning and helps avoid injury to the alveolar nerve during surgery.

6.3 AI-Assisted Virtual Surgical Planning

In conventional 3D VSP, virtual osteotomy lines were constructed on the augmented head model after which the planned jaw movements are performed in the virtual envi-

ronment based on the final occlusion, cephalometry and soft tissue simulation of the postoperative outcome. The challenge is to determine the optimal jaw movements required for the patient to achieve the desired occlusion and facial appearance. Advancements in AI are assisting clinicians to accurately simulate postoperative facial changes and to determine the most appropriate jaw positioning.

One of the first published studies in AI-assisted soft tissue prediction used a deep learning-based algorithm for soft tissue prediction in cases of BSSO advancement [26]. Despite being the first study, a higher accuracy was achieved compared to the mass tensor model used in IPS CaseDesigner (KLS Martin, Tuttlingen, Germany), with a mean absolute error for the lower face region of 1.0 ± 0.6 mm. This demonstrated the potential of deep learning to improve the accuracy of soft tissue simulations compared to conventional biomechanical models.

Recently, the facial shape change network (FSC-Net), a geometric deep learning framework designed to predict facial shape changes based on bony movements, was introduced [27]. This network operates by deforming the preoperative facial shape to the predicted postoperative outcome, while simultaneously learning the complex relationship between bone and facial tissue transformations. FSC-Net achieved a 15× increase in simulation time compared to finite element modeling methods and maintained a comparable high level of accuracy. This approach provides surgeons with a more efficient tool for predicting postoperative facial appearances, assisting them to optimize jaw movements during VSP.

To be able to perform soft tissue-based VSP, there is a necessity to be able to automatically determine the optimal jaw displacements required to achieve the desire soft tissue profile. To meet this requirement, a bidirectional 3D deep learning model known as P2P-ConvGC was developed [28]. This model not only can predict the facial soft tissue profile from manually displaced jaws; its strength is that it can also determine the specific bone movements necessary to obtain the desired soft tissue outcome. This innovation represents a significant advancement in automated soft tissue-based backward planning and is bringing orthognathic surgery closer to a more personalized surgical planning.

6.4 Challenges and Future Perspectives

In summary, AI techniques have brought significant improvements to orthognathic surgery by enhancing the accuracy and efficiency of VSP. Key processes like the segmentation of anatomical structure, cephalometric analyses and predictive modeling, which conventionally relied on extensive manual input and sophisticated biomechanical and statistical modeling, have been made faster and less observer-dependent. As a result, surgeons can focus more on critical aspects of patient care, enhancing the overall efficiency, quality and consistency in the orthognathic healthcare pathway.

Despite its transformative potential, AI-assisted VSP faces several challenges. Current AI models still struggle to fully understand the complex relationship between facial soft tissue, underlying skeletal structures and dentition. The calculation of the best-fit final occlusion, which is a key step in VSP, remains beyond the capabilities of AI to date. Furthermore, the development of robust AI models depends on the availability of large, diverse and complete datasets, which are difficult to obtain between clinics and countries. Moreover, there is a lack of a standardized validation method, which is necessary to compare the effectiveness of different AI models in orthognathic surgery in a uniform manner. Additionally, aspects such as privacy concerns, ethical considerations and the integration of AI tools into existing software and clinical workflows remain to be obstacles in the widespread adoption of AI-assisted VSP.

Looking forward, the future of AI in orthognathic surgery is bright. The integration of AI into robotic-assisted surgeries may further enhance surgical precision. With the potential to provide real-time guidance during surgery, autonomous treatment algorithms could allow surgeons to focus on more complex decision-making while AI handles routine, yet critical, tasks. The development of more generalized AI models that mimic the surgeon's thought process in initial treatment planning is also underway. This has the potential to enable AI to adopt a more holistic approach to surgical planning, making orthognathic surgery more personalized and tailored to the unique anatomical features of each patient, while still maintaining the human touch in patient care.

References

1. Donaldson CD, Manisali M, Naini FB. Three-dimensional virtual surgical planning (3D-VSP) in orthognathic surgery: advantages, disadvantages and pitfalls. J Orthod. 2021;48:52–63.
2. Kaasalainen T, Ekholm M, Siiskonen T, Kortesniemi M. Dental cone beam CT: an updated review. Phys Med. 2021;88:193–217.
3. Hegazy MAA, Eldib ME, Hernandez D, Cho MH, Cho MH, Lee SY. Dual-energy-based metal segmentation for metal artifact reduction in dental computed tomography. Med Phys. 2018;45:714–24.
4. Schmidt AMA, Grunz J-P, Petritsch B, Gruschwitz P, Knarr J, Huflage H, Bley TA, Kosmala A. Combination of iterative metal artifact reduction and virtual monoenergetic reconstruction using split-filter dual-energy CT in patients with dental artifact on head and neck CT. Am J Roentgenol. 2022;218:716–27.
5. Cassi D, De Biase C, Tonni I, Gandolfini M, Di Blasio A, Piancino MG. Natural position of the head: review of two-dimensional and three-dimensional methods of recording. Br J Oral Maxillofac Surg. 2016;54:233–40.
6. Jakobsone G, Vuollo V, Pirttiniemi P. Reproducibility of natural head position assessed with stereophotogrammetry. Orthod Craniofac Res. 2020;23:66–71.

7. Billiaert K, Al-Yassary M, Antonarakis GS, Kiliaridis S. Measuring the difference in natural head position between the standing and sitting positions using an inertial measurement unit. J Oral Rehabil. 2021;48:1144–9.
8. Smektała T, Jędrzejewski M, Szyndel J, Sporniak-Tutak K, Olszewski R. Experimental and clinical assessment of three-dimensional cephalometry: a systematic review. J Craniomaxillofac Surg. 2014;42:1795–801.
9. Baan F, van Meggelen EM, Verhulst AC, Bruggink R, Xi T, Maal TJJ. Virtual occlusion in orthognathic surgery. Int J Oral Maxillofac Surg. 2021;50:1219–25.
10. Nadjmi N, Mollemans W, Daelemans A, Hemelen GV, Schutyser F, Bergé S. Virtual occlusion in planning orthognathic surgical procedures. Int J Oral Maxillofac Surg. 2010;39:457–62.
11. Wolford LM, Chemello PD, Hilliard FW. Occlusal plane alteration in orthognathic surgery. J Oral Maxillofac Surg. 1993;51:730–40.
12. Trevisiol L, Bersani M, Lobbia G, Scirpo R, D'Agostino A. Sequencing in orthognathic bimaxillary surgery: which jaw should be operated first? A scoping review. J Clin Med. 2023;12:6826.
13. Trevisiol L, Bersani M, Martinez Garza A, Alvarado E, Arnett GW, D'Agostino A. Accuracy of virtual surgical planning in bimaxillary orthognathic surgery with mandible first sequence: a retrospective study. J Craniofac Surg. 2023;51:280–7.
14. Brown Z, Perez D, Ellis E. Sequencing in orthognathic surgery. In: Miloro M, Ghali GE, Larsen PE, Waite P, editors. Peterson's principles of Oral and maxillofacial surgery. Cham: Springer International Publishing; 2022. p. 1945–67.
15. Pereira PAA, Canellas JV, Souza RB, Tiwana PS, Medeiros PJ, Ritto FG. Three-segment versus 2-segment surgically assisted rapid maxillary expansion. Oral Surg Oral Med Oral Pathol Oral Radiol. 2022;133:264–70.
16. Gander T, Bredell M, Eliades T, Rücker M, Essig H. Splintless orthognathic surgery: a novel technique using patient-specific implants (PSI). J Craniomaxillofac Surg. 2015;43:319–22.
17. Li B, Shen S, Jiang W, Li J, Jiang T, Xia JJ, Shen SG, Wang X. A new approach of splint-less orthognathic surgery using a personalized orthognathic surgical guide system: a preliminary study. Int J Oral Maxillofac Surg. 2017;46:1298–305.
18. Wang H, Minnema J, Batenburg KJ, Forouzanfar T, Hu FJ, Wu G. Multiclass CBCT image segmentation for orthodontics with deep learning. J Dent Res. 2021;100:943–9.
19. Vinayahalingam S, Kempers S, Schoep J, Hsu T-MH, Moin DA, van Ginneken B, Flügge T, Hanisch M, Xi T. Intra-oral scan segmentation using deep learning. BMC Oral Health. 2023;23:643.
20. Ntovas P, Marchand L, Finkelman M, Revilla-León M, Att W. Accuracy of manual and artificial intelligence-based superimposition of cone-beam computed tomography with digital scan data, utilizing an implant planning software: a randomized clinical study. Clin Oral Implants Res. 2024;35:1262–72.
21. Silva TP, Hughes MM, dos Menezes LS, de Melo MFB, de Freitas PHL, Takeshita WM. Artificial intelligence-based cephalometric landmark annotation and measurements according to Arnett's analysis: can we trust a bot to do that? Dentomaxillofac Radiol. 2022;51:20200548.
22. Dot G, Schouman T, Chang S, Rafflenbeul F, Kerbrat A, Rouch P, Gajny L. Automatic 3-dimensional cephalometric landmarking via deep learning. J Dent Res. 2022;101:1380–7.
23. Vinayahalingam S, Berends B, Baan F, Moin DA, van Luijn R, Bergé S, Xi T. Deep learning for automated segmentation of the temporomandibular joint. J Dent. 2023;132:104475.
24. Berends B, Vinayahalingam S, Baan F, Flügge T, Maal T, Bergé S, de Jong G, Xi T. Automated condylar seating assessment using a deep learning-based three-step approach. Clin Oral Investig. 2024;28:512.
25. Ni F-D, Xu Z-N, Liu M-Q, Zhang M-J, Li S, Bai H-L, Ding P, Fu K-Y. Towards clinically applicable automated mandibular canal segmentation on CBCT. J Dent. 2024;144:104931.
26. Ter Horst R, van Weert H, Loonen T, Bergé S, Vinayahalingam S, Baan F, Maal T, de Jong G, Xi T. Three-dimensional virtual planning in mandibular advancement surgery: soft tissue prediction based on deep learning. J Craniomaxillofac Surg. 2021;49:775–82.
27. Ma L, Xiao D, Kim D, et al. Simulation of postoperative facial appearances via geometric deep learning for efficient Orthognathic surgical planning. IEEE Trans Med Imaging. 2023;42:336–45.
28. Bao J, Zhang X, Xiang S, et al. Deep learning-based facial and skeletal transformations for surgical planning. J Dent Res. 2024;103:809–19.

Applications of VSP in Orthognathic Surgery

Alessandro Tel and Massimo Robiony

1 Correction of II Classes

1.1 Mandibular-Only Correction with Mandibular Anterior Segmental Subapical Osteotomy (MASSO)

Clinical Analysis

A 36-years-old woman presented to our attention with a II class, division 1, dentofacial dysmorphosis. Facial analysis revealed a hypodivergent profile, prominent chin and pronounced mandibular angles. During smile, there was a normal dental exposure without gingival exposure. Maxillary protrusion was estimated normal, as confirmed by a normal range value of SNA angle, but a significant retrusion of the mandible with flattening of the cervicomandibular angle was assessed, conditioning the lower lip retraction and a severe II class malocclusion. There was no evidence of maxillary canting at clinical examination, and the superior interincisal line was centered with the facial midline (Fig. 1).

Concerning sagittal dimension in cephalometric analysis, values for SNA, SNB and ANB angles were respectively 79.5°, 75° and 6.1 °, which was coherent with the diagnosis of a mandibular retrusion with a marked overjet, as evaluated by normograms in white population [1].

Virtual Surgical Planning and Correction

A less invasive approach consisting of a mandibular-only procedure was proposed to the patient, who complained about her mandibular retrusion and the II class malocclusion. As described by Brusati [2], the subapical mandibular osteotomy is designed to increase the apical base in mandibular retrusion, at the same time optimizing inferior incisal axis to improve labio-dento-mental-morphology. It also corrects an increase in overjet both alone and as a combined procedure with the BSSO. This technique can also be used as an alternative to traditional presurgical orthodonthics to lingualize proclined incisors (instead of decompensation); however, this patient had already undergone traditional orthodontics [2].

For this specific case, a mandibular BSSO to yield 1 cm advancement at the bone gap between the proximal and distal mandibular segments was combined with a MASSO to further advance the intercanine segment until the overjet was normalized. In addition, mandibular border contouring was planned to reduce the "squared" effect of the patient's face caused by the prominence of mandibular angles and hypodivergence. A genioplasty with clockwise rotation was added to augment the height of the lower facial third and correct the effect of hypodivergence (Fig. 2).

A. Tel (✉)
Lead Specialist for VSP and 3DP, Maxillofacial Surgery Clinic, Head & Neck and Neuroscience Department, Academic Hospital of Udine, Udine, Italy
e-mail: alessandro.tel@uniud.it

M. Robiony
Chief of Maxillofacial Surgery Clinic, Director of the Postgraduate School in Maxillofacial Surgery, Chief of Head & Neck and Neuroscience Department, Academic Hospital - University of Udine, Udine, Italy
e-mail: massimo.robiony@uniud.it

© The Author(s), under exclusive license to Springer Nature Switzerland AG 2025

A. Tel, M. Robiony (eds.), *Atlas of Virtual Surgical Planning and 3D Printing for Cranio-Maxillo-Facial Surgery*,
https://doi.org/10.1007/978-3-031-94495-6_17



Fig. 1 Case 1. Preoperative clinical and occlusal evaluation

To plan MASSO, it was of utmost importance to define the level of dental roots in the intercanine region to place the cutting plane slightly inferior. For this case, patient-specific surgical guides were modeled and printed at the point-of-care (PoC), thus making the procedure fully guided (Fig. 3).

The result was an advancement of 10.4 mm at the lower interincisal midline (LIM) and of 14.7 mm at the pogonion. The postoperative photographs of the patient show the normalization of occlusion with a correct overjet and overbite and the achievement of the appropriate incisal inclination. Still some inferior midline deviation persisted, solved by postsurgical orthodontics, as well as gaps distal to the MASSO and posterior to canines, which formed as a result of the anterior segmental advancement. Postoperatively, the advancement of the inferior lip was assessed, as well as of the widening of the labiomental angle in side view. Frontally, the augmentation of the lower third was achieved, as well as a "smoothed" effect on the jawline through mandibular border ostectomies (Fig. 4).

1.2 Combined Maxillary Two-Piece and Mandibular Correction

Clinical Analysis

The evaluation of a 27-year-old lady was performed to assess a class II, division 1, malocclusion, for which the patient was a candidate for orthognathic surgery. After orthodontic decompensation, the patient revealed an increased overjet due to the lingualization of lower incisors, with a tendency to posterior cross-bite. At esthetical examination, the patient presented a biretruded profile with microgenia, widening of both nasolabial and labiomental angles, with a proportionally well-distributed height of middle and lower facial third. No maxillary canting was assessed (Fig. 5).

Cephalometric analysis revealed 78.6° for SNA angle, 70.0° for SNB and 7.8° for ANB, thus confirming the clinical diagnosis of biretrusion with a predominant mandibular retrusion and a marked maxillo-mandibular discrepancy. Occlusal plane tilt, as marked by the FHP-OcP angle, was of 10.6°.

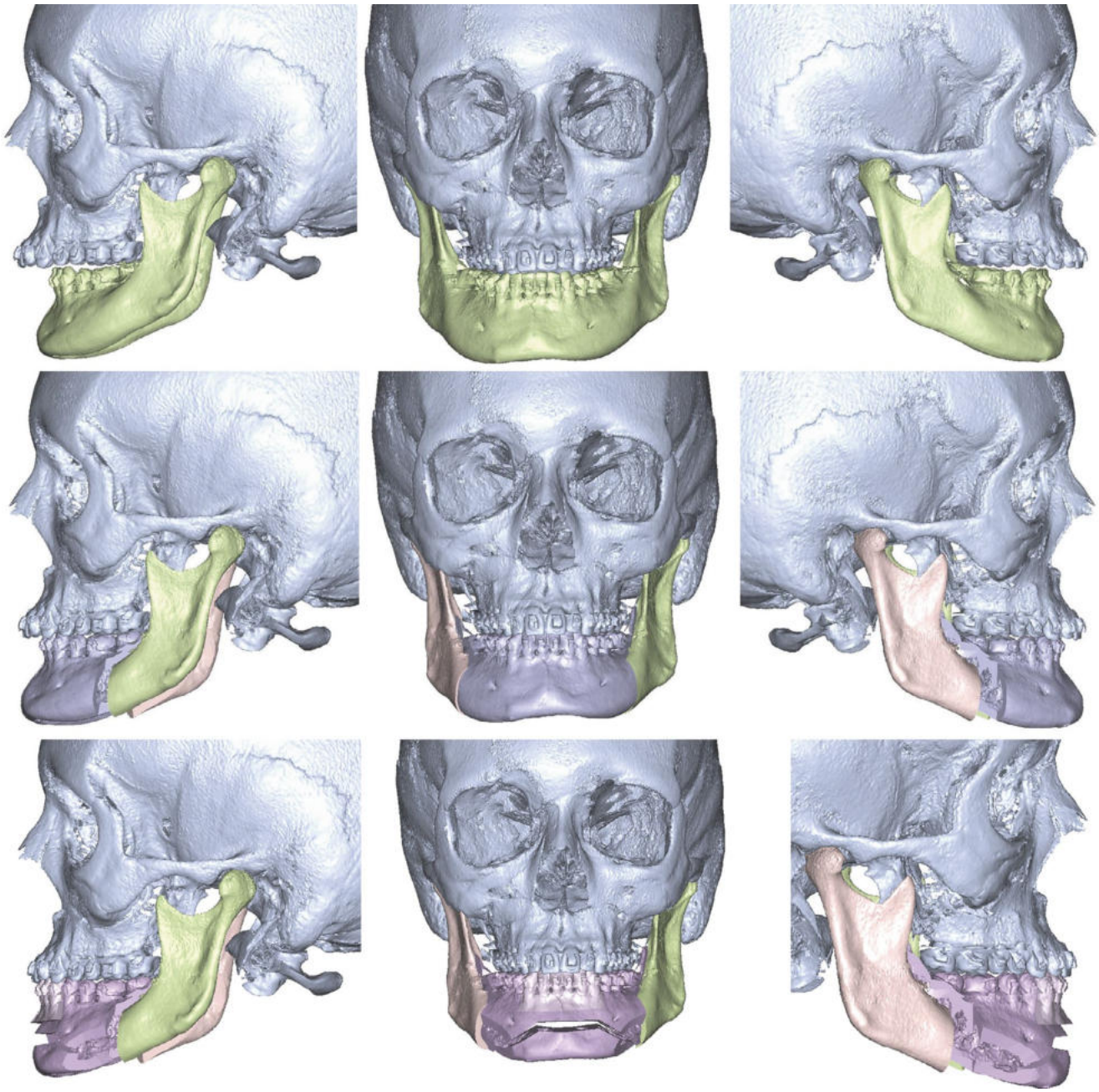


Fig. 2 Case 1. VSP with MASSO

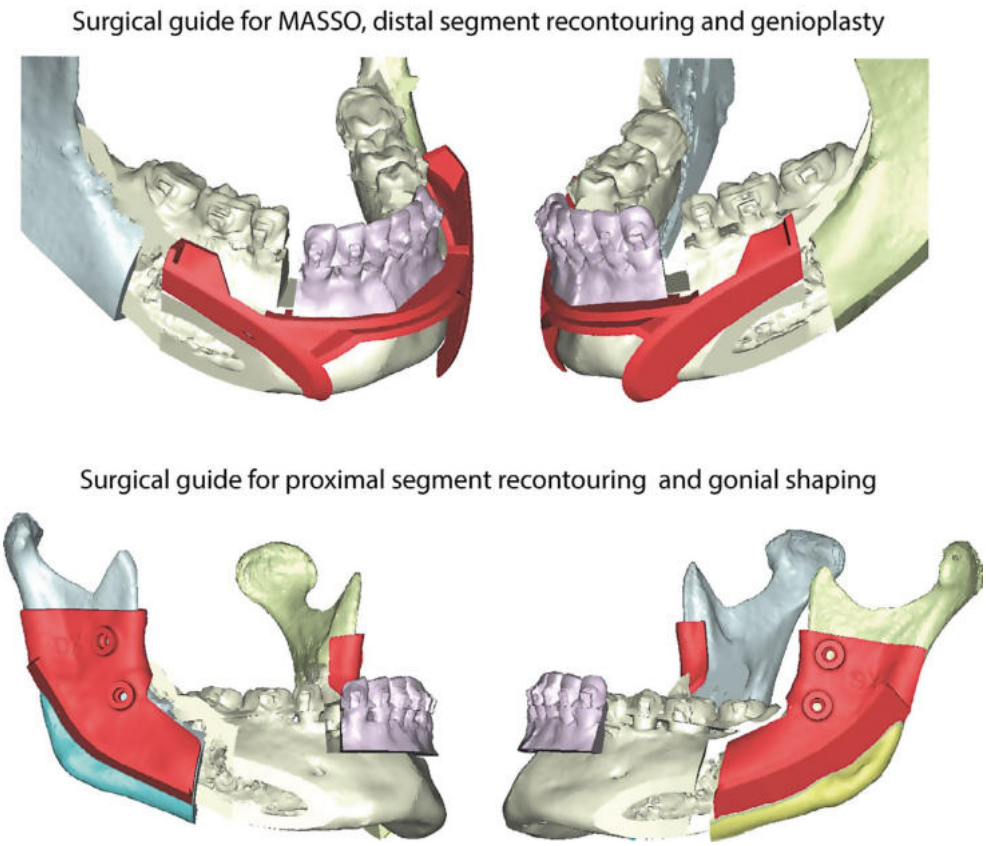


Fig. 3 Case 1. Surgical guides for gonial shaping, border contouring, genioplasty and MASSO



Fig. 4 Case 1. Postperative 3-month clinical and occlusal outcome. Postoperative orthodontic therapy was still ongoing



Fig. 5 Case 2. Preoperative clinical and occlusal evaluation

Virtual Surgical Planning and Correction

A combined bimaxillary orthognathic surgery was proposed to the patient, with a two-piece partition of the maxilla to compensate the transversal defect. VSP at first included maxillary bipartition with occlusal registration of the maxillo-mandibular complex. Skeletal repositioning was performed with the combination of a 6 mm maxillomandibular advancement, with pitch correction through a counterclockwise rotation of 2° by placing the rotational fulcrum posteriorly to reduce the slope of the occlusal plane. The corrective action of counterclockwise rotation magnified the mandibular retrusion and further enhanced chin advancement. The superior interincisal midline was considered centered with the facial midline and did not require any further centering. Yaw was corrected to neutralize as much as possible the bone interference between mandibular rami and the tooth-bearing segment. Finally, a sliding genioplasty was added to further remodel labiomental angle. The surgical sequencing was chosen as mandible first to provide a repositioned jaw for the maxillary expansion, thus requiring a single intermediate plate. A slight amount of disclusion was simulated in the mandible first intermediate position to solve interferences (Fig. 6).

The final result was the maxillo-mandibular advancement with normalization of SNA, SNB and ANB angles, which measured respectively 83.8°, 75.5° and 2.3°. The nasolabial angle was reduced, approximating 90°, as well as the labiomental angle and the cervicomandibular angle. The effect of further chin advancement appeared as an increased sagittal projection with advancement of the labialis inferior point. From the occlusal side, there was a satisfactory posterior expansion of the maxillary diameter and the restoration of an appropriate overjet and overbite. The final occlusion yielded increased stability by displacing the inferior interincisal line slightly leftward compared to the original surgical occlusion after orthodontic treatment (Fig. 7).

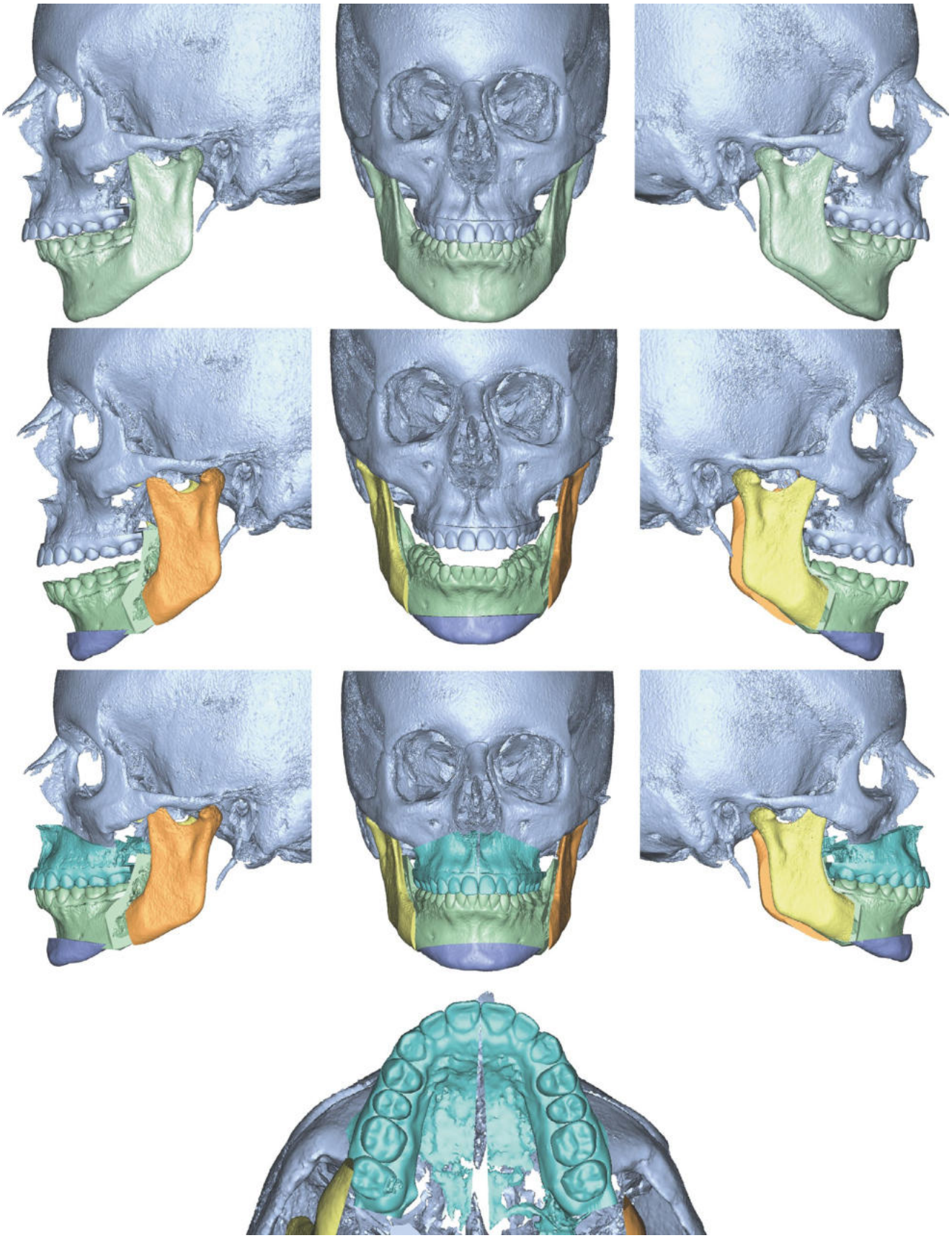


Fig. 6 Case 2. VSP with maxillary bipartition



Fig. 7 Case 2. Postoperative 1-year clinical and occlusal outcome

1.3 Combined Maxillary Three-Piece and Mandibular Correction

Clinical Analysis

A 21-year-old lady was referred to our center for the correction of a class II, division I, malocclusion. Clinical diagnosis revealed a microgenia with a hypoplasic mandible, a biretruded profile with predominant mandibular retrusion, widening of nasolabial angle and flattening of the cervicomandibular angle. Maxillary canting was ruled out. The patient presented an increased gingival exposure when smiling.

Occlusal evaluation revealed a slight bilateral crossbite with significant reduction of the transversal maxillary diameter and right-side shifting of the inferior interincisal line of approximately 2 mm. The patient was prepared for a three-piece maxillary surgery by creating a gap between lateral maxillary incisors and canines (Fig. 8).

Cephalometric analysis revealed a reduced SNA, SNB and increased ANB, of respectively 80.8°, 73.3° and 7.4°. There was slight hyperdivergence with increased pitch of the occlusal plane, confirmed by FHP-OcP angle of 9.1°.



Fig. 8 Case 3. Preoperative clinical and occlusal evaluation

Virtual Surgical Planning and Correction

A combined bimaxillary orthognathic surgery with maxillary three-piece expansion was chosen to address this case (Fig. 9). Maxillary three-piece partition was performed according to a Y design to be comparable with the model surgery setup. The maxillo-mandibular complex, consisting of the expanded three-piece maxilla and the mandible registered in the most appropriate occlusion, was established according to the physical setup performed on model surgery. The premaxillary osteotomy was performed between lateral incisors and canines and shifted slightly interiorly, allowing to yield a satisfactory overbite, whereas the lateral segments expanded providing a substantial transversal increase.

First, the superior interincisal line was checked to verify its correspondence with the facial midline. Maxillary cant was not modified. To compensate hyperdivergence leading to a high occlusal plane and retruded chin, a counterclockwise rotation with a 4 mm anterior ostectomy was planned. This enabled to normalize the occlusal plane tilt while projecting forward the chin. A mild 2 mm bimaxillary advancement was planned to further advance the maxilla and normalize the nasolabial angle. Such movements were carefully planned as a large surgical advancement of the mandible combined with an important counter-clockwise rotation involves excessive load on the condylar head, predisposing to condylar resorption [3].

In fact, literature reports that skeletal class II profiles and hyperdivergent growth patterns are more frequently related to altered TMJ load resulting in disc displacement and degenerative disorders [4]. Likewise, mandibular hypoplasia and hyperdivergence in the sagittal plane are described to be the most common growth patterns in which condylar resorption could occur after orthognathic surgery [5].

Last, yaw correction was performed accurately to minimize bone interferences by preserving the correct alignment of the interincisal lines, as rotation fulcrum was positioned in correspondence of UIM. To further sculpt the labiomental fold, a sliding geniplasty with 4 mm advancement was planned. The chosen surgical sequencing was a mandible first surgery, allowing to reposition in advance the mandible and provide the maxilla a stable skeletal base to expand upon.

The effect of VSP involved a normalization of SNA, SNB and ANB angles with the respective values of 83.2°, 75.7° and 4.1°. Occlusal plane pitch was decreased by the effect of counterclockwise rotation with resulting FGP-OcP of 4.3°. There was a smiling harmonization with reduction of gingival exposure. Mandibular advancement combined with genioplasty led to the improved jawline definition with narrowing of cervicomandibular angle and shaping of the labiomental fold (Fig. 10).

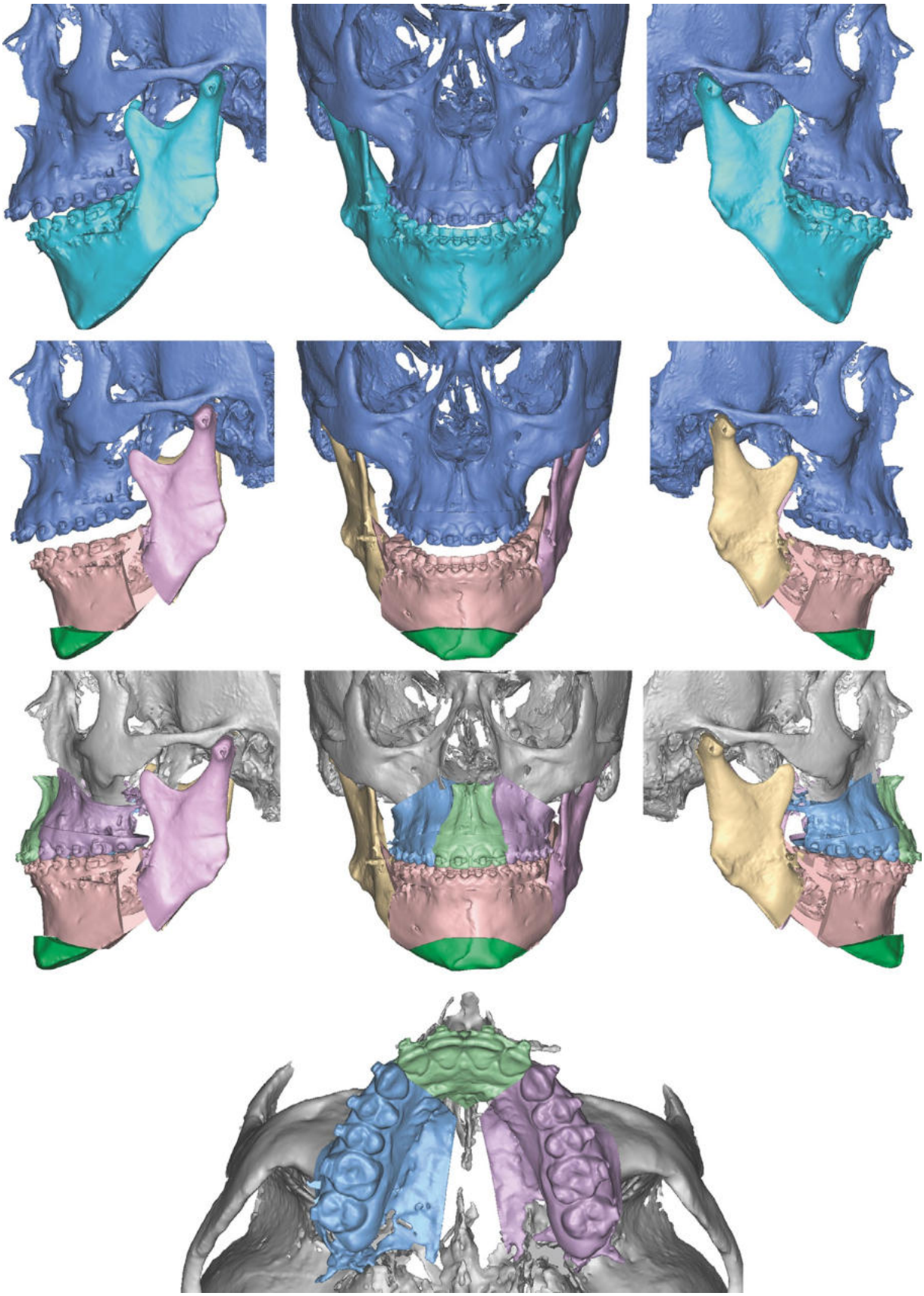


Fig. 9 Case 3. VSP with maxillary tripartition and substantial maxillary expansion



Fig. 10 Case 3. Postoperative 1-year clinical and occlusal outcome

2 Correction of III Classes

2.1 Combined Maxillo-Mandibular Repositioning in Hyperdivergent Patient with Lower Third Increase

Clinical Analysis

A 24-year-old lady was sent by her orthodontist to evaluate the surgical treatment of her class III malocclusion. The patient had a symmetric mandibular sagittal excess, with both interincisal lines centered with the facial midline. Gingival exposure was normal and symmetric during smile, showing a normally conformed maxilla without appreciable canting. The nasolabial angle was slightly widened, thereby indicating a slight maxillary retrusion. There was a significant negative overjet with a class III malocclusion, a hyperdivergent growth pattern, and a vertical excess due to the mandibular growth especially around the chin (Fig. 11).

Cephalometric analysis inspection showed the following values for SNA, SNB and ANB: 89.5°, 90.5° −2.1°, which revealed a prominent mandibular growth. Occlusal plane tilt was in normal range values (FHP-OcP = 10.7°; with a normal value of 8° 4° [6].

Virtual Surgical Planning and Correction

A combined orthognathic surgery was chosen with a maxilla first sequence. After Le Fort I osteotomy and BSSO were performed, mandibular setback was simulated to reestablish



Fig. 11 Case 4. Preoperative clinical and occlusal evaluation

a class I occlusion. To compensate the significant setback, a 5 mm advancement was planned and coupled with a 1° counterclockwise rotation to correct the hyperdivergence. No transversal movements were required, as well as roll and yaw corrections. Finally, a reduction genioplasty with the excision of a 4 mm bone and the advancement of 3 mm to redefine the flattened labiomental crease was planned (Fig. 12).

After such corrections, cephalometric values modified as follows: SNA, 96.4°; SNB, 90.0°; ANB, 2.4°.

Postoperative esthetic analysis revealed significant correction of hyperdivergence with shortening of the lower facial third, regularization of the labiomental angle and smoothly improved volume in the cheekbone contour area, with only minimal decrease of gingival exposure during smile, as maxillary impaction movements were compensated by advancement. The effect of reduction genioplasty enabled to correct the dolichofacial shape led to a more rounded jawline. From the occlusal side, there was the restoration of a normal overjet and overbite with a first-class relationship (Fig. 13).

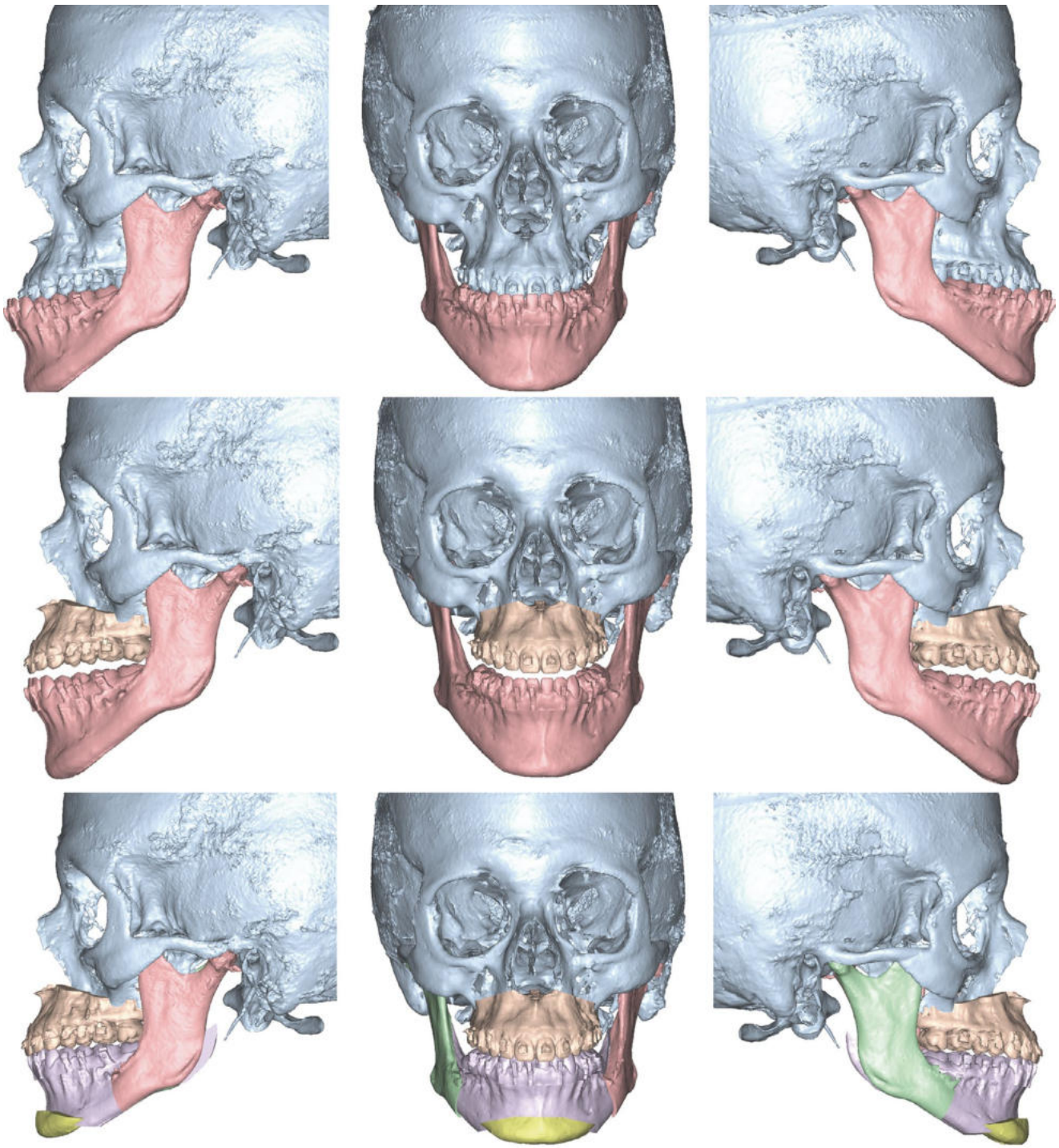


Fig. 12 Case 4. VSP



Fig. 13 Case 4. Postoperative 1-year clinical and occlusal outcome

2.2 Combined Maxillo-Mandibular Repositioning in Hyperdivergent Dolichofacial Patient with Maxillary Canting and Laterodeviation

Clinical Analysis

A 36-year-old lady followed a surgery first preparation for orthognathic surgery. At presurgical examination, she presented a typical high-occlusal plane, hyperdivergent, facial type, with mandibular laterodeviation. Maxillary canting with a vertical excess on the right side was assessed. Flatness in the cheek-malar area was assessed and related with a maxillary sagittal defect. Superior interincisal line was shifted on the right side 1 mm compared with the facial midline, while inferior interincisal line was moved 3 mm leftward compared to its superior counterpart. There was a left deviation of the pogonion on the frontal side. Labiomental angle was widened, and a substantial reduction of the cervicomandibular angle was present.

From the occlusal side, anterior crossbite with a third-class occlusion was assessed, with negative overjet and overbite (Fig. 14).

Cephalometry revealed SNA, SNB and ANB angles respectively of 83.1°, 85.9° and -2.8°.

Virtual Surgical Planning and Correction

In this case, corrective movements were established to correct hyperdivergence through counterclockwise rotation, maxillary advancement, lateral translation for deviation and roll neutralization. First, maxillo-mandibular occlusion was established through model registration, and a substantial setback of approximately 4 mm was appraised. The entire maxillo-mandibular complex in a class I relationship was advanced to compensate the entity of the mandibular setback and maintain the preoperative sagittal position of the mandible. The interincisal lines were centered with the facial midline through linear translation. Maxillary canting was corrected by placing the rotational fulcrum over the right



Fig. 14 Case 5. Preoperative clinical and occlusal evaluation

maxillomalar buttress and performing a left impaction until roll was neutralized. Finally, yaw was modified to enhance the bone-to-bone interface between the distal tooth-bearing segment and mandibular rami (Fig. 15).

The combined effect of such movements was a substantial shortening of the vertical dimension, which remarkably affected the lower third, the normalization of occlusal plane angle and the restoration of a normal divergence; an improved facial fullness around the cheek area due to maxillary advancement; and the symmetry of smile after centering the interincisal lines and correcting maxillary canting (Fig. 16).

Results on cephalometric analysis include an increase of ANB angle (1.3°), an increase of SNA angle (87.7°) and reduction of SNB angle (86.0°). Overall, UIM advanced 3.9 mm and was moved up of 4 mm.

2.3 Combined Maxillo-Mandibular Orthognathic Surgery with Midfacial Hypoplasia and Maxillo-Malar Osteotomies

Clinical Analysis

A 24-year-old patient was sent to evaluation for a severe third-class malocclusion with associated hyperdivergence and a biconcave profile. The patient revealed an exceeding, but symmetric, mandibular growth that did not condition a facial asymmetry. Maxillary canting was not assessed at clinical evaluation. The superior interincisal line appeared aligned with the facial midline, while the inferior interincisal line was deviated 3 mm left compared to its superior counterpart. Maxillary gingival exposure was normal during smile. The patient had a constant anterior open bite caused by the mandibular elongation, which he compensated with a contraction of the lips (Fig. 17).

Cephalometric analysis revealed SNA value of 85.3°, SNB of 90.4°, ANB of −4.7°, thus confirming the clinical diagnosis of a severe class III malocclusion with mandibular anterior-posterior excess.

Virtual Surgical Planning and Correction

In this case, orthognathic surgery was modified by a variation of maxillary osteotomy according to a "butterfly" design consisting in lifting the osteotomy level and revolving around the infraorbital foramen. Such osteotomy design is specifically conceived to add volume to the hypoplasic middle third and has a rejuvenating effect thanks to the resulting fullness effect it provides to the maxillo-malar area. Intraoperatively, the zygomatic contours of the butterfly design osteotomy can be further volumized by transposing the pedicled Bichat bulla flap just above the osteotomy. The variation of the maxillary osteotomy has thus the advantage of improving the final esthetic result based on the maxillary movements. This technique is carefully described in a paper by the author and his group [7] and is successfully performed using piezoelectric bone cutting and guidance provided by navigation. Due to their unconventional design, maxillo-malar osteotomies can not be simulated in traditional software for orthognathic

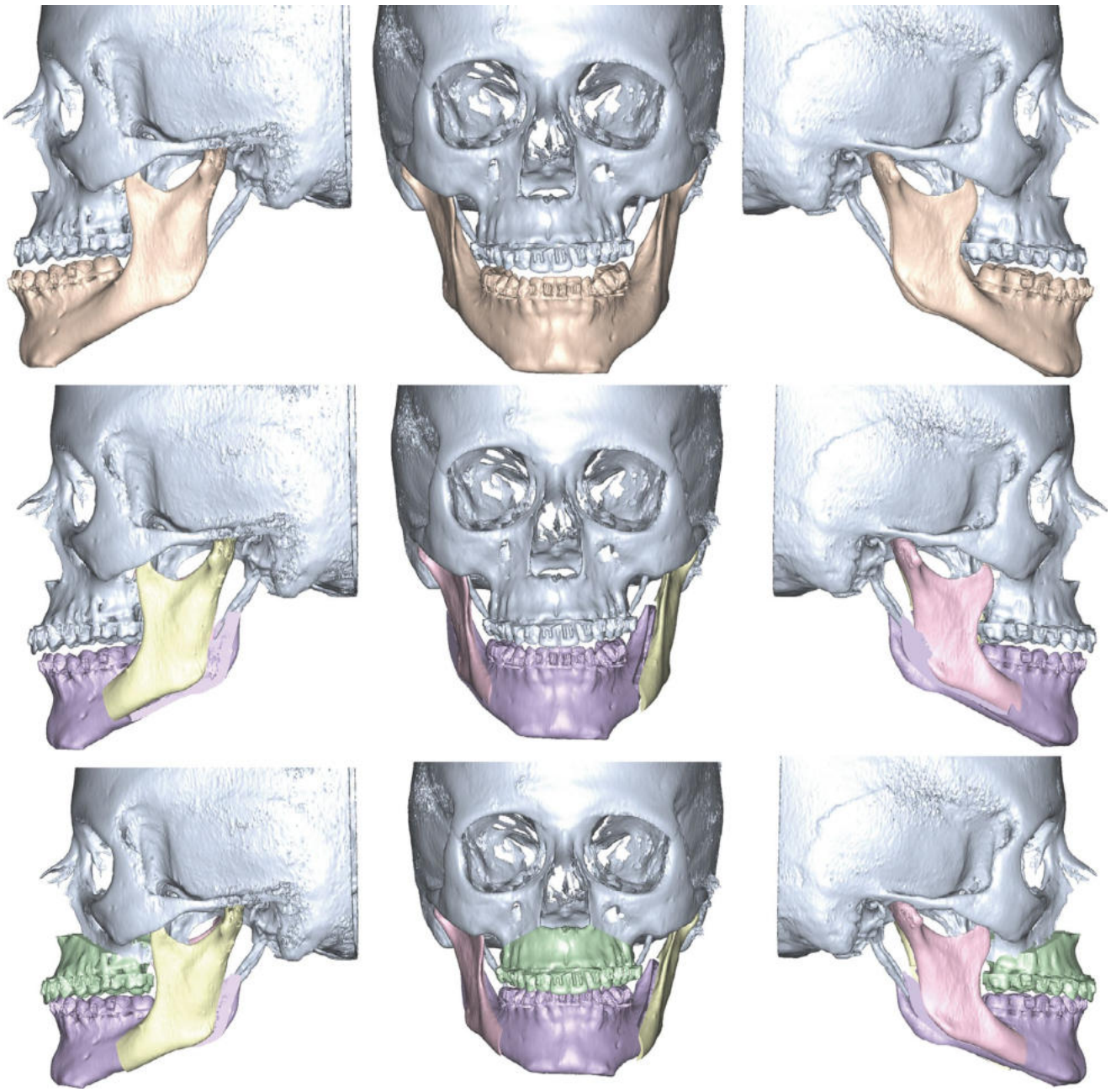


Fig. 15 Case 5. VSP



Fig. 16 Case 5. Postoperative 3-month clinical and occlusal outcome



Fig. 17 Case 6. Preoperative clinical and occlusal evaluation

surgery, as they involve curve tracing, and should be better addressed in a more comprehensive design package integrating organic modeling features, such as Geomagic Freeform.

For this patient, after maxillo-malar osteotomy design was integrated into the upper maxillary base, planned occlusion was established by registration to casted models, yielding the maxillo-mandibular complex in the desired class I occlusion. A substantial maxillo-mandibular advancement of 7 mm was performed to counteract the significant mandibular setback resulting from the occlusal correction, at the same time balancing the concave, hyperdivergent profile with an increased maxillary projection. As the 7 mm maxillary

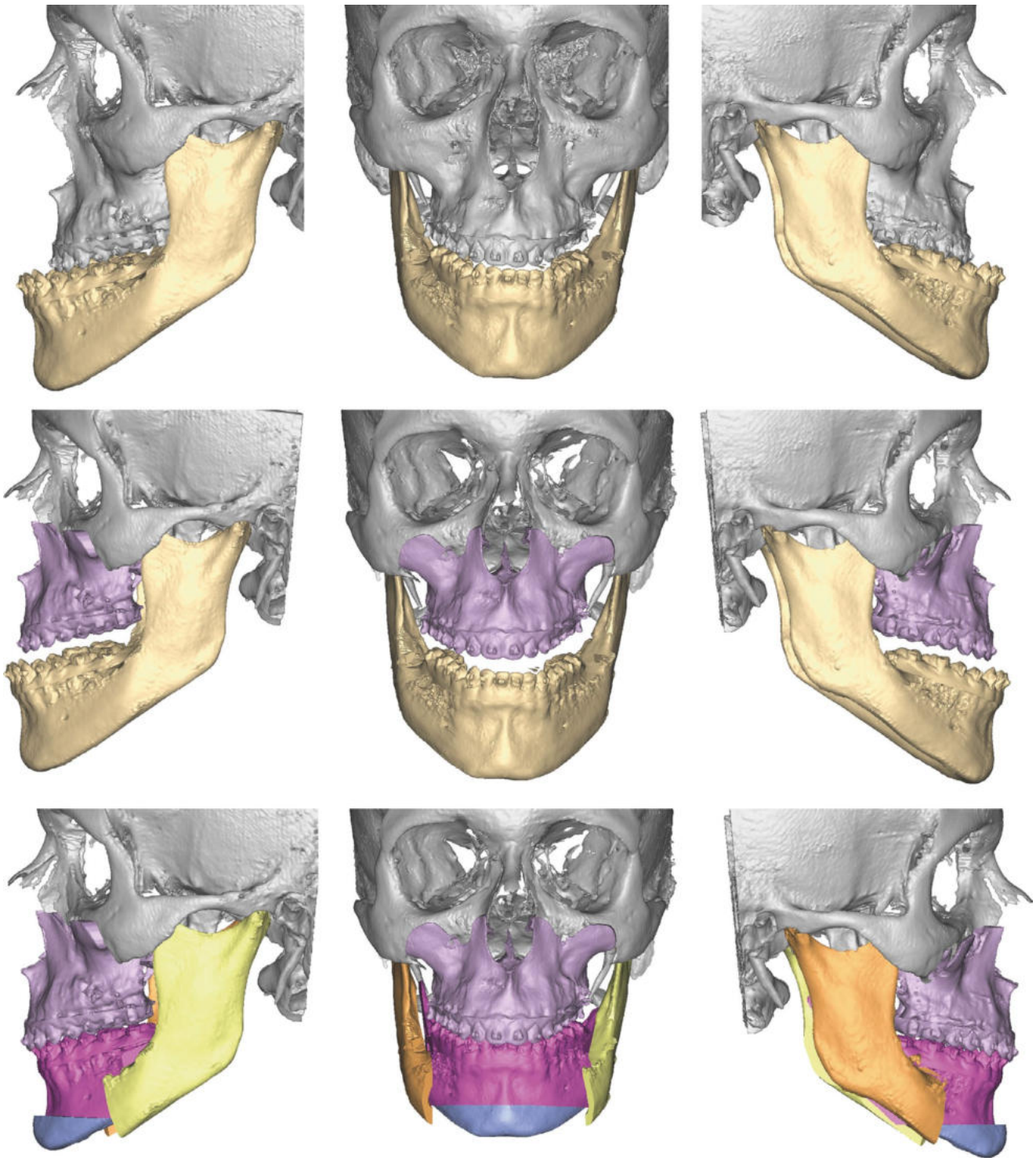


Fig. 18 Case 6. VSP

advancement would lead to a substantial increase of gingival exposure during smile, a 4 mm impaction was planned to normalize the maxillary height, which moreover shortened the dolichofacial appearance of the patient and corrected mandibular divergence. No maxillary roll correction was necessary as canting was not clinically appraised (Fig. 18).

To further remodel labiomental sulcus, a sliding genioplasty with 4 mm advancement and 3 mm of vertical reduction was planned, further shortening the lower facial third.

Cephalometry inspection revealed normalization of SNA, SNB and ANB, measuring respectively 94.3°, 87.6° and 1.2°.



Fig. 19 Case 6. Postoperative 3-month clinical and occlusal outcome

Postoperative clinical analysis revealed the correction of mandibular sagittal excess, reduction of hyperdivergence, volumization and recontouring around the cheek malar area thanks to the effect of maxillo-malar osteotomies, and a substantial reduction of the vertical excess due to the combined effect of genioplasty and maxillary impaction (Fig. 19).

3 Correction of Asymmetries

Facial asymmetries represent a complex topic of orthognathic surgery in which not just sagittal and vertical alterations need to be corrected by restoring an appropriate class I occlusion, but surgical planning must take into account all actions that aim to reestablish a symmetrical proportion between the two halves of the face. This can be challenging as in several cases there is a hypergrowth (or an hypoplasy) of one side of the face. In some patients, facial asymmetries are related to syndromes, including Goldenhar, Parry-Romberg, Moebius and Treacher-Collins syndrome, which often present hemifacial microsomia [8], but in the majority of cases they are sporadic. Among such cases, the physiopathology may be linked to the persistence of an active growth center in the mandible, in several cases located in the condyle, a condition referred to as unilateral condylar hyperplasia (UCH) [9]. UCH generally produces asymmetry predominant on the vertical dimension with maxillary canting, as the maxilla in its development follows the occlusal plane alteration induced by the asymmetric mandible. The condyle is morphologically altered, generally enlarged. This condition is known as type 2 in Obwegeser and Makek classification. However, type 1, known as hemimandibular elongation, typically presents with a horizontal asymmetry and a more laterally displaced pogonion, while the condyle is generally unaffected. The same classification also included type 3, which includes mixed forms which both exhibit type 1 and type 2 patterns and represent the most complex correction. Wolford et al. proposed more recently an updated classification system in which the same subtypes were analyzed and related with an underlying temporomandibular joint, for instance, osteochondroma in types 2a and 2b [10]. Whenever a hemimandibular hyperplasia (type 2) or a mixed form (type 3) is suspected, the patient should be evaluated for the persistence of an active growth center in the condyle using SPECT imaging to define the uptake ratio between the suspected condyle and the contralateral [11]. This allows to discriminate between progressive and nonprogressive forms of unilateral condylar hyperplasia, which benefit from different treatments. Progressive forms may benefit from proportional condylectomy alone, or condylectomy associated with orthognathic surgery, while nonprogressive forms and type 1 hemimandibular elongation are treated with orthognathic surgery. In this chapter, examples of facial asymmetries without condylectomies will be presented. Cases in which orthognathic surgery was planned with a simultaneous condylectomy will be described in Chapter "Application of VSP in Temporomandibular Joint Surgery" about virtual planning in TMJ surgery.

3.1 Combined Maxillo-Mandibular Orthognathic Surgery in a SPECT-Patient with Facial Asymmetry

Clinical Analysis

A young 27-year-old lady was evaluated for a substantial mandibular asymmetry morphologically attributable to a mixed form (type III according to Obwegeser and Makek), with predominance of mandibular elongation. The patient underwent SPECT imaging, which ruled out significant captation difference between both condyles. The mandibular shape revealed a horizontal growth vector with significant right lateral deviation of the pogonion, which caused an evident cross-bite contralateral to the elongation side and lingualization of contralateral molars. In the profile view, the patient was substantially eumorphic. Frontal analysis revealed a normal gingival exposure during smile; superior interincisal line was centered with the facial midline; a slight maxillary canting with a left vertical excess ipsilateral to the supposed side of hyperplasia was appraised by clinical photographs (Fig. 20).

CT analysis revealed an increased height of the left mandibular ramus, measured from gonion (Go) to condylon (Co), with an increased frontal deviation of the left mandibular ramus as well, conditioned by the horizontal asymmetry. On the side view, the patient was substantially normodivergent, with an increased pitch of the occlusal plane. Postoperative cephalometric analysis revealed the following values for SNA, SNB and ANB: 93.5°, 92.6°, 0.1°. FHP-OcP angle was of 8.4°.

Virtual Surgical Planning and Correction

For this patient, a combined orthognathic surgery was proposed as corrective solution for the facial activity without a diagnosis of active condylar hyperplasia. A maxilla-first sequence was chosen to prioritize the reestablishment of the correct occlusal plane cant and reposition thereafter the mandible (Fig. 21). After osteotomy design, the maxillo-mandibular complex surgical occlusion was determined by registration of models into optimal intercuspation. First, maxillary roll correction was performed with a differential impaction in the coronal plane to lift the left maxillo-malar buttress with pivot point planed in the contralateral side. Occlusal plane pitch was corrected to decrease FHP-OcP angle by performing a 3° counterclockwise rotation with a pterygoid fulcrum. A 5 mm maxillary advancement was performed to improve nasolabial angle, volumize the middle third and slightly lift the nasal tip; its effect on the increase of exposure was neutralized by the aforementioned counterclockwise rotation. A sliding advancement genioplasty was simulated to remodel labiomental fold. Last, yaw was corrected owing to the substantial interference between the tooth bearing segment and mandibular rami caused by the hemimandibular elongation component of this asymmetry.

Postoperative clinical evaluation revealed the normalization of occlusion with interincisal line alignment. A substantial centering of pogonion with the facial midline was achieved, yet some residual asymmetry was appreciable due to the different configuration of mandibular rami conditioned



Fig. 20 Case 7. Preoperative clinical and occlusal evaluation

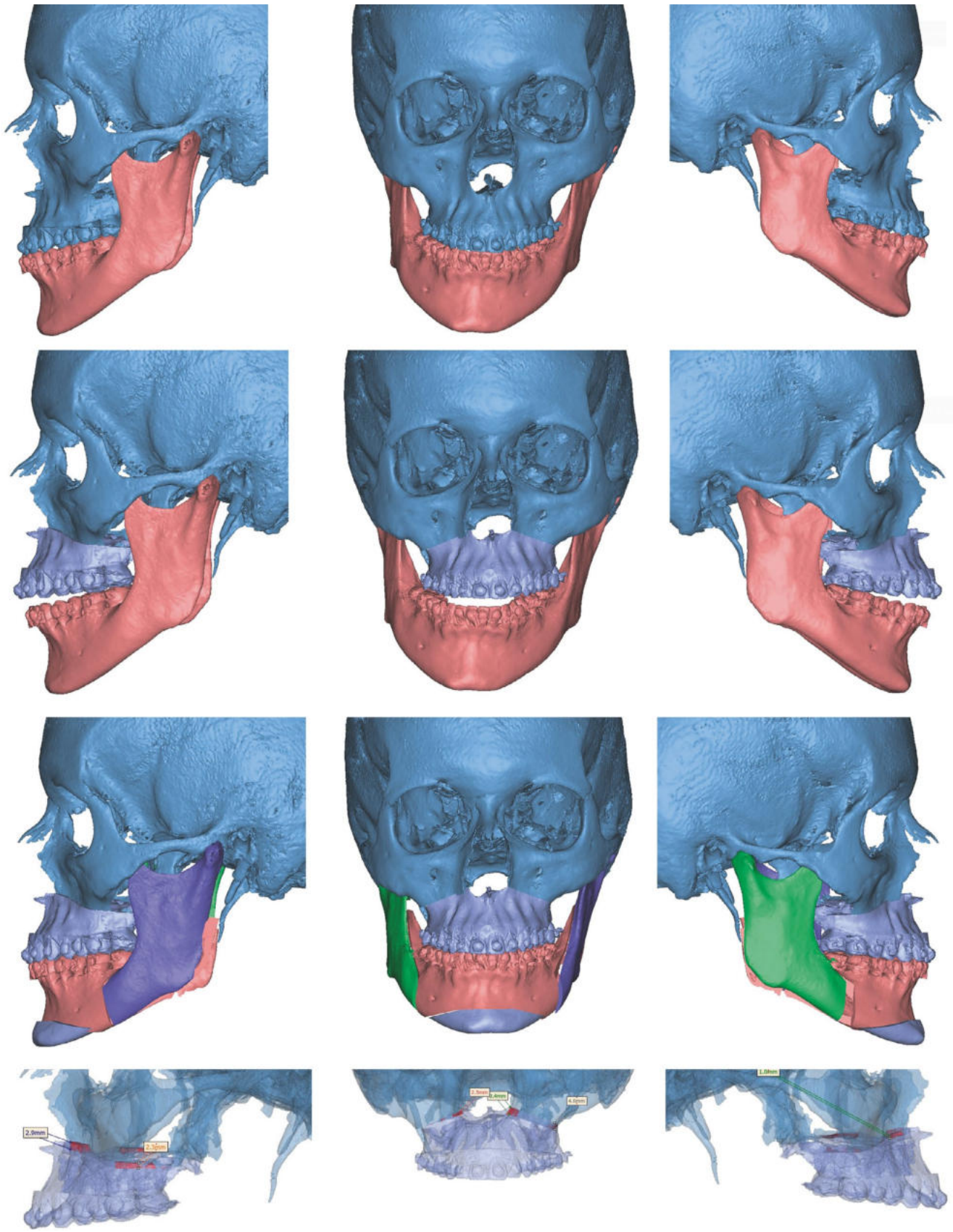


Fig. 21 Case 7. VSP



Fig. 22 Case 7. Postoperative clinical and occlusal outcome

by the hemimandibular elongation. Gingival exposure during smiling was not affected by skeletal repositioning. In side view, an improved definition of the jawline contour was achieved through normalization of hyperdivergence, with an improved visualization of the labiomental angle (Fig. 22). Postoperative cephalometric analysis revealed a SNA, SNB and ANB values respectively of 97.2°, 94.6°, 2.6°. FHP-OcP angle was of 3.7° showing normalization of divergence.

3.2 Combined Maxillo-Mandibular Orthognathic Surgery in a SPECT-Patient with Facial Asymmetry

Clinical Analysis

A young 23-year-old lady was clinically diagnosed with mandibular elongation. She presented a III class dentofacial dysmorphosis with a concave profile, a conspicuous negative overjet with inferior lip protrusion, a hyperdivergent, high occlusal plane facial pattern. The patient had lateral deviation of soft tissue pogonion, which was shifted rightward compared to the facial midline. Gingival exposure was normal during smiling. Middle third evaluation revealed hypoplasia around the malar area and the absence of maxillary canting due to increased height of maxillary alveolar bone. While maxillary canting typically characterizes hemimandibular hyperplasia, it is generally absent in hemimandibular elongation [12]. From the occlusal side, the superior interincisal line was centered with the facial midline, and the inferior interincisal line was shifted rightward about 3 mm. There was no lateral open bite, another distinctive trait of hemimandibular elongation compared to hemimandibular hyperplasia (Fig. 23).

CT inspection did not reveal a condylar enlargement on the side of elongation, which helped to rule out the coexistence of condylar hyperplasia.



Fig. 23 Case 8. Preoperative clinical and occlusal evaluation

Cephalometric analysis revealed the following measurements: SNA 79.9°, SNB 84.8°, ANB 4.9°. FHP-OcP angle was of 9.4°.

Virtual Surgical Planning and Correction

A mandible-first sequence was chosen to manage this case (Fig. 24). First, the first-class occlusion was reestablished between the distal mandibular and the Le Fort I segments. The correction of the third-class pattern, along with the laterodeviation, caused a significant mandibular setback with conspicuous bony interferences between mandibular rami and the tooth-bearing segment, partly solved implementing yaw correction by placing the fulcrum over the superior interincisal line, already centered with the facial midline. A bimaxillary advancement was performed to improve the midfacial projection, with additional 4 mm impaction to compensate for the increased lip retraction caused by the advancement. The overall effect of such movements on LIM was of 7.15 mm posterior and on pogonion of 10.94.

Last, to widen the chin, a T-shaped genioplasty with interposition of mandible-derived bone graft was performed.

Postoperative 1-year evaluation revealed the restoration of the correct relationship between the upper and lower lip, and the final result on the midface was an increased fullness around the cheekbone area with a rejuvenating effect on the patient's appearance. A normal position of the inferior lip was reestablished with lip competence. A slight decrease in the nasolabial angle was desirably achieved as a result of the bimaxillary advancement. A 1 mm decrease of gummy smile was obtained to make the patient's smiling look more natural. The soft tissue pogonion was substantially centered with the facial midline and the chin expanded as planned.

From the occlusal side, the alignment of superior and inferior interincisal lines was yielded, as well as the restoration of the correct first-class pattern both on molars and canines. A successful orthodontic closure of occlusal gaps was achieved (Fig. 25).

Planned postoperative cephalometric angles resulted as follows: SNA 83.5°, SNB 82.9°, ANB 0.7°. Final FHP-OcP angle was of 4.3°.

3.3 Combined Maxillo-Mandibular Orthognathic Surgery in a SPECT-Patient with Facial Asymmetry and Temporomandibular Joint Disorders Using Double Intraoral Vertical Ramus Osteotomy (IVRO)

Clinical Analysis

A 33-year-old lady presented to our attention for the evaluation of facial asymmetry, showing in appearance a mild hemifacial microsomia only affecting the upper maxilla and the mandible. Profile analysis did not reveal any significant sagittal discrepancies and the asymmetry was exclusively limited to the coronal plane. Smile was borderline for dental exposure and did not reveal upper gingiva. There was a right deviation of soft tissue pogonion and a maxillary canting with a shortened maxillary height on the right side as well. Superior interincisal line was slightly deviated left compared

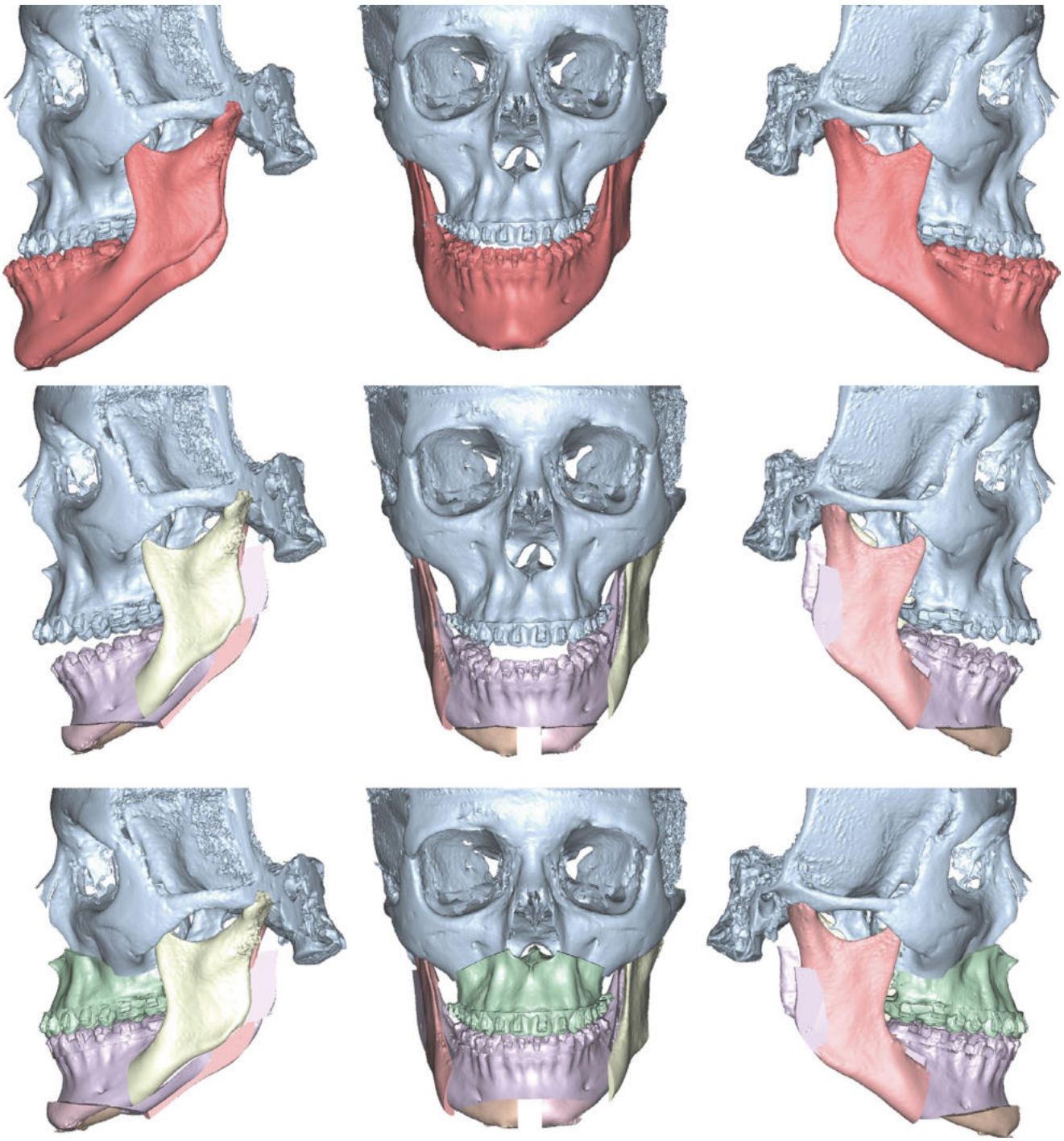


Fig. 24 Case 8. VSP (note design of a T-shaped genioplasty)



Fig. 25 Case 9. Postoperative 1-year clinical and occlusal outcome

with the half of the Cupid's arch, and the inferior interincisal line presented a 2 mm right deviation.

From the occlusal side, there was a tendency to class II malocclusion, especially in the left side, while an almost first-class relationship was preserved on the right side (Fig. 26). CT evaluation revealed reduced vertical proportions of the right hemimaxilla and hemimandible, with gonial asymmetry due to a shortened vertical height from right condylon (Co) to gonion (Go).

Cephalometric analysis assessed a preoperative amplitude of angles as follows: SNA 85.3°, SNB 82.9°, ANB 2.5°. FHP-OcP was of 15°.

The patient had been previously evaluated for temporomandibular joint disorder on both sides and underwent left TMJ arthrocentesis the year before. Inspection of the joint morphology at CT evaluation and after segmentation showed a vertical flattening of condyles, possibly responsible for the tendency to II class malocclusion. To decrease the joint load and minimize the impact of orthognathic surgery on the TMJ function, at the same time preserving it from accelerated degeneration, the choice for mandibular osteotomies was a bilateral IVRO rather than a BSSO. There are multiple evidences according to which IVRO decreased the mechanical load on the TMJ resulting in an anteroinferior displacement of the condyles, with the effect of relieving pressure on the disc and enhancing the reestablishment of the correct intraarticular equilibrium [13]. This condylotomy effect was evaluated by a series of study, including that of Bell and Yamaguchi demonstrating that the condyle moves anteroinferiorly and gradually restores its physiological position after IVRO [14]. In addition, IVRO results less harmful than BSSO for the inferior alveolar neurovascular bundle. The clinical application of IVRO has some substantial limitations owing to the limited bone contact interface it provides, as it can not address axial rotations (yaw correction) and sagittal advancements. It is useful in cases of mandibular setback for the correction of III classes and for the vertical movements, such as in case of asymmetries, as this case illustrates.



Fig. 26 Case 10. Preoperative clinical and occlusal evaluation

Virtual Surgical Planning and Correction

The resolution of maxillary canting and mandibular asymmetry required a maxillo-mandibular combined orthognathic surgery performed through a traditional Le Fort I osteotomy and a bilateral IVRO (Fig. 27). This provided the opportunity to search for a more stable occlusion, which was determined through haptical stability on plaster models, and then transferred to Le Fort I and mandibular distal segment in the VSP. A 2 mm right translation of the maxillo-mandibular complex was simulated to center the superior interincisal line, and canting correction was performed by placing the fulcrum in the right maxillo-malar buttress to lift the maxilla on the left side. The mandible was repositioned accordingly and bone contact was analyzed in proximity of IVRO. It is important to note that this VSP is ideal for scenarios in which the correction of proportions is limited to the coronal plane, as both sagittal and axial modifications strongly impair bone contact across IVRO bone interface. To decrease the load over the TMJ, there was no rigid fixation of IVRO, and the patient was left into intermaxillary rigid blockage for 40 days.

One year after surgery, the patient reported relief of TMJ symptoms. Canting correction resulted in a smile improvement with symmetrization of dental cusp exposure. The restoration of facial symmetry resulted in the compensation of hemifacial microsomia and the reciprocal centering of interincisal lines with the facial midline. There was a subsequent pogonion centering and the repositioning of mandibular angles at the same level. From the occlusal side, there was an improved stability with decreased tendency to relapse to second class (Fig. 28).

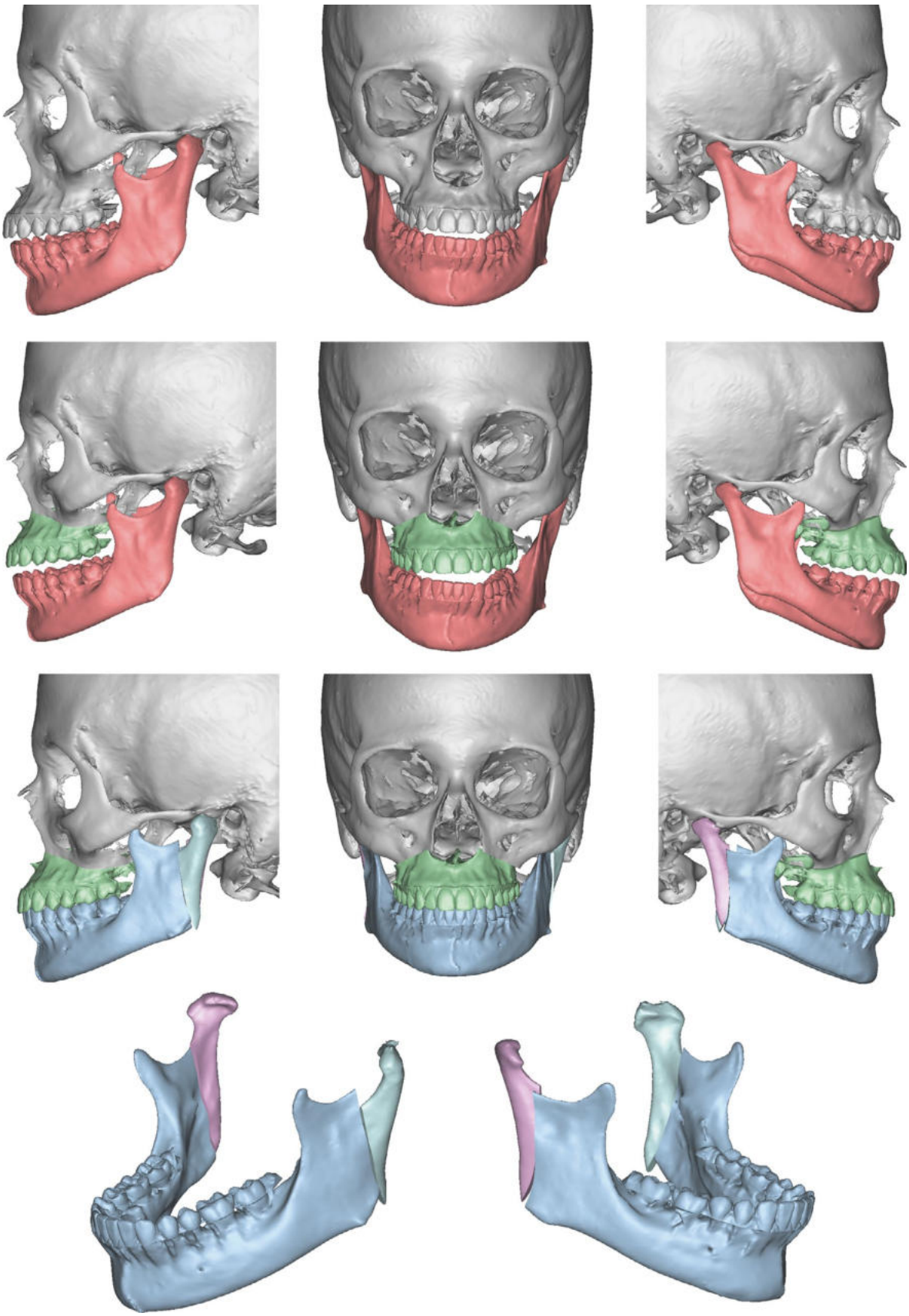


Fig. 27 Case 10. VSP with IVRO design



Fig. 28 Case 10. Postoperative 1-year clinical and occlusal outcome

4 Fully Custom Orthognathic Surgery

Fully custom surgery brings automation and predictability in orthognathic surgery. It is performed through a detailed virtual surgical planning, as seen in the previous cases, but instead of using the VSP only as a visual reference and for manufacturing splints, the VSP is shared with the manufacturer for the production of customized osteosynthesis plates. Compared with traditional orthognathic surgery, in which dental splints transfer the X and Y coordinates of the intermediate position but are unable to account for the vertical dimension (Z coordinate), and require hand modeling of plates, customized plates are modeled exactly overlying the final VSP configuration and are extruded as an offset piece from VSP geometries. This ensures a 1:1 fitting and transfers to the Le Fort I and BSSO segments the correct spatial coordinates to be reciprocally in the desired surgical occlusion, at the same time with the vertical repositioning. In this regard, it is possible to state that fully custom orthognathic surgery also accounts for the intraoperative transfer of the Z coordinate. In addition, as final spatial coordinates are included within the plate shape per definition, fully custom surgery is also referred to as "splintless" surgery. In order to define the correct sites for plate implantation, it is mandatory to exactly couple the trajectory of osteotomies with the sites for screw insertion. This can be easily performed using surgical guides, which enable to trace osteotomies and place screw holes as planned. Both surgical guides and titanium plates are manufactured from a digital design file through additive methods that generally implement selective laser sintering (SLS) or selective laser melting (SLM) 3D printing technology.

Splintless orthognathic surgery has considerable benefits in contrast with traditional orthognathic surgery: it provides a more accurate repositioning and fixation of skeletal segments [15], if favors automation in surgery with highly standardized maneuvers with subsequent leveling of expertise between experts and neophytes with unquestionable benefits on the reduction of operative time [16], and it enhances subsequent long-term skeletal stability [17]. Moreover, based on solid conceptual bases, in the Author's experience, splintless surgery might have an important role on the preservation of the natural condylar position, thus preventing condylar sag and tardive TMJ derangements, yet at the moment there are no current clinical trials confirming this statement.

The following example refers to a case of orthognathic surgery with complex rotational movements that could be best addressed with a splintless approach. Dissertation will focus on the importance of surgical guides and customized plates for the surgical automation.

4.1 Combined Advancement and Counterclockwise Rotation for Lower Third Hypoplasia Using a Fully Custom Sequence

Clinical Analysis

A 30-year-old patient was referred to our center seeking orthognathic surgery as the solution of her mandibular sagittal defect, which conditioned a micrognathia. Clinical evaluation revealed a substantially reduced vertical height of the lower third, compared with the middle third, a marked retrusion of soft tissue pogonion and a slight hyperdivergent profile. The gingival exposure during smile was substantially normal. Minimal maxillary canting was appraised at inspection of segmented CT.

From the occlusal side, the superior interincisal line was centered with the facial midline, while the inferior interincisal line showed 1 mm right deviation compared with the superior. A slight lateral open bite on the right side was present. From the occlusal side, there was a bilateral class I relationship between molars but with increased overjet between incisors (Fig. 29).

Cephalometry revealed the following angular measurements: SNA, 75.6°; SNB, 68.1°; ANB, 7.5°. FHP-OcP angle was of 12.6°.

Virtual Surgical Planning and Digital Workflow for Implant Design

For the correct management of this case, the priority was given to the mandibular advancement with the normalization of symmetry (Fig. 30). The gain in mandible sagittal projection was coupled with a 4 mm maxillary advancement, further emphasized by adding 2° counterclockwise rotation to slightly decrease divergence and improve the projection of the upper incisors tip. A minimal correction of maxillary canting was associated to equilibrate the occlusal plane. A forward sliding genioplasty was simulated to further advance pogonion and menton. Required movements were substantially conducted in the sagittal plane and the mandible was symmetrical, thus yaw correction was not needed.

Surgical planning was entirely performed at our institution by the author and was shared with the manufacturer (Materialise NV, Leuven, BE). Based on STLs from surgical planning (see "hybrid workflows," Chapter "Computer--Guided Orthognathic Surgery: State of the Art and Innovation,, Sect. 4.1), custom implants were constructed as follows (Fig. 31):

1. First, screw insertion sites were established in the final orthognathic position, taking into account bone thickness and avoidance of dental roots and inferior alveolar nerve.



Fig. 29 Case 11. Preoperative clinical and occlusal evaluation

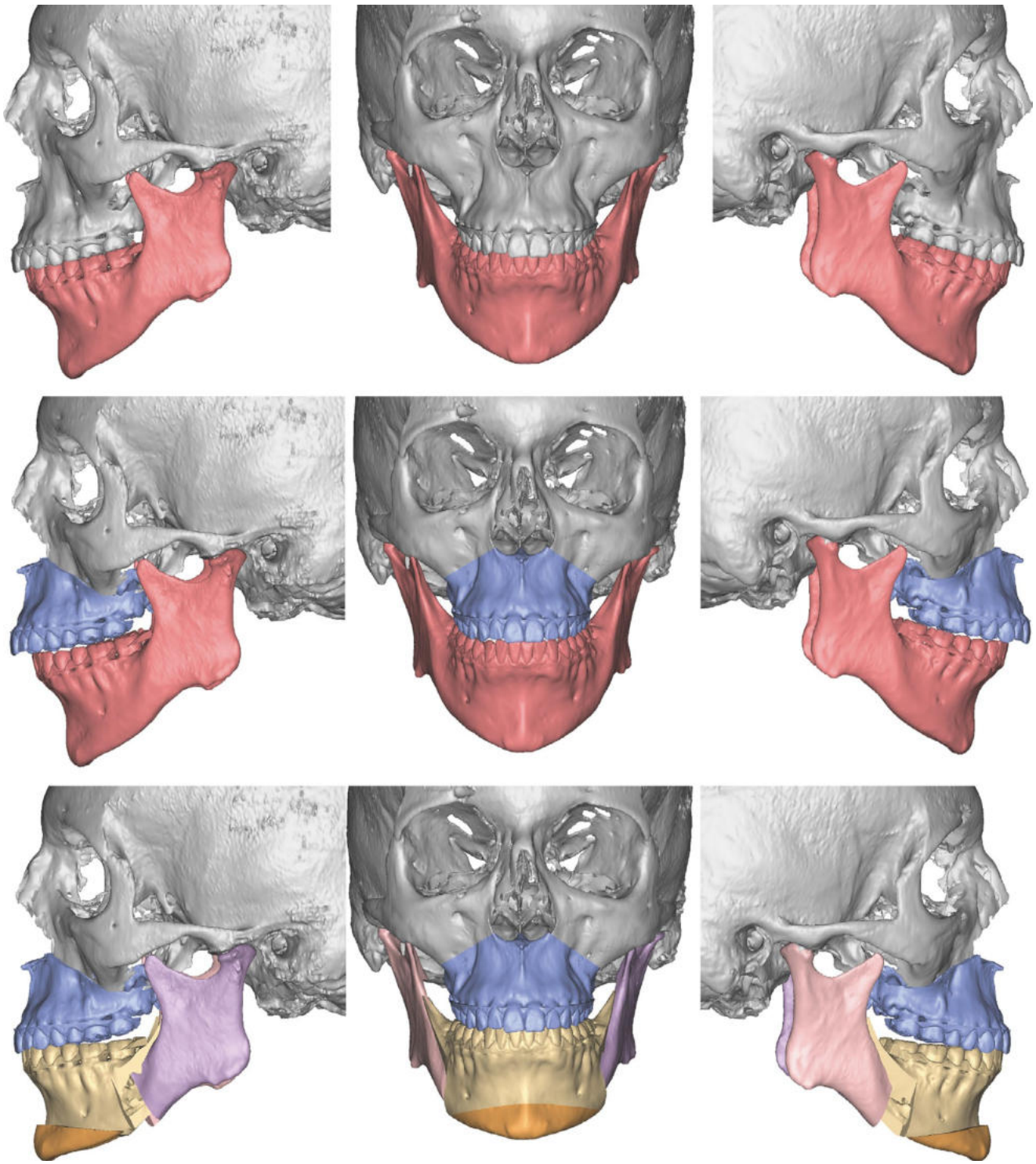


Fig. 30 Case 11. VSP delivered to the manufacturer for fully custom surgery (advanced hybrid workflow)

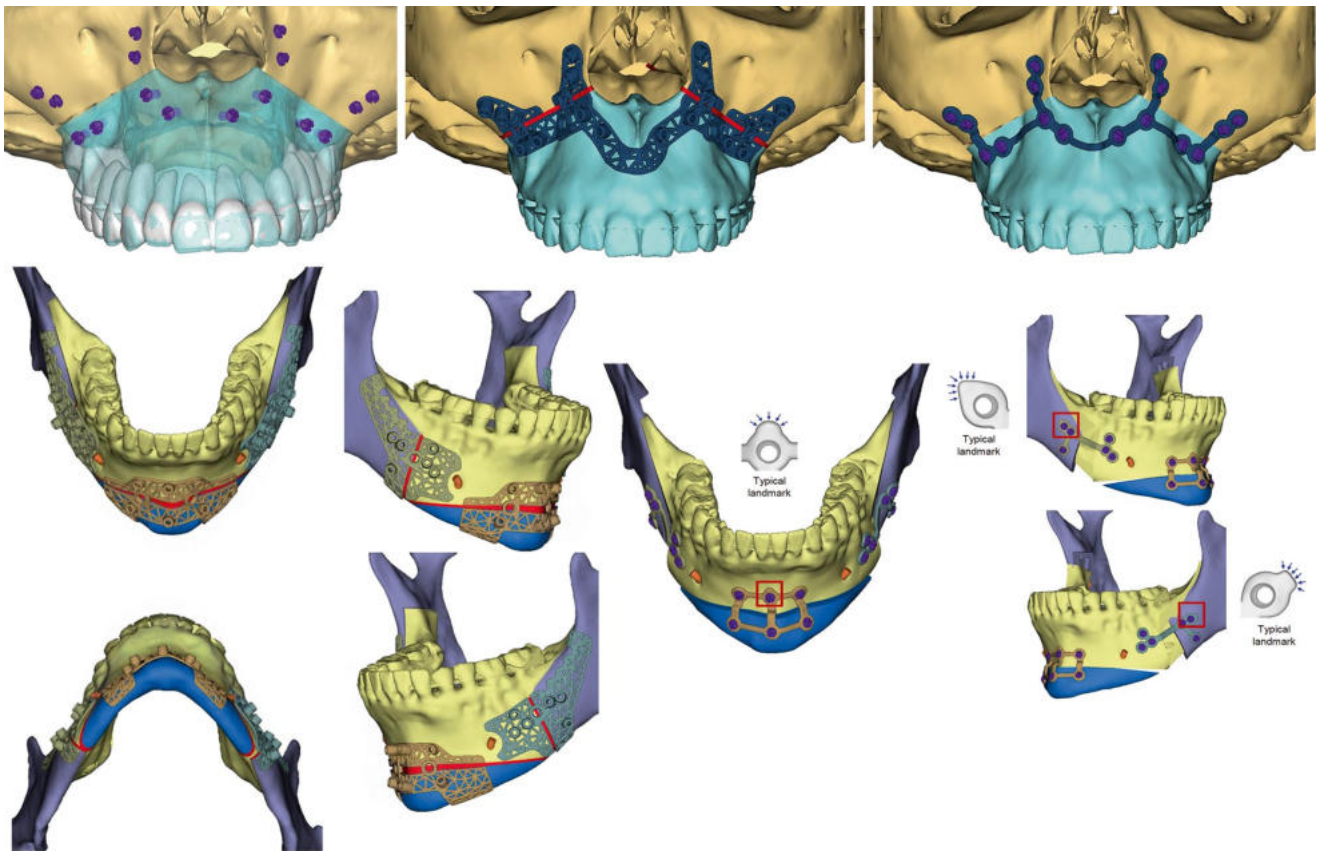


Fig. 31 Case 11. Sequences for fully custom orthognathic surgery

Such sites were marked by pins with the diameter corresponding to the screw shaft.

2. Subsequently, STLs of Le Fort and distal BSSO segments, alongside with their pins, were brought back in their preoperative position. Here, surgical guides were designed to match preoperative anatomy, allowing to drill holes in the finally planned position for screw fixation and to design osteotomies coherent with the final skeletal repositioning. In this step (especially in cases of mandibular setback surgery for III classes), surgical guides are designed to include the size of ostectomies as well.
3. Implants are designed on the final skeletal position: first, the plate projection is designed over the bone surface. This process starts with plate convergence sites (nodes) to accommodate the screw heads within them and continues with bridges that join the screw accommodation sites. Once the basic design for the plate is chosen, it is extruded with an offset value same as the desired thickness of the plate, generally 1 mm. For the maxillary plane, the authors opt for a subspinal bridging tract, which enhances the stability of the implant.

A 3D printed replica of the skull should also be available to assess the fitting stability of the implant. Surgery follows the same principles, and its steps are automated by the fully custom procedure (Fig. 32).

The result of the combined action of such movements were the 2 mm lift of the UIM alongside with its 4 mm advancement, which conditioned only a minimum gain of dental exposure at smile; the inferior incisor advanced 6 mm, while at Pog the measured advancement was of 14.5 mm with a vertical decrease of 4 mm. From the occlusal side, a minimal posterior disclusion was preferred, to be later refined with the orthodontic extrusion of molars to increase the posterior vertical height, thus increasing the stability of counterclockwise rotation and decreasing the overall stress over the TMJ (Fig. 33).

After such movements, cephalometry indexes were corrected as follows: SNA, 78.7°; SNB, 73.1°, ANB 5.6°. FHP-OcP decreased to 10.0°.

It should be noted that fully custom surgery makes invariable the surgical sequencing between a mandible-first of a maxilla-first approach: while this has relevance for traditional orthognathic surgery and the choice of the surgical sequencing should be tailored to the peculiarities of the clinical case, the automation of fully custom surgery ensures that skeletal bases are correctly positioned through custom devices independent from each other.

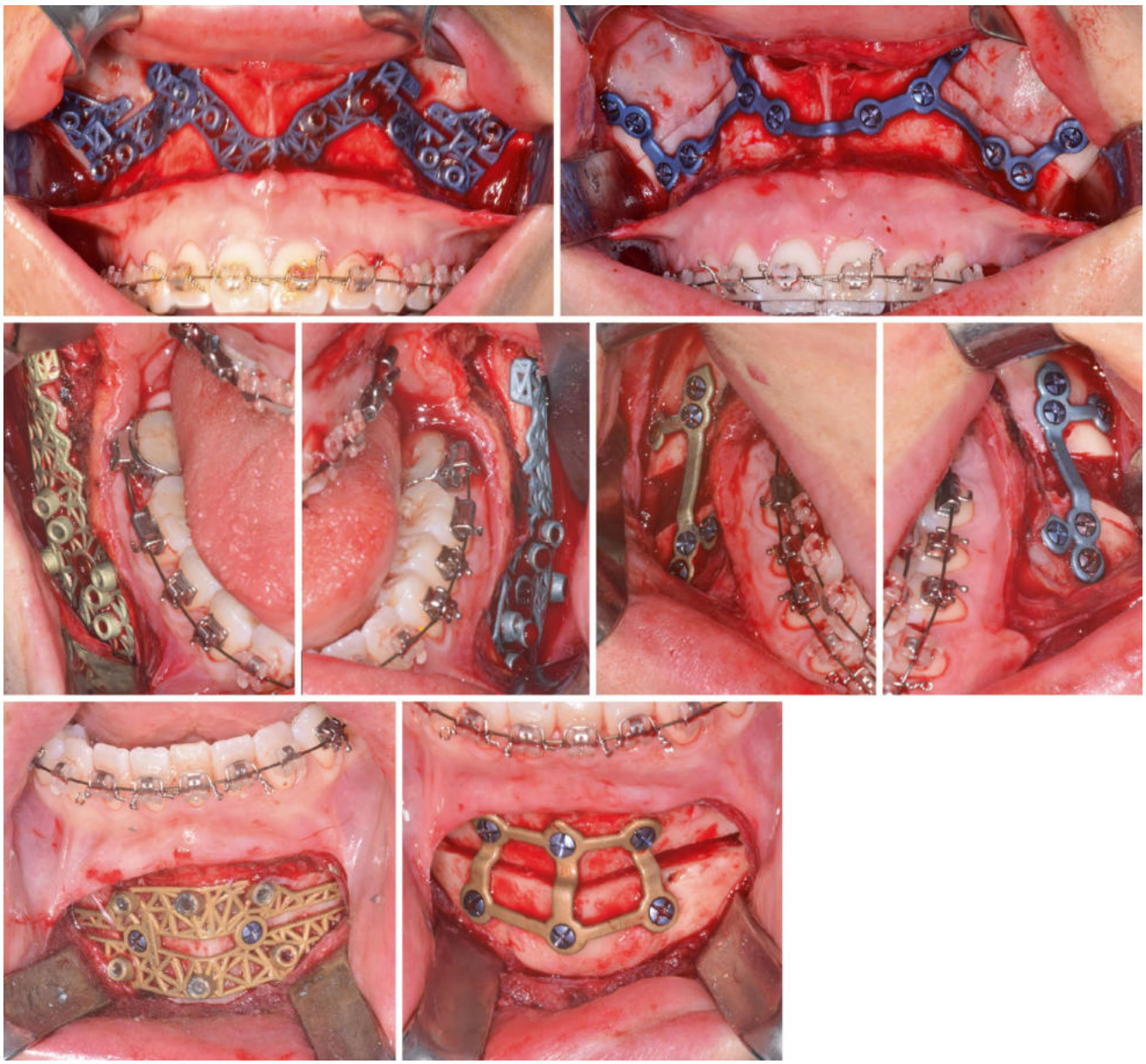


Fig. 32 Case 11. Intraoperative steps for fully custom orthognathic surgery

In conclusion, it should be noted hot the integration of VSP into clinical analysis for orthognathic surgery amplified the possibilities of dentofacial diagnosis and overcomes the classical two-dimension cephalometric models. It is virtually impossible to fit all patients within predefined normograms for cephalometric analysis, and the clinical analysis of the aforementioned cases has clearly demonstrated this concept. Facial harmonization is a delicate process and should be calibrated on the patient facial typology, biofunctional needs and the patient's requests as well. Is should not involve a radical change of the face but subtly assess which are the criticalities and correct them to equilibrate proportions. Two-dimension plots and ancient, articulator-based VTO are today completely inadequate to satisfy this complexity, and the analysis needs to be three-dimensionally performed both on skeletal and soft tissue models. In the author's perspective, in the future, the concept of cephalometry itself will become outdated, and newer forms of analysis, based on the computation of soft-tissue volumes, their relative stiffness, and the effect of underlying skeletal repositioning, all computed by artificial intelligence, are destined to become the appropriate analysis tools to plan orthognathic surgery.



Fig. 33 Case 11. Postoperative 1-year clinical and occlusal outcome

References

1. van Diepenbeek AF, Buschang PH, Prahl-Andersen B. Age-dependant cephalometric standards as determined by multilevel modeling. Am J Orthod Dentofacial Orthop. 2009;135:79–87.
2. Brusati R, Giannì AB. Anterior mandibular apical base augmentation in the surgical orthodontic treatment of mandibular retrusion. Int J Oral Maxillofac Surg. 2005;34:846–50.
3. He Z, Ji H, Du W, Xu C, Luo E. Management of condylar resorption before or after orthognathic surgery: a systematic review. J Craniofac Surg. 2019;47:1007–14.
4. Manfredini D, Segù M, Arveda N, Lombardo L, Siciliani G, Rossi A, Guarda-Nardini L. Temporomandibular joint disorders in patients with different facial morphology. A systematic review of the literature. J Oral Maxillofac Surg. 2016;74:29–46.
5. Barone S, Cosentini G, Bennardo F, Antonelli A, Giudice A. Incidence and management of condylar resorption after orthognathic surgery: an overview. Korean J Orthod. 2022;52:29–41.
6. Wolford LM, Chemello PD, Hilliard FW. Occlusal plane alteration in orthognathic surgery. J Oral Maxillofac Surg. 1993;51:730–40; discussion 740–741
7. Lazzarotto A, Tel A, Brontoladi S, Sembronio S, Costa F, Robiony M. Computer guided maxillo-malar piezoelectric osteotomies for midface augmentation. J Plast Reconstr Aesthet Surg. 2023. https://www.jprasurg.com/article/S1748-6815(22)00587-3/abstract. Accessed 30 Dec 2024
8. Bartzela TN, Carels C, Maltha JC. Update on 13 syndromes affecting craniofacial and dental structures. Front Physiol. 2017; https://doi.org/10.3389/fphys.2017.01038.
9. Obwegeser HL, Makek MS. Hemimandibular hyperplasia — Hemimandibular elongation. J Maxillofac Surg. 1986;14:183–208.
10. Wolford LM, Movahed R, Perez DE. A classification system for conditions causing condylar hyperplasia. J Oral Maxillofac Surg. 2014;72(3):567–95. https://www.joms.org/article/S0278-2391(13)01141-5/abstract. Accessed 30 Dec 2024
11. Saridin CP, Raijmakers PGHM, Shamma SA, Tuinzing DB, Becking AG. Comparison of different analytical methods used for analyzing SPECT scans of patients with unilateral condylar hyperactivity. Int J Oral Maxillofac Surg. 2009;38:942–6.
12. Nitzan DW, Katsnelson A, Bermanis I, Brin I, Casap N. The clinical characteristics of condylar hyperplasia: experience with 61 patients. J Oral Maxillofac Surg. 2008;66:312–8.
13. Ow A, Cheung LK. Skeletal stability and complications of bilateral sagittal split osteotomies and mandibular distraction osteogenesis: an evidence-based review. J Oral Maxillofac Surg. 2009;67:2344–53.
14. Bell WH, Yamaguchi Y. Condyle position and mobility before and after intraoral vertical ramus osteotomies and neuromuscular rehabilitation. Int J Adult Orthodon Orthognath Surg. 1991;6:97–104.
15. Karanxha L, Rossi D, Hamanaka R, Giannì AB, Baj A, Moon W, Del Fabbro M, Romano M. Accuracy of splint vs splintless technique for virtually planned orthognathic surgery: a voxel-based three-dimensional analysis. J Craniofac Surg. 2021;49:1–8.
16. Sánchez-Jáuregui E, Baranda- Manterola E, Ranz- Colio Á, Bueno de Vicente Á, Acero- Sanz J. Custom made cutting guides and osteosynthesis plates versus CAD/CAM occlusal splints in positioning and fixation of the maxilla in orthognathic surgery: a prospective randomized study. J Craniofac Surg. 2022;50:609–14.
17. van der Wel H, Kraeima J, Spijkervet FKL, Schepers RH, Jansma J. Postoperative skeletal stability at the one-year follow-up after splintless Le Fort I osteotomy using patient-specific osteosynthesis versus conventional osteosynthesis: a randomized controlled trial. Int J Oral Maxillofac Surg. 2023;52:679–85.

Application of VSP in Temporomandibular Joint Surgery

Salvatore Sembronio, Luca Raccampo, Massimo Robiony, and Alessandro Tel

1 TMJ Imaging

The temporomandibular joint consists of various components and tissues, making the imaging evaluation of each of them crucial for diagnosis, treatment and virtual surgical planning. Diagnostic imaging is generally performed by magnetic resonance (MR) especially to study internal derangement, yet this type of imaging is usually not applicable to virtual surgical planning (VSP). VSP needs dedicated imaging with volumetric acquisition. However, as part of the diagnostic process eventually leading to a TMJ surgical procedure, principles of diagnostic imaging will be elucidated as well.

1.1 Diagnostic TMJ Imaging

Diagnostic imaging of the TMJ is currently used to assess disc alignment and related structures, as well as degenerative changes in the bone. It is worth mentioning that acquisition should respect defined principles that are to be applied in VSP imaging as well. Diagnostic imaging is typically performed in both closed- and open-mouth positions to determine disc position and assess its reduction. For an accurate assessment of TMJ in both bone and soft tissue imaging, when performing closed-mouth sequences, it is essential that the teeth are in maximum intercuspation. If the teeth are not in this position, the spatial relationships of the TMJ components cannot be reliably assessed, potentially leading to an inaccurate diagnosis and misplacing the centric relationship of the condyle. Open-mouth imaging provides valuable information about the position of the condyle and, in MR, about the disc translation.

In MR, normally the disc and posterior attachment exhibit low-to-intermediate signal intensity on both T1 and T2 sequences. In a sagittal oblique view, a healthy TMJ disc appears biconcave, with the posterior band positioned at the 11 to 12 o'clock location relation to the condyle when the mouth is closed. The posterior band is typically the thickest portion of the disc, followed by the anterior band, with the thin intermediate zone in between. The intermediate zone lies between the convex articular surfaces, while the anterior band appears to rest on the superior head of the lateral pterygoid muscle fibers, where they insert into the pterygoid fovea. The posterior attachment consists of the temporal posterior attachment, the condylar posterior attachment, and the region where these fibers interweave and attach to the posterior band of the disc. In the open-mouth position, the condyle and disc move forward, and the area between the articular surfaces becomes the junction of the anterior band and intermediate zone. A small amount of joint fluid may sometimes be visible on T2-weighted images, which is generally considered normal.

Internal derangement usually involves anterior displacement of the posterior band, although pure mediolateral and posterior displacements are rare. In the closed-mouth position, disc displacement is considered reduced when the disc returns to its normal position upon mouth opening. Displaced discs may undergo morphological changes, including becoming rounded or biconvex, shortening along the posterior band-anterior band axis, thickening of the posterior band, and a loss of mass in the anterior band and intermediate zone. MR is typically the preferred imaging method for

S. Sembronio · L. Raccampo
Maxillofacial Surgery Clinic, Head & Neck and Neuroscience Department, Academic Hospital of Udine, Udine, Italy
e-mail: salvatore.sembronio@uniud.it; luca.raccampo@asufc.sanita.fvg.it

M. Robiony
Chief of Maxillofacial Surgery Clinic, Director of the Postgraduate School in Maxillofacial Surgery, Chief of Head & Neck and Neuroscience Department, Academic Hospital - University of Udine, Udine, Italy
e-mail: massimo.robiony@uniud.it

A. Tel (✉)
Lead Specialist for VSP and 3DP, Maxillofacial Surgery Clinic, Head & Neck and Neuroscience Department, Academic Hospital of Udine, Udine, Italy
e-mail: alessandro.tel@uniud.it

© The Author(s), under exclusive license to Springer Nature Switzerland AG 2025

A. Tel, M. Robiony (eds.), *Atlas of Virtual Surgical Planning and 3D Printing for Cranio-Maxillo-Facial Surgery*,
https://doi.org/10.1007/978-3-031-94495-6_18

evaluating TMJ disorders (TMDs) due to its excellent soft tissue contrast, enabling the assessment of various pathological conditions. Morphological changes associated with internal derangement may include increased T2 signal intensity in the bilaminar zone (posterior disc attachments) and decreased signal intensity in the disc, particularly in the posterior band. T1-weighted and proton density (PD) images provide detailed visualization of the structural and positional morphology of TMJ components, while T2-weighted imaging offers the added capability to identify abnormal fluid, such as joint effusion or bone marrow edema. Intravenous contrast can be utilized in cases where inflammatory disorders are suspected such as TMJ involvement in arthritis [1]. However, these signal changes are challenging to evaluate using current routine clinical imaging techniques. Our routine MRI protocol for TMJ assessment includes coronal oblique T1, sagittal oblique T2 with fat suppression, and sagittal oblique proton density sequences in the closed-mouth position. In the open-mouth position, sagittal oblique T2 with fat suppression and sagittal oblique proton density sequences are performed. Additionally, dynamic cine-MR sequences is typically included, which provides valuable functional information. All images are acquired with a slice thickness of 2–3 mm, high in-plane resolution, a field of view of 120 × 120 mm, and a matrix size of 320 × 224. Yet fundamental for the diagnosis of internal derangement, with today's requirements, this imaging can not be used for the reconstruction of a virtual model for VSP (Fig. 1). In the years to come, it is foreseeable that deep learning will enable a reliable segmentation of such MR exams.

1.2 VSP TMJ Imaging

The core of TMJ imaging acquired volumetrically is CT scan. The vast majority of TMJ pathological conditions are related to abnormal mandibular growth of the condyle (rarely the fossa is involved). Volumetric imaging is the basis to create a reliable 3D representation of the disease and associated deformity.

- *Skeletal structure*: Due to the higher quality of bone evaluation with CT compared with MRI, bone related TMDs are evaluated with CT. Conditions such as degenerative osteoarthritic changes in the TMJ, characterized by sclerosis, cystic changes, bony hypertrophy, and joint space narrowing, are best assessed with CT. It is also valuable for detecting other bone abnormalities, including ankylosis, infections, or tumors causing bone destruction. Compared to multidetector CT, cone-beam CT (CBCT) has the advantage of involving an inferior radiation dose, but the image has less contrast and is not based on traditional Hounsfiel Units (HU), which impairs segmentation based on thresholding. A multidetector CT scan with a resolution of 768 × 768 or at least 512 × 512 voxels and a slice thickness of 0.625 mm is suggested with a bone filter. These parameters are optimal for accurately depicting bone anatomy, including thin regions with rarefaction caused by pathological processes, and mitigate the effects of partial volume effects.
- *Angiographic imaging*: Certain pathological conditions may require the study of the anatomy of vessels in rela-

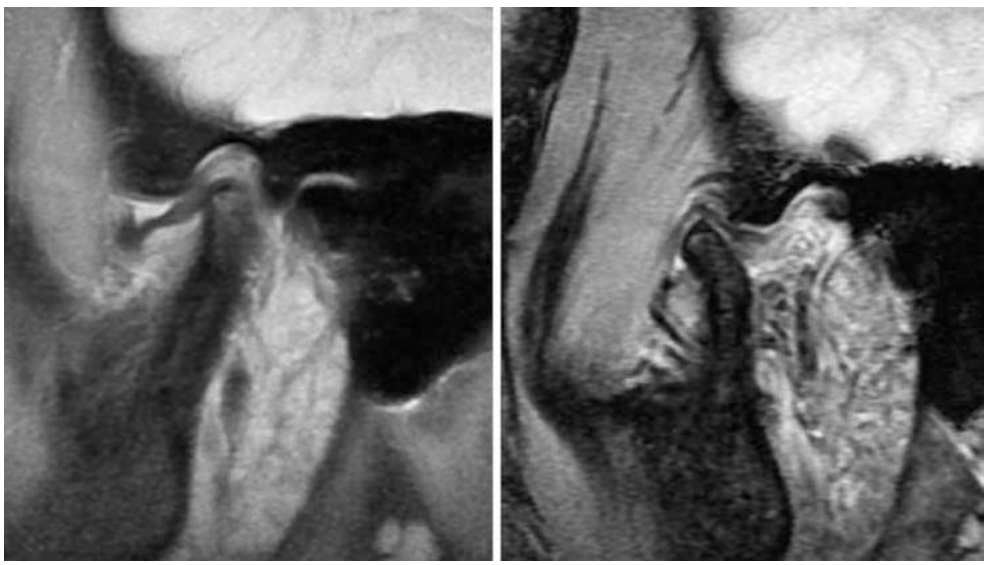


Fig. 1 Traditional MR scans to study soft tissues and, in particular, disc position. This imaging, yet providing valuable diagnostic information on the TMJ, in not usable for VSP

tionship with the TMJ. In these cases, it may be necessary to perform a CT angiography or dedicated MRI sequences that allow accurate identification and subsequent segmentation of the vessels. MR is preferrable as a CT angiography segmentation can not selectively differentiate between endovascular hyperdensity and bone hyperdensity, limitating separation of vessels from the skull base and TMJ region. Conversely, a MR with a 3D-time-of-flight (TOF) sequence with 0.5 mm slice thickness is recommended for arterial vasculature and a 3D venographic phase-contrast (PC) sequence determining proton flow velocity is useful to track the course of veins.

1.3 MRI Segmentation of the Articular Disc and Periarticular Tissues

Unless the TMJ involved by aggressive soft tissue processes, for instance, nearby tumors, magnetic resonance (MR) segmentation is not generally needed. However, a volumetric TMJ RM-imaging might be used to reconstruct a model of the disc and the capsule in a future perspective. In fact, segmentation of the articular disc is still experimental, yet supported by recent evidence in the literature [2]. Adding a model of articular disc in TMJ surgical planning might be helpful in determining its modifications in several TMJ pathologic conditions. The main limiting factor for disc segmentation is represented by its thin shape and the fact that it can be visualized exclusively in MR. 1.5 T RM coils do not provide enough resolution to reliably detect the disc, and high-resolution matrices are better acquired using 3T magnets or, in an experimental setting, 7T magnets [1].

To address this limitation, the fusion of MRI and CBCT imaging has been introduced and analyzed using deep learning [3]. The resulting fused images provide complementary data on the articular disc and osseous surfaces, aiding in more accurate diagnosis [4]. This registration process has proven to be both accurate and reliable in assessing TMJ pathology, allowing for detailed analysis of the disc shape, condylar morphology, and joint dynamics. Additionally, the fused images enable precise 3D reconstruction and quantification of TMJ structures, including the articular disc, condylar head, and articular eminence.

As seen, challenges for disc segmentation include patient motion during imaging, limited MRI sections, and the need to balance slice thickness and inter-slice spacing. While thinner slices improve resolution, they require longer scan times and increase the likelihood of motion artifacts. To mitigate cross-talk artifacts, inter-slice spacing of 10–20% of the slice thickness is often used. These constraints make achieving high-resolution 3D reconstruction for clinical use difficult. Although manual segmentation by experienced operators is accurate, it is time-intensive and highly dependent on operator expertise [5].

Accurate identification of TMJ structures in MRI images can streamline diagnosis, improve clinical outcomes, and support the development of smart applications like automated TMD diagnosis. Automatic segmentation of TMJ structures remains a critical need, with methods such as U-Net and its variants showing potential for semantic segmentation in medical imaging [6]. While most studies focus on CBCT-based segmentation, MRI offers superior reliability for imaging the articular disc.

2 Virtual Surgical Planning for TMJ Surgery: Generalities

Virtual surgical planning (VSP) and 3D printing technologies have become indispensable for improving 3D visualization of patient anatomy and simulating surgical procedures. VSP enables surgeons to safely explore various surgical options, create precise surgical guides, and design custom devices that closely align with the patient's anatomy. Given the mutual relationship between TMJ and occlusion, TMJ VSP and orthognathic VSP are mutually intertwined, and often orthognathic procedures are incorporated in such cases.

To support virtual planning, advanced imaging protocols are required to capture anatomical structures in a detailed, layer-by-layer format, encompassing bone architecture, vasculature, and soft tissues, including lesions. DICOM files from CT scans are imported into specialized software to generate 3D models of the patient's bone anatomy. The CT data is segmented using a thresholding algorithm focused on the Hounsfield Unit (HU) range for bone. The resulting segmentation mask is carefully subdivided across the TMJ and the occlusal surfaces to separate the mandible from the remaining skull (see Fig. 6, Chapter "Computer-Guided Orthognathic Surgery: State of the Art and Innovation"). Care is taken to avoid any geometry discontinuity in thin regions of the glenoid fossa and the mandibular condyle, in which the wide representation of cancellous bone and the very thin cortical layer might account for a partial volume effect with resulting voids. In this case, mask filling techniques need to be implemented to restore the geometrical integrity of the condyle, which is even more significant in case of pathological alterations, such as resorption or hyperplasia (see Fig. 5, Chapter "Computer-Guided Orthognathic Surgery: State of the Art and Innovation")

For soft tissue tumors or pathological conditions, MR imaging sequences are coregistered with DICOM coordinates of CT, and sequences specific for pathological soft tissues and vasculatures are likewise segmented to yield corresponding entities that match their correct anatomical location. Principles for vascular reconstruction match those already elucidated in previous chapters, where dynamic regional growing algorithms are used to track the course of vessels based on voxel proximity and iso-intensity. This is

especially important to define the entry of vessels in skull base foramina in extended temporomandibular joint reconstructions, as well as to track the course of the internal maxillary artery, which runs attached to the medial pole of the condyle and is a vulnerable target during such procedures (Fig. 2).

As TMJ alterations always relate with an occlusal impairment, all TMJ surgeries should be planned with careful coregistration of scanned dental impressions with the CT. This enhances dental cusps detail and enables to manufacture splints to assist mandibular repositioning during surgery, such as in case of orthognathic surgery combined to TMJ procedures (Fig. 3). Associating the desired surgical occlusion with the correct articular relationship between the condyle and the fossa is of prominent importance for such procedures.



Fig. 2 VSP imaging for the TMJ in a case of eTJR. Accurate skeletal reconstruction associated with MR coregistration for vessel tracking. Each vessel matches its respective skull base foramen

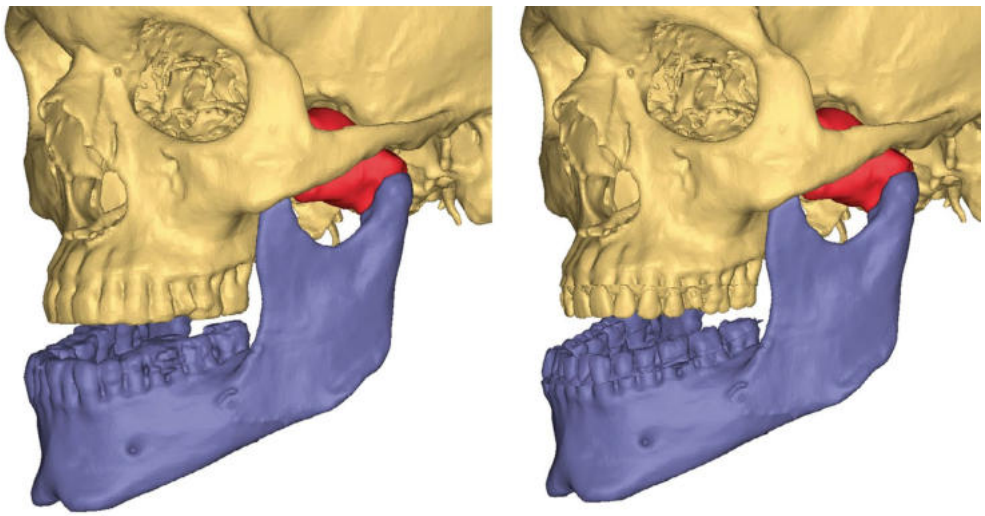


Fig. 3 Intraoral scan arch merged with VSP models in a case of giant condylar osteochondroma

3 Virtual Surgical Planning for TMJ Trauma

3.1 Condylar Fractures

Mandibular condylar fractures are among the most prevalent facial fractures and present significant management challenges. They represent 27–50% of all mandibular fractures [7]. Surgeons differ in their approach to managing these fractures, with opinions divided between conservative and surgical treatments. Condylar fractures might be caused by a direct trauma in the preauricular region, but the traumatic mechanism is often indirect, as they are caused by impact on the mandible with transmission of the force to the mandibular condyle, the less resistant structure of the mandible.

Displaced condylar fractures are unavoidably associated with malocclusion, but these fractures can lead to other complications such as mandibular movement disorders, TMJ dysfunction, and ankylosis, all of which can adversely impact a patient's physiological function. TMJ ankylosis is the utmost dreadful complication of an improper treatment of such fractures and can lead to the partial union (fibrous ankylosis) or complete fusion (osseous ankylosis) of the condyle with the skull base [8].

Advancements in imaging technology and fixation techniques have brought increased focus to fractures of the mandibular condyle. Despite this progress, there remains significant variability in classification systems for condylar fractures, with no consensus on a universally accepted approach [9]. Subjective terms like "high" and "low" fractures require clarification. We recommend the adoption of the following standardized terminology:

- *Condylar head fracture*: The fracture line originates in the articular surface and may extend beyond the joint capsule.
- *Condylar neck fracture*: The fracture line begins above the baseline of the coronoid process or sigmoid notch and, in more than half of cases, extends above this line on a lateral view.

Virtual surgical planning (VSP) is a powerful tool for managing mandibular condylar fractures, offering a detailed visual representation of the fracture site and providing essential surgical data. VSP enables comprehensive analysis of the fracture, allowing surgeons to anticipately visualize the reduction and fixation of fragments. The first step consists in the accurate analysis of the fracture, understanding the course of the fracture line itself and the number of fragments involved. In this regard, the application of the split mask algorithm found in Mimics (Materialise NV, Leuven, BE) is helpful to subdivide the initial thresholding mask into multiple fragments across the fracture line (Fig. 4).

VSP reduction maneuvers are based on anatomical reduction, which is generally intuitive, as two segments have to be engaged across the fracture line. Especially in condylar fractures, mirroring is a viable strategy, as it allows to symmetrize the posterior mandibular height, which extends from the condylon (Co) to the gonion (Go)points. Therefore, anatomical reduction is significantly facilitated by mirroring the

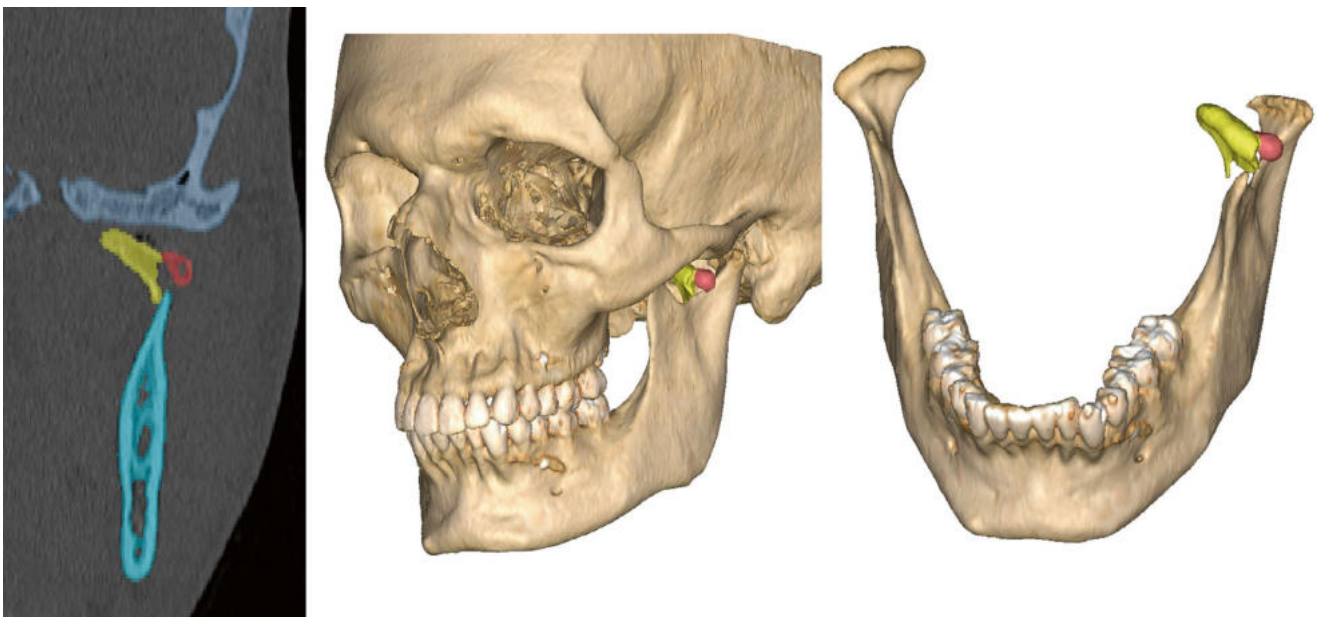


Fig. 4 Mask split applied to condylar fractures to isolate bone fragments

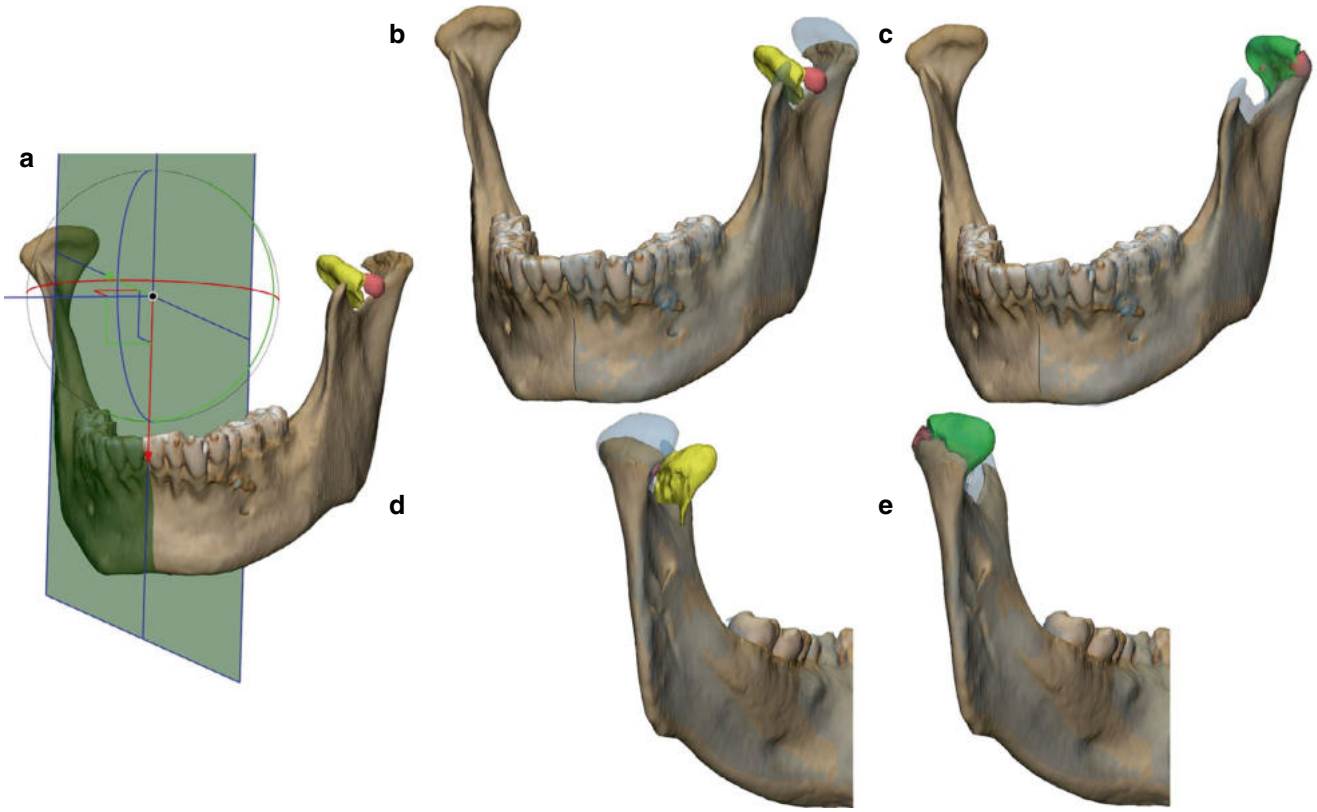


Fig. 5 Mirroring-based realignment of displaced fracture fragments through the creation of a mirrored ghost template

healthy side. For a condylar fracture of the head, anatomical reduction by reconstructing the condylar shape is generally sufficient to account for a stable occlusion, and registration of a surgical occlusion model is not routinely recommended (Fig. 5).

Another interesting possibility concerns simulation of fixation devices placement, including plates and screws, since the condyle has a small surface area and the bone is mostly cancellous, while cortical layer is remarkably thin. Therefore, it is important to intercept the most suitable regions for screw insertion. This is especially useful in mandibular condyle fractures, in which the analysis of bone thickness and quality can be vital to determine whether a screw can be placed at a given site. A wall-thickness analysis visualized by a color gradient map might be helpful in this case (Fig. 6).

3.2 Condylar Head Fracture

Clinical History

A 27year-old patient was referred to our institution after a sports injury with direct trauma to the chin and occlusal alteration, resulting in a ipsilateral precontact and a contralateral open bite. The patient was sent to CT examination using a high-resolution protocol, which revealed a left condylar head fracture with anterior-medial dislocation and a minor, tiny, bone fragment separated from the lateral condylar pole.

Virtual Surgical Planning

Segmentation was performed in Mimics using the split mask tool to separately reconstruct disrupted fragments, which were individually colored to enhance visual separation. In 3-matic, the symmetry plane was defined and a mirroring operation was performed. In this case, the mirrored mandible was cut in half to maintain exclusively the mirrored healthy side, then it was roughly aligned point-by-point to the mandibular angle on the fracture side. This maneuver enabled to symmetrize the posterior vertical height. Then, the alignment was made more coincident by applying the iterative closest point algorithm. Once the mirrored mandible was perfectly overlying on the fracture site, it was used as a digital repositioning template to reduce both the condylar head and the tiny, fractured fragment. Moreover, fixation technique was simulated by virtual insertion of two screws in the condylar head. Virtual planning in this case enabled to anticipately establish the correct length of screws and their optimal orientation (Fig. 7). A surgical guide was modeled based on the virtually reduced configuration of the condyle, acting as a physical constraint to maintain reduction of the condylar head, and with two guiding cylinders to insert screws based

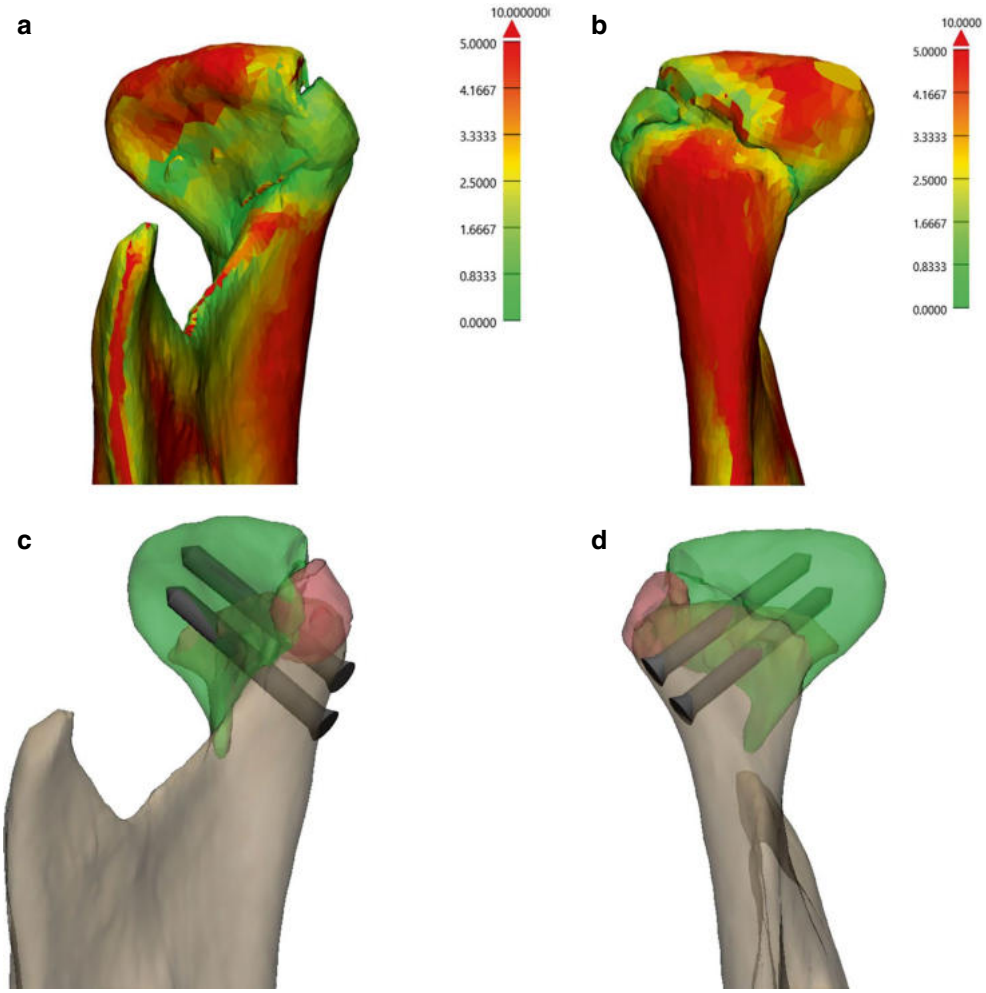


Fig. 6 Wall-thickness analysis to determine screws insertion sites

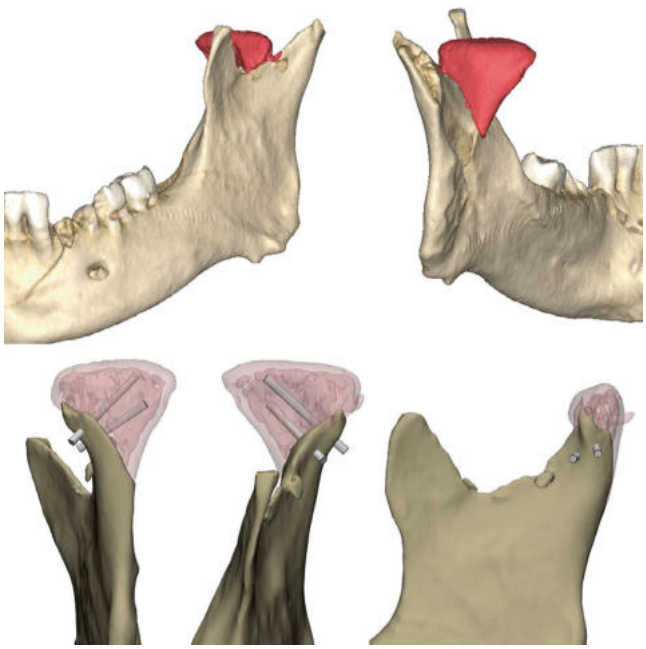


Fig. 7 VSP reduction with planned screws

on the desired direction established in VSP. Owing to the restricted field allowed by the preauricular access, guides were designed just 1.5 mm thick and 3D printed in SLA (Fig. 8).

Surgery

A preauricular incision with deep subfascial approach was used to expose the zygomatic arch and the underlying TMJ capsule, which was then incised. An Obwegeser elevator was used to retrieved the medially dislocated condylar head. Dunn-Dautrey condyle retractors were used to superficialize the condylar head and to put it into the correct anatomical relationship with the mandibular ramus. Once reduction was satisfactory, the virtual planning was inspected to analyze the best screw placement angle, and screws were placed accordingly to stabilize the condylar head (Fig. 9). Occlusion was verified.

Noteworthily, in such cases navigation might have a role to assess the correct trajectory of screw driller, as well as to identify the condylar head dislocated in depth. Surgical guides for condylar head fracture reduction represent an

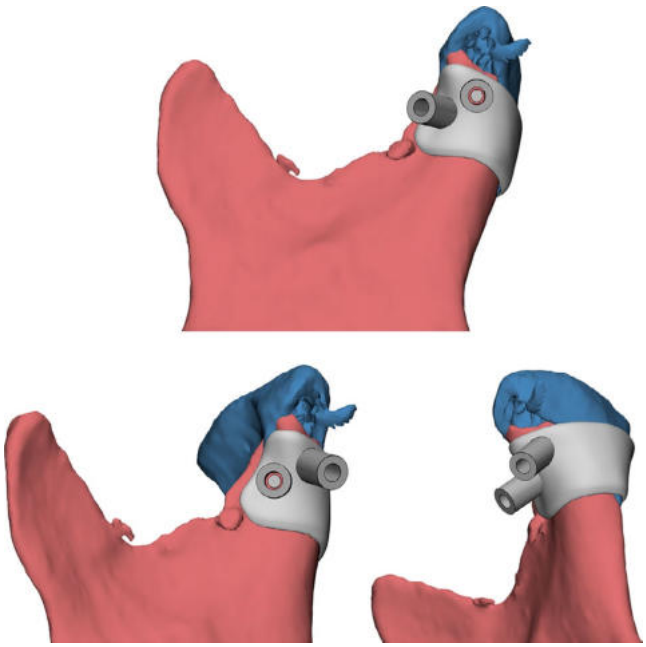


Fig. 8 CAD design of a condylar surgical guide to drive correct screw insertion

innovative attempt to bring automation in such procedures, yet they should be improved through miniaturization allowed by metal manufacturing methods.

3.3 Condylar Neck Fracture

Clinical History

The patient presented to our attention after being hit with violence by a punch in the left preauricular region. He presented an ipsilateral precontact with a contralateral open bite, which was suggestive for a left condylar fracture. CT scan was performed showing a subcondylar fracture with medial dislocation.

Virtual Surgical Planning

The mandible was segmented paying attention preserve maximal detail across the fracture line. The split mask was used first to separate the mandible from the skull base, secondly to separate the fractured fragment from the mandible. A mirrored digital template was highly useful to symmetrize

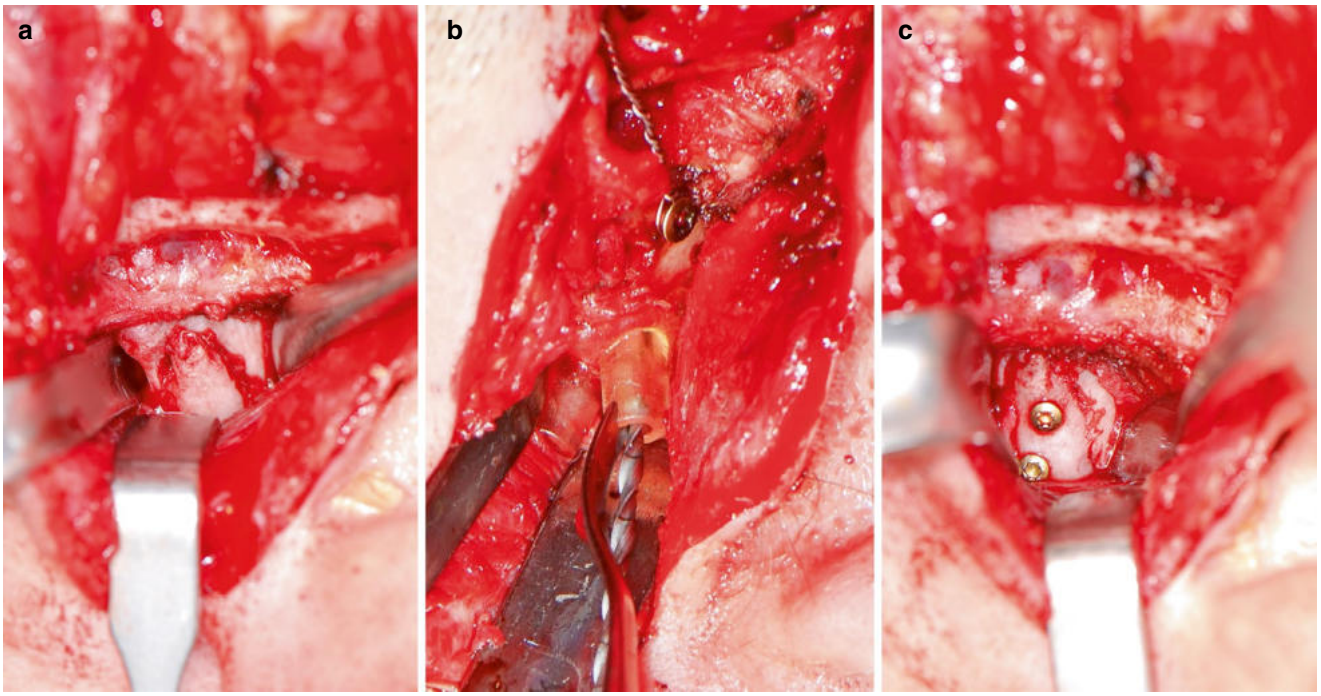


Fig. 9 Intraoperative view: (**a**) fracture; (**b**) condylar guide; (**c**) synthesis

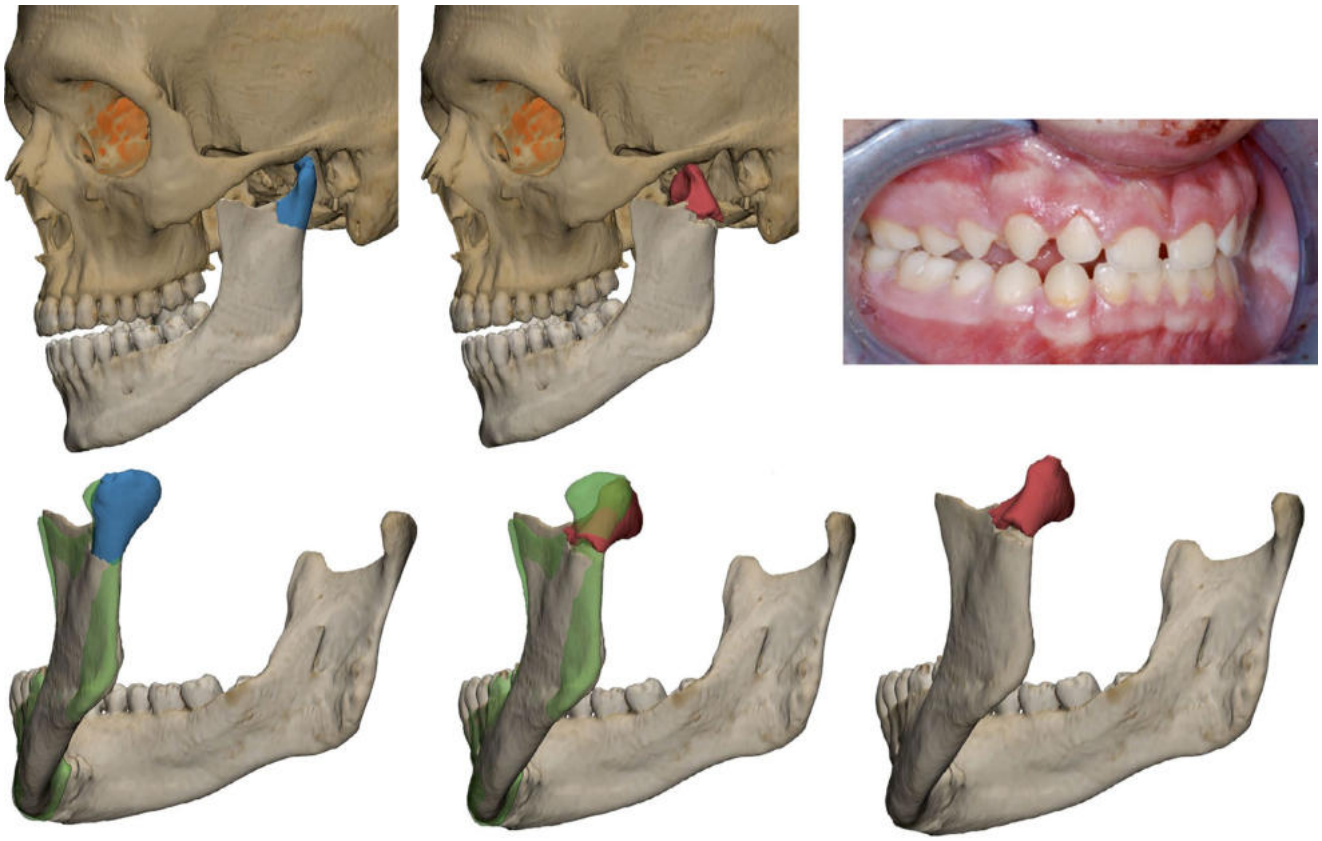


Fig. 10 Condylar neck fracture with contralateral open bite

the mandible, reducing semi-automatically the condylar shaft in the correct articular relationship, with preservation of the natural posterior facial height. A slight manual refinement was used to enhance realignment of fracture rims (Fig. 10). A rhomboid plate was modeled in Rhinoceros 8 software (McNeel, Seattle, WA, USA) using measures taken from light surface scanning, but alternatively, using dedicated software, such as Geomagic DesignX (3D Systems, Rock Hill, SC, USA) or 3-matic itself, reverse engineering is possible to convert the tessellated STL from light scanning into a CAD file. The CAD plate was then placed over the fracture line to simulate internal rigid fixation (Fig. 11).

Surgery

A retromandibular transparotid approach was chosen. Subcutaneous dissection was carried out sliding over the SMAS to reach more anteriorly the fractured site. Once in position, the SMAS fascia was minimally incised, and blunt dissection through the parotid parenchyma led to identify in depth the masseter muscle. Retractors were placed and periosteum was elevated until the fracture line was visible. Reduction was gently performed and the trapezoid plate was positioned exactly as oriented Intraoperative CT scan was performed, showing optimal reduction (Fig. 12).

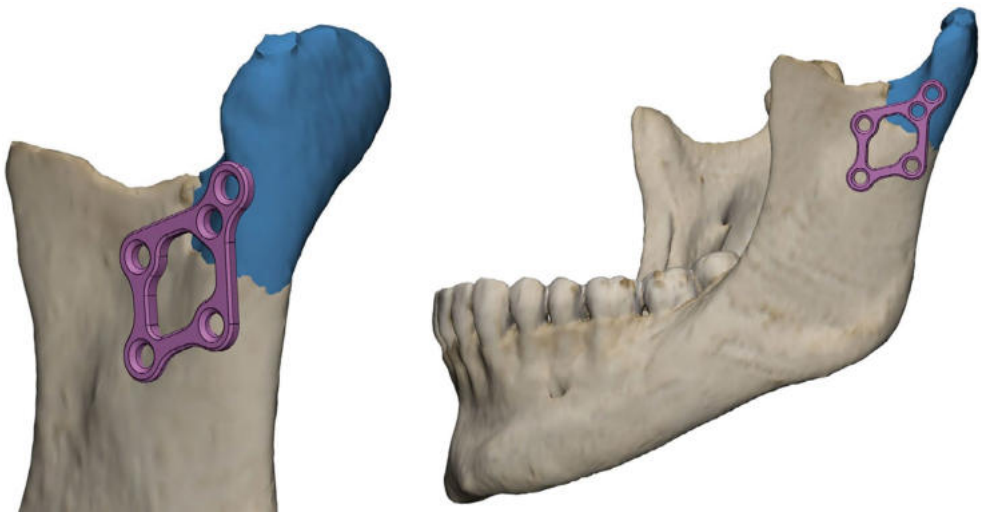


Fig. 11 Reverse engineering of a condylar plate (modelled using Autodesk Fusion) and application on the fracture site

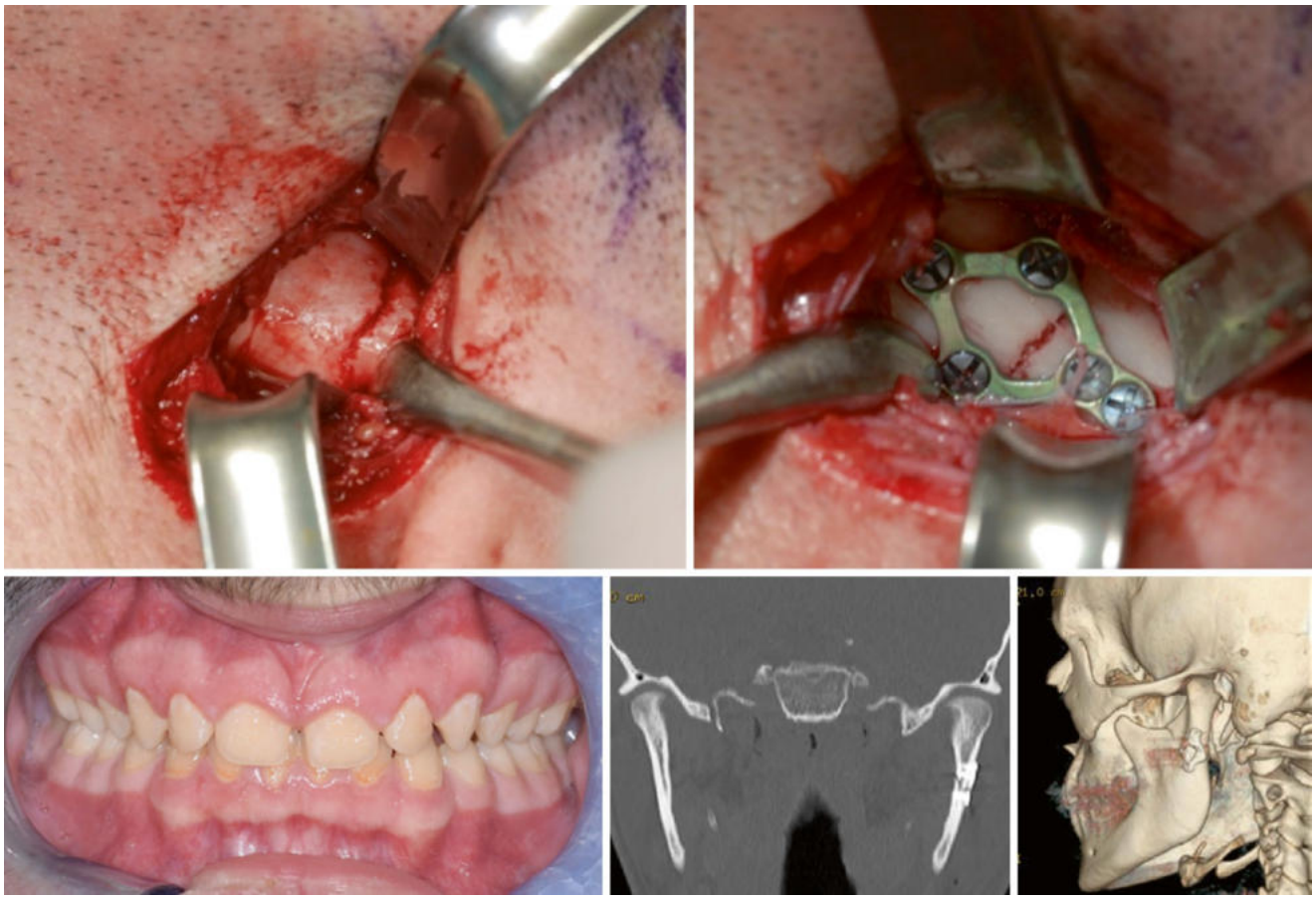


Fig. 12 Favorable clinical outcome after open reduction using retromandibular transparotid approach

4 Surgical Treatment of Condylar-Related Facial Asymmetry

Cases of facial asymmetry related to a condylar problem are most often linked to condylar hyperactivity, although some pathological conditions such as bone neoplasms affecting the mandibular condyle can lead to the development of facial asymmetry. In these cases, treatment involves the removal of the bony discrepancy affecting the affected mandibular condyle, aiming to restore a balanced facial appearance, stop growth and maintain normal function. It is also true that there are different clinically evident forms of condylar hyperactivity, for which the treatment is different; this reinforces the need for careful preoperative surgical planning and the crucial role of VSP. But it is first necessary to establish whether the disease is active to define the most suitable operative technique. The diagnosis of active condylar hyperactivity is determined with a SPECT, which shows an uptake difference between affected and unaffected condyle above 10% [10]. In active disease there are three surgical options: isolated condylar reduction, condylar reduction and delayed orthognathic surgery, and condylar reduction with simultaneous orthognathic surgery. If the pathology is no longer active, orthognathic surgery can be performed as unique treatment.

Condylar reduction can be achieved through high condylectomy or proportional condylectomy.

- High condylectomy: involves removing the upper 5 mm of the mandibular condyle. This approach targets the most active part of the condylar head, aiming to stop the overgrowth process.
- Proportional condylectomy: also known as low condylectomy, focuses on resecting the growth center and reducing posterior vertical excess. This method is particularly effective in correcting mandibular asymmetry.

When feasible, proportional condylectomy should be preferred for its ability to address growth center activity while achieving symmetry correction.

Following proportional condylectomy, a neocondyle typically forms within 12 months. This natural adaptation promotes regression of facial asymmetry and normalization of the maxillomandibular relationship. Proportional condylectomy allows the mandible to rotate on the treated side, resulting in improved facial symmetry. The approach aims to provide early intervention with a single procedure, reducing the need for conventional orthognathic treatments [11, 12]. Figure 13 illustrates a conceptual diagram for the treatment of facial asymmetry related to condylar hyperactivity, whose differential diagnosis has already been discussed in Chapter "Applications of VSP in Orthognathic Surgery" in relation to facial asymmetry.

In cases of condylar hyperactivity, the anatomy of the mandibular body and ramus-condyle unit is significantly

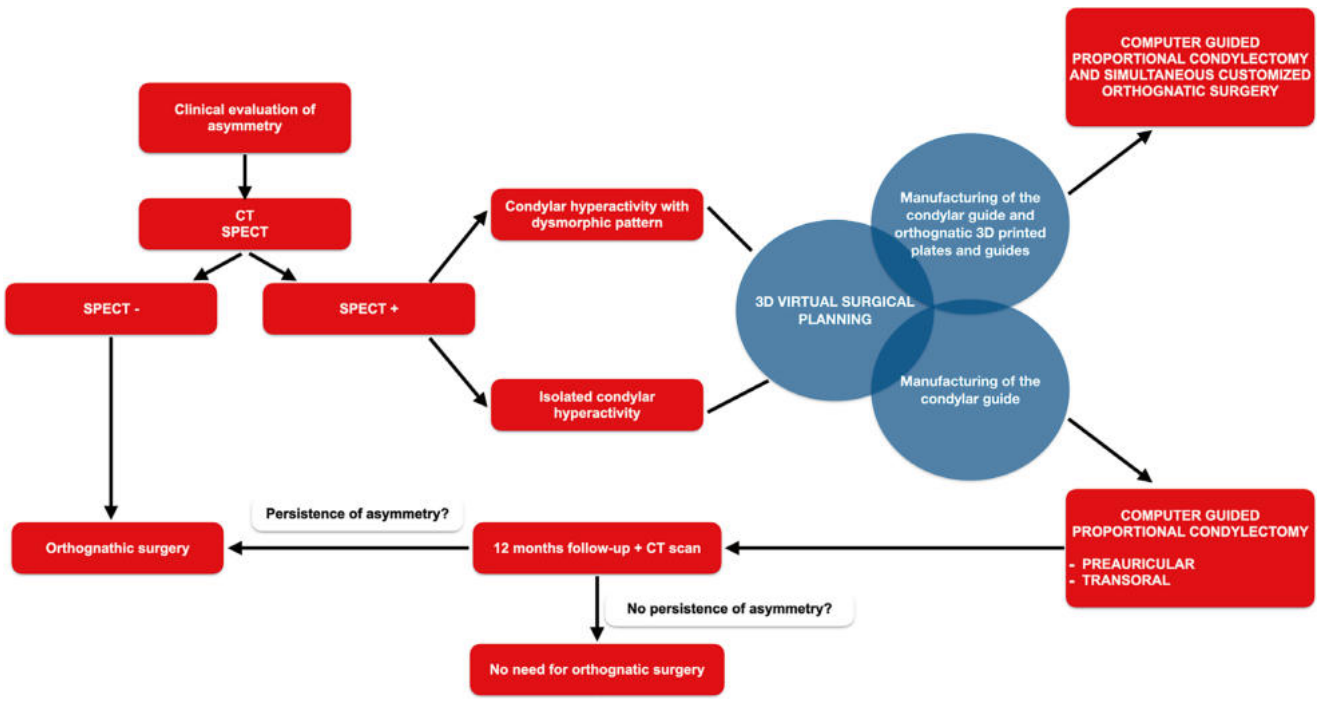


Fig. 13 Flowchart for the evaluation of condylar-related facial asymmetry

distorted, complicating the determination of reliable reference points and lines. Consequently, measurements for defining the extent of proportional condylectomy may lack accuracy. Multidetector CT is essential for a thorough understanding of the anatomical abnormalities and for VSP.

However, transferring these measurements to the operating room poses challenges, as intraoperative measurements are operator-dependent and may lack precision. The introduction of 3D printing in surgery has revolutionized the workflow, enabling to accurately reproduce the defined level for proportional condylectomy. By predicting surgical outcomes with higher reliability, these technologies enhance precision and safety during procedures, offering surgeons greater confidence in achieving optimal results.

4.1 Isolated Proportional Condylectomy: VSP Protocol

The ideal patient candidate to proportional condylectomy is that suffering of isolated condylar hyperactivity, namely a patient without any other associated dentofacial deformity. The rationale is to perform condylectomy and wait for condylar remodeling and natural correction of asymmetry. Orthognathic surgery is indicated only after condylectomy when the result is unsatisfactory.

A fully digital protocol is needed in order to perform an isolated proportional condylectomy, comprehending the following VSP steps:

1. *Natural head position definition*: First step is the orientation of the head. This step involves the definition of a standardized set of planes to correctly align the skull in the VSP software. This includes alignment on supraorbital plane (coronal reference), Frankfurt plane (sagittal reference), and midcoronal plane (axial reference).
   (a) The supraorbital plane is important for the valuation of asymmetry and should be aligned with the ideal line of the horizon. It is responsible for the coronal head tilt and all the consequent steps, including the evaluation of maxillary canting and gonial symmetry. In cases of facial asymmetry, there could be marked orbital dystopia, therefore the inferior orbital margin should not assumed to be a stable landmark. A more stable landmark is the superior orbital margin, thus a plane passing through both supraorbital notches is defined.
   (b) The midcoronal plane allows to evaluate symmetrically both facial sides and is responsible for the axial rotation of the head; it should be ideally coincident with a facial midline. As in facial asymmetry, there could be significant deviation of the columella-labial philtrum, as well as the underlying skeletal landmarks, the authors suggest considering more invariable references, for instance a plane passing through Nasion, anterior nasal spine (ANS) and the midpoint of the coronal suture (MidCor).
   (c) Frankfurt plane is used to determine the sagittal alignment of head and has least importance in the evaluation of facial asymmetry. An important landmark for the sagittal correction of facial asymmetry is the symmetry of mandibular angles, which should ideally be coincident in a sagittal view (Fig. 14).

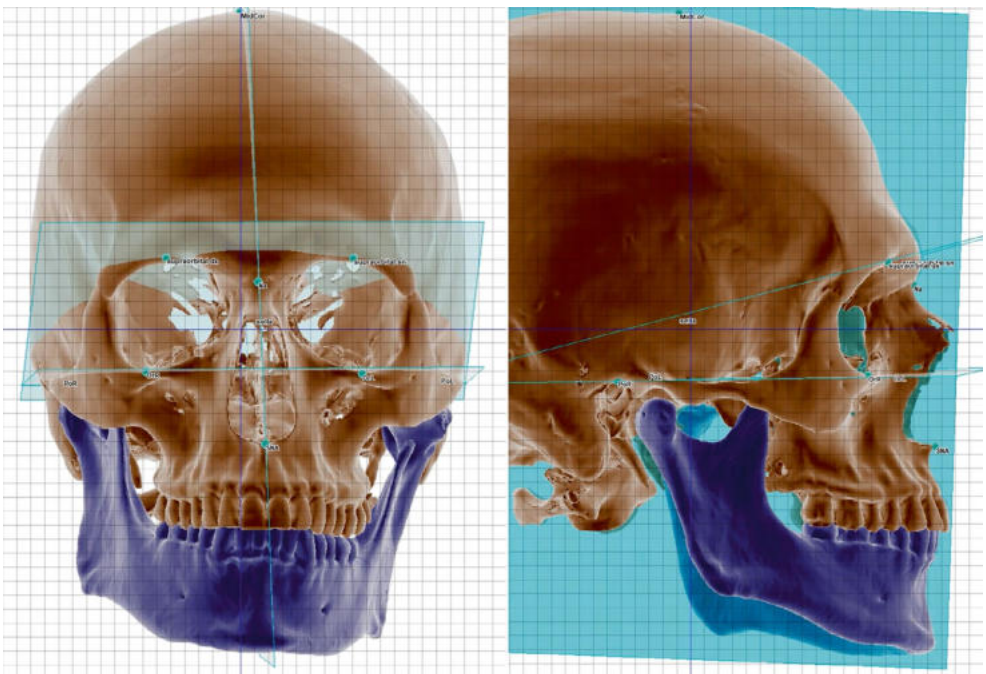


Fig. 14 Definition of reference planes to orient the skull for VSP of facial asymmetry and condylectomy

2. *Separation of the mandible and morphologic analysis*: It's important to inspect the mandible individually to evaluate its overall morphology with special regards to the hyperplastic condyle. Moreover, condylar reconstruction and cleanup is very important to reconstruct a reliable model of condylar morphology (Fig. 15).
3. *Definition of midsagittal plane and mirroring*: Next step is to evaluate the position of true midsagittal plane and subsequently mirroring of the mandible. This plane does not coincide with N-ANS-MidCor plane but is an inherent symmetry plane of the mandible itself, enabling to study its symmetry. To facilitate its location, it may be considered perpendicular to the horizon and passing through N. The evaluation of symmetry is important especially in posterior view to determine gonial discrepancy (Fig. 16).
4. *Alignment of mirrored mandible on pathologic mandible across posterior vertical height*: Point-to-point alignment is made on the mandibular ramus. Then, global registration is performed. However, global registration based on the iterative closest point (ICP) algorithm privileges alignment over the body region, where vertices are more



Fig. 15 Accurate morphological reconstruction of the condyle especially at the hyperplastic side is highly important



Fig. 16 Mandible mirroring with its inherent symmetry plane

present. Thus, subsequent manual refinement must be performed to enable overlap of both posterior vertical heights starting from the gonion. This enables to evaluate vertical discrepancy and establish the difference between condyles to set the level of proportional condylectomy (Fig. 17).

5. *Definition of the osteotomy plane and virtual condylectomy*: Once the alignment is satisfactory, the profile of the proportional condylectomy is determined by drawing a curve around the aligned condyle. The curve is drawn on a sketch passing through a point defined on the lateral condylar pole and parallel to the user's vie. The curve is used as the base to extrude the osteotomy plane. Then osteotomy and condylectomy is performed (Fig. 18).
6. *Mandibular plane equilibration*: Next step is the realignment of the mandible with rotation (fulcrum in the healthy TMJ) until the condylectomy side reaches the top of the hyperplastic condyle (to maintain the same interarticular relationship). The coincidence between the cortical profile of the hyper plastic condyle and that after condylectomy is mandatory to maintain the original interarticular space (Fig. 19).
7. *Assessment of mandibular angle symmetry verified on the side and frontal view*: Since the symmetry of the jaw is given by the position of the angles and their symmetry, bringing the angles to the same level is fundamental. Their correspondence in the sagittal view is evaluated, as well as the similarity of measurements from Gonion point (Go) to superorbital plane (or FHP if parallel to supraorbital plane). In case a discrepancy is found, it is necessary to rebalance the position of the mandibular angles to have them at the same level (Fig. 20).

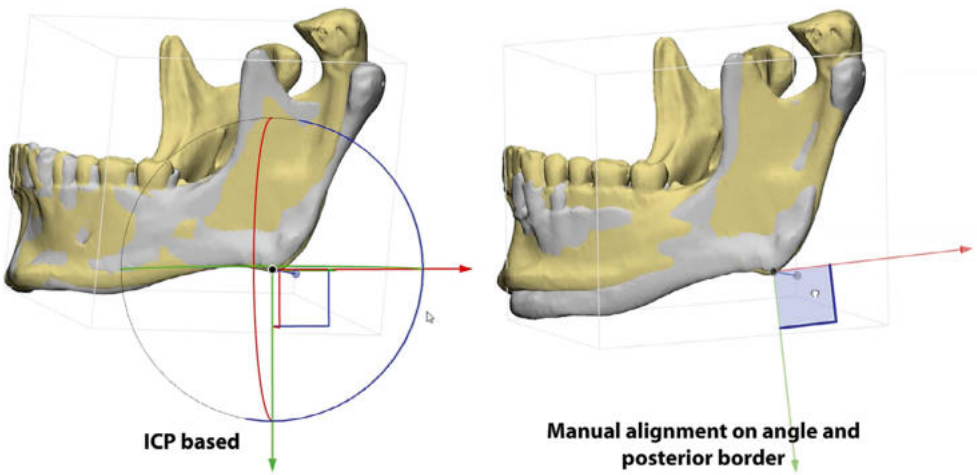


Fig. 17 establishing correspondence between Go points of the hyperplastic and the mirrored healthy side

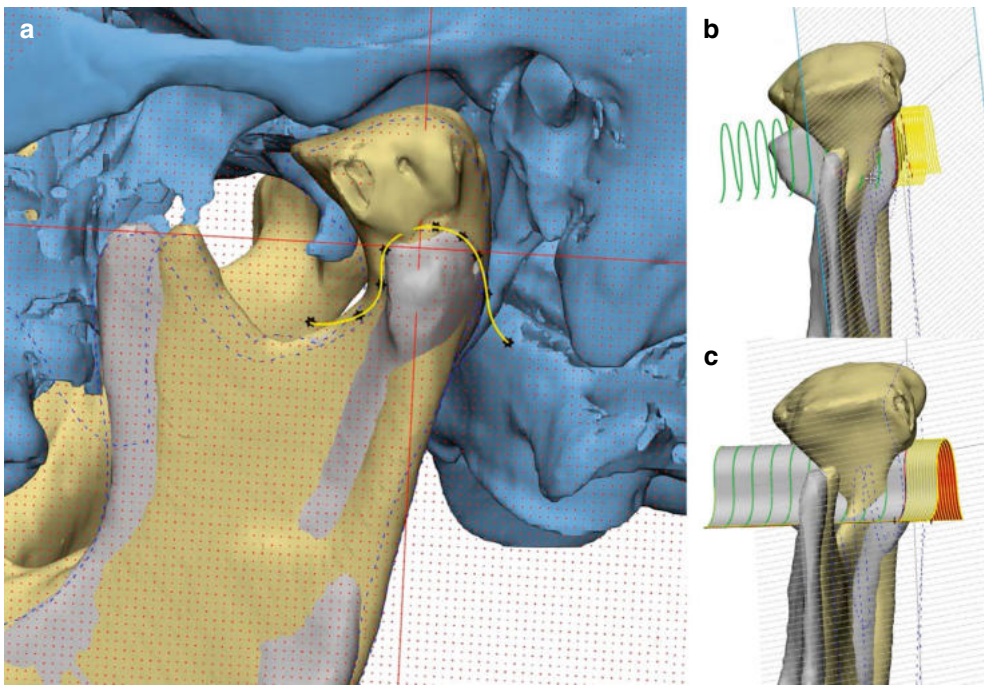


Fig. 18 Definition of the cutting profile for condylectomy (**a**) and subsequent curved plane extrusion (**b** and **c**)

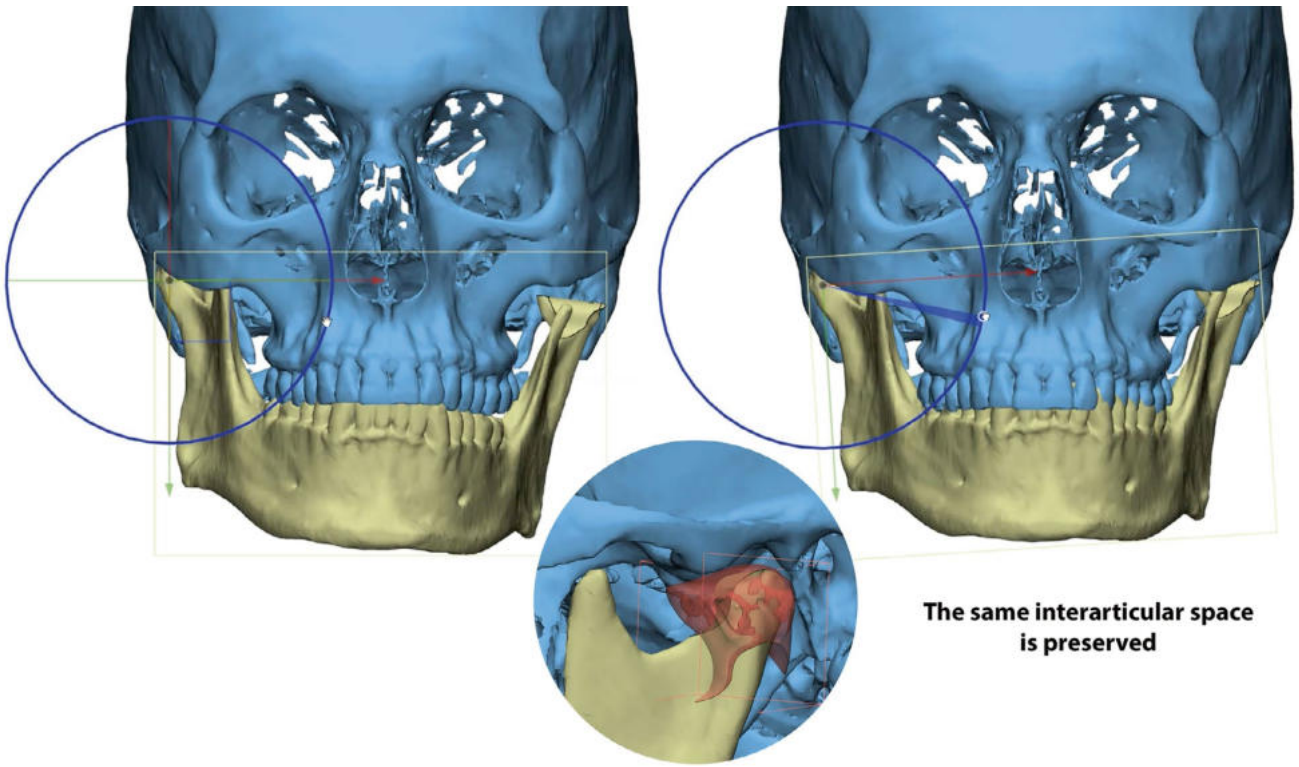
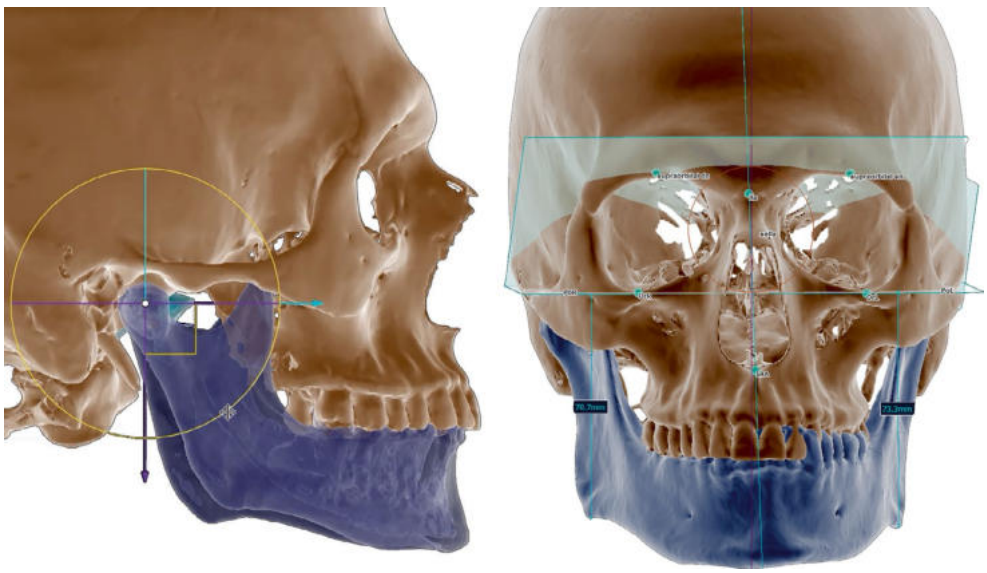


Fig. 19 Rotational compensation by placing the fulchrum at the normal side and lifting the condylectomy side at the level of interarticular space

Fig. 20 Evaluation of residual gonial asymmetry



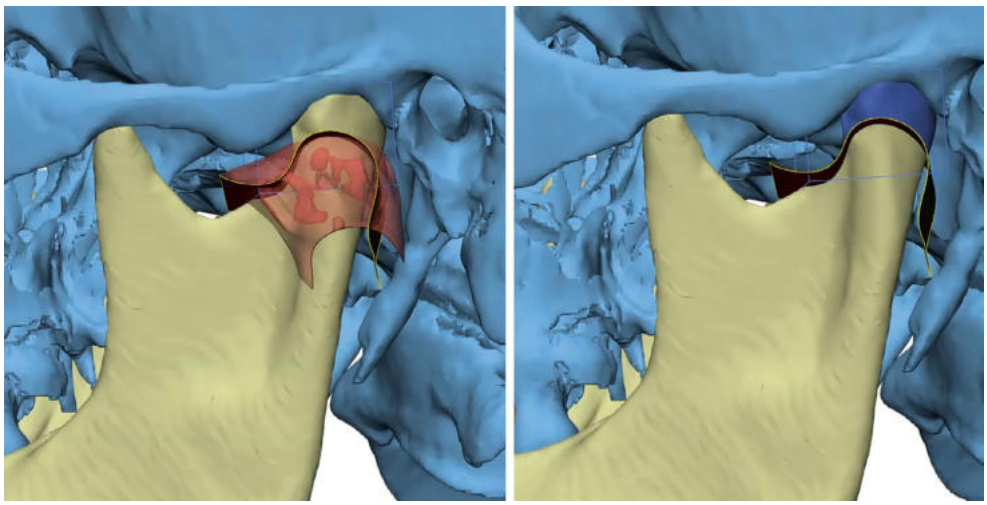


Fig. 21 While keeping the condylectomy plane at the same level, rotational compensation is performed again until gonial symmetry is achieved. This may involve a re-condylectomy

8. *Eventual remodulation of the height of the condylectomy plane to achieve angle symmetry and re-condylectomy*: Rebalancing the mandibular angles often leads to a modification in the vertical position of the condyle subject to proportional condylectomy based on contralateral mirroring. In other words, healthy side mirroring is often not sufficient to reestablish symmetry of the mandible, which needs to take into account the position of Go points. If Go from the hyperplastic side needs to be further moved up, the neocondyle is lifted, and therefore a new level of condylectomy is established to achieve angle symmetry (Fig. 21).
9. *Surgical guide modeling and 3D printing*: The surgical guide is modeled in a virtual environment and 3D printed using a biocompatible resin. The guide is usually designed 1.5 mm thick and forms a thin envelope around the lateral pole of the condyle. The guide is printed using transparent, medically certified, resin (Fig. 22).

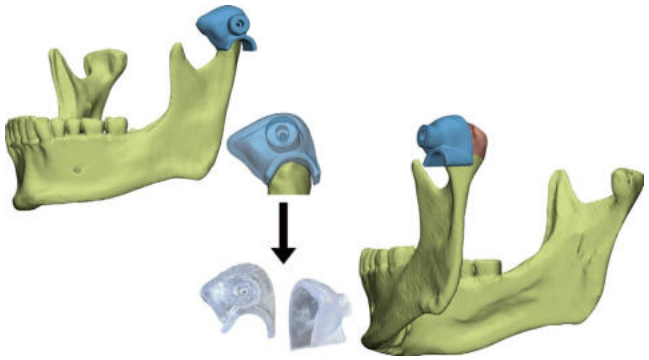


Fig. 22 Design and 3D print of a surgical guide for proportional condylectomy (preauricular approach)

4.2 Isolated Proportional Condylectomy: Surgery

This protocol should be used in any case of surgery contemplating proportional condylectomy. Isolated proportional condylectomy is traditionally performed using an external approach through the preauricular incision. This approach, conducted beneath the deep temporal fascia, provides an additional protection to the frontal branch of the facial nerve. The condylar capsule is incised and the inferior TMJ chamber is entered. Care is taken to preserve the articular disc in this procedure. Using Dunn's retractors, the lateral condylar pole is mobilized and freed, allowing to position the surgical guide. The surgical guide should be designed as thin as possible, owing to the restricted spaces. Once stable fit is found, the surgical guide clearly indicates the level of proportional condylectomy (Fig. 23).

An alternative approach, recently described (CITAZIONE NOSTRA CONDILECTOMIA INTRAORALE), consists in performing the procedure endoscopically. An incision is made above the mandibular ramus and the coronoid is exposed. As a transcoronoid pathway to the mandibular condyle is used, a strategic coronoidectomy is performed to gain access to the mandibular condyle. In this case, the surgical guide design must be modified to fit the sigmoid notch, allowing to trace the condylar osteotomy at its superior margin (Fig. 24). A screw is applied in the hyperplastic condyle with a wire loop to exert a gentle traction until the upper part of the condyle is removed (Fig. 25). Yet technically more difficult, this approach avoids an external scar and, most importantly, risks related to facial nerve injury.

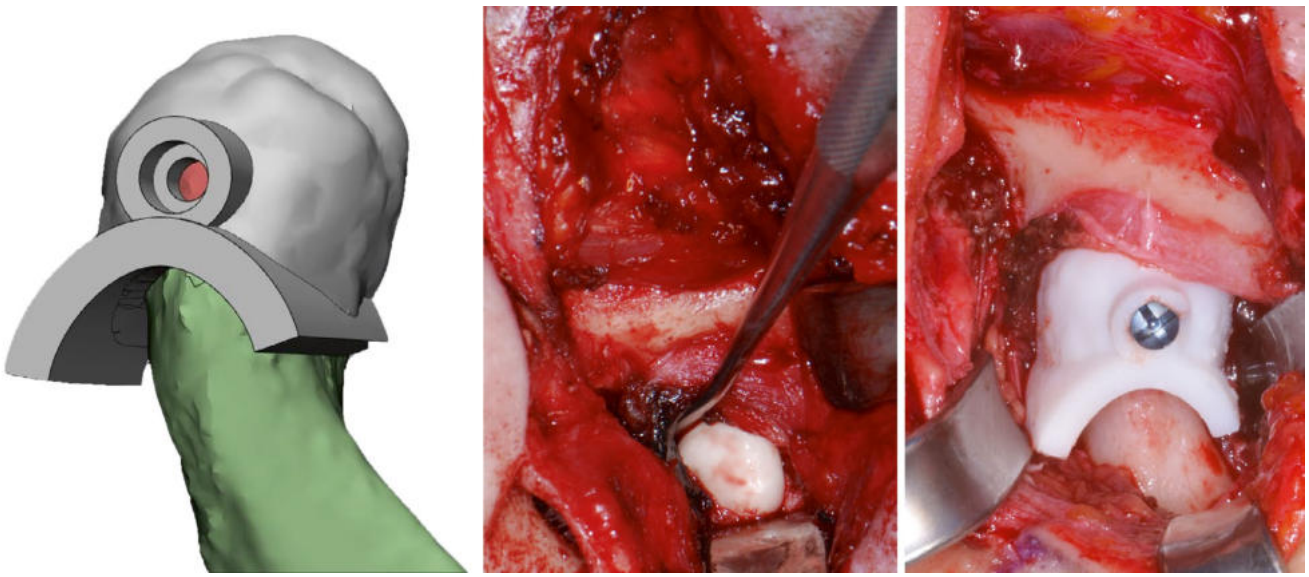


Fig. 23 Surgical view of computer-guided proportional condylectomy through a preauricular approach

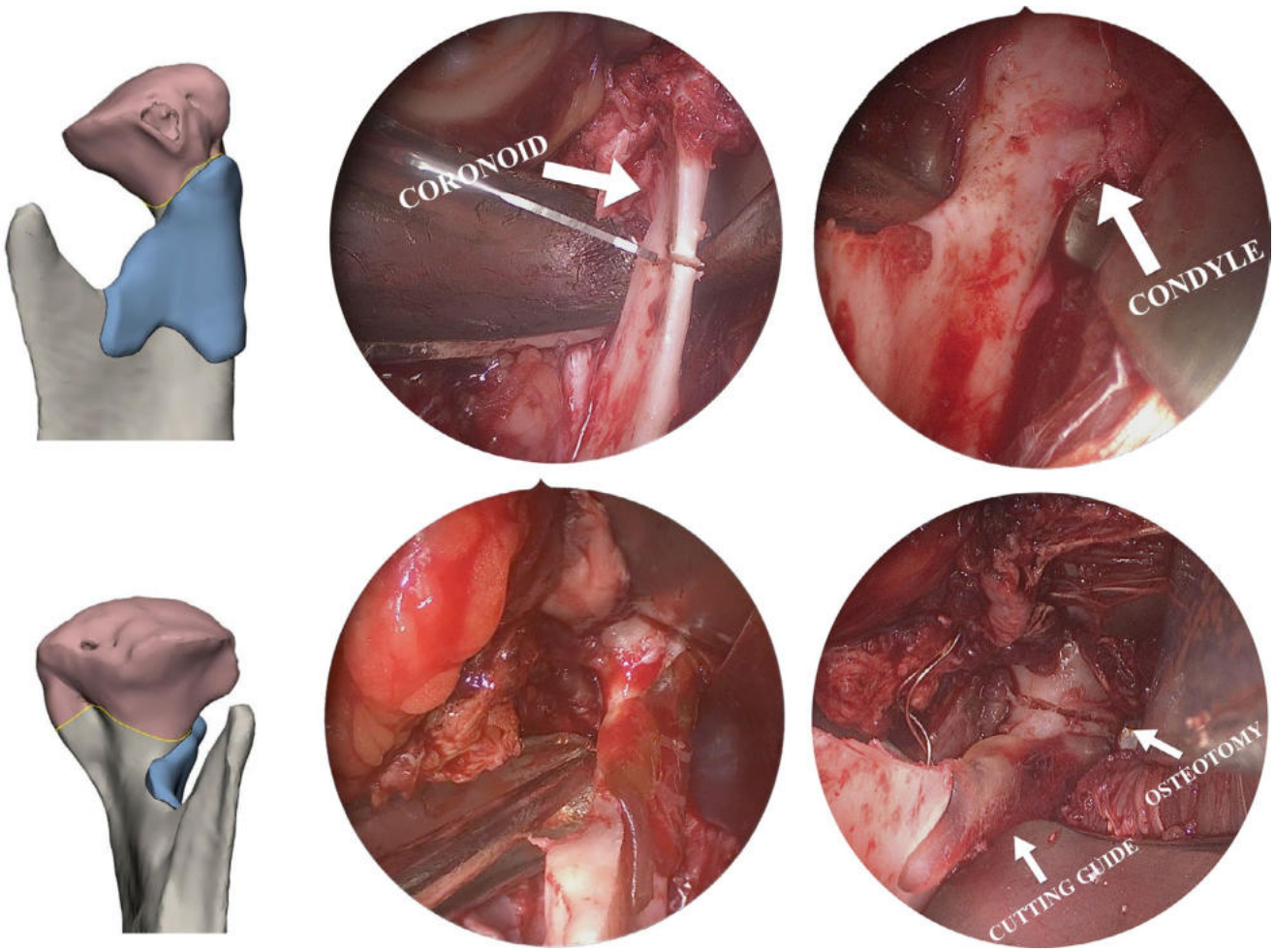


Fig. 24 Design modifications required to perform computer-guided condylectomy from an intraoral approach



Fig. 25 Resected specimen

Whatever strategy to perform the condylectomy is chosen, the expected result in the long term follow-up is the normalization of the inferior occlusal plane which, as seen, could lead to the equilibration of the maxillary occlusal plane as well through the effect of sequential orthodontic movements. This is particularly effective in growing patients, where chances to avoid a second stage orthognathic surgery are highest (Fig. 26).

4.3 Proportional Condylectomy Associated to Orthognathic Surgery: VSP Protocol

In several cases, especially when a class I dentofacial relationship is maintained, and only mild coronal asymmetry is present, proportional condylectomy alone might be sufficient. From an occlusal point of view, it is clear that as a result of the condylectomy only, the patient will present with an iatrogenic malocclusion, namely an ipsilateral precontact and a contralateral open bite. However, this may induce orthodontic readaptations resulting in ipsilateral upper molars intrusion and ipsilateral lower molars extrusion, leading to the equilibration of the occlusal plane. Especially in the growing patient, this may ultimately lead to a skeletal change with a cant correction [10].

However, if condylar hyperactivity is accompanied by dysmorphic patterns (such as class II or III dentofacial deformities), condylectomy and orthognathic surgery are planned simultaneously from the beginning. Candidates for this treatment are patients who, in addition to vertical asymmetry, also exhibit abnormal sagittal growth patterns resulting in a malocclusion not corrigible with proportional condylectomy only. This is often the case of class III unilateral condylar hyperplasia (UCH) according to Obwegeser classification (see Chapter "Applications of VSP in Orthognathic Surgery"), in which also a horizontal growth asymmetry is found, as well as morphological alterations of the mandibular body.

Proportional condylectomy associated with orthognathic surgery planned as one-stage procedure has many advantages compared with the traditional two-stage approach:

- The first, and most obvious, is to avoid the additional morbidity and discomfort associated with two surgical operations.
- However, a detailed VSP analysis according to the aforementioned protocol has the advantages of tailoring the orthognathic surgery movements on the effect of the proportional condylectomy, which is always the first step in VSP. Orthognathic surgery movements are meant to reposition skeletal based when proportional condylectomy alone is not able to restore a satisfactory facial pattern. Combining both procedures, in selected cases, might avoid performing the sagittal split osteotomy (SSO) at the condylectomy side.

The VSP steps include:

1. *Proportional condylectomy*: The workflow described in Sect. 4.1 needs to be entirely followed in any case and represent the first, unavoidable, step.
2. *Mandibular ramus repositioning (condylectomy side)*: The second step involves tracing both mandibular and maxillary osteotomies. After performing the osteotomies, the mandibular ramus of the condylectomy side is repositioned independent on the orthognathic surgical plan. The aim is to maintain the correct articular space when repositioning the new condyle (Fig. 27). In Class III cases without planned mandible advancement, a unilateral sagittal split osteotomy (SSO) can be performed, allowing repositioning of the affected ramus without requiring osteotomy. The degree of rotational compensation also affects the decision to use bilateral SSOs, as a rotational component on the coronal plane can be corrected alone by proportional condylectomy. Mandibular advancement is logically an absolute indication to bilateral SSO.
3. *Occlusion registration*: Occlusion is registered and aligned to the rsuperior dental arch, and the mandible is repositioned into the desired surgical occlusion (Fig. 28). This step is responsible for mandibular distal segment



Fig. 26 Proportional condylectomy alone in an adolescent patient was sufficient to correct facial asymmetry. From (**a**) to (**c**): preoperative appearance. From (**d**) to (**f**): 4-year follow up. (**g**) preoperative occlusion. (**h**) 4-year occlusion

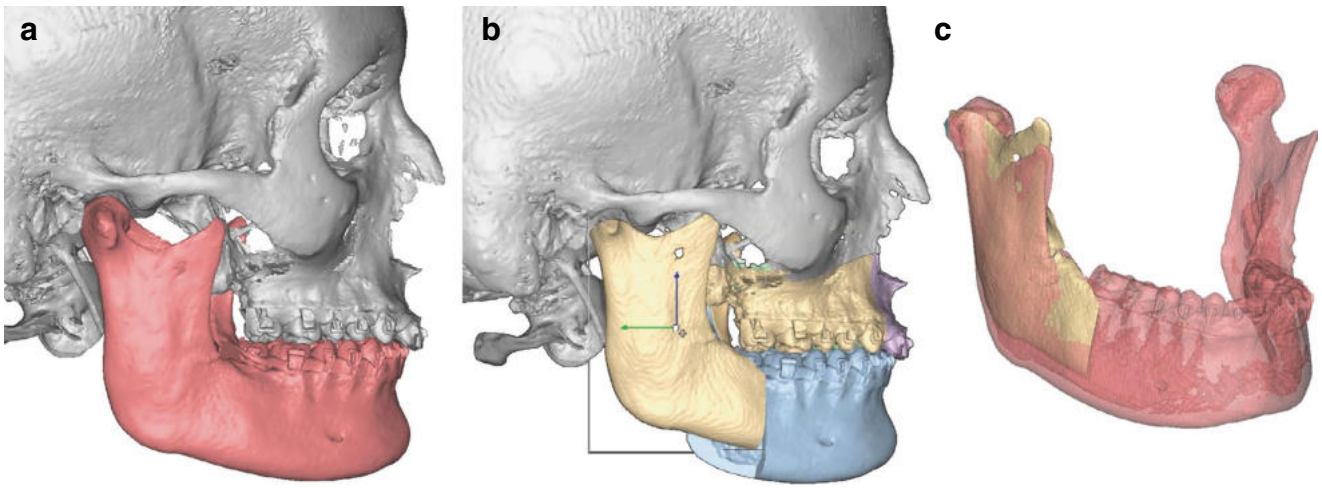


Fig. 27 Workflow for simultaneous proportional condylectomy and orthognathic surgery. After osteotomies, this first step illustrates the independent repositioning of the ramus with condylectomy in the correct relationship with the fossa

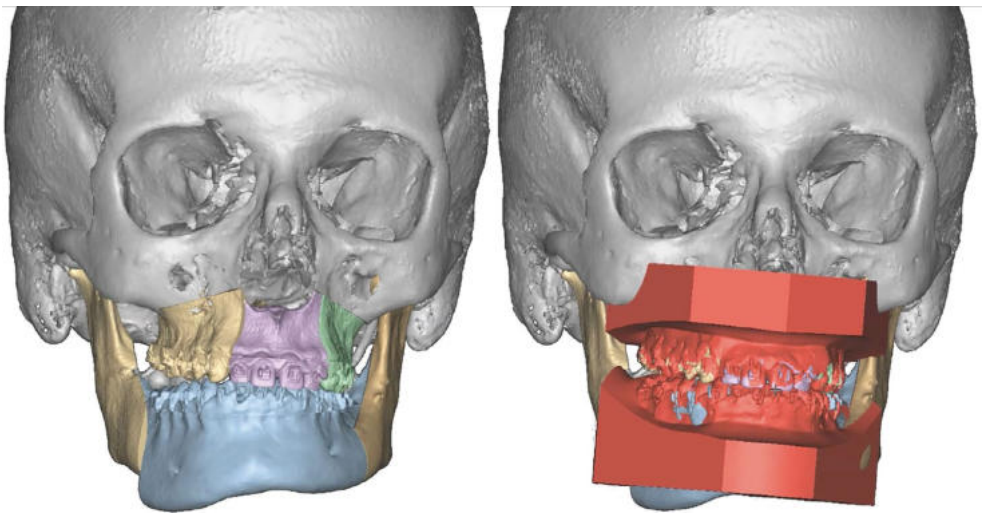


Fig. 28 Mandible repositioning in the correct occlusal relationship with the upper maxilla enables to establish the provisional movement associated with distal segment repositioning

repositioning in the desired occlusal relationship with the maxilla in a UIM value of 0. Thus, the operator is able to understand how the distal mandibular segment is repositioned in the correct occlusion.

4. *Orthognathic movements*: The maxillomandibular complex in occlusion is repositioned according to the orthognathic plan, correcting canting, yaw, pitch, and adjusting vertical and sagittal dimensions. The final position of the condylectomy ramus in relation to the orthognathic surgical plan determines whether the ipsilateral SSO is necessary or not. As mentioned, significant sagittal translations or axial rotations which create an osteotomy gap confirm that ipsilateral SSO is needed (Fig. 29). Conversely, if the result of mandibular respositioning is minimal at condylectomy side after orthognathic movements, only contralateral SSO in advised. In any case, the contralateral SSO is unavoidable to accommodate distal segment repositioning over the maxilla in the correct occlusal relationship (Fig. 30).
5. *Genioplasty and border contouring* (mandible body reshaping): Any remaining asymmetry is addressed through additional procedures, such as border recontouring and genioplasty. This is important especially in class III UCH as the mandibular body is often higher than the contralateral side, as well as to address chin defects (Fig. 31).

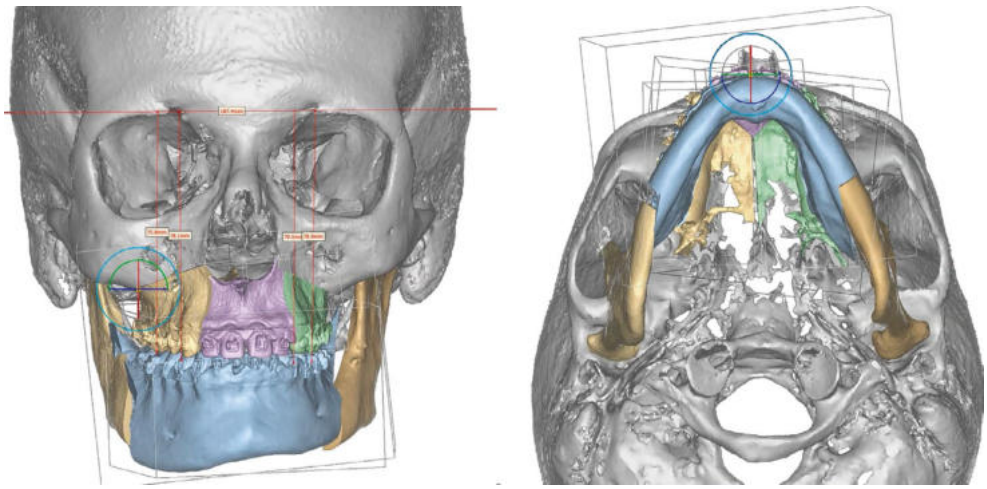


Fig. 29 Orthognathic movements. This step is crucial to define whether a single contralateral SSO is sufficient, or a bilateral SSO (BSSO) should be considered

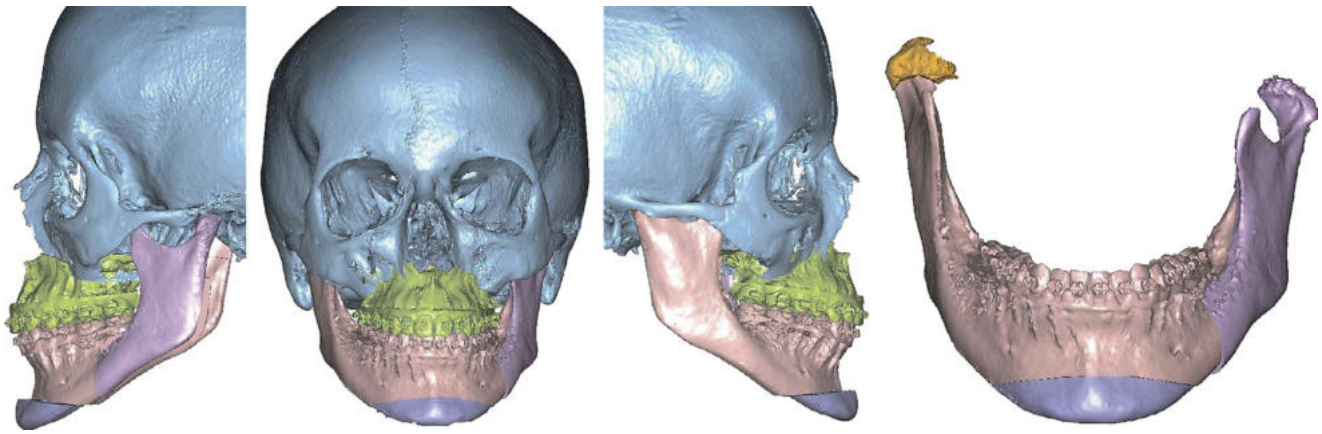


Fig. 30 VSP for a single, contralateral SSO opposite to the side of condylectomy

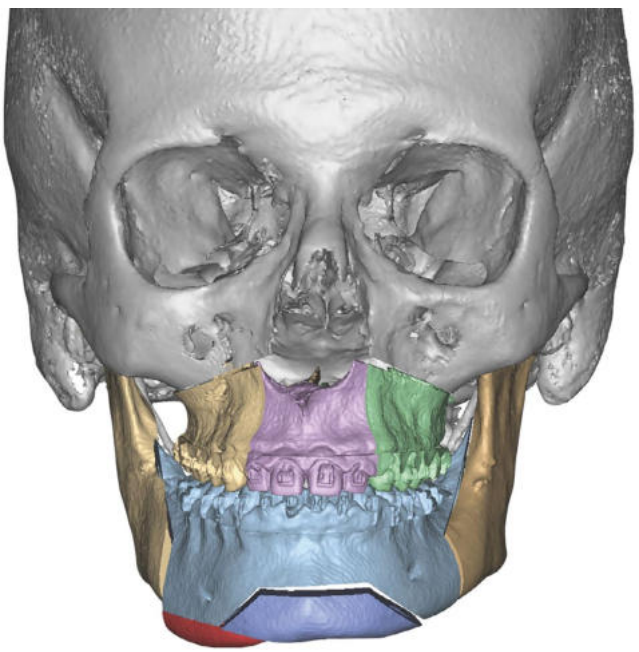


Fig. 31 Residual border asymmetry is corrected through ancillary procedures such as genioplasty and recontouring

6. *Surgical Guide Modeling and 3D Printing*: The final plan is shared with the manufacturer to create custom implants and cutting guides, including the surgical guide for proportional condylectomy, which is crucial to intraoperatively reproduce the planned level of condylectomy (Fig. 32). Fully custom surgery is highly recommended in complex procedures for its possibility to enhance automation and predictability.

4.4 Proportional Condylectomy Associated to Orthognathic Surgery: Surgical Steps

As mentioned, fully custom surgery guided by 3D printed guides and customized templates is recommended for complex procedures involving both a condylectomy and a bimaxillary orthognathic surgery [13]. Remarkably, the TMJ procedure performed to excise the hyperplastic condyle deliberately violated joint capsule and loosens the condylar attachments to the fossa. Moreover, yet condylectomy

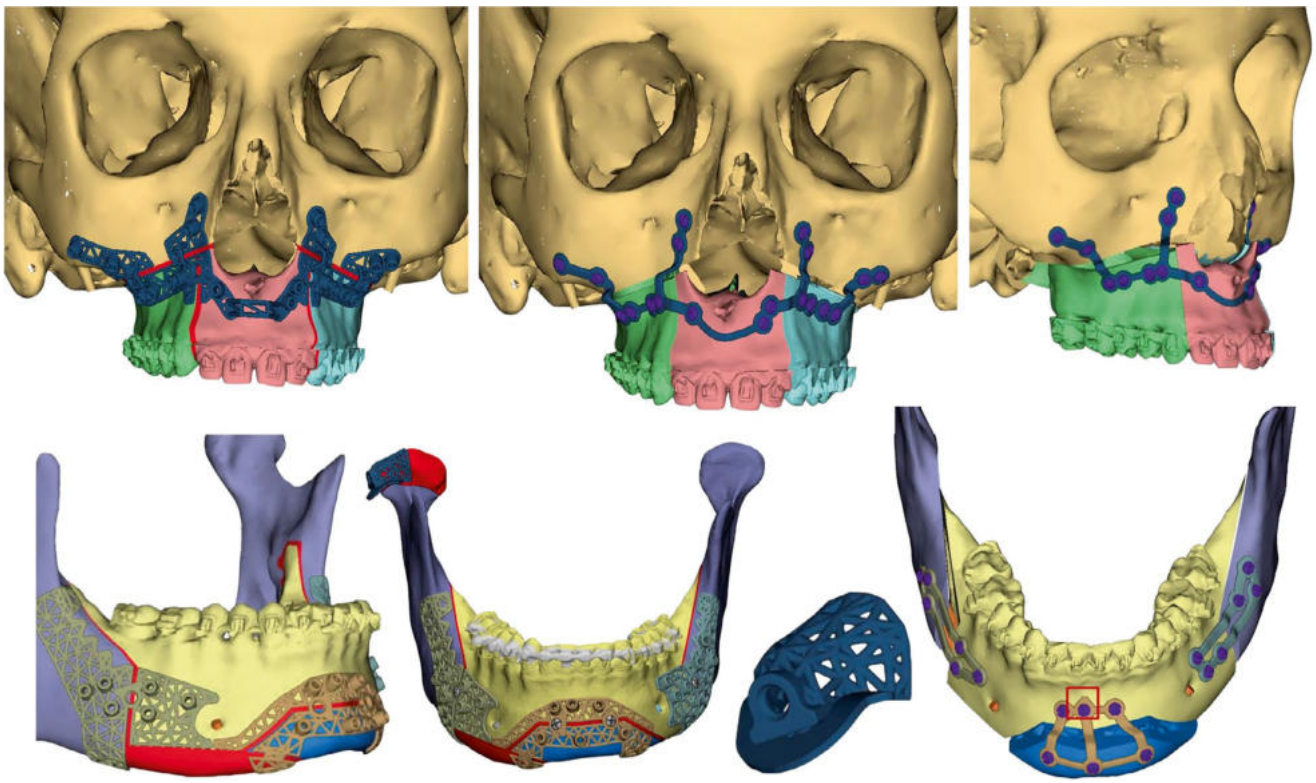


Fig. 32 Fully custom surgery: VSP shared with the manufacturer and sent back to surgeons for approval

is designed to avoid any change in the interarticular relationship between the condyle and the fossa, the intracapsular hematoma subsequent to the joint procedure results in an increase of distance between the condyle and the fossa and might be responsible for an ipsilateral open bite, even though the procedure has been correctly performed and the resulting occlusion reliably reproduced. For this reason, a fully custom surgery is able to guarantee increased reproducibility of VSP steps and trustfully reproduces skeletal movements. In particular, it is of prominent importance to assist the condylectomy itself, as even 1 mm difference for the plan might account for increased occlusal differences (Fig. 33). After condylectomy, which is advisable to perform as first step for the need of sterility in the TMJ, orthognathic bimaxillary surgery can be performed independently of a maxilla-first or mandible-first sequence, as one of the benefits of customized surgery is to prescind from the surgical order (Fig. 34).

If, for any reason, it is not possible to perform and entirely patient-specific surgery with 3D printed implants, which may be precluded in some circumstances owing to their high cost, a traditional orthognathic surgery should be performed considering the following steps:

- Taking care to meticulously separate the sterile TMJ field to the contaminated oral cavity. Every procedure in the TMJ must be performed under sterile conditions with the mouth covered.
- Start first with maxilla. Even though bimaxillary surgery is most often using mandible first sequence, and even though it might be preferrable to start surgery with the sterile part, positioning maxilla first has relevant implications. Maxillary repositioning is used as a guide to provide the correct occlusal plane for the mandible, whose repositioning might be more difficult for the concomitant TMJ procedure. This is true especially is significant occlusal plane reequilibration is needed, which happens most frequently in cases of asymmetry.
- The second step is condylectomy: after the maxilla is fixed, proportional condylectomy is performed using a preauricular approach. Although maxillary fixation can be traditionally performed, proportional condylectomy must always be a computer-guided procedure, thus a PoC printed condylar guide is necessary.
- Last step is mandibular BSSO, in which the mandible is fixed to the maxilla using MMF and plated. Using MMF with a correctly aligned maxilla has the advantage that the mandibular body repositioning prescinds from the TMJ procedure, which involves the higher variability.

The following case illustrates the effect of combined proportional condylectomy and orthognathic surgery performed through the application of this protocol and its efficacy in correcting a type 1 UCH with condylar hyperactivity determining facial asymmetry associated with a maxillomandibular dysmorphic pattern in a young patient (Fig. 35).

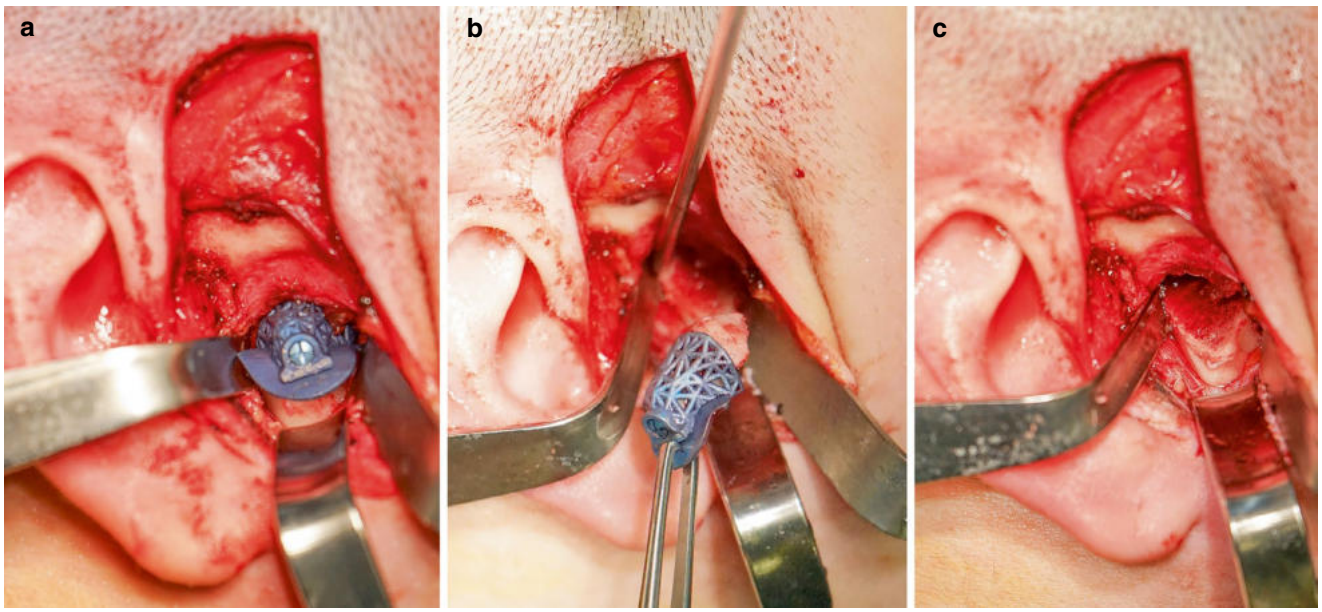


Fig. 33 Titanium guide for proportional condylectomy: surgical sequences

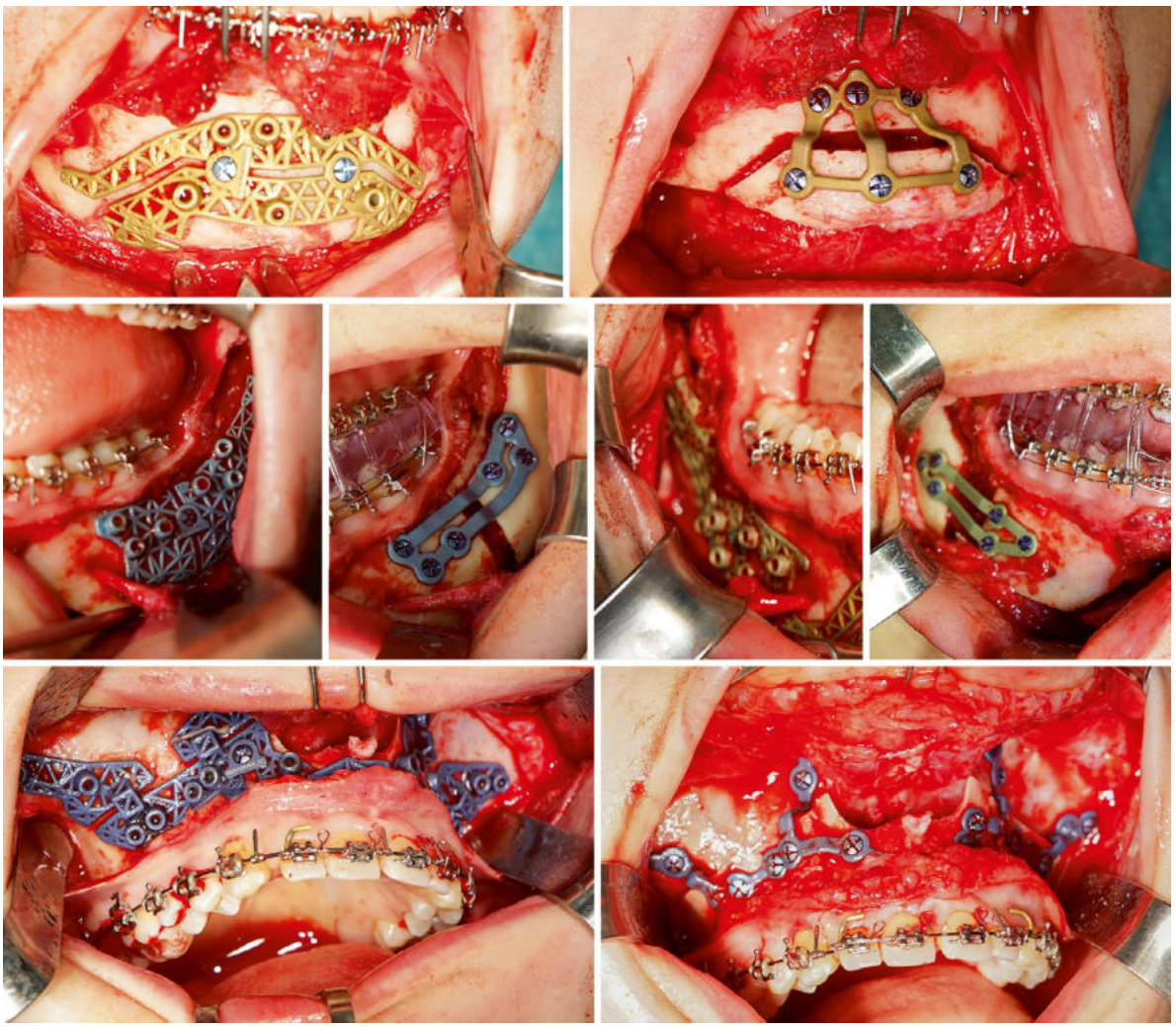


Fig. 34 Fully custom orthognathic surgery



Fig. 35 Clinical outcome of simultaneous proportional condylectomy and orthognathic surgery. From (**a**) to (**d**): preoperative clinical photographs. From (**e**) to (**h**): 4-years follow-up. (**i**) preoperative occlusion; (**j**) postoperative occlusion

5 Temporomandibular Joint Replacement (TJR)

End-stage TMJ disease can result in significant impairment of chewing and speech, impacting physical, social, and psychological well-being, as well as overall quality of life. It may also affect appearance and reduce airway space. Alloplastic TMJ replacement (TJR) is the primary treatment for this advanced condition [14, 15].

The goals of TMJ replacement include restoring the joint's functional components as closely as possible to the natural joint, with the aim of balancing posterior facial height (ramus) to prevent facial asymmetry, improving pain-free mouth opening, preventing recurrence in TMJ ankylosys, performing concurrent orthognathic surgery to address dysmorphic patterns.

Indications for alloplastic TMJ replacement generally include situations where traditional treatments failed, especially in cases of extensive damage or deformation. Key indications include:

1. disruptive degenerative disease (osteoarthritis) with severe alteration of joint function
2. refractory inflammatory arthritis unresponsive to other treatments causing the anatomical modification of the joint
3. temporomandibular joint ankylosis with impossibility to open the mouth
4. previously failed autogenous grafts (for instance, costochondral graft)
5. tissue destruction due to pathology or neoplasms, which can arise primarily within the joint, such as condylar osteomas and osteosarcomas, or represent the invasion from a nearby pathology, such as carcinomas of the oral cavity or the parotid gland
6. idiopathic or secondary condylar resorption with loss of posterior facial height
7. congenital abnormalities, such as Pruzansky-Kaban's classes II and III for hemifacial microsomia, which can occur in the context of Treacher-Collins syndrome and other related congenital malformations
8. trauma sequelae leading to severe joint disruption, for instance plurifragmented (bursted) condylar fractures
9. other systemic diseases, including juvenile idiopathic arthritis, ankylosing spondylitis, and scleroderma

Relative contraindications for alloplastic TMJ replacement include uncontrolled systemic diseases, active infections at the surgical site, and allergies to implant materials.

Advantages of alloplastic prostheses include avoiding a second surgical site related to graft harvesting, reducing surgical time, and improving biomechanical adaptation as the prostheses mimics the natural joint anatomy. Physiotherapy should start immediately, minimizing risks of heterotopic bone formation, and orthognathic surgery can be performed simultaneously for facial asymmetry correction. However, disadvantages may include the high cost of the prosthesis, material wear and biomechanical failure, potential allergic reactions, long-term stability concerns, and lack of growth potential for skeletally immature patients.

Over the last years, stock TMJ replacement prostheses have been largely superseded by customized implants, which provide an optimal adaptation to the bone surfaces of the recipient site and enhance predictability of the final result. This improvement is strictly related to advancements in design software, with the possibility to implement organic modeling, as well as sophisticated metal 3D printing techniques, including selective laser sintering, selective laser melting, and electron beam melting.

A custom TMJ prosthetic system typically consists of a ramus-condyle component, made from Ti64 Titanium alloy, and a fossa component, made from Ti64 Titanium alloy and ultra-high molecolar weight poly-ethilene (UHMWPE), coupled under pressure with the titanium structure. In addition to the implant itself, design packages and 3D printers enable to create special cutting and positioning guide, which assist the surgeon across the critical steps of ramus osteotomy and prosthesis insetting. Design conteptualization for such surgical guides has evolved over the years, starting with a basic guide for ramus osteotomy and fixation holes predrilling, and culminating in an innovative surgical guide with two assemblable components, useful not only for osteotomy and hole predrilling, but also for prosthesis insetting [16].

5.1 VSP Principles for Customized TJR

There is one core principle for VSP of TJR using customized prostheses: prosthesis design is the last phase of a process of digital planning which involves changes in the maxillo-mandibular relationship. This apparently simple statement reveals an important property of TMJ custom implants, namely the possibility to adapt to any situation, and therefore to be modelled to address any specific need. There are three types of conditions that may occur:

1. TMJ planned preserving the current occlusion: it is a rare condition since end-stage TMJ disease involves anatomical modifications that have obvious consequences on occlusion. However, it may happen for cases in which TMJ replacement is needed for a pathological process, for instance, an oncologic resection.
2. TMJ planned improving current occlusion: generally, a mandibular advancement procedure is included. This is the case, for instance, of severe condylar resorption causing a shift of the patient from a normal occlusion to a

class II occlusion. In such circumstances, placing a prosthesis accounts for ramus lengthening and thus reestablishing a correct posterior facial height.
3. TMJ planned with a combined maxillo-mandibular movement: it is the most complex setting, in which the TMJ implant must adapt to the new position of skeletal bases. In addition to translations, movements might include roll, pitch and yaw rotations; thus, customized TMJ implants are extremely versatile to allow such changes.

5.1.1 Project Setup

CT scan should be performed according to the parameters described in the previous chapters. CBCT can be used, but it involves an overall inferior quality of the segmented model, with possible voids or artifacts along skeletal surfaces, which may represent the source of inaccuracies for the implant fitting.

Intuitively, intraoral scans should always be performed on patients undergoing TMJ replacement. An occlusal registration matrix should always be acquired for patients in which occlusal changes are not planned. For patients needing a modification in their occlusion, models of dental arches should be 3D printed and assessed manually for the optimal intercuspation and then rescanned, allowing to achieve a novel occlusion registration matrix suitable for the stable surgical occlusion. Eventually, for patients with a presurgical orthodontic preparation needing simultaneous orthognathic surgery, surgical occlusion might also be established virtually, as seen in Chapter "Computer-Guided Orthognathic Surgery: State of the Art and Innovation."

Next step is the segmentation of the DICOM files from the CT scan, which are imported and processed in certified imaging software. Mask split enables to separate maxilla and mandible at their contact sites, namely the TMJ and occlusal cusps, yielding a separate mandible and maxilla, which can then be converted to STL files. Next, scanned dental arches are individually merged with the maxillary and mandibular models to achieve composite skeletal models with the improved occlusal detail.

5.1.2 VSP

Planning of ramus osteotomy is performed in a surgical planning software, such as ProPlan CMF and Enlight. It is important to establish the level of condylar ostectomy, namely the region meant to be eliminated and prosthetically replaced. This is performed by placing a cutting plane that may or may not include the coronoid process as well. Following osteotomy, the mandible is placed in the correct occlusal relationship using occlusal registration matrices acquired from scanned dental models. The mandible automatically repositions in the correct occlusal relationship.

In a combined orthognathic surgery is planned, VSP is simulated following the same principles of orthognathic surgery planning. The exception is that for a TMJ prosthesis, the BSSO is not necessary, as the required movements are already provided by the prosthesis. Moreover, screws for prosthesis fixation might conflict the SSO line. If TMJ replacement is planned only on one side, the contralateral SSO is needed, exactly as seen for proportional condylectomies.

Once skeletal bases are repositioned according to the desired orthognathic plan, the plan itself, or individual STLs, is shared with the manufacturer for prosthesis design.

5.1.3 Prosthesis Design

As mentioned at the beginning of this section, prosthesis design is the last phase of the process. It is performed in the final position of maxilla and mandible. Design software underwent significant advancements in the last years and can handle complex geometries such as anatomical entities. It depends on each company which is the optimal software: traditionally started in a purely geometric CAD environment, the interest has shifted to organic modelling software, which makes the modelling process much more intuitive and adjustable. There are some common principles that will be elucidated in relationship to the Geomagic Freeform Plus software (3D Systems Corporation, Rock Hill, SC, USA), used by the partner company GPI (GPI S.p.a., Trento, Italy):

1. Establishing the rotational fulcrum of the replaced joint. This is necessarily placed more inferior than the natural joint as the artificial fossa has a cup-like structure and is placed over the natural glenoid fossa (Fig. 36).
2. Definition of the screw position based on the location of the inferior alveolar nerve. Definition of the fitting surface of the implant, which represents the boundaries of the implant itself.
3. Extrusion of the prosthesis main body from the boundary. This happens using an "emboss" function, in which a thickness is assigned corresponding to the thickness of the final implant.

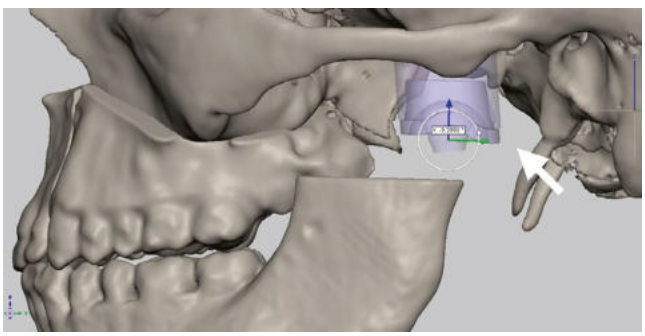


Fig. 36 Placement of the rotational fulchrum (condylar hinge) for prosthetic joint

4. A generic prosthesis head is standardized and eventually sized for each patient. It fits the prosthetic fossa and is designed to match curvature radius with compatible stability and friction. The head is positioned in the rotational fulcrum established for the prosthesis and is then connected to the prosthesis body using soft modeling brushes (Fig. 37).

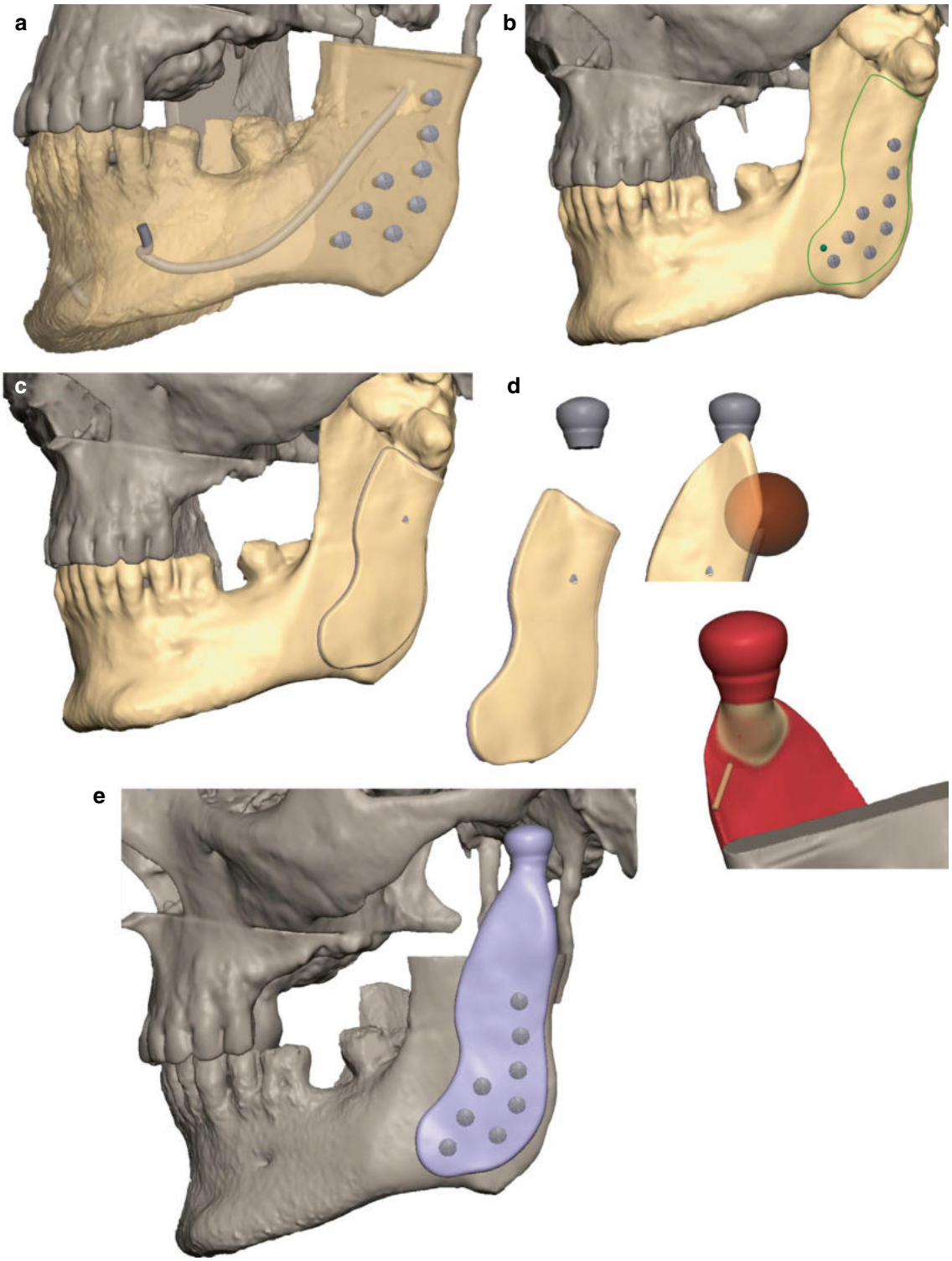


Fig. 37 Sequences for ramus component modelling using Geomagic Freeform Plus: (**a**) screw placement and avoidance of inferior alveolar nerve; (**b**) contour outlining; (**c**) contour extrusion (offset); (**d**) prosthesis head placement and connection with body flange; (**e**) complete ramus design

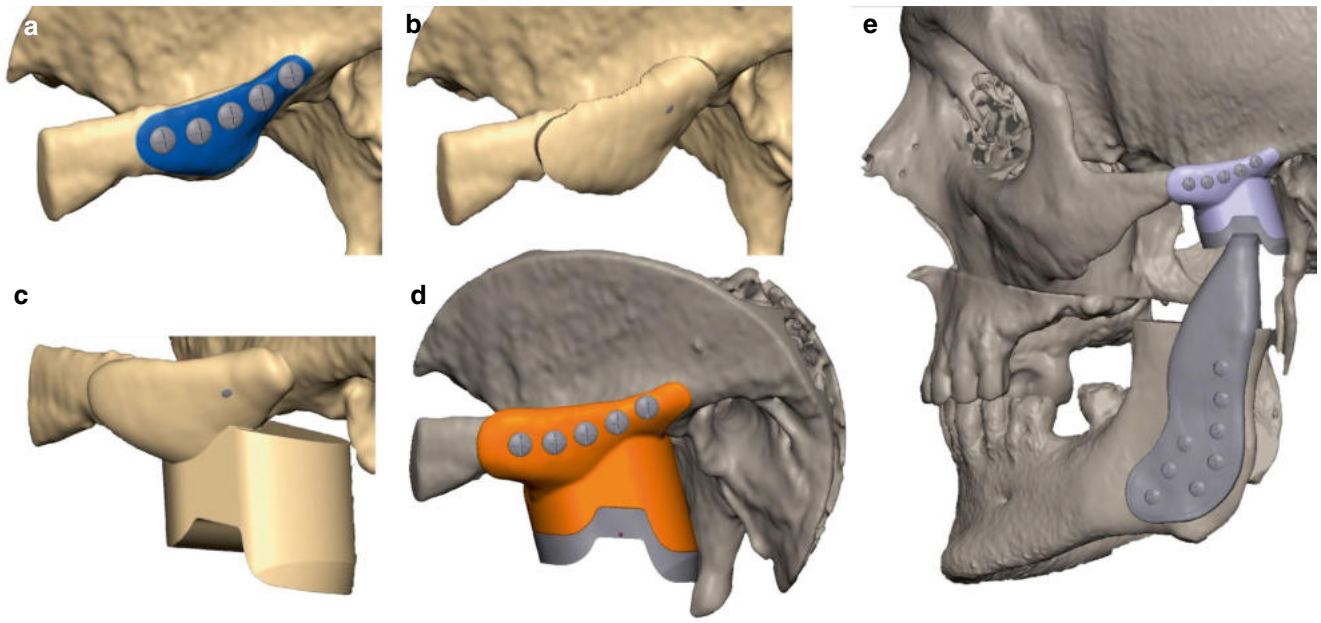


Fig. 38 Sequences for fossa component modelling using Geomagic Freeform Plus: (**a**) screw placement and marking of the area for extrusion; (**b**) extrusion; (**c**) fossa template placement and correction with extruded flange; (**d**) smoothing and refinement; (**e**) prosthesis complete

5. The same principles are applied for the fossa: screw position is established in the zygomatic arch, then an emboss function is used to extrude the thickness of the guide body.
6. A standardized fossa is connected to the guide body, matching the geometrical properties of the neocondyle. The fossa is then added another layer, corresponding to the inner UHMWPE envelope (Fig. 38).

5.1.4 Surgical Guides

The cutting guides are made of Ti6Al4V titanium alloy. They are designed to adapt to the bone resection margin, adhere in a specific position, and can be fixed by pressure to a suitably skeletonized bone surface. The guides have two components, a "core" and a "rim," with a particular geometry that enables the two units to be connected. The "core" has holes for the respective 2.7 mm screws for the mandible and 2.3 mm for the fossa (Fig. 39). The "rim" component, on the other hand, contains 2.0 mm holes for fixing to the bone. This guide system allows for the following advantages:

1. Pre-drill the bone where the fixing screws will be inserted.
2. Perform osteotomies with great precision.
3. Act as a guide by removing the "core" and leaving only the "rim" for the positioning of prostheses. This creates a sort of "installation socket" in which the guide can be inserted and three-dimensionally stabilized in the planned position.

The metal and polyamide components are produced using metal 3D printing. The ultra-high molecular weight polyethylene (UHMWPE) components are manufactured using numerically controlled milling machines.

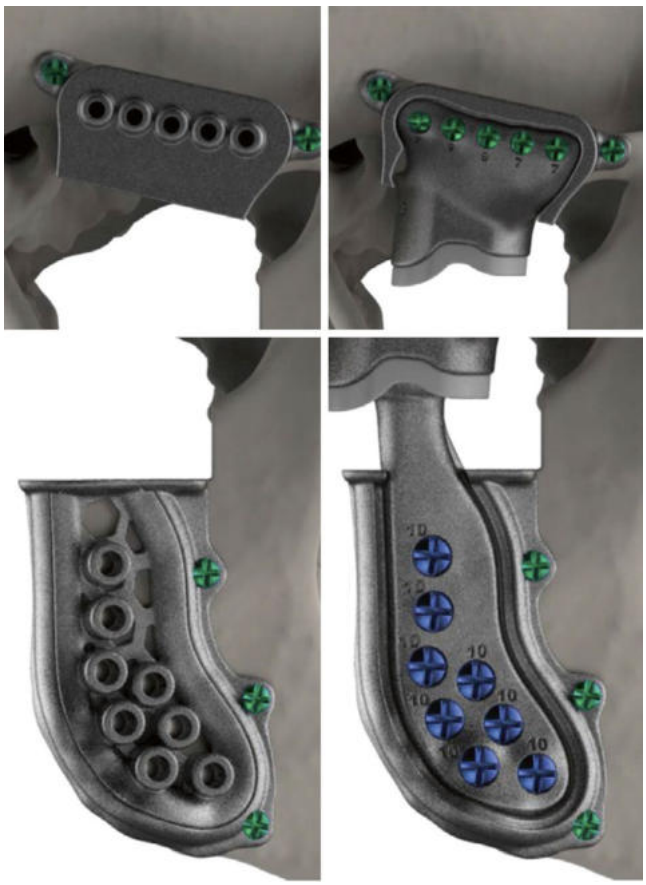


Fig. 39 Hybrid, dual-component, cutting and positioning guide for TMJ replacement

5.2 TJR for Ankylosis

Clinical History

A 65-year-old man presented to our department with progressive difficulty in mouth opening. His MMO was measured at 23 mm with a rigid end feel. He reported a history of maxillofacial trauma 3 years before, resulting in a left condylar head fracture treated conservatively. A CT scan revealed ankylotic degeneration of the left TMJ, causing a mechanical block. TMJ replacement surgery was planned (Fig. 40).

Virtual Surgical Planning (VSP)

The virtual surgical planning process was performed at our institution, and the prosthesis design and production were outsourced to the manufacturer GPI. The first step was bone segmentation to achieve anatomical polymeshes, followed by merging scanned dental arches to improve occlusal detail. The mandible was separated from the skull base and ankylosis was isolated. Osteotomy plans were designed to excise the ankylotic block. Next, the resected mandible was repositioned in a satisfactory occlusal relationship through registration with the occlusion registration mask. The prosthetic fossa and ramus components, along with their positioning and cutting guides, were customized to achieve proper maxillo-mandibular alignment. Digital tools were used for precise spatial adjustments, and surgical cutting guides were designed with attachment points for titanium osteosynthesis plates. Upon finalizing the design, STL files for the surgical guides and prosthetic components were prepared for manufacturing (Fig. 41).

Surgery

Using pre-auricular and retro-submandibular approaches, the TMJ, zygomatic arch, mandibular condylar head, and lateral mandibular ramus were exposed. Custom cutting and positioning guides were placed, avoiding the inferior alveolar nerve as planned. The ankylotic block was accessed and excised. Osteotomies were performed using a piezoelectric handpiece guided by surgical templates. The custom fossa prosthesis was positioned and fixed with pre-measured screws, and the mandibular ramus prosthesis was secured using the pre-drilled holes. The condyle's centric position within the fossa was verified, and the mandibular range of



Fig. 40 Clinical and radiological appearance of a case of left TMJ ankylosis

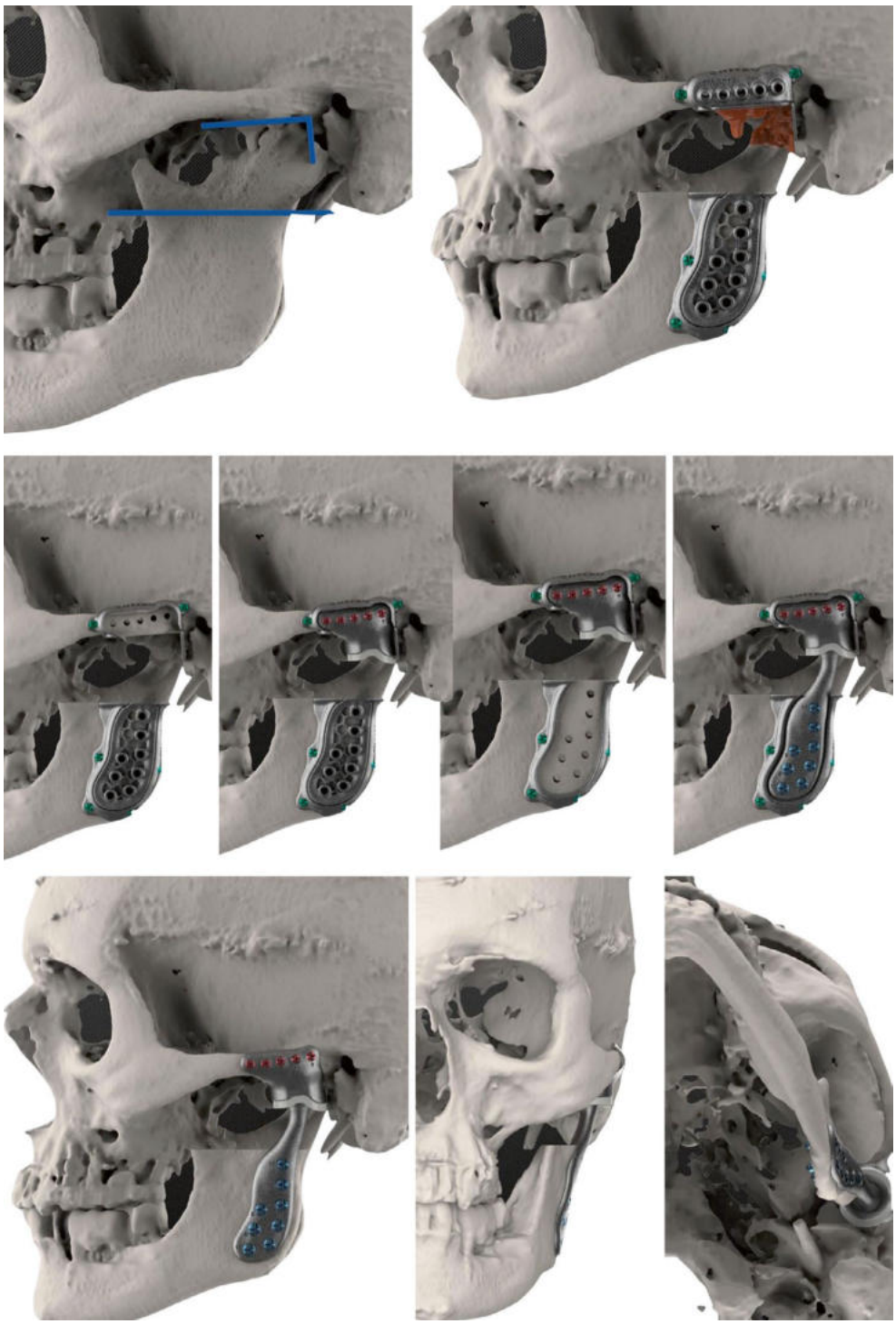


Fig. 41 VSP sequences agreed with the manufacturer (GPI S.p.a.)

motion was assessed to ensure proper alignment and functionality (Fig. 42). Clinical outcomes resulted in a stable occlusion with a normalized MMO (Fig. 43).

5.3 TJR Associated to Orthognathic Surgery

End-stage TMJ disease, when paired with the need for orthognathic surgery in adults, presents significant challenges for surgeons. This advanced stage of joint disease involves severe architectural damage to the joint, resulting in substantial functional impairment. Causes of such conditions include developmental issues, trauma, neoplasia, arthritis, failed previous surgeries, or fibrous and bony ankylosis. When treating these disorders, joint reconstruction is necessary, and three common approaches to total temporomandibular joint reconstruction (TJR) are widely recognized: autogenous bone grafting, transport distraction osteogenesis, and alloplastic replacement. The first two methods are generally used in pediatric cases.

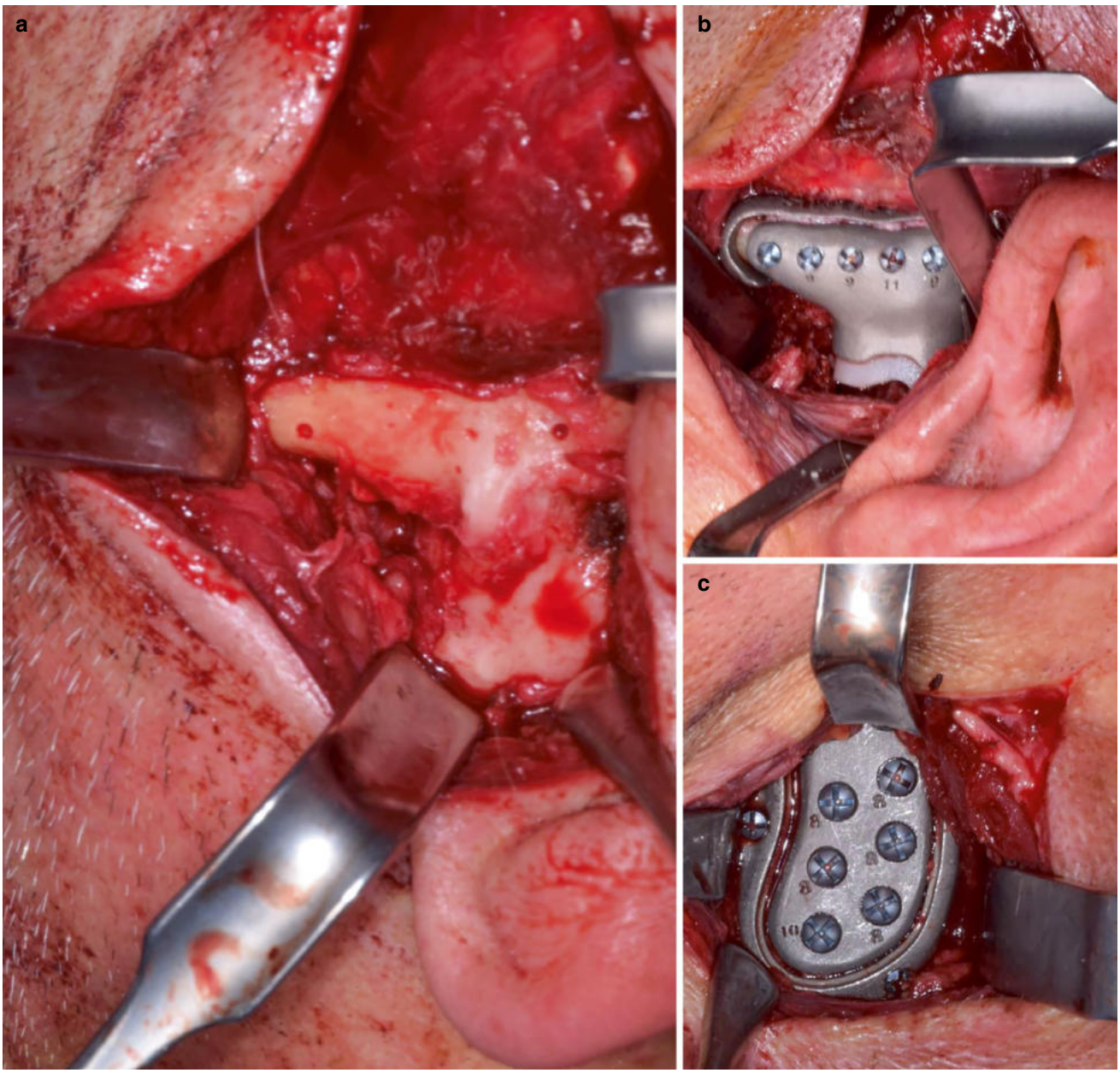


Fig. 42 Surgical sequences of TMJ replacement. Fossa prosthesis is placed through a preauricular approach, while ramus component is positioned through a retro-submandibular approach

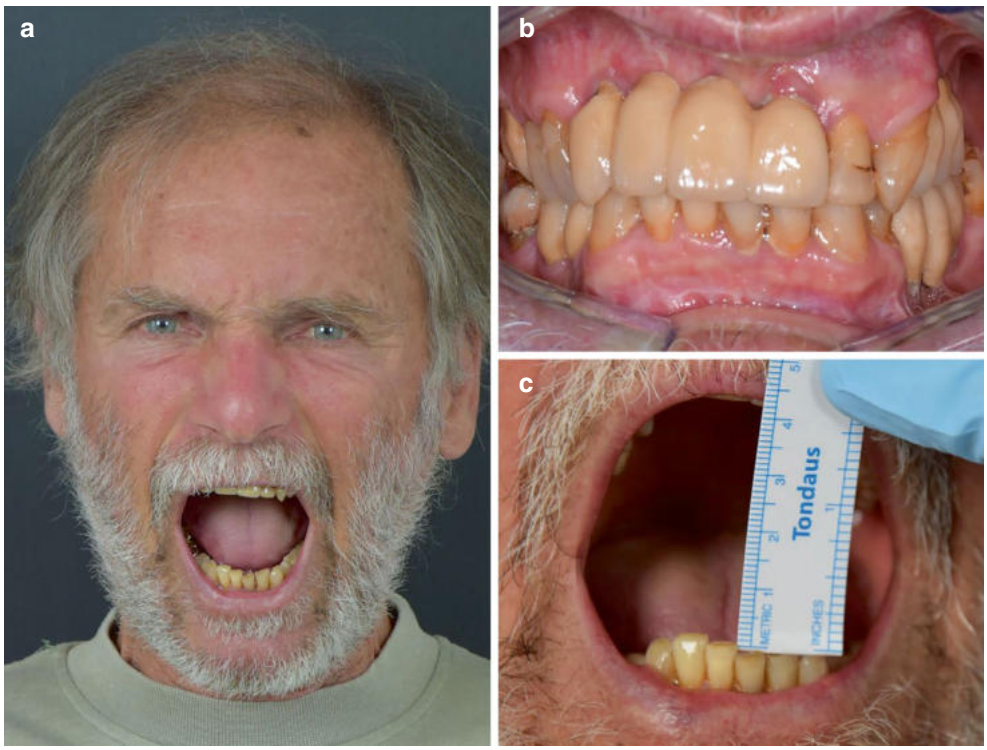


Fig. 43 Clinical outcome with (C) MMO improvement

TMDs and dentofacial deformities often occur together, with the TMDs either contributing to the jaw deformity, developing as a result of it, or both conditions arising independently. End-stage TMJ disease can negatively affect jaw position and occlusion, as seen in conditions like idiopathic condylar resorption, which leads to reduced posterior facial height, mandibular retrusion, and open bite. These patients may benefit from surgical interventions, including TJR and orthognathic surgery. A custom-made alloplastic prosthetic device offers stability, aesthetics, and improved jaw function, making TJR a preferred option. Alloplastic replacements eliminate the complications of graft harvesting and avoid the unpredictable undergrowth or overgrowth issues associated with costochondral grafts. These prostheses maintain stable mandibular position and occlusion.

Many patients benefit from mandibular advancement, particularly lengthening posterior facial height, achieved by counterclockwise rotation of the maxillomandibular complex. However, such movement can be a risk factor for TMJ issues and relapse after orthognathic surgery, especially with autogenous reconstructions. In contrast, combining prosthetic joint replacement with orthognathic surgery has proven to be highly stable since the prosthesis does not remodel or resorb. The durability of these prostheses is well-established, with reports of successful outcomes lasting over 20 years [17, 18].

For patients affected by TMDs and concurrent dentofacial deformities, both conditions can be corrected with simultaneous TMJ and orthognathic surgery in one stage or separately in two stages. Performing a single-stage procedure reduces treatment time and improves results but demands meticulous planning.

A protocol for managing custom TMJ alloplastic replacements along with simultaneous orthognathic surgery is essential, using intraoral scanning instead of stone models. This approach is renamed as "fully digital protocol," highlighting the virtual execution of each surgical step. The process begins with the acquisition of dental arches using an intraoral scanner, followed by a CT scan of the skull, using a splint with radiopaque markers for alignment (Fig. 44). After aligning the digital dental arches and CT scan, virtual surgery can be performed to simulate jaw movements, and, based on the final orthognathic plan, patient-specific devices such as plates and prostheses are designed. These components are sent to metal 3D printing.

5.3.1 Condylar Resorption Associated with Severe Retrognathia

Clinical History

This description refers to the patient presented in Fig. 44. A 32-year-old woman was referred to the Maxillofacial Surgery Department of our University due to persistent preauricular pain lasting over 5 years. She reported pain in both temporomandibular joints (TMJs), along with progressive difficulty in opening her mouth, described as a blocking sensation. Her maximum mouth opening (MMO) was measured at 24 mm. Palpation revealed tenderness in the preauricular and temporal regions bilaterally, as well as pain in the masticatory mus-

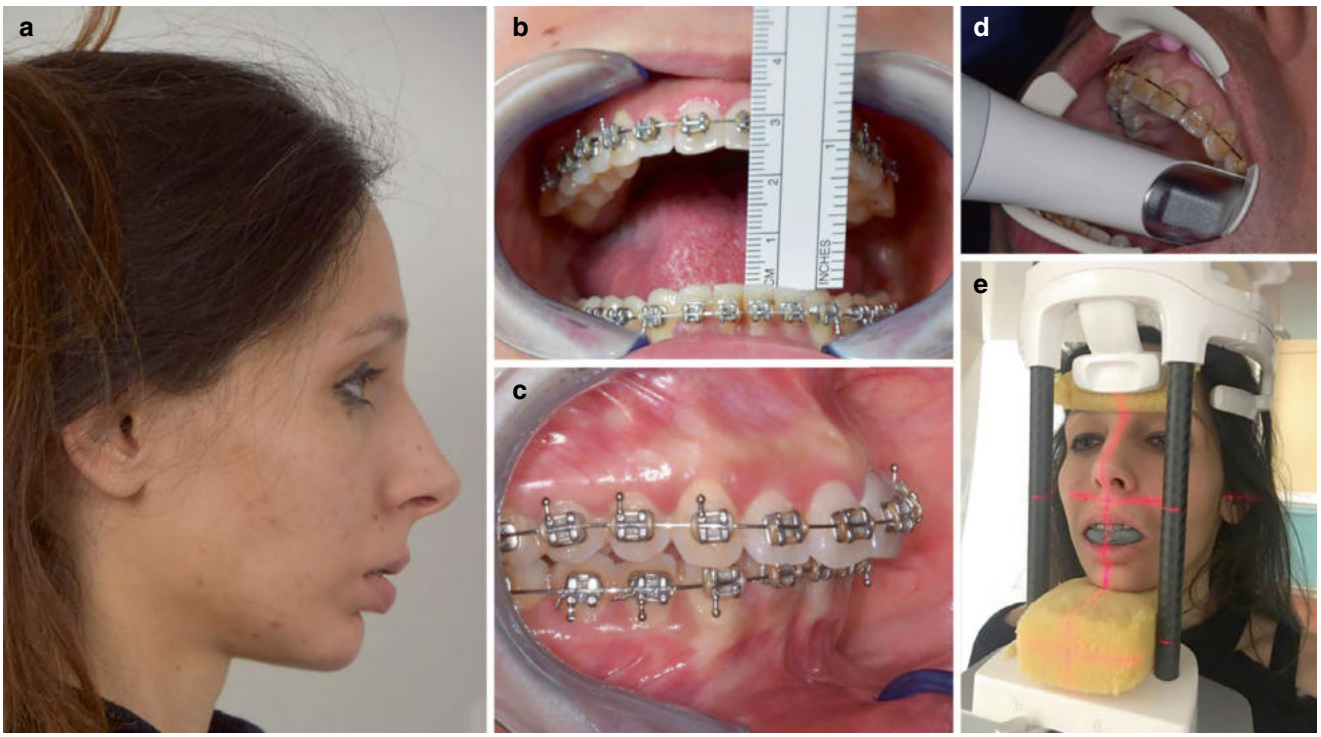


Fig. 44 Clinical appearance of severe condylar resorption with mandibular retrusion (**a**) which conditioned a significant limitation of mouth opening (**b**) and a severe class II malocclusion owing to the loss of posterior facial height (**c**). Intraoral scanning (**d**) and CBCT (**e**) integrate the study of the patient

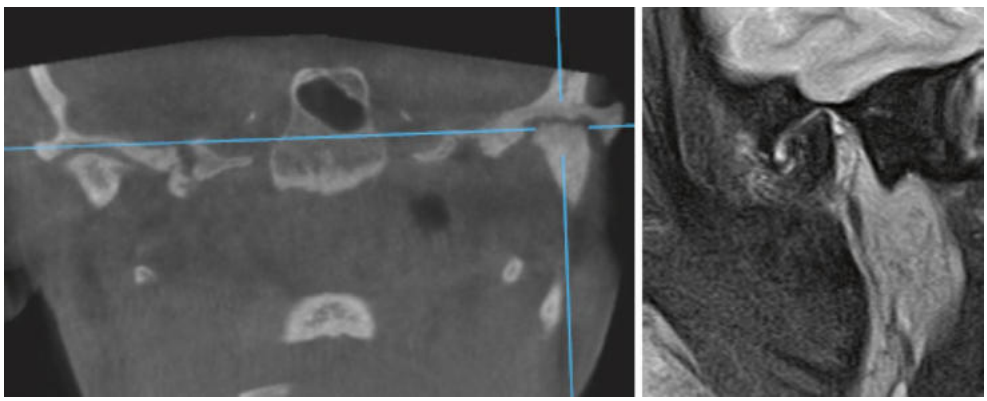


Fig. 45 Radiological appearance of the TMJ, severely destroyed

cles on both sides. The patient has class II malocclusion with severe mandibular retrusion, associated with an anterior open bite. Previous treatments, including arthrocentesis and bilateral arthroscopy, provided minimal or no relief. Imaging studies (CT and MRI) confirmed osteoarthritic degeneration of both TMJs (Fig. 45).

A comprehensive treatment plan involving a combination of orthodontic and surgical interventions, including orthognathic surgery and bilateral TMJ replacement, was devised.

Virtual Surgical Planning (VSP)

Virtual surgical planning was conducted in collaboration with the prosthesis manufacturer. The surgical team initiated the process by segmenting the bone, registering the occlusion, and planning the orthognathic and osteotomy procedures. Scanned dental arches were aligned with CT-derived dental cusps, and further adjustments were made to refine global alignment. The dental arch models were merged with CT-based models of the maxilla and mandible.

Osteotomy plans for TMJ replacement were developed, and the designs for the prosthetic fossa and ramus components, along with their positioning and cutting guides, were finalized to achieve optimal maxillo-mandibular alignment. Digital sculpting tools facilitated precise spatial positioning of the components. Surgical cutting guides were equipped

with holes for securing both the guides and titanium osteosynthesis plates. Additional procedures, including Le Fort I osteotomy and genioplasty, were planned to adapt the maxilla to the new mandibular position. Upon finalizing the plans, STL files for the surgical guides, splints, prosthetic components, and osteosynthesis plates were exported for production (Fig. 46).

Surgery

Through pre-auricular and retro-submandibular approaches, the TMJ, zygomatic arch, mandibular condylar head, and lateral mandibular ramus were exposed. Custom titanium cutting and positioning guides were securely placed, ensuring alignment and avoiding interference with the inferior alveolar nerve. Guided by surgical templates, osteotomies, including the coronoid process, were performed using a piezoelectric handpiece.

The custom fossa prosthesis was positioned and fixed with pre-measured screws. Similarly, the mandibular ramus prosthesis was secured using the pre-drilled holes. The new condylar position within the fossa was verified, and the mandibular range of motion was assessed to ensure proper alignment and function. Le Fort I osteotomy and genioplasty were then executed as planned using the surgical guide (Fig. 47).

Postoperative photographs document the normalization of the profile, with restoration of the posterior facial height (Fig. 48).

5.4 Extended Temporo-Mandibular Joint Replacement (eTMJR)

Alloplastic temporomandibular joint (TMJ) replacement is a well-established procedure in maxillofacial surgery. However, managing large excisions in this area requires a more complex reconstruction beyond the standard TMJ prosthesis. The TMJ consists of the mandibular condyle, which articulates with the glenoid fossa, a small, thin socket in the temporal bone at the skull base. The glenoid fossa represents the boundary between the mandibular condyle and the middle cranial fossa, highlighting the lateral skull base's role in the TMJ. Due to the proximity of the condyle to the middle cranial fossa, the term "temporomandibular joint and skull base" (TMJ-SB) has been coined to define this region, a key and surgically challenging area [19]. The space medial to the glenoid fossa contains large vessels and nerves, and when approaching the lateral skull base, the dura must remain intact to avoid communication with the intracranial space, preventing potentially life-threatening infections. TMJ-SB can be affected by various conditions, such as articular ankylosis, neoplasms, congenital anomalies, trauma, and osteomyelitis, impacting both aesthetics and masticatory function.

When dealing with these pathologies, reconstruction strategies must prioritize functional restoration of the TMJ. However, standard TMJ prostheses may not be suitable for extensive defects that extend beyond the TMJ to the skull base, lateral skull, and mandible. Virtual surgical planning (VSP) for TMJ reconstruction (TMJR) has enabled the design and creation of custom-made extended TMJ prostheses (eTMJR), which can replace not only the articular components but also adjacent mandibular or temporal or zygomatic bone defects, including sections of the ramus and fossa.

Accurate VSP requires the use of multiple imaging techniques and specific acquisition protocols to isolate and identify each anatomical structure in the affected region. This is crucial for accurately mapping the lesion boundaries and its relationship with nearby structures. Medial to the glenoid fossa, structures like the internal maxillary artery, the foramen ovalis (through which the mandibular nerve V3 passes), and the foramen spinosum (containing the middle meningeal artery) are present. Posteromedially, the anterior foramen lacerum, carotid canal (containing the internal carotid artery), posterior foramen lacerum (providing passage for cranial nerves IX, X, XI and the internal jugular vein), and stylomastoid foramen (housing the stylomastoid artery and facial nerve) are located. For planning an eTMJR, a CT scan, MRI, and CTA are typically required, especially if a mixed autologous/alloplastic eTMJR is planned.

The eTMJR is a safe and reliable surgical approach for selected patients with large TMJ-SB lesions. A detailed preoperative protocol and workflow are essential for achieving a successful, complex reconstruction.

5.4.1 Glenoid Fossa Osteoblastoma with Middle Skull Base Involvement

Clinical History

A 49-year-old woman was referred to the Maxillofacial Surgery Department at our University for assessment of worsening jaw pain persisting for over 3 years. She reported escalating preauricular pain near the left temporomandibular joint (TMJ), along with a progressive reduction in her ability to open her mouth. Upon examination, her MMO measured 29 mm, with a slight deviation of the chin to the left. Palpation revealed tenderness in the preauricular and temporal regions on both sides, as well as bilateral pain in the masticatory muscles. Mild swelling was observed in the left TMJ area, accompanied by articular crepitus.

CT and MRI scans revealed osteoarthritic degeneration of the left TMJ. Additionally, CT scan identified an area of altered bone density in the left temporal articular tubercle. A contrast-enhanced CT was performed for further evaluation, showing a primarily lytic lesion on the medial portion of the temporal articular eminence, with a rim of reactive sclerosis and internal matrix mineralization. Sclerotic changes were

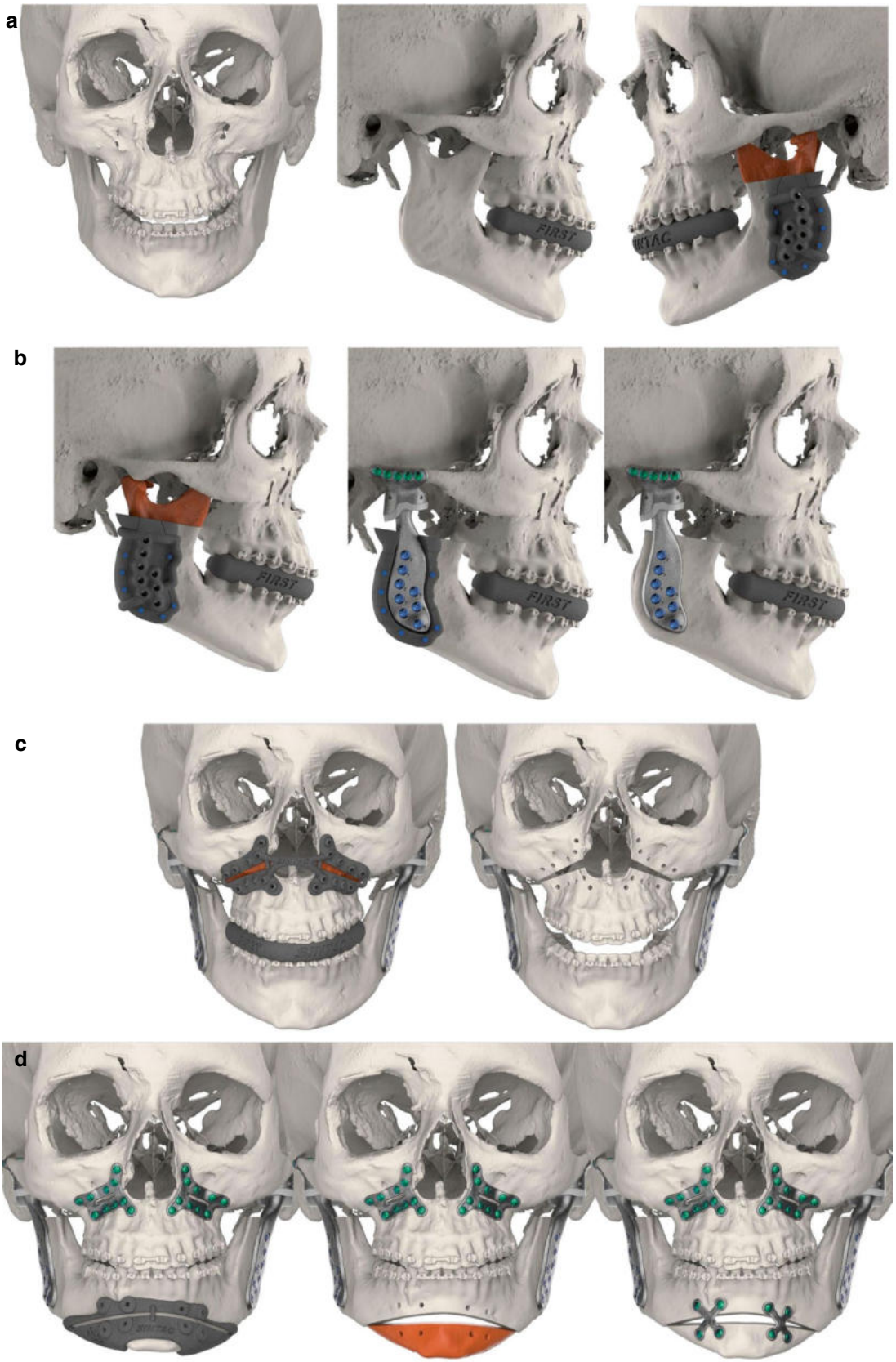


Fig. 46 VSP sequences agreed with the manufacturer (GPI S.p.a.) performed on orthognathic VSP performed by surgeons. Notably, bilateral TMJ replacement avoids the need of BSSO as the mandible is brought forward by the prosthetic ramus

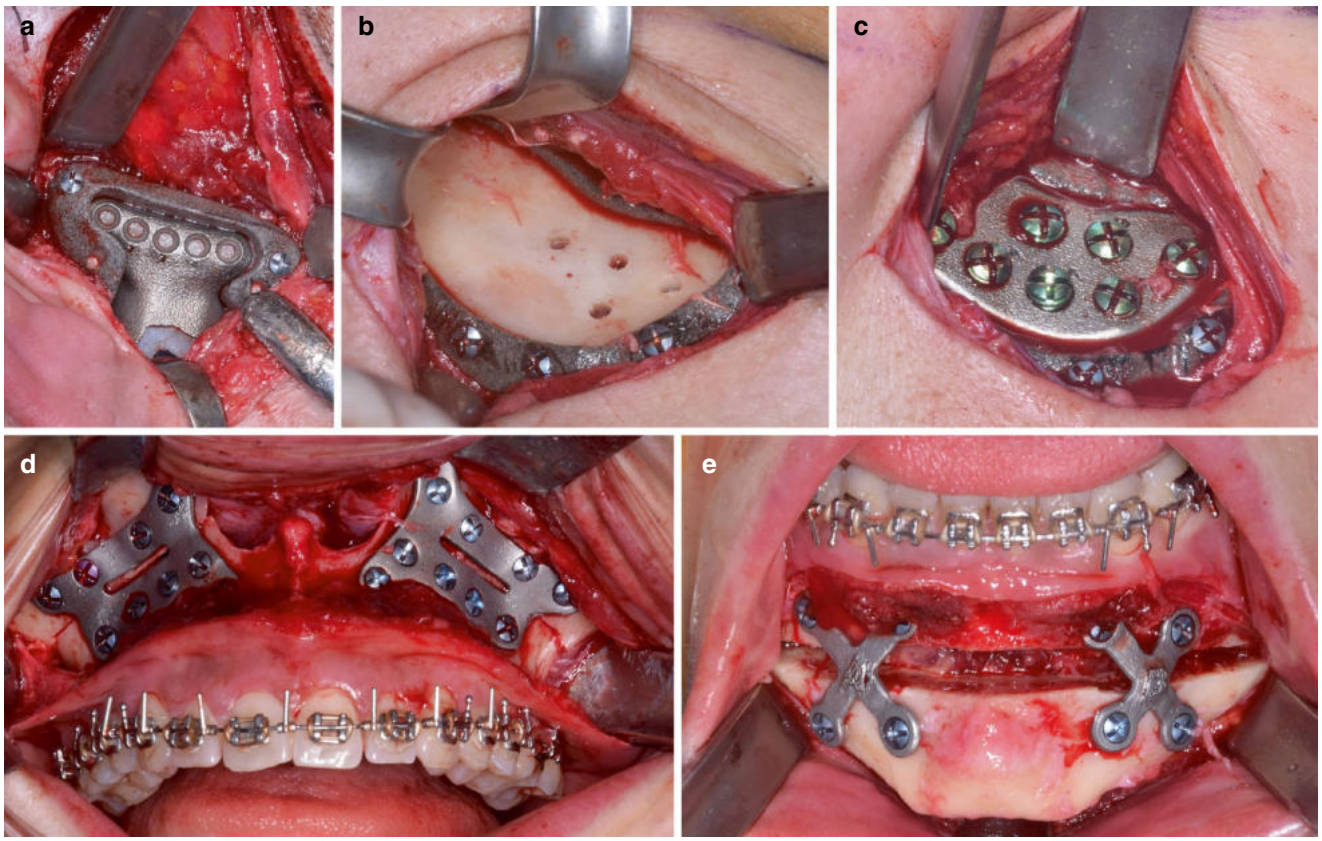


Fig. 47 Intraoperative stages using the hybrid cutting-positioning guide and customized plates

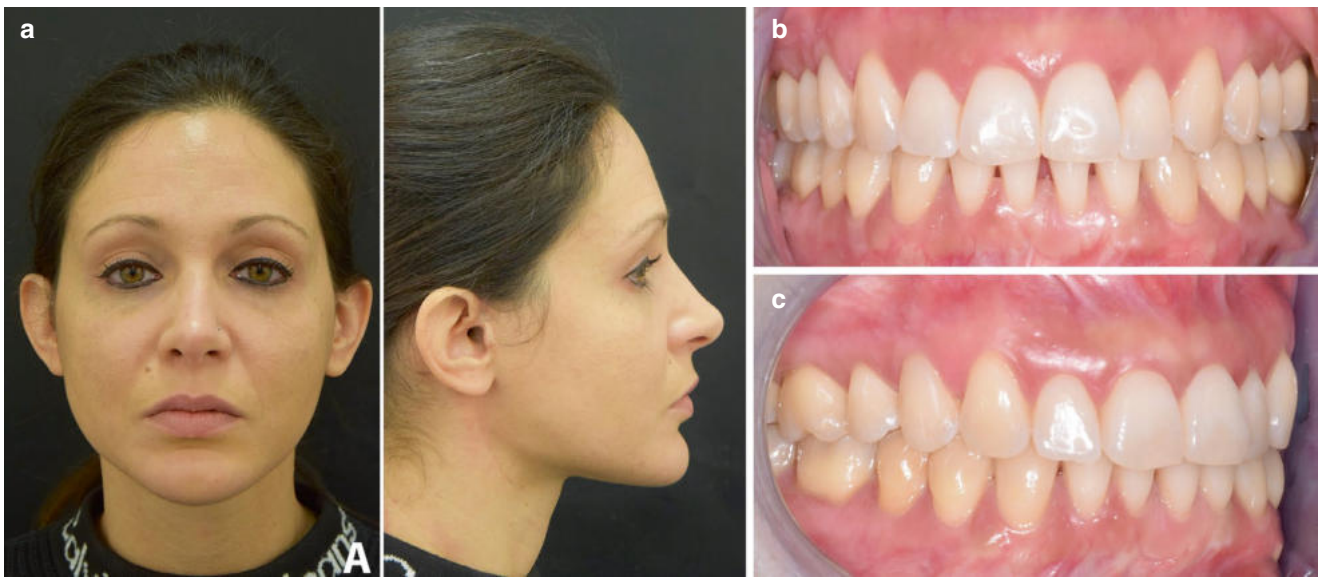


Fig. 48 Clinical appearance at 5-year follow-up

also noted in the surrounding bones, including the skull base and mandibular condyle. The radiologist suggested the lesion likely had a dystrophic or dysplastic origin. An open TMJ biopsy was planned. Under general anesthesia, a preauricular deep subfascial approach was used to access and resect the lesion. Histopathological analysis confirmed the diagnosis of osteoblastoma. The patient completed a three-year follow-up without signs of clinical or radiological recurrence. However, nearly 6 years after surgery, she returned with recurrent symptoms identical to those initially reported. A subsequent CT scan confirmed an Osteoblastoma relapse, necessitating eTMJR surgery.

VSP

First, meticulous anatomical reconstruction was performed, resulting in the creation of a reliable disease model with MR coregistration to achieve the accurate reconstruction of skull base vasculature (Fig. 49). Next, arch models were then merged with CT-based maxilla and mandible models.

Osteotomy plans were developed, and the prosthetic fossa and ramus components, along with their positioning and cutting guides, were designed to achieve the desired alignment of the maxillo-mandibular skeleton using a combined anatomical CAD modeling and soft organic sculpting tools. Surgical cutting guides were created with holes for securing both the guide and osteosynthesis titanium plates. STL files for surgical guides and prosthesis components were exported for production.

Surgery

The TMJ, zygomatic arch, mandibular condylar head, and lateral mandibular ramus were exposed via pre-auricular and retro-submandibular approaches. Custom titanium cutting and positioning guides were placed and secured, ensuring proper fit and avoiding the inferior alveolar nerve path as planned. Osteotomies were performed with a piezoelectric handpiece, guided by the surgical templates The lesion was accessed and excised under neurosurgical supervision with

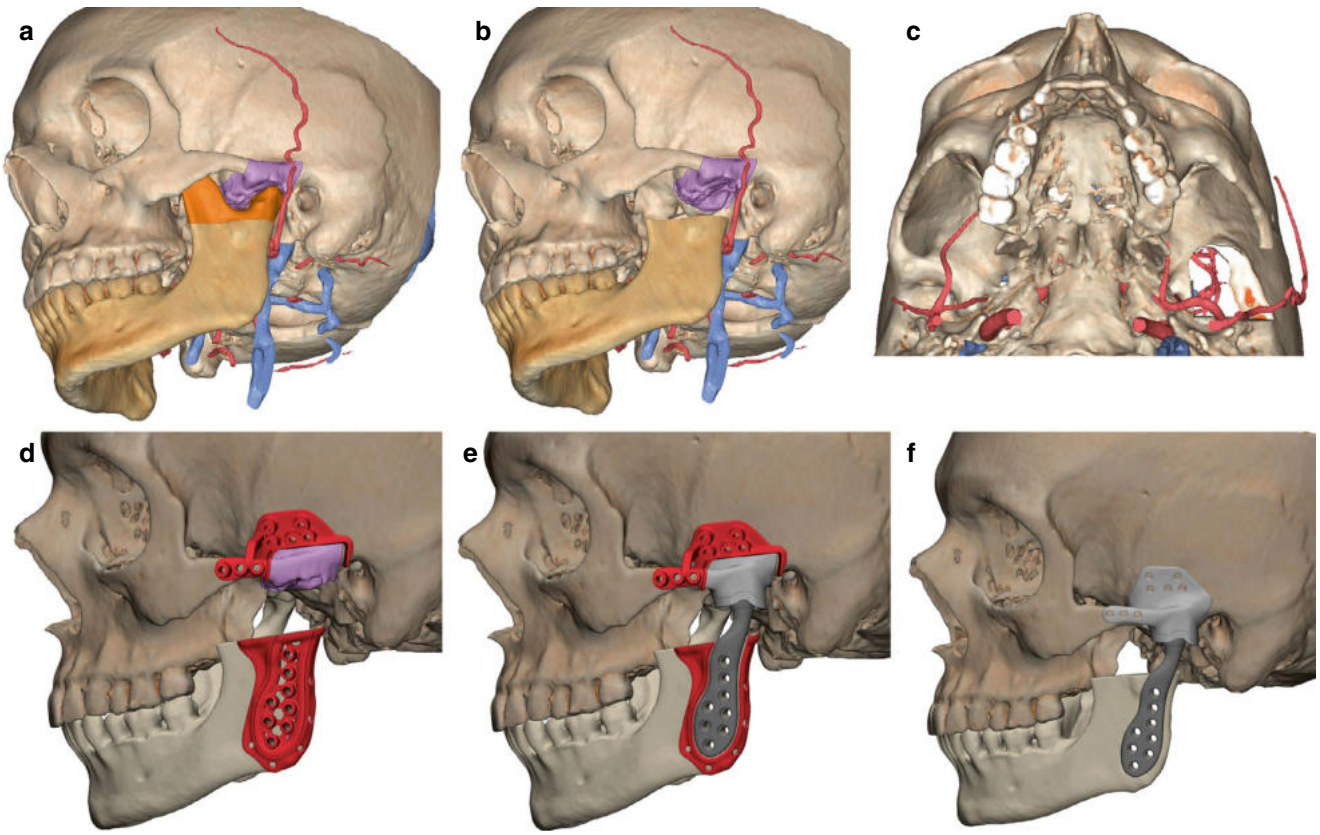


Fig. 49 VSP stages for osteoblastoma excision: (**a**) coronoidectomy is planned to widen spaces for the eTJR; (**b**) deep skull base osteotomies conducted medially until the foramen spinosum; (**c**) overview of resection in relation with skull base foramina; (**d**) design of surgical guide for osteotomies and hole predrilling. Dual-component ramus is chosen; (**e**) ramus prosthesis is placed within its socket; (**f**) eTJR

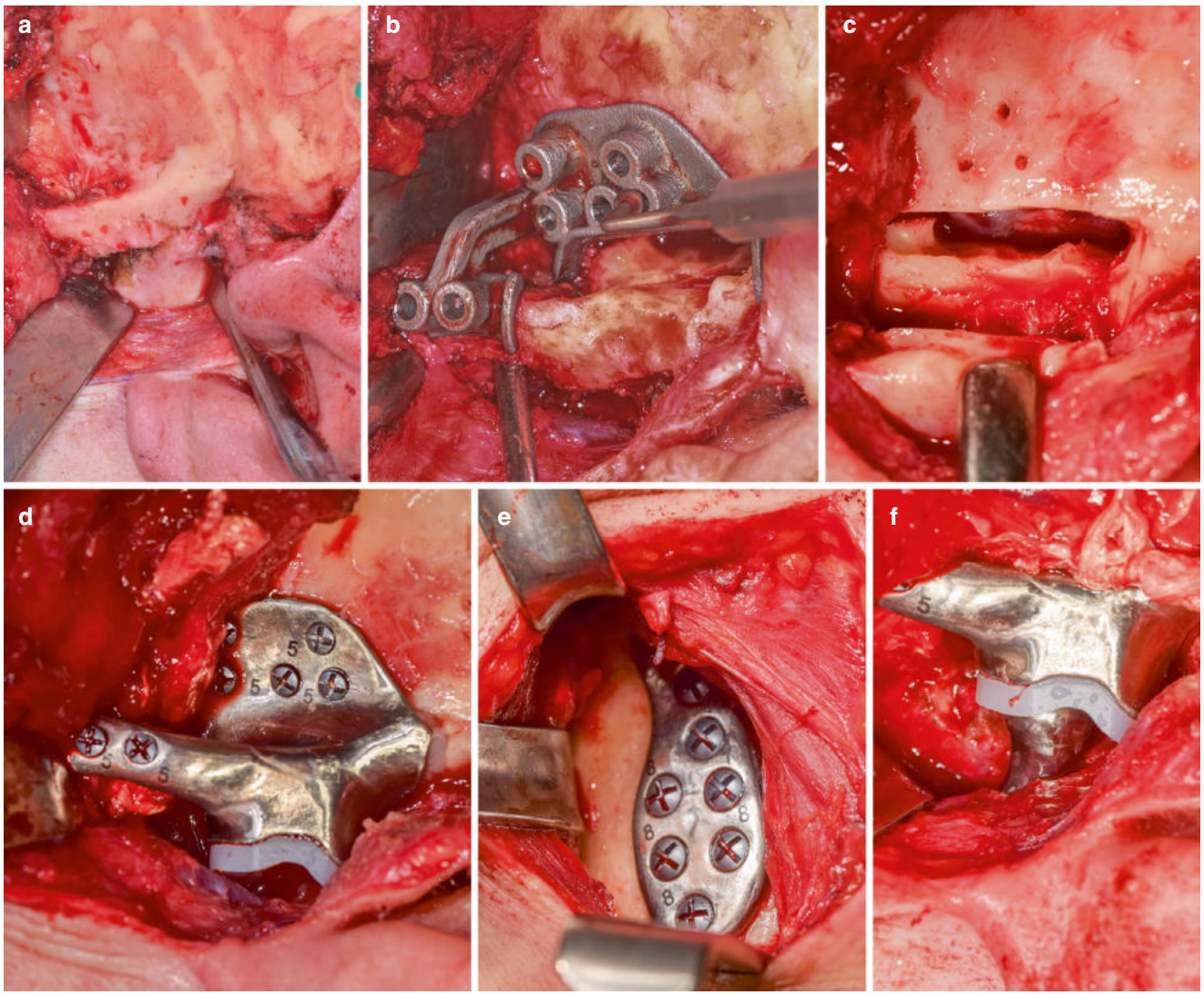


Fig. 50 Intraoperative sequences. (**a**) lesion exposure. First, a strategic condylectomy ("gap arthroplasty") to create space to the fossa; (**b**) skull base surgical guide positioned; (**c**) after temporal craniotomy is performed, the underlying temporal lobe is revealed; (**d**) fossa component; (**e**) ramus component; (**f**) articulating neojoint

the aid of navigation, as the middle cranial fossa dura was exposed. Temporal lobe dura was checked for tears and eventually reconstructed using a dural substitute. The custom fossa prosthesis was positioned and secured with screws of pre-determined lengths. Similarly, the mandibular ramus prosthesis was fixed using the same screw holes created during guide placement (Fig. 50). During the prosthesis placement, the new condyle's centric relation within the fossa was confirmed, and the mandibular range of motion was assessed to ensure proper function and alignment of the components. Postoperative CT scan showed the correct positioning of the prosthesis (Fig. 51).



Fig. 51 Postoperative CT shows optimal placement of the prosthesis

References

1. Kurup S, Crow H, Gonzalez Y, Schiffman ES, Truelove ET, Ohrbach R. A cross-sectional study of temporomandibular joint coronal plane disk position: imaging reliability and clinical utility. Oral Surg Oral Med Oral Pathol Oral Radiol. 2020;130:161–8.
2. Al-Saleh MAQ, Punithakumar K, Lagravere M, Boulanger P, Jaremko JL, Major PW. Three-dimensional assessment of temporomandibular joint using MRI-CBCT image registration. PLoS One. 2017;12:e0169555.
3. Yoon K, Kim J-Y, Kim S-J, Huh J-K, Kim J-W, Choi J. Multi-class segmentation of temporomandibular joint using ensemble deep learning. Sci Rep. 2024;14:18990.
4. Vinayahalingam S, Berends B, Baan F, Moin DA, Van Luijn R, Bergé S, Xi T. Deep learning for automated segmentation of the temporomandibular joint. J Dent. 2023;132:104475.
5. Li M, Punithakumar K, Major PW, Le LH, Nguyen K-CT, Pacheco-Pereira C, Kaipatur NR, Nebbe B, Jaremko JL, Almeida FT. Temporomandibular joint segmentation in MRI images using deep learning. J Dent. 2022;127:104345.
6. Ito S, Mine Y, Yoshimi Y, et al. Automated segmentation of articular disc of the temporomandibular joint on magnetic resonance images using deep learning. Sci Rep. 2022;12:221.
7. Zachariades N, Mezitis M, Mourouzis C, Papadakis D, Spanou A. Fractures of the mandibular condyle: a review of 466 cases. Literature review, reflections on treatment and proposals. J Craniofac Surg. 2006;34:421–32.
8. Gundlach KKH. Ankylosis of the temporomandibular joint. J Craniofac Surg. 2010;38:122–30.
9. McLeod NMH, Keenan M. Towards a consensus for classification of mandibular condyle fractures. J Craniofac Surg. 2021;49:251–5.
10. Sembronio S, Tel A, Costa F, Robiony M. An updated protocol for the treatment of condylar hyperplasia: computer-guided proportional condylectomy. J Oral Maxillofac Surg. 2019;77:1457–65.
11. Fariña R, Olate S, Raposo A, Araya I, Alister JP, Uribe F. High condylectomy versus proportional condylectomy: is secondary orthognathic surgery necessary? Int J Oral Maxillofac Surg. 2016;45:72–7.
12. Fariña R, Moreno E, Lolas J, Silva F, Martínez B. Three-dimensional skeletal changes after early proportional condylectomy for condylar hyperplasia. Int J Oral Maxillofac Surg. 2019;48:941–51.
13. Movahed R, Wolford LM. Protocol for concomitant temporomandibular joint custom-fitted total joint reconstruction and orthognathic surgery using computer-assisted surgical simulation. Oral Maxillofac Surg Clin North Am. 2015;27:37–45.
14. Lima FGGP, Rios LGC, Paranhos LR, Vieira WA, Zanetta-Barbosa D. Survival of temporomandibular total joint replacement: a systematic review and meta-analysis. J Oral Rehabil. 2024;51:775–84.
15. Ritto FG, Zuniga JR. Total temporomandibular mandibular joint alloplastic replacement as first line treatment for condylar fracture. Oral Maxillofac Surg Cases. 2023;9:100302.
16. Sembronio S, Tel A, Robiony M. The use of cutting/positioning devices for custom-fitted temporomandibular joint alloplastic reconstruction: current knowledge and development of a new system. Int J Oral Maxillofac Surg. 2021;50:530–7.
17. Sembronio S, Tel A, Robiony M. Protocol for fully digital and customized management of concomitant temporomandibular joint replacement and orthognathic surgery. Int J Oral Maxillofac Surg. 2021;50:212–9.
18. Wolford LM, Mercuri LG, Schneiderman ED, Movahed R, Allen W. Twenty-year follow-up study on a patient-fitted temporomandibular joint prosthesis: the Techmedica/TMJ concepts device. J Oral Maxillofac Surg. 2015;73:952–60.
19. Raccampo L, Sembronio S, Tel A, Robiony M. Extended complex temporomandibular joint reconstructions exploiting virtual surgical planning, navigation assistance, and custom-made prosthesis: a comprehensive protocol and workflow. JPM. 2023;13:931.

Virtual Planning and 3D Printing in Midfacial Trauma

Alessandro Tel and Massimo Robiony

1 Protocol for Reconstruction of the Virtual Trauma Patient

1.1 Segmentation

When approaching the cases of facial trauma, it is of utmost importance to reconstruct a reliable three-dimensional replica of the splanchnocranium, including all the fracture lines that are identified in the CT scan. For this purpose, CT scan should be performed trying to maximize the detailed acquisition of thin volumes, at the same time decreasing any partial volume effect that may alter the identification of even tiny fractures [1]. The authors suggest the following protocol:

- Acquisition matrix: 512 × 512 px, or even 756 × 756
- Slice thickness: 0.625 mm or at least 1 mm
- Reconstruction: bone window

DICOM data are imported within Mimics (Materialise NV, Leuven, BE) software and first a global thresholding algorithm is applied, using conventionally a threshold value of 226 HU. It is possible to apply a local segmentation by applying a ROI within the main mask in more critical areas that are subject to partial volume effect due to anatomical thinness, such as the orbital floor and the anterior maxillary wall, or less presence of compact cortical bone, for instance, the maxillary tuberosity and the mandibular condyle.

1.2 Creation of Individual Masks for Each Fractured Fragment

The most challenging task in virtual planning for trauma cases is the separation of the main mask in multiple submasks across fracture lines, each of them representing a different bone fragment. There are basically two strategies to accomplish this:

- Working on DICOMs: separation of the mask into submasks, as mentioned, using the split mask tool
- Working on STLs: reconstruction of the tessellated mesh, and use of geometrical modeling techniques to separate the main mesh into multiple subunits across the fracture lines

The first method leads to substantially higher reliability, as the polymesh often conceals fracture lines owing to inherent limitations of minimal triangle size in tessellation, as well as the fact that working in the 3D space makes some internal regions hardly accessible for the vertex separation tools. Conversely, since the split mask tool is specifically designed to separate skeletal entities into anatomically defined subunits using naturally existing boundaries, such as joints, sutures or fractures, its use is recommended as the separation is likely to occur across the fracture line, thus representing in the final submask the scalloped profile of corresponding fractured segments [2]. Therefore, it is possible to state that the separation of segmented anatomy into fractured fragments using the split mask technique leads to more anatomically correct results (Fig. 1). Once split submasks corresponding to each fractured fragments are achieved, they are converted into individual geometrical objects based on predefined tessellation settings. Further mild smoothing might be recommended to denoise 3D meshes, which tend to be multifragmented especially across fracture lines.

A. Tel (✉)
Lead Specialist for VSP and 3DP, Maxillofacial Surgery Clinic, Head & Neck and Neuroscience Department, Academic Hospital of Udine, Udine, Italy
e-mail: alessandro.tel@uniud.it

M. Robiony
Chief of Maxillofacial Surgery Clinic, Director of the Postgraduate School in Maxillofacial Surgery, Chief of Head & Neck and Neuroscience Department, Academic Hospital - University of Udine, Udine, Italy
e-mail: massimo.robiony@uniud.it

© The Author(s), under exclusive license to Springer Nature Switzerland AG 2025

A. Tel, M. Robiony (eds.), *Atlas of Virtual Surgical Planning and 3D Printing for Cranio-Maxillo-Facial Surgery*,
https://doi.org/10.1007/978-3-031-94495-6_19

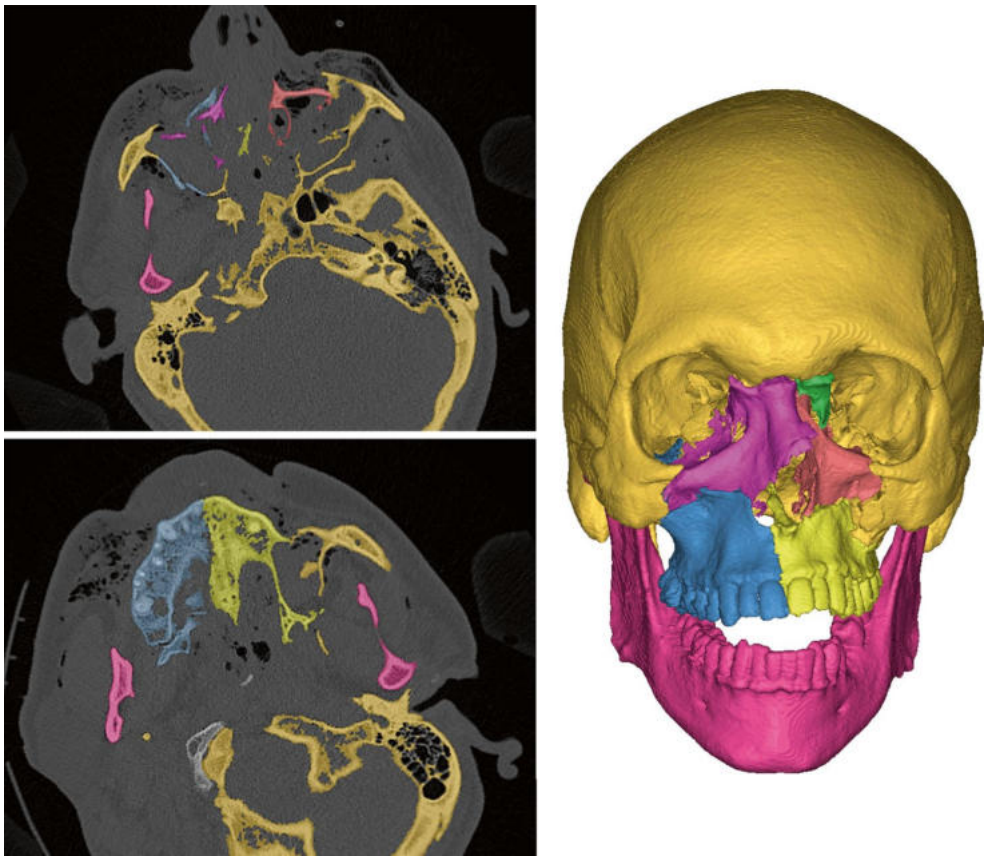


Fig. 1 Segmentation methods for complex midfacial fractures. The importance of split mask algorithm is emphasized

1.3 Techniques for Virtual Reduction of Fractures in the Craniofacial Region

Segmented anatomy, including fractures, is imported in the virtual surgical planning software to reposition displaced entities. Techniques for reduction can be divided into two main subgroups: semi-automated and manual. Semiautomated techniques employ several algorithms and might be divided into:

- *Mirroring registration*: This method starts by defining a symmetry plane within the splanchnocranium. It is intrinsically unreliable as there is always even slight asymmetry between the two halves of the craniofacial skeleton. It is advisable to place landmarks to define such symmetry plane into well recognizable anatomical landmarks, such as bony sutures, prominences, or depressions (examples include the midpoint of the frontozygomatic suture, the infraorbital foramen, the midpoint of major convexity of the zygomatic arch). Once the symmetry plane is defined, the mesh is cloned and mirrored, thus providing a reversed replica, with the normal side of the replica overlapping the fractured site of the original skull. The mirrored replica is used as a template to guide the automatic realignment of the fractured fragments within the anatomical boundaries of the normal side (Fig. 2). Intuitively, such method is exclusively limited to unilateral, sided, injuries, this being unapplicable in a variety of situations [3].
- Statistical shape modeling (SSM): It represents a much more innovative method, still under research. The interindividual variability of morphology in skulls is computed to generate a model that is the result of averaged features. The SSM model can be adapted to the individual case by modifying certain parameters to yield an instance of anatomy suitable to the case being studied. Once coefficients are set properly and the user is satisfied with the model, it can be exported and stored as STL file. The same SSM model can be used as a template for realignment, which will be logically approximate. Nevertheless, SSM can offer a reduction template also for non-sided (midline) or bilateral injuries [4, 5].
- Deep learning (DL): Constructed based on convolutional neural networks (CNN) and generative adversarial networks (GAN) [6], it uses computer learning to define the best suitable alignment of displaced fragments. Training dataset used to train the network play a crucial role, as they define the accuracy of the model. It is the most promising approach that is supposed to drive trauma reconstruction in the future of virtual surgical planning [7].

Both mirroring and SSM are imprecise methods that provide only a gross template for reduction. Therefore, due to

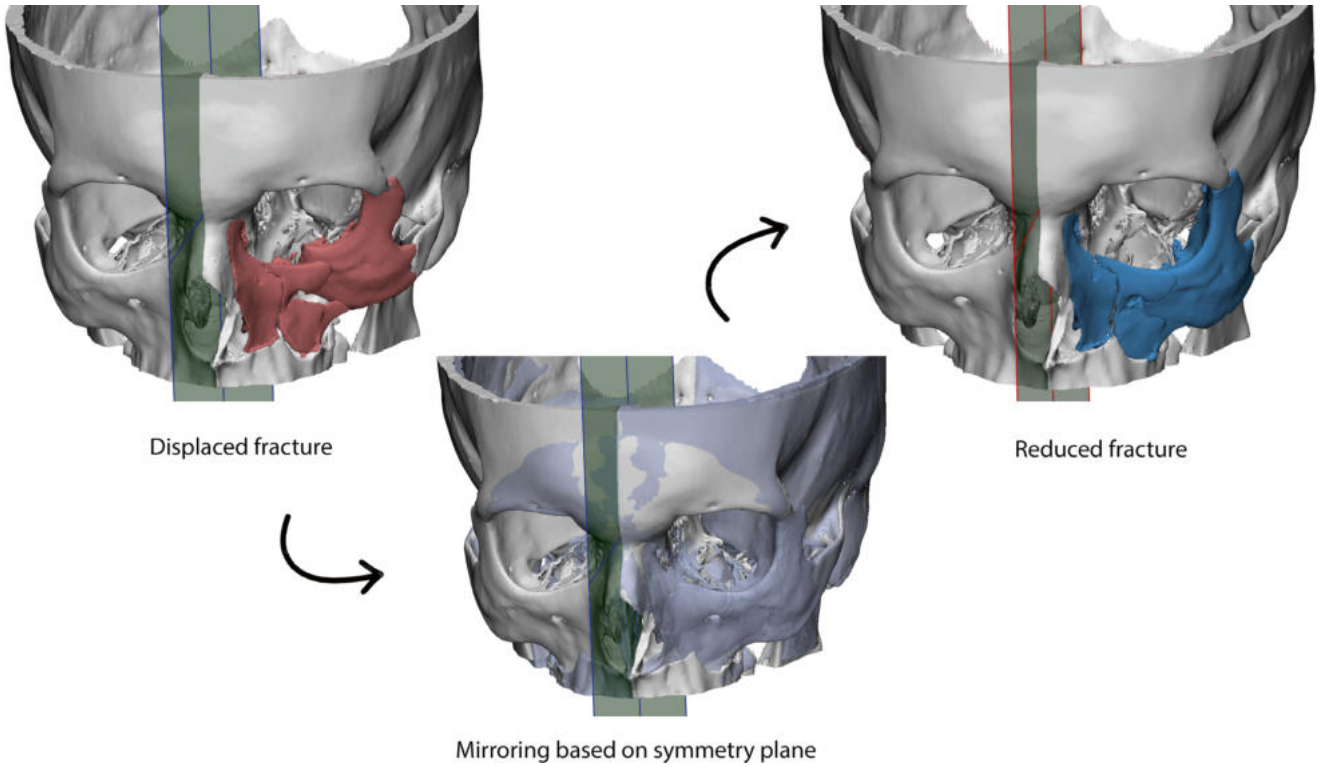


Fig. 2 Mirror-based reduction of sided ZMC injuries. As perfect symmetry is never present, minor manual adjustments are needed to achieve the optimal reduction along fractured buttresses. This is one of the core principles for reduction in occlusion-non-impairing trauma

the constitutional asymmetry of human body, any repositioned fragment using mirroring technique is supposed to further undergo manual fine-tuning to improve correspondence between fractured surfaces. This is called manual repositioning, as is the final stage of any virtual surgical planning in a trauma setting, where surgeon simulate reduction maneuvers on virtual models and prepare the model for the surgical operation.

1.4 Methods to Translate Surgical Planning in the OR for Computer-Guided Trauma Surgery

There are multiple possibilities that enable to translate surgical planning within the real patient, and they can be defined into three subtypes: techniques for anatomical reduction; techniques for occlusion restoration; and techniques for image-guided surgery. Such techniques should be used in combination, depending on the complexity of the individual case, to minimize surgical efforts, decrease surgical time and improve the accuracy of the procedure.

- *Techniques for anatomical reduction*: This method mostly involves 3D printing to create a physical replica of the virtually reduced skeleton. Not only doesit show the correctly reduced configuration to the surgeon, but it also notably provides a template to prebend osteosynthesis devices for surgery, including linear and curved plates and titanium meshes. In particular cases, but still limited to scattered reports in the literature, and strongly dependent on the expertise and resources of the center, also surgical guides to enhance reduction can be produced. Such reduction guides usually require a PoC 3D lab, as outsourcing their production to an external company is generally not suitable in an urgency setting. In addition, surgical guides may allow to predrilling holes for prebent plates according to the simulation of reduced craniofacial skeleton [8]. Due to complex anatomical surfaces of the midface and restricted accesses used (intraoral, periorbital), reduction guides have a limited, highly selected utility in midfacial trauma, whereas they are highly recommended in certain cases of mandibular multifragmented fractures (see Chapter "Virtual Planning and 3D Printing in Mandibular Fractures").
- *Techniques for occlusal restoration*: such methods often require to additionally acquire an intraoral scanning of dental arches. This can be particularly difficult in trauma cases due to pain, limited mouth opening, risk of further fragment displacement, and, especially for cases in ICU, presence of endotracheal tube in the mouth. However, when it is technically possible to acquire such impressions

in dentate patients, it is recommended to enhance the correct alignment of teeth and restoration of the correct intercuspation [9]. Intuitively, the perfect candidates for such approaches are young patients with intact teeth. There are two main solutions:

– Production of a dental splint based on the theoretical occlusion defined during the virtual surgical planning. Occlusion in VSP can be defined entirely virtually, but this method is not reliable as there are not enough sophisticated features in VSP software to simulate precontacts. As seen in orthognathic surgery chapter, some software enable for an automated surgical occlusion identification, but only when dental arches conditions are ideal, and not with interrupted arches or fractured teeth. Therefore, the best approach is still represented by 3D printing of separately aligned superior and inferior arches, which are then set into mutual intercuspation using tactile feeling by an experienced surgeon. When the most stable occlusion is found, it is further scanned and transferred to the virtual surgical planning. Surgical splints have the advantage to provide an excellent intraoperative guide that facilitates the realignment of maxillary and mandibular fragments into optimal functional relationships. Palatal fractures (maxillary sagittal fractures) are hidden to open reduction and functionally relevant; thus a contentive splint represents the optimal solution to correctly reposition bone segments (Fig. 3).
– Thermoplastic cage splints (TCS): first described by Tel and colleagues [10], they combine the workflow with splints and 3D printing with a thermoforming procedure applied on a thermoplastic foil. Alternatively, they are highly contentive cage splints printed with a minimal thickness and, occasionally, lateral connecting pins to drive the search for the optimal occlusion. The result is a highly contentive splint, which provides encasement not just to the occlusal face of teeth, bust to the whole crown and parts of the alveolar process (Fig. 4), thus providing a more accurate and faster alternative for occlusal stabilization during osteosynthesis compared to older and time-consuming methods, such as arch bars placement or manual intermaxillary ligation using IMF screws.

• *Techniques for image-guided surgery*: While the aforementioned techniques offer a physical bond for reduction maneuvers, both for displaced skeletal segments and for teeth and alveolar processes, image-guided surgery provides an interactive, real-time visual guidance without using any 3D-printed constraints. There are currently two main methods: intraoperative navigation and augmented reality.

– Intraoperative navigation takes advantage of the virtual planning and represents the visual bridge to connect surgical simulation performed in a computerized environment and the real patients. STL of reduced fragments are exported from the VSP project and imported into the navigation software, where they are used as digital reduction templates that allow to visualize the already reduced position of displaced fragments overlapped to CT scan. The surgeon can thus benefit from immediate feedback on the correct reduction maneuvers that are intraoperatively performed, including restoration of symmetry and assessment of the correct position of implants (Fig. 5). According to a robust body of literature concerning intraoperative navigation, such technology has an error margin of generally 1 mm [11, 12].

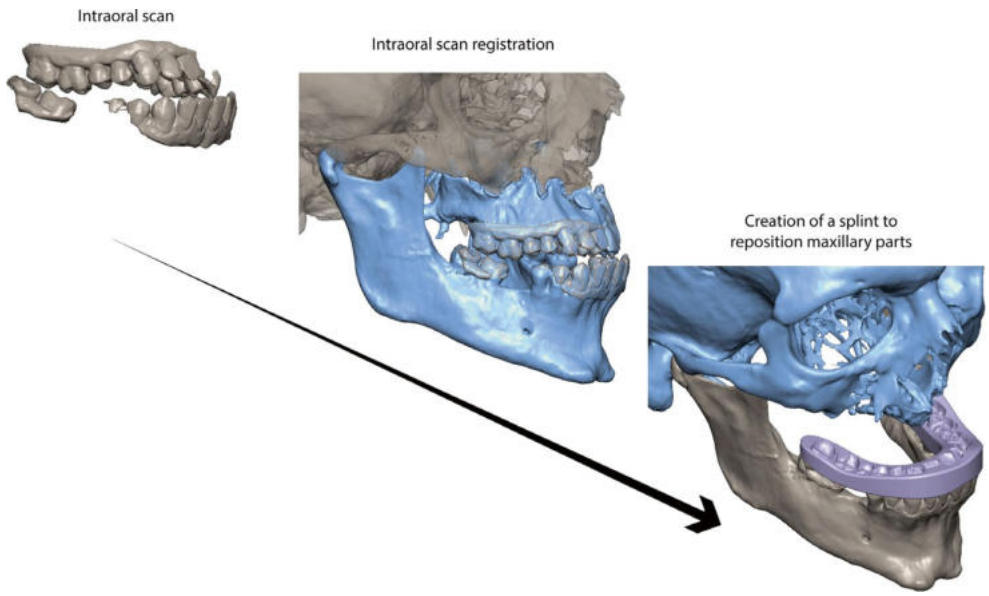


Fig. 3 Occlusion-driven repositioning of maxillary fractures. Fractured segments are merged with intraoral scans, then printed and assessed in the most stable intercuspation. The planned occlusion is used as reference to register dentate segments in the optimal configuration. A splint is then manufactured to reposition maxillary segments based on the occlusal relationship with the antagonist

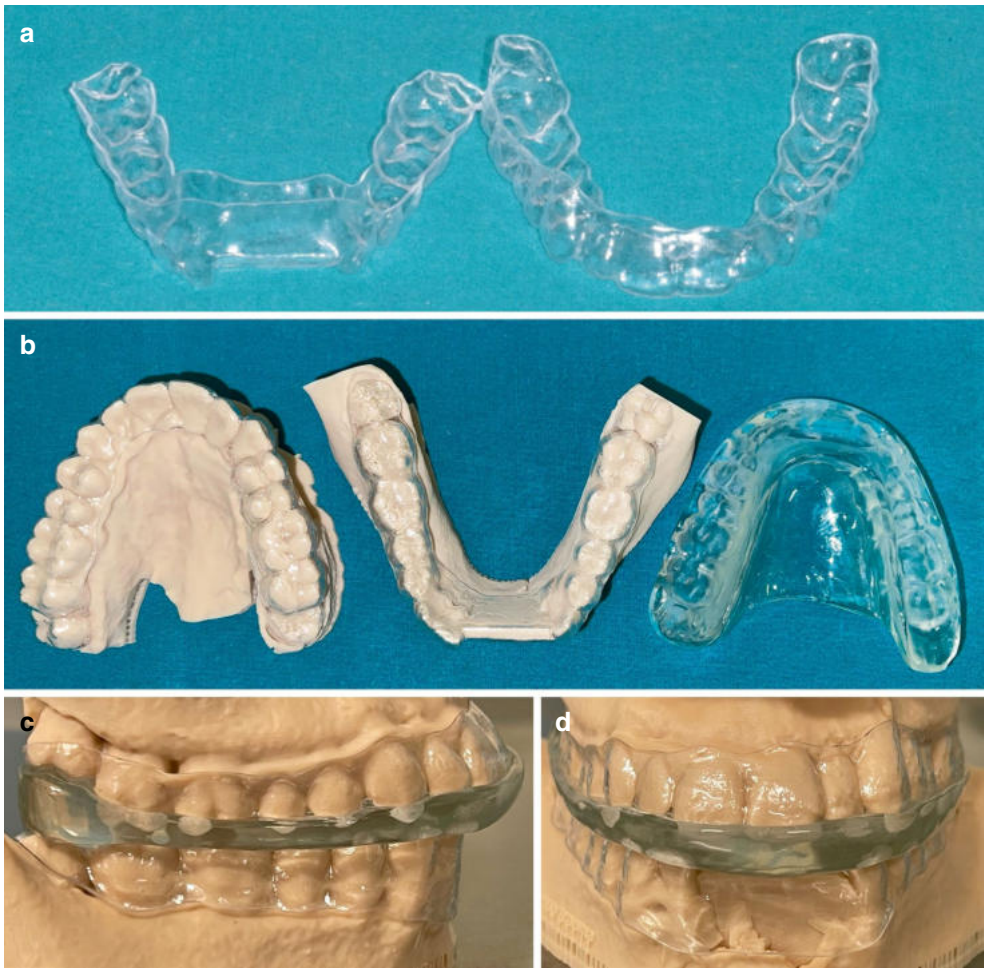


Fig. 4 TCS (occlusal aligners) for intra-arch reduction and occlusal splint (TCS-compatible) for inter-arch relationship

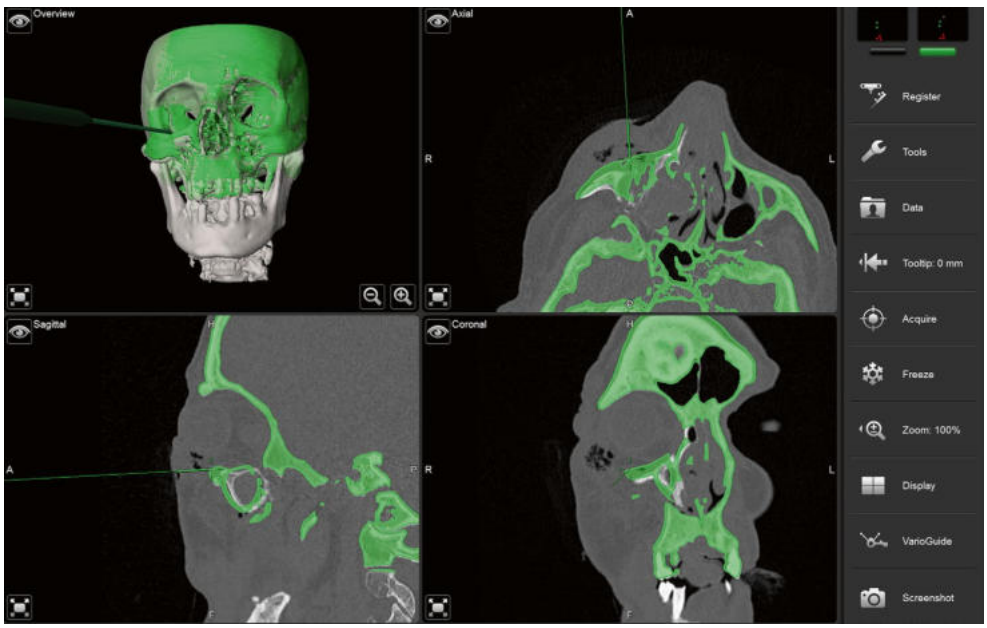


Fig. 5 VSP navigation to assess symmetry in ZMC fractures

– Augmented reality (AR) is still an experimental technology, as the crucial step is to achieve a clinically reliable registration between the virtual image of the patient superimposed to the real space, and the patient itself. Compared to navigation, it provides several advantages: first of all, it enables to translate the virtual image of the patient directly within the sight field of the surgeon; secondly, it is responsive to hand gestures without using a selective pointer; and thirdly, it avoids a cumbersome machine within the operating room. Advancements in deep learning will also improve the possibility for AR to achieve a successful, reliable, and auto-adjusting calibration [13].

1.5 Virtual Planning Workflow to Prepare 3D Printable Models of Trauma

Exported STLs of trauma cases are separate objects that are differently moved within the three-dimensional space to simulate the anatomical reduction of the fracture. Thus, they do not share any connection with each other, and printing them within a single plan would be detrimental, often resulting in print failure. Thus, it is important that one single geometry is created, based on the shape of anatomical reduction. The wrap command is highly specific and useful to this case: once separate fragments are merged hierarchically within a single entity, but still with disconnected margins, the wrap operation creates a single geometry that is exactly "wrapped" around the preexisting entity, allowing to create a topologically continuous mesh that bears the highly accurate impression of the underlying parts. It is important that the offset parameter consider three interdependent parameters:

- Gap closing distance: it measures the wrapping effect, intended as bridging effect, across gaps in the mesh. Higher values relate to larger defect area coverage (useful in case of mesh hollowing) but decrease anatomical details.
- Smallest detail, which represents the minimal geometrical detail captured when the model is wrapped.
- Resulting offset, which refers to the resulting distance of the wrapped geometry from the target entities. It should be as low as possible.

Wrapped geometries can be easily exported, remeshed, and comfortably handled to print a reducted, previously fractured, craniofacial skeleton (Fig. 6).

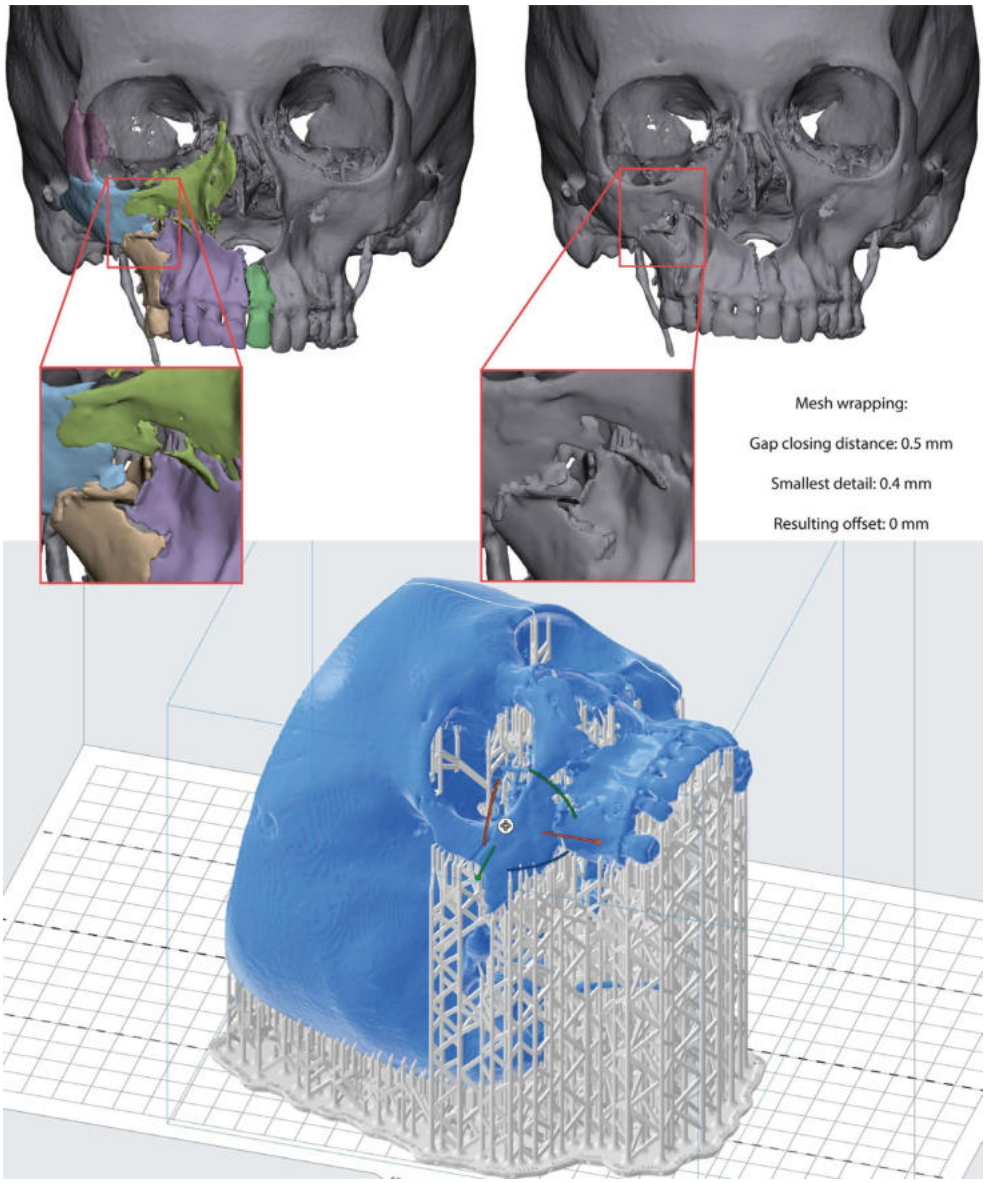


Fig. 6 Preparation of a unified trauma mesh for 3D printing. This mesh skin achieved through wrapping enables to close gaps between separate fragments

2 Practical Classification of Midfacial Trauma for VSP Purposes

It is convenient to define two major categories of midfacial trauma for which VSP is needed, as both the virtual planning workflow and the surgical sequence might vary accordingly. The main discriminator is whether the occlusion is altered or not.

- *Occlusion-impairing trauma*: this class refers to the fact that occlusion has been altered by a fracture line with displacement involving the maxillary alveolar process. Any mandibular fracture with displacement is by definition occlusion-impairing, yet mandibular fractures, owing to their peculiarities, deserve a separate dissertation and will be treated in Chap. 22. In occlusion-impairing trauma, reestablishing the correct intercuspation between teeth is the priority, and anatomical reduction must be conducted accordingly. During surgery, devices such as occlusal splints and TCS are highly recommended.
- *Occlusion-non-impairing trauma*: in this class are included ZMC fractures, orbital fractures, naso-orbito-ethmoidal fractures which do not involve the maxillary alveolar process. Anatomical reduction conducted through the aforementioned digital techniques plays the key role. Important aids during surgery are intraoperative navigation, reduction guides, plate prebending and augmented reality.

3 Occlusion-Impairing Trauma

This class includes all mandibular fractures (which are discussed in a separate chapter), as well as Le Fort I, II and III fractures, palatal fractures, and dento-alveolar fractures. Isolated Le Fort III fractures are rare, and this fracture is most often associated with other injuries with a more complex mechanism, often in panfacial trauma.

The main concept that appropriate virtual surgical planning should address is reestablishing a reliable and stable occlusion, which in several cases is difficult to achieve owing to a multitude of factors, such as the absence of any reference of preoperative occlusion (including a pre-existing, non-diagnosed malocclusion); loss or damage of several teeth, and complex multipiece fractures with misalignment on multiple vectors.

First, in such patients, dental impressions must be taken. Although alginate-based impression is the traditional and fastest method, it is not advisable in trauma for the following reasons: instability of teeth, presence of blood and debris, and presence of the oro-endotracheal tube for patients in ICU. Therefore, intraoral scanning, due to the less cumbersome optical head, is recommended. Intuitively, in patients with complex multipiece maxillary fractures, the resulting digital impressions will be misaligned. Thus, when imported into the software, each dental group must be separated across the fracture line to become an individual entity (a dental group). Each dental group must then be realigned with its bone counterpart, to have each fractured fragment matching its respective dental group. Then, dental groups are merged with fractured segments, as shown in Fig. 3. Fractured segments with improved dental detail after merging must be then individually printed, and the surgeon must determine which combination of parts yields the optimal occlusal stability (Fig. 7).

* Noteworthily, this workflow is still mixed digital + analogic and not 100% digital, but currently the manual sensation of occlusal stability is still the most reliable. In the future, algorithms will enable a fully digital arrangement of the most stable occlusion using a precontact motion analysis, but currently, as mentioned previously, automated virtual occlusion only works in ideal conditions, namely for the presurgical preparation of patients undergoing orthognathic surgery.

Concerning devices for computer-guided surgery, virtual occlusion can be satisfactorily transferred during surgery using traditional occlusal splints. However, splints can also be combined with ultrathin TCS, which, in addition to providing the interarch alignment to determine occlusion, also provide intra-arch alignment and contention of fragments, as seen in Fig. 4. Compared to traditional splints, they enable superior

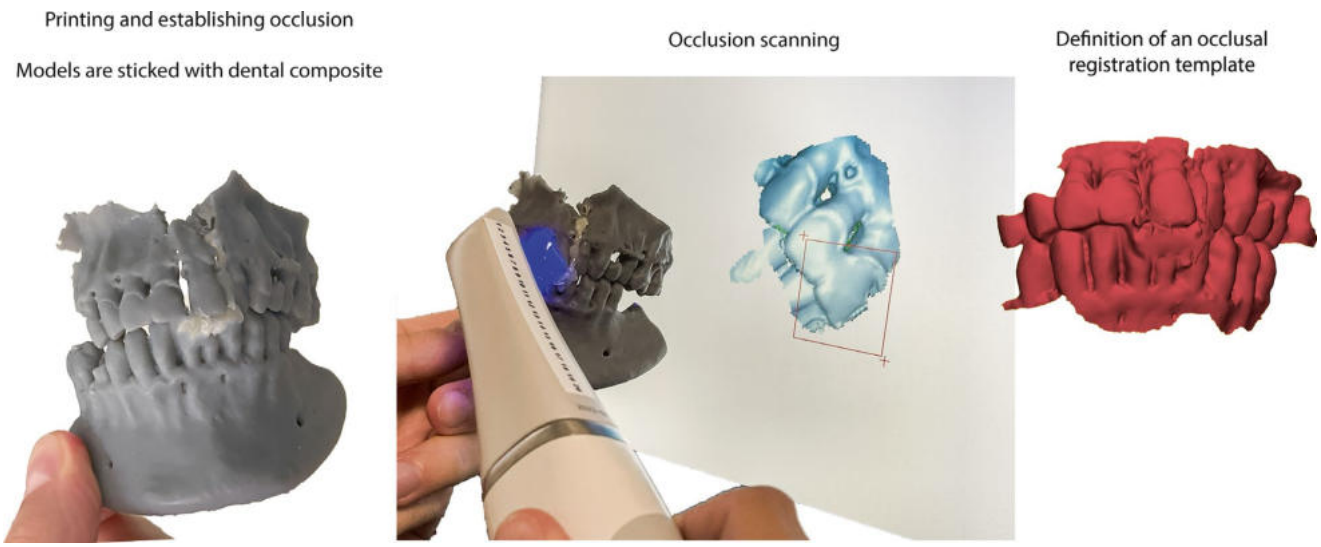


Fig. 7 Scanning workflow for occlusal planning in trauma: owing to the variability of dental arches, virtual occlusion is unreliable. Analogic occlusion is defined in the maximal stability, then a registration mask is rescanned and transferred to the VSP to align virtual trauma models

stabilization of alveolar process fragments, and allow simultaneous internal fixation, thus overcoming obsolete and painful methods such as wire fixation or arch bars plating.

3.1 Le Fort I with Sagittal Palatal Fracture: Previous Normal Occlusion

Clinical History

This patient was admitted to our department following a bicycle injury hitting his face to the ground. Clinical examination revealed a malocclusion with increased maxillary transversality, especially in the molar area, with slight maxillary impaction and open bite. CT was performed showing a Le Fort II fracture with a further palatal sagittal fracture and widening of the transverse maxillary diameter. As Le Fort II segments could not be mobilized intraoperatively, but the trauma conditioned a malocclusion, a Le Fort I osteotomy was deemed necessary to enable maxillary repositioning in a satisfactory occlusal relationship. The patient was operated on using traditional methods: IMF screws were placed symmetrically in the anterior and posterior sectors, and occlusion was determined manually on Le Fort I segments before applying the rigid intermaxillary blockage. Then, the fracture was fixed using two plates on each side and one midline, subspinal plate, which was ineffective to maintain transversality. Immediately after surgery, a malocclusion was assessed, with a persistence of posterior widening in the molar area. Postoperative CT scan confirmed the suspect of a relapse, with widening on the two maxillary halves across the palatal sagittal fracture. The case was then assigned to the digital specialist. In addition, an orthodontic appliance was positioned on each side of the Le Fort I to facilitate MMF on the splint, exactly as in orthognathic surgery.

Virtual Surgical Planning

Postoperative CT scan showing the persistence of fracture line in the hard palate was imported into Mimics and segmented. Three main objects were yielded through mask splitting: the two hemi-Le Fort I parts, divided centrally by the palatal sagittal fracture, and the mandible. Patient's occlusion was scanned on both the maxillary and the mandibular arch. STLs of scanned arches were imported into 3-matic and the maxillary arch was separated into two halves at the fracture site. Each dental group was aligned with its respective bone counterpart and merged. Models were printed and the most stabile occlusal configuration was assessed manually. Then, occlusion was made digital again by rescanning it and was imported into 3-matic. Both maxillary halves were realigned on the imported occlusion and perfect correspondence was assessed across the fracture line in the palate (Fig. 8). This crucial step demonstrates in detail how the restoration of a stable occlusion is related to the correct anatomical reduction of the fracture. Once the correct configuration of bones was determined, a contentive occlusal splint was generated to assist maxillary fracture reduction.

Surgery

A vestibular approach was performed to expose the fracture line and previously placed titanium plates, which were removed. Application of the contentive splint enabled to correct the occlusion as planned, at the same time providing a blind guidance to reduce palatal fracture through transverse diameter narrowing. The new fixation procedure was performed by plating the nasal and malar buttresses and the correct occlusion was checked (Fig. 9).

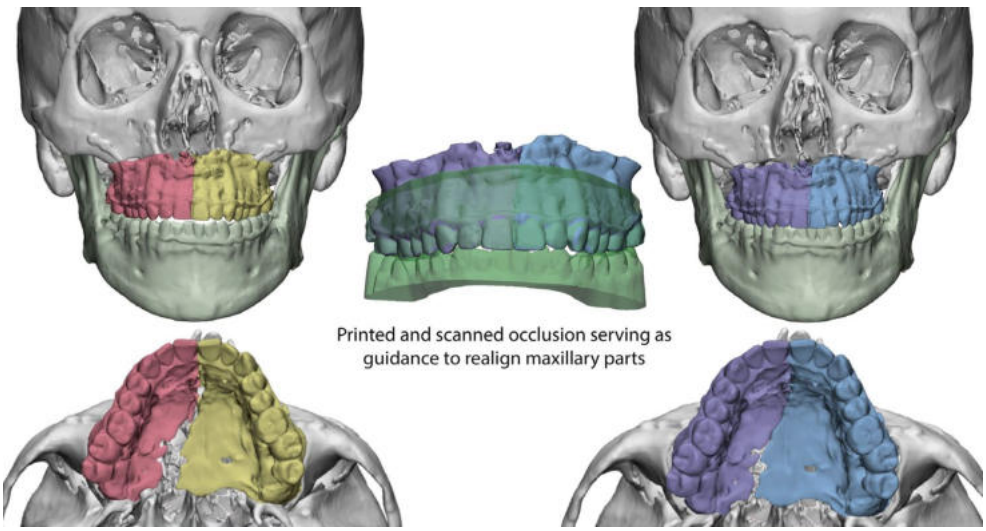


Fig. 8 Occlusion-based alignment of a maxillary fracture. Restoring the correct preoperative occlusion is associated with the anatomical reduction of fractures. This is particularly important in sagittal palatal fractures



Fig. 9 Persistence of anterior and lateral right open bite after Le Fort fracture fixation with traditional methods. This clearly shows how a conventional surgical approach is not effective in controlling the blind reduction of the sagittal palatal fracture (top panel). Middle panel: the new reduction is performed using a contentive splint designed on the virtual reduction of the sagittal palatal fracture. Bottom panel: Postoperative result, showing correction of open bite but the persistence of a slight transverse diameter reduction with left cross-bite. Oftentimes, occlusion in trauma is not optimal, unlike orthognathic surgery. Nevertheless, occlusion is overall acceptable and accounts for the efficacy of VSP

3.2 Le Fort I with Sagittal Palatal Fracture: Previous Class III Occlusion

Clinical History

In this case, a 53-year-old patient presented to our attention after falling to the ground and hitting his upper jaw against a stair step. The patient presented a malocclusion with widening of the transverse diameter and conspicuous modification of the Spee curve of the maxillary teeth. CT scan was performed showing a complex fracture pattern involving the upper jaw, with Le Fort I fracture, midline fracture extending in the osseous palate on both sides, and a nasal fracture underlying the Le Fort I and involving the piriform rim on both sides.

Virtual Surgical Planning

Accurate segmentation of the craniofacial skeleton was performed using a threshold value ideal for the best detection of the fracture line. Mask splint was applied to separate left and right components of the Le Fort I fracture. Intraoral scan was performed, and the upper maxillary impression was separated between central incisors to be realigned with the two dentate halves. The same process was repeated for the mandible, which was unaffected. 3D printing of hemi-Le Fort I segments and the mandibular arch enabled the surgeon to determine the most stable occlusion, which was rescanned to be imported back into the virtual project. Using surgical occlusion, dentoalveolar fragments were realigned and automatically repositioned in the correct arrangement. According to the achievable intercuspation, as well as previous dental reports of the patient, a class III occlusion was established to be the natural occlusion of the patient. On the final occlusal configuration in the VSP, a splint was created to guide repositioning of fragments. The

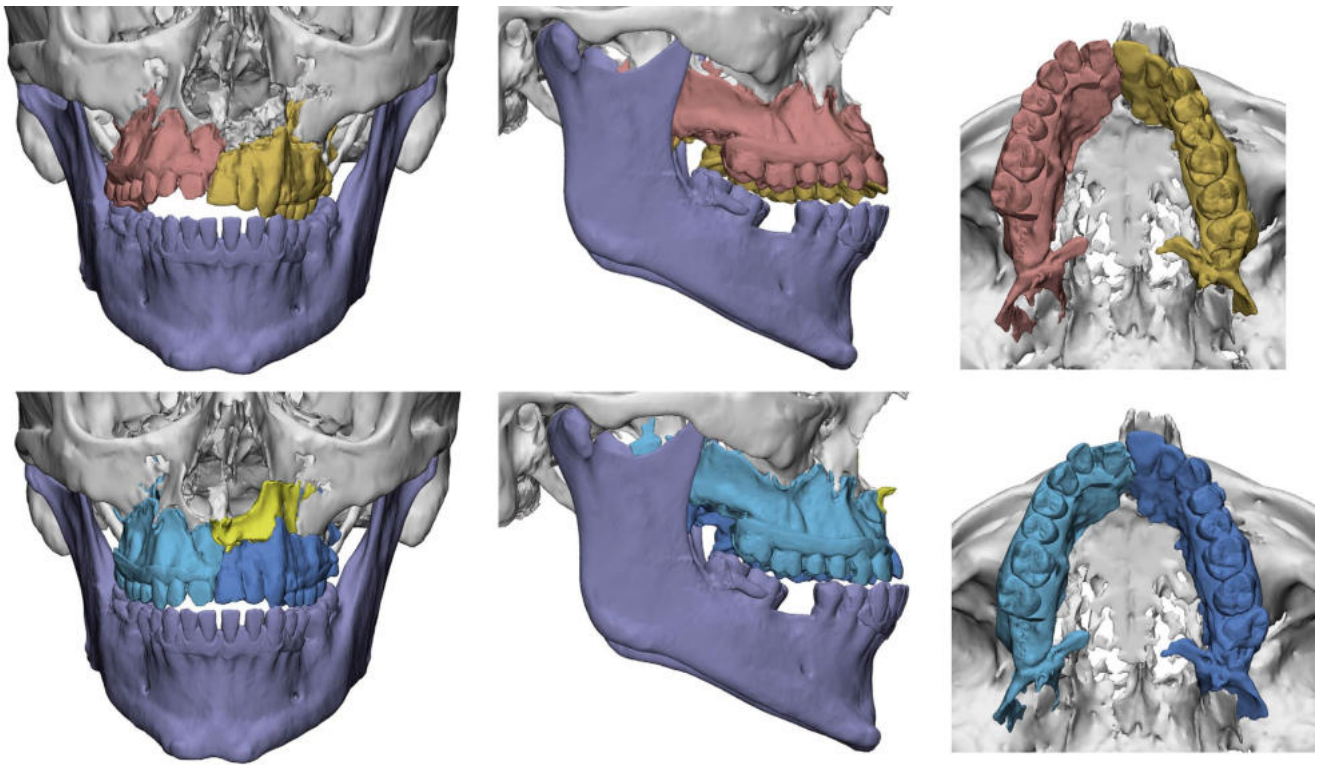


Fig. 10 VSP and reduction of multifragment Le Fort I with double palatal split. In this case, the patient had a previous, undiagnosed, class III malocclusion, which was discovered by careful virtual anatomical reduction. The patient refused a change in his preoperative occlusion by maxillary advancement

splint was designed slightly more contentively to embrace a higher portion of the dental crowns and enhance stability of dentate segments (Fig. 10).

Surgery

A maxillary vestibular incision was performed to expose the entire alveolar process of the maxilla and the fracture line, as well as the nasal buttresses up to the Le Fort I fracture line. The splint was applied, and a reduction of symmetrical hemi-Le Fort I segments was performed; then the patient was put into maxillo-mandibular fixation (MMF) on splint (Fig. 11). Anatomical reduction of paranasal fragments was accomplished, and internal rigid fixation was completed. MMF was then released to assess the correct occlusion.

* Both cases illustrate that sagittal fracture lines of the hard palate are not reachable using traditional surgical approaches (i.e., the vestibular approach); thus a reliable closed reduction is mandatory, using a contentive splint and eventually a palatal plate.

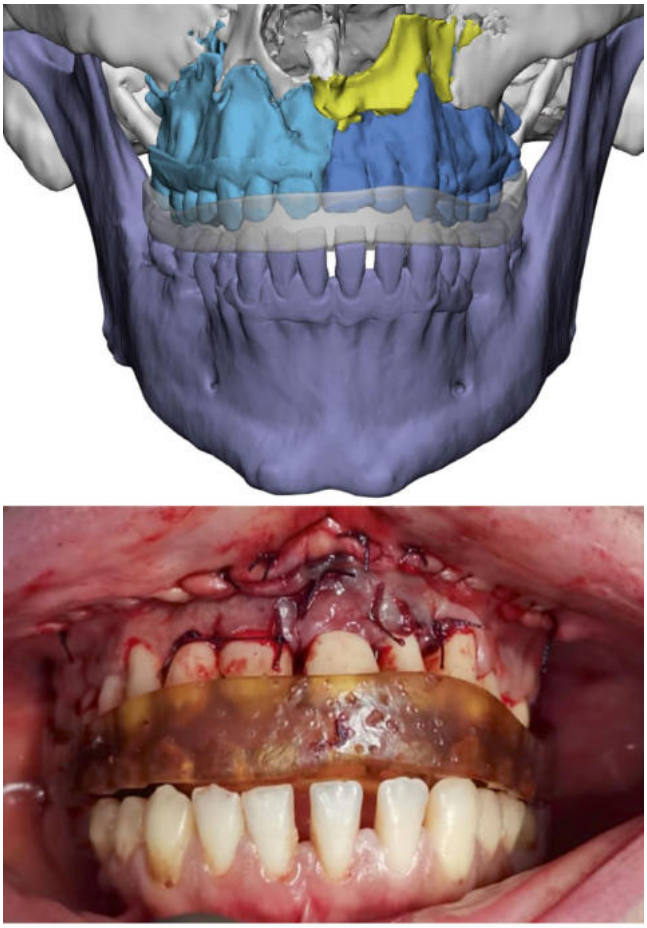


Fig. 11 Same patient as in Fig. 10. The splint enabled to perfectly engage the reduced hemi-Le Fort I segments, driving the fixation of the maxilla. The slight open mandible reveals the preexisting class III malocclusion of the patient

3.3 Le Fort I with Palatal Split in a Complex Craniofacial Trauma

Occlusion-impairing trauma in a major force impact might result in the association with different fractures, such as NOE complex (non-occlusion impairing), ZMC and orbit. However, in dentate patients, given the importance of function, mechanisms to reestablish the correct occlusion are prominent compared to anatomical reduction; thus, such traumas are treated in this section.

Clinical History

This patient was evaluated in ICU after suffering from a motorbike accident. The patient presented with a centrofacial injury with involvement of the left orbital floor, marked bilateral dislocation of the NOE complex with deviation of the nasal bones, and a Le Fort I fracture with palatal split and posterior widening, with an increase of the transversal diameter of the maxilla. ZMC complexes and the mandible were intact.

Virtual Surgical Planning

VSP in this case needed to solve both the issue of reestablishing the correct occlusion as well as the ideal anatomical repositioning of NOE fragments. Owing to the urgency setting and the presence of the oro-endotracheal tube, it was not possible to acquire intraoral scan. Thus, significant effort was made to efficiently clean up dental arch geometry reconstructed from CT scan by removing scattering artifact. Models of dental arches were 3D printed and then set manually into the most stable intercuspation. Subsequently, after restoring the correct occlusion, correspondence was verified across the maxillo-malar buttresses. Moreover, the reduction of the sagittal palatal fracture was verified once the surgical occlusion was set. Anatomical reduction of NOE fragments was carefully conducted, aiming to restore continuity on both the inferior orbital rim, pyriform rim, and fronto-nasal suture. Having three stable points, the anatomical reduction of NOE fragments was oriented through anatomical landmarks using N-points registration method and then improved manually (Fig. 12). In addition, scanned occlusion from 3D printed models served as base to design TCS both for the superior arch (exerting a contentive action to reduce the palatal split) and for the inferior arch (to drive the reduced maxilla into correct occlusal relationship). TCS were provided symmetric lateral wings to assist class I repositioning (Fig. 13).

Surgery

Once more, surgical steps followed exactly the VSP phases. IMF screws were preliminarily positioned to enable subsequent intermaxillary blockage. A vestibular intraoral access was performed to expose fractures of the anterior and lateral maxillary wall, including the whole Le Fort I, while a bilateral subciliary approach was used to expose the inferior orbital rim and the orbital floor. Glabella and nasal bones were exposed through a curved horizontal cosmetic incision.

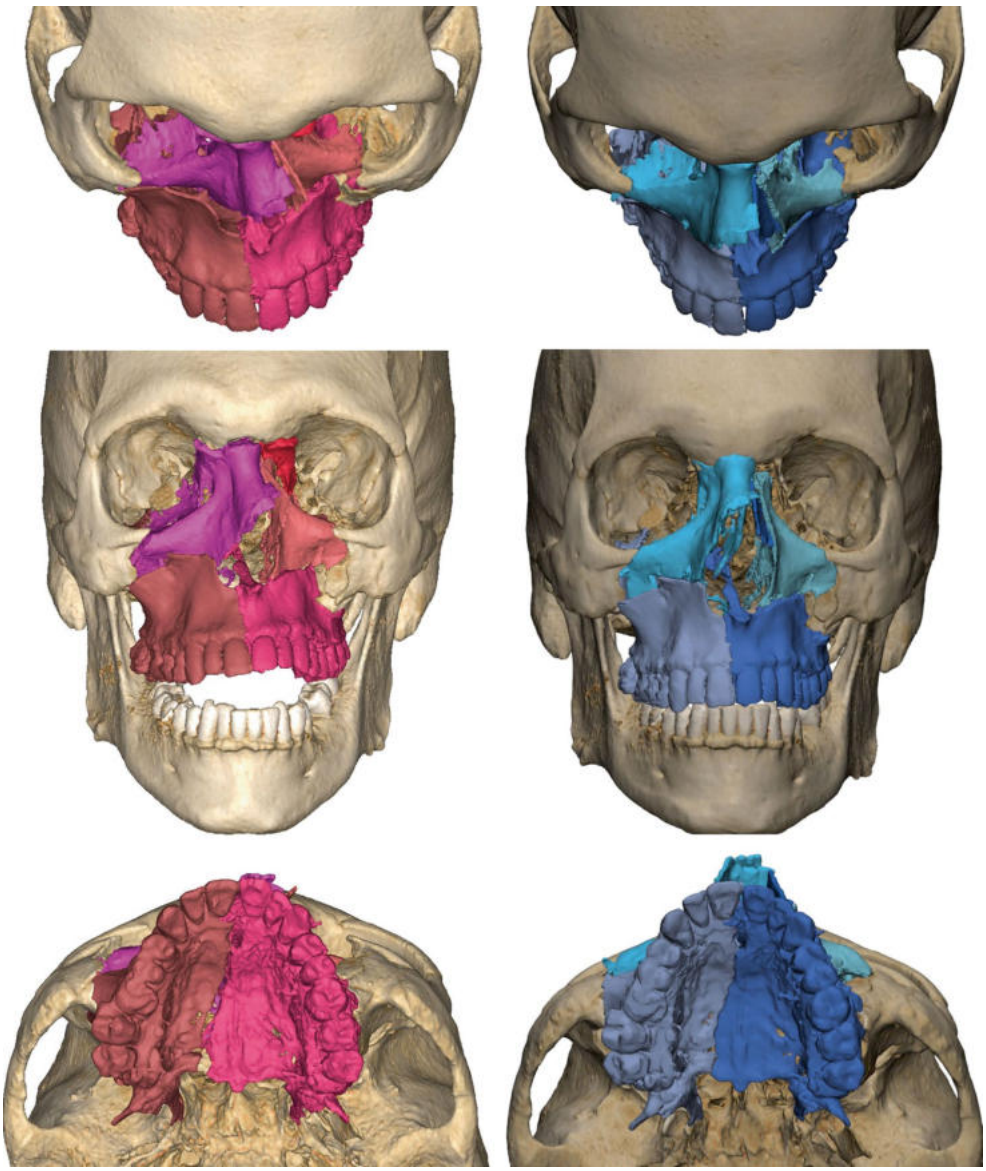


Fig. 12 VSP of complex midfacial trauma illustrated in Fig. 1. Displaced (left) and reduced (right) segments

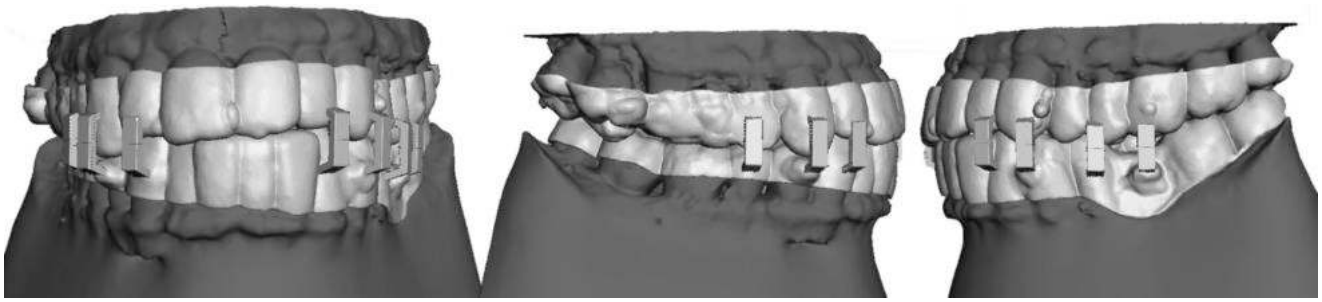


Fig. 13 Use of alternative TCS. Compared with those in Fig. 4, these are thicker and rigid, but an occlusal splint is not needed. The correspondence of lateral wings accounts for the inter-arch occlusal relationship

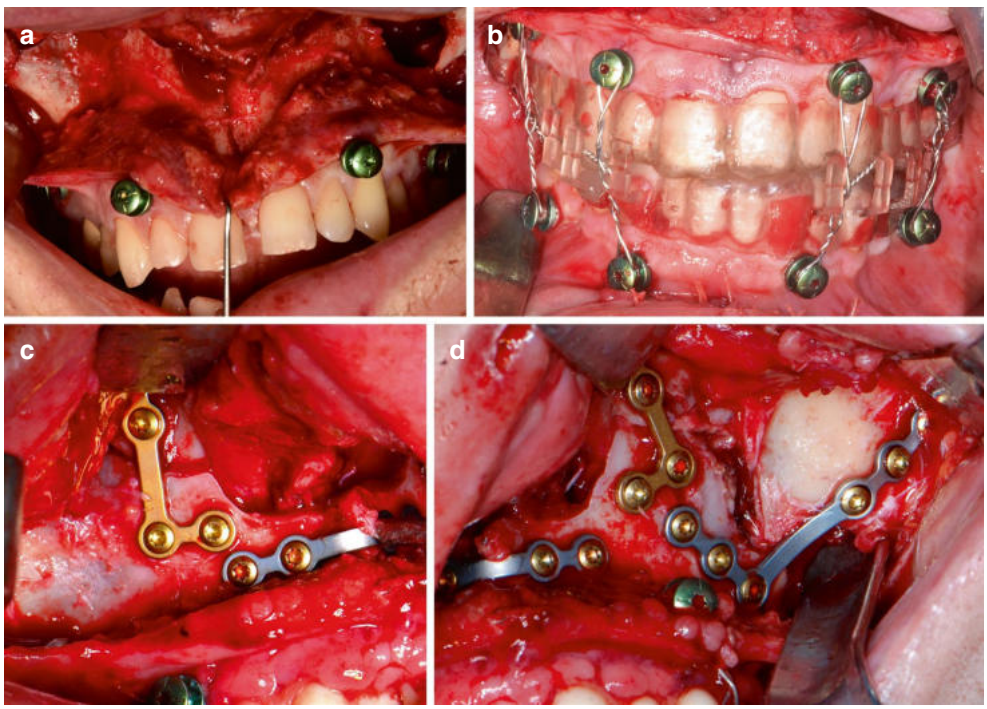


Fig. 14 Intraoperative view. A) Fractures are exposed with evidence of the sagittal midline palatal fracture; B) TCS are applied for superior arch reduction. MMF is performed by aligning lateral wings, so that the planned occlusion is verified; C) and D) plating of Le Fort buttresses to stabilize the achieved reduction

To transfer planned occlusion to the real patient, TCSs with connection pins were positioned to exert both a contentive action on the palatal split fracture and to simultaneously restore surgical occlusion. Intermaxillary blockage was performed with the TCS in place. Subsequently, plating of the Le Fort segment with stable ZMC was performed. Reduction of both NOE segments was performed based on the same stable anatomical landmarks identified in VSP and the surgical occlusion (Fig. 14). Finally, reduction and plating of the fronto-nasal suture and the nasal bones were performed by positioning a Y-shaped plate. The left orbital floor was reconstructed using a premodeled titanium implant.

Key message: In occlusion-impairing trauma, reestablishing the most stable occlusion has the priority over anatomical reduction, and this step has to be carefully accomplished within the virtual planning. Devices including occlusal splints and TCS are the most essential. Reduction guides and image-guided surgery do not play a fundamental role in the occlusion-impairing trauma of the midface.

4 Occlusion-Non-Impairing Trauma

This class includes a multitude of fracture types that involve regions higher than occlusion, notably zygomaticomaxillary complex (ZMC), isolated naso-orbito-ethmoid (NOE) complex, orbital, skull-base and cranial vault. While orbital fractures have already been discussed separately, the following section will focus predominantly on ZMC fractures, due to their prevalence.

Typical of occlusion-non-impairing trauma is the predominance of anatomical reduction and reconstruction of the natural buttresses of the craniofacial skeleton by restoring the dimensions of the splanchnocranium in terms of symmetry, diameters, and biomechanics. In VSP, techniques for anatomical reduction are essential, including mirroring for sided defects, and manual repositioning of fragments for more complex fractures. Topological mirroring, namely the mirroring of single anatomical subunits in case a fully healthy side is not available, can also be considered.

Concerning techniques for computer-assisted surgery, image-guided surgery plays the most important role, especially intraoperative navigation to navigate digital reduction templates and interactively verify if the intraoperative reduction is correct. Navigation can be performed in complex anatomical regions, does not require a broad surgical field as it is only based on a thin probe, and is optimal in regions such as ZMC, the orbital space and the skull base.

Conversely, reduction guides do not offer a considerable help in midfacial trauma, owing to the narrow spaces exposed through intraoral and periorbital incisions. In contrast, reduction guides can be highly helpful in selected cases of multifragmented mandibular fractures (see Chap. 19).

4.1 Zygomaticomaxillary Complex (ZMC) Fractures

ZMC represents an important region for the biomechanical stability of the craniofacial skeleton, as its presence is nodal to connect the force-resisting buttresses that originate from the lateral orbital rim, the zygomatic arch, and the maxillozygomatic pillar. Thus, many high-energy injuries resulting in impaction against this region of the face result in a simultaneous fracture of the three roots of the ZMC (tripodic fractures). Indeed, ZMC is the second most frequently fractured site in the face, following the mandible [14].

As a result, ZMC fractures can result in different scenarios, from entirely non-displaced to severely displaced fractures with multi-axial translocation of the ZMC, including a combination of translational and rotational movements. In addition, ZMC fractures can also be secondary; that is, they can result from trauma occurring in a different site: this is mostly typical with centrofacial injuries, causing a bilateral ZMC fracture with widening of the bizygomatic diameter and facial flattening. Because of such factors, classification of ZMC fractures has always represented a reason for major concern. Through the years, many attempts were made to classify ZMC fractures, from original classifications based on planar radiograms (Knight and North's, 1961 [15]) to the most recent taking advantage of multidetector CT scans (Zinng, Özyazgan, Bächli, Donat [16]). In 2020, the first classification entirely based on virtual surgical planning was released, taking into account not only the displacement of the fractured ZMC and other injury-related features such as comminution and laterality, but also reduction maneuvers involved during virtual surgical planning that counteract the forces causing displacement of fractured ZMC with opposing vectors, as well as the presence and site of comminution [17].

4.1.1 Case 1: Multifragmented, Completely Sided, ZMC and Maxillary Fracture with Navigation

Clinical History

This 28year-old patient was referred to our attention following a sport injury, where he was subject to a high-energy trauma in the left malar region. The patient presented with a visible asymmetry in the projection of the cheekbone area and enophtalmos due to simultaneous orbital floor fracture. CT scan revealed a multifragmented fracture involving the entire ZMC, still connected to the unfractured arch, a free segment of the inferior orbital rim, a nasomaxillary component and a fragment of the anterior antral wall.

Virtual Surgical Planning

Virtual surgical planning protocol was performed as explained, first by thresholding the whole craniofacial skeleton using a thin-structure preserving value, then the segmentation mask was splint across the fracture line to subdivide the initial mask into multiple submasks, each one corresponding to a single fractured fragment. This is a case of completely sided injury in an eumorphic patient with an overall acceptable symmetry, as seen by placing the midsagittal plane (Fig. 2). Thus, the patient was an optimal candidate for a mirroring-based semiautomatic reduction. The midsagittal plane was defined using a datum plane based on equally distant points from a theoretical midline, identified by placing two symmetrical points located in the midpoint of the frontozygomatic suture. The mirrored template was made transparent to see in depth the displaced fragments superimposed, and to determine the loss of projection from a bottom. To further enhance the correspondence of the mirrored template to the anatomy of the patient, a global registration

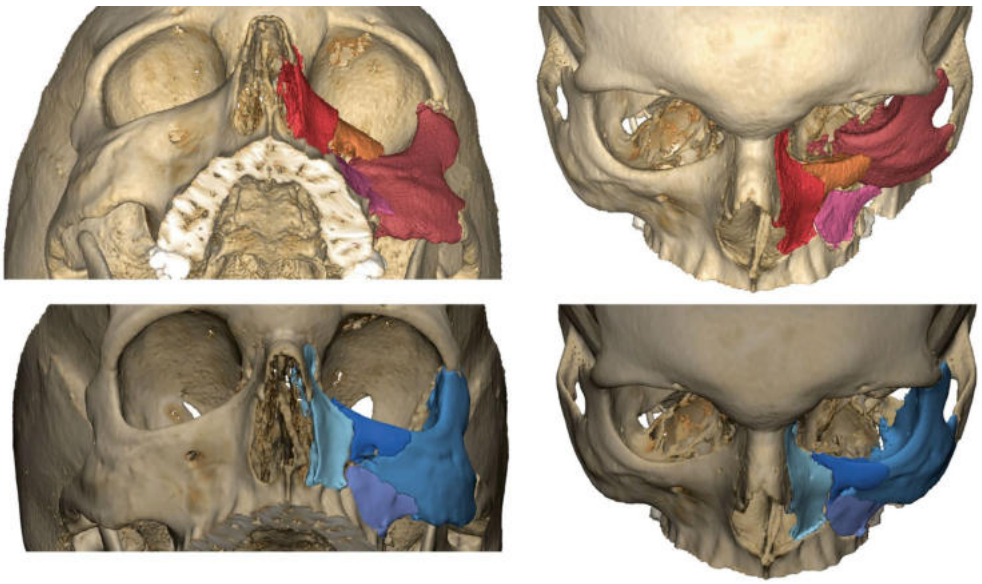


Fig. 15 VSP of complex multifragmented and severely displaced ZMC fracture. Top panel: displaced segments; bottom panel: reduced segments

based on the iterative closest point algorithm was applied. Using the mirrored template as a guide for displaced fragments repositioning, first a point-by-point preliminary alignment was performed on each fragment using the mirrored mask to realign each fractured fragment into the correct position, then the global registration algorithm was used to fine tune the registration. Minor misalignments were manually adjusted to optimize anatomical reduction (Fig. 15).

STL files of reduced fragments were exported and uploaded within the navigation system to be superimposed on the original CT scan, representing reduction templates to provide the surgeon with visual feedback on the correct reduction.

Surgery

Surgery was performed using a vestibular intraoral access according to Keen, where the ruptured anterior maxillary wall and the maxillo-malar buttress were exposed; then a transconjunctival approach was used to expose the inferior orbital rim. A percutaneous eyebrow incision was used to access the fronto-zygomatic suture. Reduction maneuvers were performed under navigational assistance and osteosynthesis plates were conformed and applied in the maxillo-malar buttress, inferior orbital rim and fronto-temporal suture (Fig. 16).

4.1.2 Case 2: Multifragmented, Orbital Rim and ZMC Fracture, Sided with 3D Printing

Clinical History

A 52-year-old lady was admitted to hospital following a facial injury while fainting and falling to the ground. Despite swelling around the maxillo-malar area, clinical examination revealed a reduction in natural projection of her left cheeckbone area. CT revealed a ZMC fracture, with two free fractured fragments around the fronto-zygomatic suture and the inferior orbital rim. In addition, the entire left orbital floor was fractured (type III according to modified Jacquery's classification) in a single macrofragment displaced internally in the maxillary sinus.

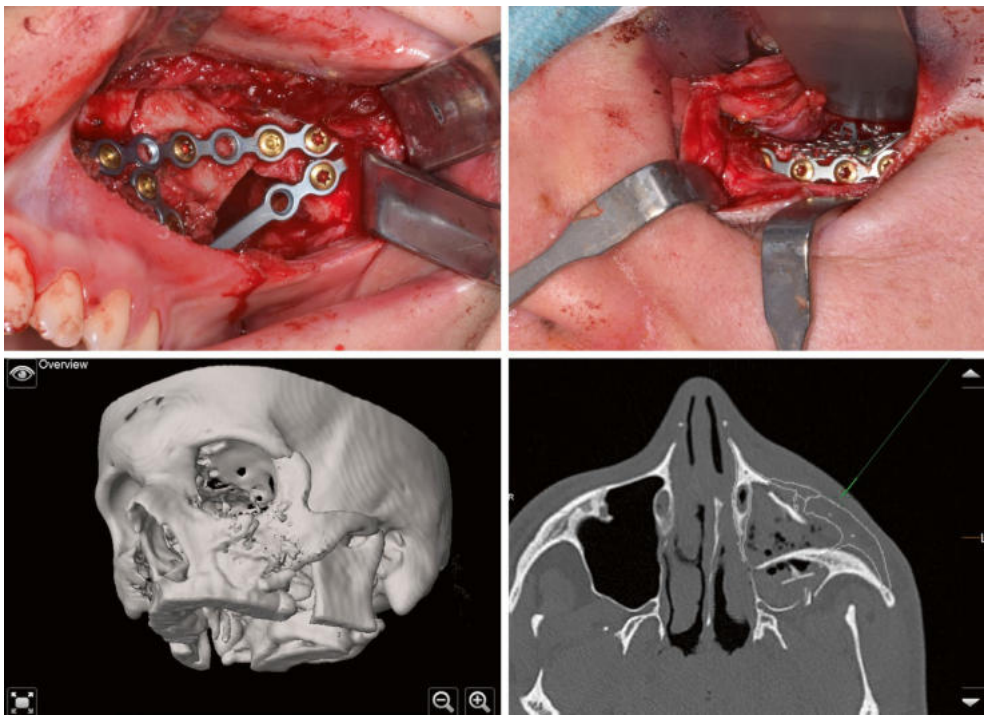


Fig. 16 Navigation-guided reduction

Virtual Surgical Planning

As previously described, a mirrored image was acquired after defining a symmetry plane. However, in this case, the craniofacial symmetry was poorer, and a considerably wider superior orbital rim diameter was assessed compared to the injured site. Interestingly, physiologic natural asymmetry made the use of mirroring technique slightly less efficient in this case. Thus, after fragments had been semi-automatically realigned, making use of the point-by-point alignment and then the object-to-mirroring global registration, the anatomical reduction was not acceptable, although if succeeded to restore symmetry in malar area projection. This case emphasizes the importance of manual reduction to improve the results of semi-automatic fragment repositioning (Fig. 17).

Moreover, a surface reconstruction within the boundaries of the broken orbital floor was used to restore the continuity of the orbital floor itself in order to allow to print a physical replica of the reduced craniofacial skeleton with an entire, anatomically reliable, orbital floor, enabling to premodel an orbital implant, as well as osteosynthesis plates). Once the reduced model was available, it was wrapped using a gap-closing distance of 2 mm, smallest detail set to 0.1 mm, and resulting offset set to 0.0710 mm. The wrapped model was imported in the software Formlabs Preform for 3D printing (Fig. 18).

Surgery

As seen in the previous case, a multiple-approach exposure of fracture sites was adopted through a maxillary vestibular approach and a subciliary incision with preseptal dissection. Plates were conformed in the 3D printed model and used once the achieved reduction was satisfactory. Moreover, prebent plates based upon a computer-guided reduction add a physical feedback sensation in terms of good positioning when the achieved reduction matches the virtual one. The orbital implant was similarly conformed and positioned over the posterior rim of the fracture contour to be granted stability and was secured to the inferior orbital rim using miniscrews (Fig. 19).

4.2 Naso-Orbito-Ethmoid Complex Fractures

NOE complex represents the central fulcrum of the splanchnocranium and has a critical relevance due to its direct contact with the orbital region, nasal bones, and anterior skull base. NOE complex is usually involved in cases of direct trauma to the midface and especially around the nasal area. In this case, the fracture can mobilize and dislocate bone fragments, which include the nasal process of the maxilla, the lacrimal bone, the inferior orbital rim and the nasal bone. The impact in the midface causes such fragments to widen and dislocate both laterally and posteriorly, causing a variety of possible clinical sequelae, including epiphora, secondary to lacrimal apparatus damage, cerebrospinal fluid rhinorrhea due to anterior skull base involvement, and telecanthus whenever the dislocated NOE fragment includes the insertion of the medial canthal ligament, which is crucial according to the well-known Markowitz and Manson classification

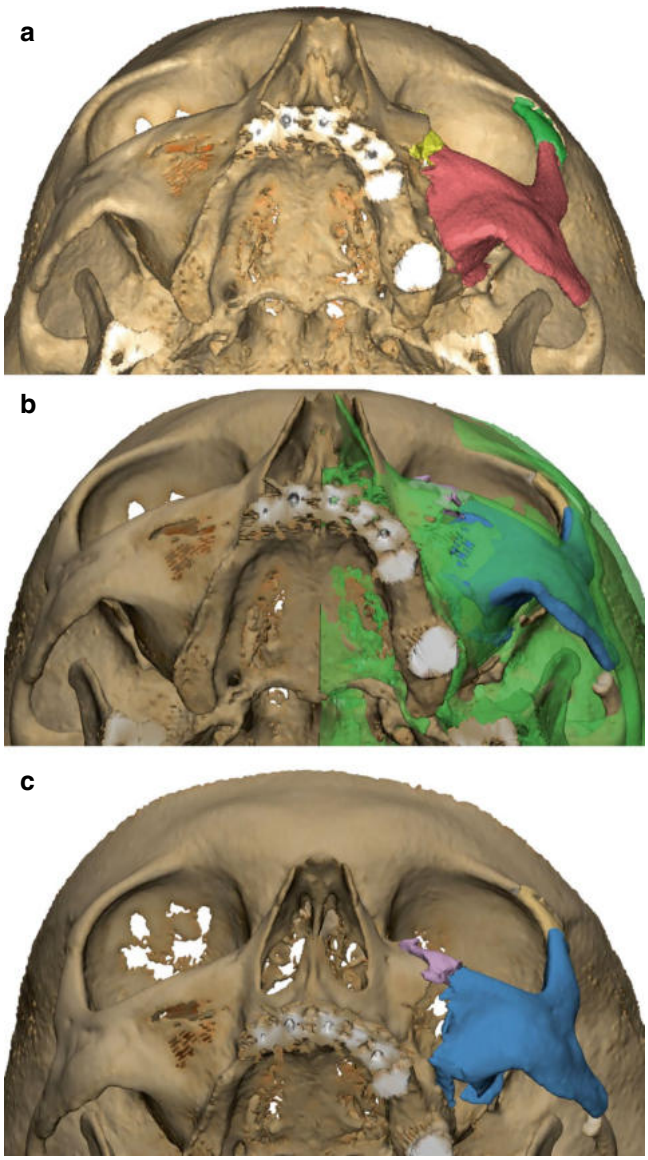


Fig. 17 Mirror-based reduction of ZMC fracture with a second fragment on the lateral orbital rim

[18]. It is often difficult that NOE complex fractures are isolate, but they are most often associated with maxillary fractures, including Le Fort I and II.

Anatomical reduction plays a prominent role in VSP for NOE segment repositioning. If a concurrent Le Fort needs to be treated, it should be firstly reduced using the concepts discussed in relation to occlusion-impairing trauma, and then NOE segments need to be precisely repositioned using anatomical reduction to fit both the reduced Le Fort and upper regions as well. In NOE fractures, nasal bone repositioning plays a key role as well, as it is responsible for the symmetry of the nasal pyramid. Like ZMC, in NOE complex fractures, navigation is the most indicated method to bridge VSP with surgery, as it enables to check the symmetry of repositioned segments, especially in correspondence with critical points, including the medial canthal tendon. The following case discusses a case of NOE fracture with a fronto-nasal separation and preserved occlusion, as prototype of an occlusion-non-impairing trauma.

4.2.1 Naso-ethmoidal Fracture with Fronto-nasal Injury

Clinical History

A 47-year-old patient was referred from the emergency department after a motorbike accident. The patient presented with a visible periorbital ecchymosis, subcutaneous emphysema, and a markedly deviated nasal pyramid. Occlusion appeared stable at clinical examination, and the patient did not complain of any modifications of teeth contact. CSF leakage was not present. CT scan was performed, showing a separated fronto-nasal fragment, with a transverse fracture line involving the outer table of the frontal sinus and a twisted axis, which conditioned a visible right nasal deviation. A second, large NOE fragment involving the left inferior orbital rim, and a third segment, including the right lacrimal bone without telecanthus, were defined as well.

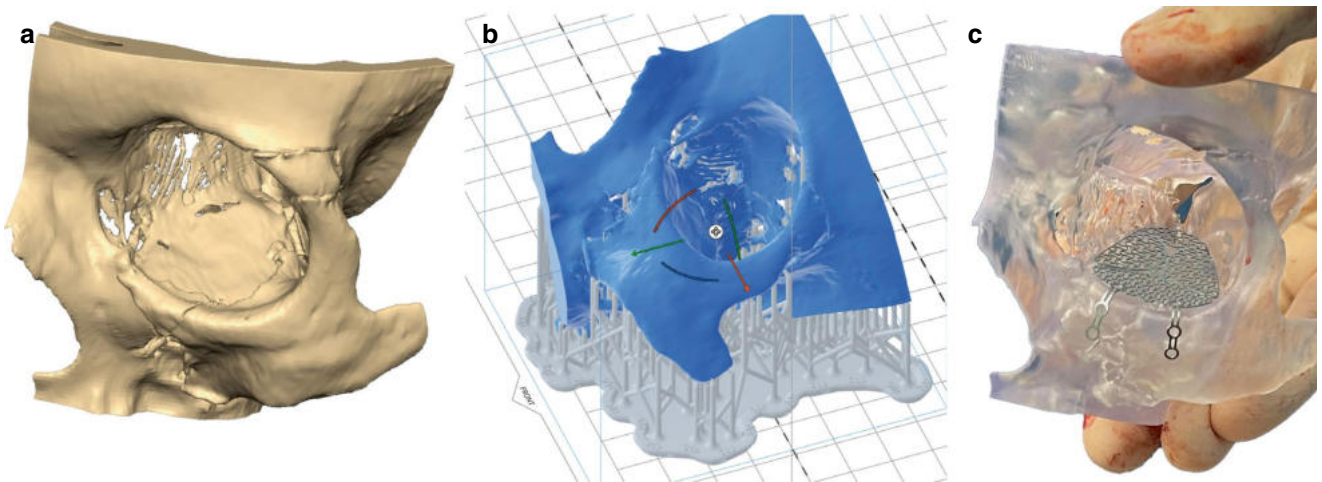


Fig. 18 Sequence of VSP steps to optimize a model for ZMC plate prebending. (**a**) Geometrical optimization with empty region filling to avoid 3D printing errors and provide a solid base to model the orbital implant; (**b**) creation of the 3D printing plan with support cage; (**c**) orbital implant modelling



Fig. 19 (**a**) and (**b**) application of prebent implants. (**c**) Comparison of the fractured orbital rim with the 3D printed model

Virtual Surgical Planning

Segmentation of the CT scan was performed, and the split mask algorithm was applied to separate the fractured fragments, as diagnosed. Each fragment was assigned a different color, and their duplicate replicas were reduced so as to inspect the differences in orientation between displaced and reduced couples. Given the central involvement typical of NOE fractures, no semi-automated method to drive realignment was available, and segments were manually repositioned with attention to recsontruct the natural buttresses and ridges, including the inferior orbital rim, at the same time prioritizing the restoration of symmetry of the nasal pyramid (Fig. 20).

Surgery

A coronal access provided the most extensive exposure of the fronto-glabellar region. Accurate reduction of the fronto-nasal separation was performed by placing Rowe's disimpaction forceps in the nasal cavity and pulling the midface upwards, until the gap was closed. Internal rigid fixation was performed, at the same access enabled control over the highest pole of the NOE fragments. A left subciliary access was used to reduce the inferior orbital rim fracture, whereas an intraoral access was used to fixate the inferior part of the left NOE fragment and to precautionally strengthen the maxillo-malar buttress, given the possible presence of a hemi Le Fort I, incomplete, fracture on the left (Fig. 21).

Key message: In occlusion-non-impairing trauma, anatomical reduction plays the prominent role and should be accurately planned. VSP is effective in predicting the correct surgical sequencing and the appropriate stable landmarks. Moreover, techniques of image-guided surgery are essential to intraoperatively verify the correct reduction using digital reduction templates imported from VSP, but also 3D printed model with plate preconfirmation can be helpful. Noteworthily, occlusion-non-impairing trauma and occlusion-impairing trauma often coexist, and each should be addressed using the appropriate planning protocols.

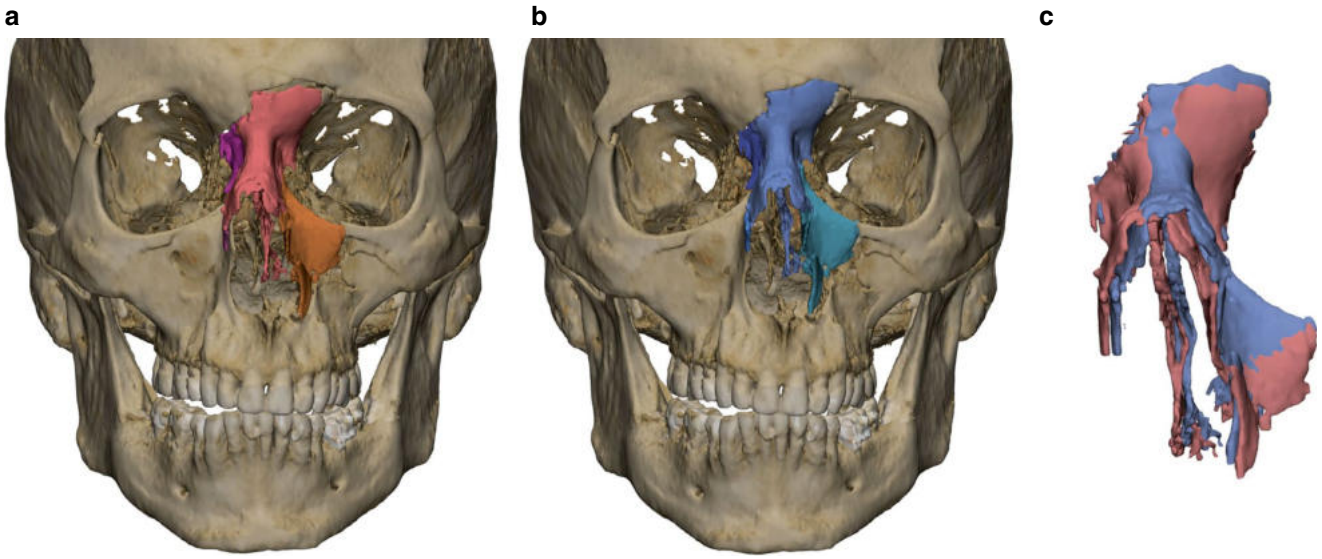


Fig. 20 (**a**) Left NOE fragment associated with a fronto-nasal separation with nasal deviation and (**b**) reduction. (**c**) illustrates the movement for reduction through overlapping

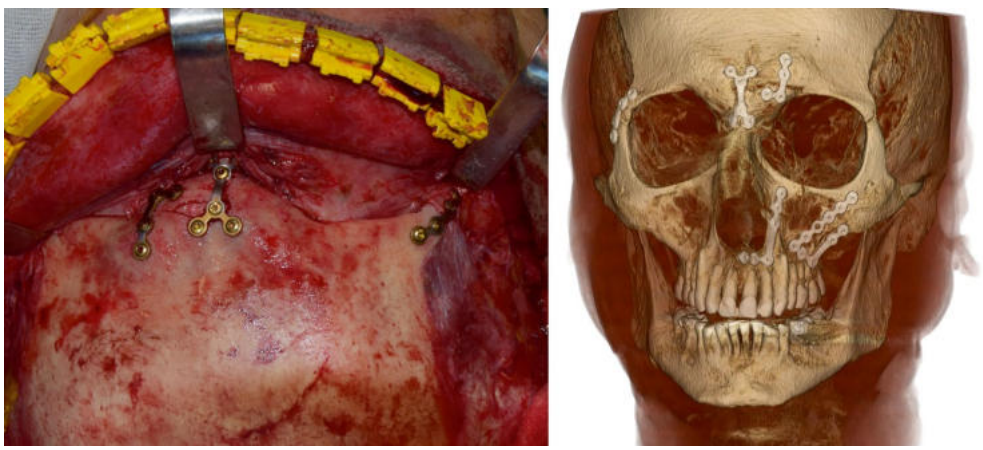


Fig. 21 Intraoperative view and postoperative CT

References

1. Mast G, Ehrenfeld M, Cornelius C-P, Litschel R, Tasman A-J. Maxillofacial fractures: midface and internal orbit-part I: classification and assessment. Facial Plast Surg. 2015;31:351–6.
2. (2024) Manual image segmentation in computer vision: a comprehensive overview of annotation techniques. In: Supervisely. https://supervisely.com/blog/complete-overview-and-comparison-of-manual-segmentation-approaches/. Accessed 12 Jan 2025.
3. Costan VV, Nicolau A, Sulea D, Ciofu ML, Boișteanu O, Popescu E. The impact of 3D technology in optimizing midface fracture treatment-focus on the zygomatic bone. J Oral Maxillofac Surg. 2021;79:880–91.
4. Semper-Hogg W, Fuessinger MA, Schwarz S, Ellis E, Cornelius C-P, Probst F, Metzger MC, Schlager S. Virtual reconstruction of midface defects using statistical shape models. J Craniomaxillofac Surg. 2017;45:461–6.
5. Gass M, Füßinger MA, Metzger MC, Schwarz S, Bähr JD, Brandenburg L, Weingart J, Schlager S. Virtual reconstruction of orbital floor defects using a statistical shape model. J Anat. 2022;240:323–9.
6. Michelutti L, Tel A, Zeppieri M, Ius T, Agosti E, Sembronio S, Robiony M. Generative adversarial networks (GANs) in the field of head and neck surgery: current evidence and prospects for the future-a systematic review. J Clin Med. 2024;13:3556.
7. Morita D, Kawarazaki A, Soufi M, Otake Y, Sato Y, Numajiri T. Automatic detection of midfacial fractures in facial bone CT images using deep learning-based object detection models. J Stomatol Oral Maxillofac Surg. 2024;125:101914.
8. Drake VE, Rizzi CJ, Greywoode JD, Vakharia KT, Vakharia KT. Midface fracture simulation and repair: a computer-based algorithm. Craniomaxillofac Trauma Reconstr. 2019;12:14–9.
9. Hussein MA, Besher A, Saad MA, Wilson AM. Versatility of hard occlusal splints in optimizing outcomes in patients with old panfacial fractures. Plast Reconstr Surg Glob Open. 2021;9:e3855.
10. Tel A, Costa F, Sembronio S, Robiony M. Contemporary management of complex craniofacial trauma: virtual planning, navigation and the novel thermoformed cage splints in a strategic, sequential, computer-guided protocol. J Craniomaxillofac Surg. 2022;50:837–47.
11. Azarmehr I, Stokbro K, Bell RB, Thygesen T. Surgical navigation: a systematic review of indications, treatments, and outcomes in Oral and maxillofacial surgery. J Oral Maxillofac Surg. 2017;75:1987–2005.

12. Jiang T, Zhu M, Chai G, Li Q. Precision of a novel craniofacial surgical navigation system based on augmented reality using an occlusal splint as a registration strategy. Sci Rep. 2019;9:501.
13. Lin L, Liu X, Gao Y, Aung ZM, Xu H, Wang B, Xie L, Yang X, Chai G. The application of augmented reality in craniofacial bone fracture reduction: study protocol for a randomized controlled trial. Trials. 2022;23:241.
14. Characteristics and epidemiology of zygomaticomaxillary complex fractures – PubMed. https://pubmed.ncbi.nlm.nih.gov/20677370/. Accessed 12 Jan 2025.
15. Knight JS, North JF. The classification of malar fractures: an analysis of displacement as a guide to treatment. Br J Plast Surg. 1961;13:325–39.
16. Zingg M, Laedrach K, Chen J, Chowdhury K, Vuillemin T, Sutter F, Raveh J. Classification and treatment of zygomatic fractures: a review of 1,025 cases. J Oral Maxillofac Surg. 1992;50:778–90.
17. Tel A, Sembronio S, Costa F, Robiony M. Scoping Zygomaticomaxillary complex fractures with the eyes of virtual reality: operative protocol and proposal of a modernized classification. J Craniofac Surg. 2021;32:552–8.
18. Markowitz BL, Manson PN, Sargent L, Vander Kolk CA, Yaremchuk M, Glassman D, Crawley WA. Management of the medial canthal tendon in nasoethmoid orbital fractures: the importance of the central fragment in classification and treatment. Plast Reconstr Surg. 1991;87:843–53.

Virtual Surgical Planning in Midfacial Oncology

Alessandro Tel and Massimo Robiony

1 Introduction to Midface Resection

Resective procedures in the midface are required to remove lesions arising in the maxillofacial area conventionally included between a line passing through the superior orbital rim and the upper teeth. This region of the splanchnocranium presents a considerable geometrical complexity and is crucial to interface the occlusal biomechanics with delicate sensory areas, including the orbit and the nasal cavity. In particular, the complex system of inner cavities represented by paranasal sinuses often represents the origin of several types of tumors, whose excision must be performed in accordance with the principles of facial disassembly illustrated by Janecka [1]. The mainstay of surgical oncology in the craniomaxillo-facial area is the three-dimensional resection of the tumor within a volume of healthy tissue and negative margins to improve the chances that resection is radical [2]. Defining the boundaries of such resection volume in a digital plan aid to conceptualize resection in complex anatomical regions and provides intraoperative feedback through image-guided surgery [3]. While VSP has a prominent role in open surgery, especially in the creation of highly selective osteotomies, the adoption of protocols for accurate anatomical reconstruction presented throughout this Atlas opens new scenarios also for endoscopic procedures that can be entirely simulated in virtual reality. Indeed, in recent years, endoscopic techniques have largely superseded traditional open approaches in favor of multimodal therapies in which surgery is not the final curative solution but, through the reduction of the lesion mass, paves the way to non-surgical therapies, including radiation with electron beams and hadrons, chemotherapy and immunotherapy [4].

A. Tel (✉)
Lead Specialist for VSP and 3DP, Maxillofacial Surgery Clinic, Head & Neck and Neuroscience Department, Academic Hospital of Udine, Udine, Italy
e-mail: alessandro.tel@uniud.it

M. Robiony
Chief of Maxillofacial Surgery Clinic, Director of the Postgraduate School in Maxillofacial Surgery, Chief of Head & Neck and Neuroscience Department, Academic Hospital - University of Udine, Udine, Italy
e-mail: massimo.robiony@uniud.it

2 Classification of Midfacial Resections for VSP Purposes

VSP applied to midfacial resective procedures allows us to define four classes: maxillectomies, resections in deep facial compartments, craniofacial resections, and virtual endoscopies.

- *Maxillectomies*: Several classification systems have been reported in the literature to standardize maxillary resections, including those proposed by Aramany, Wells, Cordeiro, and Okay [5]. Owing to its three-dimensional conceptualization, Brown and Shaw's classification of maxillectomies [6] can be effectively adapted to a novel revisitation through virtual reality. Given the importance of VSP in the anticipated definition of resection margins, it is used extensively from class I (i.e., without the creation of an oro-antral fistula, only limited to the alveolar process) to advanced classes, including orbital or nasal ablation. VSP is applied to more complex scenarios that range from class II to class VI maxillectomies.
- *Resection in deep facial compartments*: Deep facial compartments (DFC) include the pterygo-maxillo-palatine fossa, the infratemporal fossa, and the deep masticatory space (DMS). Such regions can harbor a variety of neoplasms originating mostly from salivary glands but might also be involved in infiltrative processes from advanced cancers arising in the oral cavity. A highly reliable anatomical reconstruction, especially concerning complex vascular networks contained in such spaces, is the core of VSP.
- *Craniofacial resection*: This category is broad to include complex transfacial accesses, as well as combined tran-

© The Author(s), under exclusive license to Springer Nature Switzerland AG 2025

A. Tel, M. Robiony (eds.), *Atlas of Virtual Surgical Planning and 3D Printing for Cranio-Maxillo-Facial Surgery*,
https://doi.org/10.1007/978-3-031-94495-6_20

scranial and transfacial approaches. Combined procedures are usually performed with the aim of accessing the anterior skull base through the removal of a frontal bone flap, but the pathology originates from midfacial structures, most often paranasal sinuses. For this reason, craniofacial resection is presented in this chapter and not in superior third chapters, which present examples of lesions confined exclusively in the orbit or skull vault or a combination of both [7].

- *Virtual endoscopy*: Virtual simulation of endoscopic procedures is technically challenging, as it requires to simulate not just the anatomy, but also the vision through endoscopic camera, and the animation path corresponding to the movement of the optics. Although highly preliminary in its scope, it can provide valuable information on the anatomical structures that the surgeons expect to encounter [8].

3 Protocol for Virtual Surgical Planning in Midfacial Resection

3.1 Imaging Acquisition Criteria for Multilayer Anatomical Reconstruction

Unlike the mandible, which is a bone with simple morphology and well-represented cortical layers, midfacial skeleton is a complex geometrical structure consisting of thin laminae arranged three-dimensionally and enclosing crucial structures including the orbit, nasal cavity, and deep facial compartments, as well as all vascular networks contained within. The term "multilayer anatomical reconstruction" refers to the possibility of creating a virtual model to which each anatomical layer is added starting from the skeletal backbone, which represents the basics for simulation, and improving through the addition of vascular networks, muscles, eyes, nervous structures, and glands. The aim is to customize the virtual representation of the patient, creating a sort of patient-specific virtual atlas [9]. Thus, respecting strict acquisition protocols becomes mandatory, and imaging should be acquired with the maximal technical capabilities available to any center (see also Chapter "Dedicated Acquisition Protocols in Radiology for Virtual Surgical Planning and 3D Printing").

- Skeletal anatomy: Should be acquired with high resolution using 0.625 mm thick slices and a matrix of at least 512 × 512 voxels. Threshold value for HU-based segmentation should be carefully placed, allowing the segmentation to be highly conservative of thin structures. In addition, as seen in Chapter "Virtual Surgical Planning in Craniofacial Surgery" for orbital fractures, the loss of thin missing parts caused by the intrinsic partial volume effect should be counterbalanced by the meticulous application of algorithms for thin structure reconstruction (Fig. 1).
- Soft tissue sequences: Should be acquired with contrast medium (gadolinium) for the best definition of the lesion. MR should be acquired with high spatial matrix (512 × 512 voxel), volumetric (interpolation is admitted) 1 mm thick slices, and contrast-enhanced sequences. The most effective sequence in the author's experience is VIBE (Volumetric Interpolated Breath-hold Examination), which provides the appropriate contrast to differentiate muscle bundles, glands (parotid, submandibular), and tumors, especially those that exhibit an infiltrative behavior. It provides a good contrast delineation of vessels as well and can be used for gross vessel segmentation when more specific sequences are not available. The advantage for the patient is the possibility to acquire the sequence during a single breath hold.

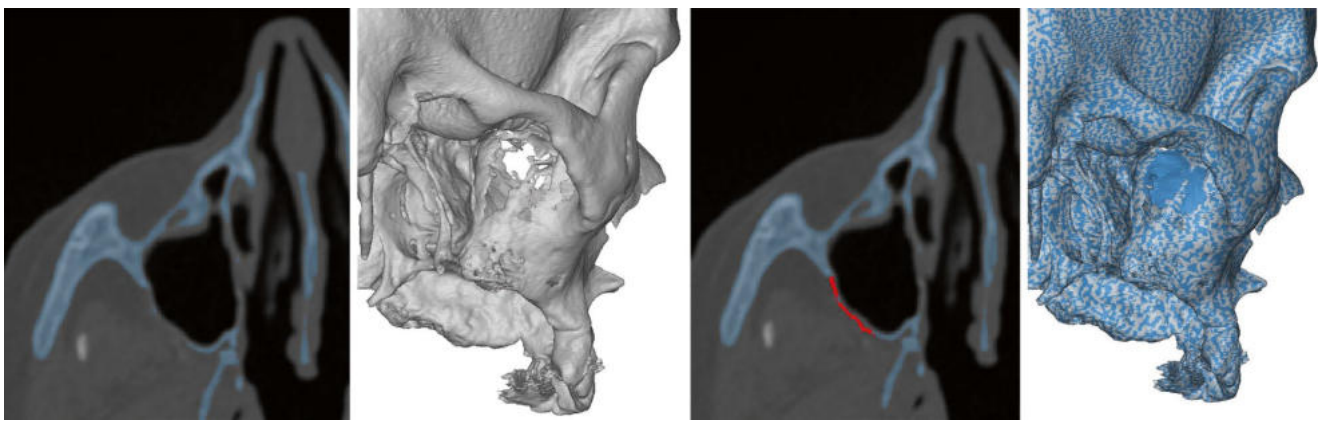


Fig. 1 Correction of thin wall artifacts is important to achieve a reliable anatomy reconstruction in the midfacial skeleton. The thin structure segmentation plugin is highly efficient in capturing such regions

- Vascular sequences: MR has to be preferred to contrast-enriched CT, owing to the absence of bone intensity in segmentation and the possibility to use sequences that are able to differentiate between arterial and venous structures. In this respect, 0.3 mm thick TOF (time-of-flight) sequence is ideal to enable easy and accurate segmentation of intracranial and extracranial vasculature, whereas 3D PCV (phased-contrast venography) or PCA (phased-contrast angiography), based on the phase shift of moving protons in blood, is excellent to track proton flow within veins [10]. In particular, lower Venc (velocity encoding) discriminates slower flow of veins from fast-flowing vessels (arteries).
- Nerve tracking sequences: Its use in virtual surgical planning is highly experimental, and segmentation of nerves is far from being clinically significant in the context of VSP (Fig. 2).

3.2 Segmentation

When multimodal imaging is used, it is essential that each imaging sequence used to delineate particular structures match the same spatial coordinate system. In contrast with the mandible (see Chapter "Virtual Surgical Planning in Midfacial Reconstruction"), coregistration of CT and MR sequences does not present relevant issues, as the skull base and the splanchnocranium are fixed landmarks. Once imaging registration is complete, segmentation steps can take place. The author suggests different segmentation techniques for different anatomical regions with the aim of minimizing inter-operator variability and including in the segmentation mask the highest quantity of voxels (and thus, of tissue):

- CT: A highly conservative thresholding algorithm (not above 200 HU) should be applied to compensate for the partial volume effect, intrinsic to thin structures, and acquire the highest quantity of bone. Moreover, a different threshold can also be used to segment the mucosal lining in case virtual endoscopy is required.
- Soft tissue: Dynamic region growing algorithms have the advantage of combining both isodensity and spatial proximity of voxels, but it may lead to inadvertently including also far regions. More recently, smart brushes based on region growing or ray casting have consistently simplified this type of segmentation.
- Vessels: In TOF sequences, due to the exclusivity of high-intensity voxels pertinent to arterial vasculature, thresholding is sufficient. In 3D PCV, dynamic region growing can be more effective (Fig. 3).

3.3 Virtual Surgical Planning of Bone Resections

The complex morphology of midfacial anatomy makes the use of conventional, plane-based osteotomies, ineffective in most cases. While positioning planes works effectively in the mandible to define the boundaries of the segment to excise, it is not possible to resect a segment of midfacial area with only two planes. Thus, other osteotomy techniques need to be considered for such a complex anatomy:

- Brush marking techniques: advanced software packages like the Mimics Innovation Suite enable to highlight all the triangles within a given brush area, that can be modified according to the resection needs (Fig. 4). This operation, however, is not exempt from errors, as new triangles need to be created to accommodate the curvilinear design of osteotomies.
- Polysculpt techniques: software like Geomagic Freeform, already mentioned in Chapter "Software Used for Virtual

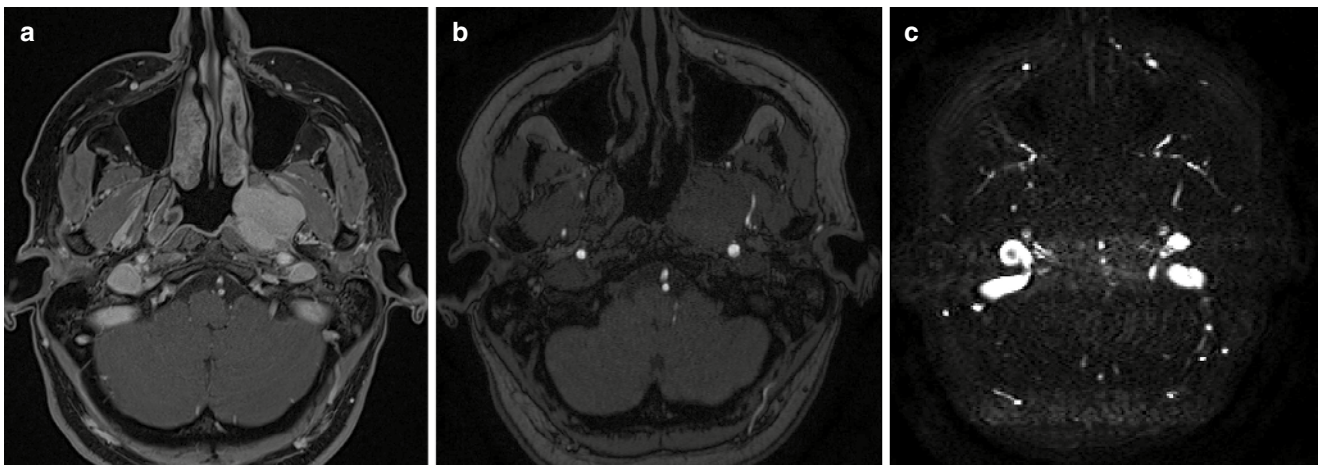


Fig. 2 Optimal MR sequences for midface VSP. Left: T1-VIBE; Center: 3D TOF; Right: Phased contrast (VEN3D)

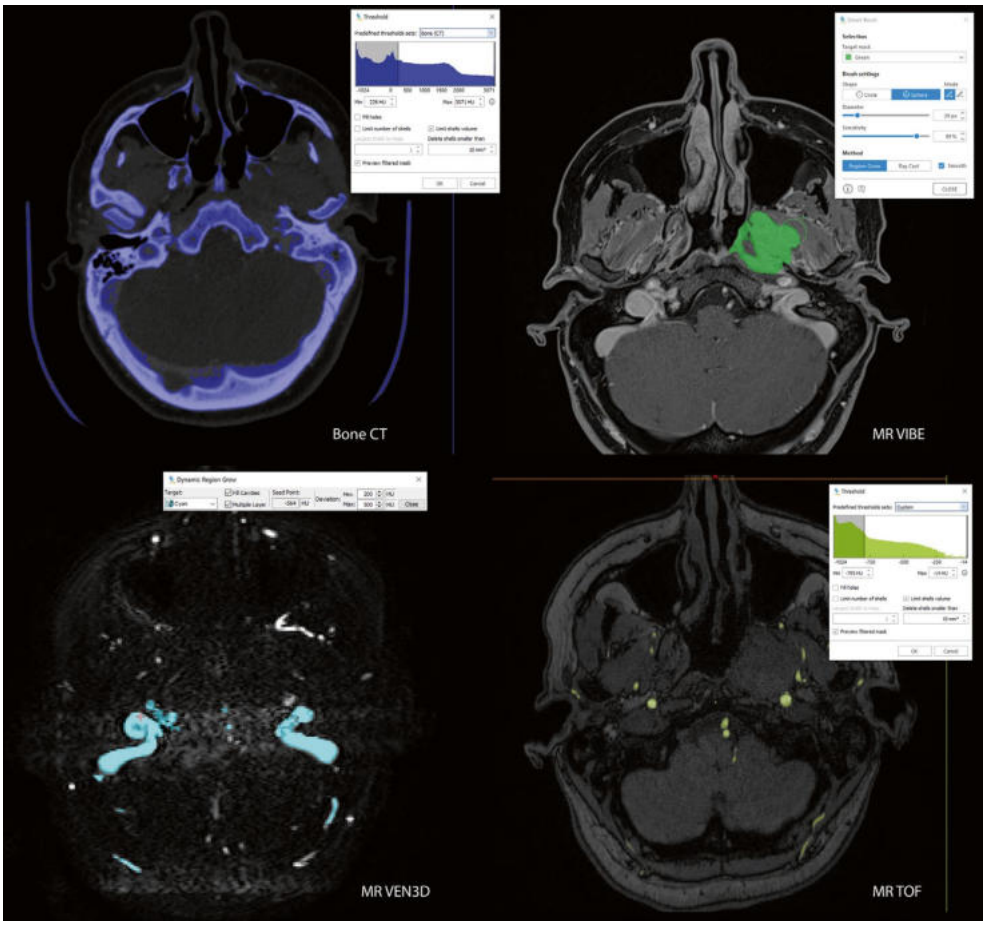


Fig. 3 Segmentation techniques for the midface. Bone CT: global thresholding; T1-VIBE (tumor): smart brush; VEN3D: dynamic region growing; TOF: global thresholding

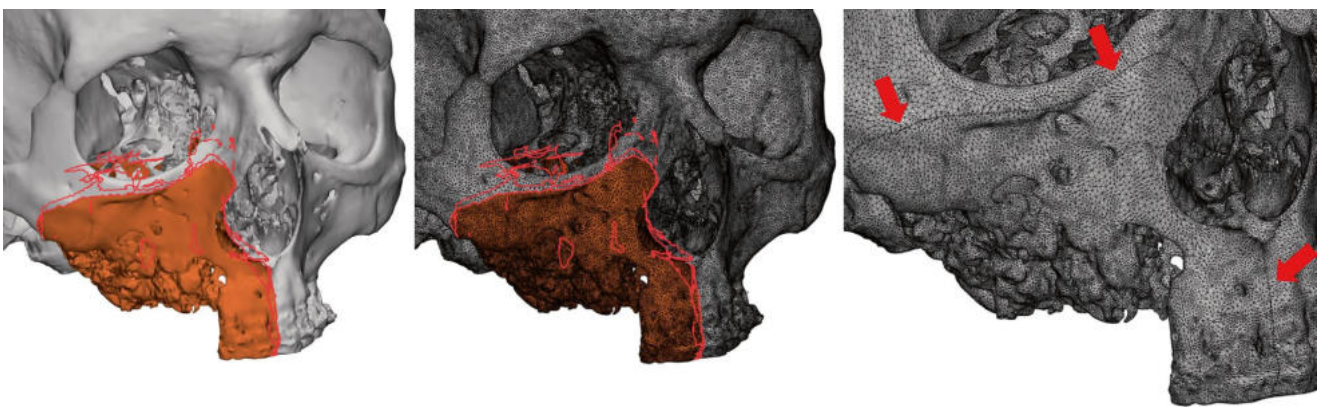


Fig. 4 Polygon-marking techniques performed on triangles can be adapted to design curvilinear cuts. Such techniques are not highly efficient as they need to create additional triangulation across the curved regions (arrows)

Surgical Planning", enables to convert triangular polygons of STL files in filled structures referred to as "clays". Clays consistently simplify the task of performing curvilinear osteotomies, especially in complex areas, such as the orbit of the deep facial compartments. Cut clays can then be reconverted into high-resolution STL files and eventually remeshed and retessellated in a lower resolution (Fig. 5).

In several cases, a mandibular osteotomy might be simulated strategically using a linear plane to assess the efficacy of a transmandibular approach on the exposure of the operative field. This is true especially for lesions located in the deep facial compartments that need to be accessed through the transmandibular corridor.

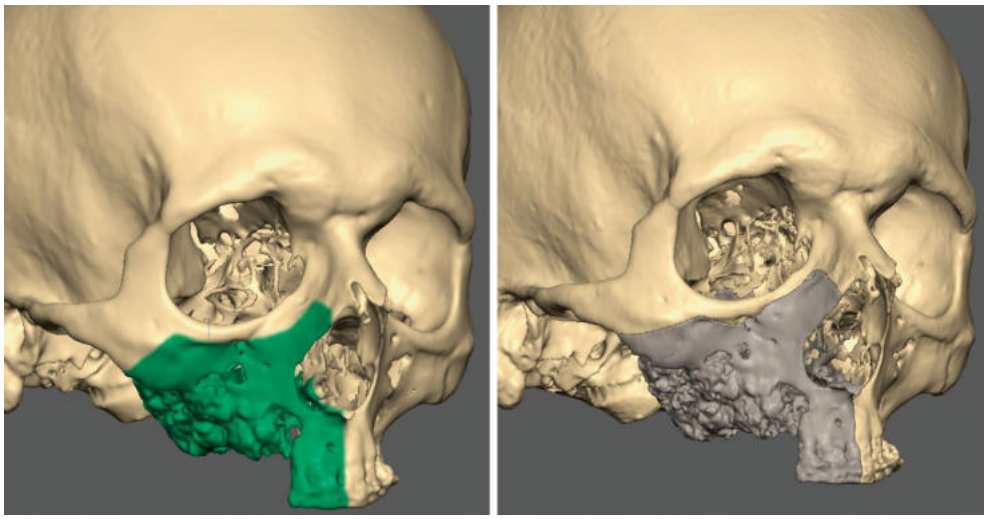


Fig. 5 Organic modelling freeform cuts are much more efficient. They are performed in clays, and only subsequently converted to polymeshes. (Software: Geomagic Freeform Plus)

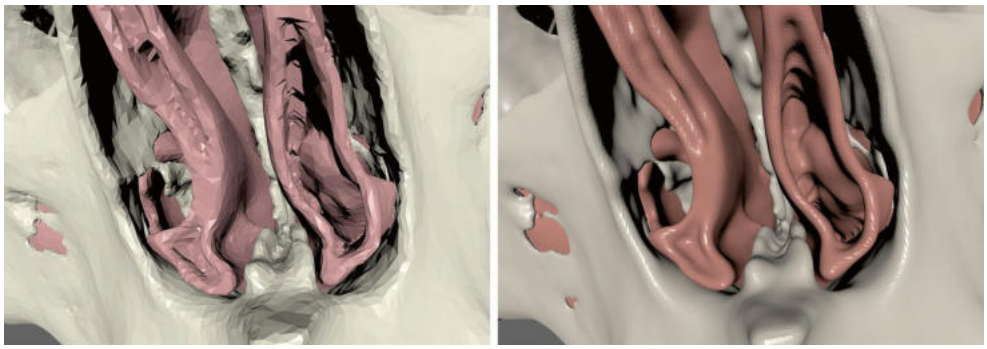


Fig. 6 Enhancing triangulation, thus resolution, accounts for improved anatomical detail as the virtual endoscope approaches the target. Computational time, however, substantially increases

3.4 Setup of Virtual Endoscopy

Virtual endoscopy refers to the possibility to perform a "fly-through" navigation of reconstructed 3D anatomy simulation with the optical properties of a surgical endoscope. It is an innovative visualization tool that can be used to anticipately simulate the field of view that the surgeon will encounter during endoscopic phases of surgery. This possibility is not available in any commercial software and requires a dedicated setup, as described by Tel et al. [9] that can be achieved within a dedicated software package. Virtual endoscopy needs the following elements to be successfully simulated:

- Definition of a vision through a camera: Animation software, such as Autodesk Maya and 3DS Max (Autodesk Inc., San Francisco, CA, USA), Maxon Cinema 4D (Maxon Computer GmbH, Bad Homburg, DE), and Blender (Blender, Amsterdam, NL), enable the possibility to add a virtual camera to the scene. The camera can be configured with optical properties, including angulation, field of view (FOV) size, and depth of field (DOF). The combination of such parameters can be used to successfully simulate the optical properties of the intended endoscope.
- Definition of a path: the path is the predicted movement that the camera will undergo within the anatomical region. The camera movement is animated through interpolation of key frames set along this path and should ideally mimic the movements made by the surgeon while holding his optics.
- High-resolution geometries: Compared to traditional VSP, in which meshes are inspected and managed with a high visual distance to simulate open procedures, such as tumor excisions and osteotomies, simulating an endoscope means approaching the geometry from an extremely close perspective; thus, it becomes mandatory to produce a high-resolution tessellation in order to avoid gross triangulation. This should be made with regards to the hardware potential of the VSP workstation, as it may involve a considerable computational effort (Fig. 6).

3.5 Techniques for Computer-Guided Surgery in Midface Resections

The complex anatomy of the midface that limits the use of simple resection planes during virtual surgical planning contributes to differentiating the indications as well as to devices

for computer-guided surgery compared to mandibular oncology. In midface resections, a prominent role is played by intraoperative navigation: the limited operative field, especially when procedures are conducted intraorally, and the need to control surgical margins in hardly accessible regions, such as the pterygopalatine fossa and the orbit, limits the indication of traditional surgical guides, which play a prominent role in mandibular resections. Moreover, as the midface is fixed to the skull where devices for navigation registration are placed (both dynamic reference frames, or DRF, positioned on the skull, as well as Mayfield's headset), navigation is highly reliable. In contrast with Mayfield's headset, typically used in neurosurgery, the DRF enables the surgeon to move the head while preserving the calibration of the navigator [11, 12].

In contrast, as mentioned, surgical guides play a limited role in midfacial oncology, as they usually require wider surgical exposures, are difficult to plane, and lack stable anchoring landmarks. Under certain circumstances, however, there may be beneficial advantages of using surgical guides: when reconstruction necessitates a bone flap or a customized implant, surgical guides have the advantage to prepare the recipient site with a superior accuracy, thus maximizing the interface area for a bone-to-bone or a bone-to-implant contact, as the guided osteotomy is more accurate than the free-hand performance.

Augmented Reality (AR) is particularly promising in the field of advanced visualization for head and neck surgery and can be highly helpful to analyze the complex anatomy of the midface and the tumors arising within. Yet the validated registration of the AR hologram to the patient is still an unsolved issue. Its uncalibrated counterpart, which is referred to as mixed reality (MR) has the unquestionable advantage of allowing the surgeon to manipulate the holographic representation of the virtual anatomy within his sight field, and its intraoperative use enables a continuous check of the patient's anatomy [13].

4 Clinical Cases

Clinical cases will be presented for each type of midfacial resection, including maxillectomies, resections in deep facial compartments, craniofacial resections, and virtual endoscopy.

4.1 Maxillectomies

It has been already anticipated that the reference classification for maxillary resection is the well-known Brown and Shaw's classification. Due to its three-dimensional conceptualization and the key role that the orbit plays in defining the classes, this classification can be effectively suited to virtual surgical planning. In addition, for virtual planning purposes, maxillectomies can also be classified according to the extent of resection along the dental arch:

- Segmental maxillectomies involve a segment of the alveolar process
- Total maxillectomies extend up to the midline
- Extended maxillectomies involve a resection beyond the midline

The most appropriate result for virtual planning results from a simplification of the aforementioned classification systems, taking into account both the vertical extension towards the orbital floor and the horizontal extension beyond the midline (Fig. 7).

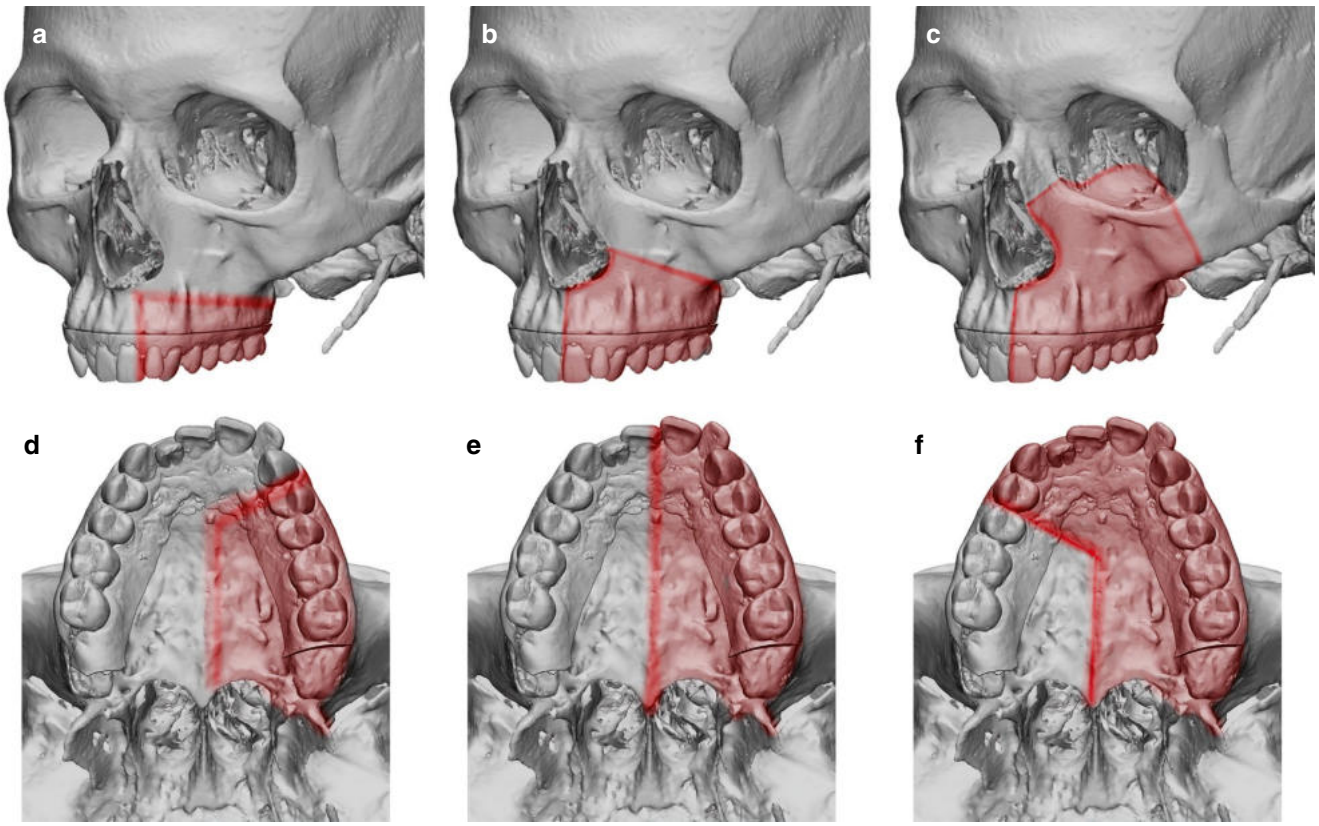


Fig. 7 Classification of maxillary resections: From (**a**) to (**b**) based on cranio-caudal extension (alveolar process, (**a**) beyond alveolar process creating a oro-antral fistla, (**b**) with orbital involvement, (**c**). From (**d**) to (**f**): based on transversal extension (ipsilateral, **d**; midline, **e**; beyond midline, **f**)

Owing to the complex design, only class I maxillectomies can be defined using linear planes, whereas when there is a higher involvement of the midface, the freehand design model for osteotomies becomes more effective and allows the surgeon a considerable freedom to selectively include parts within cured boundaries. This subsection will present several examples of maxillectomies with a thorough analysis of the implications of virtual surgical planning, demonstrating that in the vast majority of cases a freehand resection design is superior to traditional resection planes and also enables more customization of the resection area that is optimized for each single case.

4.1.1 Class II Total Maxillectomy for Mucoepidermoid Carcinoma with Simultaneous Cranioplasty

Clinical History

This patient was diagnosed with an erosive lesion causing ulceration in the oral cavity, which biopsy revealed to be a mucoepidermoid carcinoma. She underwent MR and CT examination, which revealed a bulky mass with an endophytic growth through the maxillary sinus and extensive bone erosion around the alveolar process (Fig. 8). A class II maxillectomy was planned to ensure excision of the lesion with macroscopically clean margins. Moreover, the patient presented with a cranial defect due to a previous neurosurgery for middle cerebral artery aneurysmal clipping, and she was candidate for a simultaneous cranioplasty.

Virtual Surgical Planning

At first, accurate skeletal segmentation was performed, and the soft-tissue tumor was superimposed after careful coregistration to achieve the virtualization of anatomy (Fig. 9). Given the standardized shape and the absence of any orbital involvement, a plane-based virtual planning was performed for this case. A sagittal osteotomy was performed in the midline, extending from the anterior nasal spine, through the vomerine insertion on the nasal floor, reaching the posterior nasal spine at the level of choanae. An additional horizontal osteotomy was planned from the midpoint of the nasal buttress to the root of the zygoma, continuing posteriorly to include pterygoid plates in the resection. Given the complexity of this resection, resection planes were not used, but the whole osteotomy was designed freehand. Resection margins of the virtually performed maxillectomy were inspected in their relationship with the tumor to ensure the effectiveness and feasibility of an en-bloc resection (Fig. 10). In addition, a cranioplasty based on pre-existing craniolacunia was

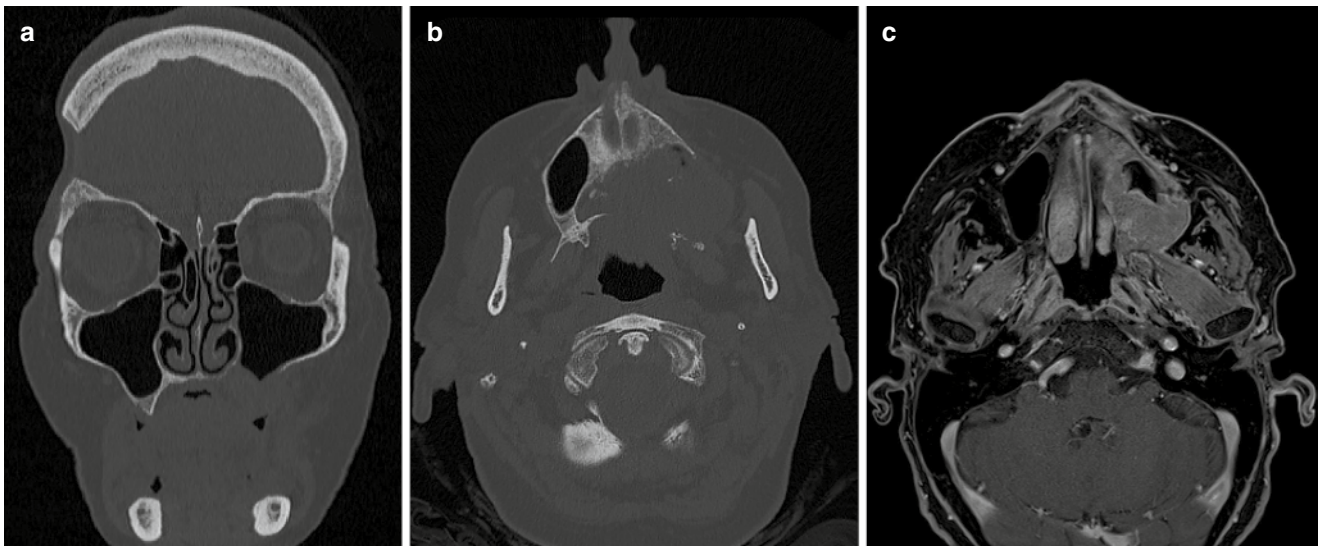


Fig. 8 CT and MR showing a highly disruptive behavior of a maxillary sinus squamocellular carcinoma. The patient also revealed a post-craniectomy defect for a previous neurosurgical procedure

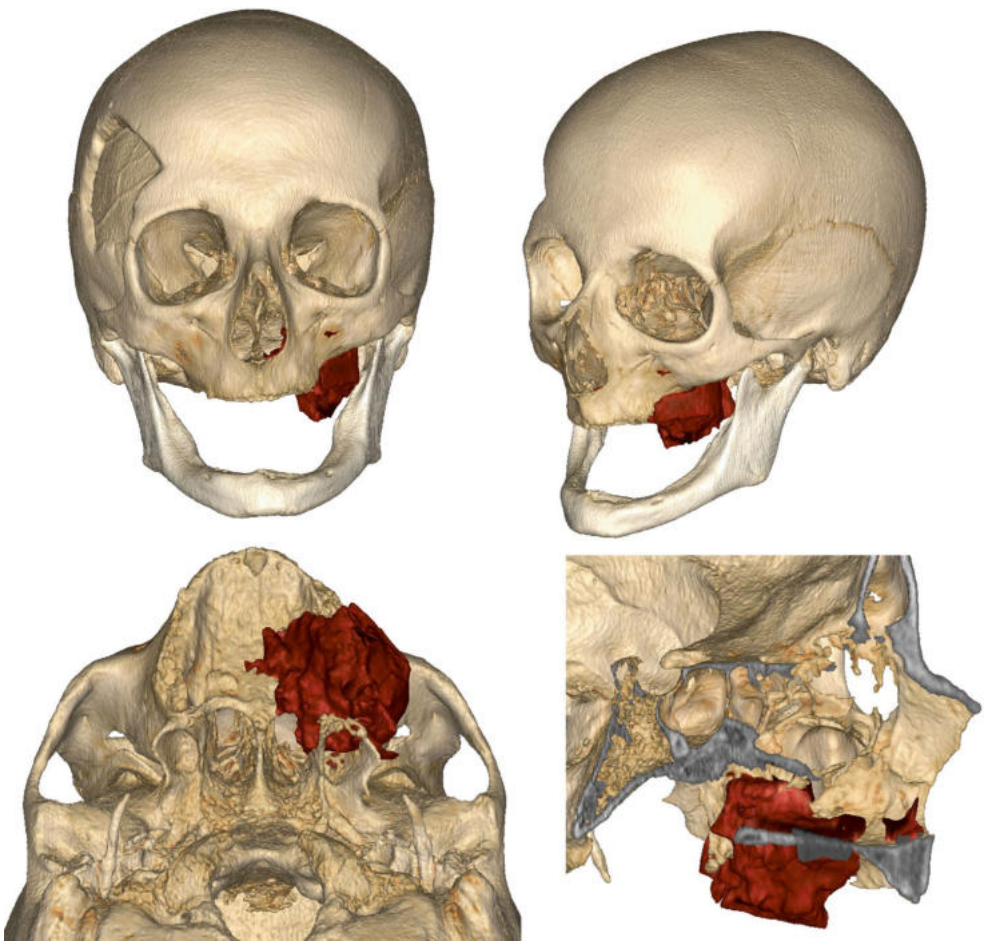


Fig. 9 VSP with voxel coloring and medial view with model cropping across the sagittal plane

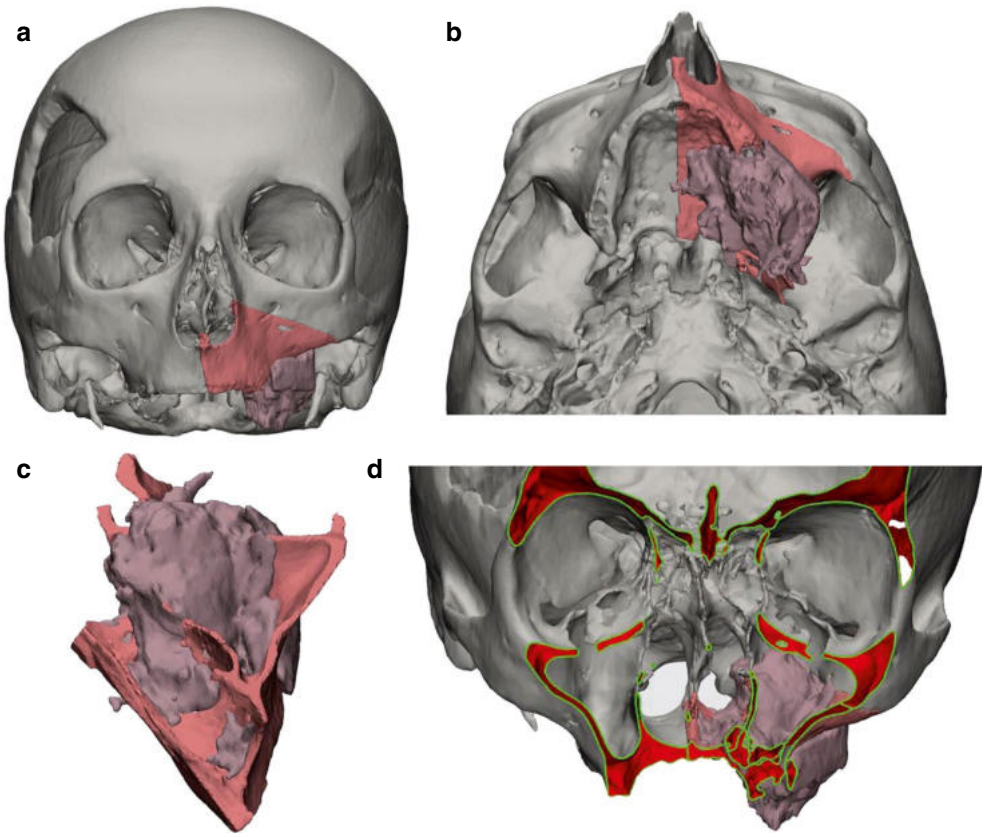


Fig. 10 Planned resection. (**c**) and (**d**) (cropped) shows that the resection is adequate also for the intrasinus extension of the tumor. (**a**) is top left, (**b**) top right, (**c**) bottom left, (**d**) bottom right

designed through a side mirroring (see Chapter "Principles of Cranial Reconstruction") (Fig. 11).

Surgery

The whole surgery was conducted intraorally. At first, the mucosal lesion was circumscribed using electrocautery, and the mucosa was incised in macroscopically healthy margins. Then, osteotomies were conducted along the palate and the anterior-lateral maxillary wall. Finally, pterygomaxillary disjunction was completed using a curved chisel, and the specimen was removed. A hemicoronal ipsilateral incision was performed, and deep subfascial dissection was used to harvest the temporalis muscle flap, which was translocated intraorally through the infratemporal fossa tunnel. A contralateral hemicoronal incision was performed to access the skull defect and perform the cranioplasty (Fig. 12).

4.1.2 Class II Total Maxillectomy for Chondroblastic Osteosarcoma

Clinical History

This patient was referred to maxillofacial consultation for a progressive and painful bulging of his right midface with loss of his corresponding upper teeth. The patient underwent CT scan showing the coexistence of addensating and rarefaction lesions around the right maxillary area. He was subject to a biopsy, which was unable to pose a histological diagnosis, showing generally a spindle cell aspect possibly associated with a sarcomatous lesion. A wide class II maxillectomy was performed and extended superiorly but with the intent of preserving the inferior orbital rim and the orbital floor.

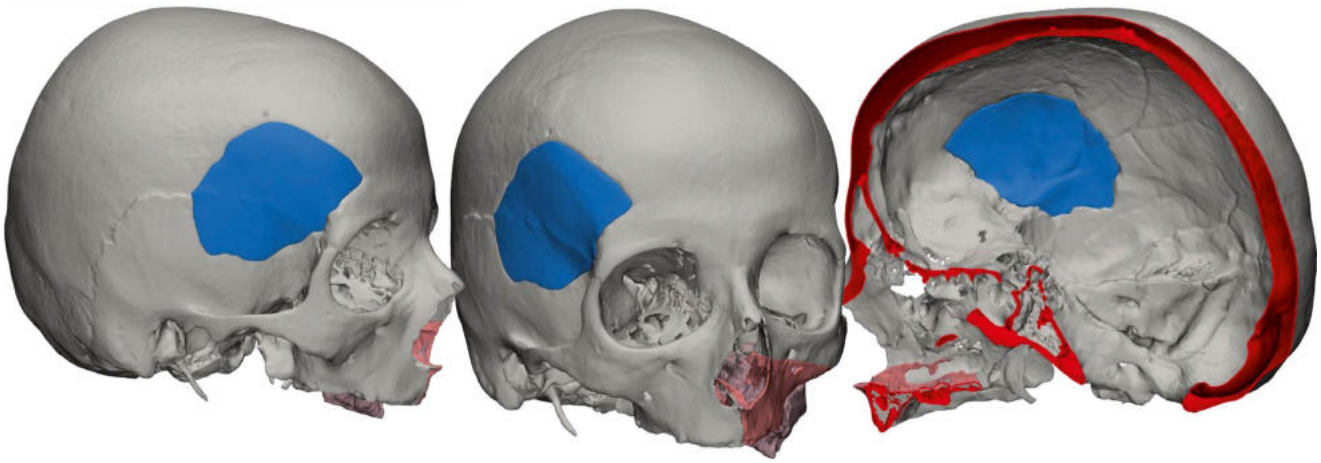


Fig. 11 Contextual planning of a cranioplasty prosthesis to fill the existing defect

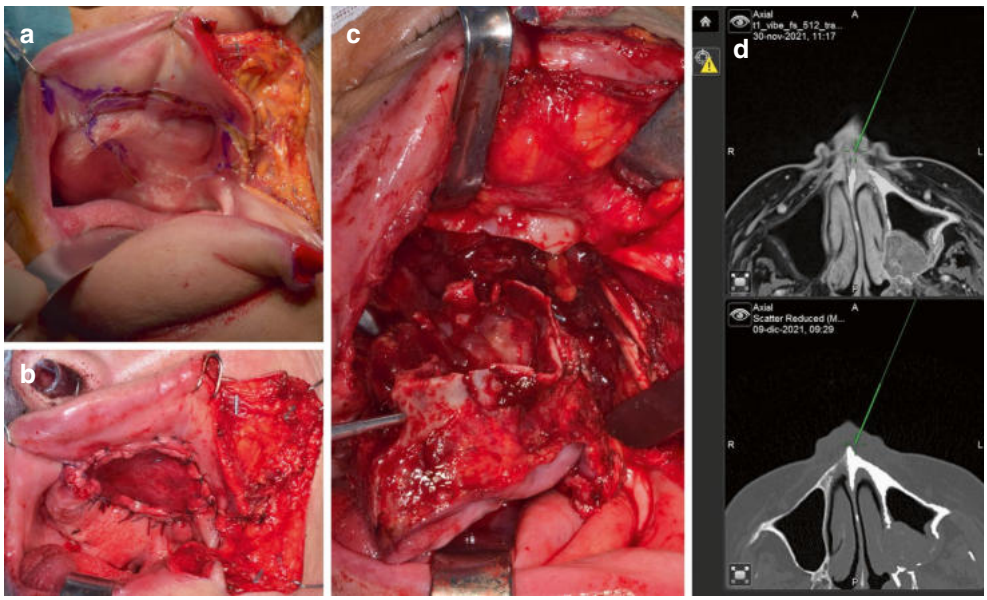


Fig. 12 Navigation of resection margins (bright contour overlapped to CT obtained as a result of resection STL mapped on DICOM ("reserse DICOMization")

Virtual Surgical Planning

A total maxillectomy was simulated by placing the mesial resection plane in the midline. The lateral resection plane was positioned slightly inferior to the inferior orbital margin and included the infraorbital nerve as well owing to its proximity to the lesion; the osteotomy was continued laterally to include a significant amount of the zygomatic body. Moreover, almost the entire nasomaxillary buttress with the piriform notch attached was included in the resection, along with the inferior and middle turbinates. Inferiorly, the anterior resection plane was prolonged up to the level of the nasal spine to include the right hemipalate. Posteriorly, the osteotomy of pterygoid plates was performed as much cranially as possible, as the inferior third of the pterygoid plates was infiltrated, along with the maxillary tuberosity and the posterior antral wall. The complexity of this resection, especially considered in its posterior component, made the use of resection planes alone inadequate, and thus the use of freehand osteotomies was required (Fig. 13). In this case, a virtual soft tissue model was not requested, as the pathology originated primitively from the bone and thus was highly detectable in CT scan.

Surgery

An intraoral approach identical to the previous case was adopted to perform the maxillectomy, still feasible despite its substantial upper extension (however, the absence of orbital involvement limited it to class II). Resection was performed under navigational guidance to check the accuracy of resection margins (Fig. 14). The temporalis muscle flap was used to reconstruct the diaphragm between the nasal and the oral cavity. The patient underwent subsequent cycles of proton therapy with concurrent cycles of chemotherapy and was free from disease after 3 years of follow-up.

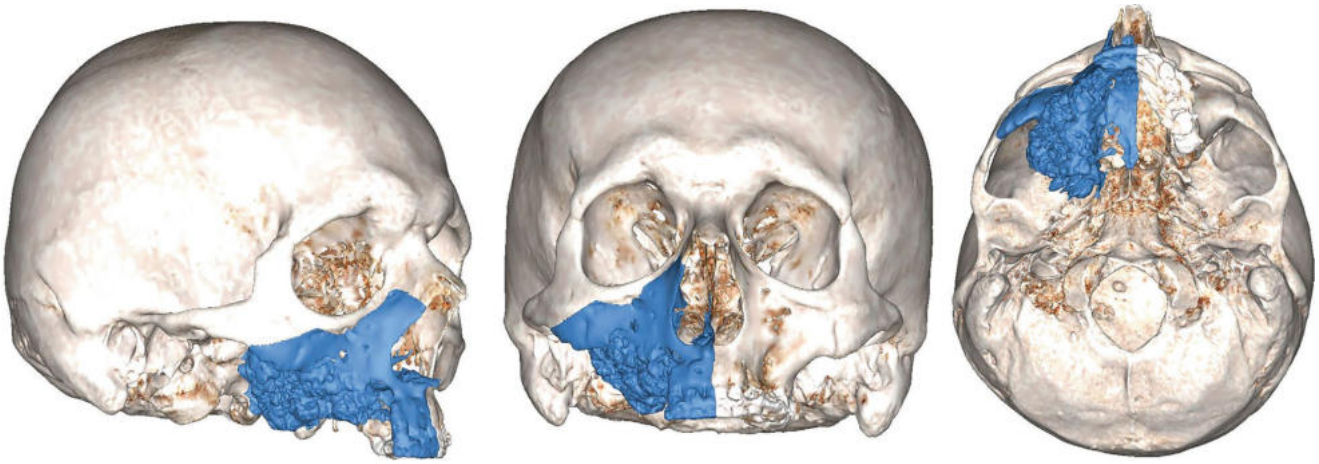


Fig. 13 Type III maxillectomy for a chondroblastic osteosarcoma

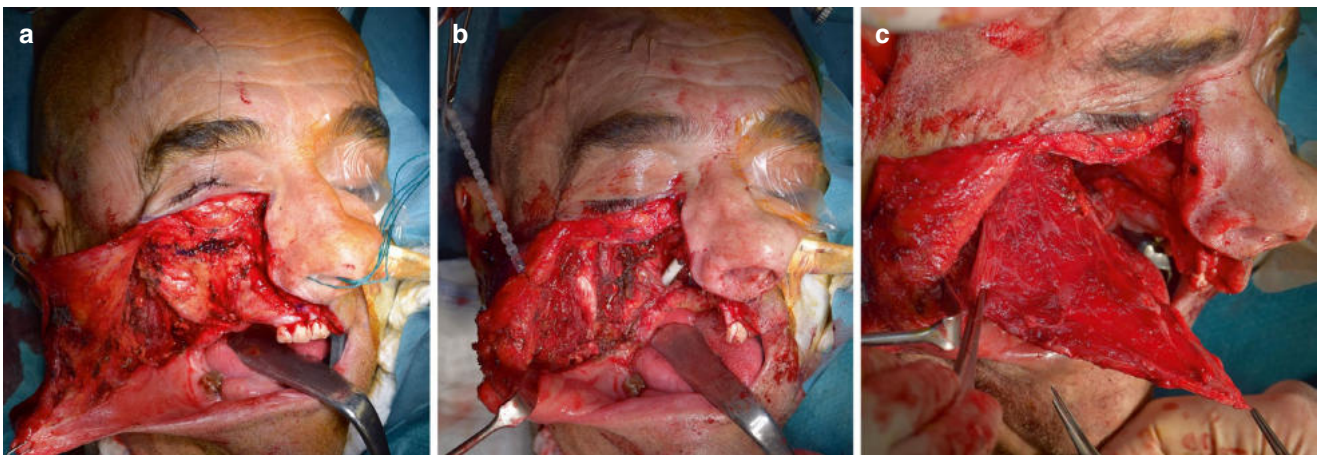


Fig. 14 Intraoperative view: (**a**) exposure; (**b**) maxillectomy; (**c**) temporalis reconstruction

4.1.3 Class II Segmental Maxillectomy with Subsequent Fibula Reconstruction for Squamocellular Carcinoma of the Palate

Clinical History

This patient was referred to our department for oral bleeding and the presence of a bulging lesion in his right hemipalate, which was biopsied and resulted in squamocellular carcinoma. The patient underwent CT scan with the high-resolution protocol, as well as MRI, to define the boundaries of the lesion, located posteriorly, with the masticator space. Additionally, the patient underwent intraoral scanning of both the dental arches, the palate mucosa and the lesion within to clarify the soft tissue resection as well. The young patient was candidate for a class II segmental maxillectomy, with preservation of the anterior maxilla mesial to element 1.4 and subsequent reconstruction of bone with a fibula free flap. This case will be continued in Chapter "Virtual Surgical Planning in Midfacial Reconstruction" from the reconstructive point of view.

Virtual Surgical Planning

CT scan was segmented with a highly conservative threshold to preserve tiny bone areas that could mark the erosion sign caused by the lesion in the posterior maxillary area. Subsequently, intraoral scan was imported as STL file and carefully aligned with the CT scan, enabling to translate the detail of dental cusps within the skeletal model. MR was registered with the CT scan, and the tumor was segmented, enabling to analyze the tumor model in relationship with the skeletal anatomy derived from CT scan. This analysis revealed that the tumor had a posterior extension beyond the level of the pterygoid plate, within the belly of the lateral pterygoid muscle. In order to define the three-dimensional cuff of tissue around the tumor to perform a radical en-bloc resection, the lateral pterygoid muscle was simulated as well. Subsequently, a class II segmental maxillectomy with poste-

rior extension to the pterygoid plate and including a subtotal excision of the lateral pterygoid muscle was planned. Care was taken to preserve the premaxilla to enhance the esthetical appearance of the patient after surgery. For this purpose, the skeletal-dental model was merged with the MR-derived tumor and lateral pterygoid muscle and the resection was simulated on such structures using a free-hand brush marking technique (Fig. 15). One peculiarity of this resection is that, in consideration of the contextual reconstruction using the fibula free flap rather than a soft-tissue flap, it was mandatory to maximize the bone-to-bone contact, thus the anterior resection margin, as well as the resection margin located in the zygomatic body, were defined using planes. The same planes were used to model resection guides enabling to prepare the surgical margins with highly precise linear cuts, to optimize the recipient site for the fibula free flap (Fig. 16). STLs of surgical planning were imported into the navigator and the full ablative procedure was checked using intraoperative navigation.

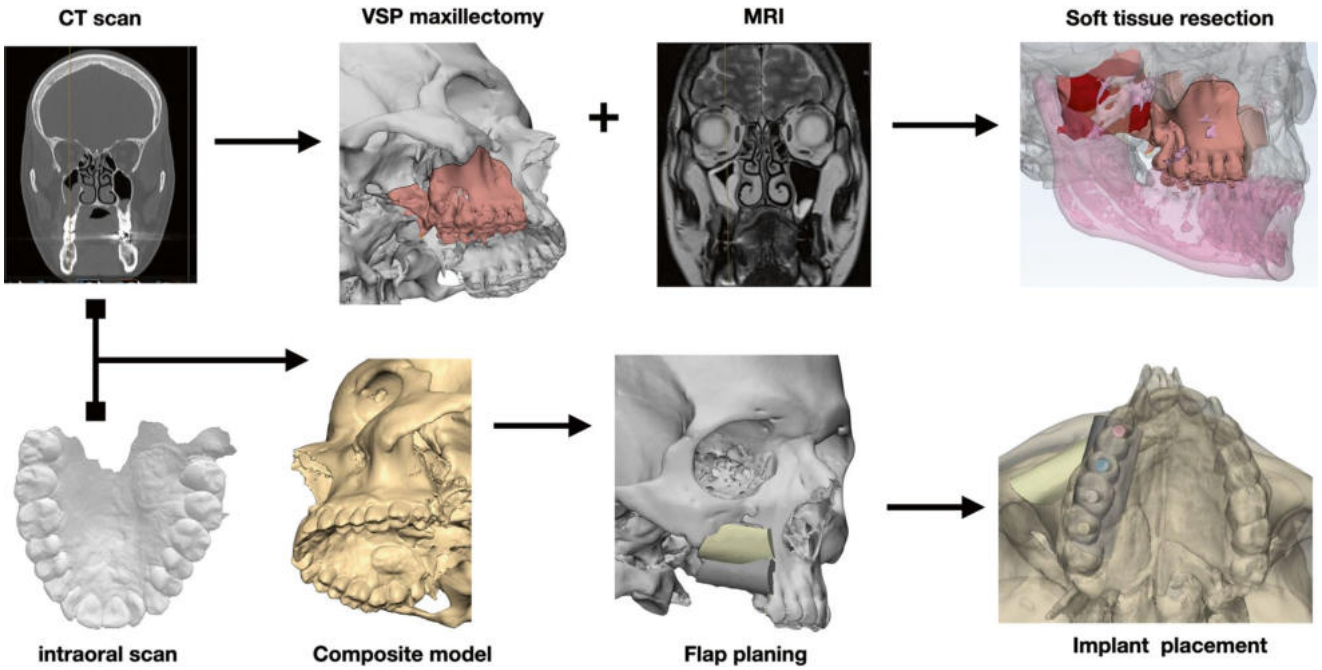


Fig. 15 Algorithm to associate maxillary resection to fibula planes for subsequent reconstruction. The core concept is associating cutting planes with those used for reconstruction, predefining linear contact interfaces

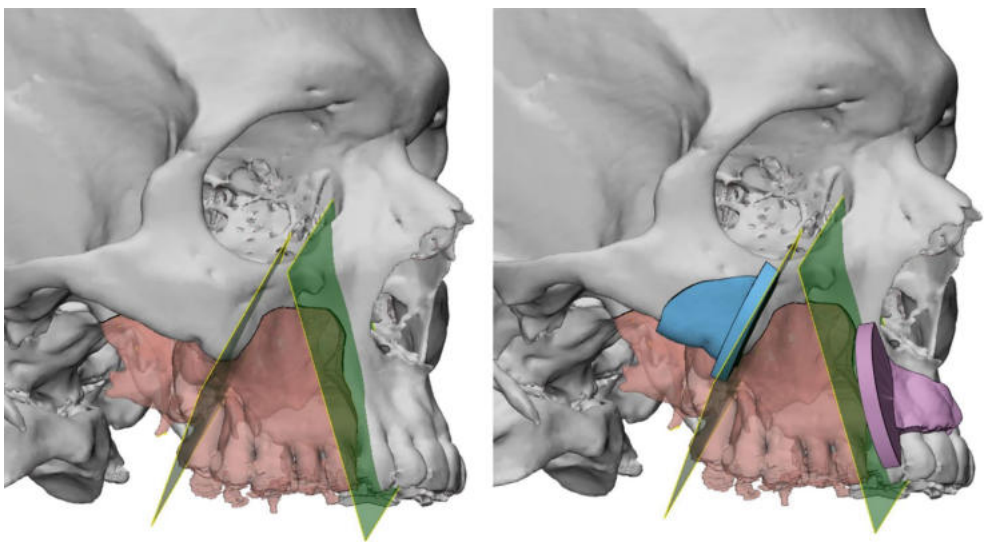


Fig. 16 Linearization of a curved resection to enable subsequent fibula reconstruction

Surgery

After the dynamic reference frame (DRF) with its three optical spheres was mounted on the patient's head and the navigator was calibrated, a Weber-Ferguson incision was designed in the right midface, starting with a midline upper lip split and continuing along the genio-nasal sulcus up to the subciliary line. A composite, myocutaneous cheek flap was elevated and rotated to uncover the underlying bone, followed by preseptal lower eyelid dissection to expose the inferior orbital margin and the whole right midface. Surgical guides were positioned on the mesial and on the distal resection margin, enabling to complete resection. Palate osteotomies and the posterior resection of the lateral pterygoid muscle belly were performed, enabling to excise the lesion within macroscopically disease-free margins. Navigational guidance assisted the accuracy of osteotomies in deep spaces, including the masticator spaces (Fig. 17). The ablated specimen was compared to its 3D printed replica showing optimal correspondence and a resection comparable to the surgical plan (Fig. 18). Neck dissection was performed before accessing the midface and prepared the vessels for microsurgical anastomoses.

4.1.4 Class III Segmental Maxillectomy for Odontogenic Myxoma Extending up to the Orbit

Clinical History

This case refers to a young lady presenting to clinical attention with a progressively swelling and a sensation of bulging in the upper left fornix. In the last weeks, she also referred to diplopia appearing in certain gaze positions. She underwent an intraoral biopsy revealing a whitish, solid tissue, whose histopathological examination revealed to be an odontogenic myxoma. The patient underwent high-resolution CT and MR according to the aforementioned protocols for the multilayer anatomical reconstruction. In addition, an intraoral scan was acquired as well to define the bulging mucosa in the oral cavity. MR revealed that the soft tissue component of the lesion extended beyond its osteoaddensating component visible at CT inspection, showing protrusion of the lesion up to the anterior-medial orbital walls, within the nasal cavity and in the infratemporal fossa (Fig. 19).

Virtual Surgical Planning

A thorough anatomical reconstruction of 3D models was mandatory to analyze the case and tailor the bone resection to be as much conservative as possible, given the nature of the lesion. First, intraoral scan was coregistered with the CT bone model to bring both the occlusal detail and the deformation of the oral mucosa in correspondence with the underlying lesion. The entire process was performed in 3-matic using a point-to-point gross alignment, then refined using global registration; voxel coloring was applied to rendering to maximize the realism. Subsequently, the tumor was segmented in multiplanar projections using the smart brush tool in Mimics, until a reliable 3D representation was yielded; care was taken to validate its anatomical relationship with the underlying bone. Given the proximity of the lesion to

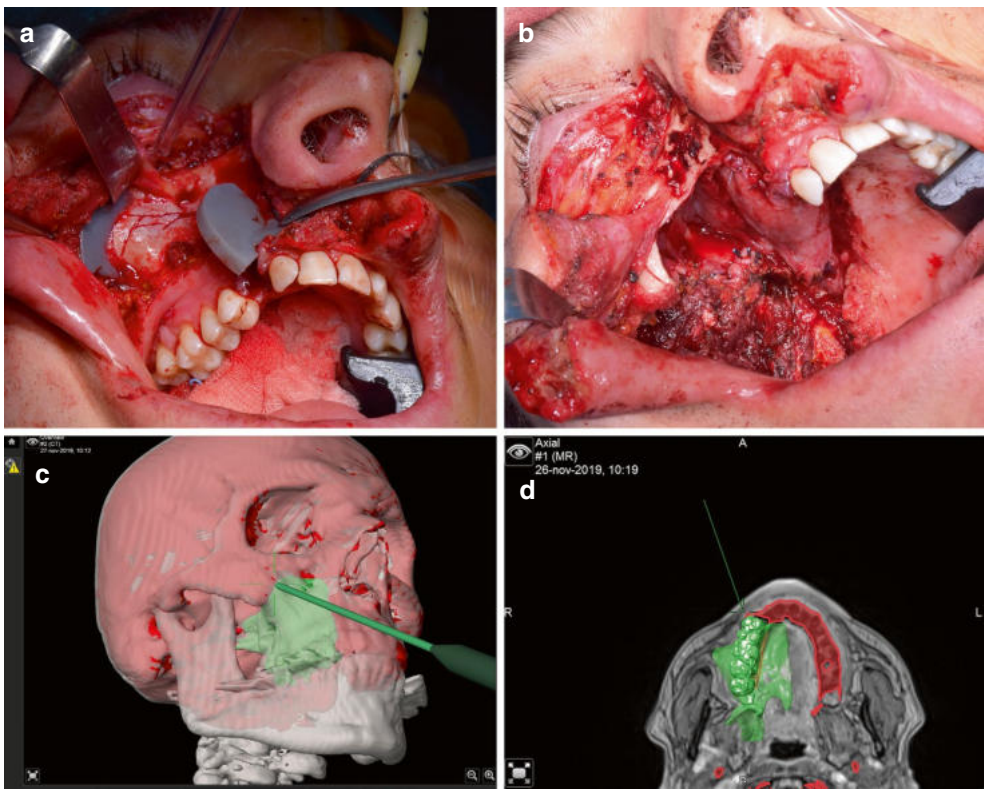


Fig. 17 Navigation of VSP for conduct a computer-guided maxillectomy

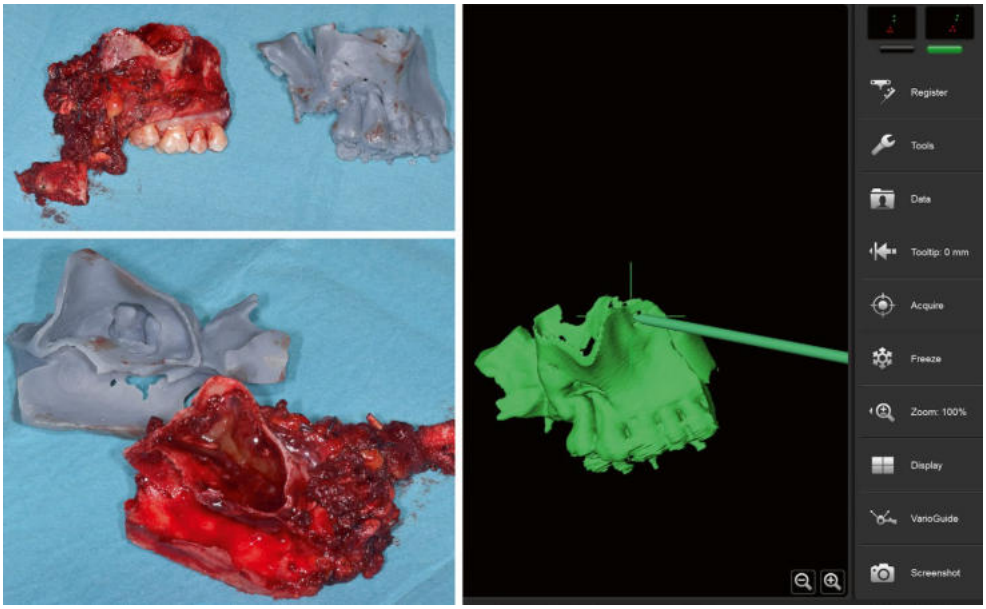


Fig. 18 Mapping resection margins ensures high correspondence between the specimen and its planned 3D printed replica

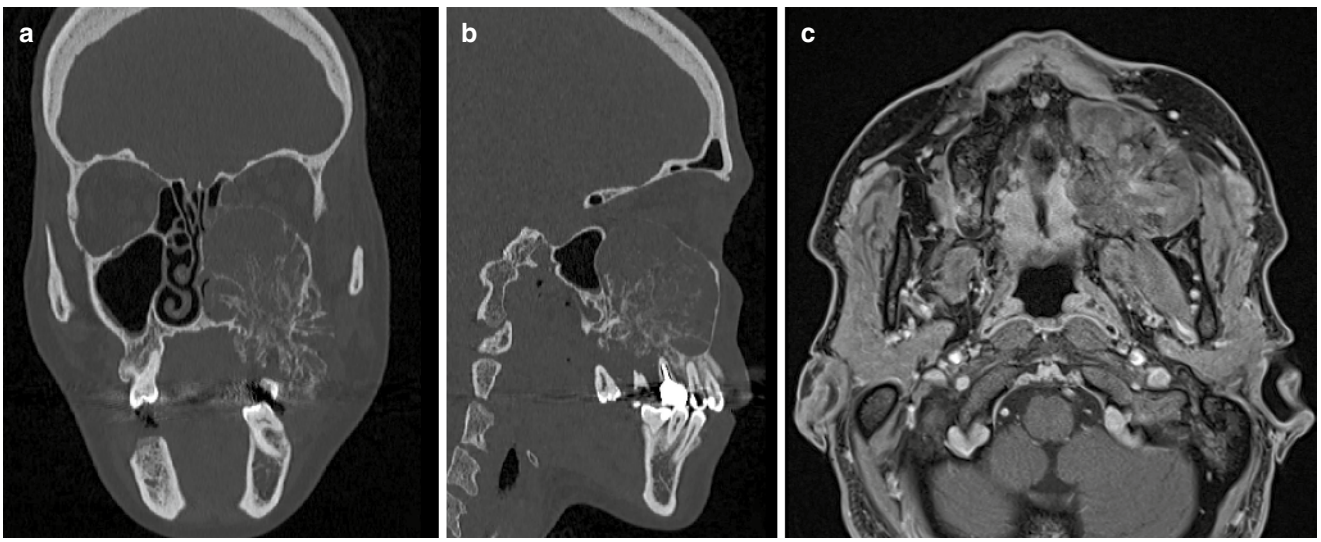


Fig. 19 Massive odontogenic myxoma seen in CT and MR T1-VIBE

eye, both the globe and extraocular muscles, as well as the optical nerve, were reconstructed. Last, TOF sequence was carefully segmented to represent the arterial vascularization; in particular, great attention was given to reconstruct the entire course of the internal maxillary artery (Fig. 20). Given such anatomical complexity, a freehand marking of the osteotomy was performed in 3-matic to yield a class III maxillectomy, extending to the entire orbital floor, but with the preservation of the premaxilla and a conspicuous amount of the nasomaxillary buttress for their positive impact on the final esthetics. Posteriorly, the resection was designed high, up to the level of the inferior orbital fissure, owing to the extent of disease in the infratemporal fossa. As the reconstruction was based on the use of a customized implant alongside with a bone flap, resection margins were optimized by placing three planes in the bone-to-metal surfaces, respectively at the level of the premaxilla, naso-maxillary buttress, and zygomatic body (Fig. 21). Based on the same planes, a

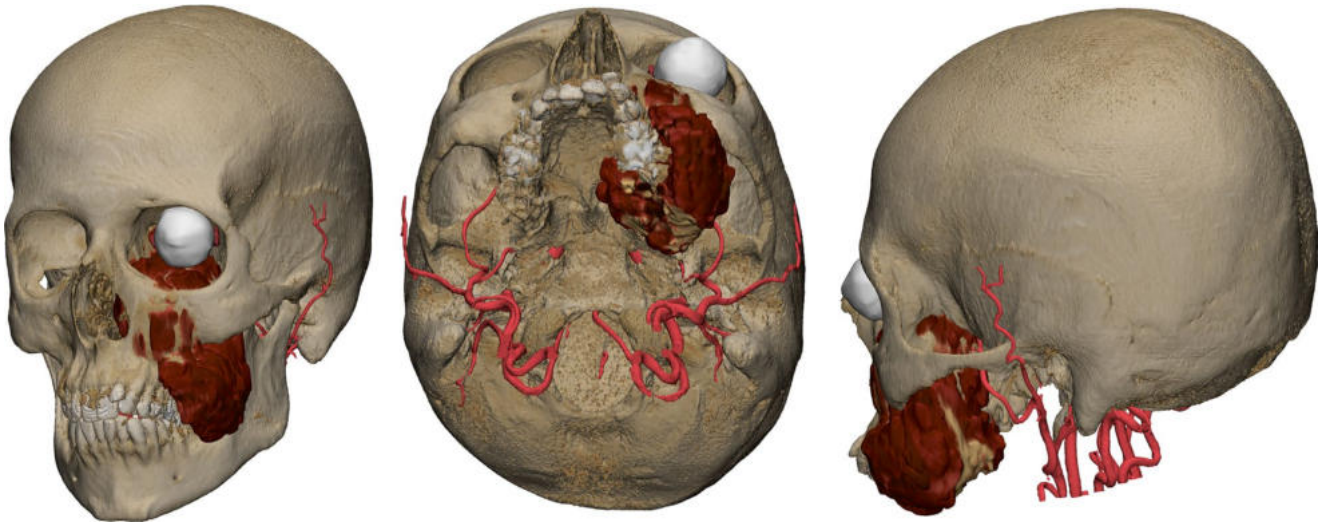


Fig. 20 High-quality segmentation with vessel merging and voxel coloring

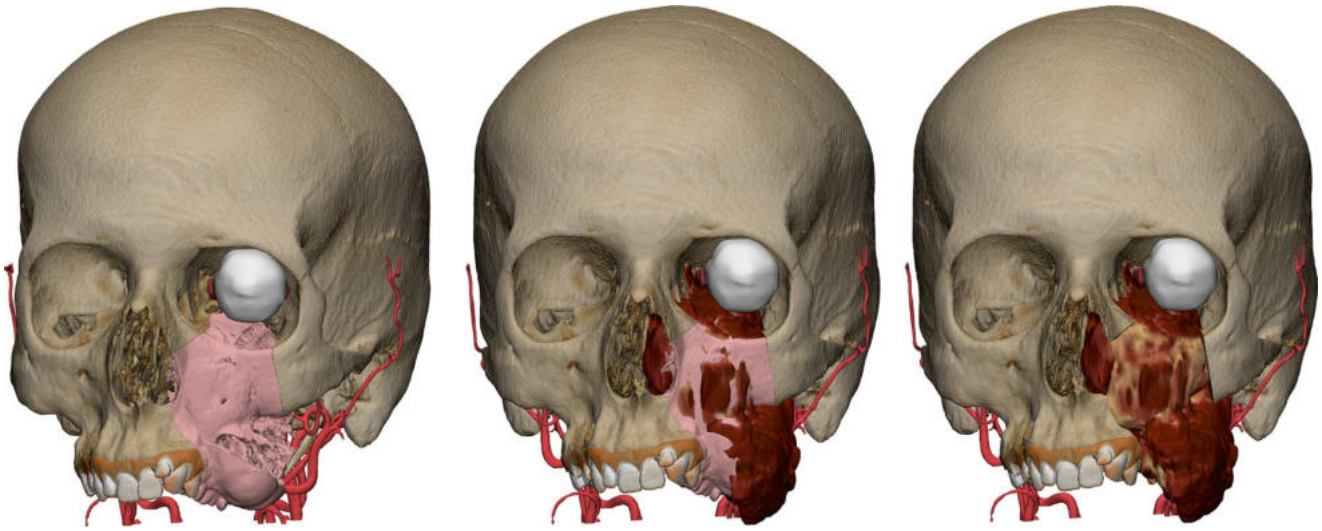


Fig. 21 Sequences of virtual resection

resection surgical guide was designed to facilitate the shaping of such bone margins across the zygomatic body, the premaxilla and the nasofrontal buttress. The guide was conceived as a triple guide system for each of the buttresses joined by curved bridges, elevated enough to enable underlying osteotomy tracing. Each screw insertion site and its corresponding guiding cylinder matched that of the final implants (Fig. 22). Resection surgical guide was printed in a biocompatible resin (Surgical Guide Resin, Formlabs, Somerville, MA) and tested in the printed replica of the skull (Fig. 23). The project was imported into Mimics Viewer (Materialise, Leuven, BE) for AR and deployed within MagicLeap 2 headset (Magic Leap, Plantation, FL, USA) to be used in AR during surgery.

Surgery

First, the navigator was calibrated to track lesion removal during surgery, and MagicLeap headset was worn by the

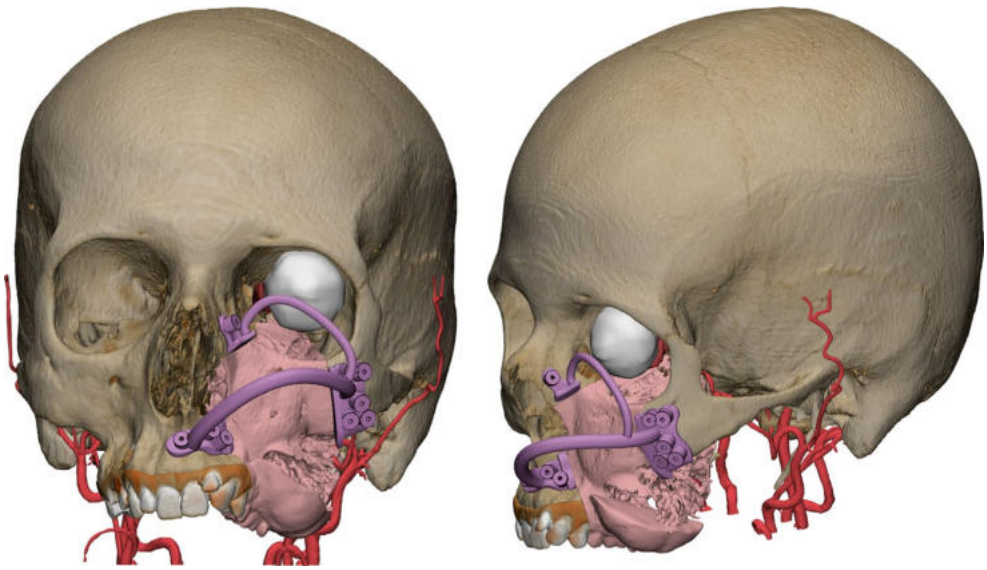


Fig. 22 Surgical guide designed in 3-matic for resection across all the craniofacial buttresses

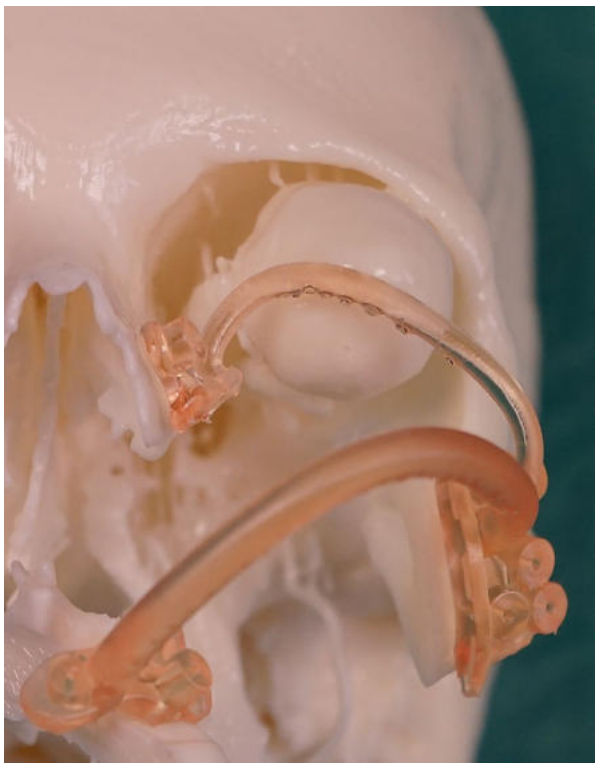


Fig. 23 3D printed surgical guide and fitting test on the craniofacial model

surgeon to position the augmented reality image overlying the patient (Fig. 24). A Weber-Fergusson incision was performed from the upper lip to the inferior eyelid crease. A cheek myocutaneous flap with upper lip split was elevated, in continuity with an orbicularis oculi flap along with palpebral skin through a preseptal dissection plane. The incision proceeded intraorally at first in the upper fornix, then curving medially distal to tooth 24 just over the palate. The palatal fibromucosa was dissected from the lesion. Accurate elevation of the periorbital layer was conducted from the tumor, which showed a pseudocapsule and could be easily mobilized. The surgical guide was placed over exposed skeletal surfaces and a stable fitting was appraised. Piezoelectric osteotomies were performed in correspondence with sites defined by VSP (Fig. 25). In addition, a midline palatal osteotomy was conducted to perform the planned maxillectomy, whose boundaries were checked with navigation to ensure their agreement with the VSP. The maxilla and the lesion were removed. Compared to a malignant tumor, the lesion was well enucleated with preservation of the mucosa of the lateral nasal wall.

4.2 Excision of Lesions Located in Deep Facial Compartments

As mentioned previously, deep facial compartments are anatomical locations of difficult access and impaired visibility that can harbor a variety of pathological lesions, both benign and malignant. Within such spaces in the splanchnocranium, it is possible to include the pterygomaxillopalatine fossa, the parapharyngeal space, the infratemporal fossa, and the deep masticatory space, which has a crucial role in neoplastic spreading as it can become infiltrated by advanced malignant processes. In particular, the deep masticatory space is highly important from both a functional and prognostic perspective: it has a strong impact on the prognosis of the disease, as tumors infiltrating such space are classified as T4b; and from the functional perspective, when its muscles become infiltrated the patient presents with trisma and limited mouth opening, a factor that contributes to complicate surgical

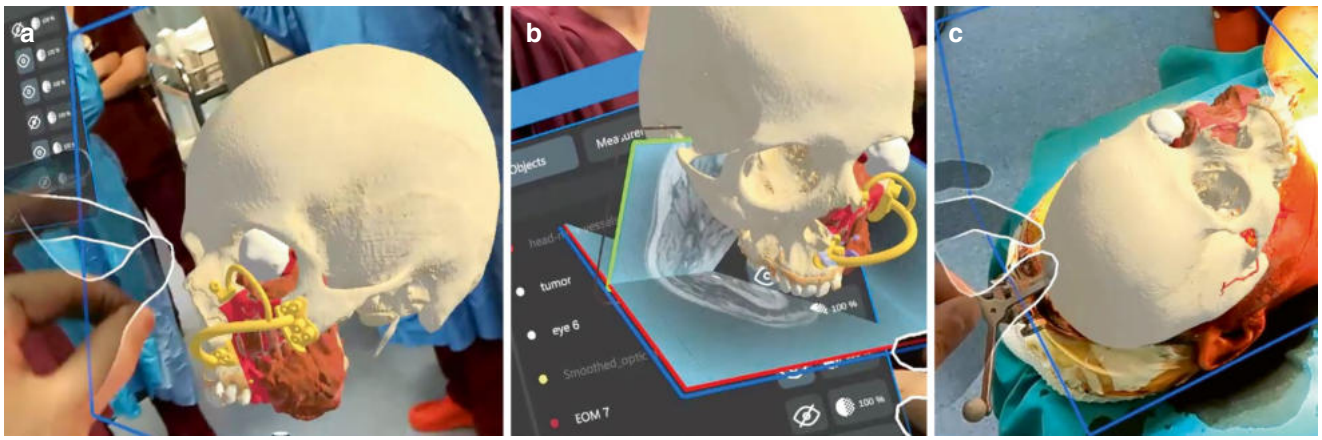


Fig. 24 Augmented reality (AR) driven resection

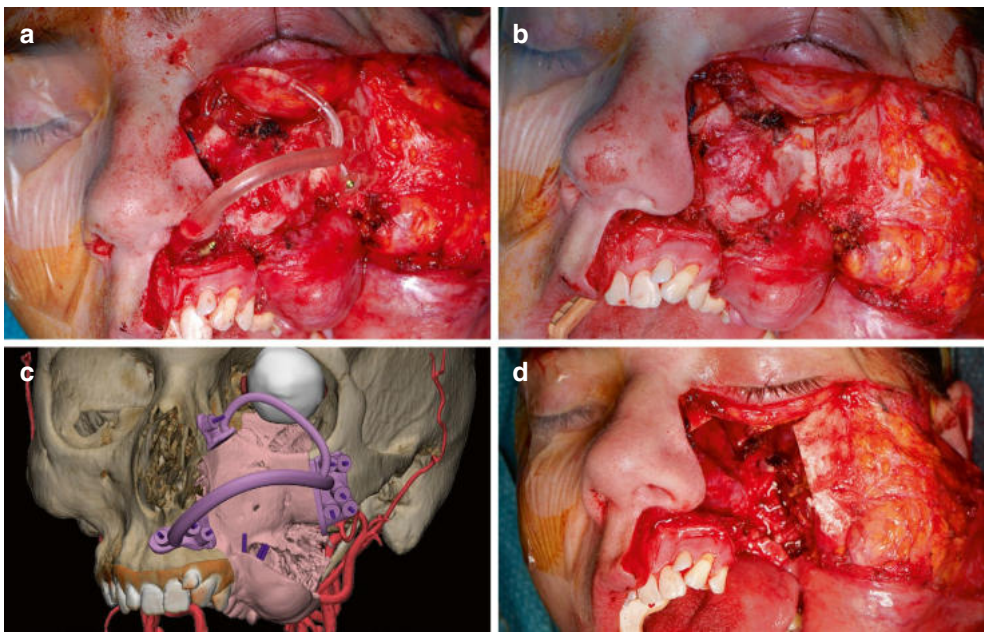


Fig. 25 Intraoperative view. Computer-guided resection using the surgical guide ensures optimal correspondence with the VSP

maneuvers. In many cases, such lesions, if resectable, are excised without reconstruction; on the other hand, if they represent the extension of head and neck tumors originating in other sites, they are generally unresectable [9].

In such regions, VSP plays a crucial role, as it allows to create patient specific virtual models that are highly impactful in elucidating the complex anatomical relationships between a tumor mass and surrounding skeletal, muscular, and vascular structures. Moreover, VSP allows to establish the most appropriate surgical accesses and to define the resection contours. Intuitively, given the restricted access possibilities, surgical guides do not significantly contribute to the excision of lesions located in such spaces. The prominent role is surely represented by image-guided surgery, which allows real-time, non-invasive, tracking of the operator position. In this regard, navigation error was estimated to be about 1 mm in the craniomaxillofacial area in an in vitro study where registration was based on anatomical landmarks [14]. The most innovative applications of image-guided surgery include augmented reality (AR), which, as shown in the previous clinical case, can assist the surgeon by bringing into his sight field an augmented perception of the underlying anatomy, including the tumor and its relationships with the crucial structures.

4.2.1 Relapse of Pleomorphic Adenoma Located in the Parapharyngeal Lobe of the Parotid

Clinical History

This 73-year-old patient was referred to our center after a routine neck ecography, which showed a mass in the parapharyngeal space. The patient was subject 20 years before to

the enucleation of a pleomorphic adenoma of the right parotid gland and did not present any related symptom. A fine needle aspiration biopsy (FNAB) was performed, with evidence of a pleomorphic adenoma, possibly related to a recurrence. MR and CT scans were performed and coregistered according to the protocol for multilayer anatomical reconstruction.

Virtual Surgical Planning

Accurate segmentation of T1 VIBE 512 × 512 px MR sequence was performed using the smart brush tool in Mimics to reconstruct the parotid gland and the tumor located at its parapharyngeal lobe (Fig. 26). Likewise, TOF 3D multi-slab sequence was segmented easily using a thresholding algorithm to reconstruct the arterial vasculature; likewise, 3D venographic phased-contrast sequences were used to segment the venous vasculature, which proved highly useful to elucidate the close relationship between the tumor, internal and external carotid artery (ICA/ECA), and the internal jugular vein (IJV) (Fig. 27). Finally, after image coregistration, CT was used to reconstruct the skeletal anatomy, and care was taken to assess that each vessel entering the intracranial space matched its skull base foramen. This can be considered a direct proof that the registration was anatomically correct. Following anatomical reconstruction of the virtual patient, a vertical ramus osteotomy (VRO) was simulated to widen the surgical corridor to excise the disease [15]. The full project was exported in the surgical navigator (Fig. 28).

Surgery

The DRF was installed and navigator calibrated. A parotidectomy-like incision (modified Blair's) was performed; the SMAS was isolated from the subcutis, the great

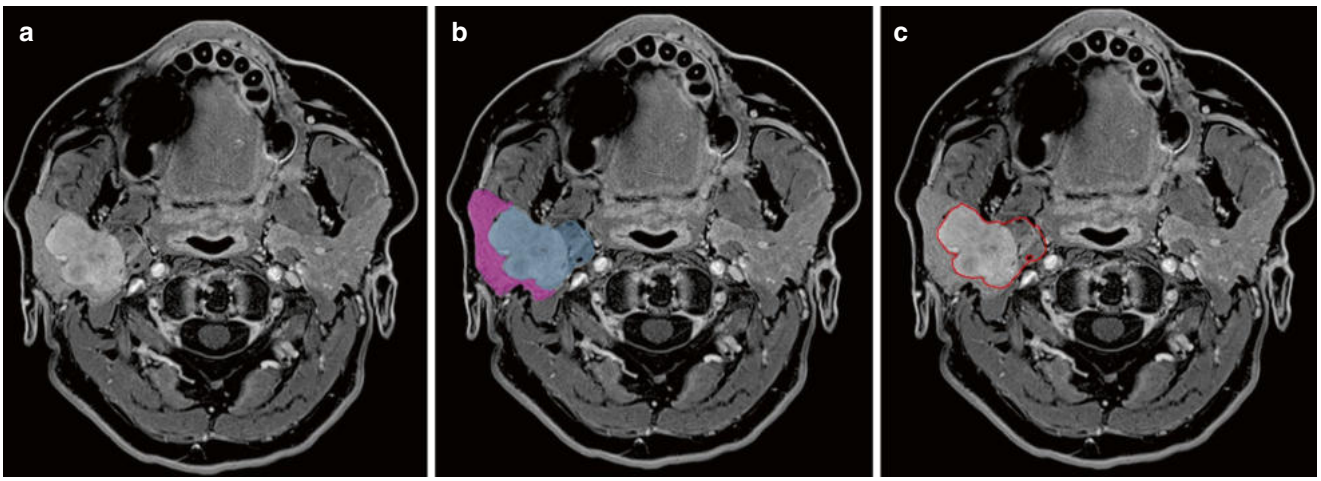


Fig. 26 Segmentation of a deep-lobe parotid pleomorphic adenoma. Segmentation masks clearly define the parotid parenchyma (purple) from the lesion (blue)

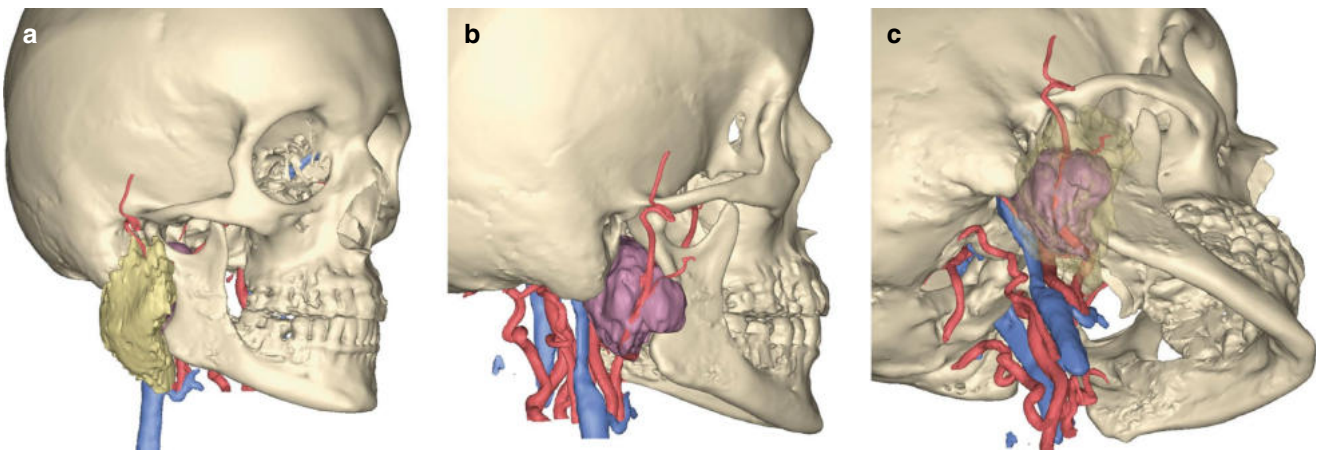


Fig. 27 Virtual model reconstruction, showing the tumor mass enveloping around the posterior mandibular border and its contact with vascular structures

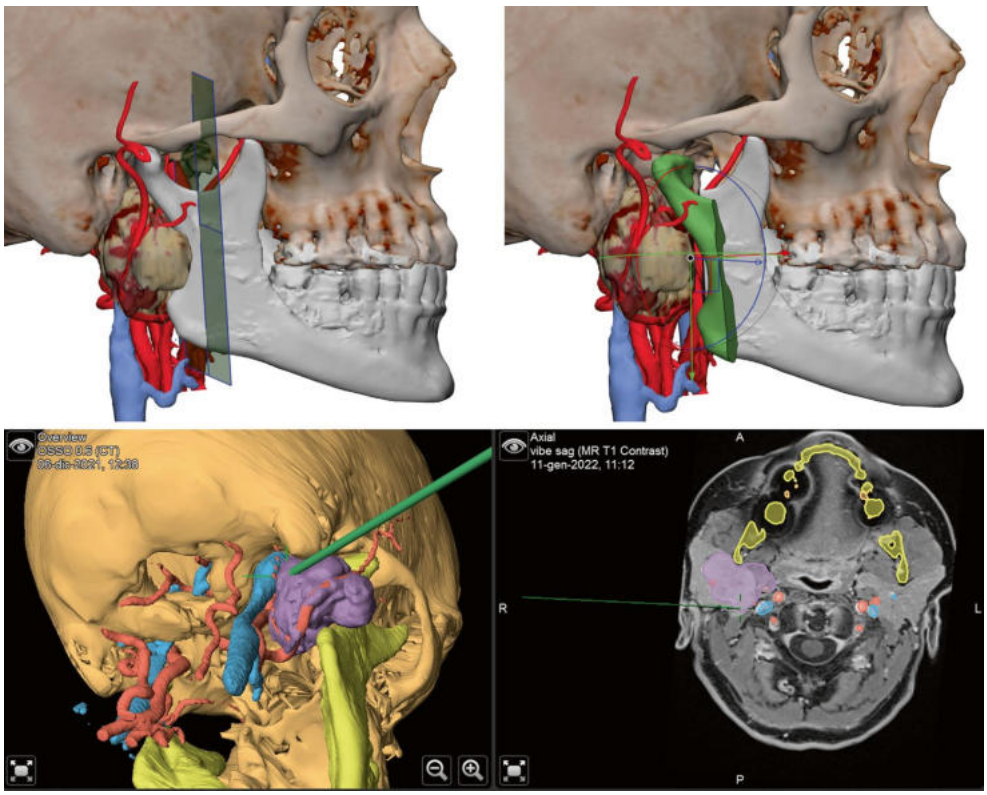


Fig. 28 Strategical VSP considers performing a vertical ramus osteotomy to efficiently expose the lesion. The level for osteotomy is decided by positioning a cut plane. In the bottom panel, navigation targeting helps identifying the lesion

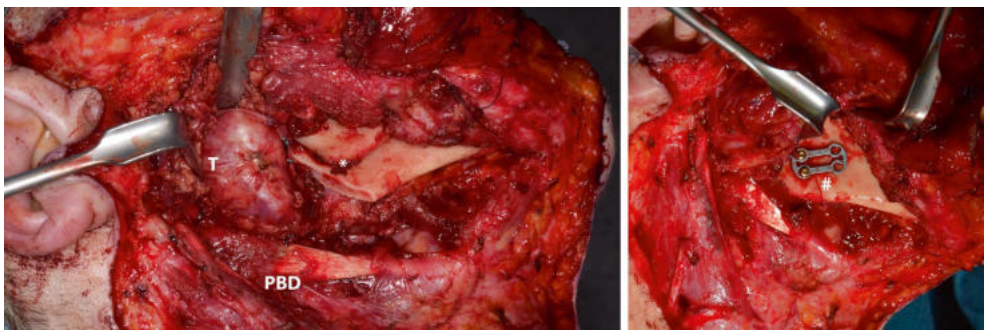


Fig. 29 Intraoperative equivalent, with VRO performed (left), and fixed with a miniplate (right)

auricular nerve was preserved, and the main trunk of the facial nerve was isolated. The parotid gland was lifted upwards, the masseter muscle incised, and a VRO was performed to create a surgical corridor to the deep lobe of the parotid in the middle of the mandibular ramus. Intraoperative navigation allowed to target the lesion, IJV, ICA, and ECA as the dissection proceeded. The lesion was selectively excised sparing nearby structures, then the mandibular osteotomy was fixated using rigid titanium plates while maintaining the correct occlusion (Fig. 29).

4.2.2 Adenoid Cystic Carcinoma Located in the Pterygomaxillopalatine Fossa

Clinical History

A 37-year-old lady was referred to ENT department for the progressive onset of left deafness. She underwent audiometric testing that did not show any neurosensory or conduction abnormality. She was then sent for MR, which revealed a mass located in the pterygomaxillopalatine fossa and parapharyngeal space in close proximity to the Eustachian tube. Owing to its location and radiological features, the mass was suspicious, and the patient was candidate for the removal of the lesion. As the lesion was located posterior to the pterygoid plates, underneath the skull base and engaging foramen rotundum and foramen ovale, it was mandatory to approach surgical planning with a proper VSP study, as well as image-guided surgery. For this reason, MR was repeated with the parameters suitable for multilayer anatomical reconstruction, and high-resolution CT scan was performed as well. Owing to the complexity of this clinical case, a double surgical approach was hypothesized, both open and endoscopic; thus, the planning was conducted accordingly.

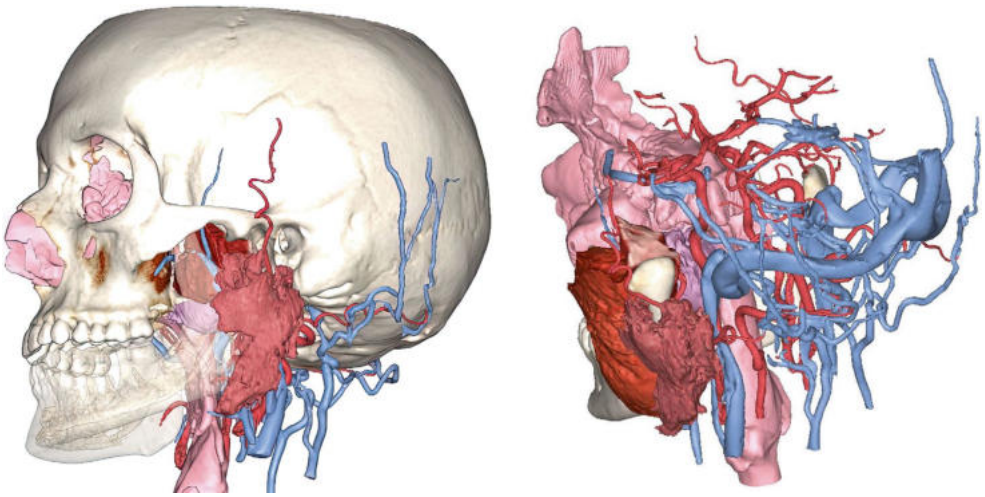


Fig. 30 Advanced virtual model creation representing a virtual anatomical reconstruction for the patient. It is achieved by maximizing the efficacy of acquisition protocols, coregistering sequences, and carefully applying segmentation methods. In addition to vascular structures, the parotid gland, masseter, lateral pterygoid and airways have been segmented

Virtual Surgical Planning

Segmentation and 3D model reconstruction had the purpose to reconstruct a high-fidelity virtual anatomical representation suitable for both open and endoscopic surgical simulation (Fig. 30).

- High resolution CT was segmented with thin-structure preserving threshold, to reconstruct thin bone structures including as much as possible of ethmoid laminae and turbinates. In addition, mucosal lining representing the walls of paranasal sinuses and airways was reconstructed using an HU range corresponding air density (between −1024 and −300 HU). The model was then hollowed by leaving a wall thickness of approximately 1 mm, enabling to reconstruct the paranasal sinus anatomy and provide a reliable environment for the virtual endoscopy.
- VEN 3D PCA sequence performed using 3T magnet and a 256 × 256 matrix enabled to effectively segment venous vasculature using a combination of thresholding and dynamic region growing. In particular, this method enabled a detailed reconstruction of the EJV, IJV, and occipital veins, including their collaterals.
- 3D TOF (or s3DI) sequence was used to segment arterial vessels from the carotid bifurcation to the Willis polygon, allowing to characterize both the external and the internal carotid artery system.
- A combination of segmentation based on both 3D FLAIR and 512 × 512 T1 VIBE sequence was used to segment the tumor, the lateral pterygoid muscle, as well as the parotid gland.

Virtual surgical planning included a strategic transmandibular approach by positioning the osteotomy plane between teeth 3.2 and 3.3. However, as the location of the lesion was high and attached to the root of pterygoid plate, an osteotomy of pterygoid plates was planned to be performed endoscopically. For this reason, virtual endoscopy was also implemented in this case (see Sect. 4.4.1). Last, a maxillary antrostomy on both the anterior and posterior antral wall was planned to enable frontal exposure of the lesion and further mobilization (Fig. 31).

Surgery

The entire procedure was conducted under navigational guidance. After the endoscopic part of the procedure, a submandibular incision with midline inferior lip split was performed to prepare the transmandibular access. The incision was continued intraorally along the lateral oral floor through the milo-hyoid muscle. The mandible was separated using piezo-surgical cut and opened to expose a straightforward surgical corridor to the lesion, whose inferior pole was detected. Intraorally, a maxillary vestibular incision was performed and the anterior-lateral maxillary antral wall was exposed; then, maxillary antrostomy was completed to gain an additional access to the higher pole of the neoplasm. After careful dissection from both the ICA and the EJV, and after ligation of the internal maxillary artery and section of the mandibular nerve at its emergence from the foramen ovale, the lesion was excised (Fig. 32). Rigid fixation of the mandible was completed using a surgical splint to preserve the preoperative occlusion of the patient. Subsequent adjuvant treatment was performed with proton therapy along the spreading pathways through cranial nerves. At three-years clinical and radiological follow-up the patient is free from disease (Fig. 33).

4.2.3 Schwannoma of the Peri-carotic Space

Clinical History

A 53-year-old patient was referred to our department for the evaluation of a temporomandibular joint (TMJ) dysfunction. She reported a previous surgery to excise a hypoglossal nerve schwannoma 15 years before, and she complained of acute pain around the mandible. MR was conducted to evaluate the TMJ, showing only mild radiological evidence of

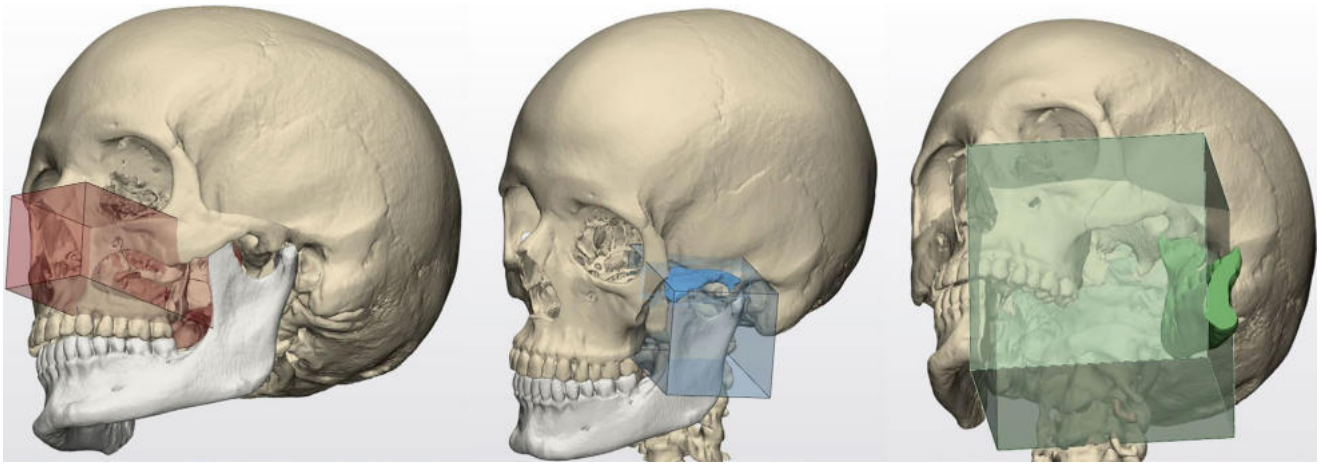


Fig. 31 Definition in VSP of access portals for the lesion: left) transmaxillary; center) transzygomatic; right) transmandibular. (Figure under CC-BY license [9])

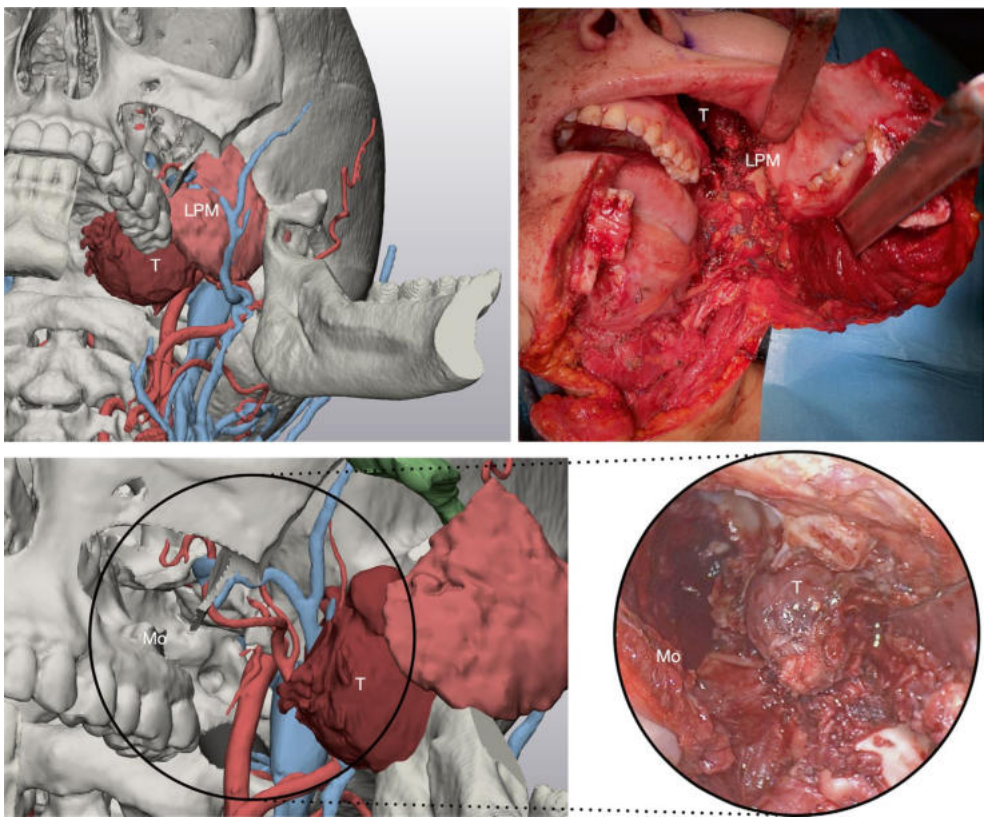


Fig. 32 Open surgery simulation by rotation of the hemimandible and removal of the anterior-lateral antral wall. Exposure of the lesion is optimally yielded, as well as its vascular relationships. (Figure under CC-BY license [9])

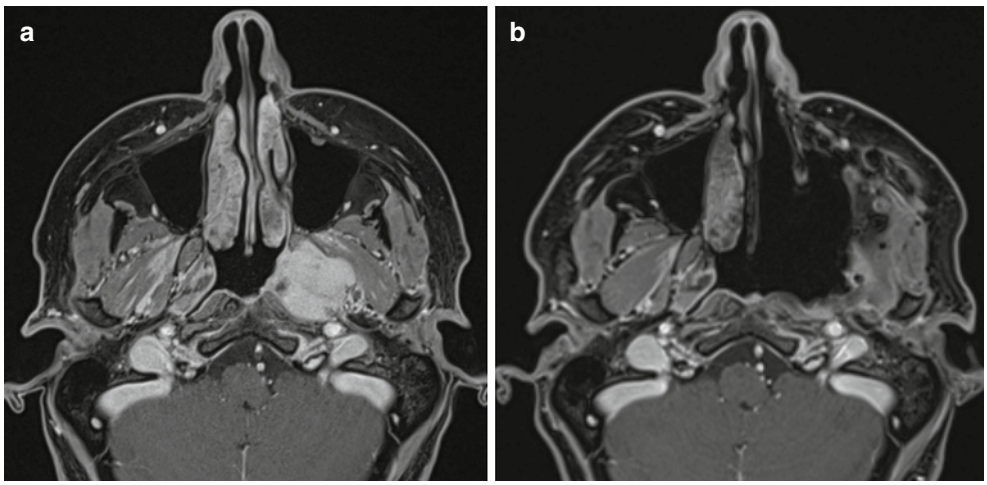


Fig. 33 Postoperative MR demonstrates the emptying of the pterygomaxillopalatine fossa. (Figure under CC-BY license [9])

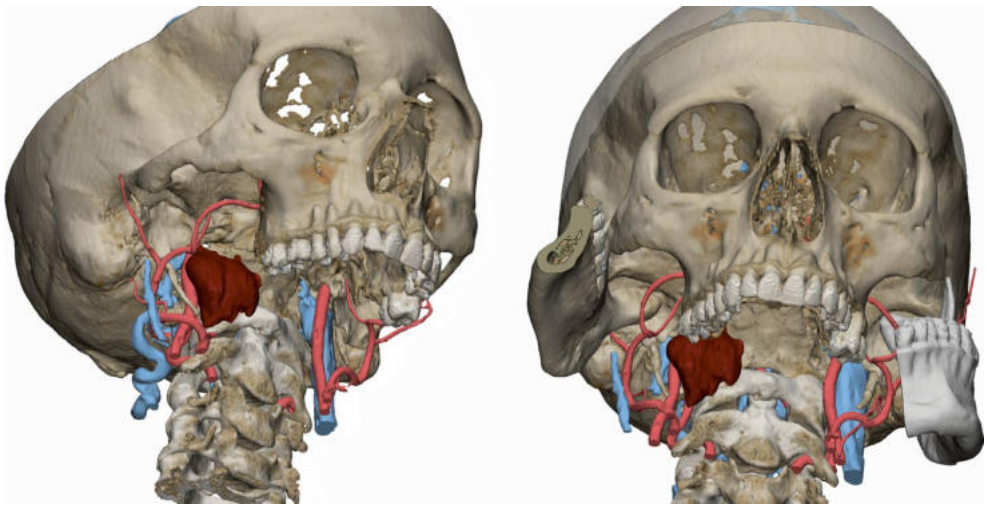


Fig. 34 Another VSP example for a case of carodid sheath schwannoma causing vascular compression. The transmandibular access was deemed optimal. (Figure under CC-BY license [21])

joint pathology but revealing a solid mass localized in the site of previous surgery, whose MR features oriented for the diagnosis of a relapsed schwannoma. The patient was thus candidate for the surgical excision of the mass, whose relationship with nearby structures, alongside with its deep location, required a careful VSP study.

Virtual Surgical Planning

The radiological acquisition protocol and segmentation techniques did not differ from the previous case. A composite model creation, including the detailed skeletal representation and vascular anatomy, was created. The tumor was carefully segmented using the smart brush tool and reconstructed in the correct spatial relationship with nearby structures thanks to accurate multi-image registration. This enables to elucidate the localization of the tumor and the best access pathways, represented by the transmandibular approach. A mandibular paramedian osteotomy was simulated and both hemimandibles were opened by positioning the rotation fulcrum within the TMJ, enabling to define the theoretical width of the transmandibular access portal, which was deemed suitable to excise the lesion (Fig. 34). STL files for each object of the surgical planning were imported in the navigation plan, allowing to effectively track the boundaries of the mass, as well as the localization of critical structures. AR was also deployed for this clinical case by importing the . mcs file of simulation within the Mimics viewer to interactive gesture control within the AR sight field provided by the Hololens.

Surgery

The transmandibular approach was prepared as previously illustrated, using a submandibular incision continuing anteriorly with a lip split approach. After the surgical corridor was widened, intraoperative navigation allowed to target the lesion, localized in the deep space and in close relationship with the ICA. Meticulous dissection from the vessel's adventitia was performed until the lesion was mobilized. The lesion was excised and sent for histopathological examination (Fig. 35).

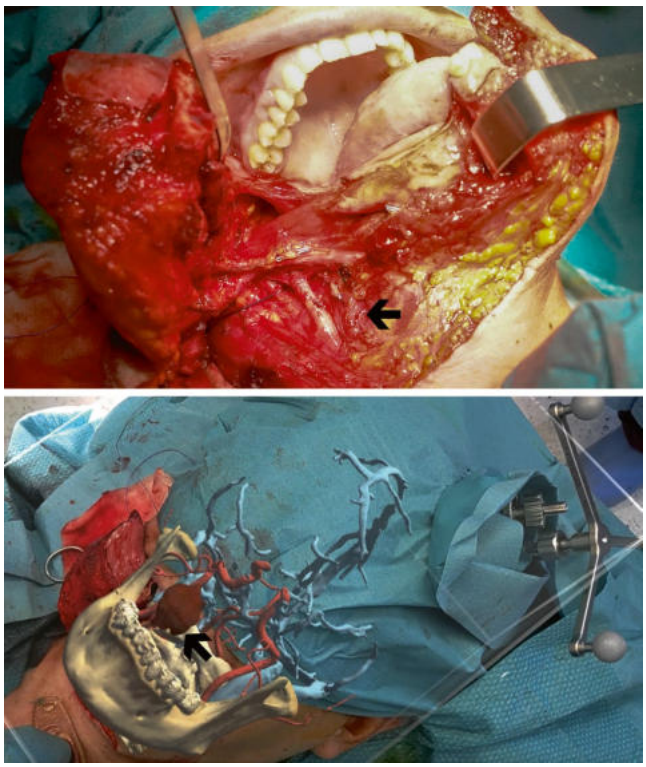


Fig. 35 AR match during open surgery. (Figure under CC-BY license [21])

4.3 Craniofacial Resection

Craniofacial resection is a complex procedure with a double surgical access from both the midface and the frontal bone to dominate and excise advanced disease arising generally in the sinonasal trait. First proposed by Ketcham [16], it remains the mainstage technique to perform en-bloc removal of resectable disease, yet there is an increasing tendency to replace this highly invasive procedure in favor of less invasive approaches, with a growing role of endoscopic debulking integrated within a multimodal approach (systemic therapy, radiation, and hadrotherapy). In this regard, the importance of neoadjuvant therapy deserves to be mentioned to select responders and to induce tumor shrinkage, allowing to operate previously unresectable disease [17]. However, within specific indications, craniofacial resection remains a curative option for patients with neoplasms of the midface and specifically for sinonasal cancers. Technology has significantly improved the accuracy and selectiveness of craniofacial resections, including the possibility to localize the deepest parts of the tumor, navigate its surgical margins, and check the proximity of vulnerable structures. Computer-guided osteotomies enable to design the specific regions of craniofacial disassembly according to the biological principles described by Janecka [18]. The well-established role of intraoperative navigation in such cases is corroborated by multiple evidences, while the application of AR introduces new scenarios for the improved visualization of the complex anatomy of this region [19].

4.3.1 Sinonasal Adenocarcinoma Approached with Navigated Craniofacial Resection

Clinical History

A 59-year-old patient sought ophthalmologic evaluation for the progressive onset of diplopia and right bulbar proptosis. He also reported nasal obstruction and epistaxis; thus, he underwent ENT evaluation with evidence of a conspicuous mass occupying the space in his left nasal cavity, highly friable and bleeding. The patient was referred to our hub center, where an endoscopic biopsy was performed, confirming adenocarcinoma non-intestinal type of the sinonasal trait. The patient underwent MR and CT using the protocol for multilayer anatomical reconstruction.

Virtual Surgical Planning

Segmentation was performed in Materialise Mimics with the same techniques described for the previous cases. In particular, the author remarks on the importance of a high-resolution acquisition for the contrast-enhanced VIBE sequence that allows accurate lesion contouring in multiplanar projections. Reconstructed 3D anatomy included the skeletal component, sinonasal tumor, eye globe, extraocular muscles, and optic nerve. The project was imported into ProPlan CMF and 3-matic for the virtual surgical planning to design osteotomies for the craniofacial dismantling, including the following components (Fig. 36):

- Flap for transcranial approach and subcranial approach: according to description by Raveh [20], to maximize bone exposure of the anterior cranial fossa, a combined transcranial and subcranial approach was conducted. A separate osteotomy was designed for the posterior wall of the frontal sinus, thus dividing in two halves the subcranial flap.
- Osteotomies for lateral rhinotomy: lateral nasal osteotomies were performed to enable the contralateral rotation of the nasal pyramid to uncover the underlying sinonasal trait.
- Maxillectomy: The excision of the infiltrated maxilla included a radical maxillectomy involving orbital exenteration (Brown's class IV).

The project with osteotomies was imported in the surgical navigator to enable intraoperative real time tracking of osteotomies and navigation of margins in virtual surgical planning.

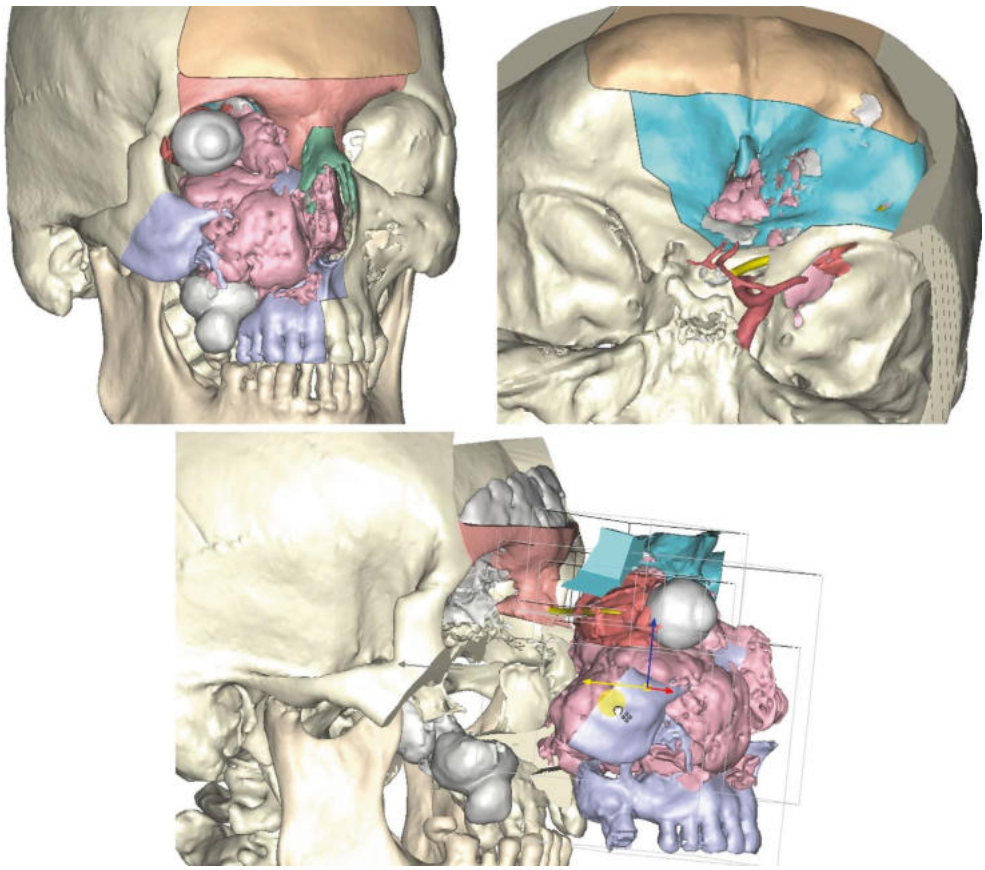


Fig. 36 VSP of craniofacial resection in a case of sinus adenocarcinoma. Accurate craniofacial dismantling is carefully studies by designing specific flaps

Surgery

The DRF was positioned, and the navigator calibrated. AR headset A coronal approach was used to expose the cranial vault up to the frontal region. During dissection, care was taken not to injure the pericranium, which would serve as source of the pedicled flap for anterior skull base sealing to prevent cerebrospinal fluid (CSF) leakage. The exposure area reached the supraorbital nerve bilaterally and the glabellar region, allowing to uncover the entire frontal bone up to the nasofrontal suture. In the midface, a Weber-Ferguson incision was used for the transfacial access, and a right cheek flap was separated. Navigated piezosurgical osteotomies were performed to complete the maxillectomy on the right side, with extension on the right orbital floor (type IV). A rhinotomy was performed to rotate the nose on the opposite side, allowing to expose the internal nasal cavity. The transfacial resection was complete with emptying of the right orbital cavity and sectioning of the optic nerve (orbital exenteration). The anterior skull base was addressed by creating a combined transcranial-subcranial approach; the frontal lobes of the brain were retracted, and osteotomies on the anterior skull base were performed under navigational guidance. The sectioned anterior skull base was pushed downwards in the midface and represented the superior limit of the resection. The specimen containing the eye, the dentate maxilla with the tumor within, and the anterior skull base was extracted from the transfacial access and sent to histopathologic examination (Fig. 37). From the reconstructive perspective, the wide breach on the anterior skull base was sealed using a multilayer technique, containing a pedicled pericranial flap, synthetic dura, and fibrin glue. Moreover, the midfacial defect was filled using a latissimus dorsi free flap, plicated and sutured on the resection margins. A multilayer skin suture was performed and a tarsorrhaphy to cover the empty eye socket.

4.3.2 Sinonasal Undifferentiated Carcinoma (SNUC) with AR and Navigation-Guided Orbito-Maxillary Resection

Clinical History

A 62-year-old lady presented with progressive left nasal obstruction and epistaxis. She performed an ENT evaluation, which found an exophytic, bleeding mass located in the left nasal fossa. An endoscopic biopsy was performed with the evidence of a sinonasal undifferentiated carcinoma. The patient was subsequently referred to our hub center, where she underwent all the diagnostic imaging performed with the aforementioned protocols for advanced virtual planning simulation.

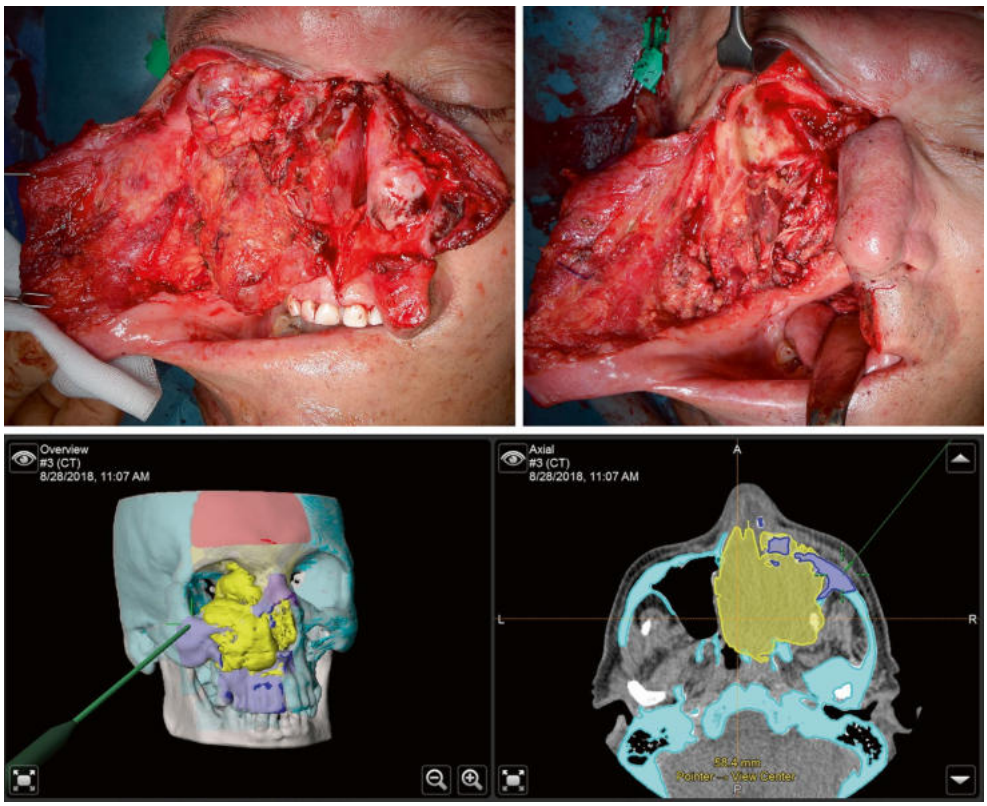


Fig. 37 Navigation-guided excision of the tumor using VSP as reference

Virtual Surgical Planning

The multilayer protocol for anatomical reconstruction is applied, and a patient-specific anatomical atlas to simulate a craniofacial resection is built through accurate segmentation processes. In particular, high-resolution CT in the bone window with conservative segmentation is used to create a reliable, thin-structure sparing, skeletal model; subsequently, sequence-specific thresholds are applied to both 3D VEN PCA and 3D TOF MR to reconstruct respectively high-resolution models of venous sinuses and the IJV system, as well as the intracranial and extracranial arterial vascularization. The eye, alongside its extraocular muscles and the optic nerve, is accurately modeled. The tumor mass is highlighted by applying selectively and in multiplanar projections the smart brush contouring with a dynamic region growing pattern. The result is a consistently accurate anatomical representation, in which voxel coloring can be applied to increase the anatomical similarity (Fig. 38).

VSP was performed using a methodology compared to the previous case, but here we highlight the increased role of freehand osteotomy drawing and the shift from ProPlan to 3-matic, as the case was more recent and the expertise of the author had increased. In particular, the following osteotomies were performed:

- Combined fronto-subfrontal flap to uncover the anterior skull base, including the supraorbital rim and the glabellar region;
- Rhinotomy, more extended on the healthy side, to enable outward contralateral rotation of the nose and uncover the inner nasal cavity;
- Maxillary osteotomy: in this case, the alveolar process and the zygomatic body were not included in the specimen, but their osteotomies were essential to enable the rotation of a composite maxillary cheek flap;
- Type V Brown's resection: included the customized design of an orbito-maxillary resection with orbital exenteration, owing to the infiltration of the inferior and medial orbital walls. The resection design included part of the left nasomaxillary buttress, the left subspinal region, the medial and inferior orbital wall.

Given the importance of an en-bloc resection and the subsequent need for rigid fixation of bone flaps, the entire anatomical model, including osteotomies and subunits, together with vessels and the tumor, was 3D printed in the University of Udine PoC 3D lab using a large-sized SLA printer (Form 3BL, Formlabs, Somerville, MA), with the aim of enhancing visualization, as well as facilitate intraoperative plating of

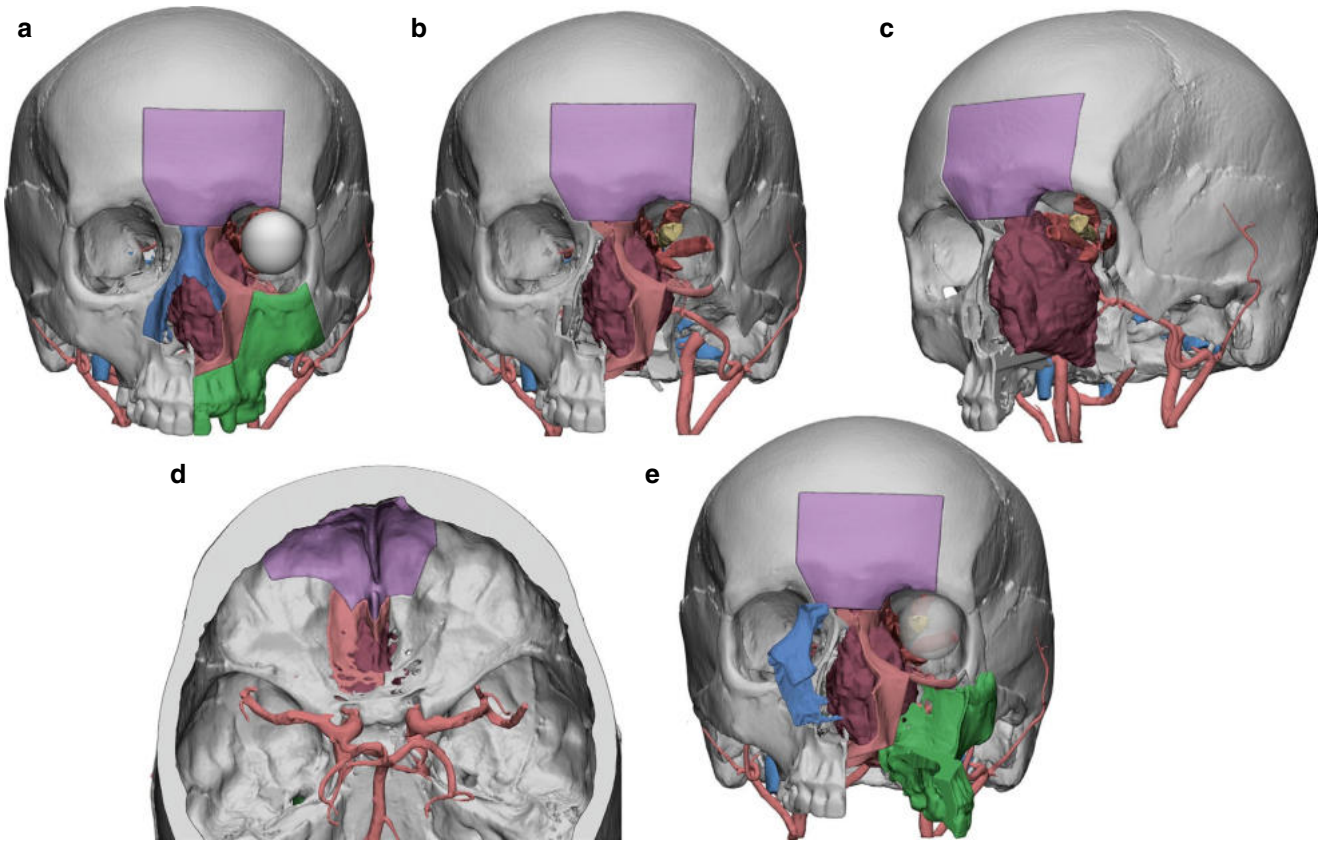


Fig. 38 A more modern VSP for craniofacial resection. The sequence of craniofacial dismantling is carefully represented. Vaascular structures are emphasized

devices for internal fixation. Moreover, the entire project was imported in Brainlab (Brainlab, Munich, DE) navigator. In addition, the 3-matic project was deployed in Mimics viewer to be displayed in AR using Hololens 2 device (Fig. 39).

Surgery

Surgical phases can be conceptually overlapped with the previous case description. It is worth mentioning that the entire surgical plan was displayed in AR. The role of navigation in anterior skull base osteotomies was crucial to drive correct execution even in blind areas, allowing constant position checking with respect to planned resection margins and vulnerable structures nearby. Concerning the reconstructive phase, the 3D printed replica enabled to assist the rigid fixation of the maxillary cheek flap and the nasal flap (Fig. 40).

4.4 Virtual Endoscopy

The term virtual endoscopy defines a technical methodology useful to simulate endoscopic surgery in VSP [9]. Although its technical features in terms of setting the computer environment have been defined in Sect. 3.4, in this section its clinical application will be described in reference to the clinical case presented in Sect. 4.2.2.

4.4.1 Adenoid Cystic Carcinoma Located in the Pterygomaxillopalatine Fossa (Continued)

To become more familiar with the concept of virtual endoscopy and understand its full potential, it is useful to refer to a case previously simulated for an open approach, in which the endoscopic sequences nevertheless proved essential to complete successful surgical excision. In addition, this clinical case features the virtual reconstruction of all the main anatomical structures and exemplifies the contribution of simulation for endoscopic procedures as well in cases of non-standardized, complex surgeries.

Virtual Surgical Planning

Before simulating the endoscopic sequence, the replica of the optic unit was subject to reverse engineering, as it provided the base geometrical body to parent the optic camera. A cylinder with the same diameter and length as the endoscope was modeled and linked with a virtual camera at its tip. Simulation was performed entirely in Autodesk Maya (Autodesk Inc., San Jose, CA, USA), a well-known software package in the movie industry. Maya's digital environment, known generally as "scene," is scoped using a separate camera in any spatial perspective (bottom, top, side, front, back). Other cameras can be created to view the scene under particular conditions:



Fig. 39 AR intraoperative match to use the holographic model as reference during surgery. (Figure under CC-BY license [19])

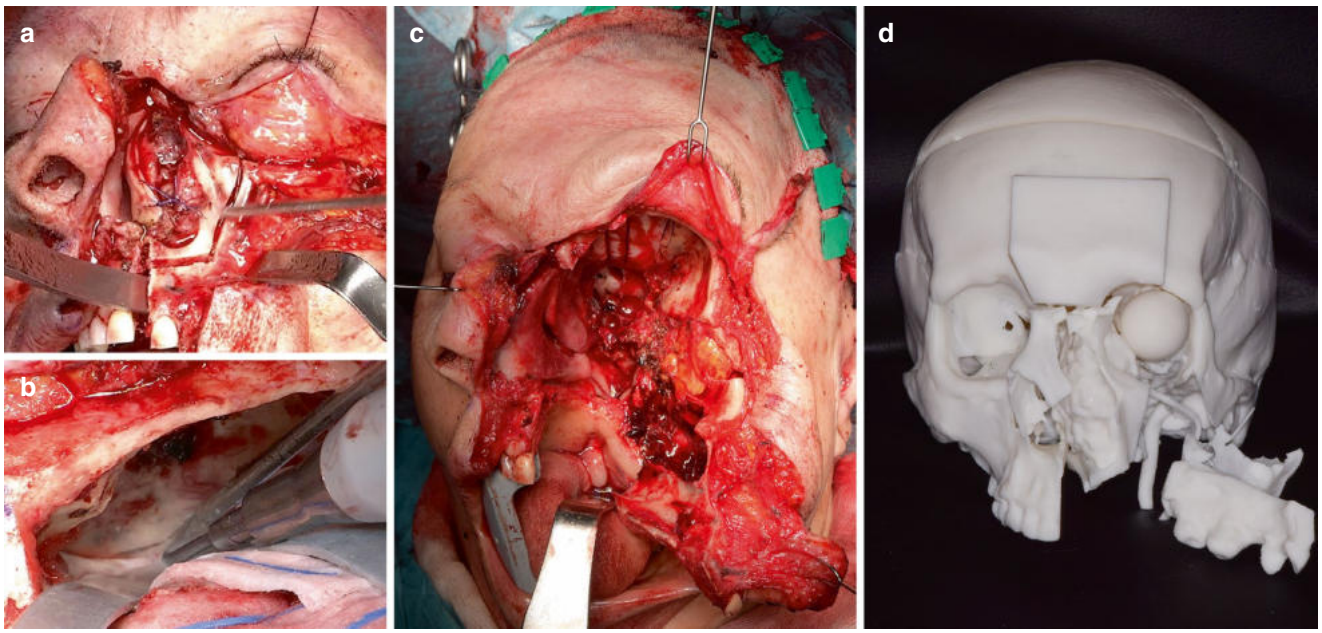


Fig. 40 3D printed model of VSP used as reference to study osteotomies for craniofacial disassembly

for this purpose, an endoscope-like camera, using the same optical properties as a real surgical endoscope, including rounded field of view, focal distance of 18 mm and image refreshing rate of 50 fps, was created and parented to the tip of the cylinder. The camera was then moved in the nasal cavity, and each relevant view was assigned a key frame in the animation bar. Such frames were then interpolated to achieve a smooth animation, showing the endoscope as it progressed within the nasal cavity, as well as its movement. During animation, each object was selectively included in an animation layer to be hidden or shown; for instance, it was possible to hide the mucosal layer to understand the vulnerable structures behind, as well as the location of the tumor. For this case in particular, the critical point was to define endoscopically the relationship between the tumor and rhinopharynx, as well as the ICA, and to assess whether it was possible to mobilize the tumor on its medial attachments before excising it from the open transmandibular corridor.

Surgery

The initial phase consisted of an inferior turbinectomy to increase space for surgical maneuvers, widening the corridor to the choanal opening. A straightforward access from the superior meatus to the sphenoid sinus was performed to evaluate sphenoid involvement. Stable landmarks for endoscopic dissection were considered the sphenoidal insertion of the vomer on the rostrum, ethmoid roof, pterygoid plates, and inside the sphenoid sinus, and the impression of the paraclival trait of ICA as lateral danger site. A medial maxillectomy extending from the antral foramen to the pterygomaxillary junction was performed to define the medial margin of the tumor. After surgery, simulation and intraoperative videos were matched to assess their correspondence, and all the main anatomical landmarks observed from the correct perspective could be localized in the virtual simulation, which therefore was effective in replicating the real view (Fig. 41).

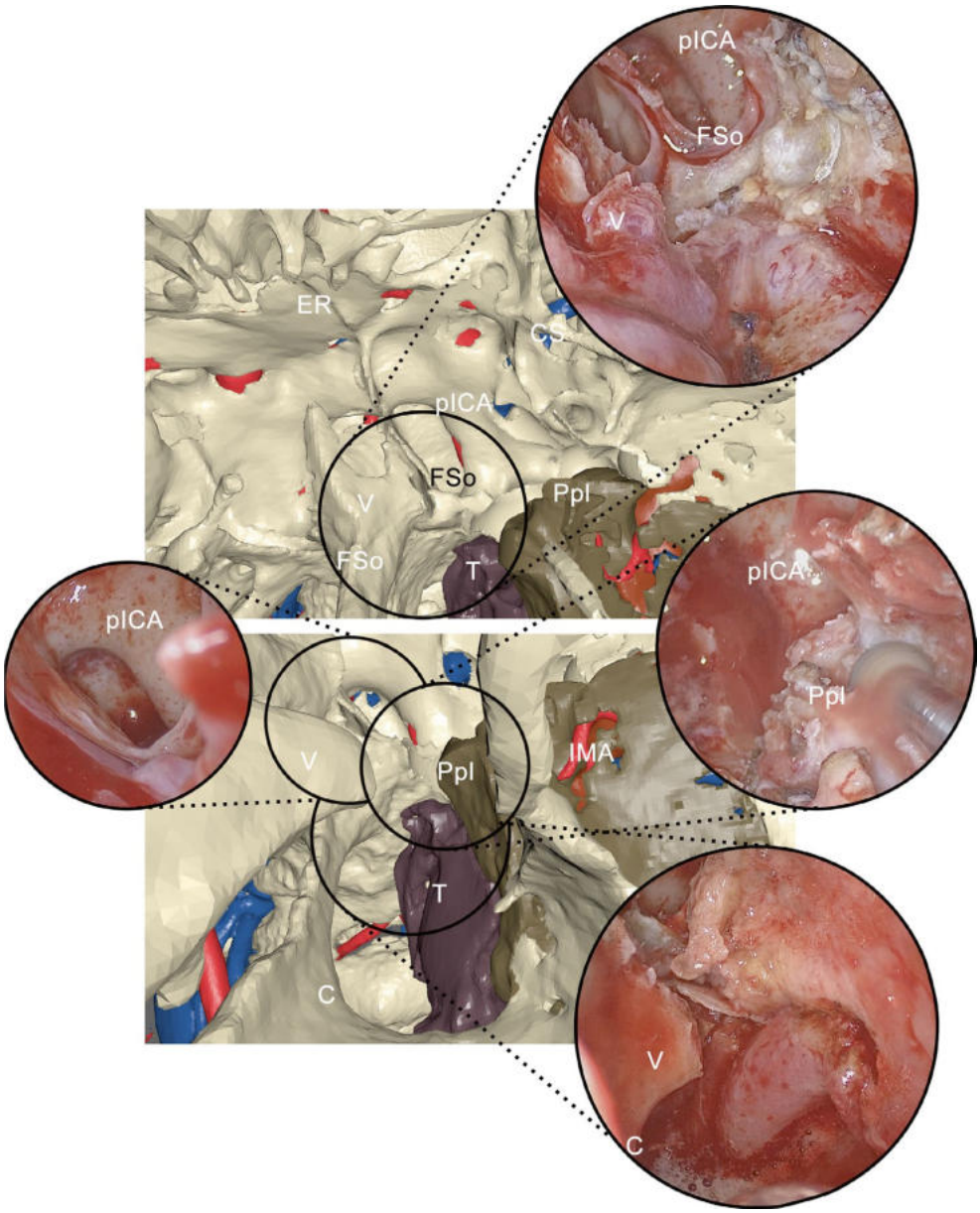


Fig. 41 Virtual endoscopy simulated for the case displayed through Figs. 30, 31 and 32. Notably, the correspondence between virtual and real endoscopic anatomy is highly evident. Endoscopy was used as auxiliary procedure to help mobilize the tumor across its medial margin. * pICA, paraclival internal carotid artery; SSo, sphenoid sinus opening; CS, cavernous sinus; ER, ethmoidal roof; V, vomer; Ppl, pterygoid plate; T, tumor; C, choana; IMA, internal maxillary artery. (Figure under CC-BY license [9])

References

1. Janecka IP, Sen CN, Sekhar LN, Nuss DW. Facial translocation for cranial base surgery. Keio J Med. 1991;40:215–20.
2. Mannelli G, Comini LV, Piazza C. Surgical margins in oral squamous cell cancer: intraoperative evaluation and prognostic impact. Curr Opin Otolaryngol Head Neck Surg. 2019;27:98–103.
3. Catanzaro S, Copelli C, Manfuso A, Tewfik K, Pederneschi N, Cassano L, Cocchi R. Intraoperative navigation in complex head and neck resections: indications and limits. Int J Comput Assist Radiol Surg. 2017;12:881–7.
4. Rajendran B. Surgical outcomes of endoscopic versus open resection for the management of sinonasal malignancies. J Korean Assoc Oral Maxillofac Surg. 2020;46:373–8.
5. Bidra AS, Jacob RF, Taylor TD. Classification of maxillectomy defects: a systematic review and criteria necessary for a universal description. J Prosthet Dent. 2012;107:261–70.
6. Reconstruction of the maxilla and midface: introducing a new classification – ScienceDirect. https://www.sciencedirect.com/science/article/abs/pii/S1470204510701133. Accessed 19 Jan 2025.
7. Cantù G, Riccio S, Bimbi G, Squadrelli M, Colombo S, Compan A, Rossi M, Pompilio M, Solero CL. Craniofacial resection for malignant tumours involving the anterior skull base. Eur Arch Otorrinolaringol. 2006;263:647–52.
8. Anand SM, Frenkiel S, Le BQH, Glikstein R. Virtual endoscopy: our next major investigative modality? J Otolaryngol Head Neck Surg. 2009;38:642–5.
9. Tel A, Bagatto D, Costa F, Sembronio S, Robiony M. Anatomical computerized exploration to excise malignancies in deep facial compartments: an advanced virtual reality protocol for a tailored surgical approach. Front Oncol. 2022;12:875990.
10. Fall S, Pagé G, Bettoni J, Bouzerar R, Balédent O. Use of phase-contrast MRA to assess intracranial venous sinus resistance to drainage in healthy individuals. AJNR Am J Neuroradiol. 2017;38:281–7.

11. Ricotta F, Cercenelli L, Battaglia S, Bortolani B, Savastio G, Marcelli E, Marchetti C, Tarsitano A. Navigation-guided resection of maxillary tumors: can a new volumetric virtual planning method improve outcomes in terms of control of resection margins? J Craniomaxillofac Surg. 2018;46:2240–7.
12. Tarsitano A, Ricotta F, Baldino G, Badiali G, Pizzigallo A, Ramieri V, Cascone P, Marchetti C. Navigation-guided resection of maxillary tumours: the accuracy of computer-assisted surgery in terms of control of resection margins – a feasibility study. J Craniofac Surg. 2017;45:2109–14.
13. Badiali G, Ferrari V, Cutolo F, Freschi C, Caramella D, Bianchi A, Marchetti C. Augmented reality as an aid in maxillofacial surgery: validation of a wearable system allowing maxillary repositioning. J Craniofac Surg. 2014;42:1970–6.
14. Sun Y, Luebbers H-T, Agbaje JO, Schepers S, Vrielinck L, Lambrichts I, Politis C. Validation of anatomical landmarks-based registration for image-guided surgery: an in-vitro study. J Craniofac Surg. 2013;41:522–6.
15. Zitsch RP, Patenaude B, Tidmore T. An extraoral parapharyngeal space approach via vertical ramus osteotomy. Am J Otolaryngol. 2007;28:330–3.
16. Ketcham AS, Wilkins RH, Van Buren JM, Smith RR. A combined intracranial facial approach to the paranasal sinuses. Am J Surg. 1963;106:698–703.
17. Amit M, Abdelmeguid AS, Watcherporn T, et al. Induction chemotherapy response as a guide for treatment optimization in sinonasal undifferentiated carcinoma. J Clin Oncol. 2019;37:504–12.
18. Tel A, Bagatto D, Tuniz F, Sembronio S, Costa F, D'Agostini S, Robiony M. The evolution of craniofacial resection: a new workflow for virtual planning in complex craniofacial procedures. J Craniofac Surg. 2019;47:1475–83.
19. Tel A, Raccampo L, Vinayahalingam S, Troise S, Abbate V, Orabona GD, Sembronio S, Robiony M. Complex craniofacial cases through augmented reality guidance in surgical oncology: a technical report. Diagnostics (Basel). 2024;14:1108.
20. The Subcranial Approach for Fronto-Orbital and Anteroposterior Skull-Base Tumors | JAMA Otolaryngology–Head & Neck Surgery | JAMA Network. https://jamanetwork.com/journals/jamaotolaryngology/article-abstract/621486. Accessed 19 Jan 2025.
21. Tel A, Zeppieri M, Robiony M, Sembronio S, Vinayahalingam S, Pontoriero A, Pergolizzi S, Angileri FF, Spadea L, Ius T. Exploring deep cervical compartments in head and neck surgical oncology through augmented reality vision: a proof of concept. J Clin Med. 2023;12:6650.

Virtual Surgical Planning in Midfacial Reconstruction

Alessandro Tel, Matthias Ureel, Maarten De Jong, Renaat Coopman, and Massimo Robiony

1 Introduction to Midface Reconstruction

Reconstruction of the midface is a complex topic. In addition to relevant functional implications including the accommodation of the eye and nasal cavity, as well as masticatory activity, this region of the splanchnocranium has a prominent esthetical relevance and is primarily responsible for the social perception of the patient. Thus, any midfacial reconstruction needs to be tailored on the single patient and must respond to criteria of symmetry, which is important especially in case of orbital involvement, biomechanical stability, to withstand masticatory forces and esthetical balance. As seen in the previous chapter, defects following ablative surgeries represent the main application field for reconstructive midfacial surgery, and the broad variety of such defects justifies a considerable array of reconstructive options. Other possible indications to midfacial reconstructive procedures include loss of tissue due to severe trauma, usually involving burst injuries, necrotizing infections, including osteoradionecrosis, and drug-related osteonecrosis.

A. Tel (✉)
Lead Specialist for VSP and 3DP, Maxillofacial Surgery Clinic, Head & Neck and Neuroscience Department, Academic Hospital of Udine, Udine, Italy
e-mail: alessandro.tel@uniud.it

M. Ureel · R. Coopman
Department of Oral & Craniomaxillofacial Surgery, Ghent University Hospital, Ghent, Belgium
e-mail: Matthias.Ureel@uzgent.be; Renaat.Coopman@uzgent.be

M. De Jong
Maastricht University Medical Center, Department of Cranio-Maxillofacial Surgery, Maastricht, the Netherlands
e-mail: maarten-dejong@hotmail.com

M. Robiony
Chief of Maxillofacial Surgery Clinic, Director of the Postgraduate School in Maxillofacial Surgery, Chief of Head & Neck and Neuroscience Department, Academic Hospital - University of Udine, Udine, Italy
e-mail: massimo.robiony@uniud.it

While in the mandible it is generally mandatory to reconstruct at least the bone continuity, and bone restoration is a preferred option, in the midface the versatility and ease of harvest of the temporalis muscle flap simplify and fasten the reconstruction of post-maxillectomy defects. The use of temporalis muscle flap provides a local reconstruction and effectively creates a diaphragm to seal off the nasal cavity from the oral cavity. Especially in elderly patients, or in case of posterior defects, this creates a permanently edentulous area that the patient might accept in favor of a less invasive and complex surgery.

However, in patients who are candidate to a dental rehabilitation, bone reconstruction becomes the ideal solution to provide support for implants. Several classification systems, including the previously mentioned Brown's, but also Aramany's and Okay's [1], have been defined to categorize the extent of maxillary ablation and subsequently tailor reconstructive strategies. In this regard, several flaps have been used for the midface, but there is no single flap that by itself can fully satisfy the morpho-functional requirements of this complex anatomical region. Virtual surgical planning (VSP) enables unprecedented control over the inset of flaps and their geometrical modeling to match anatomical characteristics demanded from the donor site. In addition, the complex anatomical and esthetical needs of the midface can be addressed by combining innovative craniofacial implants which can be fixed to traditional bone free flaps. Last, design software technology and advancements in facial scanning and color 3D printing enabled to manufacture revolutionary facial epitheses that provide a non-surgical and immediate possibility to reconstruct broad facial defects, with respect to the aesthetics and identity of the patient.

This chapter focuses on the advancements of midface reconstruction driven by VSP and explores reconstructive possibilities through a dissertation on complex cases from microsurgical bone reconstruction and craniofacial implants to facial epitheses.

© The Author(s), under exclusive license to Springer Nature Switzerland AG 2025

A. Tel, M. Robiony (eds.), *Atlas of Virtual Surgical Planning and 3D Printing for Cranio-Maxillo-Facial Surgery*,
https://doi.org/10.1007/978-3-031-94495-6_21

2 Possibilities for Computer-Guided Bone Midfacial Reconstruction

Few flaps account for the vast majority of reconstructive options in the midface, and each of them can be successfully tailored using VSP to match the characteristics of the recipient site. Moreover, the combination with facial implants provides a further impulse to highly restorative and aesthetical reconstructions.

2.1 Flaps

Among bone flaps, which are the object of virtual surgical planning, three represent the mainstay of midfacial reconstruction (Fig. 1):

- Fibula free flap: it is a highly versatile free flap, which has been considerably empowered by virtual surgical planning. It has a linear, yet slightly twisted, course and can be bended in multiple spatial axes to accommodate the variability of the recipient site. In contrast to the mandible, where bending is minimal and segments are overlapped with similar orientation (double barrel coaxial), in the midface considerable twisting and diversity in orientation (multiaxial) can be possible to reconstruct the main skeletal buttresses.
- Scapula free flap: it represents an optimal choice for the midface. Its thin shape, rather triangular and bulged along its lateral border, enables the positioning of dental implants. It can be oriented in several ways to accommodate a variety of situations: both horizontally, when the hard palate reconstruction is preferred, and vertically, when the surgeon opts for a midfacial restoration. Moreover, several parts of the scapula can be harvested to increase the versatility of reconstruction, including the parascapular region, the scapular tip, or a combination thereof [2–4].
- Deep circumflex iliac artery (DCIA) flap: this flap provides a substantial amount of bone to its recipient site but has some disadvantages: first, it has a short vascular pedicle (limited from 5 to 7 cm, thus mostly inadequate for maxillary reconstruction) and, second, its harvesting procedure is related to considerable morbidity of the donor site. The iliac crest has a natural curvature that makes it useful for the midface, yet the possibilities of flap sculpting allowed by VSP can highly overcome this apparent advantage in favor of more versatile, less invasive, flaps, such as the fibula and the scapula [5–7].

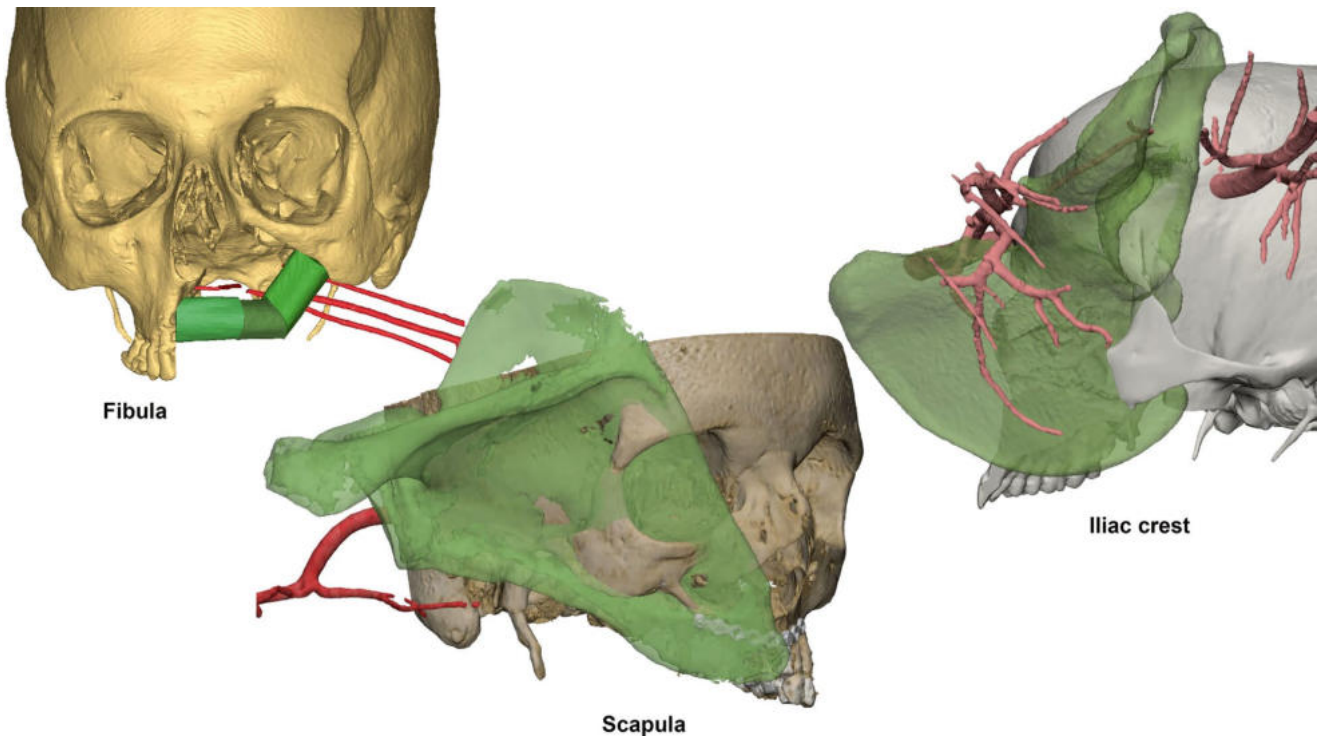


Fig. 1 Digital anatomy of the most common donor sites for osseous free flaps for midface reconstruction

2.2 Hybrid Solutions (Flap + Prosthesis)

The possibilities of additive manufacturing applied to midfacial reconstruction enable the manufacturing of highly detailed titanium prostheses in conjunction with free flap. This fastens, simplifies, and makes more accurate midfacial reconstruction, especially the complex architecture of the mesostructure, and can be extended up to the orbital floor, while bone flaps enable to transfer vital tissue to the oral cavity, including muscle, creating a sealing cuff that prevents the titanium parts from being exposed. Other than allowing for much more accurate and simplified reconstructions, the use of patient-specific implants significantly decreases the amount of bone to be harvested from the donor site, and thus makes flap harvesting procedures more conservative (Fig. 2).

2.3 Prosthesis Only

In several cases, after ablation of midfacial defect, a free flap might not be indicated, owing to patient's comorbidities, that may preclude a major surgical operation, as well as for the final aesthetical result. This is the case for instance of large facial resection for cancer with disruption of the nose, the eye, and associated parts of the midface. For such cases, an epithesis fixed on osteointegrated implants might be more suitable (Fig. 3). Recent developments in the field of hand-held structured light facial scanners, which are able not only to capture even tiny geometrical details but also accurate color textures, as well as organic modeling software, have opened significant perspectives for the improvement of such prostheses. On the manufacturing side, more recent and complex techniques such as polyjet 3D printing help create highly reliable replicas including natural-looking texture maps [8].

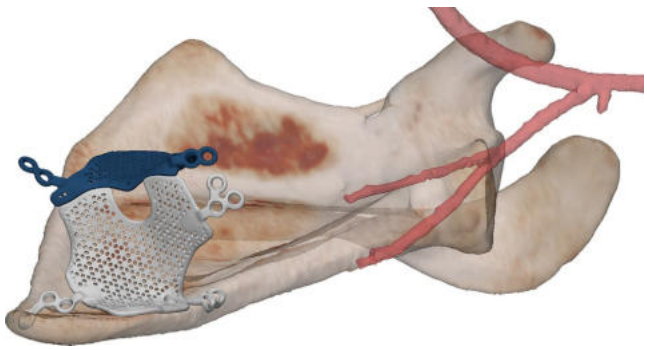


Fig. 2 Combined flap and prosthesis for midface reconstruction

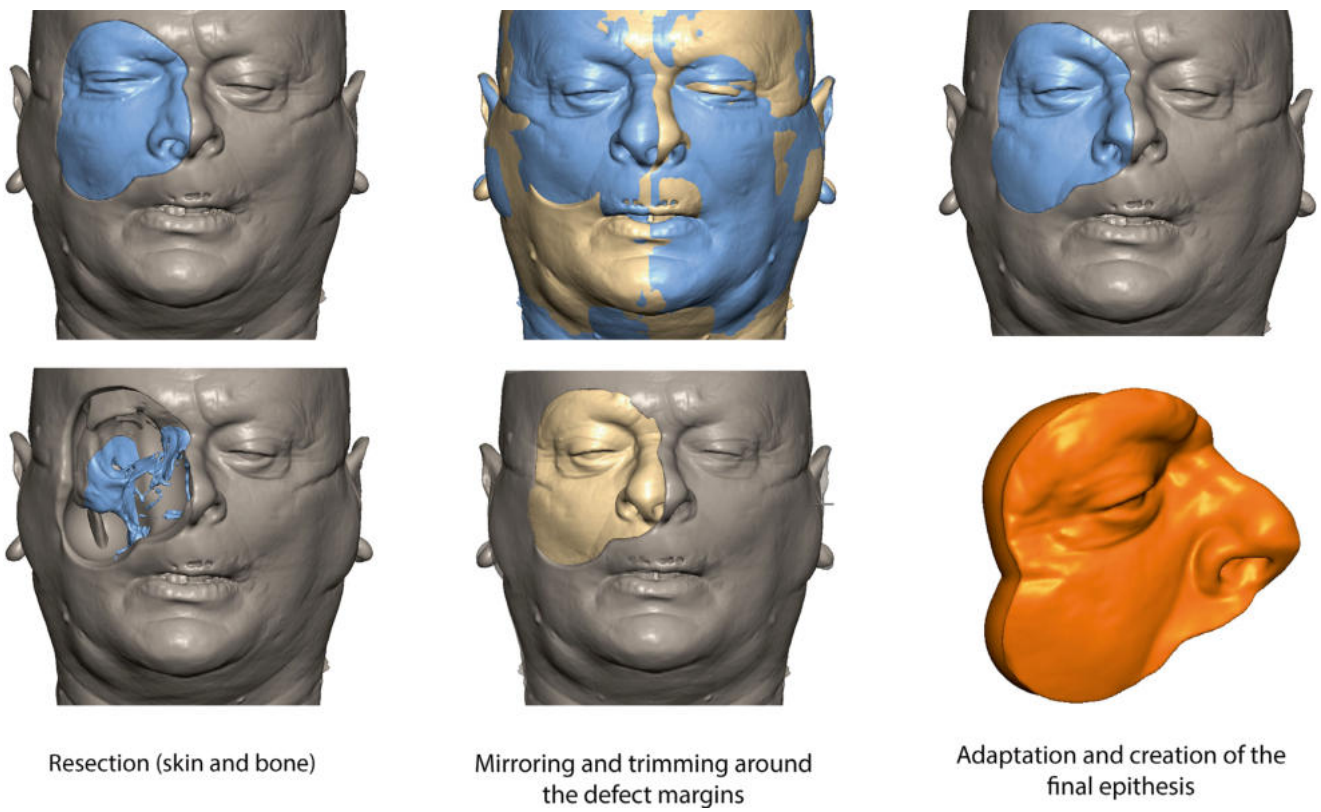


Fig. 3 Workflow for simulating soft tissue resection with clay mirroring to design a facial epithesis

3 Workflow for Computer-Guided Midface Reconstruction Using Flaps

The sequence of steps to perform a midfacial reconstruction will be detailed in the following paragraphs, starting with acquisition of images for the donor site, to flap planning and inset. Chapter "Virtual Surgical Planning in Mandibular Reconstruction" concerning mandibular reconstruction is highly specific in terms of fibula free flap, given its universally accepted role for mandibular reconstruction. A separate workflow will be described for epitheses at the end of the chapter.

3.1 CT Angiography and Segmentation for Flap Definition

In relation to any possible donor site (fibula, scapula, iliac crest), a CT angiography needs to be performed with highly specific features to maximize spatial resolution and vessel detection according to the specifications provided in Chapter "Dedicated Acquisition Protocols in Radiology for Virtual Surgical Planning and 3D Printing". The pedicle should be followed for all its length, or at least as much as possible, and should be detectable in close proximity to the donor flap. Surrounding bones should be separate to achieve virtual models of the donor bone with its vascular pedicle. In particular:

- Fibula: The peroneal artery should be clearly defined after it separates from the common trunk with the posterior tibial artery. This vessel should be identifiable as it approaches the ankle region. Between its central and distal third, the probability of locating perforators is maximal; thus, if detectable, perforators to the skin should be likewise segmented and reconstructed. The vessels must be separate from the bone, and tibia and fibula must be divided. It is useful to maintain the tibia as it facilitates to understand the orientation of the leg (Fig. 4).
- Scapula: Thoracodorsal and circumflex scapular vessels should be followed as they leave the subscapular artery, a branch of the subclavian artery. Depending on the patient's position during the acquisition (generally, with upper limbs extended overhead), the natural orientation of such vessels might be difficult to distinguish. They are generally less segmentable than the peroneal artery is, owing to less standardizable infusion time of contrast media. Segmentation for the scapula flap is difficult, as the scapula must be separated from ribs, humeral head, as well as a dense vascular network that reaches the arm. In addition, the heart and major caliber thoracic vessels have a significant contrast medium uptake and should be separated as well from the pedicle, namely the subscapular system and the thoracodorsal artery (Fig. 5). Current technology allows for the best planning of the bone reconstruction, enabling to define the shape, size, and orientation of the donor bone, yet the scapula flap is



Fig. 4 Correct 3D scene to establish a fibula flap reconstruction. Both tibias and fibulas and vascular axes need to be separately reconstructed

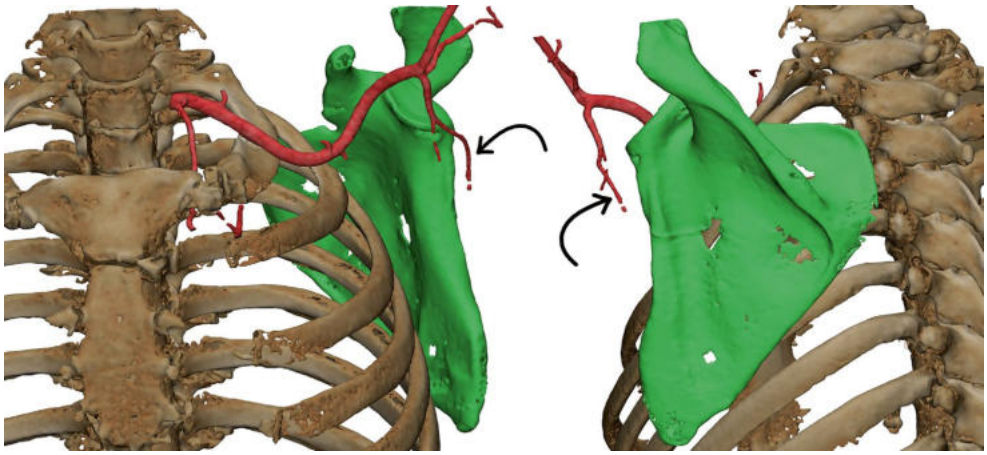


Fig. 5 Correct 3D scene to establish a scapula flap reconstruction. Scapula must be segmented after careful separation from the ribs. The vascular segmentation should emphasize the thoracodorsal artery

highly versatile and can be also harvested as chimeric flap. Interestingly, future developments of both imaging and software might allow to track small caliber vessels, even perforators, and define also the shape of soft tissue, including skin paddle and muscle cuff.

- DCIA: The deep circumflex iliac artery branches from the external iliac artery. Segmentation should be performed by placing a seed voxel in the external iliac artery and then following the DCIA as it approaches the bone on the inner margin of the iliac crest. Concerning bone, the femoral head should be removed from its acetabulum, and the ilium should be separated from the sacrum, to enable inspection of the sole donor source of the flap (Fig. 6).

3.2 Ten-Step Workflow for Virtual Surgical Planning

VSP determined the most suitable remodeling for the flap to provide the most anatomically reliable and functional reconstruction. The main issue arises from the fact that surgical software, including ProPlan CMF (Materialise NV, Leuven, BE), generally includes automated workflows for the interactive placement of bone segments, allowing to simulate the facial reconstruction while the segments are simultaneously readjusted in the donor site. This technique, for instance, is extensively used to plan mandibular reconstructions using the fibula free flap and is described in detail in Chapter "Virtual Planning and 3D Printing in Mandibular Fractures".

Therefore, given the non-exclusive use of the fibula free flap for midfacial reconstruction, the workflow presented thereafter will not consider an automated algorithm. In some circumstances, such as in cases of nonlinear (non-coaxial) orientation of segments, the automated workflows might not work for the fibula itself. In addition, the workflow will differ if a craniofacial implant is used.

1. *Definition of a virtual wax-up*: The main concern of a free-flap osseous reconstruction is to associate anatomical reconstruction with functionality. Therefore, the flap position needs to be optimized in its orientation with the future prosthetic rehabilitation. For this reason, software for digital prosthodontics such as Zirkonzahn.Modellier (Zirkonzahn, Gais, South Tyrol, IT) and Exocad (Exocad GmbH, Darmstadt, DE) offer the possibility to model a digital replica of missing crowns based on their relationship with the antagonists. This procedure, named as virtual wax-up, help define the most suitable places for dental implants, including abutments and fixtures (Fig. 7). This is a crucial step to assess to which level the bone should be planned, thus the occlusal height of the flap.
2. *Donor site transposition on the recipient site*: The donor bone is transferred in the recipient site. This preliminary orientation is essential to define the optimal side for flap harvesting, primarily in consideration to the required position of the pedicle, which represents the first criteria to define the correct harvesting site, as well as estimate the required length of the pedicle. Subsequently, the flap is repositioned in the most suitable spatial arrangement to match requirement of the recipient site in terms of curvature and replication of the resected structures, for instance, the maxillary alveolar process. Other relevant criteria include the possibility to transfer higher thickness regions of the bone where the implants are planned (Fig. 8).
3. *Design of osteotomies (1 segment):* Once the donor bone has been correctly oriented, osteotomies for the flap are created to delimitate the quantity of bone needed for midface reconstruction. Flap osteotomies must ideally share the same cutting plane as resection osteotomies. This maximizes the bone-to-bone interface and improves flap stability and healing. Once the surgeon is satisfied

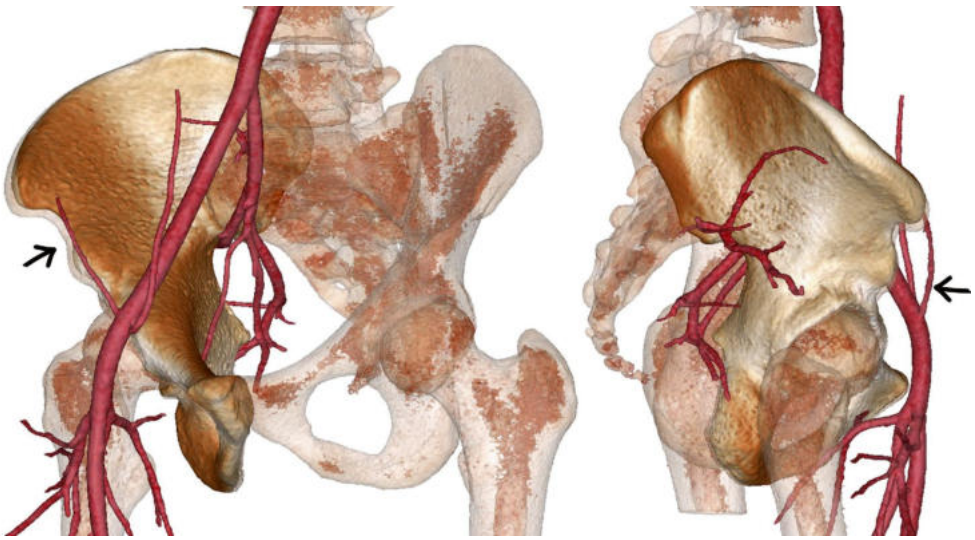


Fig. 6 Correct 3D scene to establish a DCIA flap reconstruction. The vascular segmentation should emphasize the DCIA

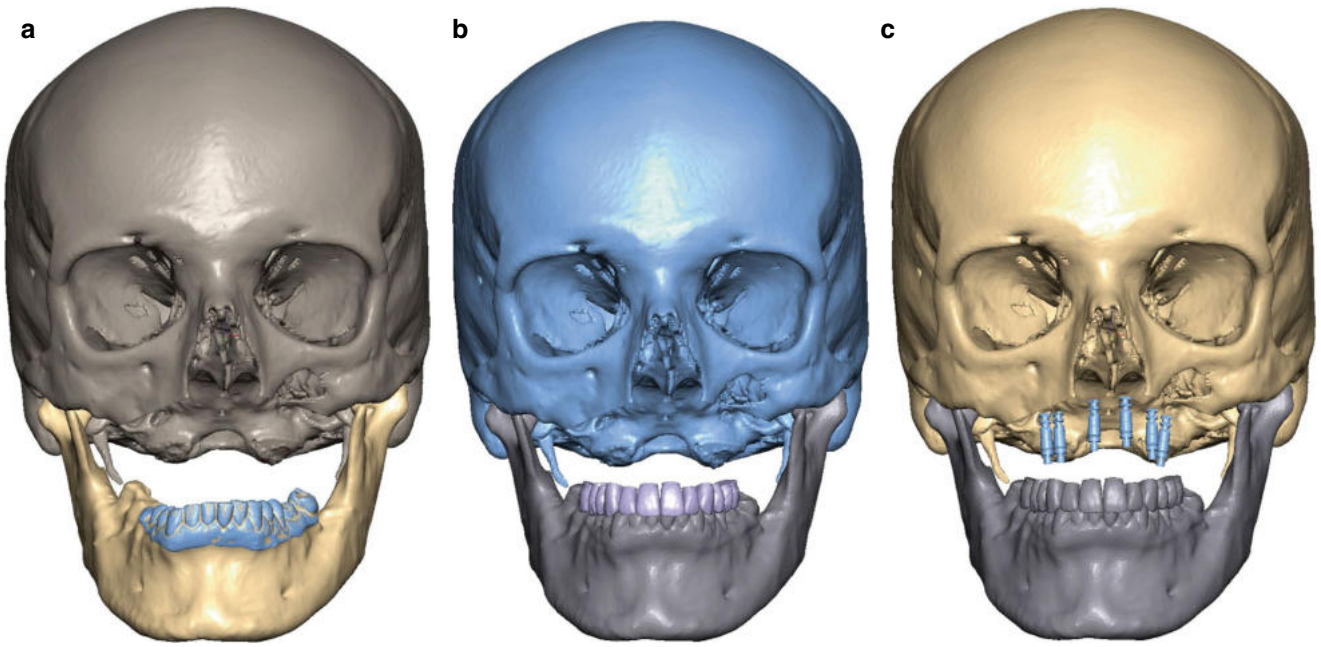


Fig. 7 Definition of the virtual wax-up in functional relationship with the mandibular antagonist for occlusion-based implant placement

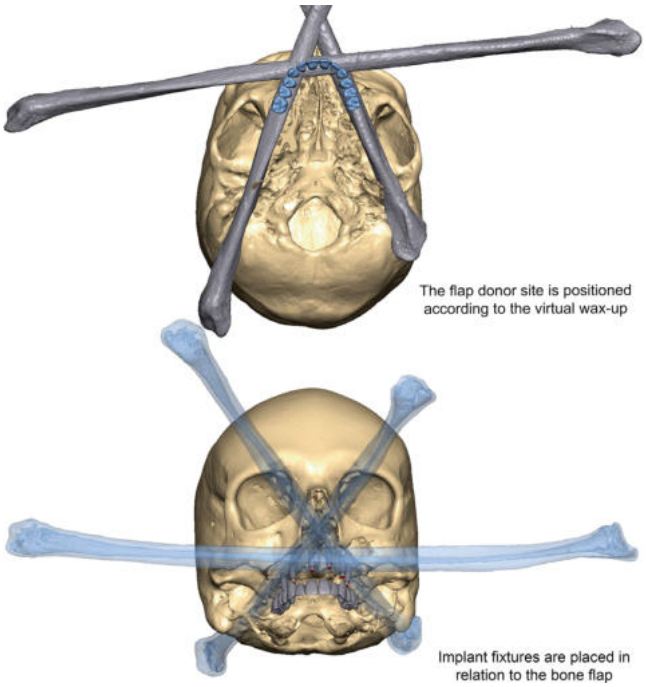


Fig. 8 Occlusion-based flap planning is performed to optimize the position of underlying bone with implant sites

with the virtual flap insetting, only the flap is left visible and the donor bone is hidden.

4. *Design of multiple osteotomies (multiple segments):* in case of more than one segment, the donor bone needs to be duplicated and moved forward/rotated to match the position of the second segment, as seen in Fig. 8. This second flap repositioning must take into account the size of the intersegmental wedge. Once satisfied with the position of this second segment, additional osteotomies are planned.
5. *Realignment of flap segment on the native donor site:* After donor site transposition has allowed to define the correct length and orientation of the flap, each segment is transposed in the donor site with a global registration method. This step is crucial and helps visualize the real quantity of bone to harvest in the donor site and represents the basic condition to design the surgical guide (Fig. 9).
6. *Definition of sites for screw and implant placement:* Each fixture is positioned in the transposed flap and then transferred to the donor site for surgical guide creation using the aforementioned alignment functions (Fig. 10). Care is taken to avoid collisions between screws and implant.
7. *Design of the surgical guide:* In the bone chosen to harvest the flap, the boundaries of realigned segments are used as base to create cutting planes. Each cutting plane is extruded inward to create the flange for the surgical guide. As will be explained in detail in Chapter "Virtual Planning and 3D Printing in Mandibular Fractures" for mandibular reconstruction, there are two types of flanges: linear, which helps perform the osteotomy outside the flange, and notch-based, which provides an inner fissure for the blade of the cutting tool. Linear flanges enable a complete cut and can be used in single segment reconstruction of in multiple segment reconstruction when each segment is widely separated from the other, whereas notch-based guides enable intersecting cuts, thus are appropriate in cases of multiple segment reconstruction with narrow intersegmental wedges (Fig. 11). Depending on the implant position in the native fibula, implant slots within the fibula guide may be designed, or a separate guide can be modelled to position implants in the oral cavity after flap insetting, especially when individual segments are short.
8. *Flap recontouring:* Further modeling of the flap can be performed, such as border trimming in correspondence of the piriform notch or the inferior orbital margin. Flap



Fig. 9 Fibula segments are realigned in the diaphysis to be used as reference for the surgical guide

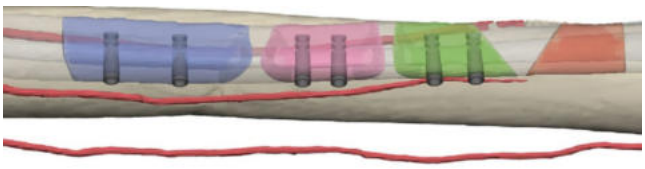


Fig. 10 Implants are inserted in segments planned for maxillary reconstruction. The most distal segment is used to reconstruct the maxillomalar buttress

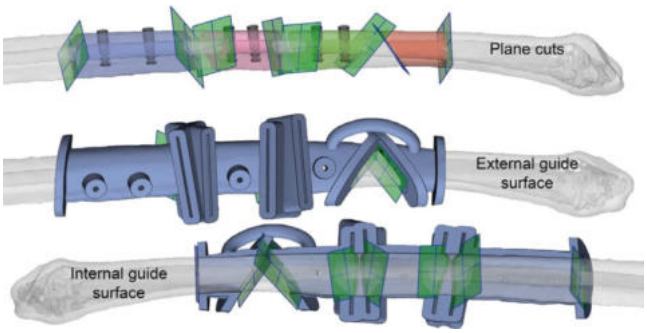


Fig. 11 Datum planes are designed tangent the extremities of fibula segments. If intersegmental wedges are too narrow and cutting flanges intersect, linear flanges are only effective at the extremities. Thus, notch-based flanges are used to allow self-intersecting cuts (central)

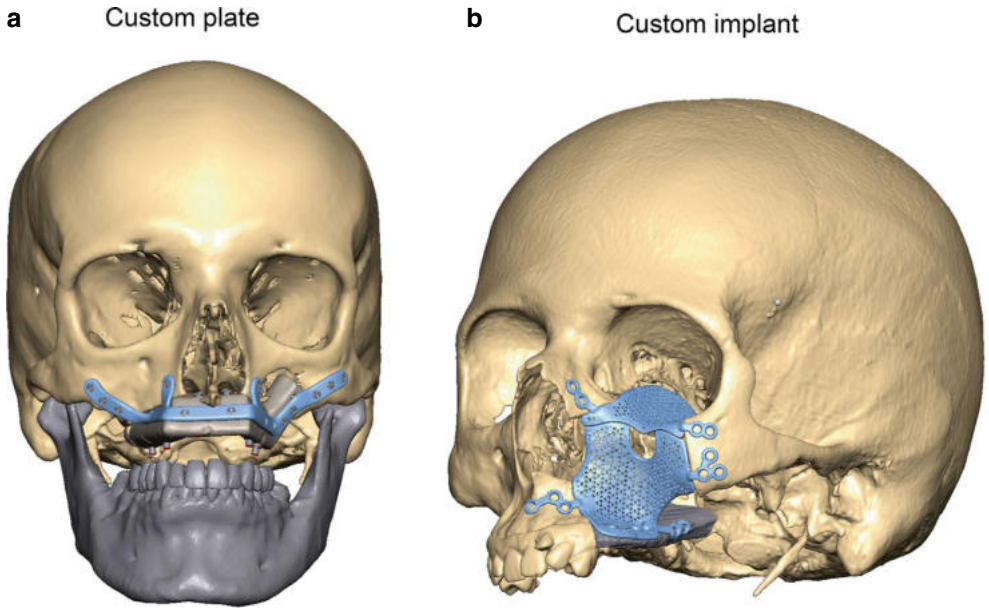


Fig. 12 Left: custom-plate; right: custom-implant

excess can be trimmed off as well if unnecessary. If needed (for example in case of flap reshaping before the insertion of a patient-specific implant), flap recontouring can be assisted by a surgical guide as well.

9. *Craniofacial implant/plate design:* Considering both the position of the flap and screws, a customized craniofacial implant or plate replicating the missing parts of the midface is modeled (Fig. 12).
   (a) In cases of implants, modeling often starts from an anatomical shape, achieved through mirroring for sided defects, or using best donor template geometry (possibly, in the near future, by generative AI). This geometrical input helps replace the missing parts, including the orbit and the midfacial buttresses (hybrid reconstructions are used almost exclusively for extended defects which most often include at least the orbital floor). The newly created geometry, representing the core of the patient-specific implant, is then added to flanges designed to perfectly overlie both the osseous flap and the resected skeleton. Usually, the implant is also added a slot for the flap to enhance flap stability, yet this slot is difficult to predict due to additional bulk volume caused by the soft tissue components of the flap. Flanges for implant fixation must use the same screw coordinates preliminarily defined for surgical guide creation with the intent of preserving the highest quantity of bone.
   (b) In cases of plates, the reconstruction model is wrapped and surfaces marked for plate fit are identified. Subsequently, the plate is extruded from the same surface and is thus granted a perfect correspondence with desired anatomy.
10. *Preparation for 3D printing*: The model containing the flap in the final reconstruction site is remeshed. As osteotomies have created separate objects, the resected skull and the flap need to be joined for a unified 3D printed replica. This is achieved by merging the objects together and applying a wrapping algorithm with minimal offset and gap closing distance. This workflow is explained in detail in Chapter "Virtual Surgical Planning in Midfacial Oncology" concerning mandibular fractures. The final model can be further remeshed to decrease computational effort and to allow the software an easier handling when layering the structure for 3D printing. Eventually, a traditional plate can be conformed using the 3D printed replica as template and can undergo reverse engineering by optical scanning or CT to be used in the VSP (see case 4.5) (Fig. 13).

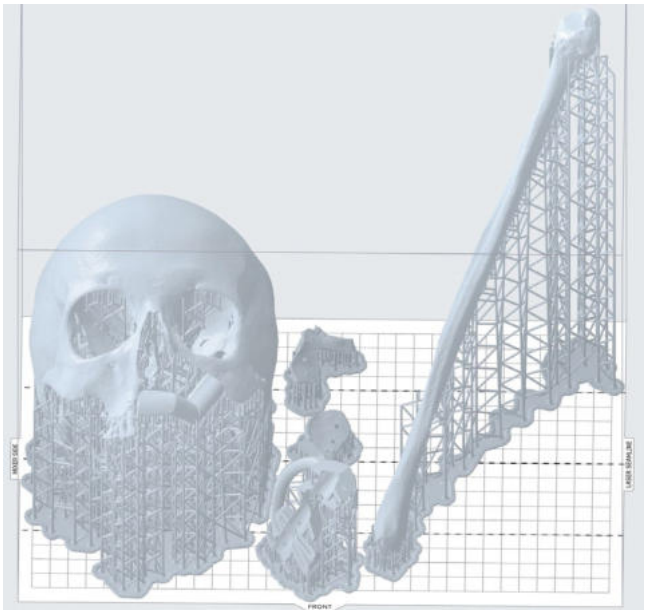


Fig. 13 3D printing project setup in Preform software

4 Clinical Cases

4.1 Biaxial Fibula Reconstruction for Class II Maxillectomy

Clinical History

This reconstruction refers to the case treated in the previous chapter in section 4. The patient was subject to a class II maxillectomy involving the alveolar process of the maxilla, the pterygoid plates, and part of the zygomatic buttress. The hypothetical reconstruction needed to take into account both the restoration of the alveolar process with implant placement and the replacement of the maxillo-malar buttress. For this reason, a biaxial, double barrel, fibula flap was considered. The fibula was preferred for its enhanced capability to be articulated in a biaxial configuration for such defect and low comorbidity.

Virtual Surgical Planning

At first, the fibula was segmented as previously described, indicating the position of the vascular pedicle. Given the involvement in the resection of both the alveolar process and the maxillo-malar buttress, a biaxial fibula flap reconstruction was chosen. Considering an axis passing through the geometric center of both the alveolar process and the maxillo-malar buttress, an "X" shape is visible, showing that axes are not linear but cross each other. During VSP, two replicas of the ipsilateral fibula were cloned in the maxillofacial defect area: the inferior, representing the alveolar process and the exit site of the pedicle, was located proximally, while the superior, intended for the maxillo-malar reconstruction, was positioned distally, including a necessary 180° rotation needed to place it above the proximal segment. The whole process was prosthetically driven, as the alveolar process segment was positioned in relation to the virtual wax-up of teeth 14, 15, and 16, representing the corresponding sites for implant placement. The proximal fibular segment was grouped with implants as a unified entity and then repositioned in the leg using realignment operations, and the same was repeated for the distal segment as well: this procedure helped assess flap segments within the fibula diaphysis, and most of all, to define the size of the intersegmental wedge enabling 180° rotation (Fig. 14). Additionally, it helped design the fibula cutting guide for flap harvest with the guiding cylinders for the insertion of implant fixtures of teeth 14, 15, and 16 (Fig. 15).

Surgery

The fibula flap harvesting procedure was performed traditionally by firstly identifying the posterior crural septum, then dissection slid to reach the interosseous membrane. Proximal and distal osteotomies were performed, and then sectioning of the interosseous membrane was enabled for fibula mobilization. The surgical guide was positioned and osteotomies for both segments of the flap were performed. Owing to the biaxial orientation of the flap, which involved reciprocal divergence between the proximal and distal segments with an increased tension over the pedicle, the intersegmental wedge was carefully excised to avoid any stretch on vessels. Implant sites were drilled using the surgical guide, and fixtures were inserted in planned positions (Fig. 16). Osteosynthesis of the flap was performed using stock plates prebent over the 3D printed replica of reconstruction (Fig. 17). To further enhance accuracy in flap insetting and fixation, the positioning of flap segments was checked using intraoperative navigation, ensuring that the distal segment could reliably replicate the orientation of the alveolar process.

4.2 Articulated Fibula Reconstruction for Bilateral Class II Maxillectomy

Clinical History

A 66-year-oldy lady reported a history of malignant disease, treated in another center with a bilateral maxillectomy, reconstruction with forearm free flap, and irradiation. Several years after radiation therapy, she was referred to our center for the progressive onset of excruciating pain in her upper jaw and secretion. She underwent a CT scan showing a conspicuous remodeling of the bone tissue with radiolucent lacunae and scalloped borders. Diagnosis of osteoradionecrosis of the jaw (ORNJ) was performed. A right, class

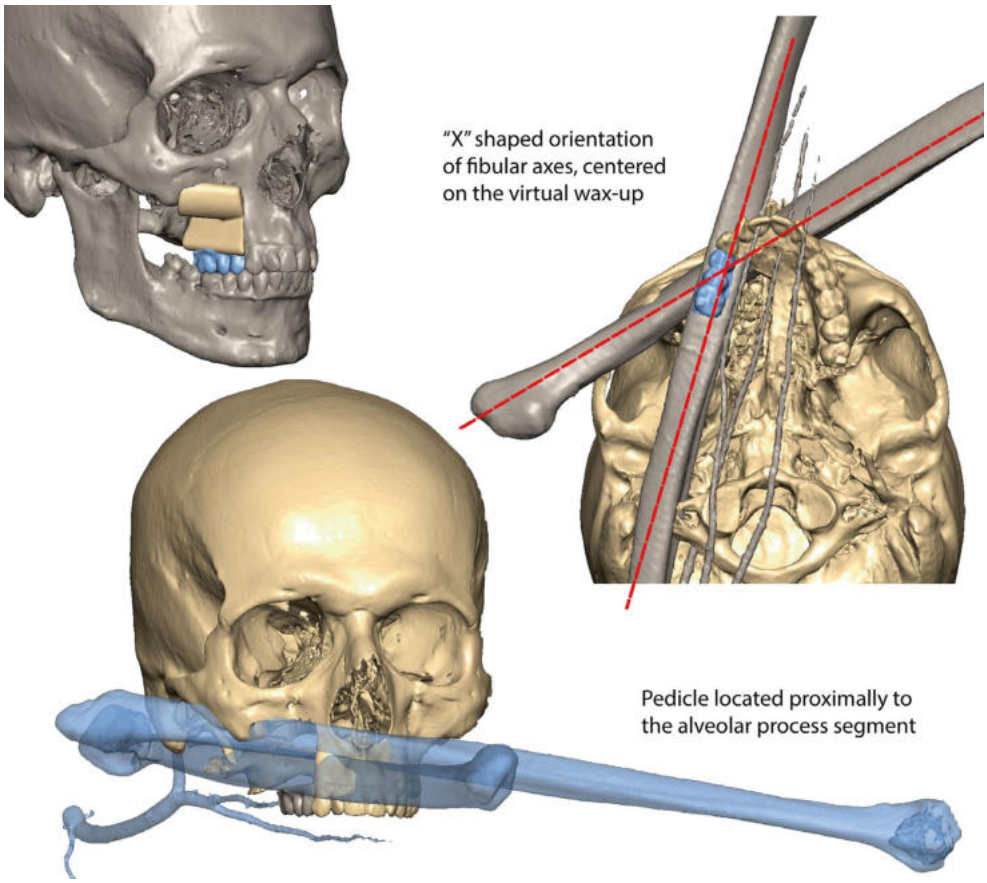


Fig. 14 VSP of biaxial fibula reconstruction to support both the alveolar process and the maxillomalar buttress. This reconstruction is based on virtual wax-up

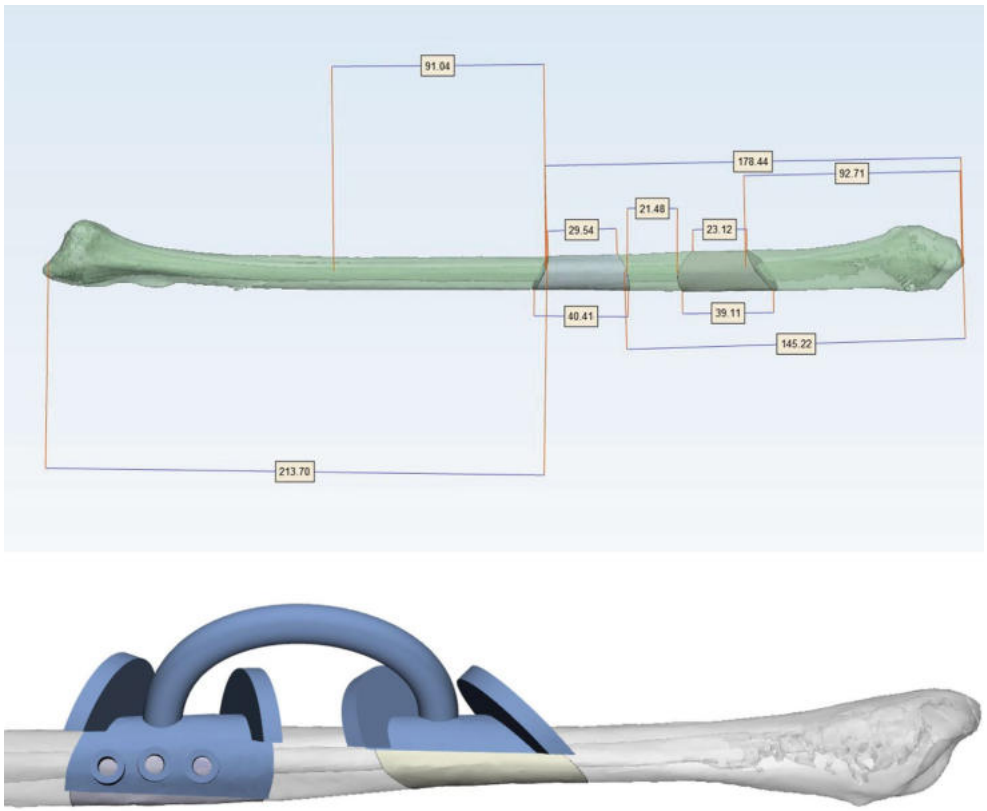


Fig. 15 VSP measurements for fibula flap harvest and creation of a surgical guide with implant slots

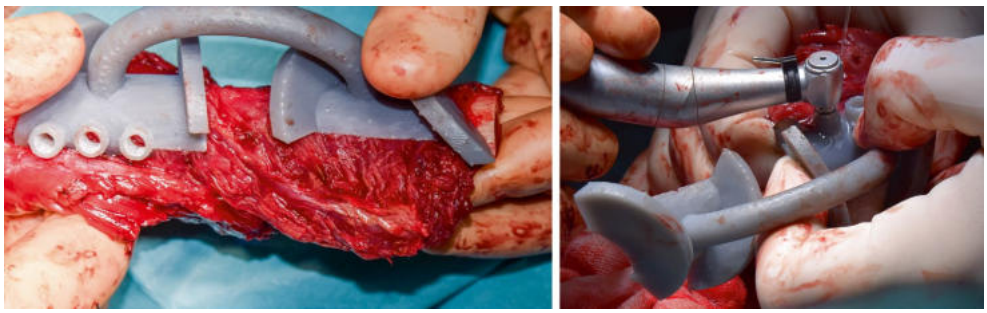


Fig. 16 Intraoperative positioning of the fibula guide and implant drilling

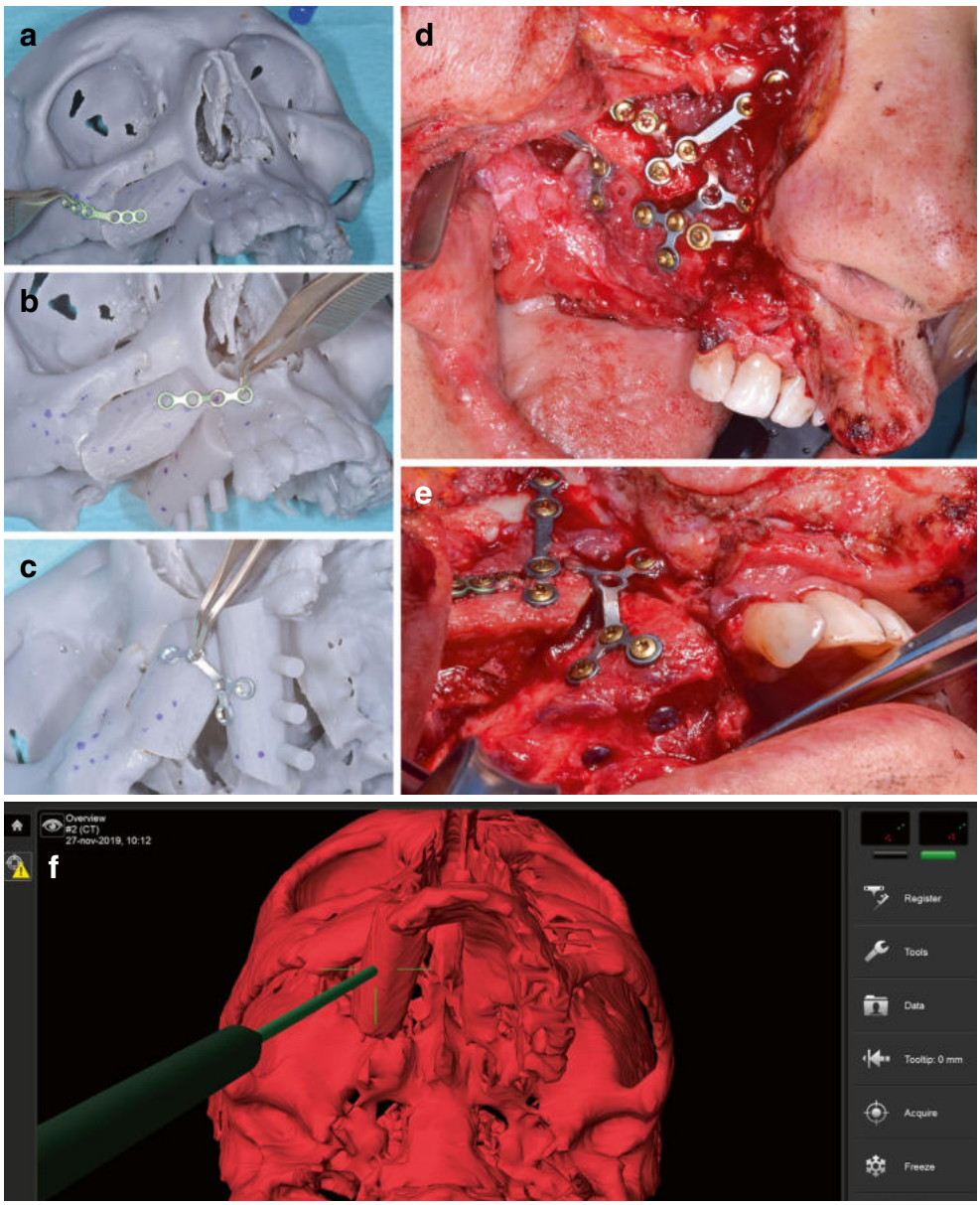


Fig. 17 Plate prebending using a 3D printed model (**a**–**c**), intraoperative sequences (**d**–**e**), and navigation of flap inset (F)

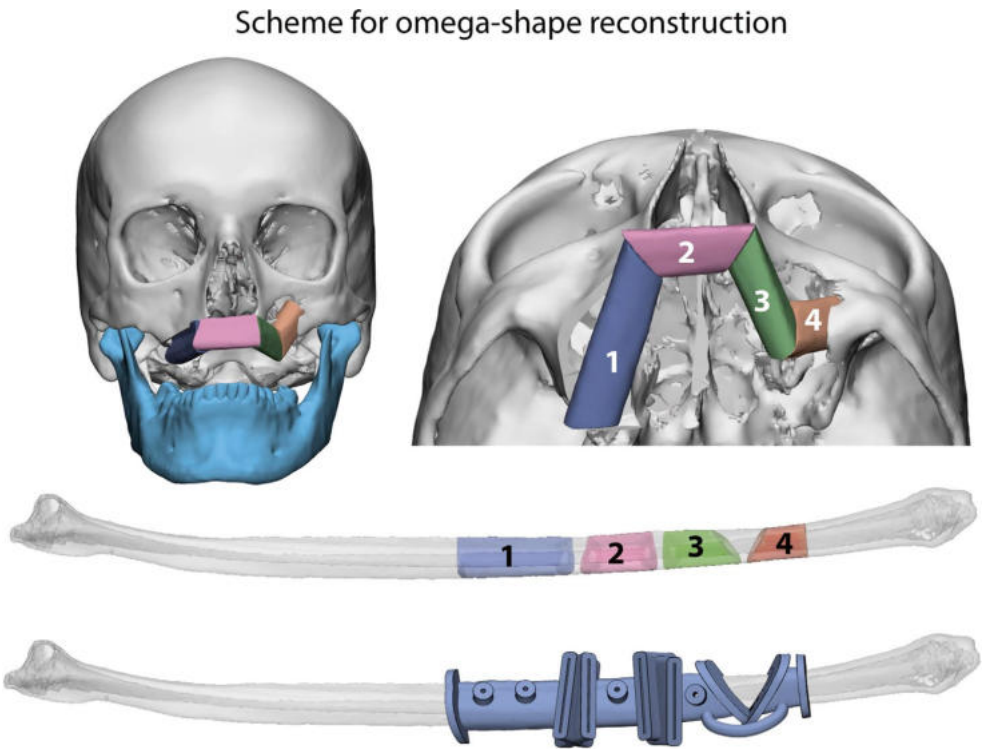


Fig. 18 VSP for omega-shaped maxillary reconstruction

II maxillectomy was proposed to the patient to remove the necrotic bone, while, on the left side, a conspicuous oro-antral communication had developed. To reconstruct the defect, an articulated reconstruction using the fibula free flap was accepted by the patient. Four segments were planned to achieve a full maxillary reconstruction using the omega-shaped fibula configuration, as described by Hanasono [9]. In addition to the classic three segments of the omega configuration, which reconstruct the alveolar process, a fourth segment was added on the left side to replace part of the missing left malar buttress. The patient was sent to CT angiography of the head and neck region to define bone geometry and evaluate the recipient vessels in the neck, depleted by previous oncologic surgery and irradiation, and lower limb CT angiography as well to plan the most appropriate fibula reconstruction. Moreover, intraoral scanning was performed to match the actual dental crowns with CT.

Virtual Surgical Planning

The VSP protocol for this case has been extensively discussed in Sect. 3.2, where its phases are described in detail. As seen in Fig. 8, omega-reconstruction is prosthetically guided, thanks to the possibility of designing a virtual wax-up based on the antagonist arch.

Before planning the reconstruction, a right maxillectomy based on Le Fort I osteotomy was planned to excise necrotic bone with the aim of optimizing the flap recipient site as well. Resection surgical guides were modeled to assist the computer-guided tracing of Le Fort I osteotomy on the right side and remove the residual bone on the left side, at the same time preparing the zygomatic buttress to receive its homologue in the fibula flap (Fig. 18).

Fibula flap planning was performed using the right leg as donor site. As the mucosal layer was intact, there was no need of a skin paddle to be included with the flap, thus the eventual position of the posterior crural septum was not taken into account. This allowed more freedom in the choice of the donor side, privileging considerations of vascular anatomy, that was preferable on the right side owing to the caliber of arteries. The pedicle position was established posterior on the right side. Thus, the distal segment, close to the malleolus, was used to reconstruct the ZMC, whereas the most proximal segment was positioned in the right posterior maxillary area so that the pedicle would exit approximately at the level of the right maxillary tuberosity. As the reconstruction involved four segments, which include a considerable amount of bone, the size of three intersegmental wedges was kept narrow to avoid bone waste. However, intuitively, the number of intersegmental wedges decreases the overall

curvature, thus the length of each wedge. All segments of midface reconstruction, along with their respective screws, were aligned to the fibula diaphysis; a surgical guide was modeled to harvest the fibula flap in its four segments (Fig. 18).

Finally, the skull with fibula segments was wrapped by minimizing surface offset and calculating a gap closure distance slightly beyond the size of the virtual osteotomy to create a unified geometry. The wrapped model was used to design a patient-specific plate, whose hole configuration was based on the position of screws (Fig. 12a). The plate was additively manufactured through titanium SLS and a replica of the skull was printed as well.

Surgery

A superior lip-split incision with perialar prolongment was performed to widen the midface up to the level of the piriform notch. The incision was continued intraorally to access the maxilla from both sides. During dissection, care was taken to preserve the palatal fibromucosa, subsequently exposing only the necrotic bone. Periosteal elevation was carried out superiorly at the level of zygomatic body, with attention not to injure the infraorbital nerve. Surgical guides were positioned, and a right Le Fort I osteotomy was performed, as well as the removal of the residual left hemimaxilla, which presented conspicuous disruption and an oro-antral communication. The fibula free flap was dissected, and surgical guide positioned to sculpt each of the four segments. The inset of the segments on the customized plate was performed with the flap still attached to its pedicle on the leg, and the full reconstructed maxilla was transferred on the recipient site, while positional accuracy was interactively checked with navigation of VSP (Fig. 19).

4.3 Horizontal Scapula with Patient-Specific Implant for Midfacial Reconstruction

This case completes the previous description in Chapter "Application of VSP in Temporomandibular Joint Surgery", paragraph 4.1.4. The complexity of this resection, the involvement of highly functional area (the alveolar process and the orbital floor), the benign nature of the disease, despite its locale extension, and the young age of the patient were all factors considered in the choice of the ideal reconstruction. After various options using the fibula free flap were initially considered, the final decision was based on the scapula free flap placed horizontally, given its possibility to geometrically replicate the same curvature of the alveolar process and reconstruct the bone of the hard palate. Likewise, to improve possibilities of craniofacial reconstruction around the orbital area, it was decided to couple the scapular flap with a patient-specific implant.

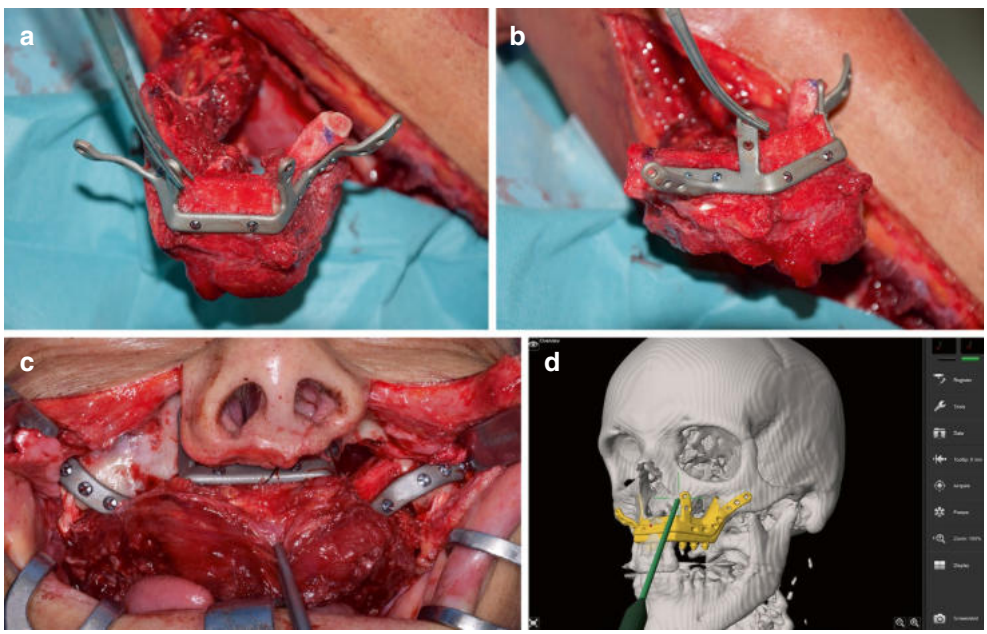


Fig. 19 (**a**, **b**) Reconstruction of the neomandible while still connected to the leg; (**c**) complete maxillary reconstruction; (**d**) navigation of flap inset

Virtual Surgical Planning

Reconstruction had to deal with the accurate segmentation of the donor site. Unlike the fibula, which can be highly standardized and represents an easy anatomical region to segment starting from a CT angiography of the lower limbs (the same considerations are true for the DCIA), segmentation for the scapular region is more challenging owing to the following reasons:

1. More complex vascular anatomy compared to the fibula free flap: the pedicle of the scapula flap is represented by the subscapular artery system, in particular, the circumflex scapular artery and the thoracodorsal artery, a branch of the subscapular system. The angular artery, specific for the scapular tip flap, is a further subdivision of the thoracodorsal artery. This region has a complex vascular network, which includes also branches of the subclavian and axillary artery to the humerus and other regions of the scapula; thus, vessel recognition is not as intuitive as in the leg.
2. Modified position of the patient during acquisition: for chest CT acquisition, the patient is positioned with his upper limbs extended above the head. This alters the position of the scapula and the course of vessels compared to traditional anatomy charts and makes it more complex to track the vessel for segmentation.
3. Separation of the scapula from multiple contact points across the ribs: the scapula bone has to be separated through its multiple contact points with the ribs; moreover, separation across the gleno-humeral and acromioclavicular joint needs to be completed.

In this specific case, for didactic purposes, 3D simulation was enriched with the segmentation of the heart and the epiaortic vessels, thyroid gland, subclavian arteries, and internal mammary arteries. The reconstruction of the cardiovascular apparatus is useful to determine as well if the contrast-enhanced CT was acquired with the appropriate timing, since, due to the proximity of the subclavian artery to the heart, the pedicle for the scapula flap has an early enhancement compared to other sites such as the DCIA and the fibula. Thus, intuitively, the heart and the thoracodorsal artery share similar enhancement time after injection of contrast medium (Fig. 20).

Once the donor site was successfully segmented, it was transposed to the recipient site, along with the pedicle. This helped search the best orientation of the bone flap to reconstruct the defect, and for this specific case, the inferior-lateral border of the ipsilateral scapula was found to have the best correspondence in terms of curvature with the mirrored healthy side. This enabled a reliable reconstruction of the missing maxillary alveolar process. As a further confirmation, the virtual wax-up of crowns in relation to the mandibular antagonist showed a compatible curvature of the dental arch and the scapular segment. This helped define the position of three dental implants in the lateral mandibular border, in the appropriate sites defined by the virtual wax-up. The pedicle position is carefully inspected to evaluate its compat-

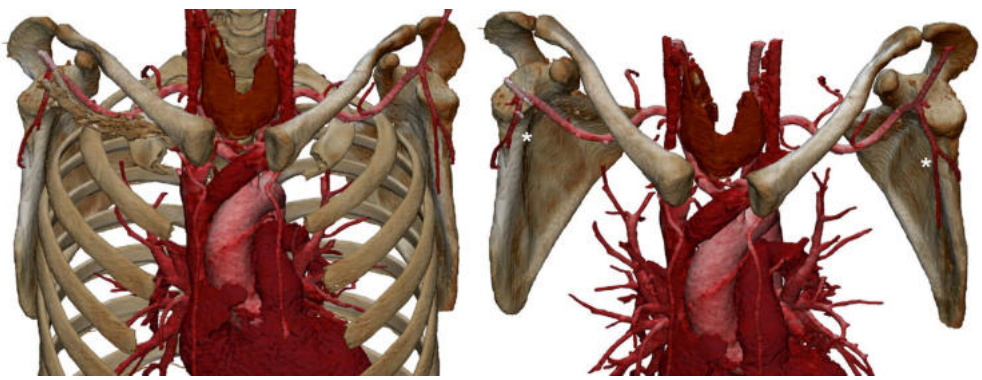


Fig. 20 Reconstruction of the thorax to isolate the epiarotic vessels and the subscapular system. Asterisks are placed in the thoracodorsal artery

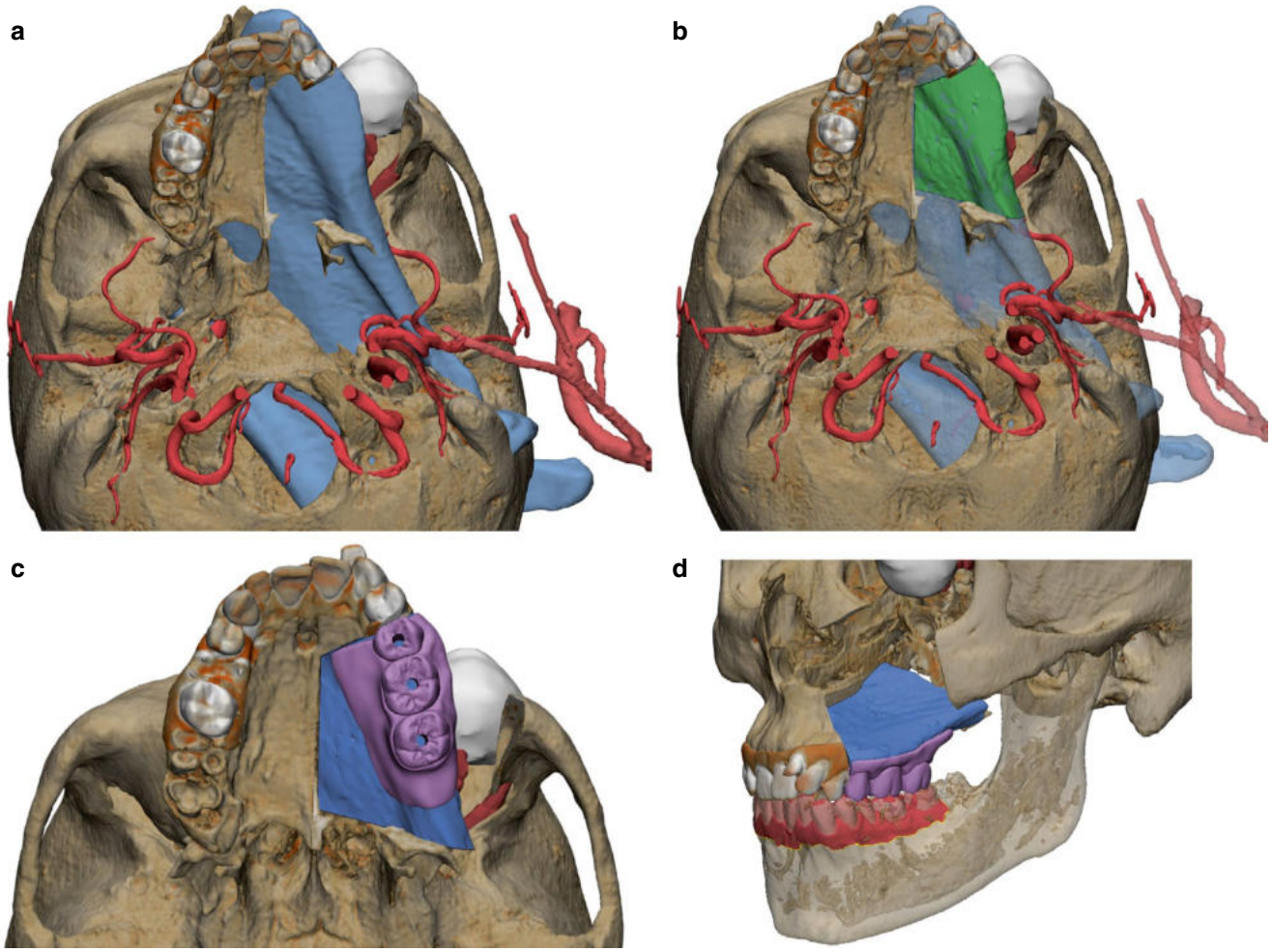


Fig. 21 The scapula and its vasculature are virtually transferred in the recipient site to determine the most suitable flap shape and orientation in relation with surrounding anatomy and wax-up

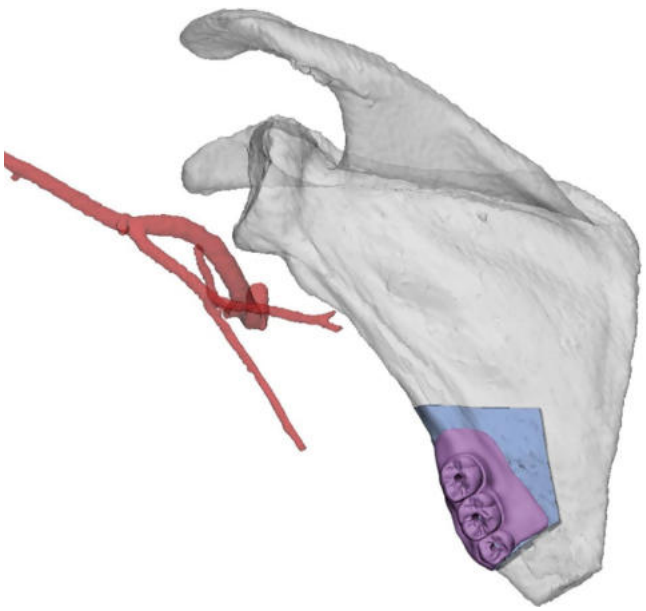


Fig. 22 Alternatively, the virtual wax-up can be transferred to the original donor site together with the flap

ibility with the surgical maneuvers: the thoracodorsal artery can be seen running posterior and lateral to the flap, in the most suitable position to be coupled with the recipient vessel and the surgical anastomosis (Fig. 21). Eventually, the virtual wax-up can be transferred back in the scapula to assess its position in relation to the flap; this makes theoretically possible to position the implants and the dental prosthesis directly in the scapula before it is transferred to the oral cavity (Fig. 22).

The surgical guide for flap harvesting was designed by matching the flap boundaries with resection planes, defining three intersecting flanges enabling to appropriately model the flap. As the scapula flap is entirely surrounded by muscles (subscapularis, teres major, and minor, infraspinatus), stable bone anchoring was searched only in the tip, which could be deperiostized, whereas both flanges and drilling cylinders were designed in "suspension," not to cause compression of the muscle cuff (Fig. 23).

Subsequently, using the mirrored side as donor template, a preliminary reconstruction of the midface was performed. This served as the base to premodel a drafted implant accord-

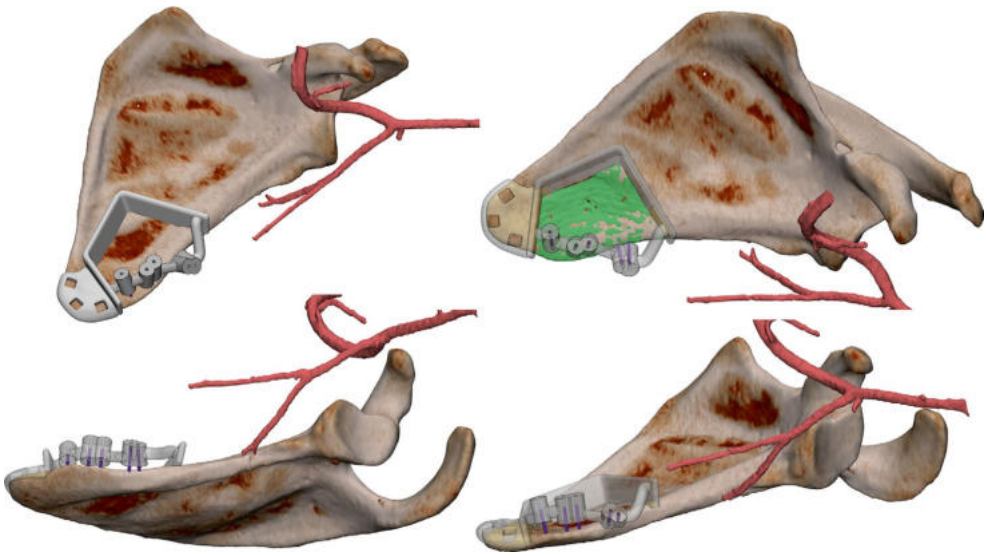


Fig. 23 Overview of surgical guide placed on the ventral surface of the scapula. The scapular angle is taken as a stable landmark for the guide, which is slightly elevated over the bone plane to avoid muscle interferences

ing to the hybrid workflow described in Chapter "Computer--Guided Orthognathic Surgery: State of the Art and Innovation" for orthognathic surgery. The drafted implant basically included the correct shape in terms of symmetry and adaptation, the appropriate location for the orbital floor, entirely reconstructed through organic modeling, and the flanges for osteosynthesis to fixate the implant both to resected buttresses and to the flap. Moreover, it helped define the sites for screws as well, which, together with the drafted implant, were shared with the manufacturer. The creation of the final implant was performed in collaboration with clinical engineers from Materialise (Materialise NV, Leuven, BE) and started from the definition of the screw position, defined by the surgeon, to the drawing of the implant contours across the strain lines, as well as the flanges for osteosynthesis, and was finally filled with a lattice structure using a trabecular pattern. The final implant was composed of two separate parts to facilitate its assembly through the transfacial access. A further, posterior flange was added to enhance the stabilization of the scapula flap and decrease the cantilever effect caused by masticatory forces (Fig. 24). Figure 25 demonstrates the perfect coincidence between planned holes for osteosynthesis, surgical guides, and the implant.

Surgery

Flap harvesting was performed in a supine position by keeping the arm lifted and rotated behind the head. An incision in the lateral thoracic wall from the axilla to 5 cm distal to the tip was performed, dissection aimed to locate the lateral margin of latissimus dorsi muscle and serratus anterior muscle. The branch to serratus anterior was identified and sectioned. Thoracodorsal artery was located and the branch to latissimus dorsi identified to harvest a chimeric flap including latissimus dorsi muscle cuff and the myo-osseous scapular tip flap. The angular branch was identified and dissected together with the flap. After releasing the scapular tip from the insertion of the serratus anterior, a wide osteotomy of the flap was conducted. The pedicle was clamped and the flap detached to be modeled on-bench using the surgical guide.

Before completing flap inset, custom implants were positioned easily through holes previously drilled to position the resection surgical guides. Following that, a tunnel through the cheek was dissected to enable pedicle position to recipient facial vessels. Flap inset was completed over the implants and stabilized using screws (Fig. 26). Accurate muscle sealing in the oral cavity helped prevent implant exposure and contamination with saliva, as the palate fibromucosa was preserved and sutured above the muscle. Figure 27 illustrates the optimal accuracy of flap inset and implant placement.

Notably, the rotator muscle cuff makes it hard to visualize predrilled holes and bone surface, and thus scapula flap is more difficult to model compared to fibula flap, where bone surface can be easily exposed to make flap harvest more accurate. Flap orientation was checked using intraoperative CT scan, which confirmed the correspondence with VSP.

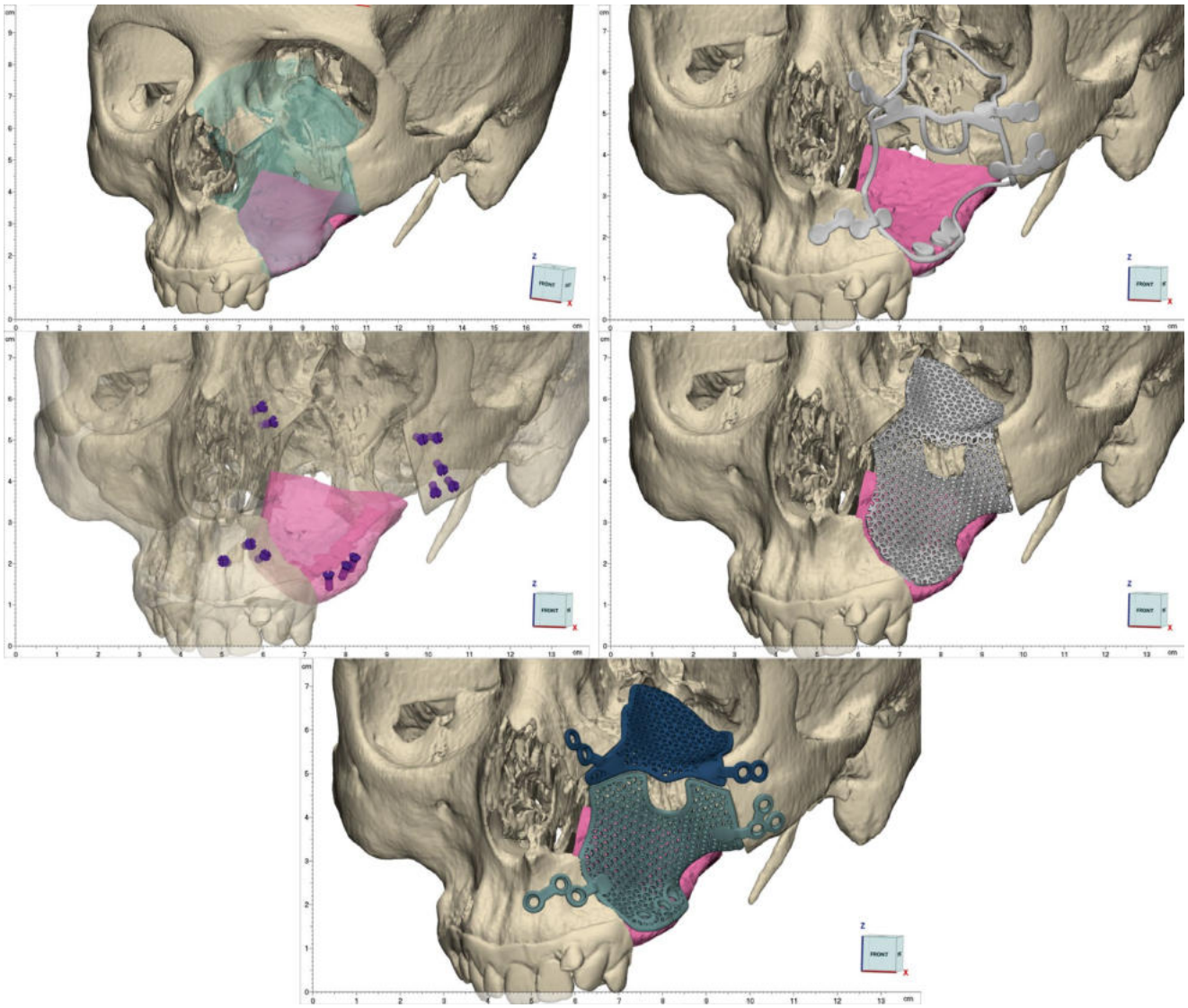


Fig. 24 Sequences of design of the customized implant by the manufacturer (Materialise NV)

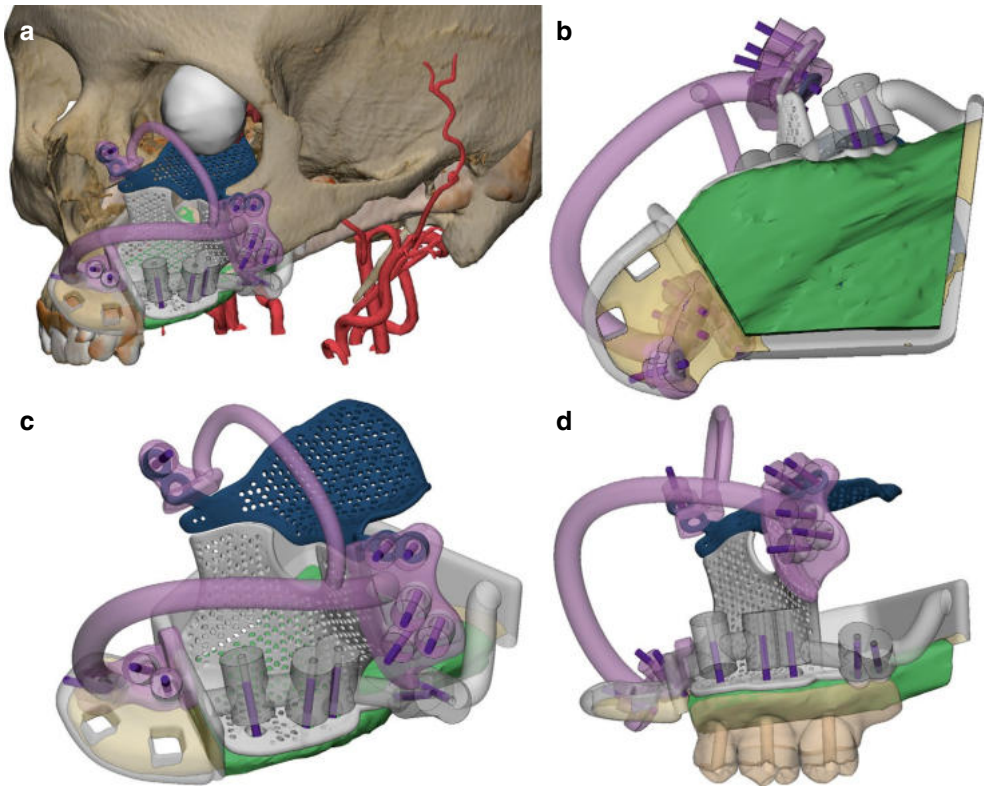


Fig. 25 Correspondence between resection guide, cutting guide, and custom implant. Overlap is best assessed in screw sites

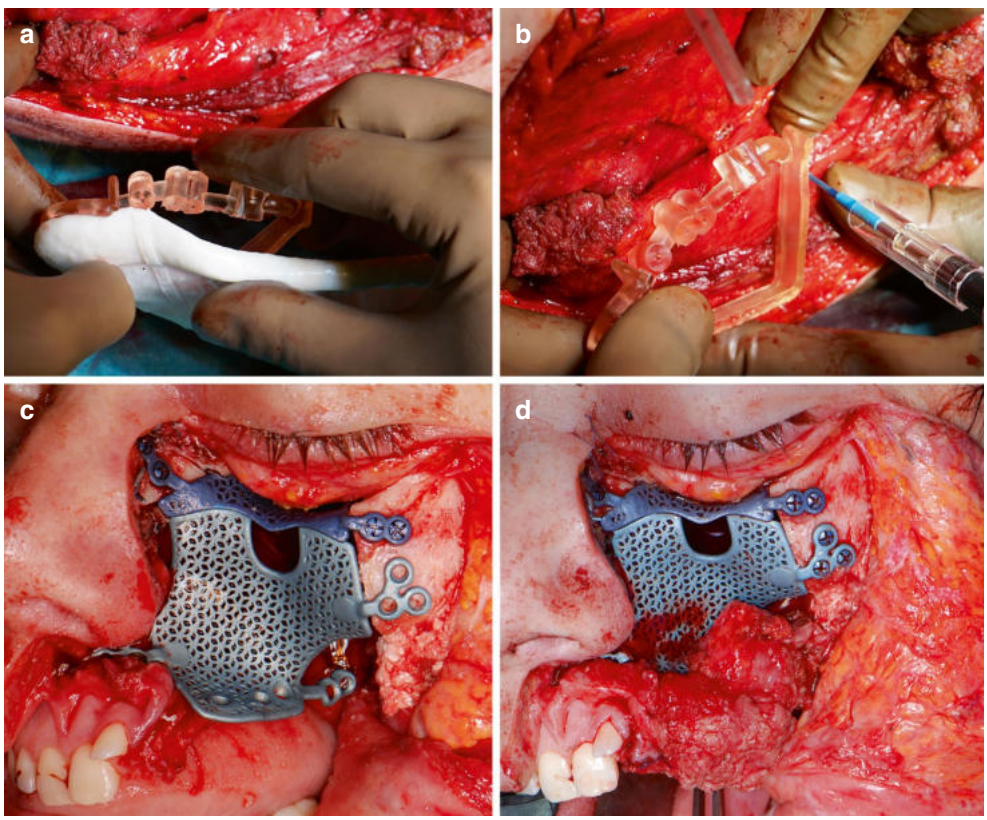


Fig. 26 Intraoperative sequences: (**a**) fitting test on 3DP models; (**b**) positioning of the guide on flap; (**c**) custom implant positioning; (**d**) implant with flap inset

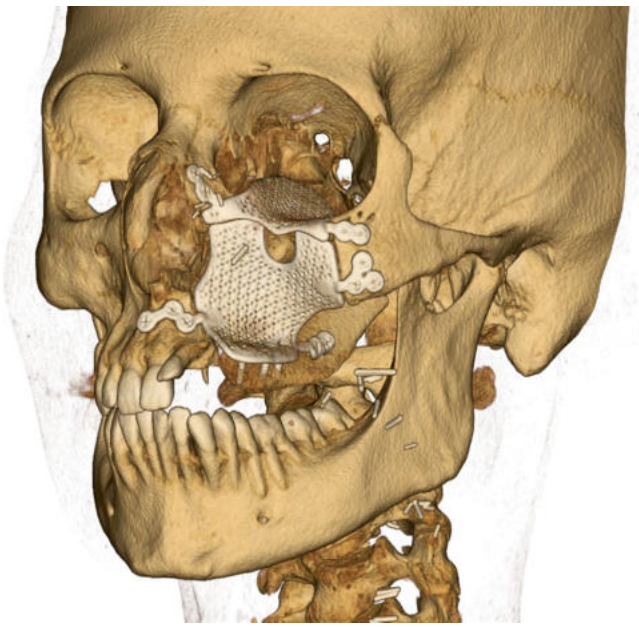


Fig. 27 Postoperative CT

4.4 Vertically Placed Scapular Tip Flap for Midfacial Reconstruction

Clinical History

A 64-year-old lady was referred to our attention owing to a previous maxillectomy with temporalis muscle reconstruction of advanced stage squamocellular carcinoma of the hard palate. The patient was subject to radiotherapy and, finally, after 7 years of clinical and radiological follow-up, she was free from disease. A class II defect according to Okay's classification was present and the patient was seeking a bone reconstruction to restore a functional mastication. Two years before, she was subject to iliac crest graft surgery, stabilized using a hand-modeled plate, but the graft eventually became infected and required removal. A microvascular reconstruction was proposed to the patient. After evaluating several flaps, in relation to the site of the defect and comorbidities related to the harvesting procedure, the choice was a scapular tip flap placed vertically to provide both the alveolar process and the skeletal framework of the mesostructure. The patient underwent angio CT scan for both the head and neck, and the thorax region. MR was not viable as this case was a secondary reconstruction and there was no further pathology to characterize.

Virtual Surgical Planning

First, head and neck CT scan was segmented. A pure bone sequence without vascular enhancement was used to reconstruct the bone structures of the midface and the mandible. Accurate metal artifact reduction was performed using dedicated filters to clear off scattering due to dental prostheses. Subsequently, the contrast-enhanced sequence was realigned to the bone sequence and segmented using a threshold value dedicated for vascular structures. Owing to the possible isointensity of the bone and vessels, a direct segmentation of such sequence would not be recommendable, as it would be impossible to separate the vessels from the bone in the 3D model. Therefore, once sequences were aligned, the bone mask was subtracted from the vascular-enhanced mask using a Boolean operation. This enabled to yield a mask for enhanced blood vessels. This step is not necessary in case a MR with dedicated vascular sequences is available. The result was a detailed 3D model of skeletal and vascular anatomy. The previously positioned titanium plate for graft fixation was digitally removed to better assess the flap recipient site.

The chest CT angiography was segmented to isolate a mask specific for left and right scapulae. Cardiovascular segmentation was performed as well to isolate epiaortic vessels at their origin from the left heart, and then subclavian arteries were followed distally through detailed segmentation until the thoracodorsal artery was identified running at the lateral scapular border. In this case, the presence of a metal body inside the right subclavian vein was a criteria to exclude reconstruction with the right scapula. The left scapula was chosen as donor side, also in light of its optimal geometrical adaptation on the recipient site (Fig. 28).

The scapula and its vascular pedicle were virtually transposed in the recipient side, and oriented favorably for both the reconstruction of the midfacial skeletal framework and the alveolar process. In this case, orientation was performed independent from a mirroring to define a balance between the symmetry of alveolar process restoration and an acceptable midfacial reconstruction as well (Fig. 29).

Surgical guides for osteotomies at the recipient site (for site preparation) and for scapula flap harvest were created using linear flanges. The guide for site preparation was made less cumbersome by designing it inside the resection site and not outside and was suspended using two fixation screws in the nasal buttress (Fig. 30).

While horizontal placement of the scapula privileges the reconstruction of the palatal vault, but has to be coupled with an implant for mesostructure restoration, a vertically placed flap enables a midfacial skeletal

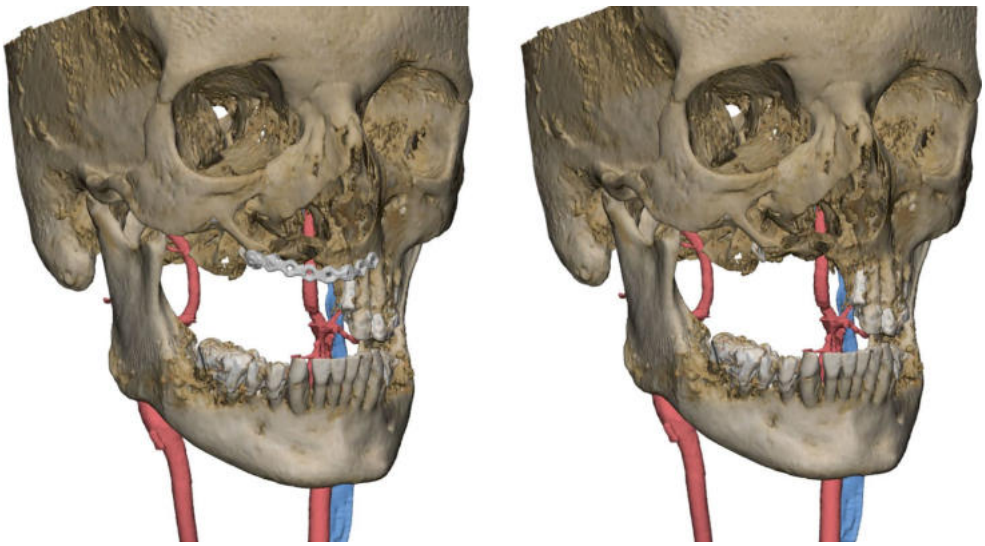


Fig. 28 Digital anatomy reconstruction outlines the maxillary defect bridged with a standard reconstruction plate and vasculature. Right: plane was separated and digitally removed

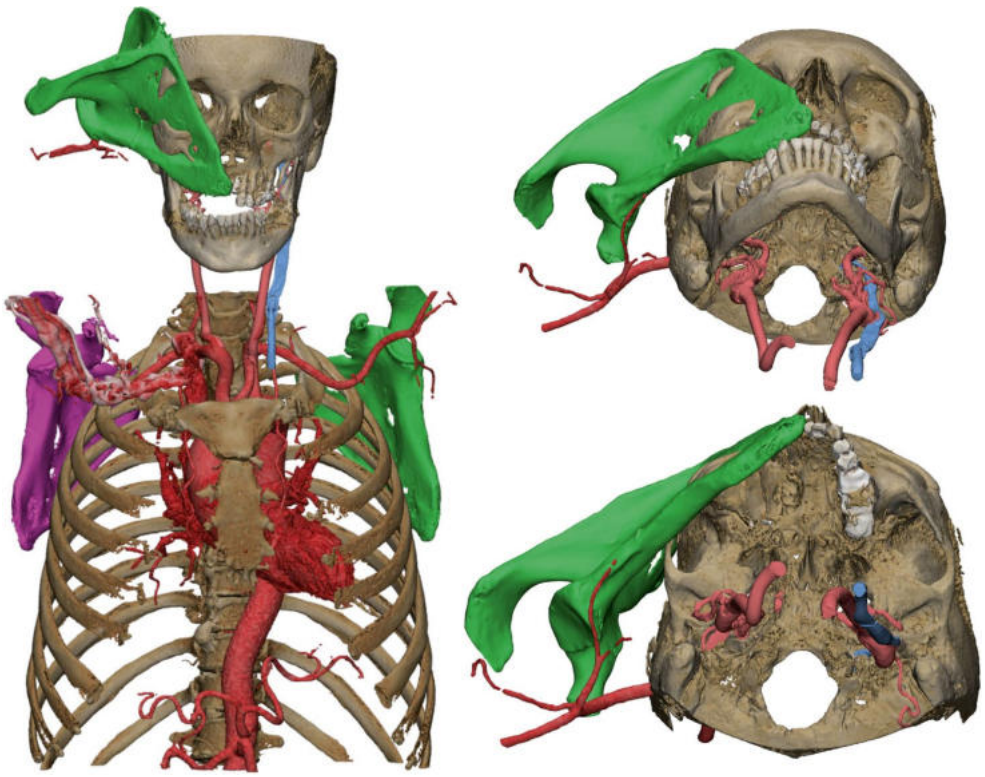


Fig. 29 Transposition of the donor scapula in the defect site to establish the most appropriate donor source and side based on vascular considerations as well

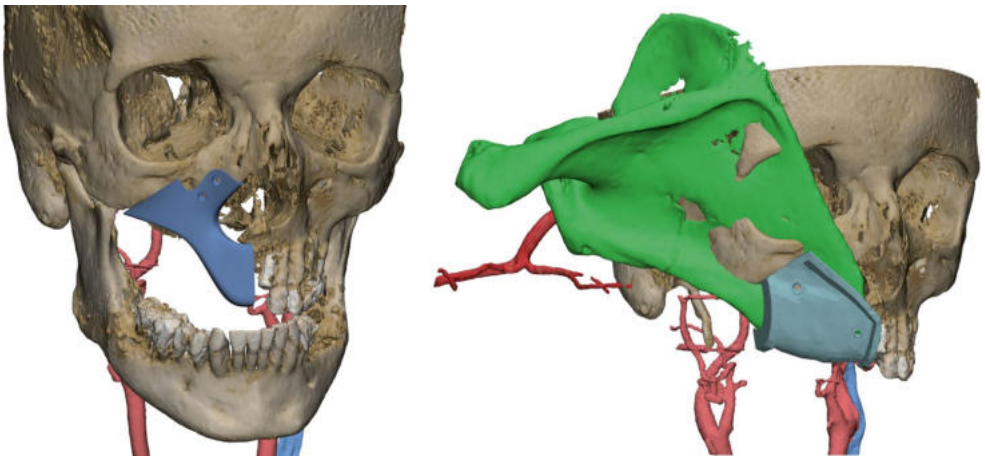


Fig. 30 Design of surgical guides based on resection margins for flap harvest (right) and defect site refinement (left)

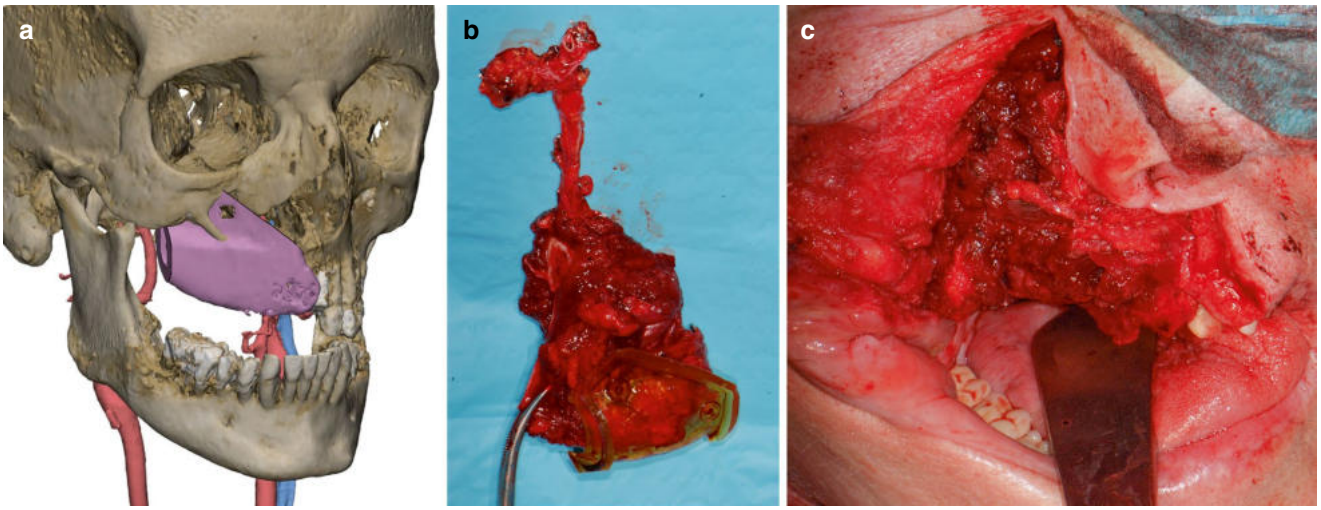


Fig. 31 Final flap VSP (**a**). On-bench modeling of the scapular tip using the surgical guide (**b**). Flap inset using a labial split approach (**c**)

replacement, privileging the mesostructure with a compromise in the optimal alveolar orientation that can be defined using VSP.

Surgery

A Weber-Fergusson incision, overlapping the previous surgical scar, was designed to access the right midface. Accurate periosteal elevation was conducted to expose the bone margins of the defect, and removal of the previous osteosynthesis plate was accomplished. The scapular tip flap was elevated from the left side after isolating the thoracodorsal pedicle, and osteotomies were accomplished using the surgical guide as reference. The flap was transferred in the defect site where it replicated the orientation defined in VSP and was stabilized using prebent plates (Fig. 31). Fixation was performed on craniofacial buttresses, as there were no drilled holes available. The oral mucosa was preserved as much as possible, and part of the muscle cuff attached to the flap was left exposed into the oral cavity to seal the underlying bone.

4.5 Fibula Reconstruction for the Midface with Reverse Engineering of a Prebent Plate

Clinical History

This patient was referred by a different institution for the reconstruction of a maxillary defect from a previous ablative procedure for a squamous cell carcinoma of the palate, reconstructed with a temporalis muscle flap. The patient underwent adjuvant radiation therapy and developed significant scarring with retraction of the corresponding upper lip. The patient sought a bone reconstruction for the possibility to prosthetically rehabilitate the area and improve her facial symmetry. A fibula free flap was chosen as reconstructive option for its three-dimensional versatility to be folded in multiple spatial vectors and for the possibility to transpose a valuable amount of muscle cuff for the reconstruction of the fornix.

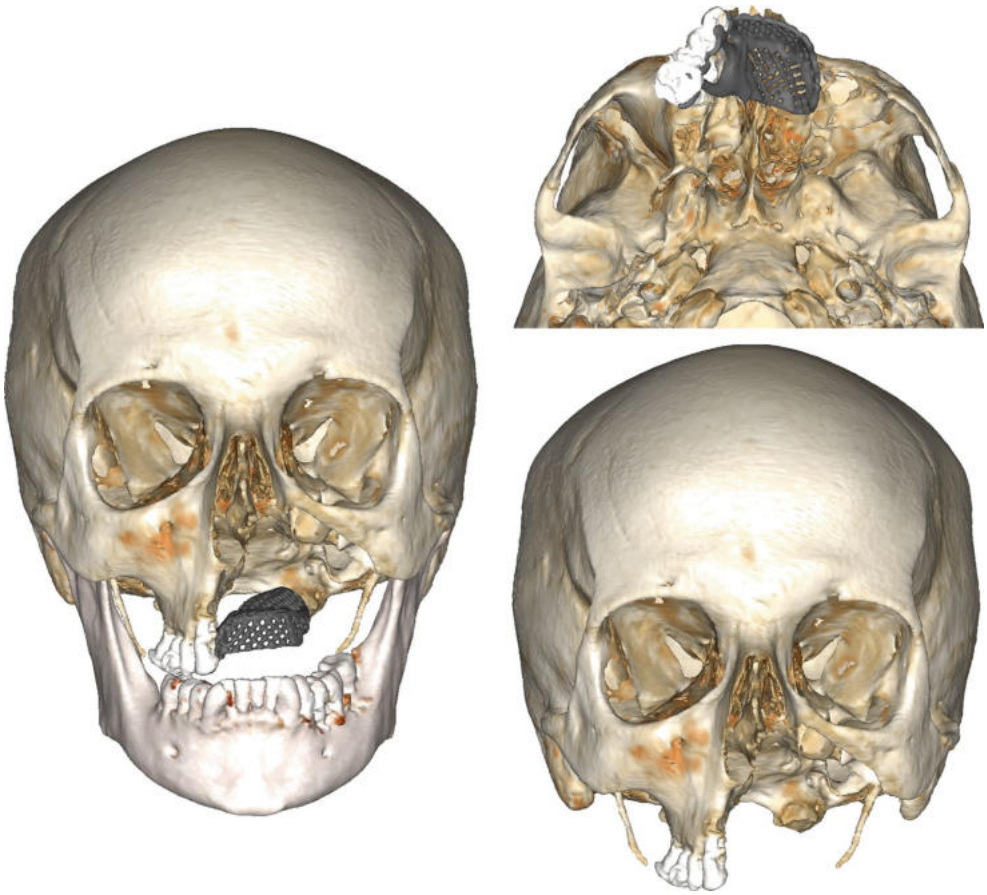


Fig. 32 Computerized anatomical reconstruction of a maxillectomy defect and removal of a mobile metal obturator after artifact reduction

Virtual Surgical Planning

- Segmentation: The patient underwent angio-CT for the lower limb and a high-quality maxillofacial CT with a filter for metal artifacts as she was using an obturator. During segmentation, care was taken to accurately separate the dental prosthesis from the bone and teeth, eliminating the residual, but conspicuous, amount of scattering caused by its metal component (Fig. 32).
- Establishing reconstruction: The maxillofacial skeleton, with the segmented donor site, was imported in Materialise Mimics Enlight CMF in the reconstruction module. Angled cutting planes were designed to conservatively refine the defect site and tailor its margins with the fibula. The left fibula was chosen, allowing to establish a posterior position for the vascular pedicle. Three segments were planned to replace respectively the premaxilla, posterior-lateral alveolar process, and maxillo-malar buttress (Fig. 33). Individual parts were exported in 3-matic for further steps.
- 3D Printing and reverse engineering: The resulting reconstruction model was wrapped using a gap closing distance of 0.5 mm and a resulting offset of 0.2 mm, and it was prepared for 3D printing in the software Preform by Formlabs. The model was used to bend a 1.5 thick reconstruction plate which was wrapped around the left malar body, all fibula segments, and the root of the right malar bone. To ensure maximal adhesion, the plate was fixed to the model using compression screws. Next, the model with the plate in place underwent CT scanning using an available intraoperative CT scan (Imaginalis, Sesto Fiorentino (FI), Italy) and segmented in Mimics, where the metal plate was separated from the resin skull, and both parts were imported back in 3-matic (Fig. 34).
- Surgical guide design: in 3-matic, the segmented resin skull was aligned with the patient's skull obtained from CT scan. This ensured that the prebent plate was correctly aligned over the VSP. The conceptual importance of this step is the possibility to apply a mechanically modeled plate to a virtual project, which is technically acknowledged as "reverse engineering." Screws were positioned in each hole of the reversed plate with appropriate size for each anatomical region. Surgical guides were modeled

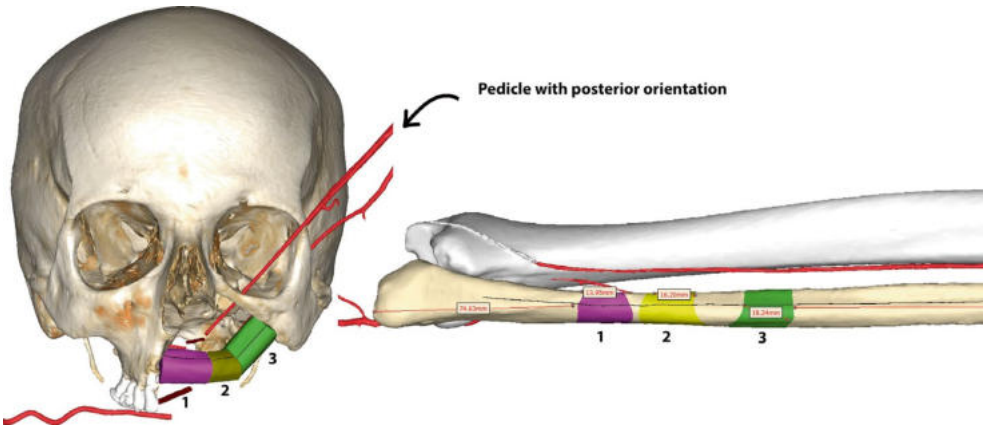


Fig. 33 VSP of fibula reconstruction with pedicle transposition to the recipient site for vascular anatomy understanding

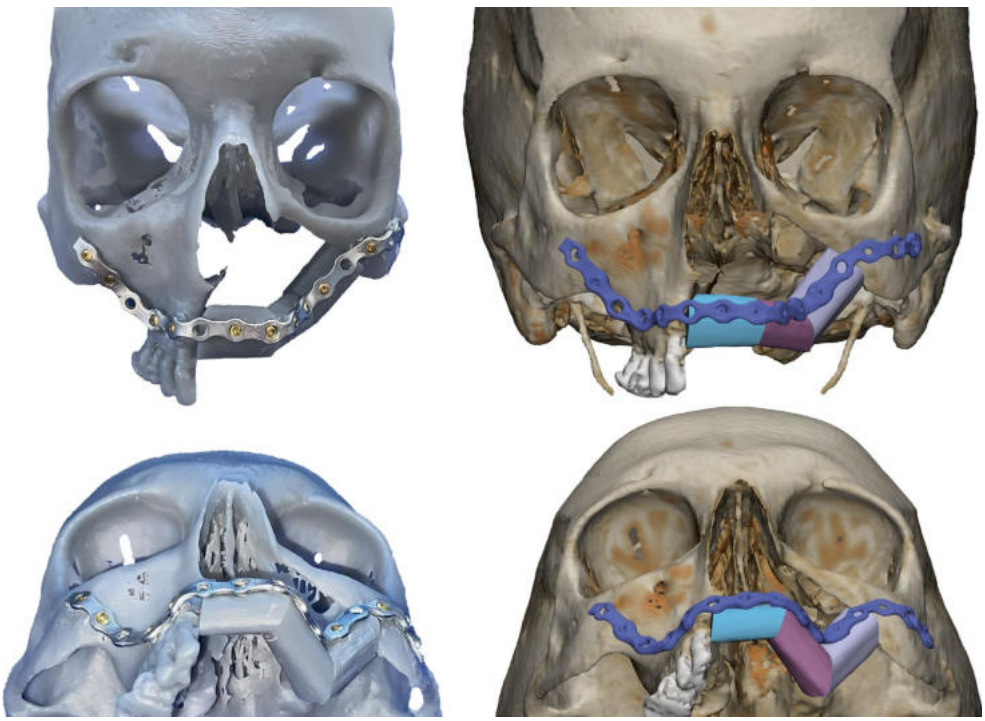


Fig. 34 3D printing of planned reconstruction and plate prebending (left). Right: reverse engineering of the plate and import in the VSP project

overlying the left and right maxillo-malar buttress with the double aim to predrill holes and refine the resection site to optimize its recipient margins for the flap. Likewise, fibula segments with their respective screws were aligned in the corresponding sites along the fibula diaphysis. A mixed surgical guide including linear flanges at the extremities and for the proximal segment, and notch-based appliances for the narrower segment, was designed, reporting, where possible, the position of fixation holes for the plate (Fig. 35). Surgical guides were 3D printed using a Formlabs Biomed Clear resin.

Essentially, this case emphasizes the versatility of the reverse engineering method which can achieve comparable results with the customized 3D-printed plate, but with a substantial reduction in costs, as the case can be managed entirely in-house.

Surgery

An intraoral incision in the right fornix and through the left temporalis muscle was performed to expose the site for reconstruction up to the malar buttresses. Surgical guides for resection were positioned to enable site preparation and predrilling of holes for the recipient site (Fig. 36). Recipient vessels in the ipsilateral neck were isolated for the anastomosis.

The fibula free flap was harvested traditionally and after proximal and distal osteotomies, and sectioning of the interosseous membrane, the fibula guide was positioned, allowing to sculp the flap exactly as planned. The three segments

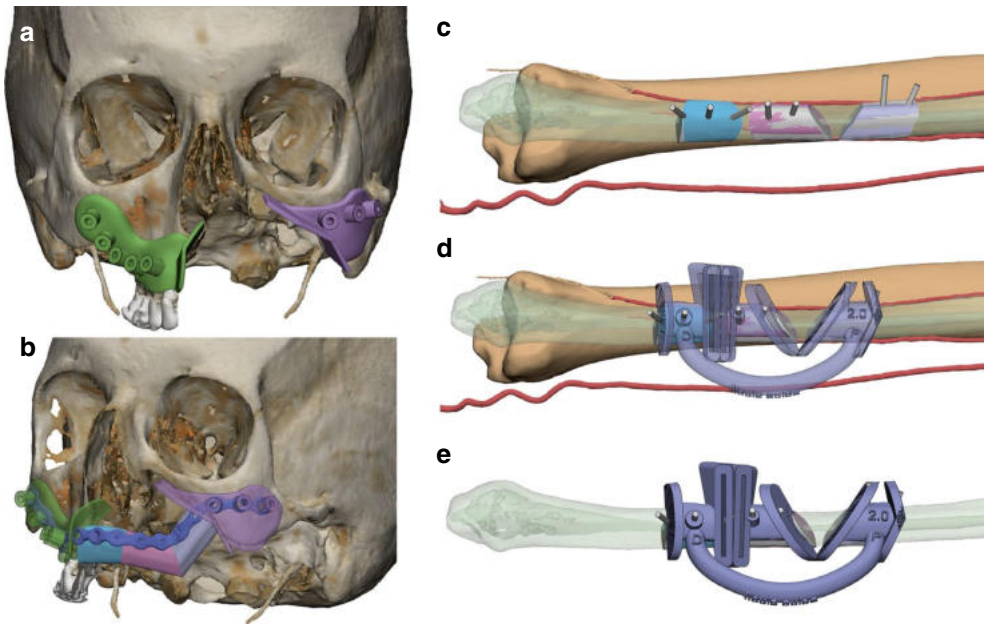


Fig. 35 Overview of guides for resection and flap harvest modeled on the holes of the reversed plate. The same holes have been physically drilled in the 3DP model

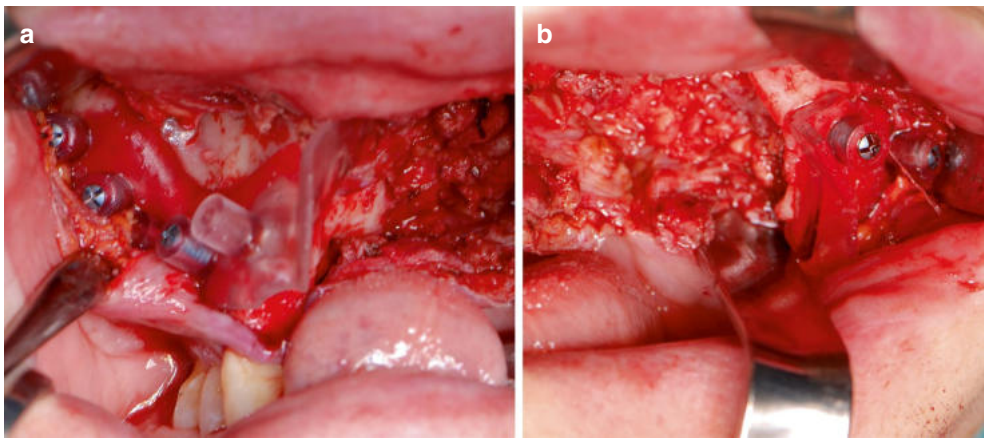


Fig. 36 Intraoperative view of computer-guided resection

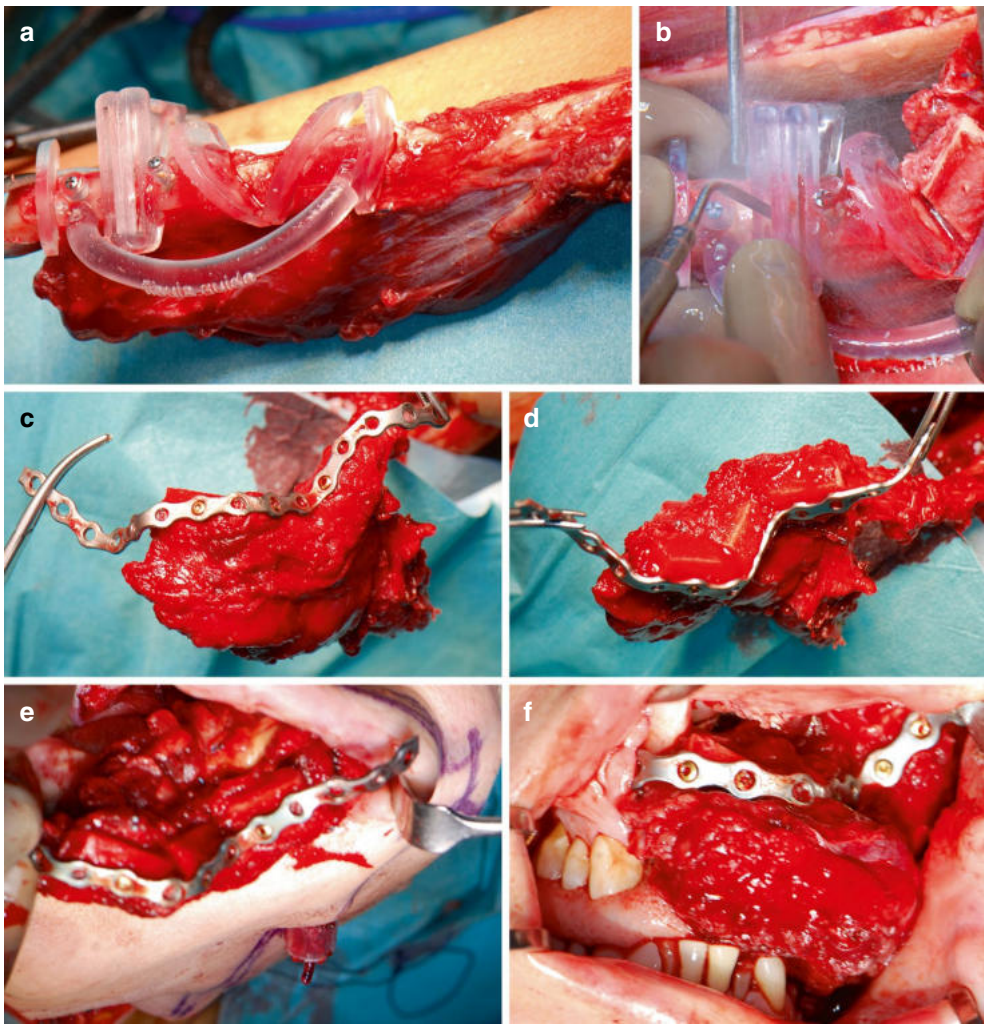


Fig. 37 Intraoperative view of computer-guided reconstruction: (**a**, **b**) fibula harvest using surgical guides; (**c**, **d**) fixation of the flap to the prebent plate. Perfect match between surgical guides holes and plate screws is achieved, thanks to reverse engineering; (**e**, **f**) flap inset

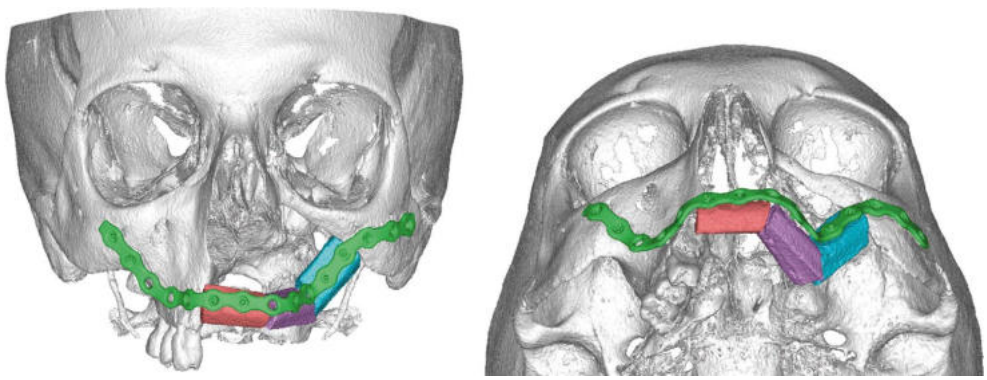


Fig. 38 Postoperative CT segmentation showing correct alignment of fibula segments

were fixed to the prebent plate while still being connected with the flap pedicle. Once sectioned, the free flap was transferred to its recipient site and both the margins of the flap and screws holes demonstrated optimal fit with the sites prepared by the surgical guides (Fig. 37). Segmentation of postoperative CT was performed to better delineate fibula segment, and accuracy with the planned procedure was verified (Fig. 38).

5 Implant-Retained Facial Prostheses

5.1 Introduction

A facial prosthesis is an artificially created custom-made medical device used to replace or restore a facial defect. They are typically made from silicone and/or acrylic to mimic the natural appearance and texture of the skin. Craniofacial or facial prostheses are used for the treatment of facial defects resulting from traumatic injury, congenital malformations, infective processes, or oncologic therapy. These facial defects can be reconstructed through surgery, prosthetic reconstruction, or a combination of both. As autologous reconstruction of ears, nose, and the orbit is difficult to achieve, auricular, nasal, and orbital prostheses are most frequently used. In extensive defects, a combination or an extension of the previously mentioned prostheses can be created. In the late 1970s, craniofacial endosseous implants were introduced by Per Ingvar Brånemark following his discovery of osseointegration of titanium in rabbit bone [10]. This development drastically improved the retention of craniofacial prostheses and results in high treatment satisfaction and quality of life for the patients [11, 12].

5.2 Surgical Technique

The goal of the treatment is to reconstruct the facial defect with an easy to use, aesthetically pleasing facial prosthesis fixed on a stable and hygienic foundation. Sometimes it is necessary to remove additional, healthy tissue to obtain this result. Thorough defect analysis and discussion with the patient and the anaplastologist are therefore crucial. Preoperative 3D imaging of the implantation area is recommended to analyze bone quality, bone volume, and the position of anatomical structures such as the frontal sinus, dental roots, dental implants, maxillary sinus, and mastoid cells. If necessary, 3D printed implant guides can be created. The implant protocol should be followed to achieve good implant stability, optimizing the chances of osseointegration. This is crucial for early implant survival. Both conventional two-stage and one-stage implant placement protocols have been described and depend on the preference of the surgical team. In general, two implants are sufficient for prosthesis retention; however, additional "sleeper" implants can be placed as backup, when one of the implants should fail.

5.3 Types of Facial Prostheses

Auricular Prosthesis
In the auricular area, the implants are placed in or on the temporal bone posterior of the external auditory canal. They should be positioned under the antihelix as this position ensures sufficient prosthetic space for the anaplastologist. The distance of the external auditory canal to the implant position is approximately 18 mm. In general, two implants are sufficient for good prosthesis retention; however, more can be placed based on the preference of the surgeon or the anaplastologist. A minimal distance of 10 mm between the implants is recommended.

Nasal Prosthesis
In the nasal area, implants can be placed in or on the nasal floor, the lateral piriform aperture, and/or the glabella. The glabella is not an ideal site, as there is little prosthetic space for the anaplastologist or prosthodontist resulting in a thicker and thus less aesthetic prosthesis. Two implants are sufficient for prosthesis retention. For a hemi- or partial nose reconstruction, one implant should suffice. It is recommended to flatten the sharp edges of the piriform aperture bone and leave 10 mm distance between the implants when placing endosseous implants in the nasal floor. The implants should be placed parallel or slightly converging and ideally follow the cortical bone of the nasal floor.

Orbital Prosthesis
In the orbital area, implants can be placed in the superior, lateral, and/or inferior orbital rim. The implants should be directed toward the center of the orbit. As the anaplastologist needs enough prosthetic space, posteriorly oriented angulated abutments are often used. It is however better to avoid these angulated abutments as they complicate peri-implant cleaning. Two implants are sufficient for retention, but due to

higher implant failure rates, many surgeons place additional implants.

5.4 Peri-implant Soft Tissue Management

Peri-implant soft tissue management is important for long-term implant survival. Ideally, the implants are surrounded by immobile, thin skin to facilitate implant cleaning and avoid skin irritation and infection. During surgery, the original skin can be thinned; however, the authors prefer the use of a split thickness skin graft placed on the periosteum.

5.5 Peri-operative Management

The operated area is covered with fat gauze and a pressure bandage for 1 week. If a split thickness skin graft was used, the donor site is treated with a sodium carboxymethylcellulose dressing. The patient receives standard pain medication and prophylactic antibiotics for 24 hours. After removal of the pressure dressing, daily cleaning of the peri-implant soft tissues with soft gauzes and physiologic water is instructed.

5.6 Complications

5.6.1 Implant Failure

The most important complication is implant failure which can be caused by forces stronger than the implant-bone interface (e.g., direct trauma to the implant and unfavorable loading), poor abutment hygiene and infections, and theoretically, all conditions impacting bone remodeling [13]. Implant failure can occur early, when the implant is unable to integrate in the bone, or late, after the implant is integrated in the bone usually after 3–6 months. It has been well established that the survival of osseointegrated implants differs according to its anatomic location. Reported implant survival rates of auricular implants range from 85 to 100%, nasal implants from 69.2 to 100%, and orbital implants from 35 to 100% [14–16]. Based on the most recent systematic review, it can be concluded that radiotherapy might negatively affect the survival of craniofacial implants, except the nasal area, which seems not to be affected [15].

5.6.2 Peri-implant Soft Tissue Infections

The most common complications of implant-retained facial prostheses are peri-abutment soft tissue reactions causing important morbidity, such as infection, overgranulation, and rarely implant failure. Peri-implant soft tissue reactions are classified by the following scales—Holgers' scale: grade 0 (no irritation), grade 1 (slight redness), grade 2 (red and moist tissue), grade 3 (red and moist tissue with granulation), and grade 4 (extensive soft tissue reaction) [17]; or by the more recent IPS-scale, with three parts, namely I-scale (inflammation), P-scale (pain), and S-scale (skin height) [18]. Skin irritation can be treated with intense hygiene measures, antibiotic ointment, and/or sliver nitrate application. More severe peri-implant infections need to be debrided and in worst case the implant must be removed and the skin thinned.

5.7 Follow-Up and Postoperative Management

Patients and their caregivers are instructed on how to clean the peri-implant soft tissues, implants, and the prosthesis. It is recommended to mechanically clean the implants daily, particularly the implant-skin interface should be thoroughly cleaned with a soft gauze and physiologic water. If appropriate hygiene at the implant site is not maintained, professional care should be organized at home and follow-up should be intensified.

Ideally, the prosthesis is removed at night and cleaned with a neutral soap. The silicone of the prothesis wears due to contact with sweat and UV-radiation. Also, the thin esthetic borders will start to wear due to frequent removal of the prosthesis. In general, the prosthesis is renewed after 18–24 months.

5.8 Timing of Prosthesis Placement

For a predictable result, soft tissue healing and implant osseointegration should be completed. Soft tissue healing usually takes about 8 weeks. Generally, prosthesis fabrication starts 12 weeks postoperatively, after completion of osseointegration. This period can be extended for patients with low bone quality or a history of radiation therapy. Before prosthesis fabrication, the implant stability can be measured by using the implant stability quotient (ISQ), periotest value, torque test, and/or radiographic evaluation.

5.9 Prosthetic Design and Production

Integrating digital production techniques into the planning, design, and manufacturing of facial prostheses offers significant advantages in terms of production speed and the predictability of the final prosthetic outcome.

The process begins with the creation of a detailed physical model of the defect, which can be achieved either through conventional impression-taking or by using an optical scanner in combination with 3D printing. CAD/CAM software is then employed to generate a virtual design of the prosthesis. This allows the creation of a multi-layered virtual model that simulates the prosthesis' position relative to surrounding soft

tissue and the placement of any implants. The model aids in the decision-making process regarding the design of the suprastructure, soft tissue adjustments, and the selection of abutments, both in terms of type and length.

Midsagittal mirroring of the virtual model can be used to project the healthy anatomy onto the defect side, restoring symmetry through easy manipulation of the digital models. In cases where the defect is located in the midface and anatomical mirroring is not feasible, a donor shape from a different individual can be utilized and adjusted accordingly.

The virtual plan and resulting models can be exported for 3D printing. These models can then be replicated in dental wax using a simple putty mold, allowing for adjustments during clinical wax fittings. Once the desired shape is achieved, the prosthesis can be refined and detailed. Using the lost wax technique, the model is then transferred into medical-grade silicone, which is custom-colored in the presence of the patient. After the silicone has cured, additional aesthetic details, such as extrinsic coloration, hair, and eyelashes, can be added to complete the prosthesis.

5.10 Clinical Examples

- *Case 1: Orbital Prosthesis*

Orbital reconstruction with an implant-retained orbital prosthesis after oncologic resection of an ethmoidal sinonasal carcinoma. Part of the skull base was resected and reconstructed with a titanium mesh and an ALT flap. For placement of the orbital prosthesis, the ALT flap was thinned until enough prosthetic space was present. The amount of prosthetic space needed was planned virtually. By using a 3D-printed polymer mold, the planning could be transferred to the operating room. The implants were placed in the inferior orbital rim as the superior and lateral orbital rim were previously resected (Figs. 39 and 40).

- *Case 2: Auricular Prosthesis*

Auricular reconstruction after resection of a malignant melanoma of the right ear. The total auricle was removed in a supraperiosteal plane to create immobile, thin peri-implant soft tissues. Two implants were placed in the mastoid area with 1 cm interimplant distance at the area of the antihelix. The incision in the neck was used for a sentinel node biopsy. A split thickness skin graft from the upper leg was taken to cover the periosteum. A pressure dressing was placed for 1 week. Postoperative healing resulted in an immobile, thin peri-implant soft tissue bed. The healthy ear is mirrored and used as a template for the prosthetic design. The final prosthetic result is visualized (Figs. 41 and 42).

- *Case 3: Nasal Prosthesis*

Prosthetic reconstruction of a partial nose defect after oncologic resection due to a squamous cell carcinoma of the right nose. Prosthetic reconstruction of partial defects

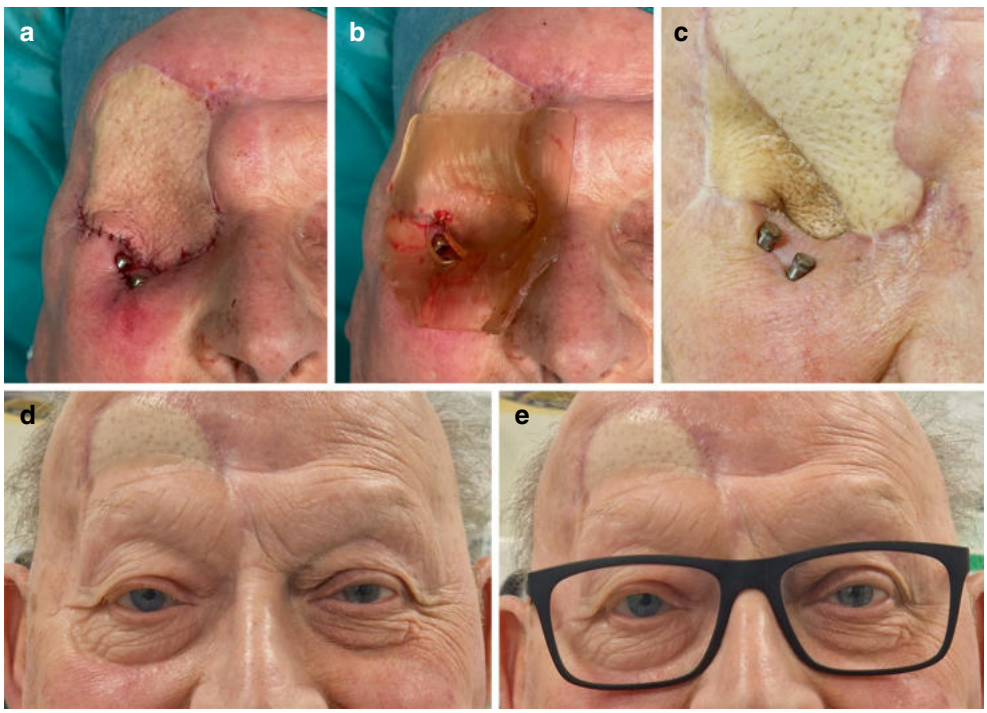


Fig. 39 Orbital reconstruction after oncologic resection. (**a**, **b**) Thinning of the ALT flap using a 3D printed mold. (**c**) Postoperative image after placement of craniofacial implants in the inferior orbital rim. (**d**, **e**) Prosthetic result. The use of glasses can improve the appearance of the prosthesis

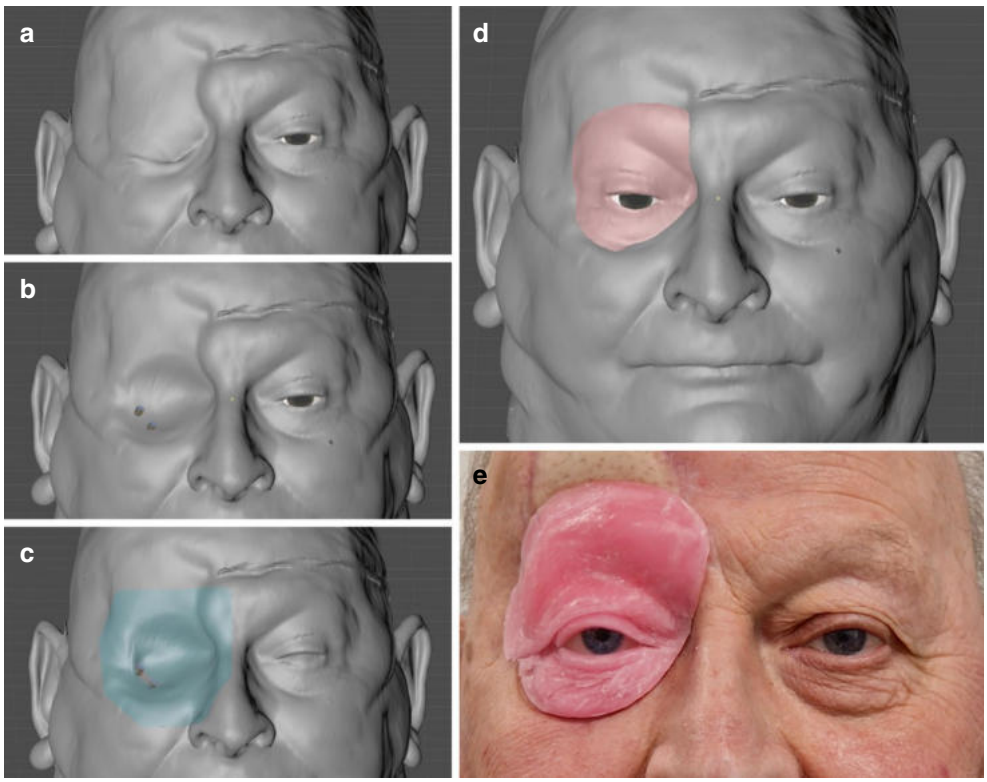


Fig. 40 Virtual planning of prosthetic space. (**a**–**c**): Virtual thinning of the excess volume and subsequent design and 3D printing of a mold, considering the position of the implants. (**d**) Midsagittal mirroring of the left eye to the right socket. (**e**) A wax model derived from a 3D printed model is fitted in multiple clinical sessions

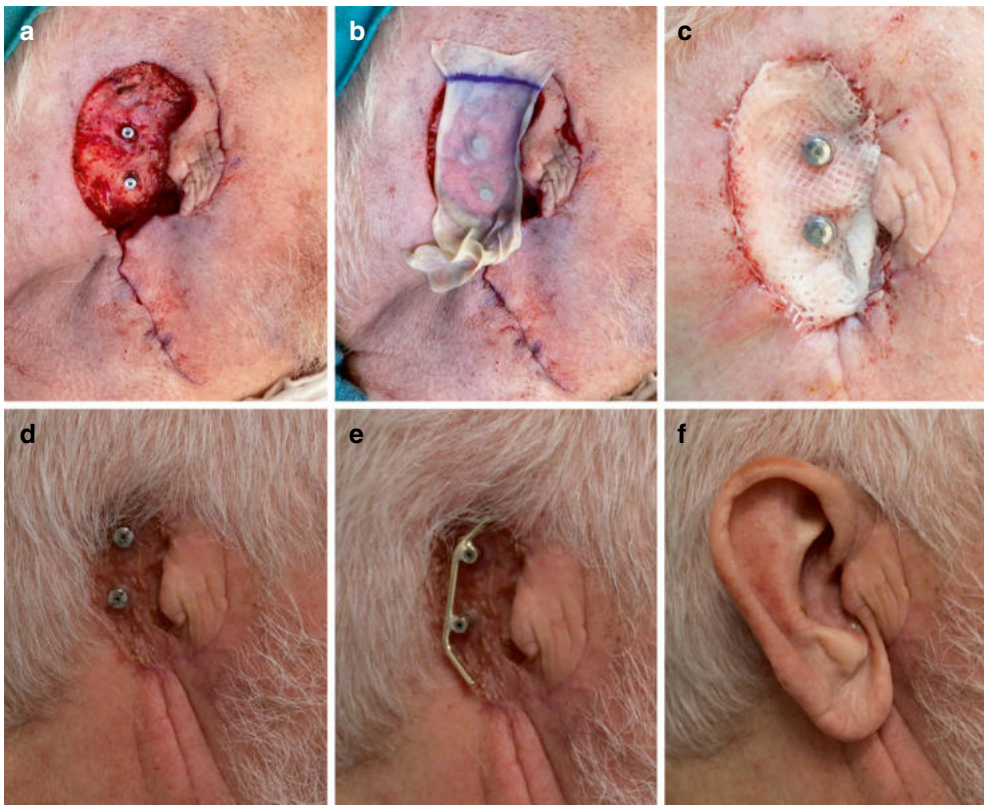


Fig. 41 (**a**) Auricular prosthetic reconstruction based on two implants placed in the mastoid bone corresponding to the location of the antihelix. Neck incision was used for sentinel node biopsy. The complete auricle was removed in a supraperiosteal plane. (**b**, **c**) A split thickness skin graft from the upper leg was placed and covered with a pressure dressing for 1 week. (**d**, **e**) Postoperative healing resulted in thin and immobile peri-implant soft tissues facilitation cleaning. (**f**) Prosthetic result

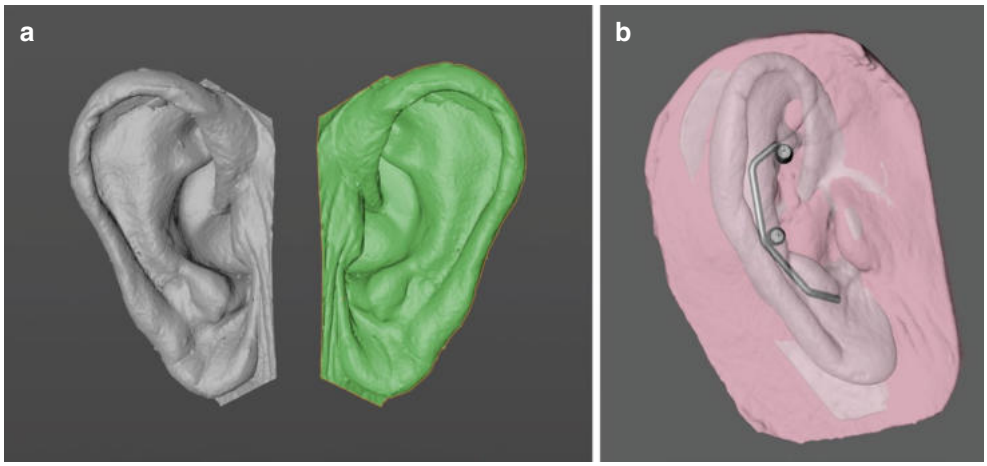


Fig. 42 Prosthetic planning for an ear reconstruction. (**a**) A contact impression of the healthy ear can be scanned with an optic scanner and mirrored using cad/cam software. This model can then be 3D-printed and transferred into wax for clinical waxfitting. (**b**) The mirrored virtual model can be positioned on the virtual model of the defect. Based on the position of the ear, the suprastructure can be designed

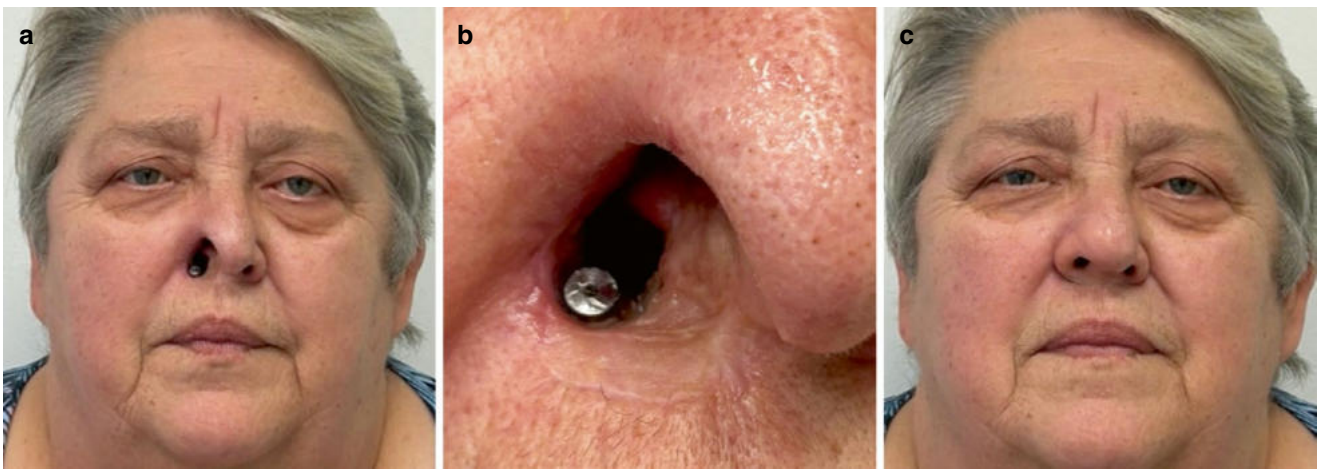


Fig. 43 (**a**) Partial prosthetic reconstruction of the right nose. One implant is placed in the nasal floor. Care was taken not to damage the dental roots. (**b**) A split thickness skin graft from the upper leg is placed around the implant. (**c**) Prosthetic result

is challenging as there is limited surgical exposure. Also, for patients it is difficult to clean the implant. In this case, one implant was placed in the nasal floor. Care was taken not to damage the dental roots. The defect was covered with a skin graft from the upper leg. By mirroring the healthy site, a nice prosthetic result can be achieved (Figs. 43 and 44).

- *Case 4: Nasal Prosthesis*

Nose reconstruction of an 11-year-old girl after total nose avulsion due to a dog bite. Immediately after the dog bite, revascularization of the avulsed nose with vascular anastomosis was attempted but failed. Due to the young age of the patient and the position of the dental roots in the nasal floor,

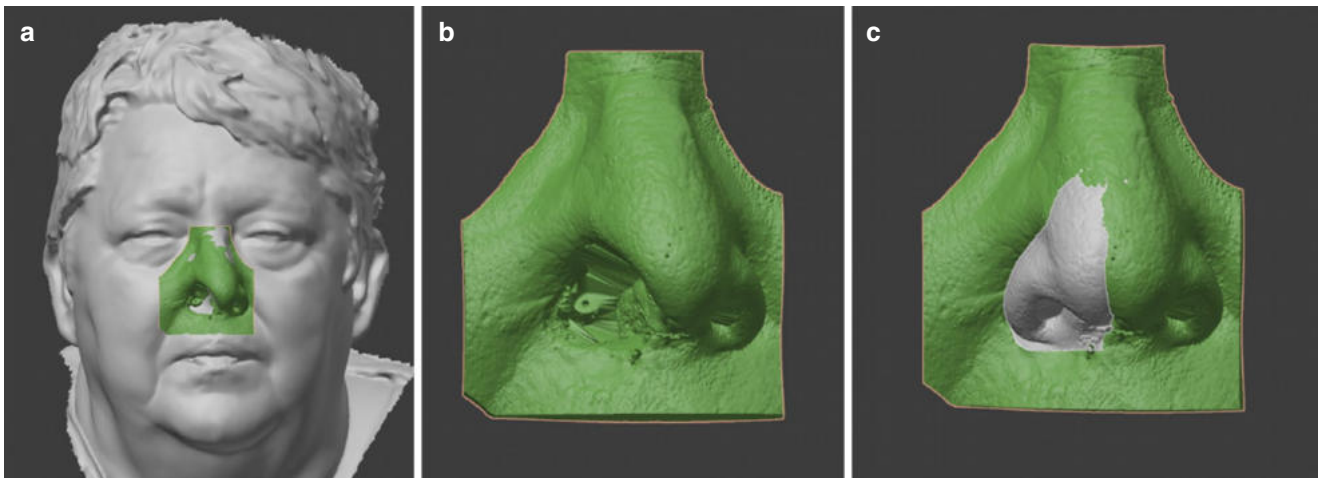


Fig. 44 (**a**, **b**) A surface scan of the nose is taken and matched with a face scan. This allows for a correct orientation of the more detailed and smaller surface scan. (**c**) The right nose is mirrored over the midsagittal plane to reconstruct the defect. This model can be printed and transferred into wax for clinical fitting

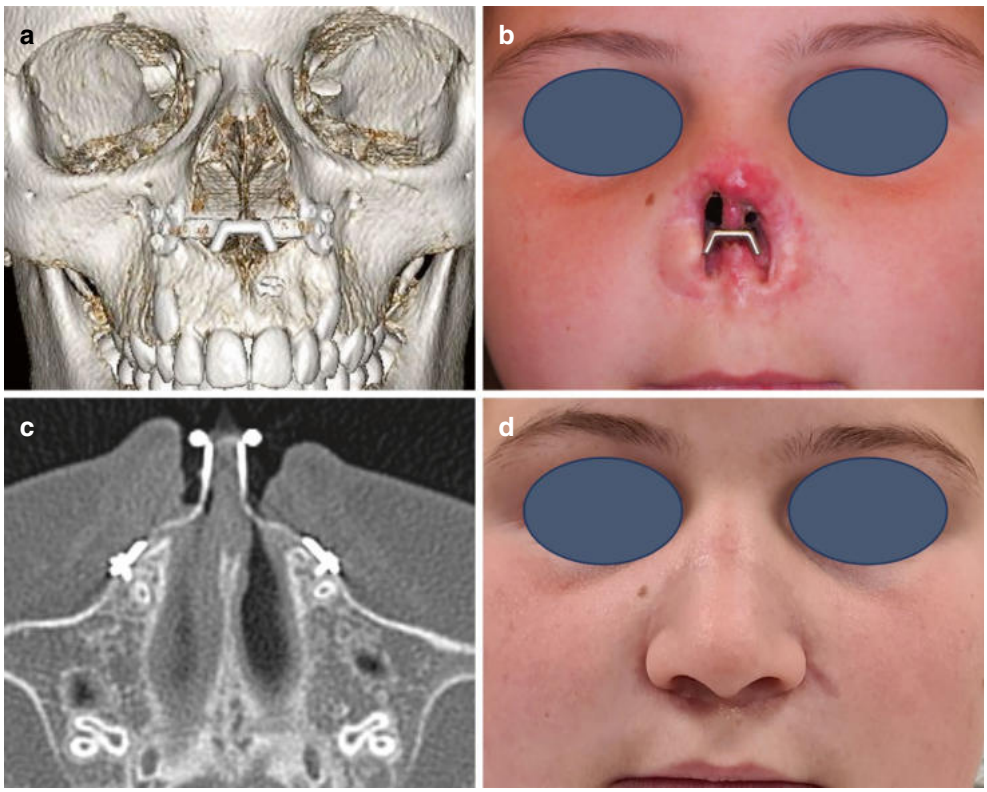


Fig. 45 Complete nose reconstruction after avulsion caused by a dog bite. (**a**) Preoperative design of the PSI by Dr. Renaat Coopman and Cadskills NV (Sint-Denijs-Westrem, Belgium). (**b**) Postoperative result with the PSI in place. (**c**) Postoperative CT-imaging demonstrating the position of the PSI just cranial of the tooth buds. (**d**) Prosthetic result. (Image derived from Ureel et al. [19])

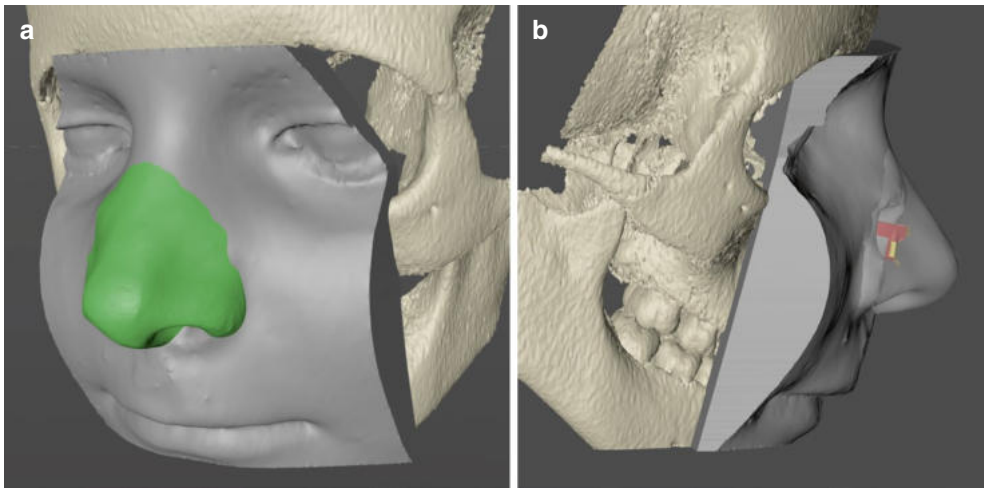


Fig. 46 Prosthetic planning. (**a**) In case of an avulsion of the nose, the original shape might be lost. If there are no previous impressions or 3D images available, a donor shape can be used. The shape can be digitally altered to fit the anatomy of the patient. Reference pictures can be used to achieve resemblance with the shape prior to the accident. (**b**) By matching the hard and soft tissue virtual models, the design can be optimized for the PSI and soft tissue positions

it was decided not to place endosseous implants. Instead, a patient specific implant (PSI) was designed and 3D printed. The implant is placed paranasal just cranial of the tooth buds in a subperiosteal plane. By matching the virtual planning and the preoperative CT soft tissue mesh, the nose can be positioned and designed. Postoperative a good position of the PSI and healthy soft tissues were seen. Postoperative imaging showed a more caudal position of the PSI compared to the preoperative planning; however, no dental roots were damaged. Close collaboration between the technical engineer, the anaplastologist, and the surgeon is essential to ensure a successful treatment outcome in these cases (Figs. 45 and 46).

References

1. Ferrari S, Ferri A, Bianchi B. Scapular tip free flap in head and neck reconstruction. Curr Opin Otolaryngol Head Neck Surg. 2015;23:115.
2. Virtual surgical guidance improves quality of life following scapular free-flap reconstruction of maxillary defects. J Oral Maxillofac Surg. https://www.joms.org/article/S0278–2391(24)00092-2/abstract. Accessed 14 Jan 2025.
3. Guide design in virtual planning for scapular tip free flap reconstruction - Kass - 2018 - Laryngoscope Investigative Otolaryngology - Wiley Online Library. https://onlinelibrary.wiley.com/doi/10.1002/lio2.162. Accessed 14 Jan 2025.
4. Swendseid BP, Roden DF, Vimawala S, Richa T, Sweeny L, Goldman RA, Luginbuhl A, Heffelfinger RN, Khanna S, Curry JM. Virtual surgical planning in subscapular system free flap reconstruction of midface defects. Oral Oncol. 2020;101:104508.
5. Zheng L, Wu W, Shi Y, Zhang J. Mandibular reconstruction with a deep circumflex iliac artery flap using computer-assisted and intraoral anastomosis techniques. J Oral Maxillofac Surg. 2019;77:2567–72.
6. Qiu S-Y, Shan X-F, Kang Y-F, Ding M-K, Zhang L, Cai Z-G. Accurate occlusion-driven maxillary reconstruction with deep circumflex iliac artery flap using computer-assisted techniques and intraoral anastomosis: a case series. Int J Oral Maxillofac Surg. 2023;52:744–52.
7. Thomas CV, McMillan KG, Jeynes P, Martin T, Parmar S. Use of a titanium cutting guide to assist with raising and inset of a DCIA free flap. Br J Oral Maxillofac Surg. 2013;51:958–61.
8. Surgical reconstruction and rehabilitation of midface defects using osseointegrated implant-supported. Maxillofacial Prosthetics. https://dtjournal.org/articles/189. Accessed 14 Jan 2025.
9. Hanasono MM, Skoracki RJ. The omega-shaped fibula osteocutaneous free flap for reconstruction of extensive midfacial defects. Plast Reconstr Surg. 2010;125:160e–2e.
10. Experimental Investigation of Microcirculation in Bone Marrow - Per-Ingvar Brånemark, 1961. https://journals.sagepub.com/doi/10.1177/000331976101200705. Accessed 14 Jan 2025.
11. Nemli SK, Aydin C, Yilmaz H, Bal BT, Arici YK. Quality of life of patients with implant-retained maxillofacial prostheses: a prospective and retrospective study. J Prosthet Dent. 2013;109:44–52.
12. Atay A, Peker K, Günay Y, Ebrinç S, Karayazgan B, Uysal Ö. Assessment of health-related quality of life in Turkish patients with facial prostheses. Health Qual Life Outcomes. 2013;11:11.
13. Granström G. Craniofacial osseointegration. Oral Dis. 2007;13:261–9.
14. Ihde S, Kopp S, Gundlach K, Konstantinović VS. Effects of radiation therapy on craniofacial and dental implants: a review of the literature. Oral Surg Oral Med Oral Pathol Oral Radiol Endod. 2009;107:56–65.
15. ElKhashab MA, Radi IAW, Elkhadem AH. Implant prognosis in irradiated versus non-irradiated nasal, orbital and auricular sites. Int J Oral Maxillofac Surg. 2020;49:636–48.
16. Chrcanovic BR, Nilsson J, Thor A. Survival and complications of implants to support craniofacial prosthesis: a systematic review. J Craniomaxillofac Surg. 2016;44:1536–52.
17. Holgers KM, Tjellstrom A, Bjursten LM, Erlandsson BE. Soft tissue reactions around percutaneous implants: a clinical study on skin-penetrating titanium implants used for bone-anchored auricular prostheses. Int J Oral Maxillofac Implants. 1987;2:35–9.
18. Kruyt IJ, Nelissen RC, Johansson ML, Mylanus EAM, Hol MKS. The IPS-scale: a new soft tissue assessment scale for percutaneous and transcutaneous implants for bone conduction devices. Clin Otolaryngol. 2017;42:1410–3.
19. Ureel M, Dadjam D, Dhooghe N, De Jong M, Coopman R. Case report: Pediatric alloplastic nose reconstruction with a 3D printed patient specific titanium implant. Front Surg. 2024; https://doi.org/10.3389/fsurg.2024.1330889.

Virtual Planning and 3D Printing in Mandibular Fractures

Alessandro Tel and Massimo Robiony

1 Generalities

The mandible is involved in most cases of facial trauma, notably, according to some reports, in 70% of patients with facial fractures. The following mean frequency percentages are based on location according to the literature: body (29%), condyle (26%), angle (25%), symphysis (17%), ramus (4%), and coronoid process (1%) [1]. As the mandible is by definition a mobile bone, any trauma with interruption of its anatomical structure results in occlusion loss and malrotation of fragments. Therefore, anatomical reduction is the most prominent aspect in mandibular fracture management, as well as restoration of occlusion. Such aspects pose considerable intraoperative challenges, as manual anatomical reduction is complex to achieve and often results in gross approximation of segments with deviations from the preoperative occlusion [2]. Moreover, a dedicated strategy is highly important when planning mandibular fracture reduction, especially when the condyle is involved: the restoration of the posterior facial height and the correct articular relationship between the condyle and glenoid fossa are crucial for the occlusion [3].

The relevant functional implications of mandibular fractures and subsequent demanding needs of surgical results cannot prescind from the adoption of VSP. Any mandibular fracture should be modernly approached, both for diagnostic purposes, but most of all for the therapeutic relevance of VSP, with volumetric imaging. Thin-sliced, high-resolution matrix CT scan is mandatory and should be acquired from menton point to include the full temporomandibular joint and the superior dental arch [4]. Whenever possible, intraoral scanning should be always performed, although there are some situations that make its acquisition complex, including severe pain associated with the fracture and trismus, which limits the mouth opening. At least 3 cm of mouth opening is needed to successfully complete intraoral scanning. Models of dental arches should be 3D printed to ensure the correct identification of the optimal intercuspation, which can be used to realign skeletal segments in VSP.

In some circumstances, it is virtually impossible to perform a manual reduction of fractures, particularly in cases of multiple or comminuted fractures, where anatomical references are lost. In such cases, performing a forward anatomical reduction using virtual models plays an essential role, as it makes available to the surgeon a correctly reduced model in the OR, minimizing the intraoperative time spent in searching the optimal alignment. A virtual software environment helps perform countless variations to the surgical planning until the desired result is achieved.

As mentioned, occlusion is a crucial element in virtual surgical planning for mandibular fractures. In trauma setting, currently available software does not allow to define the optimal intercuspation in a virtual environment, namely a virtual surgical occlusion. Virtual occlusion was developed exclusively for orthognathic surgery by some software manufacturers [5], but it is programmed to work in ideal dental conditions, with orthodontically aligned arches, which refer to the typical presurgical preparation. In trauma, algorithms are not that sophisticated to enable a virtual automatic occlusion, as several teeth might be fractured, rotated, or avulsed. Moreover, dentoalveolar fractures are typically associated with complex mandibular trauma, and occlusal stability is a major concern. Thus, it is advisable to 3D print individual dentate segments and set them manually in the optimal occlusal stability. As such occlusions are often unstable and need to be orthodontically refined, the most suitable arrange-

A. Tel (✉)
Lead Specialist for VSP and 3DP, Maxillofacial Surgery Clinic, Head & Neck and Neuroscience Department, Academic Hospital of Udine, Udine, Italy
e-mail: alessandro.tel@uniud.it

M. Robiony
Chief of Maxillofacial Surgery Clinic, Director of the Postgraduate School in Maxillofacial Surgery, Chief of Head & Neck and Neuroscience Department, Academic Hospital - University of Udine, Udine, Italy
e-mail: massimo.robiony@uniud.it

© The Author(s), under exclusive license to Springer Nature Switzerland AG 2025

A. Tel, M. Robiony (eds.), *Atlas of Virtual Surgical Planning and 3D Printing for Cranio-Maxillo-Facial Surgery*,
https://doi.org/10.1007/978-3-031-94495-6_22

ment must be defined, and then models can be scanned and transferred to the virtual surgical plan [6].

This chapter presents the importance of VSP applied to decisional and intraoperative algorithms for mandibular fractures with emphasis on complex scenarios, which can be effectively solved by VSP. Owing to their anatomical peculiarities, isolated condylar fractures have already been discussed in Chapter "Application of VSP in Temporomandibular Joint Surgery" about temporomandibular joint surgery. However, condylar fractures as part of multifocal mandibular fractures will be presented in this chapter to describe their integrated treatment.

2 Considerations for VSP in Mandibular Fractures

As the mandible is a mobile bone, it has some peculiarities that differentiate it from craniofacial and midfacial trauma without mandible involvement. While in the upper and midface navigation plays an important role in providing virtual reduction templates, in the mandible, navigation is less usable. Although some reports are present in the literature, navigation requires a more complex setup, especially concerning system calibration: given the mobility of the mandible, it is not possible to use conventional craniofacial landmarks for reduction, and a splint with reference markers attached to the inferior dental arch is necessary [7]. Therefore, we do not support the use of navigation for ordinary fracture management, except in particular cases, namely high condylar fragments with deep condyle dislocation, where navigation is useful to track the path to the condyle. Moreover, given the importance of restoring the correct mandibular arch, it is of prominent importance that technology provides physical contention templates rather than virtual guiding masks. Thus, it is intuitive that 3D printing is the leading technology to bridge virtual surgical planning with the real patient.

Devices used for mandibular fracture management can be classified as follows:

- Occlusal splints: such devices are planar jigs that bear the impression of dental arches. Once a virtual reduction plan is finalized and the achieved dental arch shape is satisfactory, the splint bears the impression of reduced dental arches, and thus enable to perform intermaxillary blockage in the correct occlusal relationship.
- Thermoplastic cage splints: such devices are the result of a thermoforming process of a thin plastic sheath around a 3D-printed model of the reduced fracture. They enable superior contention compared to simple occlusal splints and are particularly indicated for dentoalveolar trauma. They are slightly less robust and do not effectively work in fractures of the basal bone.
- Models for plate prebending: in many cases, it is useful to always print a model of the reduced anatomical structure that enables to accurately and easily preform plates for rigid internal fixation.
- Reduction surgical guides: such guides are innovative and not frequently reported in the literature. Such guides bear the negative inner impression of anatomically reduced bones. They can be designed thicker or printed in resins with superior tensile strength to accommodate needs of increased robustness. They are ideal to reduce dislocated basal bone when lines for anatomical reduction are lost. In addition, in cases of reverse engineering of prebent plates, they can also be used to predrill holes in the correct position.

In contrast with elective mandibular reconstructive surgery, such as oncology, as mandibular fractures are generally operated in an urgency setting just few days after the patient is admitted, customized 3D-printed titanium plates are hardly usable. In fact, titanium printing needs to be outsourced given the complexity of production, and delivery time is not compatible with trauma surgery, as implants need to be ordered several weeks in advance.

As mentioned in the previous chapter, trauma emphasizes even more the importance of an in-house virtual surgical planning and 3D printing laboratory within the hospital, with trained physicians in the use of technology.

3 Classification of Mandibular Fractures for Virtual Planning Purposes

It is convenient to classify mandibular fractures in several subgroups for virtual planning purposes, in terms of a unifying strategy to propose the best virtual workflow for any type of mandibular fracture. Moreover, the same classification plays an important role to define which devices need to be chosen to treat a mandibular fracture (Fig. 1).

- *Simple mandibular fractures (1 segment)*: anatomical reduction with reapproximation of the fractured fragments and reconstitution of the fracture line is needed. This procedure can be easily performed by virtual anatomical reduction, manually, or, most effectively, aided by scanning the occlusion in the correct intercuspation. Prebent plates are useful, although not essential to treat such simple cases, in which manual conformation of the plate can achieve a satisfactory result.
- *Multifocal mandibular fragments (>1 segment)*: the mandible is fractured in multiple segments of distant regions (i.e., different anatomical units). Anatomical reduction

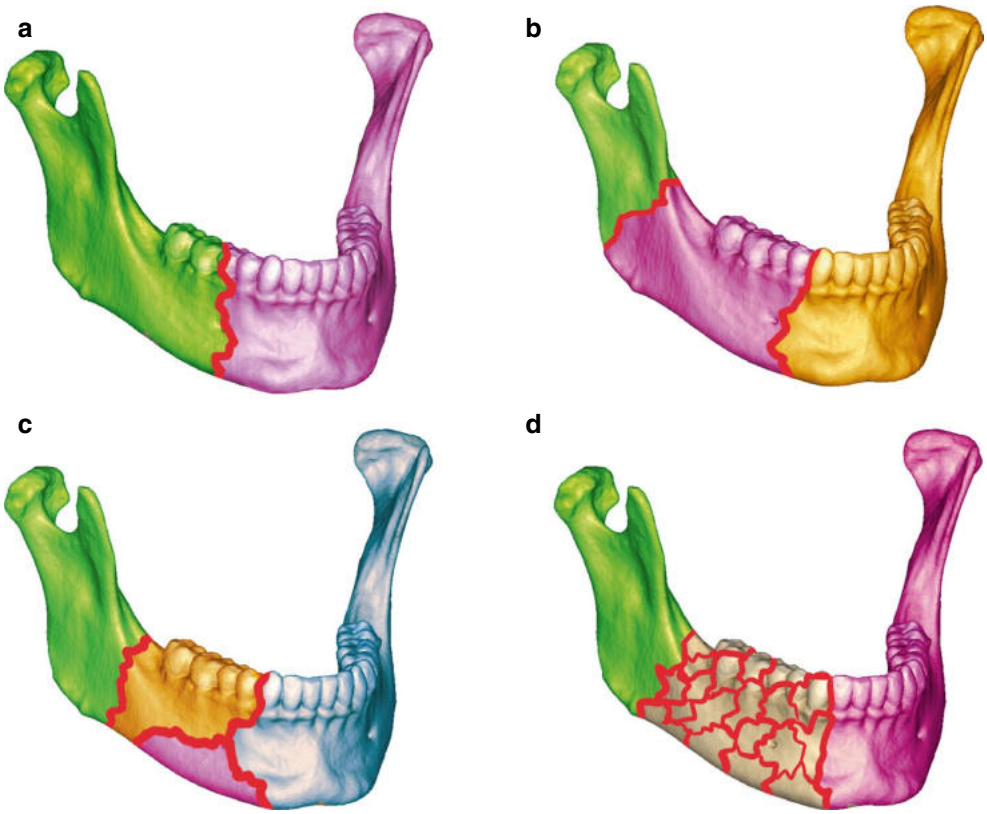


Fig. 1 Schematic classification used proposed by the author to describe mandibular fractures. (**a**) Unifocal; (**b**) multifocal; (**c**) multifragmented (but fixable); (**d**) comminuted (non fixable)

must be conducted carefully within the virtual plan. Mirroring options are most likely unavailable, except for small and laterally confined injuries. Manual reduction is often difficult, and reduction surgical guides might be useful to improve bone segment realignment. Moreover, if tooth-bearing parts are involved, traditional splints or TCS represent a highly useful option.

- *Multifragmented fractures without bone loss*: in such cases, the mandible is fractured in multiple segments within the same anatomical unit. Manual reduction of fragments has to be conducted even more accurately. It is important to separate all fracture fragments using the split mask tool. Most importantly, it is essential to identify which fragments are the most suitable to fix the plate and which are determinant for the biomechanical stability of the mandible, for instance, the largest and more vestibular fragments. TCS are often superior to traditional splints in such cases, and 3D print of a completely reduced mandible with intraoperative plate prebending is highly useful. Most importantly, such cases benefit the most from reduction surgical guides, which can be preliminarily fixed to the largest fragments and act as a reduction template to simplify the rigid fixation and the insertion of smaller fragments.
- *Multifragmented fractures with bone loss*: in such cases, it is necessary to bridge the defect using a bone graft (for small defects), or a bone free flap (for large defects), to bring novel bone tissue within the gap area. For the mandible, the fibula free flap is the most recommended choice. Virtual surgical planning has to be conducted according to the harvesting procedure of the flap, and a resection has often to be included along the reconstructive phase for optimal sizing of the recipient site. The use of splints in combination is useful to associate the mandible reconstruction with the optimal occlusal restoration.

4 Simple Mandibular Fractures (1 Segment)

Simple mandibular fractures are generally caused by direct trauma to the mandible, mostly for mandibular body, angle, and ramus. Simple mandibular are more frequent in younger population, where they have a crucial relationship with occlusion, whereas in elderly patients, they often involve edentulous mandibles.

In simple mandibular fractures, restoring intraoperatively the occlusion with maxillo-mandibular block (MMB) is often associated with a satisfactory anatomical reduction. Reestablishing the correct intercuspation drives the correct anatomical reduction of the fracture, and MMB constrains skeletal segments in the correct position for osteosynthesis. Virtual planning is useful to determine reduction maneuvers and, eventually if the surgical occlusion can be imported

within the virtual project, to manufacture an occlusal splint facilitating the maxillo-mandibular block (Fig. 2). On the contrary, edentulous mandibles require anatomical reduction of the basal bone performed most often through a bimanual reduction [8].

Owing to the anatomical engagement and ease of reestablishing the occlusion, unifocal mandibular fragments are rarely approached through VSP; thus, this chapter will provide examples of more complex clinical scenarios, in which VSP is a real game-changer in surgical strategy and simplifies procedures in the operating room.

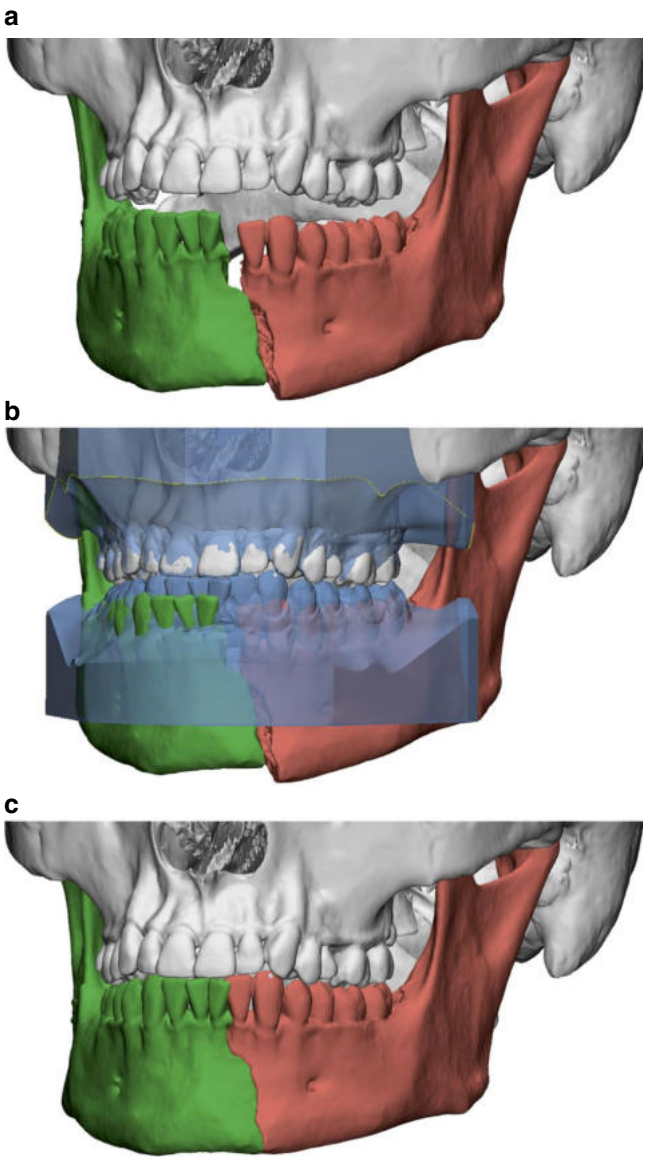


Fig. 2 Occlusion-driven reduction of mandibular fractures using the superior antagonist as template to establish the optimal intercuspation. This example refers to a class I fracture

5 Multifocal Mandibular Fragments (>1 Segment)

Multifocal mandibular fractures generally acknowledge a double trauma mechanism: a direct injury, causing a fracture at the impact point, and an indirect injury, due to the backlash on the contralateral side. The backlash generally occurs in the most vulnerable structures, represented by the high part of the ramus, including the condylar neck and head. For this reason, these fractures are generally located distant from each other. They are much more difficult to address compared to simple unifocal ones, owing to two essential reasons:

- Ascending ramus and condylar fractures cause a reduction of the posterior vertical height, which directly impacts on the occlusion.
- MMF is not as easily achievable as in unifocal fractures if the dental arch is interrupted in more than one point. In case arch bars are used to stabilize fragments, they lead to a much more unpredictable occlusion, as they can never be truly passive, other to the additional disadvantages (length of placement, periodontal damage) [9]. Thus a computer guided, occlusion-driven reduction is advised through the generation of a 3D-printed splint.

5.1 Case 1: Subcondylar, Condylar Neck, and Parasymphyseal Fracture

Clinical History

This patient was referred after a high energy trauma following a bike accident, when the patient fell off his bike and crashed into a rock wall, hitting his face. He was admitted to emergency department, where a CT scan was performed, showing a right condylar neck fracture with displacement, a left displaced subcondylar fracture, and a left parasymphyseal fracture. Given the importance of restoring the correct occlusion for this patient, an intraoral scan was performed to acquire models of dental arches.

Virtual Surgical Planning

DICOM data were imported in Mimics and segmented using dedicated threshold. Split mask was applied to each individual bone fragment to separate bones across fracture lines, and four separate parts were yielded: right condylar fragment, right hemimandible, left hemimandible, left condylar fragment. Intraoral scan was unavailable owing to the trismus and preauricular pain complained by the patient, preventing the insertion of the optical head. The project was

imported in 3-matic and anatomical reduction of condylar fractures was manually performed to restore a symmetric posterior facial height on both sides. Then, left and right hemimandibles were joined across the parasymphyseal fracture, whose anatomical reduction was carefully performed in compliance with both occlusion and a correct articular relationship between the condyle and the glenoid fossa (Fig. 3). As both condyles were fractured, it was not possible to semi-automatically reduce the displaced condyle using a mirrored reduction template, and manual reduction played a crucial role. Once the reduction was satisfactory on both occlusion and condyles, an occlusal splint was modeled to guide realignment of bone segments in the correct relationship.

Surgery

A left preauricular incision with deep subfascial approach was used in the left side to expose the capsule of the TMJ and retrieve the medially dislocated condylar stump, using an Obwegeser elevator to engage it, followed by Dunn's condyle retractors to superficialize the TMJ and achieve reduction. On the right side, a retromandibular incision was performed, with subcutaneous dissection sliding over the SMAS layer to reach the site of facture. The SMAS was incised and blunt dissection was performed through the parotid gland to avoid facial nerve branches. The bone surface was exposed and the fracture anatomically reduced, using a trapezoid plate for internal rigid fixation bilaterally. The sequence perfectly replicated the order of steps performed in virtual surgical planning. Subsequently, the splint was positioned to guide both hemimandibles in the correct anatomical relationship. After intermaxillary fixation was established with splint engagement and the parasymphyseal fracture was exposed, its anatomical reduction was subsequent. Two linear plates were positioned to complete internal rigid fixation of the mandible (Fig. 4). Postoperative CT revealed satisfactory reduction of fractures (Fig. 5).

5.2 Case 2: Parasymphyseal and Right Ramus Bifocal Fracture

Clinical History

This patient was evaluated in the emergency department after a violent injury while riding an electric scooter. The

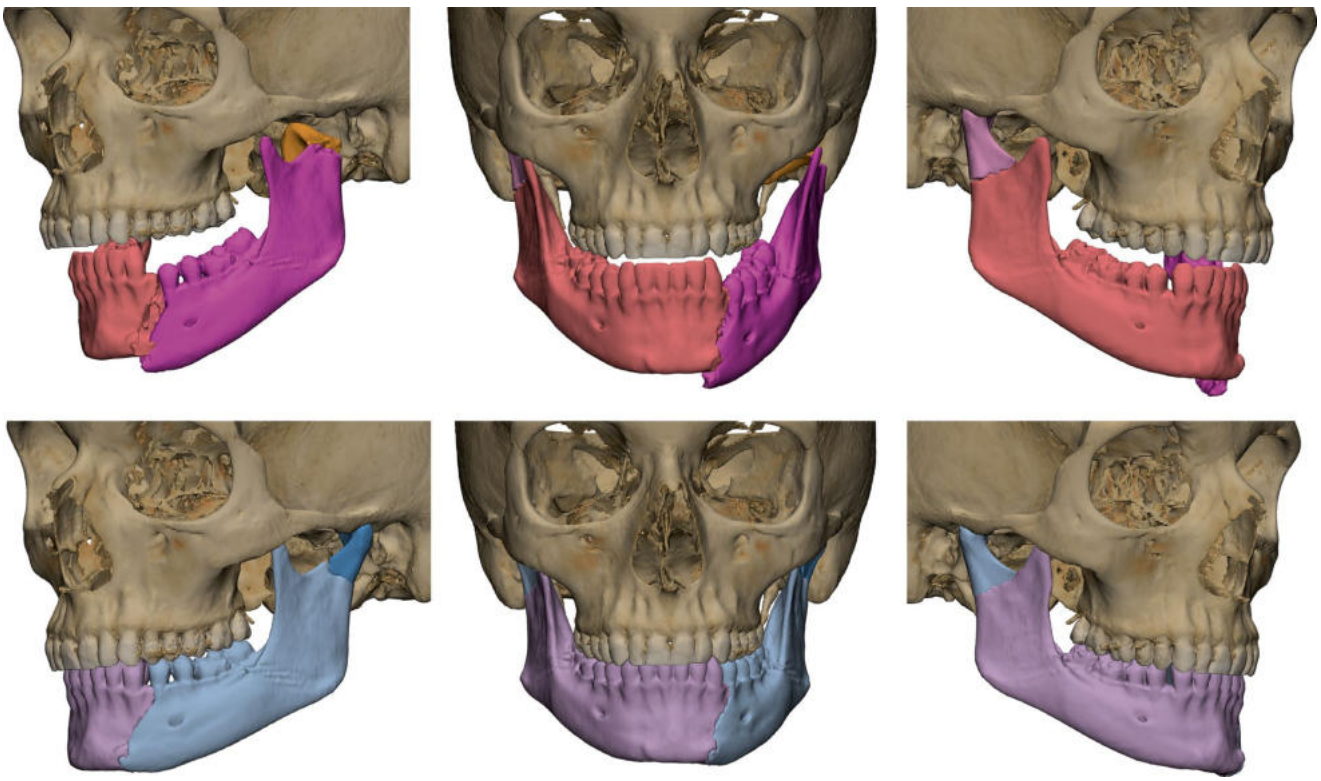


Fig. 3 Multifocal mandibular fracture, VSP. Condylar-only fractures are treated in Chapter "Application of VSP in Temporomandibular Joint Surgery" (TMJ), but they are classified in here in the context of multifocal fractures

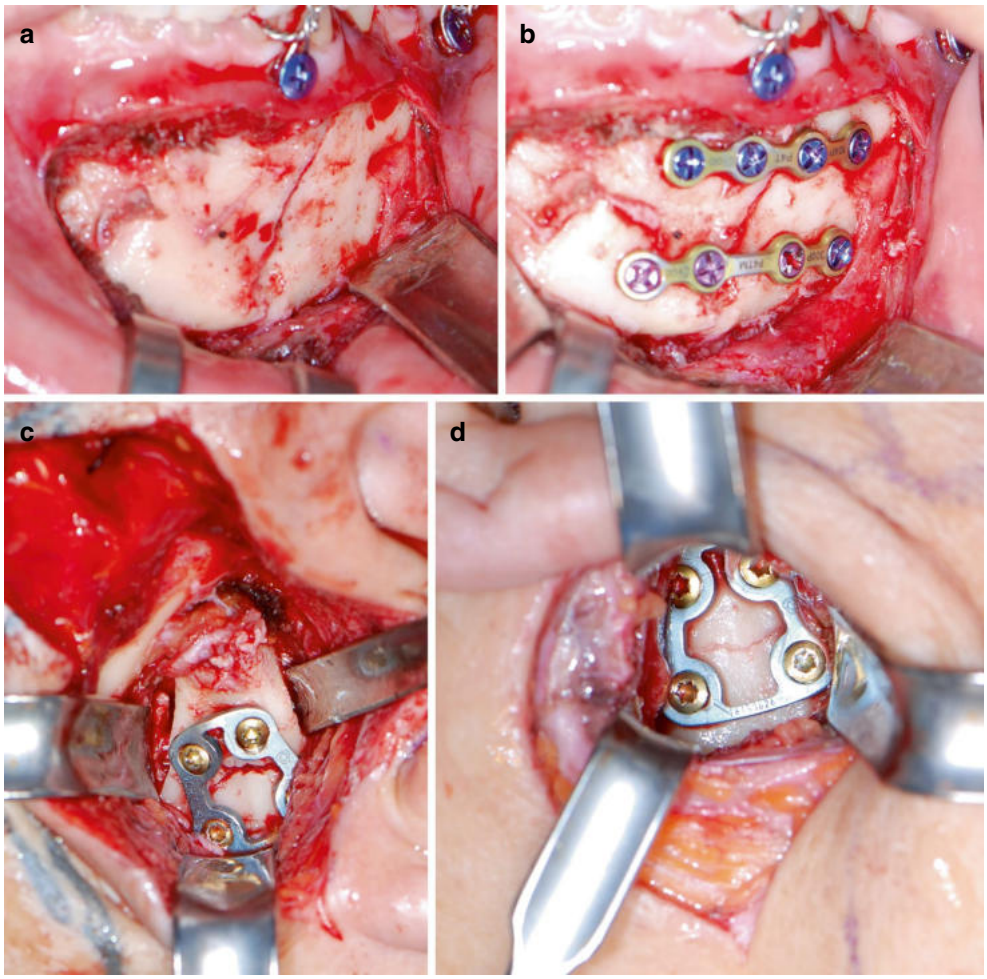


Fig. 4 Intraoperative view: (**a**) reduction and (**b**) fixation of the left parasymphyseal fracture; (**c**) fixation of the left subcondylar fracture through a preauricular approach; (**d**) fixation of the right condylar neck fracture with a retromandibular transparotid approach

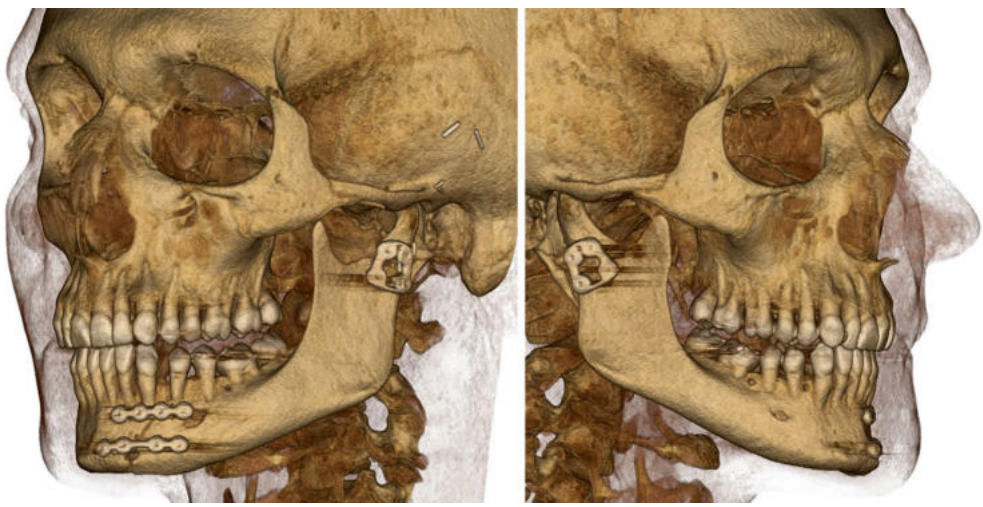


Fig. 5 Postoperative CT

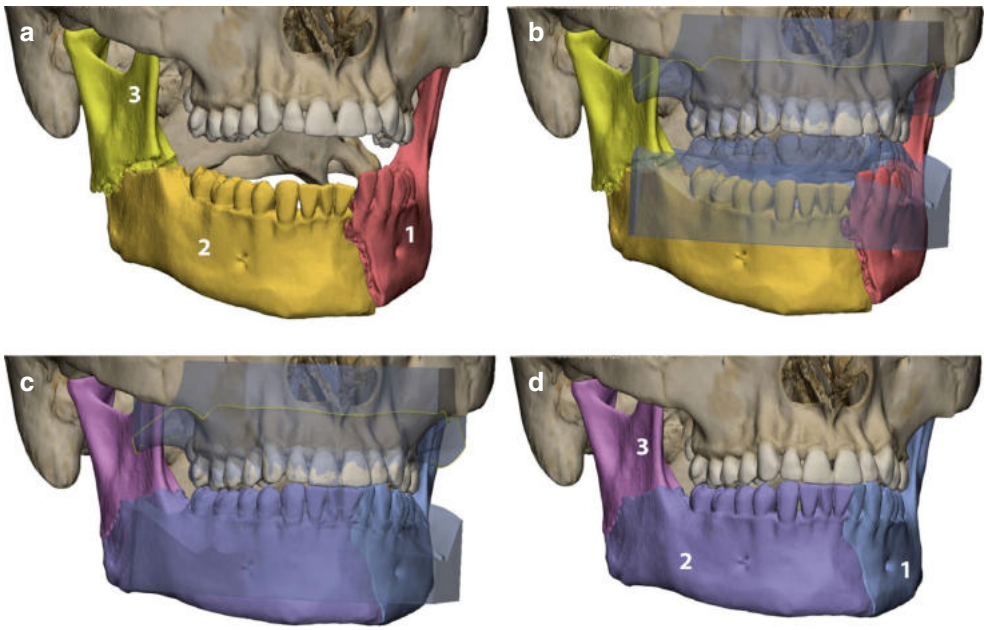


Fig. 6 Occlusion-driven realignment of a bifocal (class II) mandibular fracture

patient remained three days in ICU and, notwithstanding the presence of the oro-endotracheal tube, a visible malocclusion was assessed. The patient underwent CT scan, showing a right ramus, bicortical, fracture, and a bicortical left parasymphyseal fracture. During patient sedation, intraoral scanning was acquired, and the printed models were assessed to search the most stable occlusion, which was rescanned to be used as template driving the realignment of bone segments.

Virtual Surgical Planning

CT scan was segmented and the splint mask algorithm was used along fracture lines to reconstruct the three mandibular segments. The scanned mandibular arch was interrupted in correspondent fractured points, and each segment was aligned and merged with the relative mandibular part. This process yielded that isolated fractured segments had the detail of scanned dental cusps. The occlusion cast was aligned with the superior, integer, dental arch, and was used as a digital reduction matrix to realign both the left ramus with its half arch and the central segment. Once in the correct intercuspation, appropriate reduction at fracture sites was appraised between segments 1 and 2. At this stage, segment 3 was correctly reduced to segment 2 by placing paired points along the fracture. It is worth noting that reduction performed using occlusion as reference is entirely semi-automatic and does not involve any manual repositioning of skeletal segments, thus maximizing the likelihood of achieving the correct preoperative shape (Fig. 6). To bring such alignment in surgery, a 3D printed splint was manufactured.

Surgery

The first step consisted of fracture sites' exposure through intraoral incision: a vestibular incision overlying the parasymphyseal fracture down to the inferior mandibular border and a perimandibular vestibule incision to expose the ramus fracture. The optimal intercuspation achieved with intraoperative maxillo-mandibular fixation (MMF) did not make the use of the 3D printed splint necessary. Ramus fracture was synthesized using two linear plates in parallel, and screws were tightened using angled screwdriver (Fig. 7).

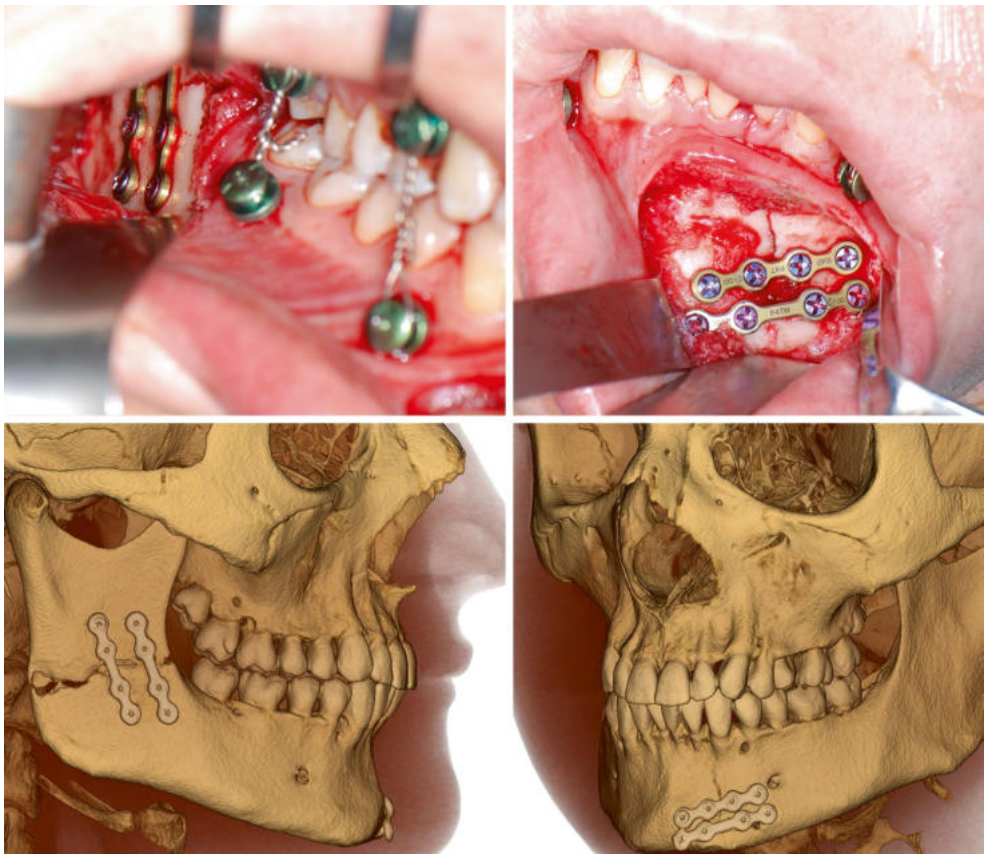


Fig. 7 Overview of intraoperative fixation and postoperative CT

5.3 Case 3: Parasymphyseal and Left Ramus Bifocal Fracture

Clinical History

This patient was evaluated in emergency department following physical assault. She presented with intense pain, trismus, and malocclusion with left-sided precontact and right open-bite. CT scan revealed displaced mandibular ramus and condylar neck fracture with angulation and loss of height, right parasymphyseal fracture, and dentoalveolar fracture of teeth 11 and 21. Intraoral scan was not feasible from trismus and intense pain; however, teeth cusp detail inferred from CT scan was sufficient as there were no metal artifacts.

Virtual Surgical Planning

CT scan was segmented and the correct application of the split mask algorithm enabled to yield different entities, accounting for left and right hemimandibles, condylar stump and ramus fracture, skull and dentoalveolar fractures. Virtual anatomical reduction of fractures was meticulous and aimed to realign the posterior mandibular border, respecting the physiological interarticular space and placing the left condyle in the centroid of the glenoid fossa. After reestablishing the posterior facial height, the reduction of the parasymphyseal fracture was determined based on the imported occlusion from a scanned 3D printed replica of the reduced maxilla and mandible placed in the most stable occlusal configuration (Fig. 8).

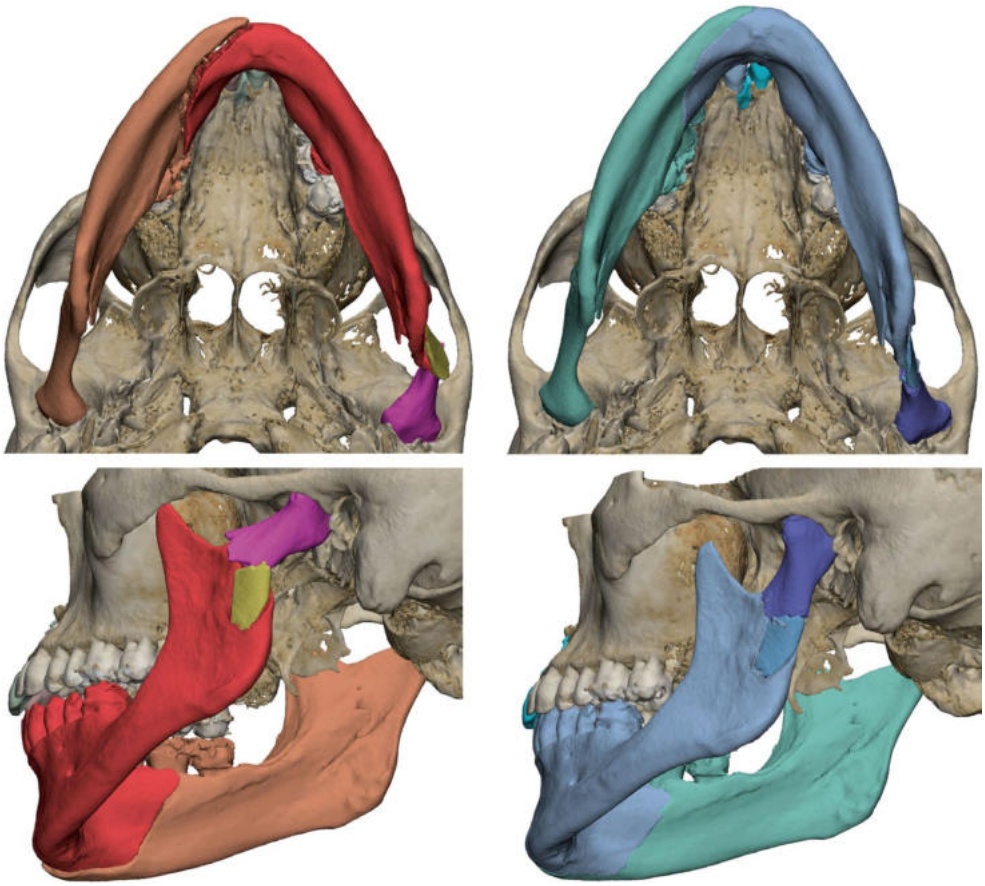


Fig. 8 VSP of multifocal (class II) mandibular fracture with subcondylar fragmentation

Surgery

A submandibular/retroangular incision was performed, aiming at first to expose the pterygomasseterine sling, which was incised at its inferior border, enabling to expose the mandible subperiosteally. This created a wide tunnel lifted by a Lagenbeck retractor, allowing to assess the most suitable reduction for the mandibular ramus, especially for the posterior border, where anatomical reduction was crucial. The posterior border was reduced using a load-bearing plate given its structural biomechanical importance, whereas the intermediate fragment was secured with a simple quadrangular plate. Subsequently, MMF was determined in the most stable intercuspal arrangement, driving the most functionally correct reduction of the parasymphyseal fracture, fixed using two load-sharing plates (Fig. 9).

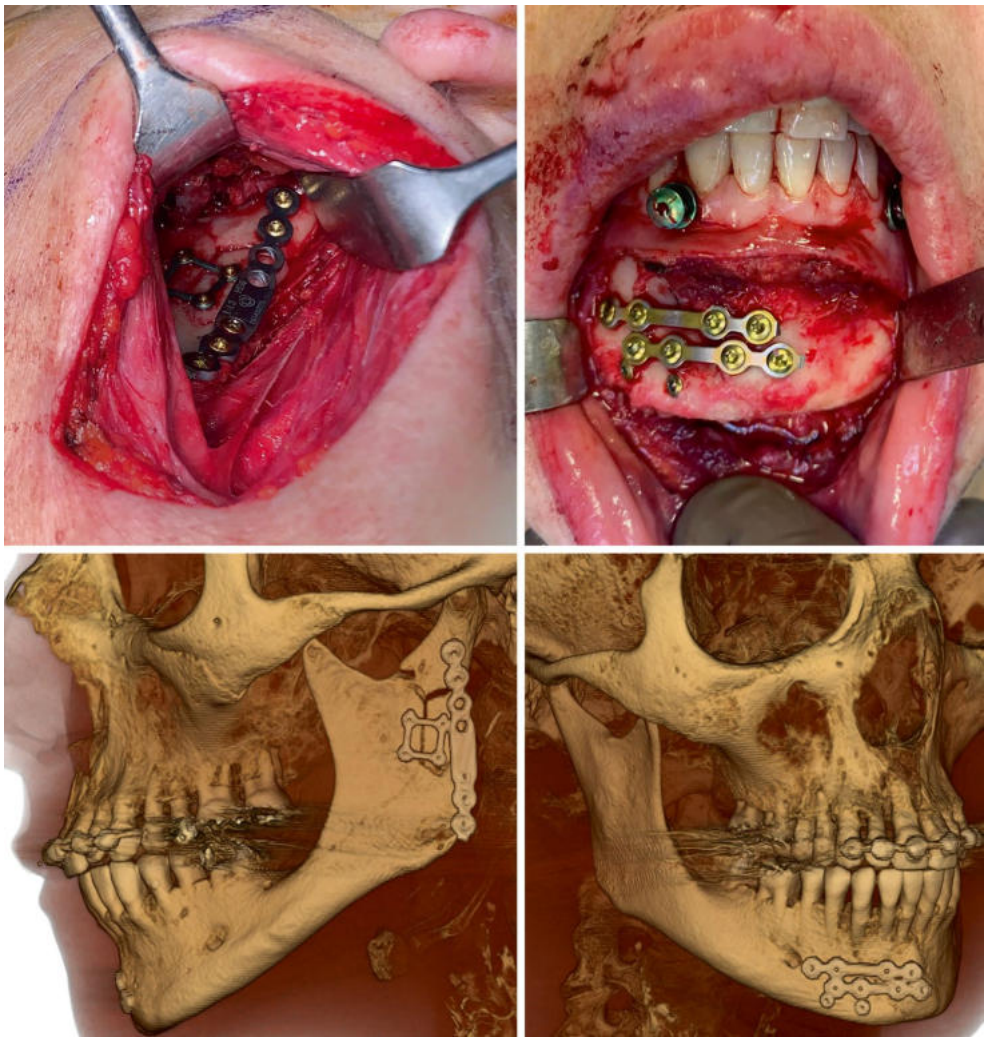


Fig. 9 Intraoperative view of fixation and postoperative CT

6 Multifragmented Mandibular Fracture Without Bone Loss

This type of fracture is caused by high-energy injuries, including car accidents and precipitations. It causes multiple fracture lines resulting in a multifocal fracture in which multiple segments of the same region are displaced, thus making anatomical reduction almost impossible using a traditional manual approach. It is of prominent importance that each segment is carefully analyzed within the virtual surgical planning, in terms of orientation and realignment with the others, as well as in terms of structural capability of being fixed to a titanium plate. Moreover, the surgical sequence of segment realignment is likewise determined within the virtual plan.

Concerning intraoperative reduction, it can be greatly enhanced by using reduction guides, which offer physical stabilization of segments within the correct realignment boundaries offered by the negative impression of virtual surgical planning. Such guide enables to assist the surgeon in fragment reduction and stabilize fractured fragments while they are fixed [10].

6.1 Case 1: Multifragmented Left Mandibular Body Fracture with Bilateral Condyle Fracture

A young, 32-year-old man suffered from car accident with a violent impact of his face against the car dashboard. The patient was intubated and transferred to ICU, where he underwent CT scan showing a complex mandibular fracture involving both condyles, with medial translocation of the condylar head and comminution, and the whole left mandibular body in multiple fragments, potentially reducible although severely dislocated. It was considered that, after proper reduction, it was possible to restore the biomechanical continuity of the mandible using a load-bearing fixation plate.

Virtual Surgical Planning

Virtual surgical planning was performed according to the following phases: segmentation, virtual reduction, surgical guide creation.

- Segmentation: Accurate segmentation was performed by setting a threshold range between 447 HU and 3017 HU to capture even the most tiny fragments. Mask split was conducted to separate larger fragments across each fracture line, with the following result: a larger, dentate, fragment; a smaller, free, segment along the inferior mandibular border, the left mandibular ramus simulating a sagittal split fracture, both condyles and the right coronoid process. Moreover, luxated teeth were also removed and not considered viable for the reduction. STLs were applied a voxel coloring method in non-fractured regions, and a full mesh coloring for fractured parts, and then were transferred in 3-matic for reduction (Fig. 10).
- Virtual reduction: As reduction was mostly unavailable in this case due to multiple teeth avulsions, virtual reduction maneuvers were essentially based on anatomical reduction: first, condyles were manually aligned with mandibular rami using the posterior mandibular border and the sigmoid notch as reference; then, the left, reduced, mandible ramus was aligned to the larger, tooth-bearing segment by searching correspondence between the inferior body contour and the angle border. Subsequently, anatomical reduction was completed by repositioning the smaller fragments in the corresponding gaps (Fig. 11). Once the mandible was satisfactorily reconstructed in its anatomical contours, it was repositioned with the aim of centering both reduced condyles in the glenoid fossa and the inferior dental arch in an acceptable position with its missing antagonist to simplify future prosthetic rehabilitation of the mandible: this was achieved by changing the rotational fulchrum to accommodate the condyle in the best centric relation with the fossa.
- Once the fragments were reduced, they were still separate objects. To design a surgical guide, it was necessary to create a single, unified entity without surface gaps. For this purpose, mesh wrapping was applied using a gap closing distance of 1 mm and a final surface offset of 0.1 mm. Once the reduced, filled mesh was achieved, the fitting surface of the guide was identified on the model and was extruded to create the base for the surgical guide. The guide was designed highly contentive in order to provide a physical boundary to relocate dislocated fragments according to the virtual reduction plan. Cylinders for screw placement were designed, allowing to secure bone fragments the achieved reduction. At the same time, the guide was designed to leave exposed the superior part of the mandible, allowing to position titanium plates, so that fixation could begin in the correct position with the guide already in place (Fig. 12).

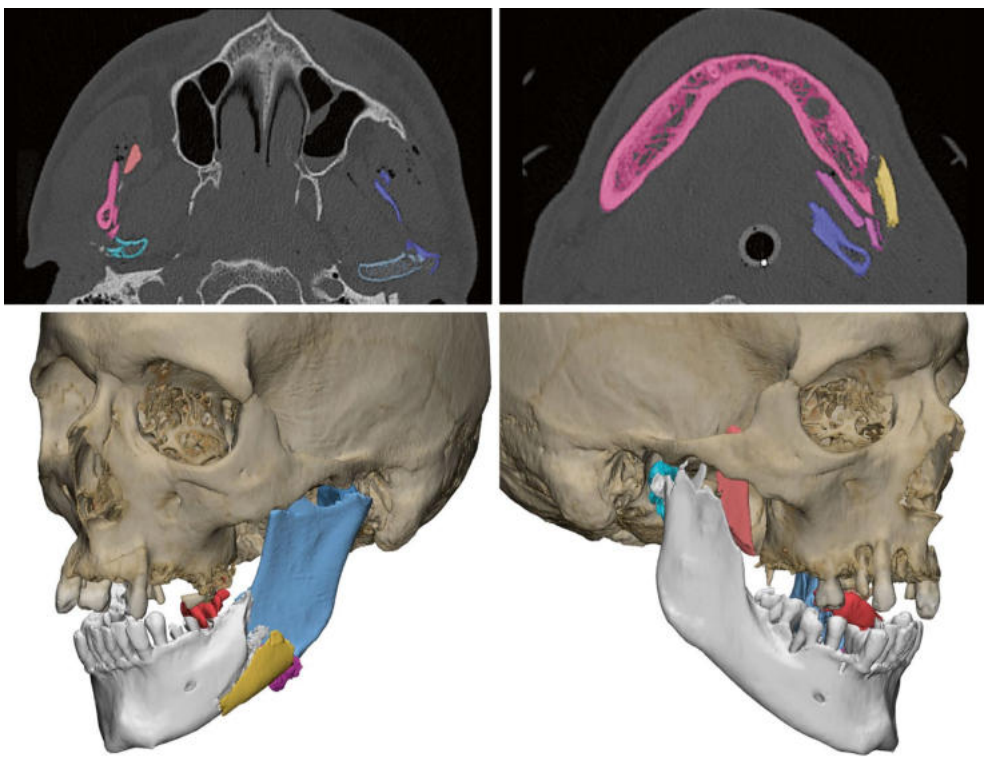


Fig. 10 Class III fracture segmentation with multiple fragments in the same anatomical unit

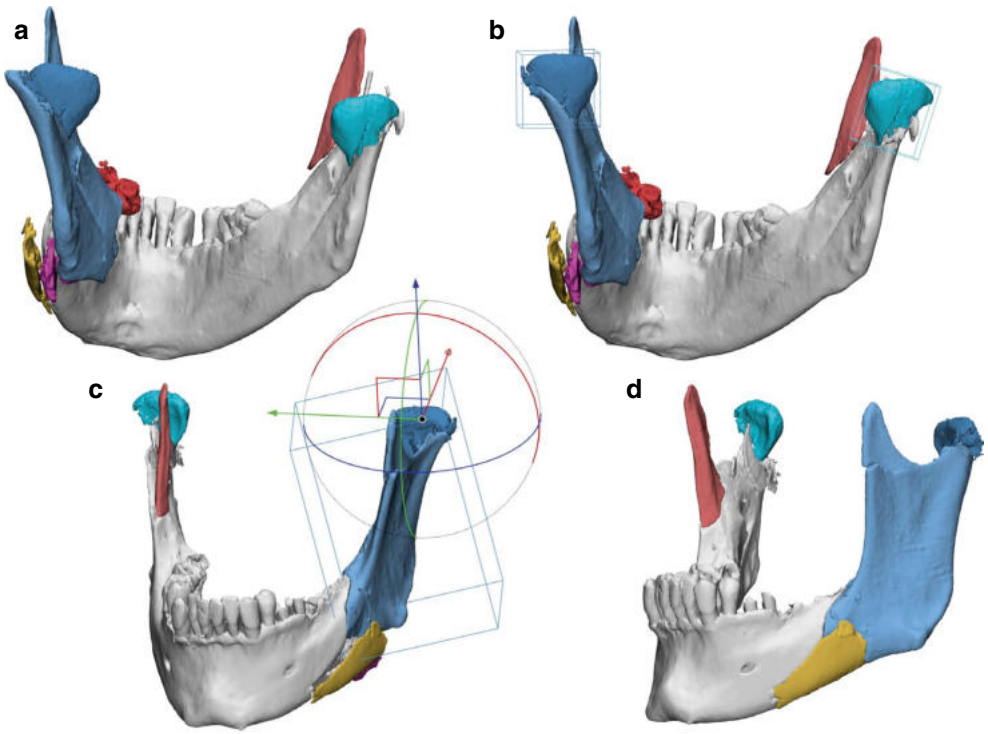


Fig. 11 Phases of reduction. (**a**) Displaced fragments; (**b**) reduction between the condyle and ramus; (**c**) alignment of reduced ramus with mandibular body (if fracture passes through the alveolar process, occlusal registration is needed in this step); (**d**) reduction of remaining fragments of basal bone (anatomical reduction)

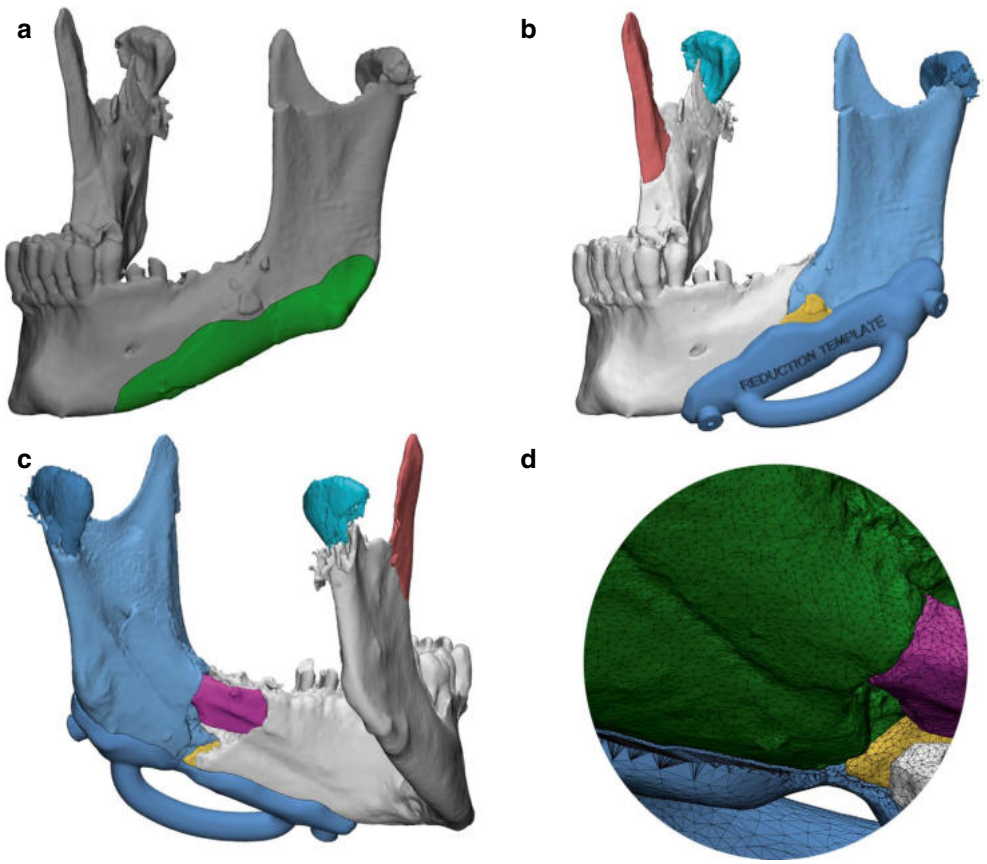


Fig. 12 Creation of a reduction template to facilitate anatomical alignment. (**a**) Definition of the fitting area using the reduced model (wrapped); (**b**) lateral view; (**c**) medial view (notably, extension is minimal to avoid problems of undercut); (**d**) particular of tessellation after further undercut removal is carried out

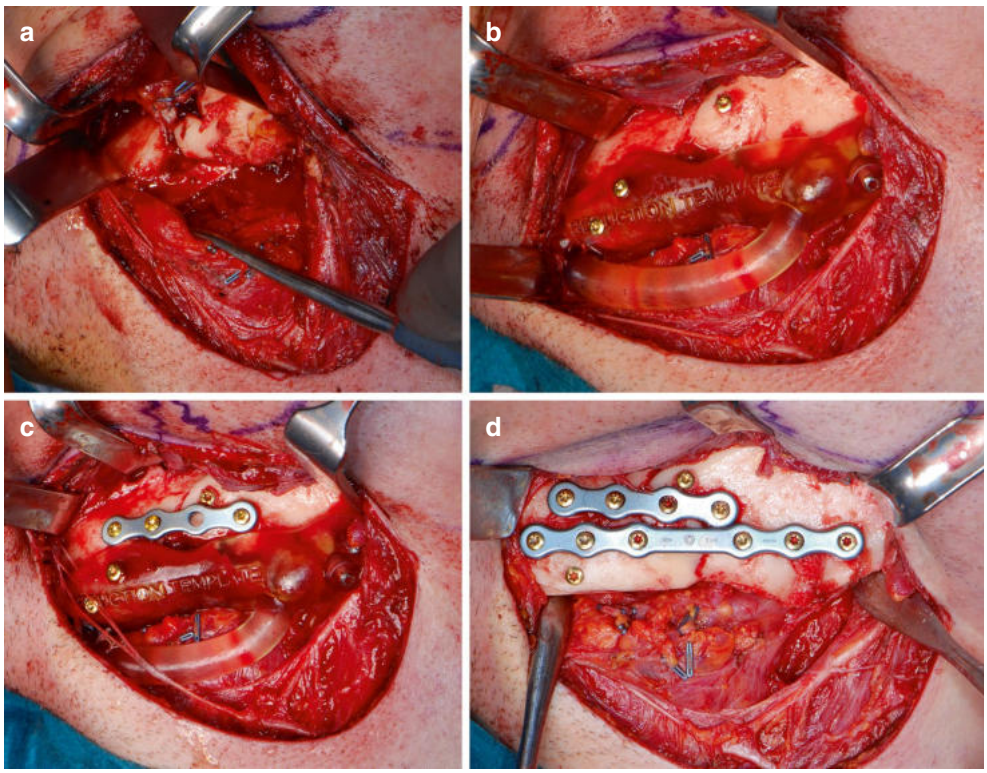


Fig. 13 Intraoperative view. (**a**) View of the fractured mandible; (**b**) surgical guide for reduction in place; (**c**) stabilization with the surgical guide in place; (**d**) optimal anatomical reduction once the guide is removed

Surgery

A submandibular incision was designed two inches inferior to the mandible contour to avoid damage of the marginalis branch of the facial nerve. Eventually, the nerve was searched and isolated. Dissection was made difficult owing to the conspicuous bleeding caused by the fracture of the cancellous component of the mandible, resulting in the hemorrhagic infarction of the muscular bellies and limited visibility. The mandibular body was exposed and fractured segments were identified (FIGURA). The surgical guide was first fixed to the tooth-bearing larger segment, and then used to realign the misoriented left mandibular ramus. Once the preliminary reduction was performed, bone segments were stabilized using bicortical screws and plates. The surgical guide was removed and a reconstruction plate was positioned to yield the final stabilization. In this case, condyles were not treated due to the excessive loss of bone with impossibility to insert fixation screws, as well as owing to the loss of teeth and any occlusal reference. It is expected that condyles will remodel and eventually readapt to the novel prosthetic occlusal rehabilitation (Fig. 13). The patient underwent postoperative CT scan to check that reduction and fixation were properly performed (Fig. 14).

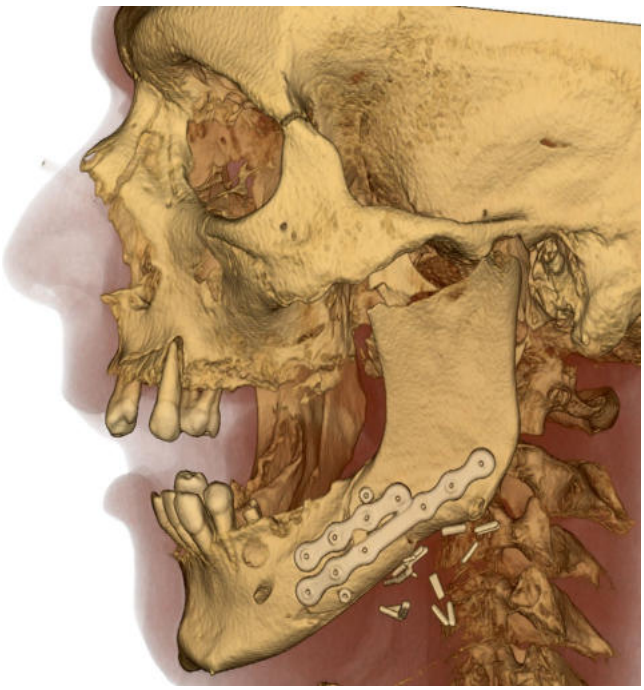


Fig. 14 Postoperative CT shows optimal reduction

7 Multifragmented Mandibular Fracture with Bone Loss

In several cases, it is not possible to perform the reduction of fragments in complex mandibular fractures, especially those caused by high-energy trauma. This is often the results of precipitation from heights of several meters, particularly violent car accidents, or ballistic trauma, including gunshot injuries. Notably, such cases require even more to use a virtual surgical planning to define the best reconstructive strategy for such patients that may consist in a microvascular free flap, especially for young, dentate patients, or, alternatively, a customized alloplastic implant, in particular in elderly patients [11].

7.1 Case: Complex Mandibular Reconstruction Using the Fibula Free Flap in Trauma Sequela

Clinical History

In this case, a 57-year-old lady was urgently referred to our department after falling from a height of several meters in a suicide attempt. She presented with a left subcondylar fracture and a multifocal mandibular body fracture, including a left parasymphyseal multifragmented fracture and a right, comminuted, body fracture with cutaneous exposure. In the first surgery, the patient was treated traditionally, trying to restore occlusion by placing arch bars with intermaxillary block, reducing the subcondylar fracture, positioning a load-bearing reconstruction plate in the right comminuted fracture, and two load sharing titanium plates across the parasymphyseal region. Surgery was performed through a mini retromandibular incision using a retroparotid approach for the condyle fracture, and from a transcutaneous, submandibular incision to dominate the fractured mandibular arch. Moreover, the patient was subject to multiple skeletal fractures, including both femurs, which required observation in intensive care unit for several days.

Ten days after surgery, a wound dehiscence with exposure of the reconstruction plate was noted within the oral cavity, with subsequent plate infection and need of its removal. Since a malocclusion was clinically appraised, plate replacement had to take into account occousal restoration.

First Virtual Surgical Planning: Plate Prebending

DICOM data was segmented in Mimics v.24.0. The reconstruction plate to be removed was virtually separated from the bone component using the split mask algorithm, not to interfere with the position of the new plate. Models of dental arches were printed to determine the most stable intercuspation, and the resulting occlusion was rescanned and imported back in the VSP, where it was used as template to realign mandibular segments. To enable plate prebending, a 3D printed replica was necessary, and the model was prepared by bridging the gap using two tube-like structures, enabling to 3D-print an uninterrupted mandibular arch. The model was printed using Grey Pro resin, with strong biomechanical properties, and a novel titanium plate was prebend on this model. Surgery was performed using the prebent plate to correct mandibular segments malposition and restore a functional occlusion (Fig. 15).

The patient stayed asymptomatic for two years, after which she came to our attention for a sudden deformity in the right parasymphyseal region and progressive occlusal alteration. She underwent a further CT scan showing the rupture of the prebent titanium plate across the region of bone gap (FOTO).

Second Virtual Surgical Planning: Fibula Reconstruction

The patient was candidate to mandibular reconstruction using a fibula free flap. A novel virtual surgical planning workflow was adopted to optimize surgery, as the following main criticalities were noted:

- Complete loss of mandible shape due to malrotation of mandibular segments after plate rupture
- Presence of the ruptured plate overlying the bone hindering the placement of surgical guides
- Absence of a preoperative occlusion to restore

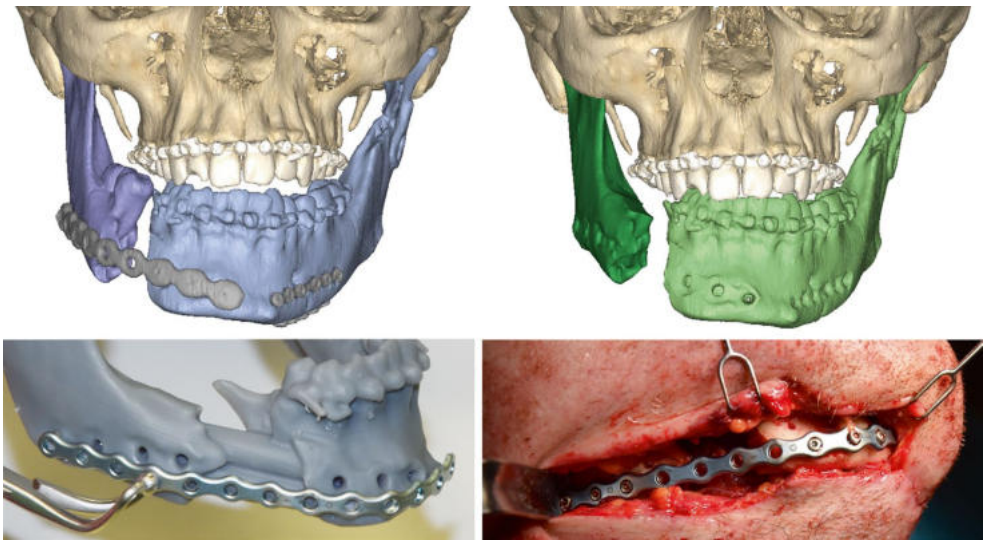


Fig. 15 VSP for the replacement of the infected plate. This second surgery was an opportunity to improve the patient's occlusion. After correctly establishing the occlusion on 3D printed models, the fracture gap was bridged using two tube-like structures. The new plate was bent over the 3D printed model in the appropriate occlusal configuration

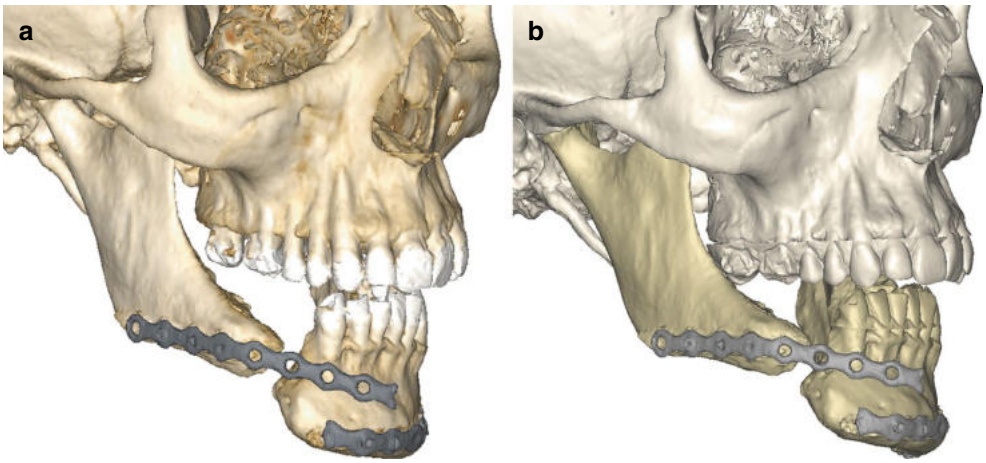


Fig. 16 (**a**) Segmentation of the broken plate; (**b**) separation of the mandible

STEP 1: Segmentation

CT was segmented and the same method based on split mask algorithm was used to separate titanium plates from the bone component. A voxel-based mesh coloring was used to enhance visualization of the bone separate from the titanium. Dental arches were scanned and matched with CT scan (Fig. 16). Moreover, angio-CT of inferior limbs was performed, and the vasculature was carefully reconstructed to rule out possible vascular abnormalities.

STEP 2: Occlusion Restoration

The patient's dental arches were scanned and processed as STL files. Following that, models were sent to 3D printing and the surgeon established the best possible occlusion based on the most stable intercuspation and stability. Notably, it may be argued that some software implementing algorithms of automatic occlusion is already available, but such methods are at initial development stage and are programmed to be effective in ideal conditions, for instance, patients with aligned teeth after orthodontic preparation that are candidate for orthognathic surgical planning (CITAZIONE). Automatic occlusion would be highly unreliable, or even detrimental, in cases of trauma with teeth rupture, partial edentulism, and misaligned teeth. Therefore, we opted for manual determination of surgical occlusion, which was rescanned to be imported in the final project (Fig. 17).

STEP 3: Occlusion-Driven Skeletal Realignment

Scanned occlusion was aligned with the superior dental arch and the left mandibular tooth-bearing segment, which was realigned. The correct position of the condyle in relationship with the glenoid fossa was inspected to evaluate its coherence with the re-established occlusion. Once satisfied, the right mandibular segment including the ramus and the angle was realigned, at first trying to reconstruct the continuity of the interrupted plate, then by optimizing its rotation with the superior dental arch. In this way, the fibula is placed in the correct position with antagonist teeth and simplifies future

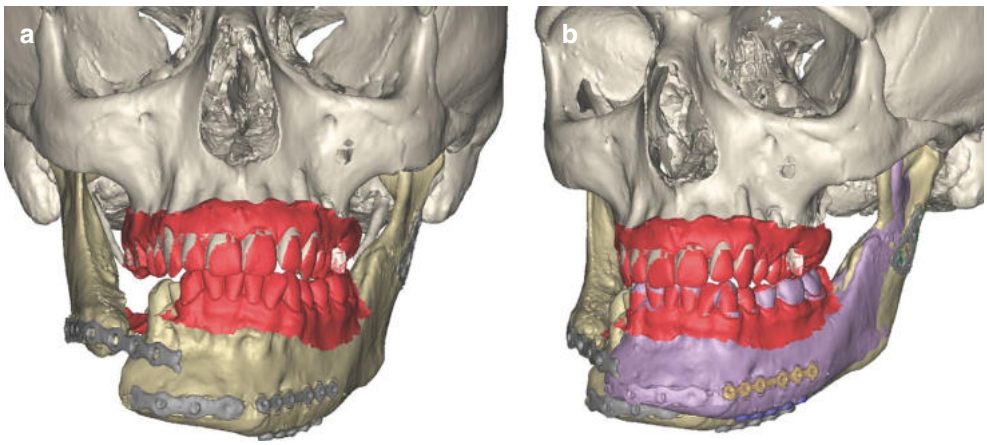


Fig. 17 Occlusal registration of the most appropriate configuration to reposition the left hemimandible

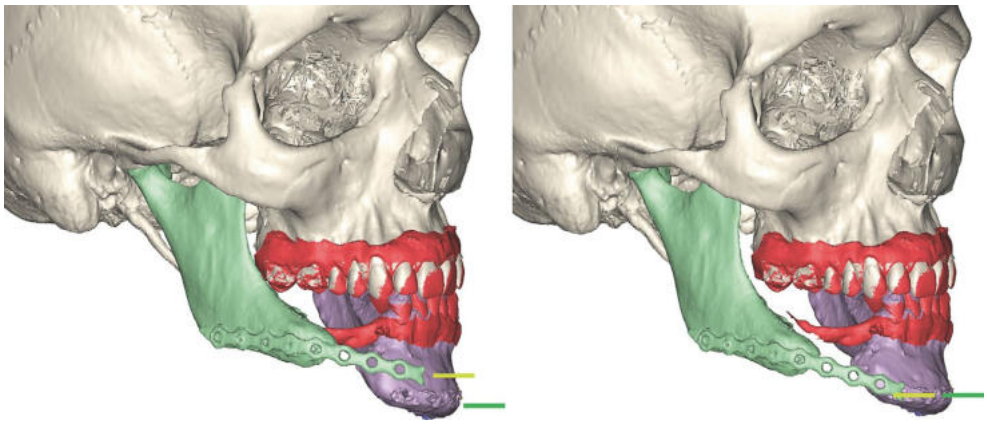


Fig. 18 Repositioning of the right ramus. To reconstruct mandibular alignment, the interrupted plate extremities were joined, and the position of the right segment was modified in the axial plane to achieve alignment with the superior dental arch

implant positioning (Fig. 18). This approach underlines the importance of orthognathic knowledge in performing reconstruction.

STEP 4: Resection

To provide a linear approximation interface between the linear osteotomies of the flap and the receiving site, osteotomies were planned on both skeletal segments of the mandible. An increased length of resection was established for the right mandibular segment with the aim to make the fibula segment longer than 3 cm to enhance its vascularization (Fig. 19).

STEP 5: Fibula Flap Planning

In the reconstruction module of ProPlan CMF, both the mandible parts and legs with their vascularization were imported. With the aim of placing the pedicle posteriorly and the muscle cuff along the posterior septum (including flexor hallucis longus and tibialis posterior), the contralateral fibula with a 180° rotation was selected. Osteotomies in the fibula were made linear and coherent with resection planes and were automatically reported along the fibula diaphysis. The fibula segment, having a triangle section, was rotated to position its superior-medial crest along the inferior mandibular border, and its wider base superiorly, offering the space to position implants (Fig. 20).

STEP 6: 3D Printing of the Mandible and Plate Prebending

As both mandible parts and the fibula segment are distinct objects and there is a 0.3 mm osteotomy gap between the flap and the mandible, models are separate and not 3D printable. Thus, a mesh wrapping with gap closing distance set to 1 mm and resulting offset of 0.1 mm was applied, yielding a composite mesh without any gap. Furthermore, an adaptive remesh was applied to regularize triangulation. The model was imported in Formlabs Preform and set for 3D printing in Formlabs 3BL printer using a Biomed Clear resin.

STEP 7: Plate Prebending and Reverse Engineering

A titanium plate was bent to closely adapt to the mode surface. Once accurately modeled, it was fixed to the mandible using titanium screws, avoiding the holes of the previous broken plates. The model with the attached plate underwent intraoperative CT scan in the OR to achieve a DICOM representation. Data were segmented as shown and the prebent plate was reconstructed in the virtual space attached to the

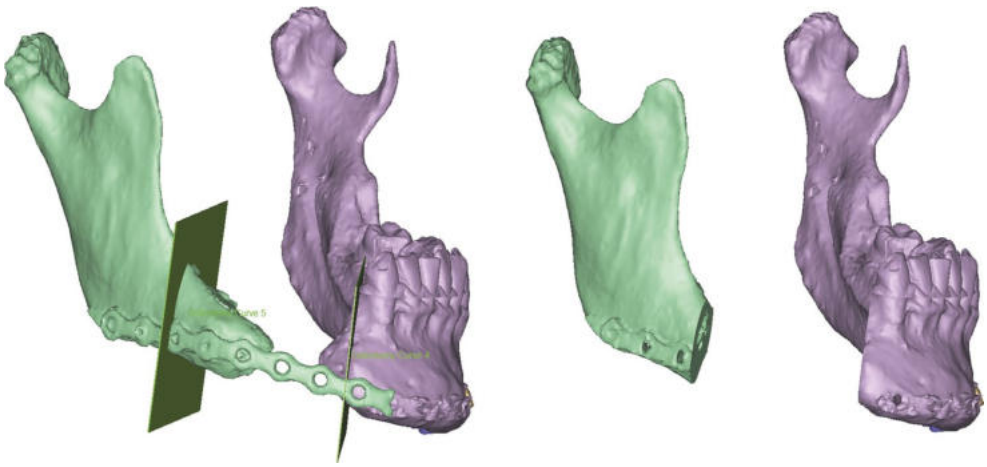


Fig. 19 Osteotomy planes are placed to define the space to inset the bone flap. Excision is planned superior to the real defect to enhance correspondence of linear planes and vascularization of the flap

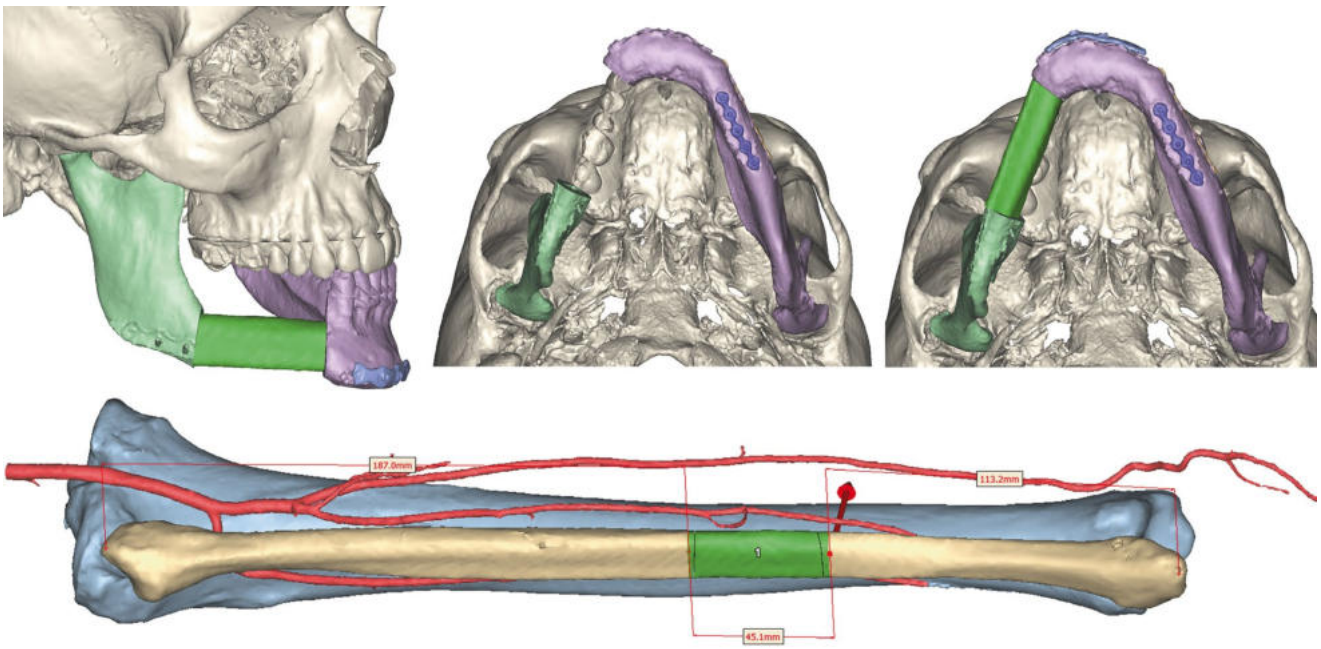


Fig. 20 Flap inset is performed according to the correspondence with the superior antagonist to optimize future occlusion. This is achieved by repositioning mandibular segments in line with the superior dental arch, as seen in Fig. 18. As illustrated in detail in Chapter "Virtual Surgical Planning in Mandibular Reconstruction", vascular considerations are mandatory to keep the pedicle posterior and lingual

model. This composite model was then aligned with the VSP project in 3-matic, enabling to transfer in the virtual plan the correct position of the prebent plate (Fig. 21). Once alignment was successful, cylinders of 2.3 mm diameter, reproducing the position of screws, were designed to enable surgical guide modeling.

STEP 8: Resection Guides

In 3-matic, resection guides were separately designed for both the mesial and distal edge of resection. While surgical guides generally fit smooth bone surfaces, engaging their anatomical fit, in this case the presence of the previously placed titanium plate represented a potential problem. At first, it was hypothesized to digitally remove the plate and place the guide over bare bone surfaces, but this is actually an unreliable step, as the virtually derived bone surface after plate removal might differ from the actual bone surface once the real plate is removed. Thus, surgical guides were designed the titanium plate already in place, bearing an additional negative impression (the plate) in their fitting surface. Once the main body of the guide was designed, notch-based structures with an inner fissure 1 mm thick were designed to guide the piezosurgical blade. Additionally, guiding tubes for hole drilling were designed around the previously positioned cylinders in the final plate position (Fig. 22).

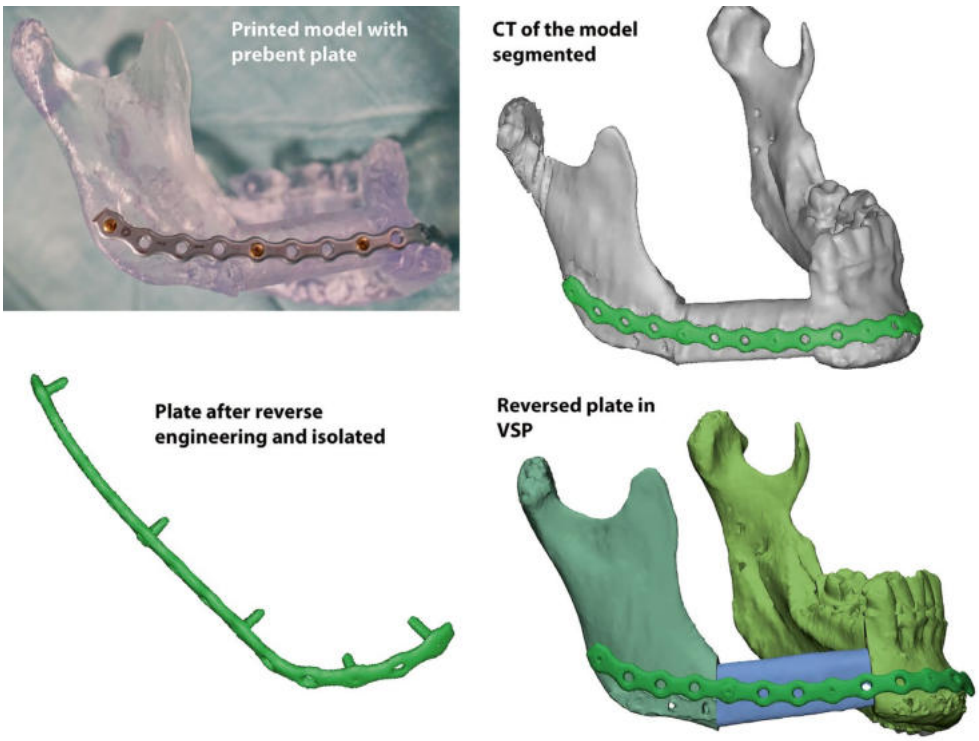


Fig. 21 Reverse engineering process of a plate conformed on a 3D-printed model. The plate is fixed using screws inserted in the polymerized resin. The model+plate undergoes CT scan, which is then segmented using a low HU value to capture the shape of the 3D printed model (slight radiopaque). Then, a different, high-density threshold is used to separately acquire the plate and screw. The model with the plate STL is aligned with the VSP so that the plate is transferred alongside in the correct position with reference to the VSP

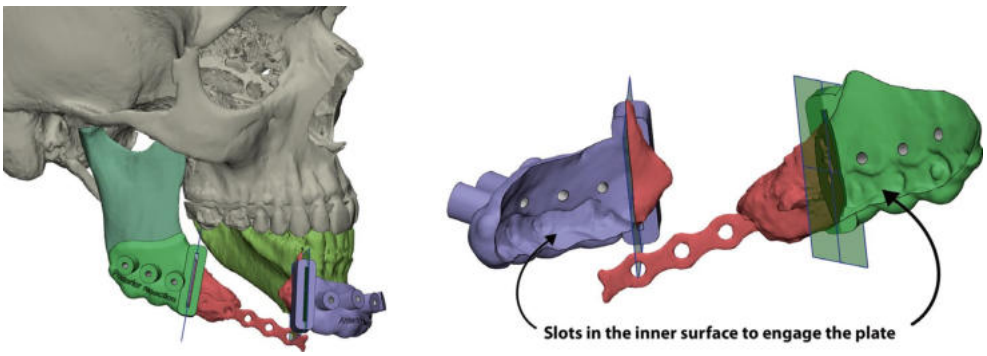


Fig. 22 Surgical guides for resection. As a plate is already on the bone, and removing it in the VSP might involve inaccuracies compared with removing it in surgery, a surgical guide fitting on the plate as well is designed, enabling to trace osteotomies outside the plate. Then, the plate is removed and osteotomy can be continued both freehand and by repositioning the surgical guide

STEP 9: Fibula Guide

To facilitate fibula guide design, the chosen fibula was aligned with its segment placed in the established place on the mandible. Once perfect alignment was found, the same principles were applied to create the fibula guide. In this case, it was preferable to use linear flanges without the inner slot to decrease possible hindrances. Guiding tubes for screw holes were designed based on the reversely engineered plate (Fig. 23).

STEP 10: Creation of the Occlusal Splint and 3D Printing

To facilitate occlusal restoration during mandible reconstruction, a splint was designed and printed together with the guides.

Surgery

A submandibular incision was designed to elevate a composite platysmatic and cutaneous flap. The posterior belly of digas-

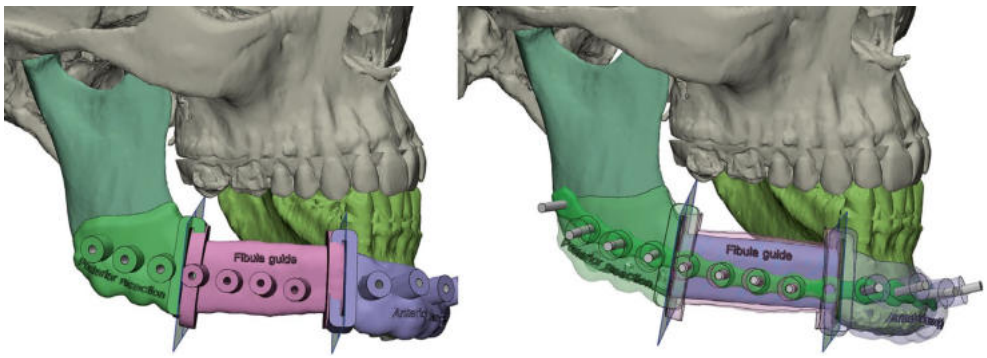


Fig. 23 Thanks to prebent plate reverse engineering, each screw hole of the plate corresponds to the screw holes of surgical guides for resection and reconstruction

tric muscle was found to determine the depth of dissection. Anteriorly, the submandibular gland was identified and luxated; facial artery was preserved, as well as the linguofacial trunk, both serving as recipient vessels of anastomosis. The mandible was exposed and the plate was identified. Mobility of the two mandibular segments was assessed. Resection surgical guides were positioned over the plate and immediate optimal fit was identified. Following that, holes were drilled inside the guiding tubes to provide the sites for screw placement of the prebent plate, as well as to secure surgical guides to the bone using screws. Osteotomies were performed within the cutting flange of surgical guides, obviously not including the bone covered by the plate (Fig. 24). The previous, broken plate was removed and osteotomies were completed, thus preparing the site to receive the fibula free flap.

Simultaneously, a second surgical team started dissecting the left fibula to elevate the flap. Once the fibula was luxated and the distal peroneal pedicle was ligated, the fibula surgical guide was positioned and fixed according to the planned position, matching the holes in the prebent plate, and osteotomies were conducted. Subsequently, the fibula segment was secured to the prebent plate using the same predrilled holes, and it was transferred in the recipient site in the man-

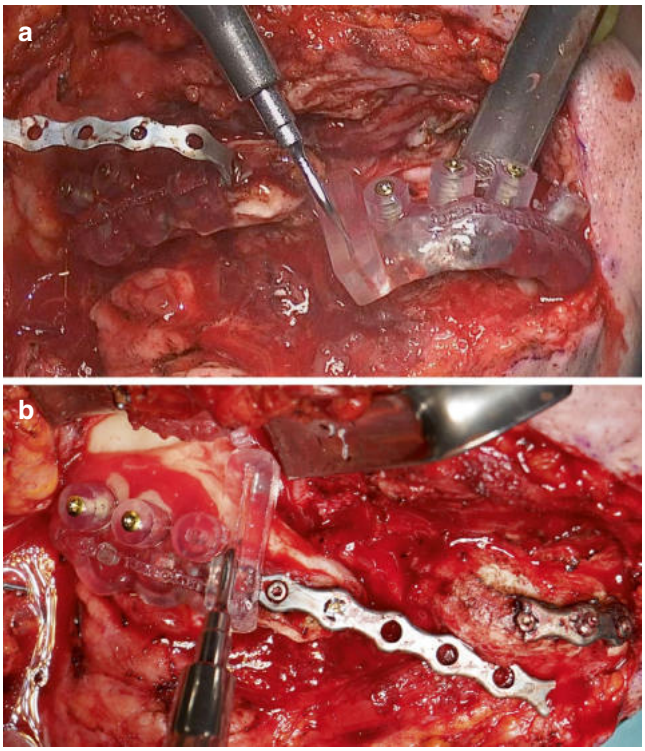


Fig. 24 Intraoperative view of double-fit surgical guides

dible while fixed to the plate. Before applying screws to the plate, the mandibular tooth-bearing segment was put into intermaxillary block using the 3D printed surgical splint to relate mandible reconstruction to the planned occlusion. During fixation, all screws matched their predrilled holes and the desired occlusion was verified after mandibular reconstruction. Anastomoses were completed and multilayer wound closure was accomplished (Fig. 25).

The patient underwent postoperative CT scan confirming the accuracy of reconstruction with a bone gap across bone interface below 1 mm on both sides of resection (Fig. 26).

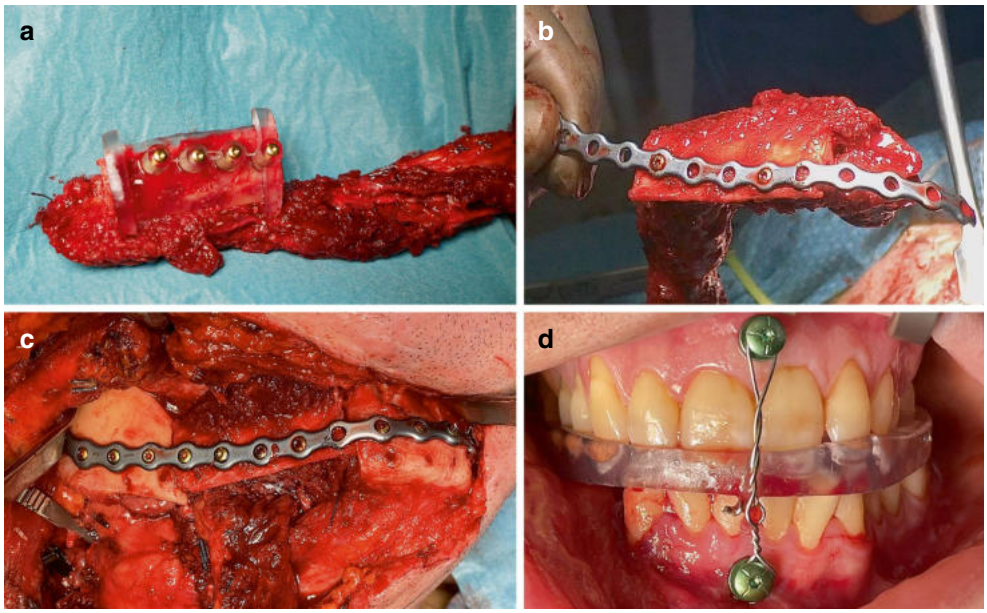


Fig. 25 Custom reconstruction with computer-automated steps. Accuracy of reconstruction is evident, as well as the predictability of the occlusal outcome

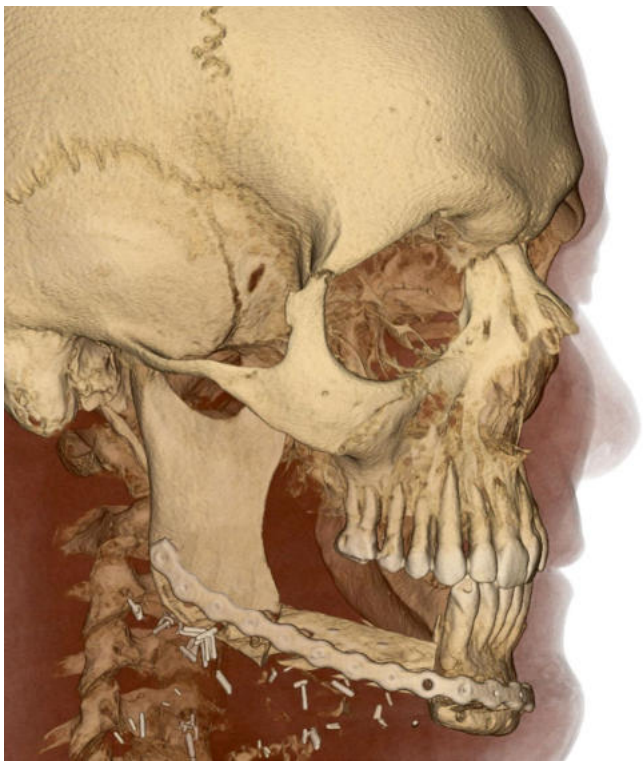


Fig. 26 Postoperative CT scan

References

1. Morris C, Bebeau NP, Brockhoff H, Tandon R, Tiwana P. Mandibular fractures: an analysis of the epidemiology and patterns of injury in 4,143 fractures. J Oral Maxillofac Surg. 2015;73:951.e1–951.e12.
2. Zhou H, Lv K, Yang R, Li Z, Li Z. Mechanics in the production of mandibular fractures: a clinical, retrospective case-control study. PLoS One. 2016;11:e0149553.
3. Walker CJ, MacLeod SPR. Anatomy and biomechanics of condylar fractures. Atlas Oral Maxillofac Surg Clin North Am. 2017;25:11–6.
4. Multidetector CT of mandibular fractures, reductions, and complications: a clinically relevant primer for the radiologist - PubMed. https://pubmed.ncbi.nlm.nih.gov/27618328/. Accessed 12 Jan 2025.
5. Baan F, van Meggelen EM, Verhulst AC, Bruggink R, Xi T, Maal TJJ. Virtual occlusion in orthognathic surgery. Int J Oral Maxillofac Surg. 2021;50:1219–25.
6. Shilo D, Capucha T, Krasovsky A, Blanc O, Emodi O, Haze A, Rachmiel A. Real-time reconstruction of comminuted mandibular fractures using 3D printing. Plast Reconstr Surg Glob Open. 2024;12:e5645.
7. de Geer AF, Brouwer de Koning SG, van Alphen MJA, van der Mierden S, Zuur CL, van Leeuwen FWB, Loeve AJ, van Veen RLP, Karakullukcu MB. Registration methods for surgical navigation of the mandible: a systematic review. Int J Oral Maxillofac Surg. 2022;51:1318–29.
8. Rozeboom AVJ, Dubois L, Bos RRM, Spijker R, de Lange J. Closed treatment of unilateral mandibular condyle fractures in adults: a systematic review. Int J Oral Maxillofac Surg. 2017;46:456–64.
9. Rai A, Datarkar A, Borle RM. Are maxillomandibular fixation screws a better option than Erich arch bars in achieving maxillomandibular fixation? A randomized clinical study. J Oral Maxillofac Surg. 2011;69:3015–8.
10. Zhuang H, Zhu B, Bu S. Short-segment drilling guides for the management comminuted mandibular fractures. J Craniofac Surg. 2022;33:e724–6.
11. Kadam D. Salvage secondary reconstruction of the mandible with vascularized fibula flap. Craniomaxillofac Trauma Reconstr. 2019;12:274–83.

Virtual Surgical Planning in Mandibular Oncology

Alessandro Tel and Massimo Robiony

1 Patients Candidate to Mandibular Resection

The indications to mandibular resection include oral cancer with involvement of the underlying bone—benign tumors arising primitively in the bone or with odontogenic etiology (ameloblastoma, ossifying fibroma), or malignant tumors such as osteosarcomas; malformations, including deforming dysplasia; and bone necrosis not responding to antibiotic therapy including bisphosphonate-related osteonecrosis of the jaw (BRONJ) and osteoradionecrosis of the jaw (ORNJ).

This chapter focuses on the methodology of virtual surgical planning (VSP) for mandibular resection and presents multiple clinical examples. The same examples will be treated in Chapter "Virtual Surgical Planning in Mandibular Reconstruction" as well from the reconstruction perspective and, thus, such chapters should be read in parallel.

2 Protocol for Virtual Surgical Planning in Mandibular Resections

A fundamental concept, when approaching any mandibular resection using VSP, is to reconstruct both a model of the skeletal mandible and the soft-tissue disease if needed. For this purpose, it is mandatory to define a standard acquisition protocol for CT and MR to optimize radiological image for both diagnostic and computer-reconstructive procedures. As seen in Chapter "Dedicated Acquisition Protocols in Radiology for Virtual Surgical Planning and 3D Printing", CT and MR have to fulfill specific requirements in terms of volumetric acquisition and visual intelligibility of the lesion, trying to emphasize as much as possible the discrimination of the lesion contours.

The most crucial phase in terms of accuracy of the entire procedure is represented by coregistration of CT and MR sequences. The main bias that needs to be ruled out is a diverse mandibular opening between CT and MR. This can be solved by using a standardized device (such as an occlusal splint) that keeps the degree of mandibular opening identical in both exams. Alternatively, acquisition is to be performed with closed mouth in maximal intercuspation, yet this might impair the separation of the mandible from the maxilla along dental arches and thus reduce the overall quality of the skeletal mandible. In addition, a metal artifact due to a dental prosthesis in the superior arch might affect the mandible as well. Once registration of both exams is achieved through validated algorithms, such as those implemented in Materialise Mimics, the soft tissue model can be reconstructed in a reliable spatial relationship with the skeletal model. Figure 1 shows segmentation of bone and soft tissue tumor for a case of ameloblastoma; to avoid any coregistration bias, both imaging sequences were acquired into maximal intercuspation, yet this worsened the metal artifact.

This virtual reconstruction represents the ideal setting to perform a mandibular resection, associating the sacrifice of bone tissue with the size of the macroscopic disease.

In contrast with midfacial resections, which involve a more complex anatomy and often require to implement curvilinear osteotomies around structures such as the pyriform rim, the orbital cavity, and the skullbase, mandibular resections are easily defined by positioning simple resection planes, whose orientation must be defined with the aim of ensuring surgical radicality of neoplasm excision and stability of reconstruction by providing a large, planar interface with the subsequent bone free flap.

A. Tel (✉)
Lead Specialist for VSP and 3DP, Maxillofacial Surgery Clinic, Head & Neck and Neuroscience Department, Academic Hospital of Udine, Udine, Italy
e-mail: alessandro.tel@uniud.it

M. Robiony
Chief of Maxillofacial Surgery Clinic, Director of the Postgraduate School in Maxillofacial Surgery, Chief of Head & Neck and Neuroscience Department, Academic Hospital - University of Udine, Udine, Italy
e-mail: massimo.robiony@uniud.it

© The Author(s), under exclusive license to Springer Nature Switzerland AG 2025

A. Tel, M. Robiony (eds.), *Atlas of Virtual Surgical Planning and 3D Printing for Cranio-Maxillo-Facial Surgery*,
https://doi.org/10.1007/978-3-031-94495-6_23

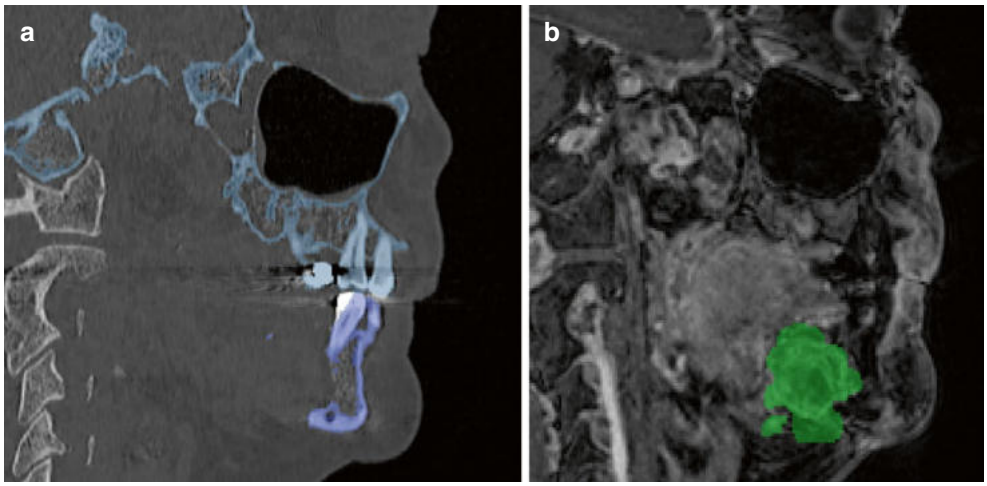


Fig. 1 After image registration, CT and MR are segmented to generate a soft tissue disease model overlapped to the skeletal model

3 Classification of Mandibular Resections for Virtual Surgical Planning Purposes

There is no currently accepted classification on mandibular resection. Historically, attempts to classify mandibular defects have been made by Urken (CRBS system, 1991) and Schultz [1, 2]. More recently, in 2016, a novel classification scheme was proposed by Brown [3], with four main categories.

However, for the purpose of virtual planning, such classification might be simplified as follows (Fig. 2):

- Marginal resection: this type of resection is indicated in cases of neoplasms (or infectious processes, like BRONJ) involving the alveolar process with absent or mild infiltration of the underlying basal bone. Marginal resection should not be indicated in cases of invasion of the cancellous component of the mandible.
- Segmental resection: it is usually indicated in case of focal, yet complete, invasion of the mandible by adjacent tumors, which often originate from the overlying epithelium, most typically in squamocellular carcinoma, or primitively in the bone (for instance, in case of sarcomas or dysplasia). In contrast with marginal resection, segmental resection entails the physical separation of the mandible in two separate parts, thus requiring an immediate reconstruction. Such resections can be further topologically subdivided in the following subtypes:
  - Anterior (typically, from canine to canine)
  - Lateral (from ipsilateral canine to angle)
  - Anterior-lateral (from contralateral canine to angle)
  - Posterior (from the mandibular angle to the mandibular ramus, without disarticulation)
- Resection with disarticulation: this type of resection includes any type of linear resection which extends posteriorly to the temporomandibular joint, with sacrifice of the mandibular condyle which is disarticulated from the joint. A particular subtype of this resection, with the anterior plane positioned in the midline, is referred to as "hemimandibulectomy."
- Total mandibulectomy: it could be classified as condyle preserving (one or both), or non-condyle preserving.

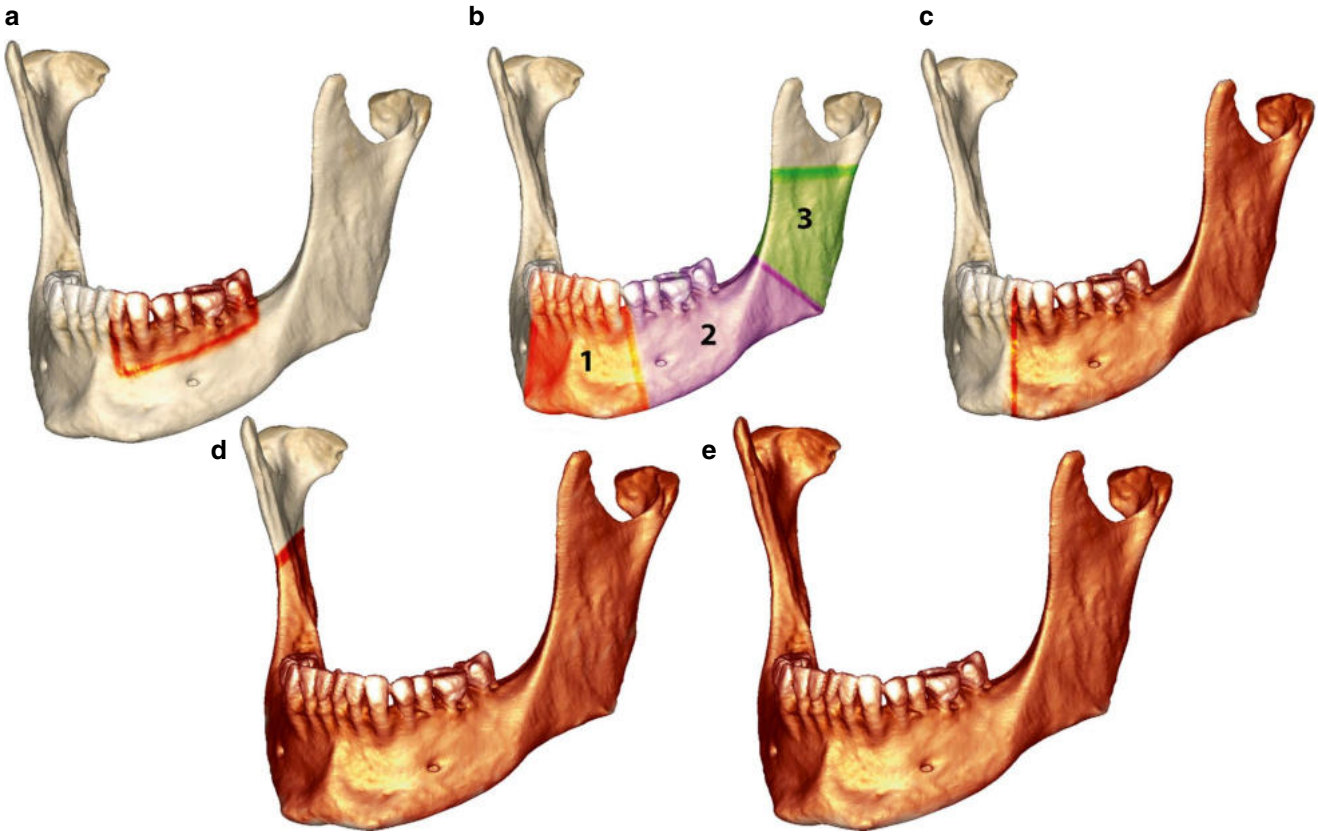


Fig. 2 Practical classification for VSP of mandibular resections: (**a**) marginal resection; (**b**) segmental resection: (1) subtype 1 (anterior), (2) subtype 2 (lateral), (3) subtype 3 (posterior); (**c**) resection with disarticulation; (**d**) condyle-preserving total mandibulectomy ("near-total mandibulectomy"); (**e**) non-condyle preserving mandibulectomy

4 Surgical Guides for Mandibular Resection

Surgical guides play the main role in enhancing the intraoperative translation of virtual surgical planning for mandibular resections [4, 5]. As seen in Chapter "Virtual Planning and 3D Printing in Mandibular Fractures" for mandibular fractures, navigation does not play a fundamental role in mandibular surgery. A wide, stable, and exposable skeletal surgery makes surgical guides the ideal device to perform computer-guided bone resections; in addition, surgical guides offer a physical interface to guide the bone cut, allowing for a controlled, straight cutting trajectory, especially when associated with ultrasonic bone cutters (Piezosurgery®). Surgical guides for resection can be easily designed by an expert operator within a medical design software and can be printed using biocompatible materials with optimal mechanical properties. Therefore, in a modern point-of-care setting, the production of surgical guides for resection is almost entirely in favor of an in-house production [6].

4.1 Ten-Step Workflow for Surgical Guide Creation for Mandibular Resection

The process of mandibular resection guides can be standardized in well-defined steps [7]:

1. The first immediate step is to define within the surgical planning software the boundaries for the mandibular resection. This is usually performed by handling and positioning the cutting plane according to the desired level, including the whole soft tissue disease to define a radical macroscopic resection. The cut with separation of bone in two halves should be performed using a thickness representative of that of the cutting instrument (0.3–0.5 mm for Piezosurgery®).
2. Fixation of mesh errors and remeshing: parts reconstructed from segmentation often contain mesh errors, including holes, overlapping triangles, back-face culling. Remeshing ensures a regular distribution of triangle

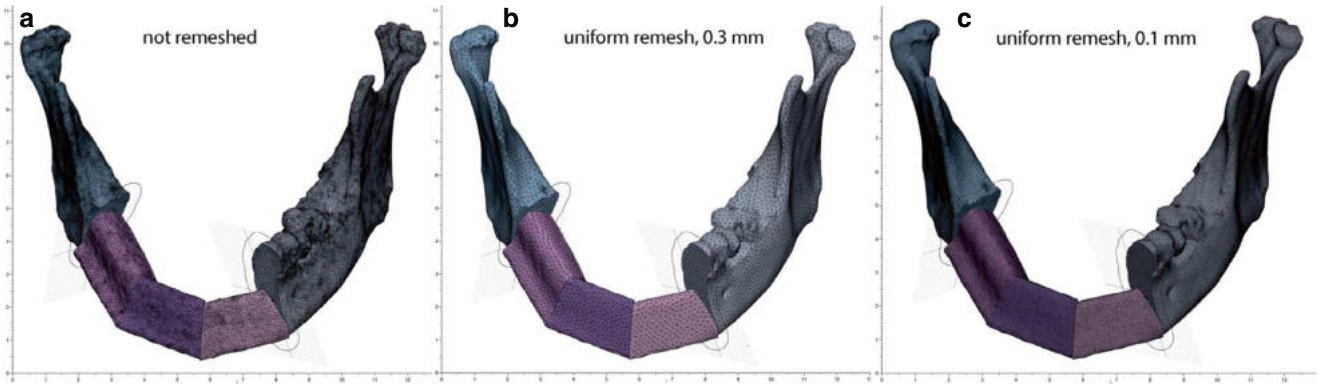


Fig. 3 Mandibular remeshing options

wireframe, allowing subsequent mesh actions to be effective without geometrical errors.

3. Identification of the fitting surface of surgical guides: using the mask brush tool, polygons are identified corresponding to the intended surface fitting area of the surgical guide. Areas of bone which can be securely exposed and represent a stable anchoring point for the surgical guide base are defined and then isolated using the smooth marking border command. In this way, the fitting surface is a selectable, separate entity (Fig. 3).
4. Creation of the base of the surgical guide: the isolated fitting surface is extruded using a coefficient equal to the intended thickness of the surgical guide. This part represents the main core of the main body of the surgical guide.
5. Creation of cutting flanges: cutting flanges are a crucial element as they represent the physical support for the cutting instrument. There are two main types of cutting flanges: linear, which enables sliding of the cutting blade in the correct direction, and notch-based, which presents an internal fissure in which the cutting blade is inserted (Fig. 4). The cutting flange must be positioned in exact coincidence with the cutting plane defined in VSP. A freeform flange can be designed using a sketch positioned on the cutting plane.
6. Creation of eventual bridges: this step is necessary only in case of "bridged" guides. Two-piece simple guides do not generally need it, although a handle can be designed to enhance intraoperative positioning.

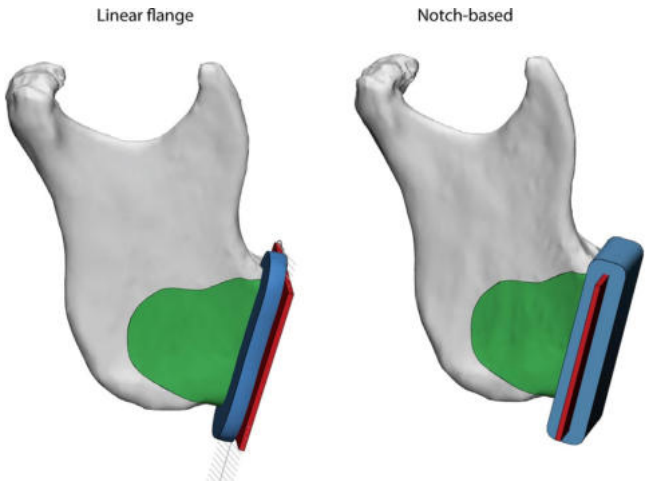


Fig. 4 Types of surgical guides for resection based on flange

7. Addition of drilling tubes: drilling tubes offer a straight path for the drilling instrument to perform holes in desired positions. Such holes might serve to fix the surgical guide to the bone, but it is more advisable that the same holes correspond to those used to secure the fixation devices (Fig. 5). In this way, the biological damage to the bone is limited to what is exclusively necessary to fix the titanium plate. It should be noted that it is possible to anticipately establish the position of fixation holes in the following situations:

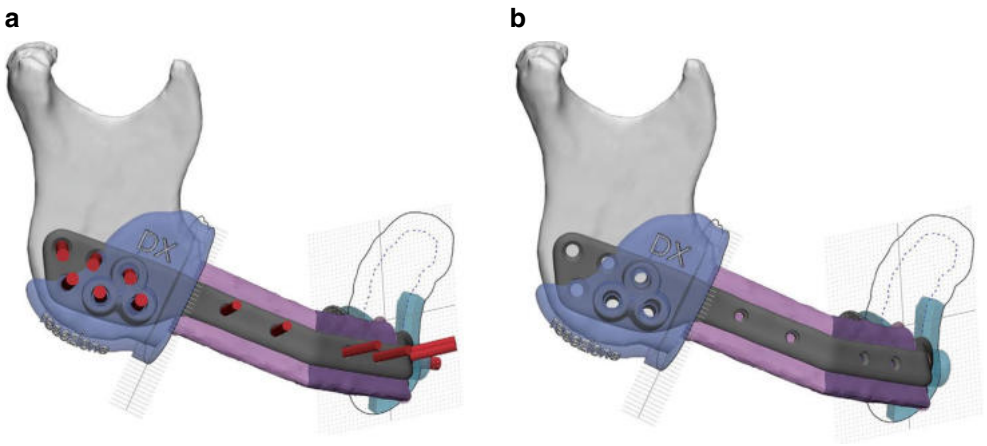


Fig. 5 Surgical guides for resection are fixed using the same holes for plate fixation, avoiding unnecessary drills

(a) Use of a customized osteosynthesis plate: in this case, the screw position used for the guide is provided to the manufacturer (or vice-versa).
(b) Reverse engineering of a premodeled titanium plate: this setting requires to 3D print the reconstructed mandible, premodel a plate on it, and fix it using screws. Then, the plane and screws are digitized using a CT scan or optical scanners, and it is possible to visualize them in the VSP.

8. Boolean operations: first the surgical guide body, flange, and handle are merged in a unique entity using a Boolean union command. This enables the creation of a unified geometry. Subsequently, the entire, non-resected, mandible is subtracted from the surgical guide to make the guide totally compatible with its recipient bone. In this operation, the author recommends applying a surface offset of 0.3 mm at least to avoid that an extremely precise fit is not replicable in the OR. This could be due to several reasons: underestimation during mask thresholding of bone quantity, presence of periosteoum remnants, presence of small fragments of soft tissue, all factors that make necessary to slightly oversize the bone impression on the cutting guide side.
9. Occasionally, despite mesh optimizing, Boolean subtraction might fail. This is due to particular features of the base mesh, for instance, small openings of the cortical surface with the creation of a geometrical tunnel communicating with the inner cancellous bone. Such tunnels are often difficult to deal with, and they are the result of both an incorrect segmentation and an unfavorable CT scan. In this case, the easiest method to solve the issue is to wrap the base model (i.e., the subtractive part) using a tunnel-occluding gap-closing distance, paying attention not to overcome an overall surface offset of 0.2–0.3 mm. Intuitively, when the wrapped surface is subtracted from the base guide, Boolean subtraction must not include the surface-offset correction, which is included in the wrapping operation.
10. Labeling: in light of the recently approved MDR (EU Medical Device Regulation, 2017/745), but also according to FDA and other regulatory entities, the medical device (including surgical guides) must be labeled with the name of the patient. Usually, a coding system with name and surname initials should be used. It is useful to mark also the device according to its role to avoid misunderstandings (i.e., resection guide vs reconstruction guide).

4.2 Classes of Surgical Guides for Mandibular Resection

Various types of surgical scenarios might require different types of surgical guides for mandibular resection. In several cases, the mandibular bone structure is completely replaced by a soft-tissue disease process, and the soft tissue tumor perforates both corticals, so that it is not possible to position a surgical guide. In other cases, a traditional surgical guide might require a surgical exposure wider than what is generally recommended by traditional approaches. In our experience, the following types of surgical resection guides can be found:

- Single-piece guide: this is the simplest type, enabling the resection along a unique resection plane. Such guides are easy to position and can be designed small, with both linear or notch-based flanges. It is useful for resection with disarticulation.
- Single-piece, tray guide: this surgical guide provides a large fitting surface and thus offers significant stability.

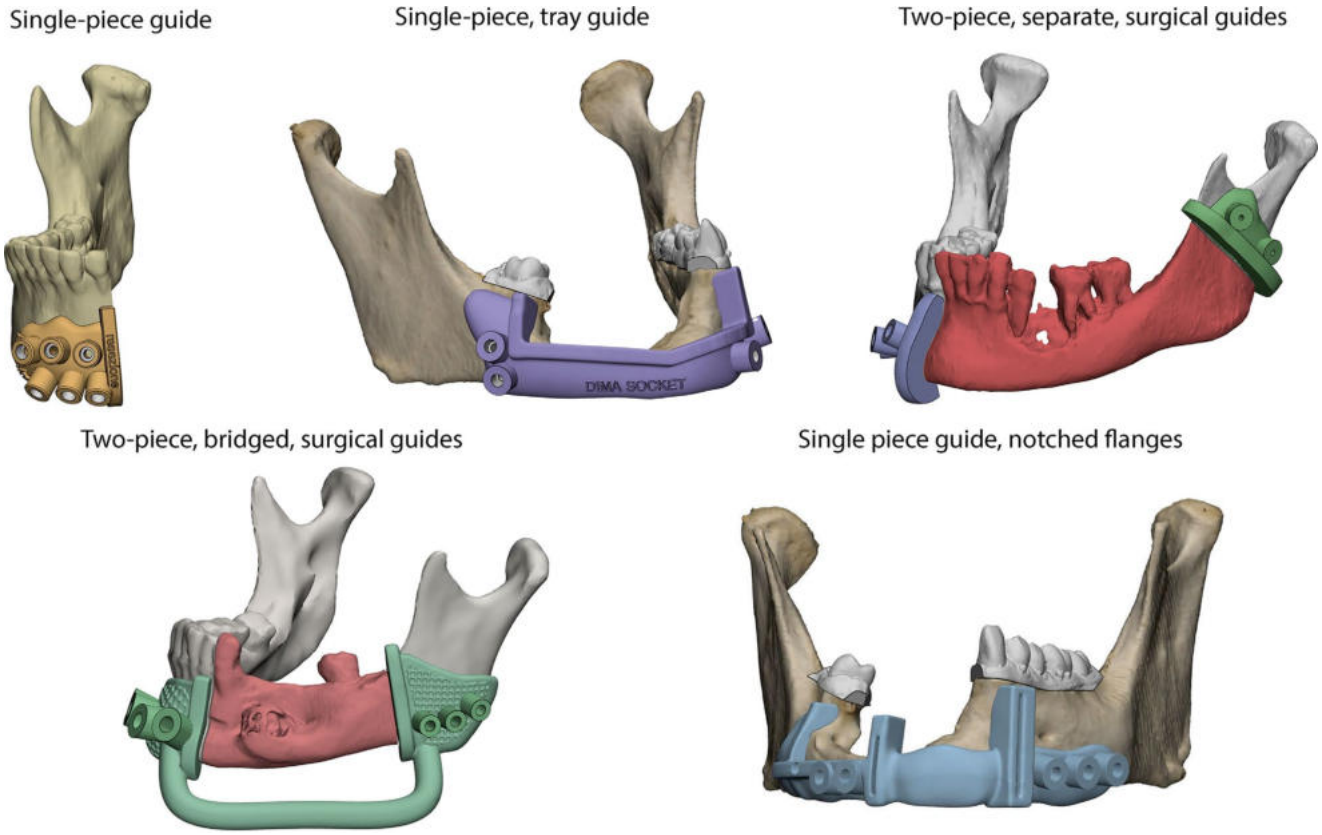


Fig. 6 Classification of surgical guides for resection based on morphological features

Instead of providing cutting flanges for osteotomies, it provides a tray to excise a superiorly oriented bone box corresponding to the intended resection. For its morphology, it is particularly suitable in marginal resections.

- Two-piece, separate, surgical guides: this type includes two independent surgical guides which are positioned mesial and distal compared to the resection site. Guides can have both a linear cutting flange, or, alternatively, a notch-based cutting flange. Advantages consist of a limited exposure of bone area to position the guide with more restricted accesses, with reduced intraoperative cluttering. Disadvantages include a less stable anchoring, and the independent movement of the two mandibular segments after resection with loss of their reciprocal orientation.
- Two-piece, bridged, surgical guides: this type is similar to the previous one, with the difference that the two parts of the guide are joined by a bridging element, represented by a curved handle. Advantages of this type of guide include the same reduced cluttering of the operating field but with preservation of mandibular segment positioning, which might favor the inset of the reconstructing flap.
- Single piece guide, notched flanges: this surgical guide is generally more cumbersome and requires wider exposure of the bone. It covers not just fitting parts but also the resection site. Notched flanges provide a fissure for bone cutting directly inside the surgical guide, allowing to trace, but not to complete, mandibular osteotomies. This type of guide has limited indications.

Surgical guide types are schematically represented in Fig. 6.

5 Clinical Cases

5.1 Resection with Disarticulation for Relapsed Mandibular Ameloblastoma Using a Single Piece Guide

Clinical History

This patient was operated 20 years before for a segmental mandibulectomy with preservation of the condylar stump and reconstruction of the bone gap using a standard titanium, reconstruction plate. The patient presented for a sudden mandibular deformity with loss of occlusion, associated with a non-painful swelling of the mouth floor. A CT scan was performed confirming the appearance of an osteolytic lesion and detachment of the titanium plate from the condylar

stump with misalignment, with a free condylar fragment. The patient underwent MR as well to define the extent of the lesion among soft tissues, which confirmed an expansive mass, with contrast enhancement, displacing the milo-hyoid muscle.

Virtual Surgical Planning

Owing to the extension of the lesion in soft tissues, a mixed virtual model was generated after merging CT and MR. The model included the mandible with the separated titanium plate, marked for removal, and the soft tissue disease, extending around the titanium plate up to the lateral skullbase, both on the buccal and on the lingual sides. A single plane was marked for resection, defined through a three-point based sketch, a 0.3 mm thick plane was achieved, and then resection with disarticulation was simulated. A single piece guide was modeled corresponding to the resection plane, and guiding cylinders for predrilling holes were modeled matching the final osteosynthesis sites (Fig. 7).

Surgery

A submandibular incision and a preauricular incision were both performed to access both the mandibular body up to the contralateral parasymphyseal region and the temporomandibular joint region. The mandible was exposed, and the titanium plate removed from the body region, while it was already avulsed from the condylar stump. The condylar stump was retrieved from the preauricular access and released from its insertion on the lateral pterygoid muscle. The plate was subsequently removed from the submandibular access. Subsequently, the single piece guide was positioned in the symphyseal region and the guided resection performed. The mobilization of the resected part of the mandibular body was conducted paying care not to violate the mucosa of the oral floor, while a milo-hyoid muscle resection was accomplished to include the soft tissue mass within a muscle cuff. The site was prepared for reconstruction (Fig. 8).

5.2 Case 2: Modified Marginal Resection in Clear Cell Carcinoma of the Alveolar Process of the Mandible

Clinical History

A patient came to our attention for painful mandibular swelling. He underwent CT scan, which revealed an osteolytic lesion, whose biopsy confirmed to be a unicystic ameloblastoma. The patient first underwent conservative enucleation of the lesion. One year later, the lesion relapsed and the patient underwent a segmental marginal mandibulectomy extended from the dental elements 4.6–3.2. Final histopathology report revealed an odontogenic clear cell carcinoma, with resection margins free from disease. The patient was then followed up with 6-month neck ecography and mandible CT for 2 years. For the subsequent reconstruction to be planned, it was mandatory to regularize the resection contours with a computer-guided marginal resection to prepare the recipient site for a microvascular reconstruction with fibula.

Virtual Surgical Planning (Version 1: Tray Resection Guide)

Segmentation was performed in Mimics using a bone thresholding algorithm. As there was not any detectable soft tissue lesion, VSP was exclusively based on a bone model.

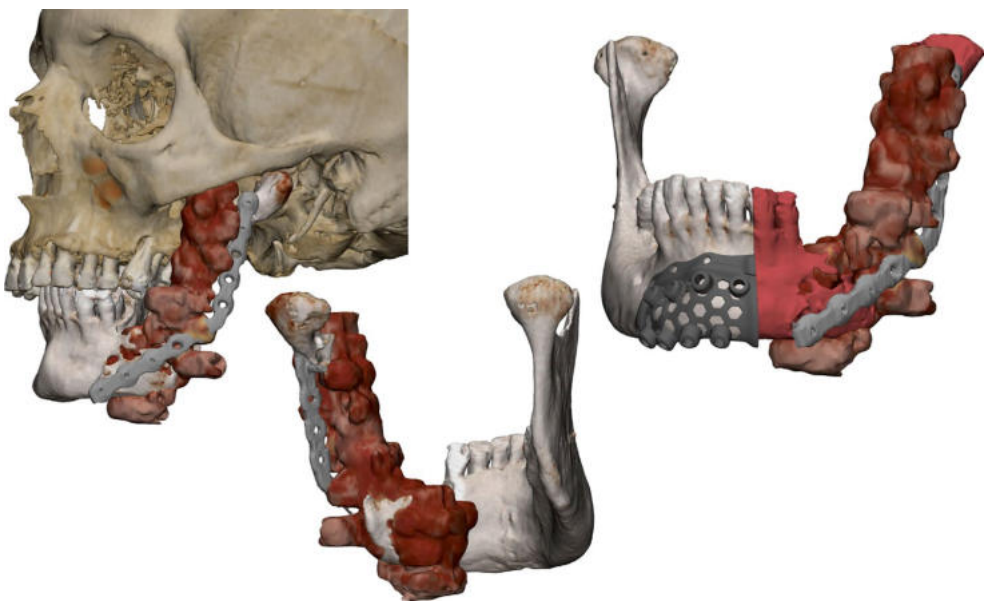


Fig. 7 Virtual model reconstruction of relapsed ameloblastoma with extensive mandibular erosion around a previously positioned titanium plate. Right panel: planned resection with surgical guide in place

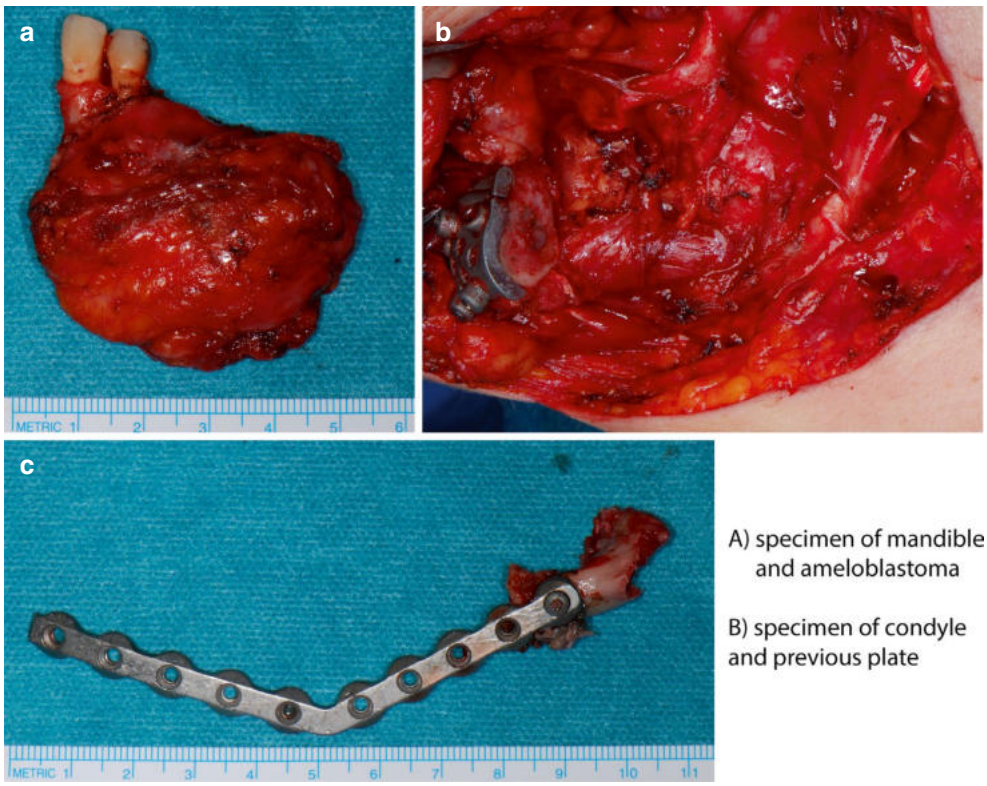


Fig. 8 Intraoperative resection and specimen

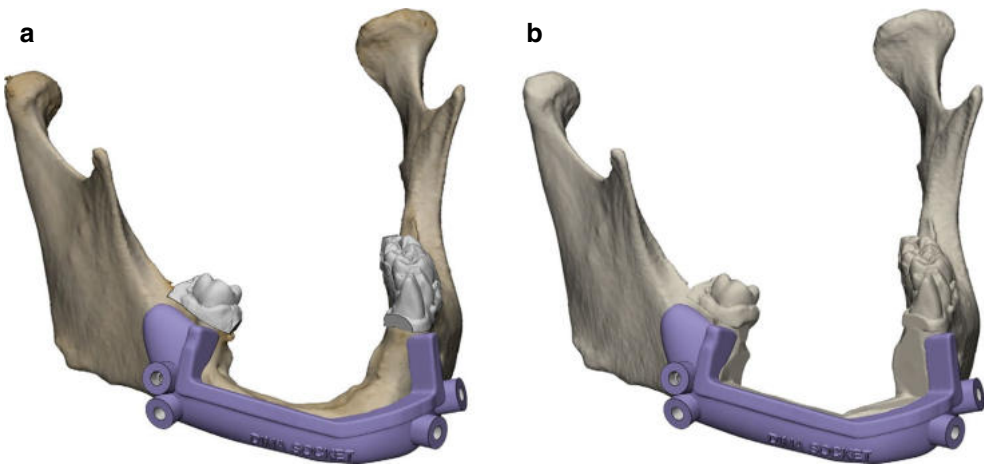


Fig. 9 Tray guide for marginal mandibulectomy

Preoperative dental arches and occlusion were scanned and merged with the reconstructed CT model. Resection boundaries were defined at both sides of the intended volume to be excised; moreover, an inferior horizontal plane was designed to represent the level of the "tray". Planes were converted into sketches, and the outline of the cutting flanges was defined. A tray surgical guide was modeled based on sketch extrusion along the three planes, after defining the fitting surface for the guide on the basal bone. Guiding tubes for holes predrilling were inserted as well (Fig. 9).

Virtual Surgical Planning (Version 2: Single Piece Guide, Notched Flanges)

After surgical planning, the patient reported persistent pain in his mandible; therefore, he underwent another CT scan showing evidence of disease progression across the mesial margin, with a cystic formation related to the pre-existent clear cell carcinoma. The virtual surgical planning was modified from a marginal resection using a tray guide to a segmental anterior resection associated with a posterior marginal resection using a single piece guide with notched flanges. In

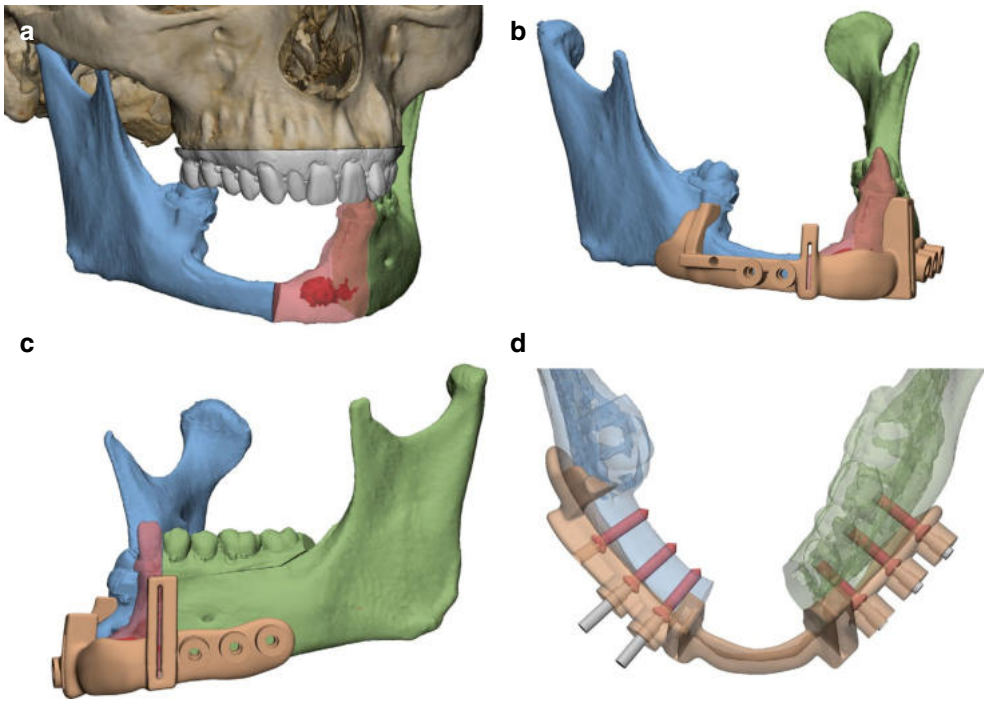


Fig. 10 Redesign and partial conversion of the tray-like guide to a guide for segmental resection with notch-based flanges

this case, we designed specifically a single piece guide with three notched flanges to assist both the posterior marginal resection with preservation of the basal bone and the anterior symphyseal segmental resection. The regularized basal bone was used to support the inset of a fibula flap for reconstruction. Thus, an additional notched flange was added between the marginal resection and the anterior segmental resection. Guiding tubes for screws predrilling were modeled, matching the final position of fixation devices (Fig. 10). It is important that the height of flanges is modeled in order not to reach the full height of the alveolar process, as osteotomies should be traced only in the basal bone, and then continued upward taking care not to violate the oral mucosa, which has to be gently released from the bone segments after osteotomies. In this way, mandibular resection can be performed using a purely external approach, as the mucosa is free from disease. Surgical guides were 3D Printed using a Formlabs Biomed Clear resin (Formlabs, Somerville, MA), which is fully autoclavable and cleared for medical use.

This case underlines the importance of an in-house 3D laboratory with trained physicians to promptly address the urgency to modify VSP in case that a discrepancy or sudden change in the plan is required. This would be hardly possible if outsourcing VSP and 3DP of guides to a third-party company, which has a longer response time; moreover, it is easier for the clinical team to implement all requested modifications as the case is well known and has previously undergone a thorough clinical, radiological, and virtual analysis.

Surgery

While previous marginal resection was conducted intraorally, this resection was performed using a cervicotomic approach, which provides a straightforward, sterile, way to the mandible, allowing to perform a safe resection with subsequent inset of a customized prosthesis and a free flap. A submandibular incision was performed, with soft tissue dissection up to the level of the posterior belly of the digastric muscle. The mandibular angle was reached, the facial vessels identified, ligated, and lifted upward in order to protect the marginalis branch of the facial nerve. An incision was performed on the mandibular periosteum and the masseter muscle, and the bone surface was exposed. While positioning resection guide, care was taken not to violate the oral mucosa in continuity with the periosteum to avoid contamination from the oral cavity. The guided piezoelectric osteotomy continued through the alveolar process by keeping the oral mucosa intact, which was gently elevated from the mobilized bone segment after completion of osteotomies (Fig. 11).

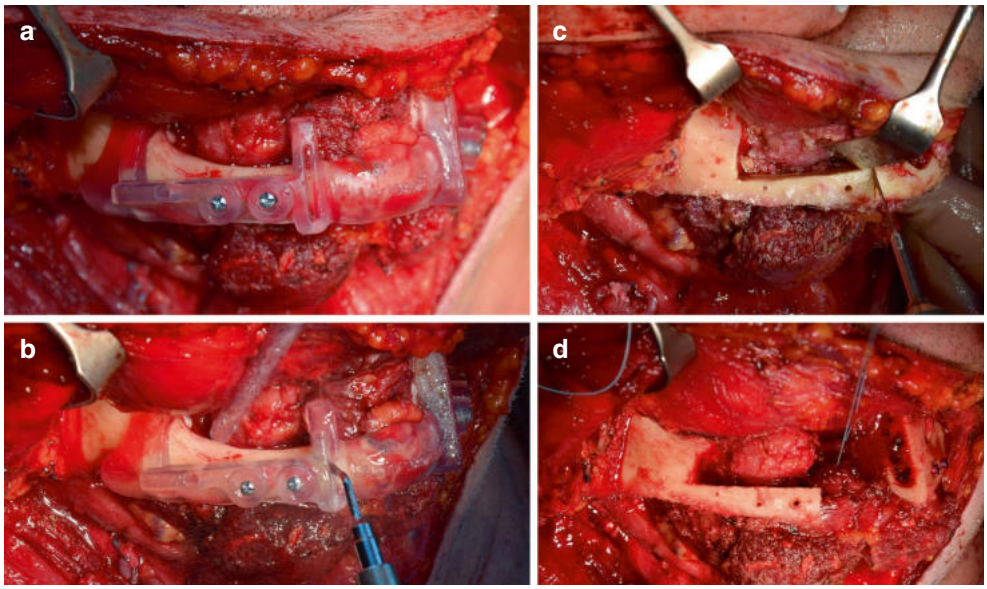


Fig. 11 Intraoperative sequences using both the tray slot and notched flanges for the symphyseal segmental resection

5.3 Segmental Lateral Resection in Mandibular Ameloblastoma Using a Bridged Surgical Guide

Clinical History

A 62-year-old patient was diagnosed with a bulky hard mass in the left mandibular body, displacing the soft tissues of the oral floor and the cheek. The patient underwent CT examination which revealed a multicystic bone lesion with inflation of the bone cortexes as well as lytic aspects. An incisional biopsy was performed confirming the diagnosis of ameloblastoma. Due to the absence of any soft tissue component of the lesion outside the bony envelope sheath, MR was not performed in this case, as CT scan provided enough information to plan the mandibular resection.

Virtual Surgical Planning

The mandible was segmented in Mimics using a thin-bone sparing threshold, enabling to preserve the tiny walls of the cystic cavity. The mandible was retessellated using a remesh algorithm to regularize the wireframe network and enhance subsequent Boolean-based actions for osteotomy. Two datum planes were defined in 3-matic, mesially between the lateral left incisor and the canine, distally in the midpoint of the antegonial notch. Datum planes were assigned based on three-point placement and then converted into polyplanes with 0.3 mm thickness. Osteotomies were performed and resection simulated and hided. Based on the remaining mandibular segments, the fitting surfaces of the guide were defined: posteriorly, around the mandibular angle with a small component along the external oblique line to allow for a stabilizing "pinching" effect; mesially, around the mandibular symphysis, including a notch to avoid injury of the contralateral mental nerve. Two linear flanges were modeled using a sketch-based extrusion along the predefined datum planes. Finally, a bridging element was added to create a two-piece, bridged, surgical guide, enabling to keep the shape of the mandibular arch after resection. As a final step, guiding tubes for holes predrilling were added for surgical guide fixation, matching the same holes used to fix the final plate (Fig. 12). Surgical guides were 3D printed using Formlabs Biomed Clear resin.

Surgery

A submandibular incision was used to access the mandible. A myocutaneous platysmal flap was elevated; blunt dissection through soft tissues was performed until the posterior belly of digastric muscle was identified to mark the correct depth plane. Anterior dissection proceeded with identification and isolation of the marginals mandibulae branch of the facial nerve, which was included in the lifted flap. An electrocautery incision was performed along the inferior mandibular border. The mandible was exposed and the two-piece, bridged surgical guide was positioned, then fixed through the predrilling guiding cylinders. The handle position was designed not to interfere with the surgical resection. Using Piezosurgery®, segmental mandibular resection was completed, with the mandible segments restrained in position through the bridging handle (Fig. 13).

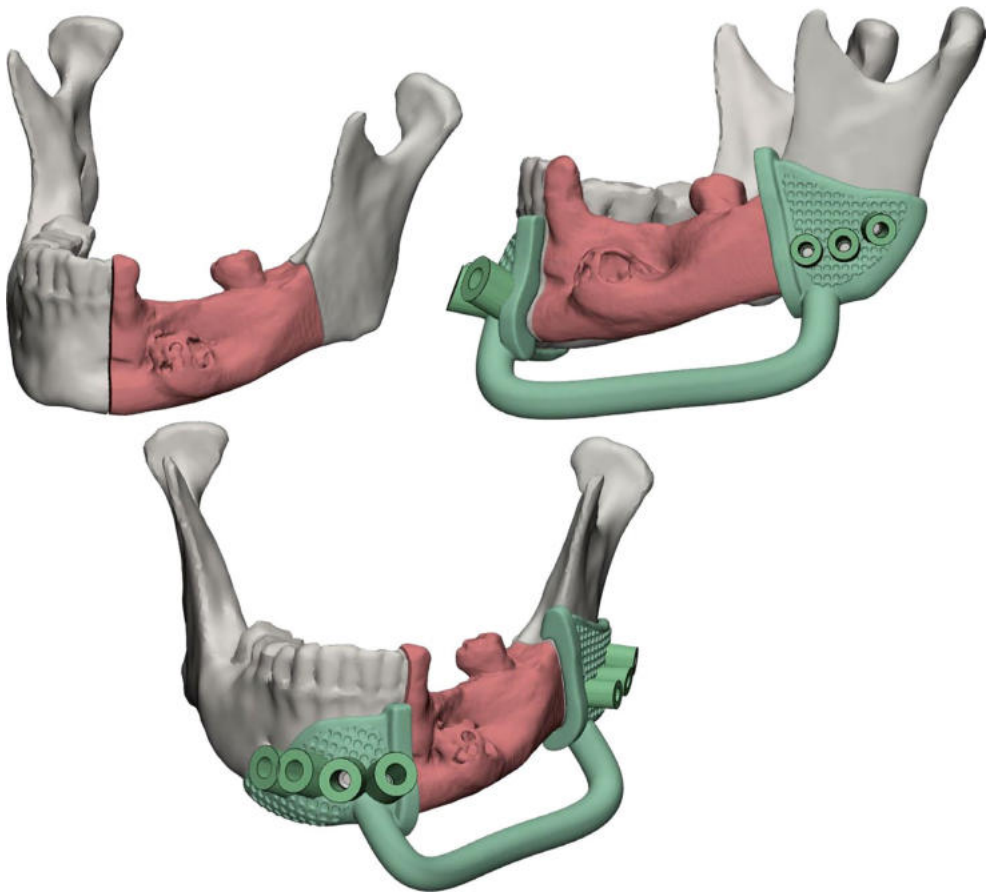


Fig. 12 VSP of segmental resection using a bridged guide

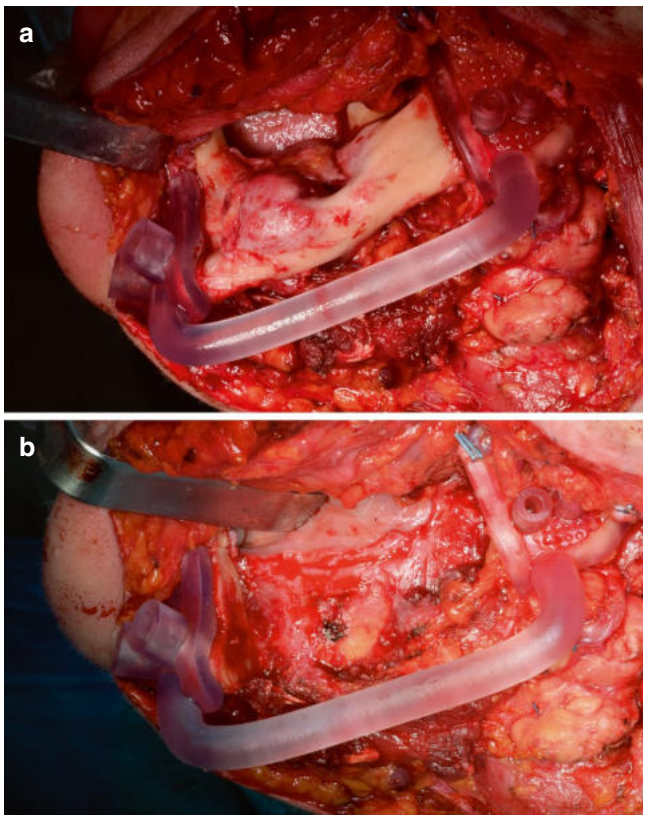


Fig. 13 Intraoperative view of computer-guided resection

5.4 Lateral Segmental Resection for Squamocellular Carcinoma pT4aN0 Using Two-Piece, Bridged, Surgical Guide

Clinical History

A young 37-year-old patient with a clinical history of recurrent oral lichen planus was sent to our attention after extraction of the inferior right third molar performed by his dentist. The postestractive site did not heal for 3 weeks and the patient referred bleeding and a sensation of a growing mass. An urgent incisional biopsy was performed with diagnosis of squamocellular carcinoma. CT scan revealed infiltration of the cortical bone of the mandible, while MR confirmed the presence of a contrast enhancing mass with invasion of the cancellous bone of the mandible. A mandibular resection with lateral pelvectomy and ipsilateral modified neck dissection was planned for this patient.

Virtual Surgical Planning

In Mimics, accurate mandibular segmentation was conducted. As the lesion was clinically well defined and presented bone erosion, CT was deemed sufficient to plan the resection. Two datum planes were positioned to define the

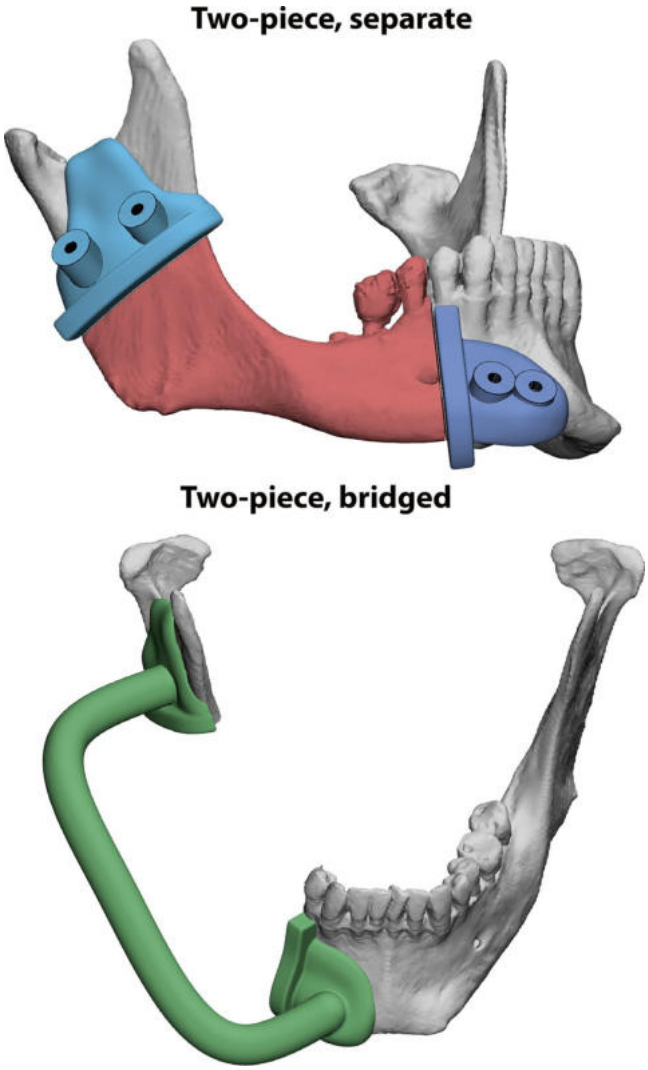


Fig. 14 PoC VSP and 3DP help design and manufacture multiple variants of guide, which can be intraoperatively assessed

segmental resection and converted in 0.3 mm thick polyplanes to cut through the bone. The resected segment was hidden, leaving the remaining mandible, which represented the base to model two separate surgical guides, prior identification of the fitting surfaces. The main body of both surgical guides was designed through fitting surface extrusion using a 3 mm thickness, and linear cutting flanges were defined from internal extrusion of datum planes. Guiding cylinders were created to assist surgical guide fixation on the mandible. Alternatively, a bridged surgical guide was also designed, allowing the intraoperative choice on both types, which were then 3D printed (Fig. 14).

Surgery

A cervical incision was designed to provide access to the neck for the modified dissection. Lymphadenectomy was performed while keeping the TN trait in continuity with the mandible. The marginalis mandibulae branch of the facial nerve was identified and preserved. Submandibular sialadenectomy was performed together with neck dissection. The mandible was exposed from the symphyseal region to the ipsilateral ramus, and surgical guides were positioned and fixed. Intraorally, floor pelvectomy was performed. The intraoperative choice was in favor of the bridged guide. Computer-guided osteotomies were completed and the specimen was sent to histopathological examination (Fig. 15). The patient underwent subsequent radiotherapy.

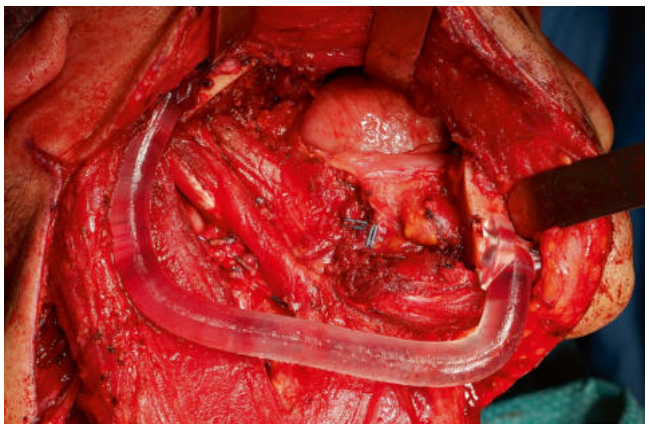


Fig. 15 Computer-guided resection using the bridged guide

5.5 Lateral Segmental Resection for Squamocellular Carcinoma pT4aN2c Using Two-Piece, Separate, Surgical Guides

Clinical History

A 58-years-old lady sought maxillofacial consultation for a painful, bleeding ulcer in the left hemimandible, associated with tooth mobility. Contrast-enhanced CT scan was performed showing a wide bony erosion in correspondence of the soft tissue lesion. MR confirmed the extent of the lesion and revealed multiple, contralateral, adenopathies. In consideration of the clinical and radiological study of the patient, CT was deemed sufficient to plan the resection. Moreover, a modified bilateral neck dissection including levels I-V, was needed as well.

Virtual Surgical Planning

Resection was planned as previously illustrated using a datum plane located between the central and lateral right incisor, then converted in a 0.3 mm thick polyplane. The second plane was positioned posterior to the mandibular angle. Subsequently, linear flanges were created through extrusion as illustrated, as well as guiding cylinders for screws. In this case, like the previous one, it was not possible to preopera-

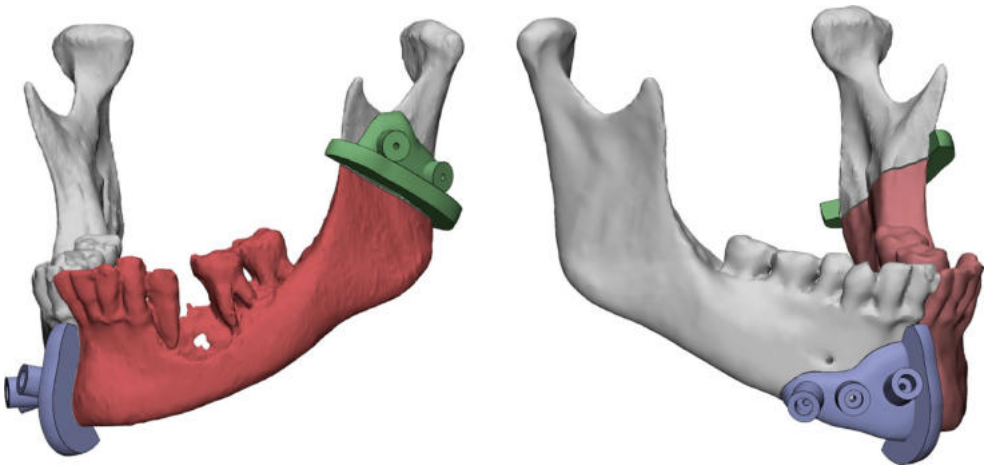


Fig. 16 Segmental resection planned using separate surgical guides

tively establish the position of fixation devices, thus the position of screws to fix surgical guides was arbitrarily defined. Boolean subtraction ensured optimal fit with a 0.2 mm free interface using offset (Fig. 16).

Surgery

The surgical approach was comparable to the previous surgery. Mandibular cutting guides were positioned and fixed on the exposed skeletal surface (Fig. 17). Osteotomies were performed using piezoelectric osteotome and the mandibular segment was removed in connection with the TN tract and the bilateral lymph-node chains.

5.6 Anterior-Lateral Segmental Resection for Squamocellular Carcinoma pT4aN3b Using Two-Piece, Separate, Surgical Guides

Clinical History

A 65-year-old lady was referred to ENT department for a large lesion of the anterior mouth floor. The patient underwent a CT scan and MR which revealed bone infiltration and a massive node metastasis with manifest extracapsular extension. Moreover, the lesion showed a deeper extension on the right lateral mouth floor. An extended, anterior-lateral, segmental resection with anterior-lateral pelvectomy was planned with bilateral neck dissection, modified lateral in the right side and supraomohyoid on the left side.

Virtual Surgical Planning

CT scan was segmented and cleared from the heavy metal artifact, due to the fact that the patient had a fixed prosthesis in the anterior mandibular region. Anterior-lateral segmental resection was planned in 3-matic using datum planes, as illustrated previously, and the resulting cutting plane was defined with a 0,3 mm thickness as well. Virtual segmental

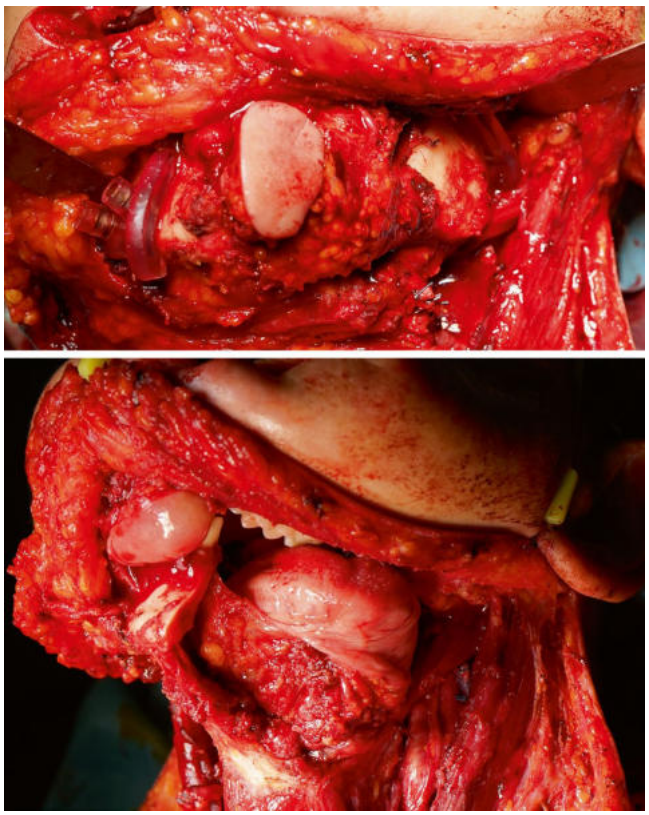


Fig. 17 Intraoperative view of resection performed using separate surgical guides

resection was performed. As the mesh wireframe presented several irregularities (Fig. 18), both healthy segments and the resection segment were remeshed. Remeshed entities facilitate the identification of fitting-surfaces for the guides as well, thus simplifying the creation of the guide base on the existing wireframe structure (Fig. 19). Given the extent of the resection, a bridged surgical guide could represent a hindrance in the surgical field; therefore a two-piece, separate, solution was chosen. Fitting surfaces were defined trying to

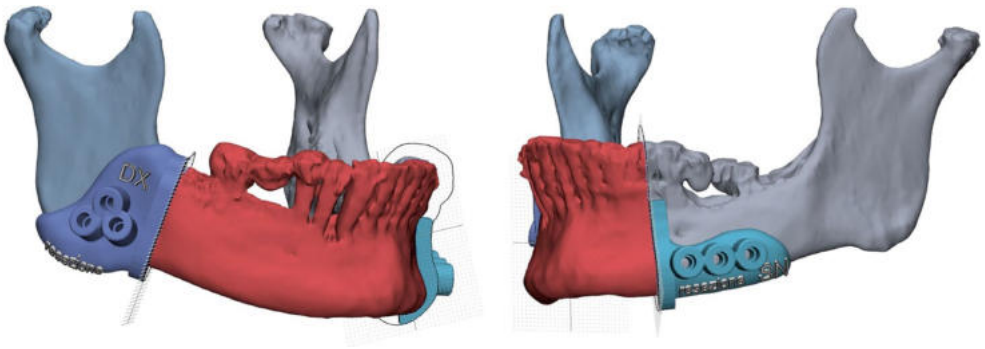


Fig. 18 VSP and design of resection by means of coupled separate surgical guides. Sketches are positioned tangent to the cutting surface to illustrate how linear flanges are achieved

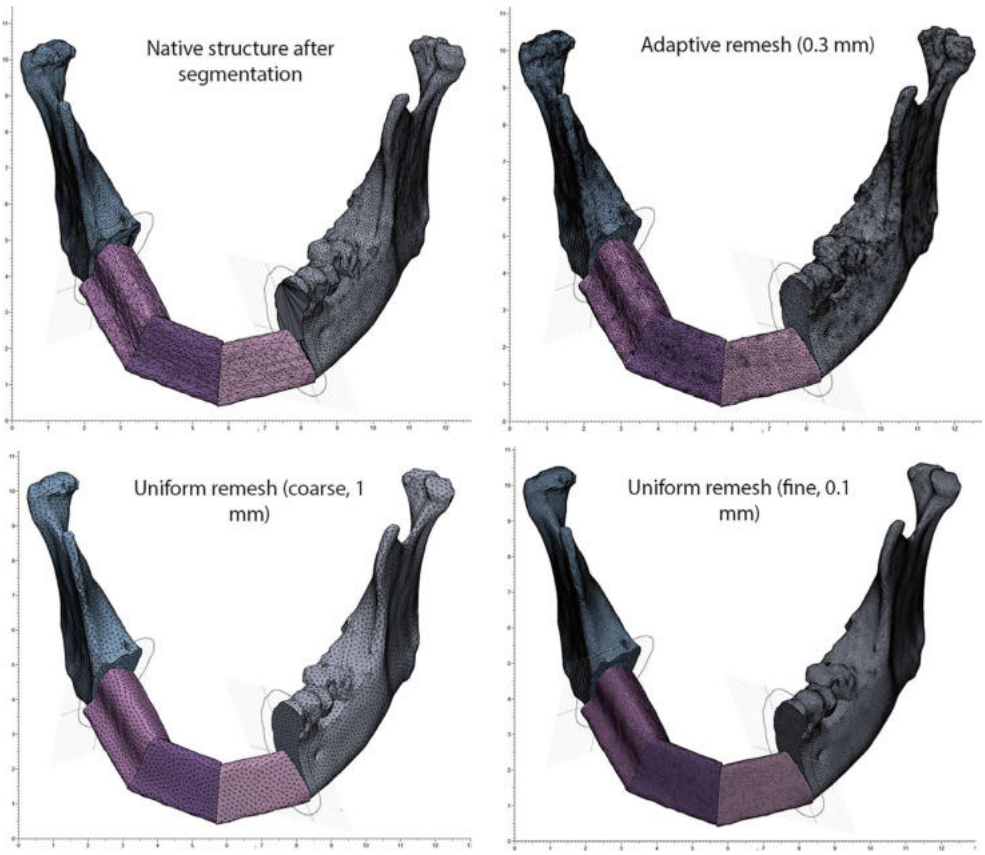


Fig. 19 Remeshing the base anatomical model is crucial as it prepares the surface to the surgical guide body extrusion. An irregular wireframe can facilitate errors

maximize the pinching effect along the external oblique line for the distal component and along the inferior mandibular border for the mesial component.

Surgery

A cervical incision was made to sculpt a visor flap and perform a mandibular degloving for the simultaneous exposure of the neck bilaterally and the mandible anteriorly. Bilateral neck dissection was performed and lymphadenectomy was kept in continuity with the mandible. Surgical guides were positioned in the exposed bone surfaces, fixed through predrilled holes, and osteotomies were performed (Fig. 20). Anterior and anterior-lateral pelvectomy was conducted intraorally to resect the oral mucosa containing the tumor. The specimen was sent to histopathological examination, and the patient was subsequently candidate to concurrent chemo-radiotherapy.

5.7 Resection with Disarticulation for Ameloblastic Carcinoma Using One-Piece Surgical Guide and Multilayer Anatomical Reconstruction

Clinical History

A 25-year-old patient came late to clinicians for a very large, progressively growing mass in his left hemiface. The lesion

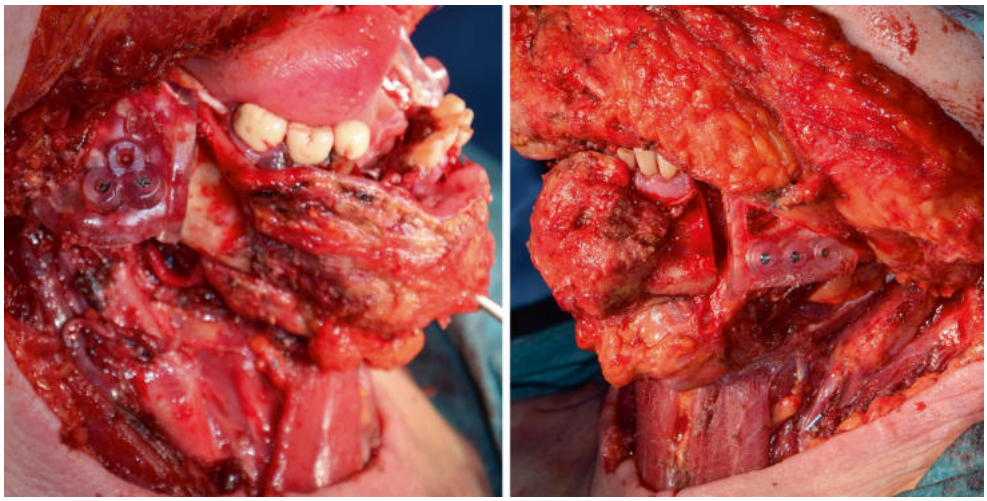


Fig. 20 Intraoperative view

involved both the external side of the mandible, the parotid region, the submandibular space, and the oral cavity in the retromolar trigone area. A biopsy was preliminarily performed with evidence of ameloblastoma. The patient underwent CT scan and RM with acquisition parameters described in chapter "Dedicated acquisition protocols in radiology for virtual surgical planning and 3D printing". Given the extent of the disease, a highly accurate virtual surgical planning was conducted to optimize the preoperative study of the patient.

Virtual Surgical Planning

A virtual reconstruction of facial anatomy was mandatory given the complexity of this case. Multiple sequences of MR were coregistered to be superimposable with CT scan. All sequences had been preliminarily acquired in closed mouth into maximal intercuspal relationship, thus minimizing a possible discrepancy between CT and MR sequences due to a mismatch in mandible opening. Once coregistration with CT scan as reference was performed, a transformation matrix was applied to each sequence to match correspondence with CT space. The following structures were segmented and reproduced in the VSP project:

- Bone: the whole maxillofacial structure was segmented. A highly respective threshold for bone was applied, in order to segment and reconstruct even the most tiny fragment of the mandible, which presented an elevated destruction. Split mask was accurately implemented to separate the condylar stump from the skullbase. As the patient did not have any metal artifact, dental cusps were satisfactorily reconstructed without acquiring intraoral scan. A voxel coloring method was used to enhance anatomical correspondence and visual understanding.
- Arterial vessels: owing to the proximity of the lesion with the critical branches from the external carotid system, it was mandatory to reconstruct a 3D representation of arteries to analyze anatomical relationship with major caliber vessels and the tumor. TOF sequence was segmented using a dynamic region growing algorithm and the resulting mask was reconstructed in a high-resolution mesh.
- Tumor: soft tissue tumor was reconstructed from 1-mm slice thickness MR VIBE sequence. This enabled to study the soft tissue extension of the tumor, thus delineating its relationship with muscles. Moreover, the cranial extension of the tumor within the infratemporal fossa was better elucidated, as well as the visualization of the skullbase to assess whether it was intact or eroded by the tumor.
- Parotid gland: this soft tissue structure was selectively segmented from the same VIBE sequence, as it needed to be resected in conjunction with the tumor, due to the continuity of the posterior side of the lesion.

The combination of all structures yielded a highly representative and trustful model of the anatomical situation of this patient, thus enabling for an accurate preoperative study with definition of the optimal resection, further enhanced by voxel coloring. After anatomical reconstruction, virtual surgical planning helped define a resection plane located between the first and second premolar. The datum plane, marked using three-points and then reoriented manually, was converted into a 0.3 mm thick polyplane for resection. The resection, including the highly subverted mandible, included the condyle as well (resection with disarticulation). The resection guide was created by establishing the fitting surface in the chin and extruding a linear flange along the datum plane marked for osteotomy. Six fixation holes were defined and guiding cylinders for predrilling were added to the surgical guides, matching the final screw sites for prosthesis osteosynthesis. Finally, the surgical guide was labeled (Fig. 21).

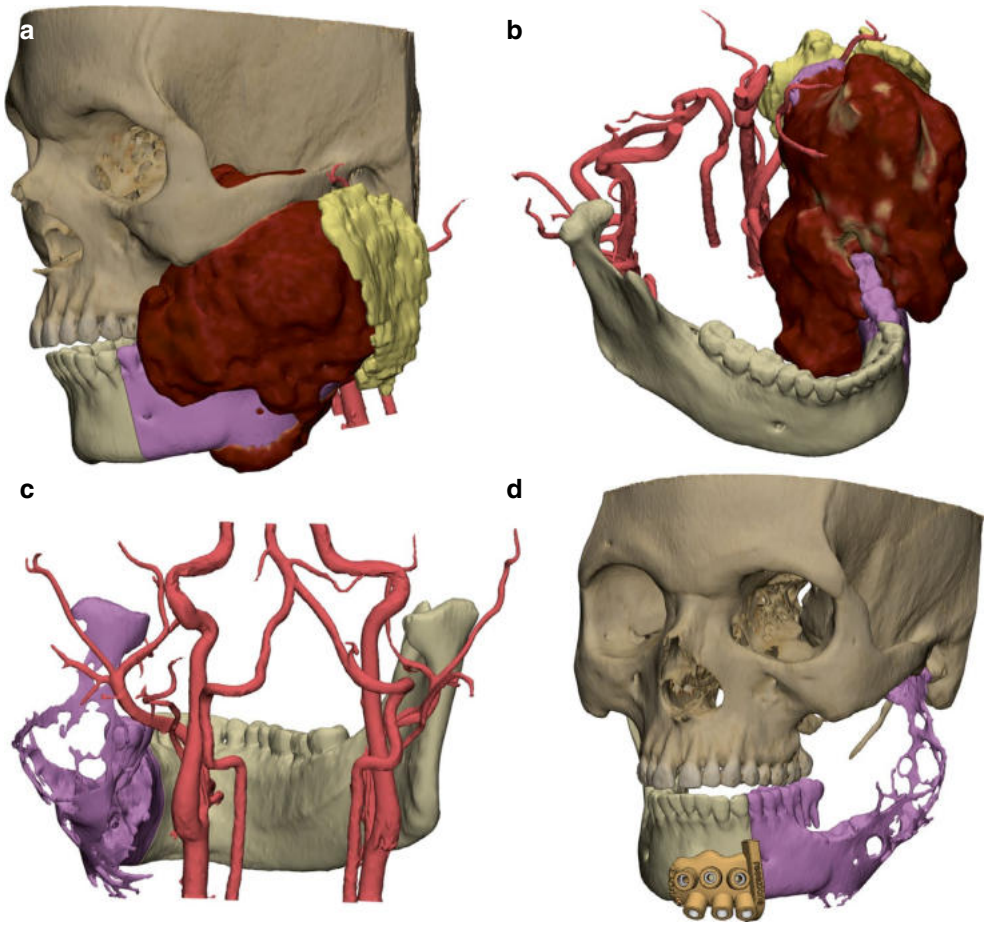


Fig. 21 Digital anatomical replicas for a case with extensive bone destruction caused by an ameloblastic carcinoma and planned resection (purple): (**a**) tumor and parotid reconstruction; (**b**) vasculature view after removing the skull; (**c**) posterior view outlines relationship with the internal maxillary artery; (**d**) planned resection with surgical guide

Surgery

A wide incision starting from a preauricular, hockey-stick design cranially was continued with a Blair-like incision with submandibular extension inferiorly. A deep subfascial approach was achieved in the temporal region, protecting the frontal branch of the facial nerve from accidental damage. The zygomatic arch was exposed by reflecting anteriorly its periosteum in continuity with the elevated deep temporal fascia. The tragal cartilage was exposed and the capsule of the TMJ identified. Inferiorly, the tragal cartilage was followed down to its pointer, and identification of the main trunk of the facial nerve was performed. Submandibular incision was joined with the preauricular approach, blunt dissection through the platysma with preservation of the marginalis mandibulae branch was performed, and then the posterior belly of the digastric muscle located as the deep level of dissection. Exposure of the mandible was completed using an intraoral incision located in the vestibule. The parotid gland was elevated, exposing the underlying, bulky, neoplasm with extended bone disruption (Fig. 22). The mandibular periosteum was elevated up to the symphyseal region, which was exposed to allow the placement of the surgical guide for resection. Piezoelectric osteotomy was performed and the mandible was separated in the region between the two left premolars. Disarticulation of the mandible was completed with incision of TMJ capsule and release of the condylar muscular insertions; discectomy was performed as well. Sectioning of mandibular musculature of the mouth floor was completed by transecting the milo-hyoid muscle. The hemimandible was sent to histopathologic examination.

5.8 Subtotal Mandibulectomy for Undifferentiated Carcinoma with Clear Cell Aspects

Clinical History

A 76-year-old patient came to our attention after a long-term mandibular swelling with facial deformation, and a gross pathological process was suspected. The tongue was hypomobile, and a massive bulging of pathologic tissue was revealed in the mouth floor at clinical examination. The patient underwent CT scan showing complete mandibular resorption and replacement of normal bone with pathologic tissue; only the left condylar head and the right mandibular ramus could be recognized. MR was performed in multiple sequences according to the aforementioned protocol, which revealed a giant pathologic mass. Biopsy was performed

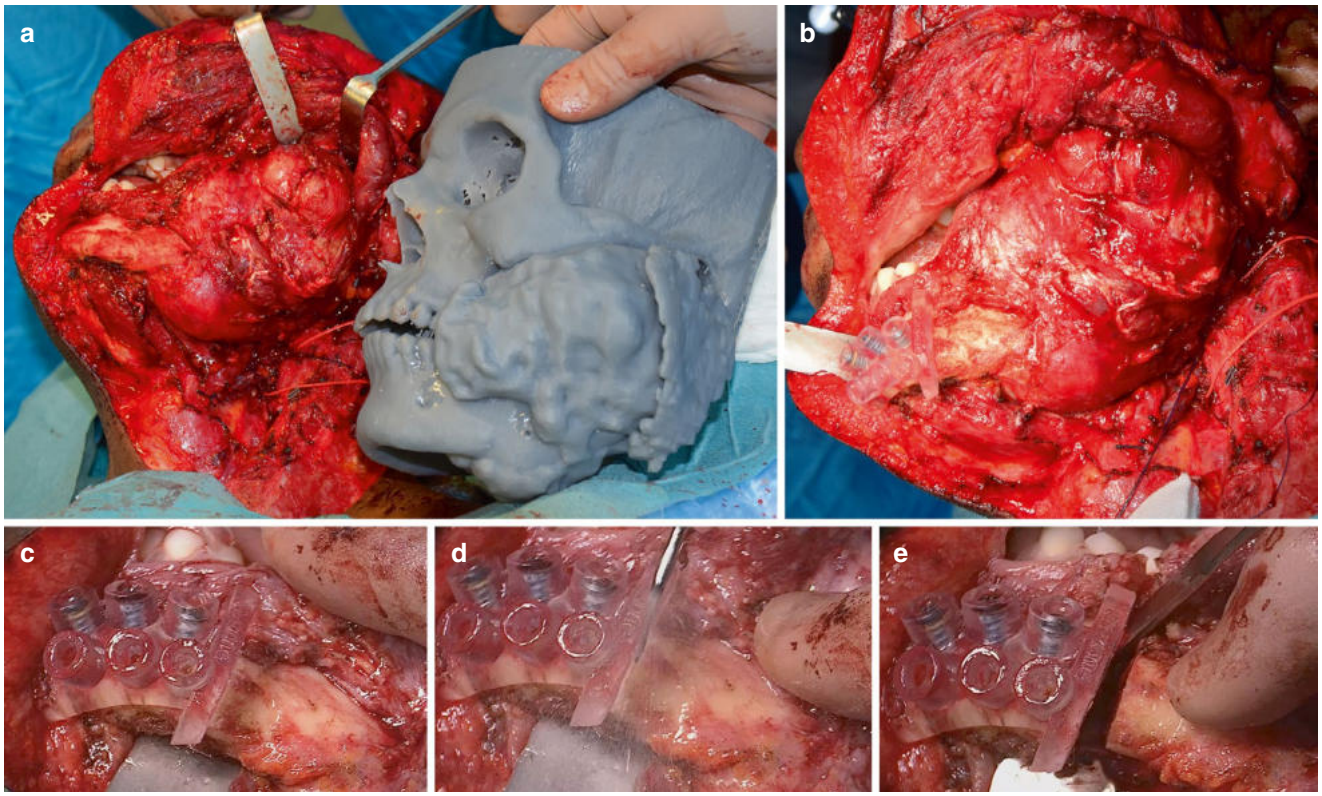


Fig. 22 Intraoperative view of computer-guided resection using a 3D printed model as reference (**a**, **b**). (**c**–**e**): guided piezo-osteotomy

with a preliminary diagnosis of clear cell tumor [8]. Given the highly destructive pattern of infiltration and dislocation of the tongue and mouth floor, an intraoral scan of the mucosal surface of the mouth floor was performed, and exported as STL file.

Virtual Surgical Planning

CT was segmented revealing the underlying bone resorption; accurate thresholding was used to preserve intact the remains of the left condylar head and the right ramus. Moreover, a skin model was reconstructed from CT scan in order to relate the soft-tissue deformity to the underlying disease process. MR was coregistered and the resulting transformation matrix was applied to each sequence. TOF sequence was segmented using dynamic region growing to identify great caliber vessels, whereas the lesion was identified using the AI-powered smart brush tool to encompass all the lesion contours (Fig. 23). The intraoral scan STL was registered with the oral floor segmented from CT scan using an iterative closest point algorithm (global registration), thus covering the oral floor and representing in the VSP the bulky, lifting effect of the underlying mass (Fig. 24). To study the infiltration of the skin, a distance-to-part analysis using different thresholds (1, 3, 5, 10 mm) was used to plan a sufficiently radical skin resection (Fig. 25). A simple one-piece surgical guide was designed to assist osteotomy of the right ramus just below the sigmoid notch. Intuitively, in total or subtotal mandibulectomies, the extent and non-selectiveness of resection do not justify the use of a surgical guide, which is useful when well-defined resection margins need to be translated in the clinical scenario. In such cases, virtual surgical planning has to focus on the most reliable definition of preoperative anatomy.

Surgery

A bilateral, modified, Apron incision was performed, with a left hemicoronal prolongation to expose the left zygomatic arch. The innominate fascia was bluntly dissected and the deep layer of temporal fascia was exposed and incised to access the zygomatic arch through the deep subfascial approach. The TMJ capsule was incised and the mandibular condyle disarticulated after discectomy was performed. From the cervical accesses, after bilateral, modified neck dissection was performed with isolation of vessels recipient for the anastomosis, the inferior mandibular border was incised and muscles of the mouth floor were disinserted from the mandible. Intraorally, a wide subtotal pelvectomy including the inferior surface of the tongue was performed and was coupled with the resection of the infiltrated skin in the mandibular symphyseal region. An en-bloc resection was performed including the whole tumor volume within macroscopically negative margins (Fig. 26).

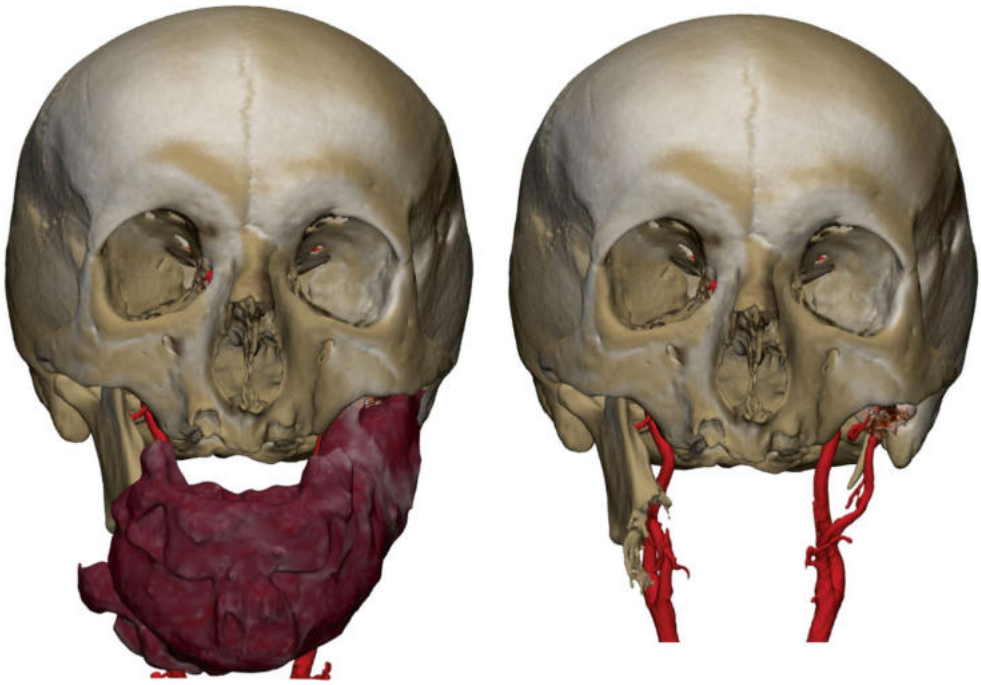


Fig. 23 Definition of tumor extension and underlying vasculature

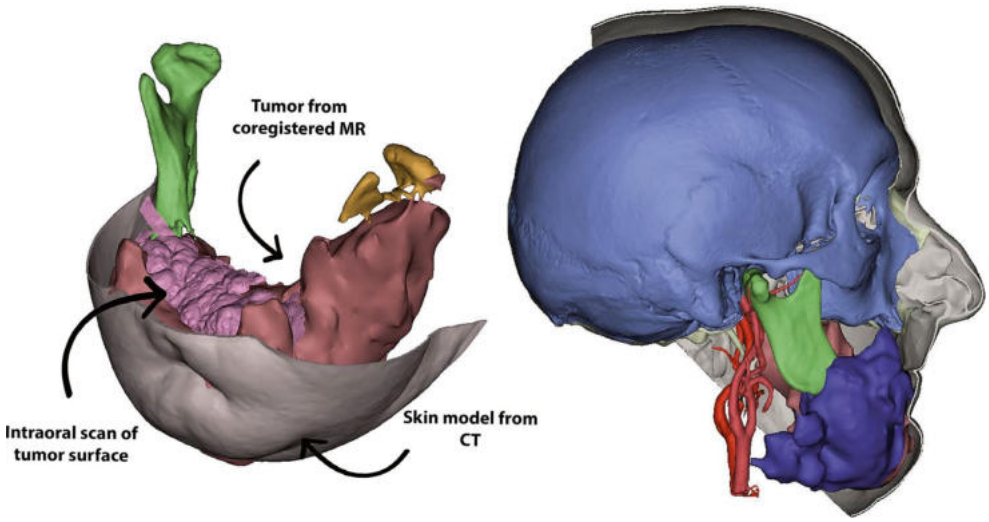


Fig. 24 Multi-tissue resection using intraoral scanning and skin reconstruction to define the need for subsequent reconstruction

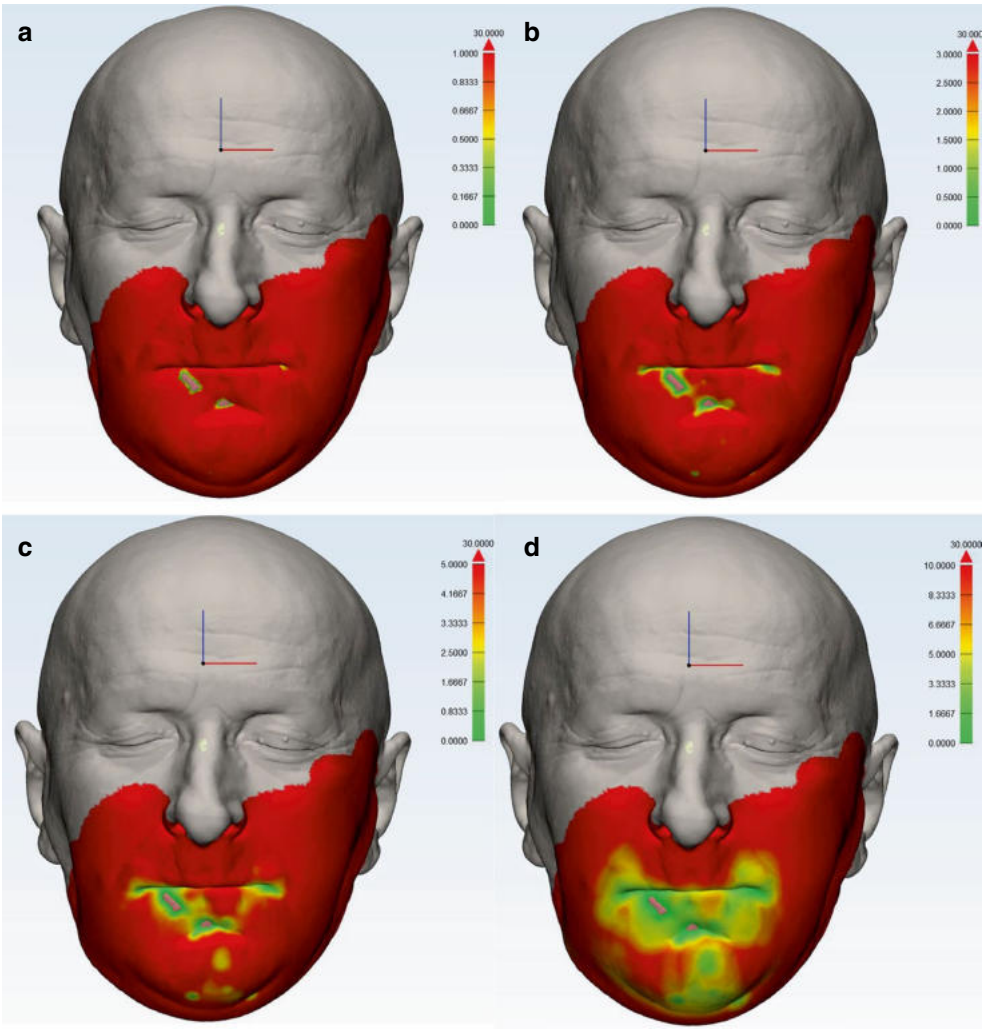


Fig. 25 Color-coded distance maps between the tumor and skin tissue to determine possible skin infiltration: (**a**) 1 mm range; (**b**) 2 mm range; (**c**) 5 mm range; (**d**) 10 mm range

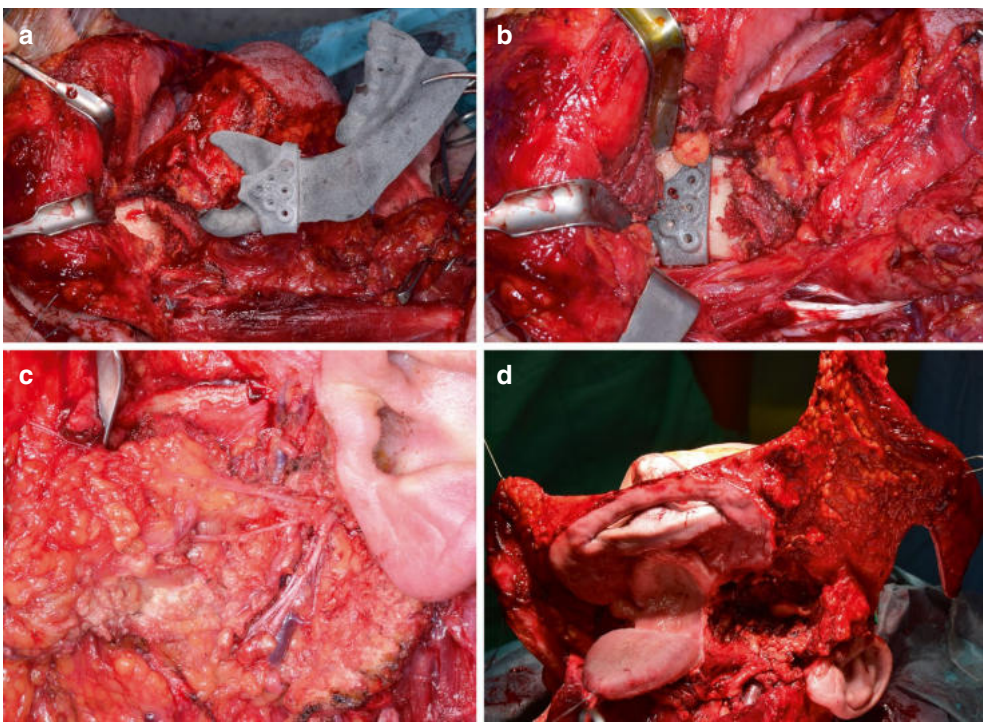


Fig. 26 Intraoperative view of near-total mandibulectomy with facial nerve preservation

References

1. Urken ML, Weinberg H, Vickery C, Buchbinder D, Lawson W, Biller HF. Oromandibular reconstruction using microvascular composite free flaps. Report of 71 cases and a new classification scheme for bony, soft-tissue, and neurologic defects. Arch Otolaryngol Head Neck Surg. 1991;117:733–44.
2. Schultz BD, Sosin M, Nam A, Mohan R, Zhang P, Khalifian S, Vranis N, Manson PN, Bojovic B, Rodriguez ED. Classification of mandible defects and algorithm for microvascular reconstruction. Plast Reconstr Surg. 2015;135:743e–54e.
3. Brown JS, Barry C, Ho M, Shaw R. A new classification for mandibular defects after oncological resection. Lancet Oncol. 2016;17:e23–30.
4. Kraeima J, Glas HH, Merema BBJ, Vissink A, Spijkervet FKL, Witjes MJH. Three-dimensional virtual surgical planning in the oncologic treatment of the mandible. Oral Dis. 2021;27:14–20.
5. Probst FA, Liokatis P, Mast G, Ehrenfeld M. Virtual planning for mandible resection and reconstruction. Innov Surg Sci. 2023;8:137–148.
6. Murtezani I, Sharma N, Thieringer FM. Medical 3D printing with a focus on Point-of-Care in Cranio- and Maxillofacial Surgery. A systematic review of literature. Ann 3D Print Med. 2022;6:100059.
7. Liu Y, Xu L, Zhu H, Liu SS-Y. Technical procedures for template-guided surgery for mandibular reconstruction based on digital design and manufacturing. Biomed Eng Online. 2014;13:63.
8. Owosho AA, Okwuosa C, Obi DI, Okiti RO, Summersgill KF. Clear cell odontogenic carcinoma of the Mandible Harboring EWSR1 rearrangement: report of a massive jaw tumor and review of diagnostic considerations. Case Rep Dent. 2021;2021:5558019.

Virtual Surgical Planning in Mandibular Reconstruction

Alessandro Tel, Matthias Ureel, Renaat Coopman, and Massimo Robiony

1 Indications to Mandibular Reconstruction

Patients candidate to mandibular reconstruction present a multitude of defects that require the reconstruction of the mandible at different extent. Such defects generally originate from oncologic resections, but they can also be due to high-energy trauma with severe comminution (see Chapter "Virtual Planning and 3D Printing in Mandibular Fractures") or infection with need of removal of necrotic bone, such as in bisphosphonate or radiation-related osteonecrosis of the jaw (BRONJ-ORNJ). This chapter addresses the main reconstructive options for mandibular reconstruction and the contribution provided by virtual surgical planning in optimizing both the surgical steps and the outcome of mandibular reconstruction *after ablative surgery*. In particular, the versatile role of the fibula free flap, empowered with computer-aided modeling, as well as customized prostheses, will be explored as the key to achieve highly accurate results. As for presented cases, the chapter will examine from the reconstruction perspective all cases that have been previously presented in Chapter "Virtual Surgical Planning in Mandibular Oncology", with the purpose of maintaining continuity and convey the logical understanding of intertwining an effective resection plan with a corresponding accurate reconstruction.

2 Possibilities for Mandibular Reconstruction

There are multiple solutions for the reconstruction of mandibular defects presented in the previous chapter:

- *Fibula free flap*: it represents the mainstay of mandibular reconstruction [1], given its versatility that make it suitable both for marginal defects and for segmental resections [2]. Its linear shape, along with a natural twisting of its axis, make it the ideal donor site for mandibular reconstruction in multiple conformational possibilities, which include bending and rotation of segments to fit each possible anatomical scenario. Its relatively low morbidity, with a low impact on patient's gait, and its double cortical section make it the ideal choice for patients needing subsequent implant placement [3].
- *Scapula free flap*: it represents another possibility but has probably less indications for mandible reconstruction compared with the midface [4]. The parascapular border has a considerably inferior length and thickness compared to the fibular diaphysis, and it provides a reduced quantity of bone compared with the fibula [5].
- *Deep Circumflex Iliac Artery (DCIA) flap*: also known simply as "iliac crest flap," it has the advantage of transferring a higher quantity of bone with thicker cortical layers . Disadvantages include a more difficult dissection, higher resorption rate, increased morbidity of the donor site, and a short vascular pedicle [6].
- *Customized prostheses*: they represent the ideal choice for a faster and more accurate replacement of missing bone segment. They can be entirely modeled in the VSP project and 3D printed in titanium using technologies including selective laser sintering (SLS), selective laser melting (SLM),

A. Tel (✉)
Lead Specialist for VSP and 3DP, Maxillofacial Surgery Clinic, Head & Neck and Neuroscience Department, Academic Hospital of Udine, Udine, Italy
e-mail: alessandro.tel@uniud.it

M. Ureel · R. Coopman
Department of Oral & Craniomaxillofacial Surgery, Ghent University Hospital, Ghent, Belgium
e-mail: Matthias.Ureel@uzgent.be; Renaat.Coopman@uzgent.be

M. Robiony
Chief of Maxillofacial Surgery Clinic, Director of the Postgraduate School in Maxillofacial Surgery, Chief of Head & Neck and Neuroscience Department, Academic Hospital - University of Udine, Udine, Italy
e-mail: massimo.robiony@uniud.it

© The Author(s), under exclusive license to Springer Nature Switzerland AG 2025

A. Tel, M. Robiony (eds.), *Atlas of Virtual Surgical Planning and 3D Printing for Cranio-Maxillo-Facial Surgery*,
https://doi.org/10.1007/978-3-031-94495-6_24

and electron beam melting (EBM). They are the ideal choice to replace segments not involved in the occlusion, including the mandibular angle and the mandibular ramus. Moreover, in elderly patients, they can provide a faster solution to bone reconstruction when future implant placement is not needed. When placed, such implants need to be buried under the tissues of the oral cavity or, whenever a wide mucosal resection for cancer is needed, a soft tissue flap, such as forearm or antero-lateral thigh flap, needs to be wrapped around them to reduce the risk of exposure. Despite advantages in shortening the overall duration of surgery, the most fearsome risk is the infection of the implant, requiring removal. This risk should be even more carefully evaluated if subsequent radiation therapy is planned on the site. In addition, customized mandibular prostheses can also include the reconstruction of the TMJ [7].

- *Combined flap + prosthesis*: this is a novel possibility made possible by recent evolution in computer-aided design that makes possible to tailor the titanium implant to the shape of the concomitant flap. This solution in the mandible has a specific indication in reconstruction of large defects in which it is also necessary to reestablish a correct mandibular height, which would require otherwise a double barrel fibula flap, with increased instability and risk of kinking of the vascular pedicle [8].

3 Digital Anatomy of the Fibula Free Flap

When approaching a case of mandibular reconstruction using the fibula free flap, it is essential to define accurately the virtual anatomy of the flap used for reconstruction. This means that a project with the segmentation of the donor regions has to be created containing at least bone and vascular structures.

3.1 CT Angiography for 3D Reconstruction

The first important step is represented by the definition of the acquisition protocol of CT angiography, which represents the ideal exam to plan mandibular reconstruction using the fibula free flap. First, CT angiography has to be acquired on both legs, starting at least above the knee regions and ending below the ankle. Acquisition matrix should be of at least 512 × 512 px, with a slice thickness as low as possible, ideally, 0,625 mm. The radiologist should pay attention to acquire an early arterial phase, and particular care should be taken to identify perforators vessels, that are useful in case a skin paddle is needed for the reconstruction of a skin or a mucosal defect (Fig. 1).

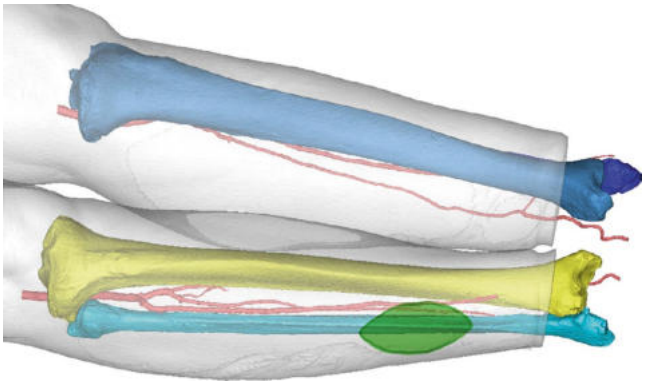


Fig. 1 Basic elements needed for mandibular reconstruction of VSP include bilateral segmentation of fibula and tibia and their respective vascular axes. Moreover, especially if perforators are visible, a soft tissue model to design the skin paddle can be created

3.2 Segmentation

In presence of a well-acquired angio-CT, segmentation thresholding should be based on vessels and not only on bone. This would not increase the quantity of bone included in segmentation, which is already maximal, but would ensure capturing all the vessel architecture as well. The first mask should therefore include both fibulas and tibas and their respective vascular axes. Secondly, mask split needs to be applied locally to separate the vascular axes from their contact points with the bone, which are minimal in presence of a well-defined CT, as vascular axes generally run far from the bone. At this point, two separate masks are yielded, including both vascular axes (femoral, popliteal, peroneal, anterior, and posterior tibial) and the skeletal anatomy of the leg. This phase is crucial to locate possible anatomical variations that should be taken into account for the surgical decision-making, for instance, the presence of a peroneal arteria magna (PAM), a congenital variation in which both the anterior and posterior tibial arteries are hypoplastic and the whole vascular supply of the leg and foot is provided by the PAM [9].

Next, skeletal mask is subdivided into singular bone masks, by separating the femoral condyles from the tibial plate, as well as the tibia from the fibula, and the ankle from both medial and lateral malleolus. The result is a project in which each bone is split into tibia, fibula, and their vessels (Fig. 2). Such objects can be converted into corresponding meshes for virtual surgical planning.

Additionally, it is also possible to reconstruct the skin in case a skin paddle is needed, to define its size and location [10], as well as muscles, which anyway require a leg MR. Muscle segmentation in fibula reconstruction is highly experimental and has been preliminarily tested by the author with encouraging results (Fig. 3).

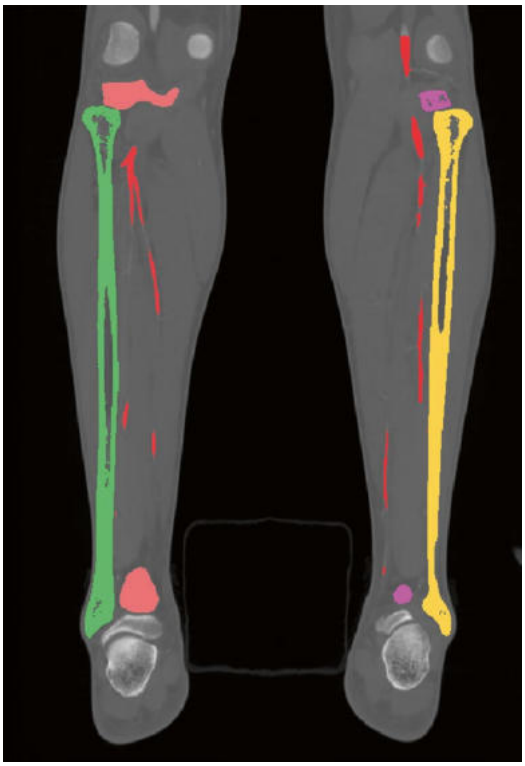


Fig. 2 Separation of vascular axis from its contact points on bones has to be carefully accomplished with the split mask tool

4 Choice of the Appropriate Site for Reconstruction

As shown in cadaver studies by Urken [11], the choice of the correct side for harvesting is based on several anatomical considerations depending on the reconstructive needs. When a skin paddle is needed, it should be considered that the posterior crural septum, which contains the perforator vessels that enter the skin paddle, is located inferiorly. This has to be established even before in contemporary vision for virtual surgical planning study. The two leading factors for strategy making are the need for an anterior or posterior pedicle, and the need of reconstructing the internal mucosa or the external skin. The vascular pedicle should always be positioned in the lingual side, where it is less vulnerable. Depending on the reconstructive needs, the combination of such anatomical factors defines four classes:

- *Contralateral fibula (anterior pedicle, inferior skin paddle):* it is ideal for ipsilateral defects that need skin reconstruction and require anterior pedicle. As the posterior crural septum is inferiorly placed, the skin paddle is rotated outwards. This represents a rare situation according to the author's experience. However, the anteriorly-placed pedicle is preferable if the vascular anastomosis

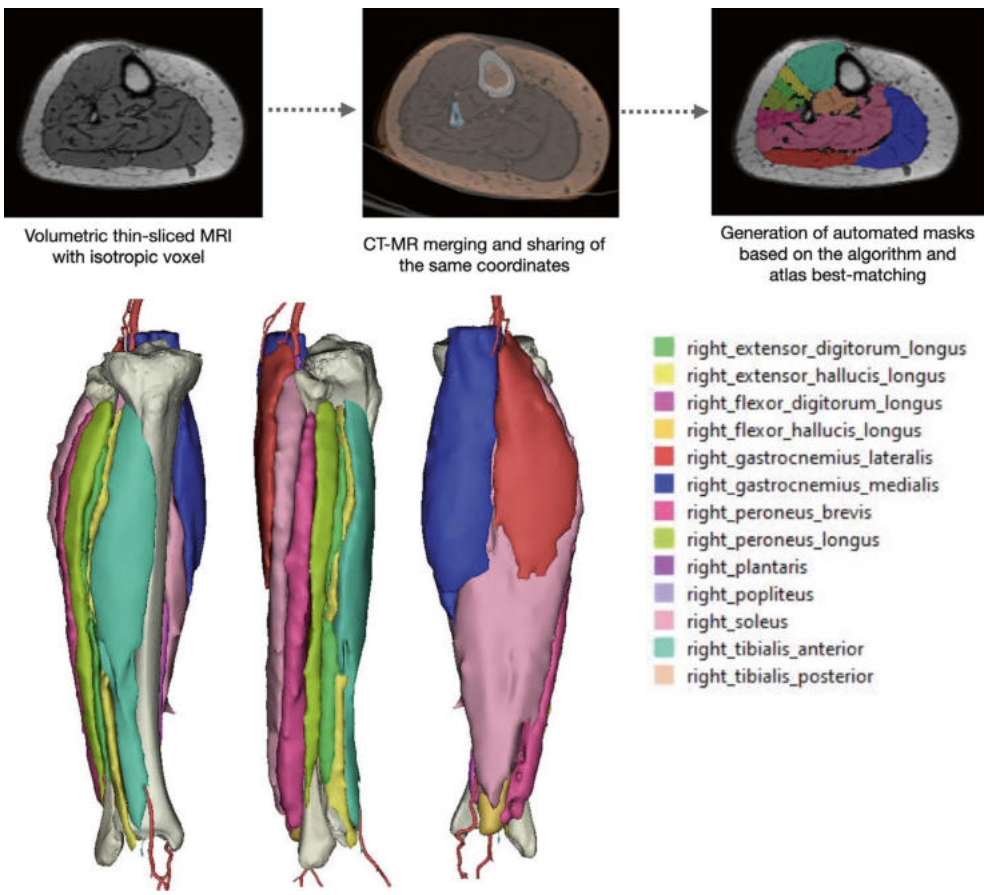


Fig. 3 Atlas-based muscle segmentation from MR can integrate basic bony and vascular reconstruction (highly experimental)

has to be performed in the contralateral side (for instance, if ipsilateral side vessels are depleted).

- *Contralateral fibula with 180° rotation (posterior pedicle, superior skin paddle):* this solution is excellent to reconstruct defect after segmental resections for oral cancer ablation. A posteriorly directed pedicle shortens the way to recipient vessels located in the neck, while the superior location of the posterior crural septum facilitates the lingual rotation of the skin paddle, making it suitable for oral mucosa suturing. This accounts for the majority of situations. Moreover, it has the advantage of placing the second operating team on the opposite side, thus avoiding possible interference with the surgical team performing the resective procedure.
- *Ipsilateral fibula (posterior pedicle, inferior skin paddle):* this is another valuable option, as it places the vascular pedicle posteriorly, thus decreasing its length to reach recipient vessels. However, as the posterior crural septum is located inferiorly, its rotation arch to reconstruct an intraoral defect increases, with augmented traction to perforator vessels. It should be considered when the contralateral, twisted, fibula is not available, whereas the difference is minimal if a skin paddle is not needed.
- *Ipsilateral fibula with 180° rotation (anterior pedicle, superior skin paddle):* in this configuration, the pedicle is located anteriorly, and the posterior crural septum with its skin paddle is located superiorly. This configuration is useful to reconstruct an intraoral defect with need of a contralateral vascular anastomosis.

Figure 4 illustrates possible reconstructive options based on the aforementioned combinations. Intuitively, the position of the skin paddle is a less limiting factor compared to the position of the pedicle. There is flexibility between a superiorly or an inferiorly oriented crural septum, which can be further compensated by axial rotation of bone segments. The surgeons should always be ready to switch between such configurations on the basis of vascular factors, including number and caliber of perforators, vessel patency, or anatomical variations.

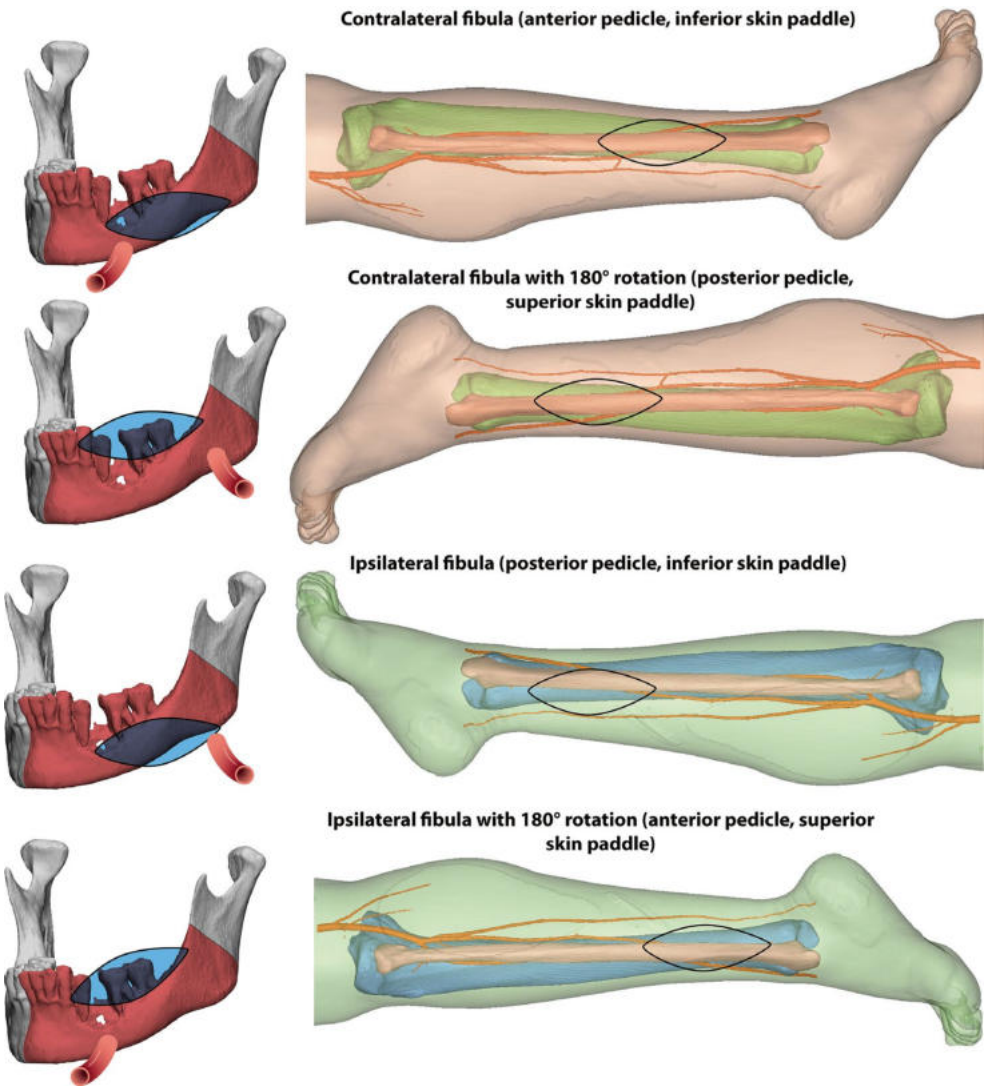


Fig. 4 Combinations described on the basis of the position of the vascular pedicle and the posterior crural septum

5 Virtual Surgical Planning in Mandibular Reconstruction Using the Fibula Free Flap

The most important aid in virtual surgical planning of a mandibular reconstruction using the fibula free flap is a software that is able to transfer every modification of fibula segments placed within the mandibular gap to the fibula diaphysis. This means that every change in length and orientation of segments positioned in the mandible can be immediately visualized in the donor region. For this purpose, the author finds that the software ProPlan CMF and its successor Enlight CMF (Materialise NV, Leuven, BE) perform efficiently. Within such software, it is important that both the surgical plan of resection and the segmentation of inferior limbs, previously described, are imported. Moreover, it is important that the orientation of the fibula flap in the mandible is defined according to both anatomical criteria, including position of the pedicle and skin paddle, and functional demands, namely the occlusal relationship with the superior antagonist. The following steps are recommended:

1. *Definition of a virtual wax-up*: when the fibula flap is positioned with the aim of providing the patient with a future prosthetic rehabilitation of the jaw, its position has to be optimized for a functional occlusal relationship. Thus, it is important that missing dental crowns are generated to be optimal for their upper antagonists, both in terms of height, Spee curve, and orientation (Fig. 5). Digital wax-up can be performed using several software available to dental technicians, including Zirkonzahn. Modellier (Zirkonzahn, Gais, South Tyrol, IT) and Exocad (Exocad GmbH, Darmstadt, DE).
2. *Preliminary positioning of the fibula segments*: according to the shape of the waxed-up arch (Fig. 6), the number, size, and orientation of fibula segments are decided. The placement of fibula segments is decided based on resection planes previously defined, and the side is chosen based on the aforementioned criteria. In order to replicate a curvature of the mandible, at least two segments are necessary. When the defect is more extended, up to three segments can be chosen. Adding more segments results in the increased removal of intersegmental wedges (sections of bone that need to be excised from the flap to enable bone bending), with subsequent devascularization and possibility of pedicle injury. A reasonable compromise

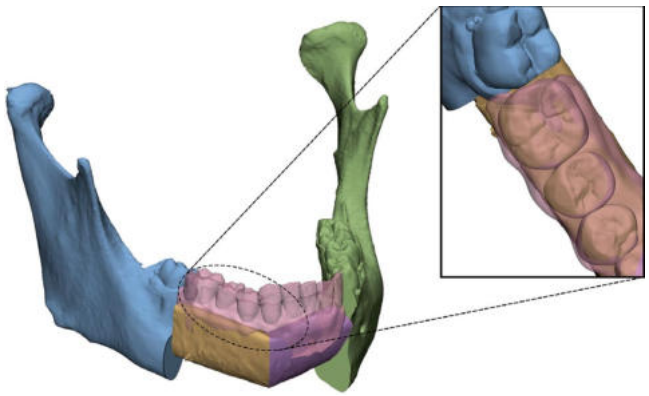


Fig. 6 Positioning of fibula segments according to occlusion

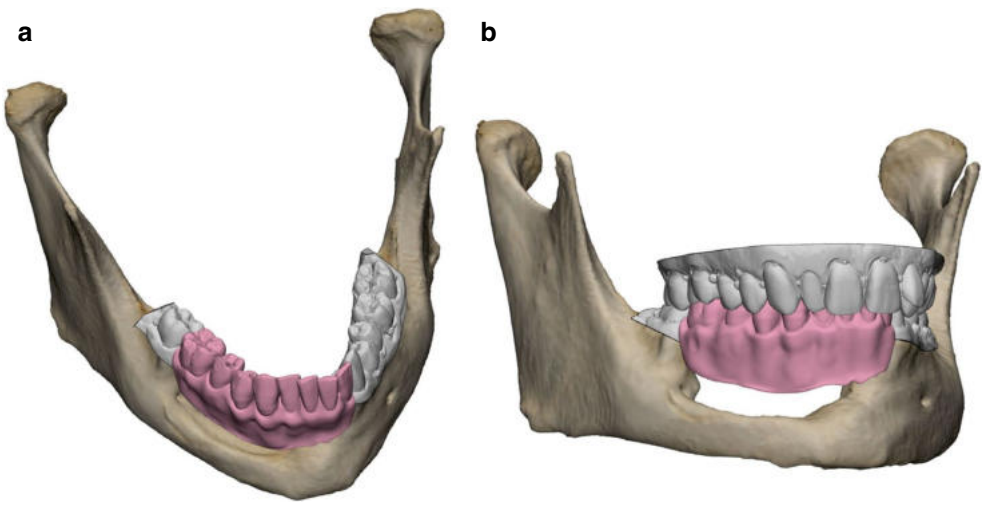


Fig. 5 Definition of digital wax-up for prosthesis-driven reconstruction

consists of avoiding an individual length for each segment inferior to 2,5–3 cm.

3. *Numbering the fibula segments*: numbering each fibula segment according to its proximity with the vascular pedicle. This enables to determine which segments is proximal and which is distal, thus the position of the vascular pedicle is placed accordingly. Newer software also allow for pedicle visualization while performing virtual surgical planning, which is highly useful in addition to the bare bone anatomy (Fig. 7).
4. *Rotation of fibula segments*: each segment is individually rotated to adapt to the natural twisting section of the fibula to the reconstructive needs. As the fibula cross-section can be approximated to a triangle, it may be decided to maintain the wider base above, providing better accommodation to the implants. Moreover, rotation of individual segments is determining to move the pedicle in the lingual side, where it is more protected. Rotation must be homogeneous across all segments and in the same direction in order to prevent twisting of the pedicle. This can be easily accomplished in the software Mimics Enlight CMF, as it allows to place a linear marker across the same face of all segments, enabling to understand their mutual rotational relationship. Similarly, this software enables to translate the relative position of the pedicle in the head and neck region, which simplifies the provisional visualization of the pedicle. Attention should be paid also to the shape of the inferior mandibular border (Fig. 8).
5. *Widening of intersegmental wedges*: This step occurs in the fibular diaphysis. Once the optimal orientation of fibula segments has been defined on the mandible, it is further optimized on the donor site to improve harvesting. First, it is important to spare at least 7 cm of bone from the apex of the lateral malleolus to ensure the ankle stability. Then, each individual segment is distanced from the other with the aim of widening intersegmental wedges to decrease the tension on the pedicle while bending, as well as to avoid interference between close osteotomies and between the flanges of surgical guides.
6. *Definition of sites for screw placement:* sites for screw placement should be anticipately defined on each man-

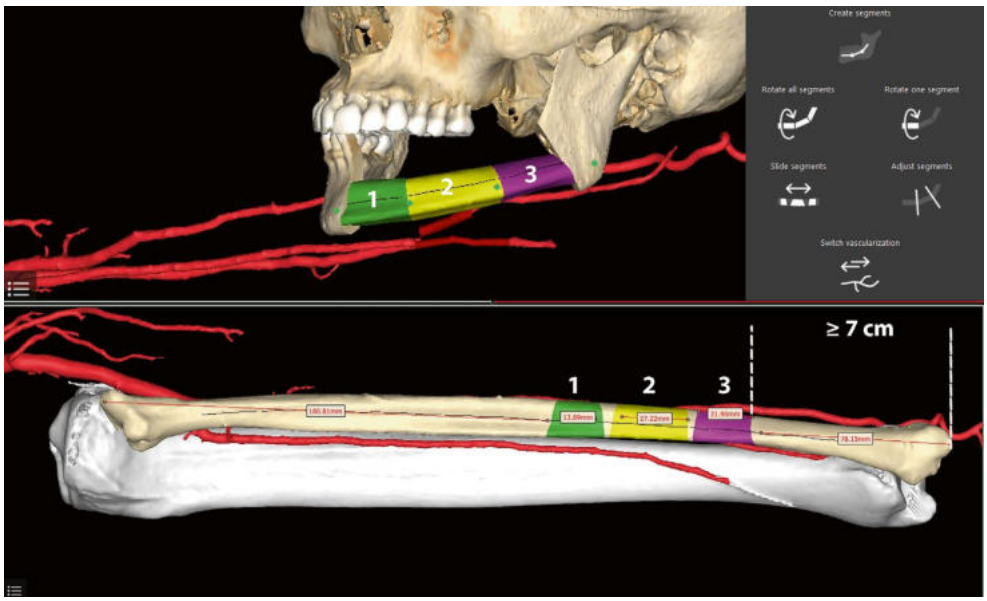


Fig. 7 Interactive fibula VSP in Mimics Enlight. Criteria for a successful reconstruction include harvesting the pedicle with preservation of the distal 7 cm of lateral malleolus; numbering segments to establish their order. This new software also enables to visualize the pedicle on the recipient site

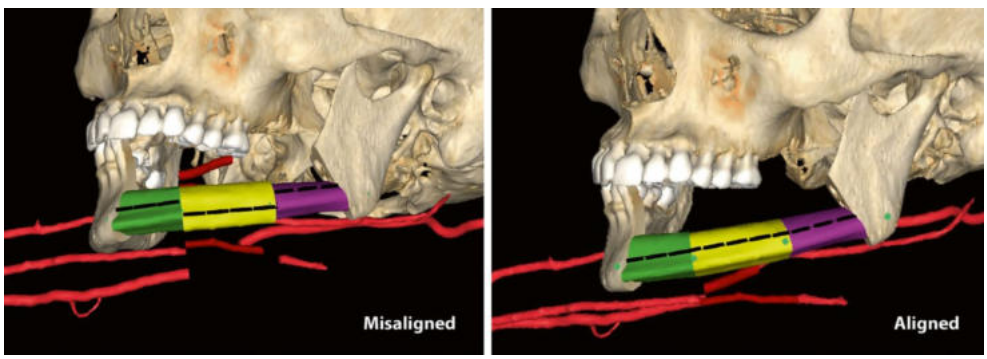


Fig. 8 Another important feature added in Enlight is a marker to assess the rotational correspondence of segments. This prevents axial kinking of the pedicle

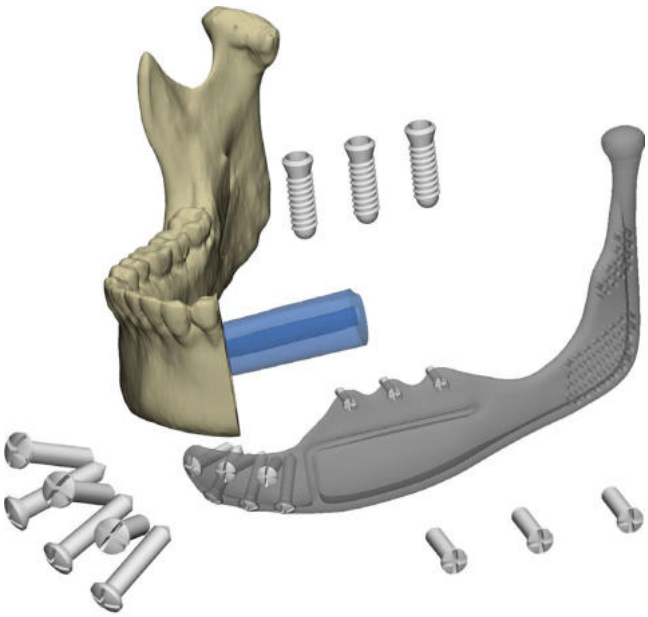


Fig. 9 Preliminary positioning of fixation screws and implant fixtures

dibular segment of the flap. Sites on the native mandible have already been drilled to ensure fixation of the surgical guide. The customized osteosynthesis plate should be designed using the same fixation holes without adding further biological damage. Then, all screw site indicators should be transferred to their corresponding segments in the fibula diaphysis, so that they can also be used to fix the surgical guide for flap harvesting (Fig. 9).

*** If a custom plate is not available, the model of mandibular reconstruction with* in situ *flap should be 3D printed, and a standard reconstruction plate can be premodeled and fixed using screws. The plate fixed on the model with screws needs to undergo CT or surface scanning to enable reverse engineering of the premodeled plate, digitization and must imported back in the VSP. At this point, the position of fixation holes can be defined in the VSP project likewise, and guides can be designed. This procedure involves more steps, but has the advantage of avoiding the purchase of a highly expensive custom titanium plate and can be managed entirely in-house*.

7. *Definition of sites for implant placement*: sites for implant placement are defined based on the digital wax-up of reconstructed crowns, so that they are optimized for the future prosthesis. In addition, implant placement and orientation are strictly limited by the presence of screws for osteosynthesis of the titanium plate, which must not collide with implants themselves (Fig. 9).
8. *Wrapping*: if a 3D printed model of the reconstructed mandible with fibula flap in situ is needed to premodel a reconstruction plate, the objects representing the resected mandible and individual fibula segments must be merged, and a wrapping operation with the same parameters reported in Chapter "Virtual Surgical Planning in Midfacial Oncology" for mandibular fractures must be performed to ensure structural integrity of the model. The wrapped model with null offset can then be 3D printed.

6 Workflow for Surgical Guide Creation for Fibula Flap Harvest

Creation of surgical guides for fibula flap harvest strictly relies upon the capability of the given software for VSP to transfer the mandibular project to the fibular diaphysis. Intersegmental wedges have already been widened after placing the fibula segments to reconstruct the defect area, and the most distal segment is planned at 7 cm (at least) from the lateral malleolus. This condition represents the substrate to perform the digital modeling of the surgical guide for harvesting, which happens through the following steps:

1. *Realignment of screw and implant-bearing segments from the mandible to the fibula diaphysis*: it is important that each implant and screw is correctly transferred to the matching position from the mandible to the fibular diaphysis. This step requires that each segment is grouped with both screws and implants, to be then aligned first point-by-point, then with a global registration method on its corresponding position in the leg (Fig. 10).
2. *Datum planes placement across osteotomies*: on each side of intersegmental wedges, datum planes are defined. Then, sketches can be generated to use the real osteotomy plane as XY coordinates to design the profile of the cutting flange (Fig. 11).
3. *Cutting guide base design:* the base of the cutting guide is defined on the external side of the fibula, which can be easily cleared from muscle insertions and soft tissue, between two consecutive flanges. It should be designed as loosely engaging, by covering less than 50% of the entire cross-sectional profile of the fibula, with a tiny pinching over the upper fibula crest (Fig. 12).
4. *Cutting flanges design:* lines drawn in sketches are extruded to crease solid geometry. As seen in guides for mandibular resection, cutting flanges can be of two types;
   (a) Linear: linear flanges require that the sketch extrusion is performed internally, allowing osteotomies to be traced exactly tangential to intersegmental wedges. Linear flanges benefit the most from intersegmental wedges widening, otherwise each flange would intersect each other, limiting the available surface to trace osteotomies (Fig. 13a).
   (b) Notch-based: notch-based flanges contain an inner fissure which drives the blade of the piezoelectric tool in a straight path. Yet slightly more cumbersome,

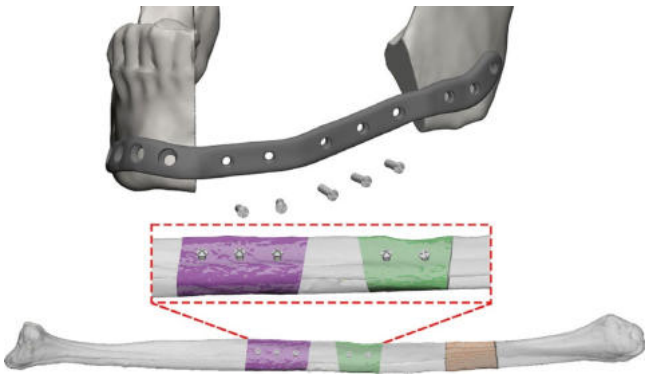


Fig. 10 Transposition of fixation screws to the recipient site

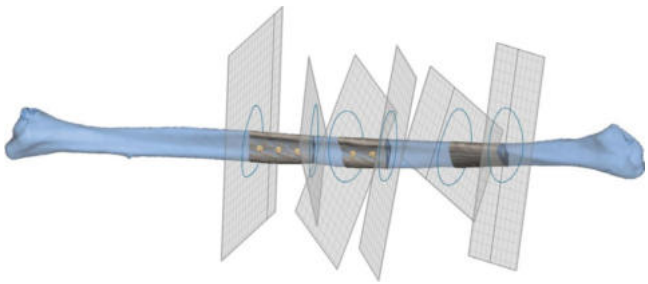


Fig. 11 The first step in surgical guide creation is the creation of cutting planes tangent to the planned segments in the fibula diaphysis

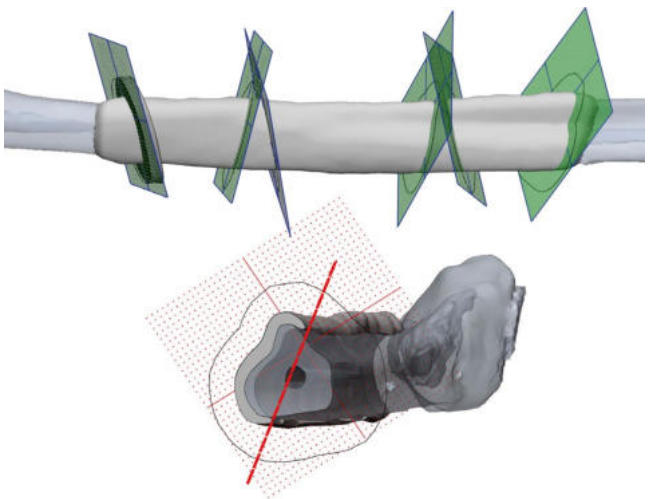


Fig. 12 The section of the fibula is projected on the datum plane as sketch and is assigned an offset corresponding to the intended height of the flange

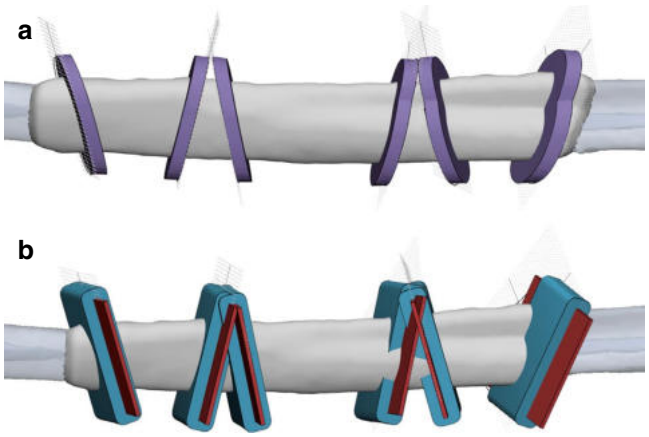


Fig. 13 Sketches on datum plane are extruded in 3D objects with the desired thickness, representing the future linear flanges (**a**). Alternatively, and more indicated for self-intersecting cuts, are notch-based flanges, for which a 3D plane is generated from the datum plane, enabling to create a slot for the cutting blade (**b**)

they have the advantage of enabling intersecting cuts, which are not possible using linear flanges. These cut slots are specifically useful when the required fibula length is demanding and intersegmental wedges have to be small in size (Fig. 13b).

5. *Addition of guiding cylinders for screws and implants:* cylinders to guide screw positioning are designed around the final screw sites and have the effect of both fixing the surgical guide to the bone and drilling the fixation holes for the final titanium plate in the fibula. As the fibula bone is more delicate compared to the mandible, the author advises to design 1.0 mm holes for a 2.0 screw system. Guiding cylinders should be designed using a telescopic internal design: an inner cylinder, 1 mm in diameter, for the screw shaft, and an outer cylinder, 2 mm in diameter, for the screw head. This ensures that the pressure applied to the screw head compresses the surgical guide to the underlying bone (Fig. 14).
6. *Addition of guiding cylinders for implants (optional):* Although it is possible to define in the same way drilling cylinders to position the implants directly in the fibula, we prefer to use a separate, intraoral, surgical guide to position the implants once the flap has already been fixated to the mandible. An intraoral surgical guide with dental anchoring is more stable and more precise; in addition, in prevents excessive manipulation of the flap while still being vulnerable in its pedicle.

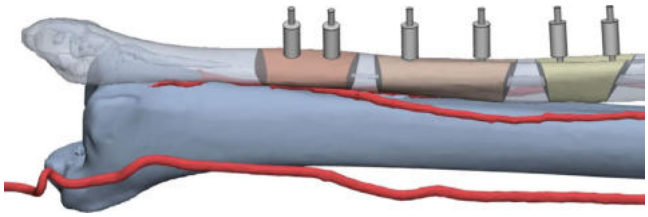


Fig. 14 Cylinders for future fixation holes are added after translating on the fibula screw positions defined in the mandible

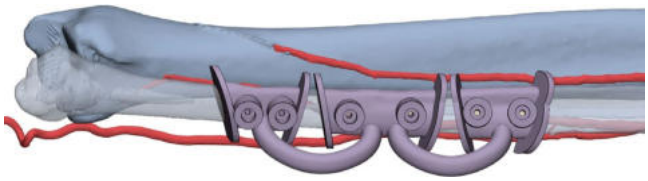


Fig. 15 The guide base is added and connected across different segments using bridges

7. *Creation of bridges:* each individual component of the surgical guide must be joined to the others to achieve a unique, solid entity, which can be placed along the whole fibula. To do so, a unique (or multiple) handle is created. The handle should not interfere with the trajectory of the surgical drill (Fig. 15).
8. *Labeling:* it is useful to label the surgical guide with both the patient's initials and the number of fibula segments.

7 Clinical Cases

Clinical cases showing mandibular reconstruction will resume the same cases treated in the previous chapter. Here, the main focus concerns strategies for mandibular reconstruction, especially virtual planning workflows implemented to solve complex mandibular defects both from an anatomical and a functional perspective. Consequently, the clinical history of each case is not reported, as it is elucidated in Chapter "Virtual Surgical Planning in Mandibular Oncology".

7.1 Case 1 (Continued): Reconstruction of a Resection Defect Using a Customized Titanium Implant

The patient herself required mandibular reconstruction to be planned using a customized patient-specific implant (PSI), as she deliberately refused a free-flap based reconstruction that had been suggested before. The patient was aware that using a PSI she would be unable to position teeth on the same mandibular side, but she opted for the advantages of a much shorter surgery and the avoidance of the leg morbidity of harvesting a fibula free flap.

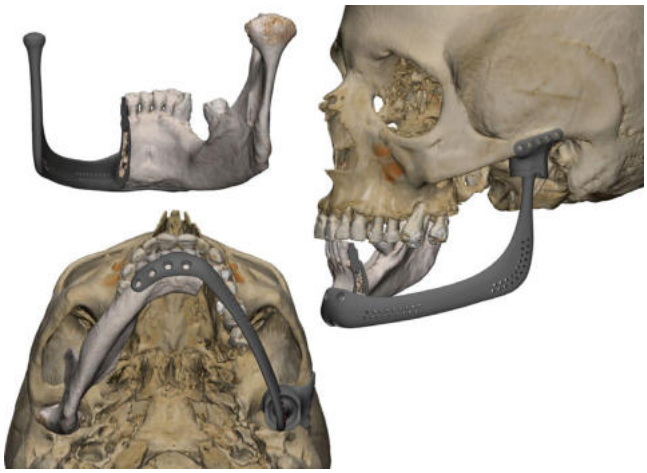


Fig. 16 VSP of extended mandibular reconstruction including TMJ with a patient-specific implant

Virtual Surgical Planning

After simulating mandibular resection with disarticulation in the VSP, an extended temporomandibular joint reconstruction (eTJR) [12] was planned with the implant's manufacturer using the software Geomagic Freeform Plus (3D Systems Corporation, Rock Hill, SC, USA). The prosthetic fossa component was positioned below the zygomatic arch, and the rotational fulchrum of the neo-TMJ was lowered accordingly. Customized flanges for the adaptation of the prosthetic fossa to the zygomatic arch were designed, thus achieving a specifically fitting fossa. The right hemimandible was mirrored to define the shape of the mandibular arch to be reconstructed with the PSI, then the overall shape was simplified and used as a template to model the shape of the mandibular component, which was then joined with the TMJ component. An anterior appendix was added to cover the right mandibular symphyseal region, where a double row of screws was added to achieve maximal stability of the implant. Last, the implant was improved by adding a grid for suturing of the masseter and milo-hyoid muscle (Fig. 16).

Surgery

First, the fossa component was positioned from the preauricular access using the deep subfascial approach. The zygomatic arch was deperiostized and the fossa component of the

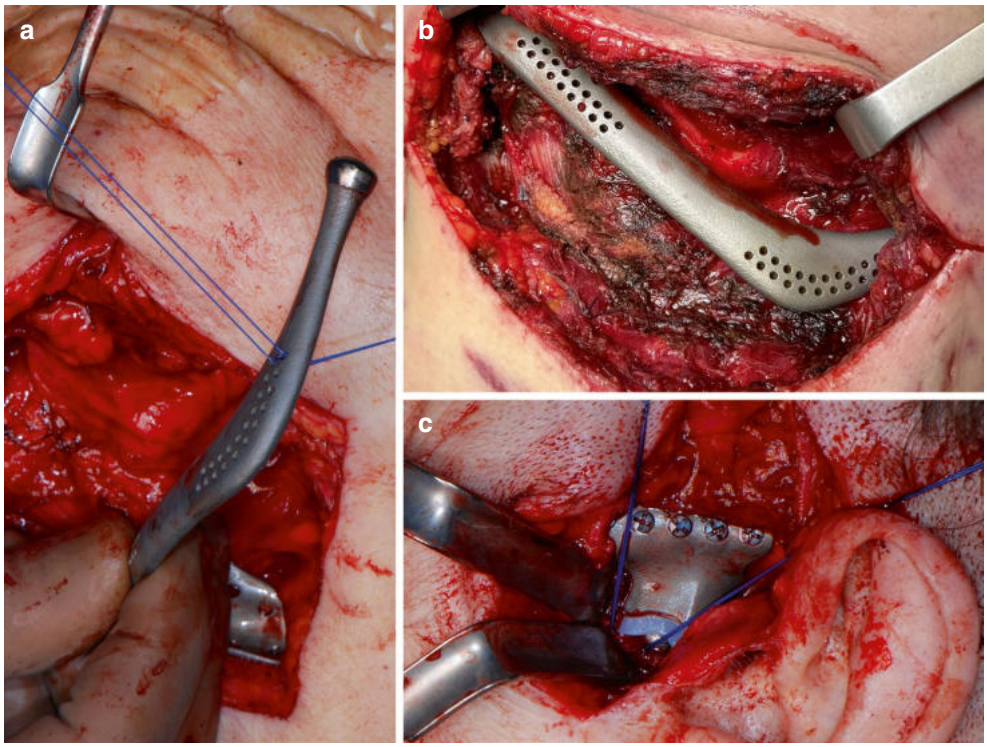


Fig. 17 (**a**) Intraoperative view with details of (**b**) ramus component and (**c**) fossa component

TMJ was positioned with a stable fitting over the natural TMJ fossa and the articular eminence. From the submandibular access, the extended mandibular prostheses was inserted, taking care to center the neo condyle with the prosthetic fossa. Subsequently, screws were tightened in the holes previously drilled to fix the resection guide. A multilayer suture was conducted (Fig. 17). Postoperative CT scan confirmed the correct placement of the implant exactly as planned (Fig. 18).

7.2 Case 2 (Continued): Reconstruction of a Marginal and Segmental Defect of the Mandible Using a Fibula Free Flap in Combination with a Patient-Specific Implant

In the previous chapter, peculiarities of this clinical case have already been elucidated, as it required a sudden change in virtual surgical planning due to the occurrence of a more anterior lesion in the time between the CT scan used for virtual surgical planning and the actual situation. The patient had previously undergone a marginal mandibular resection for a clear cell carcinoma, and during clinical and radiological follow-up, it remained stable for two years. Thus, a reconstruction of the mandible was proposed to finalize a dental rehabilitation plan, by adding bone volume using a fibula free flap to accommodate dental implants. Unfortunately, after the surgical plan for reconstruction was complete and the patient was already awaiting his reconstructive surgery, the sudden onset of pain in the symphyseal region of the mandible suggested the possible relapse of disease. The patient then underwent another CT scan showing the extension of disease beyond the anterior resection mar-

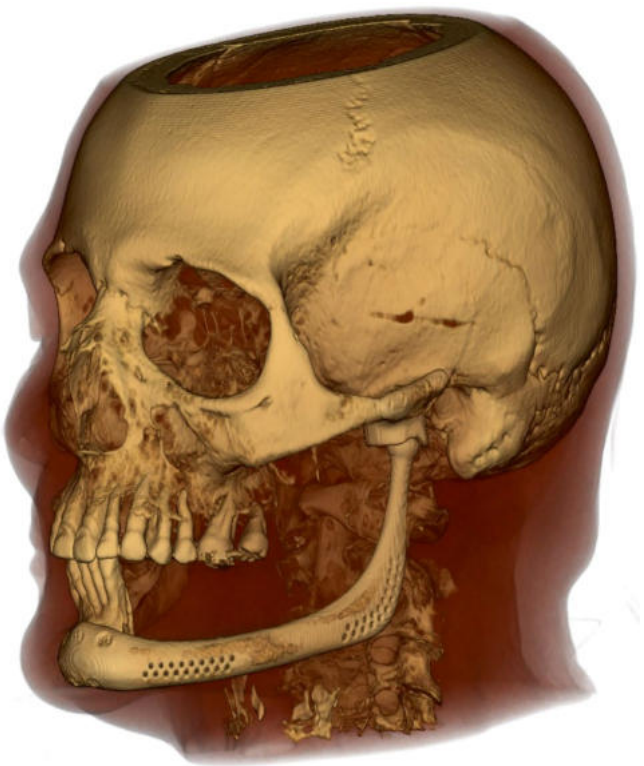


Fig. 18 Postoperative CT

gin, involving the basal bone. Then, an anterior segmental mandibular resection needed to be included in the final plan.

As mentioned in the previous chapter, this case underlines the importance of managing clinical cases within a point-of-care 3DP and VSP lab in the hospital, as it enables clinicians to fluently and rapidly shift between two different surgical plans without causing any delay for the surgical operation. For this reason, both reconstructive plans will be presented hereunder.

- Virtual Surgical Planning version 1: fibula free flap to reconstruct a marginal defect

It was already described that the marginal resection was simulated using a tray surgical guide, with regularization of the resection margin to accommodate the fibula free flap. A digital wax-up was realized in collaboration with a dental technician using Exocad, and the missing crowns of the mandibular arch were reconstructed in occlusion with their superior antagonist. Following the curvature of the dental arch, a two-segment fibula flap reconstruction was designed, with a symphyseal and a parasymphyseal segment. The ipsilateral fibula was chosen to orient the pedicle posteriorly, with segment 2, the distal one, repositioned over the symphyseal region. In the fibula diaphysis, the intersegmental wedge was slightly widened to enhance the curvature of the pedicle and avoid intersection between linear cutting flanges. Mesial and distal resection margins of the flap were made exactly coincident with those of the marginal resection, and the flap was positioned over the remaining basal bone. A two-segment surgical guide with a bridging element was created. Since a customized implant was not planned owing to the presence of basal bone as a load-bearing structure, drilling holes were randomly positioned on the fibula surgical guide to enable fixation to the bone (Fig. 19).

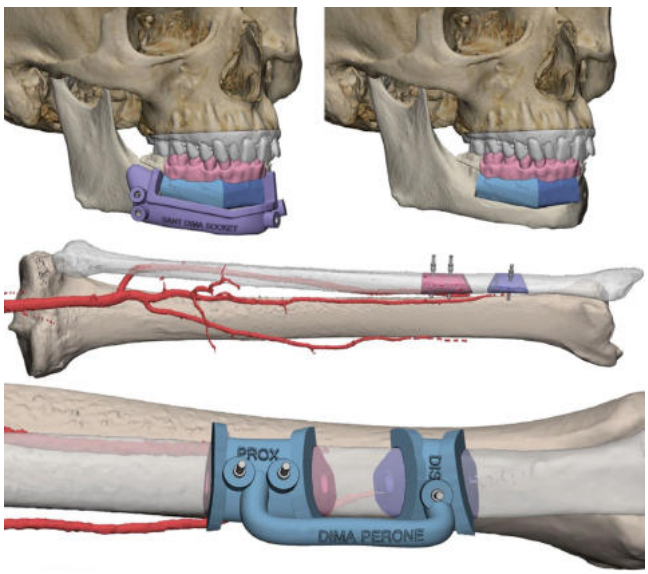


Fig. 19 VSP version 1

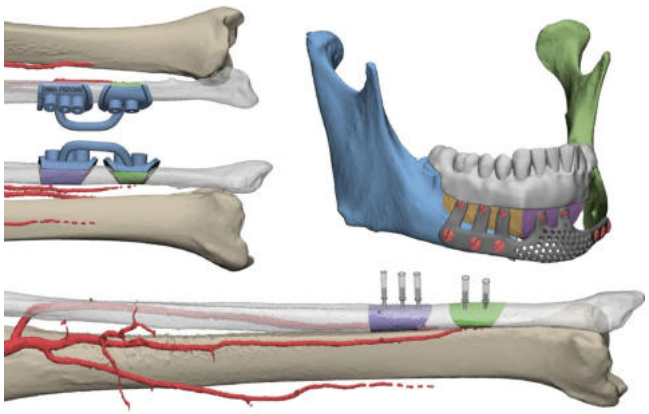


Fig. 20 VSP version 2

- Virtual Surgical Planning version 2: fibula free flap + PSI to reconstruct a posterior marginal and an anterior segmental defect

In this case, a new virtual wax-up was performed in Exocad, including as well the symphyseal region to be resected. As the chin was included in resection, due to the involvement of the basal bone in the intraosseous relapse of clear cell carcinoma, it was important to provide support in this region, which plays a crucial aesthetic relevance. Moreover, in addition to the fibula free flap folded in two segments, which was slightly more extended in its anterior component compared to the previous planning, a customized PSI reconstructing the bony chin was designed. The custom implant was planned on the final flap position and was anchored to the basal bone on both sides of the segmental resection. Finally, the virtual wax-up was used as a reference to model a surgical guide for implant placement with avoidance of the osteosynthesis screws. Since a customized implant was planned, screws position could be anticipately defined and correctly reported in the surgical guide for flap harvesting, matching the holes of the PSI without any additional drill in the fibula (Fig. 20).

*** It is worth mentioning that the PSI used for the reconstruction of the chin offered the possibility to use the same fibula reconstruction without adding another segment (in a double-barrel configuration) to replace the chin, which would add increased kinking to the pedicle and would achieve a less natural aesthetics in the chin region.*

Surgery

Through the submandibular corridor used for resection, the PSI was positioned matching resection boundaries. In particular, adaptation of the prosthetic chin with the resection

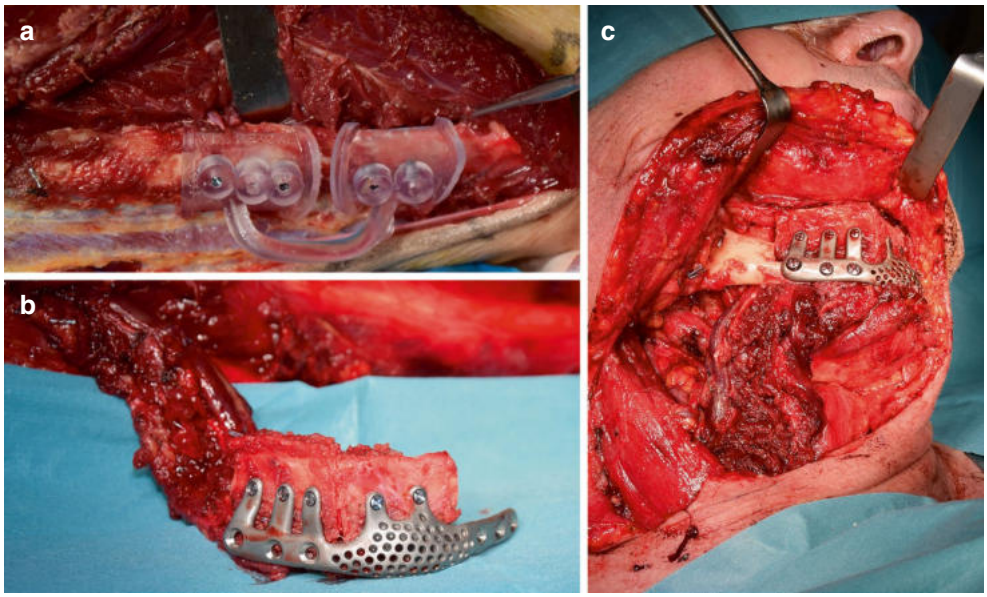


Fig. 21 Intraoperative view with (**a**) in-house 3D-printed guides and (**b**, **c**) neomandible with flap assembled on the implant

margins was carefully evaluated, and osteosynthesis to the surrounding basal bone was accomplished. Meanwhile, the surgical team involved in flap harvesting had already positioned the surgical guide on the luxated fibula and isolated the pedicle. The intersegmental wedge was excised to enable folding of the fibula in the desired configuration, the pedicle was clamped and transected, and the free flap inset was accomplished over the customized prosthesis while still being attached to the vascular pedicle. Once the pedicle was transected, the correspondence between holes drilled through the resection surgical guide and those of the implant enable to secure the customized prosthesis in the oral cavity (Fig. 21). Multilayer suturing was completed and postoperative CT was performed to assess accuracy (Fig. 22 TC post).

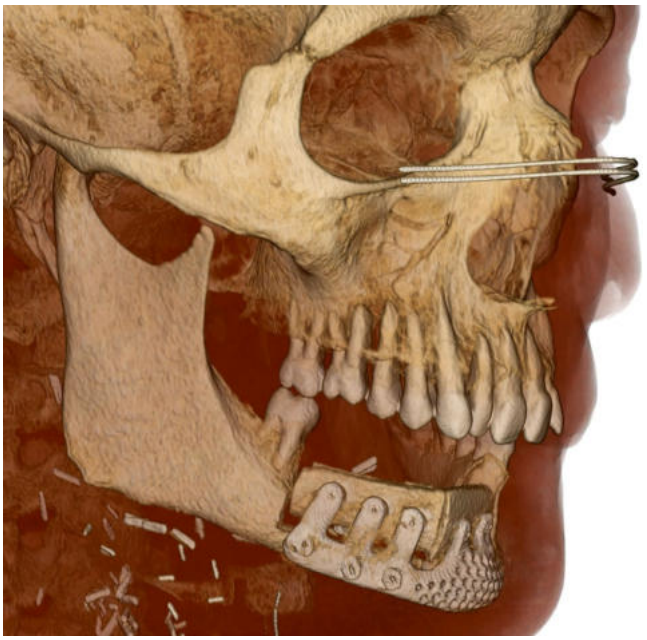


Fig. 22 Postoperative CT

7.3 Case 3 (Continued): Reconstruction of a Segmental Defect for Ameloblastoma Resection with a Three-Segment, Double Barrel, Fibula Free Flap

This case represents the first attempt—and the first success—of using point-of-care (PoC) designed and printed surgical guides for both resection and reconstruction, as this postoperative accuracy was not previously yielded using conventional surgical guides. In fact, while conventional guides are tailored to provide just the length of bone segments and cut direction to achieve the desired folded configuration, totally customized surgical guides for fibular harvest with hole matching between the mandible and the leg also provide the correct rotational arrangement, which aligns fibula segments exactly as predicted by the surgical planning. In this case, a customized osteosynthesis plate was required to the manufacturer, and it was designed on the sites for screw insertion provided by clinicians. Both surgical guides for resection, as explained in Chapter "Virtual Surgical Planning in Midfacial Reconstruction", and for reconstruction were manufactured in the in-hospital 3D printing laboratory. In addition to the improved clinical understanding and control over the entire VSP workflow, hospital institutions can benefit from a dramatical reduction of costs as the outsource exclusively the titanium implant, leaving model replica and all surgical guides to the PoC production.

Virtual Surgical Planning

At first, screw insertion sites planned for surgical guide fixation in the resective phase were considered, and replicas of 2.7 mm screws were positioned accordingly. In the reconstruction module of ProPlan CMF, fibula reconstruction was planned within resection planes using the contralateral fibula with 180° rotation: this configuration was ideal to place the vascular pedicle posteriorly. The choice of the contralateral fibula was not strictly driven by the need of a soft tissue component (as the defect to restore was exclusively osseous), but for logistic purposes, allowing a more comfortable distribution of the two surgical teams around the patient. Segment 1 (green) was thus the most proximal and was placed posteriorly, whereas segment 2 (yellow) was more distal on the fibula and placed anteriorly; these segments, replacing the basal bone, were separate from a trapezoid intersegmental wedge of 10 mm on the upper base and 15 mm in the lower base. In addition, it was considered that for successful implant placement, the height of the mandible reconstructed using two segments was not sufficient and, thus, a third segment was placed above segment 1 and 2 to restore the alveolar process. Segment 3 was distanced from segment 2 by a much wider intersegmental wedge measuring 35 mm in its bottom base, allowing the pedicle to twist upward, while being kept lingual, to enable the 180° rotation necessary to place segment 3 in a double barrel configuration. As previously mentioned, the distal edge of segment 3 was placed at least 70 mm distant from the apex of the lateral malleolus to ensure the stability of the ankle. Segments 1 and 2 were rotated to harmoniously reconstruct the inferior mandibular border, and segment 3 followed the same rotation sense to avoid potentially harmful twisting of the pedicle.

Once fibula segments were successfully placed, the final step was to decide screws position for segment 1 and 2, placed in a linear path compared to the 2.7 screws placed in the remaining mandible. Based on such coordinates, a customized plate was designed and manufactured to ensure stability of the mandible in the basal bone region, while it was considered that a standard fixation using a stock quad-shaped plate was sufficient to anchor segment 3 to segment 2 (please, refer to postoperative CT).

The screw position decided for fibular segments in the mandible was exactly transferred in the fibular diaphysis, where it was used as a reference to position guiding tubes during the construction of the surgical guide for flap harvesting. The fibula cutting guide was designed following the aforementioned principles, with datum planes positioning along the edges of each segment, inner extrusion of linear cutting flanges, and base creation between flanges. A sigmoid handle bridging all three bases of the cutting guide was designed, taking care to maintain the space for the surgical drill (Fig. 23). The surgical guide was printed in Formlabs Form 3BL using a Biomed Clear resin.

Surgery

Once surgical guide for resection was removed, sites for screw fixation were visible in the remaining segments. After dissection of the fibula free flap, creation of proximal and distal osteotomies, sectioning of the interosseous membrane, and luxation of the fibula, the pedicle was carefully isolated and the surgical guide was placed and fixed in segments 1 and 2 using guiding cylinders. Osteotomies were performed as well as excision of both the narrow and wide intersegmental wedges. The flap was folded in the final configuration and installed on the custom titanium plate using predrilled holes of segment 1 and 2, while being still attached to the vascular pedicle. Segment 3 was 180° bent and positioned above segment 2, where it was fixed using a quad-shaped stock plate. After the neo-mandible was constructed while being still connected to the leg, the pedicle was transected and the com-

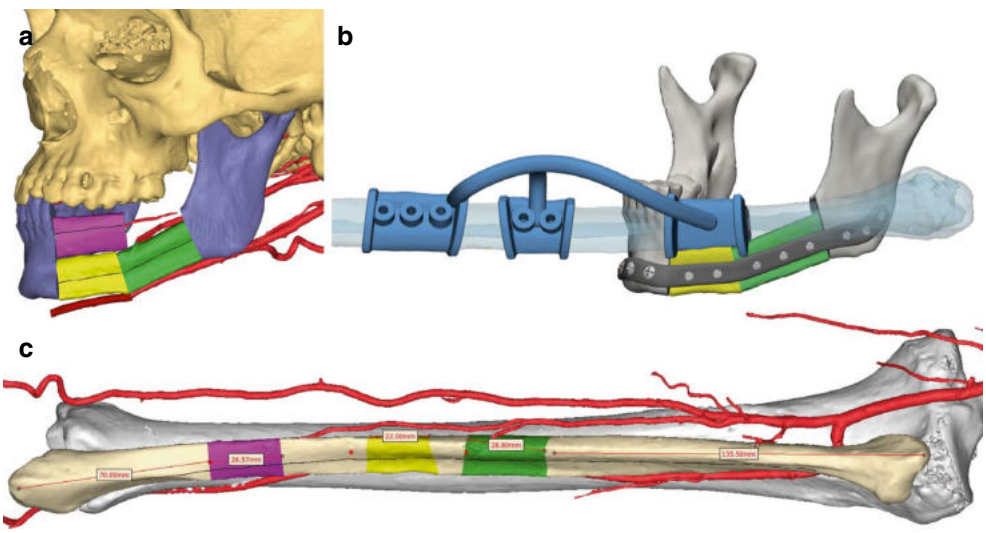


Fig. 23 (**a**) VSP of double barrel fibula reconstruction performed in ProPlan CMF. (**b**) Testing the third bone segment on the guide. A custom plane was planned after defining fixation holes; (**c**) corresponding fibula segments

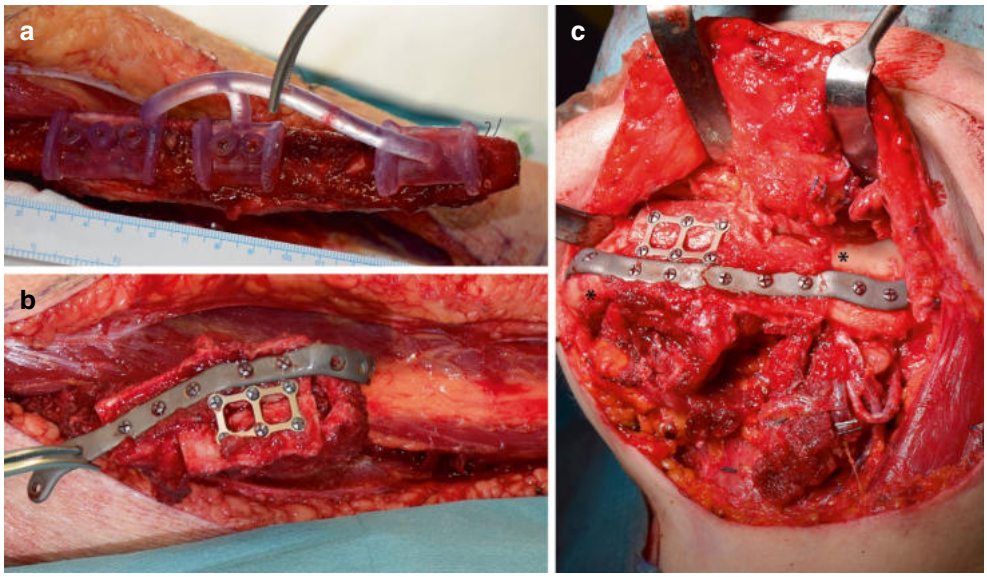


Fig. 24 Intraoperative view. (**a**) PoC resection guide; (**b**) segments fixed on plate; (**c**) final reconstruction. * demonstrates the high precision of this reconstruction in the posterior margin

posite flap was transferred to the mandibular defect area, using predrilled mandibular holes for fixation (Fig. 24). The flap engagement was exactly correspondent to the VSP. Anastomoses were performed and multilayer closure was achieved. Postoperative CT scan was performed showing the virtual absence of any bone gaps due to the highly reliable virtual and surgical workflow (Fig. 25).

7.4 Case 4 (Continued): Reconstruction of a Lateral Segmental Defect for Squamocellular Carcinoma Resection with a Two-Segment Fibula Free Flap

This case represents one of the more frequent reconstructive options, in which the continuity of the resected mandible is easily rebuilt using a two-segment, linear, configuration of the fibula free flap. This technique privileges simplicity to a more anatomical reconstruction of the mandible, which would require a two layers of bone, one for the basal bone and another for the alveolar process. However, a simpler configuration does not preclude the possibility to complete a functional rehabilitation of the mandible, since fibula segments can be placed higher than the inferior mandibular border, in order to accommodate functional implants. Moreover, the inferior the number of segments, the lesser the risk of injuring the pedicle while exciding intersegmental wedges, as well as the possibility of kinking.

Virtual Surgical Planning

The mirrored healthy hemimandible was used as reference to orient the fibula segment in the most reliable configuration for the reconstruction of the defect. The contralateral leg



Fig. 25 Postoperative CT demonstrates a highly accurate reconstruction

with 180° rotation was used to place the pedicle posteriorly and orient the posterior crural septum superiorly to deliver the skin paddle within the oral cavity. Two fibula segments were identified: segment 1, proximal to the pedicle and used to reconstruct part of the ramus, and segment 2, distal and close to the malleolus, used to reconstruct the mandibular body. The intersegmental wedge excised was slightly widened given the sharp 45° angle on both sides, necessary to enable an almost 90° bending of the fibula in the region of

the mandibular angle. Both segments, in particular segment 2, were placed in the distal third of the fibula, where the probability of identifying perforator vessels to the skin vessels is maximal (Fig. 26). Given the urgency of operating the patient as soon as possible, for this case there was no custom plate manufactured, but a standard plate was premodeled over a 3D-printed replica of the reconstructed mandible achieved through a wrapping operation.

Along the borders of fibula segments, linear cutting flanges were designed using internal extrusion of datum planes, as previously explained. Given the absence of a predefined array of screw holes, guiding cylinders were randomly placed to ensure stability of the surgical guide. A reuniting handle was placed to connect both segments of the surgical guide, which was then printed using a Biomed Clear resin.

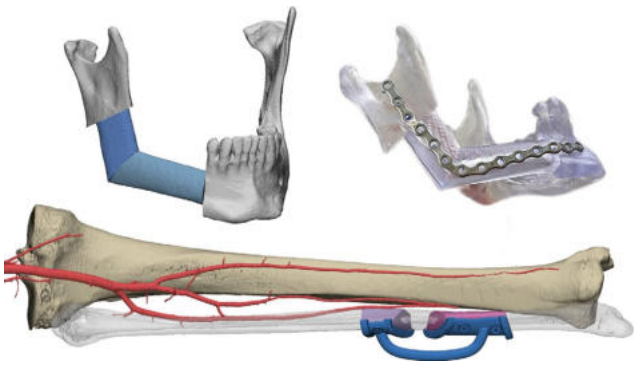


Fig. 26 VSP is used to 3D print a mandibular reconstruction model and bend a standard reconstruction plate

Surgery

The fibula free flap was mobilized and dissected as previously illustrated. The fibula cutting guide was positioned and stabilized, and osteotomies were performed with excision of the intersegmental wedge. Fibula segments were connected to the premodeled osteosynthesis plate and then fixed to the mandible (Fig. 27). Postoperative CT scan was performed, confirming an optimal result, yet slightly less accurate than the previous one, owing to the absence of predefined holes which help achieve control also on the rotational arrangement of individual fibula segments.

7.5 Case 5 (Continued): Reconstruction of a Segmental Lateral Resection for Squamocellular Carcinoma with a Three-Segment Fibula Free Flap

While the case analyzed previously refers to a standard lateral resection, more extended defects, especially those extending contralaterally, benefit from a three-segment reconstruction, which provides a more anatomical definition and decreases the amplitude of angles of intersegmental wedges, as the curvature of the mandible can be more efficiently distributed in three segments rather than in two. Also in this case, the urgency of oncologic surgery precluded the fabrication of a customized osteosynthesis plane, and, likewise, a 3D-printed mandibular model with in situ flap was produced at the PoC lab for plate prebending.

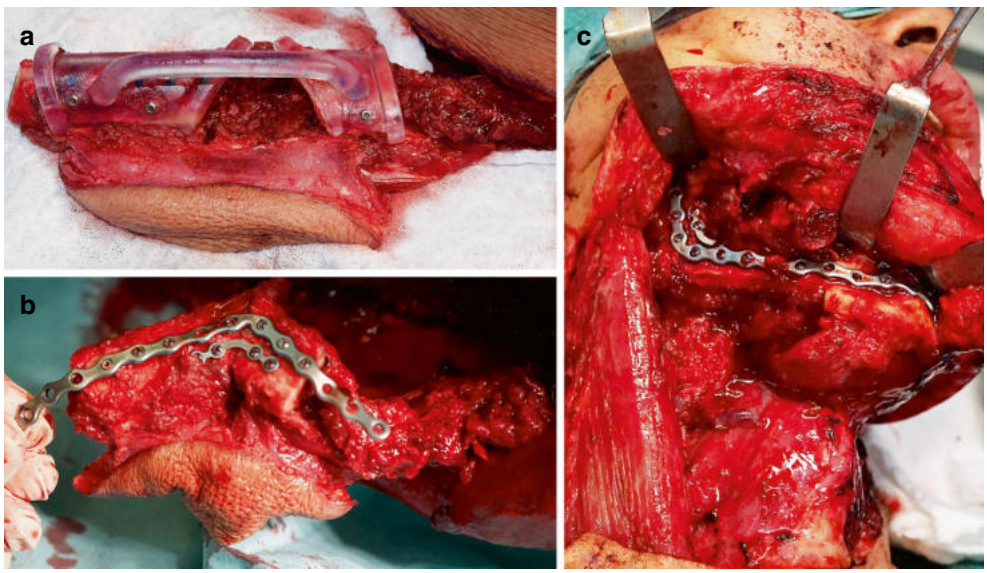


Fig. 27 Intraoperative photographs document optimal accuracy despite the lack of a patient-specific reconstruction plate

Virtual Surgical Planning

For this case, the ipsilateral fibula was used as harvesting source. A 180° rotation was applied to favorably reposition the posterior crural septum with a reduced rotation arch and decreased stress on the perforators to place the skin paddle intraorally. This case presents a situation in which the pedicle is desired in the anterior location, since, due to previous surgeries on the same side, neck vasculature on the left side was not deemed suitable as recipien t vessel for anastomosis. Placing the pedicle anterior shortens the path to contralateral recipient vessels to perform the anastomosis, as the ipsilateral side was depleted. Using the mirrored mandible as a reference template, contiguous segments were rotated by keeping the superior edge of the fibula inferiorly, where it was ideal to reconstruct the inferior mandibular border. Compared to the previous case, anatomical restoration was favored to the future implant rehabilitation.

Segment 1 was placed in the angle, segment 2 in the body, and segment 3 in the symphyseal region. The mandibular reconstruction was wrapped and transformed into a single, solid object, and 3D printed for plate prebending.

Fibula harvest guides were manufactured with the same principles, using linear cutting flanges and a mild pinching effect in less than 50% of the cross-sectional circumference of the diaphysis, to avoid excessive undercut with the impossibility to place the guide. Given the quantity of bone needed for reconstruction, intersegmental wedges were kept narrower, also in light of decreased bending angles due to the three-segment configuration. Moreover, in this case, two separate handles were preferred to a single, but more cumbersome, bridge (Fig. 28).

Surgery

Also in this case, the mandible was constructed on the mandible while keeping its connection with the vascular pedicle. The complex made of the three fibula segments fixated to the titanium plate was transferred to the mandible, where osteosynthesis to the spared bone was completed. Postoperative CT showed an acceptable accuracy of the procedure despite the lack of a customized plate (Fig. 29).

***In highly aggressive malignant pathology, time of surgery is a crucial factor. This can limit the possibility to out-*

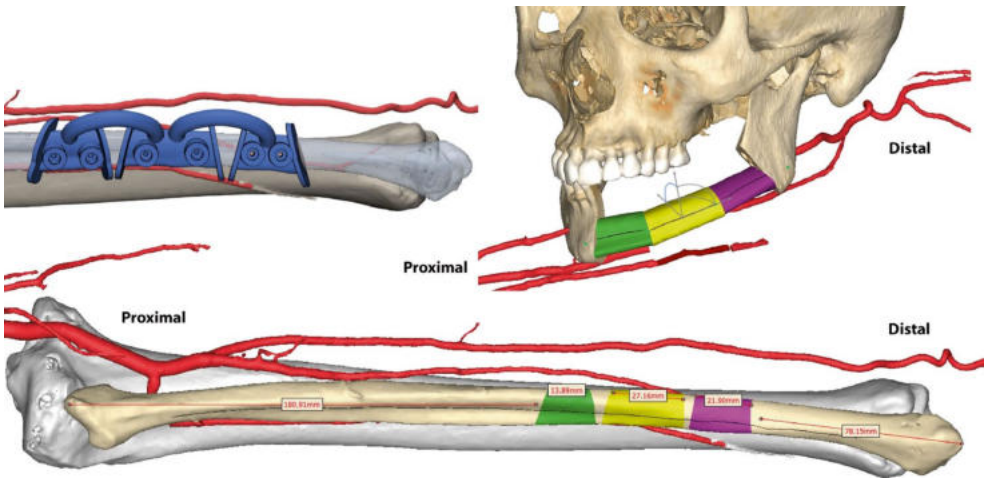


Fig. 28 VSP in Enlight CMF of an extended lateral resection of the mandible with reconstruction in 3 segments. The pedicle is visualized in the mandible as well. A surgical guide was modeled in 3-matic. A standard plate was manually bent like in the previous case

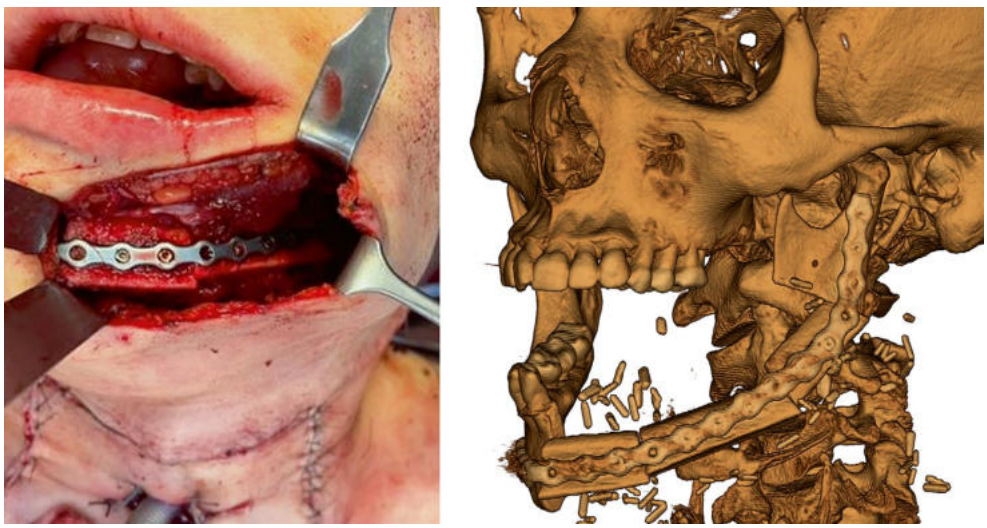


Fig. 29 Intraoperative view and postoperative CT. This case illustrates that, yet VSP was technically perfect, a manually bent plate provides less control especially on rotational movements of individual segments (a slight misalignment can be seen). In intraoprative view, the fibula can be scoped from a breach in the skin due to the excision of a cutaneous area infiltrated by the tumor.

source the production of a customized plate, which represents the gold standard in terms of accuracy to couple VSP with the surgical result. A possible and effective alternative is reverse engineering of a premodeled plate (see chapter "VSP in mandibular fractures" paragraph 5, point 6) using a 3D-printed model as reference, with slight inaccuracies introduced compared to the 3D-printed implant owing to the manual bending process.

These considerations underline the importance that hospitals in the future should be able to have immediate access to such implants, thus providing oncologic patients as well with the best possible reconstructive outcome. Nevertheless, performing such VSP and including in the planning workflow the printing of a reconstructed mandibular replica to premodel a reconstruction plate also lead to optimal results. Such results would never be possible without having a PoC 3D lab at the hospital institution where clinicians are able to plan and manufacture surgical guides by themselves.

7.6 Case 6 (Continued): Anterior-Lateral Segmental Resection for Squamocellular Carcinoma Using a Three-Segment Fibula Free Flap Reconstruction and Customized Plate

In this case, the logistics was more favorable than the previous two and it was possible to manufacture a customized plate without causing any delay to the scheduled surgery. As mentioned, while surgical guides alone are highly effective to ensure both the correct length of segments and their bending angles, predefining fixation holes which can be subsequently associated with a corresponding customized fixation plate also enables the third dimension of control of fibula free flap, namely rotational control. This ensures that fibula segments are placed in the real space exactly as planned in the 3D virtual space.

Virtual Surgical Planning

For this case, the contralateral left fibula with 180° flipping was used as donor source for the flap. In this configuration, the pedicle was placed posteriorly along the right side, while the posterior crural septum was placed superiorly, thus favoring the placement of the skin paddle in the oral cavity. Segment 1, the most proximal, was used to restore the region of the right mandibular body, and segments 2 and 3 were used to respectively rebuild the parasymphyseal and symphyseal regions. The superior fibular crest was positioned inferiorly, thanks to the 180° flipping, enabling to reconstruct the inferior mandibular border. Moreover, fibula segments were rotated inward with vestibularization of the inferior mandibular border and simultaneous lingualization of the posterior crural septum, thus further facilitating the intraoral placement of the skin paddle. Owing to the extent of the resection, intersegmental wedges were kept narrow with minimal intersection (Fig. 30). Sites for screw insertion were preliminarily decided in the fibula segments and put in continuity with those previously decided for resection guides and then used to model a customized osteosynthesis plate. Likewise, the same screw holes were transferred from the mandibular flap segments to the fibula diaphysis and used to locate the corresponding screws to plan guiding cylinders for the fibula surgical guide. The guide was designed according to the previously described workflow, using inward extrusion of sketches located at the edges of segments, with a unique handle bridging all its three compartments (Fig. 31).

Surgery

After dissection of the fibula free flap, once the fibula was separated and luxated, the surgical guide for flap harvesting was positioned on the lateral surface of the diaphysis, with a 180° flipping, as predicted by the VSP. The guide was secured through guiding cylinders for predrilled holes of 2.0 mm. Osteotomies were performed and flap segments isolated with the excision of intersegmental wedges. The customized plate

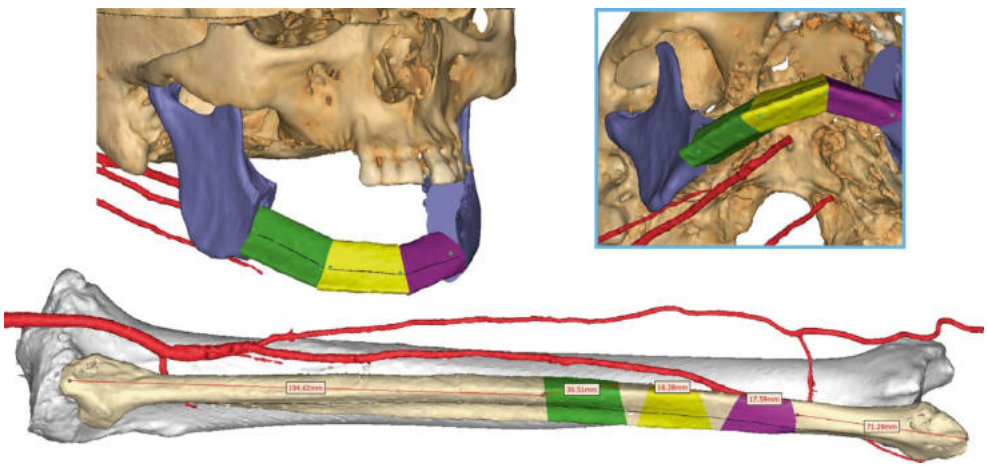


Fig. 30 VSP in Enlight CMF of an extended anterior-lateral mandibular defect. The superior, narrow fibular margin becomes the inferior mandibular margins by 180° flipping. The vascular pedicle can be seen posterior and lingual

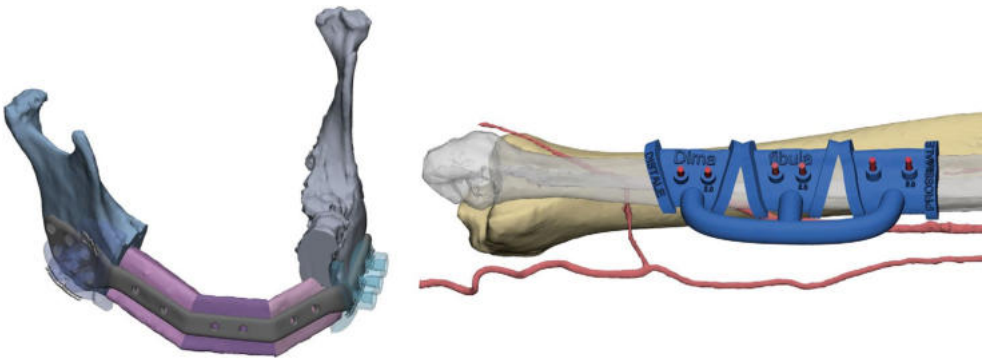


Fig. 31 PoC surgical guide and a customized osteosynthesis plate with coincident holes

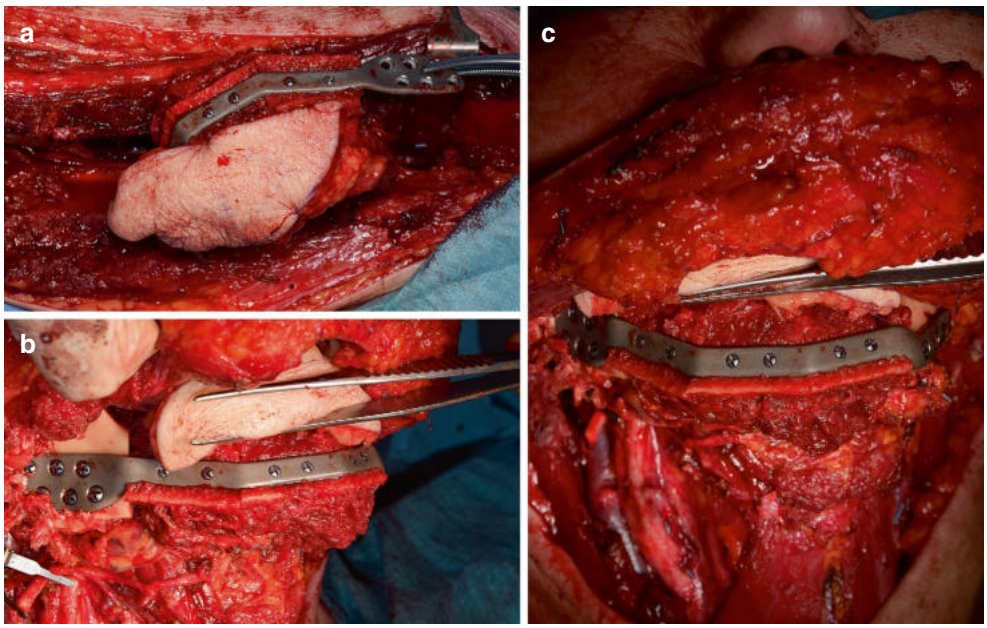


Fig. 32 Intraoperative view with excellent margin correspondence and optimal rotational control allowed by the custom plate

was fixed to the fibula flap through the same holes drilled to secure the guide. After pedicle transection, the fibula flap mounted on the customized plate was transferred to the recipient site and fixed to the resected mandible through the same holes used to secure the resection guides. Perfect compatibility with a submillimetric gap was assessed both intraoperatively and after postoperative CT scan (Fig. 32). This case shows how predefined holes and a customized fixation plate are useful for the most reliable 3D installation of the flap in its receiving site, thanks to the coincidence between the holes of surgical guides and the final plate.

7.7 Case 7 (Continued): Reconstruction of Hemi-Disarticulation of the Mandible Using a Customized Implant in Association with a Fibula Free Flap

This case exemplifies the reconstruction of a mandibular disarticulation including the temporomandibular joint, which needed an alloplastic replacement. Owing to the young age of this patient, it was decided to offer the opportunity of a future implant rehabilitation by positioning a fibula free flap. In addition, the fibula free flap alone was not sufficient to achieve a correct anatomical reconstruction, as it was placed higher to reconstruct the alveolar process, thus sacrificing the inferior mandibular border, which plays a crucial role in terms of structural stability. On the other hand, a linear configuration was preferred for the fibula free flap, avoiding a double barrel arrangement; moreover, a prosthetic solution provides a more anatomical and functionally suitable replacement for the mandibular ramus and the TMJ. Such considerations converged in the usefulness of a mixed approach, in which an alloplastic replacement was adopted for the ramus and the TMJ, embracing the mandibular border as well, while a simple, single segment, fibula free flap was placed above the implant to provide suitable bone for implant placement.

Virtual Surgical Planning

As the resection included the bone together with a wide mucosal surface, it was necessary to harvest the fibula flap

with its skin paddle. After performing Doppler ultrasound, the location of the perforator vessel was determined in the distal third of the fibula flap, and the segment was centered around the hypothetical location of the perforator vessel. For this reconstruction, the ipsilateral leg was chosen as donor source for the flap, enabling to place the pedicle posteriorly and to position the skin paddle with a slight increase in rotation of the posterior crural septum. The contralateral leg was avoided due to inferior number and pulse of perforators located at the Doppler exam.

The fibula flap was located corresponding to the resection plane and extended posteriorly to cover the full length of the alveolar process, with a slight inward rotation to enhance the position of the septum containing septo-cutaneous perforators. The position of screws was decided, as well as implant sites, to avoid any reciprocal collision. The screw position was reported correspondingly in the fibula flap, where a one-segment surgical guide with linear cutting flanges was created. Guiding tubes for predrilling and securing the guide to the bone (and subsequently fix the flap to the customized implant) were added.

Using the same holes position, and based on the healthy hemimandible mirroring, the customized implant was designed in collaboration with the commercial partner using Geomagic Freeform Plus (3D Systems Corporation, Rock Hill, SC, USA). On its inner surface, a 1 cm deep tray was added to provide additional support to the fibula flap. Grids for the insertion of the masseter and temporalis muscle were added as well. The TMJ replacement system was included in the prosthesis and was modeled through the same principles, including a condyle and a fossa (Fig. 33).

Surgery

The mandibular defect was exposed after the tumor was resected and the mandible disarticulated. Before insetting the flap and the prosthesis, the TMJ fossa was positioned through the preauricular access. After the resection of the fibula free flap was completed, the surgical guide was positioned and fixed using guiding cylinders in the predefined positions. Osteotomies were completed, and the one-segment flap with its skin paddle was mobilized while being still connected to its vascular supply in the leg. Subsequently, the mandibular prosthesis was fixed to the flap using the same screw holes used to secure the guide. The pedicle was clamped and dissected and the prosthesis combined with the flap was transferred to its recipient site, where it was fixated using the holes left by the mandibular cutting guide. Postoperative CT confirmed the elevated accuracy of reconstruction and the intimal bone contact between resection margins and the fibula flap (Fig. 34).

7.8 Case 8 (Continued): Reconstruction of a Subtotal Mandibulectomy with a Customized Prosthesis and a Latissimus Dorsi Free Flap

In this case, the extension of the resection, the exceedingly long duration of surgery, and the need of a soft tissue free flap for reconstruction did not justify the use of another bone flap for the reconstruction of the mandible. To simplify the reconstructive phase and increase anatomical reliability, a customized titanium implant was additively manufactured, including the left TMJ.

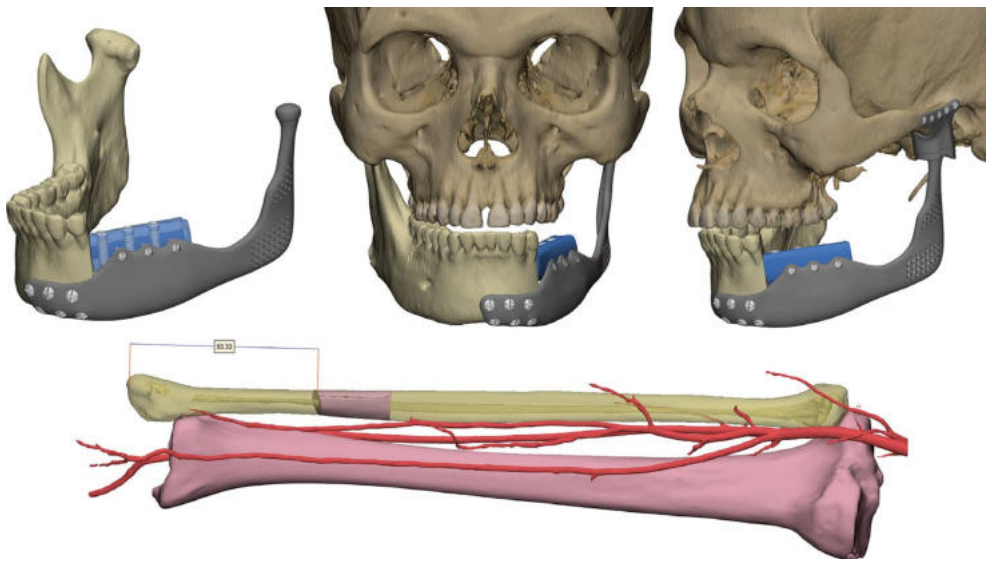


Fig. 33 Single segment VSP with prosthetic hemimandible for a case of extensive resection with disarticulation. Implants and fixation screws can be seen

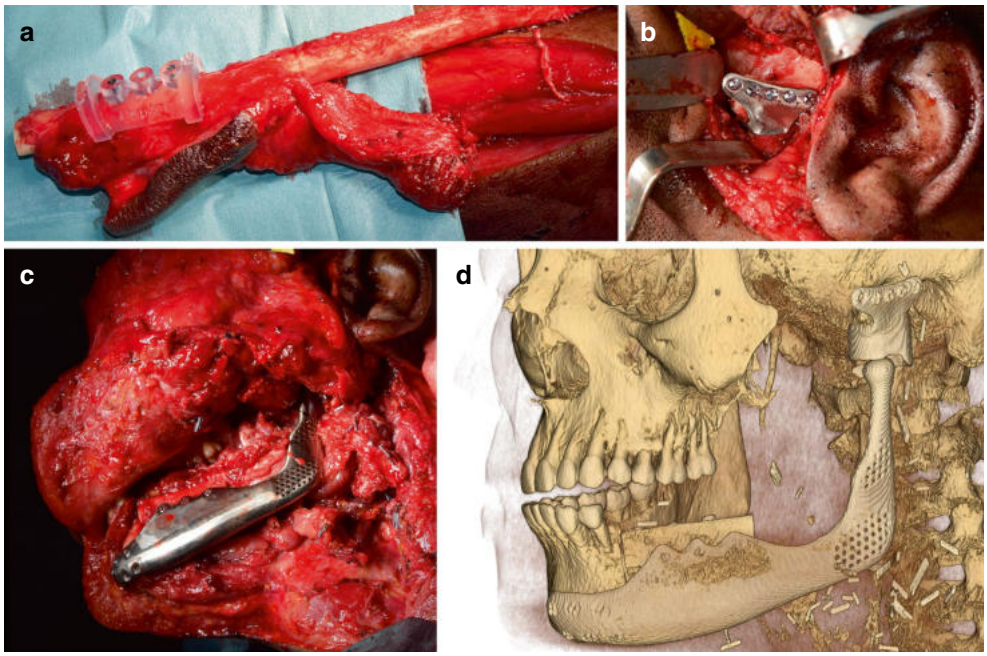


Fig. 34 Intraoperative view. (**a**) PoC guide; (**b**) prosthetic fossa; (**c**) prosthetic hemimandible + flap, (**d**) postoperative CT scan shows optimal accuracy

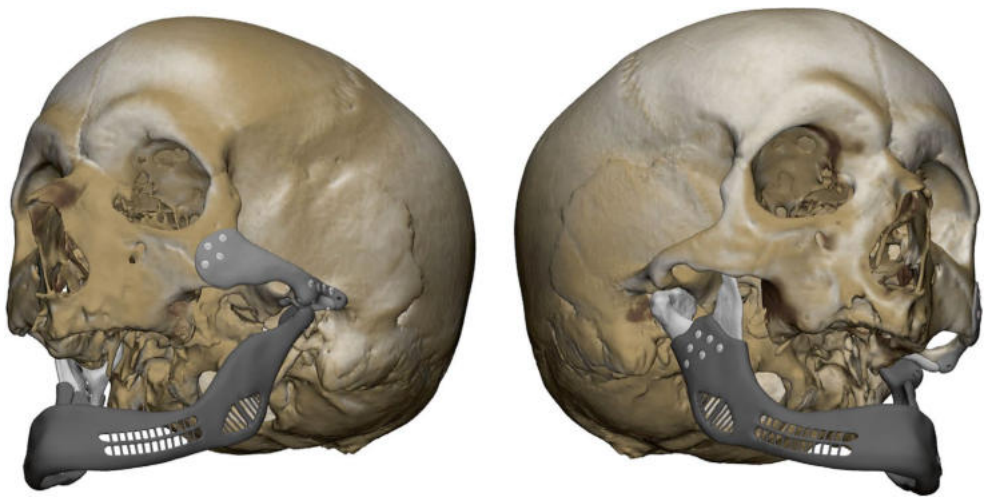


Fig. 35 VSP of reconstruction for near-total mandibulectomy with extended zygomatic arch resection. Prosthesis includes the fossa connected with the zygomatic arch

Virtual Surgical Planning

For this case, a closest donor template mandible was adopted. As this case dates back to 2019, it was not possible to implement more sophisticated technologies such as statistical shape modeling (SSM), deep learning (DL), or generative adversarial networks (GAN) [13]. Thus, the most likely mandible was chosen from a panel of patients for which 3D models of mandibles were available, basing the choice on biometric compatibility. The implant was developed in Geomagic Freeform Plus, software that converts conventional polygon-based geometries into clays, adding more freedom to the process of 3D sculpting, as explained in Chapter "Software Used for Virtual Surgical Planning". The only site for fixation holes was the remaining part of the right mandibular ramus. Multiple grids were added for muscular insertions, as well as flap suturing. The TMJ region was developed, as always, in accordance with the principles of joint replacement (Fig. 35).

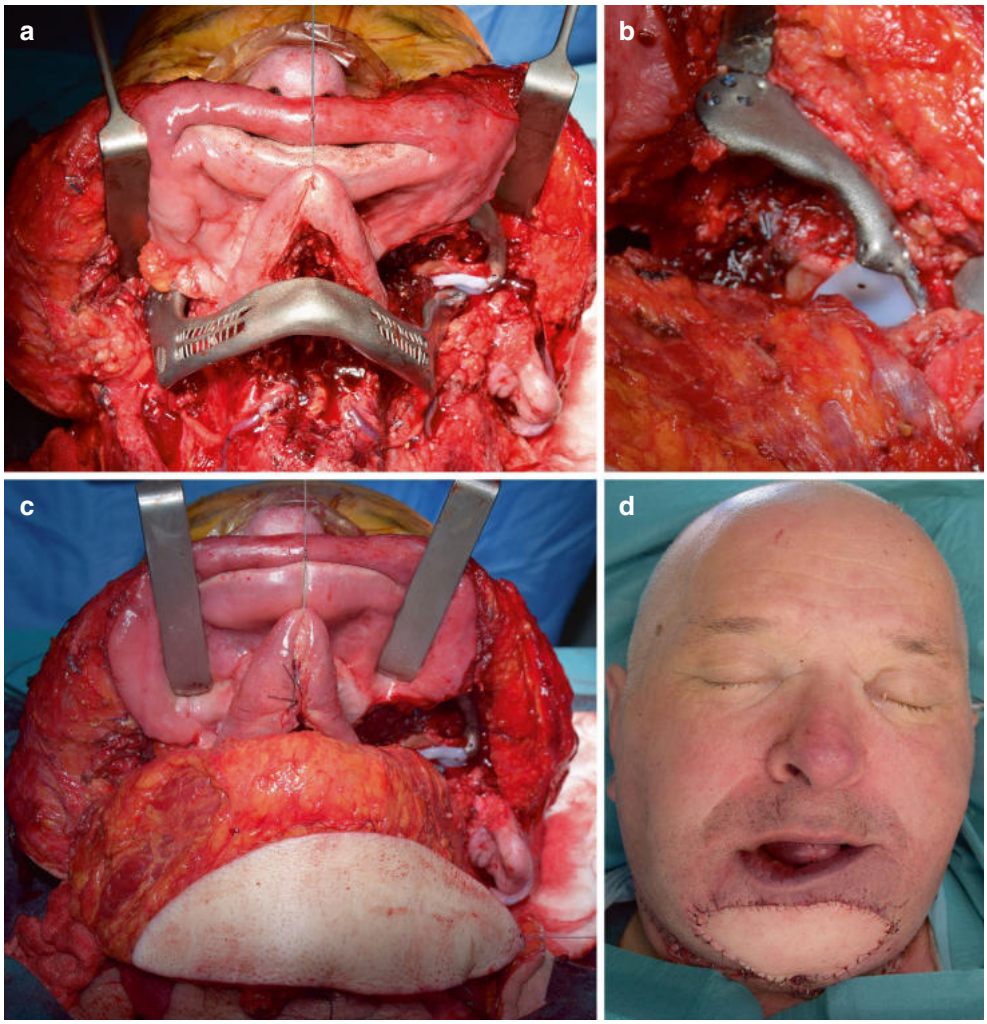


Fig. 36 Intraoperative view. (**a**) Neomandible fixed; (**b**) particular of arch and fossa; (**c**) latissimus dorsi flap enveloping the prosthesis; (**d**) immediate surgical outcome

Surgery

Once the resection phase was completed, at first the fossa component of the TMJ was installed above the articular eminence and the zygomatic arch, bridging a resection gap of the zygomatic arch itself which was segmentally resected for oncologic purposes. The mandibular prosthesis was installed and fixed with 2.7 mm screws to the resected right mandibular ramus. Subsequently, the implant was buried under a large-volume latissimus dorsi flap, which was plicated around the implant to ensure coverage and prevent it from exposure. The flap was harvested with a bulky skin paddle as well which enabled to reconstruct the skin resected from the symphyseal region, and which was sutured superiorly with the inferior lip (Fig. 36).

8 Dental Innovations in Mandibular Reconstruction

The following paragraphs showcase a pioneering workflow for one-stage prosthetical fixation of dentures in fibulas using a new, modular guide system, and innovations in vestibuloplasty after reconstructive surgery using computer-guided methods [14–16].

8.1 Case 1: In-House Manufactured Innovative Modular Stackable Guide System

1. Fibula flap VSP in Enlight® 2.0 (Materialise, Leuven, Belgium) (Fig. 37)
2. VSP of cutting guides and templates designed in 3-Matic® 18.0 (Materialise, Leuven, Belgium) (Fig. 38)
3. Design of modular stackable guide system with foot plate, attachment cylinders (blue), and connecting arms

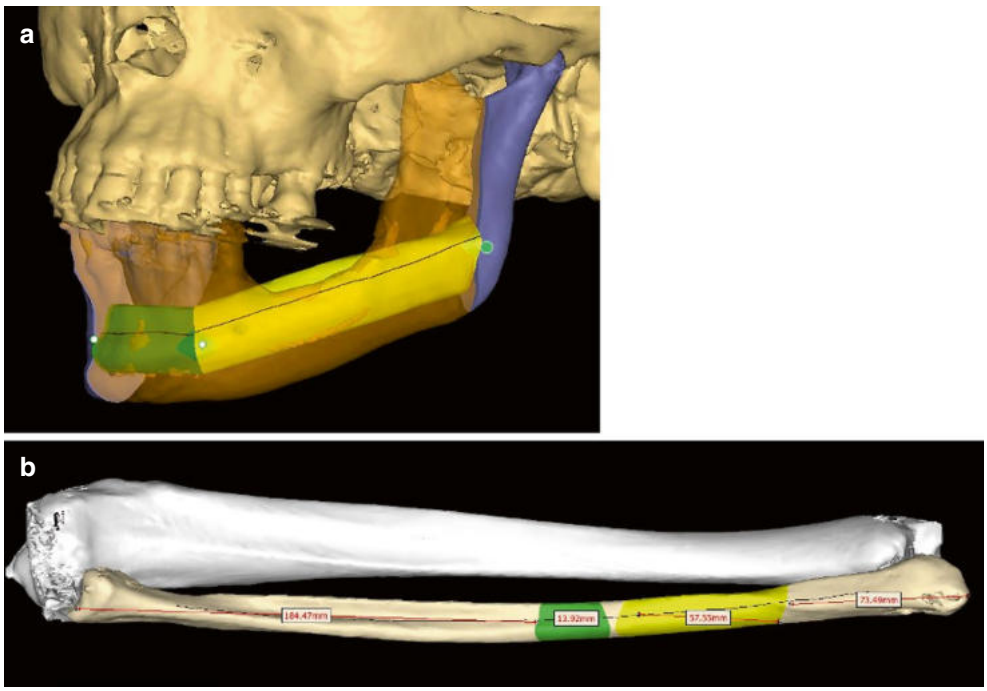


Fig. 37 (**a**) Position of the fibula segments in the native mandible after virtual tumoral resection. The height and rotation of the fibula parts are essential parameters to allow optimal implant placement. *Purple*: Remaining mandible segments; *translucent orange*: resected mandible; *green* + *yellow*: two-piece fibula for mandibular reconstruction. (**b**) Visualization of the right tibia and fibula bones. In yellow and green, the corresponding fibula parts are visible. The length of the fibular segments and distance toward lateral malleolus and fibula head are visualized (red text boxes). (Under CC BY license [14])

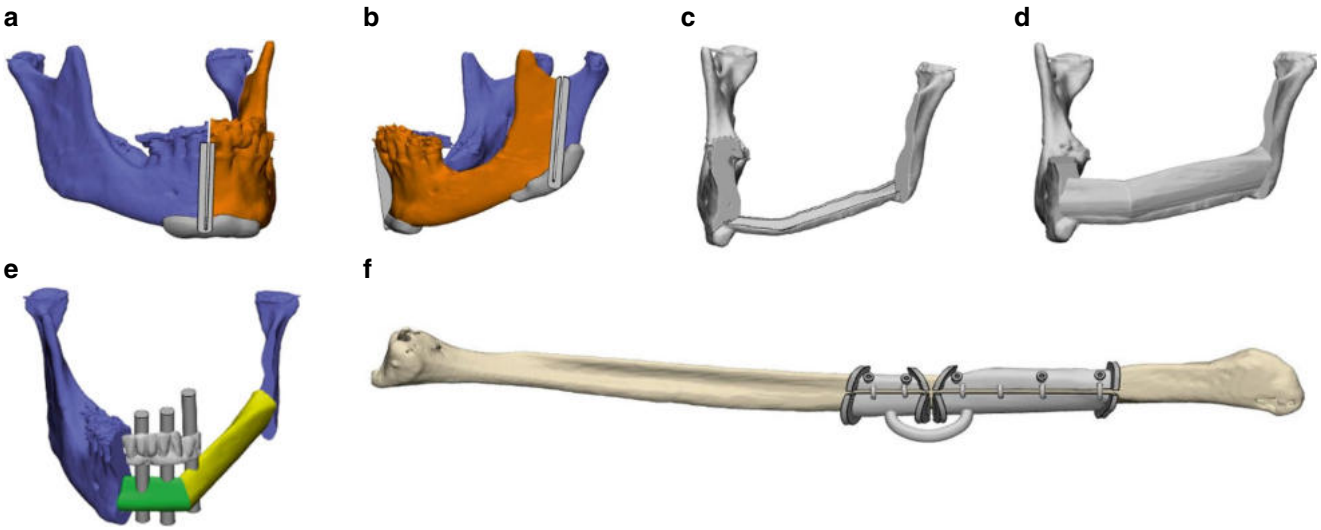


Fig. 38 (**a**, **b**) Cutting guides for the right and left mandibular osteotomy. (**c**) Positioning model with vertical support for positioning of the fibular segments. (**d**) Neomandible for prebending of the reconstruction plate. (**e**) Neomandible and intraoral scan of the dentition for height estimation of the fibula segments. The dental implant position is visualized with 5 mm diameter cylinders. (**f**) Initial cutting guide for fibula osteotomies. (Under CC BY license [14])

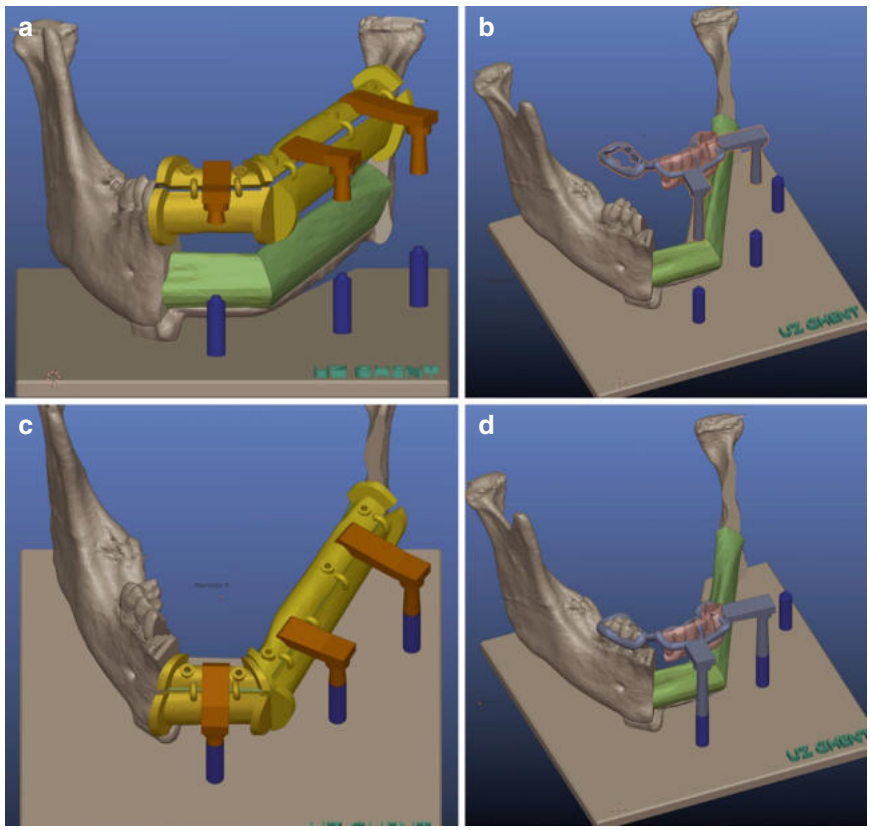


Fig. 39 (**a**, **c**) Connecting three attachment cylinders with three connecting arms to position the fibula guide and fibula parts in a correct position. (**b**, **d**) Connecting two attachment cylinders with two connecting arms and an extension toward the native dentition to position the provisional prosthesis. (Under CC BY license [14])

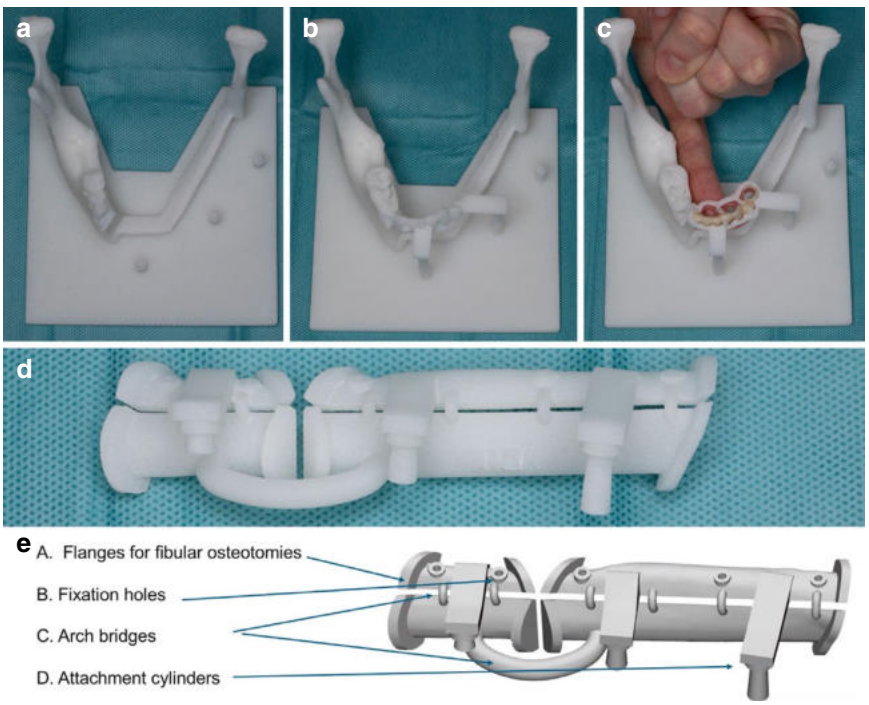


Fig. 40 (**a**) Base plate with three attachment cylinders to connect the fibula cutting guide into optimal fibular positioning. The same attachment cylinders are used for the positioning of the stackable guides for implant placement and prosthesis positioning. A supporting sleeve, bridging the remaining native mandibular parts, allows correct vertical positioning of the fibular parts. (**b**) Base plate with stackable implant drill guide connected to the attachment cylinders and to the right mandibular teeth using a supporting extension. This guide holds occlusal drill holes for positioning of the dental implants in the fibular segments. (**c**) Base plate with stackable prosthesis guide (white) and the provisional prosthesis positioned in the correct vertical dimension. (**d**, **e**) Fibula guide with sufficient contact surface to provide accurate positioning on the fibula; Sleeves for fixation to the fibula with 1.5 mm screws; 2 mm arch bridges to connect both superior and inferior surface areas; flanges serving as cutting guides; connection arms for positioning of the fibula parts on the stackable base plate; 5 mm arch bridge connecting the two fibula guide parts. (Under CC BY license [14])

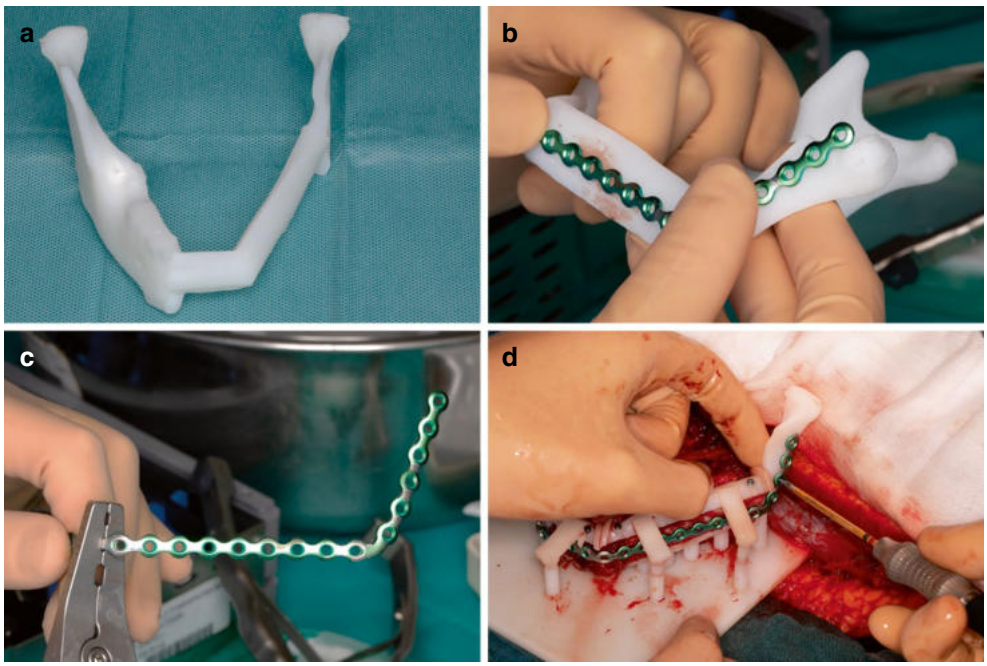


Fig. 41 (**a**) A 3D model of the neomandible. (**b**) The reconstruction plate is placed on the neomandible model, starting from the condyle. (**c**) The plate is adjusted using a surgical marker and folding pliers. (**d**) The final folded reconstruction plate is fixed to the fibular pars, guided by the stackable guides. The drill guide on the stackable guides ensures the prosthetic position independent of small rotations or translation that occurred during fibular part fixation. (Under CC BY license [14])

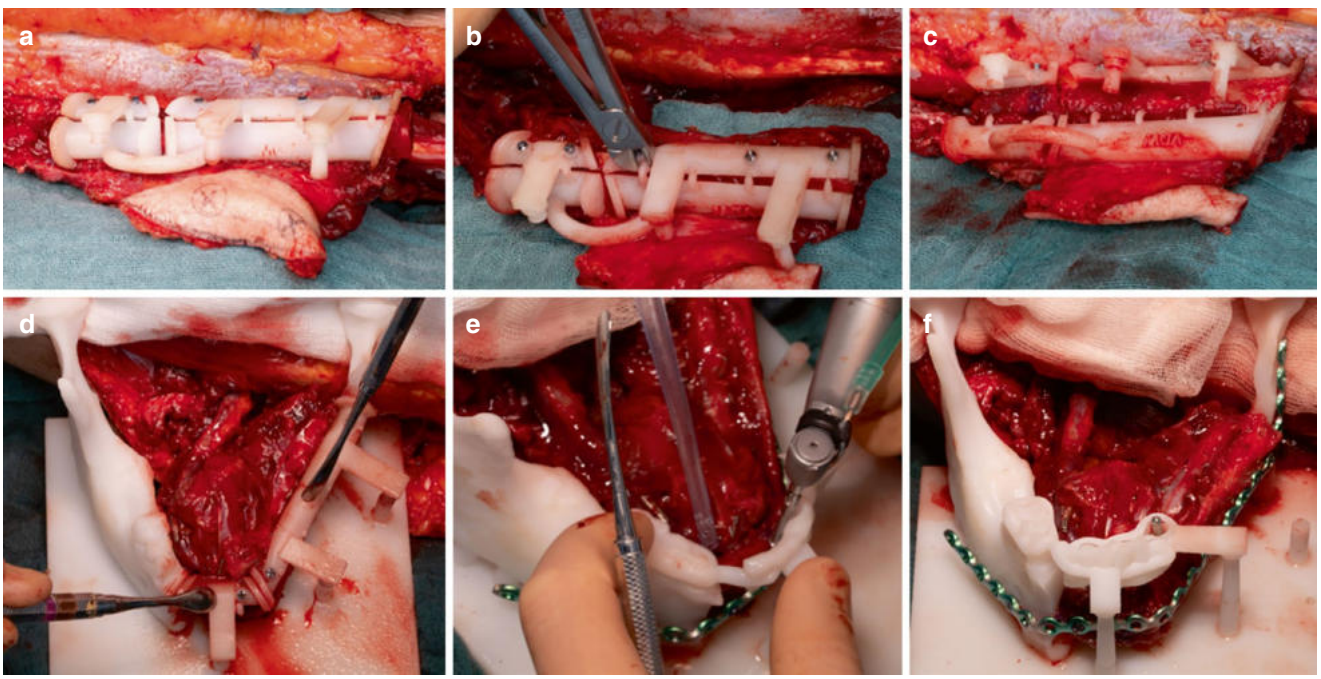


Fig. 42 (**a**) Fibula cutting guide fixed with 1.5 mm screws on the right fibula with attached skin island. (**b**, **c**) After performing the fibula osteotomies, the 2 mm arch bridges are cut to remove the lower part of the fibula cutting guide. (**d**) Positioning of the fibula parts using the connection arms of the fibula cutting guide to the base plate attachment cylinders. The lower sleeve ensures the correct vertical position of the fibula graft. (**e**) Fixation of the prebended 2.3 mm KLS Martin reconstruction plate with locking and non-locking screws. After removal of the upper part of the fibula cutting guide, the stackable implant drill guide guides correct dental implant positioning. (**f**) Placement of the stackable prosthetic guide to check implant position before connecting the provisional prosthesis. (Under CC BY license [14])



Fig. 43 (**a**) Neomandible with vascularized fibula parts positioned and fixed to the reconstruction plate. Temporary prosthesis fixed to three Bredent classic SKY 4.0x10 mm dental implants. Fibula construct still attached to the pedicle. (**b**) Fibula construct after sectioning of the pedicle with attached skin island and flexor hallucis longus muscle flap for transfer to the patient's mouth. (**c**) Fibula construct positioned in occlusion and fixed with locking and non-locking 2.3 mm screws to the mandible. (Under CC BY license [14])

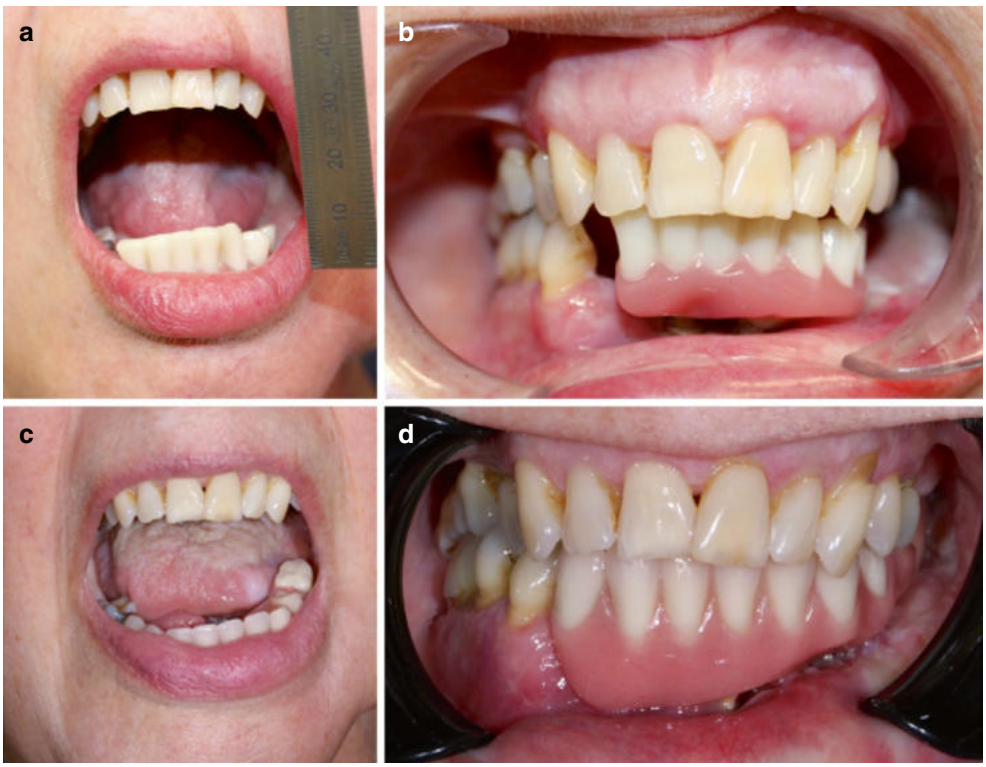


Fig. 44 Follow-up photographs 2 month (**a**, **b**) and 9 month (**c**, **d**) after surgery. (**a**) Good temporomandibular function with mouth opening of approximately 25 mm. (**b**) Provisional dental prosthesis fixed on dental implants with stable occlusion. (**c**) Stable temporomandibular function after radiochemotherapy. (**d**) Stable occlusion with the final prosthesis in place. (Under CC BY license [14])

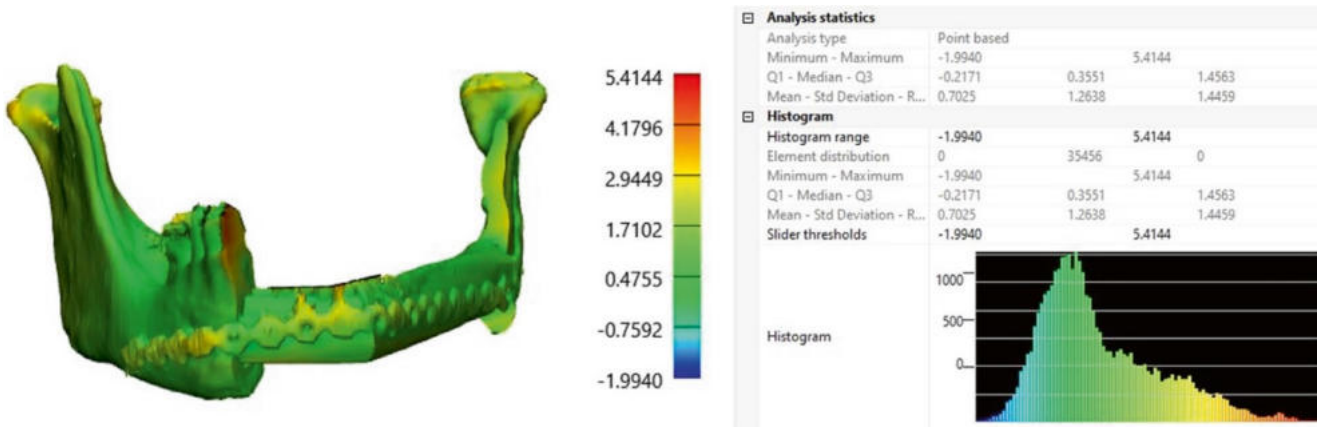


Fig. 45 Superimposition between VSP and postoperative CT. Mean difference of 0.70 mm (range −1.99–5.4 mm). (Under CC BY license [14])

(brown) in Blender v3.6 with the Blenderfordental add-on (Fig. 39)
4. 3D printing and assessment of the modular stackable guide system (Fig. 40)
5. Prebending process for the reconstruction plate (Fig. 41)
6. Surgical steps for guide positioning (Fig. 42)
7. Finalization of the fibula construct (Fig. 43)
8. Postoperative clinical images (Fig. 44)
9. Superimposition of preoperative planning and postoperative result (Fig. 45)

8.2 Case 2: Innovative 3D-Printed Implant-Retained Splint for Vestibuloplasty After Osseous Mandibular Reconstruction

The altered anatomy of the neomandible with FFF makes it difficult to fit a mucosa-supported denture. Today, computer-aided design/manufacturing (CAD/CAM) techniques allow clinicians to create customized implant-supported splints, preventing the potential recurrence of insufficient vestibular depth.

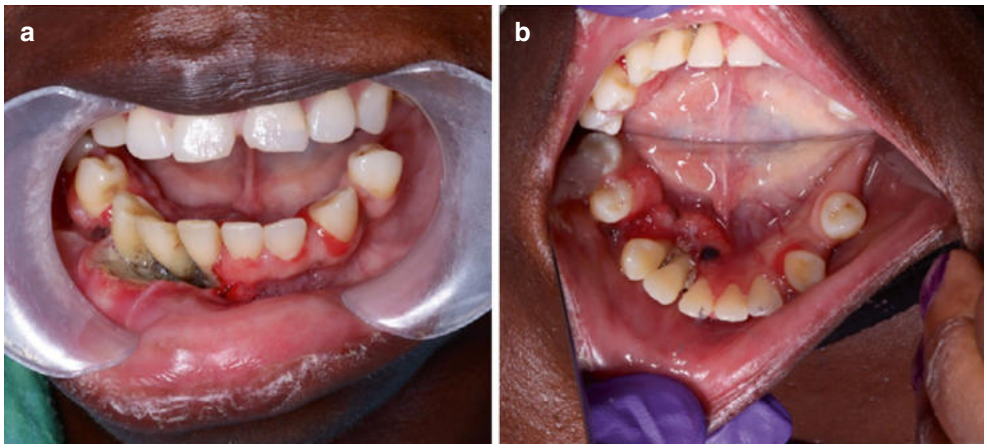


Fig. 46 (**a**, **b**) Preoperative clinical situation of squamous cell carcinoma (SCC) of the right anterior mandible

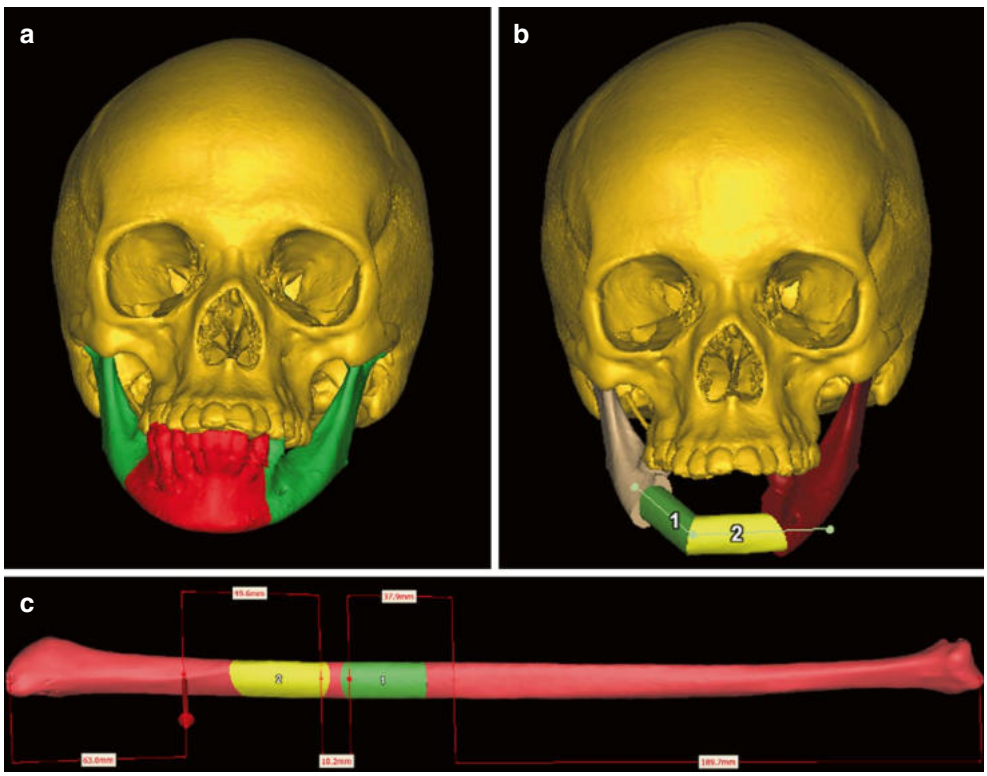


Fig. 47 (**a**) A virtual model of the patient. *Yellow*: cranium; *green*: remaining native mandible after resection; *red*: planned resection of the mandible. (**b**) Reconstruction of the mandible with a free fibular flap from the lower left leg. (**c**) Position of the fibular segments (*Yellow* & *green*) on the left lower fibular bone (*Red*)

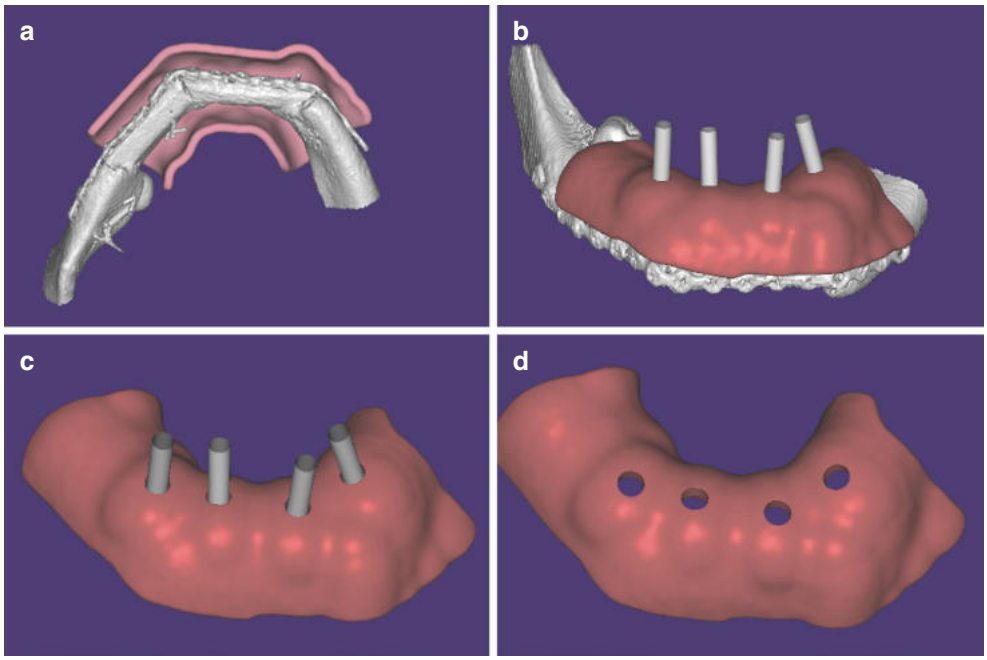


Fig. 48 (**a**) Caudal view, illustration of a 4 mm gap around the fibula. (**b**) Primary design with dental arch and buccal and lingual flanch just above the reconstruction plates. (**c**) Final design with implant sleeves (gray cylinders) making room for temporary cylinders during the intra-operative phase. (**d**) Final design after subtraction of the implant sleeves

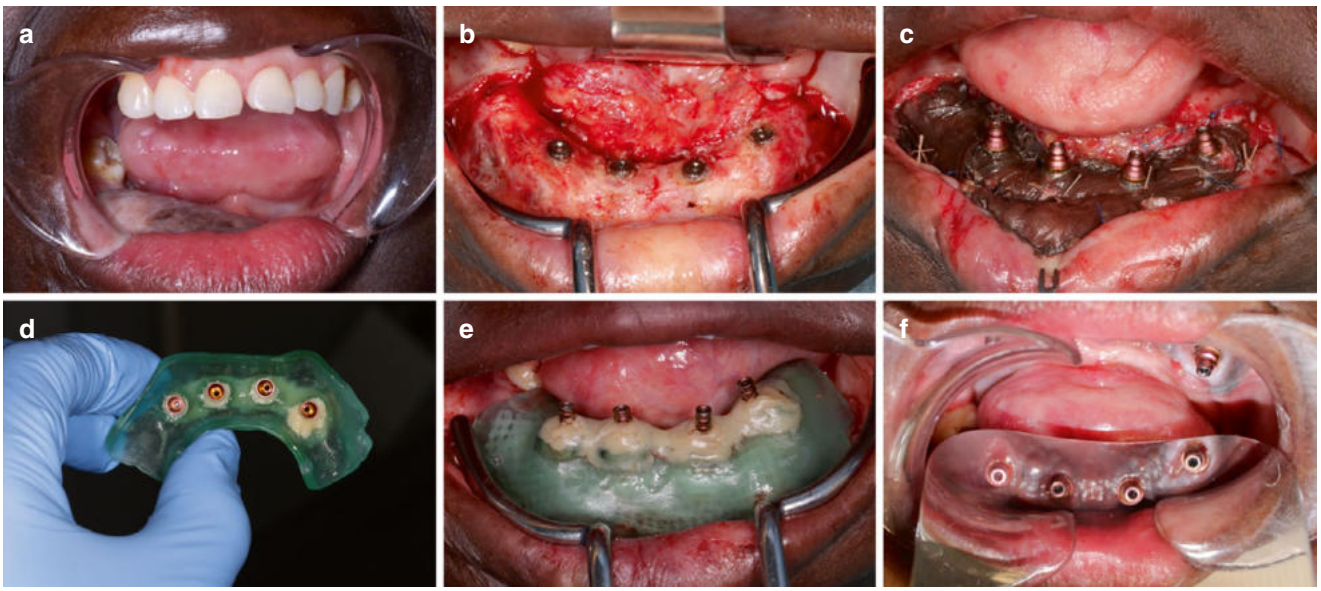


Fig. 49 (**a**) The thick FFF flap indicates the need for soft tissue modifications. (**b**) Situation after deepening of the vestibule. (**c**) Image after placement of the STG. Ethilon 5/0 and Vicryl 5/0 fix the skin flap to the new vertical vestibular level. (**d**) Implant-retained splint. Temporary cylinders are fixated with dental composite resin. (**e**) Placement of the splint on the implants compressing the wound dressing on the skin graft. Temporary cylinders are visible through the splint. (**f**) Postoperative situation (3 weeks) after removal of the splint. Reconstruction of the oral vestibule and thin keratinized gingiva has occurred

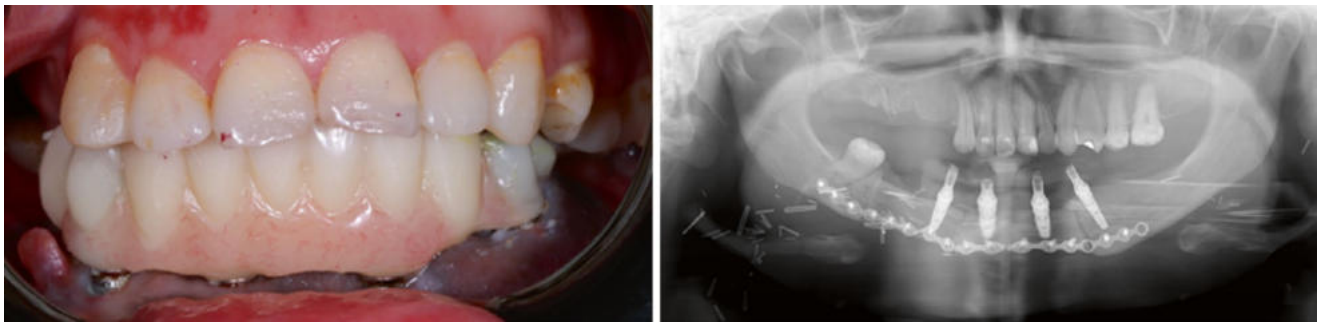


Fig. 50 Postoperative result after definitive dental restoration. Remark the space under the prosthesis to allow adequate dental hygiene

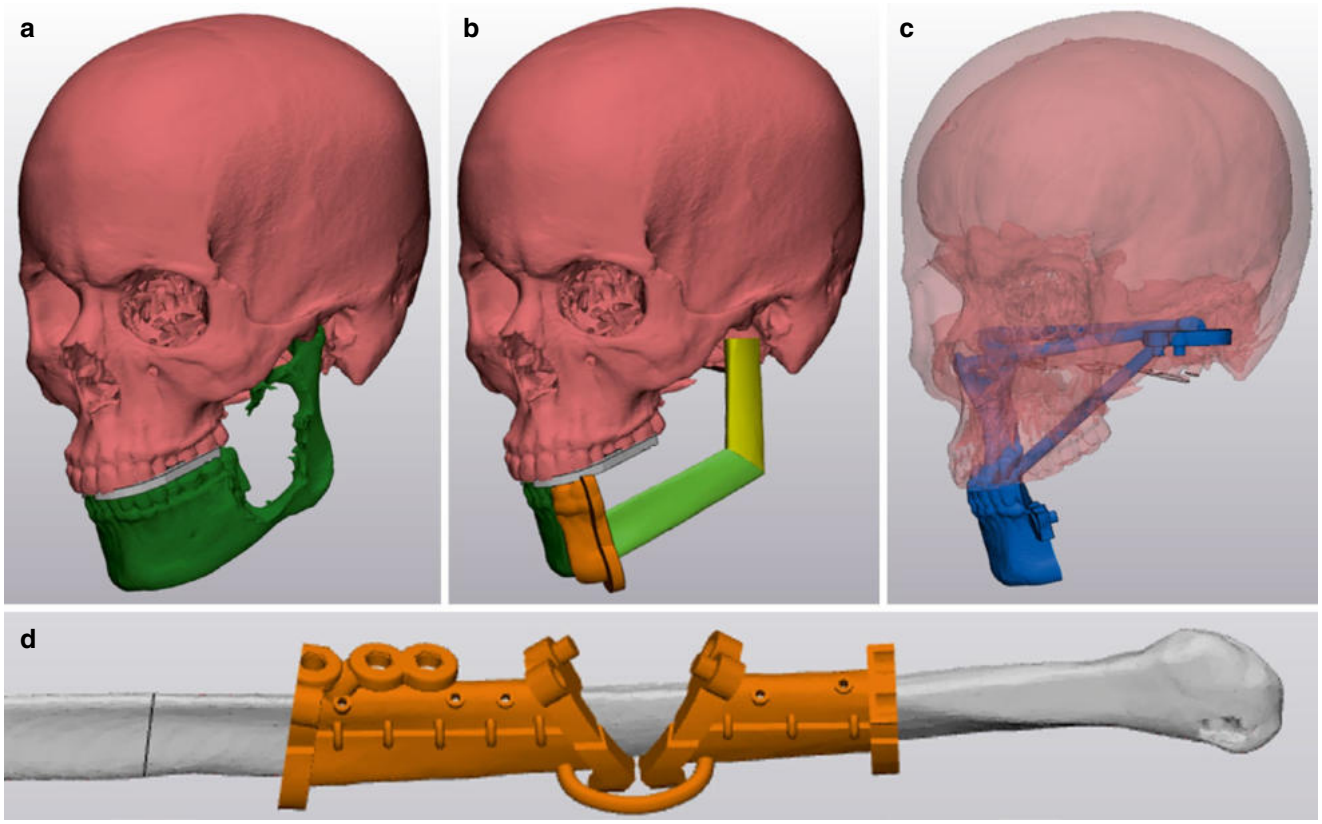


Fig. 51 (**a**) Preoperative situation of the mandible (green) and skull (red) with oral wafer for correct dental occlusion (gray). (**b**) Virtual surgical resection using a mandibular cutting guide (orange) and reconstruction with a two-segment free vascularized fibula graft (green and yellow). (**c**) Mandibular repositioning guide (blue) with cylindrical connection components to hold the surgical fibular cutting guide, allowing efficient relocation of the right condylar position. (**d**) Cutting guide for the right fibula (orange). The fibula is divided into two components. The guide consists of two horizontal sections connected by cylindrical guide bridges. This cutting guide is also equipped with a cylindrical connection system compatible with the surgical mandibular repositioning guide (Fig. 1c). Additionally, a fully guided dental implant sleeve was added using the Codiagnostix program for the placement of dental implants using an immediate loading protocol

1. Preoperative evaluation (Fig. 46)
2. VSP of the tumor resection and mandibular reconstruction (Fig. 47)
3. VSP of the implant-retained splint for vestibuloplasty (Fig. 48)
4. Intraoperative images of computer-assisted vestibuloplasty (Fig. 49)
5. Postoperative result (Fig. 50)

8.3 Case 3: Jaw-in-a-Day: Immediate Loading of Fibular Reconstruction Using Fully Guided Drill Guides

1. Virtual surgical planning of an ameloblastoma invading the left mandible using a free vascularized fibula graft from the right leg (Fig. 51)

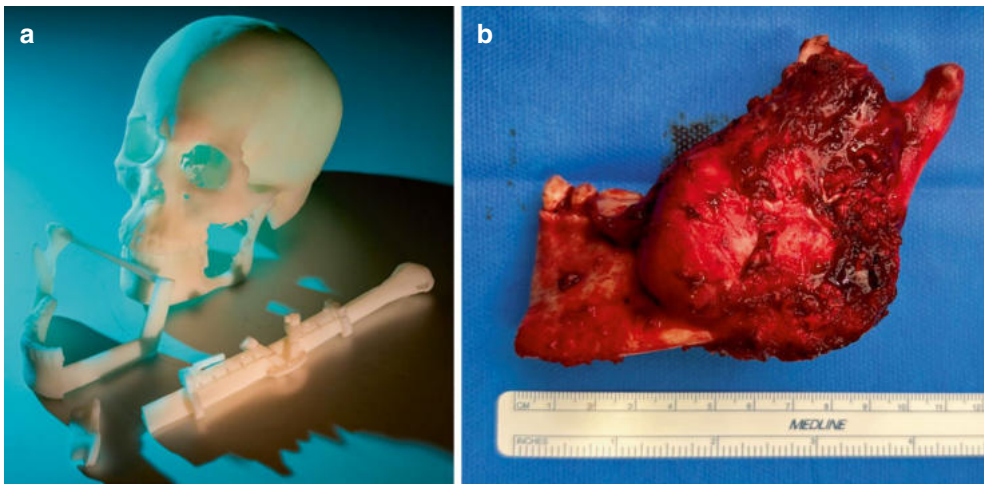


Fig. 52 (a) Clinical images of the surgical 3D models and surgical cutting guides. From left to right: mandibular neomandible, mandibular cutting guide, skull with tumor-invaded mandible in correct dental occlusion, right fibula bone with fibular cutting guide. (b) Surgical resection specimen of the ameloblastoma in the left mandible. The left condyle was completely resected

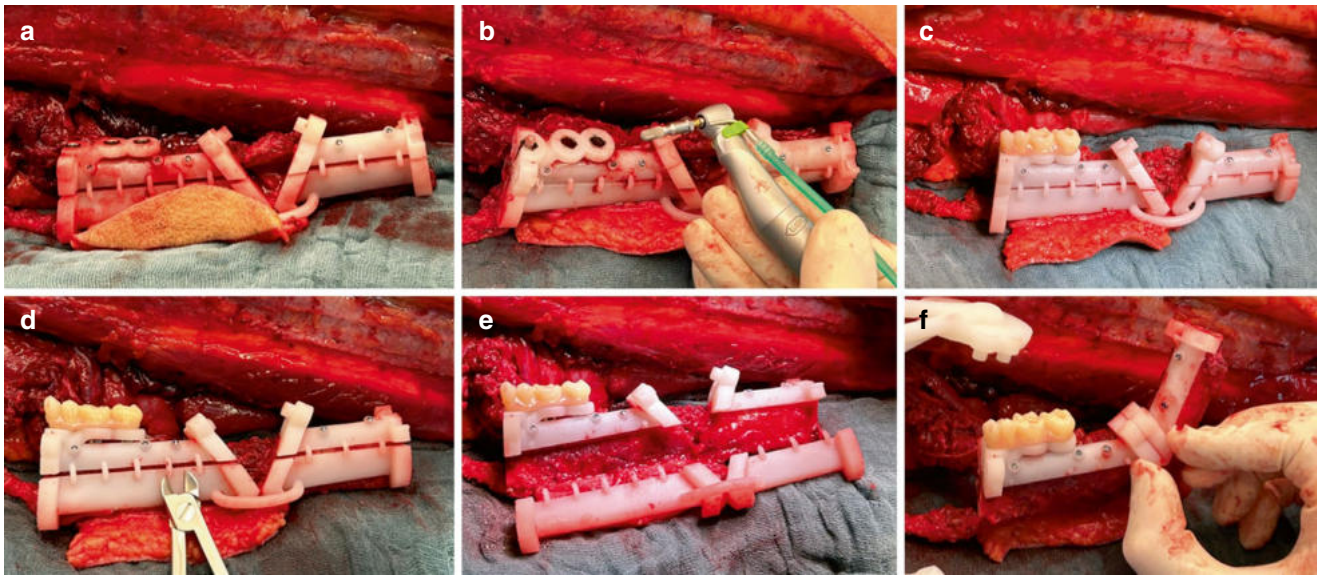


Fig. 53 (**a**) The fibular cutting guide was fixed to the right fibula using 5 KLS Martin 1.5 screws. The flanges marked the osteotomy lines and osteotomies were performed with a piezotome. (**b**) Using the fully guided drill sleeves, the drilling protocol for Bredent implants was executed and three implants (Bredent Blue SKY) were placed. The drill guide for the implants was pre-positioned at the correct height during the virtual surgical planning (VSP). (**c**) The provisional prosthesis was attached to the three placed implants using composite. (**d**) The guide bridges were separated using cutting pliers. (**e**) Removal of the inferior section of the fibular cutting guide. (**f**) The cylindrical connection system allowed the two fibular segments to be angulated in the correct position. The fibula flap remained vascularized throughout the entire procedure

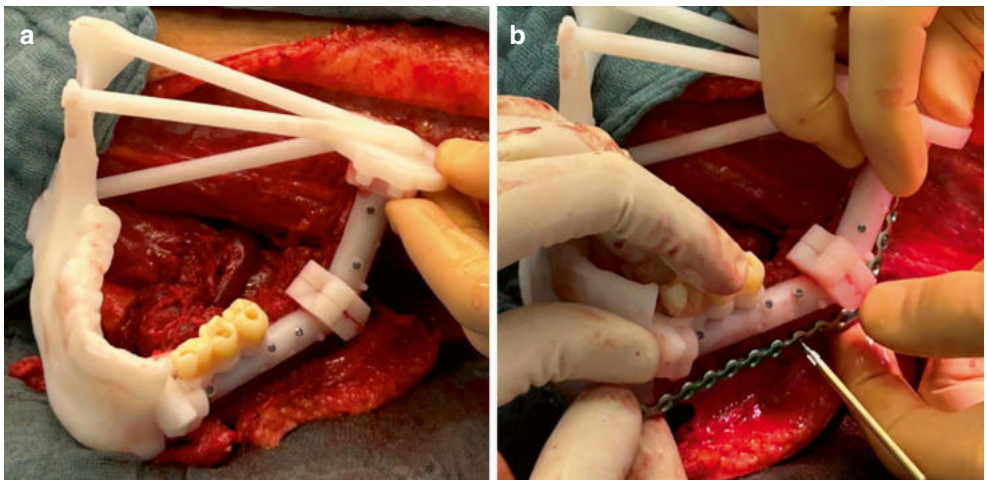


Fig. 54 (**a**) Using the cylindrical connection system, the mandibular repositioning guide and the fibular cutting guide were connected, ensuring the correct position of fibula segments according to the initial virtual surgical planning (VSP). (**b**) By removing the inferior section of the fibular cutting guide, a prebended reconstruction plate (KLS Martin 2.3) could be safely fixated to the fibular parts using KLS Martin 2.0 screws

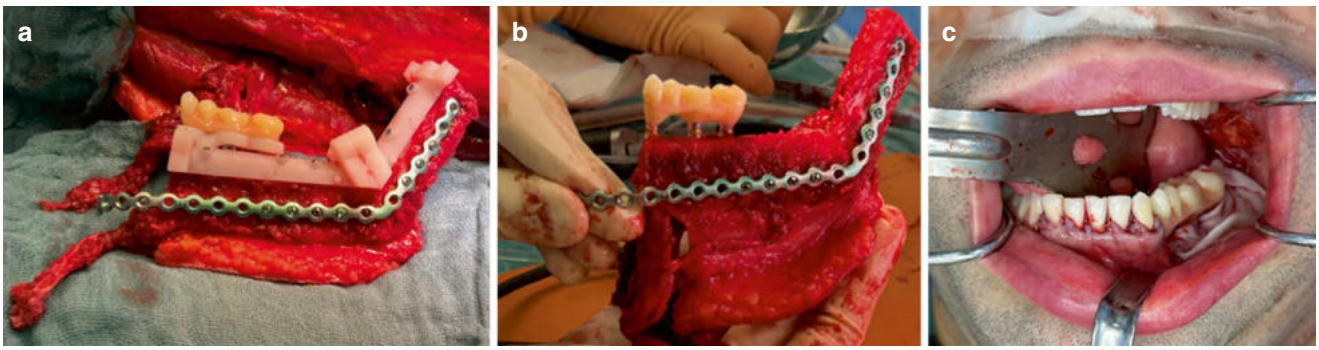


Fig. 55 (**a**) After removing the mandibular repositioning guide, the final result became visible. (**b**) The prosthetic restoration was removed from the implants to allow for the complete removal of the fibular cutting guide. The prosthesis was polished and reinserted. (**c**) Oral view of the final clinical situation. Using the oral wafer, the fibular construct was connected to the native mandible in the correct dental position. A skin graft was applied to the fibular parts and held in position using thermoplastic material

2. Clinical images of the surgical 3D models and cutting guides (Fig. 52)
3. Osteotomy of the free vascularized fibula graft and placement of dental implants following the immediate loading protocol (Fig. 53)
4. Applications of the fibula repositioning guide (Fig. 54)
5. The complete fibula reconstruction (Fig. 55)

References

1. Su Y-XR, Ganry L, Ozturk C, Lohman R, Al Afif A, McSpadden R, Frias V, Pu JJ. Fibula flap reconstruction for the mandible: why it is still the workhorse? Atlas Oral Maxillofac Surg Clin North Am. 2023;31:121–7.
2. Wallace CG, Chang Y-M, Tsai C-Y, Wei F-C. Harnessing the potential of the free fibula osteoseptocutaneous flap in mandible reconstruction. Plast Reconstr Surg. 2010;125:305–14.
3. Maben D, Anehosur V, Kumar N. Assessment of donor site morbidity following fibula flap transfer. J Maxillofac Oral Surg. 2021;20:258–63.
4. Mochizuki Y, Omura K, Harada H, Marukawa E, Shimamoto H, Tomioka H. Functional outcomes and patient satisfaction after vascularized osteocutaneous scapula flap reconstruction of the mandible in patients with benign or cancerous tumours. Int J Oral Maxillofac Surg. 2014;43:1330–8.
5. Blumberg JM, Walker P, Johnson S, et al. Mandibular reconstruction with the scapula tip free flap. Head Neck. 2019;41:2353–8.
6. Ritschl LM, Fichter AM, Grill FD, Hart D, Hapfelmeier A, Deppe H, Hedderich DM, Wolff K-D, Mücke T. Bone volume change following vascularized free bone flap reconstruction of the mandible. J Craniomaxillofac Surg. 2020;48:859–67.
7. Öhman D, Schaefer C, Nannmark U, Kjeller G, Malmström J. Mandible reconstruction with patient-specific implants: case report of five consecutive patients. Int J Oral Maxillofac Implants. 2019;34:e7–e11.
8. Tarsitano A, Ceccariglia F, Bevini M, Breschi L, Felice P, Marchetti C. Prosthetically guided mandibular reconstruction using a fibula free flap: three-dimensional Bologna plate, an alter-

native to the double-barrel technique. Int J Oral Maxillofac Surg. 2023;52:436–41.
9. Abou-Foul AK, Fasanmade A, Prabhu S, Borumandi F. Anatomy of the vasculature of the lower leg and harvest of a fibular flap: a systematic review. Br J Oral Maxillofac Surg. 2017;55:904–10.
10. Yadav PS, Ahmad QG, Shankhdhar VK, Nambi GI. Skin paddle vascularity of free fibula flap - a study of 386 cases and a classification based on contribution from axial vessels of the leg. Indian J Plast Surg. 2012;45:58–61.
11. Urken ML, Cheney ML, Blackwell KE, Harris JR, Hadlock TA, Futran N. Atlas of regional and free flaps for head and neck reconstruction: flap harvest and insetting. Lippincott Williams & Wilkins; 2012.
12. Raccampo L, Sembronio S, Tel A, Robiony M. Extended complex temporomandibular joint reconstructions exploiting virtual surgical planning, navigation assistance, and custom-made prosthesis: a comprehensive protocol and workflow. J Pers Med. 2023;13:931.
13. Michelutti L, Tel A, Zeppieri M, Ius T, Agosti E, Sembronio S, Robiony M. Generative Adversarial Networks (GANs) in the field of head and neck surgery: current evidence and prospects for the future-a systematic review. J Clin Med. 2024;13:3556.
14. Ureel M, Boderé P-J, Denoiseux B, Corthouts P, Coopman R. Mandibular reconstruction with osseous free flap and immediate prosthetic rehabilitation (jaw-in-a-day): in-house manufactured innovative modular stackable guide system. Bioengineering. 2024;11:1254.
15. Ong A, Williams F, Tokarz E, Shokri T, Hammer D, Ducic Y. Jaw in a day: immediate dental rehabilitation during fibula reconstruction of the Mandible. Facial Plast Surg. 2021;37:722–7.
16. Williams FC. History of the jaw in a day. Oral Maxillofac Surg Cases. 2023;9:100306.

Full-Face Cranio-maxillo-facial Surgery Procedures

Alessandro Tel, Federico Bolognesi, Federico Biglioli, Silvano Ferrari, and Massimo Robiony

1 Introduction

Full-face craniomaxillofacial procedures include the most advanced surgeries before facial transplantation. There are basically two conditions in which full-face procedures are performed:

- Panfacial trauma, when the craniomaxillofacial skeleton is fractured in each of its thirds, including superior third and the orbital region, the midface and the mandible
- Reconstructive procedures performed using a combination of flaps, either as trauma sequelae in highly disruptive injuries, such as ballistic trauma, or as a consequence of extensive resections performed for oncological diseases or other conditions

This chapter will detail the workflow for such extended surgeries, in which anatomical references are lost and the reconstruction of the craniomaxillofacial skeleton from a structural and functional perspective relies on the surgeon's knowledge. Virtual surgical planning plays a crucial role in defining the optimal strategy to accomplish this complex task, combining occlusal concepts with advanced anatomical reconstruction.

2 Panfacial Trauma

Panfacial trauma refers to the simultaneous presence of occlusion-impairing and occlusion-non impairing fractures across all the thirds of the craniofacial skeleton, including the cranio-orbital area, the midface, and the mandible. It is often the result of a high-energy injury, in most cases violent road accidents or precipitations from several meters. In several cases, skullbase fractures with the presence of CSF leak coexist and should be appropriately managed according to the protocols elucidated in Chapter "Virtual Planning in Frontal Sinus and Anterior Skullbase."

The most complex issue in approaching VSP for complex panfacial trauma is surgical sequencing [1]. In contrast with both occlusion-impairing and occlusion non-impairing trauma, in which an anatomical reference can be found respectively in surgical occlusion or anatomical reduction, in complex panfacial trauma, there is the alteration of all diameters and dimensions of the craniofacial skeleton, as well as the occlusion is lost. Thus, in panfacial trauma such classifications are convergent and do not define separate approaches [2].

As described by the same author [3], panfacial fractures affect each subunit of the craniofacial skeleton, by simultaneously involving upper, middle, and lower third, with the loss of aesthetical and functional relationships between facial areas.

A. Tel (✉)
Lead Specialist for VSP and 3DP, Maxillofacial Surgery Clinic, Head & Neck and Neuroscience Department, Academic Hospital of Udine, Udine, Italy
e-mail: alessandro.tel@uniud.it

F. Bolognesi
Attending Maxillofacial Surgeon, Division of Maxillofacial surgery, Head and Neck Department, San Paolo Hospital, University of Milan, Milan, Italy
e-mail: federico.bolognesi@unimi.it

F. Biglioli
Chief of Maxillofacial Surgery Department, Postgraduate School of Maxillofacial Surgery, Division of Maxillofacial surgery, Head and Neck Department, San Paolo Hospital, University of Milan, Milan, Italy
e-mail: federico.biglioli@unimi.it

S. Ferrari
Chief of Maxillofacial Surgery Department, Postgraduate School of Maxillofacial Surgery, Division of Maxillofacial surgery, University Hospital of Parma, Parma, Italy
e-mail: silvano.ferrari@unipr.it

M. Robiony
Chief of Maxillofacial Surgery Clinic, Director of the Postgraduate School in Maxillofacial Surgery, Chief of Head & Neck and Neuroscience Department, Academic Hospital - University of Udine, Udine, Italy
e-mail: massimo.robiony@uniud.it

© The Author(s), under exclusive license to Springer Nature Switzerland AG 2025

A. Tel, M. Robiony (eds.), *Atlas of Virtual Surgical Planning and 3D Printing for Cranio-Maxillo-Facial Surgery*,
https://doi.org/10.1007/978-3-031-94495-6_25

As the issue of surgical sequencing was a matter of debate in the literature [4] and no previous paper presented it under the scope of VSP, the author proposed a four-cluster classification based on common features that can be assessed in different scenarios of panfacial trauma (Fig. 1). The two main critical elements that play a role in both VSP and surgical sequencing are the following:

- Presence of any condylar fracture: it is a priority to perform the anatomical reduction of any condylar fracture before adjusting the occlusion. It suggests a bottom-up approach.
- Presence of bilateral ZMC fracture: ZMC represents the most robust region of the midface, and it is often a stable point for anatomical reduction, especially in centrofacial injuries. A unilateral ZMC does not represent a problem, as it enables to use the mirrored healthy ZMC as a reference. On the contrary, bilateral ZMC results in the loss of the facial transverse diameter, and virtual anatomical reduction has to be performed. A top-down approach can be valuable as it enables to address first issues related to facial proportions.
- When both conditions coexist (type IV), the author suggests initiating the process with a bottom-up approach, addressing first the condylar fracture reduction and related occlusal impairment. Subsequently, before performing the fixation of the maxilla to the zygomas, transverse facial proportions should be evaluated under the guidance of image-guided methods, starting with the fixation across the fronto-orbital buttresses and proceeding with the zygomatic arch and inferior orbital rim.

2.1 The Bottom-Up Approach (Occlusion-Centric)

When occlusion is lost, its reestablishment as a core functional element plays a prominent importance. This occlusion-centric approach is also referred to as "bottom-up approach" [5], indicating that reduction proceeds from the maxillomandibular complex to the upper regions of the craniomaxillofacial skeleton.

In the presence of a condylar fracture, this should be always reduced first, both in the VSP and during surgery, to reestablish the correct posterior facial height. Condylar fractures always undergo anatomical reduction [6].

In contrast with midfacial trauma or mandible trauma, seen respectively in Chapters "Virtual Planning and 3D Printing in Midfacial Trauma" and "Virtual Planning and 3D Printing in Mandibular Fractures," occlusal restoration in panfacial trauma cannot rely upon the intercuspal relationship with the unaffected antagonist, as both maxillary and mandibular fractures coexist. Thus, the occlusal relationship has to be established de novo. Thus, the correct realignment of scanned arches with the skeletal model achieved from segmentation is of prominent importance. Notably, scanned arches should be divided in points crossed by fracture lines, and individually realigned with their respective skeletal segments (Fig. 2). This step is important to improve dental cusp detail in each dentate segment, facilitating subsequent steps of reduction through thermoplastic cage splints (TCS) or conventional dental splints.

Subsequently, anatomical reduction of fractures segments within the maxilla and the mandible is accomplished, with

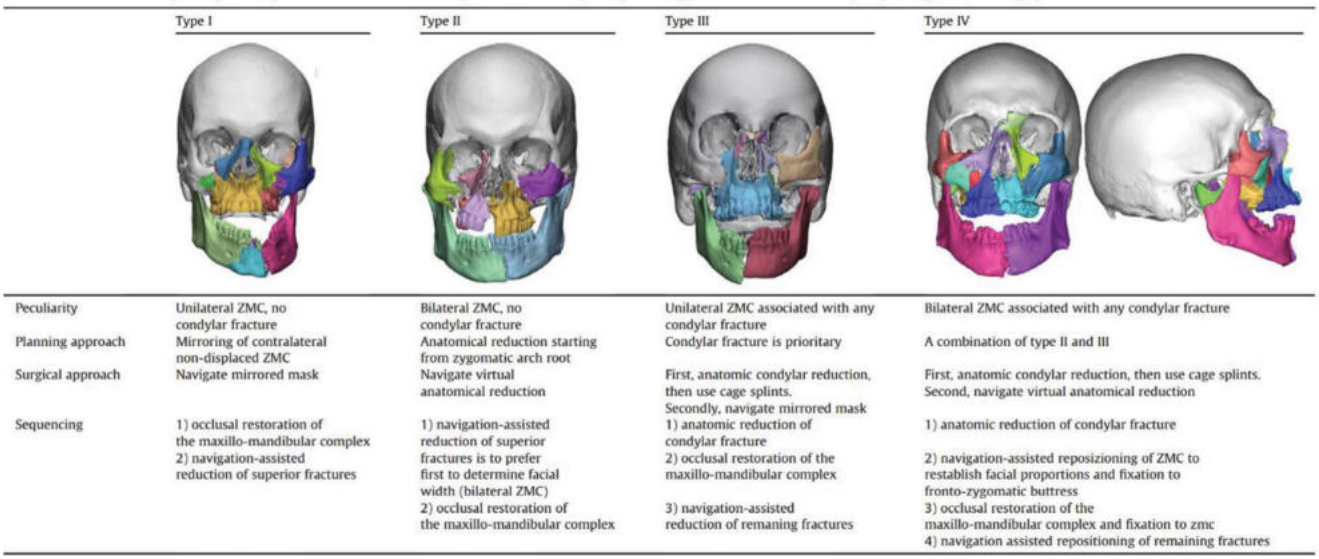


Fig. 1 Clusters identified based on planning and surgical similarities in our series of patients, and subsequent operative approaches both in Virtual Surgical Planning (VSP) and surgery

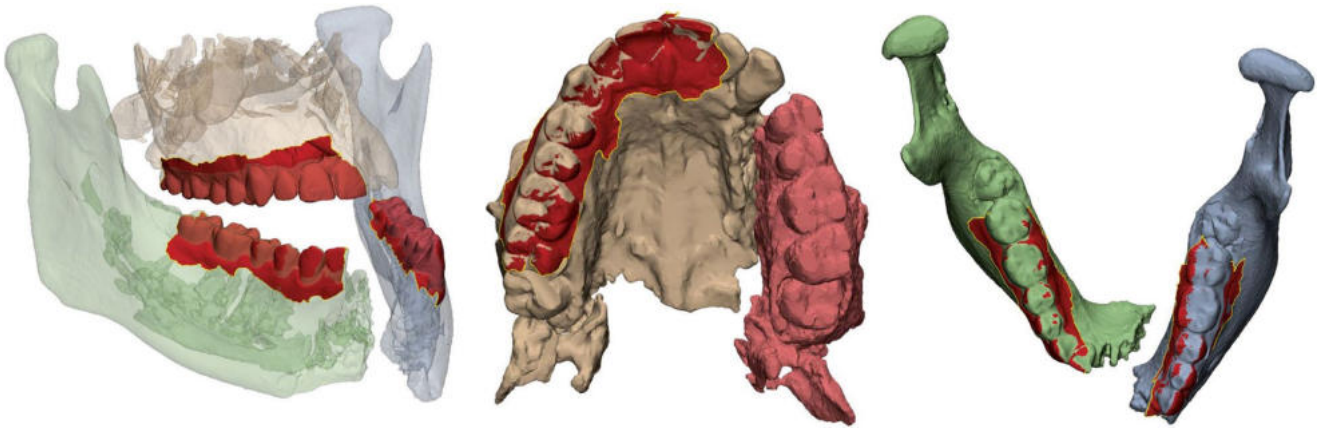


Fig. 2 **Scanned dental arches subunit realignment with corresponding skeletal fragments. It is important to maximize occlusal detail even if a full-arch scan is not achievable

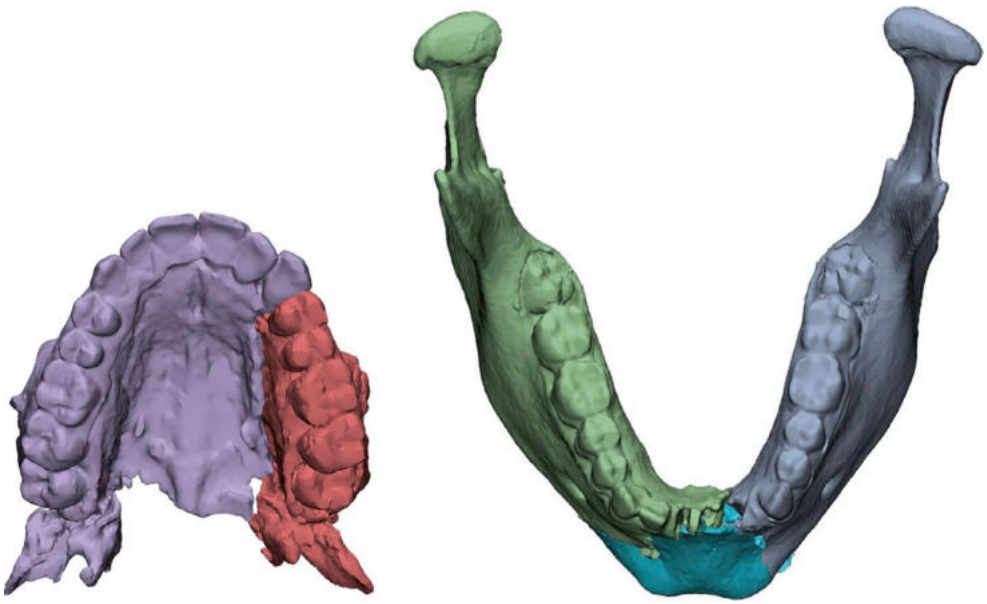


Fig. 3 Intra-arch reduction has to be coupled with anatomical reduction. The correct anatomical reduction also translates in arch integrity restoration. Reduced arches can then be 3D printed and assessed for the most stable intercuspation to define the surgical occlusion

the purpose of recreating dental arch continuity (intra-arch reduction). This step is performed entirely digital in the VSP software (Fig. 3). Once the correct engagement of dento-alveolar segments is established both in the maxilla and in the mandible, individual reduced superior and inferior dental arch models are 3D printed and set into the optimal intercuspal relationship. In this step, the experience of the surgeon in establishing both the optimal intra-arch reduction and the most stable inter-arch relationship is essential, as no entirely virtual occlusion algorithm is suitable for trauma. Once the most stable occlusion is found, it is scanned and used as a registration matrix to transfer the optimal relationship of the maxillomandibular complex (Fig. 4).

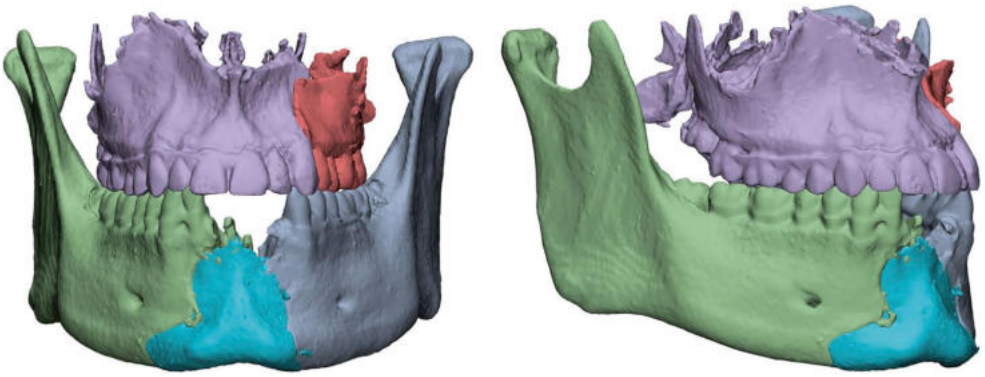


Fig. 4 Rescanned surgical occlusion is then transferred to the VSP to establish the optimal intercuspation between the reduced maxilla and mandible

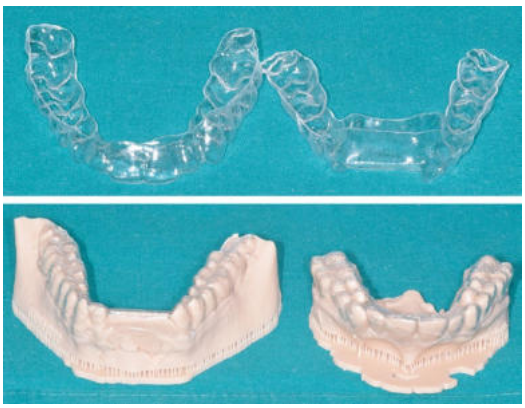


Fig. 5 TCS (reduction aligners, top panel) are passively positioned in reduced 3DP arches (bottom panel)

In this respect, computer-guided methods to restore the occlusion are based on TCS for intra-arch reduction and alignment of dento-alveolar fractures, and occlusal splints to restore inter-arch occlusal relationship. As seen in Chapter "Virtual Planning and 3D Printing in Midfacial Trauma," thermoplastic cage splints are thermoformed aligners that exert a contentive action on the dental arch, allowing to constrain segment in the virtually reduced position and providing intra-arch stabilization (Fig. 5). They can effectively replace arch bars and are entirely computer-generated on the reduction project. They are manufactured thin enough not to interfere with the occlusal splint. Eventually, a 0.3 offset is added to Boolean subtraction when creating the occlusal splint, accounting for the slight thickness of the TCS (Fig. 6). As an alternative to TCS, a single occlusal splint can be designed higher and more contentive, allowing the same contentive action as TCS.

At this point, the maxillomandibular complex in the correct occlusal relationship, along with the posterior facial height reestablished by the anatomical reduction of condylar fractures, provides the key landmark to perform reduction of upper regions, starting with the reconstruction of maxillomalar and maxillonasal buttresses. Fractures of the zygomatic arch are checked and treated to ensure the correct sagittal projection of the ZMC. Reconstruction then proceeds upward, stabilizing the inferior orbital rim and piriform rim, thus addressing NOE fractures, and is concluded by fixing the fronto-orbital rims (Fig. 7).

2.2 The Top-Down Approach (Anatomical Based)

While the bottom-up approach considers occlusion a priority and addresses it at the beginning of the sequence both in VSP and intraoperatively, and is mandatory in case a condylar fracture is assessed, the top-down approach focuses on restoring the correct facial proportions of the upper and middle thirds, using them as a stable anatomical landmark for maxillary fixation. Based on the position of the fixed maxilla, the mandible is set in the most stable occlusion [7]. This approach is recommended in cases of fractures of the zygomatic arch with severe alteration of the sagittal and trans-

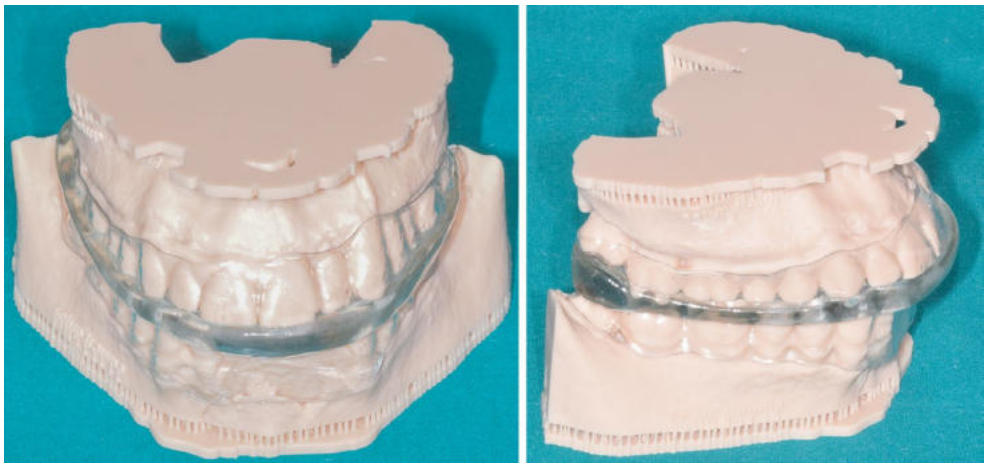


Fig. 6 A splint is extruded with a slightly increased offset (0.5 mm) to optimally fit TCS in place

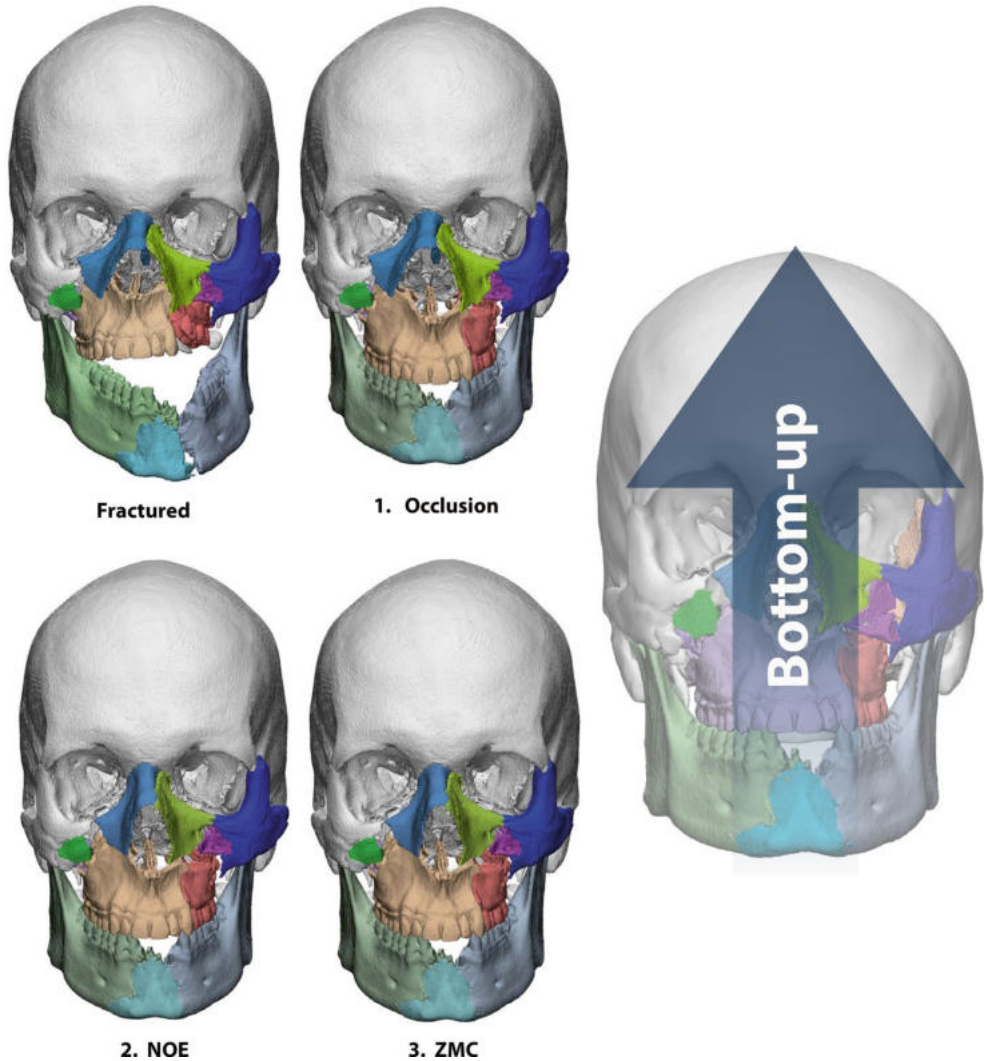


Fig. 7 Schematic illustration of the bottom-up approach, also defined "occlusion-centric" approach

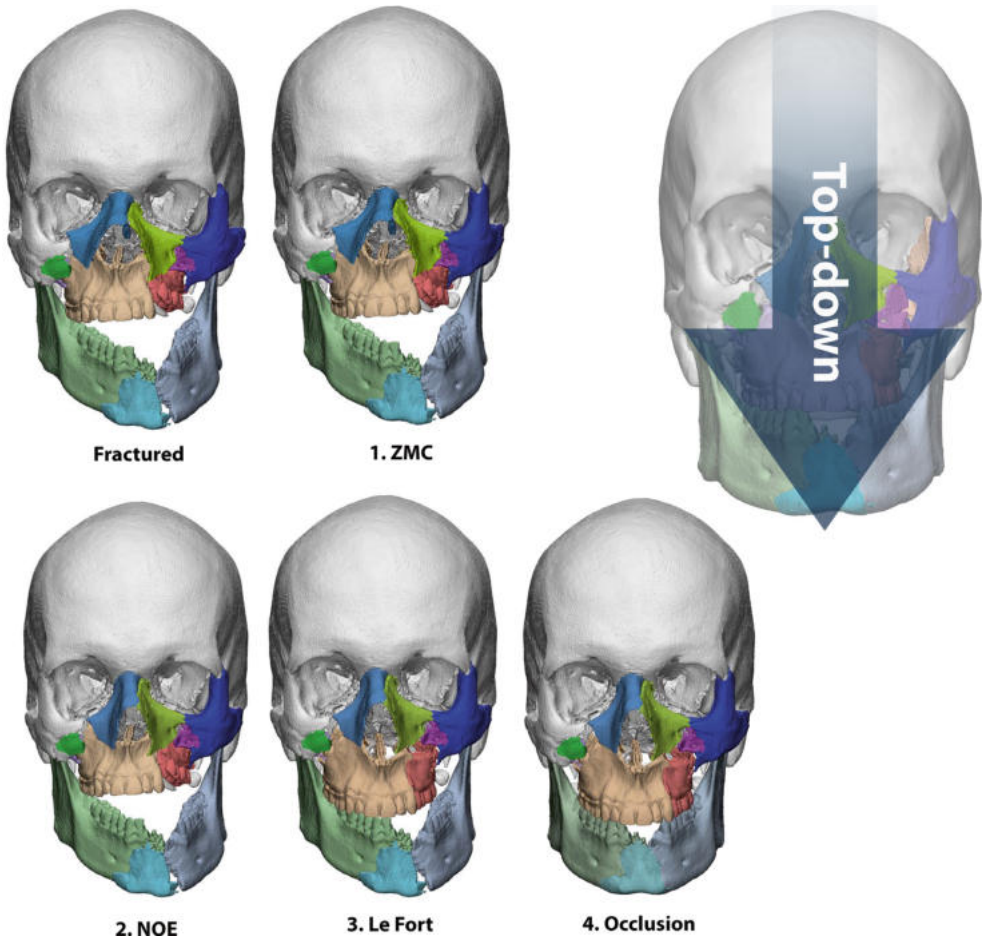


Fig. 8 Schematic illustration of the top-down approach, which privileges anatomical reduction

verse diameters, and most notably if the ZMC fracture is bilateral. In fact, a sided ZMC injury can be easily repositioned using mirroring-based methods, whereas a bilateral ZMC fracture with substantial facial enlargement is more difficult to address. In the absence of validated tools for artificial intelligence and inferential repositioning, establishing the correct facial proportions is a process left to the surgeon's experience. The author advises to address bilateral ZMC fractures by performing an accurate anatomical reduction based on the root of the zygomatic arch and the fronto-orbital rim. Respecting these two stable elements allows to effectively restore a reliable ZMC projection, both in the sagittal and in the axial planes. Figure 8 illustrates the top-down approach applied in the same case as the bottom-up approach.

Once this reduction is performed, the inferior orbital rim and the piriform aperture can be reconstructed, allowing to reposition eventual NOE fragments and reconstructing the root of the maxillonasal buttress. At this point, repositioned bone fragments are imported in Brainlab Elements (Brainlab, Munich, DE) for the navigation plan to effectively ascertain the appropriate projection during surgery (Fig. 9).

With both the maxillonasal and the maxillomalar buttresses restored, the maxilla can be effectively stabilized, acting as a repositioning template for the mandible as well. The mandible is set into the most stable occlusal configuration using an occlusal registration mask scanned from models.

2.3 Reality Beyond Schemes

A dichotomic categorization between the top-down and bottom-up approach is only conceptual and helps to establish phases of VSP. Nevertheless, both in VSP and surgery, there are situations in which sequences are interchangeable and thus should be personalized to each patient [8, 9]. For instance, a case presenting both with a bilateral ZMC and condylar fracture might benefit at first from the reduction of the condylar fracture (bottom-up), whose importance in restoring the posterior facial height has already been elucidated. However, the surgical access might be designed wider (hemicoronal rather than just preauricular) to fixate the root of the ZMC and the fronto-zygomatic rim under navigational guidance (top-down). Then, TCS and the occlusal splint are used to reposition the maxilla on the mandible in the most correct occlusal relationship (bottom-up). Subsequently, the inferior orbital rim and the nasofrontal suture might be



Fig. 9 Creation of the navigation plan by importing reduced segments in the navigation software Brainlab Elements

reduced and fixed to treat NOE fractures (top-down) and at the same time provide the maxillonasal buttress. Finally, the maxillomandibular complex, pivoted on the condylar hinge, is lifted and fixed both to the maxillomalar and the maxillonasal buttresses (bottom-up). This example illustrates how reality is much more complex and subject to variables, and how each VSP treatment plan should be highly personalized.

2.4 Case: Panfacial Trauma, Type I (Two-Piece Le Fort, NOE, Unilateral ZMC, Mandibular Multifocal, No Condyle)

This case explores the actual VSP and surgical strategy using the same patient described for the previous sections. The clinical scenario is described, and the real order of VSP and surgical procedures is detailed. The aim is to illustrate to the reader how both approaches, the top-down and the bottom-up, are interconnected and became personalized for this patient.

Clinical History

A 23-year-old patient was urgently sent to ICU after a car accident where he violently impacted against a truck. He reported multiple fractures in his limbs, pneumothorax, abdominal effusion, spleen rupture, and a complex cranio-maxillofacial trauma. The patient underwent CT scan which revealed a Le Fort I with significant posterior displacement and a parasagittal fracture with intrusion and rotation of a dentate segment, unilateral left ZMC, bilateral NOE, double mandibular parasymphyseal fracture with separation of the chin.

Consultants from maxillofacial surgery went in ICU where they performed intraoral scan using a laptop at the bed side, and STLs of severely disrupted dental arches were processed and transferred in 3-matic for processing.

Virtual Surgical Planning

Accurate segmentation with fracture-preserving thresholding was performed in Mimics, and then mask splitting helped define all subfragments needing reduction. In 3-matic, STLs of scanned dental arches were divided in correspondence of fracture lines, and each dentate segment was matched to its corresponding bone fragment isolated from CT scan, as seen in Fig. 2.

Dentate fragments were 3D printed and manually assessed to yield the most stabile surgical occlusion, which was scanned and transferred back to the VSP project. An occlusal splint was manufactured based on the scanned occlusion; moreover, 3D-printed dental arches were used as mold to shape a thermoplastic foil, enabling to create ultrathin, yet contentive, TCS, which did not interfere with occlusal splint (Figs. 5 and 6). The larger, right, Le Fort I segment was anatomically aligned with the unaffected right ZMC to restore the integrity of the piriform rim and the maxillomalar buttress. The smaller, left side of the Le Fort I, was anatomically reduced to rebuild intra-arch integrity. Likewise, occlusion was used to reposition both hemimandibles in the correct intercuspation, achieving the appropriate and functional

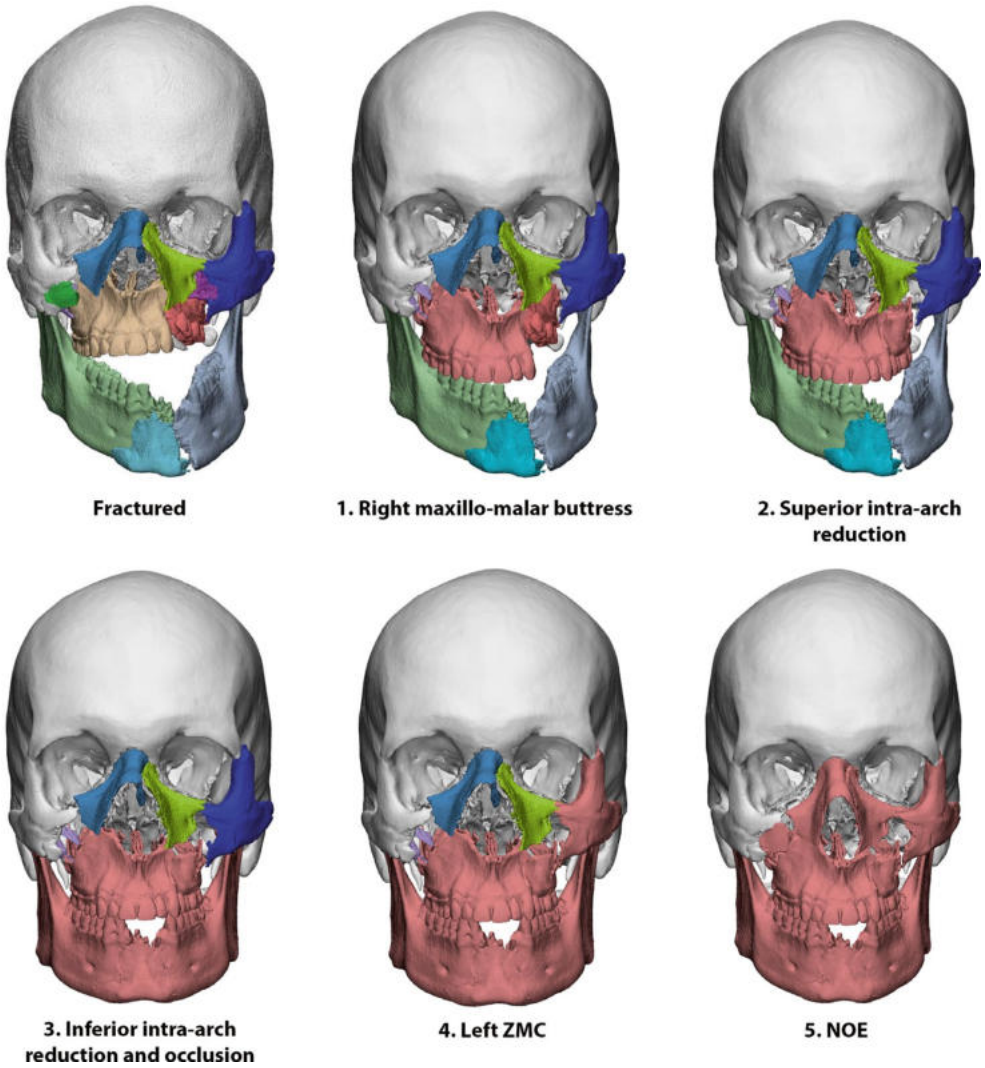


Fig. 10 The real approach to virtual (and subsequent surgical) reduction should be personalized combining elements both of the top-down and bottom-up approaches

reduction, after verifying the correct centric position of the condyle in the glenoid fossa. Last, the chin segment was anatomically reduced (bottom-up approach).

The unaffected ZMC on the right side was mirrored to create a digital repositioning template for the left displaced ZMC, providing its reduction. NOE fragments were anatomically reduced based on the fixed position of the frontonasal suture and ZMC; care was taken to effectively reconstruct the piriform rim (top-down approach). This process illustrates how the classical top-down and bottom-up approaches compenetrate each other to define a highly personalized sequence, tailored on the specific clinical case (Fig. 10).

Surgery

All fracture sites were surgically exposed using two subciliary incisions, a left frontotemporal access, a V-shaped glabellar access, an intraoral vestibular superior and inferior access for both the maxillary and the mandibular fractures. Under navigational guidance, using the mirrored mask from VSP as digital repositioning template, reduction of the right ZMC was achieved, with fixation in the frontotemporal suture with interactive control of its correct projection (Fig. 11). Le Fort I segment was mobilized and advanced using Rowe's disimpaction forceps. TCS were applied superiorly, enabling to rebuild the correct dental arch with reduction of the left Le Fort I hemi-segment, and inferiorly, facilitating the reduction of the mandibular fracture. Intermaxillary blockage was achieved with TCS in place, and le Fort segments were plated to ZMC, reconstructing the anatomical integrity of maxillomalar buttresses, as well as between each other. With both dentate hemimandible segments approached and stabilized by the TCS, reduction and

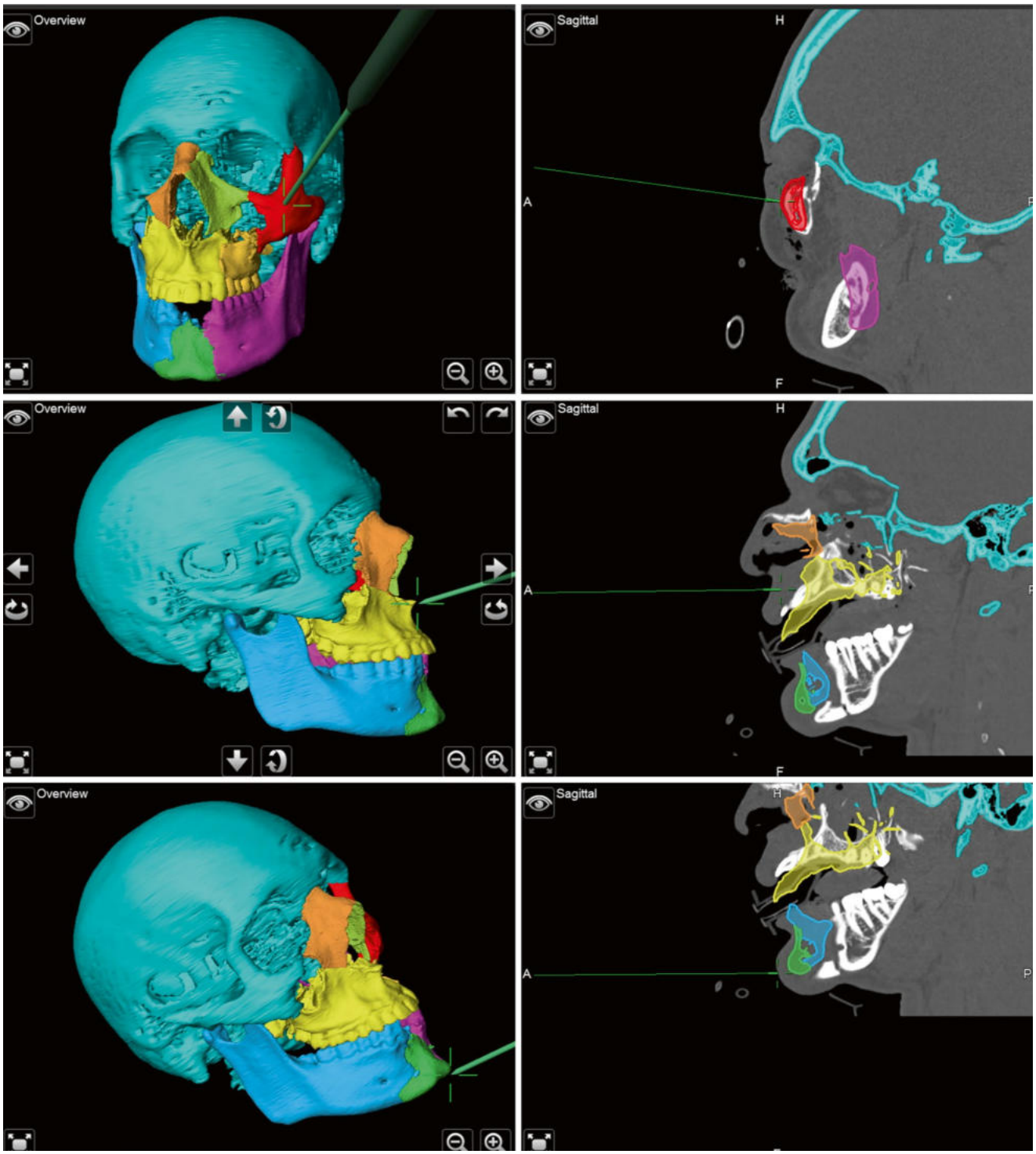


Fig. 11 Navigation of reduced STL files used as reduction mask

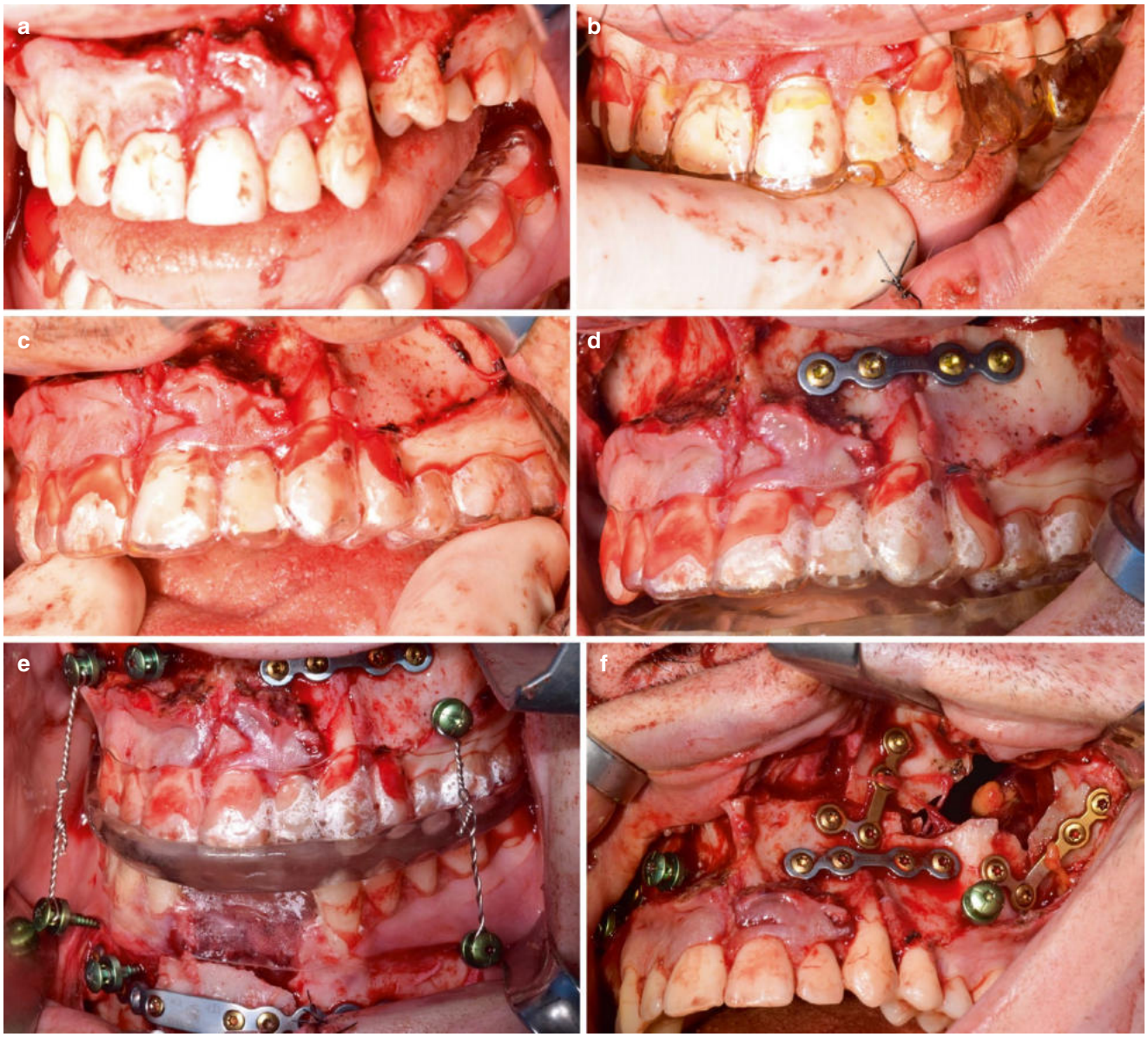


Fig. 12 Intraoperative reduction sequences based on TCS and surgical splint to establish intra-arch integrity (**a**–**d**), inter-arch coordination (**e**), and plating to the higher buttresses with the correct occlusal alignment (**f**)

fixation of the mandible and the interposed chin segment were performed with load-bearing plates (Fig. 12).

Through subciliary and glabellar incisions, reduction and fixation of NOE segments were performed using a curved plate positioned at the inferior orbital rim (Fig. 13).

2.5 Postoperative Considerations

The application of this technological protocol has substantial impacts on the accuracy of the procedure. By conducting a root mean square analysis between the overlapped VSP and postoperative CT respectively for the midface, the maxilla and the mandible, in all cases the overall deviation was around 1 mm, which is demonstrated in the color map by the wide presence of green color in the analyzed regions. Likewise, the comparison of occlusograms between VSP and postoperative CT (in the latter, intraoral scanning was not acquired, but the analysis was feasible due to the absence of metal artifacts) shows that the scheme of occlusal contacts is highly similar between the VSP and the achieved surgical outcome, thus justifying the combined use of TCS and occlusal splint (Fig. 14).

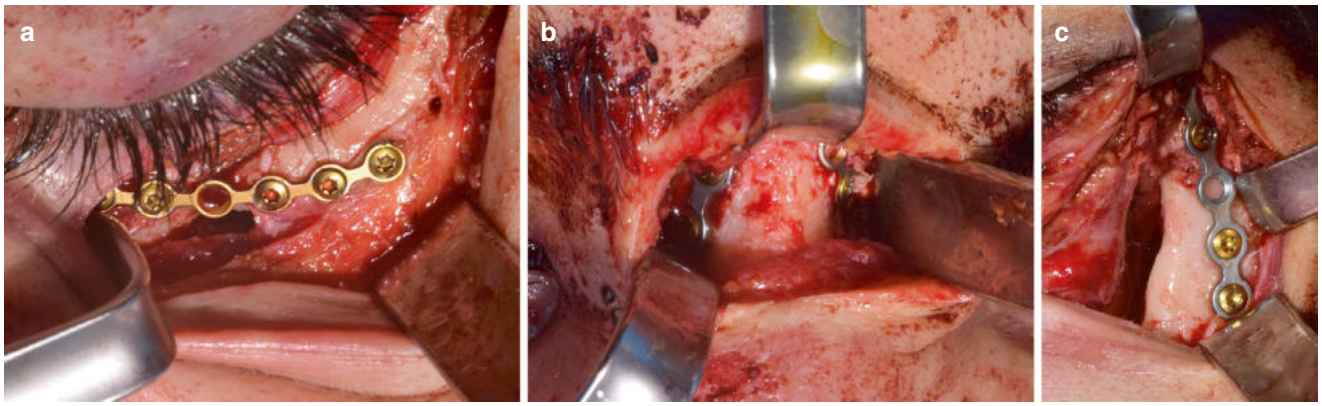


Fig. 13 Anatomical reduction of rims based on edge alignment

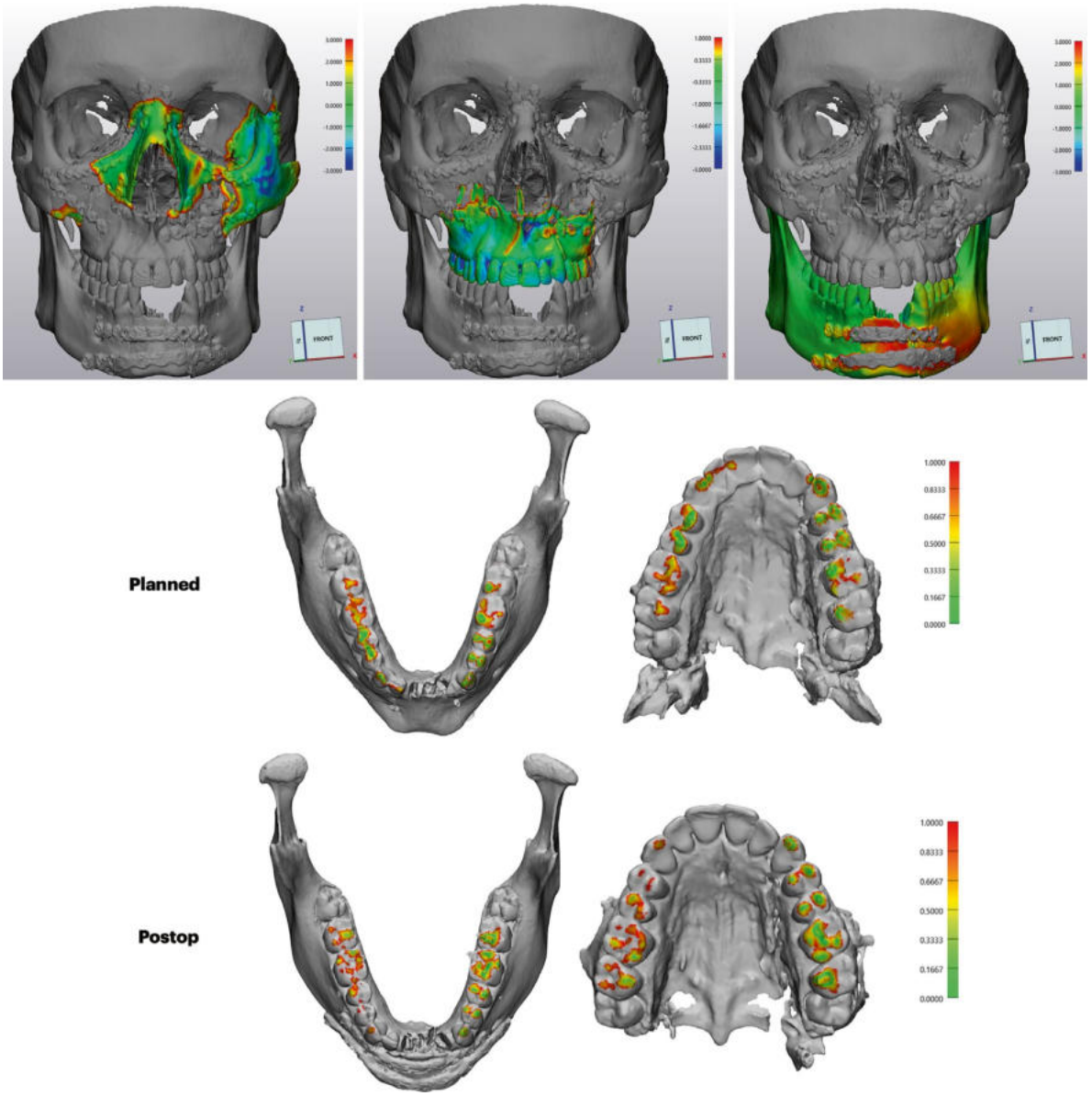


Fig. 14 Top panel: RMSE color-mapping between VSP and postoperative CT illustrating accuracy (confirmed by green color in the heatmap) for the superior midface (left), maxilla (center), and mandible (right). Bottom panel: planned and postoperative occlusogram can be superimposed

3 Full-Face Dismantling and Reconstruction

Extensive ablative procedures or disfiguring traumas pose unique challenges to surgeons. While facial transplantation is an extreme solution, performed by few centers worldwide, for those cases in which free flaps are not sufficient to replace facial tissues, and bears substantial, life-threatening risks related to rejection and immune-suppression, in several cases a combination of free flaps yields satisfactory results [10]. It is important to carefully select those cases that might benefit the most from such a complex reconstruction, first by defining the anatomical and functional units that will be replaced and secondly by choosing the optimal flap source and design to reach this objective. Virtual surgical planning is an extremely valuable resource in such cases, as it enables to perform multiple simulations to define the optimal flap combination. The present subsection will focus on double osseous flap reconstruction for the maxilla and the mandible, as only few papers have explored the possibility of combining two bone flaps for the simultaneous reconstruction of the maxilla and the mandible [11]. Moreover, the simultaneous restoration of two facial thirds is highly demanding in terms of functional requirements, as it must accommodate a stable occlusion and provide support to the eye globe and mandible articulation. An example of such reconstruction will be presented throughout this chapter, detailing the virtual workflows and its implications for a successful surgery.

3.1 Clinical Case

A 27-year-old gentleman was referred to our center for a progressive, deforming, fibrous dysplasia of the craniofacial skeleton. The patient previously underwent minor surgeries to attenuate the effect of dysplasia, without an effective result. At clinical evaluation, the patient presented with substantial mandibular deformation conditioning the impossibility of normal feeding; the abnormal dysplastic tissue occupied the oral cavity and modified the position of the tongue, compromising speech as well. Dysplasia was localized in the right hemimaxillary region and caused a substantial bulging of the right orbital floor, causing ocular dystopia and diplopia. An alteration of the normal maxillary position, with canting and obliteration of the vestibule, was observed as well (Fig. 15). This situation was hardly compatible with a normal life: as a consequence, the patient accepted extensive surgery as the only available treatment. The pro-



Fig. 15 Preoperative face and occlusion

posed surgical act included resection of the whole mandible, except the left TMJ (anatomically normal), and a class III right maxillectomy, including the orbital floor. Dysplasia involved the temporo-parietal bones and the right skullbase as well, but no cranial procedures were planned owing to their morbidity. As for reconstruction, the following plan was approved:

- Reconstruction of the mesostructure using a DCIA flap with optimal orientation to provide a functional alveolar process
- Reconstruction of the infrastructure using a three-segment fibula free flap providing the bony alveolar process, coupled with a customized implant including a temporomandibular joint prosthesis on the right side

The VSP process is developed in the following phases:

- Anatomical model creation
- Resection planning
- Definition of virtual wax-up and occlusal functionalization
- Positioning of flaps according to the digital wax-up
- Statistical shape modeling of the neomandible
- Design of implants based on the virtual project
- Design of surgical guides for resection
- Design of surgical guides for reconstruction
- Orbital reconstruction
- 3D printing

3.2 Virtual Surgical Planning

- *Anatomical model creation*: fibrous dysplasia is a pathological condition in which the bone structure is subverted initially at a microscopic level and, subsequently, the whole splanchnocranium is deformed. In this case, the patient presented with a completely inflated mandible, bulging inside the oral cavity as well as protruding externally, with a substantial alteration of symmetry. Likewise, the midface on the right side was substantially abnormal. Thus, we remark the importance of clinical analysis before any VSP is defined. For computer-guided surgery to be effective, the most reliable anatomical reconstruction of this abnormal anatomy is mandatory through accurate segmentation performed on optimal imaging. The skull was segmented using conservative thresholding values in Mimics v. 26, and split mask was applied in the TMJ and occlusal contacts to achieve a separate reconstruction of the maxilla from the mandible. TOF and VEN3D sequences were coregistered with bone CT and used to define the vasculature of the lesion. Voxel coloring was used to differentiate abnormal bone through quantitative voxel density variations, which accounted for a different color. Likewise, anatomical reconstruction of donor sites for free flap harvesting was given great importance. A high-resolution CT-angiography extending from the lumbar spine up to the proximal third of the femoral diaphysis was used for the right iliac crest, whereas a second CT-angiography was used for the left fibula, acquired from the femoral condyles to the metatarsal bones. Both CT angiographies were acquired with a 0.6 slice thickness, paying attention to acquire contrast media in the earliest phase for maximal arterial impregnation and visualization of possible perforators. Segmentation was performed using a global bone thresholding applied in pre-contrast sequences, while contrast-enhanced CT angiographies were used to delineate vascular axes and pedicles by selectively applying dynamic region growing following the vessel as distally as possible from its emergence. Subsequently, a Boolean mask subtraction was performed between vessel segmentation and bone-only segmentation, yielding a vessel-only sequence. Again, mask split was used to separate bone mask into multiple submasks, each one corresponding to a single bone. Results of 3D model creation are represented in Fig. 16.
- *Resection planning:* resection planning was performed on reconstructed 3D models to define the amount of removal. A subtotal mandibulectomy with right disarticulation was planned by simply positioning a cutting plane bisecting the left gonial angle, as the left mandibular ramus was considered to be unaffected from dysplasia. Moreover, a right maxillectomy was performed by positioning a midline cut plane; a second cut plane was positioned at the root of the zygomatic arch, and a freeform brush marking was performed over the right orbital floor. It was important to ensure that cutting interfaces receiving flaps were planar to maximize bone contact and stability (Fig. 17). STL for resection planning were imported in Brainlab Elements (Brainlab, Munich, DE) software to create a navigation plane for image-guided control of resection margins.
- *Definition of virtual wax-up and occlusal functionalization*: similar to the bottom-up approach described for panfacial trauma, the absence of references for jaw positioning except the remaining superior left hemimaxilla required a new occlusion to be defined. The new occlusion, established in software for digital dentistry (Exocad GmbH, Darmstadt, DE), consisted of mirroring the remaining left arch and designing a de novo antagonist mandibular arch. Placing the occlusion is important to define the optimal location of dental implants for prosthetic rehabilitation

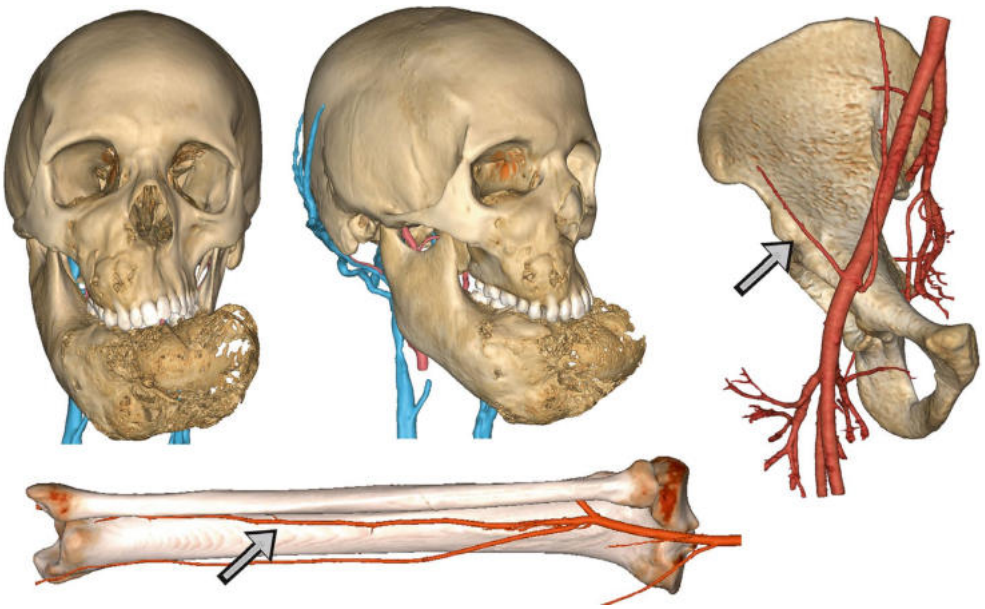


Fig. 16 Digital anatomical reconstruction for the face and donor sites of flaps including vascular anatomy for pedicles and recipient vessels. (Reprinted from [11])

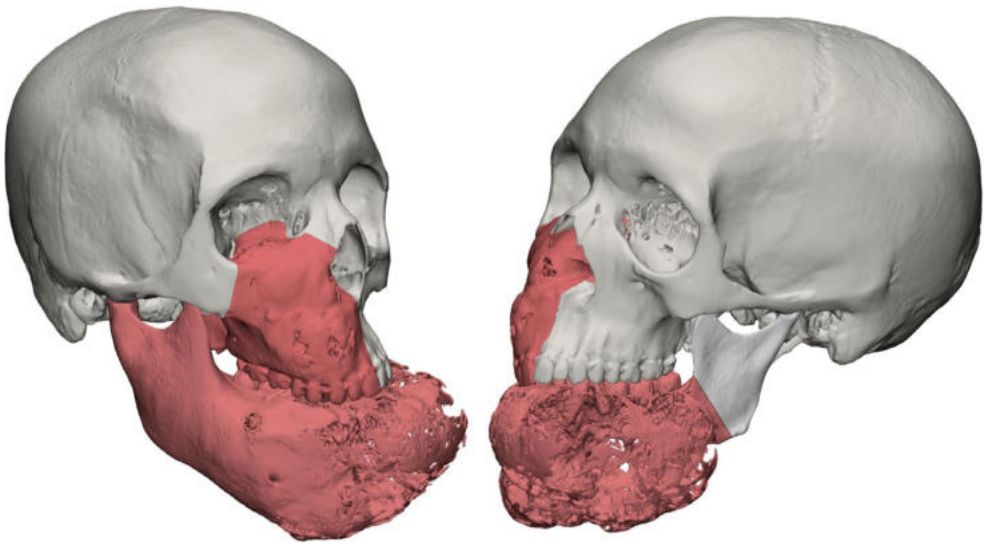


Fig. 17 Resection for the midface and the mandible as planned in 3-matic

and drives the most functional flap insetting. The concept of prosthetically driven microvascular reconstruction is supported by the literature [12] and couples anatomical reconstruction with functional demands (Fig. 18)

- *Positioning of flaps according to the digital wax-up*: as stated, the position of prosthetic crowns, defined by the virtual wax-up, drives the optimal flap inset. In addition, anatomical considerations on the position of the vascular pedicle are mandatory. In this regard, coupling the neck vascular model with the flap vascular model can facilitate the definition of optimal recipient vessel for the anastomosis. As seen in chapters about midfacial and mandibular reconstruction, the fibula (mandibular) pedicle should be ideally located posteriorly and lingually, shortening its course with the neck. Likewise, owing to the short pedicle of the DCIA flap, a connection with the facial artery was suggested and, thus, the flap has to be rotated 180° placing the superior iliac crest in correspondence of the superior alveolar process, and the pedicle posterior. Such considerations logically drive the choice of the side in which the flap is harvested. It is advisable to segment both sides of anatomy and to transpose the flap in the recipient site to find the best match in terms of anatomical orientation and correspondence with the digital wax-up (Fig. 19).
- *Statistical shape modeling of the neomandible:* the fibula flap accounts only for the alveolar process. Owing to the extension of resection and the need of reconstructing almost the whole mandible, the length of the fibula is not sufficient for a double barrel configuration, whereas it pro-

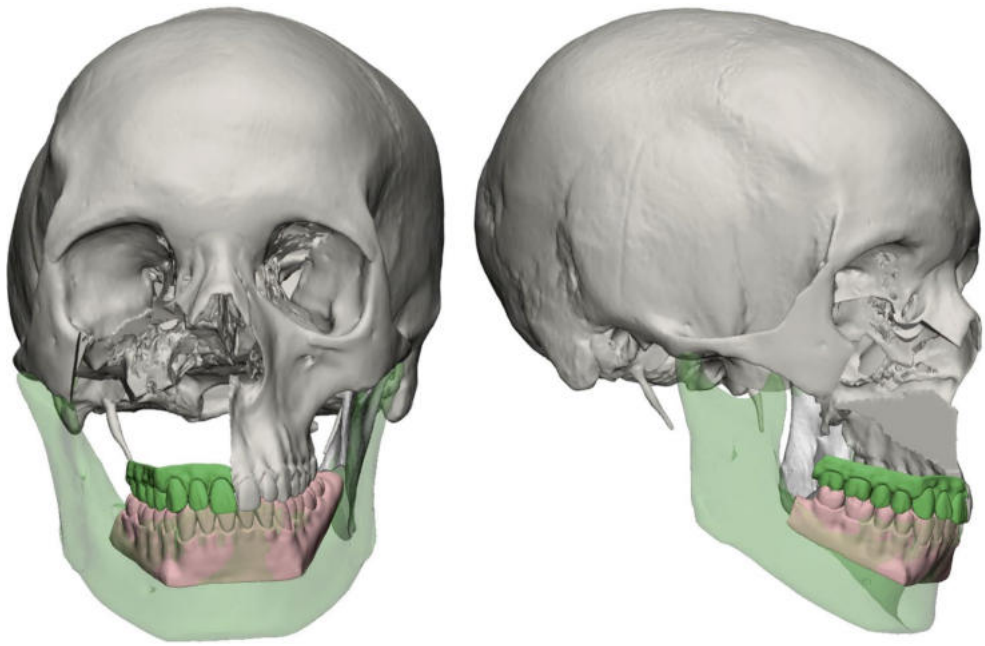


Fig. 18 Digital occlusion using virtual wax-up to mirror the remaining left maxilla and reconstruct de novo the inferior antagonist. The ghosted image refers to the SSM mandible

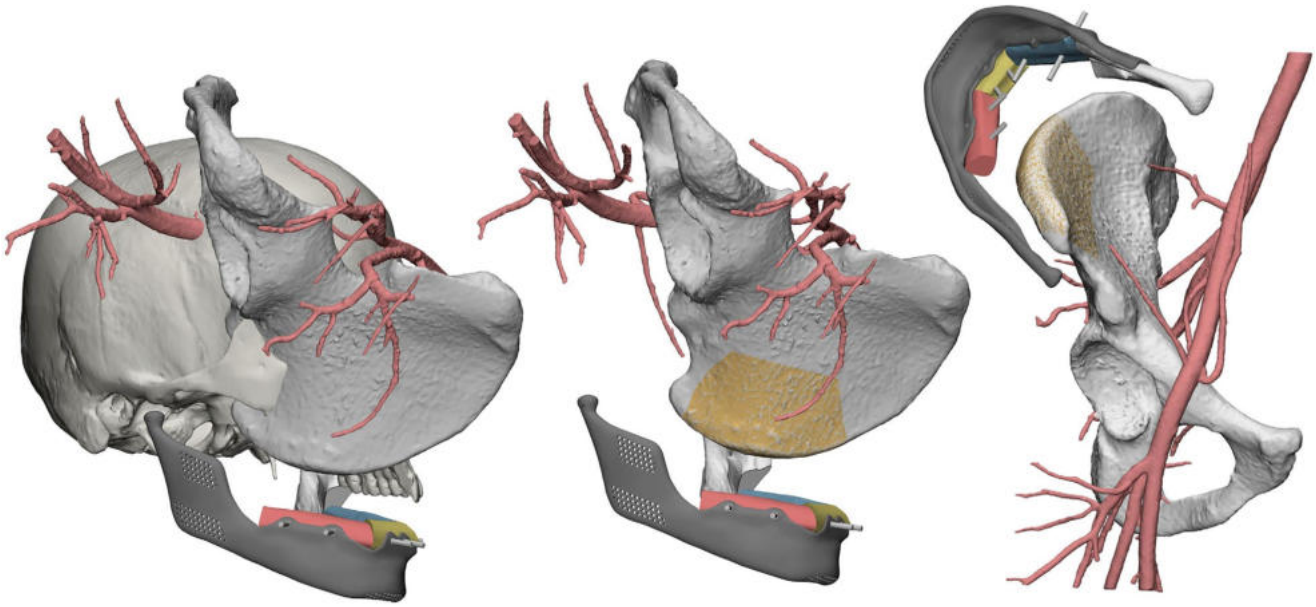


Fig. 19 Iliac crest transposition to the recipient site to define the orientation of the pedicle and the sizing of the flap itself

vides the alveolar bone for future implant positioning. Thus, a valuable principle is to replace the basal bone supporting the alveolar process with a patient-specific implant, tailored on the anatomical entity to replace [13]. In this case, the absence of any reference of the previous mandible creates a major issue in the design of the patient's implant. Without any certified deep learning method to generatively reconstruct a reliable mandible, a valuable solution is represented by statistical shape modeling (SSM), a method already debated throughout the Atlas. SSM created an average model starting from a target shape which is modified according to a population variability represented by multiple instances, each of which contains an individual anatomy. In this case, the target shape was represented by a mandible taken from a virtual donor of the same ethnicity and gender and was modified upon seven different mandibles. The combination of weights of the seven instances enabled to selectively modify the target shape according to the population variability, yielding a neomandible compatible with the patient (Fig. 20).

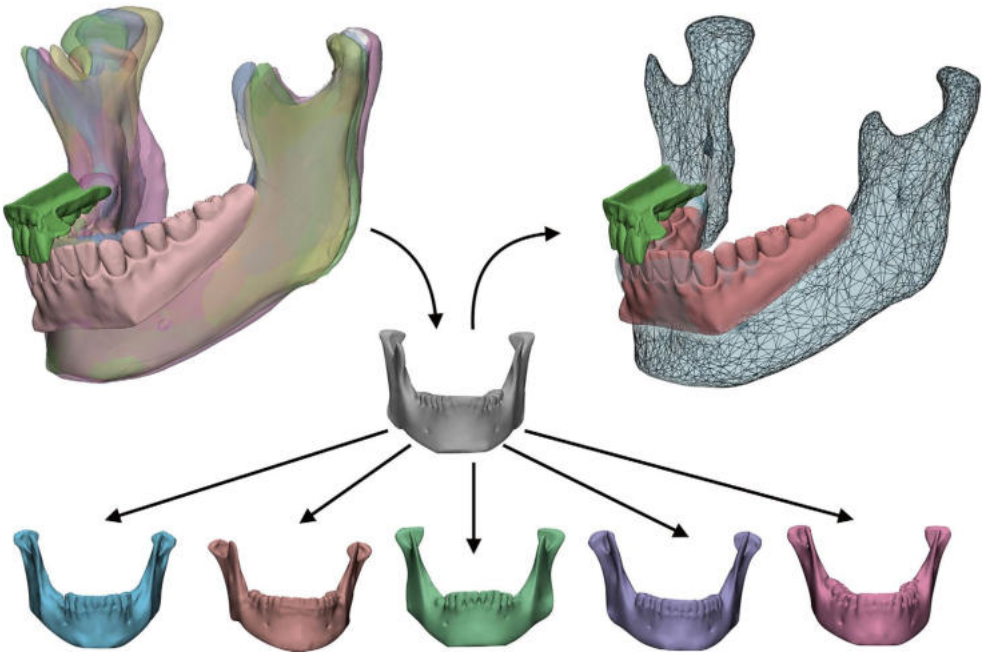


Fig. 20 SSM through computation of different mandibles (modalities, or instances) which are computer to modify a target mandible. Variating instance coefficients enables to tailor the target mandible according to the population variability

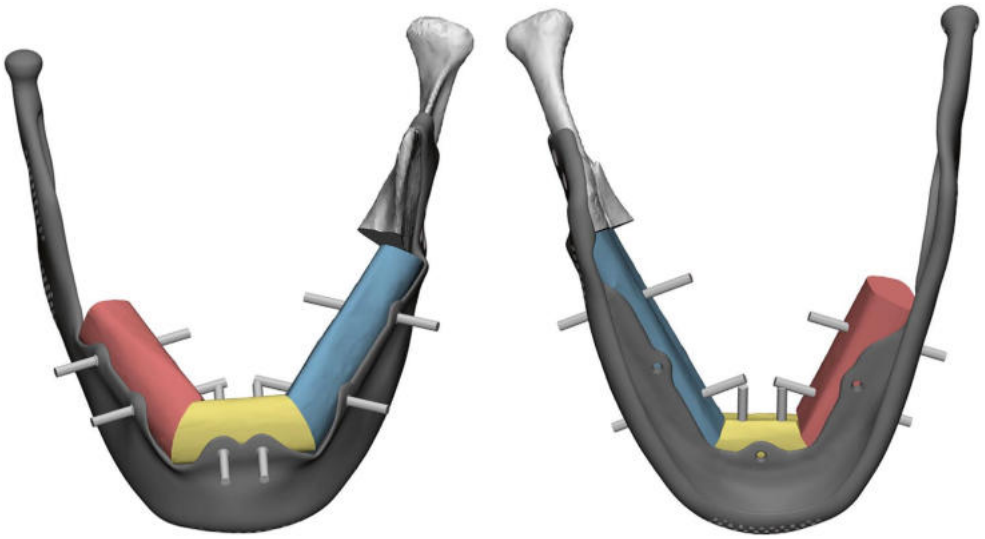


Fig. 21 Design of the mandibular PSI based on fibula flap positioning after defining sites for screw insertion

- *Design of implants based on the virtual project:* The SSM mandibular shape was used to design a custom prosthesis defining the mandibular body and ramus, including the right TMJ. The fibula flap was thus supported by the mandibular implant and served exclusively to reconstruct the alveolar process, at the same time providing a soft tissue muscular cuff to seal the oral cavity and isolate the implant preventing its communication with the oral cavity (Fig. 21).
- *Design of surgical guides*: Designing implants before surgical guides enables to anticipately define the position for screws necessary both for implant fixation to surrounding bone, as well as for flap fixation to the implant. This is conceptually important because it helps design surgical guides using the final screw holes, avoiding to drill unnecessary holes. Surgical guides enable to drill holes coincident with the final fixation points of flaps, allowing to streamline the flap inset process creating automation. For midface resection, linear flanges are created using the same cut planes defined in VSP. Resection guide is designed with multiple components joined by curved bridges, enabling to connect distant parts without interfering with surgical gestures. A double-fit mechanism is used to increase the stability of the guide, using both anatomical landmarks and an occlusal impression (Fig. 22). Concerning the surgical guide for DCIA harvest, it was designed as a simple guide with the same

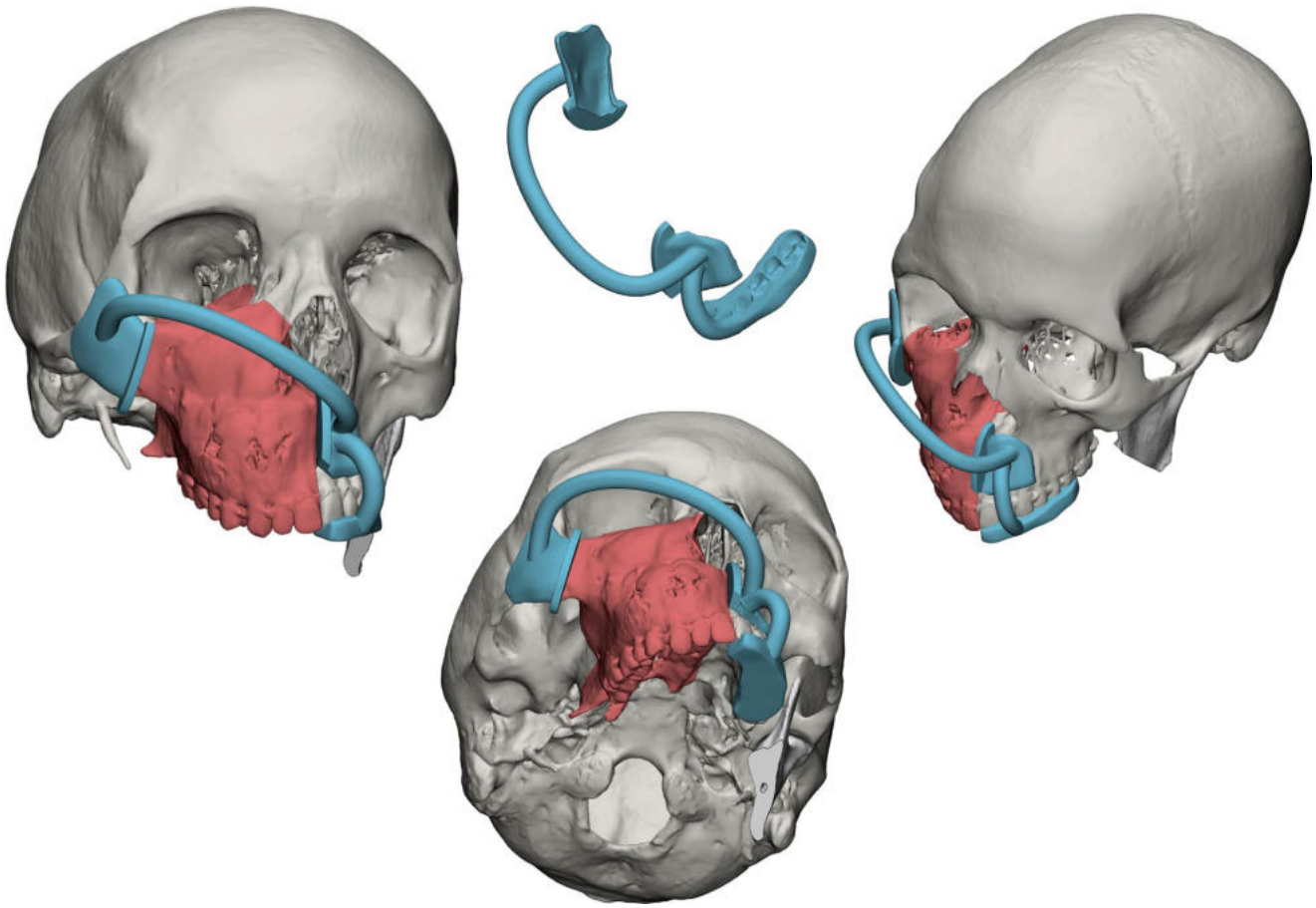


Fig. 22 Resection of the midface using a hybrid bridged guide with both skeletal and dental fit

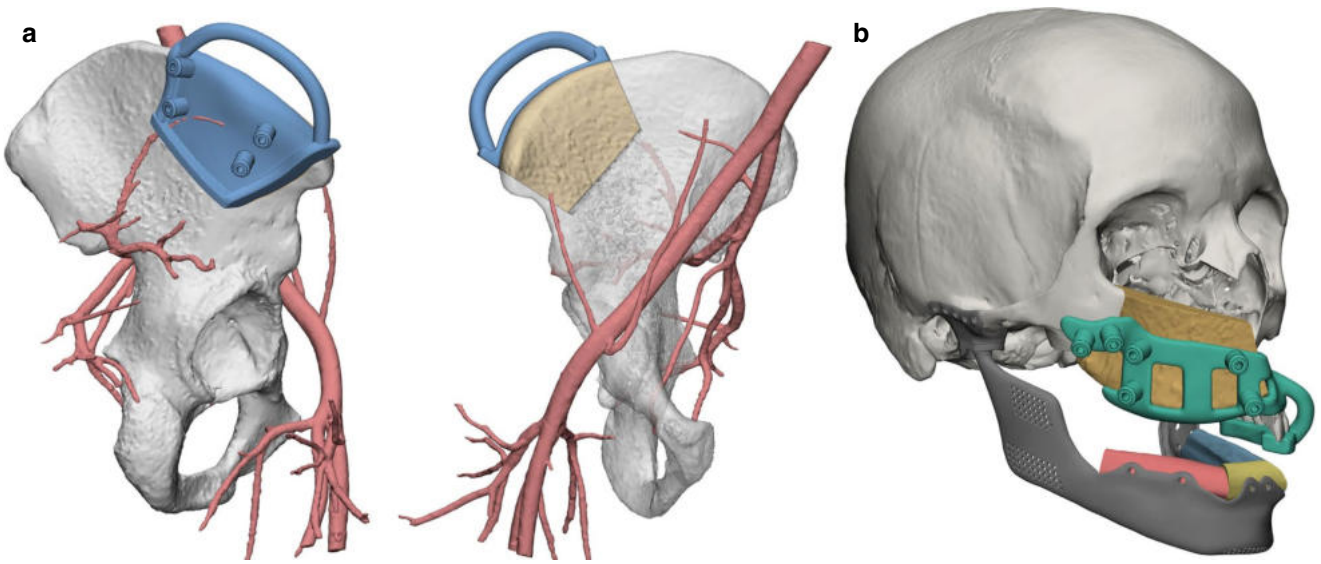


Fig. 23 Creation of a surgical guide for DCIA flap harvest (**a**) and creation of a guide for inset automation (**b**)

shape as the flap and linear flanges at its extremities. In addition, a repositioning guide to help DCIA flap inset was modeled (Fig. 23). Likewise, the surgical guide for fibula flap harvesting was created using linear flanges, given the absence of intersecting cutting wedges (Fig. 24).

- *Orbital reconstruction*: For class III maxillectomies, the reconstruction of the orbital floor is mandatory. A mirrored replica of the contralateral orbital structure was used to determine the ideal shape of the orbital floor and to preserve symmetrical volume between the orbits during reconstruction. The implant was designed following these guidelines and was made correspondent to resection margins. A molding system, which carried the negative impression of the implant, was created and 3D-printed to enable the intraoperative fabrication of an implantable orbital component made from polymethyl methacrylate (Fig. 25). Eventually, a traditional orbital implant can be prebent on the 3D printed model.

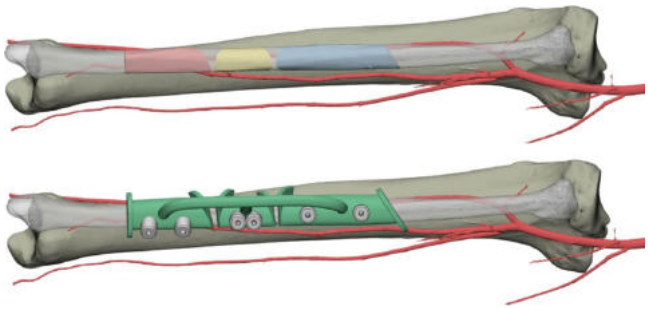


Fig. 24 Fibula segments VSP and guide design

- *3D printing:* the whole anatomical model was 3D printed in White Resin using a Formlabs Form 3BL printer. Surgical guides were printed in biocompatible resins (Biomed Clear). Customized implant was manufactured by the producer using SLS titanium printing (GPI S.p.a., Trento, Italy). The anatomical 3D-printed model was also used to prebend osteosynthesis plates (Fig. 26).

3.3 Surgery

For this case, surgery consisted of a complex sequence of procedures both during resective and reconstructive phases. Emphasis will be placed on the sequences including computer-guided automation to demonstrate that the combined use of technology helped to streamline the process, simplifying several steps.

- *Resection*: the DRF for navigated surgery was mounted on the patient's head, allowing to establish proper calibration of the navigator between the real patient and the VSP. Exposure was achieved through a visor flap cervicotomy, which at first allowed to isolate the neck vessels recipient of subsequent anastomoses. Particular attention was made to identify and protect the superior thyroid

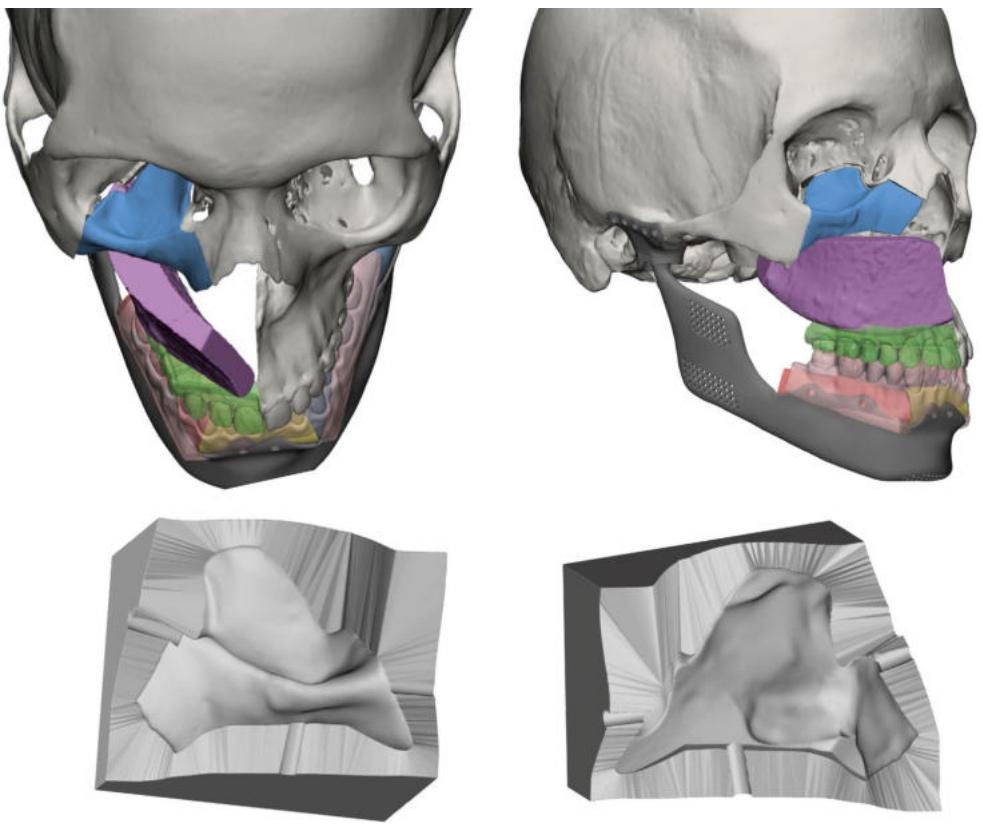


Fig. 25 Design of an orbital floor prosthesis and creation of molds for PMMA injection

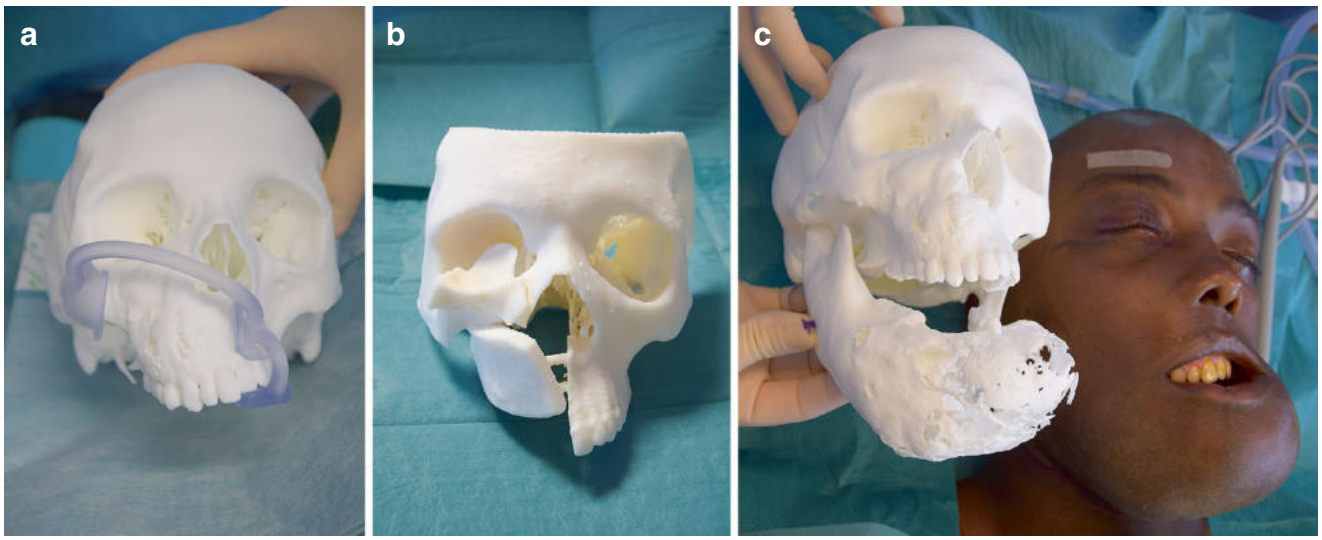


Fig. 26 (**a**) Surgical guide for resection is tested on model; (**b**) reconstruction model; (**c**) evaluation with the patient

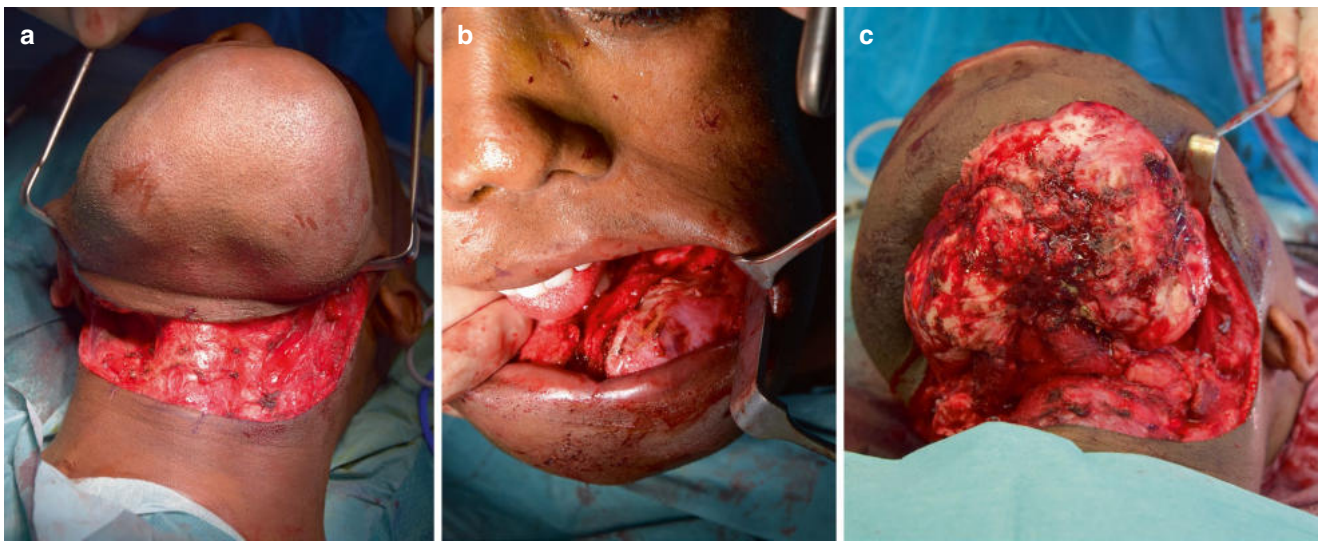


Fig. 27 (**a**) Visor flap creation for facial degloving; (**b**) intraoral exposure of the lesion; (**c**) complete exposure of the mandibular dysplasia

artery, the facial artery, and the thyrolinguofacial venous trunk on both sides. The mandible was exposed in its inferior surface. Intraorally, a vestibular incision allowed to separate the inferior lip from the pathologic mandible (Fig. 27). On the left side, a surgical guide for mandibular resection guided the mandibular angle osteotomy, while, on the right side, the incision was extended to a preauricular approach, exposing the full TMJ to complete disarticulation and at the same time enable future TMJ replacement. An intrasulcular incision was made in the superior gingiva to expose the maxillary wall, and the whole midface was approached through a facial degloving connected to the cervical visor flap. This enabled to position the resection surgical guide with double engagement, both dental and skeletal, and to complete osteotomies of the mesial and distal (malar) limit of the maxillectomy (Fig. 28). The orbital floor was approached through a subciliary incision and its circumferential osteotomy was accomplished, connecting it to the maxillectomy specimen. The whole mandible and right hemimaxilla were removed and compared to their 3D printed replicas (Fig. 29).

- *Harvesting of microsurgical bone flaps:* Left fibula free flap and right DCIA free flap were simultaneously harvested by two separate surgical teams. The fibula was modeled using the 3D-printed surgical guide, allowing to excise intersegmental wedges to the correct shape to enable bending of fibula segments based on the virtual project. The fibula was fixed to the implant using the

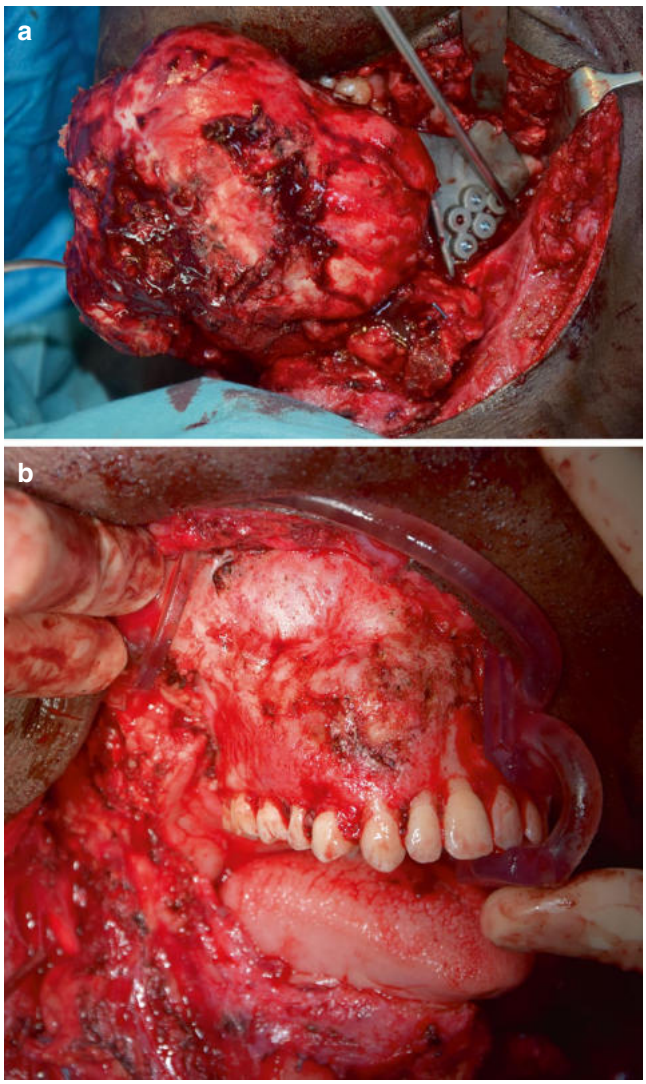


Fig. 28 (**a**) Surgical guide for left mandibular resection; (**b**) application of the guide for midface resection using the double anchoring system

holes provided by the surgical guide fixation and planned to be coincident with the implant itself. The appropriate position of the pedicle was checked and confirmed to be posterior and lingual on the left side (Fig. 30). Likewise, DCIA flap was harvested using a dedicated surgical guide and its orientation was checked to confirm that the pedicle was posteriorly directed to the recipient facial artery (Fig. 31).

- *Flap inset and reconstruction:* Through the preauricular approach, the TMJ prosthetic fossa was fixed to the zygomatic arch. The mandibular prosthesis with the mounted fibula flap was fixed to the holes on the left mandibular angle prepared through the resection guide, while, on the right side, the prosthetic neocondyle perfectly articulated with the TMJ fossa. Microsurgical anastomoses were completed. Likewise, the DCIA flap was positioned in the midface using the repositioning guide as reference to assist its optimal orientation and was fixed with prebent titanium plates. A second microvascular anastomosis was performed between the DCIA pedicle and ipsilateral facial vessels. Dental implants were positioned in bone flaps using 3D-printed drilling guides based on the virtual wax-up (Fig. 32).
- *Orbital reconstruction:* A customized replica of the orbital floor and inferior orbital rim was achieved using PMMA modeling through a small, 3D-printed, molding system. Reconstruction was effective and enabled to reestablish the correct eye globe projection (Fig. 33).

Postoperative CT illustrated the correct positioning of flaps based on the surgical plan (Fig. 34).

Three years after surgery, the patient is fit with no impairments related to flap harvesting and has a normal facial appearance. Occlusion is functionally valid, and the patient has a normal nutrition (Fig. 35).

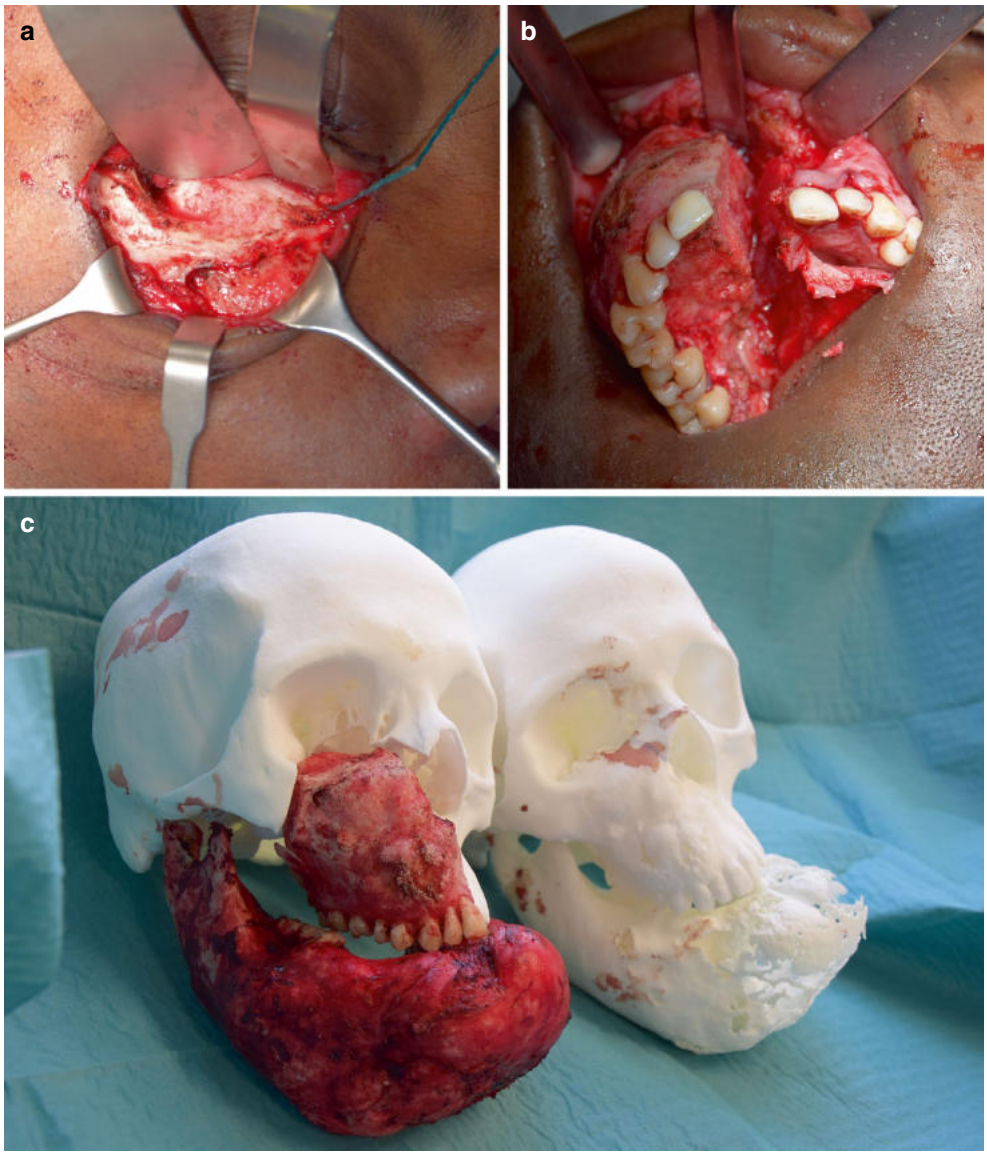


Fig. 29 (**a**) Orbital floor exposure through subciliary approach; (**b**) maxillectomy completion; (**c**) comparison between the resected specimen and 3DP model

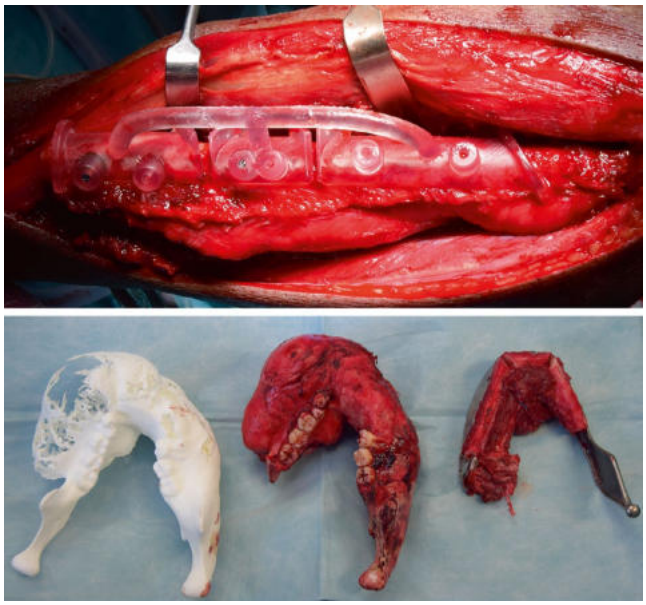


Fig. 30 Intraoperative application of fibula surgical guide (top panel). Bottom panel: comparison between resected specimen and reconstructed mandible

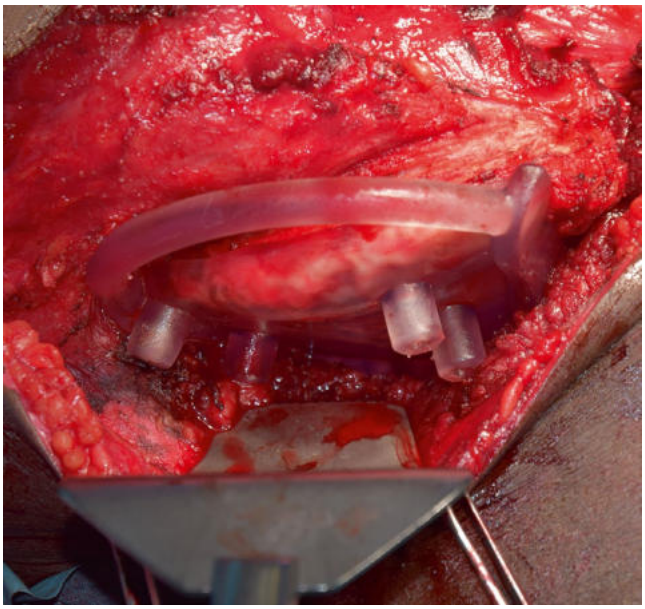
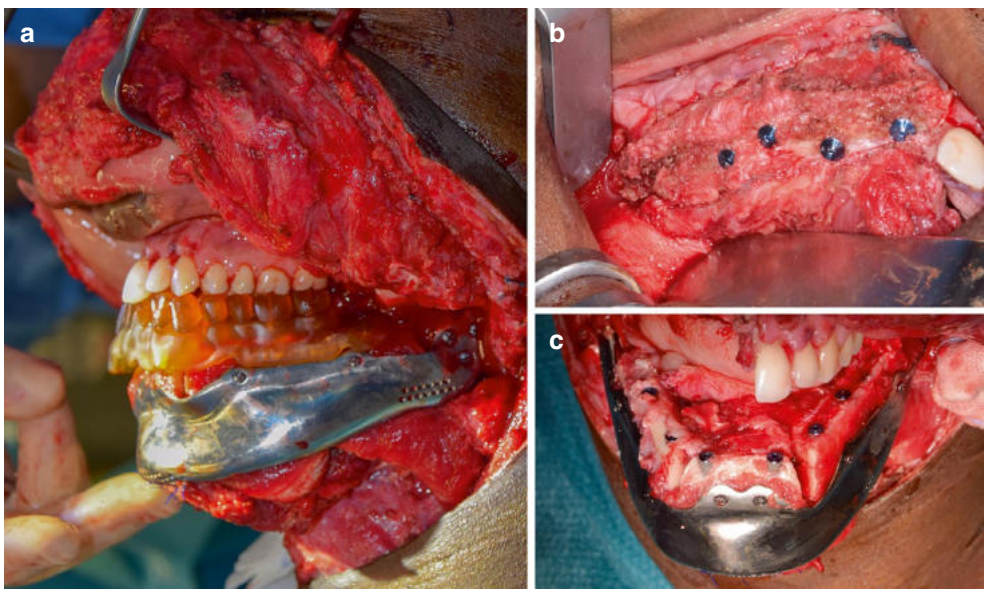


Fig. 31 Application of surgical guide for DCIA flap

Fig. 32 (**a**) Verification of the optimal intercuspation through a 3DP printed wax-up with channels for implant hole drilling. This model fits the underlying fibula reconstruction and accounts for the correct flap positioning. (**b**) DCIA implants; (**c**) fibula implants



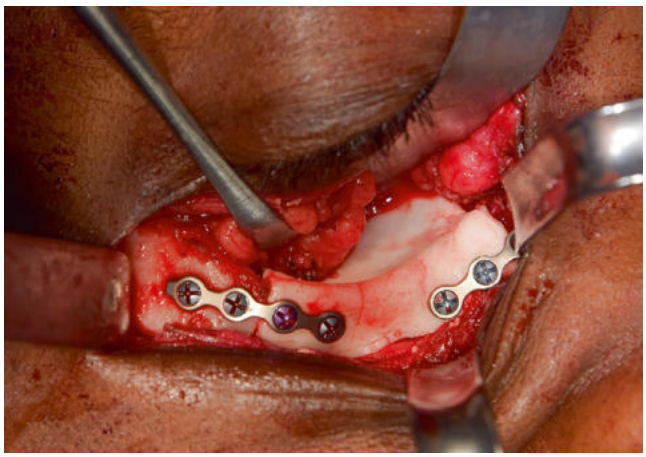


Fig. 33 PMMA orbital floor prosthesis fixed using two linear miniplates

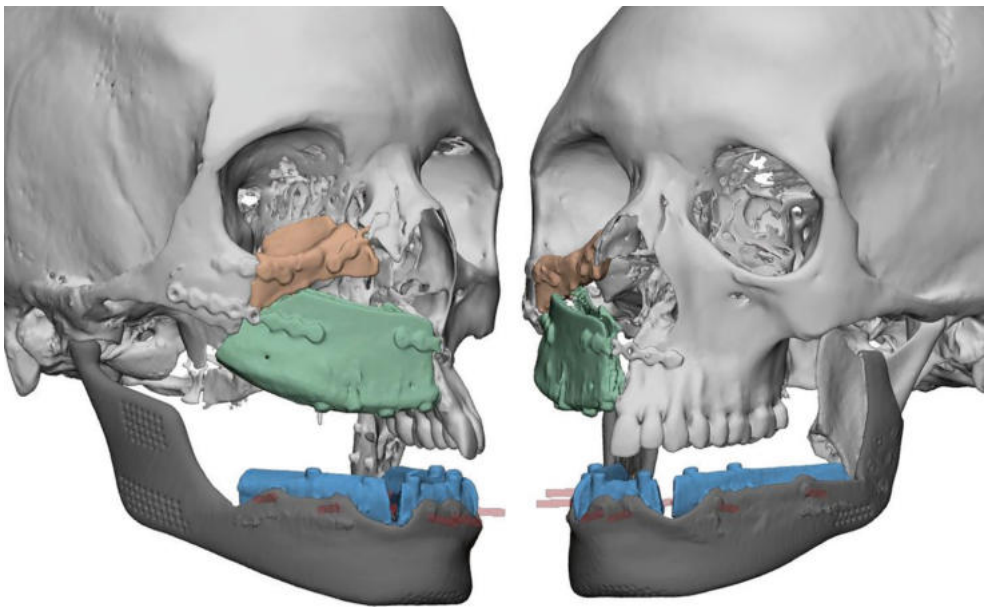


Fig. 34 Segmentation of postoperative CT



Fig. 35 Facial and occlusal outcome after denture fixation

4 Virtual Reality in Facial Nerve Reanimation

The advent of computer-assisted surgery and modern virtual surgical planning utilizing 3D reconstruction based on CT and MR has introduced a paradigm shift in the field of facial reanimation surgery. This technological advancement holds the potential to revolutionize cross-facial nerve grafting procedures by enabling precise measurement of sural nerve grafts and allowing surgeons to accurately locate and navigate donor nerves. Critical donor nerves, such as the facial nerve, the masseteric nerve, the hypoglossal nerve, and the spinal accessory nerve, may be located in specific MR sequences and traced in the VSP software in correspondent position, integrating them in a virtual model of triple innervation for facial reanimation [14](Fig. 36). Among radiologic methods, high-resolution MRI with small section thickness (<1 mm) remains the gold standard for imaging the facial nerve, especially in its intratemporal and extratemporal-intraparotid segments, as it provides better soft tissue contrast and resolution. Steady-state sequencing (neurography) and DWI implementation is also able to improve the recognition rates of facial nerve secondary branches [15]. Additionally, high-field MR neurography of the extracranial nerve with the DE3D-WE sequence is excellently suited to visualize the course of the nerves, which is due to the excellent contrast between the hypointense soft tissues and the hyperintense nerves [16]. Gaudino et al. demonstrated the use of this sequence to visualize the course of the facial nerve, which is due to the excellent contrast between the hypointense parotid gland tissue and the hyperintense facial nerve as well as the higher signal of the parotid ducts compared to the nerve structures [17].

MRI, namely steady state neurography, is also the best imaging modality to visualize the hypoglossal nerve, the trigeminal branches included the masseteric one in its intramuscular course, and the spinal accessory nerve, because of its high tissue resolution. Besides, computed tomography may have a complementary role in the delineating osseous landmarks of the hypoglossal canal [18].

Future applications of these radiological techniques in combination with real-time navigation systems promise to improve the accuracy of nerve grafting and donor nerve selection, thereby improving surgical outcomes in the reanimation of facial palsy.

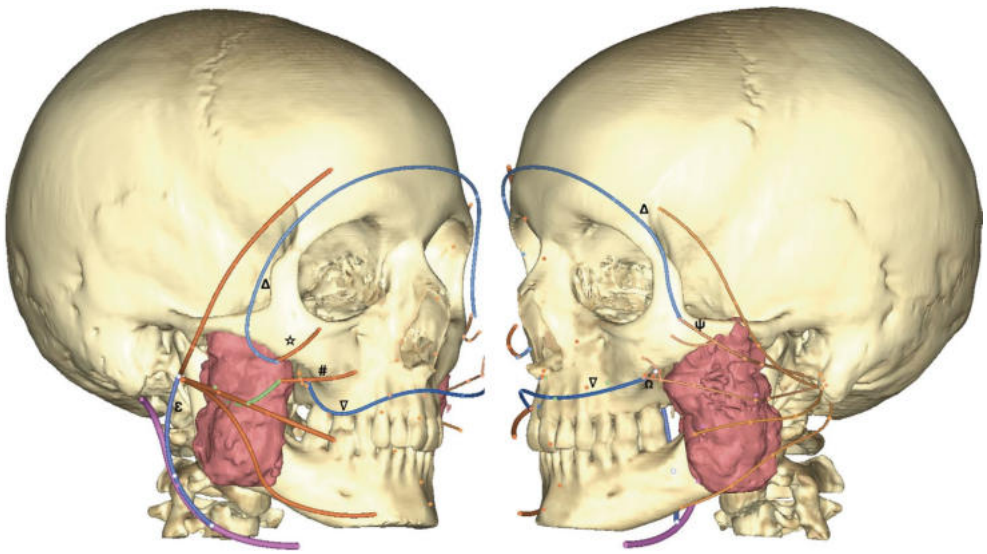


Fig. 36 3D virtual representation of the "triple innervation" technique for facial reanimation in case of recent facial palsy. Triple innervation technique is able to mix qualitative stimuli from the contralateral healthy facial nerve through cross face sural nerve grafts and quantitative stimuli from the masseteric nerve and hypoglossal nerve of the ipsilateral side.Left panel: facial palsy side of the face. The 3D figure shows the end-to-end neurography between the masseteric nerve (green) and the branch of the injured facial nerve for the great zygomatic muscle (#), the side-to-end neurography between the 30% of hypoglossus nerve (pink) and the main trunk of the injured facial nerve through a sural nerve graft (blue Ɛ) and two cross-face sural nerve grafts (blue Δ/∇). An end-to-end neurography between the free ends of the cranial cross face (Δ) is performed with the branch of the injured facial nerve for the orbicularis oculi muscle (☆), and an end-to-side neurography between the free ends of the caudal cross face (∇) is performed with the branch of the injured facial nerve for the great zygomatic muscleRight panel: healthy side of the face where two end-to-end neurographies are performed between the ends of the cross-face sural nerve grafts and the identified facial nerve branches for the contralateral orbicularis oculi muscle (ψ) and contralateral great zygomatic muscle (Ω).

5 Conclusions

This chapter is the final chapter before facial transplantation and was conceived as a synthesis of all technological possibilities presented in previous chapters. The idea is to illustrate a structured and methodological application of technology to demonstrate how it can assist the surgeon in its maneuvers but especially, as clearly seen in panfacial trauma, in conceptualizing the correct order of surgical procedures. The importance of a clinical understanding of technology is essential to establish the optimal indications for any computer-guided method, bust most of all to acknowledge its limitations. It is clear that technology, if not correctly used, can be detrimental in prolonging planning time and complicating surgical acts and, ultimately, in increasing related costs. Thus, the clinician must deeply understand the role of technology applied to each clinical situation to draw the best of its benefits, while contextualizing its application in the optimal setting.

References

1. Massenburg BB, Lang MS. Management of Panfacial Trauma: sequencing and pitfalls. Semin Plast Surg. 2021;35:292–8.
2. Ali K, Lettieri SC. Management of Panfacial Fracture. Semin Plast Surg. 2017;31:108–17.
3. Tel A, Costa F, Sembronio S, Robiony M. Contemporary management of complex craniofacial trauma: virtual planning, navigation and the novel thermoformed cage splints in a strategic, sequential, computer-guided protocol. J Craniomaxillofac Surg. 2022;50:837–47.
4. Ramakrishnan K, Palanivel I, Narayanan V, Chandran S, Narayanan J. Sequencing of fixation in Panfacial fracture: a systematic review. J Maxillofac Oral Surg. 2021;20:180–8.
5. Kochkine S, Baxter AB, McMenamy JM, Bernstein MP. Facial fractures: the "bottom-up" approach. Clin Imaging. 2023;101:167–79.
6. Yang R, Zhang C, Liu Y, Li Z, Li Z. Why should we start from mandibular fractures in the treatment of panfacial fractures? J Oral Maxillofac Surg. 2012;70:1386–92.
7. Degala S, Sundar SS, Mamata KS. A comparative prospective study of two different treatment sequences i.e. bottom up-inside out and topdown-outside in, in the treatment of Panfacial fractures. J Maxillofac Oral Surg. 2015;14:986–94.
8. de Melo WM, Sonoda CK, Shinohara EH, Garcia IR. Using the "bottom-up and outside-in" sequence for panfacial fracture management: does it provide a clinical significance? J Craniofac Surg. 2013;24:e479–81.
9. Yoon JH, Kang DH, Kim H. Sequencing of panfacial fracture surgery: a literature review and personal preference. Arch Craniofac Surg. 2022;23:256–61.
10. Joseph ST, Thankappan K, Iyer S. Reconstruction of a combined Maxillectomy and segmental Mandibulectomy defect in a seven-year-old with a single free fibula osteocutaneous flap. Craniomaxillofac Trauma Reconstr. 2017;10:73–6.
11. Tel A, Bagatto D, Sembronio S, Ferrari S, Robiony M. Double osseous flaps for simultaneous midfacial and mandible reconstruction: automation in surgical complexity within an entirely computerized workflow. Front Oncol. 2023;13:1103104.

12. Williams FC, Hammer DA, Wentland TR, Kim RY. Immediate teeth in fibulas: planning and digital workflow with point-of-care 3D printing. J Oral Maxillofac Surg. 2020;78:1320–7.
13. Wang E, Tran KL, D'heygere E, Prisman E. Predicting the premorbid shape of a diseased Mandible. Laryngoscope. 2021;131:E781–6.
14. Biglioli F, Allevi F, Rabbiosi D, Cupello S, Battista VMA, Saibene AM, Colletti G. Triple innervation for re-animation of recent facial paralysis. J Craniomaxillofac Surg. 2018;46:851–7.
15. Lee M-K, Choi Y, Jang J, Shin N-Y, Jung S-L, Ahn K-J, Kim B-S. Identification of the intraparotid facial nerve on MRI: a systematic review and meta-analysis. Eur Radiol. 2021;31:629–39.
16. Fujii H, Fujita A, Kanazawa H, Sung E, Sakai O, Sugimoto H. Localization of parotid gland tumors in relation to the Intraparotid facial nerve on 3D double-echo steady-state with water excitation sequence. Am J Neuroradiol. 2019;40:1037–42.
17. Gaudino C, Cassoni A, Pisciotti ML, Pucci R, Palma A, Fantoni N, Pantano P, Valentini V. MR-Neurography of the facial nerve in parotid tumors: intra-parotid nerve visualization and surgical correlation. Neuroradiology. 2024;66:1805–15.
18. de Sousa CR, Ventura N, de Andrade Lourenção Freddi T, da Cruz LCH, Corrêa DG. The hypoglossal nerve. Semin Ultrasound CT MRI. 2023;44:104–14.

Comprehensive Guide and Atlas to Virtual Surgical Planning in Face Transplantation

Alay R. Shah, Sachin R. Chinta, and Eduardo D. Rodriguez

1 Introduction

Face transplantation has become a transformative solution for patients suffering from severe facial deformities, offering the potential for both functional restoration and aesthetic reconstruction. Conventional reconstructive techniques often fall short in addressing the multifaceted challenges presented by complex facial trauma, burns, or congenital deformities. In such cases, facial transplantation emerges as the most viable option for restoring vital functions such as speech, mastication, facial expression, and, crucially, social reintegration [1–4].

However, the inherent complexity of face transplantation, particularly due to the intricate three-dimensional anatomy of the face, demands a high level of precision in both preoperative planning and intraoperative execution [5–11]. Virtual surgical planning (VSP) has emerged as a key tool in this process, enabling surgeons to simulate the surgery, anticipate potential challenges, and create highly accurate surgical guides and models [2]. VSP is now recognized as a critical adjunct in face transplantation, enhancing the accuracy and efficiency of these intricate procedures.

2 Indications for VSP in Face Transplantation

VSP proves especially useful in face transplantation given the variety of tissue types required to align harmoniously for optimal outcomes. In such cases, extensive skeletal damage requires meticulous planning for osteotomies, allowing the surgeon to align donor and recipient structures with precision to optimize both functional and aesthetic results. VSP technology enables the creation of custom-made cutting guides and implants, fabricated preoperatively to improve surgical accuracy and efficiency. Additionally, VSP provides detailed mapping of donor and recipient vessels to ensure efficient microvascular anastomoses with reduced ischemia times. In regard to precise soft tissue reconstruction during face transplantation, VSP aids in aligning muscles, nerves, and other tissues between donor and recipient, which is essential for restoring speech, mastication, and facial expressions [1, 2, 12–18].

3 Protocols for VSP Rendering in Face Transplantation

Our institutional protocols for utilizing VSP in face transplantation are designed to maximize the precision and efficiency of the procedure. VSP plays a multifaceted role in face transplantation by integrating advanced technologies such as three-dimensional computed tomography (3D CT), angiography, 3D printing, and stereolithographic modeling. The process begins with craniofacial CT scans of both donors and recipients, which are used to feed data into modeling software that can design customized bone-cutting guides and plan osteotomies with incredible precision. This modeling software allows for the superimposition of the donor's allograft onto the recipient's anatomy, providing surgeons with an accurate preview of surgical outcomes, thereby enhancing intraoperative alignment and reducing trial and error.

In the preoperative phase, the surgical team conducts a simulation of the entire surgery, identifying potential challenges and refining the operative approach. These simulations inform the development of 3D-printed, patient-specific cutting guides that are later sterilized and used intraoperatively to ensure accuracy. More recently, 3D printing has also

A. R. Shah · S. R. Chinta · E. D. Rodriguez (✉)
Hansjorg Wyss Department of Plastic Surgery, New York University Langone Health, New York, NY, USA
e-mail: Alay.Shah@nyulangone.org; Sachin.Chinta@nyulangone.org; Eduardo.Rodriguez@nyulangone.org

© The Author(s), under exclusive license to Springer Nature Switzerland AG 2025

A. Tel, M. Robiony (eds.), *Atlas of Virtual Surgical Planning and 3D Printing for Cranio-Maxillo-Facial Surgery*,
https://doi.org/10.1007/978-3-031-94495-6_26

been used to create masks and prosthetics for the donor, helping maintain donor integrity after procurement. Vascular mapping is employed to assess the vascular anatomy of both donor and recipient. Additionally, formal angiography is conducted through advanced angiographic techniques to ensure an optimal understanding of critical vessels for microvascular anastomosis, an essential step for reducing ischemic times and ensuring graft survival. This enables optimal planning for the harvesting of the donor's allograft, as well as the inset of the graft based on the vascular structures available in the recipient.

Stereolithographic models of the donor and recipient skulls are created to allow for the pre-bending of fixation plates before the actual surgical procedure, which helps reduce intraoperative ischemia times by minimizing the time needed to adjust skeletal fixation. Intraoperative navigation systems, adapted from intracranial and spinal surgeries, are used to provide real-time guidance with millimeter precision during critical steps such as osteotomies and allograft inset. These systems ensure that the graft is inset precisely as planned, while intraoperative CT allows for immediate adjustments if necessary.

Indocyanine Green (ICG) fluorescence angiography further enhances the intraoperative process by providing confirmation of robust allograft perfusion and venous outflow once the vascular anastomoses have been completed. After the surgery, CT imaging is again employed to assess the alignment of the allograft and measure the accuracy of the surgical outcome through cephalometric analysis, ensuring minimal deviation from the VSP plan.

4 Clinical Cases of Virtual Surgical Planning in Face Transplantation

The impact of VSP in face transplantation is best illustrated through the following clinical cases, which highlight the technology's role in enhancing both surgical precision and patient outcomes.

In the first case, a 37-year-old man who had sustained a ballistic facial injury underwent a total face, double jaw, and tongue transplantation after multiple reconstructive surgeries failed to restore adequate function (Fig. 1). Preoperative imaging, including 3D craniofacial CT and formal angiography, was used to create donor-specific titanium fixation guides and cutting templates for osteotomies. Surgical navigation software was utilized intraoperatively to guide LeFort III osteotomies, while stereolithographic models helped tailor the donor maxillary segment before vascular pedicle division. ICG angiography confirmed the viability of the allograft, and post-surgical CT imaging demonstrated minimal deviation from the virtual surgical plan, with the patient achieving normal occlusion immediately postoperatively (Fig. 2).



Fig. 1 Preoperative and postoperative images of a 37-year-old man who had sustained a ballistic facial injury and underwent a total face, double jaw, and tongue transplantation: (**a**) frontal view preoperative (**b**) frontal view postoperative. (Printed with permission from and copyrights retained by E.D.R.)

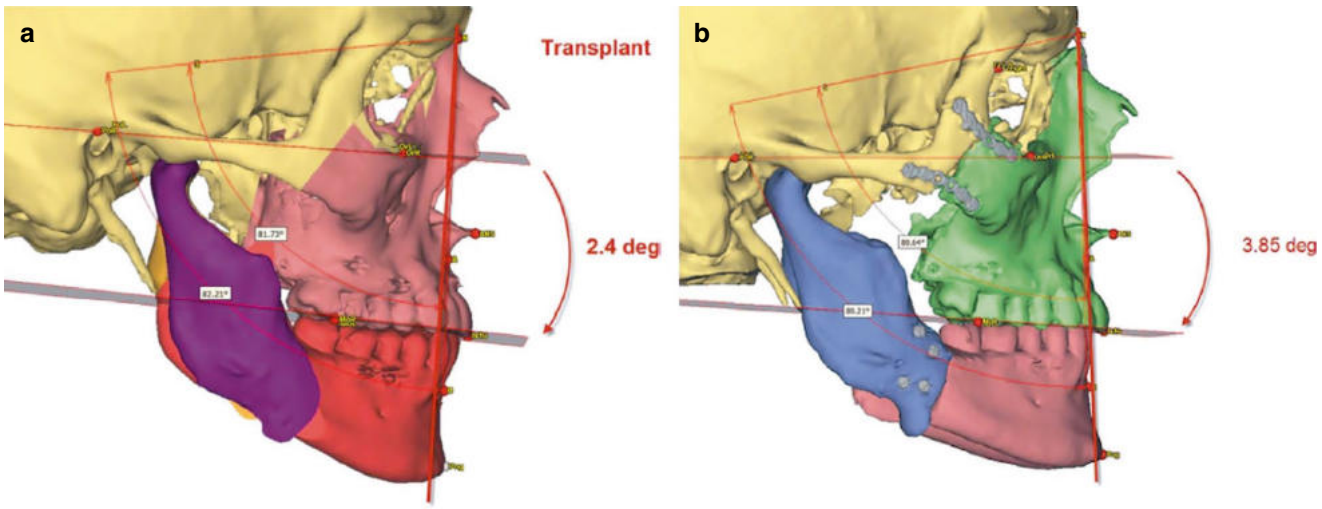


Fig. 2 (**a**) Superimposition of the preoperative CT of recipient and donor, representing the virtual surgical plan with the goal of achieving normal cephalometric indices of a sella-naison-A point of 81.73 degrees, a sella-nasion-B point of 82.21 degrees, and an occlusal angle of 2.4 degrees relative to the Frankfort horizontal plane of the recipient. (**b**) Postoperative CT of recipient post-transplant with cephalometric analysis demonstrating minimal variation from preoperative virtual surgical plan with a sella-nasion-A point of 80.64 degrees, a sella-nasion-B point of 80.21 degrees, and an occlusal angle of 3.85 degrees. (Printed with permission from and copyrights retained by E.D.R.)

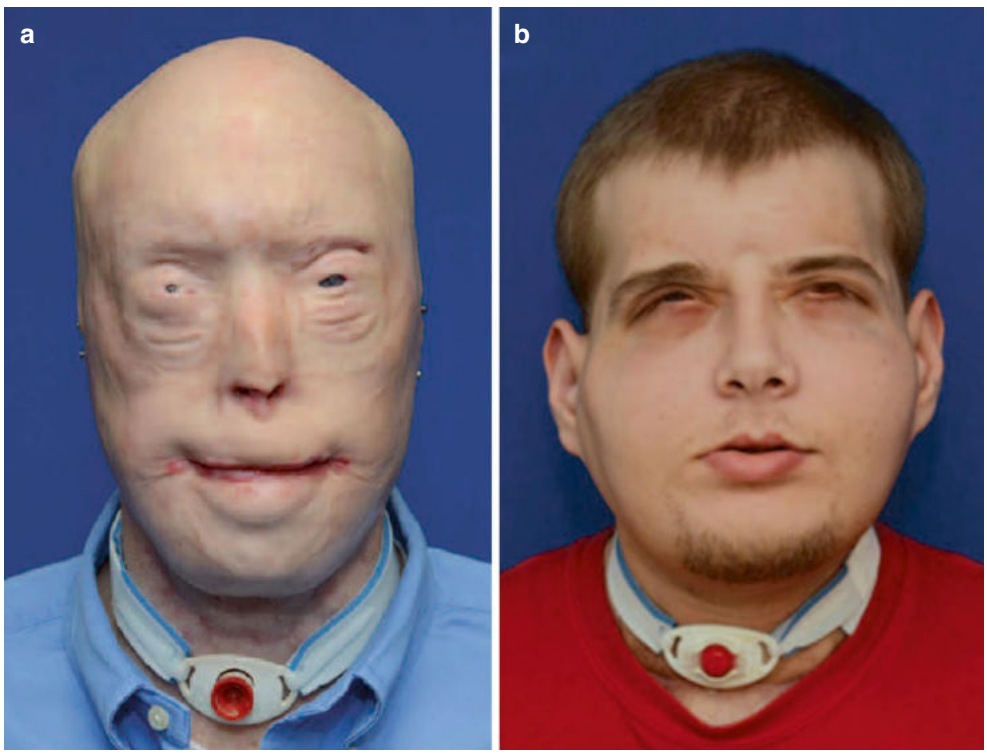


Fig. 3 Preoperative and postoperative images of a 41-year-old man who sustained severe facial burns and received a total face, scalp, eyelid, and ear transplantation: (**a**) frontal view preoperative and (**b**) frontal view postoperative. (Printed with permission from and copyrights retained by E.D.R.)

The second case involves a 41-year-old firefighter who sustained severe facial burns and underwent numerous reconstructive procedures before ultimately receiving a total face, scalp, eyelid, and ear transplantation (Fig. 3). Preoperative planning involved the use of 3D craniofacial CT and angiographic data, which were uploaded into modeling software to design osteotomies. Customized, prefabricated cutting guides were used to ensure precise bone resections (Fig. 4). During the surgery, ICG angiography was used to confirm graft perfusion, and postoperative CT confirmed that surgical outcomes closely followed the VSP plan.

In another case, a 25-year-old man with a history of ballistic injury underwent partial face and double jaw transplantation (Fig. 5). Preoperative 3D CT and angiographic data

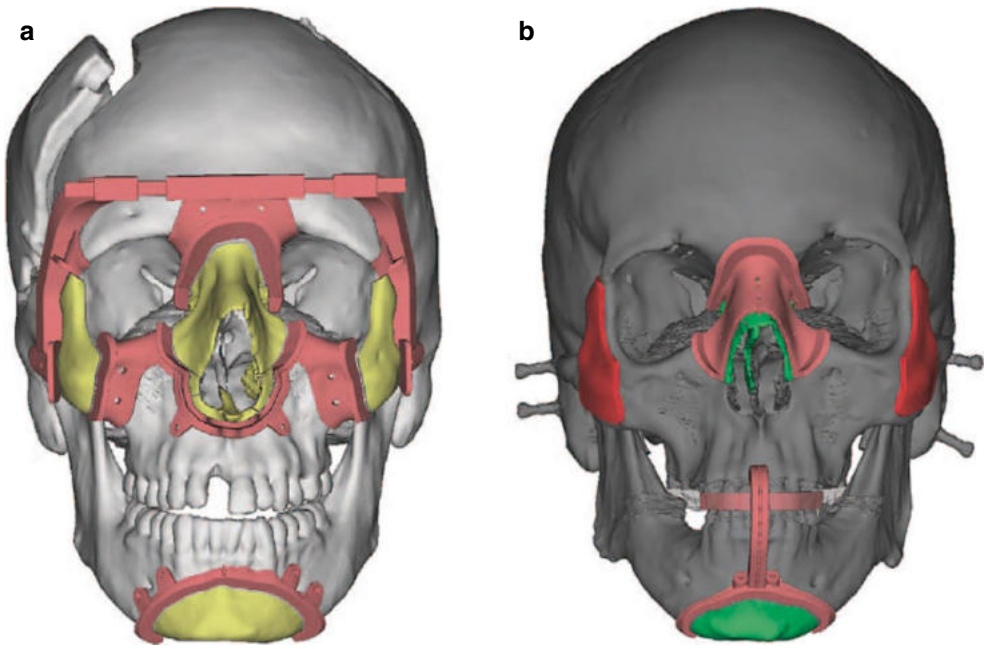


Fig. 4 Customized, prefabricated cutting guides were used to ensure precise bone resections: (**a**) donor CT with planned osteotomies of skeletal subunits (yellow) and customized cutting guides (pink) and (**b**) recipient CT with planned osteotomies of skeletal subunits to be removed (green) and customized cutting guides (pink). (Printed with permission from and copyrights retained by E.D.R.)

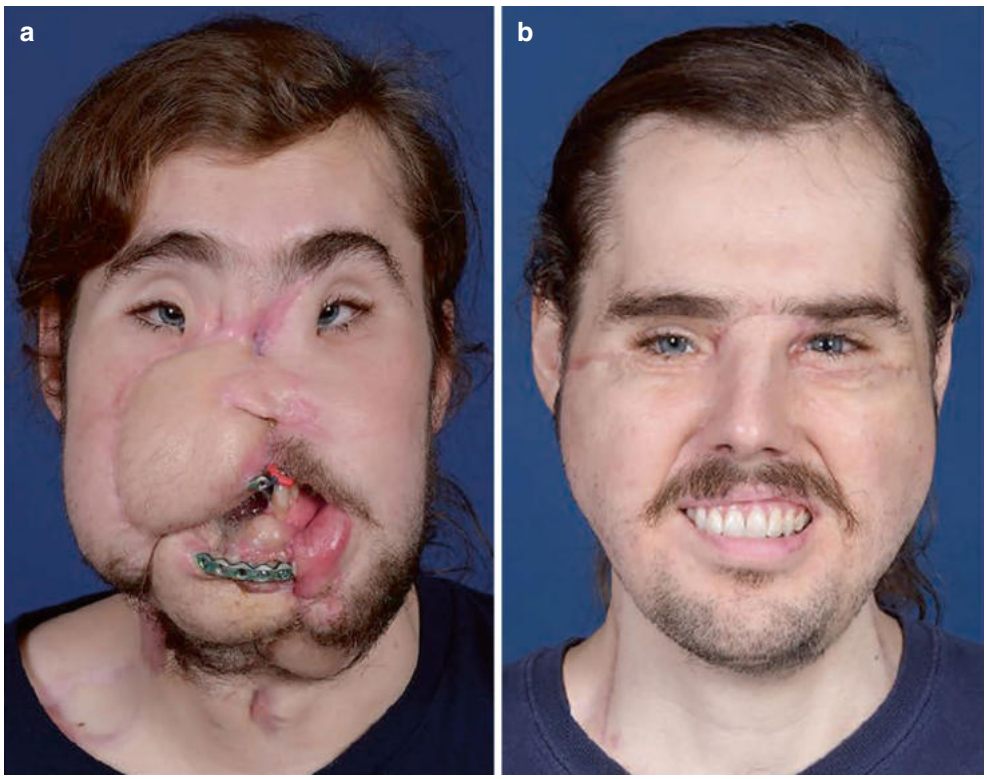


Fig. 5 Preoperative and postoperative images of a 25-year-old man with a history of ballistic injury who underwent partial face and double jaw transplantation: (**a**) frontal view preoperative and (**b**) frontal view postoperative. (Printed with permission from and copyrights retained by E.D.R.)

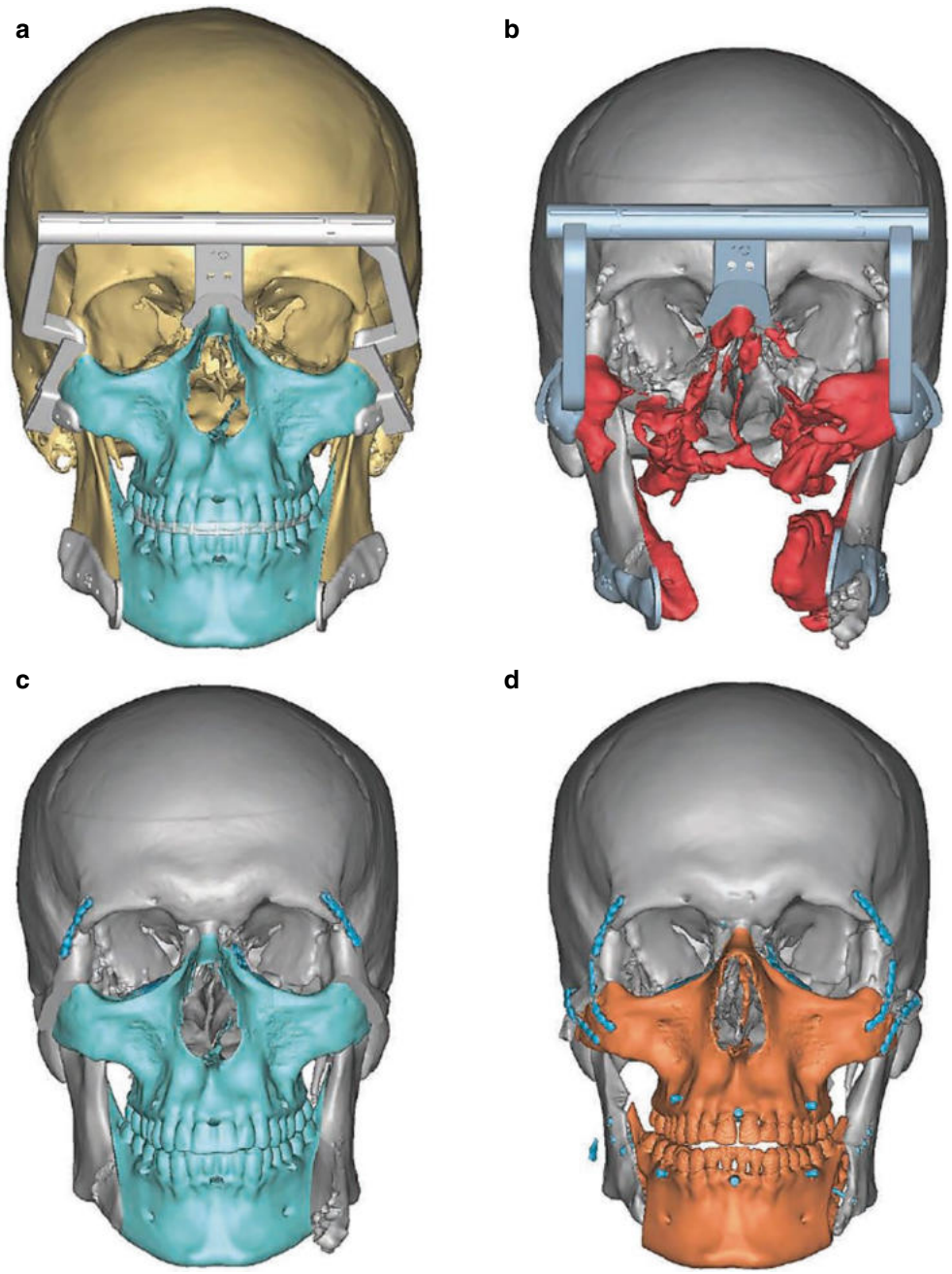


Fig. 6 Customized, prefabricated cutting guides were used to ensure precise bone resections. (**a**) Donor-specific customized cutting guides (silver) for osteotomies of skeletal segments (blue). (**b**) Recipient-specific customized cutting guides (silver) for removal of recipient skeletal segments (red). (**c**) Superimposition of donor skeletal segments (blue) onto planned recipient skeletal defect. (**d**) Postoperative CT of recipient with donor skeletal segments represented in orange. (Printed with permission from and copyrights retained by E.D.R.)

were used to create both donor and recipient cutting guides. Intraoperatively, bilateral mandibular sagittal split and LeFort III osteotomies were performed using these guides, while stereolithographic models and prefabricated dental splints ensured accurate maxillary and mandibular alignment (Fig. 6). Real-time intraoperative surgical navigation was used to confirm accurate allograft skeletal inset (Fig. 7). ICG angiography confirmed graft perfusion, and intraoperative CT was used to confirm allograft placement. Postoperative CT analysis confirmed near-perfect alignment with the VSP plan, although minor occlusal adjustments were necessary in subsequent revision surgeries.

One notable case involves a highly complex case involving a 21-year-old man who sustained burns over 80% of his

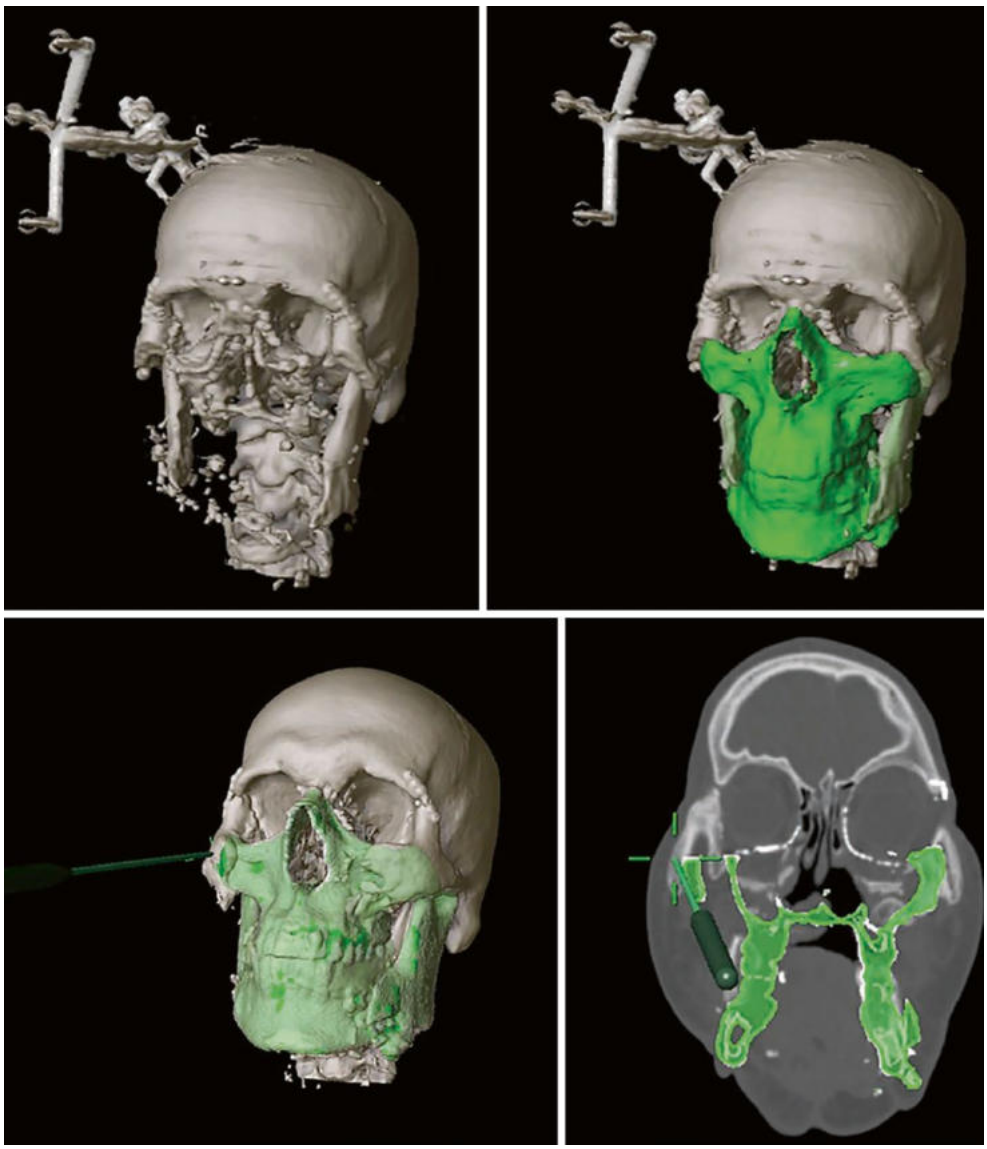


Fig. 7 Real-time intraoperative surgical navigation is utilized to confirm accurate allograft skeletal inset. Green represents the virtual surgical plan, which was compared to actual positioning of skeletal segments. Intraoperative surgical navigation was facilitated by registration device (top images), and accuracy was verified with intraoperative CT (bottom right image). (Printed with permission from and copyrights retained by E.D.R.)

body, including the face. The patient underwent the first combined face and bilateral hand transplantation (Figs. 8 and 9). Preoperative planning involved 3D craniofacial and bilateral upper extremity CT scans, which were used to create customized cutting guides and donor prosthetics to maintain integrity post-procurement. Intraoperative use of 3D-printed tags for anatomical labeling and splints for tendon repair aided in the complex procedure. Additionally, 3D-printed face mask and bilateral upper extremity prosthetics were created to maintain donor integrity after allograft procurement (Fig. 10). Post-surgical imaging confirmed that the actual outcomes closely matched the preoperative VSP, validating the accuracy of the technology even in cases of unprecedented complexity (Fig. 11).

Finally, the first combined face and whole eye transplant was performed in a 46-year-old man who suffered a high-

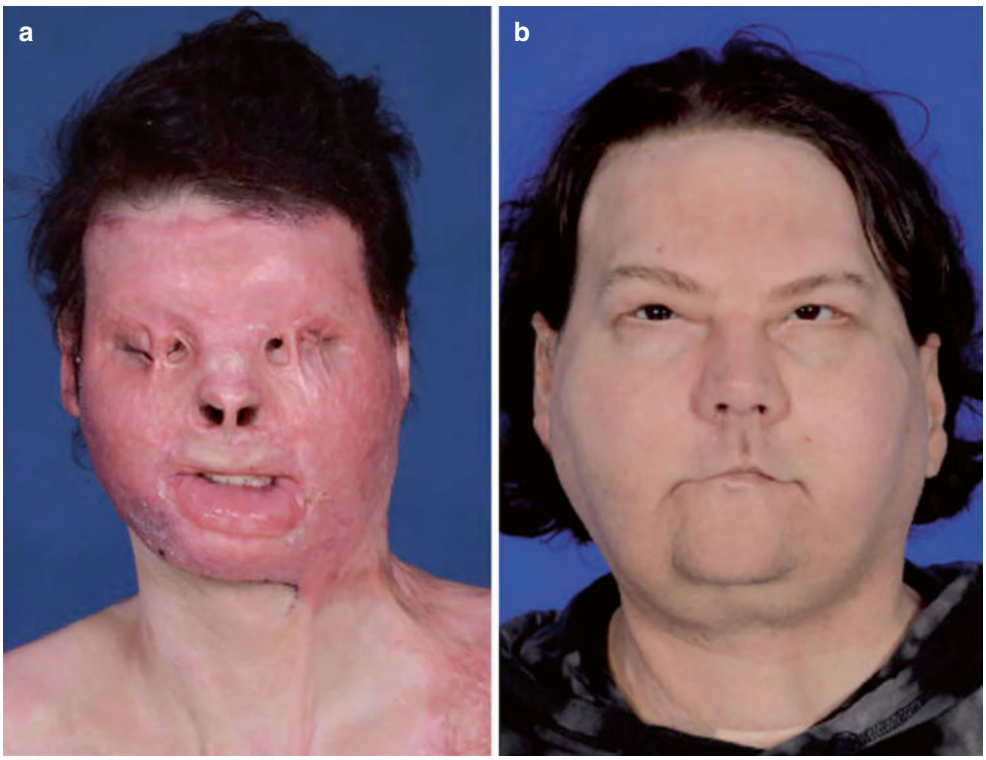


Fig. 8 Preoperative and postoperative images of a 21-year-old man who sustained burns over 80% of his body, including the face, and underwent the first combined face and bilateral hand transplantation: (**a**) frontal view preoperative and (**b**) frontal view postoperative. (Printed with permission from and copyrights retained by E.D.R.)



Fig. 9 Preoperative and postoperative images of the bilateral upper extremities: (**a**) volar view of preoperative left upper extremity, (**b**) volar view of preoperative right upper extremity, (**c**) volar view of postoperative left upper extremity, and (**d**) volar view of postoperative right upper extremity. (Printed with permission from and copyrights retained by E.D.R.)

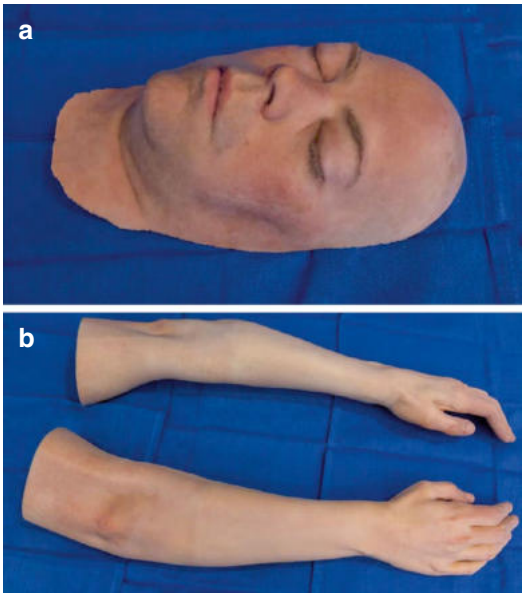


Fig. 10 High-fidelity 3D-printed face mask (**a**) and bilateral upper extremities prostheses (**b**) to maintain donor integrity after allograft procurement. (Printed with permission from and copyrights retained by E.D.R.)

voltage electrical injury, resulting in extensive facial tissue loss, including his left eye, nose, and lips (Fig. 12). VSP played a critical role in the preoperative phase by providing detailed 3D models based on CT imaging, which allowed the surgical team to meticulously plan the alignment of the facial skeleton and design customized cutting guides (Fig. 13). This facilitated the precise removal and transplantation of donor bone and soft tissue, ensuring a seamless fit between donor and recipient structures. The cutting guides also played a crucial role in allowing safe dissection of ocular structures and guiding optic nerve coaptation. In addition to guiding osteotomies, VSP enabled vascular mapping via angiography which was essential for the novel approach of connecting the donor ophthalmic artery to the superficial temporal artery to allow the face and eye allograft to be perfused via the donor external carotid system alone. Postoperative angiography confirmed retinal and choroidal perfusion, although vision was not restored. The case demonstrated the potential of VSP in managing the complexities of combined face and whole eye transplantation, particularly in addressing vascular and skeletal challenges [19].

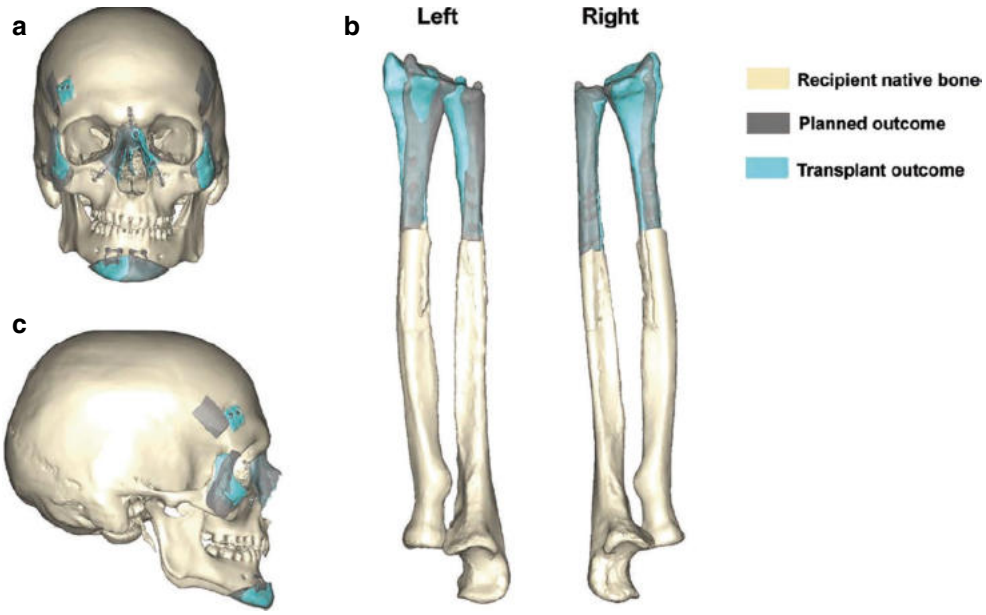


Fig. 11 Virtual surgical plan (VSP) compared to postoperative outcomes. (**a**) Frontal facial view of VSP compared to actual results, (**b**) lateral facial view of VSP compared to actual results, (**c**) VSP of bilateral upper extremities compared to actual results. (Printed with permission from and copyrights retained by E.D.R.)

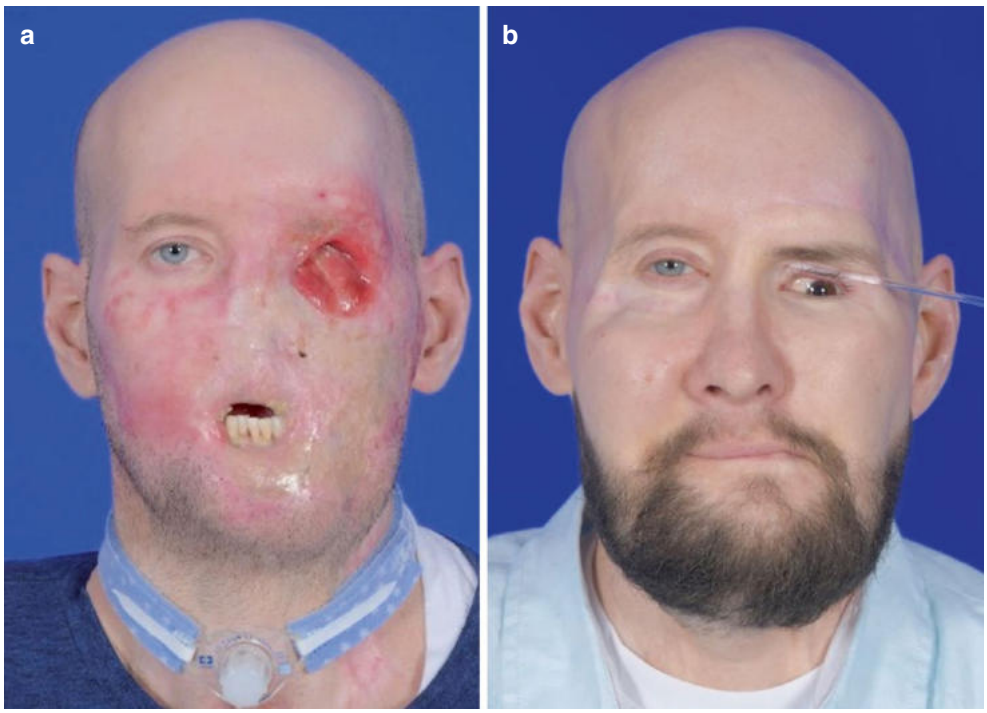


Fig. 12 Preoperative and postoperative images of a 46-year-old man who suffered a high-voltage electrical injury, resulting in extensive facial tissue loss, including his left eye, nose, and lips, who ultimately underwent the first partial face and whole eye transplantation: (**a**) frontal view preoperative and (**b**) frontal view postoperative. (Printed with permission from and copyrights retained by E.D.R.)

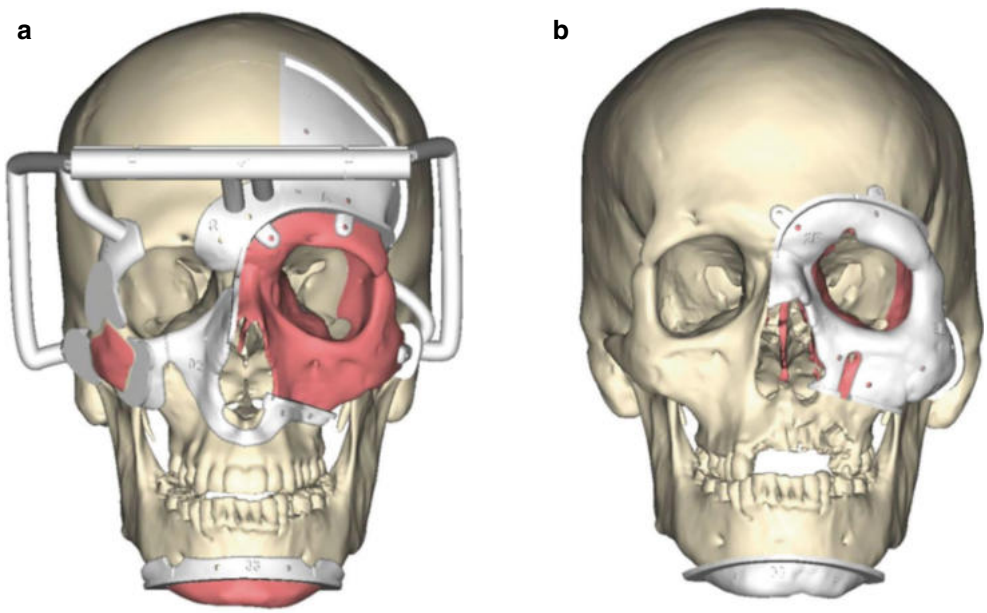


Fig. 13 Virtual surgical plan of donor and recipient osteomotomies. (**a**) 3D-printed donor-specific cutting guides were developed to harvest donor bone and soft tissue from the left orbit, zygomas, and mandible (highlighted in red). (**b**) Recipient-specific cuttings were similarly created to remove bone (in red) to allow snap fit reconstruction of transplanted bone. These guides ensure safe dissection of ocular structures and allow for highly accurate allograft placement and fixation in the recipient. (Printed with permission from and copyrights retained by E.D.R.)

5 Evolution of Virtual Surgical Planning in Face Transplantation

Since its inception, VSP has evolved significantly and is now a cornerstone of the face transplantation process. Early cases of face transplantation relied on rudimentary techniques such as physical models and cadaveric rehearsals to plan complex osteotomies and graft alignment. The first successful face transplant in 2005 utilized MRI and CT scans, along with a rigid metallic pattern created to match the recipient's anatomy to the donor graft [20, 21]. In 2008, when the first US face transplant was performed, the use of stereolithographic models based on CT data allowed for greater precision in graft harvesting and inset, though cadaveric rehearsals were still essential [5, 22].

By the time more recent cases were performed, such as those described above, the use of cutting-edge VSP technologies had dramatically reduced the need for cadaveric rehearsals and significantly increased the precision of surgical planning. The development of patient-specific cutting guides, combined with the use of real-time intraoperative navigation and ICG angiography, has allowed face transplantation to reach new levels of accuracy and efficiency. Notably, cadaveric rehearsals, which were essential in early face transplants, have decreased significantly with the advent of reliable VSP, further underscoring the technology's role in the evolution of this field.

6 Limitations of Virtual Surgical Planning

Despite the many advantages of VSP, there are still limitations to its use. One of the primary challenges is that VSP cannot completely replace clinical judgment. Intraoperative variables such as scar tissue, tissue quality, and dissection planes may still require adjustments to the original plan. Additionally, VSP is resource-intensive, requiring sophisticated software, advanced imaging modalities, and a multidisciplinary team to execute each step of the process effectively. The costs associated with the hardware and software required for VSP must be weighed against the potential benefits, though improved surgical outcomes often justify the investment.

7 Conclusions

Face transplantation offers an unparalleled opportunity to restore both function and aesthetic appearance in patients with devastating facial injuries, and VSP has proven to be an invaluable tool in facilitating these complex procedures. By enabling detailed preoperative planning, precise intraoperative navigation, and thorough postoperative assessment, VSP helps ensure that each transplantation is executed with the highest degree of accuracy possible. As face transplantation continues to evolve, VSP will undoubtedly remain a vital component of this innovative field, supporting surgeons in delivering improved outcomes and enhancing patients' quality of life.

References

1. Rifkin WJ, David JA, Plana NM, Kantar RS, Diaz-Siso JR, Gelb BE, et al. Achievements and challenges in facial transplantation. Ann Surg. 2018;268(2):260–70.
2. Ramly EP, Kantar RS, Diaz-Siso JR, Alfonso AR, Rodriguez ED. Computerized approach to facial transplantation: evolution and application in 3 consecutive face transplants. Plast Reconstr Surg Glob Open. 2019;7(8):e2379.
3. Vyas K, Bakri K, Gibreel W, Cotofana S, Amer H, Mardini S. Facial transplantation. Facial Plast Surg Clin North Am. 2022;30(2):255–69.
4. Coffman KL, Gordon C, Siemionow M. Psychological outcomes with face transplantation: overview and case report. Curr Opin Organ Transplant. 2010;15(2):236–40.
5. Siemionow MZ, Papay F, Djohan R, Bernard S, Gordon CR, Alam D, et al. First U.S. near-total human face transplantation: a paradigm shift for massive complex injuries. Plast Reconstr Surg. 2010;125(1):111–22.
6. Mohan R, Borsuk DE, Dorafshar AH, Wang HD, Bojovic B, Christy MR, et al. Aesthetic and functional facial transplantation: a classification system and treatment algorithm. Plast Reconstr Surg. 2014;133(2):386–97.
7. Lantieri L, Grimbert P, Ortonne N, Suberbielle C, Bories D, Gil-Vernet S, et al. Face transplant: long-term follow-up and results of a prospective open study. Lancet. 2016;388(10052):1398–407.
8. Dorafshar AH, Brazio PS, Mundinger GS, Mohan R, Brown EN, Rodriguez ED. Found in space: computer-assisted orthognathic alignment of a total face allograft in six degrees of freedom. J Oral Maxillofac Surg. 2014;72(9):1788–800.
9. Dorafshar AH, Bojovic B, Christy MR, Borsuk DE, Iliff NT, Brown EN, et al. Total face, double jaw, and tongue transplantation: an evolutionary concept. Plast Reconstr Surg. 2013;131(2):241–51.
10. Sosin M, Ceradini DJ, Levine JP, Hazen A, Staffenberg DA, Saadeh PB, et al. Total face, eyelids, ears, scalp, and skeletal subunit transplant: a reconstructive solution for the full face and total scalp burn. Plast Reconstr Surg. 2016;138(1):205–19.
11. Kollar B, Pomahac B. Facial restoration by transplantation. Surgeon. 2018;16(4):245–9.
12. Suchyta M, Mardini S. Innovations and future directions in head and neck microsurgical reconstruction. Clin Plast Surg. 2020;47(4):573–93.
13. Rodby KA, Turin S, Jacobs RJ, Cruz JF, Hassid VJ, Kolokythas A, et al. Advances in oncologic head and neck reconstruction: systematic review and future considerations of virtual surgical planning and computer aided design/computer aided modeling. J Plast Reconstr Aesthet Surg. 2014;67(9):1171–85.
14. Bly RA, Chang SH, Cudejkova M, Liu JJ, Moe KS. Computer-guided orbital reconstruction to improve outcomes. JAMA Facial Plast Surg. 2013;15(2):113–20.
15. Foley BD, Thayer WP, Honeybrook A, McKenna S, Press S. Mandibular reconstruction using computer-aided design and computer-aided manufacturing: an analysis of surgical results. J Oral Maxillofac Surg. 2013;71(2):e111–9.
16. Hierl T, Arnold S, Kruber D, Schulze FP, Hümpfner-Hierl H. CAD-CAM-assisted esthetic facial surgery. J Oral Maxillofac Surg. 2013;71(1):e15–23.

17. Kantar RS, Rifkin WJ, Diaz-Siso JR, Bernstein GL, Rodriguez ED. Quality improvement in facial transplantation: standard approach for novel procedures. Plast Reconstr Surg Glob Open. 2018;6(1):e1653.
18. Shah A, Chinta S, Rodriguez ED. Computerized surgical planning in face transplantation. Semin Plast Surg. 2024; s-0044-1786991
19. Ceradini DJ, Tran DL, Dedania VS, Gelb BE, Cohen OD, Flores RL, et al. Combined whole eye and face transplant: microsurgical strategy and 1-year clinical course. JAMA [Internet]. 2024; [cited 2024 Oct 23]; Available from: https://jamanetwork.com/journals/jama/fullarticle/2823414
20. Devauchelle B, Badet L, Lengelé B, Morelon E, Testelin S, Michallet M, et al. First human face allograft: early report. Lancet. 2006;368(9531):203–9.
21. Guntinas-Lichius O. Outcomes 18 months after the first human partial face transplantation. N Engl J Med. 2008;358(20):2179–80. author reply 2180
22. Siemionow M, Papay F, Alam D, Bernard S, Djohan R, Gordon C, et al. Near-total human face transplantation for a severely disfigured patient in the USA. Lancet. 2009;374(9685):203–9.

Conclusive Remarks

Medical 3D Printing: A Fruitful and Impactful Field for Collaboration and Interdisciplinarity

Giovanni Biglino, Karen Eich Hammer, Carina Hopfner, Francesco Moscato, Marina Nagel, Gunpreet Coudert Oberoi, Arnau Valls-Esteve, and Alessandro Tel

In the on-going movement toward developing a personalised approach to medicine, the availability and continuous refinement of patient-specific three-dimensional (3D) models manufactured by means of rapid prototyping (3D printing) technology represent the embodiment of this vision, when personalised unique models are used from surgical planning to customisation of implants. As schematically summarised (Fig. 1), imaging and image-based modelling are a key dimension of personalised medicine, and advances in imaging and radiology concurrent with the advent of 3D printing technology have enabled a whole field to flourish. Today, medical 3D printing and 3D medical tools (which we can indicate for brevity as 3D+, incorporating digital applications of 3D modelling such as virtual and mixed reality) and their integration with other technologies such as Artificial Intelligence have evolved from the research and academic domains to, increasingly, a true point-of-care (POC) practice, whereby models are used in a clinic, by the bedside or even in a patient's home, i.e. those settings where care is delivered.

The advancement of this field requires dialogue, research, and collaboration across multiple dimensions, from the technology itself to clinical implementation via industry. In this spirit, the European 3D in Hospitals Special Interest Group (EU3DSIG) was founded in 2022 to promote excellence in healthcare outcomes, education, research, and innovation using 3D technologies [1]. The dimensions in which the EU3DSIG intends to operate well summarise those areas that today need attention in order to continue progressing this field, and they are:

1. Fostering and curating communication channels among researchers, clinicians, and industry to create an inclusive space for knowledge sharing and collaboration
2. Collecting evidence and generating awareness around the impact of 3D technologies in POC applications, encom-

G. Biglino
Bristol Medical School, University of Bristol, Bristol, UK
e-mail: g.biglino@bristol.ac.uk

K. E. Hammer
AUH Innovation & International Affairs, Aarhus University Hospital, Aarhus, Denmark
e-mail: KAEHAM@rm.dk

C. Hopfner · M. Nagel
Department of Pediatric Cardiology & Pediatric Intensive Care Medicine, LMU Klinikum, Munich, Germany
e-mail: Carina.Hopfner@med.uni-muenchen.de; Nagel.Marina@med.uni-muenchen.de

F. Moscato
Center for Medical Physics and Biomedical Engineering, Medical University of Vienna, Vienna, Austria

Ludwig Boltzmann Institute for Cardiovascular Research, Vienna, Austria

Austrian Cluster for Tissue Regeneration, Vienna, Austria
e-mail: francesco.moscato@meduniwien.ac.at

G. C. Oberoi
Center for Medical Physics and Biomedical Engineering, Medical University of Vienna, Vienna, Austria

Austrian Center for Medical Innovation and Technology (ACMIT Gmbh), Wiener Neustadt, Austria
e-mail: gunpreet.oberoi@meduniwien.ac.at

A. Valls-Esteve
3D Unit (3D4H), Hospital Sant Joan de Déu, Esplugues de Llobregat, Spain

Innovation Department, Hospital Sant Joan de Déu, Esplugues de Llobregat, Spain
e-mail: arnau.valls@sjd.es

A. Tel (✉)
Lead Specialist for VSP and 3DP, Maxillofacial Surgery Clinic, Head & Neck and Neuroscience Department, Academic Hospital of Udine, Udine, Italy
e-mail: alessandro.tel@uniud.it

© The Author(s), under exclusive license to Springer Nature Switzerland AG 2025

A. Tel, M. Robiony (eds.), *Atlas of Virtual Surgical Planning and 3D Printing for Cranio-Maxillo-Facial Surgery*,
https://doi.org/10.1007/978-3-031-94495-6_27

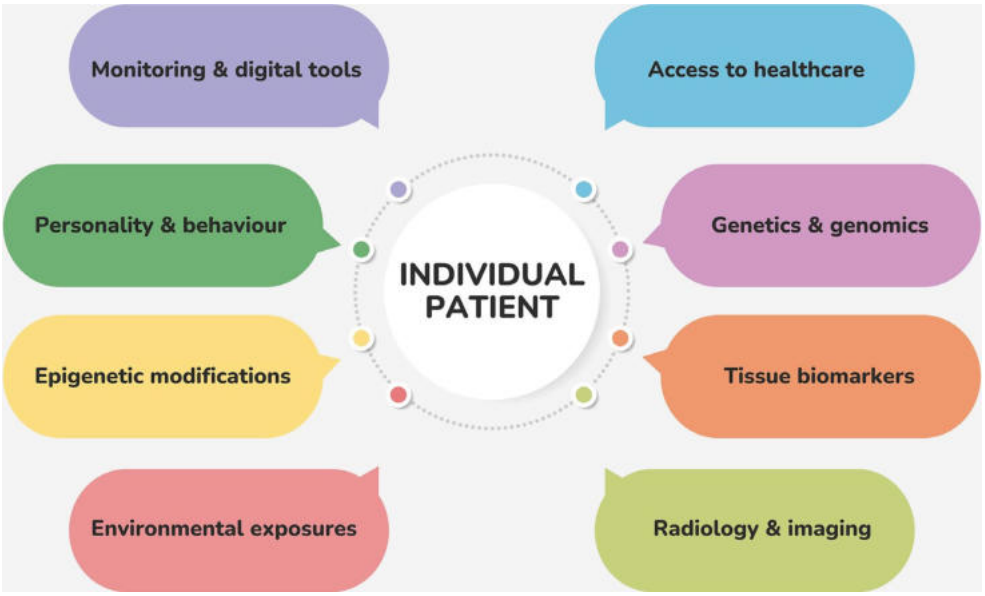


Fig. 1 A graphical representation of different domains whose integration can lead to personalised approaches in medicine, as modified from [4]

passing views from all stakeholders and across the relevant domains (academic, clinical, industry, public)
3. Advancing and innovating training and educational programs in 3D technologies and provide resources to support continuous learning
4. Coordinating work around regulation thereby providing a clear link between the policy space and the practitioners and users in this field, ensuring that the advancement and implementation of the technology are ethical, inclusive, and sustainable

As the field evolves, and as this community intends to evolve from a special interest group into a scientific society in 2025, two pillars that remain clearly and solidly at the centre of this research and clinical endeavour are collaboration and interdisciplinarity. This field brings together a breath of expertise and voices—from surgery to bioengineering, from medical education to patient experience—and it is this dialogue that makes it so exciting and valuable. However, collaboration can be a fragile and delicately precious process and caring for it starts with the recognition of its inevitability in order for progress to occur. Coming together across disciplines, finding time and space to reflect, and championing openness and inclusivity are essential for collaboration to be practiced authentically, and the field of 3D personalised medicine can be a real model for such collaborative practices. By the same token, complex problems require multiple disciplinary work. "Multiple disciplinary" has been suggested [2] as a more general term for multi-, inter-, and trans-disciplinary practices. While the latter are not interchangeable terms and they have specific additive, interactive, and holistic features, respectively, we can argue that all three domains are relevant in the space of 3D personalised medicine.

As applications of 3D modelling and printing grow across all medical applications, from paediatric cardiology to oncology to novel systems of drug delivery, maxillofacial surgery certainly represents a field where major advances have been achieved, important evidence has been documented, and innovative approaches have been pioneered, becoming one of the major surgical specialties leading the adoption of this technologies. For instance, the complementary benefits of rapid prototyping and virtual reality for surgical planning and in dealing with complex anatomical structures have been discussed early on in this area [3]. Today, this first atlas in maxillofacial applications beautifully and appropriately represents another milestone for the whole field.

References

1. Biglino G, Hopfner C, Lindhardt J, Moscato F, Munuera J, Oberoi G, Tel A, Esteve AV. Perspectives on medical 3D printing at the point-of-care from the new European 3D Printing Special Interest Group. 3D Print Med. 2023;9:14.
2. Choi and Pak. Multidisciplinarity, interdisciplinarity, and transdisciplinarity in health research, services, education and policy: 2. Promotors, barriers, and strategies of enhancement. Clin Invest Med. 2007;30(6):E224–32.
3. Robiony, et al. Virtual reality surgical planning for maxillofacial distraction osteogenesis: the role of reverse engineering rapid prototyping and cooperative work. J Oral Maxillofac Surg. 2007;65(6):1198–208.
4. Goetz LH, Schork NJ. Personalized medicine: motivation, challenges, and progress. Fertil Steril. 2018;109(6):952–63.